



International Journal of
Molecular Sciences

Special Issue Reprint

Functional Nanomaterials for Healthcare

Edited by
Monica Terracciano, Ilaria Rea, Nicola Borbone and Chiara Tramontano

mdpi.com/journal/ijms



Functional Nanomaterials for Healthcare

Functional Nanomaterials for Healthcare

Editors

Monica Terracciano

Ilaria Rea

Nicola Borbone

Chiara Tramontano



Basel • Beijing • Wuhan • Barcelona • Belgrade • Novi Sad • Cluj • Manchester

Editors

Monica Terracciano

Department of Pharmacy

University of Naples Federico II

Naples

Italy

Ilaria Rea

Institute of Applied Sciences

and Intelligent Systems

National Research Council

Naples

Italy

Nicola Borbone

Department of Pharmacy

University of Naples Federico II

Naples

Italy

Chiara Tramontano

Nanomaterials for Biomedical

Applications

Istituto Italiano di Tecnologia

Genoa

Italy

Editorial Office

MDPI

St. Alban-Anlage 66

4052 Basel, Switzerland

This is a reprint of articles from the Special Issue published online in the open access journal *International Journal of Molecular Sciences* (ISSN 1422-0067) (available at: www.mdpi.com/journal/ijms/special_issues/nanomaterials_healthcare).

For citation purposes, cite each article independently as indicated on the article page online and as indicated below:

Lastname, A.A.; Lastname, B.B. Article Title. <i>Journal Name</i> Year , Volume Number, Page Range.
--

ISBN 978-3-0365-9103-2 (Hbk)

ISBN 978-3-0365-9102-5 (PDF)

doi.org/10.3390/books978-3-0365-9102-5

© 2023 by the authors. Articles in this book are Open Access and distributed under the Creative Commons Attribution (CC BY) license. The book as a whole is distributed by MDPI under the terms and conditions of the Creative Commons Attribution-NonCommercial-NoDerivs (CC BY-NC-ND) license.

Contents

About the Editors	ix
Preface	xi
Monica Terracciano, Simas Račkauskas, Andrea Patrizia Falanga, Sara Martino, Giovanna Chianese and Francesca Greco et al. ZnO Tetrapods for Label-Free Optical Biosensing: Physicochemical Characterization and Functionalization Strategies Reprinted from: <i>Int. J. Mol. Sci.</i> 2023 , <i>24</i> , 4449, doi:10.3390/ijms24054449	1
Anna Król-Górniak, Katarzyna Rafińska, Fernanda Monedeiro, Paweł Pomastowski and Bogusław Buszewski Comparison Study of Cytotoxicity of Bare and Functionalized Zinc Oxide Nanoparticles Reprinted from: <i>Int. J. Mol. Sci.</i> 2021 , <i>22</i> , 9529, doi:10.3390/ijms22179529	16
Nika Kučuk, Mateja Primožič, Željko Knez and Maja Leitgeb Sustainable Biodegradable Biopolymer-Based Nanoparticles for Healthcare Applications Reprinted from: <i>Int. J. Mol. Sci.</i> 2023 , <i>24</i> , 3188, doi:10.3390/ijms24043188	33
Lukas Heuberger, Maria Korphidou, Olivia M. Eggenberger, Myrto Kyropoulou and Cornelia G. Palivan Current Perspectives on Synthetic Compartments for Biomedical Applications Reprinted from: <i>Int. J. Mol. Sci.</i> 2022 , <i>23</i> , 5718, doi:10.3390/ijms23105718	78
Muhammad Qasim, Andrew N. Clarkson and Simon F. R. Hinkley Green Synthesis of Carbon Nanoparticles (CNPs) from Biomass for Biomedical Applications Reprinted from: <i>Int. J. Mol. Sci.</i> 2023 , <i>24</i> , 1023, doi:10.3390/ijms24021023	109
Mahsa Mirzaei, Irini Furxhi, Finbarr Murphy and Martin Mullins Employing Supervised Algorithms for the Prediction of Nanomaterial's Antioxidant Efficiency Reprinted from: <i>Int. J. Mol. Sci.</i> 2023 , <i>24</i> , 2792, doi:10.3390/ijms24032792	132
Matteo Gasparotto, Pietro Bellet, Giorgia Scapin, Rebecca Busetto, Chiara Rampazzo and Libero Vitiello et al. 3D Printed Graphene-PLA Scaffolds Promote Cell Alignment and Differentiation Reprinted from: <i>Int. J. Mol. Sci.</i> 2022 , <i>23</i> , 1736, doi:10.3390/ijms23031736	145
Aida Şelaru, Hildegard Herman, George Mihail Vlăsceanu, Sorina Dinescu, Sami Gharbia and Cornel Baltă et al. Graphene–Oxide Porous Biopolymer Hybrids Enhance In Vitro Osteogenic Differentiation and Promote Ectopic Osteogenesis In Vivo Reprinted from: <i>Int. J. Mol. Sci.</i> 2022 , <i>23</i> , 491, doi:10.3390/ijms23010491	160
Yuting Li, Yufei Wang, Hong Shang and Jing Wu Graphene Quantum Dots Modified Upconversion Nanoparticles for Photodynamic Therapy Reprinted from: <i>Int. J. Mol. Sci.</i> 2022 , <i>23</i> , 12558, doi:10.3390/ijms232012558	186
Karolina Krajewska, Anna M. Gołkowska, Maciej Nowak, Marta Kozakiewicz-Latała, Wojciech Pudło and Andrzej Żak et al. Molecular Level Characterisation of the Surface of Carbohydrate-Functionalised <i>Mesoporous silica</i> Nanoparticles (MSN) as a Potential Targeted Drug Delivery System via High Resolution Magic Angle Spinning (HR-MAS) NMR Spectroscopy Reprinted from: <i>Int. J. Mol. Sci.</i> 2022 , <i>23</i> , 5906, doi:10.3390/ijms23115906	195

Mengwen Guo, Junhong Ling, Xinyi Xu and Xiaokun Ouyang Delivery of Doxorubicin by Ferric Ion-Modified Mesoporous Polydopamine Nanoparticles and Anticancer Activity against HCT-116 Cells In Vitro Reprinted from: <i>Int. J. Mol. Sci.</i> 2023 , <i>24</i> , 6854, doi:10.3390/ijms24076854	209
Diana Gabriela Valencia-Reséndiz, Atenea Villegas, Daniel Bahena, Kenia Palomino, Jose Manuel Cornejo-Bravo and Liliana Quintanar et al. Non-Functionalized Gold Nanoparticles Inhibit Human Papillomavirus (HPV) Infection Reprinted from: <i>Int. J. Mol. Sci.</i> 2022 , <i>23</i> , 7552, doi:10.3390/ijms23147552	226
Satish Kumar Vemuri, Satyajit Halder, Rajkiran Reddy Banala, Hari Krishnreddy Rachamalla, Vijaya Madhuri Devraj and Chandra Shekar Mallarpu et al. Modulatory Effects of Biosynthesized Gold Nanoparticles Conjugated with Curcumin and Paclitaxel on Tumorigenesis and Metastatic Pathways—In Vitro and In Vivo Studies Reprinted from: <i>Int. J. Mol. Sci.</i> 2022 , <i>23</i> , 2150, doi:10.3390/ijms23042150	237
Olakunle Oladimeji, Jude Akinyelu, Aliscia Daniels and Moganavelli Singh Modified Gold Nanoparticles for Efficient Delivery of Betulinic Acid to Cancer Cell Mitochondria Reprinted from: <i>Int. J. Mol. Sci.</i> 2021 , <i>22</i> , 5072, doi:10.3390/ijms22105072	256
Nathalie M. Malewicz, Zahra Rattray, Sebastian Oeck, Sebastian Jung, Vicente Escamilla-Rivera and Zeming Chen et al. Topical Capsaicin in Poly(lactic-co-glycolic)acid (PLGA) Nanoparticles Decreases Acute Itch and Heat Pain Reprinted from: <i>Int. J. Mol. Sci.</i> 2022 , <i>23</i> , 5275, doi:10.3390/ijms23095275	280
Nura A. Mohamed, Isra Marei, Sergio Crovella and Haissam Abou-Saleh Recent Developments in Nanomaterials-Based Drug Delivery and Upgrading Treatment of Cardiovascular Diseases Reprinted from: <i>Int. J. Mol. Sci.</i> 2022 , <i>23</i> , 1404, doi:10.3390/ijms23031404	299
Haseeb A. Khan, Uday Kishore, Hamed M. Alsulami and Salman H. Alrokayan Pro-Apoptotic and Immunotherapeutic Effects of Carbon Nanotubes Functionalized with Recombinant Human Surfactant Protein D on Leukemic Cells Reprinted from: <i>Int. J. Mol. Sci.</i> 2021 , <i>22</i> , 10445, doi:10.3390/ijms221910445	319
Mohamed K. Abdel-Rafei, Noura M. Thabet, M. I. A. Abdel Maksoud, M. Abd Elkodous, Go Kawamura and Atsunori Matsuda et al. Influence of Ce ³⁺ Substitution on Antimicrobial and Antibiofilm Properties of ZnCe _x Fe _{2-x} O ₄ Nanoparticles (X = 0.0, 0.02, 0.04, 0.06, and 0.08) Conjugated with Ebselen and Its Role Subsidised with γ -Radiation in Mitigating Human TNBC and Colorectal Adenocarcinoma Proliferation In Vitro Reprinted from: <i>Int. J. Mol. Sci.</i> 2021 , <i>22</i> , 10171, doi:10.3390/ijms221810171	334
Litty Johnson, Lorenz Aglas, Wai Tuck Soh, Mark Geppert, Sabine Hofer and Norbert Hofstätter et al. Structural Alterations of Antigens at the Material Interface: An Early Decision Toolbox Facilitating Safe-by-Design Nanovaccine Development Reprinted from: <i>Int. J. Mol. Sci.</i> 2021 , <i>22</i> , 10895, doi:10.3390/ijms221910895	374
Hyo-Dong Sung, Nayeon Kim, Yeram Lee and Eun Jung Lee Protein-Based Nanoparticle Vaccines for SARS-CoV-2 Reprinted from: <i>Int. J. Mol. Sci.</i> 2021 , <i>22</i> , 13445, doi:10.3390/ijms222413445	390

Eduard V. Karamov, Viktor F. Larichev, Galina V. Kornilaeva, Irina T. Fedyakina, Ali S. Turgiev and Andrey V. Shibaev et al. Cationic Surfactants as Disinfectants against SARS-CoV-2 Reprinted from: <i>Int. J. Mol. Sci.</i> 2022 , 23, 6645, doi:10.3390/ijms23126645	400
Andrea-Sarahí Balderrama-González, Hilda-Amelia Piñón-Castillo, Claudia-Adriana Ramírez-Valdespino, Linda-Lucila Landeros-Martínez, Erasmo Orrantia-Borunda and Hilda-Esperanza Esparza-Ponce Antimicrobial Resistance and Inorganic Nanoparticles Reprinted from: <i>Int. J. Mol. Sci.</i> 2021 , 22, 12890, doi:10.3390/ijms222312890	412
Guillem Ferreres, Sílvia Pérez-Rafael, Juan Torrent-Burgués and Tzanko Tzanov Hyaluronic Acid Derivative Molecular Weight-Dependent Synthesis and Antimicrobial Effect of Hybrid Silver Nanoparticles Reprinted from: <i>Int. J. Mol. Sci.</i> 2021 , 22, 13428, doi:10.3390/ijms222413428	441
María Mondéjar-López, Alberto José López-Jiménez, Joaquín C. García Martínez, Oussama Ahrazem, Lourdes Gómez-Gómez and Enrique Niza Thymoquinone-Loaded Chitosan Nanoparticles as Natural Preservative Agent in Cosmetic Products Reprinted from: <i>Int. J. Mol. Sci.</i> 2022 , 23, 898, doi:10.3390/ijms23020898	455

About the Editors

Monica Terracciano

Dr. Monica Terracciano is an organic chemist specializing in surface chemistry, soft interfaces, and bio/nanotechnologies for biosensing and drug delivery applications. She earned her MSc in pharmacy from the Department of Pharmacy at the University of Naples Federico II (UniNA) in 2011, with a thesis titled “Solid-Phase Synthesis of New Cisplatin Complexes with Potential Antitumor Activity”.

From 2013 to 2016, she pursued a doctoral program in “Drug Science” at UniNA (28th cycle) focused on synthesizing nanostructured materials and developing innovative chemical functionalization processes to create hybrid nanocomplexes with applications in diagnostics and targeted drug delivery. In 2016, she achieved the title of Doctor of Research with European recognition (Doctor Europaeus) by successfully defending her thesis titled “Bioengineered Porous Silica Devices for Biomedical Applications”.

From 2016 to 2019, she held a post-doctoral research fellowship, continuing her research activities at CNR-IMM, where she concentrated on chemically functionalizing and bioconjugating nanostructured materials in porous silicon for biosensing and targeted drug delivery purposes. Since 2019, she has served as an assistant professor in organic chemistry at the Department of Pharmacy at the University of Naples Federico II. Here, she joined the HybridBioSystems laboratory, where her primary role is the development of chemical protocols to create hybrid nanocomplexes for diagnostic applications and targeted drug delivery. She collaborates with various national and international research groups and actively participates in multidisciplinary research projects.

Her research results have been widely published in numerous scientific publications, with over 60 peer-reviewed articles, 7 book chapters, and more than 10 conference proceedings, thus making significant contributions to the fields of organic chemistry and nanostructured materials for biomedical applications.

Ilaria Rea

Ilaria Rea is a researcher at the Institute of Applied Sciences and Intelligent Systems of the National Research Council in Naples (ISASI NA–CNR), where she is head of the “Functional Nanomaterials and Interfaces” laboratory. Her research interests are in the field of advanced nano- and microscale materials for optical biosensing and drug delivery. Mesoporous silica/silicon nanoparticles, gold nanoparticles, nanostructured zinc oxide, and hybrid nanocomposites functionalized with antibodies, proteins, and nucleic acids are examples of materials realized in her laboratory. Her activity, made in collaboration with a multidisciplinary research team, has as its focus the *in vitro* diagnosis and treatment of human diseases such as cancer and cardiovascular ones. She is the author of more than 100 peer-reviewed scientific papers published in indexed journals, 11 book chapters, and more than 40 conference proceedings.

Nicola Borbone

Prof. Nicola Borbone is an organic chemist with specific knowledge in the fields of design, chemical-physical characterization, and evaluation of the biological roles of ODN analogues to be used as therapeutics or for biosensing applications.

He obtained his MSc in chemistry and pharmaceutical technologies at the University of Naples Federico II in 1999. In 2002, he obtained the PhD degree in “Sostanze Naturali Farmacologicamente Attive” at the University of Naples Federico II, defending a thesis on “Isolamento e caratterizzazione

strutturale di metaboliti secondari bioattivi da organismi marini e vegetali". In 2006, he got the permanent position of researcher (SSD CHIM/06) at the Department of Pharmacy of the University of Naples Federico II, and in October 2019, he got the position of associate professor in organic chemistry, founding in the same year the "HybridBioSystems" laboratory. He is the author of more than 120 peer-reviewed scientific papers published in indexed journals, 2 book chapters, and 5 conference papers.

Chiara Tramontano

Dr. Chiara Tramontano is a postdoc at the Nanomaterials for Biomedical Applications group at the Istituto Italiano di Tecnologia, where she is involved in the preparation, characterization, and biomedical applications of nanostructured materials. These materials are composed of either inorganic components or organic-inorganic materials in which various components, each with different properties such as optical, chemical, and magnetic characteristics, are carefully tailored and combined into single nano-objects.

Preface

Welcome to “Functional Nanomaterials for Healthcare”, a compilation of articles that highlights the latest developments in the synthesis and customization of advanced nanomaterials for healthcare applications. In a period when science and innovation are reshaping the landscape of healthcare, these articles provide the latest insights into the practical applications of advanced nanomaterials.

In recent years, researchers have been dedicated to synthesizing and tailoring nanomaterials for healthcare purposes. These materials play a crucial role in enhancing diagnostics, medical imaging, precise drug delivery, and supporting tissue engineering. They can even integrate diagnostics and therapies into a single solution, opening the door to exciting advancements in therapeutics and diagnostics, known as theranostics.

This reprint compiles a series of recent articles and reviews authored by experts in the field. They delve into the intricacies of advanced nanomaterial synthesis and functionalization, as well as characterization techniques, while exploring their potential medical applications.

We invite you to explore this collection of articles, which contribute significantly to the field of advanced functional nanomaterials in healthcare. Whether you are a researcher, a student, or a healthcare professional, you will discover a comprehensive overview of the latest innovations and discoveries in this dynamic field.

Monica Terracciano, Ilaria Rea, Nicola Borbone, and Chiara Tramontano

Editors



Article

ZnO Tetrapods for Label-Free Optical Biosensing: Physicochemical Characterization and Functionalization Strategies

Monica Terracciano ^{1,†} , Simas Račkauskas ^{2,†} , Andrea Patrizia Falanga ¹, Sara Martino ^{3,4},
Giovanna Chianese ³ , Francesca Greco ¹ , Gennaro Piccialli ¹ , Guido Viscardi ⁵ , Luca De Stefano ³ ,
Giorgia Oliviero ⁶ , Nicola Borbone ^{1,*} and Ilaria Rea ³

¹ Department of Pharmacy, University of Naples Federico II, Via Domenico Montesano 49, 80131 Naples, Italy

² Institute of Materials Science, Kaunas University of Technology, 51423 Kaunas, Lithuania

³ Unit of Naples, National Research Council, Institute of Applied Sciences and Intelligent Systems, Via Pietro Castellino 111, 80131 Naples, Italy

⁴ Department of Precision Medicine, University of Campania “Luigi Vanvitelli”, 80138 Naples, Italy

⁵ Department of Chemistry, NIS Interdepartmental Centre, University of Turin, Via Pietro Giuria 7, 10125 Turin, Italy

⁶ Department of Molecular Medicine and Medical Biotechnologies, University of Naples Federico II, Via S. Pansini 5, 80131 Naples, Italy

* Correspondence: nicola.borbone@unina.it; Tel.: +39-081678521

† These authors contributed equally to this work.

Abstract: In this study, we fabricated three different ZnO tetrapodal nanostructures (ZnO-Ts) by a combustion process and studied their physicochemical properties by different techniques to evaluate their potentiality for label-free biosensing purposes. Then, we explored the chemical reactivity of ZnO-Ts by quantifying the available functional hydroxyl groups (–OH) on the transducer surface necessary for biosensor development. The best ZnO-T sample was chemically modified and bioconjugated with biotin as a model bioprobe by a multi-step procedure based on silanization and carbodiimide chemistry. The results demonstrated that the ZnO-Ts could be easily and efficiently biomodified, and sensing experiments based on the streptavidin target detection confirmed these structures’ suitability for biosensing applications.

Keywords: surface characterization; quantum yield; label-free detection; zinc oxide nanostructure; surface functionalization



Citation: Terracciano, M.; Račkauskas, S.; Falanga, A.P.; Martino, S.; Chianese, G.; Greco, F.; Piccialli, G.; Viscardi, G.; De Stefano, L.; Oliviero, G.; et al. ZnO Tetrapods for Label-Free Optical Biosensing: Physicochemical Characterization and Functionalization Strategies. *Int. J. Mol. Sci.* **2023**, *24*, 4449. <https://doi.org/10.3390/ijms24054449>

Academic Editor: Kyeongsoon Park

Received: 16 January 2023

Revised: 14 February 2023

Accepted: 20 February 2023

Published: 23 February 2023



Copyright: © 2023 by the authors. Licensee MDPI, Basel, Switzerland. This article is an open access article distributed under the terms and conditions of the Creative Commons Attribution (CC BY) license (<https://creativecommons.org/licenses/by/4.0/>).

1. Introduction

The increasing interest in the earliest diagnosis has led to a considerable expansion of the biosensing field, with the continuous search for the most suitable materials for developing high-performance and low-cost detection devices [1,2]. Bulk materials lack important physicochemical properties (e.g., high surface-to-volume ratio, chemical reactivity, optical and electrical properties) needed for the development of biosensors, thus promoting the synthesis of nanostructured materials. Due to their distinct physicochemical properties, nanomaterials are appropriate as building blocks for biosensor development, providing high sensitivity and a valuable platform for analyzing single-molecular activity [3]. Among different materials, zinc oxide (ZnO) has arisen as a versatile, low-cost, and abundant metal oxide semiconductor useful to synthesize new transducer platforms for biosensor development [4–6].

Various forms of ZnO nanostructures, such as nanowires, nanotubes, tetrapods (Ts), nanorods, etc., are obtained by simple synthetic processes from low-cost materials [7,8]. The easy tuning of nanostructures’ morphology can significantly alter their physicochemical properties, such as enhancing their surface area and promoting variations in their optical,

electrical, and electrochemical responses [9]. In addition, their properties, such as their ultraviolet (UV) light sensitivity, wide bandgap (~3.37 eV), high electron transfer capability (~60 meV), and high isoelectric point (IEP ~ 9.5), make them promising materials for biosensing applications [10]. Thanks to the great progress in nanotechnology and material science, new technological methods have been developed to fabricate nanostructured ZnO templates with high surface area and advanced properties. In a previous work, we demonstrated that the emerging ZnO tetrapodal structures (ZnO-Ts), compared to ZnO nanorods and nanoparticles, have better electrochemical properties as a transducer platform for biosensing applications [10]. ZnO-Ts are characterized by four connective arms protruding from the core center at an average angle of ~110°. Their characteristic three-dimensional structure makes them better than one-dimensional nanostructures for biosensing applications due to the requisite high conductivity, limited agglomeration, and easy fabrication of electrodes and sensing devices, opening the way for the development of a label-free, multiparametric-read-out platform [4,5].

A nanostructured matrix used in biosensor development acts as both a solid support, which is used for the platform for the immobilization of sensing biomolecules (i.e., bioprobes) and as a transducer, which is able to convert target detection into an analytical read-out signal [11]. The bioprobe label can be ascribed to a variety of biomolecules spanning among simple or complex structures: single-stranded (DNA and RNA) oligonucleotides, aptamers, peptide nucleic acids (PNAs), proteins, enzymes, antibodies, peptides, etc. [7,12–17].

The fabrication of a new generation of hybrid biosensors in which biological or bio-inspired molecules are fully integrated with transducer platforms strongly depends on the functionalization and bioconjugation strategies of the device's surface [11,18]. Therefore, not only are the support's physical and chemical properties fundamental for determining the bioprobe immobilization method but the stability of the transducer surface during the functionalization and detection procedures must also be considered [19].

In this context, we explored ZnO-Ts as potential nanostructures for the development of label-free optical biosensors, paying particular attention to their physicochemical properties.

Three different ZnO-T samples (SH0, SH1, and SH2), synthesized by the combustion process and separated by centrifugation method in different size fractions, were characterized by dynamic light scattering (DLS), transmission electron microscopy (TEM), Brunauer-Emmett-Teller (BET) analyses, Fourier-transform infrared spectroscopy (FTIR), UV-vis spectroscopy, spectrofluorimetry, steady-state photoluminescence (PL), and fluorescence microscopy.

The use of ZnO-Ts as transducers in biosensor development requires the creation of coupling points for the biomolecules' immobilization (the so-called bioconjugation process), preserving the specific functionalities of biological receptors through good control of their orientation and organization on the inorganic surface [20]. To this aim, to estimate the number of hydroxyl groups (–OH) exposed on the tetrapods' surface potentially available for functionalization with the bioprobe, we functionalized the nanostructures' surface with 5'-DMT-3'-phosphoramidite-thymidine nucleotides via phosphoramidite chemistry and quantified, by colorimetric analysis, the amount of the DMT⁺ cation released in solution after coupling and acid treatment, which corresponds to the amount of reactive –OH groups exposed on the Ts' surface [21]. Then, the best T sample in terms of colloidal stability, PL quantum yield, and chemical reactivity was chemically modified and bioconjugated with biotin (used here as the bioprobe model), experiencing chemical protocols able to preserve the physicochemical properties of the matrix. To this end, ZnO nanostructures were chemically modified with a multi-step procedure consisting of a silanization step by a 3-(aminopropyl)triethoxysilane compound (APT) followed by biotin conjugation by carbodiimide chemistry [22–24]. The efficacy of the resulting ZnO-biotin biosensor was evaluated by exploiting the real-time detection of streptavidin using optical methods based on steady-state PL and fluorescence microscopy.

2. Results and Discussion

2.1. Physicochemical Characterization of Bare ZnO-Ts

ZnO-Ts were obtained by a combustion method and then separated by size into three fractions, SH0, SH1, and SH2, as described in Section 3.2. Centrifugation separates ZnO-Ts into fractions by their mass; therefore, the largest ZnO-T structures are obtained in fraction SH1, the smallest are obtained in fraction SH2, and the initial fraction, SH0, has both large SH1 and small SH2 fractions. The morphology of as-synthesized ZnO-Ts was investigated by transmission electron microscopy (TEM). The analysis revealed nanostructures characterized by the typical tetrapodal shape consisting of four connected nanorods (legs) with a diameter of 20–100 nm and a length of 100–1000 nm (Figure 1a). Different tetrapods' leg morphology could be connected to local fluctuations of synthesis conditions in the combustion chamber. The sample SH2 showed the smallest diameters and lengths; SH1 showed the biggest diameters and lengths, while SH0 had both small and big ZnO-Ts. A BET analysis (Figure S1) revealed the increase in the surface area along the series SH1 < SH0 < SH2, with corresponding values of 7.1 ± 0.1 , 8.9 ± 0.1 , and 10.8 ± 0.2 m² g⁻¹.

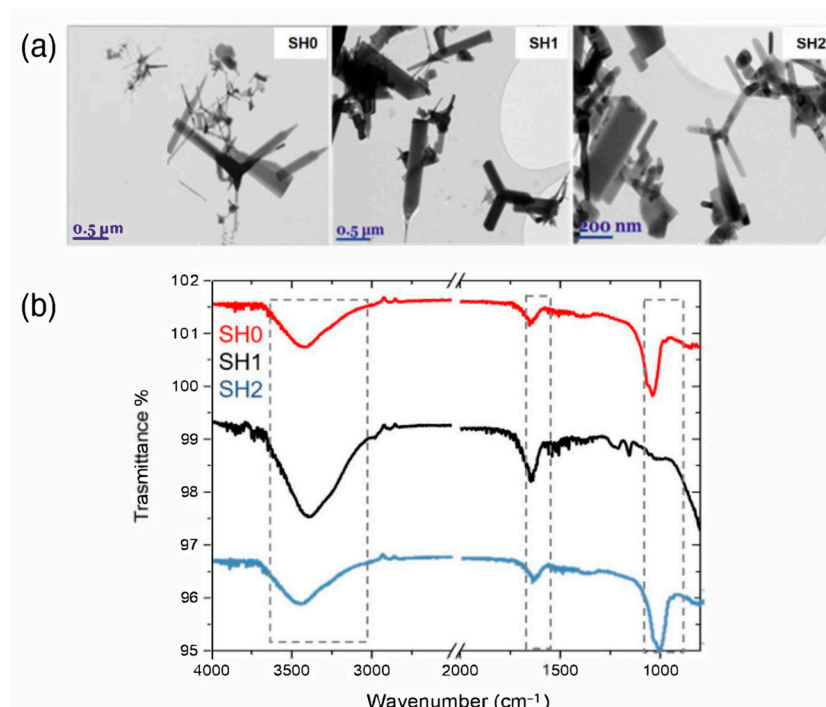


Figure 1. Morphological and chemical characterization of SH0, SH1, and SH2 ZnO-T samples. (a) TEM images showing the characteristic tetrapodal structure of ZnO-Ts. (b) ATR-FTIR spectra.

The surface chemistry of bare ZnO-T samples was investigated by attenuated total reflectance Fourier-transform infrared (ATR-FTIR) spectroscopy. The spectra reported in Figure 1b show absorption bands at 3500 cm⁻¹ and 1050 cm⁻¹ due to the O-H stretching and bending vibrations, respectively. The band at 1630 cm⁻¹, attributed to zinc carboxylate due to the synthesis process, is also evident [25,26].

Dynamic light scattering (DLS) analysis was performed to evaluate the stability of colloidal suspensions by measuring the hydrodynamic diameter (size), polydispersity index (PDI), and surface charge (zeta potential) of the three ZnO-T bare samples. To this aim, ZnO-Ts were dispersed in ultra-pure water (pH 7) at a concentration of 0.05 mg mL⁻¹ following the procedure described in Section 3.3. SH0 showed a smaller size, lower PDI, and higher zeta potential than the other samples, thus confirming the good homogeneity and stability of the SH0 ZnO-T colloidal suspension (Table 1). However, we observed that the bare ZnO-Ts had a very high tendency to agglomerate in deionized water, leading to a larger size in the DLS analyses compared to the real size determined by TEM due to the

lack of stabilizing surface chemistry [27]. Therefore, it was necessary to chemically stabilize the ZnO-Ts surface for biosensing purposes.

Table 1. Hydrodynamic diameter (size), polydispersity index (PDI), and surface charge (zeta potential) of ZnO-T samples obtained by DLS measurements. The analyses were performed in ultra-pure water (pH 7).

Sample	Size (nm)	PdI	Zeta Pot (mV)
SH0	330 ± 120	0.3	−47 ± 5
SH1	470 ± 100	0.5	−40 ± 5
SH2	600 ± 250	0.4	−43 ± 4

The absorbance of ZnO-Ts dispersed in PBS-T was investigated by UV-vis spectroscopy in the wavelength range included between 280 and 800 nm (Figure 2a). In this interval, an absorption peak at 370 nm was observed; the peak can be ascribed to the intrinsic bandgap absorption of ZnO due to the electron transitions from the valence band to the conduction band ($O2p \rightarrow Zn3d$) [28]. The fluorescence emission of ZnO-Ts in PBS-T was studied under an excitation light of 370 nm. The emission spectra of samples SH0, SH1, and SH2, reported in Figure 2b, are characterized by a broad band centered at 500 nm due to the defects present in the materials, in particular oxygen vacancies and $-OH$ groups [29,30]. A weak peak at about 420 nm can also be observed. This peak can be attributed to the transitions from Zn interstitials to the valence band [31].

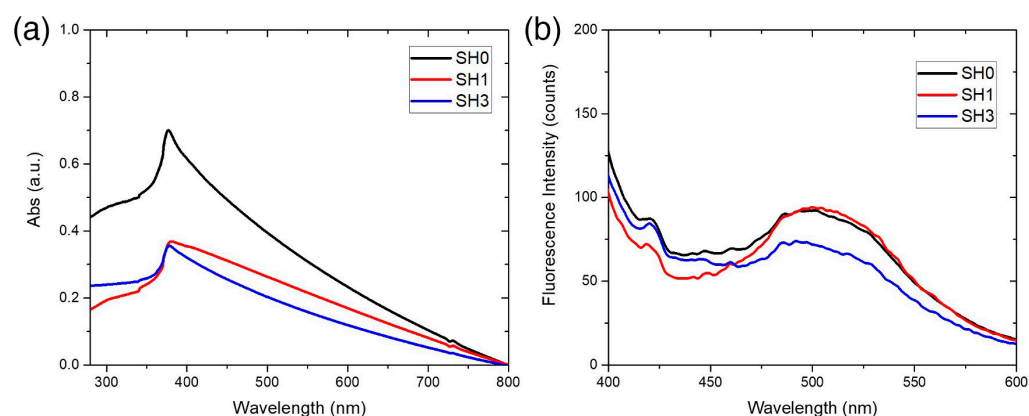


Figure 2. Optical characterization of ZnO-T samples SH0, SH1, and SH2. (a) UV-Vis absorption spectra showing an absorption peak at 370 nm. (b) Fluorescence spectra of the samples excited at 370 nm.

After this preliminary optical characterization, the fluorescence quantum yields (QYs) of SH0, SH1, and SH2 were determined by measuring the absorbance and the fluorescence intensity ($\lambda_{exc} = 370$ nm) of the samples dispersed in PBS-T at different concentrations ranging from 0.05 to 0.2 mg mL^{−1} (Figure 3a,b). QYs were estimated relative to Hoechst 33342 (Hoechst) used as a standard dye (the QY of Hoechst in DMF is 35% and calculated using the following equation:

$$\frac{QY_{ZnO\ Tds}}{n_{PBS-T}^2 \alpha_{ZnO\ Tds}} \Big|_{\lambda_{exc}} = \frac{QY_{Hoechst}}{n_{DMF}^2 \alpha_{Hoechst}} \Big|_{\lambda_{exc}} \quad (1)$$

where n is the refractive indices of the media (PBS-T or DMF) and α represents the ratio between the integrated fluorescence intensity and the absorbance at $\lambda = 370$ nm) [32,33]. The coefficients $\alpha_{SH0} = (3.6 \pm 0.4) \times 10^4$, $\alpha_{SH1} = (11.0 \pm 0.8) \times 10^4$, and $\alpha_{SH2} = (4.4 \pm 0.9) \times 10^4$ were obtained via linear regression from the plots of integrated fluorescence intensity versus absorbance for SH0, SH1, and SH2, respectively (Figure 3c).

The coefficient $\alpha_{\text{Hoechst}} = (2.3 \pm 0.1) \times 10^5$ was calculated for Hoechst in DMF. Using $n_{\text{PBS-T}} = 1.33$ and $n_{\text{DMF}} = 1.43$ as refractive indices. The QY values reported in Table 2 were determined from Equation (1).

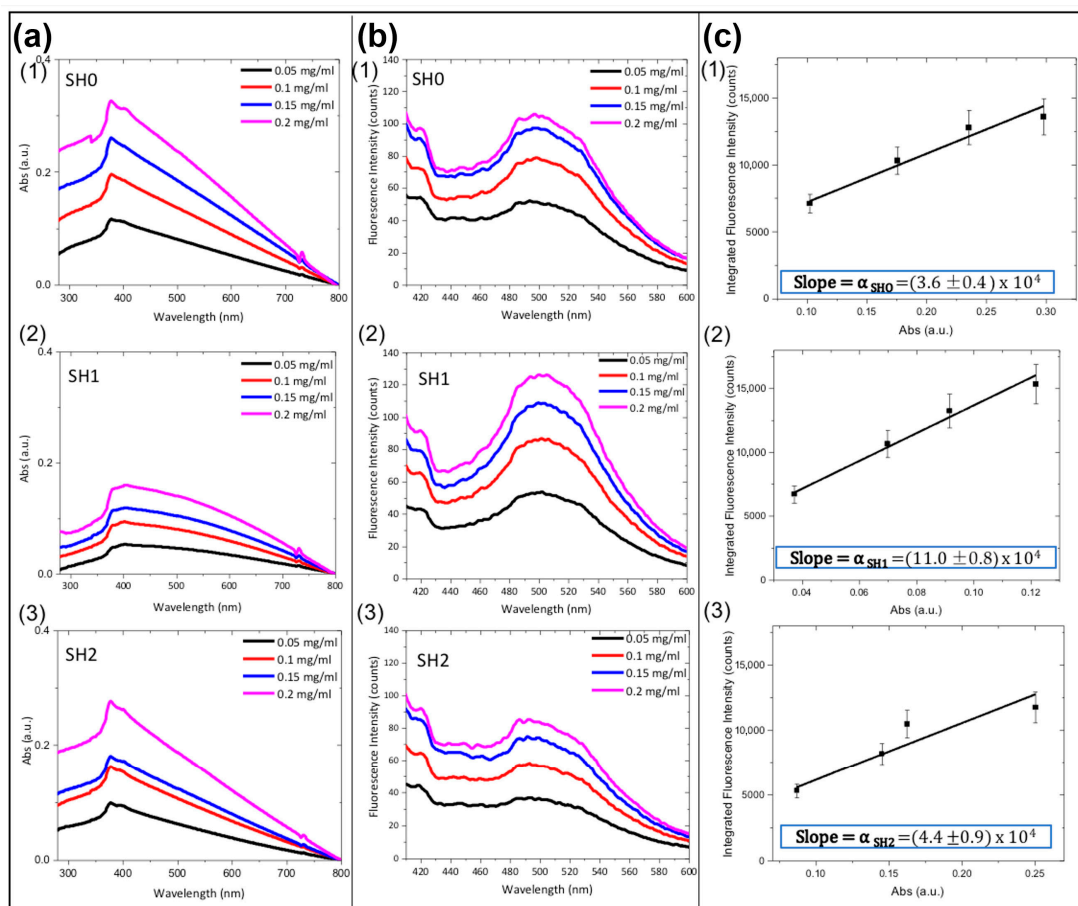


Figure 3. (a) Absorption and (b) fluorescence spectra ($\lambda_{\text{exc}} = 370$ nm) of ZnO-Ts (SH0, SH1, SH2) at different concentrations in PBS-T. (c) Corresponding integrated fluorescence intensity versus absorbance at 370 nm; the slopes of the curves were used for calculating the quantum yield (QY) of each sample.

Table 2. Relative quantum yield values calculated from Equation (1).

Sample	QY%
SH0	4.7 ± 0.6
SH1	14 ± 1
SH2	6 ± 1

2.2. Nucleotides Conjugation to ZnO-Ts by Phosphoramidite Chemistry and Quantification of Reactive Hydroxyl Groups on ZnO-T Surface

Proper surface chemical functionalization of the transducer material is paramount for biosensor development. The transducer surface is frequently functionalized to improve its physicochemical properties and enrich its functionalities. Therefore, the precise quantification of available functional groups on the transducer surface is fundamental to adequately control the chemical modification [22]. We determined the number of reactive $-\text{OH}$ groups exposed on the bare ZnO-Ts' surface using a non-conventional methodology based on nucleotide derivatization followed by a colorimetric assay. To this aim, ZnO-Ts (1, Figure 4a) were left to react with tetrazole-activated 5'-DMT-3'-phosphoramidite-thymidine nucleotides (2, Figure 4a) using the well-known phosphoramidite chemistry.

This reaction allowed the binding of T nucleotides on the ZnO surface by the fast formation of 3'-phosphite-triester groups with the –OH groups exposed on the ZnO surface (3, Figure 4a). The amount of the bonded nucleotides, which reflects the amount of the reactive –OH groups on the ZnO-Ts' surface, was assessed by spectrophotometrically quantifying the amount of the 5'-dimethoxytrityl cations (DMT⁺) released from the ZnO-T-bound 5'-DMT-protected nucleotides (3, Figure 4a) using a solution of dichloroacetic acid in dichloromethane (3% w/w). The release of the DMT⁺ cations generates a bright red-orange colored solution ($A_{\max} = 503 \text{ nm}$) whose color intensity is directly proportional to the content of –OH groups and quantifiable by the Lambert–Beer law ($\epsilon = 71,700 \text{ M}^{-1} \text{ cm}^{-1}$) as shown in Figure 4b [34]. The amount of DMT⁺ cation released in solution was 3.9 ± 0.2 , 3.5 ± 0.6 , and $1.8 \pm 0.5 \mu\text{mol mg}^{-1}$, respectively, for SH0, SH1, and SH2 (Table 3).

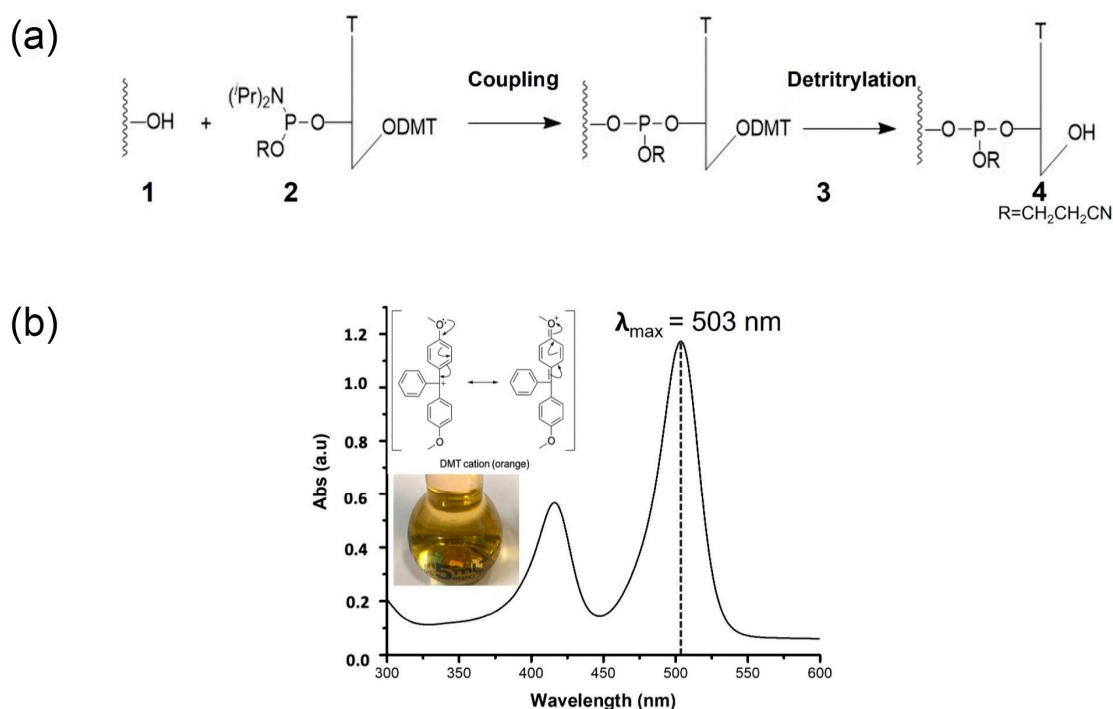


Figure 4. (a) Functionalization scheme of ZnO-Ts (1) with 5'-DMT-3'-phosphoramidite-thymidine nucleotide (2) via coupling reaction; the removal of 5'-DMT from thymidine nucleotide-bounded on ZnO-Ts surface (3) via detritylation reaction provided the ZnO-Ts surface (4). (b) Representative images of DMT cation bright red-orange colored solution resulting from detritylation where the quantity of the released DMT cation is measured by UV-vis spectroscopy at 503 nm.

Table 3. Quantification of reactive hydroxyl (–OH) groups.

Sample	–OH ($\mu\text{mol mg}^{-1}$)
SH0	3.9 ± 0.2
SH1	3.5 ± 0.6
SH2	1.8 ± 0.5

2.3. Biofunctionalization of ZnO-Ts Surface and Sensing Experiment

The selectivity of the device is another key issue in biosensor development. Selectivity is achievable by using specific bioprobes that can be either directly grown into the PSi matrix (in situ synthesis) or synthesized ex situ and then immobilized on the surface via electrostatic or covalent interactions [12,13,15]. This delicate step might affect the mobility, conformation, and functionalities of the selected bioprobes; therefore, various chemical strategies were developed to preserve the bioprobe's functionality for biosensing applications [2].

Another important aspect to consider in biosensor development is the pH of aqueous-based solutions used during biofunctionalization procedures. The pH could hugely impact the ZnO-based nanostructures and their properties considering that ZnO is an amphoteric oxide easily dissolvable in both acid and basic conditions. The metal oxide ZnO in water solution undergoes hydrolysis, creating a hydroxide coating on its surface ($\equiv\text{M-OH}$) [19]. In acid conditions, the H_3O^+ ions react with the ZnO surface, causing the dissolution of nanostructures with rapid release of $\text{Zn}^{2+}(\text{aq})$ in the alkaline condition (pH higher than 8.5) also occurs due to the dissolution of ZnO nanostructures related to their hydroxide which produces soluble species in the form of hydroxyl complexes such as $\text{Zn}(\text{OH})_2(\text{aq})$. The mechanisms of ZnO-based structures' dissolution in acid and alkaline conditions are described in detail in the "Supporting Information". Considering the results reported in the literature, the best working condition to develop a ZnO-based biosensor preserving the physicochemical properties is to use mild alkaline pH solutions [19,35,36].

The SH0 sample was chosen for the experiments of bioconjugation and optical sensing due to two main properties: the superior ability to form a stable colloidal suspension in water-based solutions, as highlighted by the measurements of DLS (Table 1), the reactive surface characterized by the presence of a larger amount of $-\text{OH}$ groups, useful for an efficient functionalization, as demonstrated by the studies of $-\text{OH}$ quantification (Table 3). The ability of the SH0 sample to act as an optical transducer of biomolecular interactions was investigated by studying selective biotin-streptavidin recognition.

Biotin, a member of the water-soluble B-complex group of vitamins, is a molecule involved in a wide range of metabolic processes in humans and other organisms. Due to the strong affinity of biotin to streptavidin, it is commonly used as a model of interaction for the development of diagnostic tools. Once the biotin slides into the tight-fitting pocket of streptavidin, the flexible loop of streptavidin folds over the biotin and acts as a lid for stable binding [23].

Biotin bioprobes were immobilized on the surface of the SH0 ZnO-Ts following the functionalization procedure schematized in Figure 5a. Firstly, the bare ZnO-Ts were silanized by the chemical reaction between the triethoxy groups of APT and the $-\text{OH}$ groups on the ZnO-TS surface, generating self-assembled monolayers covalently bonded to the surface via Zn-O-Si bonds able to passivate the surface. This chemical strategy improves the surface stability and introduces coupling points ($-\text{NH}_2$ groups) for the immobilization of the bioprobe [11,37]. The surface was then biotinylated by the reaction between the N-Hydroxysuccinimide (NHS) esters of biotin (NHS-biotin) molecules and the amine groups of the ZnO-Ts via carbodiimide chemistry at slightly alkaline conditions (pH 8), yielding stable amide bonds.

The chemical modification of the ZnO-T surface was analyzed by ATR-FTIR spectroscopy (Figure 5). As already observed by the graph reported in Figure 1, the spectrum of bare ZnO-Ts is characterized by a broad band at 3500 cm^{-1} due to the presence of $-\text{OH}$ hydroxyl groups on the sample surface [25]. After the silanization process, the ZnO-Ts-APT displayed a decrease in the signals related to $-\text{OH}$ groups involved in the covalent bond with the silane compound. The characteristic bands of APT, corresponding to the bending mode of free NH_2 at $1520\text{--}1330\text{ cm}^{-1}$ and the rocking CH_x vibration of the Si-OCH_x bond at 870 cm^{-1} , are well evident in the spectrum of the silanized sample. After the biotin immobilization, no significant changes in the FTIR spectrum were observed. The surface charge of the bare ZnO-Ts passed from $-45 \pm 10\text{ mV}$ to $5 \pm 2\text{ mV}$ after the silanization process and to $-27 \pm 18\text{ mV}$ after biotinylated, confirming the success of the ZnO-T surface functionalization. The effectiveness of the surface functionalization was also demonstrated by photoluminescence (PL) measurements performed by exposing the sample to UV laser light ($\lambda = 325\text{ nm}$) and analyzing its emission spectrum after each functionalization step. In these investigations, the sample was deposited on a silicon piece. PL measurements were preferred to standard fluorescence investigations performed in solution because they allow exploring a wider spectral range with higher resolution due to the use of high-performing source and detector devices. Figure 5d shows the PL spectra of ZnO-Ts before and after

each functionalization step. Compared to the fluorescence spectrum ($\lambda_{\text{exc}} = 370 \text{ nm}$) of bare SH0 reported in Figure 2b, its corresponding PL spectrum excited at 325 nm allows observing an intense peak at 372 nm, which can be assigned to the radiative recombination of the electron-hole pairs due to the transition from the conduction band to the valence band (excitonic emission). The visible broad band that peaked at 500 nm (green emission), related to the recombination of electrons with photo-generated holes occupying defect sites, is also well evident [38].

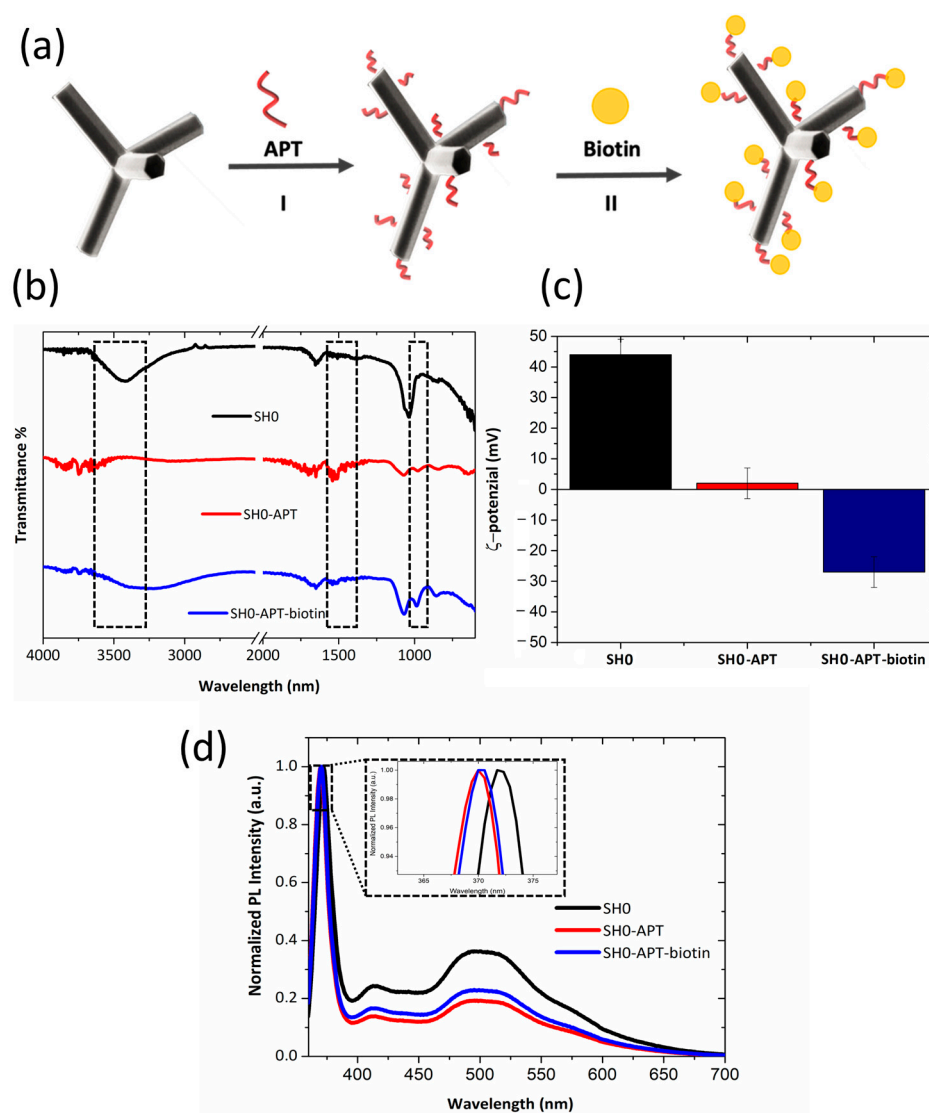


Figure 5. (a) Schematic representation of the ZnO-T surface functionalization with APT (I) and biotin (II). (b) FTIR spectrum of ZnO-Ts after each step of functionalization. (c) ζ -potential analysis. (d) PL spectra of ZnO-Ts before and after the surface functionalization.

After the silanization process, a slight shift of the peak at 372 nm towards shorter wavelengths ($\Delta\lambda = -2 \text{ nm}$) was observed; the shift can be attributed to the coordination between the APT molecules and ZnO, which affects the band gap of the material. On the other hand, the decrease in the green emission intensity (about 40%) was due to the binding of the APT molecules with the ZnO-Ts through the $-\text{OH}$ groups, reducing the availability of surface holes (i.e., the recombination centers) and, consequently, the intensity of green emission. This result agrees with the FTIR measurements highlighting the decrease in $-\text{OH}$ groups after the silanization.

After the functionalization with biotin, only a weak increase in the green emission intensity (about 15%) was monitored.

The biotinylated ZnO-Ts can interact with streptavidin, a homo-tetrameric (66 kDa) protein from the bacterium *Streptomyces avidinii* with an extraordinary affinity to biotin with a dissociation constant (K_d) in the order of $\approx 10^{-14}$ mol L⁻¹. The binding of biotin to streptavidin is one of the strongest non-covalent interactions known in nature, forming the basis for many diagnostic assays that require the formation of a specific linkage between biological macromolecules [23].

To verify the interaction between biotinylated ZnO-Ts and streptavidin, functionalized ZnO-Ts were preliminary incubated with 0.4 mM of Cy3-labelled streptavidin solution (PBS, pH 8) for 1 h under stirring (Figure 6a). After the incubation, biotinylated ZnO-Ts were washed, deposited on a silicon piece, left to dry, and analyzed by fluorescence microscopy. Figure 6b reports the fluorescence images of biotinylated ZnO-Ts before and after the incubation with fluorescent streptavidin under two different excitation wavelengths, 365 and 530 nm, respectively. The typical yellow emission of Cy3, well evident in the case of biotinylated ZnO-Ts incubated with Cy3-labeled streptavidin under an excitation of 530 nm, confirms the biomolecular interaction.

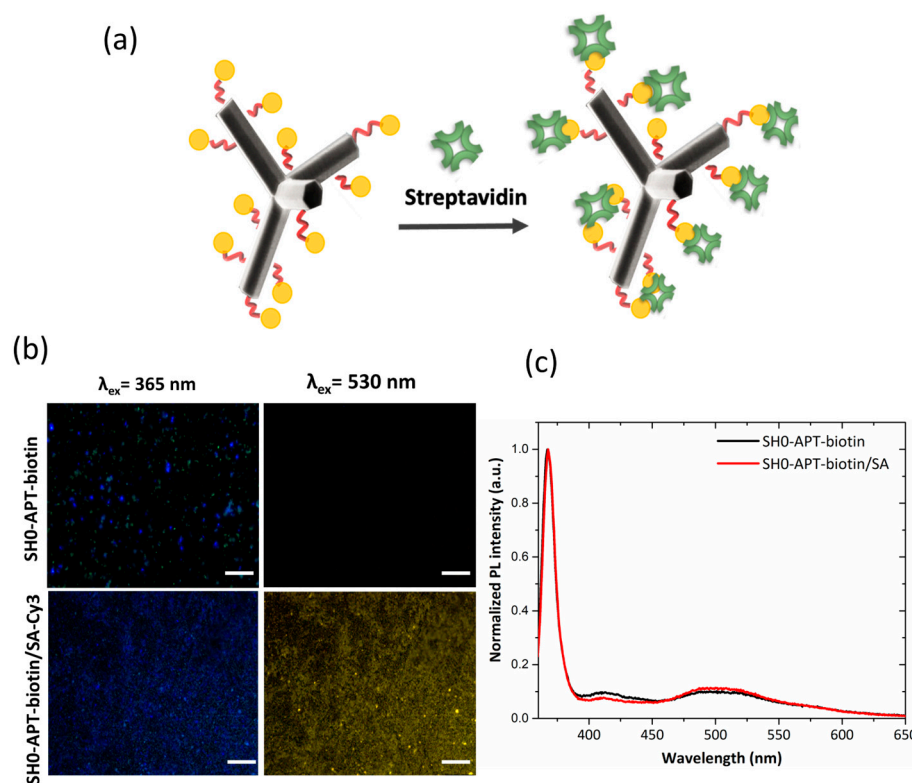


Figure 6. (a) Schematic representation of the streptavidin detection by biotinylated-ZnO-Ts. (b) Fluorescence microscope images of functionalized SH0 before and after the interaction with Cy3-labeled streptavidin. Scale bar 75 μ m. (c) Normalized PL intensity spectra of functionalized ZnO-Ts before and after the exposure to label-free streptavidin at the excitation wavelength of 325 nm.

An analogue investigation was also performed using a label-free streptavidin; in this case, the biomolecular recognition was monitored by PL analysis. The analysis did not reveal any variation in the PL spectrum.

We can conclude that the analysis of the photoluminescence emission can be a valid strategy for studying the surface functionalization of ZnO-Ts; indeed, the results are consistent with the preliminary FTIR characterization. On the contrary, the technique did not provide information on the interaction between the biotinylated ZnO-Ts and

streptavidin. The weak sensing capability could be attributed to the low specific surface area (up to $10 \text{ m}^2 \text{ g}^{-1}$) that characterizes this nanostructured material compared to other forms of nanostructured ZnO such as ZnO-NWs [39] and porous ZnO [40].

3. Materials and Methods

3.1. Materials and Reagents

Phosphate-buffered saline tablets (PBS CAS No.: P4417-50), Tween 20 (CAS No.: 9005-64-5), 3-aminopropyltriethoxysilane (APT CAS No.: 919-30-2), DMT-dT Phosphoramidite (CAS No.: 98796-51-1), tetrazole (CAS No.: 919-30-2288-94-8), deblocking solution of trichloroacetic acid in dichloromethane 3% *w/w* (CAS No.: 8-570-14); tetrahydrofuran anhydrous (THF CAS No.: 109-99-9), acetonitrile (CAS No.: 75-05-8), hydrochloric acid (HCl CAS No.: 7647-01-0), and sodium hydroxide solution (NaOH CAS No.: 1310-73-2) were all purchased from Sigma-Aldrich. Dimethyl sulfoxide (DMSO CAS No.: 67-68-5), sulfo-N-hydroxysuccinimide biotin (biotin-NHS CAS No.: 119616-38-5) water-soluble, streptavidin (SA CAS No.: 9013-20-1) from *Streptomyces avidinii*, and streptavidin–Cy3 (Cy3-SA CAS No.: S6402) from *Streptomyces avidinii* were purchased by Merck KGaA (DE). Hoechst 3342 Trihydrochloride Trihydrate-10 mg/mL solution (Hoechst CAS No.: 23491-45-4) in water was purchased from Invitrogen by Thermo Scientific. Absolute ethanol (EtOH CAS No.: A3678) was purchased from PanReac Applichem ITW Reagents. Ultra-pure water ($18 \Omega \cdot \text{cm}$) purified from a Milli-Q purification system (Millipore, Bedford, MA, USA) was used to prepare all the aqueous solutions.

3.2. ZnO Tetrapods (ZnO-Ts) Synthesis

ZnO-Ts were synthesized in a vertical reactor with heating similar to a combustion method described earlier [41]. Briefly, micron-sized Zn particles, entrained in the air, were supplied to the reactor and combusted to form a nanopowder of ZnO. Differently from the previous method, heating from the combustion of methane gas was used instead of electrical heating, and wet air was additionally supplied to the reactor to control the reaction rate. The nanopowder containing ZnO-Ts and some other forms on nanowires and nanoparticles were collected downstream of the reactor on the cellulose filter and further used in the analysis. The tetrapodal shape of the ZnO nanomaterials obtained was confirmed by in-depth TEM analysis in earlier work [41] using the same synthesis conditions. The combustion synthesis method was used because it delivers the synthesis of chemically pure ZnO-Ts in high yield, which is especially attractive for further practical application [10].

After synthesis, the as-obtained ZnO-Ts mixture was separated into 3 fractions with the help of a centrifuge (Table 4). The initial ZnO-T mixture was marked as SH0; it was suspended in isopropanol (IPA CAS No.: 67-63-0) at a concentration of 1 mg/mL, sonicated in the bath for 1 h, and further separated in the centrifuge at a rotation speed of 1000 rpm. The sediments were collected and marked as SH1. The supernatant was further centrifuged at a rotation speed of 3000 rpm; the sediments were then collected and marked as SH2. All fractions were characterized without further processing.

Table 4. Fabrication procedures of the ZnO-T samples.

ZnO-Ts Sample	Fabrication Procedure
SH0	as-obtained ZnO-Ts
SH1	SH0 dispersed in IPA, sonicated for 1 h, and centrifuged at 1000 rpm, with the sediment collected and marked as SH1
SH2	The supernatant of SH1 centrifuged at 3000 rpm, with the sediment collected and marked as SH2

3.3. ZnO-Ts Characterization

Dynamic light scattering (DLS). Each sample of ZnO-Ts (SH0, SH1, and SH2) was prepared for DLS characterization as described in the following. A stock suspension of ZnO-Ts with a concentration of 0.2 mg mL^{-1} was obtained by dispersing the powder in PBS $1\times + 0.1\%$ Tween 20 (PBS-T). Then, a sample with a concentration of 0.05 mg mL^{-1} was prepared by dispersing an aliquot of the stock suspension in ultra-pure water ($\text{pH} = 7$). The sample was centrifuged at 3500 rpm for 3 min and resuspended in ultra-pure water to completely remove the PBS-T. Before the DLS analysis, the sample was sonicated for 5 min. Hydrodynamic diameter and surface ζ -potential of ZnO-Ts were measured using a Zetasizer Nano-ZS instrument (Malvern Instrument Ltd., UK) equipped with a He-Ne laser (633 nm, scattering angle of 90° , 25°C). Size distribution and surface zeta-potential values were obtained by averaging three measurements.

UV-Vis spectroscopy. Absorption spectra of ZnO-Ts were acquired using a Jasco V-730 UV-Vis double beam spectrophotometer (Jasco Inc., Easton, PA, USA) in the wavelength range of 280–800 nm. The samples were analyzed at the concentration of 0.2 mg mL^{-1} in PBS-T using a quartz cell with a path length of 10 mm and a total volume capacity of 0.5 mL.

Fluorescence spectroscopy. Fluorescence emission spectra of ZnO-Ts were acquired using a PerkinElmer LS 55 Luminescence spectrometer (PerkinElmer Inc., Waltham, MA, USA) in the wavelength range of 380–700 nm, setting the excitation wavelength at 370 nm, and the excitation and emission bandwidth at 10 nm and 5 nm, respectively. The samples were suspended in PBS-T, and a quartz cell with a path length of 10 mm and a total volume capacity of 0.5 mL was used.

Fluorescence microscopy. Fluorescence images of ZnO-Ts were acquired using a Leica AF6000LX-DM6M-Z microscope (Leica Microsystems, Mannheim, Germany), controlled by LAS-X (Leica Application Suite; rel. 3.0.13) software and equipped with a DFC7000T Leica Camera. Fluorescence images were obtained using a $50\times$ objective and an I3 cube constituted by a 365 nm band-pass excitation filter. ZnO-Ts were dispersed in ultra-pure water (250 mg mL^{-1}), and 20 μL of the samples were left to dry on silicon pieces to acquire the images.

Brunauer-Emmett-Teller (BET) analysis. The textural parameters of the samples were determined by nitrogen adsorption–desorption isotherms at -200°C (77 K) using a Quantachrome Autosorb-iQ-KR/MP automated gas sorption analyzer. Before the analysis, the powder samples were outgassed under a vacuum at 200°C for 3 h. The specific surface area was calculated using the BET (Brunauer–Emmett–Teller) equation.

Transmission Electron Microscopy. The morphology of the samples SH0, SH1, and SH2 was investigated using a transmission electron microscope (TEM, Jeol JEM-1400, Jeol Ltd., Akishima, Japan). To this aim, the samples were dispersed in ultra-pure water at a concentration of 0.2 mg mL^{-1} and dropped on a carbon-coated copper TEM grid before air-drying overnight at room temperature.

ATR-Fourier Transform Infrared Spectroscopy. The surface chemical composition of ZnO-Ts was investigated by attenuated total reflectance Fourier transform infrared spectroscopy (ATR–FTIR). The ATR–FTIR spectra of the samples were obtained using a Nicolet iS50 (Thermo Scientific) FTIR spectrometer equipped with a Germanium (Ge) crystal element. The ATR–FTIR spectra were recorded in the wavenumber region $4000\text{--}525 \text{ cm}^{-1}$ with a resolution of 4 cm^{-1} . The measurements were carried out on dried ZnO-Ts deposited on the Ge crystal.

Photoluminescence. The photoluminescence analysis of ZnO-Ts was performed by depositing 20 μL of the samples dispersed in ultra-pure water (0.2 mg mL^{-1}) on silicon pieces; the samples were left to dry at RT before the investigations. The photoluminescence (PL) spectra of ZnO-Ts were excited by a continuous wave He–Cd laser at 325 nm (KIMMON Laser System). PL was collected at normal incidence to the surface of samples through a fiber, dispersed in a spectrometer (Princeton Instruments, SpectraPro 300i), and detected using a Peltier-cooled charge-coupled device (CCD) camera (PIXIS 100F). A long pass filter

with a nominal cut-on wavelength of 350 nm was used to remove the laser line at the monochromator inlet.

3.4. Quantum Yield (QY) Calculation

Quantum yields (QYs) of the samples SH0, SH1, and SH2 dispersed in PBS-T were calculated by measuring their absorbance and the integrated fluorescence intensity at different concentrations (0.05, 0.1, 0.15, and 0.2 mg mL⁻¹). Absorption spectra were obtained using a Jasco V-730 UV-Vis double beam spectrophotometer (Jasco Inc., Easton, PA, USA) in the wavelength range of 280–800 nm. Emission spectra were acquired using a PerkinElmer LS 55 Luminescence spectrometer (PerkinElmer Inc., Waltham, MA, USA) in the wavelength range of 410–600 nm, setting the excitation wavelength at 370 nm. The QYs of ZnO-Ts were estimated relative to Hoechst 33342 (Hoechst) used as a standard dye. To this aim, Hoechst was dispersed in DMF at the concentrations of 0.0075, 0.015, 0.025, and 0.050 mg mL⁻¹ and analyzed.

3.5. Quantification of -OH Groups

ZnO-T samples SH0, SH1, and SH2 (20 mg) reacted with tetrazole activated (18 mg) 5'-(dimethoxytrityl)-thymidine-phosphoramidite dissolved in dry THF (30 mg/mL) for 1 h at room temperature under mild stirring [34].

Then, the samples were centrifuged for 3 min at 5000 rpm and washed 10 times with acetonitrile to remove adsorbed reagents. The removal of the 5'-dimethoxytrityl protecting group from the supports bound 5'-terminal nucleotide was performed by using the deblocking solution of dichloroacetic acid in dichloromethane (3% *w/w*). The ZnO-Ts were centrifuged at 5000 rpm, and the amount of DMT in the supernatant was measured by a UV-Vis spectrometer (V-73, Jasco Europe, Italy) at 503 nm ($\epsilon = 71,700 \text{ M}^{-1} \text{ cm}^{-1}$). Functionalization of the samples was performed in triplicate.

3.6. ZnO-Ts Stability at Different pH Conditions

To investigate the stability of ZnO-Ts on exposure to acidic and alkaline conditions, ZnO-Ts were dispersed at a concentration of 0.2 mg mL⁻¹ in PBS-T at different pHs (3, 4, 5, 6, 7, and 8) for 0, 2, and 24 h. After the exposure, the samples were investigated by absorbance, fluorescence, and ATR-FTIR analyses.

3.7. ZnO-Ts Functionalization

The studies of functionalization were performed on the SH0 sample. ZnO-Ts (1 mg) of SH0 were amino-modified using APT 5% (*v/v*) in absolute EtOH (1 mL final volume) for 1 h at room temperature (RT) in mild stirring conditions [42]. The sample was centrifuged at 3500 rpm, and the supernatant was replaced twice with EtOH and once with PBS (pH = 8) to remove unreacted APT. Amino-modified ZnO-Ts (1 mg) were resuspended in biotin-NHS solution (1 mM in PBS, pH 8) and left to react for 1 h [23].

ZnO-Ts were characterized after each functionalization step by DLS, photoluminescence, and ATR-FTIR analyses.

3.8. Sensing Experiment

Two aliquots of biotinylated ZnO-Ts were incubated with 0.4 mM of SA and Cy3-SA and left to interact for 1 h with an agitation of 800 rpm. After the interaction, the samples were washed and resuspended in PBS (pH = 8).

The interaction between the biotinylated ZnO-Ts and the streptavidin was monitored by fluorescence microscopy and photoluminescence spectroscopy.

4. Conclusions

The growing advancement of the biosensor field provides a powerful driving force for the constant research and fabrication of advanced nanostructured materials with enhanced properties for developing a new generation of diagnostic devices. Zinc oxide (ZnO) is

one of the most interesting metal oxide materials used in biosensing due to its unique and versatile physicochemical properties. It has been observed that the properties of ZnO can be improved through the nanoscale-up architectural process, making ZnO-based structures suitable for biosensing applications and opening the way for the development of multiparametric, label-free transducers. In this work, we discussed the potentiality and performance of various novel ZnO-tetrapod nanostructures for label-free optical biosensing applications. The physical and chemical properties of three different ZnO-T samples (SH0, SH1, and SH2), synthesized by the combustion process and separated by a centrifugation method in different size fractions, were evaluated by DLS, TEM, BET analyses, FTIR, UV-vis spectroscopy, spectrofluorimetry, steady-state PL, and fluorescent microscopy. Then, we explored the chemical reactivity of the samples by surface coupling with monomeric oligonucleotide bases via the phosphoramidite method and quantified the available functional hydroxyl groups (–OH) on the transducer surface necessary for the subsequent functionalization steps. The best ZnO-T sample in terms of colloidal stability, PL quantum yield, and chemical reactivity was chemically modified and bioconjugated with biotin using chemical protocols able to preserve the physicochemical properties of the matrix based on silanization and carbodiimide chemistry. FTIR, zeta potential and PL analyses confirmed the successful obtainment of the biotinylated ZnO-T-based biosensor. The sensing properties of the obtained device were investigated by optical methods based on the steady-state PL and fluorescence microscopy, confirming the biotin-streptavidin interaction. Although further modifications in the synthetic process will have to be carried out to implement the chemical-physical properties of these emerging structures for label-free biosensing applications, the detailed analysis of ZnO nanostructures conducted in this study will contribute to future biosensing applications of these appealing structures.

Supplementary Materials: The following supporting information can be downloaded at: <https://www.mdpi.com/article/10.3390/ijms24054449/s1>.

Author Contributions: Conceptualization, M.T., G.O., N.B. and I.R.; data collection and interpretation, M.T., S.R., A.P.F., S.M., G.C. and F.G.; validation, G.O., G.P., L.D.S., G.V., N.B. and I.R.; writing—original draft preparation, M.T.; writing—review and editing, I.R., N.B.; visualization. All authors have read and agreed to the published version of the manuscript.

Funding: This research received funds from CN00000041 “National Center for Gene Therapy and Drugs based on RNA Technology” funded by the European Union NextGenerationEU and financed by PNRR MUR-M4C2—Investimento 1.4, CUP UNINA: E63C22000940007. M. Terracciano acknowledges financial support from PON-AIM RTDA_L1 (AIM 1873131-2). S. Račkauskas acknowledges funding from the European Regional Development Fund (project No. 01.2.2-LMT-K-718-02-0011) under a grant agreement with the Research Council of Lithuania (LMTLT).

Institutional Review Board Statement: Not applicable.

Informed Consent Statement: Not applicable.

Data Availability Statement: Data is contained within the article and supplementary material.

Conflicts of Interest: The authors declare no conflict of interest.

References

1. Holzinger, M.; Le Goff, A.; Cosnier, S. Nanomaterials for Biosensing Applications: A Review. *Front. Chem.* **2014**, *2*, 63. [CrossRef] [PubMed]
2. Moretta, R.; De Stefano, L.; Terracciano, M.; Rea, I. Porous Silicon Optical Devices: Recent Advances in Biosensing Applications. *Sensors* **2021**, *21*, 1336. [CrossRef] [PubMed]
3. Naresh, V.; Lee, N. A Review on Biosensors and Recent Development of Nanostructured Materials-Enabled Biosensors. *Sensors* **2021**, *21*, 1109. [CrossRef] [PubMed]
4. Mardosaitė, R.; Jurkevičiūtė, A.; Račkauskas, S. Superhydrophobic ZnO Nanowires: Wettability Mechanisms and Functional Applications. *Cryst. Growth Des.* **2021**, *21*, 4765–4779. [CrossRef]
5. Račkauskas, S.; Barbero, N.; Barolo, C.; Viscardi, G. ZnO Nanowire Application in Chemoresistive Sensing: A Review. *Nanomaterials* **2017**, *7*, 381. [CrossRef]

6. Tereshchenko, A.; Bechelany, M.; Viter, R.; Khranovskyy, V.; Smyntyna, V.; Starodub, N.; Yakimova, R. Optical Biosensors Based on ZnO Nanostructures: Advantages and Perspectives. A Review. *Sens. Actuator B-Chem.* **2016**, *229*, 664–677. [CrossRef]
7. Crisci, T.; Falanga, A.P.; Casalino, M.; Borbone, N.; Terracciano, M.; Chianese, G.; Gioffrè, M.; D'Errico, S.; Marzano, M.; Rea, I.; et al. Bioconjugation of a PNA Probe to Zinc Oxide Nanowires for Label-Free Sensing. *Nanomaterials* **2021**, *11*, 523. [CrossRef]
8. Rana, A.U.H.S.; Chang, S.-B.; Kim, H.-S. NH₄OH-Oriented and pH-Dependent Growth of ZnO Nanostructures via Microwave-Assisted Growth Method. *J. Nanosci. Nanotechnol.* **2018**, *18*, 2125–2127. [CrossRef]
9. Arya, S.K.; Saha, S.; Ramirez-Vick, J.E.; Gupta, V.; Bhansali, S.; Singh, S.P. Recent Advances in ZnO Nanostructures and Thin Films for Biosensor Applications: Review. *Anal. Chim. Acta* **2012**, *737*, 1–21. [CrossRef]
10. Sulciute, A.; Nishimura, K.; Gilshtein, E.; Cesano, F.; Viscardi, G.; Nasibulin, A.G.; Ohno, Y.; Račkauskas, S. ZnO Nanostructures Application in Electrochemistry: Influence of Morphology. *J. Phys. Chem. C* **2021**, *125*, 1472–1482. [CrossRef]
11. Moretta, R.; Terracciano, M.; Dardano, P.; Casalino, M.; De Stefano, L.; Schiattarella, C.; Rea, I. Toward Multi-Parametric Porous Silicon Transducers Based on Covalent Grafting of Graphene Oxide for Biosensing Applications. *Front. Chem.* **2018**, *6*, 583. [CrossRef] [PubMed]
12. Terracciano, M.; Rea, I.; Borbone, N.; Moretta, R.; Oliviero, G.; Piccialli, G.; De Stefano, L. Porous Silicon-Based Aptasensors: The next Generation of Label-Free Devices for Health Monitoring. *Molecules* **2019**, *24*, 2216. [CrossRef] [PubMed]
13. Chianese, G.; Terracciano, M.; Moretta, R.; Cappiello, P.; Vitiello, G.; Aronne, A.; Schiattarella, C.; De Stefano, L.; Rea, I. Synthesis and Surface Modification of Nanostructured F-Doped ZnO: Toward a Transducer for Label-Free Optical Biosensing. *Appl. Sci.* **2019**, *9*, 3380. [CrossRef]
14. Moretta, R.; Terracciano, M.; Borbone, N.; Oliviero, G.; Schiattarella, C.; Piccialli, G.; Falanga, A.P.; Marzano, M.; Dardano, P.; De Stefano, L.; et al. PNA-Based Graphene Oxide/Porous Silicon Hybrid Biosensor: Towards a Label-Free Optical Assay for Brugada Syndrome. *Nanomaterials* **2020**, *10*, 2233. [CrossRef] [PubMed]
15. Terracciano, M.; Galstyan, V.; Rea, I.; Casalino, M.; De Stefano, L.; Sberveglieri, G. Chemical Modification of TiO₂ Nanotube Arrays for Label-Free Optical Biosensing Applications. *Appl. Surf. Sci.* **2017**, *419*, 235–240. [CrossRef]
16. Martucci, N.M.; Rea, I.; Ruggiero, I.; Terracciano, M.; De Stefano, L.; Migliaccio, N.; Palmieri, C.; Scala, G.; Arcari, P.; Rendina, I.; et al. A New Strategy for Label-Free Detection of Lymphoma Cancer Cells. *Biomed. Opt. Express* **2015**, *6*, 1353–1362. [CrossRef]
17. Terracciano, M.; De Stefano, L.; Borbone, N.; Politi, J.; Oliviero, G.; Nici, F.; Casalino, M.; Piccialli, G.; Dardano, P.; Varra, M.; et al. Solid Phase Synthesis of a Thrombin Binding Aptamer on Macroporous Silica for Label Free Optical Quantification of Thrombin. *RSC Adv.* **2016**, *6*, 86762–86769. [CrossRef]
18. Zhang, S.; Geryak, R.; Geldmeier, J.; Kim, S.; Tsukruk, V.V. Synthesis, Assembly, and Applications of Hybrid Nanostructures for Biosensing. *Chem. Rev.* **2017**, *117*, 12942–13038. [CrossRef]
19. Fatehah, M.O.; Aziz, H.A.; Stoll, S. Stability of ZnO Nanoparticles in Solution. Influence of pH, Dissolution, Aggregation and Disaggregation Effects. *J. Colloid Sci. Biotechnol.* **2014**, *3*, 75–84. [CrossRef]
20. Terracciano, M.; Tramontano, C.; Moretta, R.; Miranda, B.; Borbone, N.; De Stefano, L.; Rea, I. Protein-Modified Porous Silicon Optical Devices for Biosensing. In *Porous Silicon for Biomedical Applications*; Elsevier: Amsterdam, The Netherlands, 2021; pp. 113–148.
21. De Stefano, L.; Oliviero, G.; Amato, J.; Borbone, N.; Piccialli, G.; Mayol, L.; Rendina, I.; Terracciano, M.; Rea, I. Aminosilane Functionalizations of Mesoporous Oxidized Silicon for Oligonucleotide Synthesis and Detection. *J. R. Soc. Interface* **2013**, *10*, 20130160. [CrossRef]
22. Terracciano, M.; Fontana, F.; Falanga, A.P.; D'Errico, S.; Torrieri, G.; Greco, F.; Tramontano, C.; Rea, I.; Piccialli, G.; De Stefano, L.; et al. Development of Surface Chemical Strategies for Synthesizing Redox-Responsive Diatomite Nanoparticles as a Green Platform for On-Demand Intracellular Release of an Antisense Peptide Nucleic Acid Anticancer Agent. *Small* **2022**, *18*, 2204732. [CrossRef] [PubMed]
23. Miranda, B.; Moretta, R.; Dardano, P.; Rea, I.; Forestiere, C.; De Stefano, L. H³ (Hydrogel-Based, High-Sensitivity, Hybrid) Plasmonic Transducers for Biomolecular Interactions Monitoring. *Adv. Mater. Technol.* **2022**, *7*, 2101425. [CrossRef]
24. Tramontano, C.; Martins, J.P.; De Stefano, L.; Kemell, M.; Correia, A.; Terracciano, M.; Borbone, N.; Rea, I.; Santos, H.A. Microfluidic-Assisted Production of Gastro-Resistant Active-Targeted Diatomite Nanoparticles for the Local Release of Galunisertib in Metastatic Colorectal Cancer Cells. *Adv. Healthc. Mater.* **2022**, 2202672. [CrossRef] [PubMed]
25. Xiong, G.; Pal, U.; Serrano, J.G.; Ucer, K.B.; Williams, R.T. Photoluminescence and FTIR Study of ZnO Nanoparticles: The Impurity and Defect Perspective. *Phys. Stat. Sol. C* **2006**, *3*, 3577–3581.
26. Thongam, D.D.; Gupta, J.; Sahu, N.K. Effect of Induced Defects on the Properties of ZnO Nanocrystals: Surfactant Role and Spectroscopic Analysis. *SN Appl. Sci.* **2019**, *1*, 1030. [CrossRef]
27. Riahimadvar, M.S.; Tajaldini, M. Fast and One-Step Synthesis of Small ZnO Nano-Tetrapods Using CO₂ Laser in Ambient Air: Physical Properties. *Phys. Scr.* **2022**, *97*, 105811. [CrossRef]
28. Khorsand Zak, A.; Majid, W.A.; Mahmoudian, M.R.; Darroudi, M.; Yousefi, R. Starch-Stabilized Synthesis of ZnO Nanopowders at Low Temperature and Optical Properties Study. *Adv. Powder Technol.* **2013**, *24*, 618–624. [CrossRef]
29. Papari, G.P.; Silvestri, B.; Vitiello, G.; De Stefano, L.; Rea, I.; Luciani, G.; Aronne, A.; Andreone, A. Morphological, Structural, and Charge Transfer Properties of F-Doped ZnO: A Spectroscopic Investigation. *J. Phys. Chem. C* **2017**, *121*, 16012–16020. [CrossRef]
30. Gonzalez-Hernandez, R.; Martinez, A.I.; Falcony, C.; Lopez, A.A.; Pech-Canul, M.I.; Hdz-Garcia, H.M. Study of the Properties of Undoped and Fluorine Doped Zinc Oxide Nanoparticles. *Mater. Lett.* **2010**, *64*, 1493–1495. [CrossRef]



31. Zeng, H.; Duan, G.; Li, Y.; Yang, S.; Xu, X.; Cai, W. Blue Luminescence of ZnO Nanoparticles Based on Non-Equilibrium Processes: Defect Origins and Emission Controls. *Adv. Funct. Mater.* **2010**, *20*, 561–572. [CrossRef]
32. Schiattarella, C.; Terracciano, M.; Defforge, T.; Gautier, G.; Della Ventura, B.; Moretta, R.; De Stefano, L.; Velotta, R.; Rea, I. Photoemissive Properties and Stability of Undecylenic Acid-Modified Porous Silicon Nanoparticles in Physiological Medium. *Appl. Phys. Lett.* **2019**, *114*, 113701. [CrossRef]
33. Hard, T.; Fan, P.; Kearns, D.R. A Fluorescence Study of the Binding of Hoechst 33258 and DAPI to Halogenated DNAs. *Photochem. Photobiol.* **1990**, *51*, 77–86. [CrossRef]
34. Rea, I.; Oliviero, G.; Amato, J.; Borbone, N.; Piccialli, G.; Rendina, I.; De Stefano, L. Direct Synthesis of Oligonucleotides on Nanostructured Silica Multilayers. *J. Phys. Chem. C* **2010**, *114*, 2617–2621. [CrossRef]
35. Fekete, M.; Riedel, W.; Patti, A.F.; Spiccia, L. Photoelectrochemical Water Oxidation by Screen Printed ZnO Nanoparticle Films: Effect of pH on Catalytic Activity and Stability. *Nanoscale* **2014**, *6*, 7585–7593. [CrossRef] [PubMed]
36. Rodrigues, J.; Pereira, S.O.; Zannoni, J.; Falcão, B.P.; Santos, N.F.; Moura, J.P.; Soares, M.R.; Rino, L.; Costa, F.M.; Monteiro, T. The Impact of Physiological Buffer Solutions on Zinc Oxide Nanostructures: Zinc Phosphate Conversion. *Mater. Today Chem.* **2022**, *23*, 100629. [CrossRef]
37. Moretta, R.; Terracciano, M.; Dardano, P.; Casalino, M.; Rea, I.; De Stefano, L. Covalent Grafting of Graphene Oxide on Functionalized Macroporous Silicon. *Open Mater. Sci.* **2018**, *4*, 15–22. [CrossRef]
38. Norberg, N.S.; Gamelin, D.R. Influence of Surface Modification on the Luminescence of Colloidal ZnO Nanocrystals. *J. Phys. Chem. B* **2005**, *109*, 20810–20816. [CrossRef]
39. Politi, J.; Dardano, P.; Caliò, A.; Iodice, M.; Rea, I.; De Stefano, L. Reversible Sensing of Heavy Metal Ions Using Lysine Modified Oligopeptides on Porous Silicon and Gold. *Sensor. Actuat. B-Chem.* **2017**, *244*, 142–150. [CrossRef]
40. Mondal, K.; Islam, M.; Singh, S.; Sharma, A. Fabrication of High Surface Area Microporous ZnO from ZnO/Carbon Sacrificial Composite Monolith Template. *Micromachines* **2022**, *13*, 335. [CrossRef]
41. Račkauskas, S.; Klimova, O.; Jiang, H.; Nikitenko, A.; Chernenko, K.A.; Shandakov, S.D.; Kauppinen, E.I.; Tolochko, O.V.; Nasibulin, A.G. A Novel Method for Continuous Synthesis of ZnO Tetrapods. *J. Phys. Chem. C* **2015**, *119*, 16366–16373. [CrossRef]
42. Terracciano, M.; Shahbazi, M.A.; Correia, A.; Rea, I.; Lamberti, A.; De Stefano, L.; Santos, H.A. Surface Bioengineering of Diatomite Based Nanovectors for Efficient Intracellular Uptake and Drug Delivery. *Nanoscale* **2015**, *7*, 20063–20074. [CrossRef] [PubMed]

Disclaimer/Publisher’s Note: The statements, opinions and data contained in all publications are solely those of the individual author(s) and contributor(s) and not of MDPI and/or the editor(s). MDPI and/or the editor(s) disclaim responsibility for any injury to people or property resulting from any ideas, methods, instructions or products referred to in the content.



Article

Comparison Study of Cytotoxicity of Bare and Functionalized Zinc Oxide Nanoparticles

Anna Król-Górniak^{1,2}, Katarzyna Rafińska^{1,2}, Fernanda Monedeiro^{1,2}, Paweł Pomastowski¹ 
and Bogusław Buszewski^{1,2,*} 

¹ Centre for Modern Interdisciplinary Technologies, Nicolaus Copernicus University in Torun, 4 Wileńska Str., 87-100 Torun, Poland; annkrol18@gmail.com (A.K.-G.); katrafinska@gmail.com (K.R.); fernandamonedeiro@hotmail.com (F.M.); pomastowski.pawel@gmail.com (P.P.)

² Environmental Chemistry and Bioanalytics, Faculty of Chemistry, Nicolaus Copernicus University in Torun, 7 Gagarina Str., 87-100 Torun, Poland

* Correspondence: bbusz@chem.umk.pl

Abstract: In this paper, a study of the cytotoxicity of bare and functionalized zinc oxide nanoparticles (ZnO NPs) is presented. The functionalized ZnO NPs were obtained by various types of biological methods including microbiological (intra- and extracellular with *Lactobacillus paracasei* strain), phytochemical (*Medicago sativa* plant extract) and biochemical (ovalbumin from egg white protein) synthesis. As a control, the bare ZnO NPs gained by chemical synthesis (commercially available) were tested. The cytotoxicity was measured through the use of (3-(4,5-dimethyl-2-thiazolyl)-2,5-diphenyl-2H-tetrazolium bromide (MTT) dye as well as lactate dehydrogenase (LDH) assays against murine fibroblast L929 and Caco-2 cell lines. As a complementary method, scanning electron microscopy (SEM) was performed to assess the morphology of the tested cells after treatment with ZnO NPs. The microscopic data confirmed the occurrence of apoptotic blebbing and loss of membrane permeability after the administration of all ZnO NPs. The reactive oxygen species (ROS) concentration during the cell lines' exposure to ZnO NPs was measured fluorometrically. Additionally, the photocatalytic degradation of methylene blue (MB) dye in the different light conditions, as well as the antioxidant activity of bare and functionalized ZnO NPs, is also reported. The addition of all types of tested ZnO NPs to methylene blue resulted in enhanced rates of photo-degradation in the presence of both types of irradiation, but the application of UV light resulted in higher photocatalytic activity of ZnO NPs. Furthermore, bare (chemically synthesized) NPs have been recognized as the strongest photocatalysts. In the context of the obtained results, a mechanism underlying the toxicity of bio-ZnO NPs, including (a) the generation of reactive oxygen species and (b) the induction of apoptosis, is proposed.

Keywords: zinc oxide nanoparticles; organic surface deposit; cytotoxicity assay; photocatalytic activity; ROS generation; toxicity mechanism



Citation: Król-Górniak, A.; Rafińska, K.; Monedeiro, F.; Pomastowski, P.; Buszewski, B. Comparison Study of Cytotoxicity of Bare and Functionalized Zinc Oxide Nanoparticles. *Int. J. Mol. Sci.* **2021**, *22*, 9529. <https://doi.org/10.3390/ijms22179529>

Academic Editors: Monica Terracciano, Ilaria Rea, Nicola Borbone and Chiara Tramontano

Received: 31 July 2021

Accepted: 30 August 2021

Published: 2 September 2021

Publisher's Note: MDPI stays neutral with regard to jurisdictional claims in published maps and institutional affiliations.



Copyright: © 2021 by the authors. Licensee MDPI, Basel, Switzerland. This article is an open access article distributed under the terms and conditions of the Creative Commons Attribution (CC BY) license (<https://creativecommons.org/licenses/by/4.0/>).

1. Introduction

Currently, zinc oxide is one of the main pillars of research in the field of nanotechnology and medicine, mainly due to its high applicability—it is widely used in many bactericidal formulations (such as ointments for controlling eczema) or in the cosmetic industry (in UV rays protection creams) [1,2]. The nanomaterials of zinc oxide, including bare nanoparticles (ZnO NPs), but also those functionalized with various types of surface modifications, attract special attention [3,4]. The concept of functionalization (inorganic core and organic deposition) is well known from the chromatographic sciences (the designing of stationary phases with specific modifications) and can be successfully applied to the nanotechnology field [5,6]. Some research groups have proposed the addition of polyethylene glycols (PEGs), which are known for their biocompatibility and biodegradation properties [7,8]. Another widely used type of functionalization is silica coating—silica is the most common material applied in analytical chemistry as column packing for liquid

chromatography [5,6], but the thin film of silica can be also used in nano deposition. It seems clear that the surface chemistry of ZnO NPs might be a decisive factor in describing the cell–nanoparticle interactions in in vitro studies. According to data in the literature, functionalized ZnO NPs consisting of an inorganic metal oxide core and organic surface deposition represent a new class of nanomaterials. Furthermore, they exhibit improved properties such as, e.g., stability, biocompatibility and toxicity, in comparison with native nanoparticles. However, not all types of the ZnO NPs' surface manipulation will result in the enhancement of such attributes. As an example, Yin et al. [9] modified ZnO NPs with a SiO₂ coating and performed a toxicity study on human lymphoblastoid cells. The experimental data proved that, regardless of the surface modification, the toxicity of bare and functionalized NPs was the same. Recently, a new approach based on the biological production of ZnO NPs was able to be suggested. Based on our latest experience, ZnO NPs can be described as functionalized due to the specific organic deposit on their surface, which comes from the bacterial biomass, for example, the probiotic *Lactobacillus paracasei* strain [10], plant extracts, e.g., *Medicago sativa* [11], or proteins, e.g., egg white protein [12], that is used in the synthesis process. The presence of characteristic organic residuals of natural origin on bio-ZnO NPs significantly increases their luminescence and antimicrobial properties [10–13]. This subject led our research group to the main motivation of the experiments presented in this paper—the interest in biologically synthesized ZnO NPs as a potentially safe agent for the treatment of oral and external bacterial infections.

Despite many potential medical applications of bio-ZnO NPs, it is necessary to consider the fact that each antimicrobial agent can be risky for human health because of its potential to reach any organ or tissue [4,14,15]. Nano-ZnO might have an impact on the loss of membrane integrity, the decrease in cells viability or even the activation of apoptosis [16]. The mechanisms underlying the nano-toxicity have been studied intensively, but there are still many questions and doubts. One of the possible toxicity mechanisms is the generation of reactive oxygen species (ROS) in cells after the nanomaterials' treatment [17,18]. The production of radicals by nano-ZnO is strongly related to the catalytic properties of this material. Zinc oxide is a wide-bandgap (3.3 eV) semiconductor and it is able to absorb the UV and other higher energy radiations, producing a hole in the valence band and a free electron in the conduction band [19]. The reactions of holes and/or electrons in ZnO NPs can further produce another activated reactive oxygen species [19,20]. The redox reactions caused by the photoinduced electrons (e⁻) and holes (h⁺) enhance the nano-ZnO photocatalytic activity [21]. The photocatalysis process is commonly used on an industrial scale for the degradation of dyes and pollutants in environmental samples, e.g., water [21–24].

On the other hand, nanomaterials can also show antioxidant activity, which means protecting cells from the damaging effects of reactive oxygen species [4,25–28]. This can be explained by the transfer of electron density located in oxygen to the odd electron located in the outer orbits of oxygen in OH• and O₂•⁻ radicals [17,29]. The totally different mode of nano-ZnO action might be associated with the concentration and colloidal stability of the used nanoparticles. Baskar et al. [26] revealed that the antioxidant activity of ZnO NPs followed a decreasing order with increasing concentrations of NP treatment. A similar result was described by Zafar with colleagues [28], who reported that, at lower concentrations, ZnO NPs showed increased 2,2-diphenyl-1-picrylhydrazyl (DPPH) activity in comparison with the higher content of nanoparticles. Moreover, according to [30], with the increasing of the concentration of ZnO NPs, the content of glutathione (GSH) in adipocyte cells also increased. Glutathione is a major antioxidant that can help prevent this process through the removal of ROS. With higher concentrations of ZnO NPs, the level of reactive oxygen species (ROS) was also increased. These results suggest the hypothesis that higher concentrations of nanomaterials exhibit pro-oxidative activity, while, at lower concentrations, the nanoparticles act as antioxidant agents [26,28,30].

According to the Food and Drug Administration (FDA) regulations, physicochemical characterization, assessment of the size distribution, in vitro and in vivo toxicology studies, and the evaluation of photocatalytic properties, are recommended for the safety assessment

of nano-ingredients [31]. Furthermore, the choice of the appropriate assay is important for the accurate assessment of NPs' cytotoxicity. Although there are clear guidelines for nanomaterials against cell lines, there is no consensus on the exact nano-ZnO toxicity mechanism. So far, the basic mechanism of nanotoxicity related to the size and concentration of NPs has been proposed. Valdiglesias with colleagues [32] tested the cytotoxic effect of ZnO NPs of around 100 nm in size on human SH-SY5Y neuronal cells with the MTT assay—the viability of the neuronal cells depended on the NPs' concentration. As for the second mechanism, the release of toxic zinc ions [33,34] or ROS production was suggested. Although the use of the ZnO NPs as photocatalysts is a great opportunity, it is important to remember that all of ROS might be responsible for lipid peroxidation, DNA damage or even the activation of apoptosis [18]. Punnoose et al. [35] demonstrated that the ZnO NP sample with the higher photocatalytic activity displayed around 1.5-fold stronger cytotoxic effect on the Hut-78 lymphoma T cell line.

However, despite numerous literature reports, the nanotoxicity mechanism is ambiguous and the specific determination of its foundations is still a challenge. Therefore, the concern for the correlation between photocatalytic activity and cytotoxicity of ZnO NPs seems to be crucial. The translation of biological and catalytic properties of ZnO to applied medicine is a novel approach and will allow the successful design of medical products such as, e.g., bed sore ointments.

Taking the above into consideration, a novel approach for evaluating the biological effect of synthesized ZnO NPs, based on complementary and interdisciplinary methods, is proposed. The present research compares the toxic potential of bare and functionalized ZnO NPs during biological synthesis via microbial (intra- and extracellular), plant-based and biochemical approaches, respectively. Cytotoxicity tests were performed on the Caco-2 and murine fibroblasts L929 cell lines using lactate dehydrogenase (LDH) and tetrazolium dye (MTT) assays. Based on the experimental data, the factors influencing the ZnO nanotoxicity (size, concentration, origin, and the presence of specific organic deposits on the surface) are demonstrated. Furthermore, the tight relationship between the oxidative potential of ZnO NPs (photocatalytic and antioxidant activity) with the cytotoxicity is shown. The described unique attributes of functionalized ZnO NPs indicate their potential for further application in medical fields. Finally, the results of the performed study support the proposed ZnO NPs' nanotoxicity mechanism.

2. Results and Discussion

2.1. Antioxidant Activity of ZnO NPs

In Figure 1, the DPPH scavenging activity of bare and functionalized ZnO NPs is presented. The obtained data indicate that the antioxidant activity of ZnO NPs depends on their concentration. At 200 µg/mL concentration, biochemically synthesized ZnO NPs (ZnO_Prot) have the highest ability to scavenge the DPPH radical ($48.87 \pm 4.21\%$), whereas the nanoparticles formed by *M. sativa* plant extract (ZnO_Phyto) and by *L. paracasei* LB3 cells (ZnO_Intra) exhibit the lowest antioxidant activity (32.54 ± 2.02 and $37.29 \pm 1.07\%$, respectively). With the decrease in the ZnO NPs' concentration, their scavenging activity increases to $84.62 \pm 1.25\%$ (ZnO_Prot), $79.59 \pm 3.54\%$ (ZnO_Phyto), $76.16 \pm 1.37\%$ (ZnO_Chem), $65.05 \pm 1.85\%$ (ZnO_Extra) and $56.31 \pm 1.21\%$ (ZnO_Intra) at 1.56 µg/mL concentration level, respectively (Figure 1). Analysis of variance (ANOVA) between the tested groups revealed the significant influence of the studied concentrations on the DPPH scavenging effect for the bio-ZnO NPs (p -value < 0.001) as compared to bare ZnO NPs.

The greatest increase in the antioxidant activity was observed for plant-based nano-ZnO (ZnO_Phyto). The higher ability of two ZnO NPs types (ZnO_Phyto and ZnO_Prot) to scavenge the DPPH radical might be related to the presence of biologically active groups on the surface of nanoparticles. As shown in the previous study [11], *Medicago sativa*, used for the biosynthesis, is a material that is rich in flavonoids, saponins or phenolic compounds. All of them have free radical scavenging abilities [36]. Interestingly, the interaction of flavonoids, such as zinc, with Me^{2+} may enhance the antioxidant properties

of the flavonoids [37]. During the biosynthesis of ZnO NPs with *M. sativa* (ZnO_Phyto), an increase in antioxidant activity was observed in comparison with a crude extract [11]. This is in a good correlation with the data obtained in present study. The next ZnO NPs with good antiradical properties were obtained from egg white protein, known as ovalbumin [12]. The data in the literature point out that proteins and peptides derived from egg white produce a good antioxidant effect [37–39]. Furthermore, the complexes of zinc with peptides [40] or amino acids (e.g., histidine) [41,42] were proven to have boosted the antioxidant properties.

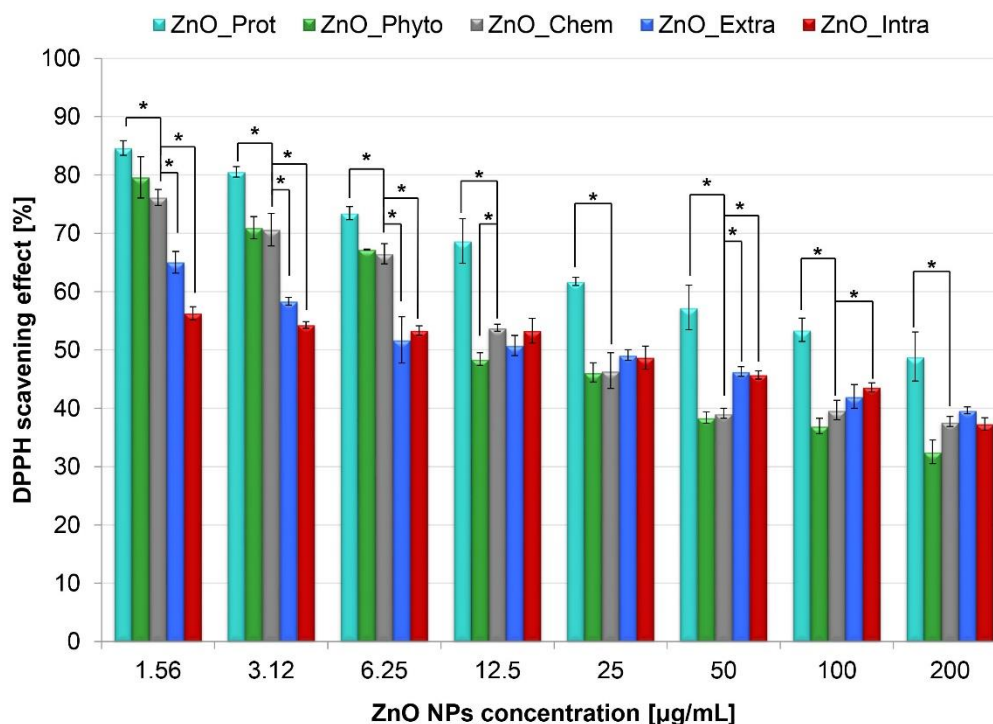


Figure 1. Antioxidant activity (%) of bare and functionalized ZnO NPs (at 200, 100, 50, 25, 12.5, 6.25, 3.12 and 1.56 µg/mL concentrations). The values are expressed as mean \pm SD values of three independent experiments ($n = 3$); * $p < 0.001$ compared to bare ZnO NPs (ANOVA).

2.2. Photocatalytic Degradation of Methylene Blue (MB) by ZnO NPs

The bare and functionalized ZnO NPs were used as a photocatalyst for the degradation of methylene blue dye under different light conditions (dark, sunlight and UV light at $\lambda = 365$ nm; Figure 2A). After 8 h of photocatalysis, the degradation of MB in the dark was the slowest in comparison with the light conditions (sunlight and UV irradiation). Moreover, for all types of tested nanoparticles, the percentage of MB degradation was in the range of 24.88 ± 1.3 – $29.12 \pm 1.4\%$ (dark). In the sunlight, at the same time (8 h), the MB degradation was found to be at the 32.37 ± 2.48 – $63.04 \pm 1.64\%$ level. The highest degradation of methylene blue was observed under UV irradiation and the percentage of this varied from 67.13 ± 1.42 to $82.22 \pm 1.1\%$. The greater efficiency of photocatalysis after UV irradiation finds its explanation in the semiconductor properties of zinc oxide. ZnO has a band gap of 3.3 eV, which corresponds to the emission in the UV region [19]. When the photon energy ($h\nu$) is equal or exceeds the band gap of the photocatalyst, the photon is absorbed. Next, the electron from the VB is excited to the CB—at the same time, the positive charge holes in the valance band are created. Then, the electron and hole pairs might take part in a series of redox reactions, leading to the formation of reactive oxygen species [20,21,31].

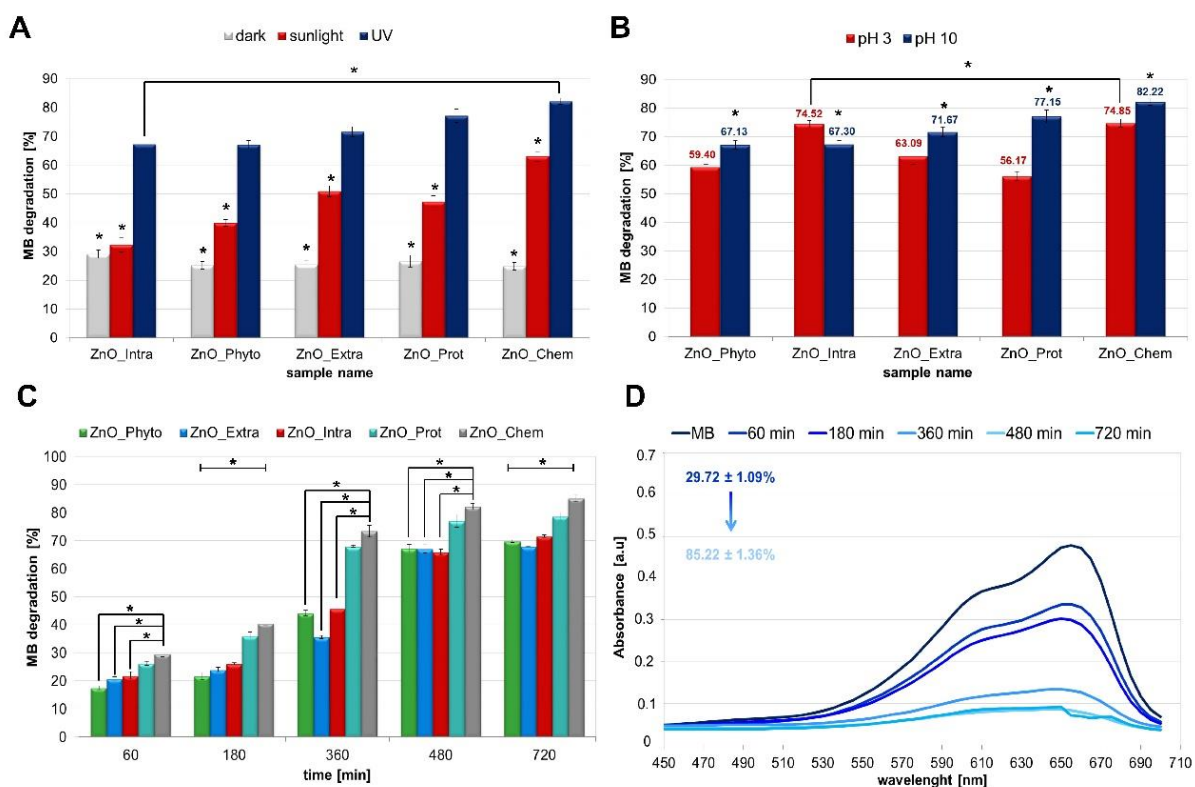


Figure 2. Photocatalytic activity of bare and functionalized ZnO NPs toward methylene blue (MB). The efficiency of MB photocatalytic degradation (%) (A) in different light conditions (dark, sunlight and UV irradiation), and (B) for different pH values (pH 3 and 10); (C) MB degradation time-dependency at pH 10 under UV irradiation; (D) UV-vis plot of MB in the presence of ZnO_Chem at pH 10 under UV irradiation. All ZnO NPs were at 1000 $\mu\text{g}/\text{mL}$ concentration. The values are expressed as mean \pm SD values of three independent experiments ($n = 3$); * $p < 0.001$ compared to bare ZnO NPs (ANOVA).

In addition to factors such as the type of irradiation or the type of nanoparticles used in photocatalysis, it is also important to consider the effect of pH [43,44]. In order to investigate the influence of pH on bare and functionalized ZnO NPs' photocatalytic activity, the degradation of MB dye was studied in acidic and alkaline conditions (Figure 2B). It was observed that the decolorization of methylene blue is strongly dependent on the pH of the solution, which plays an important role in photocatalytic degradation. From the chart (Figure 2B), it can be seen that about 56% and 77% of MB dye was degraded after 480 min illumination by the ZnO_Prot NPs at pH = 3 and pH = 10, respectively. This tendency was visible for almost all tested nanoparticles except for the ZnO_Intra NPs, which show a slightly higher ability to degrade the dye at pH = 3 (Figure 2B). The explanation of this phenomenon can be the fact that the alkaline pH value could provide a higher concentration of hydroxyl ions, which are able to react with holes and form hydroxyl radicals. In consequence, the photocatalytic degradation of methylene blue is enhanced [1,2]. Therefore, the presence of UV-irradiation and the pH value of 10 have been recognized as the most efficient conditions in terms of photocatalysis speed (Figure 2C) and were, therefore, chosen as the final experimental conditions. ANOVA on the tested experimental conditions revealed significant results (p -value < 0.001) (shown in Figure 2A–C), indicating that the type of tested ZnO NPs had a significant influence on the observed MB degradation, under all of the studied conditions. Additionally, Dunnett's post hoc test was performed in order to compare the results from each type of functionalized ZnO NPs in relation to the bare (ZnO_Chem) NPs. In addition, the average percentages of MB degradation, observed for conditions of dark, sunlight and UV light, were significantly different in all ZnO NPs ($p < 0.001$). The results of the post hoc assay are summarized in the Supplementary Material (Tables S1 and S2) and are presented in the form of asterisks in Figure 2.

Methylene blue dye shows a prominent peak at $\lambda = 665$ nm, as shown in Figure 2D. The peak intensity decreases gradually with the addition of ZnO NPs under UV irradiation and shows an increase in the MB degradation from 29.72 ± 1.09 to $85.22 \pm 1.36\%$ within 720 min. To sum up, among all tested nanoparticles, the bare chemically obtained NPs (ZnO_Chem) are considered as the most efficient photocatalysts. Those data are the opposite of the DPPH test results—the highest antioxidant activity was shown by the nanoparticles that were also the weakest photocatalysts (ZnO_Phyto). ZnO NPs synthesized by *M. sativa* aqueous extract showed a DPPH radical scavenging effect at the $79.59 \pm 3.54\%$ level (1.56 $\mu\text{g}/\text{mL}$ concentration), while the higher concentration (1000 $\mu\text{g}/\text{mL}$) of the tested nanoparticles allowed degradation only with $17.53 \pm 0.77\%$ of dye. This strongly supports the hypothesis that higher concentrations of nanomaterials exhibit pro-oxidative activity, while lower concentrations of nanoparticles act as antioxidant agents [29,45]. Furthermore, it is clear from the experimental data and our previous works [10–13] that the differences between the bare and functionalized ZnO NPs photocatalytic activity may be related to the size of the nanoparticles. Bare NPs (ZnO_Chem) were recognized as the strongest photocatalysts—the size of this nanomaterial was about 100 nm. The remaining functionalized NPs (ZnO_Prot, ZnO_Intra, ZnO_Phyto, ZnO_Extra) were smaller, at a size of 40, 16.7, 13.9 and 13.7 nm, respectively [10–13]. Thus, it can be stated that photocatalytic activity increases with the increase in the nano-ZnO particle size. The work of Kusiak-Nejman et al. [46] confirmed that the ZnO NPs' photoactivity under UV light increases mainly with the increase in the ZnO particle size. The highest phenol degradation was found for a ZnO sample with an average particle size of 71 nm [46]. Murakami et al. [47] prepared titanium(IV) oxide (TiO_2) NPs for the photocatalytic degradation of acetaldehyde. They found a size of about 40 nm to be optimal for the effectiveness of the photocatalysis process, mainly due to the optimized balance between efficient separation of redox sites and large specific surface area [47].

According to the data in the literature [19,48,49], the dyes' photo-degradation might be related to the generation of electron–hole pairs. The mechanism underlying the process described in this study is discussed later.

2.3. Cytotoxicity of ZnO NPs

To examine the cytotoxicity effect of bare and functionalized ZnO NPs in vitro, two cell lines—murine fibroblast L929 and human epithelial colorectal adenocarcinoma Caco-2—were chosen. Caco-2 cells show many morphological and biochemical similarities to intestinal cells, or enterocytes. In addition, this type of cell line is commonly used in the pharmaceutical industry as an in vitro model of the human small intestine mucosa to predict the absorption of orally administered drugs [50,51]. Moreover, Caco-2 cells were used as model to assess the toxicity of ZnO NPs in many studies [52–55]. The application of mouse fibroblast L929 cells is most frequently undertaken to evaluate cytotoxicity and may represent a sufficient in vitro screening model for skin formulations [56–58]. Furthermore, the cytotoxicity assay with mouse fibroblasts L929 is in compliance with ISO 10993-5 standards, and is often used for comparative studies of different types of nanoparticles [59].

The anti-proliferative effect was determined using two colorimetric assays—3-(4,5-dimethylthiazol-2-yl)-2,5-diphenyl tetrazolium bromide (MTT) and lactate dehydrogenase (LDH). The first of these, the MTT test, is based on the ability of mitochondrial dehydrogenase enzyme to convert yellow tetrazolium dye into formazan crystal. The rate of formazan crystal formation is directly proportional to cell viability; the untreated (positive) control is set to 100% viability [60,61]. In the LDH assay protocol, lactate dehydrogenase, as a soluble cytosolic enzyme, is released into the culture medium following the loss of membrane integrity. Then, LDH activity can be used as an indicator of cell membrane integrity and serve as a general means to assess cell viability by measuring plasma membrane permeability [62].

As shown in Figure 3A,B, the MTT results demonstrated that, for both types of cell lines, higher concentrations of ZnO NPs generated more serious cytotoxicity. At the

lowest concentration of 1.56 $\mu\text{g}/\text{mL}$, intracellularly synthesized ZnO NPs (ZnO_Intra) were able to reduce both Caco-2 and L929 cells' viability to 20.28 ± 9.54 and $26.09 \pm 6.74\%$, respectively. On the other hand, the biochemically synthesized NPs (ZnO_Prot) turned out to be the least toxic to cells—the concentration of 50 $\mu\text{g}/\text{mL}$ might be considered as an IC_{50} . At the highest concentration (100 and 200 $\mu\text{g}/\text{mL}$) (Figure 3C), all types of tested nanoparticles significantly reduced the cells' viability, while the bare and functionalized ZnO NPs were significantly more toxic to the fibroblasts L929 (Figure 3B). The work of Valdiguiesias et al. [32] also showed the concentration-dependent toxicity of nano-ZnO—significance was obtained from 25 $\mu\text{g}/\text{mL}$ for all of the treatments. Despite the crucial role of the ZnO NPs' dose, the size of the nanoparticles used should be also taken into consideration. Many papers indicate the influence of the nano-ZnO size on its further toxicity. Kang et al. [55] tested ZnO NPs at different sizes (26, 62 and 90 nm) against Caco-2 cells and observed that 26-nm ZnO NPs exhibited the highest toxicity. The different toxic effects of ZnO_Intra and ZnO_Prot NPs can be also explained by their various sizes—as mentioned above, the size of biochemically (ZnO_Prot) synthesized NPs was about 41 nm [12], whereas the ZnO_Intra NPs were smaller, at a size of 16.7 nm [10]. Furthermore, biologically synthesized NPs are functionalized by the specific organic deposit on their surface—the presence of organic residues was confirmed by the LDI-MS method in our previous study [13]. It was proven that the organic deposit plays an important role in the antibacterial action of nanomaterials. Silver [27] and zinc oxide NPs [13], naturally coated by microbial compounds, exhibit higher antibacterial effects compared with chemically synthesized nanomaterials. Intriguingly, the presence of the surface deposit might affect the cell-NPs interaction, and consequently, the intended bio-application of the obtained nanoparticles. As shown in the present paper, the extracellularly synthesized ZnO NPs, with organic deposits on their surfaces, were less toxic for Caco-2 cells than the chemically obtained NPs ($29.26 \pm 1.15\%$ and $4.81 \pm 1.57\%$, respectively, at 200 $\mu\text{g}/\text{mL}$ concentration).

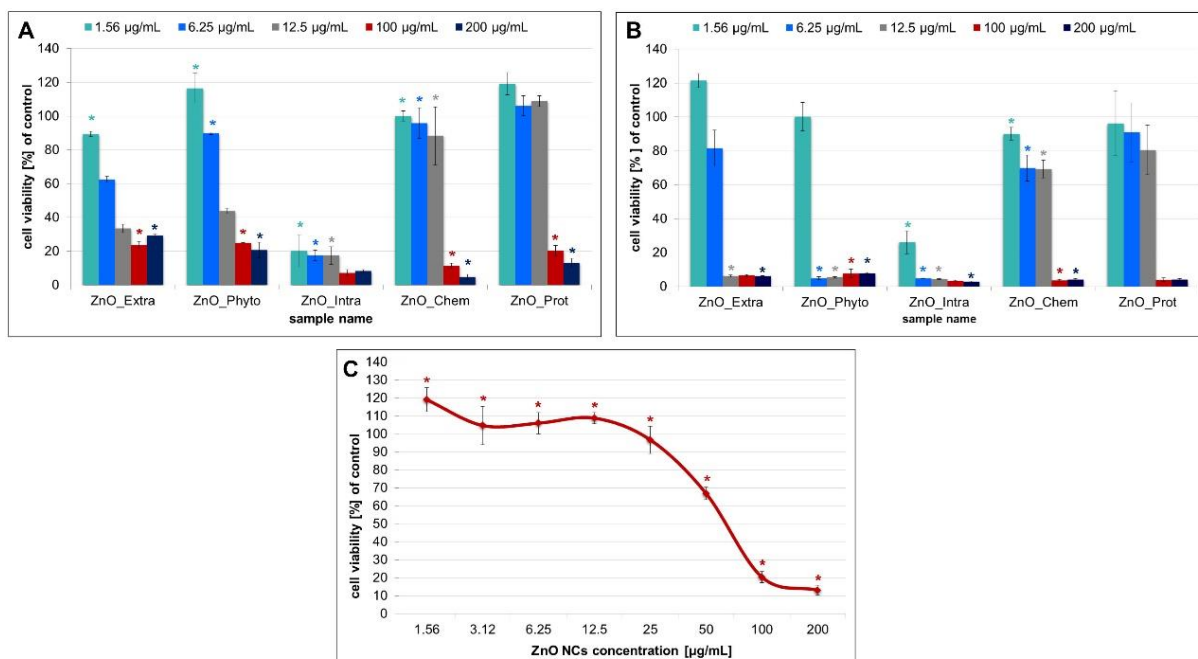


Figure 3. The MTT assay results and effects of indicated concentrations of bare and functionalized ZnO NPs on the (A) Caco-2 cells and (B) L929 cell viability. (C) the effect of different concentrations of biochemically synthesized ZnO NPs against the Caco-2 cell line. The values are expressed as mean \pm SD values of three independent experiments ($n = 3$); * $p < 0.001$ compared to bare ZnO NPs (ANOVA).

The MTT results presented in this paper are also in good correlation with the data from the photocatalytic study. The highest tested concentration of ZnO NPs resulted in

a significant reduction in the number of live cells (Figure 3) as well as in the degradation of MB dye (Figure 2A). The photocatalytic activity of nano-ZnO is connected to the toxic oxygen species [18,20,21]. In consequence, the toxicity of effect is enhanced.

The decrease in cell viability is very often correlated with apoptosis. Cell death occurred as a result of, e.g., cell membrane damage, and, in consequence, the release of LDH into the extracellular medium took place. In our study, LDH activity was measured to observe the effect of bare and functionalized ZnO NPs on membrane integrity by treating fibroblast L929 and Caco-2 cells. The results of this assay show that the enzyme release depends on the nanoparticles concentration, as shown in Figure 4. The ZnO_Chem and ZnO_Prot NPs exhibited a significant increase in LDH leakage at 25–100 µg/mL for the L929 cell line (Figure 4A,B). On the contrary, the intracellularly synthesized NPs (ZnO_Intra) already caused the release of LDH at the 1.56 µg/mL concentration level (Figure 4C) for both types of tested cells. The lack of leakage of LDH at 50–200 µg/mL was not due to a lack of ZnO_Intra NPs toxicity, but the fact that, at this concentration, the cell number was too small to give the correct results (Figure 4C). The tested nano-ZnO were more toxic against the fibroblast L929 than Caco-2 cell line. The higher sensitivity of murine fibroblasts could be explained by a different expression of specific control mechanisms, which play an important role in the differentiation and the apoptosis of various cells. One such mechanism is MAPKs (mitogen-activated protein kinases) [63]. Krüger et al. [64] showed that the addition of TiO₂ NPs activated the p38 mitogen-activated protein kinase pathways in Caco-2 cells and, furthermore, did not affect enterocyte differentiation. Another mechanism of cell lines' resistance might be associated with the induction or inhibition of the membrane transporting proteins. Guarnieri et al. [65] emphasized the correlation between metallic uptake, intracellular localization and cytotoxicity. Brück with colleagues [66] compared two different types of cells and showed that the protein expression patterns of membrane transporters in Caco-2 cells and jejunal cells differed notably. However, a detailed genomic and proteomic study regarding the exact nanotoxicity mechanism of tested nanoparticles is required to confirm the differences between the cell lines used in our study.

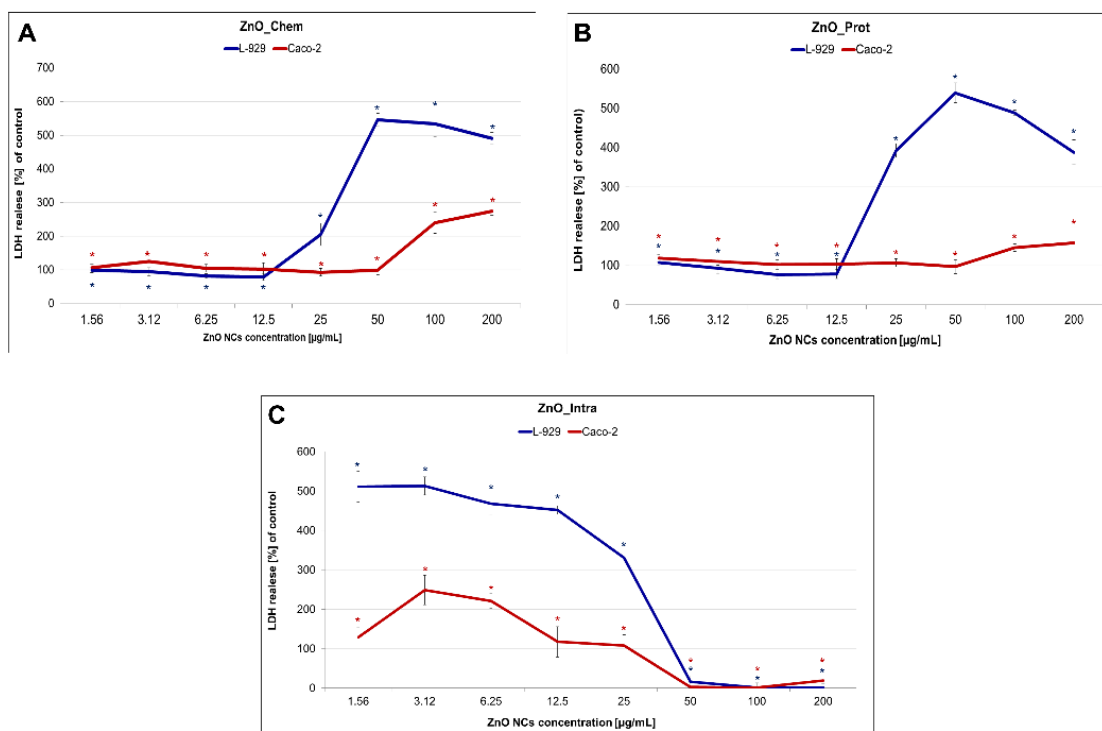


Figure 4. LDH leakage level of Caco-2 and L929 cells treated with different concentrations of (A) chemically, (B) biochemically and (C) intracellularly synthesized ZnO NPs. The values are expressed as mean \pm SD values of three independent experiments ($n = 3$); * $p < 0.001$ (ANOVA).

To observe the changes in murine fibroblast cells' morphology, scanning electron microscopy (SEM) images, after treatment with 6.25 $\mu\text{g}/\text{mL}$ of bare and functionalized ZnO NPs (the concentrations where an effect on the cell growth was noticed), were obtained. According to Figure 5, cells exposed to nano-ZnO differed significantly from the control. The L929 cells treated with the different types of nanoparticles became spherical and specific blebs were formed on their surface (Figure 5B–F). Moreover, the ZnO_Intra NPs caused the destruction of cells such as, e.g., cell membrane collapse (Figure 5D). All of the noticed morphological changes are related to the apoptosis process [67], in which the cell breaks into several vesicles, which are known as apoptotic bodies [68].

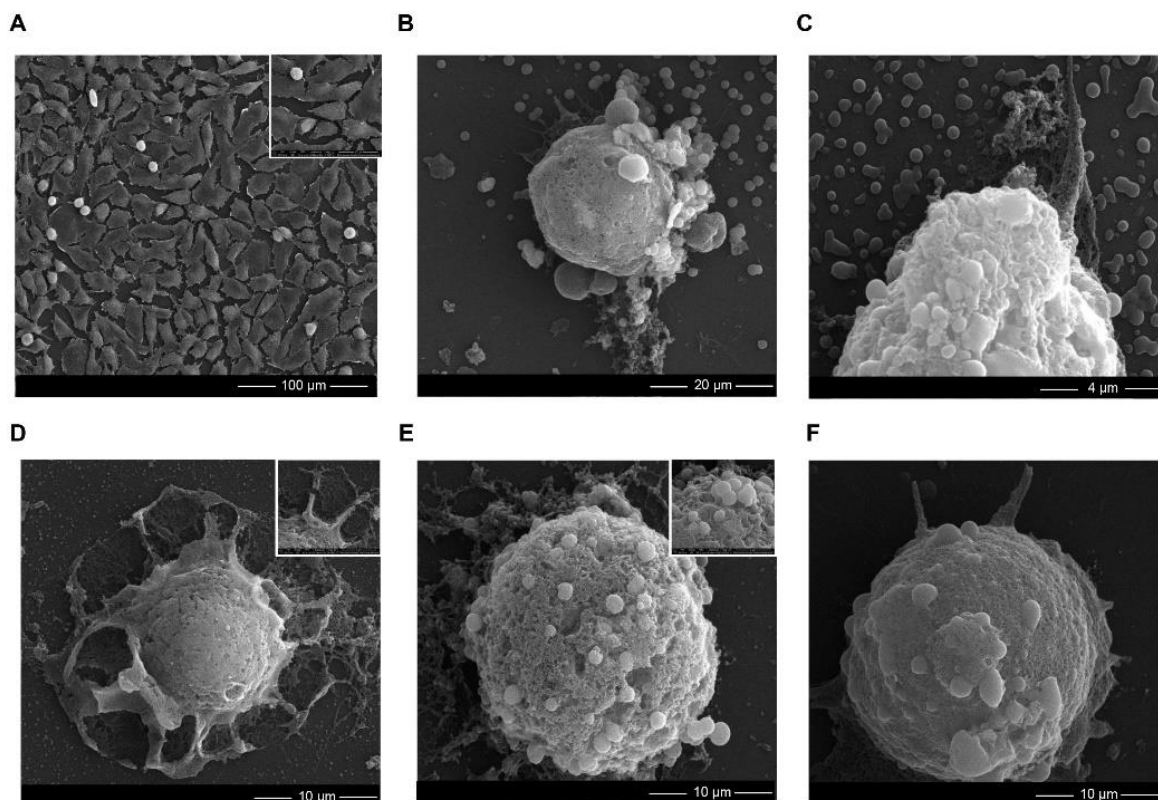


Figure 5. SEM analysis showing the morphology changes in L929 cells after the bare and functionalized ZnO NPs treatment. (A) control sample and L929 cells after the (B) extracellularly, (C) phytochemically, (D) intracellularly, (E) chemically and (F) biochemically synthesized ZnO NPs' exposure. The concentration of the used ZnO NPs was 6.25 $\mu\text{g}/\text{mL}$.

The interaction of nanoparticles with cells' surfaces leads to the loss of membrane integrity, but also presents itself in the production of reactive oxygen species (ROS). In order to detect the ROS involved in the MB degradation and the cytotoxicity of the tested bare and functionalized ZnO NPs, a fluorometric intracellular ROS Kit (Sigma-Aldrich, St. Louis, MO, USA) was used (Figure 6). Importantly, the applied kit detects superoxide and hydroxyl radicals in particular. Murine fibroblasts and human epithelium cells exposed to ZnO NPs exhibited a significant concentration-dependent increase in intracellular ROS generation. Figure 6 shows that intracellularly synthesized (ZnO_Intra) NPs cause the highest increase in ROS production—from $153.65 \pm 11.52\%$ (at 1.56 $\mu\text{g}/\text{mL}$) to $308.49 \pm 43.29\%$ (at 200 $\mu\text{g}/\text{mL}$). The observed tendency may be explained by the fact that, at higher NP concentrations, the higher amount of OH^\bullet and $\text{O}_2^{\bullet-}$ radicals production exceeds the defense capability of the cells [69]. Laurent et al. [70] and Popescu et al. [69] observed that treating cell lines with low amounts of ROS increased their proliferative rate, while further increased amounts of radicals resulted in cell death. Oxygen radicals were also found to be produced during the photocatalysis process [21]—the ZnO_Intra NPs were found to degrade the $71.67 \pm 0.47\%$ of methylene blue after 12 h and the same type of

nanocomposite showed the greatest production of ROS in tested cells. In contrast to the ZnO_Intra NPs, NPs obtained with OVA protein (ZnO_Prot) act as antioxidant agent at the lowest concentration ($75.19 \pm 29.46\%$ and $106.56 \pm 3.65\%$ for L929 and Caco-2 cell lines, respectively). For both types of tested cells, a similar trend was observed in terms of ROS production. It is strongly associated with DPPH assay results (Figure 1) and confirms the thesis that higher concentrations of nano-ZnO promote pro-oxidative activity, while lower concentrations act as antioxidant agents.

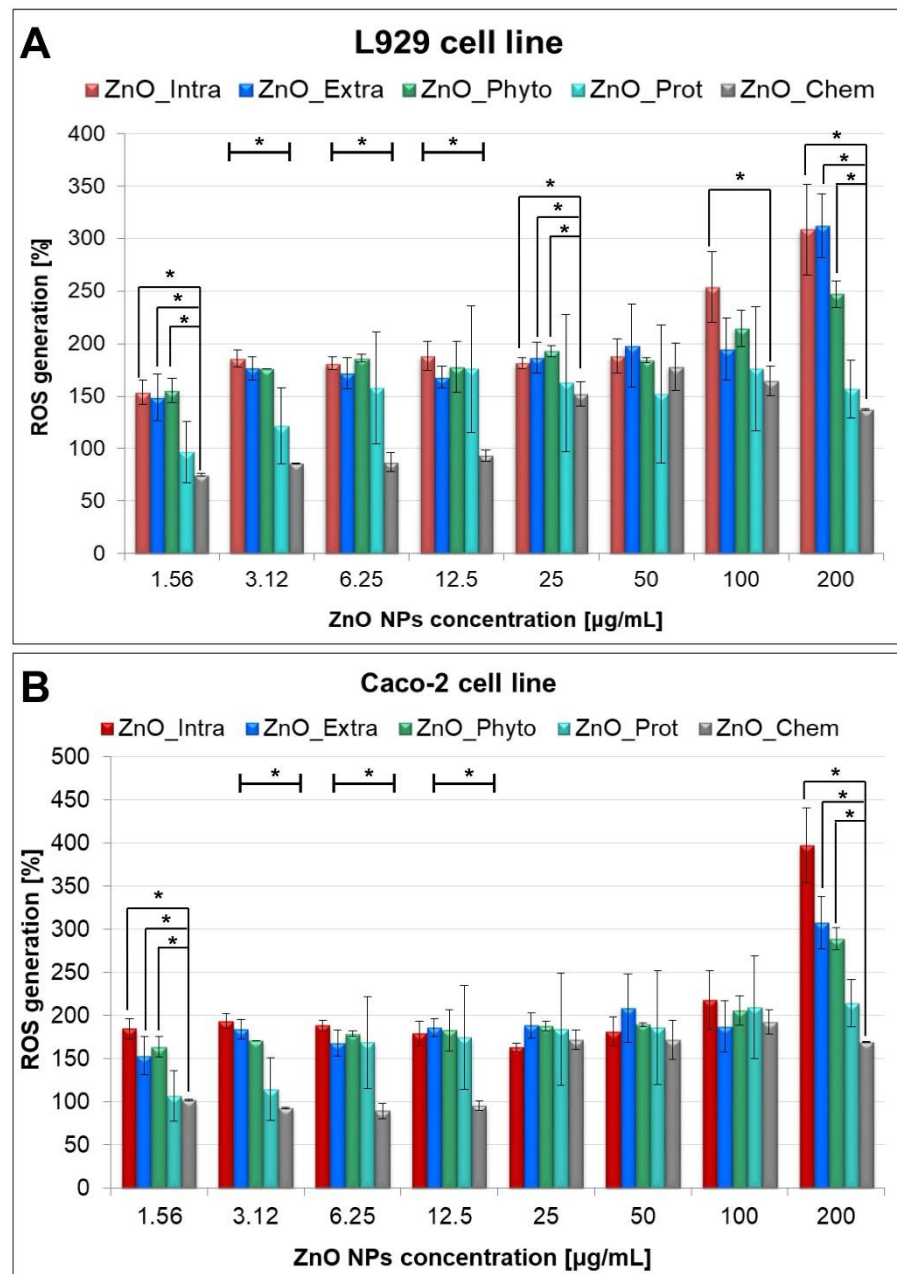


Figure 6. Concentration-dependent ROS generation by bare and functionalized ZnO-NPs in (A) L929 and (B) Caco-2 cells. The values are expressed as mean \pm SD values of three independent experiments ($n = 3$); * $p < 0.001$ compared to bare ZnO NPs (ANOVA).

In summary, based on the experimental data obtained in this study, it can be concluded that the type of biological synthesis influences the further toxic properties of functionalized ZnO NPs. The phyto- and biochemical synthesis resulted in the nanoparticles having high antioxidant activity toward the DPPH radical. It is well known that both raw sources used

for the ZnO NPs production (*Medicago sativa* extract and OVA protein [11,12]) have scavenging ability [36–39]. Furthermore, the interaction of metal ions (Me^{2+}), including zinc, with peptides [40] or flavonoids [37] might enhance the antioxidant properties. Intriguingly, the intracellular synthesis of nano-ZnO using the bacterial biomass [10] turns out to produce the most toxic nanoparticles. It might be related to their size (16.7 nm)—numerous factors, including composition, size and shape, are well known to influence nanotoxicity [71]. The crucial aspect is also the presence of organic deposits on the nanoparticles' surface, which might be the key in the reduction in ZnO NPs' toxicity. Experimental data from the actual study confirmed the presence of less cytotoxicity of extracellularly synthesized ZnO NPs [13] with organic constituents on the surface (against Caco-2 cells) compared to the bare, chemically obtained nanoparticles.

According to the data in the literature, it seems that the mechanism of toxicity depends on the aforementioned properties of the nanomaterials (size, concentration, catalytic/luminescence properties or surface characterization and coatings) [3,4,35,46]. However, the exact mechanisms and the material dependence of ZnO nanomaterials' cytotoxicity is still unclear. Metal oxide nanomaterials are well known to alter the environment around the cells and, thus, induce ROS generation [69,72]. It is also well reported that different mechanisms are proposed for nano-toxicity and one of them includes the production of radicals [4,14,17,18,73]. Based on the experimental results obtained in this study, it can be concluded that the generation of ROS plays a key role in the inhibition of cell growth, the loss of their membrane integrity and, in consequence, the apoptosis process. Moreover, the tight relationship between the harmful impact of the oxygen radical on the living cells and the bio-ZnO NPs' photocatalytic activity could clearly explain the probable mechanism of bio-ZnO NPs toxicity (Figure 7). During photocatalysis, specific electron–hole pairs are created—the reactions of holes and/or electrons in ZnO NPs lead to the production of reactive oxygen species (Figure 7B). Accordingly, the bio-NPs with greater catalytic properties also exhibited higher toxic impacts on the tested cell lines.

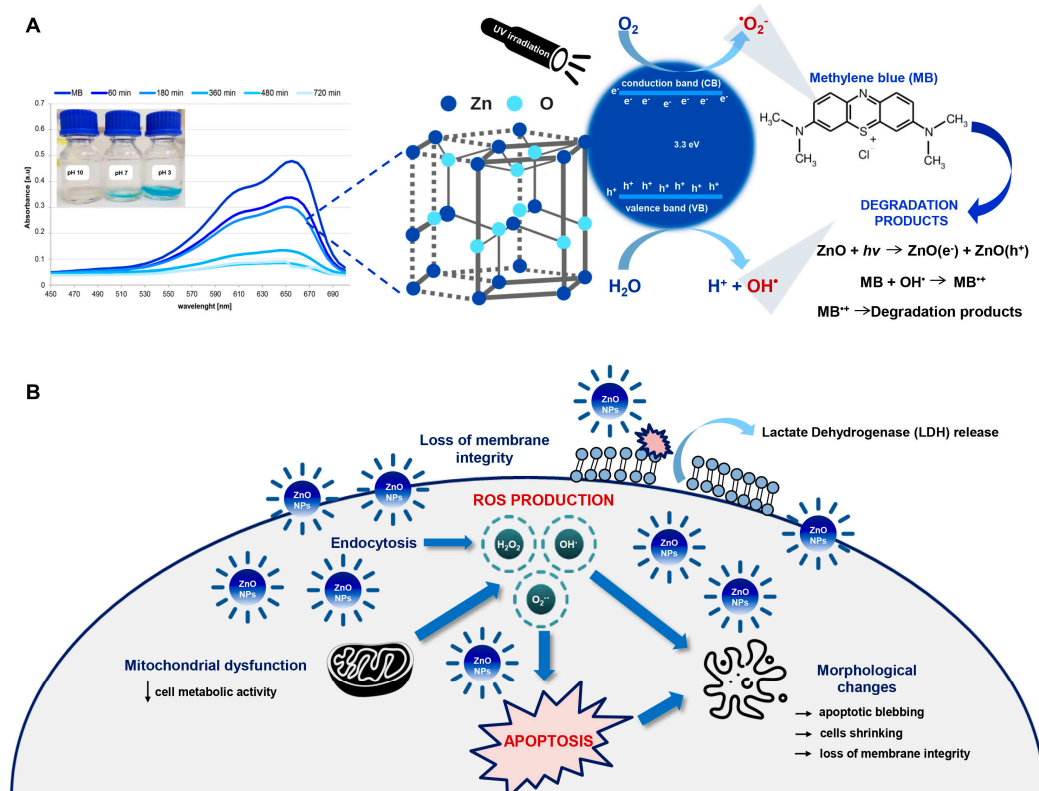


Figure 7. The proposed mechanism of (A) photocatalytic degradation of methylene blue and (B) cytotoxicity of functionalized ZnO NPs.

Despite the observed dose-dependent action of ZnO NPs, which is related to greater ROS production, attention should be also paid to another possible nanotoxicity mechanism. The smaller nanoparticles (e.g., ZnO_Intra; about 16.7 nm) have an extraordinary ability to internalize into living cells through different biological mechanisms and reach the nucleus, thereby generating genotoxic damage with the consequent triggering of apoptosis. Mittag et al. [74] investigated the cellular uptake of two differently sized ZnO NPs (<50 nm and <100 nm) against two human intestinal cell lines (Caco-2 and LT97). The outcomes of this study showed that ZnO NPs, at smaller sizes (<50 nm), led to the formation of micronuclei in LT97 cells. Micronucleus analysis is normally performed to examine whether some potentially toxic agent is able to cause chromosome damage [75]. To conclude, the smaller nanoparticles might often exhibit a strong genotoxic activity. Therefore, the undertaking of more detailed studies of ZnO NPs' genotoxicity seems to be crucial.

3. Materials and Methods

3.1. Biological Synthesis and Physicochemical Characterization of ZnO NPs

Four different biological methods of synthesis—phytochemical using *Medicago sativa* plant extract (ZnO_Phyto) [11], microbiological intracellular using *Lactobacillus paracasei* LB3 biomass (ZnO_Intra) [10], microbiological extracellular with *Lactobacillus paracasei* supernatant (ZnO_Extra) [13] and a biochemical approach with ovalbumin (OVA) protein (ZnO_Prot) [12]—were used to obtain the ZnO NPs. All biologically synthesized nanoparticles were functionalized by the presence of the specific organic deposit on their surface. ZnO_Prot, ZnO_Intra, ZnO_Phyto and ZnO_Extra NPs were found to have sizes of 40, 16.7, 13.9 and 13.7 nm, respectively. All further details of the synthesis methods as well as physicochemical characterization of all ZnO NPs are described in our previous papers.

For the comparison, in all experiments, bare chemically synthesized nano-ZnO (ZnO_Chem) NPs from Sigma-Aldrich, Poznań, Poland (CAS number: 1314-13-2; <110 nm particle size) were used.

3.2. Antioxidant Activity of ZnO NPs

Evaluation of the antioxidant activity of bare and functionalized ZnO NPs was performed using 2,2-diphenyl-1-picrylhydrazyl (DPPH) test [76]. The DPPH radical (Sigma-Aldrich, Steinheim, Germany), at 0.1 M concentration in methanol, was added to different concentrations (200, 100, 50, 25, 12.5, 6.25, 3.12 and 1.56 µg/mL) of each bio-ZnO NP at a ratio of 1:1. All samples were incubated in the dark for 30 min; after the incubation time, the UV-vis absorbance at $\lambda = 517$ nm was recorded using a NanoDrop 2000 spectrophotometer (Thermo Scientific, Waltham, MA, USA). The DPPH scavenging activity was calculated using the following equation:

$$AA\% = \frac{(A_0 - A_1)}{A_0} \times 100 \quad (1)$$

where A_0 and A_1 are absorbance of DPPH and ZnO NPs sample at $\lambda = 517$ nm, respectively. All of the experiments were prepared in triplicate.

3.3. Photocatalytic Degradation of Methylene Blue (MB) Dye by ZnO NPs

The bare and functionalized ZnO NPs were studied in terms of their catalytic properties under sunlight and UV-light ($\lambda = 365$ nm), during the degradation of methylene blue (MB) dye, according to a procedure adapted from [77]. The ZnO NPs, at 1000 µg/mL concentration, were added to the dye solutions (Aqua-Med, Łódź, Poland) at 0.015 mg/mL concentration and pH = 3 and 10. The mixture was magnetically stirred in dark conditions in order to maintain the absorption–desorption equilibrium. After the incubation, the suspension of MB dye and ZnO NPs was subjected to solar light and UV irradiation, respectively. The UV-vis spectra and absorption maxima ($\lambda = 665$ nm) were registered at fixed intervals using Varioskan TM LUX multimode microplate reader (Thermo Fisher Scientific, Waltham, MA, USA). The experiment was performed in triplicate, and the photocatalytic degradation was calculated using Equation (1), where A_0 and A_1 are the absorbance of MB

and MB with ZnO NPs sample at $\lambda = 665$ nm, respectively. As a control, the degradation of MB dye was carried out in dark conditions.

3.4. Cytotoxicity of ZnO NPs

The L929 normal mouse fibroblast cells and Caco-2 from human colon were obtained from the European Collection of Authenticated Cell Cultures. The cells were cultured as adherent monolayers in Dulbecco's modified Eagle's medium supplemented with 10% fetal bovine serum, 100 U/mL penicillin, and 100 $\mu\text{g}/\text{mL}$ streptomycin. Cells were passaged using 0.25% trypsin/EDTA every 3–4 days.

3.4.1. MTT, LDH Release and Intracellular ROS Assays

For MTT, LDH release and intracellular ROS assays, cells were cultured on 96-well plates at 2×10^5 cells/mL and incubated under 5% CO_2 at 37 °C for 24 h. When cells were adherent, ZnO NPs were added and incubated for another 24 h. In all cell experiments, the L929 and Caco-2 cells without ZnO NPs were used as controls. Then, 10 μL of Thiazolyl Blue Tetrazolium Bromide (MTT) solution (5 mg/mL in PBS) was added and incubated for 4 h at 37 °C. After incubation, medium from wells was discarded and the crystalline formazan was dissolved in DMSO. Absorbance was measured at $\lambda = 570$ nm using a Varioskan TM LUX multimode microplate reader (Thermo Fisher Scientific, Waltham, MA, USA). The results were expressed as percentages relative to the negative control—cells in standard medium without ZnO NPs that are considered as 100% viable. All experiments were performed in three independent replicates.

The LDH release assay was performed using a commercially available kit from Sigma Aldrich (Lactate Dehydrogenase Activity Assay Kit MAK066) and all samples were prepared according to the manufacturer's instructions. Absorbance was measured at $\lambda = 450$ nm using a Varioskan TM LUX multimode microplate reader (Thermo Fisher Scientific, Waltham, MA, USA). Briefly, cultured cells were incubated with bare and functionalized ZnO NPs to induce cytotoxicity and subsequently release lactate dehydrogenase (LDH). The LDH released into the medium was transferred to a new plate and mixed with 50 μL of the Reaction Mixture in each well. The plate was protected from light during the incubation (37 °C). The measurements of absorbance were taken each 5 min until the value of the most active sample was higher than the value of the highest standard in the standard curve (12.5 nmole/well). The results are presented as percentages of activity in comparison to control. All samples were run in the three independent replicates.

For reactive oxygen species measurements, the Fluorometric Intracellular ROS kit (MAK144), from Sigma-Aldrich, was used. All samples were prepared according to the manufacturer's instructions. To induce ROS, the cells, after bare and functionalized ZnO NPs treatment, were incubated in 96-well plates in a 5% CO_2 , 37 °C incubator for 24 h. After the incubation time, 100 μL of Master Reaction Mix were added to each well and the cells were incubated again in a 5% CO_2 , 37 °C incubator for 30 min. After that, the fluorescence intensities ($\lambda_{\text{ex}} = 540/\lambda_{\text{em}} = 570$ nm) were measured using a Varioskan TM LUX multimode microplate reader (Thermo Fisher Scientific, Waltham, MA, USA). Each experiment was performed in the three independent replicates.

The results of the LDH release and ROS level measurement are presented as percentages of reactive oxygen species in comparison to the control sample, and were calculated according to Kalińska et al. [78] and Lin et al. [79], respectively.

3.4.2. SEM Analysis

Adherent cells were fixed in 2.5% glutaraldehyde in PBS for 30 min and washed 3×5 min times in PBS. The next step was washing 2×2 min with dH_2O , dehydration in 95% EtOH for 1×2 min followed by 4×5 min in 100% EtOH. In the next step, cells were dehydrated 2×10 min with 100% HMDS at room temperature. Slides with cells were fixed on a holder with carbon tape and coated with Au with in a SC7620 Mini Sputter

Coater (Quorum Technologies, Lewes, UK). The cells were examined using a Quanta 3D FEG scanning electron microscope/focused ion beam (SEM/FIB).

3.4.3. Statistical Data Analysis

Significant differences among means of the groups were evaluated using one-way analysis of variance (ANOVA). The test was performed employing the software IBM SPSS Statistics v.23. Additionally, Dunnett's post hoc test was performed in order to compare the results from each type of functionalized ZnO NPs in relation to the bare (ZnO_Chem) NPs. The results of post hoc assay are summarized in the Supplementary Material (Tables S1–S6).

4. Conclusions

This study presents, for the first time, the comparative evaluation of the cytotoxicity of bare and functionalized ZnO NPs against L929 murine fibroblasts and Caco-2 cells as model cell lines. The outcomes of this work showed the dependence of ZnO NPs' concentration and size on their biological properties such as antioxidant, photocatalytic and cytotoxic activity. Moreover, the toxic action of functionalized ZnO NPs can be also connected to the presence of a specific organic deposit on their surface. Intracellularly and chemically synthesized ZnO NPs were considered to be the most toxic agent, while the ZnO NPs obtained with ovalbumin protein exhibited the lowest toxicity toward the tested cells. Intriguingly, cell lines showed different sensitivities to ZnO NP treatment—the murine fibroblast L929 was discovered to be more susceptible than Caco-2 cell lines. Accordingly, the functionalized bio-ZnO NPs might be a promising antibacterial agent when used as an oral treatment rather than in skin formulations. The ROS generation assay and SEM microscopy confirmed the oxidative stress induction and the morphological changes in the cells exposed to the ZnO NPs. Based on the data from our investigation, the bio-ZnO NPs toxicity mechanism was proposed—it is tightly related to the generation of ROS which leads to, e.g., the loss of membrane permeability, mitochondrial dysfunction and, at the highest concentrations, the apoptosis of cells.

Supplementary Materials: The following are available online at <https://www.mdpi.com/article/10.3390/ijms22179529/s1>.

Author Contributions: Conceptualization, A.K.-G., K.R., P.P. and B.B.; methodology, A.K.-G. and K.R.; software, A.K.-G. and K.R.; validation, all authors.; formal analysis, A.K.-G.; investigation, A.K.-G. and K.R.; resources, B.B.; data curation, A.K.-G. and K.R.; writing—original draft preparation, A.K.-G.; writing—review and editing, P.P. and B.B.; visualization, A.K.-G.; supervision, B.B.; project administration, B.B.; funding acquisition, P.P.; statistical analysis: F.M. All authors have read and agreed to the published version of the manuscript.

Funding: This research was funded by the National Science Centre within the framework of Opus 14 grant number 2017/27/B/ST4/02628 (2018–2021) and in the framework of the INCOOP project under the “Initiative of Excellence-Research University” (IoERU). Anna Król-Górniak obtained funds as part of the financing for a doctoral scholarship from the National Science Centre: Etiuda 7 No. 2019/32/T/ST4/00098 (2019–2020).

Institutional Review Board Statement: Not applicable.

Informed Consent Statement: Not applicable.

Data Availability Statement: Not applicable.

Conflicts of Interest: The authors declare no conflict of interest.

References

- Zhang, Y.; Nayak, T.; Hong, H.; Cai, W. Biomedical Applications of Zinc Oxide Nanomaterials. *Curr. Mol. Med.* **2013**, *13*, 1633–1645. [[CrossRef](#)] [[PubMed](#)]
- Raj, S.; Sumod, U.S.; Jose, S.; Sabitha, M. Nanotechnology in cosmetics: Opportunities and challenges. *J. Pharm. Bioallied Sci.* **2012**, *4*, 186–193. [[CrossRef](#)] [[PubMed](#)]

3. Kango, S.; Kalia, S.; Celli, A.; Njuguna, J.; Habibi, Y.; Kumar, R. Surface modification of inorganic nanoparticles for development of organic–inorganic nanocomposites—A review. *Prog. Polym. Sci.* **2013**, *38*, 1232–1261. [[CrossRef](#)]
4. Król, A.; Pomastowski, P.; Rafińska, K.; Railean-Plugaru, V.; Buszewski, B. Zinc oxide nanoparticles: Synthesis, antiseptic activity and toxicity mechanism. *Adv. Colloid Interface Sci.* **2017**, *249*, 37–52. [[CrossRef](#)]
5. Žuvela, P.; Skoczylas, M.; Liu, J.J.; Bączek, T.; Kaliszan, R.; Wong, M.W.; Buszewski, B. Column Characterization and Selection Systems in Reversed-Phase High-Performance Liquid Chromatography. *Chem. Rev.* **2019**, *119*, 3674–3729. [[CrossRef](#)] [[PubMed](#)]
6. Skoczylas, M.; Krzemińska, K.; Bocian, S.; Buszewski, B. Silica Gel and its Derivatization for Liquid Chromatography. In *Encyclopedia of Analytical Chemistry*; Meyers, R.A., Ed.; John Wiley and Sons: Hoboken, NJ, USA, 2017; pp. 1–39. [[CrossRef](#)]
7. Luo, M.; Shen, C.; Feltis, B.N.; Martin, L.; Hughes, A.E.; Wright, P.; Turney, T.W. Reducing ZnO nanoparticle cytotoxicity by surface modification. *Nanoscale* **2014**, *6*, 5791–5798. [[CrossRef](#)]
8. Karakoti, A.; Das, S.; Thevuthasan, S.; Seal, S. PEGylated Inorganic Nanoparticles. *Angew. Chem. Int. Ed.* **2011**, *50*, 1980–1994. [[CrossRef](#)] [[PubMed](#)]
9. Yin, H.; Casey, P.S.; McCall, M.J. Surface modifications of ZnO nanoparticles and their cytotoxicity. *J. Nanosci. Nanotechnol.* **2010**, *10*, 7565–7570. [[CrossRef](#)]
10. Król, A.; Railean-Plugaru, V.; Zloch, M.; Buszewski, B. Mechanism study of intracellular zinc oxide nanocomposites formation. *Colloids Surf. A Physicochem. Eng. Asp.* **2018**, *553*, 349–358. [[CrossRef](#)]
11. Król, A.; Railean-Plugaru, V.; Pomastowski, P.; Buszewski, B. Phytochemical investigation of Medicago sativa L. extract and its potential as a safe source for the synthesis of ZnO nanoparticles: The proposed mechanism of formation and antimicrobial activity. *Phytochem. Lett.* **2019**, *31*, 170–180. [[CrossRef](#)]
12. Buszewski, B.; Žuvela, P.; Król-Górniak, A.; Railean-Plugaru, V.; Rogowska, A.; Wong, M.W.; Yi, M.; Rodzik, A.; Sprynskyy, M.; Pomastowski, P. Interactions of zinc aqua complexes with ovalbumin at the forefront of the Zn²⁺/ZnO-OVO hybrid complex formation mechanism. *Appl. Surf. Sci.* **2021**, *542*, 148641. [[CrossRef](#)]
13. Pomastowski, P.; Król-Górniak, A.; Railean-Plugaru, V.; Buszewski, B. Zinc Oxide Nanocomposites—Extracellular Synthesis, Physicochemical Characterization and Antibacterial Potential. *Materials* **2020**, *13*, 4347. [[CrossRef](#)]
14. Vandebriel, R.J.; De Jong, W.H. A review of mammalian toxicity of ZnO nanoparticles. *Nanotechnol. Sci. Appl.* **2012**, *5*, 61–71. [[CrossRef](#)]
15. Zhao, J.; Stenzel, M.H. Entry of nanoparticles into cells: The importance of nanoparticle properties. *Polym. Chem.* **2018**, *9*, 259–272. [[CrossRef](#)]
16. Sruthi, S.; Ashtami, J.; Mohanan, P.V. Biomedical application and hidden toxicity of Zinc oxide nanoparticles. *Mater. Today Chem.* **2018**, *10*, 175–186. [[CrossRef](#)]
17. Fu, P.P.; Xia, Q.; Hwang, H.-M.; Ray, P.C.; Yu, H. Mechanisms of nanotoxicity: Generation of reactive oxygen species. *J. Food Drug Anal.* **2014**, *22*, 64–75. [[CrossRef](#)] [[PubMed](#)]
18. Schirmer, K. Mechanisms of Nanotoxicity. In *Nanoscience and the Environment*; Elsevier BV: Hoboken, NJ, USA, 2014; Volume 7, pp. 195–221.
19. Janotti, A.; Van de Walle, C.G. Fundamentals of zinc oxide as a semiconductor. *Rep. Prog. Phys.* **2009**, *72*, 126501. [[CrossRef](#)]
20. Nosaka, Y.; Nosaka, A. Understanding Hydroxyl Radical (•OH) Generation Processes in Photocatalysis. *ACS Energy Lett.* **2016**, *1*, 356–359. [[CrossRef](#)]
21. Nosaka, Y.; Nosaka, A.Y. Generation and Detection of Reactive Oxygen Species in Photocatalysis. *Chem. Rev.* **2017**, *117*, 11302–11336. [[CrossRef](#)]
22. Khalafi, T.; Buazar, F.; Ghanemi, K. Phycosynthesis and Enhanced Photocatalytic Activity of Zinc Oxide Nanoparticles Toward Organosulfur Pollutants. *Sci. Rep.* **2019**, *9*, 1–10. [[CrossRef](#)]
23. Pham, V.V.; Nguyen, T.D.; La, P.P.H.; Cao, M.T. A comparison study of the photocatalytic activity of ZnO nanoparticles for organic contaminants degradation under low-power UV-A lamp. *Adv. Nat. Sci. Nanosci. Nanotechnol.* **2020**, *11*, 015005. [[CrossRef](#)]
24. Balcha, A.; Yadav, O.P.; Dey, T. Photocatalytic degradation of methylene blue dye by zinc oxide nanoparticles obtained from precipitation and sol-gel methods. *Environ. Sci. Pollut. Res.* **2016**, *23*, 25485–25493. [[CrossRef](#)]
25. Singh, B.N.; Rawat, A.K.S.; Khan, W.; Naqvi, A.H.; Singh, B.R. Biosynthesis of Stable Antioxidant ZnO Nanoparticles by *Pseudomonas aeruginosa* Rhamnolipids. *PLoS ONE* **2014**, *9*, e106937. [[CrossRef](#)]
26. Baskar, V.; Nayeem, S.; Kuppuraj, S.P.; Muthu, T.; Ramalingam, S. Assessment of the effects of metal oxide nanoparticles on the growth, physiology and metabolic responses in in vitro grown eggplant (*Solanum melongena*). *3 Biotech* **2018**, *8*, 362. [[CrossRef](#)] [[PubMed](#)]
27. Viorica, R.-P.; Pawel, P.; Boguslaw, B. Use of *Lactobacillus paracasei* isolated from whey for silver nanocomposite synthesis: Antiradical and antimicrobial properties against selected pathogens. *J. Dairy Sci.* **2021**, *104*, 2480–2498. [[CrossRef](#)]
28. Zafar, H.; Ali, A.; Ali, J.S.; Haq, I.U.; Zia, M. Effect of ZnO Nanoparticles on Brassica nigra Seedlings and Stem Explants: Growth Dynamics and Antioxidative Response. *Front. Plant Sci.* **2016**, *7*, 535. [[CrossRef](#)] [[PubMed](#)]
29. Gordon, M.H. The Mechanism of Antioxidant Action in Vitro. In *Food Antioxidants*; Springer Science and Business Media LLC: Berlin/Heidelberg, Germany, 1990; pp. 1–18.
30. Muthuraman, P.; Ramkumar, K.; Kim, D.H. Analysis of Dose-Dependent Effect of Zinc Oxide Nanoparticles on the Oxidative Stress and Antioxidant Enzyme Activity in Adipocytes. *Appl. Biochem. Biotechnol.* **2014**, *174*, 2851–2863. [[CrossRef](#)] [[PubMed](#)]

31. FDA. Guidance for Industry: Safety of Nanomaterials in Cosmetic Products. Available online: <https://www.fda.gov/regulatory-information/search-fda-guidance-documents/guidance-industry-safety-nanomaterials-cosmetic-products#IIIB2> (accessed on 4 February 2021).
32. Valdiglesias, V.; Costa, C.; Kiliç, G.; Costa, S.; Pasaro, E.; Laffon, B.; Teixeira, J.P. Neuronal cytotoxicity and genotoxicity induced by zinc oxide nanoparticles. *Environ. Int.* **2013**, *55*, 92–100. [[CrossRef](#)] [[PubMed](#)]
33. Cierech, M.; Wojnarowicz, J.; Kolenda, A.; Krawczyk-Balska, A.; Prochwicz, E.; Woźniak, B.; Łojkowski, W.; Mierzwińska-Nastalska, E. Zinc Oxide Nanoparticles Cytotoxicity and Release from Newly Formed PMMA–ZnO Nanocomposites Designed for Denture Bases. *Nanomaterials* **2019**, *9*, 1318. [[CrossRef](#)] [[PubMed](#)]
34. Hackenberg, S.; Scherzed, A.; Technau, A.; Kessler, M.; Froelich, K.; Ginzkey, C.; Koehler, C.; Burghartz, M.; Hagen, R.; Kleinsasser, N. Cytotoxic, genotoxic and pro-inflammatory effects of zinc oxide nanoparticles in human nasal mucosa cells in vitro. *Toxicol. Vitro.* **2011**, *25*, 657–663. [[CrossRef](#)]
35. Punnoose, A.; Dodge, K.; Rasmussen, J.W.; Chess, J.; Wingett, D.; Anders, C. Cytotoxicity of ZnO Nanoparticles Can Be Tailored by Modifying Their Surface Structure: A Green Chemistry Approach for Safer Nanomaterials. *ACS Sustain. Chem. Eng.* **2014**, *2*, 1666–1673. [[CrossRef](#)] [[PubMed](#)]
36. Van Acker, S.A.; Berg, D.-J.V.D.; Tromp, M.N.; Griffioen, D.H.; Van Bennekom, W.P.; Van Der Vijgh, W.J.; Bast, A. Structural aspects of antioxidant activity of flavonoids. *Free. Radic. Biol. Med.* **1996**, *20*, 331–342. [[CrossRef](#)]
37. de Souza, R.F.V.; De Giovani, W.F. Synthesis, spectral and electrochemical properties of Al(III) and Zn(II) complexes with flavonoids. *Spectrochim. Acta Part A Mol. Biomol. Spectrosc.* **2005**, *61*, 1985–1990. [[CrossRef](#)] [[PubMed](#)]
38. Davalos, A.; Miguel, M.; Bartolomé, B.; López-Fandiño, R. Antioxidant Activity of Peptides Derived from Egg White Proteins by Enzymatic Hydrolysis. *J. Food Prot.* **2004**, *67*, 1939–1944. [[CrossRef](#)]
39. Abeyrathne, E.; Huang, X.; Ahn, D. Antioxidant, angiotensin-converting enzyme inhibitory activity and other functional properties of egg white proteins and their derived peptides—A review. *Poult. Sci.* **2018**, *97*, 1462–1468. [[CrossRef](#)]
40. Wang, C.; Li, B.; Wang, B.; Xie, N. Degradation and antioxidant activities of peptides and zinc–peptide complexes during in vitro gastrointestinal digestion. *Food Chem.* **2015**, *173*, 733–740. [[CrossRef](#)] [[PubMed](#)]
41. Yeomans, V.C.; Rechner, A.R.; Rice-Evans, C.A. The mechanism of action of zinc-histidine complex (Curazink[®]) as an anti-oxidant. *Free Radic. Res.* **2002**, *36*, 717–718. [[CrossRef](#)] [[PubMed](#)]
42. Williams, R.J.; Spencer, J.P.; Goni, F.M.; Rice-Evans, C.A. Zinc–histidine complex protects cultured cortical neurons against oxidative stress-induced damage. *Neurosci. Lett.* **2004**, *371*, 106–110. [[CrossRef](#)]
43. Reza, K.M.; Kurny, A.S.W.; Gulshan, F. Parameters affecting the photocatalytic degradation of dyes using TiO₂: A review. *Appl. Water Sci.* **2017**, *7*, 1569–1578. [[CrossRef](#)]
44. Azeez, F.; Al-Hetlani, E.; Arafa, M.; Abdelmonem, Y.; Nazeer, A.A.; Amin, M.O.; Madkour, M. The effect of surface charge on photocatalytic degradation of methylene blue dye using chargeable titania nanoparticles. *Sci. Rep.* **2018**, *8*, 1–9. [[CrossRef](#)]
45. Bedlovičová, Z.; Strapáč, I.; Baláž, M.; Salayová, A. A brief overview on antioxidant activity determination of silver nano-particles. *Molecules* **2020**, *25*, 3191. [[CrossRef](#)]
46. Kusiak-Nejman, E.; Wojnarowicz, J.; Morawski, A.W.; Narkiewicz, U.; Sobczak, K.; Gierlotka, S.; Lojkowski, W. Size-dependent effects of ZnO nanoparticles on the photocatalytic degradation of phenol in a water solution. *Appl. Surf. Sci.* **2021**, *541*, 148416. [[CrossRef](#)]
47. Murakami, N.; Kawakami, S.; Tsubota, T.; Ohno, T. Dependence of photocatalytic activity on particle size of a shape-controlled anatase titanium(IV) oxide nanocrystal. *J. Mol. Catal. A Chem.* **2012**, *358*, 106–111. [[CrossRef](#)]
48. Fox, M.A.; Dulay, M.T. Heterogeneous photocatalysis. *Chem. Rev.* **1993**, *93*, 341–357. [[CrossRef](#)]
49. Huszla, K.; Wysokowski, M.; Zgoła-Grześkowiak, A.; Staszak, M.; Janczarek, M.; Jesionowski, T.; Wyrwas, B. UV-light photocatalytic degradation of non-ionic surfactants using ZnO nanoparticles. *Int. J. Environ. Sci. Technol.* **2021**, *2021*, 1–16. [[CrossRef](#)]
50. Sambuy, Y.; De Angelis, I.; Ranaldi, G.; Scarino, M.L.; Stammati, A.; Zucco, F. The Caco-2 cell line as a model of the intestinal barrier: Influence of cell and culture-related factors on Caco-2 cell functional characteristics. *Cell Biol. Toxicol.* **2005**, *21*, 1–26. [[CrossRef](#)] [[PubMed](#)]
51. Sun, H.; Chow, E.C.; Liu, S.; Du, Y.; Pang, K.S. The Caco-2 cell monolayer: Usefulness and limitations. *Expert Opin. Drug Metab. Toxicol.* **2008**, *4*, 395–411. [[CrossRef](#)]
52. Kang, T.; Guan, R.; Song, Y.; Lyu, F.; Ye, X.; Jiang, H. Cytotoxicity of zinc oxide nanoparticles and silver nanoparticles in human epithelial colorectal adenocarcinoma cells. *LWT—Food Sci. Technol.* **2015**, *60*, 1143–1148. [[CrossRef](#)]
53. Song, Y.; Guan, R.; Lyu, F.; Kang, T.; Wu, Y.; Chen, X. In vitro cytotoxicity of silver nanoparticles and zinc oxide nanoparticles to human epithelial colorectal adenocarcinoma (Caco-2) cells. *Mutat. Res. Mol. Mech. Mutagen.* **2014**, *769*, 113–118. [[CrossRef](#)] [[PubMed](#)]
54. Wu, C.; Luo, Y.; Liu, L.; Xie, Y.; Cao, Y. Toxicity of combined exposure of ZnO nanoparticles (NPs) and myricetin to Caco-2 cells: Changes of NP colloidal aspects, NP internalization and the apoptosis-endoplasmic reticulum stress pathway. *Toxicol. Res.* **2019**, *8*, 613–620. [[CrossRef](#)] [[PubMed](#)]
55. Kang, T.; Guan, R.; Chen, X.; Song, Y.; Jiang, H.; Zhao, J. In vitro toxicity of different-sized ZnO nanoparticles in Caco-2 cells. *Nanoscale Res. Lett.* **2013**, *8*, 496. [[CrossRef](#)]
56. Nagaraja, S.; Basavarajappa, G.; Attimarad, M.; Pund, S. Topical Nanoemulgel for the Treatment of Skin Cancer: Proof-of-Technology. *Pharmaceutics* **2021**, *13*, 902. [[CrossRef](#)]

57. Da Silva, S.M.M.; Costa, C.R.R.; Gelfuso, G.M.; Guerra, E.N.S.; Nóbrega, Y.K.D.M.; Gomes, S.M.; Pic-Taylor, A.; Fonseca-Bazzo, Y.M.; Silveira, D.; Magalhães, P.D.O. Wound Healing Effect of Essential Oil Extracted from *Eugenia dysenterica* DC (Myrtaceae) Leaves. *Molecules* **2018**, *24*, 2. [CrossRef]
58. Gunes, S.; Tamburaci, S.; Dalay, M.C.; Gurhan, I.D. In vitro evaluation of *Spirulina platensis* extract incorporated skin cream with its wound healing and antioxidant activities. *Pharm. Biol.* **2017**, *55*, 1824–1832. [CrossRef]
59. ISO 10993-5: Biological Evaluation of Medical Devices—Part 5: Tests for In Vitro Cytotoxicity. Available online: <https://www.iso.org/standard/36406.html> (accessed on 26 August 2021).
60. Hussain, R.F.; Nouri, A.M.E.; Oliver, R.T.D. A new approach for measurement of cytotoxicity using colorimetric assay. *J. Immunol. Methods* **1993**, *160*, 89–96. [CrossRef]
61. Kumar, P.; Nagarajan, A.; Uchil, P. Analysis of Cell Viability by the MTT Assay. *Cold Spring Harb. Protoc.* **2018**, *2018*, 469–471. [CrossRef] [PubMed]
62. Kumar, P.; Nagarajan, A.; Uchil, P. Analysis of Cell Viability by the Lactate Dehydrogenase Assay. *Cold Spring Harb. Protoc.* **2018**, *2018*, 465–468. [CrossRef] [PubMed]
63. Soares-Silva, M.; Diniz, F.F.; Gomes, G.N.; Bahia, D. The Mitogen-Activated Protein Kinase (MAPK) Pathway: Role in Immune Evasion by Trypanosomatids. *Front. Microbiol.* **2016**, *7*, 183. [CrossRef] [PubMed]
64. Kruger, K.; Cossais, F.; Neve, H.; Klempt, M. Titanium dioxide nanoparticles activate IL8-related inflammatory pathways in human colonic epithelial Caco-2 cells. *J. Nanoparticle Res.* **2014**, *16*, 1–12. [CrossRef]
65. Guarnieri, D.; Sabella, S.; Muscetti, O.; Belli, V.; Malvindi, M.A.; Fusco, S.; De Luca, E.; Pompa, P.P.; Netti, P. Transport across the cell-membrane dictates nanoparticle fate and toxicity: A new paradigm in nanotoxicology. *Nanoscale* **2014**, *6*, 10264–10273. [CrossRef] [PubMed]
66. Brück, S.; Strohmeier, J.; Busch, D.; Drozdziak, M.; Oswald, S. Caco-2 cells—Expression, regulation and function of drug transporters compared with human jejunal tissue. *Biopharm. Drug Dispos.* **2016**, *38*, 115–126. [CrossRef] [PubMed]
67. Burattini, S.; Falcieri, E. Analysis of Cell Death by Electron Microscopy. *Methods Mol. Biol.* **2013**, *1004*, 77–89. [CrossRef] [PubMed]
68. Kakarla, R.; Hur, J.; Kim, Y.J.; Kim, J.; Chwae, Y.-J. Apoptotic cell-derived exosomes: Messages from dying cells. *Exp. Mol. Med.* **2020**, *52*, 1–6. [CrossRef]
69. Popescu, T.; Matei, C.O.; Vlaicu, I.D.; Tivig, I.; Kuncser, A.C.; Stefan, M.; Ghica, D.; Miclea, L.C.; Savopol, T.; Culita, D.C.; et al. Influence of surfactant-tailored Mn-doped ZnO nanoparticles on ROS production and DNA damage induced in murine fibroblast cells. *Sci. Rep.* **2020**, *10*, 1–14. [CrossRef]
70. Laurent, A.; Nicco, C.; Chéreau, C.; Goulvestre, C.; Alexandre, J.; Alves, A.; Lévy, E.; Goldwasser, F.; Panis, Y.; Soubrane, O.; et al. Controlling tumor growth by modulating endogenous production of reactive oxygen species. *Cancer Res.* **2005**, *65*, 948–956.
71. Suresh, A.K.; Pelletier, D.A.; Wang, W.; Morrell-Falvey, J.L.; Gu, B.; Doktycz, M.J. Cytotoxicity Induced by Engineered Silver Nanocrystallites Is Dependent on Surface Coatings and Cell Types. *Langmuir* **2012**, *28*, 2727–2735. [CrossRef]
72. Singh, R.; Cheng, S.; Singh, S. Oxidative stress-mediated genotoxic effect of zinc oxide nanoparticles on *Deinococcus radiodurans*. *3 Biotech* **2020**, *10*, 66. [CrossRef] [PubMed]
73. Vazquez-Munoz, R.; Borrego, B.; Juarez-Moreno, K.O.; García-García, M.; Mota-Morales, J.; Bogdanchikova, N.; Huerta-Saquero, A. Toxicity of silver nanoparticles in biological systems: Does the complexity of biological systems matter? *Toxicol. Lett.* **2017**, *276*, 11–20. [CrossRef]
74. Mittag, A.; Hoera, C.; Kämpfe, A.; Westermann, M.; Kuckelkorn, J.; Schneider, T.; Gleis, M. Cellular Uptake and Toxicological Effects of Differently Sized Zinc Oxide Nanoparticles in Intestinal Cells. *Toxics* **2021**, *9*, 96. [CrossRef] [PubMed]
75. Hayashi, M. The micronucleus test—Most widely used in vivo genotoxicity test. *Genes Environ.* **2016**, *38*, 1–6. [CrossRef] [PubMed]
76. Brand-Williams, W.; Cuvelier, M.; Berset, C. Use of a free radical method to evaluate antioxidant activity. *LWT Food Sci. Technol.* **1995**, *28*, 25–30. [CrossRef]
77. Thirukumar, P.; Atchudan, R.; Parveen, A.S.; Kalaiarasan, K.; Lee, Y.R.; Kim, S.-C. Fabrication of ZnO nanoparticles adorned nitrogen-doped carbon balls and their application in photodegradation of organic dyes. *Sci. Rep.* **2019**, *9*, 1–13. [CrossRef]
78. Kalińska, A.; Jaworski, S.; Wierzbicki, M.; Gołębiewski, M. Silver and Copper Nanoparticles—An Alternative in Future Mastitis Treatment and Prevention? *Int. J. Mol. Sci.* **2019**, *20*, 1672. [CrossRef] [PubMed]
79. Zhu, L.; Schrand, A.M.; Voevodin, A.A.; Chang, N.W.; Dai, L.; Hussain, S.M. Assessment of Human Lung Macrophages After Exposure to Multi-Walled Carbon Nanotubes Part I. Cytotoxicity. *Nanosci. Nanotechnol. Lett.* **2011**, *3*, 88–93. [CrossRef]



Review

Sustainable Biodegradable Biopolymer-Based Nanoparticles for Healthcare Applications

Nika Kučuk¹, Mateja Primožič¹, Željko Knez^{1,2}  and Maja Leitgeb^{1,2,*} 

¹ Faculty of Chemistry and Chemical Engineering, University of Maribor, Smetanova Ulica 17, 2000 Maribor, Slovenia

² Faculty of Medicine, University of Maribor, Taborska Ulica 8, 2000 Maribor, Slovenia

* Correspondence: maja.leitgeb@um.si; Tel.: +386-2-2294-462

Abstract: Biopolymeric nanoparticles are gaining importance as nanocarriers for various biomedical applications, enabling long-term and controlled release at the target site. Since they are promising delivery systems for various therapeutic agents and offer advantageous properties such as biodegradability, biocompatibility, non-toxicity, and stability compared to various toxic metal nanoparticles, we decided to provide an overview on this topic. Therefore, the review focuses on the use of biopolymeric nanoparticles of animal, plant, algal, fungal, and bacterial origin as a sustainable material for potential use as drug delivery systems. A particular focus is on the encapsulation of many different therapeutic agents categorized as bioactive compounds, drugs, antibiotics, and other antimicrobial agents, extracts, and essential oils into protein- and polysaccharide-based nanocarriers. These show promising benefits for human health, especially for successful antimicrobial and anticancer activity. The review article, divided into protein-based and polysaccharide-based biopolymeric nanoparticles and further according to the origin of the biopolymer, enables the reader to select the appropriate biopolymeric nanoparticles more easily for the incorporation of the desired component. The latest research results from the last five years in the field of the successful production of biopolymeric nanoparticles loaded with various therapeutic agents for healthcare applications are included in this review.

Keywords: nanoparticles; biopolymers; therapeutic substances; incorporation; biocompatibility; healthcare; biomedical applications



Citation: Kučuk, N.; Primožič, M.; Knez, Ž.; Leitgeb, M. Sustainable Biodegradable Biopolymer-Based Nanoparticles for Healthcare Applications. *Int. J. Mol. Sci.* **2023**, *24*, 3188. <https://doi.org/10.3390/ijms24043188>

Academic Editor: Bruno Rizzuti

Received: 29 December 2022

Revised: 1 February 2023

Accepted: 2 February 2023

Published: 6 February 2023



Copyright: © 2023 by the authors. Licensee MDPI, Basel, Switzerland. This article is an open access article distributed under the terms and conditions of the Creative Commons Attribution (CC BY) license (<https://creativecommons.org/licenses/by/4.0/>).

1. Introduction

The field of nanotechnology, which encompasses the synthesis, development, and application of nanomaterials in a size range from 1 to 100 nm, has gained increasing interest in various areas in recent years. Among other things, nanomaterials, especially nanoparticles, play an important role, especially in the field of healthcare applications, where they offer higher efficiency and lower toxicity [1–3].

Treatment of various life-threatening diseases, such as chronic diseases (e.g., cancer, heart disease, HIV/AIDS, diabetes) and severe neurological and infectious diseases, is becoming increasingly challenging. Nanomaterials are successfully addressing these challenges by finding new ways for potential treatment, intending to overcome the obstacles of conventional treatment forms [1,2,4]. Various existing formulations for the treatment of certain diseases are poorly soluble, resulting in minimal systemic bioavailability, unstable in vivo, reducing the efficacy of the drug, and causing toxic side effects, even to normal cells. Furthermore, they can cause nephrotoxicity, neurovirulence, and gastrointestinal reactions. Drug resistance may also occur, reducing the impact of further treatment [5].

Nanomaterials are defined as materials with at least one dimension smaller than 100 nm [2,6]. Compared to bulk materials, nanomaterials have different physicochemical properties, such as different shapes, surface area, size, and reactivity, leading to their exceptional performance in many applications. Nanomaterials can be classified according

to different criteria [7,8]. One is the classification into four different categories depending on the dimensionality, as shown in Figure 1. Zero-dimensional nanomaterials (0-D) include nanoparticles, fullerenes, and quantum dots. All their three dimensions are in the nanometer range. In one-dimensional nanomaterials (1-D), one dimension is outside the nanoscale, while the other two are inside the nanoscale. This classification includes nanofibers, nanorods, nanotubes, nanowires, and nanohorns. Two-dimensional nanomaterials (2-D), such as nanofilms, nanosheets, and nanolayers, have two dimensions beyond the nanoscale. The most common examples of three-dimensional nanomaterials (3-D) or bulk nanomaterials are core shells, arrays of nanotubes, and nanowires. In this category, the materials are not in the nanoscale in any dimension [2,6,9–12].

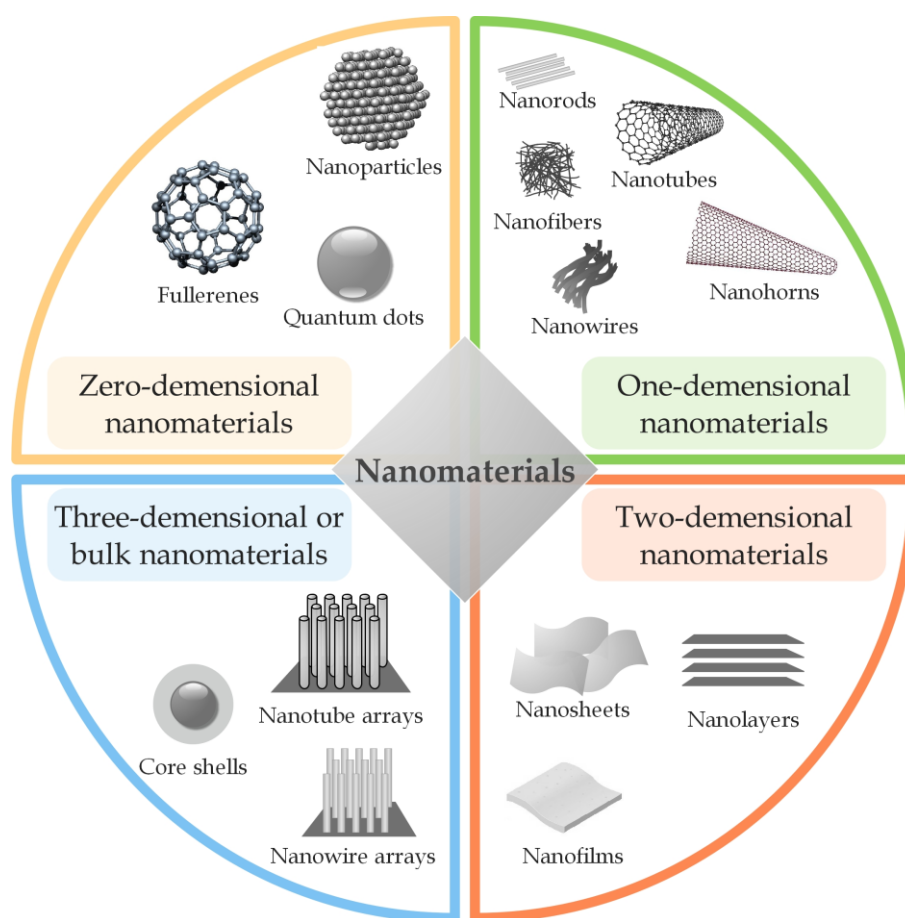


Figure 1. Classification of nanomaterials according to dimensionality (summarized from [2,6,13]).

Nanotechnology-based formulations enable better, more effective, and safer use of drugs for the prevention and treatment of various conditions, which is why the production of new nanocarriers for therapeutic agents is becoming increasingly important [1].

A variety of nanoparticles with unique physical and chemical characteristics hold promise for disease diagnosis, biological imaging, and nanomedicine applications [1,14]. They provide the ability to protect the drug from premature degradation, improve intracellular penetration, prolong release, increase absorption and efficacy of the drug at the target site, and therefore represent significant potential in the healthcare sector [4].

It is important to note that the most crucial factor in the production of nanoparticles is to avoid biological and physical barriers such as diffusion, protein adsorption, aggregation, renal or hepatic clearance, and phagocytic sequestration [14].

An important advantage of nanoparticles is that they can be reused after the removal of the incorporated component, which is an important contribution to the circular economy from an economic point of view [15].

Nanoparticles can also be divided according to their composition, meaning according to the material from which they are produced. These include in particular organic, inorganic, and carbon-based nanoparticles (Figure 2) [16]. Carbon-based nanoparticles consist only of carbon atoms and have different morphologies. They are divided into fullerenes, graphene, carbon black, carbon quantum dots, carbon nanotubes, and nanodiamonds [2,7,17,18]. Non-carbon nanoparticles are inorganic nanoparticles and can be produced from pure metals (Au, Ag, Al, Zn, Fe, Cd), metal oxides (ZnO, TiO₂, MnO₂, Fe₂O₃, Al₂O₃), semiconductors (CdS, ZnS), and ceramics (SiO₂, ZrO₂) [7,16,19]. Organic nanoparticles include proteins, lipids, polymers, carbohydrates, or other organic compounds and can be classified as synthetic or natural. They are biocompatible, biodegradable, generally non-toxic, and improve pharmacokinetic properties, bioavailability, and drug targeting. Examples are liposomes, polymersomes, micelles, polymer constructs, and protein complexes [2,19,20].

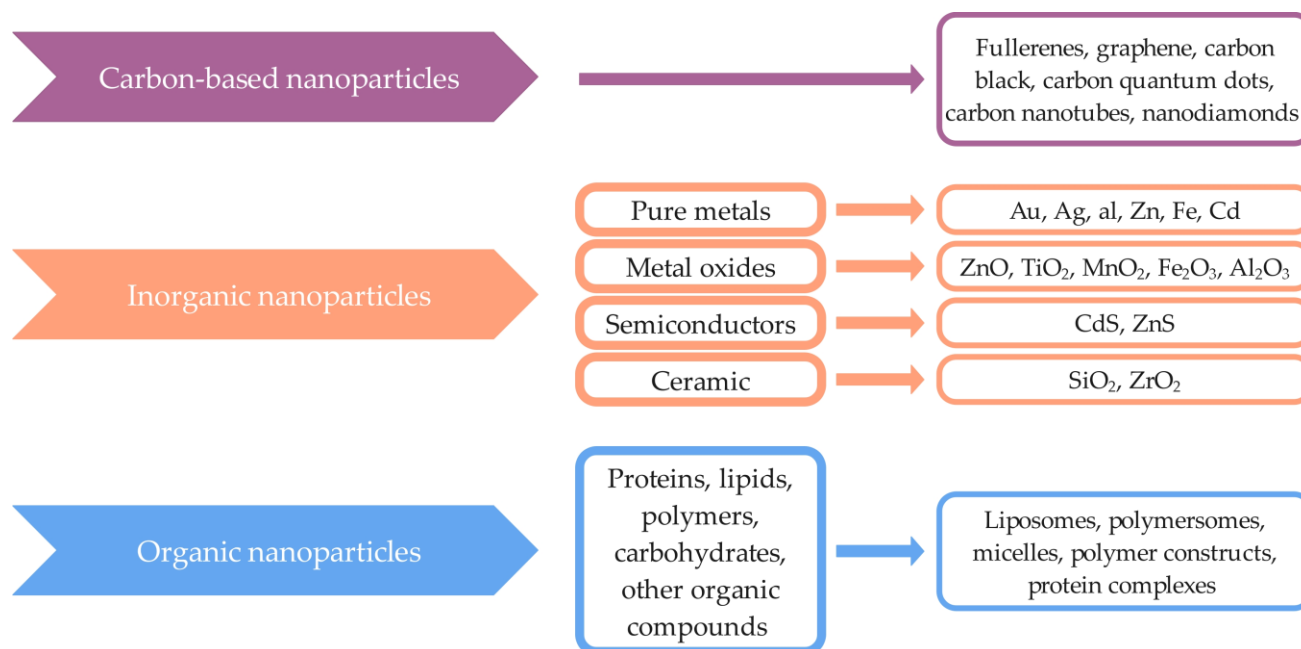


Figure 2. Classification of nanomaterials based on their chemical composition (summarized from [7,16,18]).

Inorganic nanoparticles, especially metal- and metal oxide-based nanoparticles, are among the most popular. In various applications, such as drug delivery, they are characterized by good stability and half-life of the carrier in the bloodstream, adequate biodistribution, and targeted delivery of the drug to the desired target site [21]. For example, gold nanoparticles are used for numerous diagnostic purposes [22], and silver nanoparticles are also important in biomedicine, primarily because of their antimicrobial potential [23]. Among the metal oxide nanoparticles, ZnO nanoparticles should be highlighted, which are biocompatible, non-toxic, non-expensive, and provide effective antibacterial activity and UV protection [24].

However, they are harmful to the environment, soil, water, and the organisms in them. In addition, some can be very toxic to the human body. Therefore, their use is limited because the body cannot metabolize and excrete them [3]. In contrast, biopolymeric nanoparticles are suitable for various healthcare applications due to their biocompatibility, biodegradability, nontoxicity, and other advantageous properties. The review article covers the latest research results of the last five years on nanoparticles based on natural biopolymers such as proteins and polysaccharides of animal, plant, algal, fungal, and

bacterial origin. Special emphasis is paid to the incorporation of various therapeutic agents such as bioactive agents, conventional drugs, antibiotics, and other antimicrobial agents, extracts, and essential oils into biopolymeric nanoparticles. These thus represent promising delivery systems that prevent potential adverse side effects of therapeutic agents, enable targeted delivery to target sites, and thus contribute to enhanced therapeutic efficacy and sustained release.

2. Polymeric Nanoparticles

Drug delivery systems must meet specific criteria, such as being biocompatible, biodegradable, stable, non-toxic, non-immunogenic, cost-effective, selective, easy to produce, and delivering and releasing drugs only at specific locations. When using free dosage forms, not only diseased but also healthy cells, tissues, organs, or subcellular organs can be damaged during drug administration and release. Various delivery systems, such as nanoparticles with encapsulated drugs, can successfully circumvent these limitations (Figure 3) [25–27]. Drug delivery systems also make it possible to achieve the desired therapeutic effect of drugs and, at the same time, greater efficiency and safety, as well as controlled release of the drug at the target site and prevent aggregation and reduce possible side effects of delivered drugs [25,28,29].

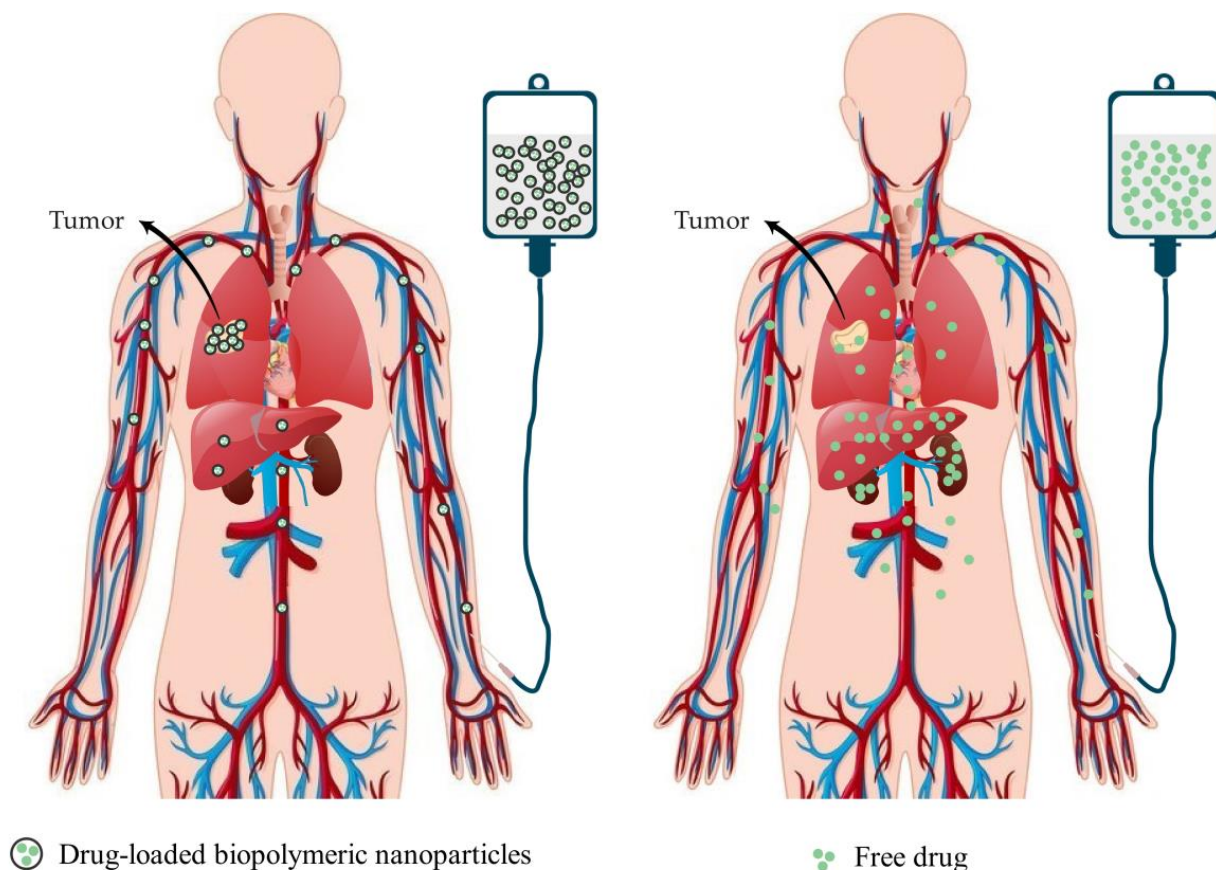


Figure 3. Biodistribution of the drug after intravenous administration when contained in biopolymeric nanoparticles (left) compared to the free drug (right) (summarized from [30]).

Polymer-based nanoparticles are important as alternative carriers for various therapeutic agents for different medicinal purposes mainly due to their biodegradability, biocompatibility, non-immunogenicity, and non-toxicity [29]. Drugs can be incorporated into polymeric nanoparticles by physical or chemical means, i.e., by various adsorption processes on their surface after the nanoparticle formation or by incorporation of drugs into the nanoparticles during the production process. The loading efficacy of therapeutic

tic agents on or into nanoparticles is mainly influenced by nanoparticle size, molecular weight and solubility of drugs, and chemical interactions between drugs and nanoparticles. The release rate of therapeutic agents from polymeric nanoparticles is primarily based on the desorption of surface-bound or adsorbed therapeutic agents, diffusion of therapeutic agents from polymeric nanoparticles, erosion of polymeric nanoparticles, and the combined process of diffusion and erosion [31,32]. Polymeric nanoparticles offer several advantages. They increase the absorption of loaded drugs, provide protection against degradation, prolong the circulation time, and ensure delivery to the target site due to their good solubility, safety and stability, and long-term release [33]. They can be of synthetic or natural origin. However, synthetic polymers can be toxic and immunogenic. Therefore, natural and biodegradable polymers offer better opportunities for nanoparticle production for various biomedical applications [29,34]. Figure 4 shows the advantages and disadvantages schematically and provides examples of synthetic and natural polymers.

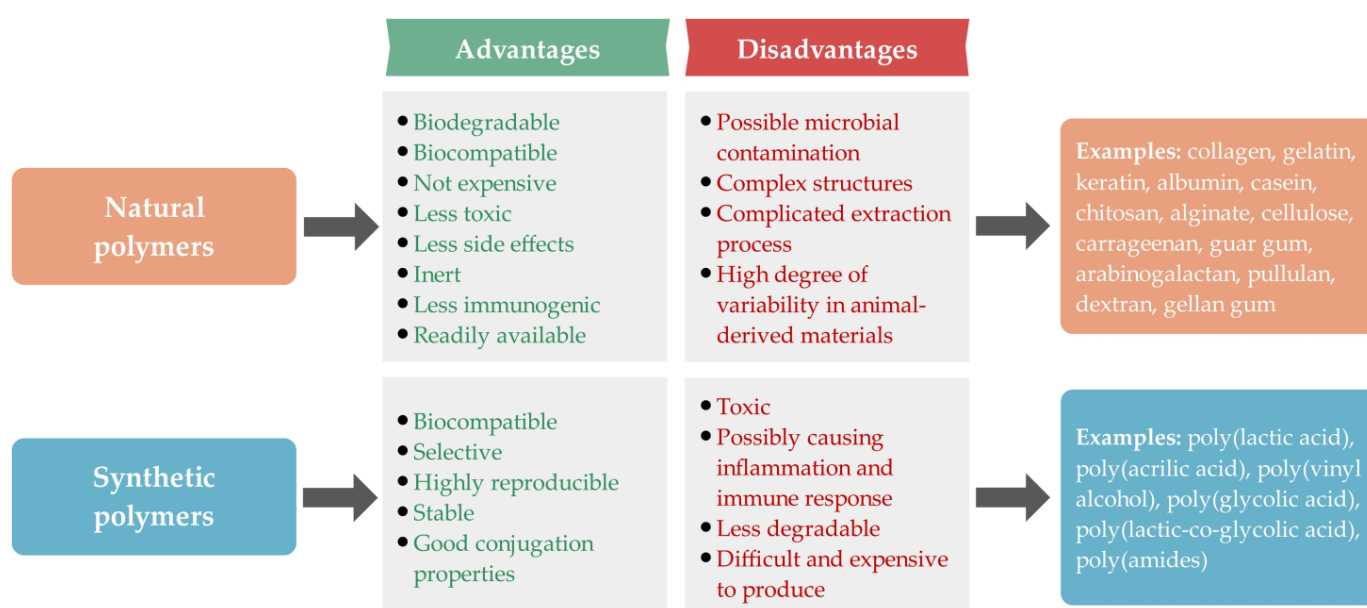


Figure 4. Advantages and disadvantages of natural and synthetic polymers (summarized from [35–37]).

2.1. Biopolymers Used for the Preparation of Biodegradable Nanoparticles

The most favorable nanoparticles for medical use must meet certain requirements, such as improved bioavailability, protection of therapeutic agents from degradation, controlled drug release, specific targeting, minimal toxicity, stability, and low cost [38], and biopolymeric nanoparticles best meet these requirements.

Biopolymeric nanoparticles comprise biopolymers—natural biological materials that are also generally recognized as safe (GRAS). Biopolymers are macromolecules composed of repeating units of monomers linked together by covalent bonds. Biopolymers such as proteins and polysaccharides are suitable for the preparation of biodegradable polymeric nanoparticles for various biomedical applications, especially for drug delivery, tissue engineering, and wound healing, as the therapeutic effect of the incorporated bioactive substances can be enhanced, and potential side effects can be reduced. This is due to their unique functions and properties, including biodegradability, biocompatibility, photoprotection, and antibacterial and antioxidant properties. In addition, they are naturally renewable, relatively inexpensive, and provide high stability in biological fluids and during storage [3,39–43]. Furthermore, various drugs and therapeutic agents can be successfully incorporated into biopolymeric nanoparticles, contributing to enhanced release at the target site [44]. Both natural polysaccharides and proteins are appropriate carriers for various therapeutic agents in the biomedical field [45]. The use of polysaccharide–protein complexes and conjugates (protein–protein, polysaccharide–polysaccharide, and protein–

polysaccharide composite nanoparticles) may be even more efficient due to their additional enhanced properties. Biopolymer composite nanoparticles offer many opportunities to improve biological functions. The preparation of protein–polysaccharide complexes can be manipulated to exhibit improved biocompatibility, biodegradability, stability, targeting, and mechanical properties [46].

Biopolymers can be obtained from various natural sources [37]. Depending on their origin, they can be divided into the animal, plant, algal, fungal, and bacterial biopolymers. Figure 5 shows a schematic representation of the biopolymers classification that can be used for the preparation of biopolymeric nanoparticles, depending on their origin, including the main representatives.

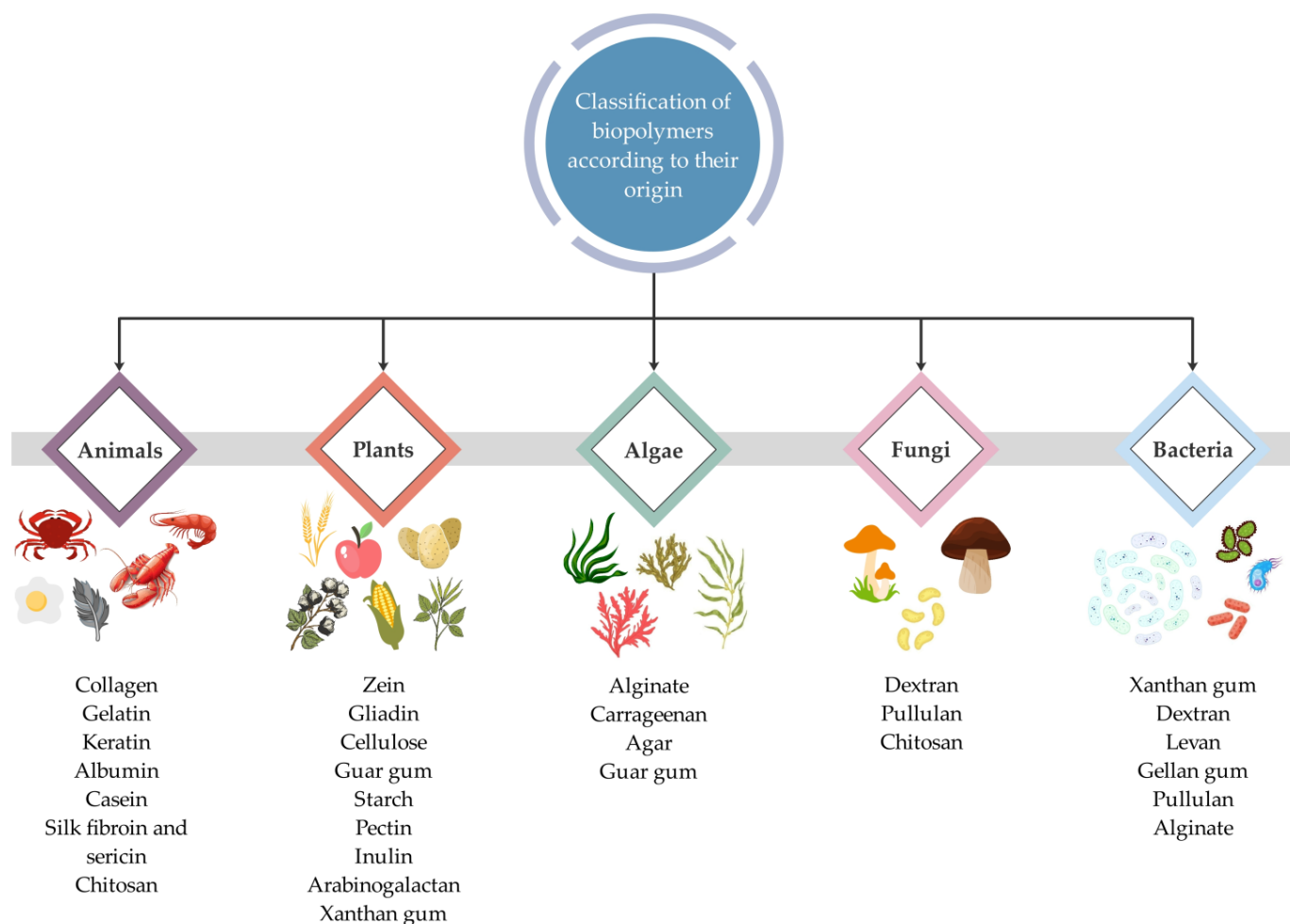


Figure 5. Classification of biopolymers based on their origin (summarized from [47,48]).

Due to their biodegradability, biocompatibility, nontoxicity, and stability, biopolymeric nanoparticles are promising nanocarrier systems for many drugs and other therapeutic agents. Through different production methods, biopolymeric nanoparticles can be successfully produced. The most commonly used methods are shown schematically in Figure 6. However, the choice of method plays a crucial role in the synthesis of nanoparticles with suitable properties, as it depends on the biopolymer used, the type of therapeutic agent, and the possible route of administration [44,49,50].

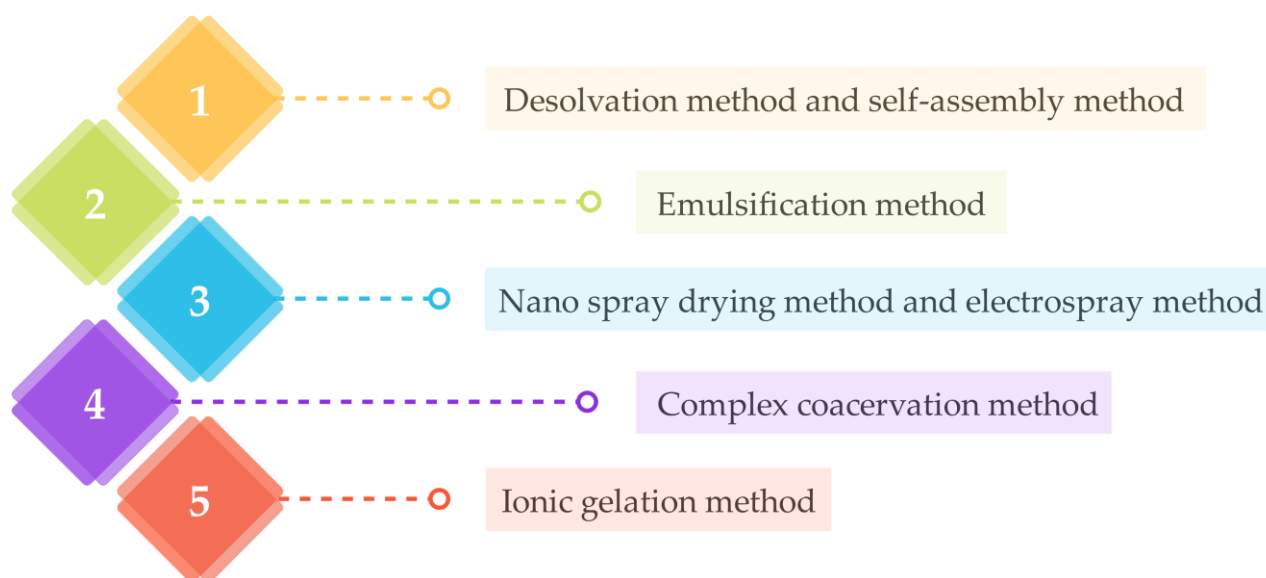


Figure 6. Schematic representation of most commonly used methods for producing biodegradable nanoparticles from biopolymers.

The desolvation method is based on using a desolvating (dehydrating) agent, such as ethanol or acetone, which changes the structure of the polymer and reduces its solubility, resulting in the formation of a precipitate of polymeric particles. This method is most commonly used to prepare protein-based nanoparticles [51–53]. The self-assembly method depends on the formation of biopolymeric nano-systems by self-assembly, both naturally and artificially, through non-covalent bonds [54,55]. The emulsification method is based on the preparation of nanoparticles by forming an emulsion system by mixing two immiscible liquids, namely the organic and aqueous phases, at very high shear. The organic solvent is then removed by evaporation to form solid nanoparticles [54,56,57]. The nano-spray drying method transforms the material from a liquid into a powder. The solution is sprayed into small droplets through a nozzle into a chamber where drying is carried out by hot gas. The evaporation of the solvent forms dry particles that collect at the bottom of the chamber. The electrospray method is based on manipulating materials on the submicron scale. The polymer solution is sprayed using high voltage through a capillary nozzle that forms aerosolized droplets containing polymer nanoparticles of colloidal size [52,54,58,59]. The complex coacervation method uses pH-dependent electrostatic interactions between biopolymers to form stable nanoparticles and coacervates [52,60]. The ionic gelation method depends on electrostatic interactions between charged polysaccharides in an aqueous medium under certain conditions. It is considered the most commonly used method for the preparation of stable polysaccharide nanoparticles [3,61–63].

2.1.1. Protein Nanoparticles

Proteins are biological macromolecules with a high molecular weight, which are inexpensive, abundant, and renewable. Their unique functionalities and properties make them ideal natural materials for the preparation of biodegradable polymeric nanoparticles. They are amphiphilic, which allows good interactions with solvents and various drugs. Protein nanoparticles are produced under mild conditions that do not require the use of toxic chemicals or organic solvents [54,64]. They offer many advantages because they are biocompatible, biodegradable, stable, have non-antigenic properties, are non-immunogenic and non-toxic, and safe.

Moreover, surface modifications of nanoparticles are also possible [52,65]. They are suitable as carriers for various substances, such as natural or chemical therapeutics, growth factors, peptides, vaccines, and nucleic acids. In this way, the potential side effects of the

drugs are eliminated, while at the same time, their therapeutic effect at the target site is increased [56]. Therefore, they can be successfully used in various biomedical applications, especially for tissue engineering and the delivery of drugs and other therapeutics [65,66].

Furthermore, various innovative protein-based nanoparticles offer enhanced properties such as biocompatibility, stability, etc. For example, intrinsically disordered proteins (IDPs) are promising nanomaterials for various medical and biotechnological purposes. They can help improve the development of drug delivery systems by enhancing the self-assembly, stimuli-responsiveness, and recognition properties of protein/peptide copolymers [67–70].

Protein-based nanoparticles can be classified according to the origin of the proteins used for their production. Proteins can be isolated from various animal and plant species. The most commonly used proteins are, for example, collagen, gelatin, and keratin. The composition of proteins depends mainly on the species from which they are obtained. Table 1 lists the most important examples of proteins and their origins suitable for protein-based nanoparticles production.

Table 1. Examples of proteins used for the production of protein-based nanoparticles.

Origin of Protein	Protein Source	Protein	Ref.
Animals	Ovalbumin and bovine serum albumin	Albumin	[71]
	Milk	Casein	[72]
	Muscles, tendons, skin, bones	Collagen	[73]
	Bones, skin, connective tissue	Gelatin	[74]
	Hair, nails, skin, feathers, wool, hooves, beaks, horns	Keratin	[75]
	Silkworm <i>Bombyx mori</i>	Silk fibroin and sericin	[76]
Plants	Wheat	Gliadin	[77]
	Corn kernel	Zein	[78]

2.1.2. Polysaccharide Nanoparticles

Polysaccharides are natural biopolymeric materials suitable for biopolymeric nanoparticle fabrication due to their exceptional structural characteristics. They consist of monosaccharide units linked together by glycosidic bonds [79]. Polysaccharides have many advantageous properties, such as biocompatibility, biodegradability, and nontoxicity. In addition, they are relatively inexpensive and readily available [79–81]. The presence of hydroxyl groups and other hydrophilic groups, such as carboxyl (e.g., in alginate) and amino groups (e.g., in chitosan), allows easy modification and functionalization of many types of polysaccharides for specific purposes [82,83].

Due to various favorable properties, polysaccharide-based nanoparticles are suitable for biomedical applications such as drug delivery and tissue engineering. In addition, they are successfully used as delivery vehicles for different therapeutic agents, including proteins, peptides, and nucleic acids. They can ensure high encapsulation efficiency of various substances and rapid and controlled release at the target site. Furthermore, polysaccharide-based biomaterials have the potential to be used in skin tissue engineering because they can absorb a large amount of water. Due to their biocompatibility and good mechanical properties, they are also increasingly used for bone and cartilage tissue engineering and are also important for the tissue engineering of nerves [80,84].

Polysaccharide nanoparticles can be divided according to the origin of the polysaccharides used for their production [85]. Polysaccharides can be isolated from animal, plant, algal, fungal, and bacterial species. They have different biological characteristics and activities due to different chemical structures and ionic nature [61]. The most well-known natural and biodegradable polysaccharides used in healthcare applications are chitosan, alginate, carrageenan, gellan gum, and dextran [86,87].

Table 2 lists the most important examples of polysaccharides and their origins used for polysaccharide-based nanoparticles production.

Table 2. Examples of polysaccharides used for the production of polysaccharide-based nanoparticles.

Origin of Polysaccharide	Polysaccharide Source	Polysaccharide	Ref.
Animal	Shells of arthropods such as crabs, prawns, shrimps, and lobsters	Chitosan	[88]
Plant	<i>Larix</i> spp.	Arabinogalactan	[89]
	Agricultural trashes: sugarcane bagasse, rice husks		[37,90]
	Plant sources: wood, cotton, jute, hemp, bamboo, coconut, wheat, rice, grass, agave, flax	Cellulose	[37,90]
	<i>Cyamopsis tetragonoloba</i>	Guar gum	[91]
	<i>Cyamopsis psoraloides</i>		[92]
	Globe artichoke, topinambur, elecampane, chicory	Inulin	[93]
	Citrus peels, apple pomace	Pectin	[94]
	Potatoes, corn, tubers, fruits, legumes, roots, cereals, rice, yams, banana wheat, sorghum	Starch	[37]
	Plant tissues (trees, cotton)	Cellulose	[95]
	Algae	<i>Nizimuddinia zanardini</i>	
<i>Sargassum latifolium</i>			[97]
<i>Cystoseira barbata</i>			[98]
<i>Ascophyllum nodosum</i>			[99]
<i>Laminaria digitata</i>		Alginate	[100]
<i>Laminaria hyperborea</i>			[101]
<i>Laminaria japonica</i>			[102]
<i>Macrocystis pyrifera</i>			[103]
<i>Sargassum wightii</i>			[104]
<i>Chondrus crispus</i>			[105]
<i>Sarcothalia crispata</i>			[106]
<i>Gigartina skottsbergii</i>		Carrageenan	[106]
<i>Eucheuma denticulatum</i>			[107]
<i>Kappaphycus alvarezii</i>			[108]
<i>Hypnea musciformis</i>	[109]		
Fungi	<i>Aureobasidium pullulans</i>		[110]
	<i>Cytaria harii</i>		[111]
	<i>Cytaria darwinii</i>		[111]
	<i>Cryphonectria parasitica</i>	Pullulan	[111]
	<i>Termella mesenterica</i>		[112]
	<i>Teloschistes falvicans</i>		[112]
	<i>Rhodotorula bacarum</i>		[112]
	<i>Saccharomyces cerevisiae</i>	Dextran	[113]
<i>Rhizopus oryzae</i>	Chitosan	[114]	

Table 2. Cont.

Origin of Polysaccharide	Polysaccharide Source	Polysaccharide	Ref.
Bacteria	<i>Lactobacillus plantarum</i>	Dextran	[115]
	<i>Weissella confuse</i>		[116]
	<i>Weissella cibaria</i>		[117]
	<i>Leuconostoc mesenteroides</i>		[118]
	<i>Leuconostoc reuteri</i>		[117]
	<i>Lactobacillus gasseri</i>	Gellan gum	[119]
	<i>Sphingomonas elodea</i>		[120]
	<i>Sphingomonas paucimobilis</i>		[120]
	<i>Leuconostoc citreum</i>	Levan	[121]
	<i>Bacillus subtilis</i>		[122]
	<i>Bacillus atrophaeus</i>		[123]
	<i>Acinetobacter nectaris</i>		[124]
	<i>Xanthomonas campestris</i>	Xanthan gum	[125]
	<i>Gluconacetobacter xylinus</i>	Cellulose	[126]
	<i>Azotobacter</i> spp.	Alginate	[127]
<i>Pseudomonas</i> spp.	[127]		

3. Animal-Based Biopolymeric Nanoparticles Used for Healthcare Applications

Biopolymers of animal origin, such as proteins and polysaccharides, play an essential and versatile role in various biomedical applications, including the production of nanoparticles, especially for drug delivery and tissue engineering.

3.1. Protein Nanoparticles of Animal Origin

For the use of biopolymeric nanoparticles for various biomedical applications as carriers of numerous therapeutic substances, proteins of animal origin are most commonly used, of which albumin, casein, collagen, gelatin, keratin, and silk proteins (fibroin and sericin) are the best known.

3.1.1. Albumin

Albumin is the main protein in blood plasma, and due to its many favorable properties, it is a versatile and suitable biomaterial for the preparation of biopolymeric nanoparticles. It is biodegradable, biocompatible, non-toxic, non-immunogenic, available in pure form, highly soluble in water and physiological fluids, and stable in the pH range between 4.0 and 9.0. It also exhibits thermal stability when heated to 60 °C for up to 10 h, as it does not cause denaturation. Albumin can be obtained from a variety of sources, including human, bovine, rat, and chicken, with bovine serum albumin (BSA), human serum albumin (HSA), egg white albumin (ovalbumin), etc. Albumin-based nanoparticles can successfully contribute to increased bioavailability, improved pharmacokinetic properties, and enhanced ability to release incorporated drugs at target sites [51,56,71,128,129].

They are successfully used as nanocarriers in the treatment and diagnosis of various diseases, as they can effectively and safely deliver nonspecifically distributed drugs in the body which can cause serious side effects [71,130]. Albumin-based nanoparticles have already been developed for the treatment of cancer, diabetes, hepatitis C, and arthritis [131,132]. Yan et al. [130] prepared albumin nanoparticles loaded with prednisolone and curcumin using a high-pressure homogenization method. Combining two therapeutic substances loaded into albumin-based biopolymeric nanoparticles has shown promise as a delivery system for combined chemotherapy in rheumatoid arthritis. By using biopoly-

meric nanoparticles, a better anti-inflammatory effect against macrophages was obtained than with a free mixture of drugs. Gawde et al. [133] came to similar conclusions that albumin nanoparticles with incorporated paclitaxel and difluorinated curcumin are suitable for the treatment of gynecologic cancers. Zhao et al. [134] also demonstrated that albumin-based nanoparticles are potential carriers for the co-delivery of paclitaxel and resveratrol for effective synergistic cancer treatment. Moreover, albumin-based nanoparticles produced by the desolvation method with incorporated methylene blue can effectively inhibit the growth of the yeast *Candida albicans* and reduce biofilm formation, as demonstrated in a study by Ambrósio et al. [135]. Using the desolvation method, the most commonly used technique for the preparation of albumin-based nanoparticles, nanoparticles with uniform size, spherical shape, and low aggregation tendency can be produced [135].

3.1.2. Collagen

Collagen is a natural biopolymer and the most abundant protein in the human body, namely the primary material of the extracellular matrix of bones, skin, muscles, cartilage, ligaments, and tendons. It accounts for more than 30% of all body proteins. Due to numerous advantages such as biocompatibility, biodegradability, non-immunogenicity, non-toxicity, tensile strength, low antigenicity, extensibility, and accessibility, it plays an essential role in the synthesis of nanoparticles in various biomedical fields, especially in drug delivery and tissue engineering [136–138]. Biodegradable and thermally stable collagen nanoparticles are suitable nanocarriers for many therapeutic and cytotoxic substances, genes, proteins, growth factors, and drugs. In dermatology, for example, they are important for administering antimicrobials and steroids. They have good absorption capacity, large contact surface area, and ensure controlled and long-term release of drugs [136,139,140].

Vijayakumar and Vaseeharan [141] synthesized non-toxic and environmentally friendly collagen-based ZnO nanoparticles with antimicrobial and antibiofilm activity against Gram-positive bacteria *Streptococcus mutans* and Gram-negative bacteria *Proteus vulgaris* and yeast *C. albicans*, and good anticancer activity against human hepatoma cancer cells (HepG2) at a very low concentration (75 µg/mL). Due to their biocompatibility and potential to mimic the extracellular matrix, collagen nanoparticles play an essential role in tissue engineering and regenerative medicine, especially in bone, cartilage, dental, vascular, corneal, and skin tissue engineering, wound healing, spinal cord injury repair, and nerve and oral mucosa regeneration [137,142,143]. In a study by Mondal et al. [144], the chemotherapeutic drug doxorubicin was successfully incorporated into gold-loaded collagen hydroxyapatite nanoparticles. The synthesized nanoparticle system is a promising material for drug delivery and an extracellular matrix for tissue engineering.

3.1.3. Other Animal-Based Protein Nanoparticles

One other important biopolymer for producing nanoparticles of animal origin, which is also promising for nanoparticle fabrication to improve bioavailability, efficacy, and controlled release, is casein, the main protein in milk and a good source of amino acids. Various therapeutic substances, such as the anticancer drug doxorubicin [145], the polyphenolic compounds resveratrol [146], curcumin [147] and quercetin [148], the antibacterial agent mequinodox [149], and the phenylpropanoid eugenol [150], have already been successfully incorporated into casein nanoparticles for use in various healthcare applications. Gelatin is another natural, water-soluble protein. Various anticancer drugs, anti-inflammatory drugs, analgesics, antimicrobial agents, and other drugs have already been successfully loaded into gelatin nanoparticles [139,151]. Keratin is a protein rich in amino acids and is fibrous and insoluble. Keratin-based nanoparticles are suitable carriers for various antitumor drugs such as doxorubicin, paclitaxel, and chlorine c6 and 9(R)-9-hydroxystearic acid, and multiple polyphenols such as rutin, quercetin, and curcumin. In addition, they are also crucial for tissue engineering and wound healing [152,153]. Fibroin and sericin are the major proteins of silk proteins. Silk protein nanoparticles are also favorable delivery systems for many

drugs, such as paclitaxel, 5-fluorouracil, doxorubicin, gemcitabine, fenofibrate, atorvastatin, methotrexate, inulin, resveratrol, and curcumin [154,155].

3.2. Polysaccharide Nanoparticles of Animal Origin

Polysaccharides of animal origin can be successfully used for various healthcare applications, with chitosan being the most important and well-known representative. It is a promising natural biomaterial for the synthesis of nanoformulations for the delivery of different therapeutic agents.

Chitosan

Chitosan is a natural biopolymer composed of N-acetyl-D-glucosamine and D-glucosamine units linked by β -1,4-glycosidic bonds. It is a cationic polysaccharide derived from chitin by demineralization and deproteinization. This is found mainly in the exoskeleton of crustaceans and insects, fish scales, and in the cell wall of fungi. Due to its exceptional physicochemical properties such as biodegradability, biocompatibility, non-toxicity, low immunogenicity, mucoadhesiveness, low cost, bio-renewability, and environmental friendliness, chitosan plays an important role in various biomedical and pharmaceutical applications. In addition, they have antitumor, antioxidant, and antimicrobial properties against the growth of Gram-positive and Gram-negative bacteria. Chitosan nanoparticles are stable, increase bioavailability, improve the solubility of poorly soluble drugs, and enhance the targeted delivery of various therapeutic compounds. Chemical modification or integration with functional materials has positive properties to improve in vivo release stability [156–163]. Chitosan-based nanoparticles can be used as nanocarriers for various drug antibiotics, proteins, vaccines, and genes [164,165]. They can be administered by nasal, intravenous, oral, and ocular routes [166].

For example, Ansari et al. [167] synthesized chitosan-based nanoparticles loaded with zinc gluconate using an ionic gelation method. They possess significant antioxidant, anti-inflammatory, and anti-arthritis potential, making them a potential alternative for the treatment of rheumatoid arthritis. Tzeyung et al. [168] prepared rotigotine-loaded chitosan nanoparticles for nose-to-brain delivery using an ionic gelation method. The nanoformulation did not cause toxicity or structural damage to the nasal mucosa, making chitosan-based nanoparticles an effective drug carrier for nose-to-brain delivery as an alternative to conventional administration routes. Yu et al. [169] synthesized dexamethasone–glycol chitosan nanoparticles that exhibited good ocular tolerance and had relatively longer precorneal retention than an aqueous solution. Therefore, these nanoparticles are relevant for ophthalmic drug administration in the treatment of various inflammatory diseases. Chitosan nanoparticles and chitosan/collagen peptide nanoparticles have been shown to be effective biopolymeric stabilizers of Pickering emulsions used for cosmetic applications [170,171]. In addition, chitosan nanoparticles have already been shown to be excellent inhibitors of bacteria, both *Escherichia coli* and *Staphylococcus aureus* [172]. Recent findings include the use of chitosan in the preparation of nanocarriers to enhance the antimetastatic properties of the entrapped drug in vitro and in vivo [173].

Table 3 summarizes examples of biopolymeric nanoparticles of animal origin for various healthcare applications, including their preparation method and the size of the synthesized nanoparticles.

Table 3. Examples of animal-based biopolymeric nanoparticles for healthcare applications.

Biopolymer	Preparation Method	Particle Size (nm)	Loaded Cargo	Healthcare Application	Ref.
HSA	Self-assembly method	<200.0	Docetaxel	Delivery of anticancer drug	[174]
HSA	High-pressure homogenization	150.4	Prednisolone and curcumin	Drug delivery for the treatment of rheumatoid arthritis	[130]

Table 3. Cont.

Biopolymer	Preparation Method	Particle Size (nm)	Loaded Cargo	Healthcare Application	Ref.
HSA	Desolvation method	<200.0	Piperine	Drug delivery for the treatment of breast cancer cells (MCF-7)	[175]
	Self-assembly method				
HSA	Coacervation method	85.0–120.0	Imipenem and ciprofloxacin	Delivery of antibiotics	[176]
BSA	Emulsification method	100.0	-	Drug delivery studies	[177]
BSA	Desolvation method	156.0–315.0	Doxorubicin	Delivery of anticancer drug	[178]
BSA	Anti-solvent precipitation method	150.0	Paclitaxel and resveratrol	Delivery of anticancer drug	[134]
BSA	Desolvation method	100.0–200.0	Methylene blue	Delivery of antifungal drugs for the treatment of <i>Candida</i> infections	[135]
Collagen	Electrospinning/electrospray method	-	-	Appropriate mimicry of the extracellular matrix for biomedical applications	[142]
Collagen	Film dispersion method	35.2–107.0	Cucurbitacin B	Oral delivery	[179]
Chitosan	Ionic gelation method	106.5	Zinc gluconate	Drug delivery for the treatment of rheumatoid arthritis	[167]
Chitosan	Emulsion-ionic gelation	40.0–100.0	Clove essential oil	Superior inhibitory effect against <i>Aspergillus niger</i>	[180]
Chitosan	Ionic gelation method	75.4	Rotigotine	Nose-to-brain drug delivery	[168]
Chitosan	Emulsion-ionic gelation	198.7–373.4	Basil essential oil	Delivery of antibacterial substances	[181]
Chitosan	Ionic gelation method	208.1	Cinnamaldehyde	Delivery of anti-quorum sensing agents	[182]
Chitosan	Ionic gelation method	174.0–898.0	Pomegranate peel extract	Controlled delivery of natural antioxidants and antimicrobials	[183]
Chitosan	Emulsification-ionic gelation method	174.0–293.0	Lemongrass essential oil	Delivery of antibacterial substances	[184]

4. Plant-Based Biopolymeric Nanoparticles Used for Healthcare Applications

Plants are a rich source of many vital substances, including various polysaccharides and proteins, promising biomaterials for producing biopolymeric nanoparticles for various biomedical applications.

4.1. Protein Nanoparticles of Plant Origin

Protein nanoparticles of plant origin are of great importance in the production of biopolymeric nanoparticles because they offer a significant advantage over protein nanoparticles of animal origin. Not only are they much cheaper and widely available, but they are also safer, as diseases from animals can be transmitted to humans through nanoparticles of animal origin. The most important representatives include zein and gliadin.

4.1.1. Gliadin

Gliadin is an important natural protein found in wheat gluten. It can be divided into four classes, namely α -, β -, γ -, and ω -gliadin, according to electrophoretic mobility. The structure of gliadin consists of a terminal region, namely a short N-terminal domain and a C-terminal domain, which is more hydrophobic due to the presence of amino acids, and a central repetitive region rich in glutamine and proline, which confers amphiphilicity to gliadin. Due to its relevant properties, it is suitable for the synthesis of nanoparticles for various therapeutic applications. They are biocompatible, biodegradable, non-toxic, and stable. Due to their hydrophobic nature and low solubility in aqueous solutions, they provide protection and controlled release of the loaded drugs [56,185–187]. Gliadin nanoparticles are suitable nanocarriers for various hydrophilic therapeutic agents [188]. Hydrophilic and amphiphilic compounds such as vitamins A and E and amoxicillin have already been successfully incorporated into gliadin nanoparticles [139].

In the study, Alqahtani et al. [189] confirmed that gliadin nanoparticles prepared by a modified antisolvent nanoprecipitation method were compatible with blood regardless of the size of the synthesized nanoparticles. Wu et al. [190] prepared potential delivery agents, resveratrol-incorporated gliadin nanoparticles, by an antisolvent precipitation method and stabilization with gum Arabic and chitosan hydrochloride. The nanocarriers prepared in this way significantly increased the release of resveratrol in water and the simulated digestive tract, thereby increasing its bioavailability. Moreover, they improved the chemical stability and antioxidant activity of the encapsulated polyphenolic compound. Sharif et al. [191] prepared zein nanoparticles with incorporated γ -oryzanol by electro-spray method. Due to the encapsulation of γ -oryzanol, the synthesized nanoparticles were rounder and smoother with a homogeneous distribution of γ -oryzanol. The synthesized γ -oryzanol-loaded gliadin nanoparticles had improved stability and decreased the proliferation of HT-29 human colon cancer cells.

4.1.2. Zein

Zein is a major plant-based protein obtained mainly from corn. It is rich in prolamin, poorly soluble in water, and resistant to high temperatures. It is divided into four classes according to different peptide chains, solubility, and molecular size, namely α -, β -, γ -, and δ -zein. Zein is biodegradable, biocompatible, and safe and therefore promising for the synthesis of natural biopolymeric nanoparticles for various healthcare applications. Namely, it offers greater bioavailability, protection, and prolonged, controlled, and more effective release of incorporated substances at the target site. Many therapeutic agents have been successfully loaded into zein-based nanoparticles, e.g., doxorubicin, heparin, 5-fluorouracil, coumarin, quercetin, resveratrol, vitamin D3, and different antimicrobials [185,192–194].

Zein-based nanoparticles are applicable nanocarriers for hydrophobic molecules to enhance their bioavailability for various therapeutic purposes. Nunes et al. [195] successfully prepared zein nanoparticles using the nanoprecipitation technique, into which they incorporated resveratrol with an efficiency of 77%. The resveratrol-loaded zein nanoparticles successfully protected resveratrol from enzymatic degradation and showed low toxicity to human colorectal cell lines Caco-2 and HT29-MTX. Using a modified phase separation method, Zhang et al. [193] prepared dodecamer peptide (G23)-functionalized polydopamine (pD)-coated curcumin-loaded zein nanoparticles. The prepared spherical nanoparticles with a diameter of about 120 nm showed excellent cellular uptake by C6 glioma cells and the ability to penetrate 3D tumor spheroids. Zein is also widely used in tissue engineering [192]. Hadavi et al. [196] synthesized zein nanoparticles as a delivery system for a bone morphogenic protein-6 (BMP6) derived peptide using a liquid–liquid phase separation method. They are promising in bone regeneration due to their low toxicity, high encapsulation efficiency, and osteoinductivity.

4.2. Polysaccharide Nanoparticles of Plant Origin

Polysaccharides are found in large amounts in various plant species and, due to their non-toxicity compared to various synthetic materials, represent an important natural and biodegradable material for the synthesis of nanoparticles. These nanoparticles are often used as nanocarriers for therapeutic agents for healthcare applications. The best-known polysaccharides of plant origin include arabinogalactan, cellulose, guar gum, inulin, pectin, and starch.

4.2.1. Pectin

Pectin is a structural polysaccharide and consists of the main chain of D-galacturonic acid units linked by α -(1,4) glycosidic bonds and side chains of galactose, arabinose, and rhamnose. It is derived from various plant sources, mainly apples, citrus fruits, and sugar beets, but algae, such as *Spirulina maxima* can also produce it. It is water-soluble, biodegradable, biocompatible, and non-toxic, making it a promising biomaterial for the preparation of nanocarrier systems for various therapeutic agents for biomedical applications [197,198]. Pectin-based nanoparticles are unique systems for targeted drug delivery in the colon because pectin is readily degraded in the colon while remaining chemically intact in the stomach and small intestine [199].

Jacob et al. [200] synthesized polysaccharide nanoparticles based on pectin extracted from citrus fruits using the ionotropic gelation method based on the difference in their degree of esterification, namely high, low, and amidated low methoxylated pectin. Magnesium (Mg^{2+}) was used as a divalent crosslinker. All three pectin samples proved to be potential delivery systems for hydrophobic drugs for oral administration. Bostanudin et al. [201] synthesized butylglyceryl-modified pectin nanoparticles by nanoprecipitation. The spherical nanoparticles produced were stable and less than 300 nm in diameter, making them appropriate drug delivery vehicles.

4.2.2. Starch

Starch is a natural biopolymer containing two different polysaccharide structures, amylose, and amylopectin. Amylose is a linear or slightly branched biopolymer and consists of glucose units linked by α -1-4 glycosidic bonds. Amylopectin is a highly branched biopolymer with short chains of glucose units linked by α -(1,4) glycosidic bonds and additional branches linked by α -1-6 glycosidic bonds. Like all other biopolymers, starch is biocompatible, biodegradable, nontoxic, nonimmunogenic, and renewable. Therefore, it represents a significant natural biopolymeric material for the preparation of nanoparticles as successful delivery systems for various drugs and bioactive substances with controlled release at the target site [202,203].

Farrag et al. [204] synthesized starch-based nanoparticles of various botanical origins into which the polyphenol quercetin was incorporated using the nanoprecipitation method. The results showed that the synthesized starch nanoparticles had a spherical shape. However, the origin of the starch had an influence on the size of the nanoparticles, the percentage of loading with quercetin, the release kinetics, and the antioxidant activity. Chin et al. [205] successfully synthesized paracetamol-loaded pH-responsive starch-citrate nanoparticles using a nanoprecipitation method. Synthesized nanocarriers are applicable for targeted drug delivery, with relatively high loading capacity and low toxicity. Chen et al. [206] demonstrated that starch-based nanoparticles could be used as nanocarriers for chemotherapeutic agents. In their study, they successfully prepared amphiphilic self-assembled glycyrrhetic acid-biotin-starch nanoparticles with encapsulated hydrophobic anticancer drug doxorubicin. The nanoformulation showed enhanced cellular uptake and cytotoxic effect on HepG2 cells as a free drug.

4.2.3. Cellulose

Cellulose is a natural structural polysaccharide and the main component of many plant tissues. It is also found in seaweed and various non-pathogenic bacterial species. It is a

linear biopolymer composed of D-glucose units linked by β -1,4-glycosidic bonds. Cellulose is the most abundant renewable biopolymer and is biocompatible, biodegradable, non-toxic, and stable under acidic conditions [95,126,207,208]. Cellulose-based nanomaterials (nanocellulose) can be used for a variety of biomedical applications, including wound healing, tissue engineering, drug delivery, bone regeneration, and as antibacterial and antifouling agents [209,210].

Chin et al. [211] demonstrated that curcumin-incorporated cellulose nanoparticles are a promising approach for curcumin delivery to the stomach and upper intestinal tract. In an in vitro study in simulated gastric fluid, higher stability and greater release of the drug were obtained. Cellulose-based nanoparticles are important for achieving target specificity and long-term efficacy in the delivery of therapeutic agents because they can be easily modified to obtain the appropriate chemical, mechanical, and physical properties [209].

4.2.4. Other Plant-Based Polysaccharide Nanoparticles

In addition to pectin and starch, there are other important biopolymers, including arabinogalactan, guar gum, and inulin, which can be used to produce nanoparticles as promising carriers for numerous therapeutics to improve their properties for healthcare applications. Most studies have been conducted primarily on the potential use of biopolymeric nanoparticles to deliver chemopreventive and chemotherapeutic agents [207,212,213]. For example, celecoxib has been successfully incorporated into guar gum nanoparticles to target colon cancer [214], as well as model drugs doxorubicin, 5-fluorouracil, rifampicin, rhodamine B, angiotensin II, antibiotic ciprofloxacin, and polyphenolic compounds, such as curcumin and caffeine. Furthermore, guar gum nanoparticles are suitable for oral as well as buccal, transdermal, and intravenous administration [215]. Inulin nanoparticles have also been developed for efficient delivery of the incorporated drug epirubicin [216]. In addition, inulin-based nanoparticles are potential carriers for unstable molecules in oral delivery systems. They ensure successful encapsulation, protection, and controlled release of quercetin for colon-targeted drug delivery [217]. Moreover, arabinogalactan-based nanoparticles are also suitable as carriers for various therapeutic agents, such as recombinant human thrombin [218].

Table 4 summarizes examples of biopolymeric nanoparticles of plant origin for use in various biomedical applications, including their preparation and the size of the synthesized nanoparticles.

Table 4. Examples of plant-based biopolymeric nanoparticles for healthcare applications.

Biopolymer	Preparation Method	Particle Size (nm)	Loaded Cargo	Healthcare Application	Ref.
Gliadin	Desolvation method	1.0–181.0	Sumatriptan	Brain-targeted drug delivery	[188]
Gliadin	Electrospray method	481.6	γ -Oryzanol	Drug delivery to reduce HT-29 cell proliferation	[191]
Zein	Nanoprecipitation method	120.0–180.0	Resveratrol	Oral drug delivery	[195]
Zein	Liquid–liquid phase separation method	379.4	BMP6-derived peptide	Bone regenerative medicine	[196]
Zein	Phase separation	37.0–112.3	Maytansine	Delivery of anticancer drug	[219]
Zein	Self-assembly method	180.0	<i>Thymbra capitata</i> essential oil	Drug delivery	[220]
Pectin	Ionotropic gelation method	700.0–850.0	-	Potential oral drug delivery	[200]
Pectin	Ionic gelation method	482.7	Metformin	Drug delivery for type 2 diabetes mellitus	[221]

Table 4. Cont.

Biopolymer	Preparation Method	Particle Size (nm)	Loaded Cargo	Healthcare Application	Ref.
Starch	Nanoprecipitation method	500.0	Quercetin	Estimation of release kinetics	[204]
Starch	Nanoprecipitation method	<250.0	Curcumin	Drug delivery for polyphenols	[222]
Starch	Nanoprecipitation method	255.0–396.0	Ginkgo biloba extracts	Oral drug delivery	[223]
Starch	Emulsification method	300.0	5-Fluorouracil	Colon-specific drug delivery	[224]
Starch	Acid hydrolysis and precipitation method	85.1	Paclitaxel	Delivery of anticancer drug	[225]
Starch	Nanoprecipitation method	105.0	Paracetamol	pH-responsive drug delivery system	[205]
Starch	Microemulsification method	282.9	Triphala Churna	Drug delivery of drugs with antimicrobial, antibiofilm, and neuroprotective effects	[226]
Cellulose	Nanoprecipitation method	70.0–365.0	Methylene blue	Sustained and controlled release	[227]
Guar gum	Emulsification method	200.0	Celecoxib	Oral drug delivery	[214]
Inulin	Emulsion solvent evaporation method	224.0–365.0	-	Intracellular stimulation of probiotics	[228]
Inulin	Spray drying method	289.8	Quercetin	Colon-targeted drug delivery	[217]

5. Algae-Based Biopolymeric Nanoparticles Used for Healthcare Applications

Algae are autotrophs, mixotrophs, and heterotrophs and are found everywhere in freshwater sources and the marine environment. They are divided into microalgae and macroalgae, and both are important for the production of various biopolymers from which nanoparticles can be successfully synthesized [229].

5.1. Polysaccharide Nanoparticles of Algal Origin

Many polysaccharides, promising biopolymeric materials for biocompatible, biodegradable, and nontoxic nanoparticles, can also be obtained from algal species. Some important biopolymers of plant origin are also produced by various algae, such as cellulose and starch. Alginate and carrageenan are among the most commonly used biopolymers of algal origin.

5.1.1. Alginate

Alginate is a natural linear and unbranched polysaccharide consisting of a repeating unit of β -D-mannuronic acid (M-blocks) and α -L-guluronic acid (G-blocks) linked by 1,4-glycosidic bonds. The physicochemical properties of alginate are based on the composition, i.e., the M/G ratio and the length and sequence of the building blocks. The high content of M and G blocks contributes significantly to the thickening and gelling properties. Alginate is mainly derived from marine algae but can also be produced by some bacterial species. Due to its important properties, such as biodegradability, biocompatibility, non-toxicity, and non-immunogenicity, alginate is an important natural biomaterial for the preparation of nanoparticles for numerous therapeutic applications. Alginate nanoparticles successfully protect the incorporated therapeutic agents and ensure the controlled release of the therapeutic agent at the target site. The release properties of therapeutic agents are influenced by the presence of monomer units in alginate [127,230–235].

Spadari et al. [236] have successfully incorporated miltefosine, a drug with great antifungal potential, into alginate nanoparticles. These have been shown to be alternative nanocarriers for antifungal drugs to treat invasive fungal infections without having a cytotoxic effect on healthy cells, as may be the case when the free drug is administered. The bacteriocins of *Lacticaseibacillus paracasei* CNCM I-5369 show good activity against Gram-negative bacteria, including *E. coli*, which contains the *mcr-1* gene that makes it resistant to the antibiotic colistin. In a study, Belguesmia et al. [237] successfully loaded alginate nanoparticles with bacteriocins, providing a successful therapeutic alternative in the fight against infections caused by Gram-negative bacteria. The results showed that antibacterial activity against *E. coli* increased significantly. Moreover, the alginate nanoparticles loaded with bacteriocins were not cytotoxic to human HT29 and animal IPEC-1 cell lines.

5.1.2. Carrageenan

Carrageenan is a linear sulfated polysaccharide obtained mainly from various species of seaweed. It is a hydrophilic biopolymer with a high molecular weight. Its polymer structure consists of 3-linked- β -D-galactopyranose and 4-linked- α -D-galactopyranose or 4-linked 3,6-anhydro- α -D-galactopyranose units. According to the structural features of the repeating disaccharide units, it can be classified into seven types, namely λ -, κ -, ι -, ν -, μ -, θ -, and ξ -carrageenan. Due to biodegradability, biocompatibility, bioavailability, non-toxicity, and thermostability, carrageenan is the ideal basis for the production of important nanoparticles based on natural polysaccharides in biomedical applications. It significantly contributes to improving the properties of incorporated therapeutic substances, increases bioavailability and durability, and prolongs the release of bioactive ingredients at the target site. In addition, carrageenan also has antioxidant, anticarcinogenic, anticoagulant, and immunomodulatory properties [61,238–241].

Fani et al. [242] used an electrospray method to synthesize carrageenan nanoparticles loaded with the sensitive bioactive compound D-limonene (R-(+)-limonene) and achieved an encapsulation efficiency of about 97%. Carrageenan-based nanoparticles were found to be effective nanocarrier systems for lipophilic compounds such as D-limonene, as both photostability and thermostability were significantly improved by encapsulation. Vijayakumar et al. [243] synthesized carrageenan-coated ZnO nanoparticles with successful antibacterial activity against MRSA. Moreover, the prepared nanoparticles had proven anti-inflammatory activity, good compatibility with human red blood cells, and were environmentally safe.

Table 5 summarizes examples of algae-based polysaccharide nanoparticles for various healthcare applications, including preparation methods and the size of produced nanoparticles.

Table 5. Examples of algal-based biopolymeric nanoparticles for healthcare applications.

Biopolymer	Preparation Method	Particle Size (nm)	Loaded Cargo	Healthcare Application	Ref.
Alginate	Ionic gelation method	-	Rifampicin	Drug delivery without systemic toxicity	[244]
Alginate	Emulsification method	279.1	Miltefosine	Antifungal drug delivery	[236]
Alginate	Emulsification method	150.0–270.0	Betamethasone sodium phosphate	Ocular drug delivery	[245]
Alginate	Ionic gelation method	400.0–1000.0	Grape pomace extract	Oral delivery	[246]
Alginate	Electrospray method	228.0	CRISPR plasmids DNA	Gene delivery	[247]

Table 5. Cont.

Biopolymer	Preparation Method	Particle Size (nm)	Loaded Cargo	Healthcare Application	Ref.
Alginate	Emulsification method	279.1	Bacteriocins from <i>L. paracasei</i>	Drug delivery for the treatment of fungal diseases caused by <i>Candida</i> spp. and <i>Cryptococcus</i> spp.	[236]
κ -Carrageenan	Electrospray method	309.5–663.8	D-limonene	Drug delivery of highly sensitive bioactive agents	[242]
κ -Carrageenan	Emulsification method	211.0	Curcumin	Drug delivery	[248]

6. Fungal-Based Biopolymeric Nanoparticles Used for Healthcare Applications

Fungi are an essential source of various natural compounds, including polysaccharides. Biodegradable and biocompatible nanoparticles, as carriers of drugs and other important therapeutic agents, can be synthesized from successfully extracted biopolymers from fungi by various methods.

Polysaccharide Nanoparticles of Fungal Origin

Pullulan is one of the most important and commonly used fungal polysaccharides for the preparation of biopolymeric nanoparticles. In addition to pullulan, the polysaccharide dextran, mainly of bacterial origin, and the protein chitosan, primarily derived from animals, can also be isolated from fungi.

Pullulan

Pullulan is a natural biopolymer obtained mainly by a fermentation process from the yeast-like fungus *A. pullulans*. The structure of pullulan contains maltotriose units linked by α -1,6 glycosidic bonds, which contributes significantly to the structural flexibility of pullulan. It is a nonionic linear exopolysaccharide easily soluble in water but insoluble in most organic solvents. Compared to other polysaccharides, the aqueous pullulan solution is stable and has a relatively low viscosity. Due to its advantageous properties, such as biodegradability, biocompatibility, non-immunogenicity, non-toxicity, non-mutagenicity, and non-carcinogenicity, pullulan is an important biomaterial for the preparation of nanoparticles based on natural polysaccharides, applicable for various biomedical use [61,111,249–251]. Pullulan-based nanoparticles are nanocarriers for various therapeutic substances, for example, antimicrobial agents and essential oils with inhibitory activity against pathogenic Gram-negative and Gram-positive bacteria and fungi, including multidrug-resistant and biofilm-forming bacteria [252].

Tao et al. [253] synthesized potential biopolymer-based nanocarriers to reduce the dose of chemotherapeutic drugs while increasing their delivery efficiency. They successfully incorporated the drug mitoxantrone into cholesterol-substituted pullulan nanoparticles, which showed successful growth inhibition of bladder cancer cells in vitro. Yuan et al. [254] synthesized cholesteryl-modified aminated pullulan nanoparticles loaded with cholesterol succinate, an acidic cholesterol ester. Sustained release of incorporated substance and cytotoxicity on Lewis lung cancer cells were obtained. In a study, Laha and Maiti [255] found that stearyl pullulan-based nanocarriers with the incorporated drug glipizide could prolong the release of the loaded drug under simulated gastrointestinal conditions. Thus, they proved to be favorable nanocarriers for poorly soluble drugs that can achieve controlled release and successfully improve the therapeutic efficiency of the incorporated drugs. Li et al. [256] demonstrated that pullulan–doxorubicin nanoparticles loaded with 1,1,2-trichlorotrifluoroethane are a new potential delivery system with a synergistic effect that significantly improves ablation and therapeutic efficacy.

Table 6 summarizes examples of polysaccharide nanoparticles of fungal origin for use in various biomedical applications, including synthesis methods and the size of nanoparticles produced.

Table 6. Examples of fungal-based biopolymeric nanoparticles for healthcare applications.

Biopolymer	Preparation Method	Particle Size (nm)	Loaded Cargo	Healthcare Application	Ref.
Pullulan	Nanoemulsification method	98.0	Ursodeoxycholic acid	Drug delivery for neuroprotective effect	[257]
Pullulan	Self-assembly method	86.4–222.3	Mitoxantrone	Delivery of anticancer drug	[253]
Pullulan	Nanoprecipitation method	<200.0	Valsartan	Delivery of cardiovascular agents	[258]
Pullulan	Emulsion solvent evaporation method	200.0	Doxorubicin	Liver-specific drug delivery	[259]
Pullulan	Self-assembly method	185.7	Methotrexate and 10-hydroxycamptothecin	Tumor-targeted drug delivery	[260]
Pullulan	Probe-sonication method	84.1	Erlotinib	Drug delivery for cervical cancer therapy	[261]

7. Bacterial-Based Biopolymeric Nanoparticles Used for Healthcare Applications

Several bacterial species can produce various bioactive compounds, including polysaccharides, from which biodegradable, biocompatible, and nontoxic nanocarriers for potential use in biomedical applications can be prepared.

7.1. Polysaccharide Nanoparticles of Bacterial Origin

Polysaccharides that are successfully used to produce biopolymeric nanoparticles of bacterial origin include dextran, xanthan gum, levan, and gellan gum, of which dextran is the best known. In addition, pullulan can also be of bacterial origin. Polysaccharide-based nanoparticles of bacterial origin can successfully enhance bioavailability and consequently reduce the side effect of the incorporated drug or other therapeutic substance.

7.1.1. Dextran

Dextran is a natural, branched exopolysaccharide with a hydrophilic nature. It is produced mainly by some Gram-positive bacteria such as *Leuconostoc* and *Streptococcus*. The main dextran chain consists of glucose monomers linked by α -1,6 glycosidic bonds and short-side branches linked by α -1,3 glycosidic bonds. However, the properties of dextran, such as branching and molecular weight, may vary depending on the bacterial strain and production conditions. Due to its advantageous properties, such as biodegradability, biocompatibility, non-toxicity, and non-immunogenicity, it is considered as a suitable biomaterial for the preparation of polysaccharide nanoparticles as delivery systems for various therapeutic agents, including proteins and nucleic acids. Moreover, dextran nanoparticles successfully reduce the potential negative side effects of incorporated substances by delivering them to the target sites in a controlled manner [262–264].

In order to minimize the local and systemic side effects of local retinoblastoma chemotherapy, Delrish et al. [265] synthesized thiolated and methylated chitosan–carboxymethyl dextran nanoparticles by the ionic gelation method. They studied their biodistribution after intravitreal injection into the eyes of rats with retinoblastoma. The diameter of the prepared biocompatible polymer nanoparticles was 34 ± 3.78 nm and 42 ± 4.23 nm, respectively. These showed increased ocular bioavailability in retinoblastoma-induced rat eyes. In a study, Han et al. [266] found that paclitaxel-loaded dextran nanoparticles decorated with the RVG29 peptide can cross the blood–brain barrier and reach intracranial

tumors. Therefore, they are suitable drug delivery systems for the treatment of C6 glioma. Jamwal et al. [267] synthesized a dextran-based insulin delivery system. An *in vitro* insulin release study was performed in an artificial gastric and artificial intestinal fluid and showed controlled release of insulin from synthesized glucose oxidase immobilized-acryloyl crosslinked dextran dialdehyde nanoparticles.

7.1.2. Other Bacterial-Based Polysaccharide Nanoparticles

Other bacterial-derived polysaccharides, such as xanthan gum, levan, and gellan gum, are also nontoxic, biodegradable, and biocompatible polymers for the synthesis of biopolymeric nanoparticles promising for biomedical applications as delivery systems. Therefore, various therapeutic substances have already been successfully incorporated into bacterial-based polysaccharide nanoparticles. For example, gellan gum and levan nanoparticles have been successfully loaded with resveratrol for oral administration [268,269], and the hydrophilic antihypertensive drug Atenolol was incorporated into gellan gum nanoparticles [270]. Moreover, a chemotherapy drug, doxorubicin, was also successfully incorporated into xanthan gum nanoparticles [271].

Table 7 summarizes examples of polysaccharide nanoparticles of bacterial origin for use in various healthcare applications, including preparation methods and size of the synthesized nanoparticles.

Table 7. Examples of bacterial-based biopolymeric nanoparticles for healthcare applications.

Biopolymer	Preparation Method	Particle Size (nm)	Loaded Cargo	Healthcare Application	Ref.
Dextran	Spray drying method	-	Rifampicin	Enhanced deep lung delivery	[272]
Dextran	Ionic gelation method	34.0–42.0	-	Ocular drug delivery	[265]
Dextran	Single emulsion evaporation method	99.8–181.3	5, 10, 15, 20-tetraphenyl-21H, 23H-porphyrine	Drug delivery for a tumor cell-targeted photodynamic therapy	[273]
Dextran	Self-assembly method	260.0	Naproxen	Anti-inflammatory drug delivery	[274]
Dextran	Solvent diffusion method	<70.0	Chloroquine diphosphate	Delivery of antimalarial drug	[275]
Dextran	Ionic gelation method	69.3	-	Antibacterial agents	[276]
Xanthan gum	Anti-solvent precipitation	149.0–241.0	Cinnamon bark extract	Controlled delivery of polyphenols	[277]
Levan	Electrohydrodynamic atomization method	82.1	Resveratrol	Drug delivery for wound healing and tissue engineering	[269]
Gellan gum	Nebulization/ionic gelation method	337.1	Resveratrol	Oral drug delivery	[268]
Gellan gum	Ionic gelation method	85.6	Atenolol	Delivery of antihypertensive drug	[270]

8. Incorporation of Different Therapeutic Substances into Biopolymeric Nanoparticles for Healthcare Applications

Biopolymeric nanoparticles are applicable for clinical use as delivery systems for various drugs, genes, and other therapeutic agents and tissue engineering. This is due to their favorable properties, especially biodegradability, biocompatibility, non-toxicity, and low induction of immune responses [278,279]. Since they allow targeted delivery of incorporated drugs to target sites, preventing toxic effects on healthy cells, they can be loaded with a high concentration of drugs, allowing enhanced therapeutic effects due to

sustained release. The loaded drug is successfully protected from metabolic processes and thus retains its bioactivity [3,84].

Free drugs require high dosages to achieve a pharmacological effect and are potentially toxic. In contrast, biodegradable biopolymer nanocarriers represent unique and effective systems for various healthcare applications due to their favorable properties and enhanced drug delivery in the human body. Moreover, they successfully reduce the potential risks and drawbacks of conventional therapies. There are several routes of administration by which therapeutic agents can be introduced into the human body using biopolymeric nanoparticles, namely the enteral (oral, ocular, nasal) or parenteral (subcutaneous, intravenous, intramuscular) route. However, the appropriate route of administration is influenced by the disease state, the desired therapeutic effect, and the bioavailability of the drug [278,280].

8.1. Incorporation and Delivery of Bioactive Compounds

Biologically active compounds, such as polyphenolic compounds, have antioxidant, anti-inflammatory, antimicrobial, antitumor, antiallergic, and other beneficial biological activities. However, they are susceptible to environmental conditions such as light, heat, and oxygen and are, therefore, chemically unstable. Furthermore, they are poorly soluble in water and are rapidly metabolized [49]. These limitations can be successfully overcome by incorporating bioactive compounds into nanocarriers, such as biopolymeric nanoparticles [195]. It has already been confirmed that encapsulation of phenolic compounds in nanoparticles significantly improves their stability, water solubility, and bioavailability, as well as their biological activity. Therefore, biopolymeric nanoparticles are suitable carriers for these compounds, as they can also reduce the required dose of bioactive compounds, further reducing potential side effects [49].

Many bioactive compounds also have good antioxidant properties. However, their potential use in the treatment of diseases caused by oxidative stress, including neurodegenerative diseases, is a significant concern because brain targeting is still a major challenge. Nanoformulations with incorporated antioxidants are promising delivery systems because they protect antioxidant molecules from degradation while allowing improved bioavailability and targeted delivery to specific organs, cells, or tissues [31].

The bioactive ingredient curcumin has many beneficial properties for human health. Therefore, many studies have already been conducted on its encapsulation in various biopolymeric nanoparticles to provide protection from rapid degradation and enhance its therapeutic effects. Das et al. [281] successfully incorporated curcumin into albumin-based nanoparticles, which showed enhanced cellular uptake and cytotoxicity in human lung carcinoma cells (A549) compared with the free compound. Hassani et al. [282] successfully encapsulated curcumin into sodium alginate–gum Arabic nanoparticles for enhanced antioxidant and drug-release properties of curcumin. The curcumin alginate–gum Arabic nanoparticles were prepared by an ionotropic gelation technique with slight modifications using calcium chloride as a crosslinker. Curcumin-loaded nanoparticles have significant therapeutic potential in preventing and treating solid malignancies. Compared with free curcumin, they showed enhanced anticancer activity against HepG2, HT29, A549, and MCF-7 cancer cells, as demonstrated by a cytotoxicity study using the MTT assay. Nogueira et al. [283] have also successfully incorporated curcumin into biopolymeric nanoparticles based on the polysaccharide carrageenan. High hydrophobicity may hinder the *in vivo* bioavailability of curcumin, reducing its therapeutic effect. Consequently, its incorporation into biodegradable nanoparticles is crucial. Curcumin-loaded carrageenan nanoparticles are a potentially effective and safe system for the treatment of bone-related diseases. Starch nanoparticles can also be used as nanocarriers for curcumin. Acevedo-Guevara et al. [222] used natural and acetylated starch from green bananas to prepare nanoparticles. Curcumin was successfully incorporated into both nanoformulations with an encapsulation efficiency greater than 80%. However, the acetylated starch nanoparticles were more successful because the acetylation of starch caused stronger hydrogen bond interaction between

curcumin and the starch matrix, making the encapsulation more effective. In addition, improved controlled release of the polyphenolic substance from the acetylated starch nanoparticles was achieved. By incorporating curcumin into ovalbumin/ κ -carrageenan nanoparticles, Xie et al. [284] demonstrated high antioxidant activity and stability in simulated gastric fluid and enhanced thermal and light stability of curcumin. Fan et al. [285] synthesized nanoparticles based on BSA and dextran for the preparation of curcumin delivery systems. The results of the study showed that the prepared nanoparticles loaded with curcumin were stable. Further, the antioxidant activity of curcumin in Caco-2 cells compared to the free bioactive compound was significantly improved. Liu et al. [286] synthesized zein nanoparticles with incorporated curcumin and stabilized dual-coating shell structure in combination with sodium caseinate (SC) and sodium alginate (SA). Zein nanoparticles stabilized with SC-SA significantly improved the photochemical stability and antioxidant activity of curcumin and enabled controlled release under simulated gastrointestinal conditions. The nanocarriers prepared in this way, therefore, have the potential to successfully deliver chemically unstable hydrophobic bioactive compounds. They can improve the water solubility, photochemical stability, and antioxidant activity of bioactive compounds such as curcumin. The same conclusions were reached by Yao et al. [287], who used zein nanoparticles loaded with curcumin and an alginate/gelatin biopolymer coating in their study. Biopolymeric materials can form stable coatings on the surface of zein and other nanoparticles made of natural polymers, which contributes to improved pH stability of nanoparticles and inhibition of particle aggregation during long-term storage [192,287]. Sorasitthyanukarn et al. [288] successfully prepared chitosan/alginate nanoparticles loaded with curcumin diglutamic acid, a prodrug of curcumin with enhanced solubility and antinociceptive activity. These were more stable than free curcumin diglutamic acid under UV radiation and in simulated gastrointestinal environments. Additionally, they showed enhanced anticancer activity against Caco-2, HepG2, and human breast cancer cells (MDA-MB-231), as well as higher in vitro cell uptake in Caco-2 cells. Therefore, the authors claim that chitosan/alginate nanoparticles are a potential system for the oral delivery of curcumin diglutamic acid for cancer treatment. In a more recent study [289], the same authors synthesized chitosan/alginate nanoparticles loaded with curcumin diethyl disuccinate, an ester prodrug of curcumin. Compared with the free therapeutic substance, these showed improved stability, bioavailability, bioaccessibility, cellular uptake, and cytotoxicity against HepG2. In addition, chitosan- κ carrageenan nanoparticles with incorporated α -mangostin, a xanthone derivative isolated from the pericarp extract of mangosteen (*Garcinia mangostana* L.), are also promising delivery systems exhibit anticancer and excellent physicochemical properties [290]. They showed increased solubility, prolonged release, and cytotoxicity against MCF-7 cancer cells.

Rathore et al. [291] incorporated silymarin, a flavonoid, into collagen-based nanoparticles. Silymarin is a bioactive compound with hepatoprotective and neuroprotective properties isolated from milk thistle. The silymarin-loaded nanoformulation showed improved therapeutic efficacy of the flavonoid against acute ischemia/reperfusion injury. Moreover, a lower drug dose can achieve an appropriate neuroprotective effect by using nanoparticles. In addition, Roy and Rhim [292] incorporated a natural antioxidant flavonoid quercetin into chitosan-based nanoparticles, which exhibited good antioxidant and antimicrobial properties. Quercetin was also successfully loaded into zein nanoparticles stabilized with soluble soybean polysaccharide. This nanoformulation significantly improved the encapsulation efficiency and photochemical stability of quercetin [293]. Cinnamaldehyde is another natural compound belonging to flavonoids. Subhaswaraj et al. [182] prepared chitosan nanoparticles loaded with cinnamaldehyde, which showed significantly higher anti-quorum sensing activity and antibiofilm activity against *Pseudomonas aeruginosa* compared to free cinnamaldehyde. Moreover, slow and sustained release of cinnamaldehyde was achieved in an in vitro release study. Liang et al. [294] incorporated the polyphenolic compound tannic acid into synthesized zein/pectin nanoparticles with an average diameter of 166 nm and achieved an encapsulation efficiency of 89%. The results showed good an-

tioxidant activity of the incorporated tannic acid, gradually released from the nanoparticles under simulated gastrointestinal conditions, especially in the small intestine.

Anacardic acid is a hydroxybenzoic acid with exceptional antimicrobial properties. Araujo et al. [295] successfully loaded anacardic acid into zein nanoparticles using a nanoprecipitation method. This method is considered an economical, environmentally friendly, low-energy, and reproducible technique. Nanoencapsulation of anacardic acid even increased antimicrobial activity against *S. aureus*, *P. aeruginosa*, and *Candida auris*. In another study, zein nanoparticles loaded with anacardic acid showed high bactericidal activity against *S. mutans* and potential antiplaque activity [296]. Bernal-Mercado et al. [297] incorporated carvacrol, a monoterpene phenol extracted from oregano and thyme essential oils, into chitosan nanoparticles, enhancing their antibacterial and antibiofilm properties against *P. aeruginosa*. Furthermore, Jain et al. [298] successfully loaded beta-carotene into zein nanoparticles prepared by a modified phase separation technique. They demonstrated enhanced cellular uptake, cytotoxicity, and improved oral biopharmaceutical performance of beta-carotene.

8.2. Incorporation and Delivery of Conventional Drugs

Selective therapeutics targeting diseased areas is a significant challenge in the treatment of many diseases, especially various forms of cancer [299]. Different anticancer drugs are poorly soluble in water and may have multiple toxic side effects, which can be successfully eliminated by incorporation into different nanocarriers [219]. Therefore, chemopreventive and chemotherapeutic agents can be successfully encapsulated into various biopolymeric nanoparticles. These offer improved stability and solubility of the drug, as well as a longer half-life in the blood due to protection from modifications caused by metabolic enzymes. In addition, drug encapsulation successfully reduces drug resistance and enables controlled drug release at the target site [31]. Nanoparticles have the ability to deliver incorporated drugs to the target organ, cells, or tissues, preventing the potentially toxic effects of drugs on healthy cells, as is the case with conventional forms of drug delivery. As a result, the amount of drug administered can also be reduced to achieve the desired therapeutic effect [300]. They are also potential gene nanocarriers due to their nanoscale size, high surface-to-volume ratio, and stability [31].

Yu et al. [219] successfully incorporated the anticancer drug maytansine with an encapsulation efficiency of 82.97% into zein nanoparticles prepared by phase separation to target the tumor and reduce the toxic side effects of the drug. Maytansin-loaded zein nanoparticles have been shown to be non-toxic and promising nanocarriers for the treatment of non-small cell lung cancer, demonstrating enhanced antitumor efficacy in A549 cells compared to the free drug. Another anticancer drug, paclitaxel, was successfully incorporated into potato starch nanoparticles by Putro et al. [225]. The cytotoxicity assay results showed good biocompatibility of the nanoparticles with 7F2 mouse osteoblast cells. Abid et al. [299] synthesized enzyme-responsive dextran-based oligoester crosslinked nanoparticles containing the anticancer drug 5-fluorouracil as a potential oral delivery system to combat colon cancer. In a study by Ding et al. [224], 5-fluorouracil was also successfully incorporated into biopolymeric particles. The synthesized retrograded starch nanoparticles showed high absorption capacity and long in vitro release of the loaded drug, making them promising nanocarriers for colon-specific controlled release of 5-fluorouracil.

Pirfenidone is a drug with anti-inflammatory and antifibrotic activity used to treat idiopathic pulmonary fibrosis. Abnoos et al. [301] incorporated pirfenidone into chitosan/alginate nanoparticles with an encapsulation efficiency of 94%. An in vitro drug release study showed sustained release of the encapsulated drug, and skin penetration of the nanoparticle-loaded pirfenidone was compared to the free drug. Kianersi et al. [245] prepared alginate nanoparticles coated with chitosan and gelatin and loaded with the anti-inflammatory drug betamethasone sodium phosphate.

Thomas et al. [302] prepared starch-modified alginate nanoparticles using the ionotropic gelation method, into which they incorporated the drug theophylline and the protein BSA as

model drugs. In vitro cytotoxicity studies showed that the nanoparticles were completely nontoxic and exhibited excellent biocompatibility. Nanoparticles prepared in this way successfully protected the incorporated drug in the acidic environment of the gastric fluid, and complete release of the drug in the intestinal fluid was achieved. Constantin et al. [303] prepared spherical nanoparticles based on a pullulan derivative incorporated with the model drug sodium diclofenac. In vitro studies revealed that the polymeric nanoparticles did not exhibit cytotoxicity at a pharmacologically relevant concentration of diclofenac and retained typical cell morphology.

Ursodeoxycholic acid is an oral drug for the treatment of primary biliary cirrhosis. Yu et al. [257] successfully demonstrated the neuroprotective effect of ursodeoxycholic acid-loaded pullulan acetate nanoparticles stabilized by poly(vinyl alcohol). Chinnaiyan et al. [221] prepared metformin-loaded pectin-based nanoparticles with an encapsulation efficiency of 68% by an ionic gelation method. The results showed reasonable stability in the presence of excess BSA and slow and sustained release of the drug at pH 6.8. In vivo stability of the nanoparticles and the possibility of prolonging the retention time of the drug in the bloodstream were demonstrated. Therefore, the pectin nanoparticles developed in this way are appropriate for enhancing the bioavailability of metformin for the successful treatment of type 2 diabetes.

8.3. Incorporation and Delivery of Antibiotics and Antimicrobial Agents

Due to increasing resistance to antibiotics and other antimicrobial agents, the search for new formulations for their administration has become increasingly important. Various metal nanoparticles are considered effective inhibitors of bacterial growth but are also highly toxic to human cells [304,305]. On the other hand, biocompatible and non-toxic biopolymeric nanoparticles also exhibit antimicrobial activity against various bacterial species [3]. Different nanoformulations, including polymeric nanoparticles in addition to liposomes, micelles, and solid lipid nanoparticles, can be considered suitable nanocarriers for antibiotics and other antimicrobial agents. Incorporating antibiotics into suitable nanoparticles can overcome antibiotic resistance, which increases the efficacy against pathogenic bacteria and contributes to the controlled release of the drug at the site of infection. In addition, encapsulation of antibiotics also has a positive effect on overcoming certain limitations, including poor solubility and stability of the drug and low permeation through biological barriers [306–308]. Thus, they can protect antibiotics from pH and/or enzymatic degradation [309].

Biopolymeric nanoparticles have been shown to be effective antibiotic carriers for combating antibiotic resistance. In vitro studies have demonstrated superior antibacterial activity against clinical isolates of multidrug-resistant *E. coli*, *Klebsiella pneumoniae*, and methicillin-resistant *S. aureus* (MRSA) compared to free antibiotics [306]. Furthermore, several antibiotics, such as colistin, can be toxic and provide low tissue penetration, so they are not commonly used. However, Scutera et al. [306] successfully incorporated the antibiotic colistin into HSA-based nanoparticles coated with chitosan. Compared to the free antibiotic, high antibacterial activity against the growth and inhibition of biofilm formation of multidrug-resistant Gram-negative bacterial species responsible for hospital-acquired severe infections (*Acinetobacter baumannii* and *K. pneumoniae*) was demonstrated. The antibacterial activity of the antibiotic imipenem and ciprofloxacin separately and in combination incorporated into albumin nanoparticles was increased, particularly against methicillin-resistant *S. aureus* and *S. mutans* [176]. Alginate/chitosan nanoparticles with incorporated antimicrobial drug tobramycin could be effectively used in the treatment of chronic infection with *P. aeruginosa* [310].

Furthermore, Liu et al. [311] prepared chitosan–sodium alginate nanoparticles into which they incorporated ϵ -polylysine, a homo-poly amino acid. In antimicrobial studies against the growth of *E. coli*, *S. aureus*, *B. subtilis*, and *Micrococcus luteus*, they showed three times higher bacteriostatic activity than free ϵ -polylysine. In vitro studies also showed prolonged release of the component from the nanoparticles. In patients with recurrent

pulmonary infections, intrapulmonary administration of antibiotics may be beneficial compared with intravenous injection. Namely, inhalation can achieve a faster onset of action and a higher concentration of therapeutic agents in the lungs. Therefore, Falciani et al. [312] prepared a nanoformulation by binding the SET-M33 peptide, a not natural antimicrobial peptide, to single-chain dextran nanoparticles. Nanoparticles have been shown to be effective against pneumonia-causing *P. aeruginosa* in a mouse model by intrapulmonary administration. In addition, the retention time of the SET-M33 peptide in the lungs was effectively improved by incorporation into dextran-based nanoparticles. Moreover, Yu et al. [313] synthesized conjugates of chitosan nanoparticles and the antimicrobial peptide microcin J25. These have significantly enhanced antimicrobial activity against Gram-negative and Gram-positive bacteria while causing no toxicity in HEK293 T and Caco-2 cell lines.

8.4. Incorporation and Delivery of Extracts

It is known that natural extracts contain various biologically active substances that have a positive effect on health. Since they can be degraded in the gastrointestinal tract, their bioavailability is often poor. For the protection of sensitive compounds, the encapsulation of the extracts in different nanocarriers is crucial. A sustainable and suitable option are natural, non-toxic, biodegradable, and biocompatible protein- or polysaccharide-based nanoparticles to enhance their bioavailability and overcome biological barriers [246].

For this purpose, Costa et al. [246] successfully incorporated bioactive grape pomace extract into alginate and chitosan nanoparticles and investigated their potential as suitable nanocarriers for oral delivery. Alginate and chitosan nanoparticles protected the extract from the gastrointestinal environment, increasing the bioavailability of polyphenolic compounds in the extract and thus enhancing antioxidant and antimicrobial activity. In addition, the encapsulation of the extract also reduced its permeability through the intestinal barrier, allowing the extract to remain in the intestine longer, thus improving the prebiotic potential of the extract. Rahimivand et al. [314] successfully synthesized alginate nanocarriers with an incorporated ethanolic extract of *Artemisia ciniformis*, which increased cytotoxicity and induced apoptosis against AGS gastric cancer cells compared with the free extract. Encapsulation successfully protected the extracts from environmental stress. Wang et al. [223] synthesized starch nanoparticles obtained from ginkgo and corn, respectively, loaded with *Ginkgo biloba* extract using the nanoprecipitation method. Starch nanoparticles proved to be promising delivery systems for *Ginkgo biloba* extract or other bioactive compounds. The extract-loaded starch nanoparticles showed sustained release compared to the free extract in artificial gastric and intestinal juices. Additionally, Nallasamy et al. [226] have prepared starch-based nanoparticles into which they have successfully incorporated Triphala Churna extract, a polyherbal formulation rich in polyphenols and vitamin C that has rejuvenating and anti-aging effects. Encapsulation in biopolymer nanoparticles increased the stability, solubility, and efficacy of the Ayurvedic drug and achieved sustained release. In addition, antioxidant and anticholinesterase activities were maintained. A strong antimicrobial activity against *Salmonella typhi*, *Shigella dysenteriae*, and *S. aureus*, as well as anti-biofilm activity against ATCC MRSA 33591 and clinical strain N7 were demonstrated. Soltanzadeh et al. [183] synthesized spherical, physically stable chitosan nanoparticles with a diameter of 174–898 nm, into which pomegranate peel extract was successfully encapsulated. The study indicates promising nano-delivery systems for extracts and the resulting protection and controlled delivery of natural, sensitive substances with antioxidant and antimicrobial properties. Furthermore, Beconcini et al. [315] incorporated cherry extract into chitosan nanoparticles, successfully protecting the antioxidants contained in the extract from degradation in the gastrointestinal tract.

8.5. Incorporation and Delivery of Essential Oils

The labile and volatile compounds in essential oils can easily evaporate or decompose and are poorly soluble in water, affecting their antioxidant and antibacterial properties.

Incorporating essential oils into nanoparticles, such as natural and biodegradable biopolymeric particles, successfully protects the essential oil components from degradation under adverse environmental conditions, extends shelf life, and contributes to controlled release [316,317].

Hadid et al. [316] successfully synthesized chitosan-based nanoparticles loaded with extracted clove bud essential oil, which exhibited better antioxidant and antimicrobial activity against *Listeria monocytogenes* and *S. aureus* compared to free essential oil. Hasheminejad et al. [180] also successfully incorporated clove essential oil into chitosan nanoparticles, which increased antifungal activity against *A. niger*. The in vitro release studies showed a controlled release of the essential oil over 56 days. By successfully encapsulating basil (*Ocimum basilicum* L.) essential oil in chitosan nanoparticles, Cai et al. [181] demonstrated enhanced antibacterial activity and strong antibiofilm activity against *E. coli* and *S. aureus*. Similarly, mandarin (*Citrus reticulata* L.) essential oil was successfully loaded into chitosan-based nanoparticles [318]. The nanoformulation successfully damaged the cell membrane of *E. coli* and *S. aureus* and inhibited biofilm formation and destroyed mature biofilms.

By incorporating essential oil from nettle leaves into chitosan nanoparticles, Bagheri et al. [319] achieved improved antioxidant activity compared to free essential oil and a more effective inhibitory effect on the growth of *E. coli* and *S. aureus*. Soltanzadeh et al. [184] incorporated the essential oil of lemongrass (*Cymbopogon commutatus*) into chitosan nanoparticles and demonstrated a time- and pH-dependent release of the essential oil in an in vitro release study. The chitosan nanoparticles also successfully retained the essential oils and preserved their bioactivity. Compared to free nanoparticles, nanoparticles with incorporated essential oil exhibited stronger antibacterial and antifungal activities. Furthermore, the essential oil of peppermint (*Mentha piperita*) and green tea (*Camellia sinensis*) [320] were also successfully loaded into chitosan nanoparticles, which exhibited enhanced thermal stability, antioxidant and antimicrobial activity. Additionally, cumin (*Cuminum cyminum*) seed essential oil was successfully encapsulated in chitosan nanoparticles [321]. Therefore, chitosan-based nanoparticles have emerged as a novel approach for the production of new pharmaceutical products with antimicrobial activity.

Furthermore, Yoncheva et al. [322] successfully encapsulated oregano essential oil in chitosan-alginate nanoparticles. The thermal stability of the oil, as well as antibacterial and antimetabolic activity compared to pure oil, was improved. In addition, an in vitro cytotoxicity test on human keratinocytes and an in vivo skin irritation test in an animal model demonstrated the safety profile of the oil-loaded nanoparticles. Merino et al. [220] incorporated *Thymbra capitata* essential oil into zein nanoparticles prepared by the self-assembly method and achieved an encapsulation efficiency of 77.8%. Compared with the essential oil in suspension, the essential oil-loaded nanoparticles exhibited enhanced antimicrobial activity. In addition, zein nanoparticles enable the controlled release of essential oils, making them beneficial nanomaterials for pharmaceutical and cosmetic purposes. Cai et al. [323] successfully incorporated tea tree essential oil into gliadin-based nanoparticles stabilized with gum Arabic.

8.6. Incorporation and Delivery of Different Therapeutic Substances: A Summary

Many studies have already been conducted testing both protein and polysaccharide nanoparticles of different origins as promising biodegradable and biocompatible delivery systems for drugs and other therapeutic agents. The aim of the studies was the improvement of bioavailability and therapeutic effect, as well as preventing possible adverse side effects of the loaded cargo.

Table 8 shows examples of drugs and other therapeutic agents incorporated into biopolymer nanoparticles, including their potential therapeutic applications.

Table 8. Examples of therapeutic agents loaded into biopolymeric nanoparticles for different biomedical purposes.

Incorporated Therapeutic Compound	Biopolymer	Administration Route	Therapeutic Application	Ref.
<i>Bioactive compounds</i>				
Sylmarin	Collagen	Intraperitoneal injection	Enhanced neuroprotective effect against acute ischemia/reperfusion injury	[291]
Cucurbitacin B	Collagen	Oral delivery	Enhanced absorption of orally administered Cucurbitacin B	[179]
Curcumin	BSA/dextran	In vitro	Enhancement of cellular antioxidant activity of curcumin in Caco-2 cells	[285]
Curcumin	Zein	Oral administration	Increased oral bioavailability	[324]
Curcumin	Zein	Intravenous injection	Potential drug delivery platform for therapy of glioblastoma	[193]
Beta-carotene	Zein	Oral administration	Enhanced cellular uptake, cytotoxicity, and improved oral biopharmaceutical performance	[298]
Anacardic acid	Zein	In vitro	Enhanced antimicrobial activity	[295]
Quercetin	Zein stabilized with soluble soybean polysaccharide	In vitro	Potential all-natural delivery systems for bioactive molecules	[293]
Morin	Starch	Intravenous injection	Therapeutic efficacy in the treatment of hyperuricemia	[325]
<i>Conventional drugs</i>				
Prednisolone and curcumin	HSA	Intravenous injection	Improved in vivo therapeutic effect in rats with rheumatoid arthritis	[130]
Paclitaxel and resveratrol	BSA	Intravenous injection	Improved suppression of tumor growth without systemic toxicity	[66]
Paclitaxel and di-fluorinated curcumin	BSA	Intravenous injection	A promising platform for treating gynecological cancers	[133]
Rotigotine	Chitosan	Nose-to-brain administration	Efficient drug delivery as an alternative to conventional routes	[168]
Zinc gluconate	Chitosan	Intraperitoneal injection	A potential alternative for the treatment of rheumatoid arthritis	[167]
Pirfenidone	Chitosan/alginate	Transdermal administration	Drug delivery for the treatment of idiopathic pulmonary fibrosis	[301]
Rifampicin	Alginate	Oral administration	No systemic toxicity and excellent safety after oral administration of nanoparticles	[244]

Table 8. Cont.

Incorporated Therapeutic Compound	Biopolymer	Administration Route	Therapeutic Application	Ref.
Maytansine	Zein	Intravenous injection	Strong anti-A549 tumor cell activity	[219]
Sumatriptan	Gliadin	Nasal administration	Effective crossing of the blood-brain barrier	[188]
Metformin	Pectin	In vitro	Oral administration for management of Type 2 Diabetes Mellitus	[221]
Ibuprofen	Starch	Oral administration	Colon-targeted drug delivery	[326]
Mitoxantrone	Pullulan	In vitro	Inhibition of the growth of bladder cancer cells (MB49)	[253]
Ursodeoxycholic Acid	Pullulan	In vitro	Increased neuroprotective effect	[257]
Paclitaxel	Dextran	Intravenous injection	Potential for C6 glioma treatment	[266]
Chloroquine diphosphate	Dextran	Parenteral administration	Treatment of malaria	[275]
<i>Antibiotics and antimicrobial agents</i>				
Colistin	HSA	In vitro	High antibacterial activity against the growth and inhibition of biofilm formation of multidrug-resistant Gram-negative bacterial species	[306]
Tobramycin	Alginate/chitosan	In vitro	Efficient delivery of antimicrobial drug	[310]
ϵ -Polylysine	Alginate/chitosan	In vitro	Delivery of antibacterial agents	[311]
SET-M33 peptide	Dextran	Intrapulmonary administration	Efficient treatment of lung infection	[312]
<i>Extracts</i>				
Pomegranate peel extract	Chitosan	In vitro	Enhanced antioxidant and antimicrobial properties	[183]
Grape pomace extract	Chitosan/alginate	Oral delivery	Improved biological activity	[246]
<i>Artemisia ciniformis</i> extract	Alginate	In vitro	Inhibition of proliferation of AGS cells	[314]
<i>Ginkgo biloba</i> extract	Starch	In vitro	Sustained release in artificial gastric and intestinal juices	[223]
<i>Essential oils</i>				
Oregano essential oil	Alginate/chitosan	Dermal administration	Enhanced antimicrobial activity	[322]
Clove essential oil	Chitosan	In vitro	Improved antioxidant and antibacterial activity	[316]
Basil essential oil	Chitosan	In vitro	Enhanced antimicrobial activity and strong antibiofilm activity	[181]
Mandarin essential oil	Chitosan	In vitro	Enhanced inhibition of biofilm formation	[318]

Table 8. Cont.

Incorporated Therapeutic Compound	Biopolymer	Administration Route	Therapeutic Application	Ref.
Lemongrass and peppermint essential oil	Chitosan	In vitro	Enhanced thermal stability, antioxidant, and antimicrobial activity	[184]
Green tea essential oil	Chitosan	In vitro	Enhanced thermal stability, antioxidant, and antimicrobial activity	[320]

9. Regulatory Aspects of Biopolymer-Based Nanoparticles

Biopolymers play a crucial role in major industrial sectors. Their sales are increasing, however, their demand for biomedical applications will grow rapidly in the coming years.

Various nanoparticles represent successful materials in numerous health applications, but there are still concerns about their safe use and long-term effects on human health. Therefore, risk management and regulatory issues remain [327]. Although biopolymeric nanoparticles are considered safe, biocompatible, biodegradable, and nontoxic, clinical studies on their safe use in drug delivery are urgently needed. Considering the many successful studies on biopolymeric nanoparticles with incorporated therapeutic agents, many companies are already developing suitable biopolymer-based nanoparticle formulations, some of which are already close to pre-clinical and clinical trials or are already in Phase 1. An example of a commercial formulation that is in Phase 1 is DE-310, which consists of a topoisomerase I inhibitor (exatecan mesylate) and a biodegradable carboxymethyl-dextran polyalcohol polymer covalently linked via a Gly-Gly-Phe-Gly peptidyl linker. In a Phase 1 clinical trial, it achieved complete remission in one of 27 patients with metastatic adenocarcinoma studied and partial remission in one patient with metastatic pancreatic cancer. In addition, it led to stabilization of disease progression in 14 patients. Delimotecan (MEN 4901/T-0128) is also a Phase 1 dextran-based nanoformulation with incorporated camptothecin (T-2513) for the treatment of solid tumors. The alginate and calcium gluconate-based formulation IK-5001 is also in Phase 1 for the prevention of ventricular remodeling and congestive heart failure. Another formulation is already in Phase 2, chitosan-based Milican, with incorporated holmium-166 for the treatment of small hepatocellular carcinoma [83].

On the other hand, some formulations containing biopolymeric nanoparticles are already successfully used and approved by the Food and Drug Administration (FDA) for various applications, including cancer treatment [52]. The first nanoformulation containing biopolymeric nanoparticles for the treatment of advanced metastatic pancreatic, breast, and non-small lung cancer is Abraxane, which the FDA has approved. Abraxane is a commercial formulation of the hydrophobic anticancer drug paclitaxel loaded into albumin-based nanoparticles. The nanoformulation is intended for intravenous administration and contains nanoparticles of 135 nm diameter [133]. Yuan et al. [328] investigated the efficacy and mechanism of two commercially available formulations to eliminate cancer stem cells *in vitro* and *in vivo*. In their study, they found that Abraxane, which contains paclitaxel-loaded albumin nanoparticles, improved the efficacy of paclitaxel in eliminating breast cancer stem cells over Taxol, a micelle formulation of paclitaxel [133].

However, the regulatory requirements for biopolymeric nanoparticles need greater attention and further research to ensure that commercial formulations can successfully overcome the challenges associated with stability and, more importantly, safety.

10. Conclusions

Research in the field of various nanoparticles as delivery systems for drugs and other therapeutic agents for healthcare applications is growing rapidly. However, synthetic nanoparticles can be toxic and have other unfavorable properties. Therefore, nanoparticles

derived from natural materials such as biopolymers of animal, plant, algal, fungal, and bacterial origin are receiving increasing attention. Namely, they offer many advantages that are important factors for their potential use as successful and safe nanocarriers for drugs in the human body. Precisely because of their biocompatibility, biodegradability, nontoxicity, antioxidant properties (natural polysaccharides), and stability, research on the potential use of protein- and polysaccharide-based nanoparticles as favorable nanocarriers for therapeutic agents as new forms of treatment has significantly increased in the last decade. Furthermore, biopolymeric nanoparticles enable efficient encapsulation of many therapeutic agents, ensuring successful protection from degradation in the gastrointestinal tract, preventing potential toxic side effects of the loaded therapeutic agents, and ensuring controlled release at the target site, making them particularly promising for oral administration.

This review aims to generally outline the current state of research in the field of promising delivery of biopolymeric nanoparticles loaded with various therapeutic agents, both drugs and antibiotics, as well as natural extracts and bioactive compounds for biomedical applications. Biopolymeric nanoparticles successfully increase the bioavailability and improve the therapeutic effect not only of drugs, antibiotics, and other antimicrobial agents but also of extracts and essential oils, especially naturally isolated bioactive compounds. As far as natural compounds and their incorporation into biopolymeric nanoparticles are concerned, most studies have been conducted on curcumin and other bioactive compounds, which have thus shown promise as nanocarriers for various biomedical purposes. However, different encapsulated extracts and essential oils show significantly enhanced antioxidant and antimicrobial activity. Therefore, nanoparticles prepared from natural biopolymers with incorporated natural extracts and bioactive compounds are a promising alternative to various conventional therapies and therapeutic agents that cause toxic side effects and cytotoxicity to healthy cells. Moreover, they may not reach the target sites at all, leading to drug resistance in patients.

Based on the reviewed literature, studies on the use of polysaccharide nanoparticles for healthcare applications predominate. Chitosan is among the most studied biopolymers for the preparation of nanoparticles for the successful delivery of various therapeutic agents, as demonstrated by numerous *in vitro* studies. It is one of the most readily available and economical biopolymers and, therefore, the most suitable for commercial application. Nevertheless, further studies are urgently needed because chitosan nanoparticles, despite their excellent potential, are less recommended for therapeutic purposes due to the possible transmission of diseases from animals to humans by animal-based nanoparticles. It should be emphasized that preclinical studies are crucial for potential commercial use. Therefore, it is recommended to focus more on plant and microbial polysaccharide-based nanoparticles. Nowadays, polysaccharides can be largely obtained from algae, which are considered to be of less concern for healthcare use. Although there is a great tendency to cultivate algae for other applications such as food applications, fuels, etc., it is reasonable to direct the cultivation towards the extraction of polysaccharides for the synthesis of algae-based nanoparticles. However, further studies are critically needed to ensure the production of the most therapeutically successful, safe, sustainable, and biodegradable biopolymeric nanoparticles for healthcare applications.

Author Contributions: N.K. and M.L. conceived and designed the article. N.K. studied the literature and wrote the manuscript. M.P. reviewed and edited the article. M.L. and Ž.K. were responsible for the financial part of the project and reviewed the article. All authors have read and agreed to the published version of the manuscript.

Funding: This research was supported by the Slovenian Research Agency (ARRS) within the frame of program P2-0046 (Separation Processes and Production Design), project No. J2-3037 (Bionanotechnology as a tool for stabilization and applications of bioactive substances from natural sources), project No. L2-4430 (Production, Isolation, and Formulation of Health Beneficial Substances from *Helichrysum italicum* for Applications in Cosmetic Industry), and young researcher ARRS fellowship contract number No. 2595/FKKT-2022.

Institutional Review Board Statement: Not applicable.

Informed Consent Statement: Not applicable.

Data Availability Statement: Not applicable.

Conflicts of Interest: The authors declare no conflict of interest.

References

- Prasad, M.; Lambe, U.P.; Brar, B.; Shah, I.; Jyoti, M.; Ranjan, K.; Rao, R.; Kumar, S.; Mahant, S.; Khurana, S.K.; et al. Nanotherapeutics: An Insight into Healthcare and Multi-Dimensional Applications in Medical Sector of the Modern World. *Biomed. Pharmacother.* **2018**, *97*, 1521–1537. [CrossRef] [PubMed]
- Joudeh, N.; Linke, D. Nanoparticle Classification, Physicochemical Properties, Characterization, and Applications: A Comprehensive Review for Biologists. *J. Nanobiotechnology* **2022**, *20*, 262. [CrossRef] [PubMed]
- Vodyashkin, A.A.; Kezimana, P.; Vetcher, A.A.; Stanishevskiy, Y.M. Biopolymeric Nanoparticles—Multifunctional Materials of the Future. *Polymers* **2022**, *14*, 2287. [CrossRef] [PubMed]
- Ingle, A.P.; Gupta, I.; Duran, N.; Rai, M. Chapter 29—Nanotherapy: A next Generation Hallmark for Combating Cancer. In *Nanostructures for Cancer Therapy*; Ficai, A., Grumezescu, A.M., Eds.; Micro and Nano Technologies; Elsevier: Amsterdam, The Netherlands, 2017; pp. 811–830; ISBN 978-0-323-46144-3.
- Xiao, X.; Teng, F.; Shi, C.; Chen, J.; Wu, S.; Wang, B.; Meng, X.; Essiet Imeh, A.; Li, W. Polymeric Nanoparticles—Promising Carriers for Cancer Therapy. *Front. Bioeng. Biotechnol.* **2022**, *10*, 1024143. [CrossRef]
- Kolahalam, L.A.; Kasi Viswanath, I.V.; Diwakar, B.S.; Govindh, B.; Reddy, V.; Murthy, Y.L.N. Review on Nanomaterials: Synthesis and Applications. *Mater. Today Proc.* **2019**, *18*, 2182–2190. [CrossRef]
- Sajid, M. Nanomaterials: Types, Properties, Recent Advances, and Toxicity Concerns. *Curr. Opin. Environ. Sci. Health.* **2022**, *25*, 100319. [CrossRef]
- Ijaz, I.; Gilani, E.; Nazir, A.; Bukhari, A. Detail Review on Chemical, Physical and Green Synthesis, Classification, Characterizations and Applications of Nanoparticles. *Green Chem. Lett. Rev.* **2020**, *13*, 223–245. [CrossRef]
- Teleanu, D.M.; Chircov, C.; Grumezescu, A.M.; Teleanu, R.I. Neurotoxicity of Nanomaterials: An Up-to-Date Overview. *Nanomaterials* **2019**, *9*, 96. [CrossRef]
- Subhan, M.A.; Choudhury, K.P.; Neogi, N. Advances with Molecular Nanomaterials in Industrial Manufacturing Applications. *Nanomanufacturing* **2021**, *1*, 75–97. [CrossRef]
- Saha, S.; Bansal, S.; Khanuja, M. Chapter 2—Classification of Nanomaterials and Their Physical and Chemical Nature. In *Nano-Enabled Agrochemicals in Agriculture*; Ghorbanpour, M., Shahid, M.A., Eds.; Academic Press: Cambridge, MA, USA, 2022; pp. 7–34; ISBN 978-0-323-91009-5.
- Xiong, R.; Grant, A.M.; Ma, R.; Zhang, S.; Tsukruk, V.V. Naturally-Derived Biopolymer Nanocomposites: Interfacial Design, Properties and Emerging Applications. *Mater. Sci. Eng. R Rep.* **2018**, *125*, 1–41. [CrossRef]
- Alkaç, İ.M.; Çerçi, B.; Timuralp, C.; Şen, F. 2—Nanomaterials and Their Classification. In *Nanomaterials for Direct Alcohol Fuel Cells*; Şen, F., Ed.; Micro and Nano Technologies; Elsevier: Amsterdam, The Netherlands, 2021; pp. 17–33; ISBN 978-0-12-821713-9.
- Kang, H.; Rho, S.; Stiles, W.R.; Hu, S.; Baek, Y.; Hwang, D.W.; Kashiwagi, S.; Kim, M.S.; Choi, H.S. Size-Dependent EPR Effect of Polymeric Nanoparticles on Tumor Targeting. *Adv. Healthc. Mater.* **2020**, *9*, 1901223. [CrossRef]
- Distaso, M. Potential Contribution of Nanotechnology to the Circular Economy of Plastic Materials. *Acta Innov.* **2020**, *37*, 57–66. [CrossRef]
- Vassal, M.; Rebelo, S.; Pereira, M.D.L. Metal Oxide Nanoparticles: Evidence of Adverse Effects on the Male Reproductive System. *Int. J. Mol. Sci.* **2021**, *22*, 8061. [CrossRef]
- Patel, K.D.; Singh, R.K.; Kim, H.-W. Carbon-Based Nanomaterials as an Emerging Platform for Theranostics. *Mater. Horiz.* **2019**, *6*, 434–469. [CrossRef]
- Khan, I.; Saeed, K.; Khan, I. Nanoparticles: Properties, Applications and Toxicities. *Arab. J. Chem.* **2019**, *12*, 908–931. [CrossRef]
- Khalid, K.; Tan, X.; Mohd Zaid, H.F.; Tao, Y.; Lye Chew, C.; Chu, D.-T.; Lam, M.K.; Ho, Y.-C.; Lim, J.W.; Chin Wei, L. Advanced in Developmental Organic and Inorganic Nanomaterial: A Review. *Bioengineered* **2020**, *11*, 328–355. [CrossRef] [PubMed]
- Wang, H.; Zhou, Y.; Sun, Q.; Zhou, C.; Hu, S.; Lenahan, C.; Xu, W.; Deng, Y.; Li, G.; Tao, S. Update on Nanoparticle-Based Drug Delivery System for Anti-Inflammatory Treatment. *Front. Bioeng. Biotechnol.* **2021**, *9*, 630352. [CrossRef]
- Chandrakala, V.; Aruna, V.; Angajala, G. Review on Metal Nanoparticles as Nanocarriers: Current Challenges and Perspectives in Drug Delivery Systems. *Emergent Mater.* **2022**, *5*, 1593–1615. [CrossRef]
- Jamkhande, P.G.; Ghule, N.W.; Bamer, A.H.; Kalaskar, M.G. Metal Nanoparticles Synthesis: An Overview on Methods of Preparation, Advantages and Disadvantages, and Applications. *J. Drug Deliv. Sci. Technol.* **2019**, *53*, 101174. [CrossRef]
- Amini, E.; Azadfallah, M. In Situ Synthesis of Silver Nanoparticles on Fiber Matrix for Preparing Antibacterial Paper. *Biointerface Res. Appl. Chem.* **2018**, *8*, 3449–3456.
- Amini, E.; Valls, C.; Yousefi, H.; Roncero, M.B. Ionic Liquid/ZnO Assisted Preparation of High Barrier Cellulose Nanocomposite Films by In Situ Ring-Opening Polymerization of Lactide Monomers. *J. Polym. Environ.* **2023**, 1–19. [CrossRef]

25. Adepu, S.; Ramakrishna, S. Controlled Drug Delivery Systems: Current Status and Future Directions. *Molecules* **2021**, *26*, 5905. [CrossRef]
26. Feitosa, R.C.; Geraldles, D.C.; Beraldo-de-Araújo, V.L.; Costa, J.S.R.; Oliveira-Nascimento, L. Pharmacokinetic Aspects of Nanoparticle-in-Matrix Drug Delivery Systems for Oral/Buccal Delivery. *Front. Pharmacol.* **2019**, *10*, 1057. [CrossRef]
27. Leitgeb, M.; Knez, Ž.; Primožič, M. Sustainable Technologies for Liposome Preparation. *J. Supercrit. Fluids* **2020**, *165*, 104984. [CrossRef]
28. Kučuk, N.; Primožič, M.; Knez, Ž.; Leitgeb, M. Exosomes Engineering and Their Roles as Therapy Delivery Tools, Therapeutic Targets, and Biomarkers. *Int. J. Mol. Sci.* **2021**, *22*, 9543. [CrossRef] [PubMed]
29. Yetisgin, A.A.; Cetinel, S.; Zuvun, M.; Kosar, A.; Kutlu, O. Therapeutic Nanoparticles and Their Targeted Delivery Applications. *Molecules* **2020**, *25*, 2193. [CrossRef]
30. Yoon, M.S.; Lee, Y.J.; Shin, H.J.; Park, C.-W.; Han, S.-B.; Jung, J.-K.; Kim, J.-S.; Shin, D.H. Recent Advances and Challenges in Controlling the Spatiotemporal Release of Combinatorial Anticancer Drugs from Nanoparticles. *Pharmaceutics* **2020**, *12*, 1156. [CrossRef] [PubMed]
31. Harish, V.; Tewari, D.; Gaur, M.; Yadav, A.B.; Swaroop, S.; Bechelany, M.; Barhoum, A. Review on Nanoparticles and Nanostructured Materials: Bioimaging, Biosensing, Drug Delivery, Tissue Engineering, Antimicrobial, and Agro-Food Applications. *Nanomaterials* **2022**, *12*, 457. [CrossRef] [PubMed]
32. Lu, X.-Y.; Wu, D.-C.; Li, Z.-J.; Chen, G.-Q. Chapter 7—Polymer Nanoparticles. In *Progress in Molecular Biology and Translational Science*; Villaverde, A., Ed.; Nanoparticles in Translational Science and Medicine; Academic Press: Cambridge, MA, USA, 2011; Volume 104, pp. 299–323.
33. Guo, S.; Fu, D.; Utupova, A.; Sun, D.; Zhou, M.; Jin, Z.; Zhao, K. Applications of Polymer-Based Nanoparticles in Vaccine Field. *Nanotechnol. Rev.* **2019**, *8*, 143–155. [CrossRef]
34. Noreen, S.; Ma, J.-X.; Saeed, M.; Pervaiz, F.; Hanif, M.F.; Ahmed, B.; Farooq, M.I.; Akram, F.; Safdar, M.; Madni, A.; et al. Natural Polysaccharide-Based Biodegradable Polymeric Platforms for Transdermal Drug Delivery System: A Critical Analysis. *Drug. Deliv. Transl. Res.* **2022**, *12*, 2649–2666. [CrossRef]
35. Gowthaman, N.S.K.; Lim, H.N.; Sreeraj, T.R.; Amalraj, A.; Gopi, S. Chapter 15—Advantages of Biopolymers over Synthetic Polymers: Social, Economic, and Environmental Aspects. In *Biopolymers and Their Industrial Applications*; Thomas, S., Gopi, S., Amalraj, A., Eds.; Elsevier: Amsterdam, The Netherlands, 2021; pp. 351–372; ISBN 978-0-12-819240-5.
36. Maghsoudi, S.; Taghavi Shahraki, B.; Rabiee, N.; Fatahi, Y.; Dinarvand, R.; Tavakolizadeh, M.; Ahmadi, S.; Rabiee, M.; Bagherzadeh, M.; Pourjavadi, A.; et al. Burgeoning Polymer Nano Blends for Improved Controlled Drug Release: A Review. *Int. J. Nanomed.* **2020**, *15*, 4363–4392. [CrossRef] [PubMed]
37. Baranwal, J.; Barse, B.; Fais, A.; Delogu, G.L.; Kumar, A. Biopolymer: A Sustainable Material for Food and Medical Applications. *Polymers* **2022**, *14*, 983. [CrossRef]
38. Lakshminarayanan, R.; Ye, E.; Young, D.J.; Li, Z.; Loh, X.J. Recent Advances in the Development of Antimicrobial Nanoparticles for Combating Resistant Pathogens. *Adv. Healthc. Mater.* **2018**, *7*, 1701400. [CrossRef]
39. Muir, V.G.; Burdick, J.A. Chemically Modified Biopolymers for the Formation of Biomedical Hydrogels. *Chem. Rev.* **2021**, *121*, 10908–10949. [CrossRef]
40. Biswas, M.C.; Jony, B.; Nandy, P.K.; Chowdhury, R.A.; Halder, S.; Kumar, D.; Ramakrishna, S.; Hassan, M.; Ahsan, M.A.; Hoque, M.E.; et al. Recent Advancement of Biopolymers and Their Potential Biomedical Applications. *J. Polym. Environ.* **2022**, *30*, 51–74. [CrossRef]
41. Kaur, G.; Kumar, V.; Mishra, A.K.; Mishra, S. Chapter 12—Toxicological Effect of Biopolymers and Their Applications. In *Bio-Based Nanomaterials*; Mishra, A.K., Hussain, C.M., Eds.; Micro and Nano Technologies; Elsevier: Amsterdam, The Netherlands, 2022; pp. 265–284; ISBN 978-0-323-85148-0.
42. Kumar, S.; Basumatary, I.B.; Mukherjee, A.; Dutta, J. An Overview of Natural Biopolymers in Food Packaging. In *Biopolymer-Based Food Packaging*; John Wiley & Sons, Ltd.: Hoboken, NJ, USA, 2022; pp. 1–28; ISBN 978-1-119-70231-3.
43. Kleber, M.; Reardon, P. Biopolymers and Macromolecules. In *Encyclopedia of Geochemistry: A Comprehensive Reference Source on the Chemistry of the Earth*; White, W.M., Ed.; Encyclopedia of Earth Sciences Series; Springer International Publishing: Cham, Switzerland, 2018; pp. 148–153; ISBN 978-3-319-39312-4.
44. Karabasz, A.; Bzowska, M.; Szczepanowicz, K. Biomedical Applications of Multifunctional Polymeric Nanocarriers: A Review of Current Literature. *Int. J. Nanomed.* **2020**, *15*, 8673–8696. [CrossRef] [PubMed]
45. Sun, X.; Wang, H.; Li, S.; Song, C.; Zhang, S.; Ren, J.; Udenigwe, C.C. Maillard-Type Protein–Polysaccharide Conjugates and Electrostatic Protein–Polysaccharide Complexes as Delivery Vehicles for Food Bioactive Ingredients: Formation, Types, and Applications. *Gels* **2022**, *8*, 135. [CrossRef] [PubMed]
46. Bealer, E.J.; Onissema-Karimu, S.; Rivera-Galletti, A.; Francis, M.; Wilkowski, J.; Salas-de la Cruz, D.; Hu, X. Protein–Polysaccharide Composite Materials: Fabrication and Applications. *Polymers* **2020**, *12*, 464. [CrossRef]
47. Pathak, N.; Singh, P.; Singh, P.K.; Sharma, S.; Singh, R.P.; Gupta, A.; Mishra, R.; Mishra, V.K.; Tripathi, M. Biopolymeric Nanoparticles Based Effective Delivery of Bioactive Compounds toward the Sustainable Development of Anticancerous Therapeutics. *Front. Nutr.* **2022**, *9*, 963413. [CrossRef] [PubMed]

48. Patra, J.K.; Das, G.; Fraceto, L.F.; Campos, E.V.R.; Rodriguez-Torres, M.d.P.; Acosta-Torres, L.S.; Diaz-Torres, L.A.; Grillo, R.; Swamy, M.K.; Sharma, S.; et al. Nano Based Drug Delivery Systems: Recent Developments and Future Prospects. *J. Nanobiotechnology* **2018**, *16*, 71. [CrossRef]
49. Nishimoto-Sauceda, D.; Romero-Robles, L.E.; Antunes-Ricardo, M. Biopolymer Nanoparticles: A Strategy to Enhance Stability, Bioavailability, and Biological Effects of Phenolic Compounds as Functional Ingredients. *J. Sci. Food Agric.* **2022**, *102*, 41–52. [CrossRef] [PubMed]
50. Pulingam, T.; Foroozandeh, P.; Chuah, J.-A.; Sudesh, K. Exploring Various Techniques for the Chemical and Biological Synthesis of Polymeric Nanoparticles. *Nanomaterials* **2022**, *12*, 576. [CrossRef]
51. Meng, R.; Zhu, H.; Wang, Z.; Hao, S.; Wang, B. Preparation of Drug-Loaded Albumin Nanoparticles and Its Application in Cancer Therapy. *J. Nanomater.* **2022**, *2022*, e3052175. [CrossRef]
52. Hong, S.; Choi, D.W.; Kim, H.N.; Park, C.G.; Lee, W.; Park, H.H. Protein-Based Nanoparticles as Drug Delivery Systems. *Pharmaceutics* **2020**, *12*, 604. [CrossRef]
53. Bora, A.; Mishra, P. Casein and Ag Nanoparticles: Synthesis, Characterization, and Their Application in Biopolymer-Based Bilayer Film. *J. Food Process. Preserv.* **2019**, *43*, e14062. [CrossRef]
54. Miao, Y.; Yang, T.; Yang, S.; Yang, M.; Mao, C. Protein Nanoparticles Directed Cancer Imaging and Therapy. *Nano Converg.* **2022**, *9*, 2. [CrossRef] [PubMed]
55. Liang, T.; Zhang, Z.; Jing, P. Black Rice Anthocyanins Embedded in Self-Assembled Chitosan/Chondroitin Sulfate Nanoparticles Enhance Apoptosis in HCT-116 Cells. *Food Chem.* **2019**, *301*, 125280. [CrossRef]
56. Jain, A.; Singh, S.K.; Arya, S.K.; Kundu, S.C.; Kapoor, S. Protein Nanoparticles: Promising Platforms for Drug Delivery Applications. *ACS Biomater. Sci. Eng.* **2018**, *4*, 3939–3961. [CrossRef] [PubMed]
57. Lindemann, H.; Kühne, M.; Grune, C.; Warncke, P.; Hofmann, S.; Koschella, A.; Godmann, M.; Fischer, D.; Heinzel, T.; Heinze, T. Polysaccharide Nanoparticles Bearing HDAC Inhibitor as Nontoxic Nanocarrier for Drug Delivery. *Macromol. Biosci.* **2020**, *20*, 2000039. [CrossRef]
58. Chopde, S.; Datir, R.; Deshmukh, G.; Dhotre, A.; Patil, M. Nanoparticle Formation by Nanospray Drying & Its Application in Nanoencapsulation of Food Bioactive Ingredients. *J. Agric. Res.* **2020**, *2*, 100085. [CrossRef]
59. Asadi, M.; Salami, M.; Hajikhani, M.; Emam-Djomeh, Z.; Aghakhani, A.; Ghasemi, A. Electrospray Production of Curcumin-Walnut Protein Nanoparticles. *Food Biophys.* **2021**, *16*, 15–26. [CrossRef]
60. Khalid, A.; Ahmed, N.; Qindeel, M.; Asad, M.I.; Khan, G.M.; ur-Rehman, A. Development of Novel Biopolymer-Based Nanoparticles Loaded Cream for Potential Treatment of Topical Fungal Infections. *Drug Dev. Ind. Pharm.* **2021**, *47*, 1090–1099. [CrossRef]
61. Plucinski, A.; Lyu, Z.; Schmidt, J.B.V.K. Polysaccharide Nanoparticles: From Fabrication to Applications. *J. Mater. Chem. B* **2021**, *9*, 7030–7062. [CrossRef]
62. Pedroso-Santana, S.; Fleitas-Salazar, N. Ionotropic Gelation Method in the Synthesis of Nanoparticles/Microparticles for Biomedical Purposes. *Polym. Int.* **2020**, *69*, 443–447. [CrossRef]
63. Kohli, K.; Mujtaba, A.; Malik, R.; Amin, S.; Alam, M.S.; Ali, A.; Barkat, M.A.; Ansari, M.J. Development of Natural Polysaccharide-Based Nanoparticles of Berberine to Enhance Oral Bioavailability: Formulation, Optimization, Ex Vivo, and In Vivo Assessment. *Polymers* **2021**, *13*, 3833. [CrossRef]
64. Habibi, N.; Mauser, A.; Ko, Y.; Lahann, J. Protein Nanoparticles: Uniting the Power of Proteins with Engineering Design Approaches. *Adv. Sci.* **2022**, *9*, 2104012. [CrossRef] [PubMed]
65. Aljabali, A.A.; Rezigue, M.; Alsharedeh, R.H.; Obeid, M.A.; Mishra, V.; Serrano-Aroca, Á.; El-Tanani, M.; Tambuwala, M.M. Protein-Based Nanomaterials: A New Tool for Targeted Drug Delivery. *Ther. Deliv.* **2022**, *13*, 321–338. [CrossRef]
66. Zhang, Y.; Sun, T.; Jiang, C. Biomacromolecules as Carriers in Drug Delivery and Tissue Engineering. *Acta Pharm. Sin. B.* **2018**, *8*, 34–50. [CrossRef] [PubMed]
67. Rizzuti, B. Nanomedicines Meet Disordered Proteins: A Shift from Traditional Materials and Concepts to Innovative Polymers. *J. Pers. Med.* **2022**, *12*, 1662. [CrossRef]
68. Santofimia-Castaño, P.; Xia, Y.; Peng, L.; Velázquez-Campoy, A.; Abián, O.; Lan, W.; Lomberk, G.; Urrutia, R.; Rizzuti, B.; Soubeyran, P.; et al. Targeting the Stress-Induced Protein NUPR1 to Treat Pancreatic Adenocarcinoma. *Cells* **2019**, *8*, 1453. [CrossRef]
69. Rizzuti, B.; Lan, W.; Santofimia-Castaño, P.; Zhou, Z.; Velázquez-Campoy, A.; Abián, O.; Peng, L.; Neira, J.L.; Xia, Y.; Iovanna, J.L. Design of Inhibitors of the Intrinsically Disordered Protein NUPR1: Balance between Drug Affinity and Target Function. *Biomolecules* **2021**, *11*, 1453. [CrossRef]
70. Bonucci, A.; Palomino-Schätzlein, M.; Malo de Molina, P.; Arbe, A.; Pierattelli, R.; Rizzuti, B.; Iovanna, J.L.; Neira, J.L. Crowding Effects on the Structure and Dynamics of the Intrinsically Disordered Nuclear Chromatin Protein NUPR1. *Front. Mol. Biosci.* **2021**, *8*, 684622. [CrossRef] [PubMed]
71. Karami, E.; Behdani, M.; Kazemi-Lomedasht, F. Albumin Nanoparticles as Nanocarriers for Drug Delivery: Focusing on Antibody and Nanobody Delivery and Albumin-Based Drugs. *J. Drug Deliv. Sci. Technol.* **2020**, *55*, 101471. [CrossRef]
72. Carter, B.G.; Cheng, N.; Kapoor, R.; Meletharayil, G.H.; Drake, M.A. Invited Review: Microfiltration-Derived Casein and Whey Proteins from Milk. *J. Dairy Sci.* **2021**, *104*, 2465–2479. [CrossRef] [PubMed]
73. Davison-Kotler, E.; Marshall, W.S.; Garcia-Gareta, E. Sources of Collagen for Biomaterials in Skin Wound Healing. *Bioengineering* **2019**, *6*, 56. [CrossRef] [PubMed]

74. Alipal, J.; Mohd Pu'ad, N.A.S.; Lee, T.C.; Nayan, N.H.M.; Sahari, N.; Basri, H.; Idris, M.I.; Abdullah, H.Z. A Review of Gelatin: Properties, Sources, Process, Applications, and Commercialisation. *Mater. Today Proc.* **2021**, *42*, 240–250. [CrossRef]
75. Donato, R.K.; Mija, A. Keratin Associations with Synthetic, Biosynthetic and Natural Polymers: An Extensive Review. *Polymers* **2020**, *12*, 32. [CrossRef]
76. Su, D.; Ding, S.; Shi, W.; Huang, X.; Jiang, L. Bombyx Mori Silk-Based Materials with Implication in Skin Repair: Sericin versus Regenerated Silk Fibroin. *J. Biomater. Appl.* **2019**, *34*, 36–46. [CrossRef]
77. Mehanna, M.M.; Mneimneh, A.T. Updated but Not Outdated “Gliadin”: A Plant Protein in Advanced Pharmaceutical Nanotechnologies. *Int. J. Pharm.* **2020**, *587*, 119672. [CrossRef]
78. Jaski, A.C.; Schmitz, F.; Horta, R.P.; Cadorin, L.; da Silva, B.J.G.; Andreaus, J.; Paes, M.C.D.; Riegel-Vidotti, I.C.; Zimmermann, L.M. Zein—A Plant-Based Material of Growing Importance: New Perspectives for Innovative Uses. *Ind. Crops Prod.* **2022**, *186*, 115250. [CrossRef]
79. Shahbaz, A.; Hussain, N.; Basra, M.A.R.; Bilal, M. Polysaccharides-Based Nano-Hybrid Biomaterial Platforms for Tissue Engineering, Drug Delivery, and Food Packaging Applications. *Starch Stärke* **2022**, *74*, 2200023. [CrossRef]
80. Sood, A.; Gupta, A.; Agrawal, G. Recent Advances in Polysaccharides Based Biomaterials for Drug Delivery and Tissue Engineering Applications. *Carbohydr. Polym. Technol. Appl.* **2021**, *2*, 100067. [CrossRef]
81. Li, Z.; Lin, Z. Recent Advances in Polysaccharide-Based Hydrogels for Synthesis and Applications. *Aggregate* **2021**, *2*, e21. [CrossRef]
82. Huh, M.S.; Lee, E.J.; Koo, H.; Yhee, J.Y.; Oh, K.S.; Son, S.; Lee, S.; Kim, S.H.; Kwon, I.C.; Kim, K. Polysaccharide-Based Nanoparticles for Gene Delivery. *Top. Curr. Chem.* **2017**, *375*, 31. [CrossRef]
83. Miao, T.; Wang, J.; Zeng, Y.; Liu, G.; Chen, X. Polysaccharide-Based Controlled Release Systems for Therapeutics Delivery and Tissue Engineering: From Bench to Bedside. *Adv. Sci.* **2018**, *5*, 1700513. [CrossRef]
84. Shokrani, H.; Shokrani, A.; Mohammad Sajadi, S.; Yazdi, M.K.; Seidi, F.; Jouyandeh, M.; Zarrintaj, P.; Kar, S.; Kim, S.-J.; Kuang, T.; et al. Polysaccharide-Based Nanocomposites for Biomedical Applications: A Critical Review. *Nanoscale Horiz.* **2022**, *7*, 1136–1160. [CrossRef]
85. Sun, Y.; Jing, X.; Ma, X.; Feng, Y.; Hu, H. Versatile Types of Polysaccharide-Based Drug Delivery Systems: From Strategic Design to Cancer Therapy. *Int. J. Mol. Sci.* **2020**, *21*, 9159. [CrossRef]
86. Khalid, A.; Ahmed, N.; Chaudhery, I.; Al-Jafary, M.A.; Al-Suhaimi, E.A.; Tarhini, M.; Lebaz, N.; Elaissari, A. Polysaccharide Chemistry in Drug Delivery, Endocrinology, and Vaccines. *Chem. Eur. J.* **2021**, *27*, 8437–8451. [CrossRef]
87. Salave, S.; Rana, D.; Sharma, A.; Bharathi, K.; Gupta, R.; Khode, S.; Benival, D.; Kommineni, N. Polysaccharide Based Implantable Drug Delivery: Development Strategies, Regulatory Requirements, and Future Perspectives. *Polysaccharides* **2022**, *3*, 625–654. [CrossRef]
88. Kou, S.G.; Peters, L.M.; Mucalo, M.R. Chitosan: A Review of Sources and Preparation Methods. *Int. J. Biol. Macromol.* **2021**, *169*, 85–94. [CrossRef]
89. Reyes-Battle, M.; Rodríguez-Talavera, I.; Sifaoui, I.; Rodríguez-Expósito, R.L.; Rocha-Cabrera, P.; Piñero, J.E.; Lorenzo-Morales, J. In vitro Amoebicidal Effects of Arabinogalactan-Based Ophthalmic Solution. *Int. J. Parasitol. Drugs Drug Resist.* **2021**, *16*, 9–16. [CrossRef]
90. Farooq, A.; Patoary, M.K.; Zhang, M.; Mussana, H.; Li, M.; Naeem, M.A.; Mushtaq, M.; Farooq, A.; Liu, L. Cellulose from Sources to Nanocellulose and an Overview of Synthesis and Properties of Nanocellulose/Zinc Oxide Nanocomposite Materials. *Int. J. Biol. Macromol.* **2020**, *154*, 1050–1073. [CrossRef] [PubMed]
91. Dehghani Soltani, M.; Meftahizadeh, H.; Barani, M.; Rahdar, A.; Hosseinikhah, S.M.; Hatami, M.; Ghorbanpour, M. Guar (*Cyamopsis tetragonoloba* L.) Plant Gum: From Biological Applications to Advanced Nanomedicine. *Int. J. Biol. Macromol.* **2021**, *193*, 1972–1985. [CrossRef] [PubMed]
92. Sharma, G.; Sharma, S.; Kumar, A.; Al-Muhtaseb, A.H.; Naushad, M.; Ghfar, A.A.; Mola, G.T.; Stadler, F.J. Guar Gum and Its Composites as Potential Materials for Diverse Applications: A Review. *Carbohydr. Polym.* **2018**, *199*, 534–545. [CrossRef]
93. Redondo-Cuenca, A.; Herrera-Vázquez, S.E.; Condezo-Hoyos, L.; Gómez-Ordóñez, E.; Rupérez, P. Inulin Extraction from Common Inulin-Containing Plant Sources. *Ind. Crops Prod.* **2021**, *170*, 113726. [CrossRef]
94. Dranca, F.; Oroian, M. Extraction, Purification and Characterization of Pectin from Alternative Sources with Potential Technological Applications. *Int. Food Res. J.* **2018**, *113*, 327–350. [CrossRef]
95. Seddiqi, H.; Oliaei, E.; Honarkar, H.; Jin, J.; Geonzon, L.C.; Bacabac, R.G.; Klein-Nulend, J. Cellulose and Its Derivatives: Towards Biomedical Applications. *Cellulose* **2021**, *28*, 1893–1931. [CrossRef]
96. Khajouei, R.A.; Keramat, J.; Hamdami, N.; Ursu, A.-V.; Delattre, C.; Laroche, C.; Gardarin, C.; Lecerf, D.; Desbrières, J.; Djelveh, G.; et al. Extraction and Characterization of an Alginate from the Iranian Brown Seaweed *Nizimuddinina zanardini*. *Int. J. Biol. Macromol.* **2018**, *118*, 1073–1081. [CrossRef]
97. Gomaa, M.; Fawzy, M.A.; Hifney, A.F.; Abdel-Gawad, K.M. Use of the Brown Seaweed *Sargassum Latifolium* in the Design of Alginate-Fucoidan Based Films with Natural Antioxidant Properties and Kinetic Modeling of Moisture Sorption and Polyphenolic Release. *Food Hydrocoll.* **2018**, *82*, 64–72. [CrossRef]
98. Trica, B.; Delattre, C.; Gros, F.; Ursu, A.V.; Dobre, T.; Djelveh, G.; Michaud, P.; Oancea, F. Extraction and Characterization of Alginate from an Edible Brown Seaweed (*Cystoseira barbata*) Harvested in the Romanian Black Sea. *Mar. Drugs* **2019**, *17*, 405. [CrossRef]

99. Montes, L.; Gisbert, M.; Hinojosa, I.; Sineiro, J.; Moreira, R. Impact of Drying on the Sodium Alginate Obtained after Polyphenols Ultrasound-Assisted Extraction from *Ascophyllum Nodosum* Seaweeds. *Carbohydr. Polym.* **2021**, *272*, 118455. [CrossRef] [PubMed]
100. Bouasria, M.; El Mendili, Y.; Benzaama, M.-H.; Pralong, V.; Bardeau, J.-F.; Hennequart, F. Valorisation of Stranded *Laminaria Digitata* Seaweed as an Insulating Earth Material. *Constr. Build. Mater.* **2021**, *308*, 125068. [CrossRef]
101. Cajnko, M.M.; Novak, U.; Likozar, B. Cascade Valorization Process of Brown Alga Seaweed *Laminaria Hyperborea* by Isolation of Polyphenols and Alginate. *J. Appl. Phycol.* **2019**, *31*, 3915–3924. [CrossRef]
102. Li, S.-Y.; Wang, Z.-P.; Wang, L.-N.; Peng, J.-X.; Wang, Y.-N.; Han, Y.-T.; Zhao, S.-F. Combined Enzymatic Hydrolysis and Selective Fermentation for Green Production of Alginate Oligosaccharides from *Laminaria Japonica*. *Bioresour. Technol.* **2019**, *281*, 84–89. [CrossRef] [PubMed]
103. Paul, S.; Salavarría, E.; Gil-Kodaka, P.; Villena, G.K. A de Novo Transcriptomic Approach to Study the Influence of Marine Water Depth in *Macrocystis pyrifera* Alginate Production. *Aquat. Bot.* **2020**, *163*, 103211. [CrossRef]
104. Janarthanan, M.; Senthil Kumar, M. Extraction of Alginate from Brown Seaweeds and Evolution of Bioactive Alginate Film Coated Textile Fabrics for Wound Healing Application. *J. Ind. Text.* **2019**, *49*, 328–351. [CrossRef]
105. Bahari, A.; Moelants, K.; Wallecan, J.; Mangiante, G.; Mazoyer, J.; Hendrickx, M.; Grauwet, T. Understanding the Effect of Time, Temperature and Salts on Carrageenan Extraction from *Chondrus Crispus*. *Algal Res.* **2021**, *58*, 102371. [CrossRef]
106. Hughes, M.H.; Prado, H.J.; Rodríguez, M.C.; Michetti, K.; Leonardi, P.I.; Matulewicz, M.C. Carrageenans from *Sarcothalia crispata* and *Gigartina skottsbergii*: Structural Analysis and Interpolyelectrolyte Complex Formation for Drug Controlled Release. *Mar. Biotechnol.* **2018**, *20*, 706–717. [CrossRef]
107. Naseri, A.; Jacobsen, C.; Sejberg, J.J.P.; Pedersen, T.E.; Larsen, J.; Hansen, K.M.; Holdt, S.L. Multi-Extraction and Quality of Protein and Carrageenan from Commercial *Spinosum* (*Eucheuma denticulatum*). *Foods* **2020**, *9*, 1072. [CrossRef]
108. Das, A.K.; Sequeira, R.A.; Maity, T.K.; Prasad, K. Bio-Ionic Liquid Promoted Selective Coagulation of κ -Carrageenan from *Kappaphycus Alvarezii* Extract. *Food Hydrocoll.* **2021**, *111*, 106382. [CrossRef]
109. Akrong, M.O.; Anning, A.K.; Addico, G.N.D.; Hogarh, J.N.; Adu-Gyamfi, A.; deGraft-Johnson, K.A.A.; Ale, M.; Meyer, A.S. Biomass and Carrageenan Yields of *Hypnea Musciformis* in Relation to Selected Environmental Variables in the Coastal Waters of Ghana. *J. Appl. Phycol.* **2022**, *34*, 2589–2601. [CrossRef]
110. Haghghatpanah, N.; Mirzaee, H.; Khodaiyan, F.; Kennedy, J.F.; Aghakhani, A.; Hosseini, S.S.; Jahanbin, K. Optimization and Characterization of Pullulan Produced by a Newly Identified Strain of *Aureobasidium Pullulans*. *Int. J. Biol. Macromol.* **2020**, *152*, 305–313. [CrossRef] [PubMed]
111. Raychaudhuri, R.; Naik, S.; Shreya, A.B.; Kandpal, N.; Pandey, A.; Kalthur, G.; Mutalik, S. Pullulan Based Stimuli Responsive and Sub Cellular Targeted Nanoplatforms for Biomedical Application: Synthesis, Nanoformulations and Toxicological Perspective. *Int. J. Biol. Macromol.* **2020**, *161*, 1189–1205. [CrossRef] [PubMed]
112. Agrawal, S.; Budhwani, D.; Gurjar, P.; Telange, D.; Lambole, V. Pullulan Based Derivatives: Synthesis, Enhanced Physicochemical Properties, and Applications. *Drug Deliv.* **2022**, *29*, 3328–3339. [CrossRef]
113. Abdulhameed, E.; Abdulsattar, J.; Majeed, H. Majeed Production, Characterization, and Antibacterial Effects of Dextran from *Saccharomyces Cerevisiae* Strains Obtained from Different Commercial Products Available in the Iraq Market. *Int. J. Pharm. Res.* **2020**, *12*, 2836–2844. [CrossRef]
114. Sebastian, J.; Rouissi, T.; Brar, S.K.; Hegde, K.; Verma, M. Microwave-Assisted Extraction of Chitosan from *Rhizopus Oryzae* NRRL 1526 Biomass. *Carbohydr. Polym.* **2019**, *219*, 431–440. [CrossRef]
115. Díaz-Montes, E. Dextran: Sources, Structures, and Properties. *Polysaccharides* **2021**, *2*, 554–565. [CrossRef]
116. Rosca, I.; Petrovici, A.R.; Peptanariu, D.; Nicolescu, A.; Dodi, G.; Avadanei, M.; Ivanov, I.C.; Bostanaru, A.C.; Mares, M.; Ciolacu, D. Biosynthesis of Dextran by *Weissella Confusa* and Its In vitro Functional Characteristics. *Int. J. Biol. Macromol.* **2018**, *107*, 1765–1772. [CrossRef]
117. Hu, Y.; Gänzle, M.G. Effect of Temperature on Production of Oligosaccharides and Dextran by *Weissella Cibaria* 10 M. *Int. J. Food Microbiol.* **2018**, *280*, 27–34. [CrossRef]
118. Hamsan, M.H.; Shukur, M.F.; Aziz, S.B.; Kadir, M.F.Z. Dextran from *Leuconostoc Mesenteroides*-Doped Ammonium Salt-Based Green Polymer Electrolyte. *Bull. Mater. Sci.* **2019**, *42*, 57. [CrossRef]
119. Jumma Kareem, A.; Abdul Sattar Salman, J. Production of Dextran from Locally *Lactobacillus* Spp. Isolates. *Rep. Biochem. Mol. Biol.* **2019**, *8*, 287–300. [PubMed]
120. Dev, M.J.; Warke, R.G.; Warke, G.M.; Mahajan, G.B.; Patil, T.A.; Singhal, R.S. Advances in Fermentative Production, Purification, Characterization and Applications of Gellan Gum. *Bioresour. Technol.* **2022**, *359*, 127498. [CrossRef] [PubMed]
121. Han, J.; Feng, H.; Wang, X.; Liu, Z.; Wu, Z. Levan from *Leuconostoc Citreum* BD1707: Production Optimization and Changes in Molecular Weight Distribution during Cultivation. *BMC Biotechnol.* **2021**, *21*, 14. [CrossRef] [PubMed]
122. Vieira, A.M.; Zahed, F.; Crispim, A.C.; de Souza Bento, E.; França, R.d.F.O.; Pinheiro, I.O.; Pardo, L.A.; Carvalho, B.M. Production of Levan from *Bacillus Subtilis* Var. Natto and Apoptotic Effect on SH-SY5Y Neuroblastoma Cells. *Carbohydr. Polym.* **2021**, *273*, 118613. [CrossRef] [PubMed]
123. Pei, F.; Ma, Y.; Chen, X.; Liu, H. Purification and Structural Characterization and Antioxidant Activity of Levan from *Bacillus Megaterium* PFY-147. *Int. J. Biol. Macromol.* **2020**, *161*, 1181–1188. [CrossRef]

124. Kirtel, O.; Öner, E.T. Chapter 6: Levan Polysaccharide for Biomedical Applications. In *Soft Matter for Biomedical Applications*; Royal Society of Chemistry: London, UK, 2021; pp. 134–154.
125. Sampaio, I.C.F.; Crugeira, P.J.L.; Soares, L.G.P.; dos Santos, J.N.; de Almeida, P.F.; Pinheiro, A.L.B.; Silveira, L. Composition of Xanthan Gum Produced by *Xanthomonas Campestris* Using Produced Water from a Carbonated Oil Field through Raman Spectroscopy. *J. Photochem. Photobiol. B Biol.* **2020**, *213*, 112052. [CrossRef]
126. Kupnik, K.; Primožič, M.; Kokol, V.; Leitgeb, M. Nanocellulose in Drug Delivery and Antimicrobially Active Materials. *Polymers* **2020**, *12*, 2825. [CrossRef]
127. Choukaife, H.; Doolaanea, A.A.; Alfatama, M. Alginate Nanoformulation: Influence of Process and Selected Variables. *Pharmaceuticals* **2020**, *13*, 335. [CrossRef]
128. Hoogenboezem, E.N.; Duvall, C.L. Harnessing Albumin as a Carrier for Cancer Therapies. *Adv. Drug Deliv. Rev.* **2018**, *130*, 73–89. [CrossRef]
129. Spada, A.; Emami, J.; Tuszyński, J.A.; Lavasanifar, A. The Uniqueness of Albumin as a Carrier in Nanodrug Delivery. *Mol. Pharm.* **2021**, *18*, 1862–1894. [CrossRef]
130. Yan, F.; Li, H.; Zhong, Z.; Zhou, M.; Lin, Y.; Tang, C.; Li, C. Co-Delivery of Prednisolone and Curcumin in Human Serum Albumin Nanoparticles for Effective Treatment of Rheumatoid Arthritis. *Int. J. Nanomed.* **2019**, *14*, 9113–9125. [CrossRef] [PubMed]
131. Kuten Pella, O.; Hornyák, I.; Horváthy, D.; Fodor, E.; Nehrer, S.; Lacza, Z. Albumin as a Biomaterial and Therapeutic Agent in Regenerative Medicine. *Int. J. Mol. Sci.* **2022**, *23*, 10557. [CrossRef] [PubMed]
132. Maurya, P.; Singh, S.; Mishra, N.; Pal, R.; Singh, N.; Parashar, P.; Saraf, S.A. Chapter 20—Albumin-Based Nanomaterials in Drug Delivery and Biomedical Applications. In *Biopolymer-Based Nanomaterials in Drug Delivery and Biomedical Applications*; Bera, H., Hossain, C.M., Saha, S., Eds.; Academic Press: Cambridge, MA, USA, 2021; pp. 465–496; ISBN 978-0-12-820874-8.
133. Gawde, K.A.; Sau, S.; Tatiparti, K.; Kashaw, S.K.; Mehrmohammadi, M.; Azmi, A.S.; Iyer, A.K. Paclitaxel and Di-Fluorinated Curcumin Loaded in Albumin Nanoparticles for Targeted Synergistic Combination Therapy of Ovarian and Cervical Cancers. *Colloids Surf. B Biointerfaces* **2018**, *167*, 8–19. [CrossRef]
134. Zhao, Y.; Cai, C.; Liu, M.; Zhao, Y.; Wu, Y.; Fan, Z.; Ding, Z.; Zhang, H.; Wang, Z.; Han, J. Drug-Binding Albumins Forming Stabilized Nanoparticles for Co-Delivery of Paclitaxel and Resveratrol: In vitro/in Vivo Evaluation and Binding Properties Investigation. *Int. J. Biol. Macromol.* **2020**, *153*, 873–882. [CrossRef] [PubMed]
135. Ambrósio, J.A.R.; Pinto, B.C.D.S.; da Silva, B.G.M.; Passos, J.C.D.S.; Beltrame Junior, M.; Costa, M.S.; Simioni, A.R. BSA Nanoparticles Loaded-Methylene Blue for Photodynamic Antimicrobial Chemotherapy (PACT): Effect on Both Growth and Biofilm Formation by *Candida Albicans*. *J. Biomater. Sci. Polym. Ed.* **2020**, *31*, 2182–2198. [CrossRef] [PubMed]
136. Arun, A.; Malrautu, P.; Laha, A.; Luo, H.; Ramakrishna, S. Collagen Nanoparticles in Drug Delivery Systems and Tissue Engineering. *Appl. Sci.* **2021**, *11*, 11369. [CrossRef]
137. Xu, N.; Peng, X.-L.; Li, H.-R.; Liu, J.-X.; Cheng, J.-S.-Y.; Qi, X.-Y.; Ye, S.-J.; Gong, H.-L.; Zhao, X.-H.; Yu, J.; et al. Marine-Derived Collagen as Biomaterials for Human Health. *Front. Nutr.* **2021**, *8*, 702108. [CrossRef]
138. Roată, C.-E.; Iacob, S.; Morărașu, S.; Livadaru, C.; Tudorancea, I.; Luncă, S.; Dimofte, M.-G. Collagen-Binding Nanoparticles: A Scoping Review of Methods and Outcomes. *Crystals* **2021**, *11*, 1396. [CrossRef]
139. Kianfar, E. Protein Nanoparticles in Drug Delivery: Animal Protein, Plant Proteins and Protein Cages, Albumin Nanoparticles. *J. Nanobiotechnology* **2021**, *19*, 159. [CrossRef]
140. Makkithaya, K.N.; Nadumane, S.; Zhuo, G.-Y.; Chakrabarty, S.; Mazumder, N.; Makkithaya, K.N.; Nadumane, S.; Zhuo, G.-Y.; Chakrabarty, S.; Mazumder, N. *Nanoparticle Based Collagen Biomaterials for Wound Healing*; IntechOpen: London, UK, 2022; ISBN 978-1-80355-412-9.
141. Vijayakumar, S.; Vaseeharan, B. Antibiofilm, Anti Cancer and Ecotoxicity Properties of Collagen Based ZnO Nanoparticles. *Adv. Powder Technol.* **2018**, *29*, 2331–2345. [CrossRef]
142. Ziaei Amiri, F.; Pashandi, Z.; Lotfibakhshaiesh, N.; Mirzaei-Parsa, M.J.; Ghanbari, H.; Faridi-Majidi, R. Cell Attachment Effects of Collagen Nanoparticles on Crosslinked Electrospun Nanofibers. *Int. J. Artif. Organs* **2021**, *44*, 199–207. [CrossRef]
143. Lo, S.; Fauzi, M.B. Current Update of Collagen Nanomaterials—Fabrication, Characterisation and Its Applications: A Review. *Pharmaceutics* **2021**, *13*, 316. [CrossRef] [PubMed]
144. Mondal, S.; Hoang, G.; Manivasagan, P.; Moorthy, M.S.; Vy Phan, T.T.; Kim, H.H.; Nguyen, T.P.; Oh, J. Rapid Microwave-Assisted Synthesis of Gold Loaded Hydroxyapatite Collagen Nano-Bio Materials for Drug Delivery and Tissue Engineering Application. *Ceram. Int.* **2019**, *45*, 2977–2988. [CrossRef]
145. Gandhi, S.; Roy, I. Doxorubicin-Loaded Casein Nanoparticles for Drug Delivery: Preparation, Characterization and in vitro Evaluation. *Int. J. Biol. Macromol.* **2019**, *121*, 6–12. [CrossRef]
146. Peñalva, R.; Morales, J.; González-Navarro, C.J.; Larrañeta, E.; Quincoces, G.; Peñuelas, I.; Irache, J.M. Increased Oral Bioavailability of Resveratrol by Its Encapsulation in Casein Nanoparticles. *Int. J. Mol. Sci.* **2018**, *19*, 2816. [CrossRef]
147. Du, X.; Jing, H.; Wang, L.; Huang, X.; Mo, L.; Bai, X.; Wang, H. PH-Shifting Formation of Goat Milk Casein Nanoparticles from Insoluble Peptide Aggregates and Encapsulation of Curcumin for Enhanced Dispersibility and Bioactivity. *LWT* **2022**, *154*, 112753. [CrossRef]
148. Peñalva, R.; Esparza, I.; Morales-Gracia, J.; González-Navarro, C.J.; Larrañeta, E.; Irache, J.M. Casein Nanoparticles in Combination with 2-Hydroxypropyl- β -Cyclodextrin Improves the Oral Bioavailability of Quercetin. *Int. J. Pharm.* **2019**, *570*, 118652. [CrossRef] [PubMed]

149. Chen, L.; Wei, J.; An, M.; Zhang, L.; Lin, S.; Shu, G.; Yuan, Z.; Lin, J.; Peng, G.; Liang, X.; et al. Casein Nanoparticles as Oral Delivery Carriers of Mequindox for the Improved Bioavailability. *Colloids Surf. B Biointerfaces* **2020**, *195*, 111221. [CrossRef]
150. Wang, Y.; Xue, Y.; Bi, Q.; Qin, D.; Du, Q.; Jin, P. Enhanced Antibacterial Activity of Eugenol-Entrapped Casein Nanoparticles Amended with Lysozyme against Gram-Positive Pathogens. *Food Chem.* **2021**, *360*, 130036. [CrossRef]
151. Madkhali, O.; Mekhail, G.; Wettig, S.D. Modified Gelatin Nanoparticles for Gene Delivery. *Int. J. Pharm.* **2019**, *554*, 224–234. [CrossRef]
152. Ferroni, C.; Varchi, G. Keratin-Based Nanoparticles as Drug Delivery Carriers. *Appl. Sci.* **2021**, *11*, 9417. [CrossRef]
153. Gao, F.; Li, W.; Deng, J.; Kan, J.; Guo, T.; Wang, B.; Hao, S. Recombinant Human Hair Keratin Nanoparticles Accelerate Dermal Wound Healing. *ACS Appl. Mater. Interfaces* **2019**, *11*, 18681–18690. [CrossRef]
154. Pham, D.T.; Tiyaboonchai, W. Fibroin Nanoparticles: A Promising Drug Delivery System. *Drug Deliv.* **2020**, *27*, 431–448. [CrossRef] [PubMed]
155. Kumar Dan, A.; Aamna, B.; De, S.; Pereira-Silva, M.; Sahu, R.; Cláudia Paiva-Santos, A.; Parida, S. Sericin Nanoparticles: Future Nanocarrier for Target-Specific Delivery of Chemotherapeutic Drugs. *J. Mol. Liq.* **2022**, *368*, 120717. [CrossRef]
156. Hu, Q.; Luo, Y. Recent Advances of Polysaccharide-Based Nanoparticles for Oral Insulin Delivery. *Int. J. Biol. Macromol.* **2018**, *120*, 775–782. [CrossRef] [PubMed]
157. Chandrasekaran, M.; Kim, K.D.; Chun, S.C. Antibacterial Activity of Chitosan Nanoparticles: A Review. *Processes* **2020**, *8*, 1173. [CrossRef]
158. Yanat, M.; Schroën, K. Preparation Methods and Applications of Chitosan Nanoparticles; with an Outlook toward Reinforcement of Biodegradable Packaging. *React. Funct. Polym* **2021**, *161*, 104849. [CrossRef]
159. Herdiana, Y.; Wathoni, N.; Shamsuddin, S.; Joni, I.M.; Muchtaridi, M. Chitosan-Based Nanoparticles of Targeted Drug Delivery System in Breast Cancer Treatment. *Polymers* **2021**, *13*, 1717. [CrossRef]
160. Aibani, N.; Rai, R.; Patel, P.; Cuddihy, G.; Wasan, E.K. Chitosan Nanoparticles at the Biological Interface: Implications for Drug Delivery. *Pharmaceutics* **2021**, *13*, 1686. [CrossRef] [PubMed]
161. Madni, A.; Kousar, R.; Naeem, N.; Wahid, F. Recent Advancements in Applications of Chitosan-Based Biomaterials for Skin Tissue Engineering. *J. Bioresour. Bioprod.* **2021**, *6*, 11–25. [CrossRef]
162. Križnik, L.; Vasić, K.; Knez, Ž.; Leitgeb, M. Hyper-Activation of β -Galactosidase from *Aspergillus Oryzae* via Immobilization onto Amino-Silane and Chitosan Magnetic Maghemite Nanoparticles. *J. Clean. Prod.* **2018**, *179*, 225–234. [CrossRef]
163. Hojnik Podrepšek, G.; Knez, Ž.; Leitgeb, M. Development of Chitosan Functionalized Magnetic Nanoparticles with Bioactive Compounds. *Nanomaterials* **2020**, *10*, 1913. [CrossRef]
164. Saeed, R.M.; Dmour, I.; Taha, M.O. Stable Chitosan-Based Nanoparticles Using Polyphosphoric Acid or Hexametaphosphate for Tandem Ionotropic/Covalent Crosslinking and Subsequent Investigation as Novel Vehicles for Drug Delivery. *Front. Bioeng. Biotechnol.* **2020**, *8*, 4. [CrossRef] [PubMed]
165. Shim, S.; Yoo, H.S. The Application of Mucoadhesive Chitosan Nanoparticles in Nasal Drug Delivery. *Mar. Drugs* **2020**, *18*, 605. [CrossRef] [PubMed]
166. Rostami, E. Progresses in Targeted Drug Delivery Systems Using Chitosan Nanoparticles in Cancer Therapy: A Mini-Review. *J. Drug Deliv. Sci. Technol.* **2020**, *58*, 101813. [CrossRef]
167. Ansari, M.M.; Ahmad, A.; Mishra, R.K.; Raza, S.S.; Khan, R. Zinc Gluconate-Loaded Chitosan Nanoparticles Reduce Severity of Collagen-Induced Arthritis in Wistar Rats. *ACS Biomater. Sci. Eng.* **2019**, *5*, 3380–3397. [CrossRef]
168. Tzeyung, A.S.; Md, S.; Bhattamisra, S.K.; Madheswaran, T.; Alhakamy, N.A.; Aldawsari, H.M.; Radhakrishnan, A.K. Fabrication, Optimization, and Evaluation of Rotigotine-Loaded Chitosan Nanoparticles for Nose-To-Brain Delivery. *Pharmaceutics* **2019**, *11*, 26. [CrossRef]
169. Yu, A.; Shi, H.; Liu, H.; Bao, Z.; Dai, M.; Lin, D.; Lin, D.; Xu, X.; Li, X.; Wang, Y. Mucoadhesive Dexamethasone-Glycol Chitosan Nanoparticles for Ophthalmic Drug Delivery. *Int. J. Pharm.* **2020**, *575*, 118943. [CrossRef] [PubMed]
170. Sharkawy, A.; Barreiro, M.F.; Rodrigues, A.E. New Pickering Emulsions Stabilized with Chitosan/Collagen Peptides Nanoparticles: Synthesis, Characterization and Tracking of the Nanoparticles after Skin Application. *Colloids Surf. A Physicochem. Eng. Asp.* **2021**, *616*, 126327. [CrossRef]
171. Ribeiro, E.F.; de Barros-Alexandrino, T.T.; Assis, O.B.G.; Junior, A.C.; Quiles, A.; Hernando, I.; Nicoletti, V.R. Chitosan and Crosslinked Chitosan Nanoparticles: Synthesis, Characterization and Their Role as Pickering Emulsifiers. *Carbohydr. Polym.* **2020**, *250*, 116878. [CrossRef] [PubMed]
172. Babae, M.; Garavand, F.; Rehman, A.; Jafarazadeh, S.; Amini, E.; Cacciotti, I. Biodegradability, Physical, Mechanical and Antimicrobial Attributes of Starch Nanocomposites Containing Chitosan Nanoparticles. *Int. J. Biol. Macromol.* **2022**, *195*, 49–58. [CrossRef]
173. Fong, S.S.; Foo, Y.Y.; Saw, W.S.; Leo, B.F.; Teo, Y.Y.; Chung, I.; Goh, B.T.; Misran, M.; Imae, T.; Chang, C.-C.; et al. Chitosan-Coated-PLGA Nanoparticles Enhance the Antitumor and Antimigration Activity of Stattic—A STAT3 Dimerization Blocker. *Int. J. Nanomed.* **2022**, *17*, 137–150. [CrossRef]
174. Qu, N.; Sun, Y.; Li, Y.; Hao, F.; Qiu, P.; Teng, L.; Xie, J.; Gao, Y. Docetaxel-Loaded Human Serum Albumin (HSA) Nanoparticles: Synthesis, Characterization, and Evaluation. *Biomed. Eng. Online* **2019**, *18*, 11. [CrossRef] [PubMed]
175. Abolhassani, H.; Shojaosadati, S.A. A Comparative and Systematic Approach to Desolvation and Self-Assembly Methods for Synthesis of Piperine-Loaded Human Serum Albumin Nanoparticles. *Colloids Surf. B Biointerfaces* **2019**, *184*, 110534. [CrossRef]

176. Shafiei, S.; Hassanshahian, M.; Shakeri, S.; Hamayeli, H. Evaluation the Antibacterial Activity of Nanoantibiotics Imipenem and Ciprofloxacin Loaded in Human Serum Albumin against Some Antibiotic-Resistant Pathogenic Bacteria. *J. Exp. Nanosci.* **2020**, *15*, 350–362. [CrossRef]
177. Demirkurt, B.; Cakan-Akdogan, G.; Akdogan, Y. Preparation of Albumin Nanoparticles in Water-in-Ionic Liquid Microemulsions. *J. Mol. Liq.* **2019**, *295*, 111713. [CrossRef]
178. Prajapati, R.; Garcia-Garrido, E.; Somoza, Á. Albumin-Based Nanoparticles for the Delivery of Doxorubicin in Breast Cancer. *Cancers* **2021**, *13*, 3011. [CrossRef] [PubMed]
179. Tang, L.; Fu, L.; Zhu, Z.; Yang, Y.; Sun, B.; Shan, W.; Zhang, Z. Modified Mixed Nanomicelles with Collagen Peptides Enhanced Oral Absorption of Cucurbitacin B: Preparation and Evaluation. *Drug Deliv.* **2018**, *25*, 862–871. [CrossRef]
180. Hasheminejad, N.; Khodaiyan, F.; Safari, M. Improving the Antifungal Activity of Clove Essential Oil Encapsulated by Chitosan Nanoparticles. *Food Chem.* **2019**, *275*, 113–122. [CrossRef]
181. Cai, M.; Wang, Y.; Wang, R.; Li, M.; Zhang, W.; Yu, J.; Hua, R. Antibacterial and Antibiofilm Activities of Chitosan Nanoparticles Loaded with Ocimum Basilicum L. Essential Oil. *Int. J. Biol. Macromol.* **2022**, *202*, 122–129. [CrossRef] [PubMed]
182. Subhaswaraj, P.; Barik, S.; Macha, C.; Chiranjeevi, P.V.; Siddhardha, B. Anti Quorum Sensing and Anti Biofilm Efficacy of Cinnamaldehyde Encapsulated Chitosan Nanoparticles against Pseudomonas Aeruginosa PAO1. *LWT* **2018**, *97*, 752–759. [CrossRef]
183. Soltanzadeh, M.; Peighambardoust, S.H.; Ghanbarzadeh, B.; Mohammadi, M.; Lorenzo, J.M. Chitosan Nanoparticles as a Promising Nanomaterial for Encapsulation of Pomegranate (*Punica Granatum L.*) Peel Extract as a Natural Source of Antioxidants. *Nanomaterials* **2021**, *11*, 1439. [CrossRef] [PubMed]
184. Soltanzadeh, M.; Peighambardoust, S.H.; Ghanbarzadeh, B.; Mohammadi, M.; Lorenzo, J.M. Chitosan Nanoparticles Encapsulating Lemongrass (*Cymbopogon Commutatus*) Essential Oil: Physicochemical, Structural, Antimicrobial and in-Vitro Release Properties. *Int. J. Biol. Macromol.* **2021**, *192*, 1084–1097. [CrossRef]
185. Reddy, N.; Rapisarda, M. Properties and Applications of Nanoparticles from Plant Proteins. *Materials* **2021**, *14*, 3607. [CrossRef] [PubMed]
186. Gomes, A.; Sobral, P.J.D.A. Plant Protein-Based Delivery Systems: An Emerging Approach for Increasing the Efficacy of Lipophilic Bioactive Compounds. *Molecules* **2022**, *27*, 60. [CrossRef] [PubMed]
187. Zhang, X.; Zhang, Z.; Liang, H.; Li, J.; Wen, L.; Geng, F.; Li, B. Influence of Solvent Polarity of Ethanol/Water Binary Solvent on the Structural, Emulsifying, Interfacial Rheology Properties of Gliadin Nanoparticles. *J. Mol. Liq.* **2021**, *344*, 117976. [CrossRef]
188. Dubey, A.; Ramteke, S.; Jain, D. Preparation and Characterization of Gliadin Nanoparticles for Brain Drug Delivery. *Asian J. Pharm. Clin. Res.* **2018**, *11*, 345–347. [CrossRef]
189. Alqahtani, M.S.; Syed, R.; Alshehri, M. Size-Dependent Phagocytic Uptake and Immunogenicity of Gliadin Nanoparticles. *Polymers* **2020**, *12*, 2576. [CrossRef]
190. Wu, W.; Kong, X.; Zhang, C.; Hua, Y.; Chen, Y.; Li, X. Fabrication and Characterization of Resveratrol-Loaded Gliadin Nanoparticles Stabilized by Gum Arabic and Chitosan Hydrochloride. *LWT* **2020**, *129*, 109532. [CrossRef]
191. Sharif, N.; Golmakani, M.-T.; Hajjari, M.M. Integration of Physicochemical, Molecular Dynamics, and in vitro Evaluation of Electrosprayed γ -Oryzanol-Loaded Gliadin Nanoparticles. *Food Chem.* **2022**, *395*, 133589. [CrossRef]
192. Abdelsalam, A.M.; Somaia, A.; Ayoub, A.M.; Alsharif, F.M.; Preis, E.; Wojcik, M.; Bakowsky, U. Surface-Tailored Zein Nanoparticles: Strategies and Applications. *Pharmaceutics* **2021**, *13*, 1354. [CrossRef]
193. Zhang, H.; van Os, W.L.; Tian, X.; Zu, G.; Ribovski, L.; Bron, R.; Bussmann, J.; Kros, A.; Liu, Y.; Zuhorn, I.S. Development of Curcumin-Loaded Zein Nanoparticles for Transport across the Blood–Brain Barrier and Inhibition of Glioblastoma Cell Growth. *Biomater. Sci.* **2021**, *9*, 7092–7103. [CrossRef] [PubMed]
194. Cardenas Turner, J.; Collins, G.; Blaber, E.A.; Almeida, E.A.C.; Arinzeh, T.L. Evaluating the Cytocompatibility and Differentiation of Bone Progenitors on Electrospun Zein Scaffolds. *J. Tissue. Eng. Regen. Med.* **2020**, *14*, 173–185. [CrossRef] [PubMed]
195. Nunes, R.; Baião, A.; Monteiro, D.; das Neves, J.; Sarmento, B. Zein Nanoparticles as Low-Cost, Safe, and Effective Carriers to Improve the Oral Bioavailability of Resveratrol. *Drug Deliv. Transl. Res.* **2020**, *10*, 826–837. [CrossRef] [PubMed]
196. Hadavi, M.; Hasannia, S.; Faghihi, S.; Mashayekhi, F.; Homazadeh, H.; Mostofi, S.B. Zein Nanoparticle as a Novel BMP6 Derived Peptide Carrier for Enhanced Osteogenic Differentiation of C2C12 Cells. *Artif. Cells Nanomed. Biotechnol.* **2018**, *46*, 559–567. [CrossRef] [PubMed]
197. Federico, O.-D.; Lizeth, L.-E.C.; Guadalupe, F.-A.K.; Zuleth, G.-R.M.; Gabriel, H.G.-R.; Alfonso, S.-V.J.; Agustín, R.-C. 7—Pectin Nanoparticles: Fabrication and Uses. In *Polysaccharide Nanoparticles*; Venkatesan, J., Kim, S.-K., Anil, S.P.d.R., Eds.; Micro and Nano Technologies; Elsevier: Amsterdam, The Netherlands, 2022; pp. 163–201; ISBN 978-0-12-822351-2.
198. Rajapaksha, D.C.; Edirisinghe, S.L.; Nikapitiya, C.; Dananjaya, S.H.S.; Kwun, H.-J.; Kim, C.-H.; Oh, C.; Kang, D.-H.; De Zoysa, M. Spirulina Maxima Derived Pectin Nanoparticles Enhance the Immunomodulation, Stress Tolerance, and Wound Healing in Zebrafish. *Mar. Drugs* **2020**, *18*, 556. [CrossRef]
199. Khotimchenko, M. Pectin Polymers for Colon-Targeted Antitumor Drug Delivery. *Int. J. Biol. Macromol.* **2020**, *158*, 1110–1124. [CrossRef]
200. Jacob, E.M.; Borah, A.; Jindal, A.; Pillai, S.C.; Yamamoto, Y.; Maekawa, T.; Kumar, D.N.S. Synthesis and Characterization of Citrus-Derived Pectin Nanoparticles Based on Their Degree of Esterification. *J. Mater. Res.* **2020**, *35*, 1514–1522. [CrossRef]

201. Bostanudin, M.F.; Arafat, M.; Sarfraz, M.; Górecki, D.C.; Barbu, E. Butylglyceryl Pectin Nanoparticles: Synthesis, Formulation and Characterization. *Polymers* **2019**, *11*, 789. [CrossRef] [PubMed]
202. Troncoso, O.P.; Torres, F.G. Non-Conventional Starch Nanoparticles for Drug Delivery Applications. *Med. Devices Sens.* **2020**, *3*, e10111. [CrossRef]
203. Campelo, P.H.; Sant'Ana, A.S.; Pedrosa Silva Clerici, M.T. Starch Nanoparticles: Production Methods, Structure, and Properties for Food Applications. *Curr. Opin. Food Sci.* **2020**, *33*, 136–140. [CrossRef]
204. Farrag, Y.; Ide, W.; Montero, B.; Rico, M.; Rodríguez-Llamazares, S.; Barral, L.; Bouza, R. Preparation of Starch Nanoparticles Loaded with Quercetin Using Nanoprecipitation Technique. *Int. J. Biol. Macromol.* **2018**, *114*, 426–433. [CrossRef]
205. Chin, S.F.; Romainor, A.N.B.; Pang, S.C.; Lee, B.K.; Hwang, S.S. PH-Responsive Starch-Citrate Nanoparticles for Controlled Release of Paracetamol. *Starch Stärke* **2019**, *71*, 1800336. [CrossRef]
206. Chen, K.; Zhang, S.; Wang, H.; Wang, X.; Zhang, Y.; Yu, L.; Ke, L.; Gong, R. Fabrication of Doxorubicin-Loaded Glycyrrhetic Acid-Biotin-Starch Nanoparticles and Drug Delivery into HepG2 Cells In vitro. *Starch Stärke* **2019**, *71*, 1800031. [CrossRef]
207. Khine, Y.Y.; Stenzel, M.H. Surface Modified Cellulose Nanomaterials: A Source of Non-Spherical Nanoparticles for Drug Delivery. *Mater. Horiz.* **2020**, *7*, 1727–1758. [CrossRef]
208. Amini, E.; Valls, C.; Roncero, M.B. Ionic Liquid-Assisted Bioconversion of Lignocellulosic Biomass for the Development of Value-Added Products. *J. Clean. Prod.* **2021**, *326*, 129275. [CrossRef]
209. Abdelhamid, H.N.; Mathew, A.P. Cellulose-Based Nanomaterials Advance Biomedicine: A Review. *Int. J. Mol. Sci.* **2022**, *23*, 5405. [CrossRef]
210. Amini, E.; Azadfallah, M.; Layeghi, M.; Talaei-Hassanloui, R. Silver-Nanoparticle-Impregnated Cellulose Nanofiber Coating for Packaging Paper. *Cellulose* **2016**, *23*, 557–570. [CrossRef]
211. Ching, Y.C.; Gunathilake, T.M.S.U.; Chuah, C.H.; Ching, K.Y.; Singh, R.; Liou, N.-S. Curcumin/Tween 20-Incorporated Cellulose Nanoparticles with Enhanced Curcumin Solubility for Nano-Drug Delivery: Characterization and in vitro Evaluation. *Cellulose* **2019**, *26*, 5467–5481. [CrossRef]
212. Zhu, M.; Huan, S.; Liu, S.; Li, Z.; He, M.; Yang, G.; Liu, S.; McClements, D.J.; Rojas, O.J.; Bai, L. Recent Development in Food Emulsion Stabilized by Plant-Based Cellulose Nanoparticles. *Curr. Opin. Colloid Interface Sci.* **2021**, *56*, 101512. [CrossRef]
213. Jiménez-Sánchez, M.; Pérez-Morales, R.; Goycoolea, F.M.; Mueller, M.; Praznik, W.; Loeppert, R.; Bermúdez-Morales, V.; Zavala-Padilla, G.; Ayala, M.; Olvera, C. Self-Assembled High Molecular Weight Inulin Nanoparticles: Enzymatic Synthesis, Physicochemical and Biological Properties. *Carbohydr. Polym.* **2019**, *215*, 160–169. [CrossRef] [PubMed]
214. Chandel, D.; Uppal, S.; Mehta, S.K.; Shukla, G. Preparation and Characterization of Celecoxib Entrapped Guar Gum Nanoparticles Targeted for Oral Drug Delivery against Colon Cancer: An In-Vitro Study. *J. Drug Deliv. Ther.* **2020**, *10*, 14–21. [CrossRef]
215. Verma, D.; Sharma, S.K. Recent Advances in Guar Gum Based Drug Delivery Systems and Their Administrative Routes. *Int. J. Biol. Macromol.* **2021**, *181*, 653–671. [CrossRef]
216. Afinjuomo, F.; Abdella, S.; Youssef, S.H.; Song, Y.; Garg, S. Inulin and Its Application in Drug Delivery. *Pharmaceuticals* **2021**, *14*, 855. [CrossRef] [PubMed]
217. Ayala-Fuentes, J.C.; Gallegos-Granados, M.Z.; Villarreal-Gómez, L.J.; Antunes-Ricardo, M.; Grande, D.; Chavez-Santoscoy, R.A. Optimization of the Synthesis of Natural Polymeric Nanoparticles of Inulin Loaded with Quercetin: Characterization and Cytotoxicity Effect. *Pharmaceutics* **2022**, *14*, 888. [CrossRef]
218. Veverka, M.; Dubaj, T.; Gallovič, J.; Veverková, E.; Šimon, P.; Lokaj, J.; Jorík, V. Formulations of Staphylococcus Aureus Bacteriophage in Biodegradable Beta-Glucan and Arabinogalactan-Based Matrices. *J. Drug Deliv. Sci. Technol.* **2020**, *59*, 101909. [CrossRef]
219. Yu, X.; Wu, H.; Hu, H.; Dong, Z.; Dang, Y.; Qi, Q.; Wang, Y.; Du, S.; Lu, Y. Zein Nanoparticles as Nontoxic Delivery System for Maytansine in the Treatment of Non-Small Cell Lung Cancer. *Drug Deliv.* **2020**, *27*, 100–109. [CrossRef]
220. Merino, N.; Berdejo, D.; Bento, R.; Salman, H.; Lanz, M.; Maggi, F.; Sánchez-Gómez, S.; García-Gonzalo, D.; Pagán, R. Antimicrobial Efficacy of *Thymbra capitata* (L.) Cav. Essential Oil Loaded in Self-Assembled Zein Nanoparticles in Combination with Heat. *Ind. Crops Prod.* **2019**, *133*, 98–104. [CrossRef]
221. Chinnaiyan, S.K.; Karthikeyan, D.; Gadela, V.R. Development and Characterization of Metformin Loaded Pectin Nanoparticles for T2 Diabetes Mellitus. *Pharm. Nanotechnol.* **2018**, *6*, 253–263. [CrossRef]
222. Acevedo-Guevara, L.; Nieto-Suaza, L.; Sanchez, L.T.; Pinzon, M.I.; Villa, C.C. Development of Native and Modified Banana Starch Nanoparticles as Vehicles for Curcumin. *Int. J. Biol. Macromol.* **2018**, *111*, 498–504. [CrossRef]
223. Wang, T.; Wu, C.; Fan, G.; Li, T.; Gong, H.; Cao, F. Ginkgo Biloba Extracts-Loaded Starch Nano-Spheres: Preparation, Characterization, and in vitro Release Kinetics. *Int. J. Biol. Macromol.* **2018**, *106*, 148–157. [CrossRef] [PubMed]
224. Ding, Y.; Lin, Q.; Kan, J. Development and Characteristics Nanoscale Retrograded Starch as an Encapsulating Agent for Colon-Specific Drug Delivery. *Colloids Surf. B: Biointerfaces* **2018**, *171*, 656–667. [CrossRef] [PubMed]
225. Putro, J.N.; Ismadji, S.; Gunarto, C.; Soetaredjo, F.E.; Ju, Y.H. A Study of Anionic, Cationic, and Nonionic Surfactants Modified Starch Nanoparticles for Hydrophobic Drug Loading and Release. *J. Mol. Liq.* **2020**, *298*, 112034. [CrossRef]
226. Nallasamy, P.; Ramalingam, T.; Nooruddin, T.; Shanmuganathan, R.; Arivalagan, P.; Natarajan, S. Polyherbal Drug Loaded Starch Nanoparticles as Promising Drug Delivery System: Antimicrobial, Antibiofilm and Neuroprotective Studies. *Process Biochem.* **2020**, *92*, 355–364. [CrossRef]

227. Chin, S.F.; Jimmy, F.B.; Pang, S.C. Size Controlled Fabrication of Cellulose Nanoparticles for Drug Delivery Applications. *J. Drug Deliv. Sci. Technol.* **2018**, *43*, 262–266. [CrossRef]
228. Kim, W.-S.; Lee, J.-Y.; Singh, B.; Maharjan, S.; Hong, L.; Lee, S.-M.; Cui, L.-H.; Lee, K.-J.; Kim, G.; Yun, C.-H.; et al. A New Way of Producing Pediocin in *Pediococcus Acidilactici* through Intracellular Stimulation by Internalized Inulin Nanoparticles. *Sci. Rep.* **2018**, *8*, 5878. [CrossRef]
229. Aswathi Mohan, A.; Robert Antony, A.; Greeshma, K.; Yun, J.-H.; Ramanan, R.; Kim, H.-S. Algal Biopolymers as Sustainable Resources for a Net-Zero Carbon Bioeconomy. *Bioresour. Technol.* **2022**, *344*, 126397. [CrossRef] [PubMed]
230. Hasnain, M.S.; Nayak, A.K.; Kurakula, M.; Hoda, M.N. Chapter 6—Alginate Nanoparticles in Drug Delivery. In *Alginates in Drug Delivery*; Nayak, A.K., Hasnain, M.S., Eds.; Academic Press: Cambridge, MA, USA, 2020; pp. 129–152; ISBN 978-0-12-817640-5.
231. Severino, P.; da Silva, C.F.; Andrade, L.N.; de Lima Oliveira, D.; Campos, J.; Souto, E.B. Alginate Nanoparticles for Drug Delivery and Targeting. *Curr. Pharm. Des.* **2019**, *25*, 1312–1334. [CrossRef]
232. Doderio, A.; Alberti, S.; Gaggero, G.; Ferretti, M.; Botter, R.; Vicini, S.; Castellano, M. An Up-to-Date Review on Alginate Nanoparticles and Nanofibers for Biomedical and Pharmaceutical Applications. *Adv. Mater. Interfaces* **2021**, *8*, 2100809. [CrossRef]
233. Li, S.; Zhang, H.; Chen, K.; Jin, M.; Vu, S.H.; Jung, S.; He, N.; Zheng, Z.; Lee, M.-S. Application of Chitosan/Alginate Nanoparticle in Oral Drug Delivery Systems: Prospects and Challenges. *Drug Deliv.* **2022**, *29*, 1142–1149. [CrossRef]
234. Rostami, E. Recent Achievements in Sodium Alginate-Based Nanoparticles for Targeted Drug Delivery. *Polym. Bull.* **2022**, *79*, 6885–6904. [CrossRef]
235. Al-Hatamleh, M.A.I.; Alshaer, W.; Hatmal, M.M.; Lambuk, L.; Ahmed, N.; Mustafa, M.Z.; Low, S.C.; Jaafar, J.; Ferji, K.; Six, J.-L.; et al. Applications of Alginate-Based Nanomaterials in Enhancing the Therapeutic Effects of Bee Products. *Front. Mol. Biosci.* **2022**, *9*, 865833. [CrossRef]
236. Spadari, C.D.C.; Bastiani, F.W.M.D.S.; Lopes, L.B.; Ishida, K. Alginate Nanoparticles as Non-Toxic Delivery System for Miltefosine in the Treatment of Candidiasis and Cryptococcosis. *Int. J. Nanomed.* **2019**, *14*, 5187–5199. [CrossRef]
237. Belguesmia, Y.; Hazime, N.; Kempf, I.; Boukherroub, R.; Drider, D. New Bacteriocins from *Lactocaseibacillus paracasei* CNCM I-5369 Adsorbed on Alginate Nanoparticles Are Very Active against *Escherichia coli*. *Int. J. Mol. Sci.* **2020**, *21*, 8654. [CrossRef]
238. Dong, Y.; Wei, Z.; Xue, C. Recent Advances in Carrageenan-Based Delivery Systems for Bioactive Ingredients: A Review. *Trends Food Sci. Technol.* **2021**, *112*, 348–361. [CrossRef]
239. BeMiller, J.N. 13—Carrageenans. In *Carbohydrate Chemistry for Food Scientists*, 3rd ed.; BeMiller, J.N., Ed.; Elsevier: Amsterdam, The Netherlands, 2019; pp. 279–291; ISBN 978-0-12-812069-9.
240. Alba, K.; Kontogiorgos, V. Seaweed Polysaccharides (Agar, Alginate Carrageenan). In *Encyclopedia of Food Chemistry*; Melton, L., Shahidi, F., Varelis, P., Eds.; Academic Press: Oxford, UK, 2019; pp. 240–250; ISBN 978-0-12-814045-1.
241. Yegappan, R.; Selvaprithiviraj, V.; Amirthalingam, S.; Jayakumar, R. Carrageenan Based Hydrogels for Drug Delivery, Tissue Engineering and Wound Healing. *Carbohydr. Polym.* **2018**, *198*, 385–400. [CrossRef]
242. Fani, N.; Enayati, M.H.; Rostamabadi, H.; Falsafi, S.R. Encapsulation of Bioactives within Electrospayed κ -Carrageenan Nanoparticles. *Carbohydr. Polym.* **2022**, *294*, 119761. [CrossRef]
243. Vijayakumar, S.; Saravanakumar, K.; Malaikozhundan, B.; Divya, M.; Vaseeharan, B.; Durán-Lara, E.F.; Wang, M.-H. Biopolymer K-Carrageenan Wrapped ZnO Nanoparticles as Drug Delivery Vehicles for Anti MRSA Therapy. *Int. J. Biol. Macromol.* **2020**, *144*, 9–18. [CrossRef]
244. Thomas, D.; KurienThomas, K.; Latha, M.S. Preparation and Evaluation of Alginate Nanoparticles Prepared by Green Method for Drug Delivery Applications. *Int. J. Biol. Macromol.* **2020**, *154*, 888–895. [CrossRef]
245. Kianersi, S.; Solouk, A.; Saber-Samandari, S.; Keshel, S.H.; Pasbakhsh, P. Alginate Nanoparticles as Ocular Drug Delivery Carriers. *J. Drug Deliv. Sci. Technol.* **2021**, *66*, 102889. [CrossRef]
246. Costa, J.R.; Xavier, M.; Amado, I.R.; Gonçalves, C.; Castro, P.M.; Tonon, R.V.; Cabral, L.M.C.; Pastrana, L.; Pintado, M.E. Polymeric Nanoparticles as Oral Delivery Systems for a Grape Pomace Extract towards the Improvement of Biological Activities. *Mater. Sci. Eng. C.* **2021**, *119*, 111551. [CrossRef]
247. Alallam, B.; Altahhan, S.; Taher, M.; Mohd Nasir, M.H.; Doolaanea, A.A. Electrospayed Alginate Nanoparticles as CRISPR Plasmid DNA Delivery Carrier: Preparation, Optimization, and Characterization. *Pharmaceuticals* **2020**, *13*, 158. [CrossRef]
248. Huang, W.; Wang, L.; Wei, Y.; Cao, M.; Xie, H.; Wu, D. Fabrication of Lysozyme/ κ -Carrageenan Complex Nanoparticles as a Novel Carrier to Enhance the Stability and in vitro Release of Curcumin. *Int. J. Biol. Macromol.* **2020**, *146*, 444–452. [CrossRef]
249. Ganie, S.A.; Rather, L.J.; Li, Q. A Review on Anticancer Applications of Pullulan and Pullulan Derivative Nanoparticles. *Carbohydr. Polym. Technol. Appl.* **2021**, *2*, 100115. [CrossRef]
250. Grigoras, A.G. Drug Delivery Systems Using Pullulan, a Biocompatible Polysaccharide Produced by Fungal Fermentation of Starch. *Environ. Chem. Lett.* **2019**, *17*, 1209–1223. [CrossRef]
251. Singh, R.S.; Kaur, N.; Hassan, M.; Kennedy, J.F. Pullulan in Biomedical Research and Development—A Review. *Int. J. Biol. Macromol.* **2021**, *166*, 694–706. [CrossRef]
252. Rai, M.; Wypij, M.; Ingle, A.P.; Trzcińska-Wencel, J.; Golińska, P. Emerging Trends in Pullulan-Based Antimicrobial Systems for Various Applications. *Int. J. Mol. Sci.* **2021**, *22*, 13596. [CrossRef]
253. Tao, X.; Tao, T.; Wen, Y.; Yi, J.; He, L.; Huang, Z.; Nie, Y.; Yao, X.; Wang, Y.; He, C.; et al. Novel Delivery of Mitoxantrone with Hydrophobically Modified Pullulan Nanoparticles to Inhibit Bladder Cancer Cell and the Effect of Nano-Drug Size on Inhibition Efficiency. *Nanoscale Res. Lett.* **2018**, *13*, 345. [CrossRef]

254. Yuan, H.; Zhong, W.; Wang, R.; Zhou, P.; Nie, Y.; Hu, W.; Tao, X.; Yang, P. Preparation of Cholesteryl-Modified Aminated Pullulan Nanoparticles to Evaluate Nanoparticle of Hydrophobic Degree on Drug Release and Cytotoxicity. *J. Nanomater.* **2020**, *2020*, e7171209. [CrossRef]
255. Laha, B.; Maiti, S. Design of Core-Shell Stearyl Pullulan Nanostructures for Drug Delivery. *Mater. Today Proc.* **2019**, *11*, 620–627. [CrossRef]
256. Li, H.; Yu, C.; Zhang, J.; Li, Q.; Qiao, H.; Wang, Z.; Zeng, D. PH-Sensitive Pullulan-Doxorubicin Nanoparticles Loaded with 1,1,2-Trichlorotrifluoroethane as a Novel Synergist for High Intensity Focused Ultrasound Mediated Tumor Ablation. *Int. J. Pharm.* **2019**, *556*, 226–235. [CrossRef]
257. Yu, K.S.; Oh, J.Y.; Kim, M.C.; Kang, S.H.; Lee, N.S.; Han, S.-Y.; Ryu, K.H.; Jeong, Y.G.; Kim, D.K. Controlled Release of Ursodeoxycholic Acid from Pullulan Acetate Nanoparticles to Modulate Glutamate-Induced Excitotoxicity in PC-12 Cells. *J. Nanomater.* **2018**, *2018*, e7130450. [CrossRef]
258. Pavaloiu, R.-D.; Sha'at, F.; Hlevca, C.; Sha'at, M.; Sevcenco, C.; Petrescu, M.; Eremia, M.; Moscovici, M. Preliminary Evaluation of Pullulan Nanoparticles Loaded with Valsartan. *Chem. Proc.* **2020**, *3*, 139. [CrossRef]
259. Yang, W.; Zhang, Y.; Wang, J.; Li, H.; Yang, H. Glycyrrhetic Acid-Cyclodextrin Grafted Pullulan Nanoparticles Loaded Doxorubicin as a Liver Targeted Delivery Carrier. *Int. J. Biol. Macromol.* **2022**, *216*, 789–798. [CrossRef]
260. Wu, S.; Yang, X.; Yang, X. Methotrexate and 10-Hydroxycamptothecin Loaded Pullulan Nanoparticles with the Targeting Property for Efficient Cancer Therapy. *Mater. Technol.* **2022**, *37*, 2777–2784. [CrossRef]
261. Bera, H.; Abosheasha, M.A.; Ito, Y.; Ueda, M. Hypoxia-Responsive Pullulan-Based Nanoparticles as Erlotinib Carriers. *Int. J. Biol. Macromol.* **2021**, *191*, 764–774. [CrossRef]
262. Ukkund, S.J.; Alke, B.; Taqui, S.N.; Syed, U.T. 1—Dextran Nanoparticles: Preparation and Applications. In *Polysaccharide Nanoparticles*; Venkatesan, J., Kim, S.-K., Anil, S., P. d, R., Eds.; Micro and Nano Technologies; Elsevier: Amsterdam, The Netherlands, 2022; pp. 1–31; ISBN 978-0-12-822351-2.
263. Huang, G.; Huang, H. Application of Dextran as Nanoscale Drug Carriers. *Nanomedicine* **2018**, *13*, 3149–3158. [CrossRef]
264. Chen, F.; Huang, G.; Huang, H. Preparation and Application of Dextran and Its Derivatives as Carriers. *Int. J. Biol. Macromol.* **2020**, *145*, 827–834. [CrossRef]
265. Delrish, E.; Ghassemi, F.; Jabbarvand, M.; Lashay, A.; Atyabi, F.; Soleimani, M.; Dinarvand, R. Biodistribution of Cy5-Labeled Thiolated and Methylated Chitosan-Carboxymethyl Dextran Nanoparticles in an Animal Model of Retinoblastoma. *J. Ophthalmic. Vis. Res.* **2022**, *17*, 58–68. [CrossRef]
266. Han, H.; Zhang, Y.; Jin, S.; Chen, P.; Liu, S.; Xie, Z.; Jing, X.; Wang, Z. Paclitaxel-Loaded Dextran Nanoparticles Decorated with RVG29 Peptide for Targeted Chemotherapy of Glioma: An in Vivo Study. *New J. Chem.* **2020**, *44*, 5692–5701. [CrossRef]
267. Jamwal, S.; Ram, B.; Ranote, S.; Dharela, R.; Chauhan, G.S. New Glucose Oxidase-Immobilized Stimuli-Responsive Dextran Nanoparticles for Insulin Delivery. *Int. J. Biol. Macromol.* **2019**, *123*, 968–978. [CrossRef]
268. Prezotti, F.G.; Boni, F.I.; Ferreira, N.N.; Silva, D.S.; Almeida, A.; Vasconcelos, T.; Sarmiento, B.; Gremião, M.P.D.; Cury, B.S.F. Oral Nanoparticles Based on Gellan Gum/Pectin for Colon-Targeted Delivery of Resveratrol. *Drug Dev. Ind. Pharm.* **2020**, *46*, 236–245. [CrossRef]
269. Cinan, E.; Cesur, S.; Erginer Haskoylu, M.; Gunduz, O.; Toksoy Oner, E. Resveratrol-Loaded Levan Nanoparticles Produced by Electrohydrodynamic Atomization Technique. *Nanomaterials* **2021**, *11*, 2582. [CrossRef]
270. Sharma, R.; Sharma, U. Formulation and Characterization of Atenolol-Loaded Gellan Gum Nanoparticles. *Indian J. Pharm. Sci.* **2021**, *83*, 60–65. [CrossRef]
271. Feng, Z.; Xu, J.; Ni, C. Preparation of Redox Responsive Modified Xanthan Gum Nanoparticles and the Drug Controlled Release. *Int. J. Polym. Mater. Polym. Biomater.* **2021**, *70*, 994–1001. [CrossRef]
272. Kadota, K.; Yanagawa, Y.; Tachikawa, T.; Deki, Y.; Uchiyama, H.; Shirakawa, Y.; Tozuka, Y. Development of Porous Particles Using Dextran as an Excipient for Enhanced Deep Lung Delivery of Rifampicin. *Int. J. Pharm.* **2019**, *555*, 280–290. [CrossRef]
273. Butzbach, K.; Konhäuser, M.; Fach, M.; Bamberger, D.N.; Breitenbach, B.; Epe, B.; Wich, P.R. Receptor-Mediated Uptake of Folic Acid-Functionalized Dextran Nanoparticles for Applications in Photodynamic Therapy. *Polymers* **2019**, *11*, 896. [CrossRef]
274. Lee, S.; Stubelius, A.; Hamelmann, N.; Tran, V.; Almutairi, A. Inflammation-Responsive Drug-Conjugated Dextran Nanoparticles Enhance Anti-Inflammatory Drug Efficacy. *ACS Appl. Mater. Interfaces* **2018**, *10*, 40378–40387. [CrossRef]
275. Kashyap, A.; Kaur, R.; Baldi, A.; Jain, U.K.; Chandra, R.; Madan, J. Chloroquine Diphosphate Bearing Dextran Nanoparticles Augmented Drug Delivery and Overwhelmed Drug Resistance in Plasmodium Falciparum Parasites. *Int. J. Biol. Macromol.* **2018**, *114*, 161–168. [CrossRef]
276. Madkhali, O.A.; Sivagurunathan Moni, S.; Sultan, M.H.; Bukhary, H.A.; Ghazwani, M.; Alhakamy, N.A.; Meraya, A.M.; Alshahrani, S.; Alqahtani, S.S.; Bakkari, M.A.; et al. Formulation and Evaluation of Injectable Dextran Sulfate Sodium Nanoparticles as a Potent Antibacterial Agent. *Sci. Rep.* **2021**, *11*, 9914. [CrossRef]
277. Muhammad, D.R.A.; Sedaghat Doost, A.; Gupta, V.; bin Sintang, M.D.; Van de Walle, D.; Van der Meeren, P.; Dewettinck, K. Stability and Functionality of Xanthan Gum-Shellac Nanoparticles for the Encapsulation of Cinnamon Bark Extract. *Food Hydrocoll.* **2020**, *100*, 105377. [CrossRef]
278. Verma, M.L.; Dhanya, B.S.; Rani, V.; Thakur, M.; Jeslin, J.; Kushwaha, R. Carbohydrate and Protein Based Biopolymeric Nanoparticles: Current Status and Biotechnological Applications. *Int. J. Biol. Macromol.* **2020**, *154*, 390–412. [CrossRef] [PubMed]

279. Ramachandraiah, K.; Hong, G.-P. Polymer Based Nanomaterials for Strategic Applications in Animal Food Value Chains. *Food Rev. Int.* **2022**, *38*, 1577–1606. [CrossRef]
280. Jain, K.K. An Overview of Drug Delivery Systems. In *Drug Delivery Systems*; Jain, K.K., Ed.; Methods in Molecular Biology; Springer: New York, NY, USA, 2020; pp. 1–54; ISBN 978-1-4939-9798-5.
281. Das, R.P.; Gandhi, V.V.; Singh, B.G.; Kunwar, A.; Kumar, N.N.; Priyadarsini, K.I. Preparation of Albumin Nanoparticles: Optimum Size for Cellular Uptake of Entrapped Drug (Curcumin). *Colloids Surf. A Physicochem. Eng. Asp.* **2019**, *567*, 86–95. [CrossRef]
282. Hassani, A.; Mahmood, S.; Enezei, H.H.; Hussain, S.A.; Hamad, H.A.; Aldoghachi, A.F.; Hagar, A.; Doolaanea, A.A.; Ibrahim, W.N. Formulation, Characterization and Biological Activity Screening of Sodium Alginate-Gum Arabic Nanoparticles Loaded with Curcumin. *Molecules* **2020**, *25*, 2244. [CrossRef]
283. Nogueira, L.F.B.; Cruz, M.A.E.; Tovani, C.B.; Lopes, H.B.; Beloti, M.M.; Ciancaglini, P.; Bottini, M.; Ramos, A.P. Curcumin-Loaded Carrageenan Nanoparticles: Fabrication, Characterization, and Assessment of the Effects on Osteoblasts Mineralization. *Colloids Surf. B Biointerfaces* **2022**, *217*, 112622. [CrossRef]
284. Xie, H.; Xiang, C.; Li, Y.; Wang, L.; Zhang, Y.; Song, Z.; Ma, X.; Lu, X.; Lei, Q.; Fang, W. Fabrication of Ovalbumin/ κ -Carrageenan Complex Nanoparticles as a Novel Carrier for Curcumin Delivery. *Food Hydrocoll.* **2019**, *89*, 111–121. [CrossRef]
285. Fan, Y.; Yi, J.; Zhang, Y.; Yokoyama, W. Fabrication of Curcumin-Loaded Bovine Serum Albumin (BSA)-Dextran Nanoparticles and the Cellular Antioxidant Activity. *Food Chem.* **2018**, *239*, 1210–1218. [CrossRef] [PubMed]
286. Liu, Q.; Jing, Y.; Han, C.; Zhang, H.; Tian, Y. Encapsulation of Curcumin in Zein/Caseinate/Sodium Alginate Nanoparticles with Improved Physicochemical and Controlled Release Properties. *Food Hydrocoll.* **2019**, *93*, 432–442. [CrossRef]
287. Yao, K.; Chen, W.; Song, F.; McClements, D.J.; Hu, K. Tailoring Zein Nanoparticle Functionality Using Biopolymer Coatings: Impact on Curcumin Bioaccessibility and Antioxidant Capacity under Simulated Gastrointestinal Conditions. *Food Hydrocoll.* **2018**, *79*, 262–272. [CrossRef]
288. Sorasitthyanukarn, F.N.; Muangnoi, C.; Ratnatilaka Na Bhuket, P.; Rojsitthisak, P.; Rojsitthisak, P. Chitosan/Alginate Nanoparticles as a Promising Approach for Oral Delivery of Curcumin Diglutamic Acid for Cancer Treatment. *Mater. Sci. Eng. C* **2018**, *93*, 178–190. [CrossRef]
289. Sorasitthyanukarn, F.N.; Muangnoi, C.; Rojsitthisak, P.; Rojsitthisak, P. Chitosan-Alginate Nanoparticles as Effective Oral Carriers to Improve the Stability, Bioavailability, and Cytotoxicity of Curcumin Diethyl Disuccinate. *Carbohydr. Polym.* **2021**, *256*, 117426. [CrossRef]
290. Wathoni, N.; Meylina, L.; Rusdin, A.; Mohammed, A.F.A.; Tirtamie, D.; Herdiana, Y.; Motoyama, K.; Panatarani, C.; Joni, I.M.; Lesmana, R.; et al. The Potential Cytotoxic Activity Enhancement of α -Mangostin in Chitosan-Kappa Carrageenan-Loaded Nanoparticle against MCF-7 Cell Line. *Polymers* **2021**, *13*, 1681. [CrossRef]
291. Rathore, P.; Arora, I.; Rastogi, S.; Akhtar, M.; Singh, S.; Samim, M. Collagen Nanoparticle-Mediated Brain Silymarin Delivery: An Approach for Treating Cerebral Ischemia and Reperfusion-Induced Brain Injury. *Front. Neurosci.* **2020**, *14*, 538404. [CrossRef] [PubMed]
292. Roy, S.; Rhim, J.-W. Fabrication of Chitosan-Based Functional Nanocomposite Films: Effect of Quercetin-Loaded Chitosan Nanoparticles. *Food Hydrocoll.* **2021**, *121*, 107065. [CrossRef]
293. Li, H.; Wang, D.; Liu, C.; Zhu, J.; Fan, M.; Sun, X.; Wang, T.; Xu, Y.; Cao, Y. Fabrication of Stable Zein Nanoparticles Coated with Soluble Soybean Polysaccharide for Encapsulation of Quercetin. *Food Hydrocoll.* **2019**, *87*, 342–351. [CrossRef]
294. Liang, X.; Cao, K.; Li, W.; Li, X.; McClements, D.J.; Hu, K. Tannic Acid-Fortified Zein-Pectin Nanoparticles: Stability, Properties, Antioxidant Activity, and in vitro Digestion. *Food Res. Int.* **2021**, *145*, 110425. [CrossRef]
295. de Araujo, J.T.C.; Martin-Pastor, M.; Pérez, L.; Pinazo, A.; Sousa, F.F.O. de Development of Anacardic Acid-Loaded Zein Nanoparticles: Physical Chemical Characterization, Stability and Antimicrobial Improvement. *J. Mol. Liq.* **2021**, *332*, 115808. [CrossRef]
296. Lima, R.A.; de Souza, S.L.X.; Lima, L.A.; Batista, A.L.X.; de Araújo, J.T.C.; Sousa, F.F.O.; Rolim, J.P.M.L.; Bandeira, T.D.J.P.G. Antimicrobial Effect of Anacardic Acid-Loaded Zein Nanoparticles Loaded on Streptococcus Mutans Biofilms. *Braz. J. Microbiol.* **2020**, *51*, 1623–1630. [CrossRef]
297. Bernal-Mercado, A.T.; Juarez, J.; Valdez, M.A.; Ayala-Zavala, J.F.; Del-Toro-Sánchez, C.L.; Encinas-Basurto, D. Hydrophobic Chitosan Nanoparticles Loaded with Carvacrol against Pseudomonas Aeruginosa Biofilms. *Molecules* **2022**, *27*, 699. [CrossRef] [PubMed]
298. Jain, A.; Sharma, G.; Kushwah, V.; Ghoshal, G.; Jain, A.; Singh, B.; Shivhare, U.S.; Jain, S.; Katare, O.P. Beta Carotene-Loaded Zein Nanoparticles to Improve the Biopharmaceutical Attributes and to Abolish the Toxicity of Methotrexate: A Preclinical Study for Breast Cancer. *Artif. Cells Nanomed. Biotechnol.* **2018**, *46*, 402–412. [CrossRef] [PubMed]
299. Abid, M.; Naveed, M.; Azeem, I.; Faisal, A.; Faizan Nazar, M.; Yameen, B. Colon Specific Enzyme Responsive Oligoester Crosslinked Dextran Nanoparticles for Controlled Release of 5-Fluorouracil. *Int. J. Pharm.* **2020**, *586*, 119605. [CrossRef] [PubMed]
300. Adeel, M.; Duzagac, F.; Canzonieri, V.; Rizzolio, F. Self-Therapeutic Nanomaterials for Cancer Therapy: A Review. *ACS Appl. Nano Mater.* **2020**, *3*, 4962–4971. [CrossRef]
301. Abnoos, M.; Mohseni, M.; Mousavi, S.A.J.; Ashtari, K.; Ilka, R.; Mehravi, B. Chitosan-Alginate Nano-Carrier for Transdermal Delivery of Pirfenidone in Idiopathic Pulmonary Fibrosis. *Int. J. Biol. Macromol.* **2018**, *118*, 1319–1325. [CrossRef] [PubMed]
302. Thomas, D.; Mathew, N.; Nath, M.S. Starch Modified Alginate Nanoparticles for Drug Delivery Application. *Int. J. Biol. Macromol.* **2021**, *173*, 277–284. [CrossRef]

303. Constantin, M.; Bucatariu, S.; Sacaescu, L.; Daraba, O.M.; Anghelache, M.; Fundueanu, G. Pullulan Derivative with Cationic and Hydrophobic Moieties as an Appropriate Macromolecule in the Synthesis of Nanoparticles for Drug Delivery. *Int. J. Biol. Macromol.* **2020**, *164*, 4487–4498. [CrossRef]
304. Singh, T.A.; Sharma, A.; Tejwan, N.; Ghosh, N.; Das, J.; Sil, P.C. A State of the Art Review on the Synthesis, Antibacterial, Antioxidant, Antidiabetic and Tissue Regeneration Activities of Zinc Oxide Nanoparticles. *Adv. Colloid Interface Sci.* **2021**, *295*, 102495. [CrossRef]
305. Horie, M.; Tabei, Y. Role of Oxidative Stress in Nanoparticles Toxicity. *Free Radic. Res.* **2021**, *55*, 331–342. [CrossRef]
306. Scutera, S.; Argenziano, M.; Sparti, R.; Bessone, F.; Bianco, G.; Bastiancich, C.; Castagnoli, C.; Stella, M.; Musso, T.; Cavalli, R. Enhanced Antimicrobial and Antibiofilm Effect of New Colistin-Loaded Human Albumin Nanoparticles. *Antibiotics* **2021**, *10*, 57. [CrossRef]
307. Lee, N.-Y.; Ko, W.-C.; Hsueh, P.-R. Nanoparticles in the Treatment of Infections Caused by Multidrug-Resistant Organisms. *Front. Pharmacol.* **2019**, *10*. [CrossRef]
308. Benoit, D.S.W.; Sims, K.R.; Fraser, D. Perspective: Nanoparticles for Oral Biofilm Treatments. *ACS Nano* **2019**, *13*, 4869–4875. [CrossRef]
309. Yeh, Y.-C.; Huang, T.-H.; Yang, S.-C.; Chen, C.-C.; Fang, J.-Y. Nano-Based Drug Delivery or Targeting to Eradicate Bacteria for Infection Mitigation: A Review of Recent Advances. *Front. Chem.* **2020**, *8*, 286. [CrossRef]
310. Hill, M.; Twigg, M.; Sheridan, E.A.; Hardy, J.G.; Elborn, J.S.; Taggart, C.C.; Scott, C.J.; Migaud, M.E. Alginate/Chitosan Particle-Based Drug Delivery Systems for Pulmonary Applications. *Pharmaceutics* **2019**, *11*, 379. [CrossRef]
311. Liu, J.; Xiao, J.; Li, F.; Shi, Y.; Li, D.; Huang, Q. Chitosan-Sodium Alginate Nanoparticle as a Delivery System for ϵ -Polylysine: Preparation, Characterization and Antimicrobial Activity. *Food Control* **2018**, *91*, 302–310. [CrossRef]
312. Falciani, C.; Zevoloni, F.; Brunetti, J.; Riolo, G.; Gracia, R.; Marradi, M.; Loinaz, I.; Ziemann, C.; Cossío, U.; Llop, J.; et al. Antimicrobial Peptide-Loaded Nanoparticles as Inhalation Therapy for *Pseudomonas Aeruginosa* Infections. *Int. J. Nanomed.* **2020**, *15*, 1117–1128. [CrossRef] [PubMed]
313. Yu, H.; Ma, Z.; Meng, S.; Qiao, S.; Zeng, X.; Tong, Z.; Jeong, K.C. A Novel Nanohybrid Antimicrobial Based on Chitosan Nanoparticles and Antimicrobial Peptide Microcin J25 with Low Toxicity. *Carbohydr. Polym.* **2021**, *253*, 117309. [CrossRef] [PubMed]
314. Rahimvand, M.; Tafvizi, F.; Noorbazargan, H. Synthesis and Characterization of Alginate Nanocarrier Encapsulating *Artemisia Ciniformis* Extract and Evaluation of the Cytotoxicity and Apoptosis Induction in AGS Cell Line. *Int. J. Biol. Macromol.* **2020**, *158*, 338–357. [CrossRef]
315. Beconcini, D.; Fabiano, A.; Zambito, Y.; Berni, R.; Santoni, T.; Piras, A.M.; Di Stefano, R. Chitosan-Based Nanoparticles Containing Cherry Extract from *Prunus Avium* L. to Improve the Resistance of Endothelial Cells to Oxidative Stress. *Nutrients* **2018**, *10*, 1598. [CrossRef]
316. Hadidi, M.; Pouramin, S.; Adinepour, F.; Haghani, S.; Jafari, S.M. Chitosan Nanoparticles Loaded with Clove Essential Oil: Characterization, Antioxidant and Antibacterial Activities. *Carbohydr. Polym.* **2020**, *236*, 116075. [CrossRef]
317. Vahedikia, N.; Garavand, F.; Tajeddin, B.; Cacciotti, I.; Jafari, S.M.; Omid, T.; Zahedi, Z. Biodegradable Zein Film Composites Reinforced with Chitosan Nanoparticles and Cinnamon Essential Oil: Physical, Mechanical, Structural and Antimicrobial Attributes. *Colloids Surf. B: Biointerfaces* **2019**, *177*, 25–32. [CrossRef]
318. Song, X.; Wang, L.; Liu, T.; Liu, Y.; Wu, X.; Liu, L. Mandarin (*Citrus reticulata* L.) Essential Oil Incorporated into Chitosan Nanoparticles: Characterization, Anti-Biofilm Properties and Application in Pork Preservation. *Int. J. Biol. Macromol.* **2021**, *185*, 620–628. [CrossRef] [PubMed]
319. Bagheri, R.; Ariaii, P.; Motamedzadegan, A. Characterization, Antioxidant and Antibacterial Activities of Chitosan Nanoparticles Loaded with Nettle Essential Oil. *J. Food Meas. Charact.* **2021**, *15*, 1395–1402. [CrossRef]
320. Shetta, A.; Kegere, J.; Mamdouh, W. Comparative Study of Encapsulated Peppermint and Green Tea Essential Oils in Chitosan Nanoparticles: Encapsulation, Thermal Stability, in-Vitro Release, Antioxidant and Antibacterial Activities. *Int. J. Biol. Macromol.* **2019**, *126*, 731–742. [CrossRef]
321. Karimirad, R.; Behnamian, M.; Dezhsetan, S. Application of Chitosan Nanoparticles Containing *Cuminum Cyminum* Oil as a Delivery System for Shelf Life Extension of *Agaricus Bisporus*. *LWT* **2019**, *106*, 218–228. [CrossRef]
322. Yoncheva, K.; Benbassat, N.; Zaharieva, M.M.; Dimitrova, L.; Kroumov, A.; Spassova, I.; Kovacheva, D.; Najdenski, H.M. Improvement of the Antimicrobial Activity of Oregano Oil by Encapsulation in Chitosan—Alginate Nanoparticles. *Molecules* **2021**, *26*, 7017. [CrossRef]
323. Cai, M.; Zhang, G.; Wang, J.; Li, C.; Cui, H.; Lin, L. Application of Glycyrrhiza Polysaccharide Nanofibers Loaded with Tea Tree Essential Oil/ Gliadin Nanoparticles in Meat Preservation. *Food Biosci.* **2021**, *43*, 101270. [CrossRef]
324. Brotons-Canto, A.; González-Navarro, C.J.; Gil, A.G.; Asin-Prieto, E.; Saiz, M.J.; Llabrés, J.M. Zein Nanoparticles Improve the Oral Bioavailability of Curcumin in Wistar Rats. *Pharmaceutics* **2021**, *13*, 361. [CrossRef]
325. Li, J.; Yang, Y.; Lu, L.; Ma, Q.; Zhang, J. Preparation, Characterization and Systemic Application of Self-Assembled Hydroxyethyl Starch Nanoparticles-Loaded Flavonoid Morin for Hyperuricemia Therapy. *Int. J. Nanomed.* **2018**, *13*, 2129–2141. [CrossRef]
326. Das, S.; Das, M.K. Synthesis and Characterization of Thiolated Jackfruit Seed Starch as a Colonic Drug Delivery Carrier. *Int. J. Appl. Pharm.* **2019**, *11*, 53–62. [CrossRef]

327. Larsson, S.; Jansson, M.; Boholm, Å. Expert Stakeholders' Perception of Nanotechnology: Risk, Benefit, Knowledge, and Regulation. *J. Nanopart. Res.* **2019**, *21*, 57. [CrossRef]
328. Yuan, H.; Guo, H.; Luan, X.; He, M.; Li, F.; Burnett, J.; Truchan, N.; Sun, D. Albumin Nanoparticle of Paclitaxel (Abraxane) Decreases While Taxol Increases Breast Cancer Stem Cells in Treatment of Triple Negative Breast Cancer. *Mol. Pharm.* **2020**, *17*, 2275–2286. [CrossRef] [PubMed]

Disclaimer/Publisher's Note: The statements, opinions and data contained in all publications are solely those of the individual author(s) and contributor(s) and not of MDPI and/or the editor(s). MDPI and/or the editor(s) disclaim responsibility for any injury to people or property resulting from any ideas, methods, instructions or products referred to in the content.



Review

Current Perspectives on Synthetic Compartments for Biomedical Applications

Lukas Heuberger ¹, Maria Korphidou ¹, Olivia M. Eggenberger ¹, Myrto Kyropoulou ^{1,2}
and Cornelia G. Palivan ^{1,2,*}

¹ Department of Chemistry, University of Basel, Mattenstrasse 24a, BPR 1096, 4058 Basel, Switzerland; lukas.heuberger@unibas.ch (L.H.); maria.korphidou@unibas.ch (M.K.); olivia.eggenberger@unibas.ch (O.M.E.); myrto.kyropoulou@unibas.ch (M.K.)

² NCCR-Molecular Systems Engineering, Mattenstrasse 24a, BPR 1095, 4058 Basel, Switzerland

* Correspondence: cornelia.palivan@unibas.ch

Abstract: Nano- and micrometer-sized compartments composed of synthetic polymers are designed to mimic spatial and temporal divisions found in nature. Self-assembly of polymers into compartments such as polymersomes, giant unilamellar vesicles (GUVs), layer-by-layer (LbL) capsules, capsosomes, or polyion complex vesicles (PICsomes) allows for the separation of defined environments from the exterior. These compartments can be further engineered through the incorporation of (bio)molecules within the lumen or into the membrane, while the membrane can be decorated with functional moieties to produce catalytic compartments with defined structures and functions. Nanometer-sized compartments are used for imaging, theranostic, and therapeutic applications as a more mechanically stable alternative to liposomes, and through the encapsulation of catalytic molecules, i.e., enzymes, catalytic compartments can localize and act in vivo. On the micrometer scale, such biohybrid systems are used to encapsulate model proteins and form multicompartmentalized structures through the combination of multiple compartments, reaching closer to the creation of artificial organelles and cells. Significant progress in therapeutic applications and modeling strategies has been achieved through both the creation of polymers with tailored properties and functionalizations and novel techniques for their assembly.

Keywords: polymers; compartments; biomedical



Citation: Heuberger, L.; Korphidou, M.; Eggenberger, O.M.; Kyropoulou, M.; Palivan, C.G. Current Perspectives on Synthetic Compartments for Biomedical Applications. *Int. J. Mol. Sci.* **2022**, *23*, 5718. <https://doi.org/10.3390/ijms23105718>

Academic Editor: Monica Terracciano

Received: 29 April 2022

Accepted: 17 May 2022

Published: 20 May 2022

Publisher's Note: MDPI stays neutral with regard to jurisdictional claims in published maps and institutional affiliations.



Copyright: © 2022 by the authors. Licensee MDPI, Basel, Switzerland. This article is an open access article distributed under the terms and conditions of the Creative Commons Attribution (CC BY) license (<https://creativecommons.org/licenses/by/4.0/>).

1. Introduction

Mimicking the structure and function of materials found in nature is a well-known strategy for developing materials with structures and functions of interest. Vesicles are nature's simplest compartments (e.g., organelles inside cells) and have existed since the first cells. While cell membranes are based on phospholipids, as they are natural amphiphiles, vesicle-forming molecules can also be synthetic. Copolymers are alternative amphiphiles that self-assemble into macromolecular assemblies [1,2]. Block copolymers, containing hydrophilic and hydrophobic regions that can be arranged in different repeating orders, have properties that can be controlled through chemical modification to support a desired application [3]. Based on the number of blocks used, amphiphilic polymers are referred to as di- or triblock copolymers, AB or ABA, respectively, with A representing the hydrophilic and B the hydrophobic block. Polyelectrolytes, polymers containing ionic or ionizable groups, also have the ability to self-assemble into synthetic compartments such as layer-by-layer (LbL) capsules or PICsomes [4]. Various molecular properties of the polymer blocks such as polydispersity, charge, block ratio and length, and molecular weight are essential to induce the supramolecular assemblies formed thereof. The addition of biomolecules changes the properties of the polymer membranes, the integration of phospholipids can change membrane mechanical properties [5–7], and membrane proteins

can alter membrane permeability [8] and even provide the desired functionality via their intrinsic bioactivity [9,10].

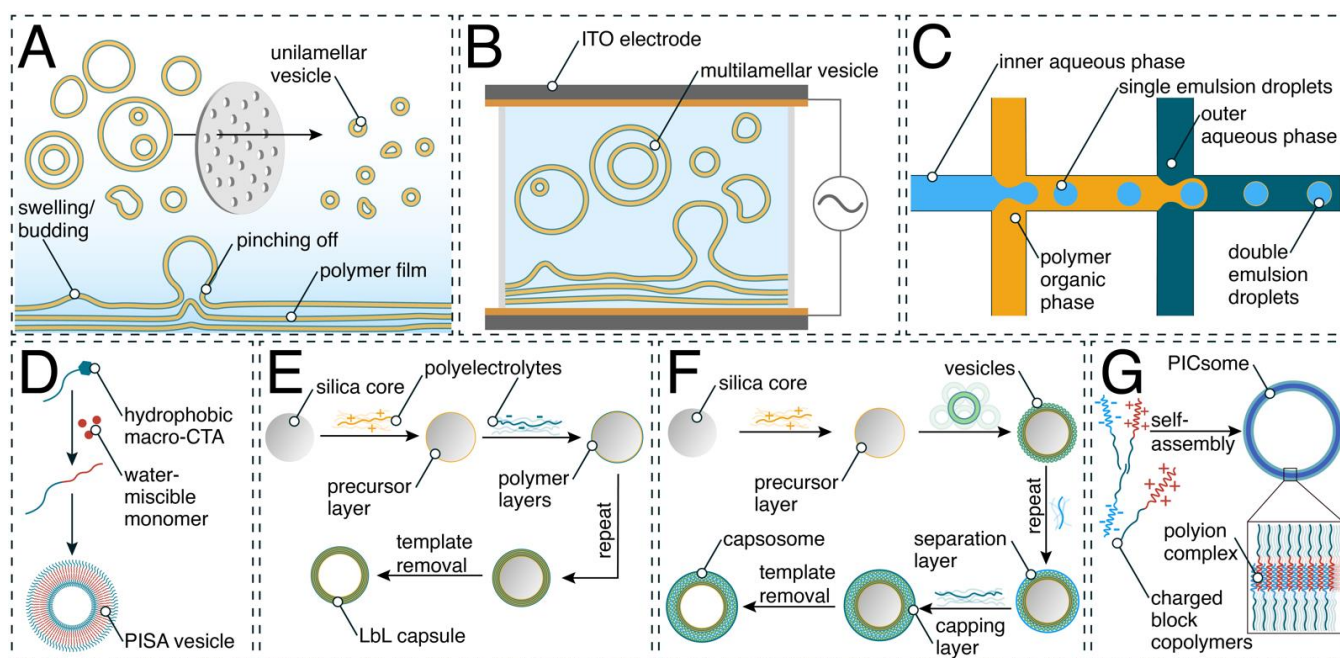
In this review, we give an overview of polymer compartments and indicate how they have been engineered when medical applications are the aim, ranging from simple drug delivery systems to artificial organelles and cells. After starting with the basic concepts of self-assembly and methods for the formation of polymer compartments, we give details on the complex requirements for medical applications and eventually cover both novel examples serving as models and systems already designed for specific medical applications. With a focus on polymer vesicles (polymersomes (<1 μm in diameter) and giant unilamellar vesicles (GUVs, 1–100 μm in diameter)), we also present other polymer compartments such as hybrid vesicles, LbL capsules, capsosomes, and PICsomes. While drug delivery systems based on polymer compartments constitute a fast-growing field, we only briefly present on these, as excellent reviews on this topic can be accessed elsewhere [11–14]. Eventually, we highlight open questions in the field and discuss how they might be solved by future studies.

2. Generation of Synthetic Compartments

A hollow cavity surrounded by a synthetic barrier (membrane, layers of polymers) represents the common architecture that forms single compartments. When more complex structures are the aim, there are two different approaches: (i) encapsulation of small nanocompartments in GUVs to generate compartments-in-compartments and (ii) zipping together compartments to generate clusters or networks [15–18].

Self-assembly of amphiphilic block copolymers in aqueous solutions can result in several types of nano- or micrometer-sized structures such as micelles, tubes, or vesicles (polymersomes and GUVs) [19,20]. Self-assembly is driven by noncovalent interactions such as the hydrophobic effect or electrostatic interactions [21]. A list of polymers commonly utilized to form compartments with a hollow-sphere architecture is presented in Table 1.

Here we present the most established self-assembly methods for nano- and micro-sized polymer vesicles (Scheme 1) and briefly describe how layer-by-layer assembly is used to generate capsules and capsosomes. In methods such as solvent switch, the block copolymer is dissolved in a water-miscible organic solvent. This is followed by the dropwise addition of an aqueous buffer to slowly replace the organic phase [22,23]. Contrarily, the cosolvent method is based on the dropwise addition of a copolymer solution to an aqueous buffer phase, which induces the self-assembly process of copolymers [24]. One drawback of these methods is the residual presence of organic solvent in the final solution, which is undesirable for biologically relevant applications. The film rehydration method (Scheme 1A) takes place in a more biocompatible manner, as the organic solution of the copolymer is completely dried, forming a film. The thin copolymer film is subsequently rehydrated with an aqueous solution, inducing the self-assembly process and resulting in supramolecular architectures (micelles, polymersomes, worm-like assemblies). When the hydrophilic–hydrophobic ratio f of the copolymers is in the range of $35 \pm 10\%$ [25], vesicles are the favored supramolecular assembly, even if the copolymers have a rather high polydispersity index (PDI) [17,26]. Film rehydration is well suited for loading polymersomes with sensitive molecules, such as enzymes and proteins, during the self-assembly process [27]. However, as this process is based on statistic loading of the desired molecules present in the rehydration solution, the encapsulation efficiency is highly dependent on their solubility and usually ranges between 5 and 20% for encapsulation of a single type of high-molecular-weight molecule, such as proteins and enzymes, and decreases even further for coencapsulation of two types of proteins [28–30].



Scheme 1. Schematic representation of selected production methods of synthetic compartments: (A) film rehydration and subsequent extrusion of block copolymers; (B) electroformation; (C) double emulsion formation with a microfluidic setup; (D) polymerization-induced self-assembly (PISA); (E) layer-by-layer (LbL) assembly; (F) assembly of capsosomes; and (G) PICsomes.

When the aim is giant unilamellar vesicles, methods used for polymersome generation are joined by other methods, including electroformation. The electroformation technique (Scheme 1B) is based on the spontaneous swelling of a dried block copolymer film that has been deposited on two electrodes of indium tin oxide (ITO)-coated glass or platinum and the consequent formation of GUVs in the presence of an aqueous solution stimulated by an electric field [17,31]. This method has a high yield of assemblies with high levels of unilamellarity [32] but is limited by a broad size dispersity and can be used only for uncharged amphiphiles to avoid electrostatic interactions affecting the self-assembly process [33]. Emulsion centrifugation is a method for the formation of GUVs wherein a water-in-oil emulsion suspension is transferred into a water phase by centrifugation [34]. The single emulsions cross a polymer monolayer at the water/oil interface and are coated by a second monolayer, resulting in a bilayered GUV. Microfluidic technology represents a step forward that has been recently used for high-throughput GUV formation with a narrow size distribution based on microdevice channel sizes and junction design [34–36]. Polymer-stabilized water–oil–water (w/o/w) double emulsions are used to form GUVs. An aqueous solution is enclosed in a layer of organic phase, consisting of the amphiphilic block copolymer dissolved in a volatile organic solvent (Scheme 1C). A flow of outer aqueous solution then pinches off the double emulsion droplets. Double emulsions can be created with a multitude of different microfluidic designs, such as glass capillaries [36,37] or molded microchannels in varying layouts [38–40]. Subsequent evaporation of the volatile organic solvent leads to the formation of a GUV with a polymer membrane. An extremely high encapsulation efficiency (99%) can be obtained by including in the inner flow the molecules (enzymes, proteins) desired to be encapsulated within the generated GUVs. The molecules planned to be entrapped in the membrane (biopores, membrane proteins) are also included in the aqueous flow at this stage [39]. Despite the high encapsulation efficiency and monodispersity, there are still limitations to using this method for GUV formation, such as its complexity and the necessity of specialized equipment.

An entirely different approach is that of polymerization-induced self-assembly (PISA), a technique that directly produces nanoassemblies during the block copolymer synthesis

(Scheme 1D) [41–43]. PISA's principle is based on the chain extension of a soluble precursor polymer block in a suitable solvent with the simultaneous use of a second polymerizing monomer, resulting in the formation of an insoluble second block, yielding polymer-somes [41–43]. The advantage of the method is its efficiency, as it combines synthesis with self-assembly and is characterized by monodispersity. On the other hand, this method is limited by decreased colloidal stability in the presence of ionic surfactants. Furthermore, PISA can only be applied for a small selection of monomers [44].

Polymer capsules are frequently formed through LbL deposition (Scheme 1E), a technique that involves the controlled adsorption of polymer layers on a sacrificial colloidal particle, alternating between oppositely charged materials, i.e., one layer of negatively charged polymer is followed by one of positively charged polymer [45–47]. Once the appropriate number of layers has been applied, the system is submerged in a solution designed to either dissolve the template or simply detach the vesicle membrane, allowing one to separate out the freshly formed vesicles. LbL capsule formation is simple yet versatile in terms of compartment size and components, including their functionality possibilities [48,49]. However, this method is limited by its dependence on the sacrificial template. Formed through a similar technique, capsosomes are capsules of which the membranes are composed of smaller vesicles. Their fabrication involves the deposition of an initial number of polymer layers onto a colloidal particle of specified size. Next, one or multiple layers of liposomes are attached, segregated by a polymeric separation layer, followed by a final deposition of several protective polymer layers (Scheme 1F) [50,51]. Assemblies of a different type, PICsomes, are the vesicular form of polyion complex (PIC) particles and are self-assembled through electrostatic interactions [23,26]. PICsomes are composed of oppositely charged block copolymers (Scheme 1G), and their membranes are semipermeable, especially to hydrophilic solutes. A major advantage of PICsomes is their facile formation—they naturally self-assemble through the mixing of their charged components [52]. One disadvantage of PICsomes is that their components typically need to be combined at equal concentrations to result in a charge-neutral vesicle, though recent experimentation has shown that charge-balance-sensitive materials can be formed by varying this ratio [53].

Table 1. Polymers used for biomedical applications.

Polymer	Method of Self-Assembly	Characteristics
Carbohydrate- <i>b</i> -PPG	Direct hydration method [54]	Forms capsosomes, inherently permeable to low-molecular-weight compounds
Chitosan	Sonication-assisted mixing (capsules) [55], LbL [56]	Biocompatible, natural polymer
CTAB	LbL [56]	Surfactant, forms micelles in the absence of another polymer
PA/DEX	LbL [57]	Biocompatible polysaccharide (anionic)
P(OEGMA300- <i>grad</i> -HPMA)	PISA [43]	Biocompatible assembly, monomers and a macromolecular precursor need to be: (i) solvophilic and (ii) compatible with each other
PA/PLA	LbL [57]	Biocompatible cationic polyelectrolyte
PAA	LbL [58]	Anionic polyelectrolyte
PAH	LbL [59,60]	Cationic polyelectrolyte
PAMAM	Mixing (PICsomes) [61]	Dendrimer (branched structure)

Table 1. Cont.

Polymer	Method of Self-Assembly	Characteristics
P(Asp-AP)	Mixing (PICsomes) [62–64]	Anionic polyelectrolyte, forms PICsomes, cannot form vesicles on its own
PATK	Mixing (PICsomes) [65]	Cationic polyelectrolyte
PBd- <i>b</i> -PEG	Double emulsion microfluidics [37]	Biocompatible
PBd- <i>b</i> -PEO	Emulsion centrifugation [34], Electroformation [66], Film rehydration [67]	Pure or as hybrid (with POPC) polymersomes for membrane protein insertion, assembly of asymmetric polymer/lipid (POPC) hybrid membranes
PBO- <i>b</i> -PG	Microfluidic double emulsion, solvent switch [68]	Biocompatible
PCL- <i>b</i> -P[Glu-stat-(Glu-ADA)]	Solvent switch [69]	Biodegradable, bone-targeting
PCL- <i>b</i> -PTrp- <i>b</i> -P(Lys-statPhe)	Solvent switch [70]	Biocompatible, biodegradable, antibacterial
PDMS- <i>b</i> -heparin	Film rehydration [71]	Forms polymersomes in combination with PMOXA- <i>b</i> -PDMS- <i>b</i> -PMOXA, forms micelles by itself
PDMS- <i>g</i> -PEO	Electroformation, Film rehydration [72]	Pure or as hybrid (with PC) polymersomes and GUVs for membrane protein insertion
PEG- <i>b</i> -PCL	Electroformation [73], film rehydration [74]	Multidomain membrane formation with lipids (DPPC)
PEG-P(CLgTMC)	Direct hydration method [75]	Biodegradable, intrinsic fluorescence
PEG- <i>b</i> -P(CPTKMA- <i>co</i> -PEMA)	Solvent exchange method [76]	Biocompatible, conjugated with camptothecin
PEG-GPLGVRG-PCL-PGPMA	Film hydration method [77]	Biocompatible, MMP-cleavable peptide and CPP-mimicking polymer
PEG- <i>b</i> -PHPMA	PISA [78]	Highly hydrated membrane, size-selective transport of molecules
PEG- <i>b</i> -PIC	Solvent exchange [79]	Biocompatible, iodine-rich for SPECT/CT and radioisotope therapy
PEG- <i>b</i> -PLA	Film rehydration [74], double emulsion microfluidics [37]	Forms polymersomes with and without lipid mixing, biodegradable
PEG- <i>b</i> -polypeptide	Mixing (PICsomes) [80]	pH-responsive, biocompatible
PEG- <i>b</i> -PAsp	Mixing (PICsomes) [62,64]	Linear polymer, forms PICsomes, micelles or hydrogels, biocompatible
PEG- <i>b</i> -PS	Solvent switch method [81,82]	Biocompatible, formation of stomatocytes, rigid assemblies
PEI- <i>b</i> -PDLLA	Microfluidic double emulsion [83]	Biocompatible, cationic assemblies, can form polymer stomatocytes
PEO- <i>b</i> -PBO	Film rehydration [84]	Forms asymmetric polymersomes
PEO- <i>b</i> -PCL	Emulsification-induced assembly [85]	Low interfacial tension solvent or SDS is needed to control the assembly
PEO- <i>b</i> -PCL- <i>b</i> -PMOXA	Film rehydration [86]	Rehydration at 62 °C due to the semi crystalline nature of the PCL block
PEO- <i>b</i> -P(CMA-stat-DEA-stat-GEMA)	Solvent exchange method [87]	Biocompatible, CMA photocrosslinking stabilization
PEO- <i>b</i> -PEHOx- <i>b</i> -PEtOz	Solvent switch, film rehydration [26]	Asymmetric membrane, can be used for directed protein insertion

Table 1. Cont.

Polymer	Method of Self-Assembly	Characteristics
PEO- <i>b</i> -PPO- <i>b</i> -PEO (Pluronics L121)	Double emulsion microfluidics [37]	Assembly via DNA linkage
PiB- <i>b</i> -PEG	Freeze–thaw extrusion [88]	Biocompatible, high chemical and thermal stability
PLys	Mixing (PICsomes) [89]	Cationic polyelectrolyte
PMA	LbL [60]	Labor-intensive LbL assembly
PMOXA- <i>b</i> -PDMS	Film rehydration [90,91], microfluidic double emulsion [39]	Formation of nano- and micro-sized vesicles in biocompatible, aqueous conditions, various channels and proteins can be inserted
PMOXA- <i>b</i> -PDMS- <i>b</i> -PMOXA	Film rehydration [71,92]	Formation of nano and micro-sized vesicles in biocompatible, aqueous conditions, various channels and proteins can be inserted
PMPC- <i>b</i> -PDPA	Film rehydration [84,93]	Formation of (asymmetric) polymersomes, can be electroporated
POEGMA- <i>b</i> -P(ST-co-VBA)	PISA [41]	Biocompatible assembly, monomers and a macromolecular precursor need to be: (i) solvophilic and (ii) compatible with each other
Poly(dopamine)	LbL [94]	Simplified LbL capsule formation
PS- <i>b</i> -PEO	Emulsification [95]	High capacity of ammonia capture in bile salt-containing buffer
PSMA-PBzMA	PISA [42]	Biocompatible assembly, monomers and a macromolecular precursor need to be: (i) solvophilic and (ii) compatible with each other
PSS- <i>b</i> -PEO- <i>b</i> -PSS	Mixing (PICsomes) [61]	Forms PICsomes with loops within the membrane when combined with poly(amidoamine) dendrimers
PVP	LbL [96]	Work-intensive LbL assembly

2.1. Surface Functionalization of Polymer Compartments

The external surfaces of compartments can be functionalized to attach different molecules with the aims of increasing their stability by cross-linking [97], attaching them on solid support to generate surfaces with nano/micro texture [98], or targeting specific biolocations (e.g., tumors [99,100] or specific organs [59,69,101,102]).

One approach to achieve external attachment of molecules is to introduce the desired chemical or reactive groups to the end of the hydrophilic copolymer block during the polymerization process [103]. The functional end groups often include hydroxyl [91,103], amine [104], and N-hydroxysuccinimidyl esters [105]. Then, by using a mixture of the end-functionalized block copolymer with a nonfunctionalized copolymer at the desired molar ratio and the methods described above, compartments bearing functional groups are formed. The molar ratio in which the functionalized copolymer is mixed is optimized to be both high enough to support the desired fraction of attached molecules after polymersomes/GUVs formation and low enough to not impede their formation. Using only functionalized polymers often leads to the formation of undesired micelles or aggregation phenomena.

Once the compartments expose the functional groups at their external interface to the environment, they can be used to further attach the desired molecules either by covalent attachment or by using molecular recognition. Covalent attachment of molecules at the compartment surface involves different chemical approaches. For example, strategies based on Cu²⁺-free

for the length of time necessary for them to reach their intended target [121]. PICsomes were functionalized with cyclic arginine-glycine-aspartic (cRGD) peptides via covalent attachment of the N-terminal cysteines of the cRGD peptides to aldehyde groups on the PICsome surface in order to specifically recognize integrins expressed at high levels in the neovascular system [122].

A second option for attaching the desired molecules at the surface of compartments is to use molecular recognition as the driving force. Among the most effective pairs of molecules involved in molecular recognition are biotin–streptavidin proteins [118,123,124] and nucleic acid hybridization [118]. A highly specific conjugation method was mediated by oligonucleotide sequences such as single-stranded DNA (ssDNA) [37,118]. In detail, azide-exposing PMOXA-*b*-PDMS polymersomes enabled coupling of dibenzocyclooctyne (DBCO)-derivatized ssDNA or its complementary oligonucleotide. Because of the specificity of complementary base pairing, DNA can be used as a means to direct the self-organization of polymersomes into more complex structures (Figure 1B) [125].

The combination of increased stability and enhanced flexibility of polymersomes with the precision of DNA hybridization leads to the formation of clusters that are both biocompatible and stable in physiological conditions. In particular, when DNA-zipped polymersome clusters were incubated with DNase I, a well-known endonuclease, the clusters maintained their structure. Additionally, polymersome–DNA clusters remained stable for up to 10 h in cell medium [120].

2.2. Assemblies of Compartments

Compartments have been used to generate more complex assemblies, either by encapsulating nanoassemblies into GUVs (compartments-in-compartments architecture) [67,71,92] or by the association of compartments and formation of networks and clusters [91,103,120]. Compartment-in-compartment architectures include various combinations of functional polymer or lipid membranes and multilayer capsules enclosed in a GUV membrane within which they can interact. The encapsulation of multiple compartments, each with distinct membranes and functionality, into a GUV membrane forms a system of increased complexity that mimics the eukaryotic cell. Such systems allow for the study of cascade reactions or signaling pathways between the environment of the GUVs and their inner compartments or in between them. While such systems allow more controlled cascade reactions, the encapsulation efficiency of nanocompartments into GUVs is still low, which generates issues of sensitivity [126]. On the contrary, clusters, which are formed by zipping together compartments into a structure similar to that of cell colonies, have an architecture that supports an increase in the encapsulation efficiency while allowing for the location of different molecules in segregated spaces at the nano scale [91,103,120]. Bioconjugation based on nucleic acid hybridization has been applied to both liposomes [127] and polymersomes [125]. For example, polymersomes decorated with exposed ssDNA were zipped to polymersomes exposing complementary ssDNA strands to form clusters that remained stable *in vitro* and *in vivo*. Another example illustrated that by using DNA as a polymer block, polymethyl acrylate-*block*-DNA (PMA-*b*-DNA) and poly(butadiene)-*block*-poly(ethylene oxide)-*block*-DNA (PBd-*b*-PEO-*b*-DNA) supported the formation of DNA-bearing giant vesicles (GUVs) that were interconnected via DNA interactions and assembled into a “vesicular island” structure [128]. A critical aspect of polymersome clusters is the control of their size to avoid aggregation. This control is achieved by optimizing the number of ssDNA strands exposed at the surface of polymersomes to support the zipping process while keeping the number of unbound ssDNA strands low [129]. The unique advantages of clusters of compartments are the possibility of having segregated spaces for different molecules and an increase in the encapsulation efficiency compared with that of compartments-in-compartments. Both types of complex compartments support multifunctionality as an essential step for advanced applications.

3. Requirements for Compartments to Be Used in Biomedical Applications

For any biologically relevant material, the transition from the research laboratory to a clinical setting is a complex procedure. This is particularly true when the final application is in the field of medicine, pharmaceutical production, or personal care [130–132]. In the case of compartments, there is a complex set of requirements, first for the copolymers used to generate the compartments and then for the compartments themselves. Therefore, for an amphiphilic block copolymer or a polyelectrolyte to be used in biomedical applications some crucial aspects need to be considered: (i) the polymers should be able to self-assemble in aqueous solutions [19,23,86]; (ii) they need to be nontoxic and biocompatible [133]; (iii) they need to have the appropriate physical characteristics (i.e., flexibility, membrane thickness) [134] in order to facilitate the functional insertion, encapsulation, and reconstitution of biomolecules [135,136]; (iv) control over their surface charge is crucial for the attachment of biomolecules or further *in vivo* applications [137]; (v) they need to maintain stability under physiological conditions [138,139] (i.e., in high temperature or salt concentration, their functionality must remain, and the availability of the encapsulated biomolecules must be sustained); and (vi) of particular import for therapeutic compartments is their ability to undergo endosomal escape so the therapeutic agent is not hindered by cells' defense mechanisms and can arrive at the pathogenic site [140–142]. Besides these, one of the most limiting factors is the fate of copolymers in the body. Therefore, their biodegradability still remains a real challenge for various copolymers that fulfill the complex list of factors aforementioned.

Second, the compartments planned to be used in medical applications should fulfill their own set of requirements. While polymersomes, capsules, and capsosomes should preserve their integrity and act as catalytic compartments, they must also allow the molecular flow of substrates and products. Their membrane can be rendered permeable by biopores such as ion channels [135,143], peptide pores [30,144], DNA nanopores [93], and natural membrane proteins [139]. While many examples of functional protein reconstitution in polymeric membranes have been shown, the increased hydrophobic mismatch of polymeric membranes as compared with lipidic ones limits the choice of membrane protein. High membrane fluidity is essential for protein incorporation, as it allows integrating proteins into membranes that are several times thicker than the protein itself and helps the protein to overcome the size mismatch between its own hydrophobic region and the hydrophobic region of the polymer membrane [134]. Furthermore, the surface charge plays a crucial role in the *in vivo* functionality, biodistribution, and cellular uptake of the systems [145,146]. Specifically, positively charged compartments have been found to be better uptaken by cells and exhibit improved biodistribution [147–149], while negatively charged ones are usually less toxic and better at specific tissue targeting [149–151].

The surface functionalization of polymersomes, capsules, and capsosomes opens up many possibilities for the assembly of complex soft compartments. However, the attachment of functional groups changes the overall charge and might induce interactions with the environment or trigger aggregation, increasing the intrinsic toxicity. Additionally, the formation of clusters of compartments increases the size of the final assembly. This limits the possible applications mainly to the intercellular matrix [152,153]. Overall, use in medical applications requires both the polymer properties (e.g., toxicity, biocompatibility) and those of the compartment (e.g., membrane composition, functionalization, size, charge) to be carefully tailored.

4. Applications of Compartments in the Biomedical Field

Numerous studies have investigated the benefits and limitations of nanometer-sized compartments for their use in imaging, therapeutics, and theranostics. As a first step, *in vitro* studies have explored the activity and cytotoxicity of the systems for these applications, while *in vivo* studies have highlighted their suitability and investigate in-depth parameters for clinical translation. Meanwhile, micrometer-sized vesicles have facilitated the modeling of cells, a crucial step in bottom-up synthetic biology aiming to bring further

insights to real-life processes. An overview of biomolecules that have been used within compartments or in their membranes is presented in Table 2.

Table 2. Biomolecules and their applications in compartments.

Biomolecule	Polymer	Location in Assembly	Application/Function
Actin	PMOXA- <i>b</i> -PDMS- <i>b</i> -PMOXA [71]	Encapsulated (in GUVs)	Polymerization to form a cytoskeleton
ATP synthase	PDMS- <i>g</i> -PEO, PBd- <i>b</i> -PEO [72,154]	Incorporated within membrane (GUVs)	ATP generation
Bacteriorhodopsin	PDMS- <i>g</i> -PEO, PBd- <i>b</i> -PEO [154]	Incorporated within membrane (GUVs)	Pumping protons across membrane
Catalase	PEG- <i>b</i> -PS [82], PAH and DEX [59]	Encapsulated with the stomata of polymer stomatocytes and LbL capsules	Conversion of hydrogen peroxide to oxygen and water for self-propelled movement
Cholesterol–DNA	PEO- <i>b</i> -PPO- <i>b</i> -PEO (Pluronic L121), PBd- <i>b</i> -PEG, PLA- <i>b</i> -PEG [37]	Incorporated within membrane (GUVs)	Clustering of polymersomes
Cytochrome <i>b</i> ₀₃ ubiquinol oxidase (Cyt <i>b</i> ₀₃)	PBd-PEO:POPC hybrid [155], PDMS- <i>g</i> -PEO and PDMS- <i>g</i> -PEO/PC hybrid [72,156]	Incorporated within membrane (polymersomes, GUVs)	Pumping protons across membrane
DNA nanopore NP-3c	PMPC- <i>b</i> -PDPA [93]	Incorporated within membrane (GUVs)	Pore formation for cross-membrane diffusion
Dopa decarboxylase (DDC)	PMOXA- <i>b</i> -PDMS [157]	Encapsulated (in polymersomes)	Production of dopamine
Erythrosine B (and its ester derivatives)	F127 Pluronic (mixed with DPPC lipids) [158]	Incorporated within membrane (polymersomes)	Photodynamic therapy
Glucose oxidase (Gox)	PMOXA- <i>b</i> -PDMS [39,91], PEG- <i>b</i> -P(CPTKMA- <i>co</i> -PEMA) [76], PATK and PEG- <i>b</i> -Pasp [65]	Encapsulated (in GUVs, polymersomes, and PICsomes)	Catalysis of glucose oxidation to hydrogen peroxide and D-glucono- δ -lactone
Gramicidin	PMOXA- <i>b</i> -PDMS [39], PMOXA- <i>b</i> -PDMS- <i>b</i> -PMOXA [71]	Incorporated within membrane	Membrane permeabilization towards ions
Horseradish peroxidase (HRP)	PMOXA- <i>b</i> -PDMS [39], PMOXA- <i>b</i> -PDMS- <i>b</i> -PMOXA [90,138], carbohydrate- <i>b</i> -PPG [54]	Encapsulated (in GUVs, polymersomes, capsosomes)	Catalysis of oxidation of organic substrates by hydrogen peroxide
Icosane	PAA and PAH (LbL) [58]	Encapsulated (in capsules)	Acting as a phase change material for thermal energy storage
Inducible nitric oxide synthase (iNOS)	PMOXA- <i>b</i> -PDMS- <i>b</i> -PMOXA [159]	Encapsulated (in polymersomes)	Oxidation of l-arginine to l-citrulline and nitric oxide (NO)
Ionomycin	PMOXA- <i>b</i> -PDMS- <i>b</i> -PMOXA [71]	Incorporated within membrane	Membrane permeabilization towards ions
Laccase	PMOXA- <i>b</i> -PDMS [120]	Encapsulated (in polymersomes)	Oxidation of phenolic and nonphenolic compounds
Lactoperoxidase (LPO)	PMOXA- <i>b</i> -PDMS [91]	Encapsulated (in polymersomes)	Oxidation of Amplex red using hydrogen peroxide

Table 2. Cont.

Biomolecule	Polymer	Location in Assembly	Application/Function
L-asparaginase	PMPC- <i>b</i> -PDPA and PEO- <i>b</i> -PBO [84], PEG- <i>b</i> -Pasp and P(Asp-AP) [64], PEG- <i>b</i> -PHPMA [78]	Encapsulated (in polymersomes, PICsomes)	Catalysis of L-asparagine to l-aspartic acid and ammonia
Lipase	PMOXA- <i>b</i> -PDMS- <i>b</i> -PMOXA [71]	Encapsulated (in polymersomes)	Catalysis of the hydrolysis of fats
Luciferase	PMOXA- <i>b</i> -PDMS [160]	Encapsulated (in polymersomes)	Bioluminescence
Melittin	PMOXA- <i>b</i> -PDMS [91,144,161]	Incorporated within membrane (polymersomes, GUVs)	Pore formation for cross-membrane diffusion
Methionine γ -lyase (MGL)	PEG-P(Asp) and PLys [63,89]	Encapsulated (in PICsomes)	Cancer therapy
Outer membrane protein F from <i>E. coli</i> (OmpF)	PMOXA- <i>b</i> -PDMS [39], PMOXA- <i>b</i> -PDMS- <i>b</i> -PMOXA [90,138]	Incorporated within membrane (GUVs, polymersomes)	Pore formation for cross-membrane diffusion
Penicillin acylase	PMOXA- <i>b</i> -PDMS- <i>b</i> -PMOXA [162]	Encapsulated (in polymersomes)	Production of antibiotic cephalixin
Rnase H	PEG- <i>b</i> -polypeptide (with single-stranded oligonucleotides) [80]	Encapsulated (in PICsomes)	Gene knockout therapy
β -galactosidase	PMOXA- <i>b</i> -PDMS [39] carbohydrate- <i>b</i> -PPG [54]	Encapsulated (in GUVs, capsosomes)	Catalysis of the hydrolysis of β -galactosides into monosaccharides
β -glucuronidase	PMOXA- <i>b</i> -PDMS [161]	Encapsulated (in polymersomes)	Cleavage of the glucuronide moiety from glucuronide-conjugates
Soluble guanylyl cyclase (sGC)	PMOXA- <i>b</i> -PDMS- <i>b</i> -PMOXA [159]	Encapsulated (in polymersomes)	Production of cyclic 3,5-guanosine monophosphate (cGMP)
Trypsin	PMPC- <i>b</i> -PDPA [93]	Encapsulated (in polymersomes)	Hydrolyzation of proteins
Tyrosinase	PMOXA- <i>b</i> -PDMS [163]	Encapsulated (in polymersomes)	Oxidation of L-DOPA
Urate oxidase (UOX)	PMOXA- <i>b</i> -PDMS- <i>b</i> -PMOXA [16]	Encapsulated (in polymersomes)	Production of hydrogen peroxide for a cascade reaction

4.1. Imaging and Theranostic Applications

Fluorescence and bioluminescence are powerful optical techniques that are often used in medical imaging. However, limitations associated with low specificity and solubility or high toxicity of imaging agents have led to an increased interest in designing nanocompartments for such applications. While nanoparticles are promising candidates for theranostic agents, they are not discussed here, as thorough reviews have been published recently [164–166].

By forming polymersomes from polyisobutylene-monomethyl-*block*-polyethylene glycol (PiB-*b*-PEG) block copolymers, triplet–triplet annihilation-based molecular photon upconversion (TTA-UC) chromophores, palladium(II) tetraphenyl tetrabenzoporphyrin and 2,5,8,11-tetra(tert-butyl)perylene were entrapped and protected by natural antioxidants [167]. This system allowed red-to-blue upconversion in aerobic conditions, which is otherwise hindered. When these polymersomes were tested on lung carcinoma cells treated

with a mixture of antioxidants in 1% oxygen, mimicking the low oxygen concentrations encountered in tumors, the upconversion emission was one order of magnitude higher, proposing a solution to the oxygen sensitivity of TTA-UC systems. Going a step further, PiB-*b*-PEG polymersomes containing one fluorescent probe in the polymer membrane and a second in the aqueous cavity served for dual fluorescent imaging (Figure 2A) [168]. In lung cancer cells, these polymersomes remained intact for 90 h postinjection and were not exocytosed but did reduce the cell proliferation. When injected in zebrafish embryos, they remained intact and active 96 h postinjection, were not excreted or degraded, and did not cause any animal death. In the same respect, the successful encapsulation of quantum dots in PMOXA-*b*-PDMS polymersomes shielded their toxic effects, as no cytotoxicity was observed when uptaken by HepG2 liver cancer cells [169]. Furthermore, they were found to be more stable than the respective liposome nanostructures which released the quantum dots in the cytoplasm of the cells. However, in comparison with free quantum dots, which are internalized rapidly but nonspecifically by living cells, the internalization of these polymersomes occurred over almost 17 h, which should be taken into consideration during the clinical translation of this system. To capitalize on the advantages of luminescence, polymersomes made of PMOXA-*b*-PDMS with encapsulated luciferase served for the *in vitro* production of strong and long-lasting luminescence, giving the system the potential to be used in biomedical imaging applications [160].

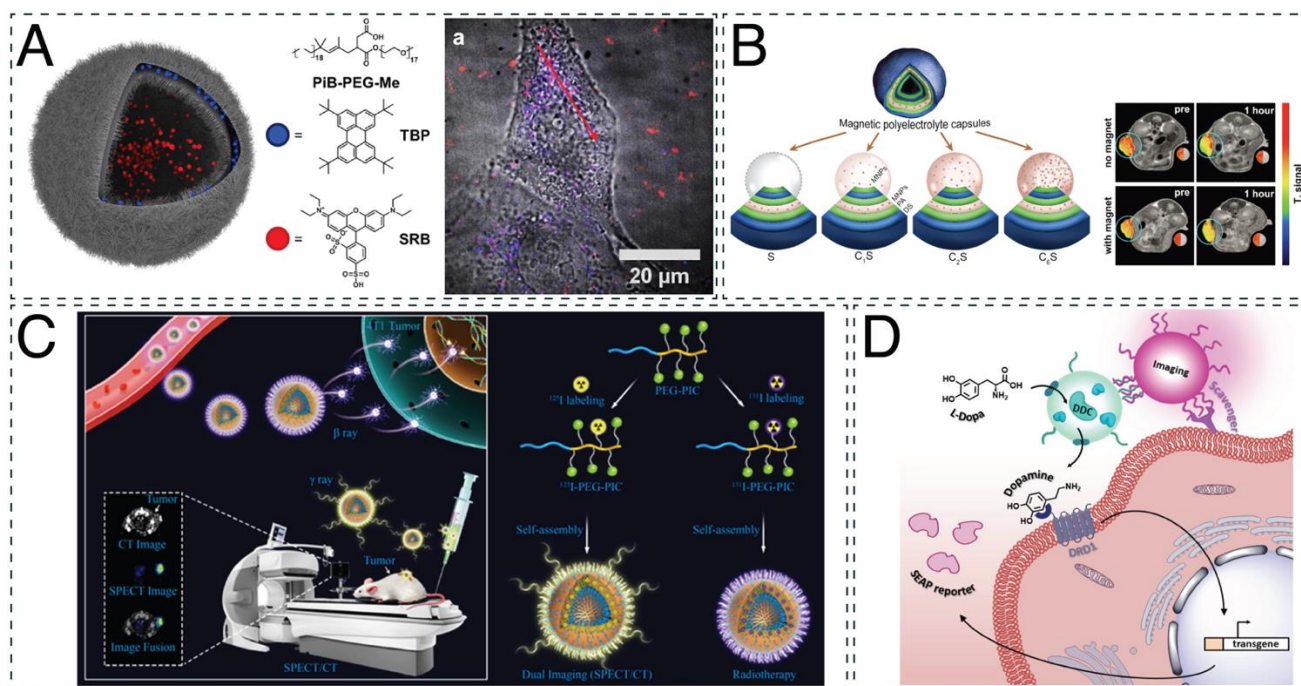


Figure 2. Imaging and theranostic applications of nanocompartments. (A) Dual fluorescence of polymersomes for optical imaging. Adapted with permission from [168]. Copyright 2018 Elsevier. (B) Magnetic LbL capsules for cancer targeting and treatment by magnetic resonance imaging (MRI). Adapted with permission from [57]. Copyright 2021 Ivyspring International Publisher. (C) Radiolabeled iodine-rich polymersomes for single-photon emission computed tomography (SPECT)/computed tomography (CT) dual imaging and cancer therapy. Reprinted with permission from [170]. Copyright 2019 American Chemical Society. (D) Theranostic DNA-zipped polymersome clusters composed of two nanocompartments: a therapeutic, dopa decarboxylase (DDC)-containing polymersome and an imaging, DY-633-containing polymersome. Reprinted with permission from [103]. Copyright 2020 John Wiley and Sons.

Moreover, a theranostic system can be established, offering the advantage of simultaneous diagnosis and treatment [114]. For example, poly(ether imide)-*block*-poly(D,L-lactide)

(PEI-*b*-PDLLA) polymersomes were recently used for neuronal restoration treatment trackable by magnetic resonance imaging (MRI) [171]. Superparamagnetic iron oxide nanoparticles (SPIONs) and the siRNA targeting the Nogo-66 receptor (NgR) gene were encapsulated in these nanocompartments. Although the application of these polymersomes led to around five times less NgR protein expression, a 30% increase in neuronal differentiation of stem cells was shown *in vitro*. In an acute ischemic stroke rat model, the polymersomes promoted the recovery of the animals better than the control group (resulting in a lower infarct volume and modified neurological severity scores (mNSS)). Employing the same principle, LbL capsules composed of magnetite nanoparticles and layers of poly-L-arginine and dextran sulfate were used in cancer treatment (Figure 2B) [57]. These capsules were traceable and directed using an external magnetic field during MRI in a mouse breast cancer model. Although they exhibited a high spleen accumulation postinjection, when a magnetic field was applied, their accumulation in the tumor increased threefold. For single-photon emission computed tomography (SPECT)/computed tomography (CT) dual imaging, polymersomes based on radiolabeled poly(ethylene glycol)-*block*-poly(iodinated carbonate) (PEG-*b*-PIC) block copolymers were tested on immunodeficient mice for the theranostic treatment of 4T1 murine breast cancer (Figure 2C) [170]. The injection of these polymersomes was found to double the lifetime of the mice and reduce the tumor volume twofold when compared with the controls. However, it should be noted that after their intravenous injection, the polymersomes accumulated in healthy organs, with a 10% higher prevalence in the spleen than at the tumor site. For enhanced photodynamic therapy, polymersomes made from poly(ethylene glycol)-*block*-poly(caprolactone-*gradient*-trimethylene carbonate) amphiphilic block copolymers (PEG-*b*-P(CLgTMC)) and a terminal block of tetraphenylethylene pyridinium-modified trimethylene carbonate (PTMC) intrinsically fluorescent polymer were loaded with BODIPY photosensitizer [75]. These polymersomes showed enhanced mitochondrial targeting and tumor accumulation in A549 tumor-bearing nude mice, reducing the size of the tumor almost five times more than in control animals. However, these results were obtained after intratumoral injections of the polymersomes to the mice, which might be a limiting factor in clinical translation. Based on the same principle, polymersomes made from poly(ϵ -caprolactone)-*block*-poly(tryptophan)-*block*-poly(lysine-*stat*-phenylalanine) were able to exhibit intrinsic blue fluorescence for bacterial monitoring and antibacterial properties [70]. When tested on *Escherichia coli* and *Staphylococcus aureus*, the planktonic bacteria were killed within 4 h of polymersome administration, at a minimum effective concentration of 600 mg/mL for *E. coli* and 62.5 mg/mL for *S. aureus*. Clusters of PMOXA-*b*-PDMS polymersomes have also served as nanotheranostics agents (Figure 2D) [103]. Generated by the hybridization of DNA exposed on their surface and separately loaded with fluorescent dyes and enzymes, they successfully targeted human embryonic kidney cells. Interestingly, the ssDNA that remained free after the cluster formation facilitated their interaction with scavenger receptors on cells. Dopa decarboxylase (DDC), the enzyme that produces the neurotransmitter dopamine, was encapsulated separately from the fluorophore DY-633, resulting in clusters serving both imaging and therapeutic purposes (such as for the treatment of atherosclerosis).

4.2. Therapeutic Applications: From *In Vitro* to *In Vivo*

4.2.1. *In Vitro* Studies

Before proceeding with any *in vivo* studies, *in vitro* evaluation of the toxicity and therapeutic potential of the nanocompartment system is of crucial importance. In one of the first studies of catalytic nanocompartments (CNCs) for antibacterial applications, penicillin acylase was encapsulated in PMOXA-*b*-PDMS-*b*-PMOXA polymersomes equipped with outer membrane protein F (OmpF) pores in the polymer membrane to facilitate the diffusion of the substrates and products [162]. These catalytic nanocompartments produced antibiotics locally and on demand and successfully inhibited the growth of *E. coli* cells. Antibacterial activity against *E. coli* and *Pseudomonas aeruginosa* was also exhibited by LbL capsules made of triclosan@cetyltrimethylammonium bromide micelles incorporated in dextran aldehyde

polyelectrolyte multilayers [56]. These capsules inhibited bacterial growth in the short term (24 h) and the long term (up to 30 days), suggesting a means of extending the life of antimicrobial coatings. However, the importance of OmpF membrane permeabilization was further established in other PMOXA-*b*-PDMS or PMOXA-*b*-PDMS-*b*-PMOXA catalytic nanocompartments, designed for enzyme replacement therapy [16,159]. When urate oxidase (UOX) or HRP was loaded in polymersomes equipped with OmpF pores, the detoxification of uric acid and prevention of H₂O₂ accumulation took place in kidney-derived HEK293T cells as a first step towards the treatment of gout and oxidative stress [16]. Similarly, a cascade reaction in situ inside epithelial cells of adenocarcinoma and myoblasts served for the production of cyclic guanosine monophosphate (cGMP), a second messenger molecule involved in a number of pathologies [159]. Inducible nitric oxide synthase (iNOS) and soluble guanylyl cyclase (sGC) were encapsulated in separate nanocompartments, and the production of cGMP was monitored by measuring the cytoplasmic calcium levels. The highest response was recorded when both of the nanocompartments were present, highlighting their potential to influence cell physiology. However, it should be noted that OmpF allowed for the diffusion of molecules only up to 600 Da, limiting the possible applications of permeabilized polymersomes [90]. Apart from OmpF, melittin biopores can also be used for membrane permeabilization [161]. Melittin-permeabilized polymersomes made from PMOXA-*b*-PDMS encapsulating β -glucuronidase were prepared to invert the glucuronidation of drugs in situ. When tested in hepatocellular carcinoma cells, they were noncytotoxic, internalized, and successfully produced the drug hymecromone over 24 h when given its glucuronide conjugate. However, when the retention of the reaction products inside the cavity is crucial, no membrane permeabilization is necessary, and the catalyst and substrate can be coencapsulated. For example, PMOXA-*b*-PDMS polymersomes encapsulating tyrosinase and L-DOPA/dopamine, the precursors of melanin/polydopamine (PDA), were incubated for 24 h in order for their polymerization to occur. The resulting melanosome mimics had the ability to cross the cellular membrane, localize around the nucleus, and offer photoprotection to immortalized human keratinocytes (HaCaT cells) under UV irradiation [163].

Clusters of CNCs encapsulating glucose oxidase (Gox; Gox-CNCs) and lactoperoxidase (LPO; LPO-CNCs) can be used for a cascade reaction that functions as protection from lung infections, treatment of hyperglycemia, and reactive oxygen species (ROS) therapy [91]. The clusters were tested on lung carcinoma epithelial cells, where they successfully consumed glucose. When amyloglucosidase was attached to the outer membrane of the Gox-CNCs, the cell viability was no different from that of Gox-LPO-CNCs, and the cells were able to metabolize amylose. PICsomes have also been used for the encapsulation of Gox [65]. These nanocompartments were made of poly([2-[[1-[(2-aminoethyl)thio]-1-methylethyl]thio]ethyl]- α,β -aspartamide) (PATK) and PEG-*block*-poly(α,β -aspartic acid) (PEG-*b*-Pasp) and tested on two breast cancer cell lines and human fibrosarcoma cells for the treatment of cancer by pyroptosis (Figure 3A). The increased cell death from pyroptosis when cells were incubated with these nanocompartments was investigated and proven by extensively analyzing the cell morphology and detecting higher levels of DNA damage and release of intracellular components in treated than in untreated cells.

Apart from polymersomes and PICsomes, LbL capsules have been investigated for their in vitro efficiency in chemophotothermal therapy [60] and oxidative stress [59]. LbL capsules made from poly(allylamine hydrochloride) (PAH) and poly(methacrylic acid) (PMA) coencapsulated doxorubicin hydrochloride with gold nanorods, as well as nimbin within the layers of the membrane (Figure 3B) [60]. Upon near-infrared (NIR) irradiation, the increased temperature of the gold nanorods led to the formation of pores and ultimate rupture of the vesicles, causing almost 90% of the encapsulated material to be released within 30 min. In leukemia monocytes, the cell death was calculated at 99%, although 50% cell death was still observed without NIR irradiation. For reducing oxidative stress, LbL capsules with tannic acid (TA) surface functionalization were successfully tested in an in vitro inflammation model [59]. Layers composed of PAH, dextran sulfate, and TA

had the ability to scavenge both H_2O_2 and radical $-OH$ while having no negative effect on the nucleus pulposus cells that they treated. While the capsules did function to reduce the concentration of H_2O_2 , they were less efficient than free enzymes because of the barrier between enzyme and substrate in the form of the polymer shell. Although LbL capsules have exhibited some very promising results when tested *in vitro*, it is important to bear in mind that their large size (2–5 μm) limits their *in vivo* use and further application.

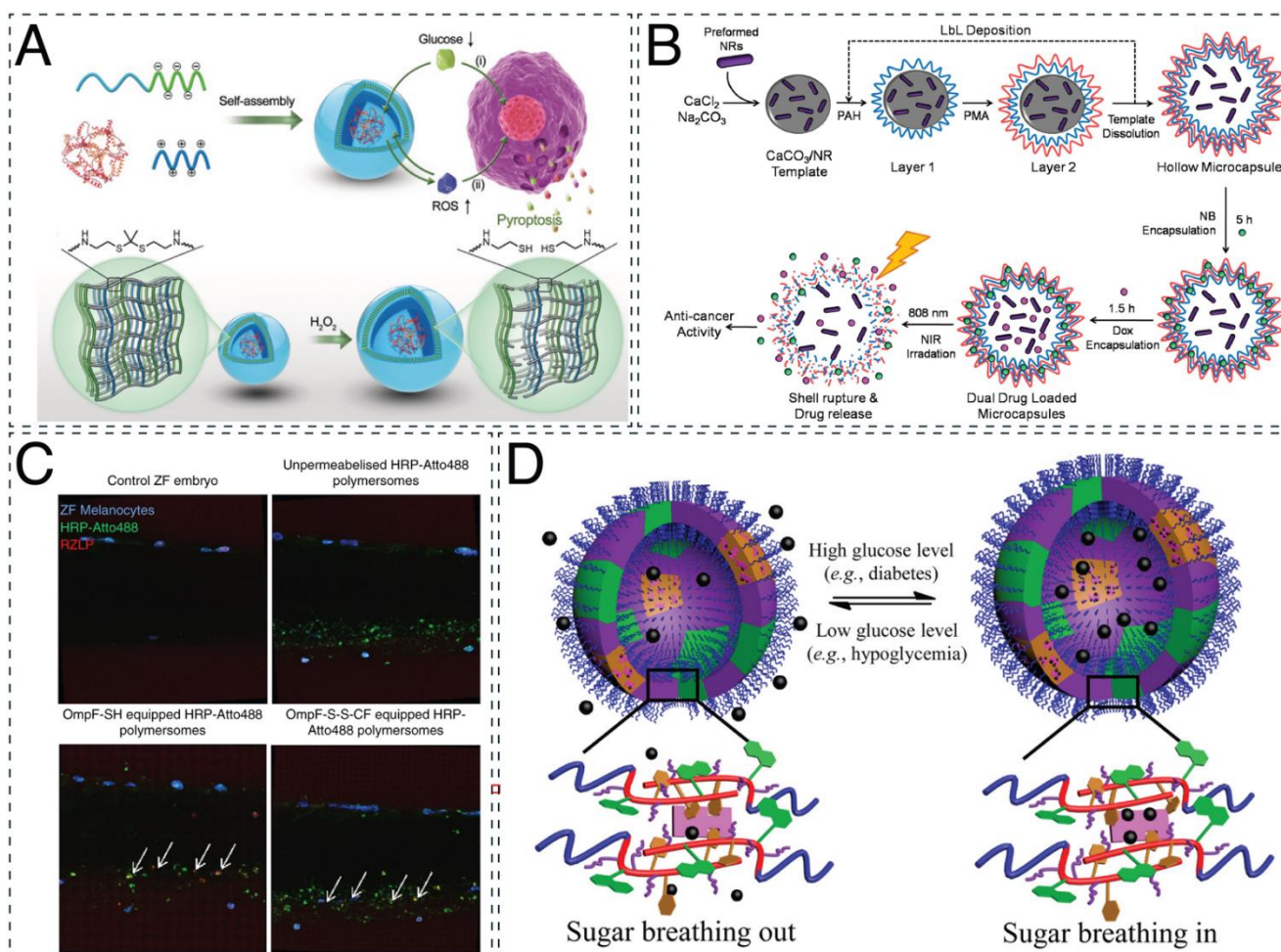


Figure 3. Therapeutic applications of nanocompartments. **(A)** Glucose oxidase-loaded PICsomes for inducing cell death by pyroptosis. Adapted with permission from [65]. Copyright 2020 John Wiley and Sons. **(B)** Layer-by-layer microcapsules for cancer chemophotothermal therapy. Reprinted with permission from [60]. Copyright 2020 Elsevier. **(C)** Biodistribution and activity of HRP-encapsulating polymersomes, acting as artificial organelles in a zebrafish embryo. Adapted with permission from [138]. Copyright 2018 Springer Nature. **(D)** Glycopolymersomes for regulating glucose levels for the treatment of diabetes mellitus. Adapted with permission from [87]. Copyright 2017 American Chemical Society.

Polymer stomatocytes are bowl-shaped polymersomes that have the ability to entrap catalytic cargo in their stomata [172,173]. When the cargo is appropriately selected (e.g., encapsulated Gox and catalase) and O_2 is generated, the stomatocytes act as nanomotors and are able to perform slow self-propelled motion [174]. This feature has been investigated for its potential use in biomedical applications such as drug delivery and ROS therapy. For example, PEG-*b*-PDLLA stomatocytes loaded with inorganic MnO_2 nanoparticles showed the ability to convert H_2O_2 into mechanical motion [83]. When tested on H_2O_2 -exposed adenocarcinoma cells, the stomatocytes had a positive effect on the cell viability

and decreased ROS induction. In another study, PEG-*b*-PS stomatocytes with platinum nanoparticles (Pt NPs) in their stomata and naphthalocyanine, a NIR light absorber, in the hydrophobic parts of the membranes were prepared [81]. They exhibited the ability to practice chemotactic-controlled movement towards H₂O₂ produced from human breast adenocarcinoma cells and allowed photothermal ablation and subsequent cell death when NIR light was applied. However, as for all nanocompartments, the size of the nanomotors remains an important aspect in their design for their further application in the biomedical area. Ultrasmall stomatocytes (approximately 150 nm) were prepared from PEG-*b*-PS block copolymer with encapsulated catalase in their stomata and evaluated for their ability to cross the membranes of HeLa cells [82]. It was found that they exhibited better cellular uptake than larger stomatocytes and presented the highest internalization values when incubated with the fuel, H₂O₂, highlighting its beneficial effect on their movement. Although the studies concerning nanomotors in biological conditions are at an early stage, they show promise for further use in biomedical applications, such as cell sorting and directional movement, taking into consideration parameters such as control over speed and direction, enzyme loading and activity, and substrate availability [175].

4.2.2. In Vivo Studies

Successful *in vitro* evaluation of nanocompartments leads to *in vivo* studies for various biomedical applications and treatments, such as enzyme replacement [78,89,120,138] and gene therapy [80], cancer [76,77], hyperammonemia [95], diabetes [87], and osteoporosis [69]. When L-asparaginase was loaded in poly(ethylene glycol)-*block*-2-hydroxypropyl methacrylate (PEG-*b*-PHPMA) polymersomes, the enzyme was more protected from proteolytic attack *in vitro* and *in vivo* than native or PEGylated enzymes. In addition, the immunogenicity was significantly reduced in an immunocompetent Balb/c mouse model, making the system a promising alternative for enzyme replacement therapy [78]. For the same purpose, PMOXA-*b*-PDMS-*b*-PMOXA polymersomes, encapsulating HRP and permeabilized with an OmpF mutant, were evaluated *in vitro* and *in vivo* in zebrafish embryos, establishing their potential to act as homeostatic artificial organelles, as they preserved their structure and detoxification ability for at least 24 h (Figure 3C) [138].

Clusters of nanocompartments were evaluated for their potential in enzyme replacement therapy, as they offer the advantage of colocalization and high cell-surface binding and accumulation [120]. DNA polymersomes encapsulating laccase, an enzyme that oxidizes mainly phenolic compounds, were tested on zebrafish embryos for their stability, cluster formation, and biodistribution. Within 30 min of injection, the clusters of nanocompartments interacted with the posterior caudal vein and preserved their architecture for at least 24 h. PICsomes have also been extensively investigated for their potential in enzyme replacement and gene therapy [80,89]. PICsomes made of α,β -polyaspartic acid, PEG-*block*-poly(α,β -aspartic acid), and poly([5-aminopentyl]- α,β -aspartamide) that contained guanidinium groups were evaluated for their *in vivo* use [62]. It is important to mention that one of the main drawbacks to the use of PICsomes in biological conditions is their sensitivity to high ionic strength, leading to their deformation in physiological environments. However, the addition of guanidinium groups increased the stability of these PICsomes, and when injected in BALB/c mice, they performed with increased circulation time in the bloodstream and no apparent aggregation. These promising results led to their further development as a dual-delivery system with Rnase H encapsulated in their cavity and single-stranded oligonucleotides in the PICsome membrane for gene knockout therapy [80]. When tested on lung carcinoma cells, the PICsomes successfully delivered their cargo, exhibiting the desired gene knockout activity. Apart from Rnase H, two methionine γ -lyase mutants were also successfully encapsulated in PEG-Pasp- and poly-L-lysine (PLys)-based PICsomes and tested on BALB/c mice [89]. Although low percentages of enzyme encapsulation were reported (3.7% and 11%) in the blood circulation, the half-lives of the enzymes increased at least 20%, and their activity remained high for at least 24 h.

For cancer treatment, polymersomes made of poly(ethylene glycol)-*block*-thioether-linked camptothecin methacrylate-co-2-(pentamethyleneimino) ethyl methacrylate encapsulating Gox and ultrasmall iron oxide nanoparticles (USIONs) were designed for precise cooperative cancer therapy [76]. These catalytic nanocompartments exhibited high efficacy in suppressing the tumor size in lung tumor-bearing mice, increasing the survival rate from 0% for untreated and camptothecin-treated animals to 80% in 90 days while their systemic toxicity remained low. Meanwhile, taking advantage of the overexpression of matrix metalloproteinases (MMPs) in tumor sites, polymersomes composed of triblock copolymers of MMP-cleavable peptide-linked poly(ethylene glycol), poly(ϵ -caprolactone) (PEG-GPLGVRG-PCL), and CPP-mimicking polymer poly(3-guanidinopropyl methacrylamide) (PGPMA) were loaded with the MMP inhibitor marimastat and colchicine, an inhibitor of microtubule formation [77]. The nanocompartments not only reduced the tumor size by almost 1.5 times in orthotopic and metastatic breast cancer-bearing mice but were successful in inhibiting its relapse after surgical abscission in almost 70% of the animals.

Polymersomes designed for the oral treatment of hyperammonemia were prepared from poly(styrene)-*block*-poly(ethylene oxide) (PS-*b*-PEO) polymersomes, encapsulating the pH-dependent fluorescent dye 8-hydroxypyrene-1,3,6-trisulfonate (HPTS), and tested on bile duct-ligated (BDL) rats [95]. These polymersomes were found to be more stable and effective for oral administration than the current liposome peritoneal treatment used in hospital settings. Meanwhile, for the treatment of diabetes mellitus, “sugar-sponges” were prepared from poly(ethylene oxide)-*block*-poly[(7-(2-methacryloyloxyethoxy)-4-methylcoumarin)-*stat*-2-(diethylamino)ethyl methacrylate-*stat*-(α -D-glucopyranosyl)ethyl methacrylate] (Figure 3D) [87]. The lectin moieties of these glycopolymersomes facilitated the uptake of glucose into their cavities when glucose concentrations were high, maintaining the blood sugar of type I diabetic KM mice at normal levels for at least 36 h. For the treatment of osteoporosis, polymersomes made from poly(ϵ -caprolactone)-*block*-poly[(L-glutamic acid)-*stat*-(L-glutamic acid-alendronic acid)] diblock copolymers were prepared, encapsulating β -estradiol. The presence of alendronic acid (ADA) in the outer membranes of these vesicles increased their affinity for hydroxyapatite, a mineral found in bones, by 20% and promoted osteogenic differentiation. Overall, a 70.4% recovery rate of total bone mineral density (BMD) and a 99.3% recovery rate of tibia BMD were reported after treating ovariectomized osteoporosis rats [69].

4.3. Vesicles as Model Systems for Organelles and Cells

While bottom-up synthetic cells have reduced complexity relative to native cells, they offer simplified views on cellular processes, supporting our understanding of complex metabolic processes. One can develop insights into the fundamental elements that control cellular behavior and function and gain greater knowledge of diseases and treatment approaches. The bottom-up strategy also offers the unique opportunity to combine artificial and biological components to create hybrid biological systems augmenting certain aspects of living systems. GUVs serve as excellent models for cells because of their size similarity and unilamellar membrane structure. There are various aspects that have to be taken into account, starting with the type of membrane and its properties up to the functionality of the whole system.

Lipids and lipid mixtures frequently serve as simplified models for cellular membranes [176–180]. However, natural cell membranes are much more complex in their composition and architecture [181]. Membrane asymmetry is an important parameter that is often overlooked but plays a major role in the function of a membrane, as it affects signal transduction and enables orientation of membrane proteins, which is crucial for their directional enzymatic activity [182,183]. Using emulsion–centrifugation, giant vesicles with an inner leaflet composed of PBd-*b*-PEO copolymer and an outer leaflet of 1-palmitoyl-2-oleoyl-sn-glycero-3-phosphocholine (POPC) were produced to mimic the asymmetry of cell membranes. However, this approach is limited to vesicles with a polymer inner leaflet and lacks long-term stability in the inverse conformation [34]. Microfluidic methods have also

been employed for the high-throughput generation of asymmetric giant vesicles but have been applied only to lipid vesicles to date [184–186]. Cellular membranes not only show an asymmetry between leaflets but possess compositional heterogeneities and form domains in a range of sizes that can contain specific proteins important for membrane trafficking, signaling, and the assembly of specialized structures [187]. By mixing the phospholipid (PL) 1,2-dipalmitoyl-sn-glycero-3-phosphocholine (DPPC) and the semicrystalline block copolymer methoxy-poly(ethylene glycol)-*block*-poly(ϵ -caprolactone) (mPEG-*b*-PCL), large PL-rich and block copolymer-rich phase-separated domains and small domains of mixed PL and copolymer (Figure 4A) can be created in hybrid GUVs. The formation of crystalline PCL and gel-like DPPC regions was confirmed through X-ray scattering and diffraction. These regions strongly influenced the PL membrane fluidity and order, indirectly influencing the mechanical and permeability properties of the membrane [73]. Polymer crystallinity plays an important role in the formation of heterogeneous membranes. When mixing the noncrystalline polymer PBd-*b*-PEO with the phospholipid POPC, no evidence for the formation of lipid-rich or polymer-rich domains was found. Membrane fluidity was shown to decrease with increasing polymer fraction by a factor of five to seven, depending on the polymer length [66]. While polymeric membranes are promising candidates for the creation of artificial cell membranes, using hybrid lipid–polymer cell membrane models combines the chemical versatility and robustness of polymers with the biocompatibility of lipids and allows for the formation of membrane domains for spatial organization.

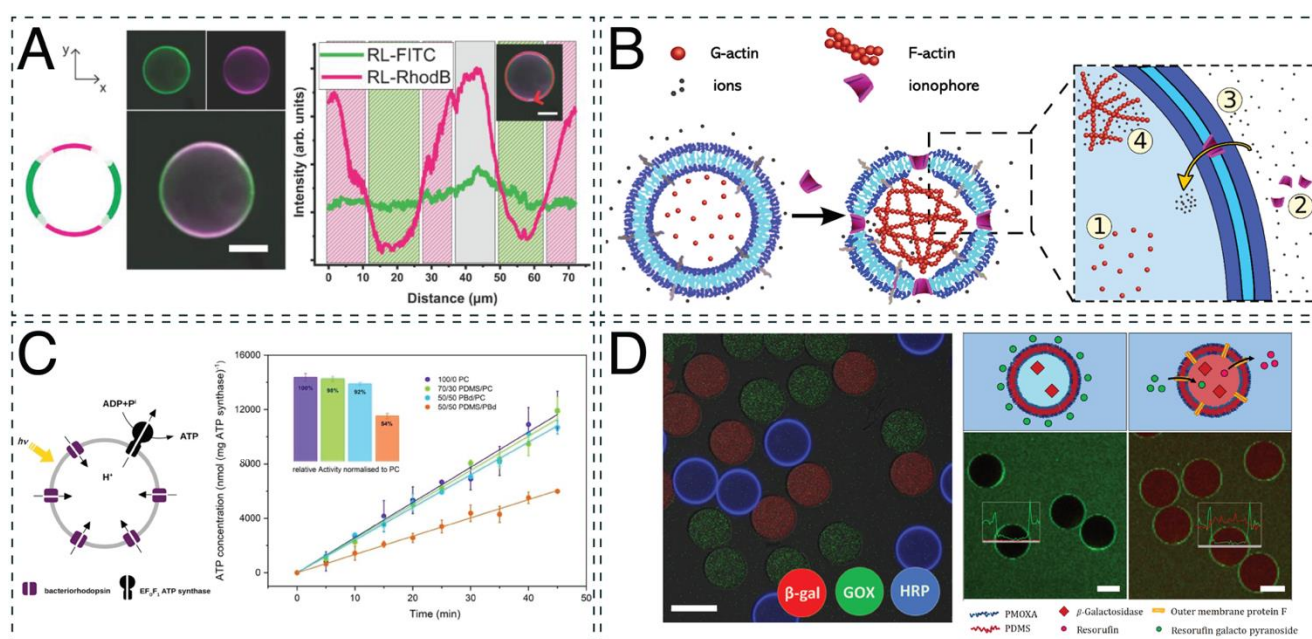


Figure 4. Applications of polymeric compartments to mimic cellular aspects. (A) Cross-sectional micrograph of DPPC-mPEG-*b*-PCL GUVs stained via fluorescein isothiocyanate (FITC, on mPEG-*b*-PCL, green) and Liss Rhod PE (in DPPC, red). Adapted with permission from [73]. Copyright 2020 MDPI. (B) Schematic representation of selective membrane permeabilization resulting in the formation of actin filaments triggered by ion import. Adapted with permission from [71]. Copyright 2020 John Wiley and Sons. (C) Schematic representation of an ATP-producing vesicle and light-driven ATP synthesis in lipid and hybrid vesicles. Adapted with permission from [154]. Copyright 2020 John Wiley and Sons. (D) CLSM micrograph of PMOXA-*b*-PDMS GUVs containing β -galactosidase enzymes labeled with Cy5 (red), glucose oxidase enzymes labeled with Oregon green 488 (green), and HRP enzymes labeled with Atto 550 (blue) (scale bar 50 μm). GUVs equipped with OmpF pores enabled the influx of resorufin galactopyranoside, which was converted to the fluorescent product resorufin (red) by β -galactosidase (scale bar 50 μm). Adapted with permission from [39]. Copyright 2020 John Wiley and Sons.

Natural membranes are constantly being remodeled in a dynamic process, enabling the adaptation of cells to their current environment [188]. Fission and fusion of vesicles are among the most important membrane remodeling processes, with the latter being promoted by the fusogenic SNARE proteins. Using SNARE proteins, membrane fusion in poly(dimethylsiloxane)-*graft*-poly(ethylene oxide) (PDMS-*g*-PEO) membranes and hybrids thereof was achieved. Through the reconstitution of SNARE proteins in polymeric membranes, a size increase and membrane protein coreconstruction using two proteins reconstructed in different polymersomes were obtained [156]. Membrane remodeling arises not only from membrane fusion but from trans-bilayer migration (flip-flop) of amphiphilic molecules [189] and was also demonstrated in asymmetric PBd-*b*-PEO/POPC membranes [34]. For those membranes, a flip-flop half-life of around 7.5 h was demonstrated, despite the size difference between the hybrid asymmetric membrane sheets, which was consistent with values reported for lipid vesicles [190,191].

Most cellular systems are compartmentalized across several length scales and sub-compartments, i.e., organelles, which are essential to spatially separate processes within cells [192]. Using multicompartmental vesicles, supramolecular assemblies with hierarchical organization, increased complexity, and subcompartments can be created. A simple example of a multicompartmentalized vesicle was obtained by (co)loading lipidic (POPC, 1,2-dimyristoyl-sn-glycero-3-phosphocholine (DMPC), phosphatidylcholine (PC), DPPC) nano-sized vesicles within PBd-*b*-PEO giant vesicles using emulsion centrifugation. Through the use of thermosensitive lipids with different release temperatures, a simple microreactor with the ability to externally stimulate contained cascade reactions on demand was created [34]. In another example, multicompartmental GUVs were formed by the encapsulation of responsive nanoparticles loaded with biomolecules inside GUVs. The nanoparticles were loaded with either enzyme substrates or biopores and disassembled in the presence of dithiothreitol (DTT), thus releasing the nanoparticles' cargo. The release of the enzyme substrates catalyzed the reaction of coencapsulated enzymes, while the release of the ion channels (gramicidin) allowed them to integrate into the vesicle membrane, causing controlled permeabilization (Figure 4B). Using this approach, a multicompartment cellular system was created that was able to change membrane permeability upon external signals, a process naturally occurring in neurons [92]. An evolution of that study examined these multicompartmental vesicles encapsulated with two different subcompartments: reduction-sensitive nanoparticles and non-reduction-sensitive heparin micelles. Upon reductive external stimuli, signaling cascades were triggered that led to the assembly of a cytoskeleton in the form of an actin network within GUVs while maintaining internal compartmentalization through reduction-insensitive compartments [71].

To understand the interaction mechanisms of cells in tissues from a bottom-up perspective, artificial cells can be assembled into tissues. Simple artificial tissues comprising GUV aggregates segregated by an artificial membrane can be used for this purpose. Using a DNA-based linking system, a multicompartment GUV network containing a mixture of GUVs, each composed of either Pluronic L121, PBd-*b*-PEG, or polylactic acid-*block*-polyethylene glycol (PLA-*b*-PEG), served for the selective assembly of polymeric vesicles. The functionalization of GUVs with cholesterol-tagged DNA mediated the linkage of the vesicles and resulted in deformation at the adhesion site. The thermal regulation of the DNA hybridization allowed the linkage that controlled the contact area between the GUVs to be switched on and off [37].

Assembling polymeric and lipidic vesicles into hierarchical structures is a promising strategy to establish cell or organelle models closer to nature. However, controlling the encapsulation of smaller vesicular structures is challenging, as it is often governed by stochastic processes, and control over the encapsulation efficiency is limited. Precise control over the encapsulated cargo and the influence thereof is essential for the creation of model systems. While membranes serve a very important role in separating aqueous compartments from their surroundings, selective transport of certain molecules across a bilayer membrane is a key requirement for any cell. A straightforward method for

introducing selective transport to hybrid GUVs is through the use of a permeable polymer. The block copolymer oligo(aspartic acid)-*block*-poly(propylene oxide) forms polymer-rich domains in a polymer/lipid hybrid membrane that are intrinsically permeable to small molecules, but the selectivity and specificity of the transport across the membrane is limited. A more challenging approach is the insertion of pores or membrane proteins into synthetic bilayer membranes to induce selective permeability. Through film rehydration, membrane proteins can be directly added to the rehydration buffer, as shown for the model biopore OmpF [90] or the membrane proteins ATP synthase and cytochrome *b₀3* ubiquinol oxidase [156]. The addition of membrane proteins to preformed vesicles presents an alternative means of protein incorporation and has been shown for OmpF and gramicidin in microfluidic double emulsion templated PMOXA-*b*-PDMS GUVs [39,68].

In cells, a majority of the energy used for chemical work is stored in the form of adenosine triphosphate (ATP). ATP drives a plethora of energy-consuming processes within a cell, such as protein biosynthesis, motility, membrane transport, and intracellular signaling. In eukaryotic cells, most ATP is produced in the mitochondrion [193], making it a biologically relevant organelle to mimic. One popular approach for this is the reconstruction of a proton pump within a polymeric or hybrid polymer/lipid membrane to generate a proton gradient that can subsequently power a reconstructed (F_0F_1)-ATP synthase for the production of ATP from adenosine diphosphate (ADP) and inorganic phosphate (P_i). This has been shown using polymersomes and GUVs made from the graft polymer PDMS-*g*-PEO and the diblock copolymer PBd-*g*-PEO (Figure 4C) [72,154]. PDMS-*g*-PEO and PDMS-*g*-PEO/PC hybrid polymersomes and GUVs served as the base for directional insertion of a proton pump into the membrane and subsequent lowering of pH inside the GUV through active transport of protons across the polymer bilayer. Rheological testing revealed that PDMS-*g*-PEO and hybrid membranes showed higher flexibility than pure PC membranes and that the insertion of protein pores into the membrane further decreased rigidity and increased membrane fluidity. The high fluidity of the copolymer was attributed to the fact that the molecular weight of the PDMS was inversely proportional to the membrane's diffusion coefficient [194]. In a similar study, the transmembrane protein F_0F_1 -ATP synthase and the light-sensitive proton pump bacteriorhodopsin were integrated into the membranes of PDMS-*g*-PEO, PBd-*b*-PEO, and polymer/lipid hybrid polymersomes. This study demonstrated enhanced long-term stability of the membrane proteins as compared with liposomes, with the highest activity and longest stability in PDMS-containing membranes [154].

Using microfluidic double emulsion templated GUV formation, bioactive cargo has been encapsulated with an encapsulation efficiency of up to 99%. Through pore formation using OmpF, catalytic GUVs were produced to create a three-step enzymatic cascade that converted fluorescein di- β -galactopyranoside (FGD) into resorufin via two intermediate steps, demonstrating a simple intracellular communication pathway (Figure 4D) that could be extended in a modular fashion [39]. Through the encapsulation of bioactive molecules, e.g., enzymes, simple model artificial cells with in situ enzymatic activity have been created that could convert substrates from outside of the GUVs. While the complete removal of organic solvent is not always trivial, this method allows for the efficient, high-throughput production of vesicles with precise control over lumen and membrane composition, which is essential for the applicability of GUVs as cell mimics [195].

5. Conclusion and Perspectives

Polymeric micro- and nanocompartments offer great versatility; they can be loaded with various functional molecules, their surfaces can be functionalized using targeting moieties, and their membranes can gain specific functions using membrane proteins. Polymer vesicles have been studied extensively, as they offer several advantages over liposomes, such as increased chemical versatility and mechanical stability, and have found applications in imaging, therapeutics, and creation of artificial cellular models.

Nanoscale polymeric vesicles, including clusters of nanocompartments, have been applied for imaging and theranostics by combining therapeutic and imaging properties. By encapsulating imaging probes (e.g., quantum dots, fluorescent dyes) and/or therapeutic compounds, potentially toxic or quenching side effects can be avoided while maintaining observable, targeted delivery. Similar approaches have been applied for therapeutic applications; cargo can be encapsulated within their cavities or loaded within their structure to increase stability, activity, and blood circulation. Specifically, through the permeabilization of enzyme-loaded polymersomes using pore proteins or pore-forming peptides, catalytic nanocompartments can be created that perform catalytic activity. This can apply to enzyme replacement therapy or on-demand drug production.

Polymeric microvesicles have mainly been used for cellular modeling and the creation of artificial cells. Using polymeric or hybrid polymer/lipid membranes, natural membranes can be mimicked in terms of membrane asymmetry or domain formation. Through reconstitution of membrane proteins, cellular signaling can be studied, and by combining nano- and micrometer-sized vesicles, structures with complex hierarchies can be built that mimic natural compartmentalized systems. Using both lipids and polymers allows for the exploitation of the advantages of both types of amphiphiles, facilitating membrane protein reconstitution while increasing the compartment's stability. Attempts have been made to mimic cytoskeleton networks, cellular movement, and inter- and intracellular communication. However, progress still needs to be made in order to gain understanding and to realize the full potential of artificial cell models.

Progress in polymer chemistry has enabled the creation of polymers with tailored properties, and because of the immense variety of chemical compositions and functionalizations, polymers can be tailored to improve biocompatibility, biodegradability, and toxicity. Even so, the production of compartments thereof is still challenging; most of the fabrication techniques are laborious and low throughput, which also complicates subsequent scale-up attempts. Using microfluidic methods enables the high-throughput production of polymeric vesicles; however, examples are still limited, in the early stages of development, and mainly applied to micrometer-sized compartments. Even though significant progress has been made in the formulation of catalytic compartments and control over the encapsulation efficiency, surface functionalization, and membrane protein reconstitution, further research is still needed to obtain insight into the structure and behavior of said compartments in a biomedical context. Hybrid materials are being investigated with significant progress; however, research is still needed to study interactions of polymeric and biological materials in order to increase biocompatibility. For therapeutic applications, most of the studies presented tested *in vitro*, and the *in vivo* studies were limited to mice. While most studies presented showed promising results, tests for the efficacy and compatibility of polymer compartments are necessary for their effective application in a medical context. Employing multifunctional materials is expected to increase applicability of polymeric compartments for patient-oriented medical strategies; incorporation of multistimulus-responsive materials that activate their functionality in response to multiple intracellular or external signals would increase the number of applications of polymeric compartments in the biomedical field.

Author Contributions: L.H., M.K. (Maria Korpidou), O.M.E. and M.K. (Myrto Kyropoulou) carried out literature research and wrote the manuscript. C.G.P. provided additional guidance and assisted in finalizing the manuscript. All authors have read and agreed to the published version of the manuscript.

Funding: The authors acknowledge financial support from the Swiss National Science Foundation, NCCR-MSE, and University of Basel. M.K. personally thanks EU ITN BIOMOLMACS (European Union's Horizon2020 research and innovation program under the Marie Skłodowska-Curie grant agreement N° 859416) for research funding and support.

Institutional Review Board Statement: Not applicable.

Informed Consent Statement: Not applicable.

Data Availability Statement: Not applicable.

Conflicts of Interest: The authors declare no conflict of interest.

Abbreviations

ADA	alendronic acid
ADP	adenosine diphosphate
AP	poly([5-aminopentyl]- α,β -aspartamide)
ATP	adenosine triphosphate
BDL	bile duct-ligated
BMD	bone mineral density
cGMP	cyclic guanosine monophosphate
CLSM	confocal laser scanning microscope
CMA	7-(2-methacryloyloxyethoxy)-4-methylcoumarin
CNC	catalytic nanocompartment
CPP	cell-penetrating peptide
CPT	camptothecin
CPTKMA	thioether-linked CPT methacrylate monomer
cRGD	cyclic arginine-glycine-aspartic
CT	computed tomography
CTAB	cetyltrimethylammonium bromide
DBCO	dibenzocyclooctyne
DDC	dopa decarboxylase
DEA	2-(diethylamino)ethyl methacrylate
DEX	dextran sulfate
DMPC	1,2-dimyristoyl-sn-glycero-3-phosphocholine
DNA	deoxyribonucleic acid
DPPC	1,2-dipalmitoyl-sn-glycero-3-phosphocholine
DTT	dithiothreitol
<i>E. coli</i>	<i>Escherichia coli</i>
FGD	fluorescein di- β -galactopyranoside
FITC	fluorescein isothiocyanate
FRAP	fluorescence recovery after photobleaching
GEMA	(α -d-glucopyranosyl)ethyl methacrylate
Gox	glucose oxidase
GUV	giant unilamellar vesicle
HPTS	8-hydroxypyrene-1,3,6-trisulfonate
HRP	horseradish peroxidase
iNOS	nitric oxide synthase
ITO	indium tin oxide
LbL	layer-by-layer
L-DOPA	levodopa/1-3,4-dihydroxyphenylalanine
LPO	lactoperoxidase
MMP	matrix metalloproteinase
mNSS	modified neurological severity scores
mPEG	methoxy-poly(ethylene glycol)
MRI	magnetic Resonance Imaging
NgR	Nogo-66 receptor
NIR	near-infrared
NP	nanoparticle
OEGMA	oligo(ethylene glycol) methyl ether methacrylate
OmpF	outer membrane protein F (from <i>Escherichia coli</i>)
PA	poly-L-arginine
PAA	poly(acrylic acid)
PAH	poly(allylamine hydrochloride)
PAMAM	poly(amidoamine)
PAsp	poly(α,β -aspartic acid)

PATK	poly([2-[[1-(2-aminoethyl)thio]-1-methylethyl]thio]ethyl]- α,β -aspartamide)
PBd	poly(1,2-butadiene)
PBO	poly(butylene oxide)
PBzMA	poly(benzyl methacrylate)
PC	phosphatidylcholine
PCL	poly(ϵ -caprolactone)
PDA	polydopamine
PDLLA	poly(D,L-Lactic Acid)
PDMS	poly(dimethylsiloxane)
PDPA	poly [2-(diisopropylamino)ethyl methacrylate]
PEG	poly(ethylene glycol)
PEHO	poly(3-ethyl-3-hydroxymethyloxetane)
PEI	poly(ether imide)
PEMA	poly(ethyl methacrylate)
PEO	poly(ethylene oxide)
PEtOz	poly(2-ethyl-2-oxazoline)
PG	poly(glycidol)
PGPMA	poly(3-guanidinopropyl methacrylamide)
PHPMA	poly(N-(2-Hydroxypropyl) methacrylamide)
P _i	inorganic phosphate
PiB	polyisobutylene
PIC	polyion complex
PISA	polymerization-induced self-assembly
PL	phospholipids
PLA	polycaprolactone
PLys	poly-lysine
PMA	polymethyl acrylate
PMOXA	poly(2-methyl-2-oxazoline)
PMPC	poly(2-methacryloyloxyethyl phosphorylcholine)
POEGMA	poly(oligo(ethylene glycol) methyl ether methacrylate)
POPC	1-palmitoyl-2-oleoyl-sn-glycero-3-phosphocholine
PS	polystyrene
PSS	poly(styrene sulfonate)
PSMA	poly(stearyl methacrylate)
PPG	poly(propylene glycol)
PPO	poly(p-phenylene oxide)
PTMC	tetraphenylethylene pyridinium modified trimethylenecarbonate
PVP	polyvinylpyrrolidone
P(CLgTMC)	poly(caprolactone-gradient-trimethylene carbonate)
ROS	reactive oxygen species
<i>S. aureus</i>	<i>Staphylococcus aureus</i>
sGC	soluble guanylyl cyclase
siRNA	small interfering ribonucleic acid
SPAAC	strain-promoted azide-alkyne cycloaddition
SPECT	single-photon emission computed tomography
SPIONs	superparamagnetic iron oxide nanoparticles
ssDNA	single-stranded deoxyribonucleic acid
TA	tannic acid
TTA-UC	triplet–triplet annihilation based molecular photon upconversion
UOX	urate oxidase
USIONs	ultrasmall iron oxide nanoparticles
VBA	poly(vinyl benzaldehyde)

References

1. Palivan, C.G.; Goers, R.; Najer, A.; Zhang, X.; Car, A.; Meier, W. Bioinspired polymer vesicles and membranes for biological and medical applications. *Chem. Soc. Rev.* **2016**, *45*, 377–411. [CrossRef]
2. Matoori, S.; Leroux, J.C. Twenty-five years of polymersomes: Lost in translation? *Mater. Horiz.* **2020**, *7*, 1297–1309. [CrossRef]
3. Feng, H.; Lu, X.; Wang, W.; Kang, N.-G.; Mays, J.W. Block copolymers: Synthesis, self-assembly, and applications. *Polymers* **2017**, *9*, 494. [CrossRef] [PubMed]
4. Kim, K.T.; Meeuwissen, S.A.; Nolte, R.J.; van Hest, J.C. Smart nanocontainers and nanoreactors. *Nanoscale* **2010**, *2*, 844–858. [CrossRef] [PubMed]
5. Go, Y.K.; Leal, C. Polymer–lipid hybrid materials. *Chem. Rev.* **2021**, *121*, 13996–14030. [CrossRef]
6. Thoma, J.; Belegriinou, S.; Rossbach, P.; Grzelakowski, M.; Kita-Tokarczyk, K.; Meier, W. Membrane protein distribution in composite polymer–Lipid thin films. *Chem. Commun.* **2012**, *48*, 8811–8813. [CrossRef]
7. Fauquignon, M.; Ibarboure, E.; Meins, J.-F. Membrane reinforcement in giant hybrid polymer lipid vesicles achieved by controlling the polymer architecture. *Soft Matter* **2021**, *17*, 83–89. [CrossRef]
8. Gilbert, R.J.; Serra, M.D.; Froelich, C.J.; Wallace, M.I.; Anderluh, G. Membrane pore formation at protein–Lipid interfaces. *Trends Biochem. Sci.* **2014**, *39*, 510–516. [CrossRef]
9. Hu, Z.; Ho, J.C.; Nallani, M. Synthetic (polymer) biology (membrane): Functionalization of polymer scaffolds for membrane proteins. *Curr. Opin. Biotechnol.* **2017**, *46*, 51–56. [CrossRef]
10. Hindley, J.W.; Law, R.V.; Ces, O. Membrane functionalization in artificial cell engineering. *SN Appl. Sci.* **2020**, *2*, 593. [CrossRef]
11. Hoang, N.H.; Lim, C.; Sim, T.; Oh, K.T. Triblock copolymers for nano-sized drug delivery systems. *J. Pharm. Investig.* **2017**, *47*, 27–35. [CrossRef]
12. Hasannia, M.; Aliabadi, A.; Abnous, K.; Taghdisi, S.M.; Ramezani, M.; Alibolandi, M. Synthesis of block copolymers used in polymersome fabrication: Application in drug delivery. *J. Control. Release* **2022**, *341*, 95–117. [CrossRef] [PubMed]
13. Mora-Huertas, C.E.; Fessi, H.; Elaissari, A. Polymer-based nanocapsules for drug delivery. *Int. J. Pharm.* **2010**, *385*, 113–142. [CrossRef] [PubMed]
14. Reimhult, E.; Virk, M.M. Hybrid lipopolymer vesicle drug delivery and release systems. *J. Biomed. Res.* **2021**, *35*, 301–309. [CrossRef]
15. Goers, R.; Thoma, J.; Ritzmann, N.; Di Silvestro, A.; Alter, C.; Gunkel-Grabole, G.; Fotiadis, D.; Müller, D.J.; Meier, W. Optimized reconstitution of membrane proteins into synthetic membranes. *Commun. Chem.* **2018**, *1*, 35. [CrossRef]
16. Belluati, A.; Craciun, I.; Liu, J.; Palivan, C.G. Nanoscale enzymatic compartments in tandem support cascade reactions in vitro. *Biomacromolecules* **2018**, *19*, 4023–4033. [CrossRef]
17. Rideau, E.; Wurm, F.R.; Landfester, K. Self-assembly of giant unilamellar vesicles by film hydration methodologies. *Adv. Biosyst.* **2019**, *3*, 1800324. [CrossRef]
18. Cabukusta, B.; Neeffjes, J. Mechanisms of lysosomal positioning and movement. *Traffic* **2018**, *19*, 761–769. [CrossRef]
19. Blanazs, A.; Armes, S.P.; Ryan, A.J. Self-assembled block copolymer aggregates: From micelles to vesicles and their biological applications. *Macromol. Rapid Commun.* **2009**, *30*, 267–277. [CrossRef]
20. Discher, D.E. Polymer vesicles. *Science* **2002**, *297*, 967–973. [CrossRef]
21. Antonietti, M.; Förster, S. Vesicles and liposomes: A self-assembly principle beyond lipids. *Adv. Mater.* **2003**, *15*, 1323–1333. [CrossRef]
22. Daubian, D.; Gaitzsch, J.; Meier, W. Synthesis and complex self-assembly of amphiphilic block copolymers with a branched hydrophobic Poly(2-Oxazoline) into multicompartiment micelles, pseudo-vesicles and Yolk/Shell nanoparticles. *Polym. Chem.* **2020**, *11*, 1237–1248. [CrossRef]
23. Wehr, R.; Gaitzsch, J.; Daubian, D.; Fodor, C.; Meier, W. Deepening the insight into poly(butylene oxide)-Block-poly(Glycidol) synthesis and self-assemblies: Micelles, worms and vesicles. *RSC Adv.* **2020**, *10*, 22701–22711. [CrossRef] [PubMed]
24. Li, B.-Y.; Li, Y.-C.; Lu, Z.-Y. The important role of cosolvent in the amphiphilic diblock copolymer self-assembly process. *Polymer* **2019**, *171*, 1–7. [CrossRef]
25. Balasubramanian, V.; Herranz-Blanco, B.; Almeida, P.V.; Hirvonen, J.; Santos, H.A. Multifaceted polymersome platforms: Spanning from self-assembly to drug delivery and protocells. *Prog. Polym. Sci.* **2016**, *60*, 51–85. [CrossRef]
26. Daubian, D.; Fillion, A.; Gaitzsch, J.; Meier, W. One-pot synthesis of an amphiphilic ABC triblock copolymer PEO-*b*-PEHOx-*b*-PEtOz and its self-assembly into nanoscopic asymmetric polymersomes. *Macromolecules* **2020**, *53*, 11040–11050. [CrossRef]
27. Parnell, A.J.; Tzokova, N.; Topham, P.D.; Adams, D.J.; Adams, S.; Fernyhough, C.M.; Ryan, A.J.; Jones, R.A. The efficiency of encapsulation within surface rehydrated polymersomes. *Faraday Discuss.* **2009**, *143*, 29–46. [CrossRef]
28. Belluati, A.; Craciun, I.; Meyer, C.E.; Rigo, S.; Palivan, C.G. Enzymatic reactions in polymeric compartments: Nanotechnology meets nature. *Curr. Opin. Biotechnol.* **2019**, *60*, 53–62. [CrossRef]
29. Pachioni-Vasconcelos, J.D.; Apolinário, A.C.; Lopes, A.M.; Pessoa, A., Jr.; Barbosa, L.R.; Rangel-Yagui, C.D. Compartmentalization of therapeutic proteins into semi-crystalline PEG-PCL polymersomes. *Soft Mater.* **2021**, *19*, 222–230. [CrossRef]
30. Lomora, M.; Garni, M.; Itef, F.; Tanner, P.; Spulber, M.; Palivan, C.G. Polymersomes with engineered ion selective permeability as stimuli-responsive nanocompartments with preserved architecture. *Biomaterials* **2015**, *53*, 406–414. [CrossRef]
31. Ibarboure, E.; Fauquignon, M.; Le Meins, J.-F. Obtention of giant unilamellar hybrid vesicles by electroformation and measurement of their mechanical properties by micropipette aspiration. *J. Vis. Exp.* **2020**, *155*, 60199. [CrossRef] [PubMed]

32. Walde, P.; Cosentino, K.; Engel, H.; Stano, P. Giant vesicles: Preparations and applications. *ChemBioChem* **2010**, *11*, 848–865. [CrossRef] [PubMed]
33. Garni, M.; Wehr, R.; Avsar, S.Y.; John, C.; Palivan, C.; Meier, W. Polymer membranes as templates for bio-applications ranging from artificial cells to active surfaces. *Eur. Polym. J.* **2019**, *112*, 346–364. [CrossRef]
34. Peyret, A.; Ibarboure, E.; Le Meins, J.-F.; Lecommandoux, S. Asymmetric hybrid polymer—Lipid giant vesicles as cell membrane mimics. *Adv. Sci.* **2018**, *5*, 1700453. [CrossRef]
35. dos Santos, E.C.; Angelini, A.; Hürlimann, D.; Meier, W.; Palivan, C.G. Giant polymer compartments for confined reactions. *Chemistry* **2020**, *2*, 470–489. [CrossRef]
36. Shum, H.C.; Kim, J.-W.; Weitz, D.A. Microfluidic fabrication of monodisperse biocompatible and biodegradable polymersomes with controlled permeability. *J. Am. Chem. Soc.* **2008**, *130*, 9543–9549. [CrossRef]
37. Luo, R.; Göpflich, K.; Platzman, I.; Spatz, J.P. DNA-based assembly of multi-compartment polymersome networks. *Adv. Funct. Mater.* **2020**, *30*, 2003480. [CrossRef]
38. Deshpande, S.; Caspi, Y.; Meijering, A.E.; Dekker, C. Octanol-assisted liposome assembly on chip. *Nat. Commun.* **2016**, *7*, 1–9. [CrossRef]
39. dos Santos, E.C.; Belluati, A.; Necula, D.; Scherrer, D.; Meyer, C.E.; Wehr, R.P.; Lörtscher, E.; Palivan, C.G.; Meier, W. Combinatorial strategy for studying biochemical pathways in double emulsion templated cell-sized compartments. *Adv. Mater.* **2020**, *32*, 2004804. [CrossRef]
40. Weiss, M.; Frohnmayer, J.P.; Benk, L.T.; Haller, B.; Janiesch, J.W.; Heitkamp, T.; Börsch, M.; Lira, R.B.; Dimova, R.; Lipowsky, R.; et al. Sequential bottom-up assembly of mechanically stabilized synthetic cells by microfluidics. *Nat. Mater.* **2018**, *17*, 89–95. [CrossRef]
41. Phan, H.; Taresco, V.; Penelle, J.; Couturaud, B. Polymerisation-induced self-assembly (PISA) as a straightforward formulation strategy for stimuli-responsive drug delivery systems and biomaterials: Recent advances. *Biomater. Sci.* **2021**, *9*, 38–50. [CrossRef] [PubMed]
42. Dorsman, I.R.; Derry, M.J.; Cunningham, V.J.; Brown, S.L.; Williams, C.N.; Armes, S.P. Tuning the vesicle-to-worm transition for thermoresponsive block copolymer vesicles prepared *via* polymerisation-induced self-assembly. *Polym. Chem.* **2021**, *12*, 1224–1235. [CrossRef]
43. Xu, S.; Corrigan, N.; Boyer, C. Forced gradient copolymerisation: A simplified approach for polymerisation-induced self-assembly. *Polym. Chem.* **2021**, *12*, 57–68. [CrossRef]
44. Canning, S.L.; Smith, G.N.; Armes, S.P. A critical appraisal of RAFT-mediated polymerization-induced self-assembly. *Macromolecules* **2016**, *49*, 1985–2001. [CrossRef]
45. Donath, E.; Sukhorukov, G.B.; Caruso, F.; Davis, S.A.; Möhwald, H. Novel hollow polymer shells by colloid-templated assembly of polyelectrolytes. *Angew. Chem. Int. Ed.* **1998**, *37*, 2201–2205. [CrossRef]
46. Eivazi, A.; Medronho, B.; Lindman, B.; Norgren, M. On the development of all-cellulose capsules by vesicle-templated layer-by-layer assembly. *Polymers* **2021**, *13*, 589. [CrossRef]
47. Elizarova, I.S.; Luckham, P.F. Layer-by-layer adsorption: Factors affecting the choice of substrates and polymers. *Adv. Colloid Interface Sci.* **2018**, *262*, 1–20. [CrossRef]
48. Kurapati, R.; Groth, T.W.; Raichur, A.M. Recent developments in layer-by-layer technique for drug delivery applications. *ACS Appl. Bio Mater.* **2019**, *2*, 5512–5527. [CrossRef]
49. Campbell, J.; Vikulina, A.S. Layer-by-layer assemblies of biopolymers: Build-Up, mechanical stability and molecular dynamics. *Polymers* **2020**, *12*, 1949. [CrossRef]
50. Francesch, M.B. Capsosomes: The revolutionary enzyme carriers. *Eur. Pharm. Rev.* **2019**, *24*, 34–36.
51. Städler, B.; Chandrawati, R.; Goldie, K.; Caruso, F. Capsosomes: Subcompartmentalizing polyelectrolyte capsules using liposomes. *Langmuir* **2009**, *25*, 6725–6732. [CrossRef] [PubMed]
52. Sun, J.; Li, Z. Polyion complexes via electrostatic interaction of oppositely charged block copolymers. *Macromolecules* **2020**, *53*, 8737–8740. [CrossRef]
53. Liu, Y.; Maruyama, T.; Kc, B.; Mori, T.; Katayama, Y.; Kishimura, A. Inducible dynamic behavior of polyion complex vesicles by disrupting charge balance. *Chem. Lett.* **2021**, *50*, 1034–1037. [CrossRef]
54. Nishimura, T.; Sasaki, Y.; Akiyoshi, K. Biotransporting self-assembled nanofactories using polymer vesicles with molecular permeability for enzyme prodrug cancer therapy. *Adv. Mater.* **2017**, *29*, 1702406. [CrossRef] [PubMed]
55. Odrobińska, J.; Gumieniczek-Chłopek, E.; Szuwarzyński, M.; Radziszewska, A.; Fiejdasz, S.; Strączek, T.; Kapusta, C.; Zapotoczny, S. Magnetically navigated core—Shell polymer capsules as nanoreactors loadable at the oil/water interface. *ACS Appl. Mater. Interfaces* **2019**, *11*, 10905–10913. [CrossRef]
56. Cai, H.; Wang, P.; Zhang, D. PH-responsive linkages-enabled layer-by-layer assembled antibacterial and antiadhesive multilayer films with polyelectrolyte nanocapsules as biocide delivery vehicles. *J. Drug Deliv. Sci. Technol.* **2019**, *54*, 101251. [CrossRef]
57. Svenskaya, Y.; Garello, F.; Lengert, E.; Kozlova, A.; Verkhovskii, R.; Bitonto, V.; Ruggiero, M.R.; German, S.; Gorin, D.; Terreno, E. Biodegradable polyelectrolyte/magnetite capsules for mr imaging and magnetic targeting of tumors. *Nanotheranostics* **2021**, *5*, 362–377. [CrossRef]
58. Seitz, S.; Ajiro, H. Self-assembling weak polyelectrolytes for the layer-by-layer encapsulation of paraffin-type phase change material icosane. *Sol. Energy Mater. Sol. Cells* **2019**, *190*, 57–64. [CrossRef]

59. Larrañaga, A.; Isa, I.L.; Patil, V.; Thamboo, S.; Lomora, M.; Fernández-Yague, M.A.; Sarasua, J.-R.; Palivan, C.G.; Pandit, A. Antioxidant functionalized polymer capsules to prevent oxidative stress. *Acta Biomater.* **2018**, *67*, 21–31. [CrossRef]
60. Sharma, V.; Vijay, J.; Ganesh, M.R.; Sundaramurthy, A. Multilayer capsules encapsulating nimbin and doxorubicin for cancer chemo-photothermal therapy. *Int. J. Pharm.* **2020**, *582*, 119350. [CrossRef]
61. Huang, J.; Li, C.; Gao, Y.; Cai, Y.; Guo, X.; Cohen Stuart, M.A.; Wang, J. Dendrimer-based polyion complex vesicles: Loops make loose. *Macromol. Rapid Commun.* **2022**, *43*, e2100594. [CrossRef] [PubMed]
62. Hori, M.; Cabral, H.; Toh, K.; Kishimura, A.; Kataoka, K. Robust polyion complex vesicles (PICsomes) under physiological conditions reinforced by multiple hydrogen bond formation derived by guanidinium groups. *Biomacromolecules* **2018**, *19*, 4113–4121. [CrossRef] [PubMed]
63. Koval, V.; Morozova, E.; Revtovich, S.; Lyfenko, A.; Chobanian, A.; Timofeeva, V.; Solovieva, A.; Anufrieva, N.; Kulikova, V.; Demidkina, T. Characteristics and stability assessment of therapeutic methionine γ -Lyase-loaded polyionic vesicles. *ACS Omega* **2022**, *7*, 959–967. [CrossRef] [PubMed]
64. Sueyoshi, D.; Anraku, Y.; Komatsu, T.; Urano, Y.; Kataoka, K. Enzyme-loaded polyion complex vesicles as in vivo nanoreactors working sustainably under the blood circulation: Characterization and functional evaluation. *Biomacromolecules* **2017**, *18*, 1189–1196. [CrossRef]
65. Li, J.; Anraku, Y.; Kataoka, K. Self-boosting catalytic nanoreactors integrated with triggerable crosslinking membrane networks for initiation of immunogenic cell death by pyroptosis. *Angew. Chem. Int. Ed.* **2020**, *59*, 13526–13530. [CrossRef]
66. Seneviratne, R.; Catania, R.; Rappolt, M.; Jeuken, L.J.; Beales, P.A. Membrane mixing and dynamics in hybrid POPC/poly(1,2-butadiene-Block-ethylene oxide) (PBd-*b*-PEO) lipid/block co-polymer giant vesicles. *Soft Matter* **2022**, *18*, 1294–1301. [CrossRef]
67. Peyret, A.; Ibarboure, E.; Pippa, N.; Lecommandoux, S. Liposomes in polymersomes: Multicompartment System with temperature-triggered release. *Langmuir* **2017**, *33*, 7079–7085. [CrossRef]
68. Wehr, R.; dos Santos, E.C.; Muthwill, M.S.; Chimisso, V.; Gaitzsch, J.; Meier, W. Fully amorphous atactic and isotactic block copolymers and their self-assembly into nano- and microscopic vesicles. *Polym. Chem.* **2021**, *12*, 5377–5389. [CrossRef]
69. Zhou, X.; Cornel, E.J.; Fan, Z.; He, S.; Du, J. Bone-targeting polymer vesicles for effective therapy of osteoporosis. *Nano Lett.* **2021**, *21*, 7998–8007. [CrossRef]
70. Yang, Y.-Y.; Chen, L.-S.; Sun, M.; Wang, C.-Y.; Fan, Z.; Du, J.-Z. Biodegradable polypeptide-based vesicles with intrinsic blue fluorescence for antibacterial visualization. *Chin. J. Polym. Sci.* **2021**, *39*, 1412–1420. [CrossRef]
71. Belluati, A.; Thamboo, S.; Najer, A.; Maffei, V.; von Planta, C.; Craciun, I.; Palivan, C.G.; Meier, W. Multicompartment polymer vesicles with artificial organelles for signal-triggered cascade reactions including cytoskeleton formation. *Adv. Funct. Mater.* **2020**, *30*, 2002949. [CrossRef]
72. Marušič, N.; Otrin, L.; Zhao, Z.; Lira, R.B.; Kyrilis, F.L.; Hamdi, F.; Kastritis, P.L.; Vidaković-Koch, T.; Ivanov, I.; Sundmacher, K.; et al. Constructing artificial respiratory chain in polymer compartments: Insights into the interplay between Bo_3 oxidase and the membrane. *Proc. Natl. Acad. Sci. USA* **2020**, *117*, 15006–15017. [CrossRef] [PubMed]
73. Go, Y.K.; Kamar, N.; Leal, C. Hybrid unilamellar vesicles of phospholipids and block copolymers with crystalline domains. *Polymers* **2020**, *12*, 1232. [CrossRef] [PubMed]
74. Khan, S.; McCabe, J.; Hill, K.; Beales, P.A. Biodegradable hybrid block copolymer—Lipid vesicles as potential drug delivery systems. *J. Colloid Interface Sci.* **2020**, *562*, 418–428. [CrossRef] [PubMed]
75. Cao, S.; Xia, Y.; Shao, J.; Guo, B.; Dong, Y.; Pijpers, I.A.; Zhong, Z.; Meng, F.; Abdelmohsen, L.K.; Williams, D.S.; et al. Biodegradable polymersomes with structure inherent fluorescence and targeting capacity for enhanced photo-dynamic therapy. *Angew. Chem. Int. Ed.* **2021**, *60*, 17629–17637. [CrossRef]
76. Ke, W.; Li, J.; Mohammed, F.; Wang, Y.; Tou, K.; Liu, X.; Wen, P.; Kinoh, H.; Anraku, Y.; Chen, H.; et al. Therapeutic polymersome nanoreactors with tumor-specific activable cascade reactions for cooperative cancer therapy. *ACS Nano* **2019**, *13*, 2357–2369. [CrossRef]
77. Li, J.; Ge, Z.; Toh, K.; Liu, X.; Dirisala, A.; Ke, W.; Wen, P.; Zhou, H.; Wang, Z.; Xiao, S.; et al. Enzymatically transformable polymersome-based nanotherapeutics to eliminate minimal relapsable cancer. *Adv. Mater.* **2021**, *33*, 2105254. [CrossRef]
78. Blackman, L.D.; Varlas, S.; Arno, M.C.; Houston, Z.H.; Fletcher, N.L.; Thurecht, K.J.; Hasan, M.; Gibson, M.I.; O'Reilly, R.K. Confinement of therapeutic enzymes in selectively permeable polymer vesicles by polymerization-induced self-assembly (pisa) reduces antibody binding and proteolytic susceptibility. *ACS Cent. Sci.* **2018**, *4*, 718–723. [CrossRef]
79. Cao, J.; Wei, Y.; Zhang, Y.; Wang, G.; Ji, X.; Zhong, Z. Iodine-rich polymersomes enable versatile SPECT/CT imaging and potent radioisotope therapy for tumor in vivo. *ACS Appl. Mater. Interfaces* **2019**, *11*, 18953–18959. [CrossRef]
80. Kim, B.S.; Naito, M.; Chaya, H.; Hori, M.; Hayashi, K.; Min, H.S.; Yi, Y.; Kim, H.J.; Nagata, T.; Anraku, Y.; et al. Noncovalent stabilization of vesicular polyion complexes with chemically modified/single-stranded oligonucleotides and peg-*b*-guanidinylated polypeptides for intracavity encapsulation of effector enzymes aimed at cooperative gene knockdown. *Biomacromolecules* **2020**, *21*, 4365–4376. [CrossRef]
81. Choi, H.; Lee, G.-H.; Kim, K.S.; Hahn, S.K. Light-guided nanomotor systems for autonomous photothermal cancer therapy. *ACS Appl. Mater. Interfaces* **2018**, *10*, 2338–2346. [CrossRef]
82. Sun, J.; Mathesh, M.; Li, W.; Wilson, D.A. Enzyme-powered nanomotors with controlled size for biomedical applications. *ACS Nano* **2019**, *13*, 10191–10200. [CrossRef] [PubMed]

83. Pijpers, I.A.; Cao, S.; Llopis-Lorente, A.; Zhu, J.; Song, S.; Joosten, R.R.; Meng, F.; Friedrich, H.; Williams, D.S.; Sánchez, S.; et al. Hybrid biodegradable nanomotors through compartmentalized synthesis. *Nano Lett.* **2020**, *20*, 4472–4480. [CrossRef] [PubMed]
84. Bueno, C.Z.; Apolinário, A.C.; Duro-Castano, A.; Poma, A.; Pessoa, A.; Rangel-Yagui, C.O.; Battaglia, G. L-asparaginase encapsulation into asymmetric permeable polymersomes. *ACS Macro Lett.* **2020**, *9*, 1471–1477. [CrossRef]
85. Jin, S.-M.; Jeon, J.; Park, M.-K.; Kim, G.H.; Lee, E. Multicompartment vesicles formation by emulsification-induced assembly of poly(ethylene oxide)-block-poly(ϵ -Caprolactone) and their dual-loading capability. *Macromol. Rapid Commun.* **2018**, *39*, 1700545. [CrossRef] [PubMed]
86. Konishcheva, E.V.; Daubian, D.; Rigo, S.; Meier, W.P. Probing membrane asymmetry of abc polymersomes. *Chem. Commun.* **2019**, *55*, 1148–1151. [CrossRef]
87. Xiao, Y.; Sun, H.; Du, J. Sugar-breathing glycopolymersomes for regulating glucose level. *J. Am. Chem. Soc.* **2017**, *139*, 7640–7647. [CrossRef]
88. Askes, S.H.; Pomp, W.; Hopkins, S.L.; Kros, A.; Wu, S.; Schmidt, T.; Bonnet, S. Imaging upconverting polymersomes in cancer cells: Biocompatible antioxidants brighten triplet-triplet annihilation upconversion. *Small Weinh. Bergstr. Ger.* **2016**, *12*, 5579–5590. [CrossRef]
89. Kulikova, V.V.; Morozova, E.A.; Anufrieva, N.V.; Koval, V.S.; Lyfenko, A.D.; Lesnova, E.I.; Kushch, A.A.; Revtovich, S.V.; Demidkina, T.V. Kinetic and pharmacokinetic characteristics of therapeutic methinonine γ -Lyase encapsulated in polyion complex vesicles. *Biochimie* **2022**, *194*, 13–18. [CrossRef]
90. Garni, M.; Einfalt, T.; Goers, R.; Palivan, C.G.; Meier, W. Live follow-up of enzymatic reactions inside the cavities of synthetic giant unilamellar vesicles equipped with membrane proteins mimicking cell architecture. *ACS Synth. Biol.* **2018**, *7*, 2116–2125. [CrossRef]
91. Maffei, V.; Belluati, A.; Craciun, I.; Wu, D.; Novak, S.; Schoenenberger, C.-A.; Palivan, C.G. Clustering of catalytic nanocompartments for enhancing an extracellular non-native cascade reaction. *Chem. Sci.* **2021**, *12*, 12274–12285. [CrossRef] [PubMed]
92. Thamboo, S.; Najer, A.; Belluati, A.; von Planta, C.; Wu, D.; Craciun, I.; Meier, W.; Palivan, C.G. Mimicking cellular signaling pathways within synthetic multicompartment vesicles with triggered enzyme activity and induced ion channel recruitment. *Adv. Funct. Mater.* **2019**, *29*, 1904267. [CrossRef]
93. Messenger, L.; Burns, J.R.; Kim, J.; Cecchin, D.; Hindley, J.; Pyne, A.L.; Gaitzsch, J.; Battaglia, G.; Howorka, S. Biomimetic hybrid nanocontainers with selective permeability. *Angew. Chem. Int. Ed.* **2016**, *55*, 11106–11109. [CrossRef] [PubMed]
94. Hosta-Rigau, L.; York-Duran, M.J.; Zhang, Y.; Goldie, K.N.; Städler, B. Confined Multiple enzymatic (cascade) reactions within poly(dopamine)-based capsosomes. *ACS Appl. Mater. Interfaces* **2014**, *6*, 12771–12779. [CrossRef]
95. Matoori, S.; Bao, Y.; Schmidt, A.; Fischer, E.J.; Ochoa-Sanchez, R.; Tremblay, M.; Oliveira, M.M.; Rose, C.F.; Leroux, J.-C. An investigation of PS-b-PEO polymersomes for the oral treatment and diagnosis of hyperammonemia. *Small* **2019**, *15*, 1902347. [CrossRef]
96. Kulygin, O.; Price, A.D.; Chong, S.-F.; Städler, B.; Zelikin, A.N.; Caruso, F. Subcompartmentalized polymer hydrogel capsules with selectively degradable carriers and subunits. *Small* **2010**, *6*, 1558–1564. [CrossRef]
97. Nishimura, T.; Toh, W.-L.; Akiyoshi, K. Synthesis and characterization of shell-cross-linked glycopolymer bilayer vesicles. *Macromol. Rapid Commun.* **2018**, *39*, 1800384. [CrossRef]
98. Liu, D.; Sun, H.; Xiao, Y.; Chen, S.; Cornel, E.J.; Zhu, Y.; Du, J. Design principles, synthesis and biomedical applications of polymer vesicles with inhomogeneous membranes. *J. Control. Release* **2020**, *326*, 365–386. [CrossRef]
99. Zhong, Y.; Meng, F.; Zhang, W.; Li, B.; van Hest, J.C.; Zhong, Z. CD44-targeted vesicles encapsulating granzyme B as artificial killer cells for potent inhibition of human multiple myeloma in mice. *J. Control. Release* **2020**, *320*, 421–430. [CrossRef]
100. Dinda, S.; Sarkar, S.; Das, P.K. Glucose oxidase mediated targeted cancer-starving therapy by biotinylated self-assembled vesicles. *Chem. Commun.* **2018**, *54*, 9929–9932. [CrossRef]
101. van Beek, L.F.; Welzen, P.L.; Teufel, L.U.; Joosten, I.; Diavatopoulos, D.A.; van Hest, J.; de Jonge, M.I. Bimodal targeting of human leukocytes by Fc- and CpG-decorated polymersomes to tune immune induction. *Biomacromolecules* **2021**, *22*, 4422–4433. [CrossRef] [PubMed]
102. Zou, Y.; Sun, Y.; Guo, B.; Wei, Y.; Xia, Y.; Huangfu, Z.; Meng, F.; van Hest, J.C.; Yuan, J.; Zhong, Z. A3 β 1 integrin-targeting polymersomal docetaxel as an advanced nanotherapeutic for nonsmall cell lung cancer treatment. *ACS Appl. Mater. Interfaces* **2020**, *12*, 14905–14913. [CrossRef] [PubMed]
103. Meyer, C.E.; Liu, J.; Craciun, I.; Wu, D.; Wang, H.; Xie, M.; Fussenegger, M.; Palivan, C.G. Segregated nanocompartments containing therapeutic enzymes and imaging compounds within dna-zipped polymersome clusters for advanced nanotheranostic platform. *Small* **2020**, *16*, 1906492. [CrossRef] [PubMed]
104. Chen, H.; Jia, H.; Tham, H.P.; Qu, Q.; Xing, P.; Zhao, J.; Phua, S.Z.; Chen, G.; Zhao, Y. Theranostic prodrug vesicles for imaging guided codelivery of camptothecin and sirna in synergetic cancer therapy. *ACS Appl. Mater. Interfaces* **2017**, *9*, 23536–23543. [CrossRef] [PubMed]
105. Egli, S.; Schlaad, H.; Bruns, N.; Meier, W. Functionalization of block copolymer vesicle surfaces. *Polymers* **2011**, *3*, 252–280. [CrossRef]
106. van Dongen, S.F.; Nallani, M.; Cornelissen, J.J.; Nolte, R.J.; van Hest, J.C. A three-enzyme cascade reaction through positional assembly of enzymes in a polymersome nanoreactor. *Chem. Eur. J.* **2009**, *15*, 1107–1114. [CrossRef]

107. Deng, Z.; Qian, Y.; Yu, Y.; Liu, G.; Hu, J.; Zhang, G.; Liu, S. Engineering intracellular delivery nanocarriers and nanoreactors from oxidation-responsive polymersomes via synchronized bilayer cross-linking and permeabilizing inside live cells. *J. Am. Chem. Soc.* **2016**, *138*, 10452–10466. [CrossRef]
108. Anajafi, T.; Yu, J.; Sedigh, A.; Haldar, M.K.; Muhonen, W.W.; Oberlander, S.; Wasness, H.; Froberg, J.; Molla, M.S.; Katti, K.S.; et al. Nuclear localizing peptide-conjugated, redox-sensitive polymersomes for delivering curcumin and doxorubicin to pancreatic cancer microtumors. *Mol. Pharm.* **2017**, *14*, 1916–1928. [CrossRef]
109. Scheerstra, J.; Wauters, A.; Tel, J.; Abdelmohsen, L.; van Hest, J. Polymersomes as a potential platform for cancer immunotherapy. *Mater. Today Adv.* **2022**, *13*, 100203. [CrossRef]
110. Fujita, S.; Motoda, Y.; Kigawa, T.; Tsuchiya, K.; Numata, K. Peptide-based polyion complex vesicles that deliver enzymes into intact plants to provide antibiotic resistance without genetic modification. *Biomacromolecules* **2021**, *22*, 1080–1090. [CrossRef]
111. Gunkel-Grabole, G.; Palivan, C.; Meier, W. Nanostructured surfaces through immobilization of self-assembled polymer architectures using thiol–ene chemistry. *Macromol. Mater. Eng.* **2017**, *302*, 1600363. [CrossRef]
112. Rigo, S.; Gunkel-Grabole, G.; Meier, W.; Palivan, C.G. Surfaces with dual functionality through specific coimmobilization of self-assembled polymeric nanostructures. *Langmuir* **2019**, *35*, 4557–4565. [CrossRef] [PubMed]
113. Simon-Gracia, L.; Hunt, H.; Scodeller, P.D.; Gaitzsch, J.; Braun, G.B.; Willmore, A.-M.; Ruoslahti, E.; Battaglia, G.; Teesalu, T. Paclitaxel-loaded polymersomes for enhanced intraperitoneal chemotherapy. *Mol. Cancer Ther.* **2016**, *15*, 670–679. [CrossRef] [PubMed]
114. Leong, J.; Teo, J.Y.; Aakalu, V.K.; Yang, Y.Y.; Kong, H. Engineering polymersomes for diagnostics and therapy. *Adv. Healthc. Mater.* **2018**, *7*, 1701276. [CrossRef] [PubMed]
115. Moreno, S.; Boye, S.; Ajeilat, H.G.; Michen, S.; Tietze, S.; Voit, B.; Lederer, A.; Temme, A.; Appelhans, D. Multivalent protein-loaded pH-stable polymersomes: First step toward protein targeted therapeutics. *Macromol. Biosci.* **2021**, *21*, 2100102. [CrossRef]
116. Egli, S.; Nussbaumer, M.G.; Balasubramanian, V.; Chami, M.; Bruns, N.; Palivan, C.; Meier, W. Biocompatible functionalization of polymersome surfaces: A new approach to surface immobilization and cell targeting using polymersomes. *J. Am. Chem. Soc.* **2011**, *133*, 4476–4483. [CrossRef]
117. Rijpkema, S.J.; Langens, S.G.; van der Kolk, M.R.; Gavriel, K.; Toebes, B.J.; Wilson, D.A. Modular approach to the functionalization of polymersomes. *Biomacromolecules* **2020**, *21*, 1853–1864. [CrossRef]
118. Moulahoum, H.; Ghorbanizamani, F.; Zihnioglu, F.; Timur, S. Surface biomodification of liposomes and polymersomes for efficient targeted drug delivery. *Bioconjug. Chem.* **2021**, *32*, 1491–1502. [CrossRef]
119. Craciun, I.; Denes, A.S.; Gunkel-Grabole, G.; Belluati, A.; Palivan, C.G. Surfaces decorated with polymeric nanocompartments for pH reporting. *Helv. Chim. Acta* **2018**, *101*, e1700290. [CrossRef]
120. Liu, J.; Craciun, I.; Belluati, A.; Wu, D.; Sieber, S.; Einfalt, T.; Witzigmann, D.; Chami, M.; Huwyler, J.; Palivan, C.G. DNA-directed arrangement of soft synthetic compartments and their behavior in vitro and in vivo. *Nanoscale* **2020**, *12*, 9786–9799. [CrossRef]
121. Chandrawati, R. Layer-by-layer engineered polymer capsules for therapeutic delivery. In *Biomaterials for Tissue Engineering: Methods and Protocols*; Chawla, K., Ed.; Methods in Molecular Biology; Springer: New York, NY, USA, 2018; pp. 73–84. ISBN 978-1-4939-7741-3.
122. Kawamura, W.; Miura, Y.; Kokuryo, D.; Toh, K.; Yamada, N.; Nomoto, T.; Matsumoto, Y.; Sueyoshi, D.; Liu, X.; Aoki, I.; et al. Density-tunable conjugation of cyclic rgd ligands with polyion complex vesicles for the neovascular imaging of orthotopic glioblastomas. *Sci. Technol. Adv. Mater.* **2015**, *16*, 035004. [CrossRef] [PubMed]
123. Hammer, D.A.; Robbins, G.P.; Haun, J.B.; Lin, J.J.; Qi, W.; Smith, L.A.; Peter Ghoroghchian, P.; Therien, M.J.; Bates, F.S. Leuko-polymersomes. *Faraday Discuss.* **2008**, *139*, 129. [CrossRef] [PubMed]
124. Di Leone, S.; Vallapurackal, J.; Yorulmaz Avsar, S.; Kyropoulou, M.; Ward, T.R.; Palivan, C.G.; Meier, W. Expanding the potential of the solvent-assisted method to create bio-interfaces from amphiphilic block copolymers. *Biomacromolecules* **2021**, *22*, 3005–3016. [CrossRef] [PubMed]
125. Liu, J.; Postupalenko, V.; Lörcher, S.; Wu, D.; Chami, M.; Meier, W.; Palivan, C.G. DNA-mediated self-organization of polymeric nanocompartments leads to interconnected artificial organelles. *Nano Lett.* **2016**, *16*, 7128–7136. [CrossRef]
126. Deng, N.-N.; Yelleswarapu, M.; Zheng, L.; Huck, W.T. Microfluidic assembly of monodisperse vesosomes as artificial cell models. *J. Am. Chem. Soc.* **2017**, *139*, 587–590. [CrossRef]
127. Rasoulianboroujeni, M.; Kupgan, G.; Moghadam, F.; Tahriri, M.; Boughdachi, A.; Khoshkenar, P.; Ambrose, J.J.; Kiaie, N.; Vashae, D.; Ramsey, J.D.; et al. Development of a DNA-liposome complex for gene delivery applications. *Mater. Sci. Eng. C* **2017**, *75*, 191–197. [CrossRef]
128. Luo, Q.; Shi, Z.; Zhang, Y.; Chen, X.-J.; Han, S.-Y.; Baumgart, T.; Chenoweth, D.M.; Park, S.-J. DNA island formation on binary block copolymer vesicles. *J. Am. Chem. Soc.* **2016**, *138*, 10157–10162. [CrossRef]
129. Meyer, C.E.; Schoenenberger, C.-A.; Liu, J.; Craciun, I.; Palivan, C.G. DNA-tethered polymersome clusters as nanotheranostic platform. *CHIMIA* **2021**, *75*, 296. [CrossRef]
130. Arun, Y.; Ghosh, R.; Domb, A.J. Biodegradable hydrophobic injectable polymers for drug delivery and regenerative medicine. *Adv. Funct. Mater.* **2021**, *31*, 2010284. [CrossRef]
131. Yorulmaz Avsar, S.; Kyropoulou, M.; Di Leone, S.; Schoenenberger, C.-A.; Meier, W.P.; Palivan, C.G. Biomolecules turn self-assembling amphiphilic block co-polymer platforms into biomimetic interfaces. *Front. Chem.* **2019**, *6*, 645. [CrossRef]

132. De Leo, V.; Milano, F.; Agostiano, A.; Catucci, L. Recent advancements in polymer/liposome assembly for drug delivery: From surface modifications to hybrid vesicles. *Polymers* **2021**, *13*, 1027. [CrossRef]
133. Rideau, E.; Dimova, R.; Schwille, P.; Wurm, F.R.; Landfester, K. Liposomes and polymersomes: A comparative review towards cell mimicking. *Chem. Soc. Rev.* **2018**, *47*, 8572–8610. [CrossRef] [PubMed]
134. Itel, F.; Najer, A.; Palivan, C.G.; Meier, W. Dynamics of membrane proteins within synthetic polymer membranes with large hydrophobic mismatch. *Nano Lett.* **2015**, *15*, 3871–3878. [CrossRef] [PubMed]
135. Lomora, M.; Itel, F.; Dinu, I.A.; Palivan, C.G. Selective ion-permeable membranes by insertion of biopores into polymersomes. *Phys. Chem. Chem. Phys.* **2015**, *17*, 15538–15546. [CrossRef] [PubMed]
136. Garni, M.; Thamboo, S.; Schoenenberger, C.-A.; Palivan, C.G. Biopores/membrane proteins in synthetic polymer membranes. *Biochim. Biophys. Acta BBA Biomembr.* **2017**, *1859*, 619–638. [CrossRef]
137. Draghici, C.; Kowal, J.; Darjan, A.; Meier, W.; Palivan, C.G. “Active surfaces” formed by immobilization of enzymes on solid-supported polymer membranes. *Langmuir* **2014**, *30*, 11660–11669. [CrossRef]
138. Einfalt, T.; Witzigmann, D.; Edlinger, C.; Sieber, S.; Goers, R.; Najer, A.; Spulber, M.; Onaca-Fischer, O.; Huwyler, J.; Palivan, C.G. Biomimetic artificial organelles with in vitro and in vivo activity triggered by reduction in microenvironment. *Nat. Commun.* **2018**, *9*, 1127. [CrossRef]
139. Edlinger, C.; Einfalt, T.; Spulber, M.; Car, A.; Meier, W.; Palivan, C.G. Biomimetic strategy to reversibly trigger functionality of catalytic nanocompartments by the insertion of PH-responsive biovalves. *Nano Lett.* **2017**, *17*, 5790–5798. [CrossRef]
140. Sun, X.; Liu, C.; Liu, D.; Li, P.; Zhang, N. Novel biomimetic vectors with endosomal-escape agent enhancing gene transfection efficiency. *Int. J. Pharm.* **2012**, *425*, 62–72. [CrossRef]
141. Rehman, Z.U.; Hoekstra, D.; Zuhorn, I.S. Mechanism of polyplex- and lipoplex-mediated delivery of nucleic acids: Real-time visualization of transient membrane destabilization without endosomal lysis. *ACS Nano* **2013**, *7*, 3767–3777. [CrossRef]
142. Wong, A.S.; Mann, S.K.; Czuba, E.; Sahut, A.; Liu, H.; Suekama, T.C.; Bickerton, T.; Johnston, A.P.; Such, G.K. Self-assembling dual component nanoparticles with endosomal escape capability. *Soft Matter* **2015**, *11*, 2993–3002. [CrossRef] [PubMed]
143. Gaur, D.; Dubey, N.C.; Tripathi, B.P. Biocatalytic self-assembled synthetic vesicles and coacervates: From single compartment to artificial cells. *Adv. Colloid Interface Sci.* **2022**, *299*, 102566. [CrossRef] [PubMed]
144. Belluati, A.; Mikhalevich, V.; Yorulmaz Avsar, S.; Daubian, D.; Craciun, I.; Chami, M.; Meier, W.P.; Palivan, C.G. How do the properties of amphiphilic polymer membranes influence the functional insertion of peptide pores? *Biomacromolecules* **2020**, *21*, 701–715. [CrossRef] [PubMed]
145. Xing, X.; Ma, W.; Zhao, X.; Wang, J.; Yao, L.; Jiang, X.; Wu, Z. Interaction between surface charge-modified gold nanoparticles and phospholipid membranes. *Langmuir* **2018**, *34*, 12583–12589. [CrossRef] [PubMed]
146. Fröhlich, E. The role of surface charge in cellular uptake and cytotoxicity of medical nanoparticles. *Int. J. Nanomed.* **2012**, 5577. [CrossRef] [PubMed]
147. Hasan, N.; Cao, J.; Lee, J.; Hlaing, S.P.; Oshi, M.A.; Naeem, M.; Ki, M.-H.; Lee, B.L.; Jung, Y.; Yoo, J.-W. Bacteria-targeted clindamycin loaded polymeric nanoparticles: Effect of surface charge on nanoparticle adhesion to MRSA, antibacterial activity, and wound healing. *Pharmaceutics* **2019**, *11*, 236. [CrossRef]
148. Jeon, S.; Clavadetscher, J.; Lee, D.-K.; Chankeshwara, S.; Bradley, M.; Cho, W.-S. Surface charge-dependent cellular uptake of polystyrene nanoparticles. *Nanomaterials* **2018**, *8*, 1028. [CrossRef]
149. Du, X.-J.; Wang, J.-L.; Iqbal, S.; Li, H.-J.; Cao, Z.-T.; Wang, Y.-C.; Du, J.-Z.; Wang, J. The effect of surface charge on oral absorption of polymeric nanoparticles. *Biomater. Sci.* **2018**, *6*, 642–650. [CrossRef]
150. Kohli, A.K.; Alpar, H.O. Potential use of nanoparticles for transcutaneous vaccine delivery: Effect of particle size and charge. *Int. J. Pharm.* **2004**, *275*, 13–17. [CrossRef]
151. El Badawy, A.M.; Silva, R.G.; Morris, B.; Scheckel, K.G.; Suidan, M.T.; Tolaymat, T.M. Surface charge-dependent toxicity of silver nanoparticles. *Environ. Sci. Technol.* **2011**, *45*, 283–287. [CrossRef]
152. Deprey, K.; Becker, L.; Kritzer, J.; Plückthun, A. Trapped! A critical evaluation of methods for measuring total cellular uptake versus cytosolic localization. *Bioconjug. Chem.* **2019**, *30*, 1006–1027. [CrossRef]
153. Sharma, A.R.; Kundu, S.K.; Nam, J.-S.; Sharma, G.; Priya Doss, C.G.; Lee, S.-S.; Chakraborty, C. Next generation delivery system for proteins and genes of therapeutic purpose: Why and how? *BioMed Res. Int.* **2014**, *2014*, e327950. [CrossRef] [PubMed]
154. Kleineberg, C.; Wölfer, C.; Abbasnia, A.; Pischel, D.; Bednarz, C.; Ivanov, I.; Heitkamp, T.; Börsch, M.; Sundmacher, K.; Vidaković-Koch, T. Light-driven ATP regeneration in diblock/grafted hybrid vesicles. *ChemBioChem* **2020**, *21*, 2149–2160. [CrossRef]
155. Khan, S.; Li, M.; Muench, S.P.; Jeuken, L.J.C.; Beales, P.A. Durable proteo-hybrid vesicles for the extended functional lifetime of membrane proteins in bionanotechnology. *Chem. Commun.* **2016**, *52*, 11020–11023. [CrossRef] [PubMed]
156. Otrin, L.; Witkowska, A.; Marušič, N.; Zhao, Z.; Lira, R.B.; Kyrilis, F.L.; Hamdi, F.; Ivanov, I.; Lipowsky, R.; Kastiritis, P.L.; et al. En route to dynamic life processes by SNARE-mediated fusion of polymer and hybrid membranes. *Nat. Commun.* **2021**, *12*, 4972. [CrossRef] [PubMed]
157. Artificial Melanogenesis by Confining Melanin/Polydopamine Production inside Polymersomes-Meyer-2021-Macromolecular Bioscience-Wiley Online Library. Available online: <https://onlinelibrary.wiley.com/doi/full/10.1002/mabi.202100249> (accessed on 27 April 2022).

158. de Freitas, C.F.; Calori, I.R.; da Silva, A.C.P.; de Castro, L.V.; Sato, F.; Pellosi, D.S.; Tessaro, A.L.; Caetano, W.; Hioka, N. PEG-coated vesicles from pluronic/lipid mixtures for the carrying of photoactive erythrosine derivatives. *Colloids Surf. B Biointerfaces* **2019**, *175*, 530–544. [CrossRef]
159. Belluati, A.; Craciun, I.; Palivan, C.G. Bioactive catalytic nanocompartments integrated into cell physiology and their amplification of a native signaling cascade. *ACS Nano* **2020**, *14*, 12101–12112. [CrossRef]
160. Catalytic Polymersomes to Produce Strong and Long-Lasting Bioluminescence—Nanoscale (RSC Publishing). Available online: <https://pubs.rsc.org/en/content/articlelanding/2021/NR/D0NR07178A#divAbstract> (accessed on 27 April 2022).
161. Korpidou, M.; Maffei, V.; Dinu, I.A.; Schoenenberger, C.-A.; Meier, W.P.; Palivan, C.G. Inverting glucuronidation of hymecromone in situ by catalytic nanocompartments. *J. Mater. Chem. B* **2022**. [CrossRef]
162. Langowska, K.; Palivan, C.G.; Meier, W. Polymer nanoreactors shown to produce and release antibiotics locally. *Chem. Commun.* **2012**, *49*, 128–130. [CrossRef]
163. Meyer, C.E.; Schoenenberger, C.-A.; Wehr, R.P.; Wu, D.; Palivan, C.G. Artificial melanogenesis by confining melanin/polydopamine production inside polymersomes. *Macromol. Biosci.* **2021**, *21*, 2100249. [CrossRef]
164. Wang, X.; Zhong, X.; Li, J.; Liu, Z.; Cheng, L. Inorganic nanomaterials with rapid clearance for biomedical applications. *Chem. Soc. Rev.* **2021**, *50*, 8669–8742. [CrossRef] [PubMed]
165. Gong, F.; Yang, N.; Wang, X.; Zhao, Q.; Chen, Q.; Liu, Z.; Cheng, L. Tumor microenvironment-responsive intelligent nanoplatforams for cancer theranostics. *Nano Today* **2020**, *32*, 100851. [CrossRef]
166. Cheng, P.; Pu, K. Molecular imaging and disease theranostics with renal-clearable optical agents. *Nat. Rev. Mater.* **2021**, *6*, 1095–1113. [CrossRef]
167. Imaging Upconverting Polymersomes in Cancer Cells: Biocompatible Antioxidants Brighten Triplet–Triplet Annihilation Upconversion—Askes-2016-Small-Wiley Online Library. Available online: <https://onlinelibrary.wiley.com/doi/10.1002/sml.201601708> (accessed on 31 March 2022).
168. Askes, S.H.; Bossert, N.; Busmann, J.; Talens, V.S.; Meijer, M.S.; Kieleyka, R.E.; Kros, A.; Bonnet, S.; Heinrich, D. Dynamics of dual-fluorescent polymersomes with durable integrity in living cancer cells and zebrafish embryos. *Biomaterials* **2018**, *168*, 54–63. [CrossRef]
169. Camblin, M.; Detampel, P.; Kettiger, H.; Wu, D.; Balasubramanian, V.; Huwyler, J. Polymersomes containing quantum dots for cellular imaging. *Int. J. Nanomed.* **2014**, *9*, 2287–2298. [CrossRef]
170. Iodine-Rich Polymersomes Enable Versatile SPECT/CT Imaging and Potent Radioisotope Therapy for Tumor in Vivo. ACS Applied Materials & Interfaces. Available online: <https://pubs.acs.org/doi/10.1021/acsami.9b04294> (accessed on 31 March 2022).
171. Lu, L.; Wang, Y.; Zhang, F.; Chen, M.; Lin, B.; Duan, X.; Cao, M.; Zheng, C.; Mao, J.; Shuai, X.; et al. MRI-Visible SiRNA nanomedicine directing neuronal differentiation of neural stem cells in stroke. *Adv. Funct. Mater.* **2018**, *28*, 1706769. [CrossRef]
172. Meeuwissen, S.A.; Kim, K.T.; Chen, Y.; Pochan, D.J.; van Hest, J.C.M. Controlled shape transformation of polymersome stomatocytes. *Angew. Chem. Int. Ed.* **2011**, *50*, 7070–7073. [CrossRef]
173. de Martino, M.T.; Tonin, F.; Bloemendal, V.R.; Hanefeld, U.; Rutjes, F.P.; van Hest, J.C. Compartmentalized cross-linked enzyme nano aggregates (c-CLEnAs) toward pharmaceutical transformations. *RSC Adv.* **2021**, *11*, 21857–21861. [CrossRef]
174. Abdelmohsen, L.K.; Nijemeisland, M.; Pawar, G.M.; Janssen, G.-J.; Nolte, R.J.; van Hest, J.C.; Wilson, D.A. Dynamic loading and unloading of proteins in polymeric stomatocytes: Formation of an enzyme-loaded supramolecular nanomotor. *ACS Nano* **2016**, *10*, 2652–2660. [CrossRef]
175. Peng, F.; Tu, Y.; Wilson, D.A. Micro/nanomotors towards in vivo application: Cell, tissue and biofluid. *Chem. Soc. Rev.* **2017**, *46*, 5289–5310. [CrossRef]
176. Lee, K.Y.; Park, S.-J.; Lee, K.A.; Kim, S.-H.; Kim, H.; Meroz, Y.; Mahadevan, L.; Jung, K.-H.; Ahn, T.K.; Parker, K.K.; et al. Photosynthetic artificial organelles sustain and control ATP-dependent reactions in a protocellular system. *Nat. Biotechnol.* **2018**, *36*, 530–535. [CrossRef] [PubMed]
177. Xu, Y.; Fei, J.; Li, G.; Yuan, T.; Li, J. Compartmentalized assembly of motor protein reconstituted on protocell membrane toward highly efficient photophosphorylation. *ACS Nano* **2017**, *11*, 10175–10183. [CrossRef] [PubMed]
178. Zhang, Y.; Zhang, X.; Kong, W.; Wang, S. Reconstitution of Caveolin-1 into artificial lipid membrane: Characterization by transmission electron microscopy and solid-state nuclear magnetic resonance. *Molecules* **2021**, *26*, 6201. [CrossRef] [PubMed]
179. Li, G.; Fei, J.; Xu, Y.; Hong, J.-D.; Li, J. Proton-consumed nanoarchitectures toward sustainable and efficient photophosphorylation. *J. Colloid Interface Sci.* **2019**, *535*, 325–330. [CrossRef] [PubMed]
180. Li, S.; Wang, X.; Mu, W.; Han, X. Chemical signal communication between two protoorganelles in a lipid-based artificial cell. *Anal. Chem.* **2019**, *91*, 6859–6864. [CrossRef]
181. Simons, K.; Sampaio, J.L. Membrane organization and lipid rafts. *Cold Spring Harb. Perspect. Biol.* **2011**, *3*, a004697. [CrossRef]
182. Devaux, P.F. Static and dynamic lipid asymmetry in cell membranes. *Biochemistry* **1991**, *30*, 1163–1173. [CrossRef]
183. Rothman, J.E.; Lenard, J. Membrane asymmetry. *Science* **1977**, *195*, 743–753. [CrossRef]
184. Arriaga, L.R.; Huang, Y.; Kim, S.H.; Aragones, J.L.; Ziblat, R.; Koehler, S.A.; Weitz, D.A. Single-step assembly of asymmetric vesicles. *Lab. Chip* **2019**, *19*, 749–756. [CrossRef]
185. Kamiya, K.; Kawano, R.; Osaki, T.; Akiyoshi, K.; Takeuchi, S. Cell-sized asymmetric lipid vesicles facilitate the investigation of asymmetric membranes. *Nat. Chem.* **2016**, *8*, 881–889. [CrossRef]

186. Lu, L.; Schertzer, J.W.; Chiarot, P.R. Continuous microfluidic fabrication of synthetic asymmetric vesicles. *Lab. Chip* **2015**, *15*, 3591–3599. [CrossRef] [PubMed]
187. Heberle, F.A.; Feigenson, G.W. Phase Separation in lipid membranes. *Cold Spring Harb. Perspect. Biol.* **2011**, *3*, a004630. [CrossRef] [PubMed]
188. Vega-Cabrera, L.A.; Pardo-López, L. Membrane remodeling and organization: Elements common to prokaryotes and eukaryotes. *IUBMB Life* **2017**, *69*, 55–62. [CrossRef]
189. van Meer, G.; Voelker, D.R.; Feigenson, G.W. Membrane lipids: Where they are and how they behave. *Nat. Rev. Mol. Cell Biol.* **2008**, *9*, 112–124. [CrossRef] [PubMed]
190. McConnell, H.M.; Kornberg, R.D. Inside-outside transitions of phospholipids in vesicle membranes. *Biochemistry* **1971**, *10*, 1111–1120. [CrossRef] [PubMed]
191. Bai, J.; Pagano, R.E. Measurement of spontaneous transfer and transbilayer movement of BODIPY-labeled lipids in lipid vesicles. *Biochemistry* **1997**, *36*, 8840–8848. [CrossRef] [PubMed]
192. Chen, A.H.; Silver, P.A. Designing biological compartmentalization. *Trends Cell Biol.* **2012**, *22*, 662–670. [CrossRef]
193. von Ballmoos, C.; Wiedenmann, A.; Dimroth, P. Essentials for ATP synthesis by F₁F₀ ATP synthases. *Annu. Rev. Biochem.* **2009**, *78*, 649–672. [CrossRef]
194. Itel, F.; Chami, M.; Najer, A.; Lörcher, S.; Wu, D.; Dinu, I.A.; Meier, W. Molecular organization and dynamics in polymersome membranes: A lateral diffusion study. *Macromolecules* **2014**, *47*, 7588–7596. [CrossRef]
195. Heuberger, L.; Palivan, C. Block copolymer giant unilamellar vesicles for high-throughput screening. *CHIMIA* **2022**, *76*, 350. [CrossRef]

Review

Green Synthesis of Carbon Nanoparticles (CNPs) from Biomass for Biomedical Applications

Muhammad Qasim ¹, Andrew N. Clarkson ^{1,*} and Simon F. R. Hinkley ^{2,*}¹ Department of Anatomy, Brain Health Research Centre and Brain Research New Zealand, University of Otago, Dunedin 9054, New Zealand² Ferrier Research Institute, Victoria University of Wellington, Wellington 5012, New Zealand

* Correspondence: andrew.clarkson@otago.ac.nz (A.N.C.); simon.hinkley@vuw.ac.nz (S.F.R.H.); Tel.: +64-3-279-7326 (A.N.C.); +64-4-463-0052 (S.F.R.H)

Abstract: In this review, we summarize recent work on the “green synthesis” of carbon nanoparticles (CNPs) and their application with a focus on biomedical applications. Recent developments in the green synthesis of carbon nanoparticles, from renewable precursors and their application for environmental, energy-storage and medicinal applications are discussed. CNPs, especially carbon nanotubes (CNTs), carbon quantum dots (CQDs) and graphene, have demonstrated utility as high-density energy storage media, environmental remediation materials and in biomedical applications. Conventional fabrication of CNPs can entail the use of toxic catalysts; therefore, we discuss low-toxicity manufacturing as well as sustainable and environmentally friendly methodology with a focus on utilizing readily available biomass as the precursor for generating CNPs.

Keywords: green synthesis; carbon nanomaterials; biomass; sustainability; biomedical



Citation: Qasim, M.; Clarkson, A.N.; Hinkley, S.F.R. Green Synthesis of Carbon Nanoparticles (CNPs) from Biomass for Biomedical Applications. *Int. J. Mol. Sci.* **2023**, *24*, 1023. <https://doi.org/10.3390/ijms24021023>

Academic Editors: Monica Terracciano, Ilaria Rea, Nicola Borbone and Chiara Tramontano

Received: 13 October 2022
Revised: 19 December 2022
Accepted: 21 December 2022
Published: 5 January 2023



Copyright: © 2023 by the authors. Licensee MDPI, Basel, Switzerland. This article is an open access article distributed under the terms and conditions of the Creative Commons Attribution (CC BY) license (<https://creativecommons.org/licenses/by/4.0/>).

1. Introduction

Carbon nanoparticles (CNPs) have demonstrated utility in a wide range of biological applications such as imaging, sensing and surface-coating. They enjoy a growing range of applications in the drug delivery of a number of biomolecules such as DNA, antibodies, and proteins. CNPs are considered the ideal candidates for metal-based sensor applications and rapid diagnostic assays due, in the main part, to their high fluorescence value. As such, they can displace gold, colored latex, silica, quantum dots, or phosphor nanoparticles, in relevant applications (Figure 1) [1–5].

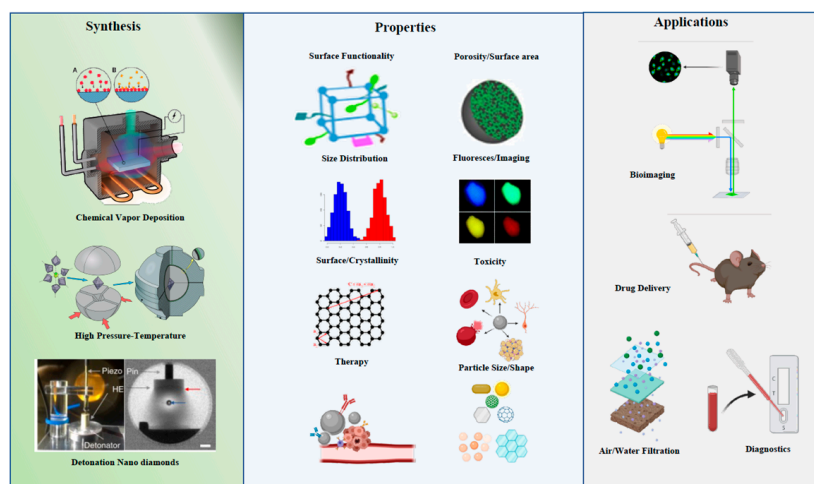


Figure 1. Synthesis, properties and applications of carbon nanoparticles.

CNPs have a range of highly desirable attributes; they exhibit low toxicity, high biocompatibility, can be readily suspended into solution [6] and can be modified post-production with a range of chemical functionality. Carbon based materials already play a critical role in many applications: electro-catalysts, electrodes in storage devices, biofuels, heterogenous catalysis and photo catalysis [7]. Carbonaceous materials form the basis of gas storage (e.g., CO₂), hydrogen capture, water purification and as additives to rectify soil properties [2]. The field of optical sensing has been extended with the discovery of highly fluorescent CNPs and carbon nanodots (CNDs) [8,9]. CNP and CND probes demonstrate remarkable properties; emission characteristics that are tunable based on particle size, high emission quantum yields, physical and chemical stability, narrow spectral bands and optimization of the surface to effect selective sensing applications [10]. Other than optical sensing, these CNPs have also seen use in applications such as photocatalysis, bioimaging and optoelectronics [11–13]. A typical example of optical sensing is the light-emitting properties of semiconductor quantum dots (QDs) used for in vitro and in vivo bioimaging [14–16] (Figure 2). QD's strong optical absorption peaks are very sensitive to the surrounding environment and medium, which enables biomolecule calorimetry to be completed [17,18]. Another significant advantage of CNPs is that they can be produced economically with high purity and are readily fabricated from naturally occurring biomass and generated utilizing green chemistry [19].

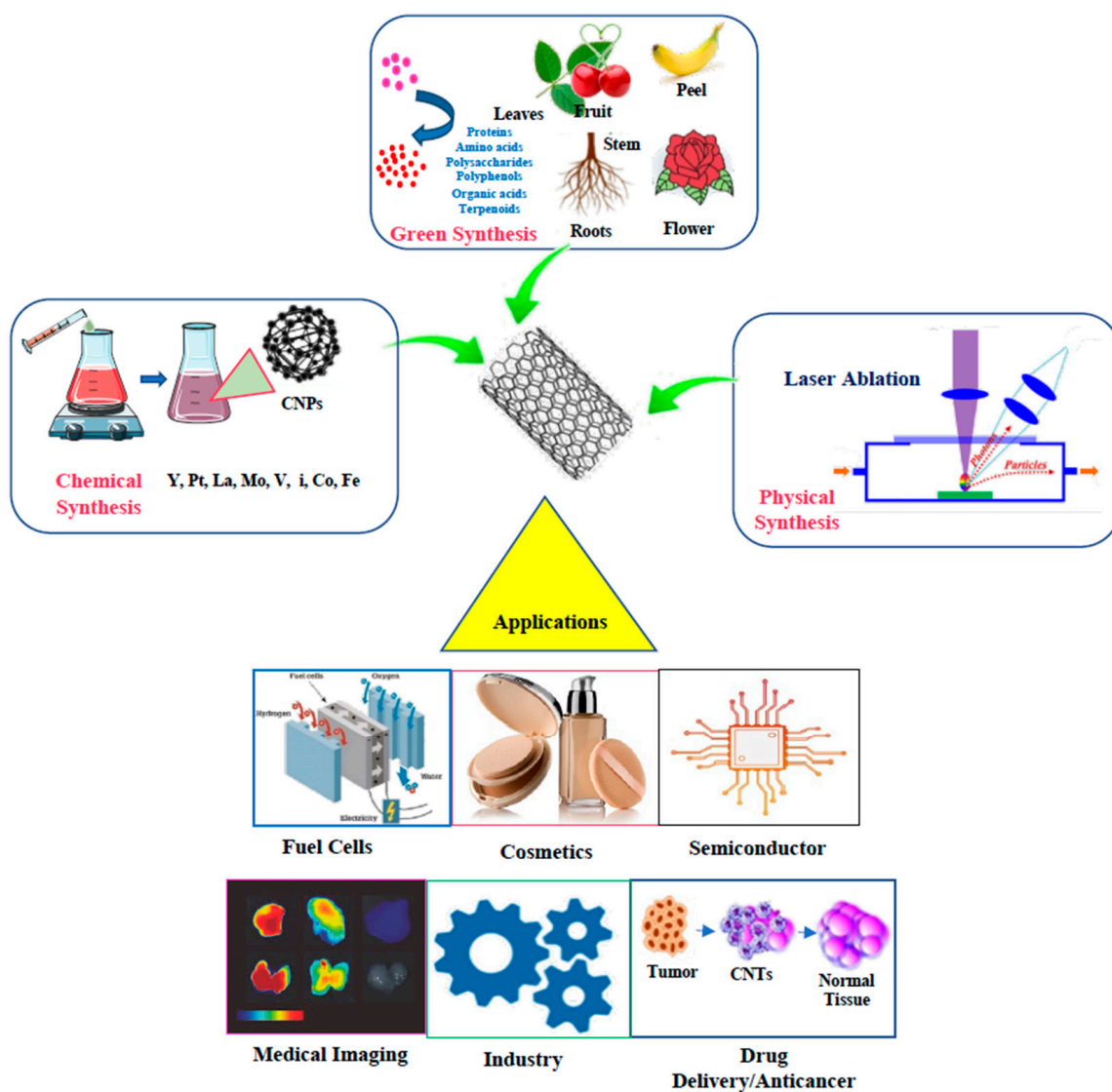


Figure 2. Types of syntheses of CNPs and example applications.

Since the pioneering studies by Sumio Iijima in 1991 with the characterization of carbon nanotubes, CNPs have been used in a number of applications. The impact of CNPs has been recognized internationally with researchers receiving the highest of scientific awards [20]. More recently, due to their adoption in the fields of medical, environmental and novel materials, industry has paved the way for the rapid development of various CNPs, such as carbon nanotubes (CNTs), QDs, graphene and nano diamonds (NDs). Based on the lattice arrangement of the main building unit carbon, CNPs are classified as either one-dimensional (1D), two-dimensional (2D) or three-dimensional (3D) structures. For instance, CNTs are 1D, graphene is 2D and NDs have a 3D structure [21,22]. Among these CNPs, CNTs are the hardest materials due to their extended aromatic C-C bond network. The arrangement of these single C-C network layers may be classified further into either single-wall carbon nanotubes (SWCNTs) or multiwall carbon nanotubes (MWCNTs) [23,24]. This C-C bond network gives a honeycomb-like arrangement. SWCNTs and MWCNTs have inter-layer distances of 0.32–0.35 nm and 2 to 50 sheets are found arranged in the tubules. This gives rise to a wide range of wall thicknesses [25]. In the case of graphene, discovered recently in single-layer form as reported by Novoselov [26], a hexagonal arrangement is generated through an extended sp^2 hybridized network.

Production of CNPs may be achieved through chemical vapor deposition (CVD), arc discharge vaporization, floating catalytic methods, laser ablation/evaporation and low temperature solid pyrolysis (Figure 2) [27–30]. However, accepted methods for the synthesis of CNPs have environmental concerns such as the high consumption of raw materials and the use of strong acids. In addition, CNP containing materials produced using these methods exhibits a limited capacity for the loading of metals oxides or post-generation modification of the particle surface [31,32]. Therefore, the focus of CN production has moved towards establishing methods that are less demanding of resources, low-cost and eco-friendly [33].

In a green-synthesis approach, biomass such as woods, leaves and low-value biomaterials, such as plant husks, have been used as the precursor for developing carbon materials. In this review we consider that a green-synthesis attribute permits inclusion. For example, a renewable feedstock, process attribute or combination therein. In some cases, green synthesis through biomass as the starting material can also replace the metal catalysts used in CNP fabrication. Based on the reaction conditions and precursor materials, different forms of CNPs such as nanofibers, nanotubes or nanoporous configurations can be generated. For instance, allotropic forms of graphitic carbon nanostructures, with a coil morphology, were fabricated by a precipitation method at 900 °C via the hydrothermal treatment of cellulose [34]. In addition, carbon nanosheets can be fabricated from lignocellulosic biomass derived from coconut coir through the action of hydrothermal carbonization followed by pyrolysis [35]. The effect of clay mineral particles has also been evaluated [36,37]. Similarly, cellulose (husk) has been used to develop carbon hollow nanostructures via a three step acid digestion process, followed by charring and high temperature pyrolysis (CO₂ laser 2200 °C) [38]. Many other types of food and agricultural waste such as proteins, chitin, lignin, carbohydrates, hemicellulose, and honeycomb have been used in the fabrication of CNPs using a green synthesis approach [19,39,40].

Herein, we describe the methods used for generating CNPs from renewable precursors and highlight some examples of their application in the environmental, energy-storage and medicinal fields.

2. Processing of Biomass

Biomass waste can be derived from either plant or animal matter as a result of processing higher-value materials, for instance leaves from trees as by product from processed wood or paper production [41]. Biomass is abundant: trees, agriculture crops, energy crops, fruits, vegetation, wood, aquatic plants and algae, general municipal waste and animal waste [7,42]. In general, such biomass materials are subjected to various processing methods to obtain energy and carbon allotropes. Two broad classifications may be made:

biochemical processing (e.g., anaerobic digestion and fermentation) and thermochemical processing (e.g., pyrolysis, combustion and gasification) [43].

The process of pyrolysis can be a highly efficient energy recovery process and has the potential to produce products ranging from char, to gas and oil [44]. Char as a by-product of energy recovery processes can act as a source for various carbon materials such as activated carbon, porous carbon and CNPs such as CNTs, graphene and fullerenes, all of which can be generated through controlled green synthesis processes [45–48]. These CNPs can be functionalized further and their surface texture and functionality modified by using different surface treatment agents and activation methods [49,50]. Final products find a wide range of applications such as environmental sensors, water purification, hydrogen capture and storage, energy conversion and air pollution control [50,51]. Generally, to obtain CNPs from the by-product of biomass processing three types of treatments are used: physical activation, chemical activation and hydrothermal carbonization (HTC) [20,52].

Physical activation is a two-step process; raw materials are subjected to pyrolysis and carbonization at a temperature below 1000 K, and in second step, subjected to controlled gasification process at high temperatures above 1150 K, in the presence of oxidizing gases (CO_2 , air, steam or a mixture of these) [53]. With steam or CO_2 as an activation gas, equipment is easy to clean, and the removal of the oxidant is straightforward. Various biomasses such as rice straw, peanut, rice husk, corn hulls, corncob, coconut shells, pecan shell and almond shells have all been used to developed CNPs using this physical activation method [54–58].

With chemical activation, a well-established single step is undertaken where a precursor is mixed with a chemical activation agent (H_3PO_4 , ZnCl_2 , KOH , K_2CO_3 , etc.) and when heated to temperatures ranging from 700 K to 1200 K, carbonization and activation occur simultaneously [59–62]. The chemical activation process results in carbon materials with high porosity and surface area ($>2000 \text{ m}^2 \text{ g}^{-1}$), and larger pore sizes [41]. The chemical activation process has advantages compared to physical activation as it is faster, requires lower conversion temperatures, is higher in carbon yield and provides a more uniformly high-porosity material. Among chemical agents, KOH is favored and since 1978 active carbon produced from KOH treatment processes has generated material with uniform porosity and a high surface area (up to $3000 \text{ m}^2 \text{ g}^{-1}$) [63].

The process of hydrothermal carbonization (HTC) is inspired by natural processes in which biological materials undergo a long, natural chemical coaling process. The application of high pressure and heat converts biomass to peat or coal over thousands to millions of years in a natural phenomenon [40]. HTC is the direct chemical imitation of this natural process but occurring over a much shorter timeframe. This process was first reported by Bergius in 1913 and remodeled by Berl and Schmidt in 1932, which is the well-known methodology for converting cellulose to activated carbon, and is still in common use today [63]. Recently, this method was shown to produce carbon materials from biomass with much milder conditions using temperatures below 500 K, pure water and self-steam pressure [40,49]. This process is considered both physical and chemical processing and is desirable due to the comparatively low temperature, cost effectiveness and overall eco-friendly synthesis. Carbohydrates and their derivatives such as hydroxymethyl furfural, glucose, xylose, furfural, sucrose and starch have all been converted to carbonaceous materials with HTC using a temperature of only $180 \text{ }^\circ\text{C}$ [64]. HTC can generate porous materials directly from biomass but, as compared to the chemical process, a less porous and lower surface area product results [40,65]. Therefore, such carbon materials are not optimal for the applications of chemical or gas adsorption, or catalysis and energy storage. To improve the porosity of carbon materials from HTC, different templates (e.g., SPA-15) or additives (and therefore more chemical-process aligned methods) such as KOH are used [66,67].

3. Carbon Nanotubes (CNTs)

CNTs were discovered in 1990 by Iijima and research into their potential has blossomed in the field of nanotechnology [68]. The unique chemical, optical, physical, thermal conductivity and electrical properties make these particles ideal for sensors, transistors, fuel cells, field emission devices and logic circuits [69–78]. CNTs and fullerenes are carbon forms that are characterized by their hollow structure. The cylindrical form is known as a nanotube, while spherical fullerenes are known as bucky balls [79,80]. The single-walled carbon nanotubes (SWCNTs) are types of CNTs that are developed by rolling single sheets of graphene into seamless cylinders [81]. Multiwalled graphene sheets are called multiwall carbon nanotubes (MWCNTs) and were discovered by the Russian scientists Radushkevich and Lukyanovich in 1951 [82], preceding SWCNTs by decades [68,83].

3.1. Biomedical Applications of CNTs

CNTs possess unique characteristics which make them an ideal candidate for various applications in biomedicine. CNTs are hydrophobic and therefore are suitable for various therapeutic and diagnostic biological applications [84]. In addition, CNTs have a high drug loading capacity, large surface area, high mechanical strength, and adequate chemical stability, which has made CNTs ideal candidates for both therapeutic and diagnostic applications, including being excellent nanocarriers for drug delivery [85]. For instance, CNTs have been shown to interact with receptors present on the cell surface that can result in greater cell loading of drugs and therefore, a reduction in the dose of a drug required to achieve an effect [86].

To date, CNTs have been utilized in a wide variety of drug delivery systems for the treatment of numerous diseases. For instance, substances such as acetylcholine, that does not cross the blood-brain-barrier, can be delivered readily to the brain using CNTs [87]. In addition, because CNTs interact with brain cells they are becoming recognized as being ideal for developing efficient gene and drug delivery systems [88]. In support of this, cell delivery of nucleic acids has become one of the prime functions for the use of CNTs [89]. In addition, groups have also used CNTs (as graphene nanosheets) to deliver angiogenic genes specific for tissue engineering and regenerative medicine to promote revascularization and cardiac repair [90]. Whilst the biological applications for CNTs are vast, much work is needed to validate their use in order to take them into the clinic.

3.2. Synthesis of CNTs

Other than the natural production of CNTs, as discussed earlier, there are many synthetic ways to develop CNTs such as electrolytic methodologies, arc discharge vaporization, laser ablation/evaporation, low temperature solid pyrolysis, chemical vapor deposition (CVD), the floating catalyst methods, and the ion bombardment growth method [27–30]. All these processes generate CNTs in moderate yield with unique morphology [91]. Some of these methods, such as CVD, laser ablation and arc discharge require an atmosphere of inert gas (such as He, N₂, or CF₄) to allow condensation of the nanoparticles to form in the cooler parts of the chamber and to minimize the chances of over-oxidation at high temperature [92].

In order to produce a large quantity of CNTs, CVD of carbon placed in a fluidized reactor at 15–150 kg/h is used [93,94]. This multidimensional process controls CNT agglomerate formation, provides delicate catalyst control at the atomic level, and keeps large scale production of CNTs at a macroscopic level [93]. The structure of CNTs can be modulated by the choice of the catalyst that acts at the atomic scale—this is one of the most important factors when producing large quantities. Generally, transition metals such as Y, Pt, La, Mo, V, Ni, Co, and Fe are used as a catalyst in the synthesis of CNT [95]. Metal is preloaded into a catalyst carrier (mostly alumina) by a process of impregnation, co-precipitation and also other processes which are common in the petrochemical industry. The calcination reduction method used for metal particle activation during or before CVD treatment gives

rise to catalytically active nanoparticles that show dual functionality as a time activator for carbon and as a template for the formation of the CNP product [96].

Metal catalysts have a significant disadvantage in that any entrained catalyst in the production of CNTs pose a significant health threat, particularly if the product destination is for *in vivo* medical applications [97]. Metal catalyst particle residue in CNTs has resulted in misalignment of plant chromosomes during the metaphase resulting in cell division arrest [98]. In the textile industry, metal residue was not readily removed by water treatment [99]. Nanoparticulate metal catalyst can inhibit fluorescent attributes of CNTs and so are not suitable for preparing materials for semiconductor based devices as their presence reduced quantum efficiency and detector life [100,101]. During the process of CVD using high temperature, metal particles vaporize and re-condense to the surface of CNTs, intimately coating the CNT surface to block their lattice vibration, and ultimately disrupting the lattice wave propagation [100].

In addition to the aforementioned conventional synthesis methods for CNTs, another important factor is cost: instrumentation, extreme temperature (700–1200 °C) and metal catalysts all contribute to CVD manufacturing economics [102,103]. Therefore, development of non-metallic, cost-effective catalysts, ideally functional and using lower temperatures, will enable better production and commercialization of CNTs to meet the obvious demands in medical, agriculture, textile and electronic fields [104].

3.3. Green Synthesis of CNTs

In order to simplify the preparation, and improve the quality and quantity of CNPs, new CVD preparation processes have been developed, which include radio-frequency enhanced CVD, plasma-enhanced (PECVD) and microwave-enhanced methodology [105,106]. In addition, spray pyrolysis has emerged as an alternative process for commercial production of CNTs [107] and is attractive due to the much reduced complexity in processing, the use of low-cost instruments, and it does not require high vacuum or the application of reducing agents. It is also highly amenable to scaled-up commercial production. In combination with a renewable biomass starting material this is a highly attractive methodology. For instance, the addition of wood sawdust in spray pyrolysis resulted in CNPs of good quality and quantity producing both carbon fibers and nanotubes [108]. Hydrogen was produced as a by-product alongside a small amount of toxic gases (NO₂, CO). Significantly, a low temperature of 750 °C (as compared to CVD to develop CNT/CE that uses a temperature of 1200 °C), resulted in the production of CNPs with a diameter of 50 nm [109].

The use of oils in spray pyrolysis has been shown to produce both MWCNT and SWCNTs. For instance, neem oil pyrolysis was used to develop uniformly aligned MWCNTs [110], whereas eucalyptus and turpentine oils produced SWCNTs with a thickness of 0.79–1.71 nm [108,111]. CNTs produced from turpentine oil developed within 60 min at 700 °C, with the size shorter than eucalyptus oil derived materials, while the turpentine oil based CNTs demonstrated a good degree of graphitization and exhibited finely resolved concentric shells. Furthermore, CNTs produced from turpentine oil contained less defects and had a notably higher current density capability and field emission strength [112]. In a similar manner, a castor oil–ferrocene mixture in an ammonia solution generated nitrogen-containing CNTs through spray pyrolysis [113] that resulted in CNTs with a distinctive bamboo shape and a wavy tube-like structure of 50–80 nm thickness.

3.4. Synthesis of CNTs from Natural Precursors

The structure and morphology of CNTs can be regulated by controlling the reaction gas, temperature, catalyst and precursors during their synthesis. Due to the high demand for CNTs worldwide [114], specifically for cancer treatment with graphene NT and medical imaging it is desirable to find eco-friendly precursors for commercial production. Biomass derived natural materials such as camphor powder, palm oil, neem oil, eucalyptus and palm tree provide alternatives to fossil-fuel based precursors such as xylene, acetylene,

methane or toluene, etc. [115]. The use of these natural precursors can produce large quantities of CNTs and through the application of appropriate processes may also be generated cost effectively [116].

The elemental analysis of edible oils has shown that they are a viable source for CNTs where the oils solids comprise 73.8% to 77.2% carbon [106]. In a recent report, coconut milk has been used as a precursor for CNP production through a simple and one step process using thermal pyrolysis at 120–150 °C. Particles were produced in only 2–5 min, without the use of any passivating or carbonizing agent [19]. In this process, carbon rich residues are separated from coconut oil by pyrolysis and when dissolved in water, exhibit blue fluorescence under UV light. A similar process was used to develop CNTs from olive oil as carbon precursor and NiCl₂ as the catalyst at 900 °C [105]. The resultant CNTs were SWCNTs with uniform surface morphology and diameters of ~27–31 nm [105]. In another study, SWCNTs were produced from vegetable oil as the carbon precursor with CNTs being produced having a diameter of 0.79–1.71 nm [117]. The MWCNTs with an aligned macrostructure of nanotubes were developed when vegetable oil was premixed with ferrocene.

A crystalline latex that was extracted from *Cinnamomum camphora* (camphor C₁₀H₁₆O) has been used as the carbon precursor for large-scale production of CNTs [118,119]. Plants of *C. camphora* are very common in the sub-tropical region including Japan, India, China and Indonesia. Thermal decomposition of camphor at 875 °C under argon produced a variety of nanotube that contained a mix of aligned CNTs, as well as multiwall and single wall CNTs [39]. The CNTs that are well aligned vertically are called vertically aligned CNTs (VACNTs) and are 1D carbon objects that are anchored atop of a solid substrate. These VACNTs are geometrically fixed compared to their counterparts, randomly oriented carbon nanotubes (CNTs). With camphor, a minute amount of catalyst was required and no amorphous carbon was produced, meaning no post deposition heat-process was required as is required in thermal decomposition methods [118]. Similar to vegetable oil, chicken fat mixed with ferrocene can be used as the precursor for CNT production [120]. Suriani et al., showed that VACNTs can be generated from chicken fat by using a ferrocene catalyst and deposition of carbon particles onto a silicon wafer substrate [107]. VACNTs demonstrate a highly crystalline structure with a D- Raman peak and G- Raman peak ratio (ID/IG) of 0.63 and in 88.2% purity with a very low amount of amorphous carbon content [107]. Coconut oil has been used as a carbon precursor for developing MWCNTs by using the CVD process [121]. Nitrogen gas was used as the carrier for evaporating the precursor and provided an inert environment. The MWCNTs so produced have a diameter of 80–90 nm (under optimum conditions). Finally, castor oil has also been used for the production of CNTs through spray pyrolysis with argon as the evaporated precursor carrier and with heating to 850 °C [121].

3.5. Biomass as the Green Catalyst for CNT Synthesis

Development of green catalyst assisted CNTs' has obvious advantages. Utilizing the biomass as both the carbon source and catalyst doubly so [103] and can provide metal impurity-free CNTs. Natural green catalysts are available in abundance at negligible cost and have been shown to operate at significantly reduced temperature. There is no requirement of costly equipment such as evaporative sputtering or controlled dip coating when green catalysts are used. Because of the ease of production and non-toxic nature of a green catalyst, there is no requirement for a clean room to optimize CNTs' growth [104].

CNT production does require a catalyst or a substrate to act as a template [122]. Biomass derivatives can act as that catalyst in CNT fabrication. Iron containing active carbon (AC) is a type of biomass-derivative that can be used as a catalyst in the synthesis of CNTs. Chen et al., demonstrated that wheat straw (AC-W), palm kernel shell (AC-P) and coconut (AC-C) contain iron as an impurity that catalyzes CNT production. If this biomass is pre-reduced with H₂, the catalyst embedded in AC can be activated [123]. Further, graphitization determines the quality of CNPs if carbon is used. When biomass is used as a

carbon precursor, or source of catalyst, or as a catalyst support, then there is a significant saving in time and energy [124]. Botanically derived volatile hydrocarbons are a rich source of carbon and can act as carbon precursors as compared to conventional gaseous precursors [118]. Camphor has been extracted from the latex of the *Cinnamomum camphora* tree and exploited to develop MWCNTs and SWCNTs produced over quartz, zeolite and silicon substrates [118,125,126]. Camphor is less toxic, cost effective and a readily available biomass. Sublimating at around 25 °C it is therefore an ideal candidate for CVD methods in the production of CNPs. When a zeolite catalyst support was impregnated with Fe–Co at atmospheric pressure and temperature of 650 °C, MWCNTs are produced in large quantity and with high purity (88%) from a pure camphor precursor, which made this process suitable for large-scale synthesis [118].

Similarly, walnut (*Juglans regia*), neem (*Azadirachta indica*), garden grass (*Cynodon dactylon*) and rose (*Rosa*) plant extracts have also been used in the production of CNTs, as they act both as source of carbon and as a catalyst due to the presence of active carbon (Figure 3) [104].

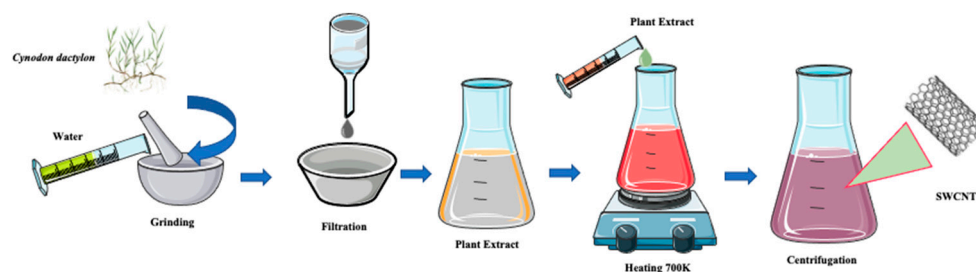


Figure 3. Green synthesis of SWCNTs from garden grass (*Cynodon dactylon*) by the CVD process.

The CNTs produced from walnut extract through the CVD process (at 575 °C) are of high quality and good yield when compared to other plant extracts that have been used. Interestingly, when the temperature was raised to 800 °C an increase in another allotrope was observed; carbon nano belts (CNBs) were detected. Their presence was confirmed using scanning electron microscopy, IR and Raman characterization [104].

Rice husk (RH) has been used as a carbon precursor as well as the source of catalyst in the production of CNTs under microwave treatment [127,128]. Rice husks are rich in lignin and cellulose, therefore they are an ideal carbon precursor [127]. The introduction of ferrocene enhanced the RH decomposition in the microwave oven induced plasma. It was observed that during this process, ferrocene was converted to non-toxic iron II, III oxide [127]. A major advantage of this green synthesis methodology of CNPs is that either non-toxic metals are produced, or no additional metals are required to be added as catalysts. This method has also been adopted for hybrid synthesis of CNT using polyaniline (PANI), forming CNT/PANI. The nickel electrodes used in the catalytic process are coated by this CNT composite material through surface modulation. This composite material is fabricated by polymerization of aniline in the presence of MWCNT-COOH in a solvent consisting of water and green solvent. The green solvent used is a mixture of ionic liquids (methyimidazolium tetrafluoroborate, [BMIM] BF₄) and mineral acids such as HCl or HNO₃. This reaction, which results in CNTs covering the surface of aniline, results in a product that is often used in electronic applications such as chemical sensors [129].

The form and function of CNPs synthesized using a green catalyst methodology is predicated by the composition of the biomass used and processing steps. For example, carbon microspheres (4–6 µm in diameter) were produced when waste cooking oil was used as the starting substrate [130]. Replacing the cooking oil with engine oil generated 4µm spherical CNPs. This difference in size was attributed to engine oils pure hydrocarbon nature, compared to waste cooking oil that is fatty acid derived where stearic palmitic linoleic and oleic acids dominate [131]. Fatty acid decomposition produces more gasses

due to the presence of oxygen, which can help in the production of filamentous structures of semi-graphics [132].

Oils are a naturally rich source of fatty acids and in turn carbon, which is used in the production of CNTs. For instance, palm oil from cooking waste has been used for the production of SWCNTs and MWCNTs via the floating-catalyst thermal CVD method [133]. Importantly, the impurities found in these oil wastes do not affect this CNT fabrication process [134].

Over the past 30 years, green chemistry has been a significant focus in the chemical industry, and the use and/or replacement of undesirable solvents one of the central themes. For example, traditional solvents have been substituted by greener solvents as new dispersants for CNT [135], e.g., room-temperature ionic liquids (RTILs). This is because RTILs do not evaporate and therefore are still present at the end of the CNT formation process. With the undesirable catalyst residue dissolved in the solvent the CNT may be recovered through centrifugation or filtration. Recently, deep eutectic solvents (DESs) have been recognized as a new type of low cost RTIL [136]. When RTILs and DESs are combined to form a porogen, they enhance the solubility of DESs, which influence the RTILs' supra molecular assembly. This may be an advantage for CNT-filled molecularly imprinted powder (MIP) preparations. A CNT-MIP composite was prepared by using RTILs and DESs' as a binary green porogen system. The RTILs [BMIM] BF₄ was chosen to stabilize a nanotube dispersion from re-aggregation [137].

4. Carbon Quantum Dots (CQDs)

Carbon quantum dots (CQDs) are one of the most important allotropes among CNPs [10]. QDs are usually just a few nanometers in size (1–5 nm) and display a myriad of desirable attributes: high photo stability, high luminescent, broad absorption spectra, low toxicity even compared to other nano-carbon forms, high quantum yield, long fluorescent life, ready surface functionalization with biological molecules, chemical inertness, biocompatibility and high emission tenability [138,139]. With such functionality, CQDs garner interest in applications from energy storage, photocatalytic activity, biosensing, drug delivery, bio-imaging, light emitting diodes, through to their use as fluorescent probes [10,138–148]. In addition, CQDs have been shown to have wide utility in nanomedicine and biomedical applications [143,148]. CQDs are semiconductor nanocrystals (2–100 nm) and impart unique electrical and optical properties. Due to their single step synthesis, and the above-mentioned qualities as well as water miscible nature, CQDs present as an alternative to traditional fluorescent dyes and inorganic semiconductors. Many environmental, physical and biosensing devices use CQDs and can be used to substitute metal based QDs.

4.1. Biomedical Applications of CQDs

The treatment of many disease conditions requires both spatial and temporal precision for drug delivery. Carbon QDs have the potential here to be superior in that they offer a dual function, that is, they are nanocarriers for specific bioactive compounds in addition they can be used for simultaneous bioimaging. One example is the use of carbon QDs conjugated with doxorubicin which revealed targeted drug release into tumor cells. Further, the fluorescence property of these carbon QDs allowed for image-guided drug delivery [149]. Whilst the update and use of carbon QDs in biological applications has been slow, based on the recently demonstrated utility for targeted drug delivery, there is hope that this will encourage others to use carbon QDs more in biological applications in the future.

4.2. Green Synthesis of CQDs

Biomass has been applied as the carbon precursor, catalyst or catalyst carrier to generate CQDs [19]. Fluorescent CQDs were synthesized by green chemical methods utilizing a wide range of natural resources, for example: pomegranate extract, D-glucose and an aqueous extract from beetroot [150,151]. A cost-effective and environmentally attractive white light emitting material for use in chemical sensing and biomedical applications was prepared through the hydrothermal treatment of pomelo peel [152]. Synthesis of carbon

dots has been carried out using naturally available carbohydrates such as glucose, sucrose, citric acid, pomelo peel, and willow bark [151–153]. The optical, physical and chemical properties of CNPs are affected by the molecular precursors employed, the specific methodology used, and the pre- and post-treatments carried out.

In another study, a by-product of coconut milk pyrolysis was used for the development of CQDs. Coconut milk is composed of a high proportion of saturated fat (lauric acid comprises ~50% of this oil) which is converted to coconut oil by thermal pyrolysis [154]. A black residue formed during thermal pyrolysis is, in general, discarded, but can be a source of CQDs through further pyrolysis that does not involve any surface passivating (coating to make the materials produced less active) or use of an acidic reagent, with the CQDs being able to be readily dispersed in water. A simple shift in pH and temperature can be used to develop blue wave length emitting CQDs to detect Fe^{3+} ions from coconut milk [154]. Similarly, leaf extracts of neem (*Azadirachta indica*) have been used to develop CQDs by a one-pot hydrothermal treatment [138]. This process was particularly eco-friendly and low cost with the resultant CQDs expressing a high fluorescent quantum yield (up to 27.2%) [155]. These CQDs were used for biosensing, displaying a peroxidase-like-mimetic activity upon oxidation of peroxidase substrate 3,3',5,5'-tetramethylbenzidine (TMB), when in contact with hydrogen peroxide (H_2O_2) (Figure 4).

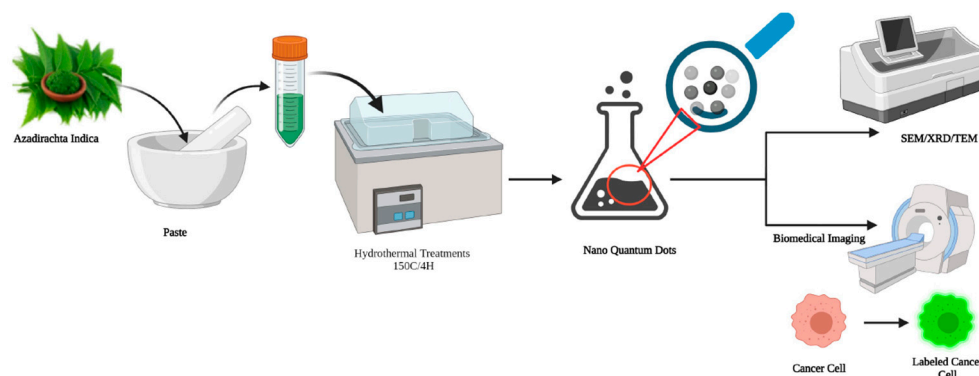


Figure 4. One-pot hydrothermal based green synthesis of nano-CQDs.

This H_2O_2 sensitive TMB oxidation property could be exploited for colorimetric detection of H_2O_2 . In support of this, the amount of ascorbic acid (AA) in solution has been detected by TMB colour change, [155,156] and the assay evaluated using different levels of ascorbic acid from fruits. This low cost and eco-friendly assay based on CQDs set a benchmark for detection of AA in real and complex biological samples. This finds utility with AA a naturally occurring reducing agent, which is highly water soluble and has demonstrated roles in a wide range of human ailments: cancer, Parkinson’s disease, cardiovascular disease, scurvy, mental illness, infertility as well as the common cold [157]. In a similar fashion, Luo et al. reported a CQD system for detecting AA in fruit [156]; the leaves of neem were processed in a one-pot hydrothermal method, devoid of any chemical reagent for passivation, resulting in CQDs uniform in size and of a high fluorescent value. This study demonstrated a cost effective and eco-friendly conversion of neem leaf to CQDs.

Similarly, sweet potato peels, cinnamon, red chili, black paper and turmeric were subjected to hydrothermal treatment to produce aqueous fluorescent CQDs with sizes ranging from 3.14 to 4.32 nm [158]. The dose-dependent toxicity (0.1 mg/mL–0.5 mg/mL) was evaluated and the toxicity recorded was dependent on the starting material. Citric acid derived CQDs showed less toxicity as compared to red chili derived CQDs. This difference was attributed to the surface functionality. A similar fluorescent CQD was developed from *Tamarindus indica* leaves by hydrothermal treatment, displaying a quantum yield of 46.6% and were used for Hg^{2+} sensing in the range from 0.01 to 0.1 mM, applicable for biomedical applications [159]. In addition to these studies, edible *Eleocharis dulcis* plant extract underwent hydrothermal treatment to generate water soluble N/P co-doped CQDs

(at 90–150 °C) and were utilized in a Fe^{3+} sensor that found utility in an anticounterfeiting application [160].

Ultrasound treatment has been used in the synthesis of CQDs. Lamellar CQDs from commercial graphite were produced in a top-down process using ultrasonication (30 min) where *Opuntia ficus indica* extract was used as the catalyst [161,162]. When the same graphite precursor was stirred at low-temperature (50 °C) and for a brief 30 min ultrasonic treatment, small (5–7 nm) CQDs were produced [145]. Another study utilized lemon peel waste developing water-soluble photoluminescent CQDs (size 1–3 nm, quantum yield 14%) with a hydrothermal process that was used for detecting Cr^{6+} (limit 73 nM) (Figure 5). These CQDs were a TiO_2 composite and demonstrated the photolytic degradation of methylene blue dye where the catalytic activity was enhanced 2.5 times as compared to TiO_2 alone. This was attributed to a better charge separation at the interface of the composite. Further, sweet potatoes have also been used as the carbon precursor, resulting in the formation of CQDs with a size of 2.0 ± 0.6 nm and quantum yield of 8.9%. The CQDs formed, when coated with (3-aminopropyl) triethoxysilane, provided an environmentally friendly sensing material for detection of oxytetracycline to concentrations as low as 15.3 ng/mL [163].

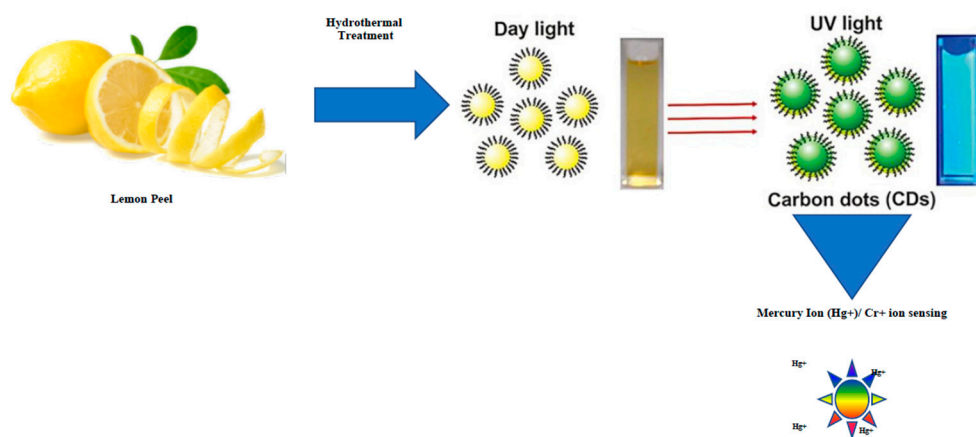


Figure 5. Schematic for the generation of water-soluble CQDs by hydrothermal treatment of lemon peel waste and their application in $\text{Hg}^{2+}/\text{Cr}^{3+}$ sensing.

5. Nano-Diamonds (NDs)

Nano-diamonds (NDs) are a new addition to the nanocarbon family, recognizable by a nanosized tetrahedral arrangement of carbon atoms. NDs were discovered accidentally when in 1963, modification of carbon through shock compression in a blast chamber generated this allotrope [164]. The detonation process is used for industrial scale production of NDs, where an inert gas or water (ice) filled enclosed chamber is used, which undergoes an explosive pressure change. Based on the gas or liquid coolant it is either a dry or wet synthesis process. This pressure blast process results in a mixture of soot, which consist of 4–5 nm sized diamond particles and other carbo allotropes and impurities [165]. NDs produced as a result of the detonation process exhibit oxygen containing function groups on their surface such as -OH and -COOH. Such chemistry can be used for further functionalization to enhance biological, physical and chemical properties in order to extend their industrial applications [166,167].

The NDs core is made of a sp^3 hybridized lattice arrangement with a disordered carbon grouping including sp^2 hybridization at the surface [168]. Their characteristic Raman spectrum [169] and low toxicity made them a useful agent for medical diagnostic applications. The diamond core contains lattice defects, which generates fluorescence-emitting colour centers [170]. These colour centers can vary to an extent that the emission covers almost the entire visible spectrum. The centers can be excited with almost any excitation wavelength; the fluorescence emitted is stable and the characteristic of photobleaching is limited. Moreover, the defect centers can be enhanced with high-energy beam treatment

followed by thermal annealing [171]. This conveys significant advantage as compared with the molecular dyes that are commonly used in biological imaging. Therefore, the defect-originated colour centers of NDs (after careful optimization) provide an ideal bioimaging tool as an alternative to molecular dyes [172].

The term ND reflects a broad range of diamond-based materials ranging from nanoscale single diamond crystals to a bulk cluster of diamonds [167,173]. There are different classifications of NDs such as nanocrystalline diamond (NCD) and ultra nanocrystalline diamond (UNCD), which is specific to the morphology generated during the crystal growth process. NCD consist of facets less than 100 nm in size, while UNCD describe materials with a particle size of less than 10 nm [174]. NDs are found naturally in interstellar dust, protoplanetary nebulae, meteorites, diamond films and in residues of detonation processes. It has been confirmed that NDs are present in primitive chondrites at a concentration of 1500 ppm along with isotopically anomalous noble gases, hydrogen, nitrogen and other elements. This confirms that natural ND were synthesized before the Sun's formation and outside of our solar system [175]. NDs, due to their unique optical, thermal, mechanical and electrical properties have a wide range of applications in physical, mechanical and biological systems. In particular, their optical transparency in the form of a diamond thin film, and a high energy band gap in their activation state, make them an ideal candidate for semiconductor applications [176]. In recent studies, various aspects of NDs have been highlighted, such as their role in NCD film fabrication from hydrogen rich and hydrogen deficient plasma, field emission properties, modifying the mechanical behavior of NCD films, chemical and bio functionalization of diamond nanowires, as well as their use for the study of non-covalent interactions [177–179].

5.1. Biomedical Applications of NDs

NDs have high biocompatibility, and are superior to other CNPs such as CNTs, carbon black or fullerenes, hence they have received significant attention for their use in biomedical applications [180]. NDs high size to surface ratio and easy functionalization with biological molecules give them an edge for both in vitro and in vivo biomedical applications such as drug delivery, single cell imaging, biosensing and protein purification. NDs can emit a specific wavelength of photoluminescence (red or green) when a specific functional molecule is embedded in their crystal lattice [181]. Therefore, they are used as enterosorbents or solid phase carriers in conjugated and non-conjugated form for small and middle size biological molecules such as drugs, proteins (lysozyme) and vaccines [182]. ND use as a probe has been reported by Cheng et al. for the detection of growth hormone receptors in single cancer cell [183]. The growth hormone molecules were covalently linked to carboxylated NDs (100 nm), which were recognized by the A549 cells growth hormone receptors. Similarly, NDs produced through a detonation process were conjugated with bovine insulin applying a physical adsorption process in aqueous solution. This material regulated sodium hydroxide adsorption based on pH. When the pH was alkaline, NDs conjugated with a vaccine at a 4:1 ratio and showed $31.3 \pm 1.6\%$ adsorption, while at neutral pH demonstrated $79.8 \pm 4.3\%$ adsorption [184].

The biocompatibility of NDs during cell division and differentiation in a single cell was assessed by Liu et al. who injected clusters of 100 nm size carboxylated NDs into cells, where cell imaging revealed that they remained in the intracellular environment for an extended time without causing cell damage [185]. It has been shown that NDs are nontoxic during cell division and differentiation thus can be used as a labelling method for tracking cell organelles in stem cells as well as cancer cells [186]. NDs used as fluorescent labels in cells demonstrate the high photostability of the colour emitted as compared to single dye molecules in photoluminescence experiments [186]. In another study, uptake of NDs in cancer and non-cancer cells such A549 human lung adenocarcinoma cells, HFL-1 fibroblast-like human fetal lung cells and Beas-2b non-tumorigenic human bronchial epithelial cells was studied and compared. It was found that in these cells, NDs uptake is mediated by

a clathrin-dependent endocytosis mechanism, with healthy cells showing higher uptake compared to cancer cells [187].

The use of NDs for single cell imaging was reported recently by Mi et al. who showed that when NDs are excited by alpha particles they quickly emit a stable and ultrabright emission [188]. Such types of fluorescent NDs enjoy application in biomedical imaging as biomarkers when functionalized with a nitrogen vacancy (NV) colour center [189], for example; femtomolar detection in immunoassays using magnetic modulation [190]. In addition, nanoscale quantum biosensors have also been used as magnetometers to measure magnetic fields and dipole moments [191–193]. Based on the data presented to date, NDs appear to be ideal agents for use as quantum biosensors, as they have good biocompatibility, are sustainable, show stable fluorescence and photostability, and have good coherence time of the NV centers [166]. Another unique trait of NDs modulated with NV centers is that they can release a far red fluorescence which is particularly useful as it differentiates from the auto fluorescent components of cells [194].

NDs use in cellular imaging is extensive, and this carbon allotrope sees additional applications as a drug formulation reagent. Aqueous solubility and membrane permeability have been classified as major factors that limit drug absorption [195]. For instance, sparingly soluble drugs were successfully formulated as demonstrated by Chen et al., where a ND cluster dispersed Purvalanol A and 4-hydroxytamoxifen in water [196]. Therefore, the enhanced aqueous solubility imparted by NDs can be used to generate optimized drug-concentrations in aqueous formulations (Figure 6). This reduces the necessity of complex formulation ingredients or production methods. In addition, the high solubility permits a tuned drug delivery where frequent low-doses (of a highly soluble ND associated drug) are more effective than infrequent high doses (of the poorly soluble drug-form) which is more effective and less likely to drive drug-resistance [197].

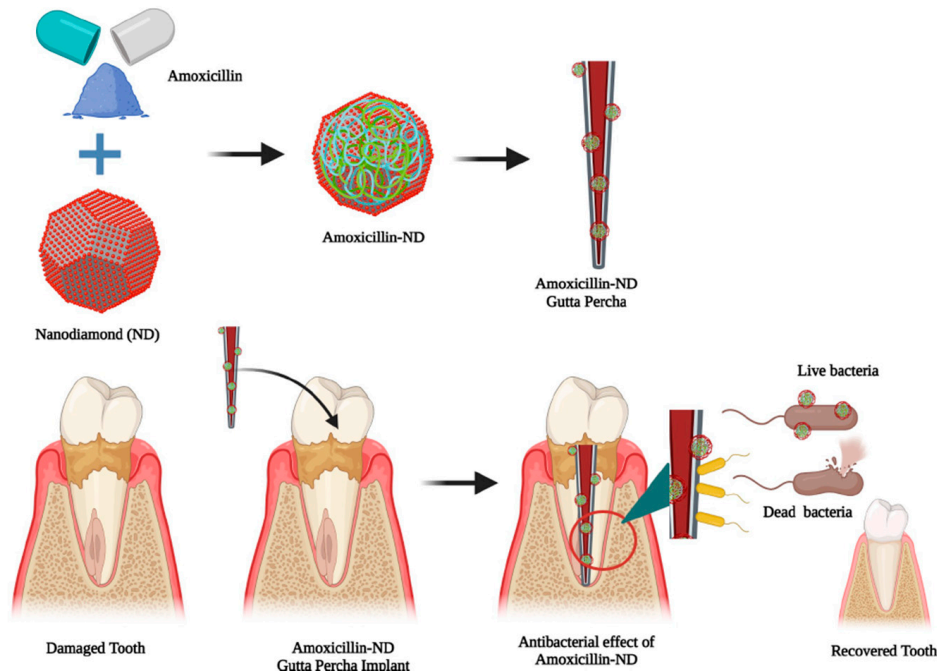


Figure 6. Nanodiamonds (NDs) used in the biological application of amoxicillin-ND aggregates imbedded in gutta-percha as a slow-release antibacterial agent.

Further, NDs have also been applied to catalyzed reactions, as oxygen reduction reactions are electrocatalysis by nitrogen-enriched carbon hybridized nanodiamonds (N-doped CND) [198].

5.2. Towards the Green Synthesis of NDs

There is a growing field of the biomedical applications of NDs [199] but their synthesis in a green-chemistry or green-precursor sense is very limited, notably being absent in reviews [200,201]—even of those focused on green-synthetic processes [202]. Simple and relatively environmentally friendly synthesis of ND's from coal in solution by laser ablation has been demonstrated, and while not a renewable resource this is a low-energy path to ND generation [203]. The green synthesis of carbon nanodiamonds by green synthesis presents an opportunity for future development.

6. Graphene

The graphene lattice has a honeycomb-like structure due to the sp^2 hybridized carbon-carbon network [79] and can be synthesized using both top-down and bottom-up methods. Mechanical and chemical approaches for the synthesis of graphene involve silicon carbide (SiC) for exfoliation of graphite [204], titanium carbide (TiC) [205], tantalum carbide (TaC), unzipping of CNTs [206–208], metals such as Co, Ni, Pt, Cu, Ir, Ru [209,210], solvothermal synthesis [211], chemical vapor deposition (CVD) and organic synthesis [212]. Further, graphene oxide (GO) reduction has also been used in the production of graphene [213]. For this reduction process, pre-reduced GO is preferred over non-reduced GO due to its high conductivity. In 1962, Boehm and colleagues were the first to reported low cost and large scale synthesis of graphene through the reduction in GO using hydrazine [212]. The production of graphene through chemical reduction in GO is well established; however, it remains hard to produce large panels of graphene through this process [213,214]. A major limitation is the incorporation of impurities, mainly not fully reduced oxide species, which results in poor electronic properties. Despite extensive advancements in materials sciences, this remains a big challenge to develop a cost-effective process for the high-quality production of graphene.

Green chemistry is paving a way to solve this challenge to some extent. Ruan and colleagues have reported the use of low cost carbon resources such as food, agriculture waste materials and insects, which has resulted in the production of high quality single layer graphene sheets directly from a copper foil surface when in the presence of argon, without using any purification steps [215]. Similarly, sugar (glucose) in the presence of ammonia solution as the reducing agent, reduced glucose oxide into graphene nano sheet [39]. Similarly, dextran as used by Kim et al. reduced GO for the production of graphene. Due to the biocompatible nature of dextran this process was highly eco-friendly [216]. Triethylamine or *Ginkgo biloba* extract are also reported as reducing and stabilizing agents for green chemical synthesis of graphene. Similarly, the amino acid glycine can also be used as a reducing agent to generate graphene oxide [217–219].

Molecular probes or biological molecules interact with GO dynamically allowing the investigation of special biological functions or responses as detected by changes to Raman scattering patterns and unique fluorescence observations [220]. Graphene nanomaterials were effective in the biosensing of genetic materials; e.g., single and double stranded DNA and RNA [221]. Their highly selective biosensing ability is attributed to a strong ionic interaction with positively charged nucleobase to negatively charged carboxyl groups on the GO surface, high electrochemical nature and fast π - π stacking between the nucleobases and honeycomb carbon structure. Using these properties the group of Rahighi fabricated reduced graphene nanowire (RGNW) as a biochip for detection of the four bases of DNA with the potential to detect at the remarkably low sub-femtomol level [222]. Similarly Zhang et al. functionalized GO with -COOH and with polyaniline (PANI) to fabricate two different type of GO such as GO-COOH and GO-PANI to detect DNA, also at very low concentrations (10^{-6} to 10^{-14} mol/L) [223]. Graphene nanoparticles have been adopted widely to the field of drug delivery and sustained release applications. Pei et al. delivered the well-studied oncology therapeutic doxorubicin to PEGylated nano graphene oxide (pGO) and showed its sustained delivery of the cytotoxin with a twofold increased anticancer effect [224].

7. Conclusions

High carbon content biomass can be used to synthesized CNPs through simple, green, low cost, and time efficient methods, often with minimal additional chemical or solvent components. Fruit waste is an excellent resource, readily available and requires no additional preconditioning. These biomasses may be manipulated further to produced varieties of CNPs according to their applications. CNPs such as CNTs (SWCNTs, MWCNTs), NDs and QDs have been used for delivery biomolecules (drugs, vaccine, mRNA, DNA, etc.), biosensing for diagnosis of cancer and other diseases, as antimicrobial agents (e.g., antibacterial, antifungal and antiviral) and as coating materials. They are also used as composite materials for 3D bioprinting and tissue engineering. These CNPs have wide ranging applications and significance yet there exists significant opportunity to enhance and simplify their production and purification processes to develop more efficient CNPs and CNPs based devices to improve human wellbeing.

Author Contributions: Conceptualization, M.Q. and A.N.C.; writing—original draft preparation, M.Q.; writing—review and editing, A.N.C. and S.F.R.H.; editing, revision, supervision, project administration and funding A.N.C. and S.F.R.H. All authors have read and agreed to the published version of the manuscript.

Funding: This research was supported by “Regenerative Therapies”, Ministry for Business, Innovation and Employment (NZ) grant number CONT-52128-ENDRP-RSCHTRUSTVIC.

Institutional Review Board Statement: Not applicable.

Informed Consent Statement: Not applicable.

Data Availability Statement: Not applicable.

Conflicts of Interest: The authors declare no conflict of interest.

References

- Liu, Z.; Robinson, J.T.; Tabakman, S.M.; Yang, K.; Dai, H. Carbon materials for drug delivery & cancer therapy. *Mater. Today* **2011**, *14*, 316–323. [CrossRef]
- Panwar, N.; Soehartono, A.M.; Chan, K.K.; Zeng, S.; Xu, G.; Qu, J.; Coquet, P.; Yong, K.-T.; Chen, X. Nanocarbons for Biology and Medicine: Sensing, Imaging, and Drug Delivery. *Chem. Rev.* **2019**, *119*, 9559–9656. [CrossRef] [PubMed]
- Sagbas, S.; Sahiner, N. Carbon dots: Preparation, properties, and application. In *Nanocarbon and Its Composites*; Khan, A., Jawaid, M., Mohamed Asiri, I., Mohamed Asiri, A., Eds.; Woodhead Publishing: Sawston, UK, 2018; pp. 651–676.
- Mendes, R.G.; Bachmatiuk, A.; Büchner, B.; Cuniberti, G.; Rummeli, M.H. Carbon nanostructures as multi-functional drug delivery platforms. *J. Mater. Chem. B* **2013**, *1*, 401–428. [CrossRef] [PubMed]
- Liu, Y.; Dong, X.; Chen, P. Biological and chemical sensors based on graphene materials. *Chem. Soc. Rev.* **2012**, *41*, 2283–2307. [CrossRef] [PubMed]
- Manzetti, S.; Gabriel, J.-C.P. Methods for dispersing carbon nanotubes for nanotechnology applications: Liquid nanocrystals, suspensions, polyelectrolytes, colloids and organization control. *Int. Nano Lett.* **2019**, *9*, 31–49. [CrossRef]
- Linares, N.; Silvestre-Albero, A.M.; Serrano, E.; Silvestre-Albero, J.; García-Martínez, J. Mesoporous materials for clean energy technologies. *Chem. Soc. Rev.* **2014**, *43*, 7681–7717. [CrossRef]
- Baker, S.N.; Baker, G.A. Luminescent Carbon Nanodots: Emergent Nanolights. *Angew. Chem. Int. Ed.* **2010**, *49*, 6726–6744. [CrossRef]
- Shen, J.; Zhu, Y.; Yang, X.; Li, C. Graphene quantum dots: Emergent nanolights for bioimaging, sensors, catalysis and photovoltaic devices. *Chem. Commun.* **2012**, *48*, 3686. [CrossRef]
- Li, H.; Kang, Z.; Liu, Y.; Lee, S.-T. Carbon nanodots: Synthesis, properties and applications. *J. Mater. Chem.* **2012**, *22*, 24230–24253. [CrossRef]
- Liu, L.; Li, Y.; Zhan, L.; Liu, Y.; Huang, C. One-step synthesis of fluorescent hydroxyls-coated carbon dots with hydrothermal reaction and its application to optical sensing of metal ions. *Sci. China Chem.* **2011**, *54*, 1342–1347. [CrossRef]
- Wee, S.S.; Ng, Y.H.; Ng, S.M. Synthesis of fluorescent carbon dots via simple acid hydrolysis of bovine serum albumin and its potential as sensitive sensing probe for lead (II) ions. *Talanta* **2013**, *116*, 71–76. [CrossRef] [PubMed]
- Wang, Y.X.Y.L.; Ming, Z. Research on seismic behavior and cost estimation of a new concrete filled steel tube frame structure. *Adv. Mat. Res.* **2011**, *335*, 1231–1234.
- Medintz, I.L.; Uyeda, H.T.; Goldman, E.R.; Mattoussi, H. Quantum dot bioconjugates for imaging, labelling and sensing. *Nat. Mater.* **2005**, *4*, 435–446. [CrossRef] [PubMed]
- Efros, A.L.; Nesbitt, D.J. Origin and control of blinking in quantum dots. *Nat. Nanotechnol.* **2016**, *11*, 661–671. [CrossRef]

16. Oh, E.; Liu, R.; Nel, A.; Gemill, K.B.; Bilal, M.; Cohen, Y.; Medintz, I.L. Meta-analysis of cellular toxicity for cadmium-containing quantum dots. *Nat. Nanotechnol.* **2016**, *11*, 479–486. [CrossRef] [PubMed]
17. Ali, M.R.K.; Wu, Y.; Ghosh, D.; Do, B.H.; Chen, K.; Dawson, M.R.; Fang, N.; Sulchek, T.A.; El-Sayed, M.A. Nuclear Membrane-Targeted Gold Nanoparticles Inhibit Cancer Cell Migration and Invasion. *ACS Nano* **2017**, *11*, 3716–3726. [CrossRef]
18. Chen, Y.; Xianyu, Y.; Jiang, X. Surface Modification of Gold Nanoparticles with Small Molecules for Biochemical Analysis. *Acc. Chem. Res.* **2017**, *50*, 310–319. [CrossRef]
19. Roshni, V.; Ottor, D. Synthesis of carbon nanoparticles using one step green approach and their application as mercuric ion sensor. *J. Lumin.* **2015**, *161*, 117–122. [CrossRef]
20. Shen, Y. Carbothermal synthesis of metal-functionalized nanostructures for energy and environmental applications. *J. Mater. Chem. A* **2015**, *3*, 13114–13188. [CrossRef]
21. Villarreal, C.C.; Pham, T.; Ramnani, P.; Mulchandani, A. Carbon allotropes as sensors for environmental monitoring. *Curr. Opin. Electrochem.* **2017**, *3*, 106–113. [CrossRef]
22. Bhattacharya, D.; Jana, D. Twin T-graphene: A new semiconducting 2D carbon allotrope. *Phys. Chem. Chem. Phys.* **2020**, *22*, 10286–10294. [CrossRef]
23. Baughman, R.H.; Zakhidov, A.A.; de Heer, W.A. Carbon Nanotubes—The Route toward Applications. *Science* **2002**, *297*, 787–792. [CrossRef]
24. Ni, Z.; Li, Q.; Yan, L.; Gong, J.; Zhu, D. Welding of multi-walled carbon nanotubes by ion beam irradiation. *Carbon* **2008**, *46*, 376–378. [CrossRef]
25. Anzar, N.; Hasan, R.; Tyagi, M.; Yadav, N.; Narang, J. Carbon nanotube—A review on Synthesis, Properties and plethora of applications in the field of biomedical science. *Sens. Int.* **2020**, *1*, 100003. [CrossRef]
26. Novoselov, K.S.; Geim, A.K.; Morozov, S.V.; Jiang, D.; Zhang, Y.; Dubonos, S.V.; Grigorieva, I.V.; Firsov, A.A. Electric field effect in atomically thin carbon films. *Science* **2004**, *306*, 666–669. [CrossRef] [PubMed]
27. Tan, G.; Mieno, T. Synthesis of single-walled carbon nanotubes by arc-vaporization under high gravity condition. *Thin Solid Films* **2010**, *518*, 3541–3545. [CrossRef]
28. Yang, F.; Wang, X.; Zhang, D.; Yang, J.; Luo, D.; Xu, Z.; Wei, J.; Wang, J.-Q.; Xu, Z.; Peng, F.; et al. Chirality-specific growth of single-walled carbon nanotubes on solid alloy catalysts. *Nature* **2014**, *510*, 522–524. [CrossRef] [PubMed]
29. Liu, J.; Lu, J.; Lin, X.; Tang, Y.; Liu, Y.; Wang, T.; Zhu, H. The electronic properties of chiral carbon nanotubes. *Comput. Mater. Sci.* **2017**, *129*, 290–294. [CrossRef]
30. Ci, L.; Li, Y.; Wei, B.; Liang, J.; Xu, C.; Wu, D. Preparation of carbon nanofibers by the floating catalyst method. *Carbon* **2000**, *38*, 1933–1937. [CrossRef]
31. Ateia, M.; Koch, C.; Jelavić, S.; Hirt, A.; Quinson, J.; Yoshimura, C.; Johnson, M. Green and facile approach for enhancing the inherent magnetic properties of carbon nanotubes for water treatment applications. *PLoS ONE* **2017**, *12*, e0180636. [CrossRef]
32. Chen, B.; Zhu, Z.; Ma, J.; Yang, M.; Hong, J.; Hu, X.; Qiu, Y.; Chen, J. One-pot, solid-phase synthesis of magnetic multiwalled carbon nanotube/iron oxide composites and their application in arsenic removal. *J. Colloid Interface Sci.* **2014**, *434*, 9–17. [CrossRef]
33. Thambiraj, S.; Shankaran, D.R. Green synthesis of highly fluorescent carbon quantum dots from sugarcane bagasse pulp. *Appl. Surf. Sci.* **2016**, *390*, 435–443. [CrossRef]
34. Sevilla, M.; Fuertes, A.B. Graphitic carbon nanostructures from cellulose. *Chem. Phys. Lett.* **2010**, *490*, 63–68. [CrossRef]
35. Omoriyekomwan, J.E.; Tahmasebi, A.; Dou, J.; Wang, R.; Yu, J. A review on the recent advances in the production of carbon nanotubes and carbon nanofibers via microwave-assisted pyrolysis of biomass. *Fuel Process. Technol.* **2021**, *214*, 106686. [CrossRef]
36. Barin, G.B.; Gimenez, I.D.F.; da Costa, L.P.; Filho, A.G.S.; Barreto, L.S. Hollow carbon nanostructures obtained from hydrothermal carbonization of lignocellulosic biomass. *J. Mater. Sci.* **2013**, *49*, 665–672. [CrossRef]
37. Barin, G.B.; Gimenez, I.D.F.; da Costa, L.P.; Filho, A.G.S.; Barreto, L.S. Influence of hydrothermal carbonization on formation of curved graphite structures obtained from a lignocellulosic precursor. *Carbon* **2014**, *78*, 609–612. [CrossRef]
38. Herring, A.M.; McKinnon, J.T.; McCloskey, B.D.; Filley, J.; Gneshin, K.W.; Pavelka, R.A.; Kleebe, H.-J.; Aldrich, D.J. A Novel Method for the Templated Synthesis of Homogeneous Samples of Hollow Carbon Nanospheres from Cellulose Chars. *J. Am. Chem. Soc.* **2003**, *125*, 9916–9917. [CrossRef]
39. Titirici, M.-M.; White, R.J.; Brun, N.; Budarin, V.L.; Su, D.S.; del Monte, F.; Clark, J.H.; MacLachlan, M.J. Sustainable carbon materials. *Chem. Soc. Rev.* **2015**, *44*, 250–290. [CrossRef]
40. Hu, B.; Wang, K.; Wu, L.; Yu, S.-H.; Antonietti, M.; Titirici, M.-M. Engineering Carbon Materials from the Hydrothermal Carbonization Process of Biomass. *Adv. Mater.* **2010**, *22*, 813–828. [CrossRef]
41. Gao, Z.; Zhang, Y.; Song, N.; Li, X. Biomass-derived renewable carbon materials for electrochemical energy storage. *Mater. Res. Lett.* **2017**, *5*, 69–88. [CrossRef]
42. McKendry, P. Energy production from biomass (part 1): Overview of biomass. *Bioresour. Technol.* **2002**, *83*, 37–46. [CrossRef] [PubMed]
43. McKendry, P. Energy production from biomass (part 2): Conversion technologies. *Bioresour. Technol.* **2002**, *83*, 47–54. [CrossRef] [PubMed]
44. Pütün, A.E.; Özbay, N.; Önal, E.P.; Pütün, E. Fixed-bed pyrolysis of cotton stalk for liquid and solid products. *Fuel Process. Technol.* **2005**, *86*, 1207–1219. [CrossRef]

45. Primo, A.; Atienzar, P.; Sanchez, E.; Delgado, J.M.; García, H. From biomass wastes to large-area, high-quality, N-doped graphene: Catalyst-free carbonization of chitosan coatings on arbitrary substrates. *Chem. Commun.* **2012**, *48*, 9254–9256. [CrossRef] [PubMed]
46. Su, D.S. The Use of Natural Materials in Nanocarbon Synthesis. *ChemSusChem* **2009**, *2*, 1009–1020. [CrossRef] [PubMed]
47. Tay, T.; Ucar, S.; Karagöz, S. Preparation and characterization of activated carbon from waste biomass. *J. Hazard. Mater.* **2009**, *165*, 481–485. [CrossRef] [PubMed]
48. Marriott, A.; Hunt, A.; Bergström, E.; Wilson, K.; Budarin, V.; Thomas-Oates, J.; Clark, J.; Brydson, R. Investigating the structure of biomass-derived non-graphitizing mesoporous carbons by electron energy loss spectroscopy in the transmission electron microscope and X-ray photoelectron spectroscopy. *Carbon* **2013**, *67*, 514–524. [CrossRef]
49. Titirici, M.-M.; Antonietti, M. Chemistry and materials options of sustainable carbon materials made by hydrothermal carbonization. *Chem. Soc. Rev.* **2010**, *39*, 103–116. [CrossRef]
50. Su, D.S.; Centi, G. A perspective on carbon materials for future energy application. *J. Energy Chem.* **2013**, *22*, 151–173. [CrossRef]
51. Nie, J.-Q.; Zhang, Q.; Zhao, M.-Q.; Huang, J.-Q.; Wen, Q.; Cui, Y.; Qian, W.-Z.; Wei, F. Synthesis of high quality single-walled carbon nanotubes on natural sepiolite and their use for phenol absorption. *Carbon* **2011**, *49*, 1568–1580. [CrossRef]
52. Liu, J.; Deng, Y.; Li, X.; Wang, L. Promising Nitrogen-Rich Porous Carbons Derived from One-Step Calcium Chloride Activation of Biomass-Based Waste for High Performance Supercapacitors. *ACS Sustain. Chem. Eng.* **2016**, *4*, 177–187. [CrossRef]
53. El-Hendawy, A.-N.A.; Samra, S.; Girgis, B. Adsorption characteristics of activated carbons obtained from corncobs. *Colloids Surfaces A Physicochem. Eng. Asp.* **2001**, *180*, 209–221. [CrossRef]
54. Zhang, T.; Walawender, W.P.; Fan, L.; Fan, M.; Daugaard, D.; Brown, R. Preparation of activated carbon from forest and agricultural residues through CO₂ activation. *Chem. Eng. J.* **2004**, *105*, 53–59. [CrossRef]
55. Ioannidou, O.; Zabaniotou, A. Agricultural residues as precursors for activated carbon production—A review. *Renew. Sustain. Energy Rev.* **2007**, *11*, 1966–2005. [CrossRef]
56. Daifullah, A.A.M.; Yakout, S.M.; Elreefy, S.A. Adsorption of fluoride in aqueous solutions using KMnO₄-modified activated carbon derived from steam pyrolysis of rice straw. *J. Hazard. Mater.* **2007**, *147*, 633–643. [CrossRef] [PubMed]
57. Aworn, A.; Thiravetyan, P.; Nakbanpote, W. Preparation and characteristics of agricultural waste activated carbon by physical activation having micro- and mesopores. *J. Anal. Appl. Pyrolysis* **2008**, *82*, 279–285. [CrossRef]
58. Balci, S.; Doğu, T.; Yücel, H. Characterization of activated carbon produced from almond shell and hazelnut shell. *J. Chem. Technol. Biotechnol.* **1994**, *60*, 419–426. [CrossRef]
59. Caturla, F.; Molina-Sabio, M.; Rodríguez-Reinoso, F. Preparation of activated carbon by chemical activation with ZnCl₂. *Carbon* **1991**, *29*, 999–1007. [CrossRef]
60. Lillo-Ródenas, M.; Cazorla-Amorós, D.; Linares-Solano, A. Understanding chemical reactions between carbons and NaOH and KOH: An insight into the chemical activation mechanism. *Carbon* **2003**, *41*, 267–275. [CrossRef]
61. Prahaz, D.; Kartika, Y.; Indraswati, N.; Ismadji, S. Activated carbon from jackfruit peel waste by H₃PO₄ chemical activation: Pore structure and surface chemistry characterization. *Chem. Eng. J.* **2008**, *140*, 32–42. [CrossRef]
62. Hayashi, J.; Horikawa, T.; Takeda, I.; Muroyama, K.; Ani, F.N. Preparing activated carbon from various nutshells by chemical activation with K₂CO₃. *Carbon* **2002**, *40*, 2381–2386. [CrossRef]
63. US4082694A; Active Carbon Process and Composition. BP Corp North America: Houston, TX, USA, 1978.
64. Titirici, M.-M.; Antonietti, M.; Baccile, N. Hydrothermal carbon from biomass: A comparison of the local structure from poly- to monosaccharides and pentoses/hexoses. *Green Chem.* **2008**, *10*, 1204–1212. [CrossRef]
65. Titirici, M.-M.; White, R.J.; Falco, C.; Sevilla, M. Black perspectives for a green future: Hydrothermal carbons for environment protection and energy storage. *Energy Environ. Sci.* **2012**, *5*, 6796–6822. [CrossRef]
66. Sevilla, M.; Fuertes, A.B.; Mokaya, R. High density hydrogen storage in superactivated carbons from hydrothermally carbonized renewable organic materials. *Energy Environ. Sci.* **2011**, *4*, 1400–1410. [CrossRef]
67. Titirici, M.-M.; Thomas, A.; Antonietti, M. Replication and Coating of Silica Templates by Hydrothermal Carbonization. *Adv. Funct. Mater.* **2007**, *17*, 1010–1018. [CrossRef]
68. Iijima, S. Helical microtubules of graphitic carbon. *Nature* **1991**, *354*, 56–58. [CrossRef]
69. Kong, J.; Franklin, N.R.; Zhou, C.; Chapline, M.G.; Peng, S.; Cho, K.; Dai, H. Nanotube Molecular Wires as Chemical Sensors. *Science* **2000**, *287*, 622–625. [CrossRef]
70. Ghosh, S.; Sood, A.K.; Kumar, N. Carbon Nanotube Flow Sensors. *Science* **2003**, *299*, 1042–1044. [CrossRef]
71. Sun, X.; Li, R.; Villers, D.; Dodelet, J.; Désilets, S. Composite electrodes made of Pt nanoparticles deposited on carbon nanotubes grown on fuel cell backings. *Chem. Phys. Lett.* **2003**, *379*, 99–104. [CrossRef]
72. Saha, M.S.; Li, R.; Sun, X.; Ye, S. 3-D composite electrodes for high performance PEM fuel cells composed of Pt supported on nitrogen-doped carbon nanotubes grown on carbon paper. *Electrochem. Commun.* **2009**, *11*, 438–441. [CrossRef]
73. Gupta, C.; Maheshwari, P.H.; Dhakate, S.R. Development of multiwalled carbon nanotubes platinum nanocomposite as efficient PEM fuel cell catalyst. *Mater. Renew. Sustain. Energy* **2016**, *5*, 2. [CrossRef]
74. Chen, Y.; Wang, J.; Liu, H.; Li, R.; Sun, X.; Ye, S.; Knights, S. Enhanced stability of Pt electrocatalysts by nitrogen doping in CNTs for PEM fuel cells. *Electrochem. Commun.* **2009**, *11*, 2071–2076. [CrossRef]
75. Zhu, W.; Bower, C.; Zhou, O.; Kochanski, G.; Jin, S. Large current density from carbon nanotube field emitters. *Appl. Phys. Lett.* **1999**, *75*, 873–875. [CrossRef]

76. Rueckes, T.; Kim, K.; Joselevich, E.; Tseng, G.Y.; Cheung, C.-L.; Lieber, C.M. Carbon Nanotube-Based Nonvolatile Random Access Memory for Molecular Computing. *Science* **2000**, *289*, 94–97. [CrossRef] [PubMed]
77. Bachtold, A.; Hadley, P.; Nakanishi, T.; Dekker, C. Logic Circuits with Carbon Nanotube Transistors. *Science* **2001**, *294*, 1317–1320. [CrossRef]
78. Postma, H.W.C.; Teepen, T.; Yao, Z.; Grifoni, M.; Dekker, C. Carbon Nanotube Single-Electron Transistors at Room Temperature. *Science* **2001**, *293*, 76–79. [CrossRef]
79. Saba, N.; Jawaid, M.; Fouad, H.; Allothman, O.Y. Nanocarbon: Preparation, properties, and applications. In *Nanocarbon and Its Composites*; Khan, A., Jawaid, M., Mohamed Asiri, I., Mohamed Asiri, A., Eds.; Woodhead Publishing: Sawston, UK, 2018; pp. 327–354. [CrossRef]
80. Vedhanarayanan, B.; Praveen, V.K.; Das, G.; Ajayaghosh, A. Hybrid materials of 1D and 2D carbon allotropes and synthetic π -systems. *NPG Asia Mater.* **2018**, *10*, 107–126. [CrossRef]
81. Zhang, M.; Li, J. Carbon nanotube in different shapes. *Mater. Today* **2009**, *12*, 12–18. [CrossRef]
82. Radushkevich, L.; Lukyanovich, V. About the structure of carbon formed by thermal decomposition of carbon monoxide on iron substrate. *J. Phys. Chem.* **1952**, *26*, 88–95.
83. Monthieux, M.; Kuznetsov, V.L. Who should be given the credit for the discovery of carbon nanotubes? *Carbon* **2006**, *44*, 1621–1623. [CrossRef]
84. Kunzmann, A.; Andersson, B.; Thurnherr, T.; Krug, H.; Scheynius, A.; Fadeel, B. Toxicology of engineered nanomaterials: Focus on biocompatibility, biodistribution and biodegradation. *Biochim. Biophys. Acta (BBA)-Gen. Subj.* **2011**, *1810*, 361–373. [CrossRef] [PubMed]
85. Chou, C.-C.; Hsiao, H.-Y.; Hong, Q.-S.; Chen, C.-H.; Peng, Y.-W.; Chen, H.-W.; Yang, P.-C. Single-Walled Carbon Nanotubes Can Induce Pulmonary Injury in Mouse Model. *Nano Lett.* **2008**, *8*, 437–445. [CrossRef] [PubMed]
86. Chen, J.; Chen, S.; Zhao, X.; Kuznetsova, L.V.; Wong, S.S.; Ojima, I. Functionalized Single-Walled Carbon Nanotubes as Rationally Designed Vehicles for Tumor-Targeted Drug Delivery. *J. Am. Chem. Soc.* **2008**, *130*, 16778–16785. [CrossRef]
87. Yang, Z.; Zhang, Y.; Yang, Y.; Sun, L.; Han, D.; Li, H.; Wang, C. Pharmacological and toxicological target organelles and safe use of single-walled carbon nanotubes as drug carriers in treating Alzheimer disease. *Nanomed. Nanotechnol. Biol. Med.* **2010**, *6*, 427–441. [CrossRef]
88. Bardi, G.; Nunes, A.; Gherardini, L.; Bates, K.; Al-Jamal, K.T.; Gaillard, C.; Prato, M.; Bianco, A.; Pizzorusso, T.; Kostarelos, K. Functionalized Carbon Nanotubes in the Brain: Cellular Internalization and Neuroinflammatory Responses. *PLoS ONE* **2013**, *8*, e80964. [CrossRef] [PubMed]
89. Karimi, M.; Solati, N.; Ghasemi, A.; Estiar, M.A.; Hashemkhani, M.; Kiani, P.; Mohamed, E.; Saeidi, A.; Taheri, M.; Avci, P.; et al. Carbon nanotubes part II: A remarkable carrier for drug and gene delivery. *Expert Opin. Drug Deliv.* **2015**, *12*, 1089–1105. [CrossRef] [PubMed]
90. Pau, A.; Hasan, A.; Al Kindi, H.; Gaharwar, A.K.; Rao, V.T.S.; Nikkhah, M.; Shin, S.R.; Krafft, D.; Dokmeci, M.R.; Shum-Tim, D.; et al. Injectable Graphene Oxide/Hydrogel-Based Angiogenic Gene Delivery System for Vasculogenesis and Cardiac Repair. *ACS Nano* **2014**, *8*, 8050–8062. [CrossRef]
91. Pumera, M. Nanomaterials meet microfluidics. *Chem. Commun.* **2011**, *47*, 5671–5680. [CrossRef]
92. Mittal, G.; Dhand, V.; Rhee, K.; Kim, H.-J.; Jung, D.H. Carbon nanotubes synthesis using diffusion and premixed flame methods: A review. *Carbon Lett.* **2015**, *16*, 1–10. [CrossRef]
93. Wei, F.; Zhang, Q.; Qian, W.-Z.; Yu, H.; Wang, Y.; Luo, G.-H.; Xu, G.-H.; Wang, D.-Z. The mass production of carbon nanotubes using a nano-agglomerate fluidized bed reactor: A multiscale space–time analysis. *Powder Technol.* **2008**, *183*, 10–20. [CrossRef]
94. Wang, Y.; Wei, F.; Luo, G.; Yu, H.; Gu, G. The large-scale production of carbon nanotubes in a nano-agglomerate fluidized-bed reactor. *Chem. Phys. Lett.* **2002**, *364*, 568–572. [CrossRef]
95. Dupuis, A.-C. The catalyst in the CCVD of carbon nanotubes—A review. *Prog. Mater. Sci.* **2005**, *50*, 929–961. [CrossRef]
96. Harris, P.J.F. *Carbon Nanotubes and Related Structures*; Cambridge University Press: Cambridge, UK, 1999; pp. 1–279. [CrossRef]
97. Panyala, N.R.; Mendez, E.P.; Havel, J. Silver or silver nanoparticles: A hazardous threat to the environment and human health? *J. Appl. Biomed.* **2012**, *6*, 117–129. [CrossRef]
98. Masarovičová, E.; Kráľová, K. Metal Nanoparticles and Plants/Nanocząstki Metaliczne I Rośliny. *Ecol. Chem. Eng.* **2013**, *20*, 9–22. [CrossRef]
99. Velusamy, S.; Roy, A.; Sundaram, S.; Mallick, T.K. A Review on Heavy Metal Ions and Containing Dyes Removal through Graphene Oxide-Based Adsorption Strategies for Textile Wastewater Treatment. *Chem. Rec.* **2021**, *21*, 1570–1610. [CrossRef]
100. Liu, T.-Y.; Zhang, L.-L.; Yu, W.-J.; Li, S.-S.; Hou, P.-X.; Cong, H.-T.; Liu, C.; Cheng, H.-M. Growth of double-walled carbon nanotubes from silicon oxide nanoparticles. *Carbon* **2013**, *56*, 167–172. [CrossRef]
101. Jean-Luc, B.; Bruno, D. Contamination Monitoring and Analysis in Semiconductor Manufacturing. *Semicond. Technol.* **1999**, *1999*, 57–78. [CrossRef]
102. Liu, B.; Ren, W.; Gao, L.; Li, S.; Pei, S.; Liu, C.; Jiang, C.; Cheng, H.-M. Metal-Catalyst-Free Growth of Single-Walled Carbon Nanotubes. *J. Am. Chem. Soc.* **2009**, *131*, 2082–2083. [CrossRef]
103. Tripathi, N.; Moinuddin, M.G.; Islam, S.S. Growth of SWNTs using $\text{Cu}(\text{NO}_3)_2$ and CuO a systematic study on role of oxygen in growth of CNTs. In Proceedings of the 2015 Annual IEEE India Conference (INDICON), New Delhi, India, 17–20 December 2015; pp. 1–3. [CrossRef]

104. Tripathi, N.; Pavelyev, V.; Islam, S.S. Synthesis of carbon nanotubes using green plant extract as catalyst: Unconventional concept and its realization. *Appl. Nanosci.* **2017**, *7*, 557–566. [CrossRef]
105. Hamid, Z.; Azim, A.; Mouez, F.A.; Rehim, S. Challenges on synthesis of carbon nanotubes from environmentally friendly green oil using pyrolysis technique. *J. Anal. Appl. Pyrolysis* **2017**, *126*, 218–229. [CrossRef]
106. Szabó, A.; Perri, C.; Csató, A.; Giordano, G.; Vuono, D.; Nagy, J.B. Synthesis Methods of Carbon Nanotubes and Related Materials. *Materials* **2010**, *3*, 3092–3140. [CrossRef]
107. Kamalakaran, R.; Terrones, M.; Seeger, T.; Kohler-Redlich, P.; Rühle, M.; Kim, Y.A.; Hayashi, T.; Endo, M. Synthesis of thick and crystalline nanotube arrays by spray pyrolysis. *Appl. Phys. Lett.* **2000**, *77*, 3385–3387. [CrossRef]
108. Ghosh, P.; Afre, R.A.; Soga, T.; Jimbo, T. A simple method of producing single-walled carbon nanotubes from a natural precursor: Eucalyptus oil. *Mater. Lett.* **2007**, *61*, 3768–3770. [CrossRef]
109. Bernd, M.G.S.; Bragança, S.R.; Heck, N.; Filho, L.C.D.S. Synthesis of carbon nanostructures by the pyrolysis of wood sawdust in a tubular reactor. *J. Mater. Res. Technol.* **2017**, *6*, 171–177. [CrossRef]
110. Kumar, R.; Tiwari, R.S.; Srivastava, O.N. Scalable synthesis of aligned carbon nanotubes bundles using green natural precursor: Neem oil. *Nanoscale Res. Lett.* **2011**, *6*, 92. [CrossRef]
111. Afre, R.A.; Soga, T.; Jimbo, T.; Kumar, M.; Ando, Y.; Sharon, M. Vertically aligned carbon nanotubes at different temperatures by spray pyrolysis techniques. *Int. J. Mod. Phys. B* **2006**, *20*, 4965–4972. [CrossRef]
112. Ghosh, P.; Soga, T.; Tanemura, M.; Zamri, M.; Jimbo, T.; Katoh, R.; Sumiyama, K. Vertically aligned carbon nanotubes from natural precursors by spray pyrolysis method and their field electron emission properties. *Appl. Phys. A* **2009**, *94*, 51–56. [CrossRef]
113. Awasthi, K.; Kumar, R.; Raghubanshi, H.; Awasthi, S.; Pandey, R.; Singh, D.; Yadav, T.P.; Srivastava, O.N. Synthesis of nano-carbon (nanotubes, nanofibres, graphene) materials. *Bull. Mater. Sci.* **2011**, *34*, 607–614. [CrossRef]
114. De Volder, M.F.L.; Tawfick, S.H.; Baughman, R.H.; Hart, A.J. Carbon nanotubes: Present and future commercial applications. *Science* **2013**, *339*, 535–539. [CrossRef]
115. Jain, N.; Gupta, E.; Kanu, N.J. Plethora of Carbon Nanotubes Applications in Various Fields—A State-of-the-Art-Review. *Smart Sci.* **2022**, *10*, 1–24. [CrossRef]
116. Makgabutlane, B.; Nthunya, L.N.; Maubane-Nkadimeng, M.S.; Mhlanga, S.D. Green synthesis of carbon nanotubes to address the water-energy-food nexus: A critical review. *J. Environ. Chem. Eng.* **2021**, *9*, 104736. [CrossRef]
117. Ghosh, P.; Soga, T.; Afre, R.A.; Jimbo, T. Simplified synthesis of single-walled carbon nanotubes from a botanical hydrocarbon: Turpentine oil. *J. Alloys Compd.* **2008**, *462*, 289–293. [CrossRef]
118. Kumar, M.; Ando, Y. Carbon nanotubes from camphor: An environment-friendly nanotechnology. *J. Phys. Conf. Ser.* **2007**, *61*, 129. [CrossRef]
119. Andrews, R.J.; Smith, C.F.; Alexander, A. Mechanism of carbon nanotube growth from camphor and camphor analogs by chemical vapor deposition. *Carbon* **2006**, *44*, 341–347. [CrossRef]
120. Suriani, A.; Dalila, A.; Mohamed, A.; Rosmi, M.; Mamat, M.; Malek, M.; Ahmad, M.; Hashim, N.; Isa, I.; Soga, T.; et al. Parametric study of waste chicken fat catalytic chemical vapour deposition for controlled synthesis of vertically aligned carbon nanotubes. *Cogent Phys.* **2016**, *3*, 1247486. [CrossRef]
121. Paul, S.; Samdarshi, S. A green precursor for carbon nanotube synthesis. *New Carbon Mater.* **2011**, *26*, 85–88. [CrossRef]
122. Huang, S.; Cai, Q.; Chen, J.; Qian, Y.; Zhang, L. Metal-Catalyst-Free Growth of Single-Walled Carbon Nanotubes on Substrates. *J. Am. Chem. Soc.* **2009**, *131*, 2094–2095. [CrossRef]
123. Chen, X.-W.; Timpe, O.; Hamid, S.B.; Schlögl, R.; Su, D.S. Direct synthesis of carbon nanofibers on modified biomass-derived activated carbon. *Carbon* **2009**, *47*, 340–343. [CrossRef]
124. Rinaldi, A.; Tessonnier, J.-P.; Schuster, M.E.; Blume, R.; Girgsdies, F.; Zhang, Q.; Jacob, T.; Hamid, S.B.A.; Su, D.S.; Schlögl, R. Dissolved Carbon Controls the Initial Stages of Nanocarbon Growth. *Angew. Chem. Int. Ed.* **2011**, *50*, 3313–3317. [CrossRef]
125. Kumar, M.; Ando, Y. Single-wall and multi-wall carbon nanotubes from camphor—A botanical hydrocarbon. *Diam. Relat. Mater.* **2003**, *12*, 1845–1850. [CrossRef]
126. Kumar, M.; Okazaki, T.; Hiramatsu, M.; Ando, Y. The use of camphor-grown carbon nanotube array as an efficient field emitter. *Carbon* **2007**, *45*, 1899–1904. [CrossRef]
127. Asnawi, M.; Azhari, S.; Hamidon, M.N.; Ismail, I.; Helina, I. Synthesis of Carbon Nanomaterials from Rice Husk via Microwave Oven. *J. Nanomater.* **2018**, *2018*, 2898326. [CrossRef]
128. Kure, N.; Hamidon, M.N.; Azhari, S.; Mamat, N.S.; Yusoff, H.M.; Isa, B.M.; Yunusa, Z. Simple Microwave-Assisted Synthesis of Carbon Nanotubes Using Polyethylene as Carbon Precursor. *J. Nanomater.* **2017**, *2017*, 2474267. [CrossRef]
129. Nguyen, V.H.; Shim, J.-J. Green Synthesis and Characterization of Carbon Nanotubes/Polyaniline Nanocomposites. *J. Spectrosc.* **2015**, *2015*, 297804. [CrossRef]
130. Datta, A.; Dutta, P.; Sadhu, A.; Maiti, S.; Bhattacharyya, S. Single-step scalable conversion of waste natural oils to carbon nanowhiskers and their interaction with mammalian cells. *J. Nanoparticle Res.* **2013**, *15*, 1808. [CrossRef]
131. Cárdenas, J.; Orjuela, A.; Sánchez, D.L.; Narváez, P.C.; Katryniok, B.; Clark, J. Pre-treatment of used cooking oils for the production of green chemicals: A review. *J. Clean. Prod.* **2021**, *289*, 125129. [CrossRef]
132. Suriani, A.B.; Nor, R.; Rusop, M. Vertically aligned carbon nanotubes synthesized from waste cooking palm oil. *J. Ceram. Soc. Jpn.* **2010**, *118*, 963–968. [CrossRef]

133. Pasha, M.A.; Shafiekhani, A.; Vesaghi, M. Hot filament CVD of Fe–Cr catalyst for thermal CVD carbon nanotube growth from liquid petroleum gas. *Appl. Surf. Sci.* **2009**, *256*, 1365–1371. [CrossRef]
134. Bazaka, K.; Jacob, M.V.; Ostrikov, K. Sustainable Life Cycles of Natural-Precursor-Derived Nanocarbons. *Chem. Rev.* **2016**, *116*, 163–214. [CrossRef]
135. Fukushima, T.; Kosaka, A.; Ishimura, Y.; Yamamoto, T.; Takigawa, T.; Ishii, N.; Aida, T. Molecular Ordering of Organic Molten Salts Triggered by Single-Walled Carbon Nanotubes. *Science* **2003**, *300*, 2072–2074. [CrossRef]
136. Zhang, L.-S.; Gao, S.-P.; Huang, Y.-P.; Liu, Z.-S. Green synthesis of polymer monoliths incorporated with carbon nanotubes in room temperature ionic liquid and deep eutectic solvents. *Talanta* **2016**, *154*, 335–340. [CrossRef] [PubMed]
137. Booker, K.; Bowyer, M.C.; Holdsworth, C.I.; McCluskey, A. Efficient preparation and improved sensitivity of molecularly imprinted polymers using room temperature ionic liquids. *Chem. Commun.* **2006**, *16*, 1730–1732. [CrossRef] [PubMed]
138. Zhou, J.; Lin, P.; Ma, J.; Shan, X.; Feng, H.; Chen, C.; Chen, J.; Qian, Z. Facile synthesis of halogenated carbon quantum dots as an important intermediate for surface modification. *RSC Adv.* **2013**, *3*, 9625–9628. [CrossRef]
139. Li, H.; He, X.; Kang, Z.; Huang, H.; Liu, Y.; Liu, J.; Lian, S.; Tsang, A.C.H.; Yang, X.; Lee, S.-T. Water-Soluble Fluorescent Carbon Quantum Dots and Photocatalyst Design. *Angew. Chem. Int. Ed.* **2010**, *49*, 4430–4434. [CrossRef]
140. Dong, Y.; Wang, R.; Li, G.; Chen, C.; Chi, Y.; Chen, G. Polyamine-Functionalized Carbon Quantum Dots as Fluorescent Probes for Selective and Sensitive Detection of Copper Ions. *Anal. Chem.* **2012**, *84*, 6220–6224. [CrossRef]
141. Wang, F.; Chen, Y.-H.; Liu, C.-Y.; Ma, D.-G. White light-emitting devices based on carbon dots' electroluminescence. *Chem. Commun.* **2011**, *47*, 3502–3504. [CrossRef]
142. Li, X.; Wang, H.; Shimizu, Y.; Pyatenko, A.; Kawaguchi, K.; Koshizaki, N. Preparation of carbon quantum dots with tunable photoluminescence by rapid laser passivation in ordinary organic solvents. *Chem. Commun.* **2011**, *47*, 932–934. [CrossRef]
143. Wang, Q.; Huang, X.; Long, Y.; Wang, X.; Zhang, H.; Zhu, R.; Liang, L.; Teng, P.; Zheng, H. Hollow luminescent carbon dots for drug delivery. *Carbon* **2013**, *59*, 192–199. [CrossRef]
144. Ding, H.; Cheng, L.-W.; Ma, Y.-Y.; Kong, J.-L.; Xiong, H.-M. Luminescent carbon quantum dots and their application in cell imaging. *New J. Chem.* **2013**, *37*, 2515–2520. [CrossRef]
145. Liu, H.; Ye, T.; Mao, C. Fluorescent Carbon Nanoparticles Derived from Candle Soot. *Angew. Chem. Int. Ed.* **2007**, *46*, 6473–6475. [CrossRef]
146. Zhu, S.; Meng, Q.; Wang, L.; Zhang, J.; Song, Y.; Jin, H.; Zhang, K.; Sun, H.; Wang, H.; Yang, B. Highly photoluminescent carbon dots for multicolor patterning, sensors, and bioimaging. *Angew. Chem. Int. Ed.* **2013**, *52*, 3953–3957. [CrossRef]
147. Luo, P.G.; Sahu, S.; Yang, S.-T.; Sonkar, S.K.; Wang, J.; Wang, H.; LeCroy, G.E.; Cao, L.; Sun, Y.-P. Carbon “quantum” dots for optical bioimaging. *J. Mater. Chem. B* **2013**, *1*, 2116–2127. [CrossRef]
148. Yang, S.-T.; Cao, L.; Luo, P.G.; Lu, F.; Wang, X.; Wang, H.; Mezziani, M.J.; Liu, Y.; Qi, G.; Sun, Y.-P. Carbon Dots for Optical Imaging In Vivo. *J. Am. Chem. Soc.* **2009**, *131*, 11308–11309. [CrossRef]
149. Ross, S.; Wu, R.-S.; Wei, S.-C.; Ross, G.M.; Chang, H.-T. The analytical and biomedical applications of carbon dots and their future theranostic potential: A review. *J. Food Drug Anal.* **2020**, *28*, 677–695. [CrossRef]
150. Hu, S.; Wei, Z.; Chang, Q.; Trinchì, A.; Yang, J. A facile and green method towards coal-based fluorescent carbon dots with photocatalytic activity. *Appl. Surf. Sci.* **2016**, *378*, 402–407. [CrossRef]
151. Peng, H.; Travas-Sejdic, J. Simple Aqueous Solution Route to Luminescent Carbogenic Dots from Carbohydrates. *Chem. Mater.* **2009**, *21*, 5563–5565. [CrossRef]
152. Lu, W.; Qin, X.; Liu, S.; Chang, G.; Zhang, Y.; Luo, Y.; Asiri, A.M.; Al-Youbi, A.O.; Sun, X. Economical, Green Synthesis of Fluorescent Carbon Nanoparticles and Their Use as Probes for Sensitive and Selective Detection of Mercury(II) Ions. *Anal. Chem.* **2012**, *84*, 5351–5357. [CrossRef]
153. Yang, Y.; Cui, J.; Zheng, M.; Hu, C.; Tan, S.; Xiao, Y.; Yang, Q.; Liu, Y. One-step synthesis of amino-functionalized fluorescent carbon nanoparticles by hydrothermal carbonization of chitosan. *Chem. Commun.* **2012**, *48*, 380–382. [CrossRef]
154. Preethi, M.; Viswanathan, C.; Ponpandian, N. A green path to extract carbon quantum dots by coconut water: Another fluorescent probe towards Fe³⁺ ions. *Particuology* **2021**, *58*, 251–258. [CrossRef]
155. Yadav, P.K.; Singh, V.K.; Chandra, S.; Bano, D.; Kumar, V.; Talat, M.; Hasan, S.H. Green Synthesis of Fluorescent Carbon Quantum Dots from *Azadirachta indica* Leaves and Their Peroxidase-Mimetic Activity for the Detection of H₂O₂ and Ascorbic Acid in Common Fresh Fruits. *ACS Biomater. Sci. Eng.* **2019**, *5*, 623–632. [CrossRef]
156. Luo, X.; Zhang, W.; Han, Y.; Chen, X.; Zhu, L.; Tang, W.; Wang, J.; Yue, T.; Li, Z. N,S co-doped carbon dots based fluorescent “on-off-on” sensor for determination of ascorbic acid in common fruits. *Food Chem.* **2018**, *258*, 214–221. [CrossRef] [PubMed]
157. Gökmen, V.; Kahraman, N.; Demir, N.; Acar, J. Enzymatically validated liquid chromatographic method for the determination of ascorbic and dehydroascorbic acids in fruit and vegetables. *J. Chromatogr. A* **2000**, *881*, 309–316. [CrossRef] [PubMed]
158. Vasimalai, N.; Vilas-Boas, V.; Gallo, J.; Cerqueira, M.F.; Menéndez-Miranda, M.; Costa-Fernández, J.M.; Diéguez, L.; Espiña, B.; Fernández-Argüelles, M.T. Green synthesis of fluorescent carbon dots from spices for in vitro imaging and tumour cell growth inhibition. *Beilstein J. Nanotechnol.* **2018**, *9*, 530–544. [CrossRef] [PubMed]
159. Bano, D.; Kumar, V.; Singh, V.K.; Hasan, S.H. Green synthesis of fluorescent carbon quantum dots for the detection of mercury(ii) and glutathione. *New J. Chem.* **2018**, *42*, 5814–5821. [CrossRef]
160. Bao, R.; Chen, Z.; Zhao, Z.; Sun, X.; Zhang, J.; Hou, L.; Yuan, C. Green and Facile Synthesis of Nitrogen and Phosphorus Co-Doped Carbon Quantum Dots towards Fluorescent Ink and Sensing Applications. *Nanomaterials* **2018**, *8*, 386. [CrossRef] [PubMed]

161. Madrigal-Bujaidar, E.; Cerón-Montes, G.I.; Reyes-Miranda, J.; Vergara-Hernández, E.; Álvarez-González, I.; Morales-Ramírez, D.J.; Francisco-Martínez, L.E.; Garrido-Hernández, A. Structural, luminescence and geno/cytotoxicity study of carbon dots derived from *Opuntia ficus-indica* (L.) Mill. *New J. Chem.* **2020**, *44*, 942–950. [CrossRef]
162. Tyagi, A.; Tripathi, K.M.; Singh, N.; Choudhary, S.; Gupta, R.K. Green synthesis of carbon quantum dots from lemon peel waste: Applications in sensing and photocatalysis. *RSC Adv.* **2016**, *6*, 72423–72432. [CrossRef]
163. Liu, H.; Ding, L.; Chen, L.; Chen, Y.; Zhou, T.; Li, H.; Xu, Y.; Zhao, L.; Huang, N. A facile, green synthesis of biomass carbon dots coupled with molecularly imprinted polymers for highly selective detection of oxytetracycline. *J. Ind. Eng. Chem.* **2019**, *69*, 455–463. [CrossRef]
164. Danilenko, V.V. On the history of the discovery of nanodiamond synthesis. *Phys. Solid State* **2004**, *46*, 595–599. [CrossRef]
165. Dolmatov, V.Y. Detonation synthesis ultradispersed diamonds: Properties and applications. *Russ. Chem. Rev.* **2001**, *70*, 607–626. [CrossRef]
166. Chipaux, M.; Van Der Laan, K.J.; Hemelaar, S.R.; Hasani, M.; Zheng, T.; Schirhagl, R. Nanodiamonds and Their Applications in Cells. *Small* **2018**, *14*, e1704263. [CrossRef] [PubMed]
167. Mahdavi, M.; Mahmoudi, N.; Anaran, F.R.; Simchi, A. Electrospinning of Nanodiamond-Modified Polysaccharide Nanofibers with Physico-Mechanical Properties Close to Natural Skins. *Mar. Drugs* **2016**, *14*, 128. [CrossRef] [PubMed]
168. Mochalin, V.N.; Shenderova, O.; Ho, D.; Gogotsi, Y. The properties and applications of nanodiamonds. *Nat. Nanotechnol.* **2011**, *7*, 11–23. [CrossRef] [PubMed]
169. Thapliyal, V.; Alabdulkarim, M.E.; Whelan, D.R.; Mainali, B.; Maxwell, J.L. A concise review of the Raman spectra of carbon allotropes. *Diam. Relat. Mater.* **2022**, *127*, 109180. [CrossRef]
170. Gruber, A.; Drabenstedt, A.; Tietz, C.; Fleury, L.; Wrachtrup, J.; von Borczyskowski, C. Scanning Confocal Optical Microscopy and Magnetic Resonance on Single Defect Centers. *Science* **1997**, *276*, 2012–2014. [CrossRef]
171. Yu, S.-J.; Kang, M.-W.; Chang, H.-C.; Chen, K.-M.; Yu, Y.-C. Bright Fluorescent Nanodiamonds: No Photobleaching and Low Cytotoxicity. *J. Am. Chem. Soc.* **2005**, *127*, 17604–17605. [CrossRef]
172. Perevedentseva, E.; Lin, Y.-C.; Jani, M.; Cheng, C.-L. Biomedical applications of nanodiamonds in imaging and therapy. *Nanomedicine* **2013**, *8*, 2041–2060. [CrossRef] [PubMed]
173. Shenderova, O.A.; Zhirnov, V.V.; Brenner, D.W. Carbon nanostructures. *Crit. Rev. Solid State Mater. Sci.* **2006**, *27*, 227–356. [CrossRef]
174. Williams, O.; Nesladek, M.; Daenen, M.; Michaelson, S.; Hoffman, A.; Osawa, E.; Haenen, K.; Jackman, R. Growth, electronic properties and applications of nanodiamond. *Diam. Relat. Mater.* **2008**, *17*, 1080–1088. [CrossRef]
175. Huss, G.R. Meteoritic Nanodiamonds: Messengers from the Stars. *Elements* **2005**, *1*, 97–100. [CrossRef]
176. Kharisov, B.I.; Kharissova, O.V.; Chvez-Guerrero, L. Synthesis techniques, properties, and applications of nanodiamonds. *Synth. React. Inorg. Met.-Org. Nano-Met. Chem.* **2010**, *40*, 84–101. [CrossRef]
177. Zhang, S.; Ali, N. *Nanocomposite Thin Films and Coatings: Processing, Properties and Performance*; Imperial College Press: London, UK, 2007; pp. 1–615. [CrossRef]
178. Yang, N.; Uetsuka, H.; Williams, O.A.; Osawa, E.; Tokuda, N.; Nebel, C.E. Vertically aligned diamond nanowires: Fabrication, characterization, and application for DNA sensing. *Phys. Status Solidi* **2009**, *206*, 2048–2056. [CrossRef]
179. Kong, X.-L. Nanodiamonds Used as a Platform for Studying Noncovalent Interaction by MALDI-MS. *Chin. J. Chem.* **2008**, *26*, 1811–1815. [CrossRef]
180. Zhang, X.-Q.; Lam, R.; Xu, X.; Chow, E.K.; Kim, H.-J.; Ho, D. Multimodal Nanodiamond Drug Delivery Carriers for Selective Targeting, Imaging, and Enhanced Chemotherapeutic Efficacy. *Adv. Mater.* **2011**, *23*, 4770–4775. [CrossRef]
181. Vijayanthimala, V.; Chang, H.-C. Functionalized fluorescent nanodiamonds for biomedical applications. *Nanomedicine* **2009**, *4*, 47–55. [CrossRef]
182. Schrand, A.M.; Hens, S.A.C.; Shenderova, O.A. Nanodiamond Particles: Properties and Perspectives for Bioapplications. *Crit. Rev. Solid State Mater. Sci.* **2009**, *34*, 18–74. [CrossRef]
183. Cheng, C.-Y.; Perevedentseva, E.; Tu, J.-S.; Chung, P.-H.; Liu, K.-K.; Chao, J.-I.; Chen, P.-H.; Chang, C.-C. Direct and In Vitro observation of growth hormone receptor molecules in A549 human lung epithelial cells by nanodiamond labeling. *Appl. Phys. Lett.* **2007**, *90*, 163903. [CrossRef]
184. Shimkunas, R.A.; Robinson, E.; Lam, R.; Lu, S.; Xu, X.; Zhang, X.-Q.; Huang, H.; Osawa, E.; Ho, D. Nanodiamond–insulin complexes as pH-dependent protein delivery vehicles. *Biomaterials* **2009**, *30*, 5720–5728. [CrossRef]
185. Liu, K.-K.; Wang, C.-C.; Cheng, C.-L.; Chao, J.-I. Endocytic carboxylated nanodiamond for the labeling and tracking of cell division and differentiation in cancer and stem cells. *Biomaterials* **2009**, *30*, 4249–4259. [CrossRef] [PubMed]
186. Faklaris, O.; Garrot, D.; Joshi, V.; Druon, F.; Boudou, J.-P.; Sauvage, T.; Georges, P.; Curmi, P.A.; Treussart, F. Detection of Single Photoluminescent Diamond Nanoparticles in Cells and Study of the Internalization Pathway. *Small* **2008**, *4*, 2236–2239. [CrossRef]
187. Perevedentseva, E.; Hong, S.-F.; Huang, K.-J.; Chiang, I.-T.; Lee, C.-Y.; Tseng, Y.-T.; Cheng, C.-L. Nanodiamond internalization in cells and the cell uptake mechanism. *J. Nanopart. Res.* **2013**, *15*, 1834. [CrossRef]
188. Mi, Z.; Chen, C.-B.; Tan, H.Q.; Dou, Y.; Yang, C.; Turaga, S.P.; Ren, M.; Vajandar, S.K.; Yuen, G.H.; Osipowicz, T.; et al. Quantifying nanodiamonds biodistribution in whole cells with correlative iono-nanoscopy. *Nat. Commun.* **2021**, *12*, 4657. [CrossRef] [PubMed]
189. Boruah, A.; Saikia, B.K. Synthesis, Characterization, Properties, and Novel Applications of Fluorescent Nanodiamonds. *J. Fluoresc.* **2022**, *32*, 863–885. [CrossRef] [PubMed]

190. Hui, Y.Y.; Chen, O.J.; Lin, H.-H.; Su, Y.-K.; Chen, K.Y.; Wang, C.-Y.; Hsiao, W.W.-W.; Chang, H.-C. Magnetically Modulated Fluorescence of Nitrogen-Vacancy Centers in Nanodiamonds for Ultrasensitive Biomedical Analysis. *Anal. Chem.* **2021**, *93*, 7140–7147. [CrossRef]
191. Doherty, M.W.; Manson, N.B.; Delaney, P.; Jelezko, F.; Wrachtrup, J.; Hollenberg, L.C. The nitrogen-vacancy colour centre in diamond. *Phys. Rep.* **2013**, *528*, 1–45. [CrossRef]
192. Haziza, S.; Mohan, N.; Loe-Mie, Y.; Lepagnol-Bestel, A.-M.; Massou, S.; Adam, M.-P.; Le, X.L.; Viard, J.; Plancon, C.; Daudin, R.; et al. Fluorescent nanodiamond tracking reveals intraneuronal transport abnormalities induced by brain-disease-related genetic risk factors. *Nat. Nanotechnol.* **2016**, *12*, 322–328. [CrossRef]
193. Glenn, D.R.; Lee, K.; Park, H.; Weissleder, R.; Yacoby, A.; Lukin, M.D.; Lee, H.; Walsworth, R.L.; Connolly, C.B. Single-cell magnetic imaging using a quantum diamond microscope. *Nat. Methods* **2015**, *12*, 736–738. [CrossRef]
194. Carter, S.D.; Mageswaran, S.K.; Farino, Z.J.; Mamede, J.I.; Oikonomou, C.M.; Hope, T.J.; Freyberg, Z.; Jensen, G.J. Distinguishing signal from autofluorescence in cryogenic correlated light and electron microscopy of mammalian cells. *J. Struct. Biol.* **2018**, *201*, 15–25. [CrossRef]
195. O'Driscoll, C.; Griffin, B. Biopharmaceutical challenges associated with drugs with low aqueous solubility—The potential impact of lipid-based formulations. *Adv. Drug Deliv. Rev.* **2008**, *60*, 617–624. [CrossRef]
196. Chen, M.; Pierstorff, E.D.; Lam, R.; Li, S.-Y.; Huang, H.; Osawa, E.; Ho, D. Nanodiamond-Mediated Delivery of Water-Insoluble Therapeutics. *ACS Nano* **2009**, *3*, 2016–2022. [CrossRef]
197. Zur Wiesch, P.A.; Kouyos, R.; Engelstädter, J.; Regoes, R.R.; Bonhoeffer, S. Population biological principles of drug-resistance evolution in infectious diseases. *Lancet Infect. Dis.* **2011**, *11*, 236–247. [CrossRef] [PubMed]
198. Van Hung, T.; Karunakaran, R.; Tung, T.T.; Dang, N.N.; Nguyen, S.X.; Losic, D. Nitrogen-doped carbon-coated nanodiamonds for electrocatalytic applications. *J. Phys. D Appl. Phys.* **2020**, *54*, 085303. [CrossRef]
199. Jariwala, D.H.; Patel, D.; Wairkar, S. Surface functionalization of nanodiamonds for biomedical applications. *Mater. Sci. Eng. C* **2020**, *113*, 110996. [CrossRef] [PubMed]
200. Khan, M.B.; Khan, Z.H. Nanodiamonds: Synthesis and applications. In *Nanomaterials and Their Applications*; Springer: Singapore, 2018; pp. 1–26. [CrossRef]
201. Arnault, J.-C. Nanodiamonds: From synthesis to applications. In *Handbook of Carbon-Based Nanomaterials*; Elsevier: Amsterdam, The Netherlands, 2021; pp. 209–246. [CrossRef]
202. Verma, S.K.; Das, A.K.; Gantait, S.; Panwar, Y.; Kumar, V.; Brestic, M. Green synthesis of carbon-based nanomaterials and their applications in various sectors: A topical review. *Carbon Lett.* **2021**, *32*, 365–393. [CrossRef]
203. Xiao, J.; Liu, P.; Yang, G.W. Nanodiamonds from coal under ambient conditions. *Nanoscale* **2015**, *7*, 6114–6125. [CrossRef]
204. Gobin, A.M.; Watkins, E.M.; Quevedo, E.; Colvin, V.L.; West, J.L. Near-Infrared-Resonant Gold/Gold Sulfide Nanoparticles as a Photothermal Cancer Therapeutic Agent. *Small* **2010**, *6*, 745–752. [CrossRef]
205. Zhang, C.; Lv, W.; Zhang, W.; Zheng, X.; Wu, M.-B.; Wei, W.; Tao, Y.; Li, Z.; Yang, Q.-H. Reduction of Graphene Oxide by Hydrogen Sulfide: A Promising Strategy for Pollutant Control and as an Electrode for Li-S Batteries. *Adv. Energy Mater.* **2014**, *4*, 1301565. [CrossRef]
206. Shan, C.; Zhao, W.; Lu, X.L.; O'Brien, D.J.; Li, Y.; Cao, Z.; Elias, A.L.; Cruz-Silva, R.; Terrones, M.; Wei, B.; et al. Three-Dimensional Nitrogen-Doped Multiwall Carbon Nanotube Sponges with Tunable Properties. *Nano Lett.* **2013**, *13*, 5514–5520. [CrossRef]
207. Kabiri, S.; Tran, D.N.; Altalhi, T.; Losic, D. Outstanding adsorption performance of graphene-carbon nanotube aerogels for continuous oil removal. *Carbon* **2014**, *80*, 523–533. [CrossRef]
208. Nardecchia, S.; Carriazo, D.; Ferrer, M.L.; Gutiérrez, M.C.; del Monte, F. Three dimensional macroporous architectures and aerogels built of carbon nanotubes and/or graphene: Synthesis and applications. *Chem. Soc. Rev.* **2013**, *42*, 794–830. [CrossRef]
209. Voiry, D.; Yang, J.; Kupferberg, J.; Fullon, R.; Lee, C.; Jeong, H.Y.; Shin, H.S.; Chhowalla, M. High-quality graphene via microwave reduction of solution-exfoliated graphene oxide. *Nanomaterials* **2016**, *353*, 1413–1415. [CrossRef] [PubMed]
210. Vecera, P.; Holzwarth, J.; Edelhalthammer, K.F.; Mundloch, U.; Peterlik, H.; Hauke, F.; Hirsch, A. Solvent-driven electron trapping and mass transport in reduced graphites to access perfect graphene. *Nat. Commun.* **2016**, *7*, 12411. [CrossRef] [PubMed]
211. Sha, J.; Li, Y.; Salvatierra, R.V.; Wang, T.; Dong, P.; Ji, Y.; Lee, S.-K.; Zhang, C.; Zhang, J.; Smith, R.H.; et al. Three-Dimensional Printed Graphene Foams. *ACS Nano* **2017**, *11*, 6860–6867. [CrossRef] [PubMed]
212. Chen, L.; He, L.; Wang, H.S.; Wang, H.; Tang, S.; Cong, C.; Xie, H.; Li, L.; Xia, H.; Li, T.; et al. Oriented graphene nanoribbons embedded in hexagonal boron nitride trenches. *Nat. Commun.* **2017**, *8*, 14703. [CrossRef]
213. Phiri, J.; Gane, P.; Maloney, T.C. General overview of graphene: Production, properties and application in polymer composites. *Mater. Sci. Eng. B* **2017**, *215*, 9–28. [CrossRef]
214. Ren, S.; Rong, P.; Yu, Q. Preparations, properties and applications of graphene in functional devices: A concise review. *Ceram. Int.* **2018**, *44*, 11940–11955. [CrossRef]
215. Ruan, G.; Sun, Z.; Peng, Z.; Tour, J.M. Growth of Graphene from Food, Insects, and Waste. *ACS Nano* **2011**, *5*, 7601–7607. [CrossRef]
216. Kim, Y.-K.; Kim, M.-H.; Min, D.-H. Biocompatible reduced graphene oxide prepared by using dextran as a multifunctional reducing agent. *Chem. Commun.* **2011**, *47*, 3195–3197. [CrossRef]
217. Gurunathan, S.; Han, J.W.; Park, J.H.; Eppakayala, V.; Kim, J.-H. Ginkgo biloba: A natural reducing agent for the synthesis of cytotocompatible graphene. *Int. J. Nanomed.* **2014**, *9*, 363–377. [CrossRef]

218. Bose, S.; Kuila, T.; Mishra, A.K.; Kim, N.H.; Lee, J.H. Dual role of glycine as a chemical functionalizer and a reducing agent in the preparation of graphene: An environmentally friendly method. *J. Mater. Chem.* **2012**, *22*, 9696–9703. [CrossRef]
219. Gurunathan, S.; Han, J.W.; Kim, J.-H. Green chemistry approach for the synthesis of biocompatible graphene. *Int. J. Nanomed.* **2013**, *8*, 2719–2732. [CrossRef] [PubMed]
220. Kim, J.; Park, S.-Y.; Kim, S.; Lee, D.H.; Kim, J.H.; Kim, J.M.; Kang, H.; Han, J.-S.; Park, J.W.; Lee, H.; et al. Precise and selective sensing of DNA-DNA hybridization by graphene/Si-nanowires diode-type biosensors. *Sci. Rep.* **2016**, *6*, 31984. [CrossRef] [PubMed]
221. Tang, L.; Wang, Y.; Li, J. The graphene/nucleic acid nanobiointerface. *Chem. Soc. Rev.* **2015**, *44*, 6954–6980. [CrossRef] [PubMed]
222. Akhavan, O.; Ghaderi, E.; Rahighi, R. Toward Single-DNA Electrochemical Biosensing by Graphene Nanowalls. *ACS Nano* **2012**, *6*, 2904–2916. [CrossRef]
223. Cheng, D.; Yang, L.; Li, X.; Zhou, J.; Chen, Q.; Yan, S.; Li, N.; Chu, M.; Dong, Y.; Xie, Z.; et al. An Electrochemical DNA Sensing Platform Using Carboxyl Functionalized Graphene as the Electrode Modified Material. *J. Electrochem. Soc.* **2017**, *164*, H345. [CrossRef]
224. Pei, X.; Zhu, Z.; Gan, Z.; Chen, J.; Zhang, X.; Cheng, X.; Wan, Q.; Wang, J. PEGylated nano-graphene oxide as a nanocarrier for delivering mixed anticancer drugs to improve anticancer activity. *Sci. Rep.* **2020**, *10*, 2717. [CrossRef] [PubMed]

Disclaimer/Publisher’s Note: The statements, opinions and data contained in all publications are solely those of the individual author(s) and contributor(s) and not of MDPI and/or the editor(s). MDPI and/or the editor(s) disclaim responsibility for any injury to people or property resulting from any ideas, methods, instructions or products referred to in the content.



Article

Employing Supervised Algorithms for the Prediction of Nanomaterial's Antioxidant Efficiency

Mahsa Mirzaei ¹, Irini Furxhi ^{1,2,*}, Finbarr Murphy ¹ and Martin Mullins ¹

¹ Department of Accounting and Finance, Kemmy Business School, University of Limerick, V94PH93 Limerick, Ireland

² Transgero Limited, Newcastle West, V42V384 Limerick, Ireland

* Correspondence: irini.furxhi@ul.ie; Tel.: +353-85-106-9771

Abstract: Reactive oxygen species (ROS) are compounds that readily transform into free radicals. Excessive exposure to ROS depletes antioxidant enzymes that protect cells, leading to oxidative stress and cellular damage. Nanomaterials (NMs) exhibit free radical scavenging efficiency representing a potential solution for oxidative stress-induced disorders. This study aims to demonstrate the application of machine learning (ML) algorithms for predicting the antioxidant efficiency of NMs. We manually compiled a comprehensive dataset based on a literature review of 62 in vitro studies. We extracted NMs' physico-chemical (P-chem) properties, the NMs' synthesis technique and various experimental conditions as input features to predict the antioxidant efficiency measured by a 2,2-diphenyl-1-picrylhydrazyl (DPPH) assay. Following data pre-processing, various regression models were trained and validated. The random forest model showed the highest predictive performance reaching an $R^2 = 0.83$. The attribute importance analysis revealed that the NM's type, core-size and dosage are the most important attributes influencing the prediction. Our findings corroborate with those of the prior research landscape regarding the importance of P-chem characteristics. This study expands the application of ML in the nano-domain beyond safety-related outcomes by capturing the functional performance. Accordingly, this study has two objectives: (1) to develop a model to forecast the antioxidant efficiency of NMs to complement conventional in vitro assays and (2) to underline the lack of a comprehensive database and the scarcity of relevant data and/or data management practices in the nanotechnology field, especially with regards to functionality assessments.

Keywords: nanomaterials; nanoparticles; machine learning; antioxidant; reactive oxygen species



Citation: Mirzaei, M.; Furxhi, I.; Murphy, F.; Mullins, M. Employing Supervised Algorithms for the Prediction of Nanomaterial's Antioxidant Efficiency. *Int. J. Mol. Sci.* **2023**, *24*, 2792. <https://doi.org/10.3390/ijms24032792>

Academic Editors: Ilaria Rea, Nicola Borbone, Monica Terracciano and Chiara Tramontano

Received: 15 December 2022

Revised: 25 January 2023

Accepted: 29 January 2023

Published: 1 February 2023



Copyright: © 2023 by the authors. Licensee MDPI, Basel, Switzerland. This article is an open access article distributed under the terms and conditions of the Creative Commons Attribution (CC BY) license (<https://creativecommons.org/licenses/by/4.0/>).

1. Introduction

Reactive Oxygen Species (ROS) are molecules that contain one or more unpaired electrons in their orbitals and can lead to the formation of free radicals, e.g., superoxide ($O_2^{\bullet-}$), hydroxyl ($\bullet OH$), peroxy ($ROO\bullet$) or hydrogen peroxide H_2O_2 . ROS are generated during normal cellular functions as a by-product of aerobic metabolism and are essential to regulate physiological functions in biological systems [1]. However, exposure to exogenous factors such as heavy metals or ionizing radiation can trigger the excessive generation of ROS. The disruption of the equilibrium of ROS leads to oxidative modifications of biological systems at a molecular level, causing damage to cellular components, such as DNA, lipids and proteins. Moreover, it leads to the acceleration of cellular death which underlies several diseases [2]. Therefore, it is necessary to reduce or eliminate the excess of free radicals. Free radicals can be eliminated or detoxified by a selection of antioxidative enzymes or antioxidants [3]. Therapeutic approaches for preventing oxidative damage are currently at the core of medical research, including the use of antioxidants [4].

The antioxidant efficiency (anti-ox) is defined as the ability of molecules to scavenge the free radicals. Antioxidant compounds (natural or synthetic) control autoxidation by preventing the formation of free radicals or interrupting their spread by neutralizing them

which delays or inhibits the damage to the target cells, decreasing oxidative stress, enhancing immune function and increasing longevity [5,6]. Numerous studies have investigated the anti-ox properties of various materials [7–9]. Conventional antioxidants are designed to reduce ROS in biological systems [10]. However, clinical investigations have shown that traditional molecules provide little to no protection or even, in some instances, increase the risk of mortality [11]. Ghorbani [12] demonstrated that antioxidants show inadequate effects due to their unspecific distribution and poor retention in disease sites. Therefore, the need for an efficient, safe yet more specific antioxidant is undeniable.

Nanotechnology has gained tremendous attention due to its potential to treat diseases and it is growing rapidly within the medicinal disciplines [13–15]. Nanomaterials (NMs) are particles with unique features such as a high surface-to-volume ratio, biocompatibility, redox and catalytic properties and are used in many fields such as the pharmaceutical industry, textile, cosmetics, food, water treatment, and particularly in health-related biological fields [16–19]. Nanomedicines overcome limitations such as non-specific distribution, high renal clearance, low delivery efficiency and inadequate in vivo bioavailability [20,21].

There are numerous organic and inorganic NMs exhibiting strong ROS-scavenging activities [22,23]. Studies have demonstrated promising results in developing a novel class of antioxidants (nano-antioxidants) to overcome the challenges associated with conventional antioxidants [12]. The potential use of NMs to reduce damages related to oxidative stress and prevent diseases is the subject of intense scientific research [20,24]. The potential use of NMs in treatments of degenerative Alzheimer's disease, cancer, metabolic diseases and chronic inflammatory diseases has been reported [25,26]. Ghorbani [12] demonstrated that NMs have stable anti-ox activity with specific pharmacokinetic actions, intrinsic ROS-scavenging properties and fewer adverse effects.

In recent decades, there has been considerable interest in digitising the information in medical and pharmaceutical disciplines and the use of such data to explain biological phenomena [27]. As more data becomes available, the application of artificial intelligence (AI) becomes increasingly valuable for analysing the data. AI technology, implemented in various fields, e.g., molecular medicine, drug development and nanotechnology, provides great reproducibility and timeliness to accomplish a variety of tasks [28–30]. This approach is data intensive [31] and has been applied in fields of medicine including disease prediction [32], the discovery of new medicine [33], the prediction of drug responses [34], medicine's toxicity [35], nanotoxicity [36], antimicrobial resistance [37], antibiotic resistance [38] and the antibacterial capacity of NMs [39], to mention a few. In the era of data, machine learning (ML) models, a sub-field of AI, can improve the predictions of toxicological and functional effects and provide insights into the design of NMs and/or strategies to eliminate exposure and minimize risks, contributing to sustainable and safe-by-design approaches (SSbD) [31,40,41]. The ML approach is a promising tool as it is time- and cost-effective reducing the number of tests required while allowing the researcher to be more effective by providing them precise forecasts. Furthermore, the traditional risk assessment is transforming into digital frameworks consisting of new approach methodologies (NAMs) without the need for animal testing [42,43].

ML models have been used to predict anti-ox activities, for example, Karydas [44] successfully developed an ML model to assess cherries' free radical scavenging capacity where in their analysis they utilised the 2,2-diphenyl-1-picrylhydrazyl (DPPH) and folin-ciocalteu (FCR) lowering capacity as outputs while sensing indices, soil attributes, climatic, topographic and hydrographic data were used as input features. They employed and achieved an extreme gradient boosting (XGBoost) algorithm with an accuracy of $R^2 = 0.89$. They employed important attribute analysis using the F-score method and determined the variables that affect the antioxidant capacity of cherries. Another example is from Idowu and Fatokun [45], which examined supervised and unsupervised algorithms to correlate polyphenol's antioxidant activity (output feature) to molecular descriptors, with parameters regulating in vivo antioxidant behaviour (input features). Olsen [46] demonstrated the use of a deep convolutional neural network (CNN) to predict the anti-ox efficiency measured

by a DPPH assay based on the properties of 687 peptides. They demonstrated that the model can be used to estimate the potential of a protein's peptides to scavenge free radicals.

Given the time-consuming, expensive and work-intensive nature of NMs' synthesis, having a computational method that can predict the anti-ox properties is beneficial. In addition, due to the large number of NMs' P-chem possible combinations and the impact of experimental variables, it is not feasible to evaluate all of them using conventional laboratory tests to determine the ones with the highest capacities. In this work, we manually compiled a dataset derived from a literature review of in vitro studies in different mediums that can be used by other researchers to train models, augment the dataset with additional features, fill data gaps through grouping approaches and predict the efficiency of NMs to scavenge free radicals. Despite the limited data available [47], we explored ML tools and we were able to predict the anti-ox efficiency of NMs and we also demonstrated which attributes have a substantial impact on the predictions. To the best of our knowledge, no study has been undertaken on the use of ML tools to predict the scavenging efficiency of NMs. This novel study contributes significantly to the existing research by proposing a model that can fit the SSbD framework, in the functionality dimension [31]. This tool utilizes P-chem properties, exposure conditions and the method of NMs' synthesis preparations. A random forest algorithm demonstrated the highest accuracy, reaching an $R^2 = 0.83$.

2. Results

2.1. Data Pre-Processing

Due to high missing values among the input-related data collected, we selected NMs' type, core size, shape, dosage, coating as well as the synthesis process, medium used, absorbance and duration as the input features for the model. This data cleansing resulted in a final dataset consisting of 10 columns and 1027 rows. Table 1 shows the percentages of missing values among the initial input variables: core size (3%), HDS (78.30%), shape (15.68%), EE (90.34%), ZP (65.09%), PDI (82.05%), SA (99.51), dosage (9.86%), temperature (76.33%), pH (98.62%) and thermal stability (86.59%).

Table 1. The primary and final input variables in dataset I and dataset II.

Category	Variables	Type	DATASET I		DATASET II			
			Min-Max or Labels	Data Transformation	Methods of Determination	Missing Values %		
Physico-chem properties	Core Size	Numeric	3.7–313 (nm), NaN	Selected	3.7–313 (nm), NaN	SEM, EDX, TEM, DLS, etc.,	3.06	
	Hydrodynamic Size		32–752 (nm), NaN	Eliminated due to high NaN	–	DLS	78.30	
	Encapsulation Efficiency		59.7–237 (%), NaN		–	DLS	90.34	
	Zeta Potential		–20.6–46.8 (mV), NaN		–	DLS	65.09	
	Polydispersity Index		0.145–1.76, NaN		–	DLS	82.05	
	Surface Area		52.2–135.5 (m ² /g), NaN		–	–	99.51	
	Dosage		0–200,000 (µg/mL), NaN	Selected	0–200,000 (µg/mL), NaN	–	9.86	
	Synthesis Technique		Green, Chemical	Selected	Green, Chemical	–	–	
	Shape		Nominal	Spherical, Hexagonal, Rod, Spherical/Rod, Dendrimer, Triangular, Cubic	Selected	Spherical, Hexagonal, Rod, Spherical/Rod, Dendrimer, Triangular, Cubic	TEM, HRTEM, SEM, FESEM, EDX, XRD	15.68
	NMs' Type			Ag, ZnTe, CdTe, Chs, Se, Nd/ZnO, Au, Cu, CdSe, Chs/AL, AL, NaCas/GA, TiO ₂ , MgO, etc.,	Selected	Ag, ZnTe, CdTe, Chs, Se, Nd/ZnO, Au, Cu, CdSe, Chs/AL, etc.,	XRD, EDX, SEM, FESEM, TEM, HRTEM, etc.,	–
Coating	Allium sativum, areca catechu nut, Carboxymethyl cellulose (CMC), carboxymethyl cellulose (CMC)/curcumin, CCS, etc.,	Simplified: Transformed into Binary	Coated, Uncoated	SEM, EDX, TEM, DLS, XRD, HRTEM, STEM, FTIR	–			

Table 1. Cont.

Category	Variables	Type	DATASET I		DATASET II		
			Min-Max or Labels	Data Transformation	Methods of Determination	Missing Values %	
Exposure	Medium Used for Antioxidant Evaluation	Nominal	Extract, Solution, Emulsion, Food, Nanocomposites, Coating films	Selected	Extract, Solution, Emulsion, Food, Nanocomposites, Coating films	–	–
	Temperature	Numeric	0–37 (°C), NaN	Eliminated due to high NaN	–	–	76.33
	pH		7–7.4, NaN		–	–	98.62
	Thermal Stability		12–600, NA	–	TGA	86.59	
	Spectrophotometer Absorbance		517–540, NaN	Selected	517–540, NaN	–	–
	Duration		0–2190 (h), NaN	Selected	0–2190 (h), NaN	–	–

The HDI, EE, PDI, SA, ZP, temperature, pH and thermal stability columns were excluded due to the presence of numerous missing values. Null data in core size, dosage and shape were replaced with the mean (for numeric features) or mode value (for nominal features) [48]. Additionally, to avoid overfitting the model, the coating was transformed to a binary feature (coated and uncoated).

2.2. Model Validation

Following data homogenization and pre-processing, we trained and compared several regression models. The models are trained with the training dataset comprising 70% of the data (719 rows). Internal 10-fold cross validation is performed to optimize the hyper parameters and to ensure the models’ robustness and goodness-of-fit. Following the model training, we performed model validation using 308 rows out of 1027 (30% of data) as a test set (external validation) to evaluate the final tuned predictivity. As shown Figure 1, the external validation of the RF model outperformed the other regression models exhibiting the lowest error with MAE at 7.8, RMSE at 12.7 and the highest accuracy displaying a $R^2 = 0.83$.

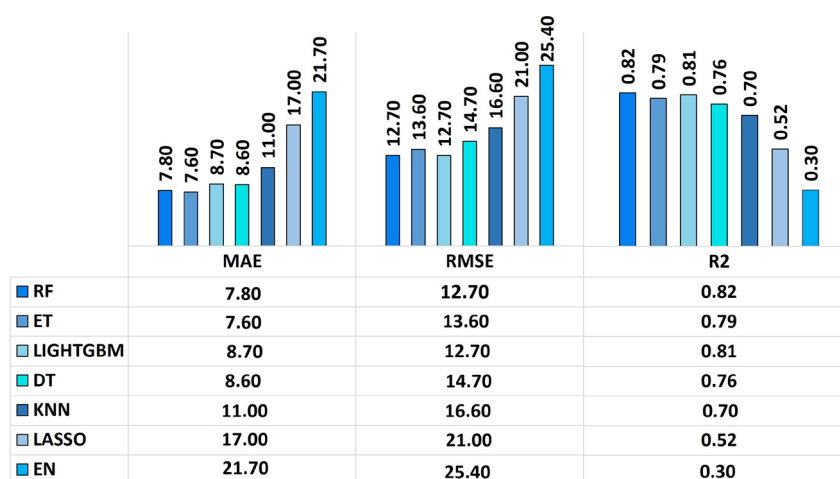


Figure 1. External models’ validation metrics from the test dataset (30%). Comparison of the seven regression models (columns used for this evaluation includes type of NMs, medium used, core-size, shape, synthesis techniques, coating, dosage, absorbance, duration).

Nonlinear regression models (RF and ET) outperform linear models (LASSO and EN) because they exhibit more parameters (properties of training data learned during the learning process). RF is excellent at processing categorical, binary and numeric features, making it ideal for working with high-dimensional data with minimal pre-processing requirements.

Figure 2 presents the validation curve of the RF algorithm derived from the internal validation dataset (70%), the values of the training and cross-validation score are close, indicating the model goodness of fit and robustness of the training model.

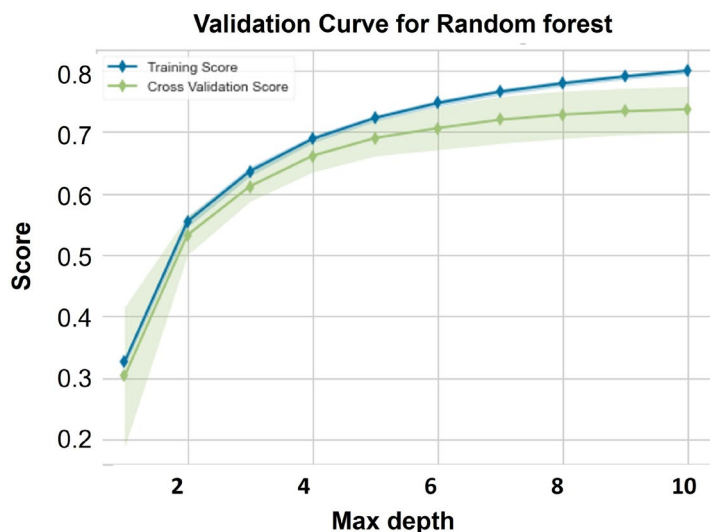


Figure 2. The internal model validation curve of RF model for the training score and the cross-validation score. x-axis represents the hyperparameter of the tree depth, y-axis represents the score (accuracy) of the model.

Depicted in Figure 3 are the prediction error of the predicted values against the actual values. It shows that the predicted values produced by our model (0.83) are close to the observed targets from the dataset. In regression models, prediction error measures how effectively the model predicts the response variable and as can be seen, the predicted values are relatively close to the actual values.

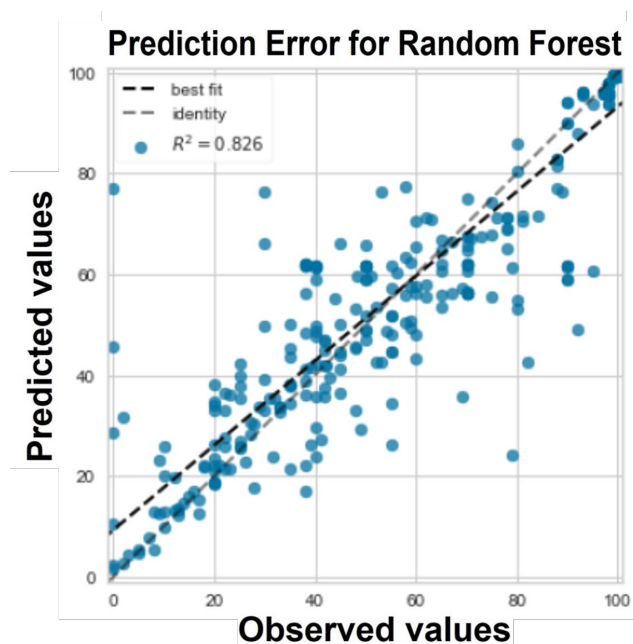


Figure 3. The prediction error by the RF regression model, the x-axis represents the actual (observed) values and the y-axis represents the predicted values.

2.3. Model Prediction

Attribute Importance

The feature importance in the RF model is calculated using the impurity Gini-based feature importance (or Mean Decrease in Impurity). Figure 4 presents the attribute importance analysis performed by RF. As illustrated, NMs' type, core-size and dosage appeared as the top three most important attributes influencing the prediction of the outcome.

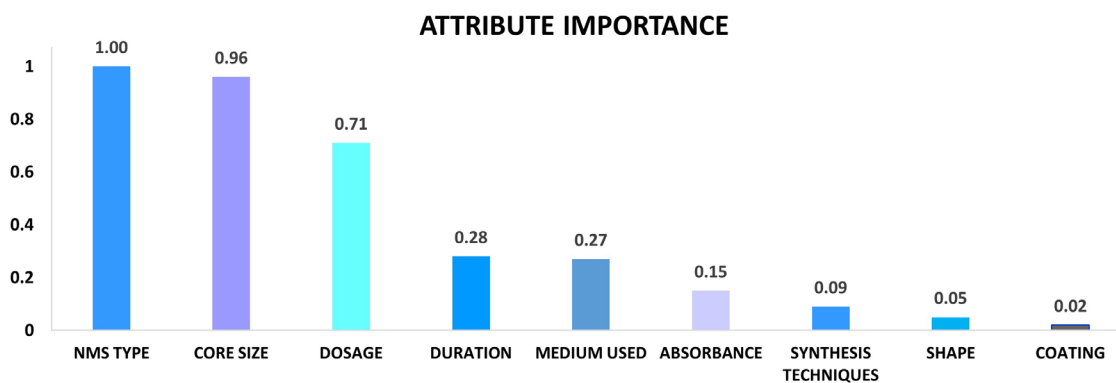


Figure 4. Attribute importance generated by random forest model, y-axis represents the variable importance from 0 to 1, x-axis represents the attributes.

The duration of exposure, the medium used and the absorbance are relatively important attributes that affect the prediction. The synthesis techniques, shape and coating (presence or absence) have relatively less effect on the prediction.

3. Discussion

The purpose of this research was initially to (i) gather data from the literature related to the anti-ox efficiency of NMs, (ii) to present the landscape of data gaps related to functionality assessments, (iii) to apply a tool to demonstrate the feasibility of ML for this outcome and iv) to identify significant factors influencing the prediction of the outcome.

Tremendous efforts are being put together to create databases with complete datasets and also many initiatives to promote the FAIR (findable, accessible, interoperable and reusable) principles are being created in the nano-domain [49,50]. To the best of our knowledge, there is no publicly accessible database that collects and summarizes data on the P-chem characteristics, functionality, application and production of NMs and at the same time links this information to safety aspects. Such a database could enhance the correlation between functionality and safety and thus support the SSbD paradigms [51]. In this study, we manually built a dataset that adheres to the FAIR principles: it is findable (10.5281/zenodo.6584826, accessed on 26 May 2022), accessible (open access), interoperable (containing the methodology and source of data as well as experimental parameters) and reusable in order to aid data scientists to accelerate the nano-informatics field. We collected data on P-chem experimental settings, such as TEM, SEM, FESEM, HRTEM, XRD, EDX, UV-vis spectroscopy and FTIR, and employed them to measure and evaluate intrinsic properties such as size, morphology, chemical composition and extrinsic properties such as encapsulation efficiency, polydispersity index and zeta potential. The various methodologies have an impact on the features' quality and homogeneity of information. However, due to the lack of data, we utilized all the available information. When more data becomes available and FAIR, attributes generated through one technique will reflect more scientifically sound choices for these modeling purposes.

To evaluate the free radical scavenging capacity, we gathered data from six different methods such as DPPH, ABTS, NO, H₂O₂, OD and metal chelating. However, we selected the DPPH assay as the outcome due to substantial missing values among the other techniques. According to the literature, ABTS and DPPH assays are recommended with

ABTS considered lengthy and expensive. It is challenging to conclude which approach is the most suitable for assessing the anti-ox activity. Bedlovičová [52] examined DPPH and ABTS assays, and they concluded that DPPH assay is inexpensive and simpler. When more information becomes available it could be feasible to utilize all the assays under one dataset if the parameters affecting the measurements become transparent with an increased variability due to data size. Another factor regarding the quality of data is the comparable measurements (unit metrics), which makes it difficult to merge a homogeneous dataset that contains all the knowledge gained through valuable experimental research. This may obstruct the advancement of a data-driven research. Thus, our work points out the shortcoming in current data management practices and reporting schemes in the field of nanotechnology. A uniform and homogenous system for reporting data on properties and experimental conditions will help to improve the quality of data and completeness.

Regarding P-chem characteristics, only 35%, 22%, 10%, 18% and 1% of the selected studies reported ZP, HDS, EE, PDI and SA of NMs, respectively. Therefore, due to a substantial number of missing values, we were unable to incorporate all these data. Therefore, for this study we employed the type of NM, medium used, core-size, shape, synthesis techniques, coating, dosage, absorbance, duration and DPPH variables. However, the performance of the models was compared by including ZP values computed with an ML missing values imputation methodology, and/or including shape (Supplementary Materials, Tables S1–S3). These properties are important in determining the activity of NMs. Regarding the core size, dosage and shape, the missing values were replaced with the mean or mode value. Thus, we stress that future research should report as many P-chem properties as feasible to allow the usage of intrinsic and/or extrinsic properties information. For experimental settings, we obtained data on the medium used, temperature, pH, thermal stability, spectrometers absorbance and exposure duration. However, the majority of them were excluded due to substantial number of missing values.

We utilized a model that adheres to OECD (organization for economic co-operation and development) principles (https://github.com/mahsa-mirzaei/NMAOP_M-M_wo-ZP-/blob/main/AOP_M%26M_wo%20ZP%20.ipynb, accessed on 18 January 2023), has a well-defined approach and is validated and built to an explicit endpoint derived from one assay [53]. The RF model surpasses all other models, with the highest R^2 value, $R^2 = 0.83$. In the nano domain, ML tools have been implemented to predict and assess the toxicity and functionality of NMs [54]. Furxhi [55] investigated NF's toxicity, whereas Mirzaei [39] and Mirzaei [56] assessed the antibacterial properties of NMs as such or coated on textiles, respectively. However, to our knowledge, no similar studies that predict the anti-ox capacity of NMs have been published. This approach is the initial step toward assisting researchers in discovering NMs with a high capacity and determining their P-chem properties and/or experimental settings. Despite these limitations, our findings are congruent with the previous literature [57–59]. The RF model's attribute importance analysis showed P-chem characteristics including type and core-size as influential variables on the prediction of the outcome, followed by shape, zeta potential and synthesis techniques. Researchers have investigated the anti-ox efficiency of numerous NMs and discovered that properties including particle core size, chemical composition, surface charge and surface coating have an impact on their anti-ox capacity [60–63]. According to Sharpe [57], the type of NM, core-size and dosage are among the most pivotal components. Fafal [59] stated that different synthesis techniques can affect the anti-ox capacity of NMs, they demonstrated that green techniques could have relatively higher activity. Nevertheless, the other characteristics such as ZP, EE and PDI can be equally valuable and play an important role. A study by Ruktanonchai [64], indicated that the ZP is a useful tool to predict the physical stability of NMs, and the PDI can show the size distributions. Kim [58] identified that particle-size, ZP, EE and PDI can enhance the release property and as a result improve the activity. One limitation of our study is the categorical representation of NMs in our dataset which are converted into binary representation through one-hot encoding. The categorical attributes can be changed only when the chemical composition of the NMs is available or swapped

with theoretical descriptors. Future studies should focus on the accurate representation of the intrinsic properties related to the composition, in order to be used with ML applications.

Significant numbers of NMs have been evaluated to date, resulting in a large pool of information scattered through the literature; it becomes increasingly challenging to analyze all NMs using traditional test methods. Accordingly, the demand for computational methods increases. We investigated inorganic and organic NMs to develop a model with good predictability ($R^2 = 0.83$). In addition to complementing conventional in vitro testing, this approach is substantially more cost-effective and time-efficient. The capacities of algorithms can be exploited to fulfill new approach methodologies [65]. Once safety can be integrated with the functionality of NMs, the modeling tools will allow the development and optimization of NMs with desired properties while ensuring worker, public and environmental safety, and functionality.

4. Materials and Methods

Figure 5 depicts an overview of the workflow followed. First, a literature review of studies investigating the efficiency of NMs via in vitro experiments was performed. P-chem properties of NMs, exposure conditions, measurement equipment-related features, characterization methodologies and assays used for assessing the anti-ox efficiency were extracted. Following an investigation of the dataset's completeness, data pre-processing was carried out, including normalization [66], one-hot encoding [67] and data split [68]. Several regression models were trained and validated using a variety of performance parameters in order to identify a model with high predictability. To train ML models, we used Scikit-learn and PyCaret library [69]. Finally, importance attribute analysis, a supervised technique that identifies and ranks the variables was used [70].

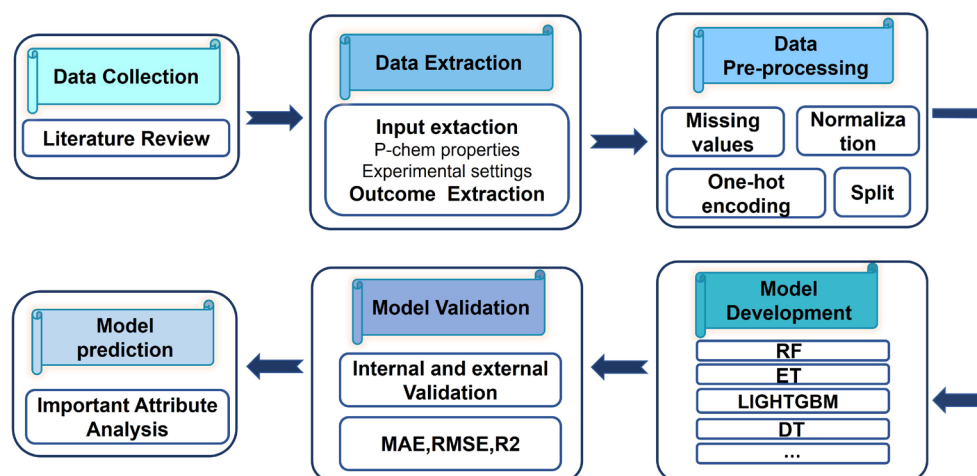


Figure 5. Model development workflow.

4.1. Data Collection

In order to compose a high-quality dataset, a great amount of data must be integrated in a harmonized fashion which is the most challenging aspect of the ML workflow. A literature search was conducted for studies that investigated NMs' antioxidant efficiency with quantitative results from 2013 to 2021. Following keywords were used 'antioxidants', 'free radicals', 'ROS', 'Oxidative stress', 'RNS', 'nanoparticles', 'nanofoms' and 'nanomaterials'. We selected 73 studies that investigated different organic and inorganic NMs with in vitro experiments. We excluded 11 studies due to binary or qualitative results. From the studies gathered, the following information was manually extracted:

Input-related collection: (1) information related to NMs' P-chem properties such as the NM type, core-size, coating, hydrodynamic size (HDS) and its polydispersity index (PDI), shape, surface area (SA), zeta potential (ZP) and encapsulation efficiency (EE); (2) ex-

perimental conditions such as the methods of NMs' synthesis such as chemical (top-down and bottom-up approach) and green (bottom down approach employing natural extracts or microorganisms and biological components as reducing agents), the culture medium for the anti-ox activity evaluation, information related to the application of the NF (pharmaceutical and food packaging, nanomedicine, etc.), pH, temperature, thermal stability, absorbance and duration of the test. In addition, the characterization methodologies used, i.e., scanning electron microscopy (SEM), field emission scanning electron microscopy (FESEM), transmission electron microscopy (TEM), high-resolution transmission electron microscopy (HRTEM), X-ray Diffraction (XRD), energy dispersive X-Ray (EDX), Fourier transform infrared spectroscopy (FTIR), dynamic light scattering (DLS) and Ultraviolet-visible spectroscopy (UV-vis spectroscopy) to evaluate the P-chem properties were collected.

Output-related collection: various assays can be used to assess the anti-ox efficiency of NPs including 2,2-diphenyl-1-picrylhydrazyl (DPPH), 2,2'-azino-bis (3-ethylbenzothiazoline-6-sulfonic acid (ABTS), nitric oxide (NO) or total radical-trapping antioxidant potential (TRAP). After collecting the above information, we selected the DPPH assay that measures the anti-ox efficiency of NMs as the output to be predicted, since it is the most popular, rapid, inexpensive and simple test [69]. In addition, the DPPH assay appeared as the most frequent assay (resulting in sufficient data points for modelling purposes) in the literature search and by choosing one assay we reflect the homogeneity of the experimental data measurements.

4.2. Model Development

Data pre-processing: PyCaret executes missing value imputation and categorical one-hot encoding. The missing values in the numerical features are replaced with the mean value of the features in the training dataset, whereas the missing values in categorical features are imputed with the most frequent or the mode value [70]. Rafsunjani [48] compared several imputation techniques and found that mean imputation performed the best for handling missing values. One-hot encoding was performed since regression models cannot handle categorical features. Normalization was used to rescale numerical values to reduce the impact of magnitude in the deviation without altering the differences in the range of values. The dataset was split into training (internal, 70% of the dataset to fit the model and to test goodness of fit) and test set (external, 30% of the dataset for evaluation of predictability).

Model development: We trained several regression models including Random Forest (RF), Light Gradient Boosting Machine (LIGHTGBM), Extra Trees (ET), Decision Tree (DT), K-Nearest Neighbors (KNN), Least Absolute Shrinkage And Selection Operator (LASSO), Elastic Net (EN) Least Angle Regression (LAR), passive aggressive regressor (PAR), Lasso Least Angle Regression (LLAR), Huber Regressor (HUBER), Adaboost Regressor (ADA), Bayesian Ridge (BR), Ridge Regression (RIDGE), Gradient Boosting Machine (GBM) and Orthogonal Matching Pursuit (OMP). All models were evaluated and compared to find the best model with good predictivity. The following seven models are selected for reporting in this study: RF is a supervised algorithm that employs both decision trees and bagging techniques. These decision trees organize attributes by arranging them by their values. RF executes feature selection, each tree calculates the significance of a feature based on its ability to improve the integrity of the leaves [71]. LIGHTGBM is a gradient boosting algorithm that uses decision trees. Different data points play different roles in the computation of the information gain. Higher gradient data points will have a greater influence on the information acquisition [49]. ET algorithm generates a large number of the unpruned decision or regression trees from the training dataset and then combines the predictions of multiple decision trees. ET possess similar properties as RF, randomly samples the features at each split point. Nevertheless, differs from RF, where it splits nodes by selecting cut-points entirely at random and fits each decision tree to the entire training dataset [50]. DT is a decision support technique that employs a binary model to display the hidden association between the input and outputs, also known as a pattern recognition capable of categorizing input variables into categories. It has some limitations such as failing to recognize the

impact of weak attributes [51]. The KNN technique works on the principle that comparable/similar samples exist in the vicinity and have a higher probability. KNN approach finds distances between a new data point and all existing training data points, then selects the nearest data points (k) to the query [52]. LASSO is used for the regularization of data models. It conducts feature selection and can minimize model complexity while preventing overfitting. It executes L1 penalty, providing a type of automatic feature selection that has the effect of shrinkage of coefficients and thus input variables that do not provide much to the prediction set to zero [53]. EN is a standardized or penalized linear regression approach that is commonly used to solve high-dimensional feature space regression problems. EN automatically chooses variables, promoting continuous shrinkage [54].

Model validation: 10-fold cross-validation was performed on the training set (70%) to optimize the hyperparameters and to ensure robustness. The mean absolute error (MAE), root mean square error (RMSE) and coefficient of determination (R^2) were employed to assess the performance of the models. In addition, the external data (30% of data) was used to assess the predictability of the models.

Attributes importance: A supervised approach that ranks features that are important for predicting the outcome was performed once the best model was selected [55]. The value of attributes varies from 0 to 1, with 1 representing the most information gain. In a regression model, the concept of “variance reduction” is used to guide the feature selection for internal nodes. Thus, we can evaluate how each feature reduces the impurity of the split (the feature with the highest reduction is chosen for the internal node). We measure the average impurity reduction for each feature across all trees in the RF model representing the feature relevance:

$$I_g(f) = \sum_M w_{p,n} \sum_M \Delta i_f(\tau, M)$$

where I_g is the Gini importance which identifies the frequency of a particular feature (f) chosen for the split and the importance of the feature's value. Gini impurity reduction resulting from any peak split $\Delta i_f(\tau, M)$ is assembled individually for each feature nodes τ in the M number of weighted trees in the forest [71].

5. Conclusions

Researchers from multiple domains are interested in the application of nano-antioxidants for the prevention and treatment of oxidative stress-mediated disorders. We demonstrate the application of an RF algorithm to predict the efficiency of nano-antioxidants. The attribute importance analysis demonstrated the NMs' P-chem characteristics such as type and core-size to have a significant impact on the predictions along with the exposure concentration (dosage). Furthermore, this paper emphasizes the significance of a consistent and systematic reporting structure and comparable measurement techniques indicating that their absence can result in an obstacle for modelling purposes. This is an important finding for policymakers and research funding bodies alike. The ability to predict functionalities represents a great opportunity in the healthcare field. Additionally, it will assist insurers and other stakeholders in the healthcare ecosystem to determine whether it is safe and beneficial (profitable) to invest in the development of nano-antioxidant therapies. Future research should therefore attempt to address this challenge through data capturing templates from empirical researchers that facilitate the construction of a comprehensive dataset.

Supplementary Materials: The following supporting information can be downloaded at: <https://www.mdpi.com/article/10.3390/ijms24032792/s1>.

Author Contributions: Conceptualization, M.M. (Mahsa Mirzaei) and I.F.; methodology, M.M. (Mahsa Mirzaei); formal analysis, M.M. (Mahsa Mirzaei); data curation, M.M. (Mahsa Mirzaei); writing—original draft preparation M.M. (Mahsa Mirzaei); writing—review and editing, F.M. and M.M. (Martin Mullins); visualization, M.M. (Mahsa Mirzaei) and I.F.; supervision, I.F., F.M. and M.M. (Martin Mullins); funding acquisition: I.F. All authors have read and agreed to the published version of the manuscript.

Funding: This research was funded by the European Union's Horizon 2020 research and innovation programme under grant agreement no. 862444.

Institutional Review Board Statement: Not applicable.

Informed Consent Statement: Not applicable.

Data Availability Statement: Dataset available at: 10.5281/zenodo.6584826, accessed on 26 May 2022.

Conflicts of Interest: The authors declare no conflict of interest.

References

1. Mittler, R. ROS are good. *Trends Plant Sci.* **2017**, *22*, 11–19. [CrossRef] [PubMed]
2. Sies, H.; Jones, D.P. Reactive oxygen species (ROS) as pleiotropic physiological signalling agents. *Nat. Rev. Mol. Cell Biol.* **2020**, *21*, 363–383. [CrossRef] [PubMed]
3. Di Meo, S.; Venditti, P. Evolution of the knowledge of free radicals and other oxidants. *Oxidative Med. Cell Longev.* **2020**, *2020*, 9829176. [CrossRef]
4. Alkadi, H. A review on free radicals and antioxidants. *Infect. Disord. -Drug Targets* **2020**, *20*, 16–26.
5. Gulcin, İ. Antioxidants and antioxidant methods: An updated overview. *Arch. Toxicol.* **2020**, *94*, 651–715. [CrossRef] [PubMed]
6. Mirzaei, A.; Mirzaei, M.; Mirzaei, N. Antioxidant activity of the Pistacia atlantica in carbon tetrachloride intoxicated rats in Iran. *Clin. Biochem.* **2011**, *44*, S329–S330. [CrossRef]
7. Mirzaei, A.; Mohammadi, J.; Mirzaei, N.; Mirzaei, M. The Antioxidant Capacities and Total Phenolic Contents of Some Medicinal Plants in Iran. *J. Adv. Biomed. Sci.* **2011**, *1*, 160–167.
8. Mirzaei, A.; Toori, M.A.; Mirzaei, N.; Shirazi, R.G. Antioxidant, antimicrobial and antimutogenic potential of 4 Iranian medicinal plants. *Life Sci. J.* **2013**, *10*, 1085–1091.
9. Toori, M.A.; Mirzaei, M.; Mirzaei, N.; Lamrood, P.; Mirzaei, A. Antioxidant and hepatoprotective effects of the internal layer of oak fruit (Jaft). *J. Med. Plants Res.* **2013**, *7*, 24–28.
10. Poprac, P.; Jomova, K.; Simunkova, M.; Kollar, V.; Rhodes, C.J.; Valko, M. Targeting Free Radicals in Oxidative Stress-Related Human Diseases. *Trends Pharm. Sci.* **2017**, *38*, 592–607. [CrossRef]
11. Morry, J.; Ngamcherdtrakul, W.; Yantasee, W. Oxidative stress in cancer and fibrosis: Opportunity for therapeutic intervention with antioxidant compounds, enzymes, and nanoparticles. *Redox Biol.* **2017**, *11*, 240–253. [CrossRef] [PubMed]
12. Ghorbani, M.; Derakhshankhah, H.; Jafari, S.; Salatin, S.; Dehghanian, M.; Falahati, M.; Ansari, A. Nanozyme antioxidants as emerging alternatives for natural antioxidants: Achievements and challenges in perspective. *Nano Today* **2019**, *29*, 100775. [CrossRef]
13. Zhou, J.; Kroll, A.V.; Holay, M.; Fang, R.H.; Zhang, L. Biomimetic nanotechnology toward personalized vaccines. *Adv. Mater.* **2020**, *32*, 1901255. [CrossRef] [PubMed]
14. Doroudian, M.; MacLoughlin, R.; Poynton, F.; Prina-Mello, A.; Donnelly, S.C. Nanotechnology based therapeutics for lung disease. *Thorax* **2019**, *74*, 965–976. [CrossRef]
15. Grodzinski, P.; Kircher, M.; Goldberg, M.; Gabizon, A. *Integrating Nanotechnology into Cancer Care*; ACS Nano, National Cancer Institute, National Institutes of Health: Rockville, MD, USA, 2019; Volume 13, pp. 7370–7376.
16. Ijaz, I.; Gilani, E.; Nazir, A.; Bukhari, A. Detail review on chemical, physical and green synthesis, classification, characterizations and applications of nanoparticles. *Green Chem. Lett. Rev.* **2020**, *13*, 223–245. [CrossRef]
17. Liandi, A.R.; Cahyana, A.H.; Yunarti, R.T.; Wendari, T.P. Facile synthesis of magnetic Fe₃O₄@Chitosan nanocomposite as environmentally green catalyst in multicomponent Knoevenagel-Michael domino reaction. *Ceram. Int.* **2022**, *48*, 20266–20274. [CrossRef]
18. Nelson, B.C.; Johnson, M.E.; Walker, M.L.; Riley, K.R.; Sims, C.M. Antioxidant Cerium Oxide Nanoparticles in Biology and Medicine. *Antioxidants* **2016**, *5*, 15. [CrossRef]
19. Fadaka, A.; Aluko, O.; Awawu, S.; Theledi, K. Green Synthesis of Gold Nanoparticles using Pimenta dioica Leaves Aqueous Extract and Their Application as Photocatalyst, Antioxidant, and Antibacterial Agents. *J. Multidiscip. Appl. Nat. Sci.* **2021**, *1*, 78–88. [CrossRef]
20. Kumar, H.; Bhardwaj, K.; Nepovimova, E.; Kuča, K.; Singh Dhanjal, D.; Bhardwaj, S.; Bhatia, S.K.; Verma, R.; Kumar, D. Antioxidant functionalized nanoparticles: A combat against oxidative stress. *Nanomaterials* **2020**, *10*, 1334. [CrossRef]
21. Khalil, I.; Yehye, W.A.; Etxeberria, A.E.; Alhadi, A.A.; Dezfooli, S.M.; Julkapli, N.B.M.; Basirun, W.J.; Seyfoddin, A. Nanoantioxidants: Recent Trends in Antioxidant Delivery Applications. *Antioxid.* **2019**, *9*, 24. [CrossRef] [PubMed]
22. Valgimigli, L.; Baschieri, A.; Amorati, R. Antioxidant activity of nanomaterials. *J. Mater. Chem. B* **2018**, *6*, 2036–2051. [CrossRef]
23. Saravanakumar, G.; Kim, J.; Kim, W.J. Reactive-Oxygen-Species-Responsive Drug Delivery Systems: Promises and Challenges. *Adv. Sci.* **2017**, *4*, 1600124. [CrossRef]
24. Jampilek, J.; Kralova, K. Potential of nanonutraceuticals in increasing immunity. *Nanomaterials* **2020**, *10*, 2224. [CrossRef] [PubMed]
25. Rehman, A.; John, P.; Bhatti, A. Biogenic Selenium Nanoparticles: Potential Solution to Oxidative Stress Mediated Inflammation in Rheumatoid Arthritis and Associated Complications. *Nanomaterials* **2021**, *11*, 2005. [CrossRef] [PubMed]

26. Chauhan, P.S.; Tayal, S.; Jha, N. Nano-Antioxidants, A Next-Generation Therapeutic Strategy. In *Antioxidant-Based Therapies for Disease Prevention and Management*; Apple Academic Press: New York, NY, USA, 2021; pp. 1–20.
27. Hamet, P.; Tremblay, J. Artificial intelligence in medicine. *Metabolism* **2017**, *69*, S36–S40. [CrossRef] [PubMed]
28. Ibrahim, I.; Abdulazeez, A. The role of machine learning algorithms for diagnosing diseases. *J. Appl. Sci. Technol. Trends* **2021**, *2*, 10–19. [CrossRef]
29. Patel, V.; Shah, M. Artificial intelligence and machine learning in drug discovery and development. *Intell. Med.* **2022**, *2*, 134–140. [CrossRef]
30. OECD. Available online: <https://oecd.ai/en/dashboards/policy-areas/PA11> (accessed on 28 January 2023).
31. Furxhi, I.; Perucca, M.; Blosi, M.; Lopez de Ipiña, J.; Oliveira, J.; Murphy, F.; Costa, A.L. ASINA Project: Towards a Methodological Data-Driven Sustainable and Safe-by-Design Approach for the Development of Nanomaterials. *Front. Bioeng. Biotechnol.* **2022**, *9*, 805096. [CrossRef] [PubMed]
32. Dahiwade, D.; Patle, G.; Meshram, E. Designing Disease Prediction Model Using Machine Learning Approach. In Proceedings of the 2019 3rd International Conference on Computing Methodologies and Communication (ICCMC), Erode, India, 27–29 March 2019; pp. 1211–1215.
33. Carracedo-Reboredo, P.; Liñares-Blanco, J.; Rodríguez-Fernández, N.; Cedrón, F.; Novoa, F.J.; Carballal, A.; Maojo, V.; Pazos, A.; Fernandez-Lozano, C. A review on machine learning approaches and trends in drug discovery. *Comput. Struct. Biotechnol. J.* **2021**, *19*, 4538–4558. [CrossRef] [PubMed]
34. Adam, G.; Rampášek, L.; Safikhani, Z.; Smirnov, P.; Haibe-Kains, B.; Goldenberg, A. Machine learning approaches to drug response prediction: Challenges and recent progress. *npj Precis. Oncol.* **2020**, *4*, 19. [CrossRef]
35. Pu, L.; Naderi, M.; Liu, T.; Wu, H.-C.; Mukhopadhyay, S.; Brylinski, M. eToxPred: A machine learning-based approach to estimate the toxicity of drug candidates. *BMC Pharmacol. Toxicol.* **2019**, *20*, 2. [CrossRef] [PubMed]
36. Furxhi, I.; Murphy, F. Predicting in vitro neurotoxicity induced by nanoparticles using machine learning. *Int. J. Mol. Sci.* **2020**, *21*, 5280. [CrossRef] [PubMed]
37. Chowdhury, A.S.; Call, D.R.; Broschat, S.L. PARGT: A software tool for predicting antimicrobial resistance in bacteria. *Sci. Rep.* **2020**, *10*, 11033. [CrossRef]
38. Li, L.-G.; Yin, X.; Zhang, T. Tracking antibiotic resistance gene pollution from different sources using machine-learning classification. *Microbiome* **2018**, *6*, 93. [CrossRef]
39. Mirzaei, M.; Furxhi, I.; Murphy, F.; Mullins, M. A machine learning tool to predict the antibacterial capacity of nanoparticles. *Nanomaterials* **2021**, *11*, 1774. [CrossRef] [PubMed]
40. Tsalidis, G.A.; Soeteman-Hernández, L.G.; Noorlander, C.W.; Saedy, S.; van Ommen, J.R.; Vijver, M.G.; Korevaar, G. Safe-and-Sustainable-by-Design Framework Based on a Prospective Life Cycle Assessment: Lessons Learned from a Nano-Titanium Dioxide Case Study. *Int. J. Environ. Res. Public Health* **2022**, *19*, 4241. [CrossRef]
41. Gottardo, S.; Mech, A.; Drbohlavová, J.; Małyska, A.; Bøwadt, S.; Riego Sintes, J.; Rauscher, H. Towards safe and sustainable innovation in nanotechnology: State-of-play for smart nanomaterials. *NanoImpact* **2021**, *21*, 100297. [CrossRef]
42. Stucki, A.O.; Barton-Maclaren, T.S.; Bhuller, Y.; Henriquez, J.E.; Henry, T.R.; Hirn, C.; Miller-Holt, J.; Nagy, E.G.; Perron, M.M.; Ratzlaff, D.E.; et al. Use of new approach methodologies (NAMs) to meet regulatory requirements for the assessment of industrial chemicals and pesticides for effects on human health. *Front. Toxicol.* **2022**, *4*, 964553. [CrossRef]
43. Ramanarayanan, T.; Szarka, A.; Flack, S.; Hinderliter, P.; Corley, R.; Charlton, A.; Pyles, S.; Wolf, D. Application of a new approach method (NAM) for inhalation risk assessment. *Regul. Toxicol. Pharmacol.* **2022**, *133*, 105216. [CrossRef]
44. Karydas, C.; Iatrou, M.; Kouretas, D.; Patouna, A.; Iatrou, G.; Lazos, N.; Gewehr, S.; Tseni, X.; Tekos, F.; Zartaloudis, Z.; et al. Prediction of antioxidant activity of cherry fruits from UAS multispectral imagery using machine learning. *Antioxidants* **2020**, *9*, 156. [CrossRef]
45. Idowu, S.O.; Fatokun, A.A. Artificial Intelligence (AI) to the Rescue: Deploying Machine Learning to Bridge the Biorelevance Gap in Antioxidant Assays. *SLAS Technol. Transl. Life Sci. Innov.* **2020**, *26*, 16–25. [CrossRef]
46. Olsen, T.H.; Yesiltas, B.; Marin, F.I.; Pertseva, M.; García-Moreno, P.J.; Gregersen, S.; Overgaard, M.T.; Jacobsen, C.; Lund, O.; Hansen, E.B.; et al. AnOxPePred: Using deep learning for the prediction of antioxidative properties of peptides. *Sci. Rep.* **2020**, *10*, 21471. [CrossRef] [PubMed]
47. Furxhi, I. Health and environmental safety of nanomaterials: O Data, Where Art Thou? *NanoImpact* **2022**, *25*, 100378. [CrossRef] [PubMed]
48. Rafsunjani, S.; Safa, R.S.; Al Imran, A.; Rahim, M.S.; Nandi, D. An empirical comparison of missing value imputation techniques on APS failure prediction. *Int. J. Inf. Technol. Comput. Sci* **2019**, *2*, 21–29. [CrossRef]
49. Thompson, M.; Burger, K.; Kaliyaperumal, R.; Roos, M.; da Silva Santos, L.O.B. Making FAIR easy with FAIR tools: From creolization to convergence. *Data Intell.* **2020**, *2*, 87–95. [CrossRef]
50. Wilkinson, M.D.; Dumontier, M.; Aalbersberg, I.J.; Appleton, G.; Axton, M.; Baak, A.; Blomberg, N.; Boiten, J.-W.; da Silva Santos, L.B.; Bourne, P.E.; et al. The FAIR Guiding Principles for scientific data management and stewardship. *Sci. Data* **2016**, *3*, 160018. [CrossRef] [PubMed]
51. Tavernaro, I.; Dekkers, S.; Soeteman-Hernández, L.G.; Herbeck-Engel, P.; Noorlander, C.; Kraegeloh, A. Safe-by-Design part II: A strategy for balancing safety and functionality in the different stages of the innovation process. *NanoImpact* **2021**, *24*, 100354. [CrossRef]

52. Bedlovicova, Z.; Strapac, I.; Balaz, M.; Salayova, A. A Brief Overview on Antioxidant Activity Determination of Silver Nanoparticles. *Molecules* **2020**, *25*, 3191. [CrossRef]
53. Gramatica, P. Principles of QSAR modeling: Comments and suggestions from personal experience. *Int. J. Quant. Struct.-Prop. Relatsh.* **2020**, *5*, 61–97. [CrossRef]
54. Furxhi, I.; Murphy, F.; Mullins, M.; Arvanitis, A.; Poland, C.A. Practices and trends of machine learning application in nanotoxicology. *Nanomaterials* **2020**, *10*, 116. [CrossRef]
55. Furxhi, I.; Murphy, F.; Mullins, M.; Poland, C.A. Machine learning prediction of nanoparticle in vitro toxicity: A comparative study of classifiers and ensemble-classifiers using the Copeland Index. *Toxicol. Lett.* **2019**, *312*, 157–166. [CrossRef] [PubMed]
56. Mirzaei, M.; Furxhi, I.; Murphy, F.; Mullins, M. A Supervised Machine-Learning Prediction of Textile's Antimicrobial Capacity Coated with Nanomaterials. *Coatings* **2021**, *11*, 1532. [CrossRef]
57. Sharpe, E.; Andreescu, D.; Andreescu, S. Artificial Nanoparticle Antioxidants. In *Oxidative Stress: Diagnostics, Prevention, and Therapy*; American Chemical Society: Washington, DC, USA, 2011; Volume 1083, pp. 235–253.
58. Kim, E.S.; Baek, Y.; Yoo, H.J.; Lee, J.S.; Lee, H.G. Chitosan-Tripolyphosphate Nanoparticles Prepared by Ionic Gelation Improve the Antioxidant Activities of Astaxanthin in the In Vitro and In Vivo Model. *Antioxidants* **2022**, *11*, 479. [CrossRef] [PubMed]
59. Fafal, T.; Taştan, P.; Tüzün, B.; Ozyazici, M.; Kivcak, B. Synthesis, characterization and studies on antioxidant activity of silver nanoparticles using *Asphodelus aestivus* Brot. *aerial part extract*. *South Afr. J. Bot.* **2017**, *112*, 346–353. [CrossRef]
60. Sandhir, R.; Yadav, A.; Sunkaria, A.; Singhal, N. Nano-antioxidants: An emerging strategy for intervention against neurodegenerative conditions. *Neurochem. Int.* **2015**, *89*, 209–226. [CrossRef]
61. Cîrcu, M.; Nan, A.; Borodi, G.; Liebscher, J.; Turcu, R. Refinement of magnetite nanoparticles by coating with organic stabilizers. *Nanomaterials* **2016**, *6*, 228. [CrossRef]
62. Samuel, E.L.; Duong, M.T.; Bitner, B.R.; Marciano, D.C.; Tour, J.M.; Kent, T.A. Hydrophilic carbon clusters as therapeutic, high-capacity antioxidants. *Trends Biotechnol.* **2014**, *32*, 501–505. [CrossRef]
63. Verma, A.K. Anti-oxidant activities of biopolymeric nanoparticles: Boon or bane. *J. Pharm. Res.* **2014**, *8*, 871–876.
64. Ruktanonchai, U.; Bejrapha, P.; Sakulkhu, U.; Opanasopit, P.; Bunyapraphatsara, N.; Junyaprasert, V.; Puttipipatkachorn, S. Physicochemical Characteristics, Cytotoxicity, and Antioxidant Activity of Three Lipid Nanoparticulate Formulations of Alpha-lipoic Acid. *AAPS PharmSciTech* **2009**, *10*, 227. [CrossRef] [PubMed]
65. Ball, N.; Bars, R.; Botham, P.A.; Cuciureanu, A.; Cronin, M.T.D.; Doe, J.E.; Dudzina, T.; Gant, T.W.; Leist, M.; van Ravenzwaay, B. A framework for chemical safety assessment incorporating new approach methodologies within REACH. *Arch. Toxicol.* **2022**, *96*, 743–766. [CrossRef]
66. Jo, J.-M. Effectiveness of normalization pre-processing of big data to the machine learning performance. *J. Korea Inst. Electron. Commun. Sci.* **2019**, *14*, 547–552. [CrossRef]
67. Seger, C. *An Investigation of Categorical Variable Encoding Techniques in Machine Learning: Binary Versus One-Hot and Feature Hashing*; EECS: Stockholm, Sweden, 2018; p. 34. Available online: <http://urn.kb.se/resolve?urn=urn:nbn:se:kth:diva-237426> (accessed on 28 January 2023).
68. Brownlee, J. *Data Preparation for Machine Learning Data Cleaning, Feature Selection, and Data Transforms in Python*; Machine Learning Mastery: San Juan, Argentina, 2020.
69. Pedregosa, F.; Varoquaux, G.; Gramfort, A.; Michel, V.; Thirion, B.; Grisel, O.; Blondel, M.; Prettenhofer, P.; Weiss, R.; Dubourg, V. Scikit-learn: Machine learning in Python. *J. Mach. Learn. Res.* **2011**, *12*, 2825–2830.
70. Mishra, S.; Mallick, P.K.; Tripathy, H.K.; Bhoi, A.K.; González-Briones, A. Performance Evaluation of a Proposed Machine Learning Model for Chronic Disease Datasets Using an Integrated Attribute Evaluator and an Improved Decision Tree Classifier. *Appl. Sci.* **2020**, *10*, 8137. [CrossRef]
71. Disha, R.A.; Waheed, S. Performance analysis of machine learning models for intrusion detection system using Gini Impurity-based Weighted Random Forest (GIWRF) feature selection technique. *Cybersecurity* **2022**, *5*, 1. [CrossRef]

Disclaimer/Publisher's Note: The statements, opinions and data contained in all publications are solely those of the individual author(s) and contributor(s) and not of MDPI and/or the editor(s). MDPI and/or the editor(s) disclaim responsibility for any injury to people or property resulting from any ideas, methods, instructions or products referred to in the content.



Article

3D Printed Graphene-PLA Scaffolds Promote Cell Alignment and Differentiation

Matteo Gasparotto ^{1,†} , Pietro Bellet ^{1,†}, Giorgia Scapin ^{2,*}, Rebecca Busetto ¹, Chiara Rampazzo ³ ,
Libero Vitiello ^{3,4,5} , Dhvanit Indravadan Shah ² and Francesco Filippini ^{1,*}

- ¹ Synthetic Biology and Biotechnology Unit, Department of Biology, University of Padua, 35131 Padua, Italy; matteo.gasparotto.1@phd.unipd.it (M.G.); pieter.bellet@studenti.unipd.it (P.B.); rebecca.busetto@studenti.unipd.it (R.B.)
- ² Garuda Therapeutics, Cambridge, MA 02142, USA; dhvanit.shah@garudatx.com
- ³ Department of Biology, University of Padua, 35131 Padua, Italy; chiara.rampazzo.1@unipd.it (C.R.); libero.vitiello@unipd.it (L.V.)
- ⁴ Interuniversity Institute of Myology (IIM), Administrative headquarters University of Perugia, Piazza Lucio Severi 1, 06132 Perugia, Italy
- ⁵ Inter-Departmental Research Center for Myology (CIR-Myo), University of Padua, 35131 Padua, Italy
- * Correspondence: giorgia.scapin@garudatx.com (G.S.); francesco.filippini@unipd.it (F.F.)
- † These authors contributed equally to this work.

Abstract: Traumas and chronic damages can hamper the regenerative power of nervous, muscle, and connective tissues. Tissue engineering approaches are promising therapeutic tools, aiming to develop reliable, reproducible, and economically affordable synthetic scaffolds which could provide sufficient biomimetic cues to promote the desired cell behaviour without triggering graft rejection and transplant failure. Here, we used 3D-printing to develop 3D-printed scaffolds based on either PLA or graphene@PLA with a defined pattern. Multiple regeneration strategies require a specific orientation of implanted and recruited cells to perform their function correctly. We tested our scaffolds with induced pluripotent stem cells (iPSC), neuronal-like cells, immortalised fibroblasts and myoblasts. Our results demonstrated that the specific “lines and ridges” 100 µm-scaffold topography is sufficient to promote myoblast and fibroblast cell alignment and orient neurites along with the scaffolds line pattern. Conversely, graphene is critical to promote cells differentiation, as seen by the iPSC commitment to neuroectoderm, and myoblast fusions into multinuclear myotubes achieved by the 100 µm scaffolds containing graphene. This work shows the development of a reliable and economical 3D-printed scaffold with the potential of being used in multiple tissue engineering applications and elucidates how scaffold micro-topography and graphene properties synergistically control cell differentiation.

Keywords: graphene; G+; PLA; Grafylon; scaffold; neuronal differentiation; stem cells; 3D printing; regenerative medicine



Citation: Gasparotto, M.; Bellet, P.; Scapin, G.; Busetto, R.; Rampazzo, C.; Vitiello, L.; Shah, D.I.; Filippini, F. 3D Printed Graphene-PLA Scaffolds Promote Cell Alignment and Differentiation. *Int. J. Mol. Sci.* **2022**, *23*, 1736. <https://doi.org/10.3390/ijms23031736>

Academic Editors:
Monica Terracciano, Ilaria Rea,
Nicola Borbone and
Chiara Tramontano

Received: 14 December 2021

Accepted: 31 January 2022

Published: 3 February 2022

Publisher's Note: MDPI stays neutral with regard to jurisdictional claims in published maps and institutional affiliations.



Copyright: © 2022 by the authors. Licensee MDPI, Basel, Switzerland. This article is an open access article distributed under the terms and conditions of the Creative Commons Attribution (CC BY) license (<https://creativecommons.org/licenses/by/4.0/>).

1. Introduction

It is the well-known features of the tissue environment, such as the mechanical, electrical, and molecular cues, which play a pivotal role in regulating cell differentiation, proliferation, shape and orientation. Therefore, the ability of scaffolds to mimic tissue environmental stimuli is crucial in regenerative medicine and tissue engineering projects [1]. Decellularised tissues from animal donors or human cadavers are promising ‘physiological’ scaffolds encapsulating the natural composition and the three-dimensional organisation of the extracellular matrix (ECM) [2]; however, antigens from such scaffolds may elicit adverse immune responses leading to transplant failure [3], and the batch-to-batch variability would impair the reliability of protocols and results [4]. To alleviate these issues, in recent years the focus has switched to the design and development of synthetic biocompatible polymers

and nanocomposites which represent a much more attractive option for drug delivery, biosensors and tissue engineering applications [5]. Among them, Poly-L-Lactic Acid (PLA) has proven reliable for tissue engineering manufacturing, as it shows low immunogenicity, batch variation and easy modulation of its physical and biochemical features by blending with different nanofillers [6].

PLA-based scaffolds are self-standing and can be used for cell growth and differentiation. In vivo, bare PLA is degraded by non-enzymatic hydrolysis of ester bonds [7]. Although it is fully reabsorbed, degradation rate is very slow, and PLA residues can be detected up to 5.5 years in the human body even after it loses its functions as biomaterial [8]. Such features make PLA scaffolds suitable for planned reabsorption [9] and are therefore the preferred base materials for the fabrication of artificial tissue or scaffolds for tissue regeneration [10].

Since cells have micro and nanoscale sensitivity and are able to respond to an extracellular environment presenting a variety of spatially defined cues in the sub-micron to micron scale, the incorporation of nanomaterial in biocompatible polymers greatly improves the scaffold performance by mimicking the multiple environmental stimuli of the chosen tissue [4,11]. Among the plethora of nanomaterials available, graphene and its derivatives are attractive candidates for developing tissue engineering scaffolds due to their tuneable electrical conductivity, excellent mechanical properties, biocompatibility, chemically modifiable surface, and nanoscale dimension matching cell surface receptors and extracellular matrix (ECM) nanotopography [12]. Graphene consists of a two-dimensional monolayer of sp^2 hybridised carbon atoms bonded in a hexagonal lattice [13]. Although its physico-chemical properties make it an attractive material in several fields [14–16], its use for biological applications has been shown to have a dose- and time-dependent toxicity [17–19]. Since its first discovery, several derivatives, including graphene oxide (GO) and reduced graphene oxide (rGO) have been developed to both reduce fabrication costs and modulate physico-chemical properties [20–22]. Particularly, properties of graphene-based nanomaterials (GBN) are strongly influenced by several factors, including shape, size, lateral dimension, surface chemistry and defect density. GO and rGO based nanomaterials are less hydrophobic than graphene-based ones, thus showing reduced aggregation and improved biocompatibility; however, toxicity of bare GBN is still a matter of concern. For instance, cytotoxicity of GO flakes used for neuronal differentiation of stem cells has been found to be strongly dependent on flake dimensionality, whereas surface roughness was responsible for better cell attachment and proliferation [23]. Surfaces with large flakes of GO or rGO are the most biocompatible for mesenchymal stem cells propagation and do not affect their proliferation and survival [24]. It has been shown that incorporation of GBN into polymeric matrices can further reduce their toxicity and, at the same time, improve properties of the dispersing matrix [25].

In neural regenerative projects, incorporation of graphene in polymeric scaffolds endows them with nanoroughness, which contributes to cell anchoring and modulation of cell morphology, and allows the establishment of tight contact with the growth cone that guides the spreading of developing neurites [26]. Since for regenerating axons it is critical to reach their correct targets, the development of scaffolds incorporating patterns of graphene could provide the physical guidance cues to allow neurite elongation facilitating nerve formation [27]. In addition, neuronal differentiation of stem cells or precursor cells is boosted by electrically conductive scaffolds mimetic of the neural tissue electroactive properties [12,28,29]. As graphene is electrically conductive and its conductivity is stable in biological environments, its incorporation in polymeric scaffolds can reduce the polymer electrical resistance and offer a permissive environment for neuronal differentiation.

Electrical and nanotopographical stimuli are not only important for the neuronal cell physiology but also play a vital role in multiple cellular process like myoblast fusion and wound healing. After skeletal muscle injury, myoblast precursors first migrate to the damaged site, then they align longitudinally, and finally they fuse their membranes to form multinuclear myotubes [30]. Since such geometrical directionality has a close relationship

with function, the simulation of the ECM natural topography is a critical factor in the generation of muscle tissue engineering scaffolds [31]. Like myoblasts, fibroblasts are sensitive to topographical cues that play a critical role in the wound healing process. Fibroblast alignment allows deposition of highly anisotropic ECM and collagen fibres which support the wound healing process whilst reducing the scar tissue formation [32]. By being strongly dependent on ionic channel activation and Ca^{2+} concentration [30], myoblast fusion is facilitated by electrically conductive scaffolds. Likewise, the wound regeneration process is accelerated by conductive materials supporting the transmission of endogenous/exogenous electrical stimuli [33]. Therefore, scaffolds bearing graphene patterns have great potential in providing contact guidance to alignment, ECM protein-like nanofeatures to stimulate intracellular-responsive pathways, and electrically conductive properties which finally enhance myoblast membrane fusion [34,35] and wound healing [36–39].

Although graphene-based nanocomposite scaffolds can modulate cell fate, even small variations in their composition can have unpredictable effects on cellular response [40]. In recent years, fused deposition manufacturing (FDM) 3D-printing has emerged as a cost-effective, reliable, and reproducible tool to rapidly generate scaffold for cell growth with desired micro-topographical features. The main drawback of FDM is the inherent presence of wrinkles on the surface of objects due to the side-by-side deposition of extruded material; however, even those micro-topographic imperfections (i.e., grooves, pillars, and ridges) have been shown to influence migration and orientation of various cell lines [41].

In this work, we exploited FDM to develop 3D printed scaffolds based on either PLA or graphene@PLA with defined patterns and we tested them with different cell types to assess how scaffolds influence cell behaviour. Such scaffolds resulted to be biocompatible and to promote the alignment of neuronal, fibroblast and myoblast cells due to their 3D printed topographies. In addition, the scaffolds containing the graphene could stimulate the differentiation of induced pluripotent stem cells (iPSCs) to neuroectodermal precursors and promote the myoblast membrane fusion to generate multinuclear myotubes. In summary, we obtained state-of-the-art and cost-effective scaffolds with the potential for being applied in multiple regenerative medicine applications. Such scaffolds intrinsic properties can directly stimulate the desired cell behaviour, without addition of any exogenous factor.

2. Results

2.1. 3D Printing

Scaffold design and printing parameters were optimised to obtain a regular pattern of creases at increasing distance, to test whether an increase in pattern spacing could influence cell alignment and differentiation. Ultimately, we opted for two series of micropatterned scaffolds that correspond to two different printing techniques: (i) 100 μm -spaced scaffolds (100 μm) and (ii) 400 μm -spaced scaffolds (400 μm). The 100 μm series was designed so that neighbouring filament depositions were at a distance comparable with that of a cell in its larger dimension. These scaffolds were built vertically from the printing table to take advantage of the higher resolution of the z printing axis, though alterations on the printing bed led to a more consistent ~ 100 μm pattern. Such increase in resolution also involves an increase in roughness, as single lines of filament are extruded on top of each other making the scaffold surface not completely even. To fix this predicament, the 400 μm series took advantage of the smooth surface of the build table itself to yield objects with a flat surface. Scaffolds were printed upside-down: a single line of material was deposited back-and-forth on the xy plane, spaced apart by 400 μm (much higher than the average diameter of a cell soma). Then, the build plate was lowered, and fused filament was poured in larger quantities, higher temperature, and lower speed along a complementary path, so it could expand and completely fill in the empty spaces. Therefore, ridges form only in near proximity of the initial path: this allows to obtain flat surfaces with wrinkles roughly every 400 μm .

Using the methods described above, we were able to create micropatterned scaffolds made entirely of PLA or graphene@PLA, as seen in Figure 1.

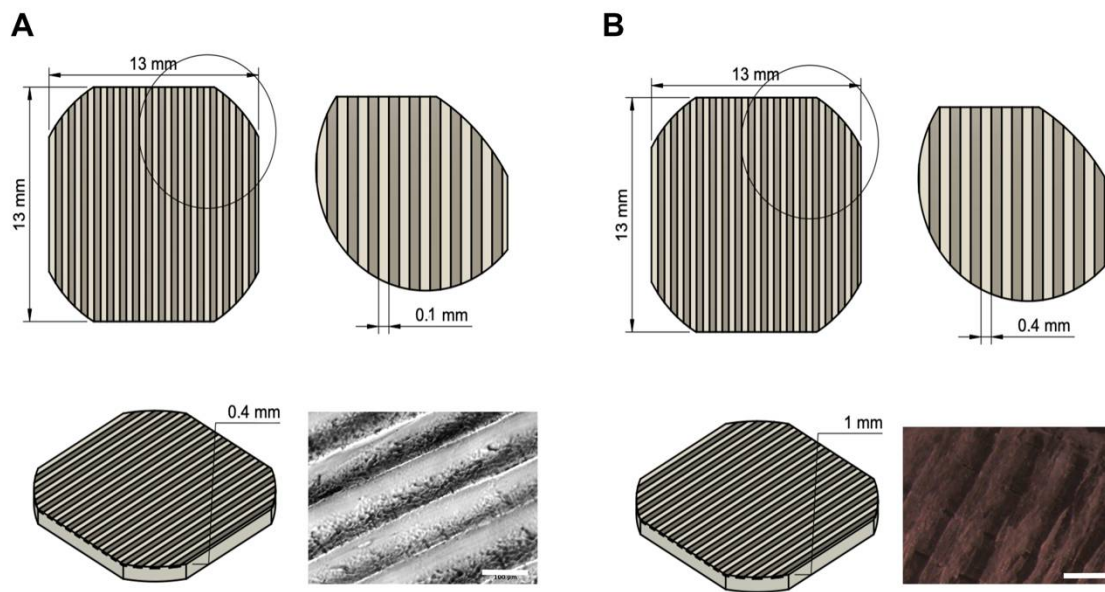


Figure 1. Frontal, lateral and axonometric views of scaffold design. (A) 100 μm series (B) 400 μm series. Scalebar of the fourth image of each panel is 100 μm and 400 μm , respectively.

2.2. Cell Viability and Proliferation

Carbon-based nanofillers, including graphene, have been reported to be biocompatible at concentrations up to 3–5% in either PLA [42] or other matrices [43] and although graphene concentration in graphene@PLA is as low as roughly 1%, i.e., similar to already validated, graphene@PLA flat scaffolds [29,40], we tested viability and proliferation of cells cultured onto both graphene@PLA and corresponding pure PLA filaments to exclude that any negative effects from eventual impurities impaired biocompatibility. Figure 2A shows that viability of SH-SY5Y cells at 24 h (Day 1) and 72 h (Day 3) after seeding onto graphene@PLA and corresponding pure PLA scaffolds is not significantly different from cells seeded onto plates used as control. Viability ranges between 90 and 100%, and slightly lower values at Day 1 are known to depend on post-detachment stress [42].

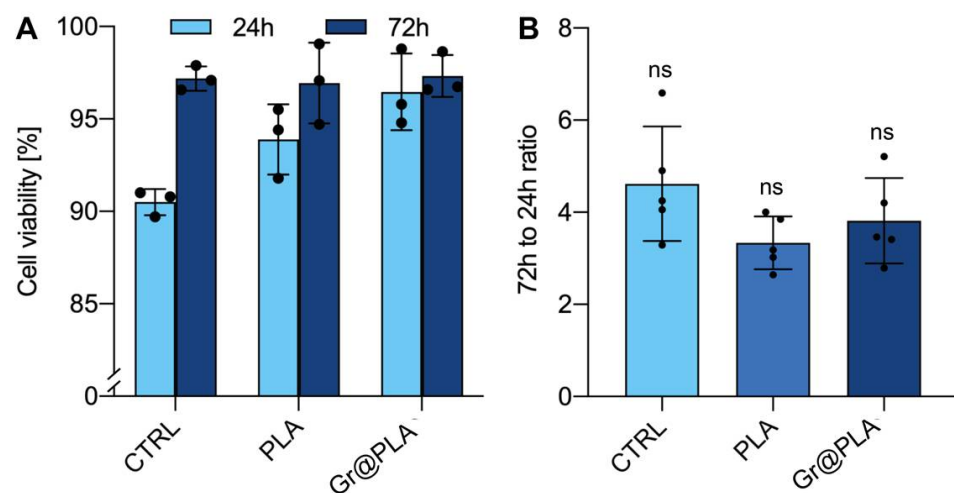


Figure 2. Effects of bare Poly-L-lactic acid (PLA) or graphene@PLA (Gr@PLA) on SH-SY5Y. (A) Cell viability at either 24 or 72 h after cell seeding. Lower values at 24h are due to post-detachment stress. (B) Cell proliferation expressed as ratio between number of cells at 72h and 24h after seeding. Scaffolds do not significantly interfere with cell proliferation. All data represent the mean \pm SD of at least three independent experiments. Statistical significance was determined with one-way ANOVA with Tukey’s correction.

Once cytotoxicity was excluded, we checked eventual effects on cell proliferation, because exogenous materials eventually stimulating cell division are potentially tumorigenic. Figure 2B shows that proliferation of cells grown on the scaffolds is never significantly different from control, suggesting scaffolds do not alter cell proliferation.

2.3. 100 μm Graphene@PLA Scaffolds Promote Neuronal Commitment and Neurite Sprouting whilst Directing Neurite Elongation

To test whether the bio-printed scaffolds could promote the neuronal differentiation of pluripotent stem cells, we cultured iPSCs onto the scaffolds with ectoderm-inducing media and we performed gene and protein expression analyses. As shown in Figure 3A,B graphene-containing scaffolds promote the expression of the transcription factor PAX6, which is the master regulator of the neuroectoderm specification [44] and of Nestin, an intermediate filament protein mainly expressed by neural progenitor cells with an important role in cellular remodelling [45]; however, cells did not seem to follow the spatial organisation of the scaffold (not shown), possibly because they are still too immature and not yet extending neurites.

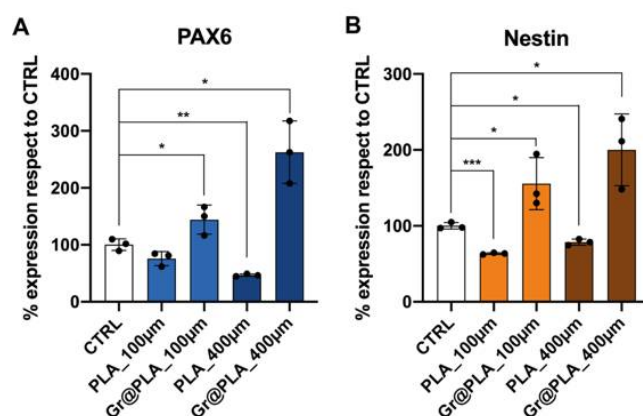


Figure 3. Neuroectodermal commitment of iPSCs grown onto 3D-printed scaffolds. (A) PAX6 and (B) Nestin expression increases when cells are cultured on graphene@PLA (Gr@PLA) scaffolds. All data represents the mean \pm SD of at least three independent experiments. Statistical significance was determined with a two tailed *t*-test. Significance at $p < 0.05$ (*), $p < 0.01$ (**) and $p < 0.001$ (***) between samples is reported. CTRL condition consists of cells seeded onto common 24-well plates.

Therefore, to investigate if the scaffold pattern could trigger the neurite sprouting and orient their elongation, we used the neuronal-like cell line SH-SY5Y. This cell line is characterised by neuroblast-like, non-polarised cell bodies with few truncated processes. Moreover, cells grow in clusters and express immature neuronal markers, which make them resemble immature catecholaminergic neurons [46]. Upon differentiation, SH-SY5Y cells express mature neuronal markers, such as the neurotrophin receptor (TrKB) and increase their neurite length and number [47,48].

Although scaffolds did not result in a significant increase in neurite length or number (Supplementary Figure S1), they were able to strongly influence cell cluster formation. Specifically, we analysed the contact guidance of SH-SY5Y by considering the angle between the pattern and the trajectory of processes and we addressed the alignment in terms of percentage of neurites within a specific angle range on the total number of neurites. As shown in Figure 4, SH-SY5Y better align on 100 μm scaffolds compared to 400 μm . This is probably due to the different dimensionality of the two micropatterns. The 400 μm series has 400 μm -wide flat surfaces divided by creases: since SH-SY5Y neurites reach only ~ 100 μm in length, smooth surfaces are vast enough to be sensed as non-patterned and neurites sprout randomly ($\sim 20\%$ in each angle range). On the other hand, 100 μm scaffolds are designed with a denser pattern, so non-aligned neurites forcefully get into contact with it, resulting in a higher percentage of orienteered neurites.

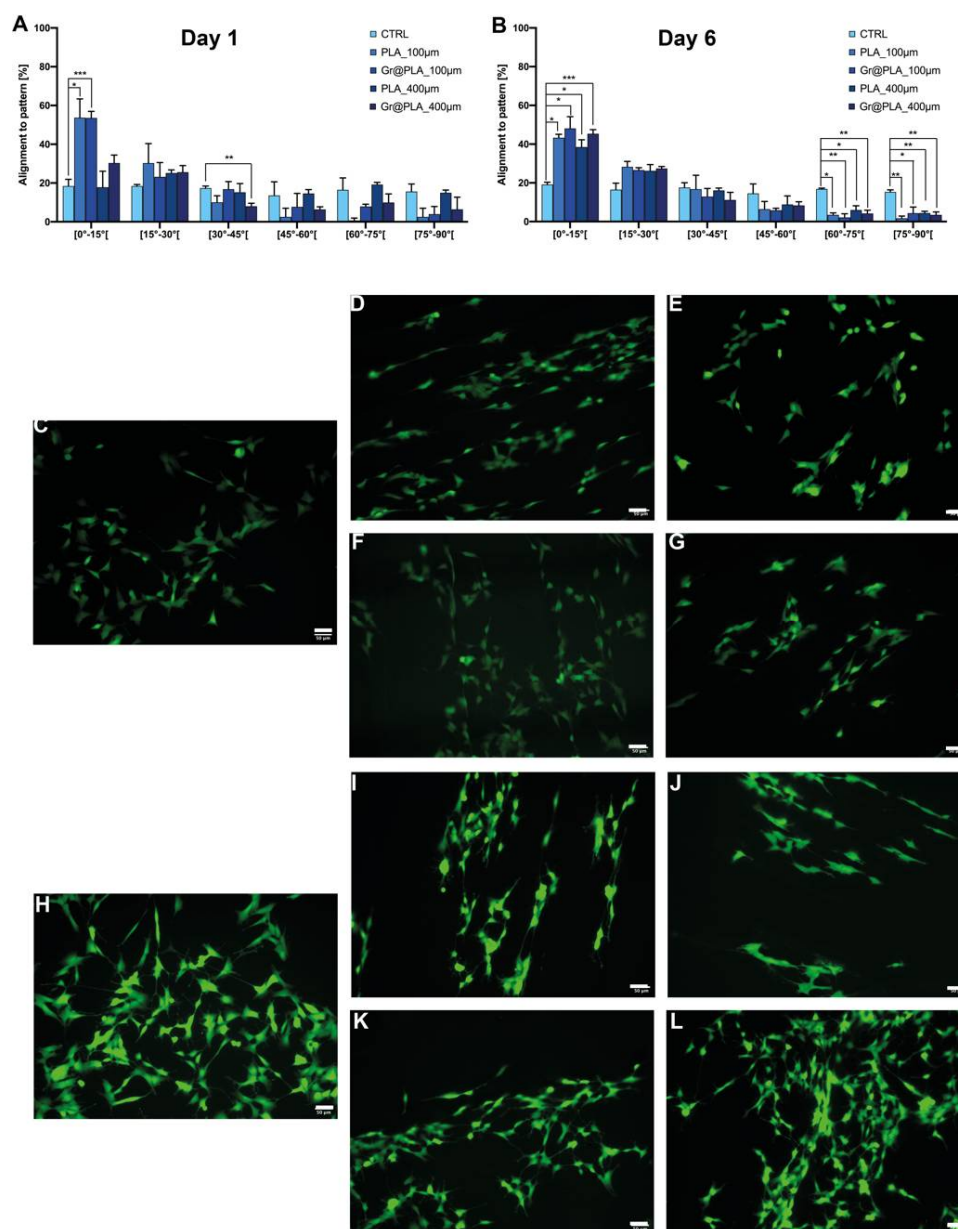


Figure 4. Alignment of SH-SY5Y cells to scaffold patterning. Values are at (A) day 1 and (B) day 6 from cell seeding. Cell orientation is influenced by scaffold patterning independently of its composition. CTRL condition consists of cells seeded onto common 24-well plates. All data represents the mean \pm SD of at least three independent experiments. Statistical significance was determined with two-way ANOVA with Dunnet's correction; significance at $p < 0.05$ (*), $p < 0.01$ (**) and $p < 0.001$ (***) between samples is reported, (C–L) representative fields of cells grown onto scaffolds. (C) Day 1 control, (D) Day 1 PLA₁₀₀ μ m, (E) Day 1 PLA₄₀₀ μ m, (F) Day 1 Gr@PLA₁₀₀ μ m, (G) Day 1 Gr@PLA₄₀₀ μ m, (H) Day 6 control, (I) Day 6 PLA₁₀₀ μ m, (J) Day 6 PLA₄₀₀ μ m, (K) Day 6 Gr@PLA₁₀₀ μ m, (L) Day 6 Gr@PLA₄₀₀ μ m. Scalebar 50 μ m.

Together, whilst the graphene presence in the scaffold boosts the iPSC commitment to neuroectoderm, the specific 100 μ m printing pattern orient the neurite elongation along the scaffold aligned features.

2.4. Contact Guidance Is Influenced by 3D-Printing Method and Promotes Myoblast Fusion into Multinuclear Myotubes When Combined with Graphene Cues

Cell alignment is critical for the fibroblast deposition of anisotropic matrix favouring wound healing and for the myoblast fusion into multinuclear myotubes. Given the ability of our 3D printed scaffolds to affect neurite orientation, we hypothesised that scaffold composition and pattern could also affect contact guidance of fibroblasts and myoblast leading to an aligned cell organisation. We tested contact guidance as the percentage of cells with a specific angle with respect to scaffold pattern. We analysed cell morphology on the scaffold at 48 h and 168 h after cell seeding for immortalised fibroblasts and at 72 h after cell seeding for immortalised myoblasts.

As shown in Figure 5, hTERT-immortalised fibroblasts seeded onto scaffolds were aligned to the printing axis, whereas control cells displayed random orientation.

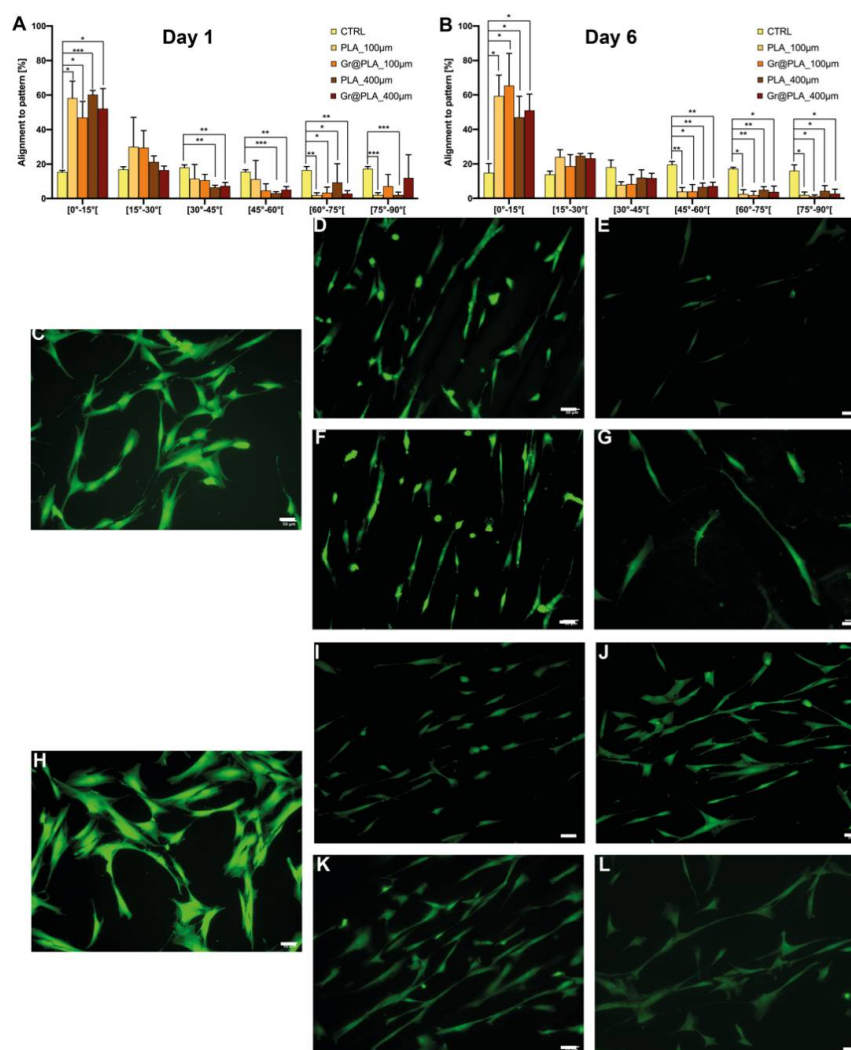


Figure 5. Alignment of hTERT-immortalised fibroblasts to scaffold patterning. Values are at (A) day 1 and (B) day 6 from cell seeding. Cell growth is influenced by scaffold patterning independently of its composition. CTRL condition consists of cells seeded onto common 24-well plates. All data represent the mean \pm SD of at least three independent experiments. Statistical significance was determined with two-way ANOVA with Dunnet's correction; significance at $p < 0.05$ (*), $p < 0.01$ (**) and $p < 0.001$ (***) between samples is reported, (C–L) representative fields of cells grown onto scaffolds. (C) Day 1 control, (D) Day 1 PLA_100 μ m, (E) Day 1 PLA 400 μ m, (F) Day 1 Gr@PLA_100 μ m, (G) Day 1 Gr@PLA_400 μ m, (H) Day 6 control, (I) Day 6 PLA_100 μ m, (J) Day 6 PLA 400 μ m, (K) Day 6 Gr@PLA_100 μ m, (L) Day 6 Gr@PLA_400 μ m. Scalebar 50 μ m.

This was expected, as fibroblasts are known to be highly responsive to topographical cues. 100 μm scaffolds have an increased density of topographical stimuli; thus, we were expecting a higher percentage of aligned cells on those scaffolds compared to 400 μm . However, this was not the case, as alignment on 400 μm and 100 μm at day 6 is not meaningfully different. Intriguingly, Miyoshi and co-workers [49] found fibroblasts to migrate and align along the longitudinal axis of micropatterned surfaces, therefore, the vast majority of cells moved near scaffold ridges and experienced contact guidance, independently from scaffold pattern dimensionality and graphene presence.

We recently reported reduced graphene oxide (rGO) PLA composite scaffolds to be able to increase the expression of pro-myogenic markers on human circulating multipotent cells [40]; however, manually cast scaffolds were unable to increase fusion index of primary myoblasts in culture. We then wondered if the improved control over surface roughness and pattern of 100 μm and 400 μm printed scaffold could solve this issue. As shown in Figure 6A, cell alignment ability seems to be independent of the scaffold composition but rather on the topographies generated by the 3D printing process. Conversely, when analysing the ability of cells to fuse their membranes, we found that the 100 μm -graphene@PLA scaffolds almost doubled the fusion index of control cells, whilst 400 μm - graphene@PLA scaffolds and PLA-only scaffold were unable to improve the cell membrane fusion capacity (Figure 6B).

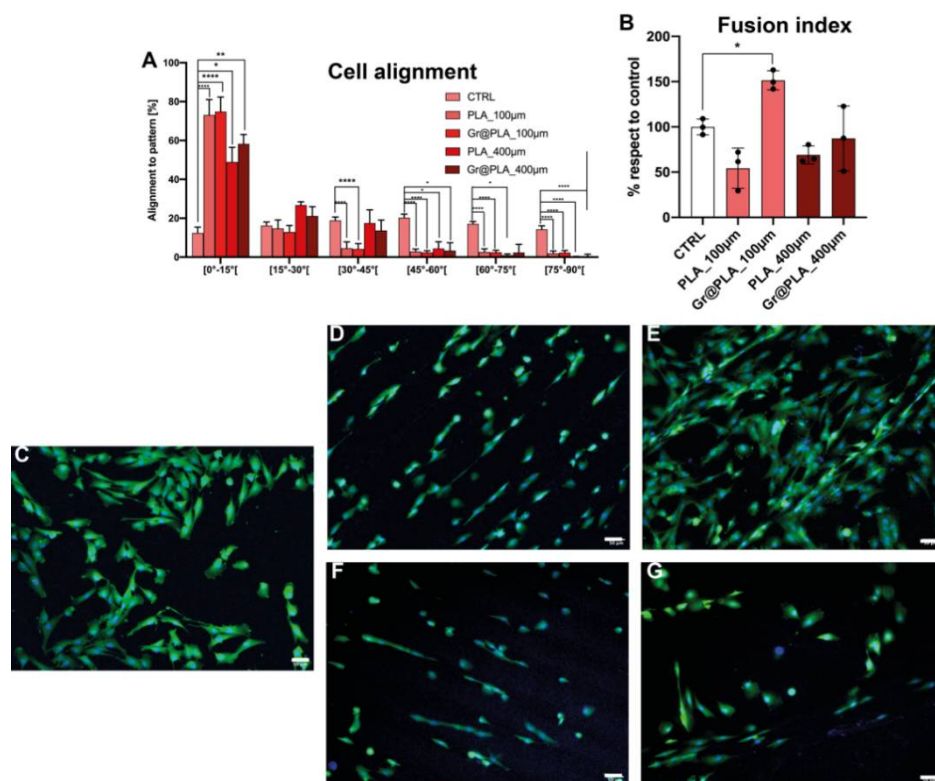


Figure 6. Effects of 3D-printed scaffolds on myoblasts. (A) Myoblasts alignment to scaffold pattern is strongly influenced by scaffold dimensionality, however it is independent from scaffold composition. (B) Fusion index is strongly increased by the combined effects of graphene and patterning. CTRL condition consists of cells seeded onto common 24-well plates. All data represents the mean \pm SD of at least three independent experiments. Statistical significance of panel (A) with two-way ANOVA with Dunnet's correction, whereas that of panel (B) was determined with one-way ANOVA with Tukey's correction; significance at $p < 0.05$ (*), $p < 0.01$ (**), $p < 0.001$ (***) and $p < 0.0001$ (****) between samples is reported, (C–G) representative fields of cells grown onto scaffolds. (C) control, (D) PLA_100 μm , (E) PLA 400 μm , (F) Gr@PLA_100 μm , (G) Gr@PLA_400 μm .

Altogether, such data suggest that contact guidance and alignment are purely regulated by the scaffold features provided by the 3D-printing process, whilst cell behaviours like membrane fusion are controlled by a combination of 3D-printed cues and graphene incorporation.

3. Discussion

Although nervous, muscle, and connective tissues can partially regenerate after injury, in chronic damages or after traumas, their endogenous self-regeneration is impaired and, consequently, tissue engineering approaches are promising therapeutic tools; however, despite the advances in microfabrication techniques, tissue engineering applications are still struggling to develop immune-compatible biomaterials, retaining the features of the natural tissue of interest. Therefore, it is critical to develop reliable, reproducible, and economically affordable synthetic scaffolds which could provide sufficient biomimetic cues to promote the desired cell behaviour without triggering graft rejection and transplant failure. Poly-L-lactic acid-based scaffolds demonstrated high versatility in promoting cell growth and differentiation. We previously found that rGO@PLA based scaffolds could modulate cell commitment toward the neuronal or muscle fate [40]; however, manual casting of scaffolds proved unreliable and expensive. Here, we took advantage of cost-effective fused deposition manufacturing 3D-printing technology and commercially available nanocomposite filaments to design biocompatible scaffolds which can be used as a platform for different tissue engineering applications. We found that both PLA and graphene@PLA filaments do not significantly alter cell vitality as viability was found to be above 90%. Moreover, a 3- to 5-fold increase in cell number between 24 h and 72 h after seeding was found in all condition tested and is compatible with the 27 h doubling time of the SH-SY5Y cell line [46], indicating scaffolds do not alter cell proliferation. When iPSCs were seeded onto scaffolds, we found graphene could increase expression of Pax6 and Nestin, independently on scaffold micro-topography, suggesting commitment toward the neuronal lineage. Conversely, no condition tested was found to induce an enhancement in neurite sprouting or elongation of the more mature cell line SH-SY5Y. As SH-SY5Y cell differentiation has been associated with a decrease in cell proliferation, this is in agreement with reported observations on proliferation rate [50]. Moreover, SH-SY5Y growth appears strongly oriented toward scaffold topography. Albeit cells are strongly oriented both on day 1 and day 6, differences observed between the 100 μm and 400 μm class might be due to cell migration timing. Evidence reported in the literature suggests migration of proliferating SH-SY5Y is poor and substrate dependent [51,52]. 3D printed scaffolds proved to influence cells outside the neuronal lineage, as micro-topographical features influenced orientation of hTERT-immortalised fibroblasts and myoblasts. Strikingly, myoblasts seeded onto 100 μm scaffolds containing graphene, showed an increase in fusion rate into multinuclear cells, indicating patterning and graphene are both required to favour myotube formation. In conclusion, here we show the development of a reliable and economical FDM printed scaffold with the potential of being used in multiple tissue engineering applications, and we elucidate how micro-topographies provided by the 3D printed line pattern and the nano-topographies/conductive properties provided by the graphene incorporation synergistically control cell differentiation.

4. Materials and Methods

4.1. 3D-Printing

Poly-L-lactic acid (PLA) and graphene@PLA (GRAFYLON[®] 3D) ϕ 1.75 mm filaments were purchased from FILOALFA, Ozzero, Italy. GRAFYLON[®] 3D consists of G+ Graphene Plus (Directa Plus, Lomazzo, Italy) dispersed in pure PLA. G+ Graphene Plus is made up of pristine graphene nanoplatelets (GNPs), which are obtained by purely physical treatments of natural graphite, thus avoiding any chemical treatments with organic solvents or acids, and just exploiting water, temperature and pressure to reduce the graphite thickness to the nanometric level. G+ Graphene Plus GNPs have a lateral dimension in the micrometer range, whilst the thickness is in the nanometer scale (<https://graphene-plus.com/> accessed

on 19 January 2022). The 3D-printable scaffolds were designed using Fusion 360 (v2.0.9719, Autodesk, San Rafael, CA 94903, USA), whilst 100 μm -micropatterned scaffolds were developed as $50 \times 50 \times 15$ mm hollowed cubes with 1.0 mm wall width and presented regularly alternated materials every 50 μm . Final scaffolds were cut from the cube into round-edged squares of approximately 13.0×13.0 mm and 1.0 mm in height, well suited for 24-well plates. To obtain scaffolds with a patterning much higher than average cell length, 400 μm -patterned scaffolds were designed directly as $13.0 \times 13.0 \times 1.0$ mm round-edged squares with a 400 μm -wide pattern. STL files were imported in Simplify3D (v4.1.2, Cincinnati, OH 45241, USA) and slicing presets were configured. Layer height and nozzle temperature varied based on the type of support and material: 100 μm scaffold series was printed with 0.050 mm layer height, 100% infill at 195 °C for both PLA and graphene@PLA, whereas 400 μm series was printed with 0.1 mm layer height, 100% infill, 195 °C for graphene@PLA and 0.2 mm layer height, 100% infill, 215 °C for PLA. To improve first layer adhesion, the printing plate was coated with a saturated solution of sucrose in water. Specifically, the sucrose solution was dispersed onto the glass-slide printing plane. The printing plane was then heated to 40 °C and water was left to evaporate to create a sticky film over the glass. Models were printed by fused deposition manufacturing (FDM) with a NG dual 3D printer (Sharebot, Nibionno, Italy). After printing, scaffolds were sterilised under UV-light, 30 min on all sides after a 30 min wash in 75% ethanol. Pure PLA and graphene@PLA 3D-printed scaffolds were pre-incubated for 3h in DMEM/F-12 10% FBS (growth medium).

4.2. SH-SY5Y Cell Culture and Differentiation

Exponentially growing human neuroblastoma-derived SH-SY5Y cells were cultured with Dulbecco's Modified Eagle Medium/Nutrient Mixture F-12, GlutaMAX™ supplement (DMEM/F-12, Gibco™, Fisher Scientific Italia, Rodano, Italy), enriched with 10% heat-inactivated foetal bovine serum (FBS, Euroclone) and 25 $\mu\text{g}/\text{mL}$ gentamicin (Sigma-Aldrich, St. Louis, MO, USA), in a humidified atmosphere of 5% of CO_2 in air at 37 °C. Cells were split into 25 cm^2 flasks (Sarstedt, Nümbrecht, Germany) every 2 days. Cell differentiation was induced by treating cells with all-trans-retinoic acid (RA, Sigma-Aldrich) at 10mM concentration and lowering the FBS in the culture medium to 2% (differentiation medium) 24 h after seeding. In undifferentiated control samples, Dimethylsulfoxide (in which RA is dissolved) was added as the equivalent amount.

4.3. Immortalised Fibroblast Cell Culture

hTERT-immortalised fibroblasts were cultured in high glucose Dulbecco's Modified Eagle Medium, GlutaMAX™ and pyruvate supplement (DMEM, Gibco™) enriched with 10% FBS, MEM non-essential amino acids (NEAA, Gibco™), 50 U/mL penicillin and 50 $\mu\text{g}/\text{mL}$ streptomycin (Pen/Strep, Gibco™) in a humidified atmosphere of 5% of CO_2 in air at 37 °C. Cells were split into 75 cm^2 vented flasks (Sarstedt, Nümbrecht, Germany) every 3 days.

4.4. Immortalised Myoblasts Cell Culture

Immortalised human myoblasts, obtained by double transduction with hTERT and cdk4, were kindly supplied by the Institut de Myologie (Pitié-Salpêtrière Hospital, Paris, France). These myoblasts (wt AB1190) were cultured with a growth medium containing F12 supplemented with 20% FBS (Invitrogen Life Technologies, Waltham, MA, USA), 25 $\mu\text{g}/\text{mL}$ fetuin (Invitrogen Life Technologies), 5 ng/mL hEGF (ImmunoTools GmbH, Friesoythe, Germany), 0.5 ng/mL bFGF (ImmunoTools GmbH), 5 $\mu\text{g}/\text{mL}$ insulin (Sigma-Aldrich), and 0.2 $\mu\text{g}/\text{mL}$ dexamethasone (Sigma-Aldrich).

4.5. Cell Proliferation Assay

Cell proliferation was measured using the resazurin reduction assay. The assay is based on the reduction of the non-fluorescent indicator dye resazurin to the highly fluorescent

resorufin (Ex 569 nm, Em 590 nm) by viable cells. Cells were seeded onto scaffolds or 24-well plates as control (time 0) and cell number was evaluated at 24 h and 72 h after seeding. At each time point, the culture medium was replaced by resazurin solution (resazurin, 15 µg/mL in growth medium; Sigma-Aldrich) and cells were incubated for 4 h in the dark at 37 °C, 5% CO₂. Absorbance at 590 nm was detected using a Fluoroskan Ascent fluorometer (Fisher Scientific Italia, Rodano, Italy) and background values from blank samples were subtracted. To infer the number of cells in each sample, a titration curve was obtained by performing the assay on a known number of cells seeded onto control gelatin/poly-*L*-lysine coated wells. The number of cells in each condition tested was determined by linear regression from the titration curve and cell proliferation was determined as the ratio of the number of cells 72 h and 24 h after seeding.

4.6. Cell Viability Assay

Cell viability was assessed with CytoTox-ONE™ Homogeneous Membrane Integrity Assay, (Promega Italia, Milano, Italy), which is based on the estimation of the LDH released by dead cells. According to manufacturer protocol, cells were grown onto scaffolds for 24h or 72h. At each time point, an equal volume of CytoTox-ONE™ Reagent was added and samples were incubated for 10 min. Reaction was then stopped with blocking solution and fluorescence at 590 nm was detected using a Fluoroskan Ascent fluorometer (Fisher Scientific Italia). A negative (medium without cells) and positive (cells lysed with Promega Lysis Solution) control were used to determine blank and maximal LDH release. Toxicity was then evaluated using:

$$\text{Percent Cytotoxicity} = 100 \cdot \frac{\text{Sample} - \text{Blank}}{\text{Maximum LDH Release} - \text{Blank}}$$

4.7. Differentiation and Contact Guidance Analysis

Cells were seeded onto different types of 3D-printed scaffolds and morphology was evaluated at 24 h (Day 1) and 168 h (Day 6) (SH-SY5Y cells and immortalised fibroblasts) or 72 h (Day 3, myoblasts) after seeding. Based on each line proliferation rate, a different number of cells was seeded for observation at day 1 and 6. Specifically, proliferative SH-SY5Y were seeded 35 k/well for Day 1 and 20 k/well for Day 6. Fibroblasts were seeded 20 k/well for Day 1 and 10 k/well for Day 6. Finally, myoblasts were seeded onto scaffolds and gelatin-coated control wells at 25 k cells/well density. Culture medium was refreshed every 2 days.

Cells were visualised after incubation with calcein acetoxymethyl ester (Calcein-AM, Biotium, Fremont, CA 94538, USA), 1 µM in Hank's Balanced Salt Solution (HBSS, Gibco™, Fisher Scientific Italia) and 10 µg/mL Hoechst 33258 (Invitrogen Life Technologies) for 30 min in the dark at 37 °C and 5% CO₂. Medium was then replaced with fresh HBSS and cells were observed with a DMI4000 microscope (Leica, Wetzlar, Germany) at 10× magnification with a GFP and DAPI filter. Ten images per well were recorded; the first two fields were set to correspond to the centre of the well. Next, fields were then selected in the periphery of the well (N, NE, E, SE, S, SW, W, NW, in respect to the centre), so that images could be representative of the whole well. Images were evaluated with Fiji suite v. 2.3 [53]. Cells were counted by manually counting nuclei. Overall, between 1000 and 2000 cells were recorded per condition. SH-SY5Y differentiation was evaluated considering neurite outgrowth and elongation. Neurite length was measured using Fiji suite [53] by tracing the path of the neurite from the tip to the junction between the neurite and cell body. Processes were considered neurites when their length was longer than 50 µm and neuritogenic properties were analysed in terms of total number of neurites to cell ratio and their mean length as described in [54]. Contact guidance on neurite growth and fibroblast and myoblasts orientation was evaluated comparing the angle (0–90°) between the trajectories of neurites or cell bodies and the pattern. Cells were sorted into 15° classes, and data are presented as percentage of cells in a given class respect to the total number of

cells. Cells or neurites were considered aligned if their angle did not exceed 15° respect to pattern angle. All experiments were performed in triplicate.

4.8. Fusion Index Analysis

Myoblasts were stained with 2 µM Calcein-AM (Biotium) in HBSS (Gibco™, Fisher Scientific Italia) and 10 µg/mL Hoechst 33258 (Invitrogen Life Technologies) for 45 min in dark at 37 °C and 5% CO₂. Cells were visualised under a DM4000B fluorescent microscope (Leica) using GFP and DAPI filter. Fusion index, which describes the number of nuclei inside myotubes as a percentage of the total number of nuclei, was evaluated.

4.9. iPSC Culture and Neuroectodermal Induction

iPSCs (A18945, ThermoFisher, Waltham, MA, USA) were cultured on a Matrigel substrate (Corning, Somerville, MA, USA) with mTeSR media (Stemcell Technologies, Vancouver, BC, Canada) and maintained at 37 °C, 5% CO₂, 95% humidity. For neuroectodermal induction, cells were detached from the culture dish when 70% confluent with TripLE (ThermoFisher) incubation for 5 min at 37 °C to obtain a single cell suspension. Next, 200K cells/well were seeded onto Matrigel coated wells or on scaffolds placed in a 24-well plate in mTeSR supplemented with 2µM of Y-27632 Dihydrochloride (Peprotech EC, London, UK). 24h after seeding, culture media was replaced with the ectodermal inducing media (R & D systems, Minneapolis, MI, USA) and cultured for additional 3 days. On day 4, cultures were stopped to perform RT-qPCR and immunofluorescence.

4.10. RT-qPCR

Media was removed from the wells, cells were incubated with TRIzol (ThermoFisher) for 5 min at RT, and RNA extraction was performed using the RNeasy Micro Kit (Qiagen) following the manufacturer instruction. Next, cDNA synthesis was achieved by using the iScript cDNA Synthesis Kit (Bio-Rad, Hercules, CA, USA) following manufacturer instruction.

Gene expression was then analysed by qPCR. 1 µl of cDNA was used for each reaction that was performed using SYBR green (Quantabio, Beverly, MA, USA) in a final reaction volume of 20 µL. The thermal cycler was set as follows: 9' at 95 °C followed by 30 cycles consisting of 30" melting at 95 °C + 30" annealing at 60 °C + 35" extension at 72 °C. GAPDH expression was used as the housekeeping control for normalization. The comparative CT method ($2^{-\Delta\Delta ct}$) was used to quantify gene expression. Melting curve analysis was performed to ensure all transcripts under investigation would be represented by a single peak, as an index for specificity (melting ramp from 70 to 95 °C). *PAX6* [44] and *NESTIN* [55] expression relative to *GAPDH* was performed by using the following primers:

```
PAX6_FW_GTCCATCTTTGCTTGGGAAA
PAX6_RV_TAGCCAGGTTGCGAAGAAGT
NESTIN_FW_GTCAGGTCTGGAAGGTC
NESTIN_RV_TAAGAAAGGCTGGCACAGGT
GAPDH_FW_ACGAATTTGGCTACAGCAACAGGG
GAPDH_RV_TCTACATGGCAACTGTGAGGAGG
```

4.11. Statistical Analysis

Data are presented as a Mean ± Standard Deviation (Mean ± SD) unless otherwise noted. Cytotoxicity, Viability and fusion index data were analysed using one-way ANOVA with Tukey's correction, as the mean of each dataset was compared to the mean of all the others. Two-way ANOVA with Dunnet's correction was used to analyse cell alignment data, as the mean of each dataset was compared to that of the control condition.

5. Conclusions

Reliability of scaffold for tissue engineering is an issue that regenerative medicine must address, especially when research innovations are translated to clinical practice. Particularly, they have to combine standardised nanocomposite formulations and ease of

fabrication with robust and consistent biological response. In graphene-based nanocomposite scaffolds, issues with biocompatibility may even arise from just using different batches of the same GBN, as flakes dimensionality, type and amount of chemical impurities, may vary due to different purification strategies [13]. In this work, we used a graphene@PLA nanocomposite filament consisting as a matrix of pure PLA, a polymer that is FDA-certified for regenerative medicine, and, as nanofiller, graphene G+, which is produced by means of a physical method ensuring the absence of any chemical contaminant. Even though the absence of cytotoxicity for neuronal-like cells and other cellular types of carbon-based nanomaterials dispersed in PLA was already established by several works, hand-made fabrication of such nanocomposite scaffolds may result in unpredictable influence on cell fate and differentiation [40]. Whilst retaining the biocompatibility feature of pure PLA as a matrix and conductivity feature of pristine graphene as nanofiller, FDM 3D-printing with the graphene@PLA and pure PLA filaments used in this work also excluded hand-made batch variation effects on cell growth and differentiation. Furthermore, 3D-printing allowed at the same time to investigate the effect of topographic patterning of scaffolds on cell orientation. In this pilot study, we exploited the effect of scaffolds with different topography and composition on growth, commitment and/or differentiation of iPSCs, neuronal-like cells, immortalised fibroblasts, and primary myoblasts, demonstrating that the specific scaffold topography can promote cell alignment, whereas the presence of graphene promoted iPSC commitment to neuroectoderm and myoblast fusion into multinuclear myotubes.

Supplementary Materials: The following supporting information can be downloaded at: <https://www.mdpi.com/article/10.3390/ijms23031736/s1>.

Author Contributions: M.G. and P.B. performed most of the experiments and wrote the manuscript; G.S. performed experiments on iPSCs and contributed writing the manuscript; R.B. performed experiments on myoblasts, C.R., L.V. and D.I.S. supported the project, F.F. conceived and supervised the project and wrote the manuscript. All authors have read and agreed to the published version of the manuscript.

Funding: This work was supported by funding from the Padua University (Project PRID Seed 2018 to FF and ‘Mille e una lode’ fellowship to PB) and the CaRiPaRo foundation (PhD fellowship to MG).

Acknowledgments: We thank Yuriko Suemi Hernandez Gomez for help with cytotoxicity and proliferation tests and Sara Schiavon for help with fluorescence microscopy.

Conflicts of Interest: The authors declare no conflict of interest.

References

1. Sampogna, G.; Guraya, S.Y.; Forgione, A. Regenerative medicine: Historical roots and potential strategies in modern medicine. *J. Microsc. Ultrastruct.* **2015**, *3*, 101–107. [CrossRef] [PubMed]
2. Kobayashi, E. Challenges for Production of Human Transplantable Organ Grafts. *Cell Med.* **2017**, *9*, 9–14. [CrossRef] [PubMed]
3. Badylak, S.F. Decellularized allogeneic and xenogeneic tissue as a bioscaffold for regenerative medicine: Factors that influence the host response. *Ann. Biomed. Eng.* **2014**, *42*, 1517–1527. [CrossRef] [PubMed]
4. Edgar, L.; McNamara, K.; Wong, T.; Tamburrini, R.; Katari, R.; Orlando, G. Heterogeneity of Scaffold Biomaterials in Tissue Engineering. *Materials* **2016**, *9*, 332. [CrossRef] [PubMed]
5. Follmann, H.D.M.; Naves, A.F.; Araujo, R.A.; Dubovoy, V.; Huang, X.; Asefa, T.; Silva, R.; Oliveira, O.N. Hybrid Materials and Nanocomposites as Multifunctional Biomaterials. *Curr. Pharm. Des.* **2017**, *23*, 3794–3813. [CrossRef]
6. Simamora, P.; Chern, W. Poly-L-lactic acid: An overview. *J. Drugs Dermatol.* **2006**, *5*, 436–440.
7. Ulery, B.D.; Nair, L.S.; Laurencin, C.T. Biomedical Applications of Biodegradable Polymers. *J. Polym. Sci. B Polym. Phys.* **2011**, *49*, 832–864. [CrossRef] [PubMed]
8. Tsuji, H.; Ikarashi, K. In vitro hydrolysis of poly(L-lactide) crystalline residues as extended-chain crystallites. Part I: Long-term hydrolysis in phosphate-buffered solution at 37 °C. *Biomaterials* **2004**, *25*, 5449–5455. [CrossRef]
9. Santoro, M.; Shah, S.R.; Walker, J.L.; Mikos, A.G. Poly(lactic acid) nanofibrous scaffolds for tissue engineering. *Adv. Drug Deliv. Rev.* **2016**, *107*, 206–212. [CrossRef]
10. Bharadwaz, A.; Jayasuriya, A.C. Recent trends in the application of widely used natural and synthetic polymer nanocomposites in bone tissue regeneration. *Mater. Sci. Eng. C Mater. Biol. Appl.* **2020**, *110*, 110698. [CrossRef]
11. Dvir, T.; Timko, B.P.; Kohane, D.S.; Langer, R. Nanotechnological strategies for engineering complex tissues. *Nat. Nanotechnol.* **2011**, *6*, 13–22. [CrossRef] [PubMed]

12. Bellet, P.; Gasparotto, M.; Pressi, S.; Fortunato, A.; Scapin, G.; Mba, M.; Menna, E.; Filippini, F. Graphene-based scaffolds for regenerative medicine. *Nanomaterials* **2021**, *11*, 404. [CrossRef] [PubMed]
13. Liao, C.; Li, Y.; Tjong, S.C. Graphene Nanomaterials: Synthesis, Biocompatibility, and Cytotoxicity. *Int. J. Mol. Sci.* **2018**, *19*, 3564. [CrossRef] [PubMed]
14. Zhao, Y.; Li, X.; Zhou, X.; Zhang, Y. Review on the graphene based optical fiber chemical and biological sensors. *Sens. Actuators B Chem.* **2016**, *231*, 324–340. [CrossRef]
15. Li, K.; Zhao, X.; Wei, G.; Su, Z. Recent Advances in the Cancer Bioimaging with Graphene Quantum Dots. *Curr. Med. Chem.* **2018**, *25*, 2876–2893. [CrossRef]
16. Madni, A.; Noreen, S.; Maqbool, I.; Rehman, F.; Batool, A.; Kashif, P.M.; Rehman, M.; Tahir, N.; Khan, M.I. Graphene-based nanocomposites: Synthesis and their theranostic applications. *J. Drug Target.* **2018**, *26*, 858–883. [CrossRef]
17. Vallabani, N.V.S.; Mittal, S.; Shukla, R.K.; Pandey, A.K.; Dhakate, S.R.; Pasricha, R.; Dhawan, A. Toxicity of graphene in normal human lung cells (BEAS-2B). *J. Biomed. Nanotechnol.* **2011**, *7*, 106–107. [CrossRef]
18. Nasirzadeh, N.; Azari, M.R.; Rasoulzadeh, Y.; Mohammadian, Y. An assessment of the cytotoxic effects of graphene nanoparticles on the epithelial cells of the human lung. *Toxicol. Ind. Health* **2019**, *35*, 79–87. [CrossRef]
19. Fujita, K.; Take, S.; Tani, R.; Maru, J.; Obara, S.; Endoh, S. Assessment of cytotoxicity and mutagenicity of exfoliated graphene. *Toxicol. Vitro.* **2018**, *52*, 195–202. [CrossRef]
20. Skákalová, V.; Kotrusz, P.; Jergel, M.; Susi, T.; Mittelberger, A.; Vretenár, V.; Šiffalovič, P.; Kotakoski, J.; Meyer, J.C.; Hulman, M. Chemical Oxidation of Graphite: Evolution of the Structure and Properties. *J. Phys. Chem. C* **2018**, *122*, 929–935. [CrossRef]
21. Zhong, Y.L.; Tian, Z.; Simon, G.P.; Li, D. Scalable production of graphene via wet chemistry: Progress and challenges. *Mater. Today* **2015**, *18*, 73–78. [CrossRef]
22. Oliveira, A.E.F.; Braga, G.B.; Tarley, C.R.T.; Pereira, A.C. Thermally reduced graphene oxide: Synthesis, studies and characterization. *J. Mater. Sci.* **2018**, *53*, 12005–12015. [CrossRef]
23. Wychowanec, J.K.; Litowczenko, J.; Tadyszak, K. Fabricating versatile cell supports from nano- and micro-sized graphene oxide flakes. *J. Mech. Behav. Biomed. Mater.* **2020**, *103*, 103594. [CrossRef]
24. Sekuła-Stryjewska, M.; Noga, S.; Dźwigońska, M.; Adamczyk, E.; Karnas, E.; Jagiełło, J.; Szkaradek, A.; Chytrosz, P.; Boruczowski, D.; Madeja, Z.; et al. Graphene-based materials enhance cardiomyogenic and angiogenic differentiation capacity of human mesenchymal stem cells in vitro—Focus on cardiac tissue regeneration. *Mater. Sci. Eng. C Mater. Biol. Appl.* **2021**, *119*, 111614. [CrossRef]
25. Cirillo, G.; Peitzsch, C.; Vittorio, O.; Curcio, M.; Farfalla, A.; Voli, F.; Dubrovskaya, A.; Iemma, F.; Kavallaris, M.; Hampel, S. When polymers meet carbon nanostructures: Expanding horizons in cancer therapy. *Future Med. Chem.* **2019**, *11*, 2205–2231. [CrossRef]
26. He, Z.; Zhang, S.; Song, Q.; Li, W.; Liu, D.; Li, H.; Tang, M.; Chai, R. The structural development of primary cultured hippocampal neurons on a graphene substrate. *Colloids Surf. B Biointerfaces* **2016**, *146*, 442–451. [CrossRef]
27. Fang, X.; Guo, H.; Zhang, W.; Fang, H.; Li, Q.; Bai, S.; Zhang, P. Reduced graphene oxide-GelMA-PCL hybrid nanofibers for peripheral nerve regeneration. *J. Mater. Chem. B* **2020**, *8*, 10593–10601. [CrossRef]
28. Scapin, G.; Bertalot, T.; Vicentini, N.; Gatti, T.; Tescari, S.; De Filippis, V.; Marega, C.; Menna, E.; Gasparella, M.; Parnigotto, P.P.; et al. Neuronal commitment of human circulating multipotent cells by carbon nanotube-polymer scaffolds and biomimetic peptides. *Nanomedicine* **2016**, *11*, 1929–1946. [CrossRef]
29. Scapin, G.; Salice, P.; Tescari, S.; Menna, E.; De Filippis, V.; Filippini, F. Enhanced neuronal cell differentiation combining biomimetic peptides and a carbon nanotube-polymer scaffold. *Nanomed. Nanotechnol. Biol. Med.* **2015**, *11*, 621–632. [CrossRef]
30. Lehka, L.; Rędownicz, M.J. Mechanisms regulating myoblast fusion: A multilevel interplay. *Semin. Cell Dev. Biol.* **2020**, *104*, 81–92. [CrossRef]
31. Kim, J.; Leem, J.; Kim, H.N.; Kang, P.; Choi, J.; Haque, M.F.; Kang, D.; Nam, S. Uniaxially crumpled graphene as a platform for guided myotube formation. *Microsyst. Nanoeng.* **2019**, *5*, 53. [CrossRef] [PubMed]
32. Xu, L.; Gao, S.; Zhou, R.; Zhou, F.; Qiao, Y.; Qiu, D. Bioactive Pore-Forming Bone Adhesives Facilitating Cell Ingrowth for Fracture Healing. *Adv. Mater.* **2020**, *32*, 1907491. [CrossRef] [PubMed]
33. Korupalli, C.; Li, H.; Nguyen, N.; Mi, F.-L.; Chang, Y.; Lin, Y.-J.; Sung, H.-W. Conductive Materials for Healing Wounds: Their Incorporation in Electroactive Wound Dressings, Characterization, and Perspectives. *Adv. Healthc. Mater.* **2021**, *10*, e2001384. [CrossRef]
34. Palmieri, V.; Sciandra, F.; Bozzi, M.; De Spirito, M.; Papi, M. 3D Graphene Scaffolds for Skeletal Muscle Regeneration: Future Perspectives. *Front. Bioeng. Biotechnol.* **2020**, *8*, 383. [CrossRef] [PubMed]
35. Zhang, Y.; Le Fric, A.; Chen, M. 3D anisotropic conductive fibers electrically stimulated myogenesis. *Int. J. Pharm.* **2021**, *606*, 120841. [CrossRef]
36. Zhang, Q.; Du, Q.; Zhao, Y.; Chen, F.; Wang, Z.; Zhang, Y.; Ni, H.; Deng, H.; Li, Y.; Chen, Y. Graphene oxide-modified electrospun polyvinyl alcohol nanofibrous scaffolds with potential as skin wound dressings. *RSC Adv.* **2017**, *7*, 28826–28836. [CrossRef]
37. Tang, P.; Han, L.; Li, P.; Jia, Z.; Wang, K.; Zhang, H.; Tan, H.; Guo, T.; Lu, X. Mussel-Inspired Electroactive and Antioxidative Scaffolds with Incorporation of Polydopamine-Reduced Graphene Oxide for Enhancing Skin Wound Healing. *ACS Appl. Mater. Interfaces* **2019**, *11*, 7703–7714. [CrossRef]

38. Liang, Y.; Zhao, X.; Hu, T.; Chen, B.; Yin, Z.; Ma, P.X.; Guo, B. Adhesive Hemostatic Conducting Injectable Composite Hydrogels with Sustained Drug Release and Photothermal Antibacterial Activity to Promote Full-Thickness Skin Regeneration During Wound Healing. *Small* **2019**, *15*, e1900046. [CrossRef]
39. Li, J.; Liu, X.; Tomaskovic-Crook, E.; Crook, J.M.; Wallace, G.G. Smart graphene-cellulose paper for 2D or 3D “origami-inspired” human stem cell support and differentiation. *Colloids Surfaces B Biointerfaces* **2019**, *176*, 87–95. [CrossRef]
40. Tonellato, M.; Piccione, M.; Gasparotto, M.; Bellet, P.; Tibaudou, L.; Vicentini, N.; Bergantino, E.; Menna, E.; Vitiello, L.; Di Liddo, R.; et al. Commitment of autologous human multipotent stem cells on biomimetic poly-l-lactic acid-based scaffolds is strongly influenced by structure and concentration of carbon nanomaterial. *Nanomaterials* **2020**, *10*, 415. [CrossRef]
41. Kalaskar, D.M.; Alshomer, F. Micro- and Nanotopographical Cues Guiding Biomaterial Host Response. In *In Situ Tissue Regeneration*; Elsevier: Amsterdam, The Netherlands, 2016; pp. 137–163.
42. Vicentini, N.; Gatti, T.; Salerno, M.; Hernandez Gomez, Y.S.; Bellon, M.; Gallio, S.; Marega, C.; Filippini, F.; Menna, E. Effect of different functionalized carbon nanostructures as fillers on the physical properties of biocompatible poly(L-lactic acid) composites. *Mater. Chem. Phys.* **2018**, *214*, 265–276. [CrossRef]
43. Cheng, X.; Wan, Q.; Pei, X. Graphene Family Materials in Bone Tissue Regeneration: Perspectives and Challenges. *Nanoscale Res. Lett.* **2018**, *13*, 289. [CrossRef] [PubMed]
44. Zhang, X.; Huang, C.T.; Chen, J.; Pankratz, M.T.; Xi, J.; Li, J.; Yang, Y.; Lavaute, T.M.; Li, X.-J.; Ayala, M.; et al. Pax6 is a human neuroectoderm cell fate determinant. *Cell Stem Cell* **2010**, *7*, 90–100. [CrossRef] [PubMed]
45. Bernal, A.; Arranz, L. Nestin-expressing progenitor cells: Function, identity and therapeutic implications. *Cell. Mol. Life Sci.* **2018**, *75*, 2177–2195. [CrossRef]
46. Kovalevich, J.; Langford, D. Considerations for the use of SH-SY5Y neuroblastoma cells in neurobiology. *Methods Mol. Biol.* **2013**, *1078*, 9–21. [CrossRef]
47. Kaplan, D.R.; Matsumoto, K.; Lucarelli, E.; Thiele, C.J. Induction of TrkB by retinoic acid mediates biologic responsiveness to BDNF and differentiation of human neuroblastoma cells. Eukaryotic Signal Transduction Group. *Neuron* **1993**, *11*, 321–331. [CrossRef]
48. Lopes, F.M.; Schröder, R.; da Frota, M.L.C.J.; Zannotto-Filho, A.; Müller, C.B.; Pires, A.S.; Meurer, R.T.; Colpo, G.D.; Gelain, D.P.; Kapczinski, F.; et al. Comparison between proliferative and neuron-like SH-SY5Y cells as an in vitro model for Parkinson disease studies. *Brain Res.* **2010**, *1337*, 85–94. [CrossRef]
49. Miyoshi, H.; Adachi, T. Topography design concept of a tissue engineering scaffold for controlling cell function and fate through actin cytoskeletal modulation. *Tissue Eng. Part B Rev.* **2014**, *20*, 609–627. [CrossRef] [PubMed]
50. Xie, H.; Hu, L.; Li, G. SH-SY5Y human neuroblastoma cell line: In vitro cell model of dopaminergic neurons in Parkinson’s disease. *Chin. Med. J.* **2010**, *123*, 1086–1092. [PubMed]
51. Joshi, S.; Guleria, R.; Pan, J.; DiPette, D.; Singh, U.S. Retinoic acid receptors and tissue-transglutaminase mediate short-term effect of retinoic acid on migration and invasion of neuroblastoma SH-SY5Y cells. *Oncogene* **2006**, *25*, 240–247. [CrossRef]
52. Dwane, S.; Durack, E.; Kiely, P.A. Optimising parameters for the differentiation of SH-SY5Y cells to study cell adhesion and cell migration. *BMC Res. Notes* **2013**, *6*, 366. [CrossRef] [PubMed]
53. Schindelin, J.; Arganda-Carreras, I.; Frise, E.; Kaynig, V.; Longair, M.; Pietzsch, T.; Preibisch, S.; Rueden, C.; Saalfeld, S.; Schmid, B.; et al. Fiji: An open-source platform for biological-image analysis. *Nat. Methods* **2012**, *9*, 676–682. [CrossRef] [PubMed]
54. Gasparotto, M.; Hernandez Gomez, Y.S.; Peterle, D.; Grinzato, A.; Zen, F.; Pontarollo, G.; Acquasaliente, L.; Scapin, G.; Bergantino, E.; De Filippis, V.; et al. NOG-Derived Peptides Can Restore Neuritogenesis on a CRASH Syndrome Cell Model. *Biomedicines* **2022**, *10*, 102. [CrossRef]
55. Dahlstrand, J.; Lardelli, M.; Lendahl, U. Nestin mRNA expression correlates with the central nervous system progenitor cell state in many, but not all, regions of developing central nervous system. *Dev. Brain Res.* **1995**, *84*, 109–129. [CrossRef]



Article

Graphene–Oxide Porous Biopolymer Hybrids Enhance In Vitro Osteogenic Differentiation and Promote Ectopic Osteogenesis In Vivo

Aida Şelaru ^{1,†}, Hildegard Herman ^{2,†}, George Mihail Vlăsceanu ^{3,4,†}, Sorina Dinescu ^{1,5,*}, Sami Gharbia ^{1,2}, Cornel Baltă ², Marcel Roşu ², Ciprian V. Mihali ², Mariana Ioniţă ^{3,4}, Andrada Serafim ⁴, Horia Iovu ^{4,6}, Anca Hermenean ^{2,*} and Marieta Costache ^{1,5}

- ¹ Department of Biochemistry and Molecular Biology, University of Bucharest, 91-95 Splaiul Independentei, 050095 Bucharest, Romania; aida.selaru@bio.unibuc.ro (A.Ş.); samithgh2@hotmail.com (S.G.); marieta.costache@bio.unibuc.ro (M.C.)
 - ² “Aurel Ardelean” Institute of Life Sciences, Vasile Goldis Western University of Arad, 86 Revolutiei, 310025 Arad, Romania; hildegard.i.herman@gmail.com (H.H.); baltacornel@gmail.com (C.B.); ramrosu@gmail.com (M.R.); mihaliciprian@yahoo.com (C.V.M.)
 - ³ Faculty of Medical Engineering, University Politehnica of Bucharest, 1-7 Gh. Polizu, 011061 Bucharest, Romania; vlasceanu.georgemihail@yahoo.ro (G.M.V.); mariana.ionita@polimi.it (M.I.)
 - ⁴ Advanced Polymer Materials Group, University Politehnica of Bucharest, 1-7 Gh. Polizu, 011061 Bucharest, Romania; andrada.serafim@gmail.com (A.S.); horia.iovu@upb.ro (H.I.)
 - ⁵ Research Institute of the University of Bucharest, University of Bucharest, 050095 Bucharest, Romania
 - ⁶ Academy of Romanian Scientists, 54 Splaiul Independentei, 050094 Bucharest, Romania
- * Correspondence: sorina.dinescu@bio.unibuc.ro (S.D.); anca.hermenean@gmail.com (A.H.)
† These authors contributed equally to this work.



Citation: Şelaru, A.; Herman, H.; Vlăsceanu, G.M.; Dinescu, S.; Gharbia, S.; Baltă, C.; Roşu, M.; Mihali, C.V.; Ioniţă, M.; Serafim, A.; et al. Graphene–Oxide Porous Biopolymer Hybrids Enhance In Vitro Osteogenic Differentiation and Promote Ectopic Osteogenesis In Vivo. *Int. J. Mol. Sci.* **2022**, *23*, 491. <https://doi.org/10.3390/ijms23010491>

Academic Editors: Monica Terracciano and Daniel Arcos

Received: 5 December 2021

Accepted: 29 December 2021

Published: 1 January 2022

Publisher’s Note: MDPI stays neutral with regard to jurisdictional claims in published maps and institutional affiliations.



Copyright: © 2022 by the authors. Licensee MDPI, Basel, Switzerland. This article is an open access article distributed under the terms and conditions of the Creative Commons Attribution (CC BY) license (<https://creativecommons.org/licenses/by/4.0/>).

Abstract: Over the years, natural-based scaffolds have presented impressive results for bone tissue engineering (BTE) application. Further, outstanding interactions have been observed during the interaction of graphene oxide (GO)-reinforced biomaterials with both specific cell cultures and injured bone during in vivo experimental conditions. This research hereby addresses the potential of fish gelatin/chitosan (GCs) hybrids reinforced with GO to support in vitro osteogenic differentiation and, further, to investigate its behavior when implanted ectopically. Standard GCs formulation was referenced against genipin (Gp) crosslinked blend and 0.5 wt.% additivated GO composite (GCsGp/GO 0.5 wt.%). Pre-osteoblasts were put in contact with these composites and induced to differentiate in vitro towards mature osteoblasts for 28 days. Specific bone makers were investigated by qPCR and immunolabeling. Next, CD1 mice models were used to assess de novo osteogenic potential by ectopic implantation in the subcutaneous dorsum pocket of the animals. After 4 weeks, alkaline phosphate (ALP) and calcium deposits together with collagen synthesis were investigated by biochemical analysis and histology, respectively. Further, ex vivo materials were studied after surgery regarding biomineralization and morphological changes by means of qualitative and quantitative methods. Furthermore, X-ray diffraction and Fourier-transform infrared spectroscopy underlined the newly fashioned material structuration by virtue of mineralized extracellular matrix. Specific bone markers determination stressed the osteogenic phenotype of the cells populating the material in vitro and successfully differentiated towards mature bone cells. In vivo results of specific histological staining assays highlighted collagen formation and calcium deposits, which were further validated by micro-CT. It was observed that the addition of 0.5 wt.% GO had an overall significant positive effect on both in vitro differentiation and in vivo bone cell recruitment in the subcutaneous region. These data support the GO bioactivity in osteogenesis mechanisms as being self-sufficient to elevate osteoblast differentiation and bone formation in ectopic sites while lacking the most common osteoinductive agents.

Keywords: graphene oxide; biopolymer blends; biomineralization; ectopic bone formation; osteoinduction; ex vivo analysis

1. Introduction

The field of regenerative medicine and tissue engineering (TE) has emerged as a necessity for tissue substitutes in the case of major trauma. Therefore, the development of novel biomaterials to efficiently support tissue repair and regeneration is a serious matter in this research area. Thus, the goal of BTE relies on generating the expected support for the repair of bone defects based on biocompatible scaffolds with unique properties that enhance cell adhesion and formation of new bone extracellular matrix (bECM) and tissue.

High-performing artificial bone substitutes raise critical issues since engaging in the fabrication of autografts with equal performance to the “gold standard” is still technologically out of reach. Particularly in BTE, calcium (Ca^{2+}) mineral-enriched scaffolds possess the ability to generate osteogenic signaling in osteoprogenitor populations [1]. Most mineral-based substrates investigated for these purposes successfully cover the mechanical features [2] but lack in the areas of morphological mimesis, pore interconnectivity, and pairing with organic compounds, unless they are supplied from allo-/xeno-graft sources. Even so, immunogenicity and unpredictable resorption rates can occur with low prospects of restraint [3].

Over the years, several polymers, mostly natural compounds, have been found to successfully mimic the bECM, thus generating a perfect microenvironment for cell proliferation, which is an important feature for BTE-designed scaffolds [4]. Fish gelatin, a derivate of a major component of the ECM, allures with good biocompatibility [5], high degradability rate [6] and low immunogenicity [7], while chitosan, due to its structural resemblance with glycosaminoglycans naturally sited in bECM, augments cell adhesion [8]. Therefore, gelatin and chitosan-based scaffolds have been demonstrated to meet the expected results in the case of osteogenic differentiation and engagement in bone repair [9,10]. Genipin is mostly used as a crosslinking agent for scaffold development due to its low toxicity and biosafety features [11–13]. Modern techniques in biomaterial design include the reinforcement of natural scaffolds with bioactive nanostructures. The oxygen-containing functional groups found in the GO structure ensure a great interaction with cellular proteins, hence significantly contributing to cellular behavior [14] in terms of cell growth and viability. GO has turned out to be a reliable nano-component due to its biocompatibility, which has been addressed in several studies over the years [15,16].

This carbon-based material turned out to present remarkable physiochemical characteristics, which have resulted in good biocompatibility and proper support for a plethora of next-generation targeted biomedical applications. Its versatility and tunable compatibility with robust and diverse materials captivated the focus in the research on skin [17] and adipose [18] regeneration, muscle (cardiac and skeletal [19]) engineering, nerve [20], as well as de novo cartilage and bone tissue [21]. GO demonstrated excitingly good interaction with many kinds of cell types, such as stem cells [22,23], neural cells [24,25], cardiomyocytes [26] and endothelial [27] cells and osteoblasts [28], while the non-toxic effect of GO-reinforced materials has been numerously reported in both in vitro and in vivo experimental conditions [29,30]. Even though there is not a global consensus on the drawbacks that GO additivities can be associated with, many results support that the impact of GO in the osteogenic development is rather positive, as long as the concentration of GO is not very high (~0.5 wt.%) [31–33].

Interestingly, studies have observed that the implantation of a scaffold engineered for BTE purposes at an ectopic site still has the means to recruit bone cells and to generate bone tissue, even if not surrounded by it [34]. Exquisite studies reported the implantation of BTE-designed scaffolds in other areas (e.g., subcutaneously/in muscle) in order to prove the osteoinductive and osteoconductive properties of the scaffolds [35–38]. These unique events have been proven for biomaterials such as β -tricalcium phosphate scaffolds [39], hydroxyapatite-based materials [40] and also phosphate graphene composites [41].

In our previous studies, we developed a new scaffold composed of fish gelatin/chitosan crosslinked with genipin (GCsGp) and reinforced with various GO:biopolymer mass ratios [15,42]. Appertaining on preliminary results, including thorough biocompatibility, we

concluded and highlighted that the macromolecule network best performs if reinforced with 0.5 wt.% GO.

Predicated on these positive outcomes, we designed a study whose novelty is manifold: (i) complete characterization of partially investigated new BTE promising materials, (ii) survey of their specific osteoinductive features manifesting in ectopic sites and (iii) pioneering structural analysis of this kind of ex vivo sample. Firstly, we substantiated the materials' characterization to the full extent, building on our previous findings on these types of composites. In this stage, we assessed their intrinsic osteoinductive properties in ectopic sites in mice models. Thus, by implantation in a non-osteogenic area, the number of variables involved in bone formations was reduced, eliminating the effects of bone stimulating cytokines, bone-forming cells and potentially bone-promoting mechano-transduction, and therefore, the onset of osteogenesis was attributed exclusively to the scaffold itself.

Cell-laden hydrogels such as acid-g-chitosan-g-poly(*N*-isopropyl acrylamide) [43], bone morphogenetic protein-2 embedded collagen [44] or thiolated chitosan [45] exhibited promising bone formation when injected subcutaneously; furthermore, chitosan/calcium phosphate putties developed ectopic bone-like tissue when implanted intramuscularly.

To the best of our knowledge, our formulations are the only cell-barren polymer hybrids of this kind that manifest ectopic osteogenesis while lacking bone progenitor recruitment cues, differentiating inducers or Ca^{2+} and PO_4^{3-} rich substrates. In addition, we showed that its remarkable behavior is strengthened by the presence of graphene oxide, known for synergistically promoting bone differentiation in hydroxyapatite composites [46] or as an osteomimetic support designed by phosphate functionalization of graphenic sheets [41].

Last but not least, we exploited these results from more than one perspective, and the paper advances a creative means to approach the explanted mineralized scaffolds from the standpoint of the engineer, issuing an uncommon process of physico-chemical characterizations meant to support and refine established immunohistological techniques.

2. Results and Discussion

The fish gelatin/chitosan crosslinked with genipin and reinforced with different GO biopolymer scaffolds have been previously analyzed by our group for their good physico-chemical properties and biocompatibility [15,42]. The in vitro osteogenic potential analysis and the de novo bone-forming capacity in vivo was compared for three materials: i. GCs (to evaluate the baseline osteoinductivity of an unmodified hybrid substrate); ii. GCsGp (to survey whether the osteoinductivity is conditioned by the biopolymer network crosslinking) and iii. GCsGp/GO 0.5 wt.% (to apprehend the contribution of GO to the de novo process of osteogenesis). These outcomes are supported by some studies which have focused on chitosan or gelatin-based materials enriched with graphene and its derivatives [22,47–49]. Thus, we used physical and morphological characterization of the material before implantation and on day 28 post-implantation in order to evaluate de novo osteoinductive properties of the materials by supplementation with GO in the absence of bone stimulating cytokines, bone-forming cells and potentially bone-stimulation mechano-transduction. The early stage of the osteogenesis under the material's support was evaluated by using biological tests, respectively biochemical, histochemical methods and specific analysis of early and late markers of osteogenesis, both in vitro and in vivo.

2.1. A Priori Scaffold Characterization

Engineered biomaterials for BTE can issue and propagate stimuli in cells regulating their early contact with a new lodging substrate, familiarization, adjustment and ultimately their phenotype outcome. This is most likely to occur due to the materials' chemistry, physio-mechanical properties and distinctively tweaked nanostructuration [50].

Swollen freeze-dried GCs, GCsGp and GCsGp/GO 0.5% scaffolds, after reaching equilibria (2 h) [15], were subjected to mechanical testing meant to assess the effect of crosslinking and GO reinforcements generated within the GCs network with regards to compressibil-

ity. The measured values of E (plotted in Figure 1a as the average values \pm SD) portray an expected image whereby the stiffness of the materials is augmented first by Gp crosslinking and additionally via GO embedding. In particular, compression modulus values are as following: $E_{GCs} > E_{GCsGp} > E_{GCsGp/GO\ 0.5\%}$ (81.67 kPa > 126.67 kPa > 179.50 kPa).

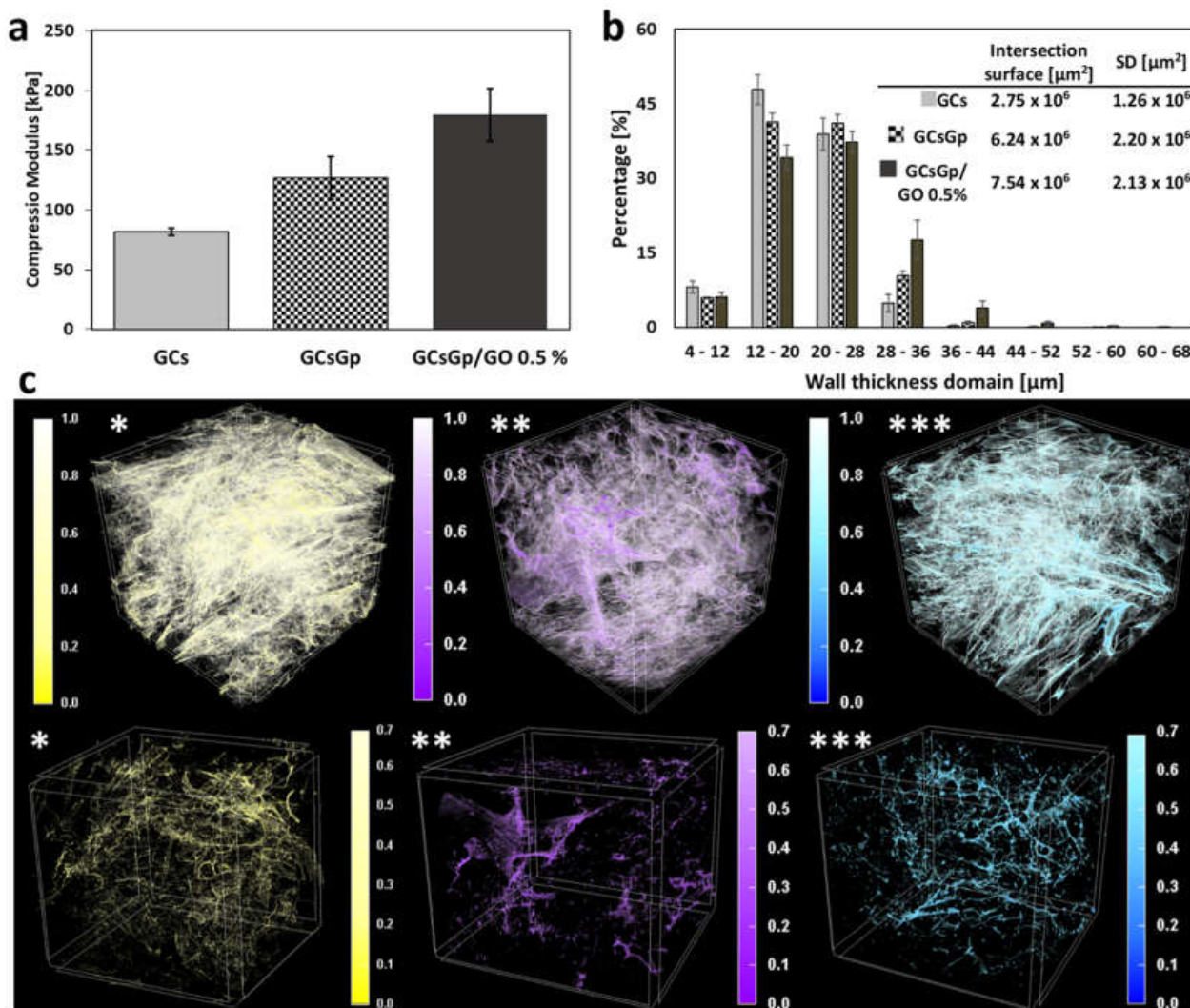


Figure 1. (a) Plotting of the compression modulus of hydrated materials, before implantation; (b) histogram depiction of the wall thickness size domain calculated in CTAn (Bruker); (c) color-highlighted 3D renderings of (*) GCs, (**) GCsGp and (***) GCsGp/GO 0.5% scaffold captured in CTVox.

The porous dry networks of the components were investigated by micro-CT analysis with the purpose of endorsing the mechanical behavior. Figure 2b consists of a chart of the incidence (in percentages) of dimensional domains as calculated for the scaffold walls. Gp, as well as consequent GO reinforcement, are able to customize the solid phase templating as a result of the GCs chains densification through crosslinking and additional centers of physical interactions supplied by the carbon nanomaterial within. As a consequence, scaffold walls tend to become thicker and stiffer—in agreement with the tendency of the detrimental shift the ratio of thinner walls exhibit with Gp and GO supplementation (Figure 1b). Moreover, the estimation of “intersection surface” values, areas of higher solid density where congruent walls meet, merge and overlap, support the theory according to which crosslinking and GO composing of biopolymer blend favor the materialization of areas of variable density and stiffness.

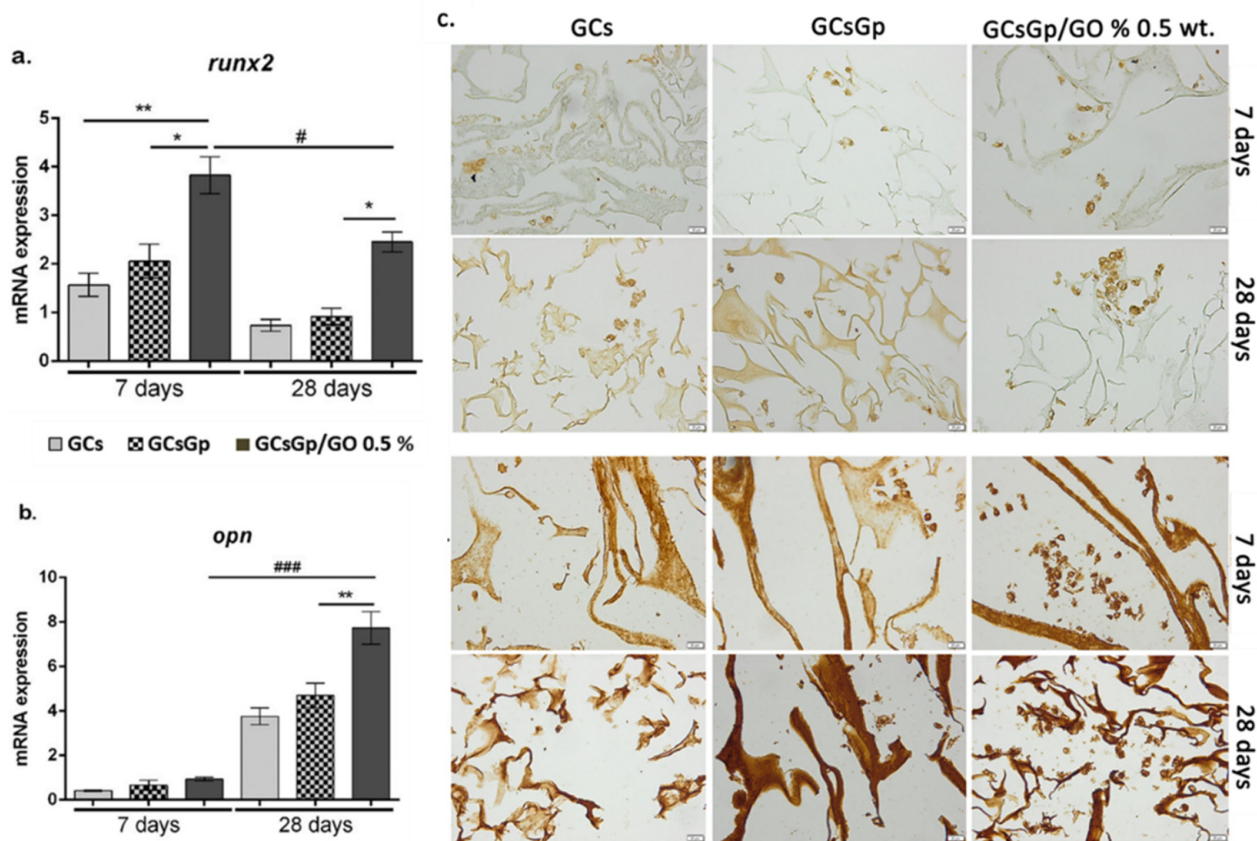


Figure 2. In vitro osteogenic profile analyses of runx2 (a) and opn (b) gene expression in differentiated 3T3-E1 cells in contact with GCsGp/GO materials with statistical significance #### $p < 0.001$; ** $p < 0.01$; #, * $p < 0.05$; (c) immunohistochemical runx2 and opn expression in differentiated 3T3-E1 cells in contact with GCsGp/GO materials.

In order to provide a visual representation of the stiffness gradient, we depicted in Figure 1c a generic colored representation of the scaffold walls, pigmented in direct proportionality with the initial grey tones CT images possessed based on X-ray absorbance. Therefore, the areas where the colors are more pronounced feature superior agglomerations of solid matter (thicker walls), and the pale areas are associated with the finest layouts of the scaffolds. The classic greyscale (0–255) was converted in a reduced unit bar (0–1) for each colorized microtomography, and wall distribution was depicted both unaltered and 30% attenuated in the (0.7–1) region in order to highlight the volume spread of durotactic nuclei.

In the case of GCs, they seem homogeneously spread within the sample volume, however light-consistent and sheer (Figure 1c *). GCsGp, on the other hand, features the coarsest associations of high-density domains but remotely distributed and preferentially toward the outer region of the scaffold (Figure 1c **). Antithetically, the GO composite (Figure 1c ***) displays a very interesting distribution of durotactic poles, with the highest isotropy in terms of both 3D distribution and dimensional extent. Consequently, its intrinsic structuration enables it to manifest the best mechanical performance in wet states, endorsed by synergistic Gp reticulation and GO embedding.

2.2. Effects of Graphene–Oxide Porous Biopolymer Hybrids on In Vitro Osteogenesis

In vitro osteogenic profile of GO-biopolymer composite resulted from experimental assay trials against 3T3-E1 cell line. During the differentiation of pre-osteoblasts, Runx-related transcription factor 2 (runx2) is a master transcription factor, which is responsible for the regulation of other important osteoblast markers such as collagen type I alpha I (Col1a1) and osterix (SP7) [12]. In this study, qPCR evaluation of runx2 gene expression was evaluated after 7 and 28 days of osteogenic induction (Figure 2a) and revealed that

murine pre-osteoblast differentiated successfully started the differentiation towards the osteogenic lineage. At 7 days, significant levels of runx2 expressions were found on the composites enriched with 0.5% wt.% GO as compared to the controls, GCs ($p < 0.01$) and GCsGp ($p < 0.05$). No significant differences were observed between the two tested controls, GCs and GCsGp, respectively. The expression on day 28 was found to be significantly ($p < 0.05$) lower as compared to the levels found after 7 days. This can be explained by the fact that runx2 acts in a stage-dependent manner during this process and is considered an early osteogenic marker, which is expected to present in higher expression levels within the first week of osteogenic differentiation. Moreover, it has been stated that the two isoforms of runx2, namely type I and type II, regulate different stages of a bone cell. Thus, runx2 type I is present in pre-osteoblasts [51], whereas runx2 type II is necessary for terminal phases of the osteogenic differentiation [52,53]. This comes in support of our results, which highlight that runx2 expression is still present after 28 days. Even so, the differences remained similar to those found at 7 days between the composites; namely, runx2 expression on GCsGp/GO 0.5% wt.% systems was found to be significantly higher ($p < 0.05$) as compared to GCs and GCsGp.

At the same time, expression of the osteopontin (opn) gene (Figure 2b) was evaluated by qPCR. During osteogenesis, opn is highly expressed, as it produces an important protein, which is present in the bECM when cells achieve the stage of mature osteoblasts [31]. As compared to runx2, its levels of expression at 7 days of osteogenic differentiation were barely detectable as opn is a late osteogenic marker, which is expressed during the last weeks of osteogenesis.

Therefore, significant opn expression levels ($p < 0.001$) were found after 28 days of induction for the composite containing 0.5% wt.% GO in comparison to the expression levels found after 7 days of osteogenic induction (Figure 2b) on the same composite. Moreover, qPCR results for opn expression indicated a significantly increased ($p < 0.01$) expression on GCsGp/GO 0.5 wt.% in comparison to GCsGp control, after 28 days of osteogenic induction. As these results are in concordance with the one obtained in the case of runx2 expression, no significant opn expression levels were found on the two tested controls. Thus, these results suggest that incorporation of GO to GCsGp materials has significantly supported in vitro osteogenic differentiation of 3T3-E1 cells. A similar study has underlined that the addition of GO to composites based on poly(lactic-co-glycolid) acid surfaces [54] may enhance the expression of runx2 and opn during in vitro 3T3-E1 osteogenic differentiation. Moreover, it has been reported that in the presence of titanium surfaces with reduced GO [55], osteoblasts present a higher expression of opn bone marker.

A similar pattern was recorded for immunohistochemical expression of both RUNX2 and OPN osteogenic markers (Figure 2c). Here, it can be observed that the expression of both makers is present in the tested biosystems. The staining reveals the presence of differentiated cells within the pores of the material, by expression of RUNX2. Another study demonstrated that human mesenchymal stem cells have been found with a higher protein expression of RUNX2 in the presence of GO-collagen scaffold when compared to the collagen control [56]. The immunohistochemical staining for OPN expression showed a more pronounced expression for the composites enriched with GO, as compared to the GCs and GCsGp scaffolds. The expression of OPN and OCN by 3T3-E1 pre-osteoblasts has also been investigated by Lee et al. [46] in composites based on hydroxyapatite reinforced with reduced GO, where it was underscored that the presence of GO had an important contribution to the osteogenic differentiation of pre-osteoblasts. Moreover, cell clusters are predominantly present in the systems where GO was added, supporting once again the idea that the addition of GO has a beneficial impact on the cellular behavior during cell-scaffold interactions. These results come in support of the gene expression patterns found by qPCR, thus demonstrating the achievement of mature osteoblasts from 3T3-E1 precursors in contact with GO-enriched scaffolds.

Cell morphology and distribution within the biocomposites were qualitatively evaluated by SEM. The obtained images revealed 7 days post-induction that cell adhesion

occurred on all composites (Figure 3(A1–A3)). Interestingly, cells on GCsGp/GO 0.5% wt.% formed groups and populated the scaffolds’ pores. It can be observed that morphologically these cells present the characteristics of osteoblast precursors, namely a smooth surface structure with low amounts of mineral accumulation.

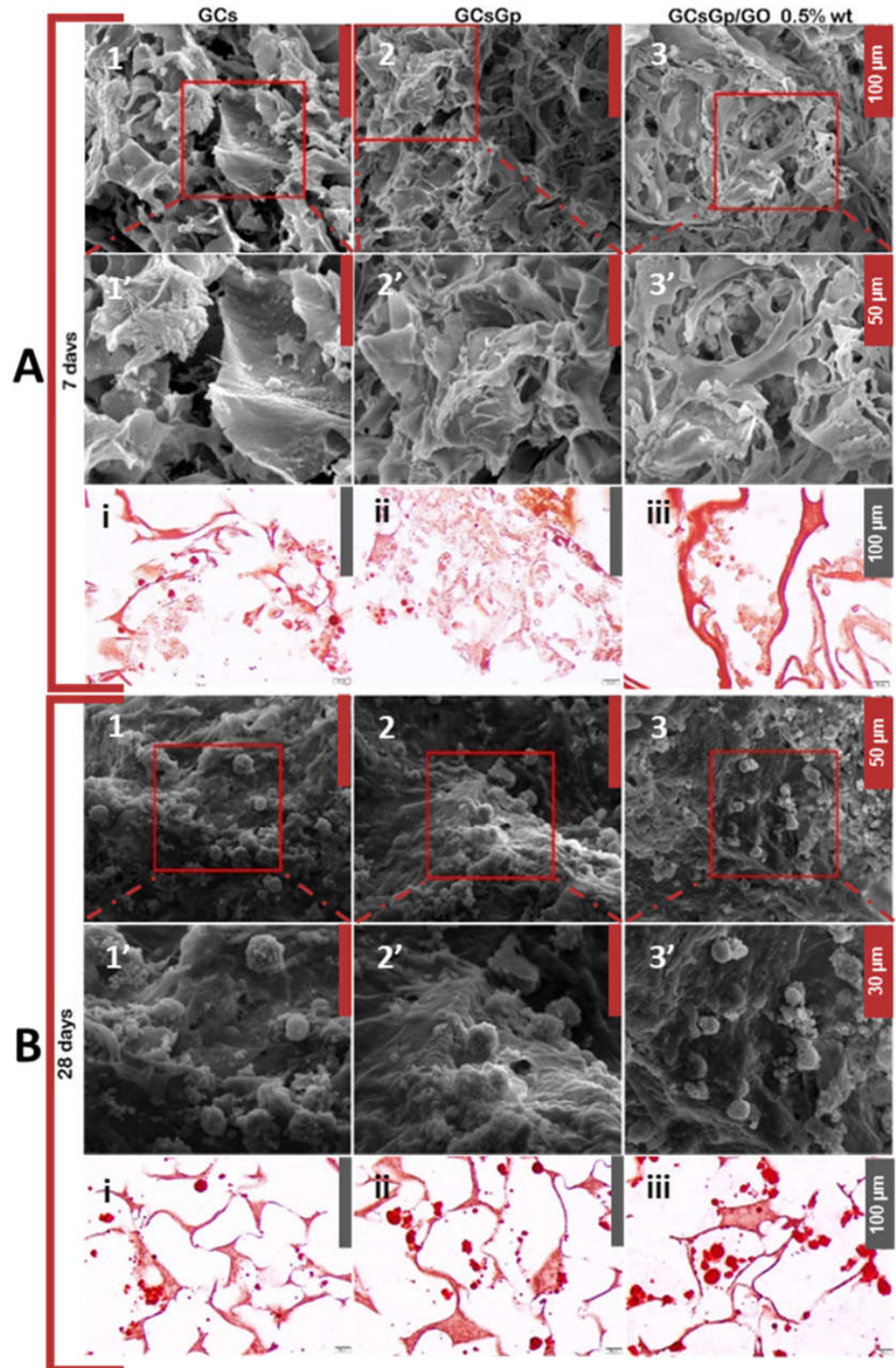


Figure 3. Qualitative evaluation of cellular distribution and morphology in GCsGp/GO scaffolds during 7 (A1–A3) and 28 (B1–B3) days of osteogenic differentiation using SEM while the A1’–A3’ and B1’–B3’ subsets depict corresponding close-ups of the areas marked in red squares above; qualitative evaluation of in vitro calcium accumulation in bECM using ARS histological staining at after 7 (Ai–Aiii) and 28 (Bi–Biii) days.

After 28 days of *in vitro* differentiation, cell adhesion and spread are reconfirmed. It can be observed that cells exhibit different morphological features in opposition to those captured 7 days post-induction. In this latter case, it can be clearly distinguished that cells secreted a mineralized matrix on the surface and cells presented a cuboidal shape, thus demonstrating the presence of mature osteoblasts in the pores of the materials.

ARS is a widely used histological staining to evaluate extracellular bone matrix accumulation and namely to qualitatively certify the observations on the SEM images. Seven days after osteogenic induction, only low amounts of calcium were detected in all scaffolds by ARS histological staining (Figure 3(Ai–Aiii)). Even so, these low quantities demonstrate the inception of the osteogenic differentiation in murine pre-osteoblasts. No significant differences were observed between the three tested composites within 7 days from induction. Twenty-eight days after induction, significant calcium accumulation can be observed in all the materials, in contrast to those found on day 7 (Figure 3(Bi–Biii)). It can be noticed that GO-enriched materials presented significantly more calcium aggregates in comparison to GCs and GCsGp scaffolds. Therefore, GO embedding in crosslinked GCs featuring the best pre-osteoblast differentiation motifs for *in vitro* osteogenesis is also confirmed by ARS staining.

Our previous studies [57–59] on GO-based composites underlined the active engagement of the 2D nanomaterial in cell adhesion and differentiation but also its welcome nature to catalyze cell viability and proliferation. Furthermore, we prove that functional GO-reinforced GCsGp scaffolds could serve as an osteoinductive matrix *in vivo*: seizing native cells to the site and harnessing differentiation into osteoblast in a non-osteogenetic area. We chose to study ectopic bone formation in the subcutaneous dorsal space of mice because osteoinductivity is clearly demonstrated, while the ability to develop bone in this non-specific location is more challenging and, thus, more persuasive of the innate properties of the scaffold [41,60,61].

2.3. Effects of Graphene–Oxide Porous Biopolymer Hybrids on Ectopic Bone Formation

In the *in vivo* study, we investigated the ectopic osteogenic differentiation potential of the scaffolds, without any advantage (dedicated cells, specific matrix, suitable growth factors) provided by an osteogenic area, wherein osteoblastic differentiation is stimulated by different signaling pathways (BMP, NF- κ B, MAPK, Wnt) [62].

In vivo osteogenesis stimulated by GO addition in GCs networks was evaluated by quantitative analysis of biomarkers (seric ALP, *opn* and *runx2*) and the span of bECM deposits. Furthermore, by confocal microscopy, protein expression of *opn* and *runx2* was illustrated, while histological staining results were captured under the light microscope. All of the mice survived until the retrieval of the implanted specimens, and there were no general or local complications.

ALP is an early marker of osteogenic differentiation. The serum expression variations of ALP based on the nature of the scaffolds are not very high and borderline significant, but it still registers an increase with the addition of Gp, however, and is hindered by the presence of GO (Figure 4a). Of note, the presence of Gp as a crosslinking agent in the second tested control in this present study has channelled beneficial effects with respect to *in vitro* osteogenic differentiation, along the same lines with other studies that have explored the addition of this biomolecule in scaffolds designed for BTE [62,63].

The profile of osteogenic differentiation in implanted GCs, GCsGp and GCsGp/GO 0.5% wt.% was evaluated by qPCR analysis for two osteogenic markers, namely *runx2* and *opn*. qPCR results indicated that 28 days post insertion, cells populated the material, since both osteogenic *opn* and *runx2* genes were expressed *in vivo* (Figure 4b).

At the scaffold implantation site, the early osteogenesis process was quickly activated, showing an increased gene expression of the essential transcription factor *runx2* toward Gp and Gp/GO enhanced scaffolds [64]. Furthermore, cell differentiation into mineralized matrix producing osteoblast phenotype was also stimulated by the GO enriched substrate during late osteogenesis, as shown by the immunopositivity of *opn*, which was strongly

expressed 28 days after implantation. In a similar pattern, it was documented for *runx2* and *opn* during osteoblast differentiation in vitro.

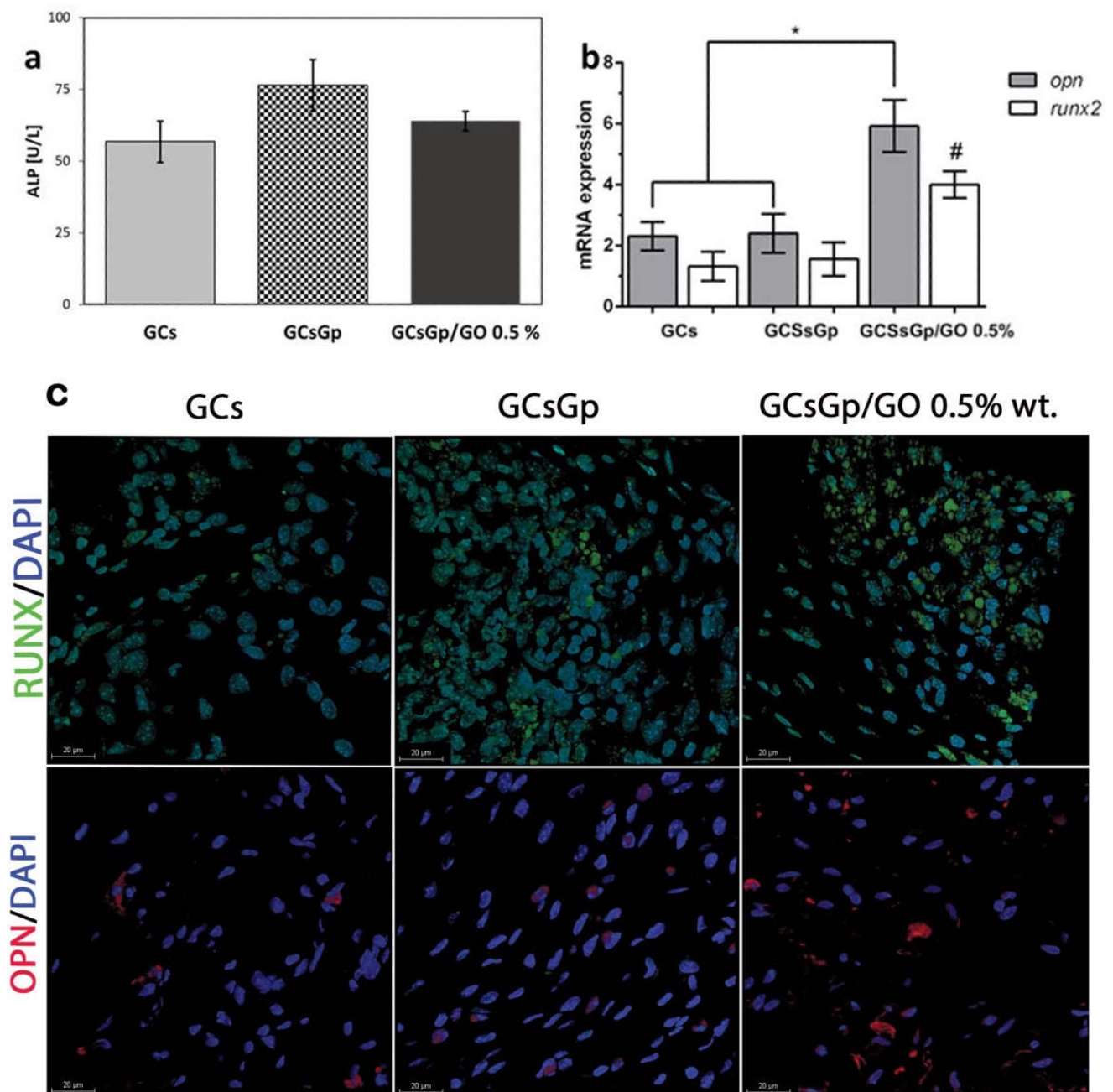


Figure 4. (a) Seric ALP activity 28 days post-implantation of GCs, GCsGp and GCsGp/GO 0.5% wt.% Scaffolds to mice; in vivo osteogenic profile analyses (b) mRNA expression of *opn* and *runx2* four weeks post-implantation (statistical significance #,* $p < 0.05$); (c) confocal microscopy protein expression of *opn* (red) and *runx2* (green) and cell nuclei stained in blue four weeks post-implantation.

After 28 days of in vivo state, both gene expressions were significantly lower in GCs and GcsGp compared to the GO-reinforced scaffold ($p < 0.05$). These data suggest the initiation of in vivo osteogenesis for all tested compositions, but with a significant stimulation per the scaffold containing 0.5% GO. Thus, these results indicate that the addition of GO brings an important contribution to the triggering and maturation of in vivo osteogenic differentiation. The confocal microscopy revealed the same pattern for

opn and runx2 positivity (Figure 4c). It can be noticed that runx2 protein expression (green labeling) has been evidenced in the case of all three tested composites after 28 days of *in vivo* ectopic implantation, suggesting the presence of bone cells within the structure of the scaffold. Conversely, runx2 expression is stronger for all compositions as green staining fluorescence is visually clearest. It is better regulated *in vivo* rather than *in vitro*, advancing the idea that the master osteoblast regulator and transcription factor, promoter of key collagen I, ALP, opn and osteocalcin downstream genes [65], better intervene in support of osteoblast phenotype when in genuine physiological media. The obtained images indicate a more intense labeling in the case of a GCsGp/GO 0.5% system. The same can be stated in the case of opn protein expression (labeled in red), which has been found to be better outlined in the system where GO was added. opn, nonetheless, down-regulates osteoclasts cycles, is involved in bone matrix resorption, as it can bind calcium phosphates, and most likely connects superficial cell receptors to the support matrix through its specific RGD sequence [66]. For simply being expressed at the implantation site, one can analogize the resembling phenomena of the native bone metabolism cycle to the incipient event of ectopic bone formation within the implanted scaffolds.

Histological examination of the samples by H&E, Gömöri trichrome and ARS staining was performed under a light microscope, which enabled the detection of cell infiltration on all of the retrieved scaffolds implanted subcutaneously (Figure 5a). H&E staining demonstrated that the number of cells spread into the GCsGp/GO 0.5% network is superior to cell percolation observed against the controls. Furthermore, the highest amount of EC matrix found embedded in the scaffold pores corresponds to GO composite too. The GCs control, in particular, exhibits the poorest ECM penetration in the interconnected pore network; still, well-defined sectors were formed, preferentially following the durotaxis gradient (Figure 1c).

Gömöri's trichrome staining was green positive in all samples, yet distinctly significant for GCsGp/GO 0.5% scaffold ($p < 0.001$). In this respect, collagen subsequently connected to create basic fibrous frameworks supporting bone formation. When reported to the bare GCs control, the production and in bulk pore occupancy by the secreted collagen was increased 3.7-fold upon GO and Gp supplementation and only by $1.2\times$ for the scaffold reinforced with crosslinking agent alone (Figure 5b). Moreover, we assert that calcium mineral deposits developed against the foreign matrix of GCsGp/GO 0.5% and overlapped across the collagen Gömöri's positive areas is a prompt but firm mark of ectopic bone formation. According to ARS staining, ectopic bone formation commenced mainly in GO-filled scaffold ($p < 0.001$ compared to GCs), while less evidence of mineralization could be identified in the two controls. In those cases, the nuclei of mineralization are rather disconnected or in the process of convergence (Figure 5c).

The three staining assays concur in regards to the matter of the composition best endowed to support *de novo* bone tissue ingrowth. Twenty-eight days post-implantation, functional GO-reinforced 3D scaffold implants exhibited a better cellular infiltration and matrix production compared to GCs and GCsGp. Conformal to these intermediary staining outcomes, GO composites behaviorly outdo the *in vivo* performance of the controls. By its distinct nature, GCsGp/GO 0.5% excels at indulging the ectopic percolation of individual osteoblasts and finally the formation of the organic/inorganic osteogenic matrix.

GO embedded polymer-based frameworks for bone regeneration have been previously reported by us [59]. Our experimental results support the finding that GO promotes ectopic osteogenesis, as we have previously shown that with increasing graphene concentration in chitosan scaffolds implanted in bone defects, early and late osteogenesis marker expression is stimulated [57]. Other studies suggested innate osteoinductivity for GO, but the effects were weak under those conditions [19,67,68].

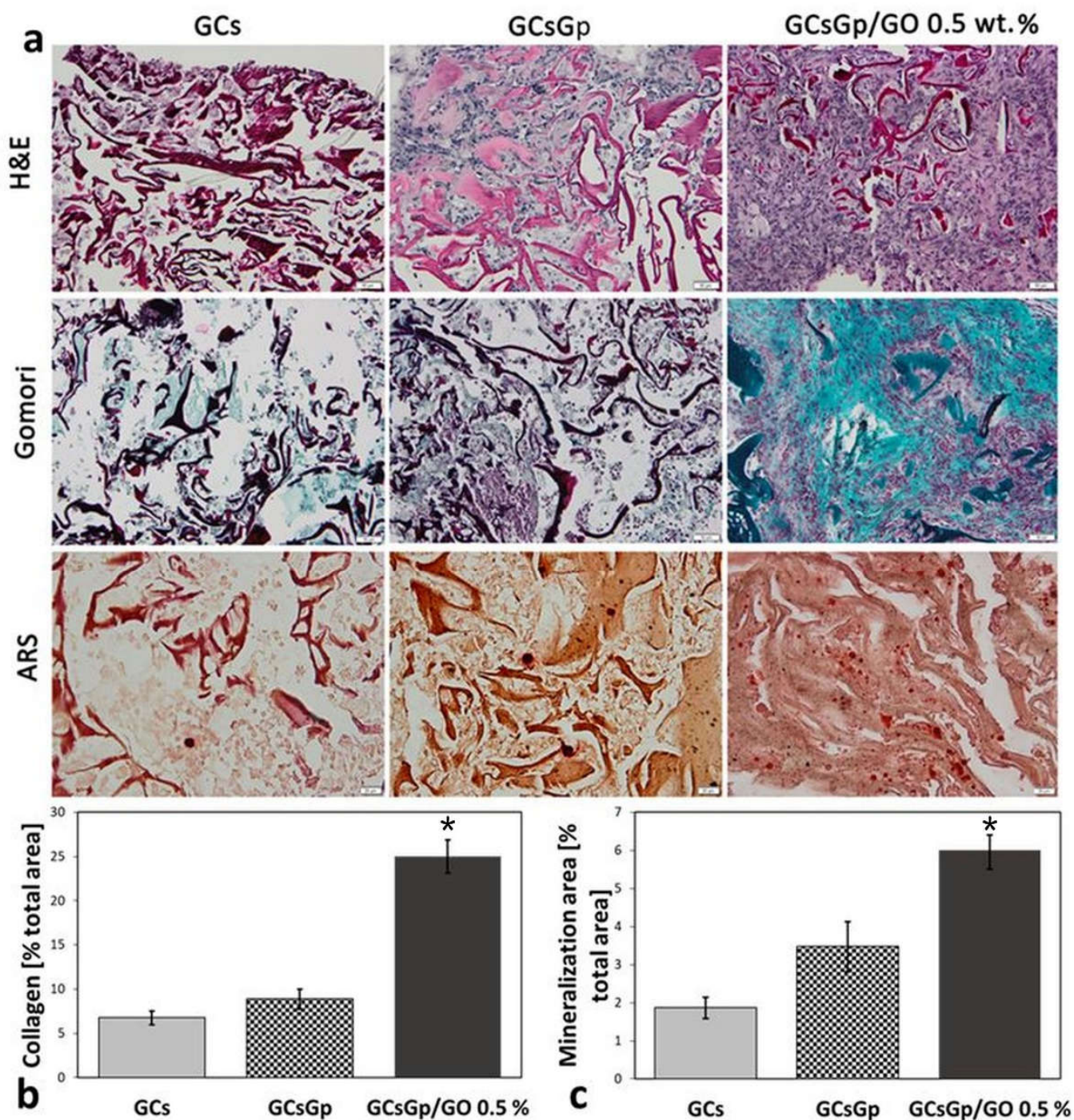


Figure 5. Histological analysis of the ectopic bone occurrence in GCs, GCsGp and GCsGp/GO 0.5% wt.% Scaffolds 28 days post-implantation. (a) Representative H&E, Gomöri trichrome and ARS stainings. Scale Bar 20 µm; (b) The analysis of the area of collagen domains according to Gömöri staining indicated that significantly more collagen was secreted within GCsGp/GO 0.5% wt.% Group as opposed to GCs group ($* p < 0.001$); (c). ARS staining indicates that significantly more calcium mineral deposits are present in the GCsGp/GO 0.5% wt.% group than GCs group ($* p < 0.001$).

2.4. Dynamic Changes in Graphene–Oxide Porous Biopolymer Hybrids during Ectopic Bone Formation

Biomaterials, after explantation on day 28 after surgery, are only occasionally characterized from the morphological point of view and scarcely structurally. This lot, however, after retrieval, was subjected to some unconventional analyses to uncover possible clues

pointing towards the certification of biochemical and immunohistochemical results. Firstly, μ CT provided the global image of ectopic mineral formed inside each specimen, and customized image data analysis allowed a volumetric assessment of bone amount. By SEM, sharpened morphological aspects were provided, while some new bECM structuration theories were outlined empirically. FTIR and XRD spectra granted fundamental insight into the bi-phasic nature of the neotissue, from the angle of its patterning with respect to the remnant scaffold and the layout of the implant after long exposure to physiological media. In addition, structural analysis enables the corroboration of the osteoblast's phenotype with the structuration of authentic bone by way of associating detected attributes of the explants to the acknowledged particularities of genuine tissue.

GO intrinsic osteoconductivity is also highlighted by the results obtained through SEM (Figure 6) and μ CT (Figure 7) investigations. The SEM images of functional GO-reinforced GCsGp scaffolds showed a higher population of cell scaffolds with a differentiated phenotype towards osteoblasts and extensively secreted matrix, compared to GCsGp and GCs, respectively (Figure 6). On the pristine polymer scaffolds, bECM was formed in a lower amount and, based on the image contrast and surface texture, with a higher organic:inorganic ratio. The new collagenous deposits appear to be heavily laden with inorganic phase, most probably germinal calcium phosphates; still, it is not until the matter of GO composition that the phosphate phase of the ECM exceeds the organic quota. Furthermore, roughness is a heightened, topographical feature that favors the adhesion of circulating bone progenitor cells and the growth of tissue overall.

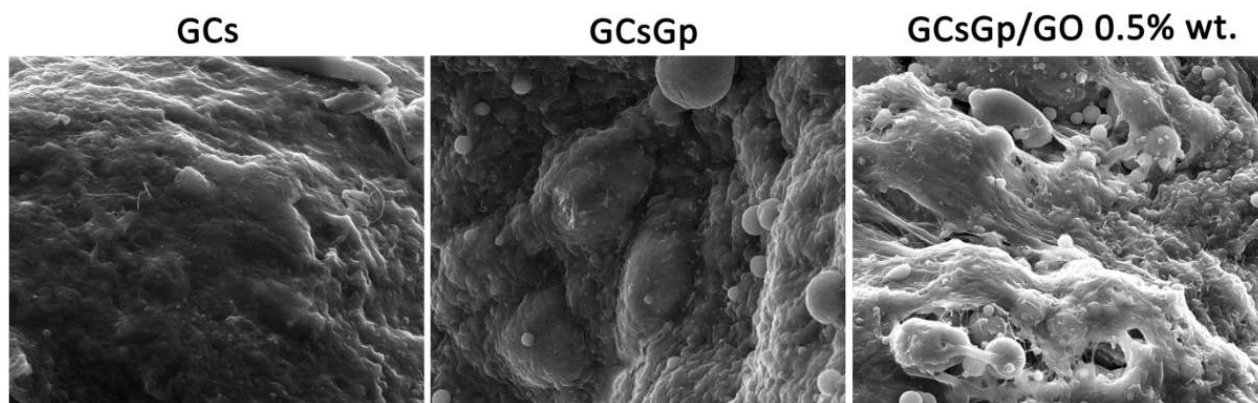


Figure 6. SEM micrographs of GCs, GCsGp and GCsGp/GO 0.5% wt.% scaffolds 28 days post-implantation.

Moreover, these findings are supported by the E modulus measurement. $E_{GCsGp/GO 0.5\%}$ despite being within the order of kPa while native bone sites reach 26 GPa [69], significantly favors the bone formation compared to the two control subjected in our study. GO, besides patterning the architecture of the 3D network [15], provides loci of amplified stiffness that delineates cell-friendly durotactic gradients [58], in particular, beneficial for BTE [70].

μ CT rendering showed that the biomineral deposits after 28 days of subcutaneous implantation reside preferentially on the outskirts of the scaffold, penetrating the volume to a lower extent. This phenomenon might be due to the fact that, initially, the recruited progenitor cells populate the interface of the living tissue with the artificial material. The proliferation within the volume can also be influenced by the size of the pores and the cell's robustness to infiltrate through the interconnecting channels.

The resolution of the scan is 1.5 μ m (pixel equivalent), so individual cells cannot be displayed; however, the aspect of the inorganic phase of the newly formed bECM suggests that tissue formation occurs in clusters casually spread at the interphase. These organizational domains feature a dense and compact aspect, as well as rough topography, resulted from the agglomeration of quasi-spherical phosphate deposits with slight irregularities. Incipient clusters of mineralization can also be identified in the innermost areas of the scaffolds, adhered to the resilient stiffer walls.

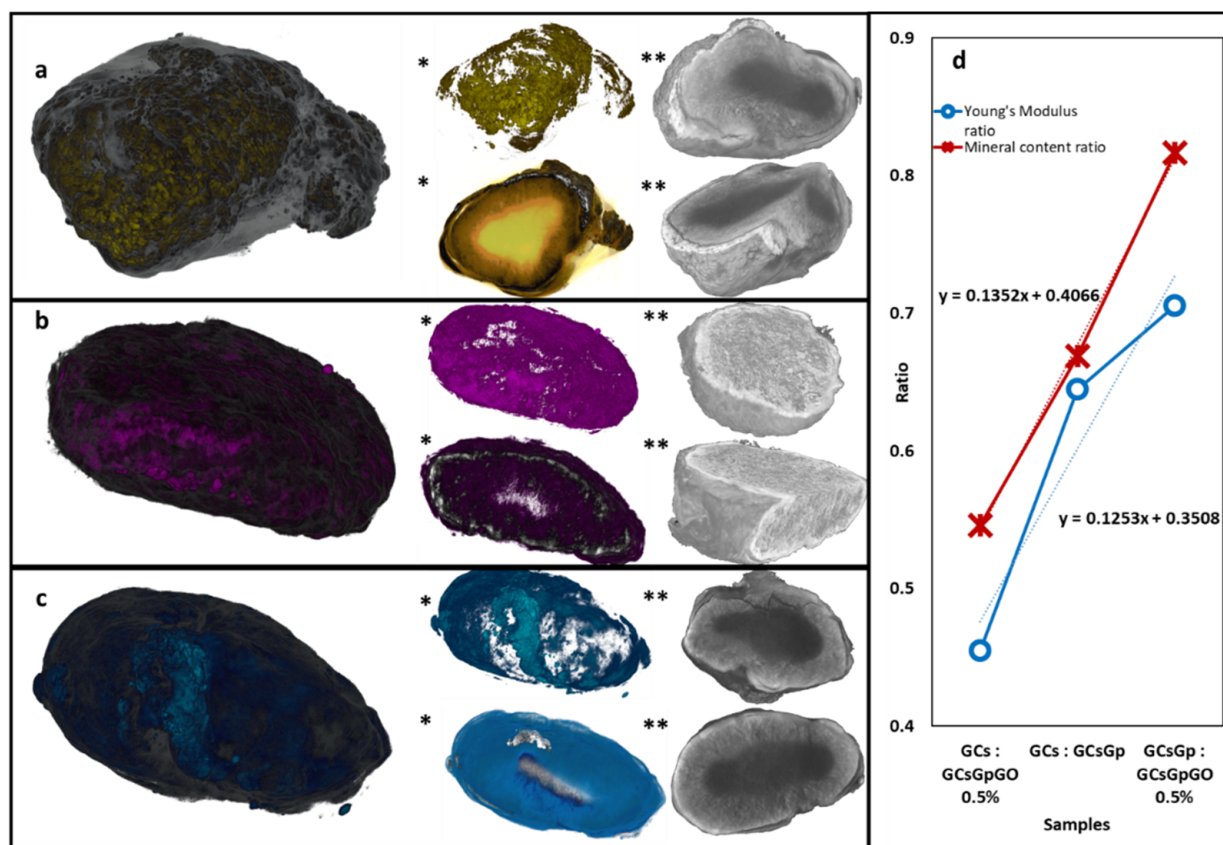


Figure 7. Colorized μ CT images of (a) GCs, (b) GCsGp and (c) GCsGp/GO 0.5% wt.% scaffolds explanted 28 days; (*) marks indicate captures whereby the bi-phasic nature of the samples was separately highlighted and (**) marks indicate sectional views of the central morphology of the samples. (d) Charted data correlating mechanical properties and mineral formation based on the constitutional nature of the composites.

The 3D analysis enables the visualization of the dense crystalline phosphate agglomeration in light shades of gray and white while the lower density domains (original porous composite and collagenous share of the bECM) in darker tones. For a better visualization, in Figure 7a,a*,b,b*,c,c*, the mineral deposits were depicted in colors and the organic phase in white. Figure 7a**,b**,c** illustrates various angles and cross-sections of the tomograms without color alterations. Crystalline domains are contrastingly highlighted from the non-mineralized areas and delineate a gradient density sketch whereby the explant resembles a light-cored/dense-shelled model, as depicted in the cross-sectional views in Figure 8. Furthermore, the porous architecture of the materials is preserved in all compositions, even in the case of the uncrosslinked control. This remarkable stability might be due to the fact that the subcutaneous implantation inferred space constrictions, which limited the expected solvability.

The CT datasets processing enabled the determination of organic/inorganic fractions in each composite, as cataloged in Table 1. Considering the scanning resolution, the total volume of the object was calculated by counting the three-dimensional pixel building blocks (voxel) of the tomograms and translating the voxel size to metric units; the object volume does not include the volume of the pores within. Mineral volume and non-mineral volume were determined by establishing a threshold level in the gray scale pallet of each tomogram, a clear separation of the inorganic/organic phases based on the image contrast. These quantitative data are detailed in Table 1, and the mineral percentage in each composition (vs. the object volume) is consistent with immunohistochemical and biomarkers assays and substantiates these findings.

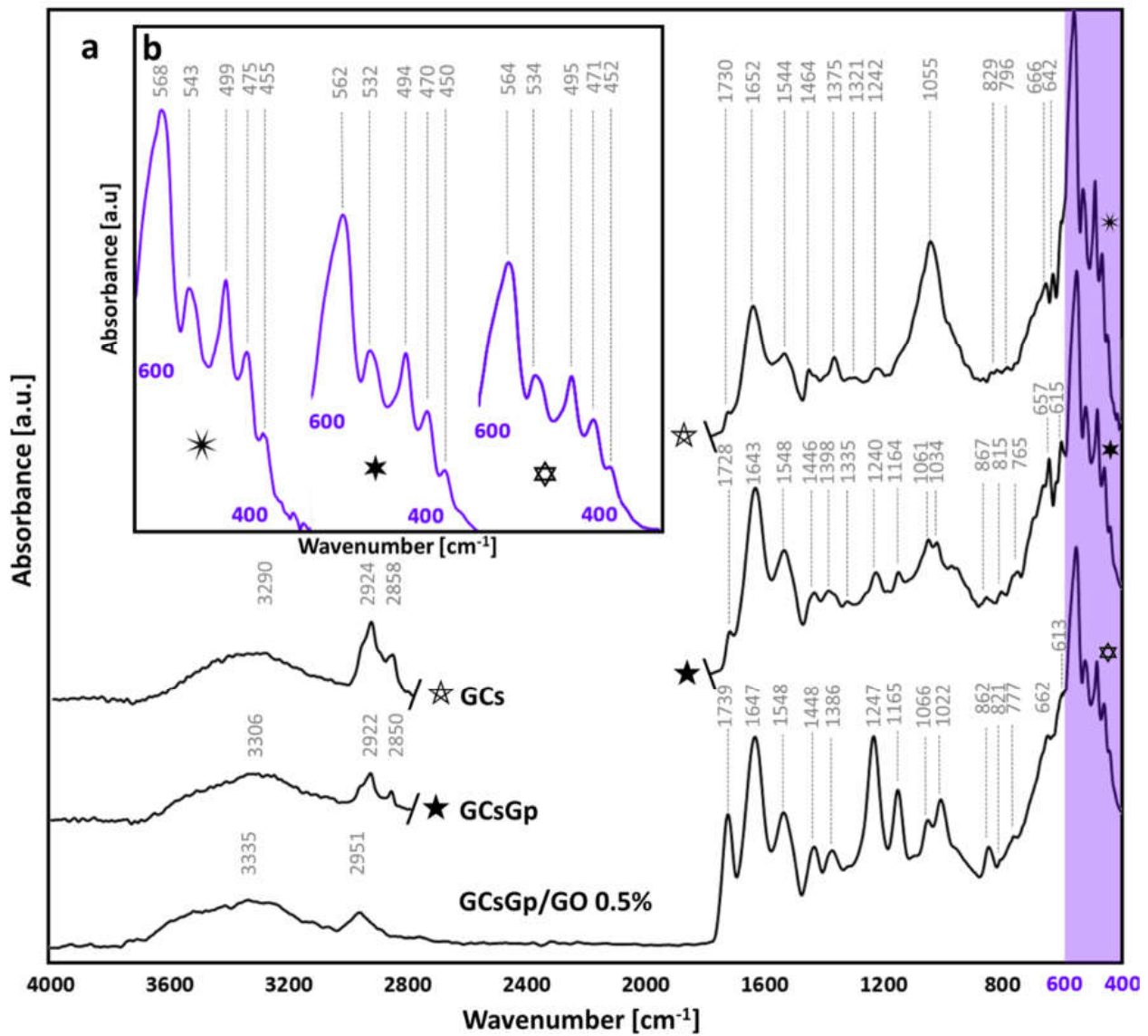


Figure 8. (a) FTIR spectra of GCs, GCsGp and GCsGp/GO 0.5% wt.% scaffolds explanted after 28 days; (b) close-up on the 400-600 cm⁻¹ fingerprint domain specific to natural phosphates.

Table 1. Quantitative μ CT measurements performed on the GCs, GCsGp and GCsGp/GO 0.5% samples.

Ex Vivo Sample	Object (Total) Volume (mm ³)	Mineral Volume (mm ³)	Non-Mineral Volume (mm ³)	Mineral Percentage (%)
GCs	9.85	2.11	7.74	21.47
GCsGp	9.33	2.99	6.34	32.05
GCsGp/GO 0.5%	10.11	3.96	6.15	39.23

In addition, we plotted the mineral ratios of pairing composites against compression modulus ratios (Figure 7d) to survey the correspondence between the mechanics and osteogenesis, indicating linear and univocal proclivity between the two features. The durotaxis (cell guidance according to stiffness gradients) of GCs, GCsGp and GCsGp/GO 0.5% can be pinpointed by unified interpretation of compression test results and quantitative μ CT data; the ratios between the E values and mineral formation follow a linear slope of direct proportionality. Durotaxis by itself confined the performance of the formulations (under both in vivo and in vitro angles) to linear variability.

The nature of the dense crystalline domains in particular was further overviewed by FTIR and XRD. Figure 8 depicts the FTIR complex spectra of the explanted materials merging specific signal of both initial scaffolds and de novo material formation. The νOH broad domain of $3600\text{--}3000\text{ cm}^{-1}$ displays a shredded profile due to the plethora of local maximums of absorption connected to H bonding in remains of the initial implanted materials, the newly formed hybrid bECM and the interface of the two (Figure 8a). Furthermore, as some suggest, the domain can be seen as a heterogeneous area where proteic νNH signals (often $\sim 3400\text{ cm}^{-1}$) [71] mingle with the νOH band [30]. Thoroughly addressing the convoluted band in similar scaffolding materials can be of remarkable interest in understanding the structural evolution of bioactive materials for BTE during the process of integration and regeneration. Symmetric and asymmetric stretching of the C–H bond appear within the $3000\text{--}2800\text{ cm}^{-1}$ range, indicating either specific to residues on the polysaccharide backbone [72] or lipidic tainting/formations in the bECM [73,74]; in GCs (2924 and 2858 cm^{-1}) and GCsGp (2922 and 2850 cm^{-1}), the maximum of absorption manifests slight shifts probably due to the important variations in the amount of new mineral formations and the molecular constraints that emerge as a result. In the GO composite, the symmetric stretching signal disappears as a broad domain in which a maximum of 2951 cm^{-1} is singularized.

Regarding protein structuration, amide I, II and III signals occur in all compositions. A signal at $\sim 1730\text{ cm}^{-1}$ distinguishes with the Gp crosslinking and, consequently, with a GO addition that can be attributed to $\nu\text{C}=\text{O}$ in amide I. Furthermore, the peaks in the range of $1700\text{--}1500\text{ cm}^{-1}$ are linked to amidic vibrations [75]. The amide II signal is weaker in GCs (1544 cm^{-1}) due to the less chemically stable structure and incidental gelatin dissolution and increases with the control material's crosslinking and compositing, manifesting a blue shift towards 1547 cm^{-1} [76]. Nonetheless, amide I fingerprint redshifts in GCsGp and GCsGp/GO 0.5% (towards 1643 and 1647 cm^{-1}) [77]. In a similar fashion, the signals are stronger as a result of the collagen-based organic matrix formed in vivo and probably also as a result of the tendency of gelatin to renature to collagenic triple helical form. Amide III absorption peaks in the $1247\text{--}1240\text{ cm}^{-1}$ range [78]. GCs and GCsGp also exhibit weaker peaks at 1321 and 1375 cm^{-1} and 1335 and 1398 cm^{-1} , which can be attributed to CO_2 saturation of Ca^{2+} phosphates, whereas the GO composite features a stronger single peak at 1386 cm^{-1} [79,80]. Such variations indicate intimate interactions of mineral phases with the organic artificial matrix as well as the collagenous bECM. With respect to control, Gp and GO customization of the fish gelatin–chitosan hybrid generates material structurations that more resemble the natural bone molecular architecture [81]. Crosslinking on its own could partly renature the gelatin structure, while GO was shown to pattern the protein's helicity closer to its natural state [82]. Moreover, the appearance of more defined peaks is supported by the protein rich content of the bECM secreted in the in vivo models. Initial matrix footprints emerge at $\sim 1450\text{ cm}^{-1}$, where δCH_2 signals lodge, related in particular to the proline ring [83].

In GCs, the strongest signal originates at 1055 cm^{-1} for the vibrations of νPO_4^{3-} moiety in stoichiometric apatite formations [84]. After GCs crosslinking and GO embedding, its broadness is diminished and the peaks are split to 1061 , 1034 and 1066 , 1022 cm^{-1} , respectively [85]. The lower wavenumbers emerging are indications of CO_3^{2-} substitutions of Ca^{2+} and, thus, of fluctuations in crystallinity. The $1061/1034$ and $1066/1022$ ratios are flipped since the lower wavenumber absorbance is more enhanced in the case of GCsGp/Go 0.5% and still, within the domain of $1000\text{--}900\text{ cm}^{-1}$, particularly for the unsubstituted (crystalline) apatitic environment, a sharpening tendency is observed [85]. The decline in the crystallinity of in vivo biominerals is also partway supported by the 1164 cm^{-1} (in GCsGp) and 1165 cm^{-1} (GCsGp/Go 0.5%) peaks of less crystalline apatites; in addition, within the range of $900\text{--}750\text{ cm}^{-1}$, pyrophosphate specific signals emerge as markers of less ordered Ca^{2+} domains while above 600 cm^{-1} , νOH vibrations from stoichiometric hydroxyapatite are highlighted.

In the fingerprint region of $600\text{--}400\text{ cm}^{-1}$ (Figure 8b), the control (*) features a very strong peak at 568 cm^{-1} originating from PO_4^{3-} ions, consistent with νPO_4^{3-} vibrations in natural bones. For the crosslinked (⊗) and GO inlayed composition (⊛), redshifts occur towards 562 and 564 cm^{-1} , but not outside of the characteristics of ideal crystallinity of native bone structures [86,87]. Similarly, the position of the 475 cm^{-1} peak (νPO_4^{3-}) in the control is pushed to lower wavenumbers. Intermediary vibrations were detected at 538 ± 5 , 496 ± 3 and $452 \pm 3\text{ cm}^{-1}$ assigned to δPO_4^{3-} in apatites with various stoichiometrical coefficients [85,88].

The main target of XRD studies was to establish the influence of GO on GC composites' general mode of structuration and ability to encourage osteoinduction by crystallinity index determination. According to the spectra displayed in Figure 9a, the XRD pattern of unloaded composite consists of two diffraction peaks located at 8.5° and 11.7° , one weak diffraction at 17.9° and a broad band around 21.5° [2]. The intensity maxima at 8.5° and 17.9° are assigned to the G domains (organized/unorganized). Their correspondent d-spacing values of 1.03 and 0.49 nm are in direct relation to the diameter of triple helical structures (lateral packing of gelatin) and to the isotropic amorphous region (the distance between amino-acid components), respectively [89,90]. The peak from 11.7° and the broadening domain at 21° ascribe to the semi-crystalline chitosan [91,92].

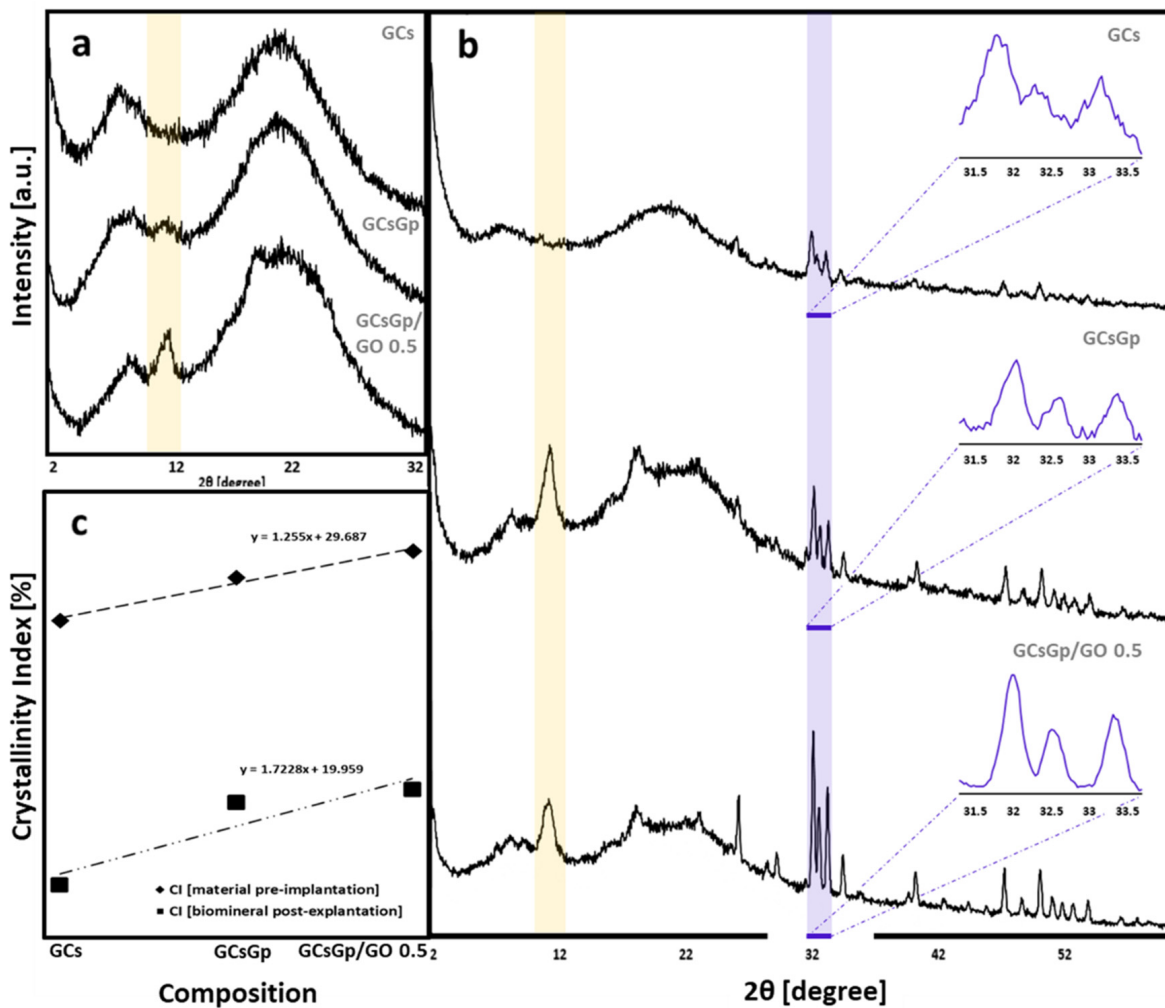


Figure 9. XRD spectra of GCs, GCsGp and GCsGp/GO 0.5% wt.% (a) before implantation and (b) after explanation; (c) crystallinity index of the three scaffold compositions.

XRD spectra revealed that the addition of GO within the GCs matrix seems to cause alterations [2] within the unmodified samples spectrum, as the 11.7° peak associated with

chitosan's crystal I [93] and 21° band paired to the crystal II structure [94] significantly sharpen. Hence, it can be assumed that the identified sharpening is associated with a higher degree of crystallinity of the polysaccharide [95]; crystallization firstly occurred after crosslinking and accelerated with the GO embedding [30] within the matrix. This is confirmed by the crystallinity index (CI) that resulted from

$$CI = [(I_{cr} - I_{am})/I_{110}] \times 100, \quad (1)$$

where I_{cr} is the maximum intensity of the diffraction peak of Cs, and I_{am} is the intensity of amorphous diffraction at $2\theta = 16^\circ$ [96]. CI values determined for GCs, GCsGp and GCsGp/GO 0.5% were: 30.84°, 32.4° and 33.55°, plotted in Figure 9c against the ones calculated for the ex vivo specimens.

G–Cs interactions partially result from hydrogen bonds and electrostatic interactions between carbonyl, amino and hydroxyl groups in polymer chains and genipin crosslinking. Generally, they facilitate the miscibility of the protein and polysaccharide but impede gelatin renaturation by decreasing the number of triple helices in the composite mass [97]. Nonetheless, by adding GO, gelatin renaturation reoccurs, as indicated by the 8.5° peak individualization.

The lack of GO signals within the FTIR spectra can be due to equipment limitations of detecting both the well dispersed and low amounts of GO sheets. Nevertheless, XRD characterization pointed out the fact that once GO sheets are incorporated within the hybrids, a slight sharpening of the maximum at 21° occurs, as well as an increase in intensity for the peak at 11.7° can be observed, suggesting that GO holds the ability to promote GCs crystalline features. With respect to the GCs pair affinity, the partial overlapping of the 17.9° peak with the 21° band is the result of crosslinking between the different species' chains. The absence of GO specific intensity maximum from the composite's spectra supports the idea of adequate GO nanosheet dispersion throughout the materials volume.

The XRD patterns of explanted scaffold (Figure 9b) reveal the tendency of the material to rearrange in more ordered patterns with Gp and moreover with GO addition. Explanted GCs exhibit a rather amorphous structuration with the exception of three sharper but weak peaks in the range of 31–34°. These signals appear in the more complex scaffolds too, featuring fewer broad extents and stronger intensities. Furthermore, the existence of sharp peaks, which generally characterize the hydroxyapatite at 25.9°, 28.9°, 31.9°/32.4°/32.0°, 32.3°/32.1°/32.0°, 33.0°/33.2°/33.2°, 46.7°, 49.8° and 53.2° corresponding to the diffraction planes (002), (120), (121), (112), (300), (222), (123) and (004) [98], respectively, indicate the presence of native-similar bECM in the explant structure. Meanwhile, the patterns of the crosslinked and composite matrices show two broad diffraction peaks centered at 2θ 11° and a broad band above 16°, which indicates their semi-crystalline nature. The peak identified at 11°, as well as the broad band are attributed to the semi-crystalline structure of chitosan and the unorganized and endorsed organized domains of gelatin.

The XRD spectra suggest that overall crystallinity increases in the following order: GCs < GCsGp < GCsGp/GO 0.5%. The CI index calculated for the three specimens follow the same trend—linearly correlated with the CI of original scaffolds. This suggests that FTIR analysis cannot support crystallinity observations on its own; to reiterate, the FTIR spectra pointed out that upon customizing the control material, contrasting variations in stoichiometric and non-stoichiometric apatite vibrations were detected, with difficulty in providing a substantial judgment on the most ordered composition.

3. Materials and Methods

3.1. Scaffold Preparation

Graphene oxide powder, crab shell-derived medium molecular weight chitosan with 75–85% deacetylation degree, coldwater fish gelatin, genipin (purity > 98%—HPLC grade), and acetic acid (99.7%) were purchased from Sigma Aldrich (St. Louis, MO, USA) and used without prior purification. The composites' synthesis was carried out in double distilled water.

Gelatin/chitosan (GCs), genipin crosslinked gelatin/chitosan blend (GCsGp) and 0.5 wt.% graphene oxide-reinforced genipin crosslinked gelatin/chitosan blend (GCsGp/GO 0.5%) scaffolds were prepared under identical conditions as previously reported [13]. Briefly, a GO dispersion procedure was carried out using a VCX 750 ultrasonic device from Sonics and Materials, Inc. (Newton, CT, USA) provided with a Ti-6Al-4V probe tip and a 750 W processor operating at 20 kHz. The amplitude of the probe tip vibrations was set at 70% throughout the 1 h GO exfoliation procedure. Gelatin was solubilized in water/GO aqueous dispersions (5% *w/v*) and mixed with the chitosan solution prepared in mild acidic solution (1% *v/v*). For a total of 50 mL solution, 8.33 mL of gelatin solution was homogenized with 41.67 mL chitosan solution. The crosslinking was carried out with genipin (1% *w/w*). Next, materials were frozen at $-80\text{ }^{\circ}\text{C}$ and freeze-dried ($-55\text{ }^{\circ}\text{C}$).

3.2. Former Material Characterization

3.2.1. Compression Tests

Compression tests were performed using a Brookfield CT3 texture analyzer equipped with a 4500 g cell. Freeze-dried samples with a diameter of 5 mm and a height of 3 mm were swollen at equilibrium, removed from the aqueous media and blotted dry before testing. The compressions were performed at a speed of 0.05 mm/s at room temperature. All measurements were performed in triplicate. A stress–strain graph was plotted using the dedicated software, and the compression modulus (E) was computed at 2% strain (in the linear part of the curve).

3.2.2. Micro-Computed Tomography (μCT)

Freeze dried specimens of the GCs, GCsGp and GCsGp/GO 0.5% wt.% scaffold batch were scanned with Bruker μCT 1272 high-resolution equipment under the following conditions: no filter, 45 kV source voltage, 200 μA current intensity, 550 ms exposure per frame. The scanning was performed while samples rotated 180° , with a rotation step of 0.15. Every recorder projection was the averaged result of 6 acquisitions. Throughout the scaffold lot, the scanning resolution (image pixel size) was fixed at 4 μm . Tomogram reconstruction was performed in Bruker NRecon 1.7.1.6 software (Kontich, Belgium) and rendered in CTvox 3.3.0.0 (Bruker), while sample analysis was performed in CTAn 1.17.7.2 software (Bruker, Kontich, Belgium). For each composite, 4 cylindrical volume-of-interest (VOI) datasets (constrained in terms of diameter and height) were extracted. VOIs were subjected to an image-processing task list consisting of thresholding, despeckling, and 3D analysis (to quantify wall thickness and “intersection surface”). Wall thickness distribution was depicted while the values calculated for the intersection surface are tabulated in the adjacent inset (both with standard deviation \pm SD).

3.3. In Vitro and In Vivo Biological Assessment

3.3.1. In Vitro Differentiation of 3T3-E1 Cell Line in Contact with GCsGp/GO Biomaterials

Murine pre-osteoblasts from the MC 3T3-E1 cell line (ATCC) were seeded on GCs, GCsGp and GCsGp/GO composites at a density of 6.5×10^5 cells/cm² and incubated for 24 h in standard conditions (37 $^{\circ}\text{C}$, 5% CO₂ and humidity). Then, culture media was discharged and replaced with a commercially available osteogenic induction cocktail media (StemPro Osteogenesis Differentiation Kit, Thermo Fischer Scientific, Waltham, MA, USA). The osteogenic process was monitored for 28 days of in vitro cell culture and the differentiation media was changed every 3 days. The in vitro differentiation was evaluated at 7 and 28 days post-induction.

3.3.2. Animals and Subcutaneous Mouse Model of Ectopic Bone Formation

CD1 male mice (6 weeks old, weight: 20–25 g) were used. Mice handling was carried out in accordance with the EU Directive 2010/63/EU and national legislation (Law No.43/2014). All experimental procedures have been approved by the Vasile Goldis Western University Ethics Committee for Research. Animals were housed in individually

IVC cages, with ad libitum access to food/water, with standard conditions of temperature/relative humidity and a light/dark cycle of 12/12 h.

Surgical procedures were executed under anesthesia by intraperitoneal (i.p.) administration of 100 mg/kg b.w. ketamine hydrochloride and 10 mg/kg b.w. xylazine hydrochloride. Scaffolds were implanted ectopically into a subcutaneous pocket in the dorsum of the animals (Figure 10), randomly assigned to three groups (n = 10/group): 1 (GCs), 2 (GCsGp), 3 (GCsGp/GO 0.5 wt.%). After 28 days, mice were euthanatized, and the subcutaneous explants were removed and collected for further analysis.

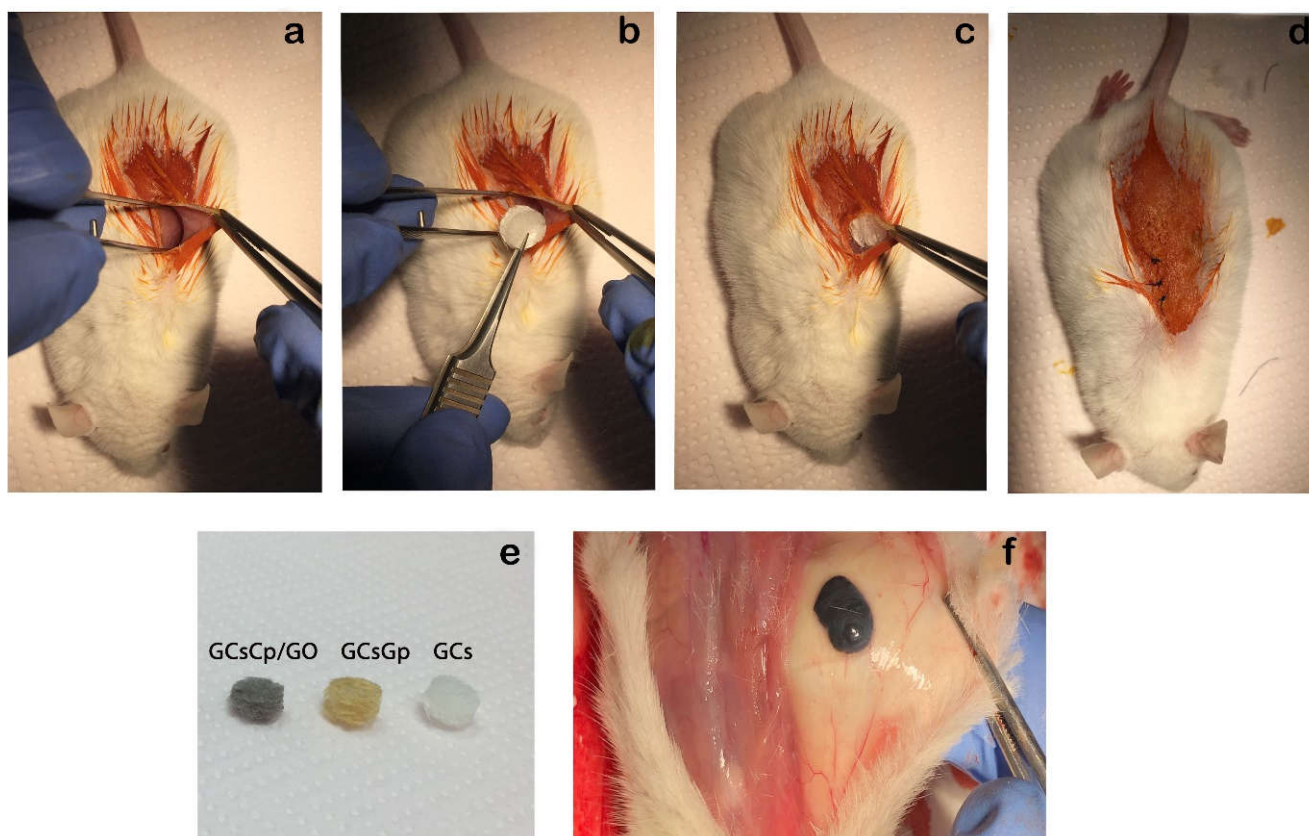


Figure 10. Experimental design. (a) Preparation of subcutaneous pocket in the dorsum of mice; (b,c) ectopic subcutaneous implantation of the scaffold; (d) closure of the overlying skin; (e) scaffolds before implantation; (f) GCsGp/GO 0.5% wt.% scaffold 28 days after subcutaneously implantation to mice.

3.3.3. Biochemistry

Blood samples were collected by cardiac puncture into sterile containers, without anticoagulant. Biochemical analysis was carried out to determine the serum level of alkaline phosphatase (ALP) using a biochemical analyzer (Mindray BS-120, ShenzhenMindray Bio-Medical Electronics).

3.3.4. Histology

The *in vitro* samples and the *in vivo* explants were fixed for 24 h in 4% paraformaldehyde, embedded in paraffin and cut in 5.0 μm thick sections. All samples were stained with Hematoxylin and Eosin (H&E) for morphological analysis and Alizarin Red S (ARS), to label calcium deposits as indicative of mineralization from cells displaying an osteogenic phenotype. *Ex vivo* explants were also stained by a Gömöri's trichrome kit (Leica Biosystems) to demonstrate collagen synthesis. Microscopic sections were analyzed with an Olympus BX43 microscope.

3.3.5. Immunohistochemistry

Immunohistochemical staining was performed on *in vitro* slides, with anti-mouse RUNX2 (diluted at 1:100; sc-390715, Santa Cruz Biotechnology, CA, USA) and OPN (diluted at 1:100; sc-73631, Santa Cruz Biotechnology, CA, USA) primary antibodies. For visualization, Novocastra Peroxidase/DAB kit (Leica Biosystems, Nussloch, Germany) was utilized, according to the manufacturers' instructions.

3.3.6. Immunofluorescence

The *in vivo* sections were incubated with primary antibodies against RUNX2 (diluted at 1:100; sc-390715, Santa Cruz Biotechnology, CA, USA) and OPN (diluted at 1:100; sc-73631, Santa Cruz Biotechnology, CA, USA), and then with secondary antibody conjugated with Alexa Fluor 488 fluorescent dye (diluted at 1:200; A-11029, Thermo Fischer Scientific, Waltham, MA, USA). Finally, cell nuclei were visualized by DAPI and viewed under the confocal Leica TCS SP8 microscope system (Leica Biosystems, Nussloch, Germany).

3.3.7. qPCR Analysis of Osteogenic Markers

Total RNA isolation was achieved by using TRIzol (Thermo Fisher Scientific, Waltham, MA, USA) and further RNA integrity number (RIN) was analyzed using an Agilent 2100 bioanalyzer. cDNA was synthesized using an iScript DNA synthesis kit (BioRad, Hercules, CA, USA) and was amplified by PCR using Veriti 96-well Thermal Cycler (Applied Biosystems, Waltham, MA, USA). qPCR was performed using SYBR Select Master Mix (Thermo Fisher Scientific, Waltham, MA, USA) and Viia7 equipment (Thermo Fisher Scientific, Waltham, MA, USA). Every sample was evaluated in triplicate and the gene expression of glyceraldehyde 3-phosphate dehydrogenase (GAPDH) was used as a reference gene (Table 2).

Table 2. List of primers used for qPCR analysis of osteogenic differentiation in 3T3-E1/GCsGp/GO biosystems.

Genes	Primers
<i>opn</i>	Forward: 5'-CTGGCAGCTCAGAGGAGAAG-3 Reverse: 5'-TTCTGTGGCGCAAGGAGATT-3
<i>runx2</i>	Forward: 5'-ATCCCCATCCATCCACTCCA-3 Reverse: 5'-GGGGTGTAGGTAAAGGTGGC-3'
<i>gapdh</i>	Forward: 5'-AACTTTGGCATTGTGGAAGG-3' Reverse: 5'-ACACATTGGGGGTAGGAACA-3'

3.3.8. Statistical Analysis

The resulted data were statistically evaluated using one-way ANOVA method followed by a Bonferroni multiple comparison test. For this matter, GraphPad Prism 6.0 software (San Diego, CA, USA) for Windows 10 was used. All results are presented as mean \pm SD of $n = 3$ experiments, and p -values < 0.05 were considered to be statistically significant.

3.4. Ex Vivo Material Characterization (28 Days Post-Implantation)

3.4.1. Fourier-Transform Infrared Spectrometry (FTIR)

FTIR investigations were carried on a SHIMADZU 8900 (Kyoto, Japan) on the subcutaneously explants, collected 28 days after material's implantation, under Attenuated Total Reflectance (ATR) mode. The spectra resulted from the average of 32 acquisition with a resolution of 4 cm^{-1} over the range of $400\text{--}4000 \text{ cm}^{-1}$.

3.4.2. X-ray Diffraction (XRD)

X-ray diffraction measurements were performed at room temperature using a Panalytical X'Pert Pro MPD (Malvern, UK) instrument provided with a Cu $K\alpha$ radiation

source. For analogy reasons, XRD spectra were recorded before implantation and 28 days post-implantation.

3.4.3. Scanning Electron Microscopy (SEM)

Both of the *in vitro* and *in vivo* samples were processed according to the technique described previously [33] and analyzed under scanning electron microscope—Quanta Inspect F SEM device equipped with a field emission gun (Fei Company, Hillsboro, OR, USA) with 1.2 nm resolution.

3.4.4. Micro-Computed Tomography

Explanted scaffolds were scanned with the same equipment as before the surgical procedure, under different parameters: 50 kV source voltage, 200 μ A source current, 1200 ms exposure, 1.5 μ m image pixel size. The rotation step was increased to 0.2° while the scan was performed upon a 360° sample rotation to avoid artifacts that may appear due to the presence of high-density mineral. Every projection was the averaged result of 3 acquisitions. Reconstruction, 3D illustration and bone mineral analysis were carried out in the same dedicated pieces of software provided by Bruker.

4. Conclusions

The aim of this study was to design a porous biopolymer hybrid as solutions to the lack of autologous bone needed to regenerate large defects in orthopedics. This is a pioneering account that graphene oxide incorporation in fish gelatin/chitosan/genipin scaffolds up-regulates both osteogenic differentiations *in vitro* and above all bone formation in ectopic sites when implanted in mice models.

To sum up, the data presented in this paper demonstrated that the addition of GO to the GCsGp composite enhances the expression of *runx2* and *opn* during osteogenic differentiation. Moreover, data on collagen production and ectopic calcium deposits within the explanted composites originated from histology staining and underlined the capacity of the biomaterial alone to recruit bone cells in an ectopic site. Further, μ CT results provided a measure of quality control over the Ca^{2+} biomineral survey. Overall, GCsGp/GO 0.5% wt was validated as the material with the strongest osteoinductive character, emphasizing, once again, the high gain from low GO supplementation of the polysaccharide-protein conjugate.

Bone formation within artificial materials is a process that is far from being fully comprehended down to its finely tuned mechanisms especially in the case of multi-component materials, which lack well-known bone-forming inducers and are structurally extremely complex. The present study covers the multi-angle investigation of a substrate of G and Cs, which we customized to a more bone-oriented scaffold by Gp crosslinking and GO embedding. These optimizations lead to a composite with osteoinduction-friendlier chemistry, crystallinity and durotaxis. The previously discussed results corroborate an overview understanding of material structuration and the GO-enabled features that best favor best the bone tissue formation in the experiment designed for this study. Quantitatively, the bECM secreted by the cells recruited to the implantation site was higher in the GO composite with the remark that the stoichiometry of *in situ* formed apatite was slightly below the GCs and GCsGp.

Among our perspectives, we consider addressing this issue upon a longer timeframe in order to gain insights on the osteoinductive manifestation of GCsGpGO materials and its aftereffects with respect to time. The variety of physical particularities and key chemical signals it provided enables the ranking of this survey as the first report on the osteogenic differentiation *in vitro* and bone formation in ectopic sites on the echelon of Ca^{2+} free GO embedded GCs blends.

Author Contributions: Conceptualization, S.D., M.I., A.H. and M.C.; data curation, S.D., M.I., A.H. and M.C.; formal analysis, H.H., G.M.V., S.D., C.B. and A.S.; funding acquisition, M.I., A.H. and M.C.; investigation, A.S., H.H., G.M.V., S.D., S.G., A.S. and A.H.; methodology, A.S., H.H., G.M.V.,

S.D., S.G., C.B., M.R., C.V.M., M.I., A.S. and A.H.; project administration, M.I., A.H. and M.C.; resources, M.I., A.H. and M.C.; software, A.Ş., G.M.V. and C.V.M.; supervision, S.D., M.I., A.H. and M.C.; validation, A.Ş., H.H., G.M.V. and S.G.; visualization, A.Ş., H.H., G.M.V., S.D., S.G., M.I. and A.H.; writing—original draft, A.Ş., H.H., G.M.V., S.D. and A.H.; writing—review and editing, A.Ş., G.M.V., S.D., M.I., H.I., A.H. and M.C. All authors have read and agreed to the published version of the manuscript.

Funding: This work was supported by a grant from the National Authority for Scientific Research and Innovation, Operational Program Competitiveness Axis 1-Section E Program co-funded from European Regional Development Fund “Investments for Your Future” under Project No. 154/25.11.2016, P_37_221/2015, SMIS code 108117, “A novel graphene biosensor testing osteogenic potency; capturing best stem cell performance for regenerative medicine” (GRABTOP). Additionally, the in vitro biological testing was supported by a grant from the Romanian Ministry of Research and Innovation, CNCS-UEFISCDI grant number PN-III-P1-1.2-PCCDI-2017-0782/REGMED, within PNCDI III. This research was also supported by the National Council for Higher Education Funding (CNFIS) providing institutional development funds- project No. CNFIS-FDI-2021-0583.

Institutional Review Board Statement: The study was conducted according to the guidelines of the Declaration of Helsinki and approved by the Ethics Committee of Vasile Goldis Western University (Certificate no. 131 issued on 13 December 2018).

Informed Consent Statement: Not applicable.

Acknowledgments: The micro-computer tomography experiments were possible due to European Regional Development Fund through Competitiveness Operational Program 2014–2020, Priority axis 1, ID P_36_611, SMIS code 107066, INOVABIOMED. Biological research and infrastructure development were supported by CNFIS-FDI-2021-0583 grant.

Conflicts of Interest: The authors declare no conflict of interest.

References

- Nikolova, M.P.; Chavali, M.S. Recent advances in biomaterials for 3D scaffolds: A review. *Bioact. Mater.* **2019**, *4*, 271–292. [CrossRef] [PubMed]
- Foroutan, S.; Hashemian, M.; Khosravi, M.; Nejad, M.G.; Asefnejad, A.; Saber-Samandari, S.; Khandan, A. A Porous Sodium Alginate-CaSiO₃ Polymer Reinforced with Graphene Nanosheet: Fabrication and Optimality Analysis. *Fibers Polym.* **2021**, *22*, 540–549. [CrossRef]
- Di Silvio, L.; Jayakumar, P. Cellular response to osteoinductive materials in orthopedic surgery. In *Cellular Response to Biomaterials*; Di Silvio, L., Ed.; Woodhead Publishing: Cambridge, UK, 2009; Volume 1, pp. 313–343. [CrossRef]
- Filippi, M.; Born, G.; Chaaban, M.; Scherberich, A. Natural polymeric scaffolds in bone regeneration. *Front. Bioeng. Biotechnol.* **2020**, *8*, 474. [CrossRef] [PubMed]
- Şelaru, A.; Drăguşin, D.-M.; Olăreţ, E.; Serafim, A.; Steinmüller-Nethl, D.; Vasile, E.; Iovu, H.; Stancu, I.-C.; Costache, M.; Dinescu, S. Fabrication and Biocompatibility Evaluation of Nanodiamonds-Gelatin Electrospun Materials Designed for Prospective Tissue Regeneration Applications. *Materials* **2019**, *12*, 2933. [CrossRef] [PubMed]
- Hayashi, Y.; Yamada, S.; Guchi, K.Y.; Koyama, Z.; Ikeda, T. Chitosan and fish collagen as biomaterials for regenerative medicine. *Adv. Food Nutr. Res.* **2012**, *65*, 107–120. [CrossRef] [PubMed]
- Lynn, A.K.; Yannas, I.V.; Bonfield, W. Antigenicity and immunogenicity of collagen. *J. Biomed. Mater. Res.* **2004**, *71*, 343–354. [CrossRef]
- LogithKumar, R.; KeshavNarayan, A.; Dhivya, S.; Chawla, A.; Saravanan, S.; Selvamurugan, N. A review of chitosan and its derivatives in bone tissue engineering. *Carbohydr. Polym.* **2016**, *151*, 172–188. [CrossRef]
- Ranganathan, S.; Balagangadharan, K.; Selvamurugan, N. Chitosan and gelatin-based electrospun fibers for bone tissue engineering. *Int. J. Biol. Macromol.* **2019**, *133*, 354–364. [CrossRef]
- Maji, K.; Dasgupta, S.; Pramanik, K.; Bissoyi, A. Preparation and evaluation of gelatin-chitosan-nanobioglass 3D porous scaffold for bone tissue engineering. *Int. J. Biomater.* **2016**, *2016*, 9825659. [CrossRef]
- Dimida, S.; Barca, A.; Cancelli, N.; De Benedictis, V.; Raucci, M.G.; Demitri, C. Effects of genipin concentration on cross-linked chitosan scaffolds for bone tissue engineering: Structural characterization and evidence of biocompatibility features. *Int. J. Polym. Sci.* **2017**, *2017*, 8410750. [CrossRef]
- Wang, G.; Zheng, L.; Zhao, H.; Miao, J.; Sun, C.; Ren, N.; Wang, J.; Liu, H.; Tao, X. In vitro assessment of the differentiation potential of bone marrow-derived mesenchymal stem cells on genipin-chitosan conjugation scaffold with surface hydroxyapatite nanostructure for bone tissue engineering. *Tissue Eng. Part A* **2011**, *17*, 1341–1349. [CrossRef]
- Janfada, A.; Asefnejad, A.; Khorasani, M.T.; Joupari, M.D. Reinforcement of electrospun polycaprolacton scaffold using KIT-6 to improve mechanical and biological performance. *Polym. Test.* **2020**, *84*, 106391. [CrossRef]

14. Zhang, B.; Wei, P.; Zhou, Z.; Wei, T. Interactions of graphene with mammalian cells: Molecular mechanisms and biomedical insights. *Adv. Drug Deliv. Rev.* **2016**, *105*, 145–162. [CrossRef]
15. Vlaseanu, G.M.; Şelaru, A.; Dinescu, S.; Balta, C.; Herman, H.; Gharbia, S.; Hermenean, A.; Ionita, M.; Costache, M. Comprehensive appraisal of graphene–oxide ratio in porous biopolymer hybrids targeting bone-tissue regeneration. *Nanomaterials* **2020**, *10*, 144. [CrossRef]
16. Patel, S.K.; Choi, S.H.; Kang, Y.C.; Lee, J.K. Eco-friendly composite of Fe₃O₄-reduced graphene oxide particles for efficient enzyme immobilization. *ACS Appl. Mater. Interfaces* **2017**, *9*, 2213–2222. [CrossRef]
17. Mahmoudi, N.; Eslahi, N.; Mehdipour, A.; Mohammadi, M.; Akbari, M.; Samadikuchaksaraei, A.; Simchi, A. Temporary skin grafts based on hybrid graphene oxide-natural biopolymer nanofibers as effective wound healing substitutes: Preclinical and pathological studies in animal models. *J. Mater. Sci. Mater. Med.* **2017**, *28*, 73. [CrossRef]
18. Chu, J.; Shi, P.; Yan, W.; Fu, J.; Yang, Z.; He, C.; Deng, X.; Liu, H. PEGylated graphene oxide-mediated quercetin-modified collagen hybrid scaffold for enhancement of MSCs differentiation potential and diabetic wound healing. *Nanoscale* **2018**, *10*, 9547–9560. [CrossRef] [PubMed]
19. Bin Jo, S.; Erdenebileg, U.; Dashnyam, K.; Jin, G.-Z.; Cha, J.-R.; El-Fiqi, A.; Knowles, J.C.; Patel, K.D.; Lee, H.-H.; Lee, J.-H.; et al. Nano-graphene oxide/polyurethane nanofibers: Mechanically flexible and myogenic stimulating matrix for skeletal tissue engineering. *J. Tissue Eng.* **2020**, *11*. [CrossRef]
20. Saravanan, S.; Sareen, N.; Abu-El-Rub, E.; Ashour, H.; Sequiera, G.L.; Ammar, H.I.; Gopinath, V.; Shamaa, A.A.; Sayed, S.; Moudgil, M.; et al. Graphene Oxide-Gold Nanosheets Containing Chitosan Scaffold Improves Ventricular Contractility and Function After Implantation into Infarcted Heart. *Sci. Rep.* **2018**, *8*, 15069. [CrossRef] [PubMed]
21. Krukiewicz, K.; Putzer, D.; Stüendl, N.; Lohberger, B.; Awaja, F. Enhanced Osteogenic Differentiation of Human Primary Mesenchymal Stem and Progenitor Cultures on Graphene Oxide/Poly(methyl methacrylate) Composite Scaffolds. *Materials* **2020**, *13*, 2991. [CrossRef]
22. Li, M.; Xiong, P.; Yan, F.; Li, S.; Ren, C.; Yin, Z.; Li, A.; Li, H.; Ji, X.; Zheng, Y.; et al. An overview of graphene-based hydroxyapatite composites for orthopedic applications. *Bioact. Mater.* **2018**, *3*, 1–18. [CrossRef]
23. Kim, J.; Choi, K.S.; Kim, Y.; Lim, K.-T.; Seonwoo, H.; Park, Y.; Kim, D.-H.; Choung, P.-H.; Cho, C.-S.; Kim, S.Y.; et al. Bioactive effects of graphene oxide cell culture substratum on structure and function of human adipose-derived stem cells. *J. Biomed. Mater. Res. Part A* **2013**, *101*, 3520–3530. [CrossRef]
24. Bramini, M.; Alberini, G.; Colombo, E.; Chiacchiaretta, M.; DiFrancesco, M.L.; Maya-Vetencourt, J.F.; Maragliano, L.; Benfenati, F.; Cesca, F. Interfacing graphene-based materials with neural cells. *Front. Syst. Neurosci.* **2018**, *12*, 12. [CrossRef]
25. Verre, A.F.; Faroni, A.; Iliut, M.; Silva, C.; Mury, C.; Reid, A.J.; Vijayaraghavan, A. Improving the glial differentiation of human Schwann-like adipose-derived stem cells with graphene oxide substrates. *Interface Focus* **2018**, *8*, 20180002. [CrossRef]
26. Li, X.P.; Qu, K.Y.; Zhou, B.; Zhang, F.; Wang, Y.Y.; Abodunrin, O.D.; Zhu, Z.; Huang, N.P. Electrical stimulation of neonatal rat cardiomyocytes using conductive polydopamine-reduced graphene oxide-hybrid hydrogels for constructing cardiac microtissues. *Colloids Surf. B Biointerfaces* **2021**, *205*, 111844. [CrossRef]
27. Mukherjee, S.; Sriram, P.; Barui, A.K.; Nethi, S.K.; Veeriah, V.; Chatterjee, S.; Suresh, K.I.; Patra, C.R. Graphene oxides show angiogenic properties. *Adv. Healthc. Mater.* **2015**, *4*, 1722–1732. [CrossRef] [PubMed]
28. Di Carlo, R.; Di Crescenzo, A.; Pilato, S.; Ventrella, A.; Piattelli, A.; Recinella, L.; Chiavaroli, A.; Giordani, S.; Baldrighi, M.; Camisasca, A.; et al. Osteoblastic Differentiation on Graphene Oxide-Functionalized Titanium Surfaces: An In Vitro Study. *Nanomaterials* **2020**, *10*, 654. [CrossRef] [PubMed]
29. Maleki, M.; Zarezadeh, R.; Nouri, M.; Sadigh, A.R.; Pouremamali, F.; Asemi, Z.; Kafil, H.S.; Alemi, F.; Yousefi, B. Graphene Oxide: A Promising Material for Regenerative Medicine and Tissue Engineering. *Biomol. Concepts* **2020**, *11*, 182–200. [CrossRef] [PubMed]
30. Mollaqaem, V.K.; Asefnejad, A.; Nourani, M.R.; Goodarzi, V.; Kalae, M.R. Incorporation of graphene oxide and calcium phosphate in the PCL/PHBV core-shell nanofibers as bone tissue scaffold. *J. Appl. Polym. Sci.* **2020**, *138*. [CrossRef]
31. Zeng, Y.; Zhou, M.; Chen, L.; Fang, H.; Liu, S.; Zhou, C.; Sun, J.; Wang, Z. Alendronate loaded graphene oxide functionalized collagen sponge for the dual effects of osteogenesis and anti-osteoclastogenesis in osteoporotic rats. *Bioact. Mater.* **2020**, *5*, 859–870. [CrossRef]
32. Du, Z.; Wang, C.; Zhang, R.; Wang, X.; Li, X. Applications of Graphene and Its Derivatives in Bone Repair: Advantages for Promoting Bone Formation and Providing Real-Time Detection, Challenges and Future Prospects. *Int. J. Nanomed.* **2020**, *ume 15*, 7523–7551. [CrossRef]
33. Fang, H.; Luo, C.; Liu, S.; Zhou, M.; Zeng, Y.; Hou, J.; Chen, L.; Mou, S.; Sun, J.; Wang, Z. A biocompatible vascularized graphene oxide (GO)-collagen chamber with osteoinductive and anti-fibrosis effects promotes bone regeneration in vivo. *Theranostics* **2020**, *10*, 2759–2772. [CrossRef] [PubMed]
34. Du, Z.; Feng, X.; Cao, G.; She, Z.; Tan, R.; Aifantis, K.E.; Zhang, R.; Li, X. The effect of carbon nanotubes on osteogenic functions of adipose-derived mesenchymal stem cells in vitro and bone formation in vivo compared with that of nano-hydroxyapatite and the possible mechanism. *Bioact. Mater.* **2020**, *6*, 333–345. [CrossRef] [PubMed]
35. Chai, Y.C.; Kerckhofs, G.; Roberts, S.J.; Van Bael, S.; Schepers, E.; Vleugels, J.; Luyten, F.P.; Schrooten, J. Ectopic bone formation by 3D porous calcium phosphate-Ti6Al4V hybrids produced by perfusion electrodeposition. *Biomaterials* **2012**, *33*, 4044–4058. [CrossRef] [PubMed]

36. Calabrese, G.; Giuffrida, R.; Forte, S.; Salvatorelli, L.; Fabbi, C.; Figallo, E.; Gulisano, M.; Parenti, R.; Magro, G.; Colarossi, C.; et al. Bone augmentation after ectopic implantation of a cell-free collagen-hydroxyapatite scaffold in the mouse. *Sci. Rep.* **2016**, *6*, 36399. [CrossRef] [PubMed]
37. Chen, Z.; Zhang, Q.; Li, H.; Wei, Q.; Zhao, X.; Chen, F. Elastin-like polypeptide modified silk fibroin porous scaffold promotes osteochondral repair. *Bioact. Mater.* **2020**, *6*, 589–601. [CrossRef]
38. Karimi, M.; Asefnejad, A.; Aflaki, D.; Surendar, A.; Baharifar, H.; Saber-Samandari, S.; Khandan, A.; Khan, A.; Toghraie, D. Fabrication of shapeless scaffolds reinforced with baghdadite-magnetite nanoparticles using a 3D printer and freeze-drying technique. *J. Mater. Res. Technol.* **2021**, *14*, 3070–3079. [CrossRef]
39. Ye, X.; Yin, X.; Yang, D.; Tan, J.; Liu, G. Ectopic Bone Regeneration by Human Bone Marrow Mononucleated Cells, Undifferentiated and Osteogenically Differentiated Bone Marrow Mesenchymal Stem Cells in Beta-Tricalcium Phosphate Scaffolds. *Tissue Eng. Part C Methods* **2012**, *18*, 545–556. [CrossRef]
40. Li, W.; Zheng, Y.; Zhao, X.; Ge, Y.; Chen, T.; Liu, Y.; Zhou, Y. Osteoinductive Effects of Free and Immobilized Bone Forming Peptide-1 on Human Adipose-Derived Stem Cells. *PLoS ONE* **2016**, *11*, e0150294. [CrossRef]
41. Arnold, A.M.; Holt, B.D.; Daneshmandi, L.; Laurencin, C.T.; Sydlik, S.A. Phosphate graphene as an intrinsically osteoinductive scaffold for stem cell-driven bone regeneration. *Proc. Natl. Acad. Sci. USA* **2019**, *116*, 4855–4860. [CrossRef]
42. Vlasceanu, G.M.; Crica, L.E.; Pandele, A.M.; Ionita, M. Graphene oxide reinforcing genipin crosslinked chitosan-gelatin blend films. *Coatings* **2020**, *10*, 189. [CrossRef]
43. Liao, H.-T.; Chen, C.-T.; Chen, J.-P. Osteogenic Differentiation and Ectopic Bone Formation of Canine Bone Marrow-Derived Mesenchymal Stem Cells in Injectable Thermo-Responsive Polymer Hydrogel. *Tissue Eng. Part C Methods* **2011**, *17*, 1139–1149. [CrossRef]
44. Bae, I.-H.; Jeong, B.-C.; Kook, M.-S.; Kim, S.-H.; Koh, J.-T. Evaluation of a Thiolated Chitosan Scaffold for Local Delivery of BMP-2 for Osteogenic Differentiation and Ectopic Bone Formation. *BioMed Res. Int.* **2013**, *2013*, 878930. [CrossRef] [PubMed]
45. Zhang, Q.; He, Q.-F.; Zhang, T.-H.; Yu, X.-L.; Liu, Q.; Deng, F.-L. Improvement in the delivery system of bone morphogenetic protein-2: A new approach to promote bone formation. *Biomed. Mater.* **2012**, *7*, 045002. [CrossRef] [PubMed]
46. Lee, J.H.; Shin, Y.C.; Lee, S.-M.; Jin, O.S.; Kang, S.H.; Hong, S.W.; Jeong, C.-M.; Huh, J.B.; Han, D.-W. Enhanced Osteogenesis by Reduced Graphene Oxide/Hydroxyapatite Nanocomposites. *Sci. Rep.* **2015**, *5*, 18833. [CrossRef] [PubMed]
47. Mahanta, A.K.; Patel, D.K.; Maiti, P. Nanohybrid Scaffold of Chitosan and Functionalized Graphene Oxide for Controlled Drug Delivery and Bone Regeneration. *ACS Biomater. Sci. Eng.* **2019**, *5*, 5139–5149. [CrossRef] [PubMed]
48. Wan, C.; Frydrych, M.; Chen, B. Strong and bioactive gelatin–graphene oxide nanocomposites. *Soft Matter* **2011**, *7*, 6159–6166. [CrossRef]
49. Depan, D.; Pesacreta, T.C.; Misra, R.D.K. The synergistic effect of a hybrid graphene oxide–chitosan system and biomimetic mineralization on osteoblast functions. *Biomater. Sci.* **2013**, *2*, 264–274. [CrossRef] [PubMed]
50. Ventre, M.; Causa, F.; Netti, P.A. Determinants of cell–material crosstalk at the interface: Towards engineering of cell instructive materials. *J. R. Soc. Interface* **2012**, *9*, 2017–2032. [CrossRef]
51. Choi, K.Y.; Lee, S.W.; Park, M.H.; Bae, Y.C.; Shin, H.I.; Nam, S.; Kim, Y.J.; Kim, H.J.; Ryoo, H.M. Spatio-temporal expression patterns of Runx2 isoforms in early skeletogenesis. *Exp. Mol. Med.* **2002**, *34*, 426–433. [CrossRef]
52. Xiao, Z.S.; Hjelmeland, A.B.; Quarles, L.D. Selective deficiency of the “bone-related” Runx2-II unexpectedly preserves osteoblast-mediated skeletogenesis. *J. Biol. Chem.* **2004**, *279*, 20307–20313. [CrossRef]
53. Bruderer, M.; Richards, R.G.; Alini, M.; Stoddart, M.J. Role and regulation of RUNX2 in osteogenesis. *Eur. Cell Mater.* **2014**, *28*, 269–286. [CrossRef]
54. Fu, C.; Yang, X.; Tan, S.; Song, L. Enhancing cell proliferation and osteogenic differentiation of MC3T3-E1 pre-osteoblasts by BMP-2 delivery in graphene oxide-incorporated PLGA/HA biodegradable microcarriers. *Sci. Rep.* **2017**, *7*, 12549. [CrossRef]
55. Liu, M.; Hao, L.; Huang, Q.; Zhao, D.; Li, Q.; Cai, X. Tea polyphenol-reduced graphene oxide deposition on titanium surface enhances osteoblast bioactivity. *J. Nanosci. Nanotechnol.* **2018**, *18*, 3134–3140. [CrossRef]
56. Kang, S.; Park, J.B.; Lee, T.J.; Ryu, S.; Bhang, S.H.; La, W.G.; Noh, M.K.; Hong, B.H.; Kim, B.S. Covalent conjugation of mechanically stiff graphene oxide flakes to three-dimensional collagen scaffolds for osteogenic differentiation of human mesenchymal stem cells. *Carbon* **2015**, *83*, 162–172. [CrossRef]
57. Hermenean, A.; Codreanu, A.; Herman, H.; Balta, C.; Rosu, M.; Mihali, C.V.; Ivan, A.; Dinescu, S.; Ionita, M.; Costache, M. Chitosan-graphene oxide 3D scaffolds as promising tools for bone regeneration in critical-size mouse calvarial defects. *Sci. Rep.* **2017**, *7*, 16641. [CrossRef] [PubMed]
58. Ignat, S.-R.; Lazăr, A.D.; Şelaru, A.; Samoilă, I.; Vlăsceanu, G.M.; Ioniță, M.; Radu, E.; Dinescu, S.; Costache, M. Versatile Biomaterial Platform Enriched with Graphene Oxide and Carbon Nanotubes for Multiple Tissue Engineering Applications. *Int. J. Mol. Sci.* **2019**, *20*, 3868. [CrossRef]
59. Dinescu, S.; Ionita, M.; Ignat, S.-R.; Costache, M.; Hermenean, A. Graphene oxide enhances chitosan-based 3D scaffold properties for bone tissue engineering. *Int. J. Mol. Sci.* **2019**, *20*, 5077. [CrossRef] [PubMed]
60. Salgado, C.L.; Teixeira, B.I.B.; Monteiro, F.J.M. Biomimetic composite scaffold with phosphoserine signaling for bone tissue engineering application. *Front. Bioeng. Biotechnol.* **2019**, *7*, 206. [CrossRef]

61. Shabani, I.; Haddadi-Asl, V.; Soleimani, M.; Seyedjafari, E.; Hashemi, S.M. Ion-exchange polymer nanofibers for enhanced osteogenic differentiation of stem cells and ectopic bone formation. *ACS Appl. Mater. Interfaces* **2014**, *6*, 72–82. [CrossRef] [PubMed]
62. Osta, B.; Lavocat, F.; Eljaafari, A.; Miossec, P. Effects of interleukin-17A on osteogenic differentiation of isolated human mesenchymal stem cells. *Front. Immunol.* **2014**, *5*, 425. [CrossRef]
63. Komori, T. Signaling networks in RUNX2-dependent bone development. *J. Cell. Biochem.* **2011**, *112*, 750–755. [CrossRef]
64. Ling, M.; Huang, P.; Islam, S.; Heruth, D.P.; Li, X.; Zhang, L.Q.; Li, D.-Y.; Hu, Z.; Ye, S.Q. Epigenetic regulation of Runx2 transcription and osteoblast differentiation by nicotinamide phosphoribosyltransferase. *Cell Biosci.* **2017**, *7*, 27. [CrossRef]
65. Choi, J.-W.; Shin, S.; Lee, C.Y.; Lee, J.; Seo, H.-H.; Lim, S.; Lee, S.; Kim, I.-K.; Lee, H.-B.; Kim, S.W.; et al. Rapid Induction of Osteogenic Markers in Mesenchymal Stem Cells by Adipose-Derived Stromal Vascular Fraction Cells. *Cell. Physiol. Biochem.* **2017**, *44*, 53–65. [CrossRef]
66. Dubey, N.; Bentini, R.; Islam, I.; Cao, T.; Castro Neto, A.H.; Rosa, V. Graphene: A versatile carbon-based material for bone tissue engineering. *Stem Cells Int.* **2015**, *2015*, 804213. [CrossRef]
67. Prasad, S.; Suresh, S.; Wong, R. Osteogenic potential of graphene in bone tissue engineering scaffolds. *Materials* **2018**, *11*, 1430. [CrossRef]
68. Shadjou, N.; Hasanzadeh, M. Graphene and its nanostructure derivatives for use in bone tissue engineering: Recent advances. *J. Biomed. Mater. Res. Part. A* **2016**, *104*, 1250–1275. [CrossRef] [PubMed]
69. Morgan, E.F.; Unnikrisnan, G.U.; Hussein, A.I. Bone mechanical properties in healthy and diseased states. *Annu. Rev. Biomed. Eng.* **2018**, *20*, 119–143. [CrossRef] [PubMed]
70. Hadden, W.J.; Young, J.L.; Holle, A.; McFetridge, M.L.; Kim, D.Y.; Wijesinghe, P.; Taylor-Weiner, H.; Wen, J.H.; Lee, A.; Bieback, K.; et al. Stem cell migration and mechanotransduction on linear stiffness gradient hydrogels. *Proc. Natl. Acad. Sci. USA* **2017**, *114*, 5647–5652. [CrossRef] [PubMed]
71. Kourkoumelis, N.; Zhang, X.; Lin, Z.; Wang, J. Fourier transform infrared spectroscopy of bone tissue: Bone quality assessment in preclinical and clinical applications of osteoporosis and fragility fracture. *Clin. Rev. Bone Miner. Metab.* **2019**, *17*, 24–39. [CrossRef]
72. Xu, W.; Wang, W.; Hao, L.; Zhao, W.; Liu, H.; Wang, X. Effect of generation number on properties of fluoroalkyl-terminated hyperbranched polyurethane latexes and its films. *J. Appl. Polym. Sci.* **2020**, *137*, 49215. [CrossRef]
73. Lui, K.; Jackson, M.; Sowa, M.G.; Ju, H.; Dixon, I.M.; Mantsch, H.H. Modification of the extracellular matrix following myocardial infarction monitored by FTIR spectroscopy. *Biochim. Biophys. Acta* **1996**, *1315*, 73–77. [CrossRef]
74. Wang, X.-F.; Li, M.-L.; Fang, Q.-Q.; Zhao, W.-Y.; Lou, D.; Hu, Y.-Y.; Chen, J.; Wang, X.-Z.; Tan, W.-Q. Flexible electrical stimulation device with Chitosan-Vaseline[®] dressing accelerates wound healing in diabetes. *Bioact. Mater.* **2021**, *6*, 230–243. [CrossRef]
75. Abasalta, M.; Asefnejad, A.; Khorasani, M.T.; Saadatabadi, A.R. Fabrication of carboxymethyl chitosan/poly (ϵ -caprolactone)/doxorubicin/nickel ferrite core-shell fibers for controlled release of doxorubicin against breast cancer. *Carbohydr. Polym.* **2021**, *257*, 117631. [CrossRef]
76. Liu, H.; Lin, M.; Liu, X.; Zhang, Y.; Luo, Y.; Pang, Y.; Chen, H.; Zhu, D.; Zhong, X.; Ma, S.; et al. Doping bioactive elements into a collagen scaffold based on synchronous self-assembly/mineralization for bone tissue engineering. *Bioact. Mater.* **2020**, *5*, 844–858. [CrossRef]
77. de Campos Vidal, B.; Mello, M.L.S. Collagen type I amide I band infrared spectroscopy. *Micron* **2011**, *42*, 283–289. [CrossRef]
78. Unal, M.; Jung, H.; Akkus, O. Novel Raman spectroscopic biomarkers indicate that postyield damage denatures bone's collagen. *J. Bone Miner. Res.* **2016**, *31*, 1015–1025. [CrossRef]
79. Mata-Miranda, M.M.; Guerrero-Ruiz, M.; Gonzalez-Fuentes, J.R.; Hernandez-Toscano, C.M.; Garcia-Andino, J.R.; Sanchez-Brito, M.; Vazquez-Zapien, G.J. Characterization of the biological fingerprint and identification of associated parameters in stress fractures by FTIR spectroscopy. *Biomed. Res. Int.* **2019**, *2019*, 1241452. [CrossRef] [PubMed]
80. Smirnov, I.V.; Rau, J.V.; Fosca, M.; De Bonis, A.; Latini, A.; Teghil, R.; Kalita, V.I.; Fedotov, A.Y.; Gudkov, S.V.; Baranchikov, A.E.; et al. Structural modification of titanium surface by octacalcium phosphate via Pulsed Laser Deposition and chemical treatment. *Bioact. Mater.* **2017**, *2*, 101–107. [CrossRef] [PubMed]
81. Imbert, L.; Gourion-Arsiquaud, S.; Villarreal-Ramirez, E.; Spevak, L.; Taleb, H.; van der Meulen, M.C.H.; Mendelsohn, R.; Boskey, A.L. Dynamic structure and composition of bone investigated by nanoscale infrared spectroscopy. *PLoS ONE* **2018**, *13*, e0202833. [CrossRef] [PubMed]
82. Ionita, M.; Crica, L.E.; Tiainen, H.; Haugen, H.J.; Vasile, E.; Dinescu, S.; Costache, M.; Iovu, H. Gelatin–poly(vinyl alcohol) porous biocomposites reinforced with graphene oxide as biomaterials. *J. Mater. Chem. B* **2016**, *4*, 282–291. [CrossRef]
83. Banc, A.; Desbat, B.; Cavagnat, D. Ab initio calculations of proline vibrations with and without water: Consequences on the infrared spectra of proline-rich proteins. *Appl. Spectrosc.* **2011**, *65*, 817–819. [CrossRef] [PubMed]
84. Balan, V.; Mihai, C.-T.; Cojocaru, F.-D.; Uritu, C.-M.; Dodi, G.; Botezat, D.; Gardikiotis, I. Vibrational spectroscopy fingerprinting in medicine: From molecular to clinical practice. *Materials* **2019**, *12*, 2884. [CrossRef] [PubMed]
85. Boskey, A.L.; Spevak, L.; Ma, Y.; Wang, H.; Bauer, D.C.; Black, D.M.; Schwartz, A.V. Insights into the bisphosphonate holiday: A preliminary FTIR study. *Osteoporos. Int.* **2018**, *29*, 699–705. [CrossRef] [PubMed]
86. Schuetz, R.; Fix, D.; Schade, U.; Aziz, E.F.; Timofeeva, N.; Weinkamer, R.; Masic, A. Anisotropy in bone demineralization revealed by polarized far-IR spectroscopy. *Molecules* **2015**, *20*, 5835–5850. [CrossRef]

87. Lopes, C.D.C.A.; Limirio, P.H.J.O.; Novais, V.R.; Dechichi, P. Fourier transform infrared spectroscopy (FTIR) application chemical characterization of enamel, dentin and bone. *Appl. Spectrosc. Rev.* **2018**, *53*, 747–769. [CrossRef]
88. Woess, C.; Unterberger, S.H.; Roider, C.; Ritsch-Martel, M.; Pemberger, N.; Cemper-Kiesslich, J.; Hatzler-Grubwieser, P.; Parson, W.; Pallua, J.D. Assessing various Infrared (IR) microscopic imaging techniques for post-mortem interval evaluation of human skeletal remains. *PLoS ONE* **2017**, *12*, e0174552. [CrossRef] [PubMed]
89. Liu, F.; Antoniou, J.; Li, Y.; Ma, J.; Zhong, F. Effect of sodium acetate and drying temperature on physicochemical and thermomechanical properties of gelatin films. *Food Hydrocoll.* **2015**, *45*, 140–149. [CrossRef]
90. Benbettaieb, N.; Karbowiak, T.; Brachais, C.-H.; Debeaufort, F. Impact of electron beam irradiation on fish gelatin film properties. *Food Chem.* **2016**, *195*, 11–18. [CrossRef]
91. Youssef, A.M.; Abou-Youcef, H.; El-Sayed, S.M.; Kamel, S. Mechanical and antibacterial properties of novel high performance chitosan/nanocomposite films. *Int. J. Biol. Macromol.* **2015**, *76*, 25–32. [CrossRef]
92. Li, Z.; Yang, F.; Yang, R. Synthesis and characterization of chitosan derivatives with dual-antibacterial functional groups. *Int. J. Biol. Macromol.* **2015**, *75*, 378–387. [CrossRef]
93. Naito, P.K.; Ogawa, Y.; Kimura, S.; Iwata, T.; Wada, M. Crystal transition from hydrated chitosan and chitosan/monocarboxylic acid complex to anhydrous chitosan investigated by X-ray diffraction. *J. Polym. Sci. B Polym. Phys.* **2015**, *53*, 1065–1069. [CrossRef]
94. Jampafuang, Y.; Tongta, A.; Waiprib, Y. Impact of crystalline structural differences between α - and β -chitosan on their nanoparticle formation via ionic gelation and superoxide radical scavenging activities. *Polymers* **2019**, *11*, 2010. [CrossRef]
95. Cheng, J.; Zhu, H.; Huang, J.; Zhao, J.; Yan, B.; Ma, S.; Zhang, H.; Fan, D. The physicochemical properties of chitosan prepared by microwave heating. *Food Sci. Nutr.* **2020**, *8*, 1987–1994. [CrossRef]
96. Song, X.; Liu, L.; Wu, X.; Liu, Y.; Yuan, J. Chitosan-Based Functional Films Integrated with Magnolol: Characterization, Antioxidant and Antimicrobial Activity and Pork Preservation. *Int. J. Mol. Sci.* **2021**, *22*, 7769. [CrossRef]
97. Tronci, G.; Russell, S.J.; Wood, D.J. Photo-active collagen systems with controlled triple helix architecture. *J. Mater. Chem. B* **2013**, *1*, 3705–3715. [CrossRef] [PubMed]
98. El-Meliegy, E.; Abu-Elsaad, N.I.; El-Kady, A.M.; Ibrahim, M.A. Improvement of physico-chemical properties of dextran-chitosan composite scaffolds by addition of nano-hydroxyapatite. *Sci. Rep.* **2018**, *8*, 12180. [CrossRef] [PubMed]



Article

Graphene Quantum Dots Modified Upconversion Nanoparticles for Photodynamic Therapy

Yuting Li [†], Yufei Wang [†], Hong Shang ^{*} and Jing Wu ^{*}

School of Science, China University of Geosciences (Beijing), Beijing 100083, China

^{*} Correspondence: shanghong@cugb.edu.cn (H.S.); wujing@cugb.edu.cn (J.W.);

Tel.: +86-10-8232-2758 (H.S. & J.W.)

[†] These authors contributed equally to this work.

Abstract: Photodynamic therapy (PDT), as a novel technique, has been extensively employed in cancer treatment by utilizing reactive oxygen species (ROS) to kill malignant cells. However, most photosensitizers (PSs) are short of ROS yield and affect the therapeutic effect of PDT. Thus, there is a substantial demand for the development of novel PSs for PDT to advance its clinical translation. In this study, we put forward a new strategy for PS synthesis via modifying graphene quantum dots (GQDs) on the surface of rare-earth elements doped upconversion nanoparticles (UCNPs) to produce UCNPs@GQDs with core-shell structure. This new type of PSs combined the merits of UCNPs and GQDs and produced ROS efficiently under near-infrared light excitation to trigger the PDT process. UCNPs@GQDs exhibited high biocompatibility and obvious concentration-dependent PDT efficiency, shedding light on nanomaterials-based PDT development.

Keywords: photodynamic therapy; photosensitizer; upconversion nanoparticles; graphene quantum dots; reactive oxygen species



Citation: Li, Y.; Wang, Y.; Shang, H.; Wu, J. Graphene Quantum Dots Modified Upconversion Nanoparticles for Photodynamic Therapy. *Int. J. Mol. Sci.* **2022**, *23*, 12558. <https://doi.org/10.3390/ijms232012558>

Academic Editors: Ilaria Rea, Nicola Borbone, Monica Terracciano and Chiara Tramontano

Received: 3 October 2022

Accepted: 18 October 2022

Published: 19 October 2022

Publisher's Note: MDPI stays neutral with regard to jurisdictional claims in published maps and institutional affiliations.



Copyright: © 2022 by the authors. Licensee MDPI, Basel, Switzerland. This article is an open access article distributed under the terms and conditions of the Creative Commons Attribution (CC BY) license (<https://creativecommons.org/licenses/by/4.0/>).

1. Introduction

Photodynamic therapy (PDT) is an emerging cancer treatment method combining light, oxygen, and a photosensitizer (PS) to produce highly cytotoxic reactive oxygen species (ROS) that cause cancer cell death [1–3]. Two kinds of mechanisms (type I and II) are involved in the PDT process. In most cases, the type II mechanism needs to transform ground-state triplet oxygen ($^3\text{O}_2$) into highly reactive singlet oxygen ($^1\text{O}_2$) and is limited by the concentration of O_2 . Different from the type II route, the type I process takes place through either electron or hydrogen atom abstraction by exciting PSs from the substrate and performs well even under low O_2 conditions [4,5]. Compared with conventional cancer therapy methods, PDT is superior in minimal side effects, low cumulative toxicity, precise targeting therapy with no damage to neighboring normal tissues, and long-term therapeutic effect [6]; however, inherent shortages of PDT impede its clinical translation, such as limited depth of light penetration, inefficient ROS generation, and lacking ideal PSs.

In recent years, nanoparticles (NPs) have been tried to be used as PSs toward solving the associated problems with PDT [7,8]. Upconversion nanoparticles (UCNPs) are a new type of optical nanomaterials composed of rare earth elements with low bandgap and featured with narrow emission bands and excellent photostability [9–12]. The upconversion luminescence of UCNPs provides an alternative way to overcome the existing drawbacks of PDT [13]. The near-infrared (NIR) excitation light of UCNPs is a transparent window in tissue and permits deep tissue penetration. Besides that, due to the adjustable doped ratio of rare earth elements, the intramolecular charge transfer can be realized via excited state absorption and energy transfer, which provides a promising pathway for electron transfer aiding ROS generation [14,15]. Meanwhile, versatile nanocomposites based on UCNPs can be designed due to their easy surface functionalization and show great potential for PDT applications.

In this work, UCNPs (NaYF₄:Yb/Er) were modified with graphene quantum dots (GQDs) to obtain a composite (UCNPs@GQDs) which was used as PSs for PDT in the NIR therapeutic window. The surface of UCNPs was activated by the N-doped GQDs, which were synthesized by using folic acid (FA) as a carbon source. GQDs were selected as the modification agent due to their rich valence band could stabilize electrons/holes [16]. GQDs displayed some advantages which were beneficial for PDT, such as excellent photoluminescent features, corrosion resistance, high water solubility, high photo/pH-stability, in vitro and in vivo biocompatibility, and efficient ROS generation [17,18]. Here, the ROS generation performance was dramatically promoted in the composite of UCNPs@GQDs due to the up-convert energy transition and Dexter excitation transfer (DET), which was identified by photoluminescence (PL) spectra. ROS production was accompanied by the chemical adsorption of oxygen, which was reduced by the photo-induced electrons to be O₂^{•-} and then was oxidized to be ¹O₂ by holes. Significantly, upon protonation, the charge separation was further increased due to the improved light absorption capacity and limited electron-hole recombination. Combined with the excellent charge separation and promoted oxygen diffusion and ROS release, the modified UCNPs led to excellent PDT performance through the type I mechanism.

2. Results

2.1. Characterization of UCNPs@GQDs

The morphology of UCNPs@GQDs was examined by transmission electron microscopy (TEM) and scanning electron microscope (SEM) (Figures 1a and S1b). UCNPs@GQDs exhibited a core-shell structure, and the thickness of the shell was about 1.8 nm. All of the nanoparticles displayed similar shapes and equal sizes. UCNP lattice was observed, and the width of lattice fringes was 0.51 nm which was consistent with the characteristic packing of UCNP demonstrating the core-shell structure of UCNPs@GQDs. Elemental mapping images in Figure S2 also proved this and showed that the distribution of elements C, N, and O was consistent with that of elements Y and Yb. The X-ray diffraction (XRD) patterns of the synthesized GQDs, UCNPs, and UCNPs@GQDs are presented in Figure 1b. XRD profile of UCNP clearly revealed their crystallization of the α phase (JCPDS 77-2042) [19]. The obvious peak located at 25° in the XRD pattern of GQDs arose from the 002-lattice plane [20]. The XRD pattern of UCNPs@GQDs demonstrated their well-crystallized structure, which was the same as that of UCNP. The zeta potential of GQDs, UCNPs, and UCNPs@GQDs was detected in pH = 7 aqueous medium and is shown in Figure 1c. It exhibited that the zeta potential of GQDs was opposite to that of UCNP. That was why the two particles were mutually combined to form a composite. Meanwhile, the decrease in zeta potential for UCNPs@GQDs proved the successful loading of GQDs. The detailed bond structure on the UCNPs@GQDs surface was confirmed by X-ray photoelectron spectroscopy (XPS) spectra (Figure 1d–f). In the high-resolution XPS spectra of C 1s of UCNPs@GQDs, C=C (284.2 eV), C-O (284.9 eV), and C=O (288.4 eV) peaks were observed and demonstrated the existence of GQDs on the surface of UCNP. The high-resolution XPS spectra of Y 3d also confirmed this result. In addition to the presence of the Y-F (161.2 eV) peak of NaYF₄, Y-O (159.2 eV) peak also presented with higher strength, possibly because the oxygen-containing functional groups existing on the surface of GQDs filled within lattice defects of NaYF₄. As a result, DET may occur between GQDs and UCNP. The convergence of the XPS profiles of C 1s and Y 3d was good, demonstrating the credibility of these data (Figure S3).

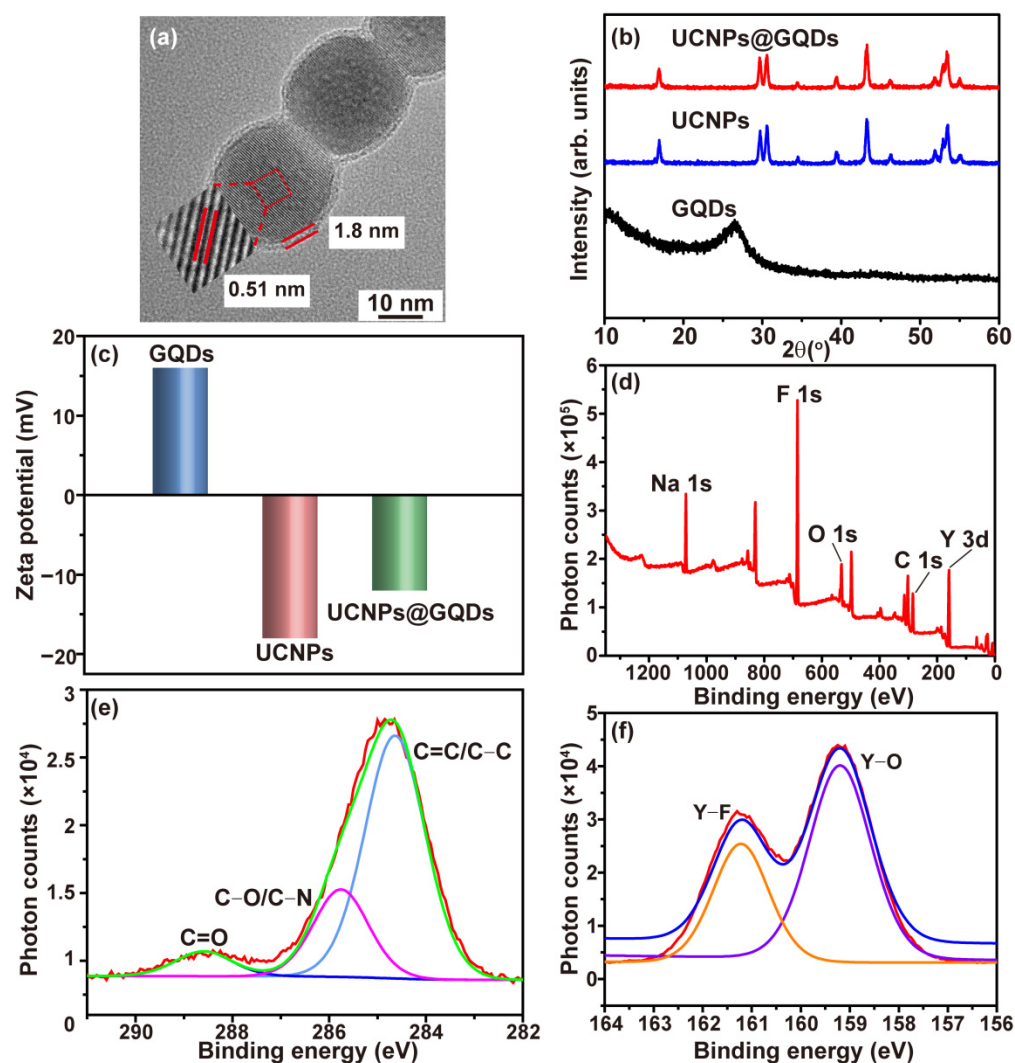


Figure 1. Characterization of UCNPs@GQDs. (a) HRTEM image of UCNPs@GQDs. The inset was the lattice fringes of UCNPs. (b) XRD pattern of UCNPs@GQDs. (c) Zeta potential of GQDs, UCNPs, and UCNPs@GQDs. (d) XPS survey spectrum of UCNPs@GQDs. (e) High-resolution C 1s XPS profiles of UCNPs@GQDs. (f) High-resolution Y 3d XPS profiles of UCNPs@GQDs.

As one kind of carbon dot, GQDs also have excitation wavelength-dependent PL emission [21]. GQDs emission exhibited a red shift as the excitation light shifted to a longer wavelength (Figure 2a). The strongest emission of GQDs was located at 412 nm when the excitation wavelength was 350 nm. Such properties were inherited in UCNPs@GQDs PL spectra, which also had the red-shift effect and gave the maximum emission at the wavelength of 382 nm excited by the light of 320 nm (Figure 2b). The PL emission of UCNPs@GQDs gives them the potential to be fluorescent imaging materials. The decrease in emission intensity of UCNPs@GQDs was referred to as the result of the blocking of $n-\pi^*$ transitions of oxygen-containing functional groups on the surface of GQDs. Based on XPS spectra, the oxygen-containing functional groups partially filled in the lattice defects of UCNPs, making some n -electrons participate in forming feedback bonds, which weakened the PL emission of UCNPs@GQDs. These results indirectly proved the successful formation of the core-shell structure in UCNPs@GQDs. Meanwhile, under the irradiation of 980 nm laser, the main emission peaks of the UCNPs located at 407, 525, 543, and 657 nm and were attributed to ${}^2\text{H}_{9/2} \rightarrow {}^4\text{I}_{15/2}$, ${}^2\text{H}_{11/2} \rightarrow {}^4\text{I}_{15/2}$, ${}^4\text{S}_{3/2} \rightarrow {}^4\text{I}_{15/2}$, ${}^4\text{F}_{9/2} \rightarrow {}^4\text{I}_{15/2}$ transitions of Er^{3+} ions, respectively. GQDs gave a broad UV-Vis absorption band which centered at ~ 310 nm but had no overlap with the emission of UCNPs, indicating there was no

Förster resonance energy transfer between UCNPs and GQDs (Figure 2c) [22,23]. The emission spectra of UCNPs@GQDs, UCNPs, and GQDs were detected through exciting by a 980 nm laser to explore the possible energy transfer mechanism between the UCNPs and GQDs. Compared with the emission spectrum of UCNPs, the main emission peak located at 543 nm significantly dropped as well as a new emission peak appeared at 354 nm in the emission spectrum of UCNPs@GQDs (Figure 2d). The new emission at the short wavelength availed electron ionization in high-energy states to generate ROS in an aqueous environment. The emission intensity of UCNPs@GQDs was dramatically quenched by GQDs, giving a promise for cytotoxic $^1\text{O}_2$ generation [24]. The inset photograph in Figure 2d also clearly showed that the upconversion luminescence of UCNPs was partially quenched by the incorporated GQDs. Pure GQDs gave no upconversion emission irradiated by the 980 nm laser. As a result, the synthesized UCNPs@GQDs can be used as a potential PDT agent activated by NIR lights.

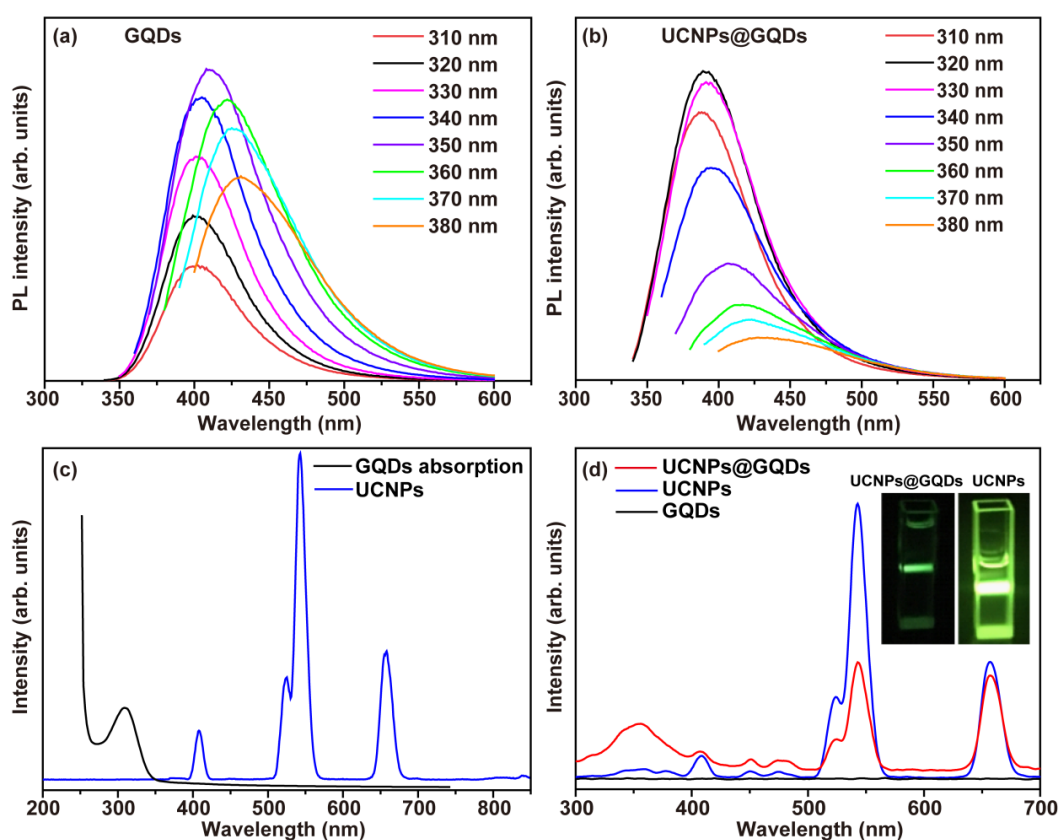


Figure 2. Optical properties of UCNPs@GQDs. (a) PL spectra of GQDs detecting with different excitation wavelengths. (b) PL spectra of UCNPs@GQDs detecting with different excitation wavelengths. (c) The spectral overlap of GQDs absorption and UCNPs emission ($\lambda_{\text{ex}} = 980$ nm). (d) Upconversion luminescence spectra of UCNPs@GQDs, UCNPs, and GQDs ($\lambda_{\text{ex}} = 980$ nm). The inset is the photograph of UCNPs@GQDs and UCNPs upon 980 nm laser irradiation.

2.2. In Vitro ROS Detection for UCNPs@GQDs

$\cdot\text{OH}$ and $^1\text{O}_2$ are two kinds of ROS that are cytotoxic to cancer cells and can kill them by activating cell apoptosis or necrosis by attacking organic compounds encountered in the PDT process. Room-temperature electron paramagnetic resonance (EPR) spectra were collected to detect $\cdot\text{OH}$ generated by UCNPs@GQDs under the irradiation of a 980 nm laser. DMPO was utilized as a specific detection reagent for $\cdot\text{OH}$ to examine the variation of $\cdot\text{OH}$ generation with the irradiation time. In Figure 3a, the characteristic 1:2:2:1 EPR signals (marked with red asterisk symbols) were assigned to DMPO- $\cdot\text{OH}$ and confirmed the generation of $\cdot\text{OH}$, which increased with the time of laser irradiation. In this system, DMPO

was oxidized by $^1\text{O}_2$ to be 5,5-dimethyl-2-oxopyrroline-1-oxyl (DMPOX), which gave triplet signals in EPR spectra (marked with black square symbols), indicating the existence of $^1\text{O}_2$ in this system. Meanwhile, $^1\text{O}_2$ generation was further detected by two specific fluorescent probes, Singlet Oxygen Sensor Green (SOSG) and 1,3-diphenylisobenzofuran (DPBF). SOSG was sensitive to $^1\text{O}_2$, while it did not react with $\cdot\text{OH}$ or superoxide. SOSG reacted with $^1\text{O}_2$ to give green FL, which became more intense with the increasing amount of $^1\text{O}_2$. As shown in Figures 3b and S4a,b, the FL intensity of SOSG rapidly increased with the presence of both UCNP and UCNP@GQDs under the 980 nm laser irradiation. Compared with the FL intensity curve of UCNP, the slope of the curve of UCNP@GQDs was larger, indicating more $^1\text{O}_2$ generation induced by UCNP@GQDs. Then, $^1\text{O}_2$ production of UCNP@GQDs was investigated by DPBF, which was a commercial fluorescent probe and irreversibly reacted with $^1\text{O}_2$ to be 1,2-dibenzoylbenzene (DBB) (Figure S4c). The conjugated structure in DBB was broken and resulted in the decrease of absorbance of DPBF. Upon irradiation by a 980 nm laser, the absorbance intensities were decreased by UCNP and UCNP@GQDs, while GQDs brought no effect on the absorbance intensity (Figures 3c and S3d). Both UCNP and UCNP@GQDs induced $^1\text{O}_2$ generation. The irradiation time was longer, and the decrease in the absorbance intensity was faster (Figure S4e,f). The slope of the curves in Figure 3c represented the efficiency of $^1\text{O}_2$ generation. It was obvious that the efficiency of $^1\text{O}_2$ generation induced by UCNP@GQDs was higher than that of UCNP. All these results demonstrated the capability of UCNP@GQDs for ROS generation, which is promising for their application in PDT.

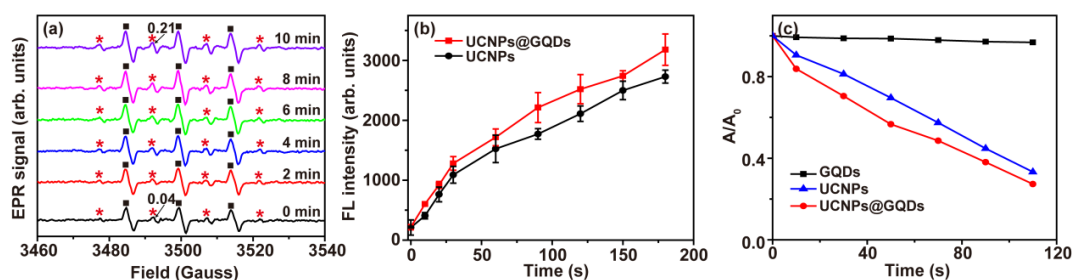


Figure 3. In vitro $^1\text{O}_2$ detection for UCNP@GQDs. (a) EPR spectra of UCNP@GQDs were detected under the irradiation of a 980 nm laser for different times. DMPO was used as the specific scavenger agent to detect $\cdot\text{OH}$ generation. The EPR signals marked with red asterisk symbols were assigned to DMPO- $\cdot\text{OH}$. The EPR signals marked with black square symbols were assigned to $^1\text{O}_2$. (b) FL intensity curves of SOSG were detected at 525 nm upon treatment by UCNP and UCNP@GQDs and subsequent 980 nm laser irradiation in different time duration. (c) Absorption decay curves of DPBF were detected at 420 nm upon treatment by UCNP@GQDs and subsequent 980 nm laser irradiation in different time duration.

2.3. PDT Assessment for UCNP@GQDs

Before PDT assessment, the cytotoxicity of UCNP@GQDs was evaluated by Live/Dead assay kit to make sure whether their biocompatibility was appropriate for PDT tests. A series of UCNP@GQDs concentrations ranging from 0.16 to 1600 $\mu\text{g}\cdot\text{mL}^{-1}$ were assessed in order to test all the concentrations used in PDT tests. Without NIR laser irradiation, the cells treated by UCNP@GQDs exhibited high cell viability, which was above 80% at the concentration even up to 1600 $\mu\text{g}\cdot\text{mL}^{-1}$ suggesting the good biocompatibility of the synthesized UCNP@GQDs (Figures 4a and S5a). UCNP@GQDs-treated cells followed by NIR laser irradiation had an apparently declined cell viability compared with the dark group demonstrating UCNP@GQDs had perfect PDT efficacy for tumor cells (Figures 4b and S5b). The data in Figures 4b and S4c also indicate that UCNP@GQDs displayed poor toxicity to the cells under dark conditions.

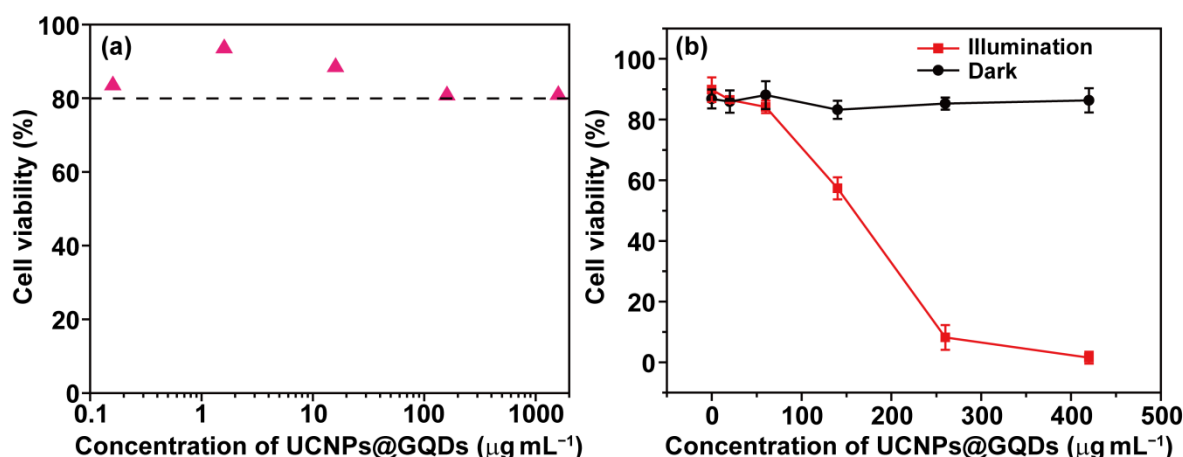


Figure 4. PDT assessment for UCNPs@GQDs. (a) Biocompatibility of UCNPs@GQDs was assessed without irradiation of a 980 nm laser. (b) Cell viability of HeLa cells treated by UCNPs@GQDs was determined by Live/Dead assay kit.

High ROS generation is indispensable for a PS and plays an important role in the PDT process. The amount of ROS is kept low in a normal intracellular microenvironment of cancer cells and easily neutralized by *in vivo* antioxidants. PS can break this balance by inducing a large amount of ROS generation and initiating cell apoptosis. Dihydroethidium (DHE) was used as a specific FL probe to detect intracellular ROS generation induced by UCNPs@GQDs under NIR laser irradiation. Intracellular DHE gave blue FL emission ($\lambda_{\text{ex}} = 370 \text{ nm}$) before illumination and reacted with ROS to give red FL emission ($\lambda_{\text{ex}} = 535 \text{ nm}$) after illumination. As shown in Figure 5, the red FL of ROS augmented with the increase in UCNPs@GQDs concentration, and the results were consistent with the data on cell viability.

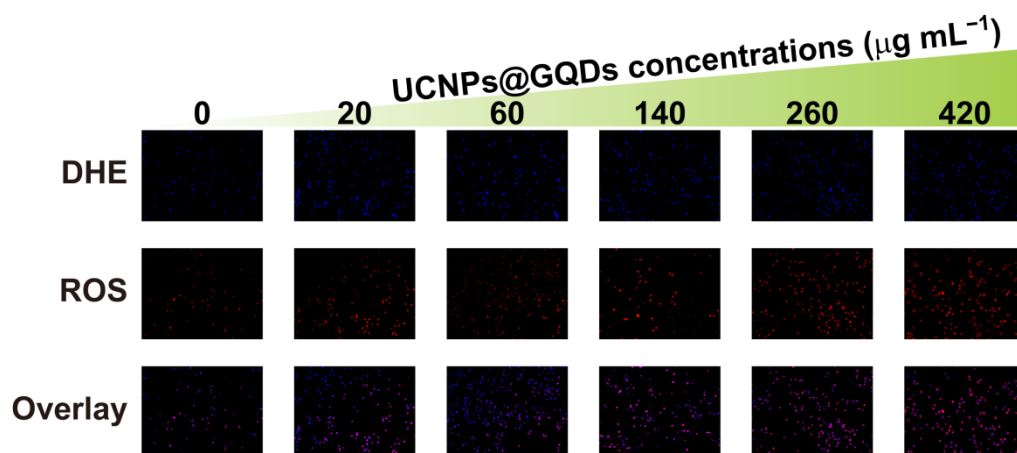


Figure 5. Intracellular ROS detection using DHE as the specific fluorescent probe. HeLa cells were treated with different concentrations of UCNPs@GQDs and illuminated by a 980 nm laser.

3. Discussion

Here, GQDs-modified UCNPs were used as a novel PS in the PDT process induced by NIR light. The composite UCNPs@GQDs were facilely prepared and exhibited excellent biocompatibility. Cytotoxic ROS was efficiently generated upon NIR light irradiation. As a result, this work provides a novel paradigm with highly integrated functionalities, which exhibits excellent prospects not only for imaging-guided PDT but also encourages us to further explore new types of multifunctional NPs for biomedical applications.

4. Materials and Methods

4.1. Reagents and Materials

FA, oleic acid, 1-octadecene, and Tris-HCl buffer were all purchased from Sigma-Aldrich Chemical Co. Ltd. (St. Louis, MO, USA). Ethanol (99.7%) and sodium hydroxide were purchased from Sinopharm Chemical Reagent Co. Ltd. (Shanghai, China). Hydrochloric acid (HCl), methanol (MeOH), and cyclohexane were supplied by Beijing Chemical Reagent Co. Ltd. (Beijing, China). SOSG, DPBF, and DHE were purchased from Leyan reagent Co. Ltd. All chemical reagents were used as received without further purification.

4.2. Apparatus

High-resolution TEM (HRTEM) images were recorded by a JEOL-1400 transmission electron microscope (JEOL, Tokyo, Japan). The PL spectra were performed on an Agilent Cary Eclipse spectrofluorometer (F-7000, Hitachi, Japan). The slit width was set as 5 nm. The voltage of the photomultiplier tube (PMT) was controlled to be 700 V. UV-vis absorption spectra were collected on a PerkinElmer Lambda 950 spectrophotometer. SEM images were taken on a field emission scanning electron microscope (FESEM, Carl Zeiss AG, Germany). XRD spectra were collected on Bruker D8 diffractometer with the Cu K α radiation. XPS was measured by an X-ray photoelectron spectrometry (AXIS SUPRA, SHIMADZU, Japan). EPR spectra were measured on a Bruker E500 spectrometer.

4.3. Material Synthesis

4.3.1. Synthesis of GQDs

GQDs were synthesized according to a previous method with some modifications [25]. Then, 10 mg FA was dissolved in 15 mL of deionized water. It was uniformly dispersed under ultrasonic conditions and then transferred into a 25 mL Teflon-lined stainless-steel autoclave. The FA solution was heated at 240 °C for 6 h. After cooling to room temperature, a dark brown liquid was obtained and centrifuged at 12,000 rpm for 10 min to remove the sediment. The product was freeze-dried and stored at room temperature for further use. The obtained N-doped GQDs were sphere-like NPs of about 2–3 nm size (Figure S1a) and consisting of nitrogen and functional groups of –OH, –NH₂, and –COOH.

4.3.2. Synthesis of UCNPs

The coprecipitation method was adopted to synthesize the UCNPs (NaYF₄:Yb/Er) following a recipe from the literature with some slight modifications [26]. Then, 3.2 mL Y(OAc)₃ (0.2 M), 720 μ L Yb(OAc)₃ (0.2 M), 80 μ L Er(OAc)₃ (0.2 M), and 6 mL oleic acid were mixed well in a 100 mL two-neck flask, and the reaction was carried out at 150 °C for 30 min under vigorous stirring to evaporate the water. Then, 14 mL 1-octadecene was added to the mixture, and the reaction was kept at 150 °C for another 30 min. After that, the temperature of the mixture was cooled to ~50 °C. Then, 4 mL NaOH solution (0.5 M, dissolved in MeOH) was mixed with 8 mL NH₄F solution (0.4 M) and quickly added into the reaction system, which was kept at 50 °C for 30 min. Then, the temperature of the system was warmed up to 100 °C and held for 20 min to remove MeOH. After three cycles of pumping and charging with high-purity nitrogen, the reaction was carried out at 290 °C for 2 h under nitrogen protection. After the reaction was completed and cooled to room temperature, ethanol, cyclohexane, 2 M HCl:ethanol (V:V = 1:1), and deionized water were used to clean the reactant by centrifugation, and the solid was collected for subsequent use.

4.3.3. Synthesis of UCNPs@GQDs

In total, 4 mL GQDs (1 mg·mL⁻¹) were uniformly mixed with 12.8 mg UCNPs and then sonicated for 20 min. Subsequently, the mixture was loaded into a Teflon line stainless steel autoclave and reacted at 80 °C for 6 h. After the reaction, it was cooled to room temperature. The product was mixed with deionized water and centrifuged twice at 12,000 rpm for 15 min. The solid was collected and dispersed in 0.05 M Tris-HCl buffer (pH = 7.4) for further use.

4.4. Assessment of $^1\text{O}_2$ Generation

SOSG was used as a $^1\text{O}_2$ indicator to evaluate the $^1\text{O}_2$ generation [27]. SOSG reacted with $^1\text{O}_2$ to give bright green fluorescence (FL) ($\lambda_{\text{ex}}/\lambda_{\text{em}} = 504/525$ nm). GQDs, UCNPs, or UCNPs@GQDs were suspended in 2 mL water at the concentration of $500 \mu\text{g}\cdot\text{mL}^{-1}$ in the presence of $10 \mu\text{M}$ SOSG. The mixed suspension was exposed to laser irradiation ($0.8 \text{ W}\cdot\text{cm}^{-2}$, 980 nm) for 0, 10, 20, 30, 60, 90, 120, and 180 s, and the FL at different time points was measured with a fluorimeter. Further, $^1\text{O}_2$ generation was monitored by DPBF via UV-vis spectroscopy [28]. DPBF ($100 \mu\text{g}\cdot\text{mL}^{-1}$) was dispersed in GQDs, UCNPs, or UCNPs@GQDs solutions. Then, the mixed solution was irradiated by a 980 nm laser with the power of $0.8 \text{ W}\cdot\text{cm}^{-2}$. The change of absorption of DPBF at 412 nm was recorded over time.

4.5. PDT Tests

4.5.1. Biocompatibility of UCNPs@GQDs

HeLa cells were seeded at a density of 1×10^4 cells per well in a 96-well plate and cultured at 37°C for 24 h in a 5% CO_2 environment. After that, the culture medium was replaced by a series of UCNPs@GQDs solutions (dissolved in Tris-HCl) with concentration gradients (1.6×10^{-4} , 1.6×10^{-3} , 1.6×10^{-2} , 0.16, and $1.6 \text{ mg}\cdot\text{mL}^{-1}$) and the cells continued to be cultured for 24 h. Afterwards, cell apoptosis was analyzed by staining cells with a Live/Dead assay kit (Calcein-AM/EthD-1, Invitrogen, CA, USA). The stained cells were observed by an FL confocal microscope, and the data were analyzed by the program Image-Pro Plus 6.0. Three independent experiments were carried out with the same concentration gradients of UCNPs@GQDs solutions.

4.5.2. Cell Apoptosis Assays

HeLa cells were seeded at a density of 1×10^4 cells per well in a 96-well plate and cultured at 37°C for 24 h in a 5% CO_2 environment. The 96-well plate is numbered from top to bottom and from left to right. The No. 1–3 rows on the 96-well plate were used for PDT tests, and the No. 4–6 rows were used as the control groups without NIR laser irradiation. After 24 h cell culture, UCNPs@GQDs solutions were infused into the wells in rows 1–6. The wells in rows No. 7 and 8 were infused with blank Tris-HCl buffer solution. Cells were incubated with UCNPs@GQDs for 6 h. After that, a 980 nm laser beam with the power of $0.8 \text{ W}/\text{cm}^2$ was used to irradiate the cells in No. 1–3 and 7 rows for 20 min, and the irradiation was stopped for 1 min every 1 min. After another 48-h incubation, the cells were stained by a Live/Dead assay kit and observed by an FL confocal microscope. For intercellular ROS detection, the cells were stained by DHE and observed by an FL confocal microscope. The data were analyzed by the program Image-Pro Plus 6.0.

Supplementary Materials: The following supporting information can be downloaded at: <https://www.mdpi.com/article/10.3390/ijms232012558/s1>.

Author Contributions: Y.L. and Y.W. equally contributed to this work. Methodology, data analysis, and draft writing, Y.L.; methodology and data analysis, Y.W.; writing—review and editing, H.S.; supervision, project administration, and funding acquisition, J.W. All authors have read and agreed to the published version of the manuscript.

Funding: This research was funded by the National Natural Science Foundation of China (Nos. 21874120 and 22001240), Beijing Natural Science Foundation (No. 2222022), and the Fundamental Research Funds for the Central Universities (Nos. 2652019112 and 2652018004).

Institutional Review Board Statement: Not applicable.

Informed Consent Statement: Not applicable.

Conflicts of Interest: The authors declare no conflict of interest.

References

- Karges, J. Clinical development of metal complexes as photosensitizers for photodynamic therapy of cancer. *Angew. Chem. Int. Edit.* **2022**, *61*, e202112236. [CrossRef] [PubMed]
- Pham, T.C.; Nguyen, V.N.; Choi, Y.; Lee, S.; Yoon, J. Recent strategies to develop innovative photosensitizers for enhanced photodynamic therapy. *Chem. Rev.* **2021**, *121*, 13454–13619. [CrossRef] [PubMed]
- Yang, Y.; Zeng, Z.; Almatrafi, E.; Huang, D.; Zhang, C.; Xiong, W.; Cheng, M.; Zhou, C.; Wang, W.; Song, B.; et al. Core-shell structured nanoparticles for photodynamic therapy-based cancer treatment and related imaging. *Coord. Chem. Rev.* **2022**, *458*, 214427. [CrossRef]
- Tabrizi, P.F.; Wennige, S.; Berneburg, M.; Maisch, T. Susceptibility of soda- and sodb-deficient escherichia coli mutant towards antimicrobial photodynamic inactivation via the type i-mechanism of action. *Photoch. Photobio. Sci.* **2018**, *17*, 352–362. [CrossRef]
- Huang, L.; Zhao, S.; Wu, J.; Yu, L.; Singh, N.; Yang, K.; Lan, M.; Wang, P.; Kim, J.S. Photodynamic therapy for hypoxic tumors: Advances and perspectives. *Coord. Chem. Rev.* **2021**, *438*, 213888. [CrossRef]
- Dolmans, D.E.J.G.; Fukumura, D.; Jain, R.K. Photodynamic therapy for cancer. *Nat. Rev. Cancer* **2003**, *3*, 380–387. [CrossRef]
- Choi, J.; Sun, I.C.; Hwang, H.S.; Yoon, H.Y.; Kim, K. Light-triggered photodynamic nanomedicines for overcoming localized therapeutic efficacy in cancer treatment. *Adv. Drug Deliver. Rev.* **2022**, *186*, 114344. [CrossRef]
- Zhou, S.Y.; Li, D.D.; Lee, C.; Xie, J. Nanoparticle phototherapy in the era of cancer immunotherapy. *Trends Chem.* **2020**, *2*, 1082–1095. [CrossRef]
- Han, S.Y.; Yi, Z.G.; Zhang, J.B.; Gu, Q.F.; Liang, L.L.; Qin, X.; Xu, J.H.; Wu, Y.M.; Xu, H.; Rao, A.; et al. Photon upconversion through triplet exciton-mediated energy relay. *Nat. Commun.* **2021**, *12*, 3704. [CrossRef]
- Han, S.Y.; Deng, R.R.; Gu, Q.F.; Ni, L.M.; Huynh, U.; Zhang, J.B.; Yi, Z.G.; Zhao, B.D.; Tamura, H.; Pershin, A.; et al. Lanthanide-doped inorganic nanoparticles turn molecular triplet excitons bright. *Nature* **2020**, *587*, 594. [CrossRef]
- Yi, Z.G.; Luo, Z.C.; Qin, X.; Chen, Q.S.; Liu, X.G. Lanthanide-activated nanoparticles: A toolbox for bioimaging, therapeutics, and neuromodulation. *Acc. Chem. Res.* **2020**, *53*, 2692–2704. [CrossRef] [PubMed]
- Zheng, K.Z.; Loh, K.Y.; Wang, Y.; Chen, Q.S.; Fan, J.Y.; Jung, T.; Nam, S.H.; Suh, Y.D.; Liu, X.G. Recent advances in upconversion nanocrystals: Expanding the kaleidoscopic toolbox for emerging applications. *Nano Today* **2019**, *29*, 100797. [CrossRef]
- Liu, Y.; Meng, X.; Bu, W. Upconversion-based photodynamic cancer therapy. *Coord. Chem. Rev.* **2019**, *379*, 82–98. [CrossRef]
- Li, Y.; Jia, D.L.; Ren, W.; Shi, F.; Liu, C.H. A versatile photoinduced electron transfer-based upconversion fluorescent biosensing platform for the detection of disease biomarkers and nerve agent. *Adv. Funct. Mater.* **2019**, *29*, 1903191. [CrossRef]
- Xu, H.; Han, S.Y.; Deng, R.R.; Su, Q.Q.; Wei, Y.; Tang, Y.A.; Qin, X.; Liu, X.G. Anomalous upconversion amplification induced by surface reconstruction in lanthanide sublattices. *Nat. Photonics* **2021**, *15*, 732–737. [CrossRef]
- Yan, Y.; Gong, J.; Chen, J.; Zeng, Z.; Huang, W.; Pu, K.; Liu, J.; Chen, P. Recent advances on graphene quantum dots: From chemistry and physics to applications. *Adv. Mater.* **2019**, *31*, 1808283. [CrossRef] [PubMed]
- Zhang, X.L.; Wei, C.B.; Li, Y.; Yu, D.S. Shining luminescent graphene quantum dots: Synthesis, physicochemical properties, and biomedical applications. *TrAC Trends Anal. Chem.* **2019**, *116*, 109–121. [CrossRef]
- Chung, S.; Revia, R.A.; Zhang, M.Q. Graphene quantum dots and their applications in bioimaging, biosensing, and therapy. *Adv. Mater.* **2021**, *33*, 1904362. [CrossRef]
- Vukovic, M.; Dinic, I.; Jardim, P.; Marković, S.; Veselinović, L.; Nikolić, M.; Mancic, L. The low-temperature sonochemical synthesis of up-converting β NaYF₄:Yb,Er mesocrystals. *Adv. Powder Technol.* **2022**, *33*, 103403. [CrossRef]
- Kumar, S.; Ojha, A.K.; Ahmed, B.; Kumar, A.; Das, J.; Materny, A. Tunable (violet to green) emission by high-yield graphene quantum dots and exploiting its unique properties towards sun-light-driven photocatalysis and supercapacitor electrode materials. *Mater. Today Commun.* **2017**, *11*, 76–86. [CrossRef]
- Ghosh, S.; Chizhik, A.M.; Karedla, N.; Dekaliuk, M.O.; Gregor, I.; Schuhmann, H.; Seibt, M.; Bodensiek, K.; Schaap, I.A.T.; Schulz, O.; et al. Photoluminescence of carbon nanodots: Dipole emission centers and electron–phonon coupling. *Nano Lett.* **2014**, *14*, 5656–5661. [CrossRef] [PubMed]
- Wu, L.; Huang, C.; Emery, B.P.; Sedgwick, A.C.; Bull, S.D.; He, X.; Tian, H.; Yoon, J.; Sessler, J.L.; James, T.D. Förster resonance energy transfer (fret)-based small-molecule sensors and imaging agents. *Chem. Soc. Rev.* **2020**, *49*, 5110–5139. [CrossRef] [PubMed]
- Zu, F.; Yan, F.; Bai, Z.; Xu, J.; Wang, Y.; Huang, Y.; Zhou, X. The quenching of the fluorescence of carbon dots: A review on mechanisms and applications. *Microchim. Acta* **2017**, *184*, 1899–1914. [CrossRef]
- Zhang, D.; Wen, L.; Huang, R.; Wang, H.; Hu, X.; Xing, D. Mitochondrial specific photodynamic therapy by rare-earth nanoparticles mediated near-infrared graphene quantum dots. *Biomaterials* **2018**, *153*, 14–26. [CrossRef] [PubMed]
- Liu, H.F.; Li, Z.H.; Sun, Y.Q.; Geng, X.; Hu, Y.L.; Meng, H.M.; Ge, J.; Qu, L.B. Synthesis of luminescent carbon dots with ultrahigh quantum yield and inherent folate receptor-positive cancer cell targetability. *Sci. Rep.* **2018**, *8*, 1086. [CrossRef]
- Wang, F.; Deng, R.; Liu, X. Preparation of core-shell nagdf4 nanoparticles doped with luminescent lanthanide ions to be used as upconversion-based probes. *Nat. Protoc.* **2014**, *9*, 1634–1644. [CrossRef]
- Hou, W.Y.; Yuan, Y.; Sun, Z.Z.; Guo, S.X.; Dong, H.W.; Wu, C.F. Ratiometric fluorescent detection of intracellular singlet oxygen by semiconducting polymer dots. *Anal. Chem.* **2018**, *90*, 14629–14634. [CrossRef]
- Wang, X.H.; Yu, Y.X.; Cheng, K.; Yang, W.; Liu, Y.A.; Peng, H.S. Polylysine modified conjugated polymer nanoparticles loaded with the singlet oxygen probe 1,3-diphenylisobenzofuran and the photosensitizer indocyanine green for use in fluorometric sensing and in photodynamic therapy. *Microchim. Acta* **2019**, *186*, 842. [CrossRef]



Communication

Molecular Level Characterisation of the Surface of Carbohydrate-Functionalised Mesoporous silica Nanoparticles (MSN) as a Potential Targeted Drug Delivery System via High Resolution Magic Angle Spinning (HR-MAS) NMR Spectroscopy

Karolina Krajewska ¹, Anna M. Gołkowska ¹, Maciej Nowak ¹, Marta Kozakiewicz-Latała ¹,
Wojciech Pudło ², Andrzej Żak ³, Bożena Karolewicz ¹, Yaroslav Z. Khimyak ⁴ and Karol P. Nartowski ^{1,*}

¹ Department of Drug Form Technology, Wrocław Medical University, Borowska 211A, 50-556 Wrocław, Poland; karolina.krajewska@student.umw.edu.pl (K.K.); anna.golkowska@student.umw.edu.pl (A.M.G.); maciej.nowak@umed.wroc.pl (M.N.); marta.kozakiewicz-latala@umw.edu.pl (M.K.-L.); bozena.karolewicz@umed.wroc.pl (B.K.)

² Department of Chemical Engineering and Process Design, Silesian University of Technology, M. Strzody 7 Str., 44-100 Gliwice, Poland; wojciech.pudlo@polsl.pl

³ Faculty of Mechanical Engineering, Wrocław University of Science and Technology (WUST), Wybrzeże Wyspińskiego 27, 50-370 Wrocław, Poland; andrzej.zak@pwr.edu.pl

⁴ School of Pharmacy, University of East Anglia, Norwich Research Park, Norwich NR4 7TJ, UK; y.khimyak@uea.ac.uk

* Correspondence: karol.nartowski@umw.edu.pl; Tel.: +48-71-784-05-69



Citation: Krajewska, K.; Gołkowska, A.M.; Nowak, M.; Kozakiewicz-Latała, M.; Pudło, W.; Żak, A.; Karolewicz, B.; Khimyak, Y.Z.; Nartowski, K.P. Molecular Level Characterisation of the Surface of Carbohydrate-Functionalised Mesoporous silica Nanoparticles (MSN) as a Potential Targeted Drug Delivery System via High Resolution Magic Angle Spinning (HR-MAS) NMR Spectroscopy. *Int. J. Mol. Sci.* **2022**, *23*, 5906. <https://doi.org/10.3390/ijms23115906>

Academic Editors: Monica Terracciano, Ilaria Rea, Nicola Borbone and Chiara Tramontano

Received: 24 April 2022

Accepted: 20 May 2022

Published: 25 May 2022

Publisher's Note: MDPI stays neutral with regard to jurisdictional claims in published maps and institutional affiliations.

Abstract: Atomistic level characterisation of external surface species of mesoporous silica nanoparticles (MSN) poses a significant analytical challenge due to the inherently low content of grafted ligands. This study proposes the use of HR-MAS NMR spectroscopy for a molecular level characterisation of the external surface of carbohydrate-functionalised nanoparticles. MSN differing in size (32 nm, 106 nm, 220 nm) were synthesised using the sol-gel method. The synthesised materials displayed narrow particle size distribution (based on DLS and TEM results) and a hexagonal arrangement of the pores with a diameter of ca. 3 nm as investigated with PXRD and N₂ physisorption. The surface of the obtained nanoparticles was functionalised with galactose and lactose using reductive amination as confirmed by FTIR and NMR techniques. The functionalisation of the particles surface did not alter the pore architecture, structure or morphology of the materials as confirmed with TEM imaging. HR-MAS NMR spectroscopy was used for the first time to investigate the structure of the functionalised MSN suspended in D₂O. Furthermore, lactose was successfully attached to the silica without breaking the glycosidic bond. The results demonstrate that HR-MAS NMR can provide detailed structural information on the organic functionalities attached at the external surface of MSN within short experimental times.

Keywords: mesoporous silica nanoparticles; MSN; porous materials; functionalisation; NMR; HR-MAS NMR; surface



Copyright: © 2022 by the authors. Licensee MDPI, Basel, Switzerland. This article is an open access article distributed under the terms and conditions of the Creative Commons Attribution (CC BY) license (<https://creativecommons.org/licenses/by/4.0/>).

1. Introduction

Porous materials are solids that have pores, cavities, channels or fissures with depths greater than the width [1]. Three types of porous materials can be distinguished based on the pore size: microporous (pore diameter < 2 nm), mesoporous (pore diameter 2–50 nm) and macroporous (pore diameter > 50 nm) [1]. Mesoporous silica materials are synthesised using the sol-gel method in the presence of an acidic or basic catalyst [2–4]. The first synthesis of MCM-41 (Mobil Crystalline Materials/Mobil Composition of Matter)-type mesoporous silica particles was described in 1992 by Beck et al., which enabled

particles characterised by a hexagonal pore arrangement with a pore size of 2–10 nm to be obtained [5,6]. In the MSN synthesis, the source of silica is usually TEOS (tetraethoxysilane), whose alkoxy groups undergo hydrolysis to silane groups, followed by homo- (reaction of silane groups with each other) and heterocondensation (reaction of alkoxy groups with silane groups) resulting in the formation of Si-O-Si siloxane bridges. Silica condensation occurs on a template (e.g., CTAB, cetyltrimethylammonium bromide) that forms cylindrically organised micelles. The surfactant (template) is removed by solvent extraction or calcination (at about 550 °C) leading to the final product. The particle size, pore size or shape can be modified by controlling the reaction conditions [7].

Mesoporous silica nanoparticles (MSN) have two surfaces, an outer surface and an inner surface, both covered with silanol (Si-OH) groups which allow their covalent conjugation with different types of functional groups such as carboxylates, amines, phosphonates, polyethylene glycol, octadecyl and carboxylate/octadecyl groups to name a few [8,9]. This property of MSN can be utilised for the synthesis of targeted drug delivery systems that can selectively bind to different cellular receptors or cell compartments [3,10]. One can distinguish between two methods of surface functionalisation: grafting and co-condensation. Co-condensation is a process that allows the direct functionalisation of silica during the material synthesis process. Typically, R-TMS or R-TEOS organosilanes, where R is the organic functional group and TMS or TES (trimethoxysilane and triethoxysilane, respectively) are added to the reaction either together with TEOS or immediately after the addition of TEOS, which ensures the incorporation of the organosilanes into the final product. This method is mainly preferred for the functionalisation of the inner surface of nanoparticles [11]. In contrast, grafting is a post-synthetic method of attaching organic or inorganic functional groups to the MSN surface. The reaction requires the condensation of organosilanes of the (R'O)₃SiR type (where R stands for an organic radical) with reactive -Si-OH end groups in an anhydrous solvent, e.g., toluene. Grafting allows the preparation of hydrothermally stable MSN using classical synthesis methods and the subsequent selective functionalisation of the outer surface of these materials [7,12,13]. The grafting method was used in this work to functionalise nanoparticles with an amine group, galactose and lactose.

The unique properties of MSN, e.g., a high degree of ordering of their internal porous structure, hydrothermal stability and the possibility of surface modification has led to the application of MSN in many branches of science, including nanotechnology, medicine or pharmaceutical drug delivery [3,14–17]. A number of reports have demonstrated that the functionalisation of the MSN external surface is desirable for targeted cancer therapy applications as it increases the efficiency of material penetration into the tumour microenvironment [3,8,17–21]. MSN can also be used as novel carriers for nucleic acids in emerging gene therapies. Mukherjee and co-workers investigated the possibility of hepatitis C therapy using galactose-functionalised MSN with encapsulated shDNA. The presence of galactose at the silica surface was responsible for their selective uptake by liver cells that overexpress the asialoglycoprotein receptor. The plasmid shDNA encapsulated in the particles acted as a precursor for in situ siRNA production that binds to the target HCV mRNA sequence causing its degradation. Biodistribution studies in an in vivo model showed an increased uptake of galactose-modified silica in the liver compared to other organs. Further in vitro infection studies showed a significant (94%) reduction in viral RNA after shDNA delivery using Gal-AMSN in a HCV-JFH1 cell culture [21].

Understanding the spatial distribution of the functional groups at the silica surface is important for the rational design of new MSN for targeted drug delivery. The molecular structure of functionalised MSN can be analysed with solid-state NMR spectroscopy [22–24]. This method allows the chemical characterisation of the material structure along the surface species, enabling an investigation into the local environment of different nuclei (e.g., ¹H, ²⁹Si and ¹³C) to obtain distance information, the degree of organic functionalisation or the dynamics of functional groups [25]. The main limitation for the broad application of solid-state NMR spectroscopy for the characterisation of organically modified silica materials is the low sensitivity of the method which is mostly pronounced in the case of nanomaterials

that possess functionalities exclusively at the external surface of the particles. Furthermore, the ^1H NMR spectra of solids often show very broad lines due to the presence of strong dipolar couplings or orientation-dependent interactions (e.g., chemical shift anisotropy) even under RF decoupling or high rates of magic angle spinning (MAS). Structural analysis using the abovementioned methods is usually performed on dried powders, which does not reproduce the behaviour of MSN in an aqueous environment [26]. It should be considered that complex chemical transformations that do not occur in the solid phase may occur in biorelevant fluids (e.g., aggregation or opsonisation) [27]. For this reason, the development of novel methods for the structural analysis of functionalised nanomaterials is crucial for understanding their structure and dynamics in solutions. Recently, Tataurova et al. [28] authors used solution-state NMR spectroscopy to determine the number of bound and released ligands or groups that were exchanged upon the hydrothermal treatment of functionalised mesoporous silicas [29,30].

Advantages of solid- and solution-state NMR can be combined in the so called High Resolution Magic Angle Spinning (HR-MAS) technique that allows the analysis of materials that swell and become partially soluble or form true solutions even when some solids are still present. High resolution spectra are obtained due to spinning the sample at the 'magic angle' ($\theta = 54.7^\circ$) with respect to the static magnetic field, which enables the strong anisotropic interactions to be overcome and as a consequence the width of the signals can be reduced. One of the advantages of this NMR technique is its timing. High resolution two-dimensional spectra (e.g., ^1H - ^{13}C HSQC) in HR-MAS can be acquired in much less time (as short as 30 min) compared to the spectra obtained using solid state ^1H - ^{13}C HETCOR NMR techniques (several hours to several days) [31,32].

In this work we propose for the first time the application of HR-MAS NMR spectroscopy for the molecular level characterisation of the surface of functionalised MCM-41-type MSN in an aqueous medium in minutes. For this purpose, silica nanoparticles varying in size (32 nm, 106 nm, 220 nm) were synthesised and then their external surface was functionalised with APTES (amino group donor), galactose and lactose using the grafting method following the removal of the templating agent (Figure 1, Scheme 1). The size, shape and hexagonal structure of the particles were confirmed using DLS, low angle PXRD and N_2 physisorption analysis corroborated with TEM imaging. The presence of organic functionalities at the silica surface was confirmed with ^1H - ^{29}Si CP/MAS NMR, HR-MAS NMR spectroscopy and with FTIR. The development of a novel analytical technique for the molecular level understanding of functionalised nanomaterials enables a knowledge-based design of advanced functionalised nanocarriers for targeted drug delivery.

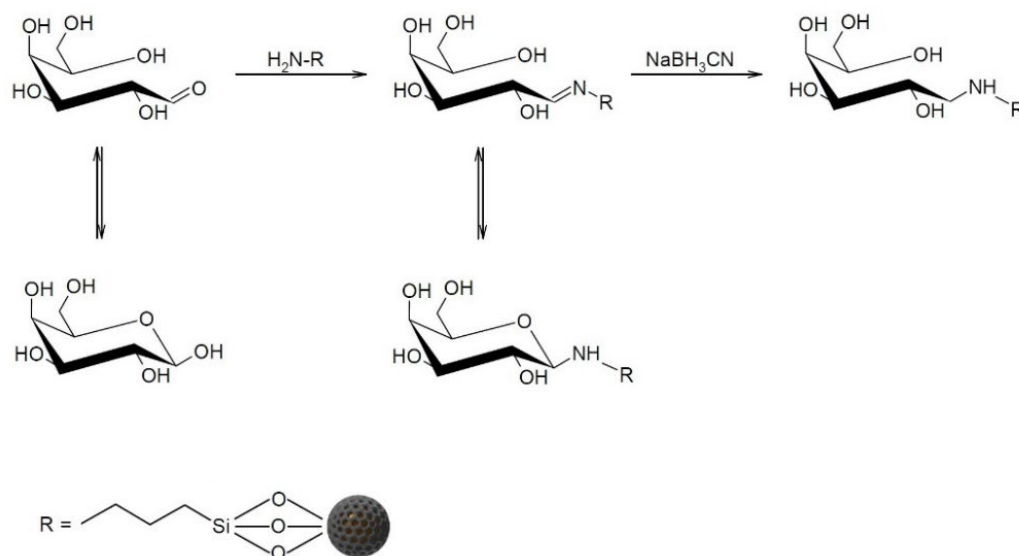
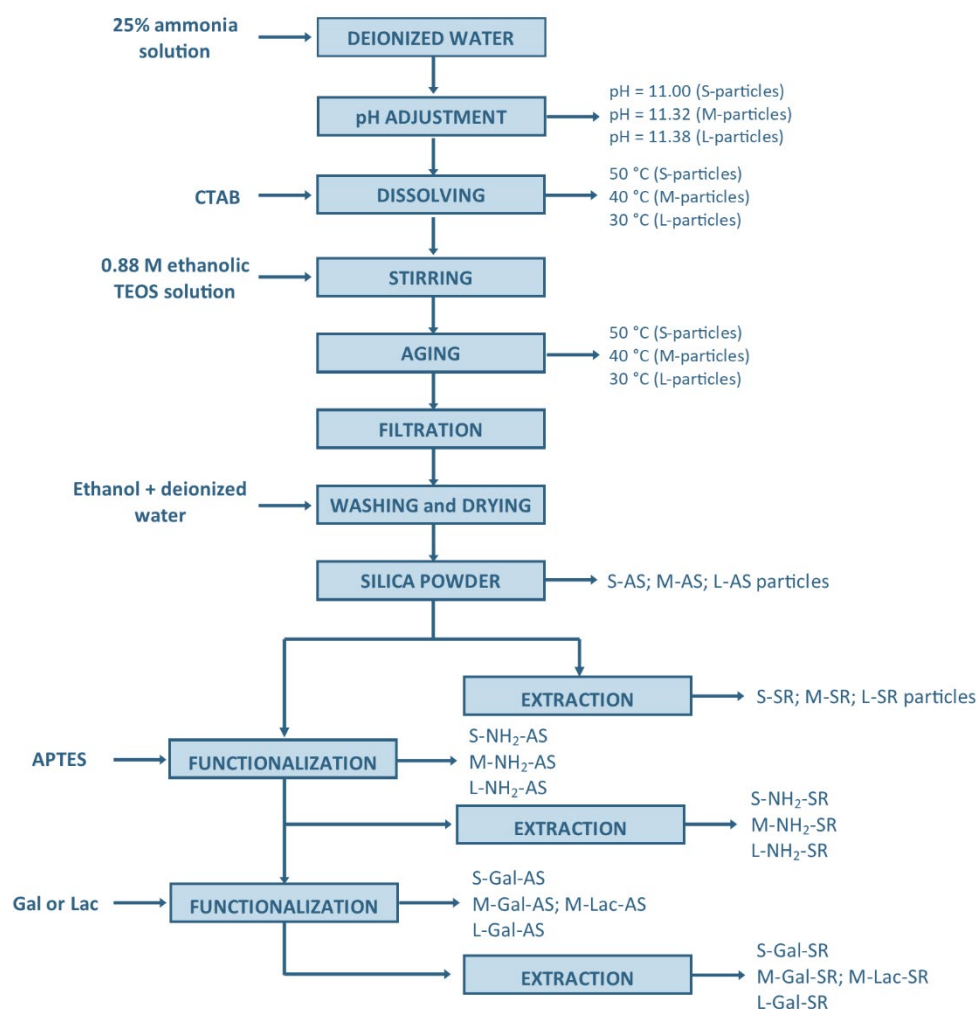


Figure 1. Reductive amination of galactose with amino-functionalised MSN.



Scheme 1. Flowchart presenting the synthesis, functionalisation and extraction steps required to obtain galactose and lactose-functionalised MSN particles. The abbreviations used for the materials labelling: S—small—32 nm particles; M—medium—106 nm particles; L—large—220 nm particles; AS—as synthesised; SR—surfactant removed; NH₂—amino functionalised particles; Gal—galactose; Lac—lactose.

2. Results and Discussion

The successful synthesis of MSN (Scheme 1) was confirmed by a combination of analytical techniques which enabled an assessment of the size of the particles, BET surface area, pore volume and architecture as well as the formation of specific bonds. The main manuscript provides a detailed characterisation of the ‘M’ particles, while the analysis of ‘S’ and ‘L’ particles is provided in the Supplementary Materials (Figures S1–S10), which proves that the approach is applicable for nanoparticles with different sizes.

2.1. Particle Size, Morphology and Pore Architecture

The particle size was confirmed directly by TEM (Figure 2) imaging and the results were supported indirectly by dynamic light scattering (DLS) analysis (Figure 3). The obtained particles were 32 nm (PDI = 0.261) (for the ‘S’ materials), 106 nm (PDI = 0.163) (for the ‘M’ materials) and 220 nm (PDI = 0.165) (for the ‘L’ materials) in diameter, respectively. The particle sizes observed in the TEM images were slightly smaller than the particle sizes determined by the DLS studies due to the differences in the analytical principle used in both methods. The size of the particles obtained from DLS analysis is the hydrodynamic diameter, which takes into account the diameter of the particle along with the solvation layer adsorbed on its surface.

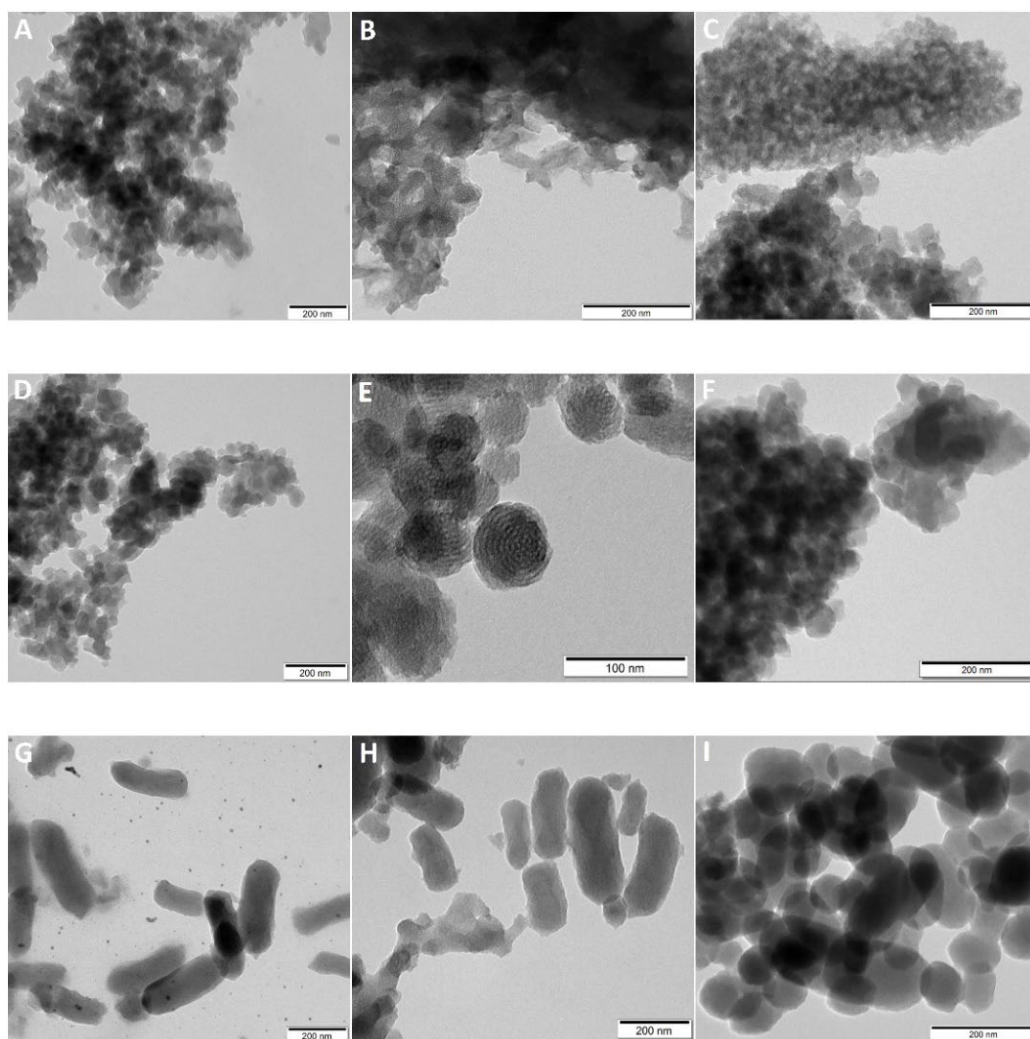


Figure 2. TEM images of particles: (A) S-SR, (B) S-NH₂-SR, (C) S-Gal-SR, (D) M-SR, (E) M-NH₂-SR, (F) M-Gal-SR, (G) L-SR, (H) L-NH₂-SR, (I) L-Gal-SR.

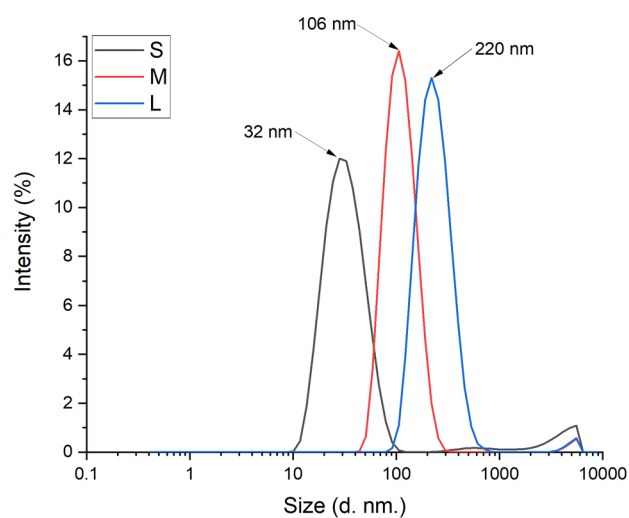


Figure 3. Particle size distribution obtained from DLS measurements.

Low angle PXRD (Figure 4, Supplementary Materials, Figures S2 and S4) measurements were also performed to confirm the hexagonal arrangement of the pores before

and after surfactant removal. Three intense peaks indexed as reflections (100), (110) and (200) characteristic of MCM-41 type materials were observed, confirming the hexagonal arrangement of the pores. The pore architecture was preserved as evidenced by the contrast noted in the structure in the TEM images (Figure 2). The 'L' particles, despite the altered morphology to a rod-like shape, did not differ from the other particles in pore architecture.

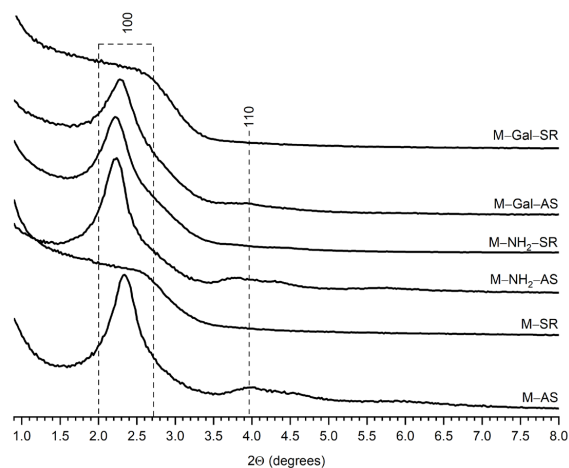


Figure 4. Low angle PXRD patterns of the 'M' particles functionalised with APTES (M-NH₂) and galactose (M-Gal) before (AS) and after (SR) template removal.

The strong FTIR vibrational bands of the synthesised materials (M-SR, and M-AS, Figure 5, for 'S' and 'L' materials see Supplementary Materials Figures S1 and S3) characteristic of asymmetric stretching vibrations of Si-O-Si groups were centred at 1030 cm⁻¹ and 784 cm⁻¹. The peaks at 564 cm⁻¹ and 426 cm⁻¹ corresponded to the bending vibrations of Si-O-Si groups. The peak seen at 956 cm⁻¹ was attributed to the stretching of the Si-OH bond. The observed broad peaks centred at 3200 cm⁻¹ indicated O-H groups and adsorbed water. Similarly, the peak at 1646 cm⁻¹ corresponded to the bending vibrations of the O-H group of adsorbed water.

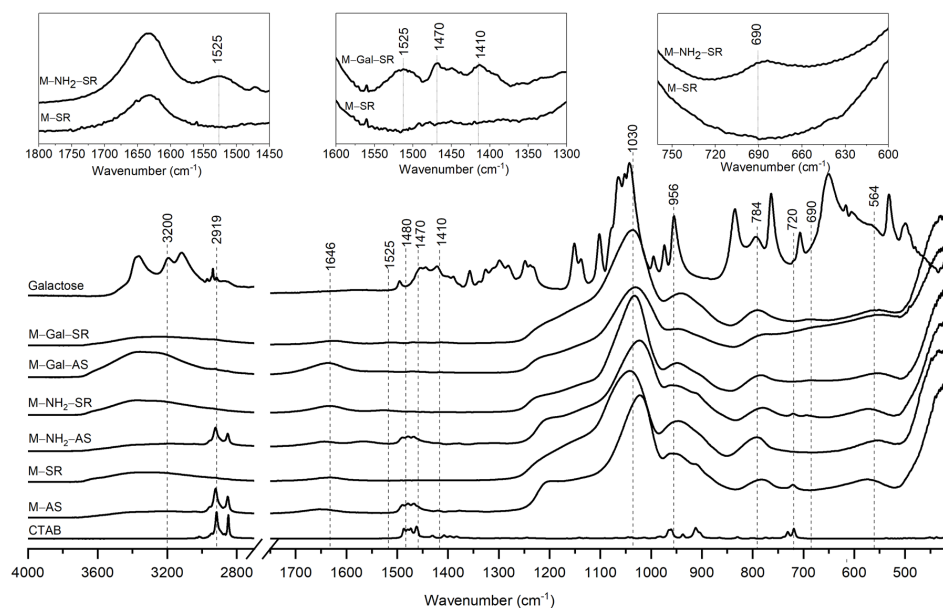


Figure 5. FTIR spectra of the 'M' particles functionalised with APTES (M-NH₂) and galactose (M-Gal) before (AS) and after (SR) template removal. FTIR spectra of CTAB and galactose are given for comparison. The insets at the top of the figure represent the zoomed spectra with peaks that prove the presence of the NH₂ and Gal functionalities.

In the spectra of AS materials, the peaks located at 2919 cm^{-1} , 1480 cm^{-1} and 720 cm^{-1} corresponded to the surfactant template (CTAB) present in the silica pores. Their disappearance in the spectra of SR-labelled materials indicated the successful removal of the template.

2.2. Surface Functionalisation with GAL and LAC

MSN functionalised with galactose ('S', 'M' and 'L') or lactose (only 'M' particles) displayed no change in particle morphology while increased aggregation was observed across all functionalised materials (Figure 2). Furthermore, TEM images confirmed the presence of the pores in the functionalised materials. This was corroborated with N_2 adsorption-desorption isotherms (Supplementary Materials, Figure S5 and Table S1). The presence of the reflections (100), (110) and (200) in low angle PXRD (Figure 4, Supplementary Materials Figures S2 and S4) traces confirmed the presence of the hexagonal arrangement of the pores in the functionalised particles while some loss of signal intensity was observed after surfactant removal. Loss of signal intensity was associated with the difference in the scattering power/scattering contrast between the amorphous silicate wall and amorphous sorbate in the mesoporous structure as well as the presence of organic groups close to the pore openings.

To confirm the presence of NH_2 , Gal and Lac groups at the surface of functionalised materials, FTIR and NMR analyses were performed. Although FTIR is frequently used to confirm the presence of organic groups at the silica surface, for the materials that have an external surface that is exclusively functionalised the application of this method is challenging due to (i) the low content of organic functionalities, i.e., <3%, of the material mass as well as (ii) substantial broadening of the peaks that represents a lack of long-range ordering. The low intensity bands at wavenumbers of 1525 cm^{-1} and 690 cm^{-1} indicated the successful attachment of the amino groups (Figure 5 insets, Supplementary Materials Figures S1 and S3). The appearance of the vibrational bands at 1470 and 1410 cm^{-1} can be assigned to the presence of galactose molecules at the silica surface (Figure 5 insets, Supplementary Materials Figures S1 and S3). It is important to notice that the reductive amination of galactose led to the opening of the galactose ring (Figure 1). Therefore, it is expected that some of the FTIR peaks characteristic for galactose will disappear or undergo substantial shifts, making the molecular level characterisation of the functionalised materials based on FTIR spectra extremely challenging.

In contrast, the solid-state ^1H - ^{29}Si CP/MAS and ^1H - ^{13}C HSQC NMR spectrum of M-Gal-SR particles obtained under HR-MAS conditions provided a wealth of structural information. At least nine distinct signals were observed in the spectrum (Figure 6, see Supplementary Materials Figures S6–S9 for 'S' and 'L' particles) proving the successful functionalisation with the aminopropylene group (peaks 1, 2 and 3), followed by the attachment of the galactose functionality (peaks 4–9) via reductive amination. In comparison to the neat galactose ^1H - ^{13}C HSQC spectrum (Supplementary Materials, Figure S7), in the spectrum of the M-Gal-SR particles, a substantial shift of anomeric carbon towards a higher field (ca. 40 ppm shift in ^{13}C spectrum; ca. 2 ppm in ^1H spectrum) was observed (peak 4), indicating an opening of the galactopyranose ring following the attachment of amine. Furthermore, peak 4 was composed of three resonances similarly to peak 2 in the aminopropylene group. This may indicate slight differences in the environment of both sites once being grafted as T1, T2 or T3 sites that have frequently been described for organofunctionalised mesoporous silica materials [25]. The ^1H - ^{29}Si CP/MAS NMR spectrum displayed only Q sites for neat L-SR particles while the presence of T sites was observed in the spectra of L- NH_2 -SR and L-Gal-SR particles (Supplementary Materials, Figure S6).

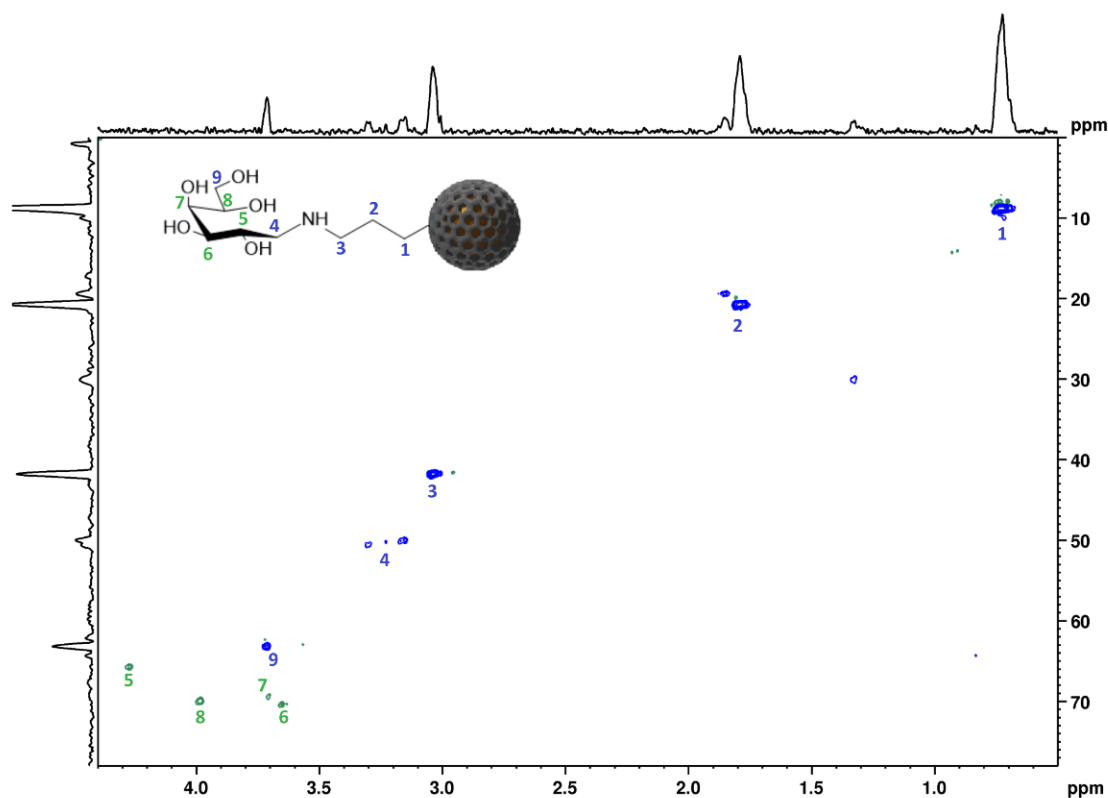


Figure 6. ^1H - ^{13}C HSQC HR-MAS NMR spectrum of galactose functionalised M-GAL-SR particles. The spectra assignment was made based on the NMR spectra predictor available at nmrdp.org (accessed on 20 March 2022) as well as using the reference spectra available at hmdb.ca (accessed on 20 March 2022) [33–35].

In order to investigate the possibility of attaching galactose to the material while preserving its structure (without breaking the ring), the functionalisation of ‘M-NH₂-AS’ particles with lactose (a sugar composed of galactose and glucose units), was performed (Figure 7). This system also enabled us to evaluate the applicability of HR-MAS NMR spectroscopy for a more complex system that has disaccharide at the surface (at least 15 sites were expected in the spectrum). The TEM image (Figure 7A) confirmed the preservation of particle structure and morphology and the presence of the pores after functionalisation and surfactant removal. The FTIR analysis (Figure 7C) confirmed the presence of amino functionality (peaks at 1525 and 690 cm⁻¹) as well as the presence of lactose (low intensity, broad bands at 1470 and 1410 cm⁻¹). The PXRD patterns (Figure 7B) of the particles after surfactant removal displayed a decrease and a broadening of the peaks that could be attributed to the loss of signal intensity due to the difference in the scattering power/scattering contrast between the amorphous silicate wall and the amorphous sorbate in the mesoporous structure.

The functionalisation of the particle surface with lactose was also confirmed by a HSQC NMR study (Figure 8). The obtained spectrum displayed 15 signals that were assigned to the structure of lactose-functionalised particles. In comparison to the spectra of neat lactose (Supplementary Materials, Figure S10), the substantial shift of anomeric carbon of glucose towards a higher field (ca. 40 ppm shift in ^{13}C spectrum; ca. 2 ppm in ^1H spectrum) was observed (peak 4) indicating an opening of the glucose ring following the attachment of amine, leaving the galactose ring intact. This may be of great importance in the development of novel galactose-functionalised MSN-based carriers for targeted delivery to the liver [21,36,37]. Similar to the galactose-functionalised particles, some of the peaks were present in more than one environment which can be attributed to the different binding motifs of APTES to silanol groups.

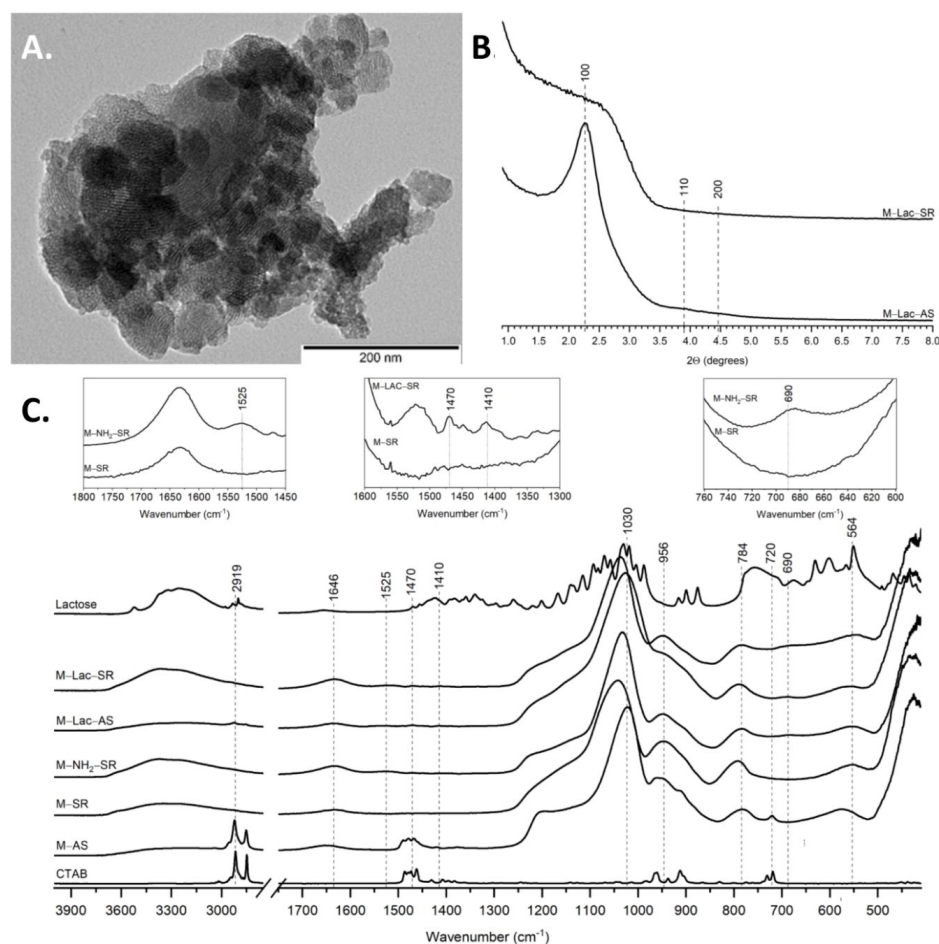


Figure 7. (A) TEM image of M–Lac–SR particles; (B) low angle PXRD patterns of M–Lac particles before (AS) and after (SR) template removal; (C) FTIR spectra of ‘M’ particles functionalised with APTES (M–NH₂) and lactose (M–Lac) before (AS) and after (SR) template removal. FTIR spectra of CTAB and lactose are given for comparison. The insets at the top of the figure represent zoomed spectra with peaks that prove the presence of NH₂ and lactose functionalities.

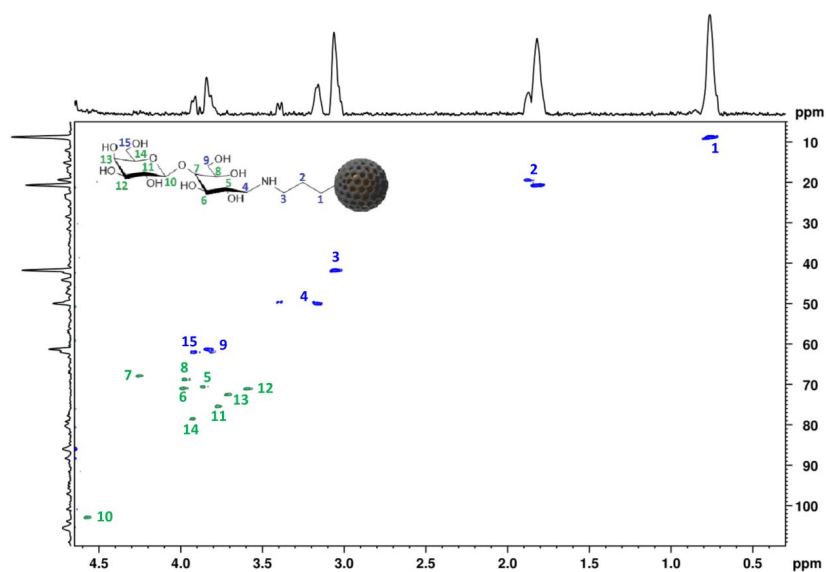


Figure 8. ¹H–¹³C HSQC HR-MAS NMR spectrum of M–Lac–SR particles. The spectra assignment was made based on the NMR spectra predictor available at nmrdb.org (on 20 March 2022) as well as the use of the reference spectra available at hmdb.ca (on 20 March 2022) [33–35].

3. Materials and Methods

Three types of MCM-41 silica nanoparticles differing in size (S—32 nm, M—106 nm, L—220 nm) were synthesised using the sol-gel method. All chemicals were purchased from Sigma-Aldrich, USA. Tetraethoxysilane (TEOS) was used as the silica precursor and hexadecyltrimethylammonium bromide (CTAB) was used as the template, while (3-aminopropyl)triethoxysilane (APTES), D-(+)-galactose and lactose were used to functionalise the material surface in the presence of sodium cyanoborohydride (NaBH_3CN) and a borate buffer.

3.1. MSN Synthesis

MCM-41 type MSN were synthesised (see Scheme 1) according to the previously reported procedure [38]. The NH_4OH solution was prepared by diluting 25% ammonia solution in water. The pH was adjusted to 11.00, 11.32 and 11.38 in order to provide the control over materials size (particles labelled S—small, M—medium, L—large). The solution was heated to 50 (S—particles), 40 (M—particles) or 30 (L—particles) °C and CTAB was added and stirred until dissolved. In a separate beaker, 0.88 M ethanolic TEOS solution was prepared and added dropwise into ammonia water. The solution was stirred for 1 h. After this time stirring was turned off and the solution was allowed to age at a constant temperature. After 18 h, the product (AS—as synthesised, S-AS, M-AS, L-AS) was filtered, washed with deionised water and ethanol and dried. The obtained material was divided into two parts. One was destined for subsequent functionalisation and the remaining part was extracted for 24 h in a mixture of ethanol and hydrochloric acid to remove the surfactant. The product (SR—surfactant removed, S-SR, M-SR, L-SR) was filtered, washed with water and ethanol and dried.

3.2. MSN Functionalisation

To functionalise the external surface of the nanoparticles, a grafting method was used. Parts of dried, templated particles of a given size (S-AS, M-AS, L-AS) were suspended in 100 mL of toluene. Then (3-aminopropyl)triethoxysilane (APTES) was added and allowed to stand for 20 h. After this time, the product (labelled: S- NH_2 -AS, M- NH_2 -AS, L- NH_2 -AS) was filtered, washed several times with ethanol and deionised water and allowed to dry. One part of the dried material was destined for further functionalisation, and the other was subjected to template removal in a mixture of ethanol and HCl following the procedure described above in the Section 3.1. MSN Synthesis.

Gal/Lac were grafted on the silica surface by reductive amination using NaBH_3CN as a reducing agent. The obtained particles (S- NH_2 -AS, M- NH_2 -AS, L- NH_2 -AS) were suspended in a borate buffer (pH 9). Then 50 mg of galactose was added and stirred for 15 min. After this time, sodium cyanoborohydride (NaBH_3CN) was added to the mixture and stirred overnight. The product (S-Gal-AS, M-Gal-AS, L-Gal-AS) was filtered, washed several times with ethanol and water and dried. The surfactant was removed by 24 h extraction in a mixture of ethanol and HCl. The final product (S-Gal-SR, M-Gal-SR, L-Gal-SR) was filtered, washed extensively with water and ethanol and dried. For lactose functionalisation, M- NH_2 -AS particles were selected. All steps were performed in the same manner as for galactose functionalisation, the amount of added lactose was 95 mg and the resultant products were labelled M-Lac-AS and M-Lac-SR.

3.3. Particle Size and Shape

Hydrodynamic diameters of the synthesised particles were determined by dynamic light scattering. The measurements were performed with Zetasizer Nano ZS ZEN3600 (Malvern Instruments Ltd., Malvern, UK) equipped with a laser light source ($\lambda = 633$ nm) and a detector operating at a 173° scattering angle. The 1 mL samples were taken directly from the synthetic mixture at the end of the aging step and investigated immediately. Experiments were run at 25 ± 0.1 °C. Each sample was measured at least 5 times. The

values of hydrodynamic diameters presented in this work are based on the intensity weighted size distribution.

The materials after filtration, functionalisation and surfactant removal were imaged with transmission electron microscopy (TEM; Hitachi H-800 microscope) providing a direct measure of the diameter of the particles as well as the presence of pores within the silica. The materials prior to the analysis were dispersed in ethanol and a drop of the obtained suspension was placed on the carbon on copper grids (Agar S160) and analysed after solvent evaporation.

3.4. Low Angle Powder X-ray Diffraction

The architecture of the hexagonal pores was confirmed using low angle PXRD (D2 Phaser Bruker, Billerica, MA, USA) with Cu K α radiation (1.5418 Å) and a LynxEye detector. Each material was analysed in the range of 2θ 0.65–8° with 0.02° increment and 1 s irradiation time per step.

3.5. N₂ Adsorption

Nitrogen adsorption–desorption isotherms for S–SR, M–SR, L–SR, L–NH₂–SR and L–Gal–SR particles were measured using an autosorb iQ gas sorption system and ASiQwin software (Quantachrome Instruments, Boynton Beach, FL, USA) or ASAP 2020 (Micromeritics, Norcross, GA, USA) at 77 K. Samples were outgassed under a high vacuum at 313 K for 16 h prior to the analysis. The BET specific surface area (S_{BET}) and the volume of monolayer coverage were determined using the Brunauer–Emmett–Teller (BET) equation [39] in the linear range of the adsorption curve (0.1–0.25 P/P_0). The pore size and distribution curves were calculated using N₂ adsorption on silica at 77 K and the NLDFT cylindrical pore equilibrium model as implemented in the ASiQwin™ software (ver. 5.2, Quantachrome Instruments, Boynton Beach, FL, USA).

3.6. Fourier Transformed Infrared Spectroscopy (FTIR)

FTIR spectra of the as–synthesised (AS), surfactant–removed (SR) and functionalised materials were acquired using a Nicolet iS50 FTIR spectrometer (Thermo Scientific, Waltham, MA, USA) in the attenuated total reflectance (ATR) mode. All measurements were carried out in the wavelength range of 400–4000 cm^{−1} at a 4 cm^{−1} resolution with at least 512 scans per measurement.

3.7. Nuclear Magnetic Resonance (NMR) Spectroscopy

All HR-MAS and solution-state NMR spectra were acquired using a Bruker AVANCE III™ NMR spectrometer, consisting of the 54 mm bore superconducting, actively shielded Ascend™ magnet operating at 600.13 MHz and 150.91 MHz for ¹H and ¹³C, respectively. The spectra of the functionalised materials were acquired using a dual inverse high-resolution magic angle spinning (HR-MAS) probe ¹H/¹³C, ²H-lock; (optimised for ¹H observation); equipped with a single axis magic angle gradient. The samples were packed in Kel-F inserts, soaked with D₂O until wetted and transferred to 4 mm zirconia rotors. The 1D ¹H MAS and 2D ¹H–¹³C HSQC spectra of the materials were acquired at 4 kHz MAS rate.

²⁹Si solid-state NMR spectra of L–SR, L–NH₂–SR and L–Gal–SR particles were acquired using a Bruker 300 MHz Avance III spectrometer with a double resonance probe operating at frequencies 300.13 MHz and 59.63 MHz for ¹H and ²⁹Si, respectively. The materials were packed into Kel-F inserts and transferred to the 4 mm zirconia rotors and analysed at an MAS rate of 4 kHz. The materials were characterised using ¹H–²⁹Si (CP/MAS) NMR (²⁹Si $\pi/2$ pulse length 4.5 μ s with a contact time of 2 ms, SPINAL64 decoupling was used during signal acquisition, 2048 transients were acquired with a recycle delay of 30 s). The Hartmann–Hahn conditions for ¹H–²⁹Si CP/MAS NMR experiments were set with kaolinite. The ²⁹Si chemical shifts were recorded with respect to TMS.

4. Conclusions

Three types of MCM-41 type mesoporous silica nanoparticles, differing in size (S—32 nm, M—106 nm, L—220 nm), were synthesised and their surface was functionalised with galactose ('S', 'M' and 'L' particles) or lactose ('M' particles). The synthesised materials displayed a narrow particle size distribution ('S' particles PDI = 0.261; 'M' particles PDI = 0.163; 'L' particles PDI = 0.165) and a hexagonal arrangement of pores with a diameter of ca. 3 nm. The pore architecture and the structure and morphology of the particles did not change after surface functionalisation with functional groups. The presence of saccharides covalently attached at the materials surface was confirmed using the combined application of FTIR and HR-MAS NMR spectroscopy. The use of HR-MAS NMR spectroscopy for the characterisation of organic groups attached at the silica surface enabled the successful functionalisation of the particles to be confirmed. High resolution 2D ^1H - ^{13}C HSQC spectra were obtained within 2 h compared to the few days that would be required to acquire ^1H - ^{13}C HETCOR solid-state NMR spectrum. Wider application of HR-MAS NMR may enable the development of new spectroscopic methods to study the interactions of targeted nanocarriers with proteins and complex biological systems in biorelevant media.

Supplementary Materials: The following supporting information can be downloaded at: <https://www.mdpi.com/article/10.3390/ijms23115906/s1>.

Author Contributions: Conceptualization, K.P.N. and K.K.; methodology, K.P.N., M.N., M.K.-L. and Y.Z.K.; investigation, K.K., K.P.N., A.M.G., A.Ż. and W.P.; resources, B.K., K.P.N., Y.Z.K. and A.Ż.; writing—original draft preparation, K.K., A.M.G., M.N., M.K.-L., W.P., A.Ż., B.K., Y.Z.K. and K.P.N.; writing—review and editing, K.K., K.P.N., A.M.G., M.N., M.K.-L., W.P., A.Ż., B.K., Y.Z.K. and K.P.N.; supervision, K.P.N. and Y.Z.K.; funding acquisition, Y.Z.K., K.P.N. and B.K. All authors have read and agreed to the published version of the manuscript.

Funding: This research was funded by the Ministry of Science and Higher Education in Poland via grant number SUBK.D190.22.022. K.P.N. is grateful for an access to NMR facility at University of East Anglia.

Institutional Review Board Statement: Not applicable.

Informed Consent Statement: Not applicable.

Data Availability Statement: The data supporting the reported results are available upon request from the authors.

Conflicts of Interest: The authors declare no conflict of interest.

References

1. Thommes, M.; Kaneko, K.; Neimark, A.V.; Olivier, J.P.; Rodriguez-Reinoso, F.; Rouquerol, J.; Sing, K.S.W. Physisorption of Gases, with Special Reference to the Evaluation of Surface Area and Pore Size Distribution (IUPAC Technical Report). *Pure Appl. Chem.* **2015**, *87*, 1051–1069. [CrossRef]
2. Wu, S.-H.; Mou, C.-Y.; Lin, H.-P. Synthesis of Mesoporous Silica Nanoparticles. *Chem. Soc. Rev.* **2013**, *42*, 3862. [CrossRef] [PubMed]
3. Giret, S.; Man, M.W.C.; Carcel, C. Mesoporous-Silica-Functionalized Nanoparticles for Drug Delivery. *Chem. A Eur. J.* **2015**, *21*, 13850–13865. [CrossRef]
4. Narayan, R.; Nayak, U.Y.; Raichur, A.M.; Garg, S. Mesoporous Silica Nanoparticles: A Comprehensive Review on Synthesis and Recent Advances. *Pharmaceutics* **2018**, *10*, 118. [CrossRef] [PubMed]
5. Kresge, C.T.; Leonowicz, M.E.; Roth, W.J.; Vartuli, J.C.; Beck, J.S. Ordered Mesoporous Molecular Sieves Synthesized by a Liquid-Crystal Template Mechanism. *Nature* **1992**, *359*, 710–712. [CrossRef]
6. Beck, J.S.; Vartuli, J.C.; Roth, W.J.; Leonowicz, M.E.; Kresge, C.T.; Schmitt, K.D.; Chu, C.T.W.; Olson, D.H.; Sheppard, E.W. A New Family of Mesoporous Molecular Sieves Prepared with Liquid Crystal Templates. *J. Am. Chem. Soc.* **1992**, *114*, 10834–10843. [CrossRef]
7. Trewyn, B.G.; Slowing, I.I.; Giri, S.; Chen, H.T.; Lin, V.S.Y. Synthesis and Functionalization of a Mesoporous Silica Nanoparticle Based on the Sol-Gel Process and Applications in Controlled Release. *Acc. Chem. Res.* **2007**, *40*, 846–853. [CrossRef]

8. Shahabi, S.; Döscher, S.; Bollhorst, T.; Treccani, L.; Maas, M.; Dringen, R.; Rezwani, K. Enhancing Cellular Uptake and Doxorubicin Delivery of Mesoporous Silica Nanoparticles via Surface Functionalization: Effects of Serum. *ACS Appl. Mater. Interfaces* **2015**, *7*, 26880–26891. [CrossRef]
9. Slowing, I.; Trewyn, B.G.; Lin, V.S.Y. Effect of Surface Functionalization of MCM-41-Type Mesoporous Silica Nanoparticles on the Endocytosis by Human Cancer Cells. *J. Am. Chem. Soc.* **2006**, *128*, 14792–14793. [CrossRef]
10. Niculescu, V.C. Mesoporous Silica Nanoparticles for Bio-Applications. *Front. Mater.* **2020**, *7*, 36. [CrossRef]
11. Bharti, C.; Gulati, N.; Nagaich, U.; Pal, A. Mesoporous Silica Nanoparticles in Target Drug Delivery System: A Review. *Int. J. Pharm. Investig.* **2015**, *5*, 124. [CrossRef] [PubMed]
12. Vivero-Escoto, J.L.; Trewyn, B.G.; Lin, V.S.-Y. *Mesoporous Silica Nanoparticles: Synthesis and Applications*; Annual Review of Nanoresearch; World Scientific Publishing Co. Pte Ltd.: Singapore, 2009; Volume 3, pp. 191–231.
13. Hoffmann, F.; Cornelius, M.; Morell, J.; Fröba, M. Silica-Based Mesoporous Organic-Inorganic Hybrid Materials. *Angew. Chem. Int. Ed.* **2006**, *45*, 3216–3251. [CrossRef] [PubMed]
14. Möller, K.; Bein, T. Talented Mesoporous Silica Nanoparticles. *Chem. Mater.* **2017**, *29*, 371–388. [CrossRef]
15. Tang, F.; Li, L.; Chen, D. Mesoporous Silica Nanoparticles: Synthesis, Biocompatibility and Drug Delivery. *Adv. Mater.* **2012**, *24*, 1504–1534. [CrossRef] [PubMed]
16. Li, Z.; Zhang, Y.; Feng, N. Mesoporous Silica Nanoparticles: Synthesis, Classification, Drug Loading, Pharmacokinetics, Biocompatibility, and Application in Drug Delivery. *Expert Opin. Drug Deliv.* **2019**, *16*, 219–237. [CrossRef] [PubMed]
17. Argyo, C.; Weiss, V.; Bräuchle, C.; Bein, T. Multifunctional Mesoporous Silica Nanoparticles as a Universal Platform for Drug Delivery. *Chem. Mater.* **2014**, *26*, 435–451. [CrossRef]
18. Mamaeva, V.; Sahlgren, C.; Lindén, M. Mesoporous Silica Nanoparticles in Medicine—Recent Advances. *Adv. Drug Deliv. Rev.* **2013**, *65*, 689–702. [CrossRef]
19. Slowing, B.I.I.; Trewyn, B.G.; Giri, S.; Lin, V.S.-Y. Mesoporous Silica Nanoparticles for Drug Delivery and Biosensing Applications. *Adv. Funct. Mater.* **2007**, *17*, 1225–1236. [CrossRef]
20. Mackowiak, S.A.; Schmidt, A.; Weiss, V.; Argyo, C.; Von Schirnding, C.; Bein, T.; Bräuchle, C. Targeted Drug Delivery in Cancer Cells with Red-Light Photoactivated Mesoporous Silica Nanoparticles. *Nano Lett.* **2013**, *13*, 2576–2583. [CrossRef]
21. Mukherjee, M.B.; Mullick, R.; Reddy, B.U.; Das, S.; Raichur, A.M. Galactose Functionalized Mesoporous Silica Nanoparticles as Delivery Vehicle in the Treatment of Hepatitis C Infection. *ACS Appl. Bio Mater.* **2020**, *3*, 7598–7610. [CrossRef]
22. Caldarelli, S.; Meden, A.; Tuel, A. Solid-State Nuclear Magnetic Resonance Study of the Microporous Aluminophosphate AlPO₄-41. *J. Phys. Chem. B* **1999**, *103*, 5477–5487. [CrossRef]
23. Davidowski, S.K.; Holland, G.P. Solid-State NMR Characterization of Mixed Phosphonic Acid Ligand Binding and Organization on Silica Nanoparticles. *Langmuir* **2016**, *32*, 3253–3261. [CrossRef] [PubMed]
24. Mao, K.; Rapp, J.L.; Wiench, J.W.; Pruski, M. Characterization of nanostructured organic-inorganic hybrid materials using advanced solid-state NMR spectroscopy. In Proceedings of the Materials Research Society Symposium Proceedings, Ames, IA, USA, 5 January 2009; Volume 1184, pp. 175–183.
25. Kobayashi, T.; Singappuli-Arachchige, D.; Wang, Z.; Slowing, B.I.I.; Pruski, M. Spatial Distribution of Organic Functional Groups Supported on Mesoporous Silica Nanoparticles: A Study by Conventional and DNP-Enhanced ²⁹Si Solid-State NMR. *Phys. Chem. Chem. Phys.* **2017**, *19*, 1781. [CrossRef] [PubMed]
26. Lee, D.; Monin, G.; Duong, N.T.; Lopez, I.Z.; Bardet, M.; Mareau, V.; Gonon, L.; De Paëpe, G. Untangling the Condensation Network of Organosiloxanes on Nanoparticles Using 2D ²⁹Si-²⁹Si Solid-State NMR Enhanced by Dynamic Nuclear Polarization. *J. Am. Chem. Soc.* **2014**, *136*, 13781–13788. [CrossRef]
27. Dai, F.R.; Sambasivam, U.; Hammerstrom, A.J.; Wang, Z. Synthetic Supercontainers Exhibit Distinct Solution versus Solid State Guest-Binding Behavior. *J. Am. Chem. Soc.* **2014**, *136*, 7480–7491. [CrossRef]
28. Tataurova, Y.; Sealy, M.J.; Larsen, R.G.; Larsen, S.C. Surface-Selective Solution NMR Studies of Functionalized Zeolite Nanoparticles. *J. Phys. Chem. Lett.* **2012**, *3*, 425–429. [CrossRef]
29. Yu, C.; Zhu, L.; Zhang, R.; Wang, X.; Guo, C.; Sun, P.; Xue, G. Investigation on the Mechanism of the Synthesis of Gold (I) Thiolate Complexes by NMR. *J. Phys. Chem. C* **2014**, *118*, 10434–10440. [CrossRef]
30. Hens, Z.; Moreels, I.; Martins, J.C. In Situ ¹H NMR Study on the Trioctylphosphine Oxide Capping of Colloidal InP Nanocrystals. *ChemPhysChem* **2005**, *6*, 2578–2584. [CrossRef]
31. Alam, T.M.; Jenkins, J.E. *HR-MAS NMR Spectroscopy in Material Science*; InTech: Houston, TX, USA, 2012.
32. Moestue, S.; Sitter, B.; Bathen, T.F.; Tessem, M.-B.; Susann Gribbestad, I. HR MAS MR Spectroscopy in Metabolic Characterization of Cancer. *Curr. Top. Med. Chem.* **2010**, *11*, 2–26. [CrossRef]
33. Banfi, D.; Patiny, L. www.nmrdb.org: Resurrecting and Processing NMR Spectra On-Line. *Chim. Int. J. Chem.* **2008**, *62*, 280–281. [CrossRef]
34. Steinbeck, C.; Krause, S.; Kuhn, S. NMRShiftDB—Constructing a Free Chemical Information System with Open-Source Components. *J. Chem. Inf. Comput. Sci.* **2003**, *43*, 1733–1739. [CrossRef] [PubMed]
35. Castillo, A.M.; Patiny, L.; Wist, J. Fast and Accurate Algorithm for the Simulation of NMR Spectra of Large Spin Systems. *J. Magn. Reson.* **2011**, *209*, 123–130. [CrossRef] [PubMed]

36. Gary-Bobo, M.; Hocine, O.; Brevet, D.; Maynadier, M.; Raehm, L.; Richeter, S.; Charasson, V.; Loock, B.; Morère, A.; Maillard, P.; et al. Cancer Therapy Improvement with Mesoporous Silica Nanoparticles Combining Targeting, Drug Delivery and PDT. *Int. J. Pharm.* **2012**, *423*, 509–515. [CrossRef]
37. Oh, H.; Jo, H.-Y.; Park, J.; Kim, D.-E.; Cho, J.-Y.; Kim, P.-H.; Kim, K.-S. Galactosylated Liposomes for Targeted Co-Delivery of Doxorubicin/Vimentin siRNA to Hepatocellular Carcinoma. *Nanomaterials* **2016**, *6*, 141. [CrossRef] [PubMed]
38. Lin, Y.S.; Haynes, C.L. Impacts of Mesoporous Silica Nanoparticle Size, Pore Ordering, and Pore Integrity on Hemolytic Activity. *J. Am. Chem. Soc.* **2010**, *132*, 4834–4842. [CrossRef] [PubMed]
39. Brunauer, S.; Emmett, P.H.; Teller, E. Adsorption of Gases in Multimolecular Layers. *J. Am. Chem. Soc.* **1938**, *60*, 309–319. [CrossRef]



Article

Delivery of Doxorubicin by Ferric Ion-Modified Mesoporous Polydopamine Nanoparticles and Anticancer Activity against HCT-116 Cells In Vitro

Mengwen Guo, Junhong Ling , Xinyi Xu and Xiaokun Ouyang *

School of Food and Pharmacy, Zhejiang Ocean University, Zhoushan 316022, China

* Correspondence: xkouyang@zjou.edu.cn

Abstract: In clinical cancer research, photothermal therapy is one of the most effective ways to increase sensitivity to chemotherapy. Here, we present a simple and effective method for developing a nanotherapeutic agent for chemotherapy combined with photothermal therapy. The nanotherapeutic agent mesoporous polydopamine-Fe(III)-doxorubicin-hyaluronic acid (MPDA-Fe(III)-DOX-HA) was composed of mesoporous polydopamine modified by ferric ions and loaded with the anticancer drug doxorubicin (DOX), as well as an outer layer coating of hyaluronic acid. The pore size of the mesoporous polydopamine was larger than that of the common polydopamine nanoparticles, and the particle size of MPDA-Fe(III)-DOX-HA nanoparticles was 179 ± 19 nm. With the presence of ferric ions, the heat generation effect of the MPDA-Fe(III)-DOX-HA nanoparticles in the near-infrared light at 808 nm was enhanced. In addition, the experimental findings revealed that the active targeting of hyaluronic acid to tumor cells mitigated the toxicity of DOX on normal cells. Furthermore, under 808 nm illumination, the MPDA-Fe(III)-DOX-HA nanoparticles demonstrated potent cytotoxicity to HCT-116 cells, indicating a good anti-tumor effect in vitro. Therefore, the system developed in this work merits further investigation as a potential nanotherapeutic platform for photothermal treatment of cancer.



Citation: Guo, M.; Ling, J.; Xu, X.; Ouyang, X. Delivery of Doxorubicin by Ferric Ion-Modified Mesoporous Polydopamine Nanoparticles and Anticancer Activity against HCT-116 Cells In Vitro. *Int. J. Mol. Sci.* **2023**, *24*, 6854. <https://doi.org/10.3390/ijms24076854>

Academic Editors: Ilaria Rea, Nicola Borbone, Monica Terracciano and Chiara Tramontano

Received: 23 February 2023

Revised: 24 March 2023

Accepted: 3 April 2023

Published: 6 April 2023



Copyright: © 2023 by the authors. Licensee MDPI, Basel, Switzerland. This article is an open access article distributed under the terms and conditions of the Creative Commons Attribution (CC BY) license (<https://creativecommons.org/licenses/by/4.0/>).

Keywords: mesoporous polydopamine; ferric ions; doxorubicin (DOX); hyaluronic acid target modification

1. Introduction

Colon cancer is a disease with a high morbidity and mortality rate worldwide, which may be attributable to poor diet and a reversed work schedule [1,2]. Although academic research on colon cancer treatment has never stopped, the incidence of colon cancer continues to rise [3–5]. Currently, the primary anticancer treatments include surgery, chemotherapy, and radiotherapy [6–8]. Chemotherapy using doxorubicin (DOX), a broad-spectrum anthracycline antitumor drug, is widely used to develop model drugs for tumor-targeted drug delivery systems [9–12]. However, a single chemotherapy regimen can lead to several serious side effects, cancer metastasis, and tumor resistance [13,14]. Studies have demonstrated that chemotherapy combined with photothermal therapy (PTT) can reduce the heat resistance of tumor cells and that the heat generated by PTT can alleviate tumor hypoxia to further promote chemotherapy [15–17]. Thus, combined photothermal and chemotherapeutic treatment can effectively mitigate the drawbacks of monotherapy. With the ongoing development of nanotechnology, it has been found that nanodrug delivery systems can be used for targeted drug delivery to the tumor site, reduce dosage, and enhance the anticancer activity of chemotherapeutic drugs [18–20]. This type of loading system is typically biocompatible, degradable, and modifiable [21,22].

Polydopamine (PDA), a natural melanin polymer formed by the self-aggregation of dopamine (DA) [23], can be decomposed in the weakly acidic tumor microenvironment [24]. PDA has many applications in multifunctional surface modification due to its natural nontoxicity, biodegradability, and high absorptivity in the near-infrared region (NIR) [25].

Therefore, PDA has numerous applications in tumor photothermal therapy. However, the lack of photothermal performance hinders its chemotherapeutic effects. Studies have shown that PDA strongly chelates metal ions, and the addition of metal ions to PDA can significantly improve the photothermal conversion efficiency of PDA nanoparticles [26].

In addition, we selected mesoporous polydopamine nanoparticles (MPDA) as drug carriers to increase the loading rate of chemotherapeutic drugs. With a specific surface area and pore size, MPDA nanoparticles can effectively increase the loading capacity of chemotherapeutic drugs [27]. During drug administration, mesoporous nanoparticles exhibit severe drug leakage. Therefore, an appropriate encapsulant is typically used when designing the drug delivery system [28]. Hyaluronic acid (HA) is highly hydrophilic, which can increase the stability of MPDA nanoparticles and also has a targeting effect due to the expression of specific receptors on the surface of tumor cells [29]. As an encapsulant, HA can therefore reduce drug loss and cytotoxicity.

Here, we designed and synthesized a photothermal–chemotherapy combined drug delivery system (MPDA-Fe(III)-DOX-HA) by introducing ferric ions to enhance the photothermal effect of the mesoporous PDA nanoparticles loaded with the chemotherapeutic drug doxorubicin and encapsulated with hyaluronic acid. The simplify preparation process is shown in Figure 1.

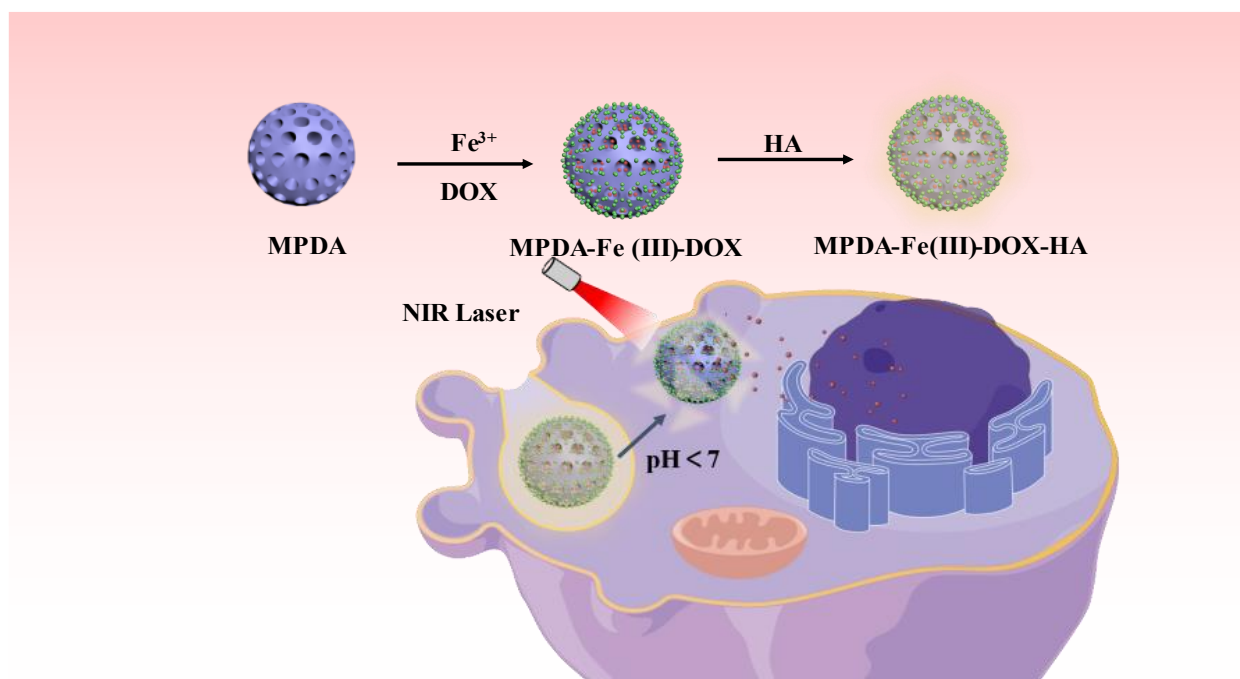


Figure 1. Schematic representation of the preparation of MPDA-Fe(III)-DOX-HA nanoparticles and their anti-tumor activity.

MPDA-Fe(III)-DOX-HA nanoparticles were gathered near tumor cells via the active target of HA. Due to the sensitivity of tumor cells to temperature, 808 nm near-infrared light irradiation caused polydopamine nanoparticles to generate a substantial amount of heat and inhibit the growth of tumors. Subsequently, PDA disintegrated in a weakly acidic environment, releasing the chemotherapeutic drug doxorubicin, which, when combined with the photothermal effect, killed tumor cells. In summary, the MPDA-Fe(III)-DOX-HA delivery system not only increased the efficacy of chemotherapy but also decreased cytotoxicity, indicating that photothermal combined with chemotherapy is a promising strategy for treating tumors and that tumors can be destroyed by the synergistic effect of the two treatments.

2. Results

2.1. BET Analysis

The N₂ adsorption–desorption isotherms of PDA and MPDA were measured (Figure 2a,b, with the pore size distribution in the top right corner). Both PDA and MPDA had typical Langmuir IV isotherms, as shown in Figure 2a,b, indicating that both PDA and MPDA may have pore structures [30]. The pore size curve of PDA in Figure 2a shows that the existing pore structure may have larger pores caused by mutual adhesion and polymerization of PDA, so the pore content of mesopores is relatively low. In Figure 2b, the specific surface area of MPDA is shown to be 36.824 m²g^{−1}, which is significantly larger than that of non-mesoporous PDA spheres (17.126 m²g^{−1}), indicating that MPDA is more suitable for drug loading as a drug carrier than PDA.

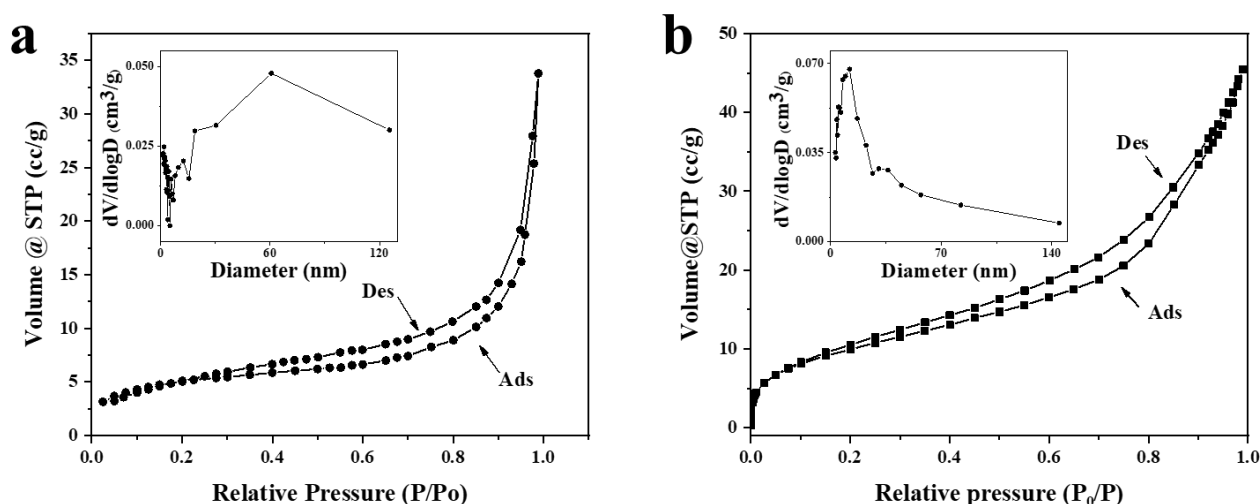


Figure 2. N₂ Adsorption and desorption isotherms, as well as size analysis of PDA nanoparticles (a) and MPDA nanoparticles (b). The abbreviations Ads and Des in the figures refer to adsorption and desorption, respectively.

As shown in Figure 2, an H4-type hysteresis loop caused by capillary agglomeration occurs in the P/P₀ range of 0.2–0.9. The average pore size of MPDA is 3.827 nm (Figure 2b), and that of PDA is 1.347 nm (Figure 2a), with poor pore size distribution. Based on these findings, it can be concluded that the mesoporous structure of MPDA can provide a larger specific surface area for drug loading and improve the drug loading capacity.

2.2. SEM and Particle Size Analysis

SEM images of various nanomaterials obtained in the experiment are shown in Figure 3. Results indicate that the addition of TMB could optimize the preparation of MPDA. Figure 3a shows that the PDA nanoparticles without the TMB template lack a mesoporous structure and have a non-uniform particle size distribution with an average particle size of 296 nm. The MPDA particles prepared with TMB have a distinct mesoporous structure and a uniform particle size. The results of optimizing the elution conditions of the template are shown in Figure 3b,c. MPDA nanoparticles with a relatively uniform distribution and small particle size (133 ± 18 nm) were obtained in the studies using acetone–ethanol and ethanol as the elution templates and acetone–ethanol as the eluent (Figure 3b). In contrast, the MPDA nanoparticles (Figure 3c) prepared after the removal of the template using ethanol as the eluent had a non-uniform particle size distribution and a mean particle size of 156 ± 21 nm. Therefore, the acetone–ethanol elution condition was selected as the subsequent elution condition.

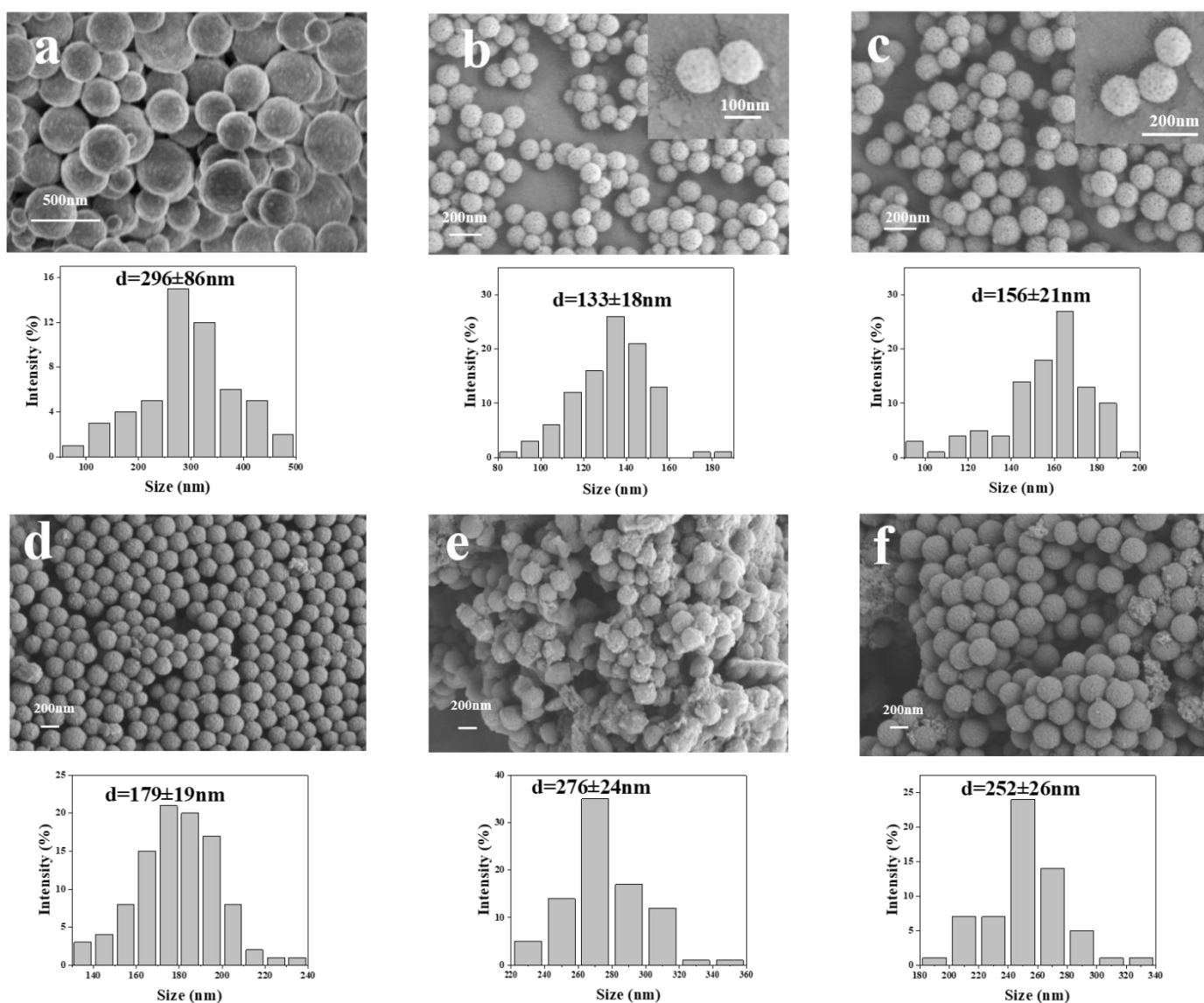


Figure 3. SEM and particle size analysis template-free dopamine nanoparticles (a), acetone-ethanol elution dopamine nanoparticles (b), anhydrous ethanol elution dopamine nanoparticles (c), m (MPDA-Fe(III)-DOX:HA) = 1:1 (d), m (MPDA-Fe(III)-DOX:HA) = 1:2 (e), m (MPDA-Fe(III)-DOX:HA) = 1:3 (f).

In this study, the effect of HA modification at different proportions on the particle size of MPDA drug-loaded nanoparticles was investigated. When comparing Figure 3d–f to Figure 3b, HA was successfully coated on the MPDA particles. The HA-modified MPDA nanoparticles are distributed evenly because the hydrophilicity of HA improves the dispersibility of nanoparticles in the solution. Figure 3d–f correspond to m (MPDA-Fe(III)-DOX:HA) = 1:1, m (MPDA-Fe(III)-DOX:HA) = 1:2, and m (MPDA-Fe(III)-DOX:HA) = 1:3, respectively. When m (MPDA-Fe(III)-DOX:HA) = 1:1 was used instead of m (MPDA-Fe(III)-DOX:HA) = 1:2, 1:3, the prepared nanoparticles were more evenly distributed with an average particle size of 179 ± 19 nm. Therefore, m (MPDA-Fe(III)-DOX:HA) = 1:1 was selected for the preparation of the MPDA nanoparticles as drug carriers.

2.3. Zeta Potential Analysis

As shown in Figure 4a, the surface potential of MPDA was -10.86 mV. After doxorubicin was loaded into MPDA, the surface potential of MPDA-Fe(III)-DOX increased to -1.42 mV (Figure 4b), which may be because the negative charge of the MPDA carrier itself

was significantly reduced due to the chelation of metal ions on the surface and the loading of DOX drugs. The surface electronegativity of MPDA nanoparticles was significantly increased after HA modification due to the strong electronegativity of the carboxyl group in sodium hyaluronate. As shown in Figure 4b, the surface potential of MPDA-Fe(III)-DOX-HA modified by HA was more electronegative than that of MPDA-Fe(III)-DOX, reaching -9.17 mV (Figure 4b). The zeta potential of MPDA modified with HA was also investigated. As shown in Figure 4d–f, the zeta potential of the HA-modified MPDA nanoparticles was deprotonated by the carboxyl group on the HA surface. The electronegativity of MPDA nanoparticles with a higher proportion of HA modification was higher, indicating that HA was successfully modified on the surface of MPDA.

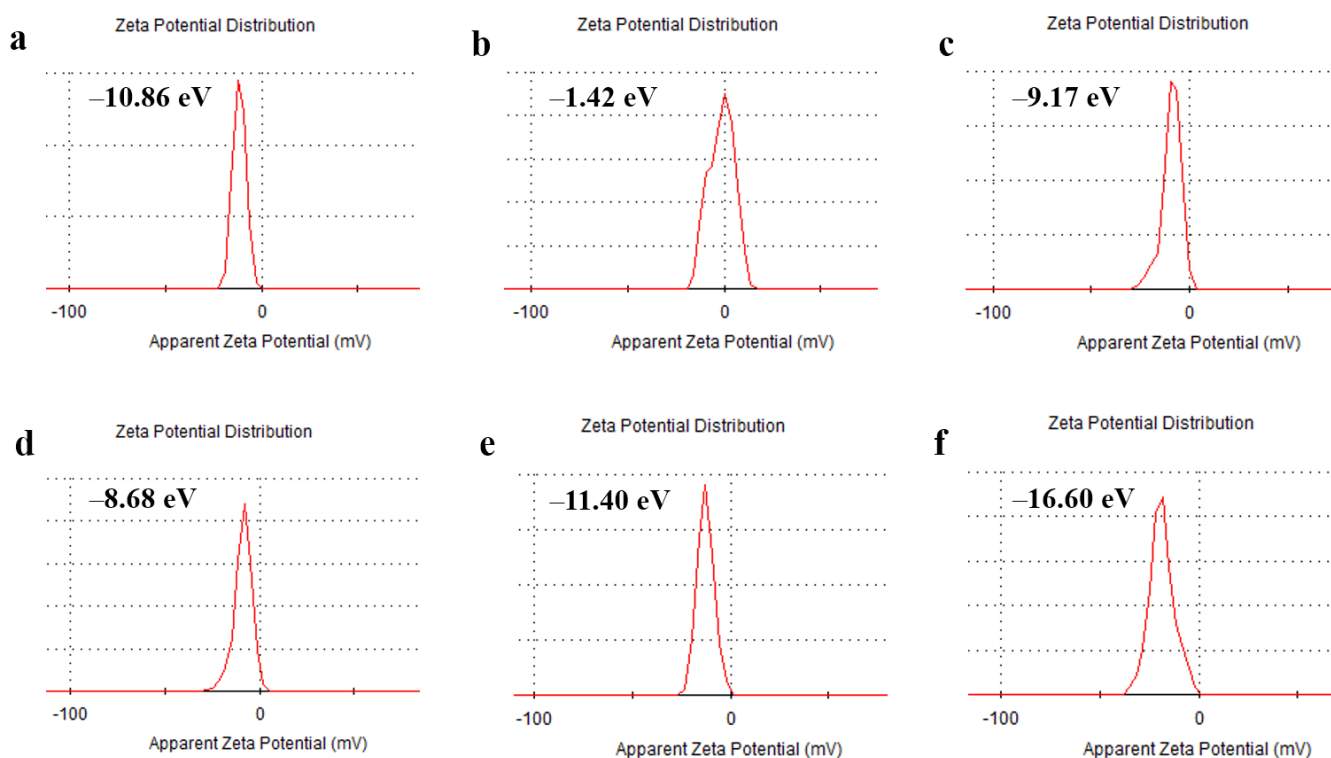


Figure 4. Zeta potentials of (a) MPDA, (b) MPDA-Fe(III)-DOX, (c) MPDA-Fe(III)-DOX-HA, (d) m (MPDA-Fe(III)-DOX): m (HA) = 1:1, (e) m (MPDA-Fe(III)-DOX): m (HA) = 1:2, (f) m (MPDA-Fe(III)-DOX): m (HA) = 1:3.

2.4. FTIR Analysis

The infrared absorption of MPDA, MPDA-Fe(III)-DOX, and MPDA-Fe(III)-DOX-HA nanoparticles was investigated using infrared spectroscopy. As shown in Figure 5, the absorption peaks of PDA are at 1630 cm^{-1} (the telescopic vibration peak of the aromatic ring and the bending vibration peak of N–H) [31], 1380 cm^{-1} (the phenolic C–O–H bending vibration), 1120 cm^{-1} (C–O vibration) [32], and 2921 cm^{-1} (the C–H telescopic vibration peak caused by aromatic and aliphatic C–H) [33]. This further indicates that PDA is prepared. The absorption peak at 1745 cm^{-1} could be attributed to the C=O stretching vibration peak [34]. The peak intensities at 2921 cm^{-1} and 1745 cm^{-1} were significantly reduced after DOX loading and HA modification, which was due to the reduction of the aldehyde group caused by the participation of Fe in chelation after DOX loading. The bands at 546 and 521 cm^{-1} in MPDA-Fe(III)-DOX-HA are attributed to the elastic and contractile vibration peaks of Fe–O [35], indicating that some free Fe ions may be involved in the chelation of HA and that the HA layer on the drug-loaded nanoparticles has been modified.

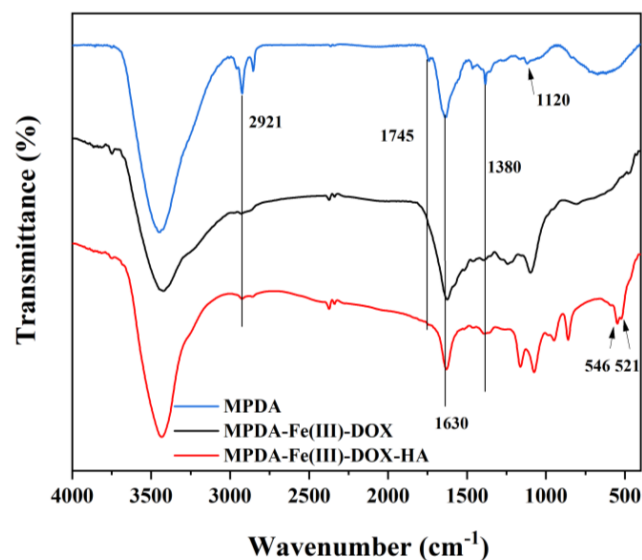


Figure 5. Comparison of the IR spectra of nanoparticles at different steps.

2.5. XPS Analysis

The X-ray photoelectron spectroscopy results of MPDA, MPDA-Fe(III)-DOX, and MPDA-Fe(III)-DOX-HA are shown in Figure 6a,b. The full spectrum in Figure 6a shows that each material contains C, N, and O elements [36]. Because of the relatively low content of Fe, we further analyzed the Fe 2p spectra of MPDA-Fe(III)-DOX-HA and MPDA-Fe(III). The peak in MPDA-Fe(III) indicates that Fe was chelated successfully on MPDA [37]. The Fe content of MPDA-Fe(III)-DOX-HA decreased, which could be attributed to the relatively low Fe content on the surface of HA-modified nanoparticles.

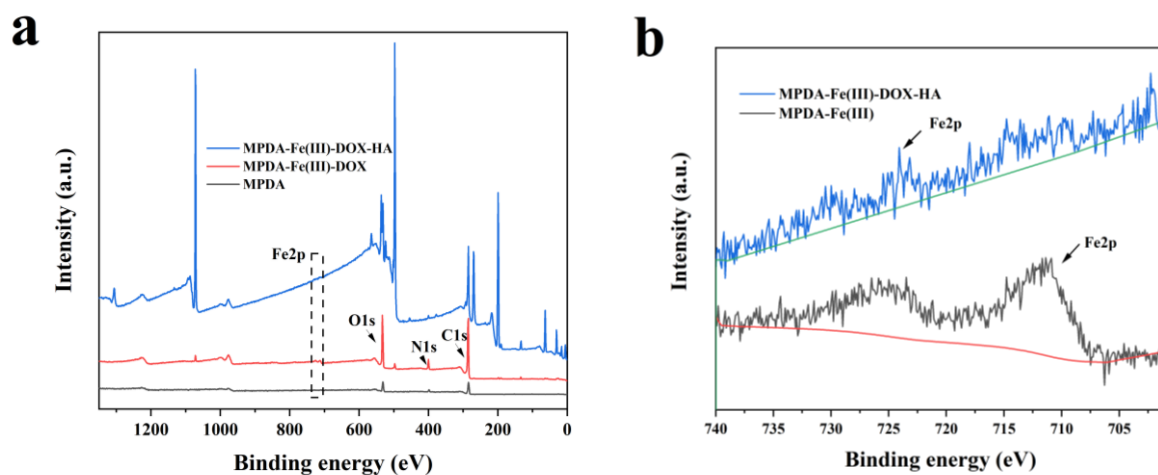


Figure 6. Spectrum of XPS (a), spectral comparison of Fe 2p in XPS before and after HA inclusion (b). The green and red lines in (b) are both background lines.

2.6. Photothermal Conversion Capability Analysis

As a photothermal agent, PDA has a strong near-infrared absorption capacity and an absorption capacity in the 808 nm near-infrared band [38]. Ferric ions were added to the MPDA preparation process to improve the infrared absorption capacity and photothermal efficiency of the obtained MPDA nanoparticles [39]. In this study, the ferric ion addition ratio was optimized. The effects of different ferric ion addition ratios on the photothermal efficiency of MPDA nanoparticles were investigated under irradiation conditions of 808 nm and 2 W/cm^2 . Figure 7a shows that the prepared nanoparticles had the best heating effect when the dopamine (DA):Fe ratio was 3:1.

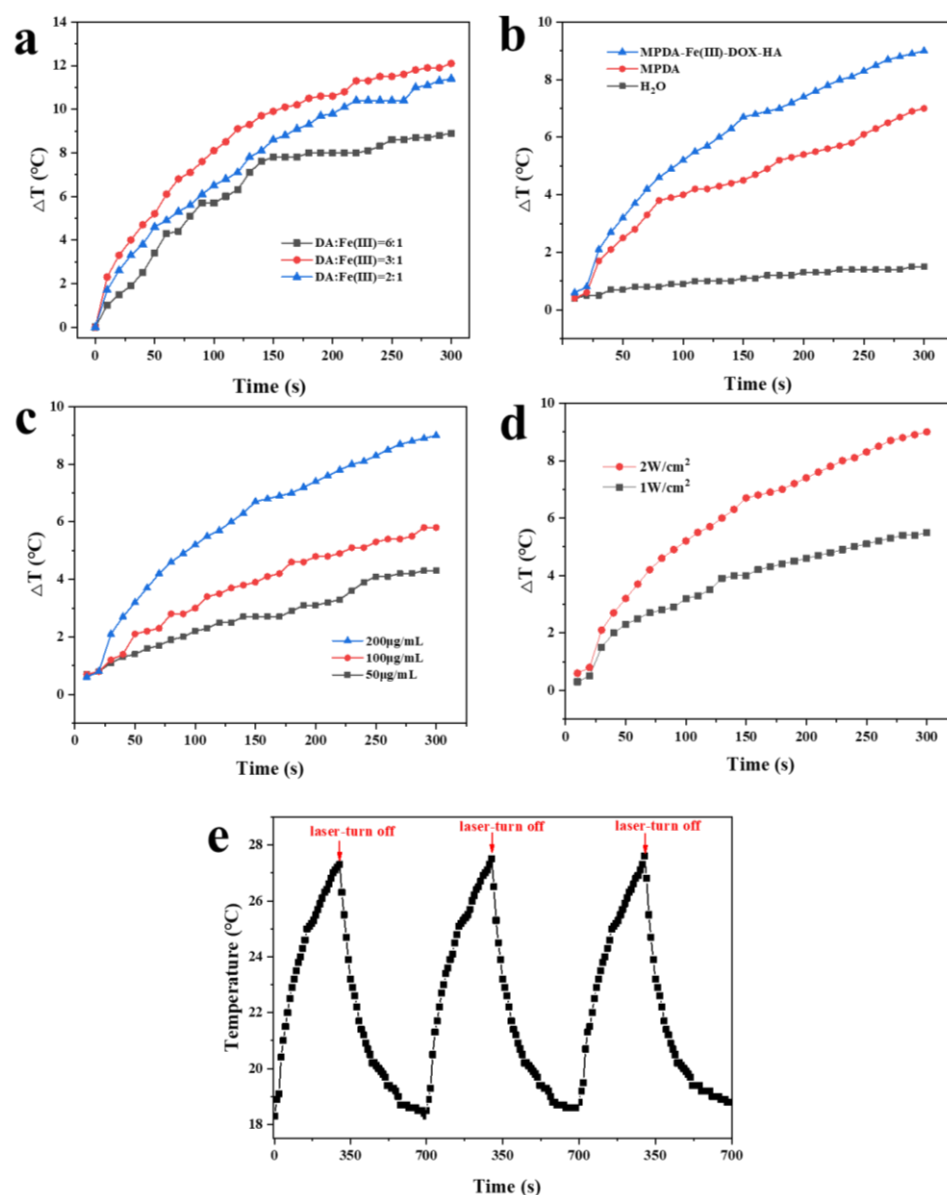


Figure 7. After 5 min of 2 W/cm^2 NIR laser irradiation, the temperature difference curve of different DA:Fe molar ratio (a), materials (b), and MPDA-Fe(III)-DOX-HA concentration (c). Temperature difference curve for a 1 mg/mL MPDA-Fe(III)-DOX-HA solution at various laser powers (d). The temperature change per 10 s of 5 min irradiation by a 2 W/cm^2 NIR laser after three cycles of cooling to room temperature (e).

Figure 7b shows the photothermal experiments on samples from various preparation steps. MPDA-Fe(III)-DOX-HA demonstrated good photothermal conversion ability, whereas the pure water temperature in the control group changed slightly. Under the irradiation of different powers of near-infrared laser (Figure 7c) and 808 nm near-infrared light for 10 min (1 W/cm^2 and 2 W/cm^2), the 2 W/cm^2 laser exhibited a superior photothermal conversion effect.

The photothermal performance of MPDA-Fe(III)-DOX-HA was further evaluated by dispersing MPDA-Fe(III)-DOX-HA in an aqueous solution at varying concentrations (50, 100, and $200 \mu\text{g/mL}$). As shown in Figure 7c, the temperature of the MPDA-Fe(III)-DOX-HA solution varied in a concentration-dependent manner. The increase in temperature of the MPDA-Fe(III)-DOX-HA solution ($200 \mu\text{g/mL}$) from $18.3 \text{ }^\circ\text{C}$ to $27.3 \text{ }^\circ\text{C}$ indicates that MPDA-Fe(III)-DOX-HA could effectively convert near-infrared light into thermal energy.

In this study, the photothermal stability of MPDA-Fe(III)-DOX-HA was further evaluated using cyclic laser irradiation. As shown in Figure 7e, the highest temperature reached by MPDA-Fe(III)-DOX-HA was relatively stable after three cycles of laser irradiation, indicating that MPDA-Fe(III)-DOX-HA possessed good photothermal stability.

2.7. DOX Loading and Release Analysis

Table 1 shows that when the DA to Fe(III) molar ratio is 6:1, 3:1, or 2:1, the drug loading rate and encapsulation efficiency of the obtained nano-sized drug-loaded particles (MPDA-Fe(III)-DOX-HA) are $80.41 \pm 0.84\%$, $16.08 \pm 0.16\%$; $84.90 \pm 0.68\%$, $16.98 \pm 0.13\%$; and $81.87 \pm 1.26\%$, $16.35 \pm 0.25\%$, respectively. The loading effect of MPDA-Fe(III)-DOX-HA was optimal when the DA to Fe(III) molar ratio was 3:1.

Table 1. Drug loading capacity of nano-system with different DA to Fe(III) molar ratios.

Molar Ratios of DA:Fe(III)	6:1	3:1	2:1
Loading Capacity (LC)	$80.41 \pm 0.84\%$	$84.90 \pm 0.68\%$	$81.87 \pm 1.26\%$
Encapsulation Efficiency (EE)	$16.08 \pm 0.16\%$	$16.98 \pm 0.13\%$	$16.35 \pm 0.25\%$

To investigate the drug release behavior of MPDA-Fe(III)-DOX-HA, PBS and ABS buffer were used to simulate the internal body environment and the tumor microenvironment, respectively. As shown in Figure 8, the drug release rate increased by nearly 30% to 53.1% under the simulated tumor microenvironment when compared to the normal PBS environment. This indicates that MPDA-Fe(III)-DOX-HA had a more potent disintegration and release capacity in acidic environments, which may be due to the instability of the dopamine structure in an acidic solution, which increased the drug release [40]. Additionally, protonation of amine groups in DOX at acidic pH results in higher solubility of DOX and faster drug release [41].

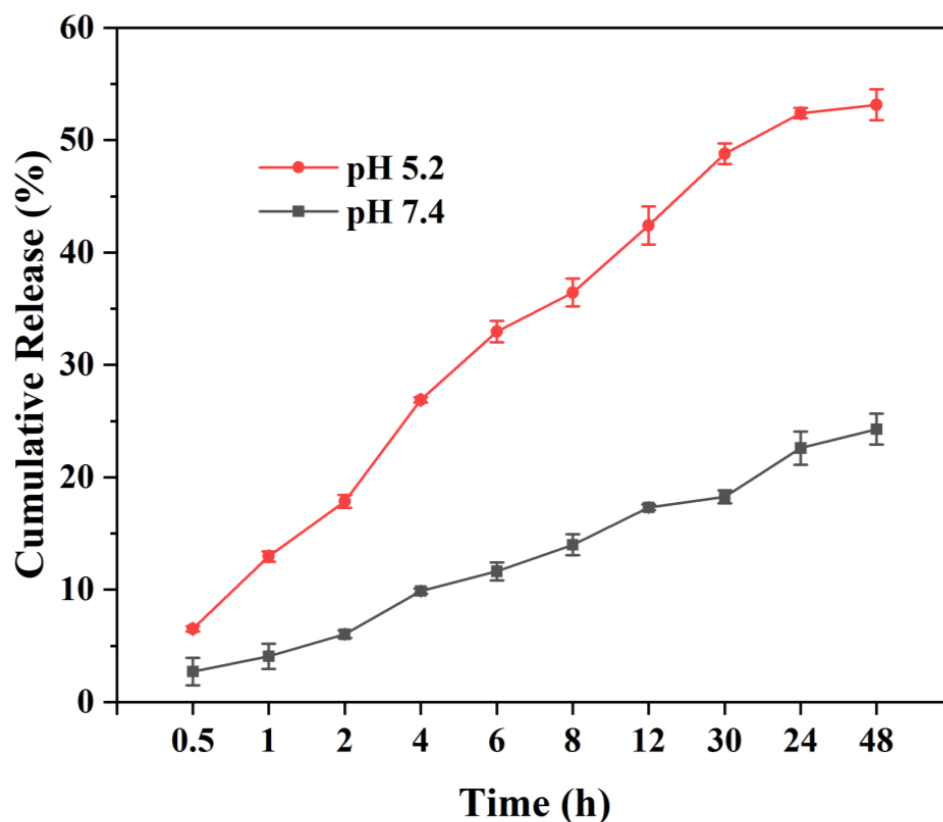


Figure 8. The ability of MPDA-Fe(III)-DOX-HA to release DOX in different pH environments.

2.8. Cytotoxicity Analysis

Nanodrug carriers are used for drug delivery, and their toxicity should be determined [42]. In this study, the MTT assay was used to determine the toxicity of DOX, MPDA-Fe(III)-DOX, and MPDA-Fe(III)-DOX-HA on L929 and HCT-116 cells. As shown in Figure 9a, freely available DOX, MPDA-Fe(III)-DOX, and MPDA-Fe(III)-DOX-HA had no significant toxicity to mouse fibroblasts. The survival rate of cells receiving MPDA-Fe(III)-DOX was 66.94% at a DOX concentration of 20 $\mu\text{g}/\text{mL}$, which may be attributed to the targeting effect of MPDA-Fe(III)-DOX without a modification layer in a normal cell culture environment [43]. DOX release was uncontrolled, so its release capacity was high, resulting in increased toxicity to normal cells [44]. The survival rate of MPDA-Fe(III)-DOX increased to 79.28% after HA modification. Survival rates were greater than 80% at the remaining DOX concentrations.

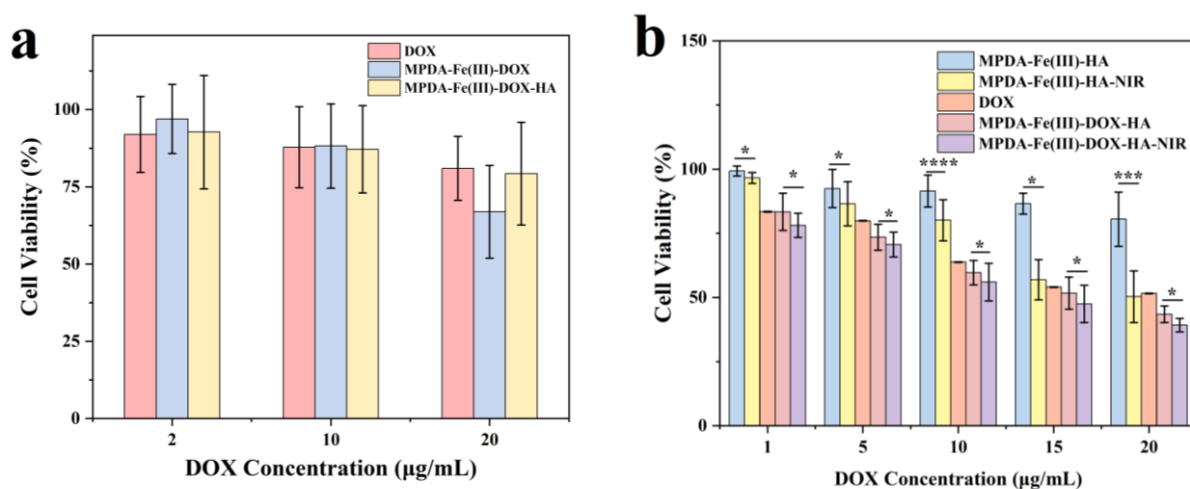


Figure 9. Cytotoxicity analysis using the MTT method (toxicity of different concentrations of drug delivery system on L929 cells (a), toxicity of different concentrations of drug delivery system to HCT-116 cells under different NIR (b)) (* $p < 0.05$; *** $p < 0.001$; **** $p < 0.0001$).

The toxicity of varying DOX concentrations (calculated by release rate) was evaluated using HCT-116 cells. The results indicated that the drug-loaded nanoparticles MPDA-Fe(III)-HA had no significant toxicity on tumor cells (survival rate $> 80\%$), as shown in Figure 9b, but the survival rate in the corresponding MPDA-Fe(III)-HA-NIR group was only 50.29% at a DOX concentration of 20 $\mu\text{g}/\text{mL}$, due to the photothermal properties of the nanoparticles. As demonstrated in the MPDA-Fe(III)-DOX-HA experimental group, at a DOX concentration of 20 $\mu\text{g}/\text{mL}$, the tumor cell viability was significantly different in the NIR group, indicating that MPDA-Fe(III)-DOX-HA had good photothermal properties and could work in conjunction with DOX to kill tumor cells (Figure 9b). At this time, the tumor cell viability was reduced to 39.1%. In comparison to the free DOX group and the MPDA-Fe(III)-DOX-HA group, the MPDA-Fe(III)-DOX-HA-NIR group exhibited significant inhibition at the same drug concentration. The enhanced cytotoxicity was caused by the thermal effect generated by near-infrared radiation in combination with the action of DOX.

2.9. Cellular Uptake Analysis

This study investigated the distribution of DOX after 4 h and 8 h of incubation of HCT-116 cells with drug-loaded nanoparticles, as well as the tumor cell uptake of MPDA-Fe(III)-DOX-HA nanoparticles. CD44 receptors are highly expressed in HCT-116 cells [45]. Tumor cell uptake of MPDA-Fe(III)-DOX (without HA modification) and MPDA-Fe(III)-DOX-HA (HA-modified) nanoparticles were compared. In addition, the differences in nanoparticle uptake behavior with and without near-infrared light irradiation were investigated. As shown in Figure 10, the fluorescence intensity of HCT-116 cells treated with Hoechst

33,258 increased with culture time. At the same time, the fluorescence intensity of DOX in cells increased over time, indicating that the nanoparticles were ingested rather than attached to the cell surface. In addition, when compared to MPDA-Fe(III)-DOX nanoparticles, MPDA-Fe(III)-DOX-HA demonstrated higher DOX fluorescence intensity at varying uptake times, indicating that the HA-modified nanoparticles could enhance nanoparticle uptake by tumor cells. The DOX fluorescence intensity of tumor cells in the near-infrared light irradiation group was higher than in the group without NIR light irradiation because the heat generated after the near-infrared light irradiation could promote drug release by the nanocarriers [46].

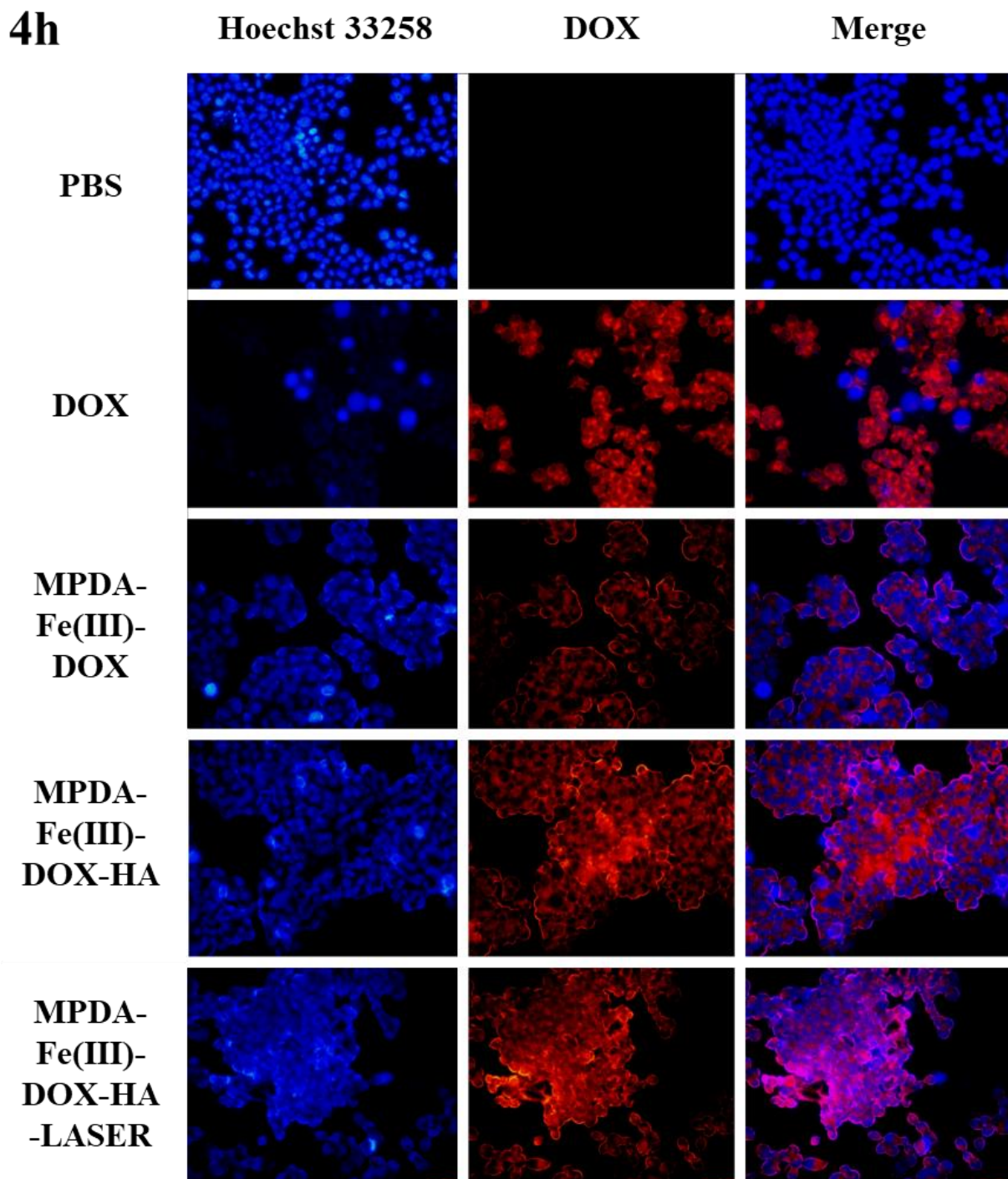


Figure 10. Cont.

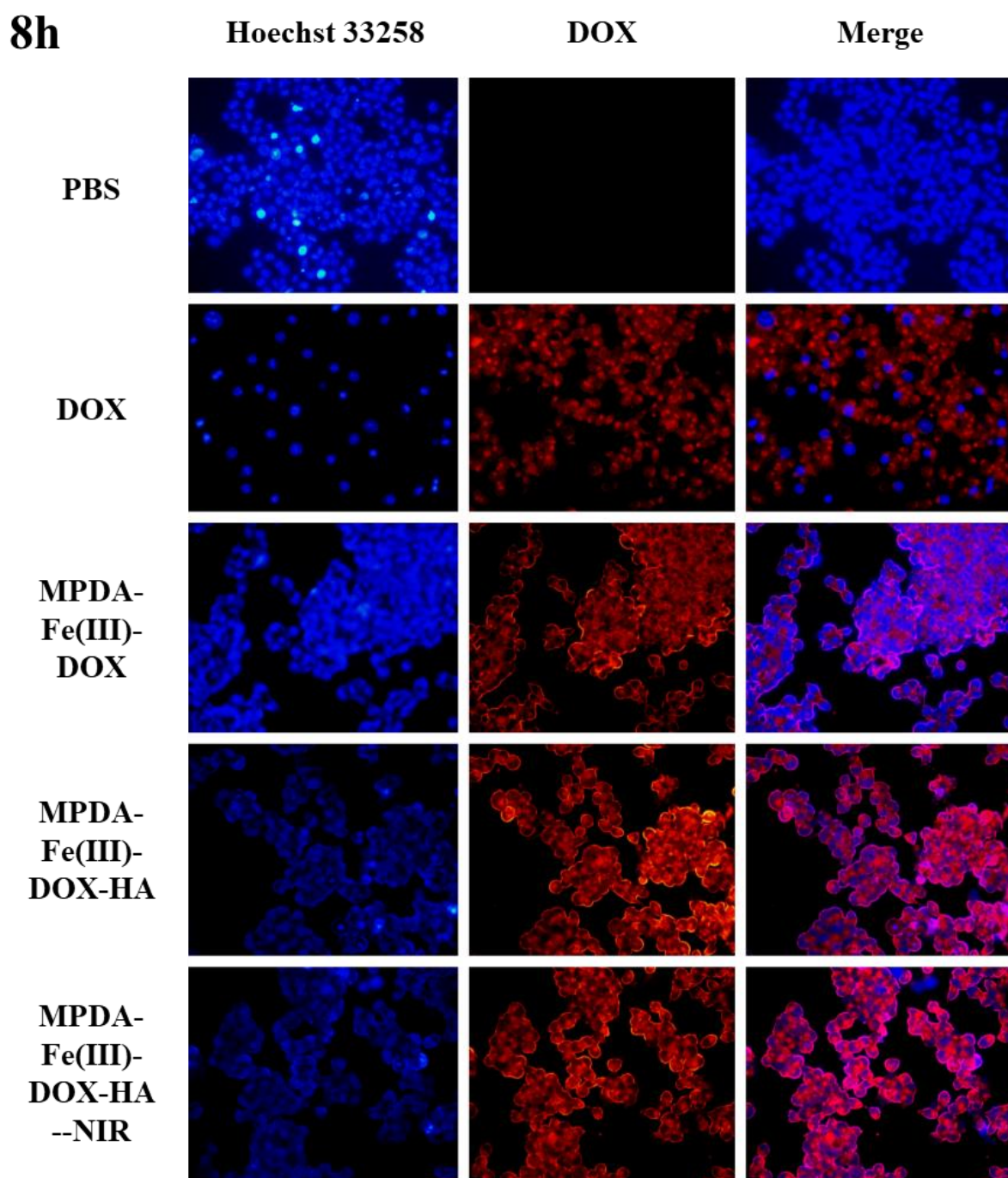


Figure 10. The cell survival and uptake capacity of the free DOX, MPDA-Fe(III)-DOX, MPDA-Fe(III)-DOX-HA, and MPDA-Fe(III)-DOX-HA-NIR groups cultured in HCT-116 cells for 4 h and 8 h at the same DOX concentration.

3. Discussion

Overall, our studies establish that the MPDA-Fe(III) prepared by adding trivalent ferric ions significantly improved the photothermal effect of MPDA, which was consistent with the conclusion in the relevant literature that metal ions enhanced the photothermal effect of polymers [47]. However, we found that the photo-conversion of MPDA-Fe(III)-DOX-HA was lower than that of MPDA-Fe(III), possibly due to the chelation of some iron ions by HA. However, photothermal cycling experiments showed that MPDA-Fe(III)-DOX-HA still had good photothermal stability.

In addition, we have found in the cell experiment that the mesoporous polydopamine has good biocompatibility, and the killing effects of free doxorubicin within a certain concentration range on normal cells and cancer cells are different, which may be related to the action mechanism of doxorubicin. At the same time, the cell experiment also showed the targeting effect of hyaluronic acid. The material encapsulated by hyaluronic acid could reduce the toxic effect on L929 cells. In addition, experiments on cancer cell HCT-116 cells proved that MPDA-Fe(III)-DOX-HA had a good killing effect on tumor cells, and the differential expression of this nanodrug delivery system in normal cells indicated that it is a potential good platform for cancer drug delivery.

4. Materials and Methods

4.1. Materials

Doxorubicin hydrochloride (DOX · HCl, 98%) was purchased from Shanghai Haoyun Chem Technology Co., Ltd. (Shanghai, China) F127 (Biochemical Reagent, BR) was purchased from Sigma-Aldrich (Shanghai, China) Trading Co., Ltd. (Shunan, Japan) Hyaluronic acid (97%, 40 KDa–100 KDa) was purchased from Shanghai Macklin Biochemical Co., Ltd. (Shanghai, China) Ammonia (NH₃·H₂O, Analytical Reagent, AR) was purchased from Sinopharm Chemical Reagent Co., Ltd. (Shanghai, China) Dopamine hydrochloride (DA · HCl, 98%), 1,3,5-trimethylbenzene (TMB, AR, 97%), and FeCl₃·6H₂O (AR, 99%) were purchased from Shanghai Aladdin Bio-Chem Technology Co., Ltd. (Shanghai, China) L929 mouse epithelial cells (SCSP-5039) and HCT-116 cells (TCHu 99) were purchased from National Collection of Authenticated Cell Cultures.

4.2. Synthesis of Mesoporous Polydopamine (MPDA) Nanoparticles

Mesoporous polydopamine (MPDA) nanoparticles were prepared using the one-pot method [48], and in the classic experiment, TMB was added to optimize the preparation of MPDA nanoparticles. First, 250 mg of F127 and 100 µL of TMB were added to 10 mL of 50% ethanol. After 5 min of ultrasonic treatment, 75 mg of DA · HCl was added, followed by 450 µL of ammonia to adjust the pH value. The mixture was magnetically stirred for 24 h before being centrifuged at 12,000 rpm for 12 min at 25 °C. The precipitate was washed three times with acetone:ethanol (1:3; *v:v*). To compare the effect of TMB on MPDA nanoparticles, MPDA nanoparticles without TMB were prepared without changing any other parameters.

4.3. Preparation of MPDA-Fe(III)-DOX Nanoparticles

The MPDA nanoparticles were first prepared according to the molar ratios (DA:Fe) of 6:1, 3:1, and 2:1. The obtained MPDA nanoparticles and ferric chloride were dissolved in the above molar ratio in PBS and vortexed at 1000 rpm for 5 min to obtain three different iron-crosslinked MPDA (MPDA-Fe(III)) nanoparticles. DOX in various concentrations was dissolved in PBS, and the three ferric crosslinked MPDA nanoparticles were added in turn. The supernatant was obtained by centrifugation at 11,000 rpm for 10 min. The performance of the three ferric crosslinked loaded DOX was evaluated, and the best one, MPDA-Fe(III) nanoparticle-loaded DOX, was optimized to obtain MPDA-Fe(III)-DOX for the subsequent experiments.

4.4. Hyaluronic Acid-Based Modification of Nanoparticles

In the experiment, the optimal MPDA-Fe(III)-DOX was used for HA modification, and the mass ratios of MPDA-Fe(III)-DOX to HA were 1:1, 1:2, and 1:3. High-speed centrifugation was used after thorough mixing to obtain MPDA-Fe(III)-DOX-HA modified with varying proportions of HA. Zeta potential values and SEM images were evaluated to obtain the optimal proportion of HA.

4.5. Characterization of Nanocarrier

4.5.1. Brunner–Emmett–Teller (BET) Measurements

In this study, the IQ3 automatic specific surface and porosity analyzer was used to determine the specific surface area and pore volume of the nanocarrier via adsorption. The N₂ adsorption–desorption isotherms were determined in continuous adsorption mode at 77.35 K, and the specific surface area, pore size, and pore volume were determined using BET and BJH methods.

4.5.2. Scanning Electron Microscopy (SEM)

The nanoparticles were dispersed in an ethanol solution, sampled, dropped onto tin-foil paper, and sprayed with gold after natural drying. The morphology of the nanoparticles was examined under a scanning electron microscope.

4.5.3. Fourier Transform Infrared Spectroscopy (FTIR)

Experimentally obtained nanoparticles were dried and sample-prepared before infrared spectrum analysis using the Bruker Tensor II infrared spectrometer.

4.5.4. X-ray Photoelectron Spectroscopy (XPS)

The X-ray photoelectron spectrum of the nanocarrier was analyzed, and the changes in the energy spectrum of the nanocarrier were compared before and after drug loading.

4.5.5. DOX Loading and In Vitro Release

1. Standard curve

The standard curve of DOX was plotted using ultraviolet spectrophotometry. Following the preparation of 10 mg DOX in 1 mg/mL mother solution with H₂O, the mother solutions were diluted to obtain 2, 4, 8, 10, and 16 µg/mL DOX solutions. At 480 nm, the absorbance value was measured, and the standard curve of DOX was plotted.

2. Loading rate and encapsulation efficiency

The nanocarrier was added to a 100 µg/mL DOX solution, oscillated and loaded overnight, and centrifuged at 11,000 rpm for 10 min. The supernatant was taken to determine DOX content. The centrifuged precipitate was lyophilized and weighed. The loading rate and encapsulation efficiency of MPDA-Fe(III) nanoparticles were calculated.

The loading capacity (LC) and encapsulation efficiency (EE) were calculated using the following formulas:

$$LC = \frac{W_0 - W_1}{W_2} \times 100\% \quad (1)$$

$$EE = \frac{W_0 - W_1}{W_0} \times 100\% \quad (2)$$

The W_0 , W_1 , and W_2 represent the initial DOX addition, the DOX content of the supernatant after centrifugation, and the weight of the centrifuged precipitate after freeze-drying, respectively.

4.5.6. In Vitro Release

The release capacity of MPDA-Fe(III)-DOX-HA at different pH values was determined using dialysis. The dialysis bag (MW = 3500) was packed with the same amount of MPDA-Fe(III)-DOX-HA in PBS (pH = 7.4) or acetic acid buffer (pH = 5.2). After sealing, it was dispersed in the corresponding 200 mL buffer to simulate the normal human internal environment and tumor microenvironment, and the release process of the drugs in vivo was examined. Under constant temperature oscillation at 150 rpm and 37 °C, 2 mL of dialysate in the beaker was collected, and 2 mL of the corresponding buffer was added at a certain time point for continuous release for 48 h. The DOX content of the dialysate was measured, and the ratio to the initial DOX content was calculated to plot the release curve.

4.5.7. Photothermal Conversion Efficiency

MPDA, MPDA-Fe(III)-DOX, and MPDA-Fe(III)-DOX-HA solutions were prepared in 100 μL deionized water at a concentration of 200 $\mu\text{g}/\text{mL}$, and the temperature rise was measured under near-infrared laser irradiation ($2\text{ W}/\text{cm}^2$, 5 min). The nanomaterial solutions with different concentrations (50, 100, and 200 $\mu\text{g}/\text{mL}$) and power densities (1 and $2\text{ W}/\text{cm}^2$) were irradiated for 5 min to evaluate the photothermal effects at different irradiation powers. The 200 $\mu\text{g}/\text{mL}$ MPDA-Fe(III)-DOX-HA solution was irradiated with a near-infrared laser ($2\text{ W}/\text{cm}^2$) for 5 min and allowed to naturally cool to $25\text{ }^\circ\text{C}$. The photothermal conversion rate of MPDA-Fe(III)-DOX-HA was then calculated.

4.5.8. Cytotoxicity

The MTT assay was used to evaluate the cytotoxicity of drugs and nano-systems to L929 and HCT-116 cells. L929 mouse epithelial cells and HCT-116 cells were cultured in Gibco MEM medium and Gibco DMEM medium, respectively, supplemented with 10% fetal bovine serum and 100 $\mu\text{g}/\text{mL}$ streptomycin in a humidified atmosphere with 5% CO_2 at a constant temperature of $37\text{ }^\circ\text{C}$ to the logarithmic phase. The cells were seeded in a 96-well plate at a density of 5×10^4 cells per well. After 18 h of incubation, 20 μL of samples with different concentration gradients were added to each well. After 12 h of coincubation, the illumination group was irradiated with a near-infrared light for 10 min. After 12 h, 20 μL MTT solution (5 mg/mL) was added to each well in the dark, followed by 4 h of incubation. After incubation, the solution was carefully removed from the wells, and 150 μL DMSO was added to each well. After shaking in the dark for 10 min, the absorbance was measured using a microplate reader at an absorbance of 490 nm, and the ratio of the absorbance of the drug-co-cultured cells to the absorbance of the medium reference was calculated to measure the survival rate of various cells.

4.5.9. Uptake of Nanomaterials by Tumor Cells

The uptake of nanomaterials by tumor cells and their targeting to HA were evaluated. HCT-116 tumor cells were used to assess cellular uptake (the cell surface contains CD44 receptors), and the cellular uptake of the HA-modified nanocarrier was compared to that of the non-HA-modified nanocarrier. HCT-116 cells were seeded into 6-well plates (containing 1 mL of culture medium) at a density of 1×10^6 cells per well and grown for 24 h. Subsequently, 1 mL of PBS, DOX, MPDA-Fe(III)-DOX, and MPDA-Fe(III)-DOX-HA were added (the equivalent DOX concentration in each group was 10 $\mu\text{g}/\text{mL}$), followed by an incubation of 4 or 8 h. After adding the samples, the irradiated group was incubated with near-infrared light (808 nm , $2\text{ W}/\text{cm}^2$) for 10 min. After incubation, cells were washed three times with PBS and stained with 1 mL of Hoechst 33,258 for 25 min. After discarding the staining agent, the cells were again washed three times with PBS before being observed under a fluorescence inverted microscope.

4.5.10. Statistical Analysis

The results were expressed as mean \pm SD. Statistical analysis was performed using one-way analysis of variance (ANOVA) and *t*-test. $p < 0.05$ was considered statistically significant.

5. Conclusions

In this study, mesoporous polydopamine nanoparticles (MPDA) were prepared using the template method, and an integrated photothermal–chemotherapy platform (MPDA-Fe(III)-DOX-HA) was subsequently established. MPDA-Fe(III)-DOX-HA had a uniform particle size of ($133 \pm 18\text{ nm}$), a high drug-loading capacity for DOX ($84.90 \pm 0.68\%$), and a high release capacity at $\text{pH} = 5.2$ (release rate: 53.1%). Photothermal experiments revealed that the MPDA nanoparticles with surface-modified ferric ions had greater photothermal conversion ability and good photothermal stability. In addition, under local irradiation with an 808 nm near-infrared laser, MPDA-Fe(III)-DOX-HA exhibited strong cytotoxicity to HCT-116 cells, whereas targeted modification of hyaluronic acid reduced the cytotoxicity

of nanoparticles to normal cells. The results showed that MPDA-Fe(III)-DOX-HA exhibited good biocompatibility and anti-tumor effect, which could be used as a reference for further research into photothermal–chemotherapy combination therapy in the future.

Author Contributions: Conceptualization, X.O.; Investigation, M.G. and X.X.; Project administration, J.L. All authors have read and agreed to the published version of the manuscript.

Funding: This work was financially supported by the Basic Public Welfare Research Project of Zhejiang Province (LTGY23H180008).

Data Availability Statement: Not applicable.

Acknowledgments: We acknowledge Yingjie Wang for the software support for this work.

Conflicts of Interest: The authors declare no conflict of interest.

References

- O’Keefe, S.J.D. Diet, microorganisms and their metabolites, and colon cancer. *Nat. Rev. Gastroenterol. Hepatol.* **2016**, *13*, 691–706. [CrossRef] [PubMed]
- Thanikachalam, K.; Khan, G. Colorectal Cancer and Nutrition. *Nutrients* **2019**, *11*, 164. [CrossRef] [PubMed]
- Amidon, S.; Brown, J.E.; Dave, V.S. Colon-Targeted Oral Drug Delivery Systems: Design Trends and Approaches. *Aaps Pharmscitech* **2015**, *16*, 731–741. [CrossRef] [PubMed]
- Lee, S.H.; Bajracharya, R.; Min, J.Y.; Han, J.W.; Park, B.J.; Han, H.K. Strategic Approaches for Colon Targeted Drug Delivery: An Overview of Recent Advancements. *Pharmaceutics* **2020**, *12*, 68. [CrossRef]
- Mojarad-Jabali, S.; Mahdinloo, S.; Farshbaf, M.; Sarfraz, M.; Fatahi, Y.; Atyabi, F.; Valizadeh, H. Transferrin receptor-mediated liposomal drug delivery: Recent trends in targeted therapy of cancer. *Expert Opin. Drug Deliv.* **2022**, *19*, 685–705. [CrossRef]
- Barkat, A.; Beg, S.; Panda, S.K.; Alharbi, K.S.; Rahman, M.; Ahmed, F.J. Functionalized mesoporous silica nanoparticles in anticancer therapeutics. *Semin. Cancer Biol.* **2021**, *69*, 365–375. [CrossRef]
- Edis, Z.; Wang, J.L.; Waqas, M.K.; Ijaz, M.; Ijaz, M. Nanocarriers-Mediated Drug Delivery Systems for Anticancer Agents: An Overview and Perspectives. *Int. J. Nanomed.* **2021**, *16*, 1313–1330. [CrossRef]
- Gothwal, A.; Khan, I.; Gupta, U. Polymeric Micelles: Recent Advancements in the Delivery of Anticancer Drugs. *Pharm. Res.* **2016**, *33*, 18–39. [CrossRef]
- Zare, H.; Ahmadi, S.; Ghasemi, A.; Ghanbari, M.; Rabiee, N.; Bagherzadeh, M.; Karimi, M.; Webster, T.J.; Hamblin, M.R.; Mostafavi, E. Carbon Nanotubes: Smart Drug/Gene Delivery Carriers. *Int. J. Nanomed.* **2021**, *16*, 1681–1706. [CrossRef]
- Yi, G.; Ling, J.; Jiang, Y.; Lu, Y.; Yang, L.-Y.; Ouyang, X.k. Fabrication, characterization, and in vitro evaluation of doxorubicin-coupled chitosan oligosaccharide nanoparticles. *J. Mol. Struct.* **2022**, *1268*, 133688. [CrossRef]
- Wenningmann, N.; Knapp, M.; Ande, A.; Vaidya, T.R.; Ait-Oudhia, S. Insights into Doxorubicin-induced Cardiotoxicity: Molecular Mechanisms, Preventive Strategies, and Early Monitoring. *Mol. Pharmacol.* **2019**, *96*, 219–232. [CrossRef]
- Mirzaei, S.; Gholami, M.H.; Hashemi, F.; Zabolian, A.; Farahani, M.V.; Hushmandi, K.; Zarrabi, A.; Goldman, A.; Ashrafizadeh, M.; Orive, G. Advances in understanding the role of P-gp in doxorubicin resistance: Molecular pathways, therapeutic strategies, and prospects. *Drug Discov. Today* **2022**, *27*, 436–455. [CrossRef]
- Liu, C.; Jiang, F.; Xing, Z.; Fan, L.; Li, Y.; Wang, S.; Ling, J.; Ouyang, X.-K. Efficient Delivery of Curcumin by Alginate Oligosaccharide Coated Aminated Mesoporous Silica Nanoparticles and In Vitro Anticancer Activity against Colon Cancer Cells. *Pharmaceutics* **2022**, *14*, 1166. [CrossRef]
- Ghosh, S. Cisplatin: The first metal based anticancer drug. *Bioorganic Chem.* **2019**, *88*, 102925. [CrossRef]
- Kalluru, P.; Vankayala, R.; Chiang, C.S.; Hwang, K.C. Photosensitization of Singlet Oxygen and In Vivo Photodynamic Therapeutic Effects Mediated by PEGylated W18O49 Nanowires. *Angew. Chem. -Int. Ed.* **2013**, *52*, 12332–12336. [CrossRef]
- Lee, W.; Lee, C.; Kim, K. Injectable composite hydrogel embedded with eutectic Ga/In liquid metal particles for photothermal and chemotherapy against breast cancer. *Tissue Eng. Part A* **2022**, *28*, 332.
- Patel, V.; Rajani, C.; Tambe, V.; Kalyane, D.; Anup, N.; Deb, P.K.; Kalia, K.; Tekade, R.K. Nanomaterials assisted chemophotothermal therapy for combating cancer drug resistance. *J. Drug Deliv. Sci. Technol.* **2022**, *70*, 103164. [CrossRef]
- Aghajanzadeh, M.; Zamani, M.; Kouchi, F.R.; Eixenberger, J.; Shirini, D.; Estrada, D.; Shirini, F. Synergic Antitumor Effect of Photodynamic Therapy and Chemotherapy Mediated by Nano Drug Delivery Systems. *Pharmaceutics* **2022**, *14*, 322. [CrossRef]
- Mujokoro, B.; Adabi, M.; Sadroddiny, E.; Adabi, M.; Khosravani, M. Nano-structures mediated co-delivery of therapeutic agents for glioblastoma treatment: A review. *Mater. Sci. Eng. C-Mater. Biol. Appl.* **2016**, *69*, 1092–1102. [CrossRef]
- Nejati, K.; Rastegar, M.; Fathi, F.; Dadashpour, M.; Arabzadeh, A. Nanoparticle-based drug delivery systems to overcome gastric cancer drug resistance. *J. Drug Deliv. Sci. Technol.* **2022**, *70*, 103231. [CrossRef]
- Neamtu, I.; Rusu, A.G.; Diaconu, A.; Nita, L.E.; Chiriac, A.P. Basic concepts and recent advances in nanogels as carriers for medical applications. *Drug Deliv.* **2017**, *24*, 539–557. [CrossRef] [PubMed]

22. George, A.; Shah, P.A.; Shrivastav, P.S. Natural biodegradable polymers based nano-formulations for drug delivery: A review. *Int. J. Pharm.* **2019**, *561*, 244–264. [CrossRef] [PubMed]
23. Alfieri, M.L.; Weil, T.; Ng, D.Y.W.; Ball, V. Polydopamine at biological interfaces. *Adv. Colloid Interface Sci.* **2022**, *305*, 102689. [CrossRef] [PubMed]
24. Liu, C.; Ling, J.; Yang, L.-Y.; Ouyang, X.-k.; Wang, N. Chitosan-based carbon nitride-polydopamine-silver composite dressing with antibacterial properties for wound healing. *Carbohydr. Polym.* **2023**, *303*, 120436. [CrossRef] [PubMed]
25. Acter, S.; Jahan, N.; Vidallon, M.L.P.; Teo, B.M.; Tabor, R.F. Mesoporous Polydopamine Nanobowls Toward Combined Chemo- and Photothermal Cancer Therapy. *Part. Part. Syst. Character.* **2022**, *39*, 2200015. [CrossRef]
26. Seth, A.; Derami, H.G.; Gupta, P.; Wang, Z.Y.; Rathi, P.; Gupta, R.; Cao, T.; Morrissey, J.J.; Singamaneni, S. Polydopamine-Mesoporous Silica Core-Shell Nanoparticles for Combined Photothermal Immunotherapy. *ACS Appl. Mater. Interfaces* **2020**, *12*, 42499–42510. [CrossRef] [PubMed]
27. Batul, R.; Tamanna, T.; Khaliq, A.; Yu, A. Recent progress in the biomedical applications of polydopamine nanostructures. *Biomater. Sci.* **2017**, *5*, 1204–1229. [CrossRef]
28. Choukaife, H.; Seyam, S.; Alallam, B.; Doolaanea, A.; Alfatama, M. Current Advances in Chitosan Nanoparticles Based Oral Drug Delivery for Colorectal Cancer Treatment. *Int. J. Nanomed.* **2022**, *17*, 3933–3966. [CrossRef]
29. Suner, S.S.; Ari, B.; Onder, F.C.; Ozpolat, B.; Ay, M.; Sahiner, N. Hyaluronic acid and hyaluronic acid: Sucrose nanogels for hydrophobic cancer drug delivery. *Int. J. Biol. Macromol.* **2019**, *126*, 1150–1157. [CrossRef]
30. Wu, D.; Duan, X.; Guan, Q.; Liu, J.; Yang, X.; Zhang, F.; Huang, P.; Shen, J.; Shuai, X.; Cao, Z. Mesoporous Polydopamine Carrying Manganese Carbonyl Responds to Tumor Microenvironment for Multimodal Imaging-Guided Cancer Therapy. *Adv. Funct. Mater.* **2019**, *29*, 1900095. [CrossRef]
31. Guan, H.D.; Wang, L.C.; Zhang, J.X.; Xing, Y.X.; Cai, K.Y. Selective Enrichment of Polydopamine in Mesoporous Nanocarriers for Nuclear-Targeted Drug Delivery. *Part. Part. Syst. Character.* **2018**, *35*, 1800011. [CrossRef]
32. Zheng, X.Y.; Zhang, J.X.; Wang, J.; Qi, X.Q.; Rosenholm, J.M.; Cai, K.Y. Polydopamine Coatings in Confined Nanopore Space: Toward Improved Retention and Release of Hydrophilic Cargo. *J. Phys. Chem. C* **2015**, *119*, 24512–24521. [CrossRef]
33. Du, P.F.; Yan, J.H.; Long, S.; Xiong, H.J.; Wen, N.C.; Cai, S.D.; Wang, Y.R.; Peng, D.M.; Liu, Z.B.; Liu, Y.F. Tumor microenvironment and NIR laser dual-responsive release of berberine 9-O-pyrazole alkyl derivative loaded in graphene oxide nanosheets for chemo-photothermal synergetic cancer therapy. *J. Mater. Chem. B* **2020**, *8*, 4046–4055. [CrossRef] [PubMed]
34. Zhang, Q.; Chen, B.; Wu, D.; Peng, Z.H.; Qiao, X.S.; Chao, X.L.; Yang, Z.P. Controllable synthesis of (Ba_{0.85}Ca_{0.15})(Zr_{0.1}Ti_{0.9})O₃ submicron sphere by hydroxide co-precipitation method. *Ceram. Int.* **2020**, *46*, 28285–28291. [CrossRef]
35. Wang, X.; Liu, X.J.; Xiao, C.W.; Zhao, H.; Zhang, M.Y.; Zheng, N.N.; Kong, W.Y.; Zhang, L.; Yuan, H.K.; Zhang, L.J.; et al. Triethylenetetramine-modified hollow Fe₃O₄/SiO₂/chitosan magnetic nanocomposites for removal of Cr(VI) ions with high adsorption capacity and rapid rate. *Microporous Mesoporous Mater.* **2020**, *297*, 110041. [CrossRef]
36. Liu, J.-S.; Peng, S.-J.; Li, G.-F.; Zhao, Y.-X.; Meng, X.-Y.; Yu, X.-R.; Li, Z.-H.; Chen, J.-M. Polydopamine Nanoparticles for Deep Brain Ablation via Near-Infrared Irradiation. *ACS Biomater. Sci. Eng.* **2020**, *6*, 664–672. [CrossRef]
37. Wilson, D.; Langell, M.A. XPS analysis of oleylamine/oleic acid capped Fe₃O₄ nanoparticles as a function of temperature. *Appl. Surf. Sci.* **2014**, *303*, 6–13. [CrossRef]
38. Bhartiya, P.; Chawla, R.; Dutta, P.K. Folate receptor targeted chitosan and polydopamine coated mesoporous silica nanoparticles for photothermal therapy and drug delivery. *J. Macromol. Sci. Part A-Pure Appl. Chem.* **2022**, *59*, 810–817. [CrossRef]
39. Xiao, J.-D.; Jiang, H.-L. Metal–Organic Frameworks for Photocatalysis and Photothermal Catalysis. *Acc. Chem. Res.* **2019**, *52*, 356–366. [CrossRef]
40. Yan, Q.; Liu, L.; Wang, T.; Wang, H. A pH-responsive hydrogel system based on cellulose and dopamine with controlled hydrophobic drug delivery ability and long-term bacteriostatic property. *Colloid Polym. Sci.* **2019**, *297*, 705–717. [CrossRef]
41. Jazani, A.M.; Shetty, C.; Movasat, H.; Bawa, K.K.; Oh, J.K. Imidazole-Mediated Dual Location Disassembly of Acid-Degradable Intracellular Drug Delivery Block Copolymer Nanoassemblies. *Macromol. Rapid Commun.* **2021**, *42*, 2100262. [CrossRef] [PubMed]
42. Stankic, S.; Suman, S.; Haque, F.; Vidic, J. Pure and multi metal oxide nanoparticles: Synthesis, antibacterial and cytotoxic properties. *J. Nanobiotechnology* **2016**, *14*, 73. [CrossRef]
43. Chiu, H.I.; Samad, N.A.; Fang, L.; Lim, V. Cytotoxicity of targeted PLGA nanoparticles: A systematic review. *RSC Adv.* **2021**, *11*, 9433–9449. [CrossRef] [PubMed]
44. Zhang, S.; Liu, Y.; Gan, Y.; Qiu, N.; Gu, Y.; Zhu, H. Conjugates of TAT and folate with DOX-loaded chitosan micelles offer effective intracellular delivery ability. *Pharm. Dev. Technol.* **2019**, *24*, 253–261. [CrossRef]
45. Gary-Bobo, M.; Brevet, D.; Benkirane-Jessel, N.; Raehm, L.; Maillard, P.; Garcia, M.; Durand, J.O. Hyaluronic acid-functionalized mesoporous silica nanoparticles for efficient photodynamic therapy of cancer cells. *Photodiagnosis Photodyn. Ther.* **2012**, *9*, 256–260. [CrossRef] [PubMed]
46. Haine, A.T.; Niidome, T. Drug Delivery Systems Controlled by Irradiation of Near Infrared Light. *J. Photopolym. Sci. Technol.* **2015**, *28*, 705–710. [CrossRef]

47. Lee, Y.D.; Shin, H.J.; Yoo, J.; Kim, G.; Kang, M.K.; Lee, J.J.; Bang, J.; Yang, J.K.; Kim, S. Metal complexation-mediated stable and biocompatible nanoformulation of clinically approved near-infrared absorber for improved tumor targeting and photonic theranostics. *Nano Converg.* **2021**, *8*, 36. [CrossRef]
48. Chen, F.; Xing, Y.; Wang, Z.; Zheng, X.; Zhang, J.; Cai, K. Nanoscale Polydopamine (PDA) Meets π - π Interactions: An Interface-Directed Coassembly Approach for Mesoporous Nanoparticles. *Langmuir* **2016**, *32*, 12119–12128. [CrossRef]

Disclaimer/Publisher's Note: The statements, opinions and data contained in all publications are solely those of the individual author(s) and contributor(s) and not of MDPI and/or the editor(s). MDPI and/or the editor(s) disclaim responsibility for any injury to people or property resulting from any ideas, methods, instructions or products referred to in the content.



Article

Non-Functionalized Gold Nanoparticles Inhibit Human Papillomavirus (HPV) Infection

Diana Gabriela Valencia-Reséndiz ¹, Atenea Villegas ², Daniel Bahena ³, Kenia Palomino ⁴, Jose Manuel Cornejo-Bravo ⁴ , Liliana Quintanar ² , Giovanni Palomino-Vizcaino ^{5,*} and Luis Marat Alvarez-Salas ^{1,*}

- ¹ Laboratorio de Terapia Génica, Departamento de Genética y Biología Molecular, Centro de Investigación y de Estudios Avanzados del I.P.N., Av. Instituto Politécnico Nacional 2508, Ciudad de México 07360, Mexico; dgvalr@gmail.com
 - ² Departamento de Química, Centro de Investigación y de Estudios Avanzados del I.P.N., Av. Instituto Politécnico Nacional 2508, Ciudad de México 07360, Mexico; avillegas@cinvestav.mx (A.V.); lilianaq@cinvestav.mx (L.Q.)
 - ³ Laboratorio Avanzado de Nanoscopia Electrónica (LANE), Centro de Investigación y de Estudios Avanzados del I.P.N., Av. Instituto Politécnico Nacional 2508, Ciudad de México 07360, Mexico; dbahenau@cinvestav.mx
 - ⁴ Laboratorio de Biofarmacia, Facultad de Ciencias Químicas e Ingeniería, Universidad Autónoma de Baja California, Calzada Universidad 14418, Col. Parque Industrial Internacional, Tijuana 22424, Mexico; kenia.palomino@uabc.edu.mx (K.P.); jmcornejo@uabc.edu.mx (J.M.C.-B.)
 - ⁵ Facultad de Ciencias de la Salud, Unidad Valle de las Palmas, Campus Tijuana, Universidad Autónoma de Baja California, Boulevard Universitario 1000, Valle de las Palmas, Tijuana 21500, Mexico
- * Correspondence: gpalomino@uabc.edu.mx (G.P.-V.); lalvarez@cinvestav.mx (L.M.A.-S.)



Citation: Valencia-Reséndiz, D.G.; Villegas, A.; Bahena, D.; Palomino, K.; Cornejo-Bravo, J.M.; Quintanar, L.; Palomino-Vizcaino, G.; Alvarez-Salas, L.M. Non-Functionalized Gold Nanoparticles Inhibit Human Papillomavirus (HPV) Infection. *Int. J. Mol. Sci.* **2022**, *23*, 7552. <https://doi.org/10.3390/ijms23147552>

Academic Editors: Ilaria Rea, Nicola Borbone, Monica Terracciano and Chiara Tramontano

Received: 14 June 2022

Accepted: 4 July 2022

Published: 7 July 2022

Publisher's Note: MDPI stays neutral with regard to jurisdictional claims in published maps and institutional affiliations.

Abstract: The spontaneous interaction between human papillomavirus type 16 (HPV16) L1 virus-like particles (VLPs) and non-functionalized gold nanoparticles (nfGNPs) interferes with the nfGNPs' salt-induced aggregation, inhibiting the red–blue color shift in the presence of NaCl. Electron microscopy and competition studies showed that color-shift inhibition is a consequence of direct nfGNP–VLP interaction and, thus, may produce a negative impact on the virus entry cell process. Here, an in vitro infection system based on the HPV16 pseudovirus (PsV) was used to stimulate the natural infection process in vitro. PsVs carry a pseudogenome with a reporter gene, resulting in a fluorescent signal when PsVs infect a cell, allowing quantification of the viral infection process. Aggregation assays showed that nfGNP-treated PsVs also inhibit color shift in the presence of NaCl. High-resolution microscopy confirmed nfGNP–PsV complex formation. In addition, PsVs can interact with silver nanoparticles, suggesting a generalized interaction of metallic nanoparticles with HPV16 capsids. The treatment of PsVs with nfGNPs produced viral infection inhibition at a higher level than heparin, the canonical inhibitor of HPV infection. Thus, nfGNPs can efficiently interfere with the HPV16 cell entry process and may represent a potential active component in prophylactic formulations to reduce the risk of HPV infection.

Keywords: gold nanoparticles; nanoprophyllaxis; viral inhibition; human papillomavirus; HPV; pseudovirus; viral infection inhibition; nanocomplex formation



Copyright: © 2022 by the authors. Licensee MDPI, Basel, Switzerland. This article is an open access article distributed under the terms and conditions of the Creative Commons Attribution (CC BY) license (<https://creativecommons.org/licenses/by/4.0/>).

1. Introduction

Infection by the high-risk human papillomavirus (HPV) is the most significant risk factor in the development of malignant tumors of the anogenital tract, including cervical cancer. Despite the increasing use of prophylactic vaccines against HPV infection, cervical cancer is still a primary health threat for women living in developing countries. Vaccine cost, inadequate healthcare infrastructure and socio-cultural issues are some of the main reasons for this apparent lack of effectivity. Hence, there is still a pressing need for new and efficient strategies for HPV transmission control, detection and treatment [1,2].

Genital dysplasia and cervical cancer are associated with a subset of HPVs referred to as high risk, consisting of HPV types 16, 18, 31, 33, 45, 52 and 58. HPVs are small (50 nm) icosahedral viruses with an 8 kb double-stranded circular DNA genome, encoding eight early and late genes. Early genes regulate cellular transformation, and early and late viral DNA replication. The late genes code for the L1 and L2 proteins, which self-assemble within the host cell nucleus to encapsidate the viral DNA and constitute infective virions. High-risk HPVs infect mucosal genital epithelia, where the key event is the binding of the positively charged viral capsid to heparan sulfate (HS), a negatively charged linear oligosaccharide attached to a protein core on the cell surface [3].

Gold nanoparticles (GNPs) are biocompatible Au clusters from 1 to 100 nm in size. GNPs display distinctive physicochemical properties depending on their size and shape, including surface plasmon resonance (SPR) and fluorescence enhancement effects [4]. Different forms of GNPs have been used as small-volume, ultra-sensitive label-free optical sensors, leading to the development of several biomedical applications, such as real-time imaging and biosensing, as well as the delivery of either genes or anti-tumor drugs for cancer diagnosis and therapy, respectively. An easily noticeable red to blue color shift results from particle–particle plasmonic coupling of GNPs. While in suspension in water, GNPs electrostatically repulse each other, maintaining a stable color. However, the presence of counterions (i.e., Na^{++}) neutralizes electrostatic repulsion and the distance between the GNPs decreases, producing near-field coupling that results in bigger particle size and a strong enhancement of the localized electric field within the interparticle spacing, leading to a pronounced color shift. The clearly distinguishable color shift facilitates detection readout to such a degree that it can be performed with the naked eye [4].

GNP conjugation (functionalization) with biomolecules has been extensively reported in several biodetection methods. Non-functionalized GNPs (nfGNPs) in water suspension will eventually aggregate and precipitate as metallic gold powder. However, nfGNP stabilization by protective or capping agents, such as thiols or citrate, prevents uncontrolled aggregation, allowing long-term storage. The capping agent generally forms a monolayer coat (ligand shell) that plays a critical role against aggregation, thus improving solubility and electron-transfer efficiency while allowing controlled shape and assembly. The ability to integrate nfGNPs into biological systems relies on the basic understanding of their interactions with electrolytes, macromolecules and metabolites adsorbed onto their surface by electrostatic, hydrophobic, van der Waals and dispersive forces forming a dense coating known as the biocorona. Such a coating shields the original nfGNP surface properties acting as a “complex” surfactant interface modifying their size and composition, thus defining the physiological response and interaction with living systems including viruses [5].

Our group first reported the spontaneous interaction between HPV16 L1 virus-like particles (VLPs) and nfGNPs, which resulted in the stabilization of purified VLPs and the inhibition of the nfGNPs’ salt-induced aggregation. Ionic-competition and genetic data showed that the nature of an nfGNP–VLP interaction was mainly hydrophobic [6]. Furthermore, nfGNPs covered substantial areas on the VLPs’ surface, suggesting that nfGNPs may be used as a steric inhibitor of the HPV-16 virion interaction with the host cell surface receptor, thus blocking infection. The present work showed, for the first time, the interaction of nfGNPs with functional HPV16 PsVs and characterized the effect of the PsVs in the nfGNPs’ aggregation process and the impact of the nfGNPs in the HPV virion cell entrance process *in vitro*. Aggregation assays showed that PsVs can inhibit the nfGNPs’ color shift in the presence of NaCl in a dose-dependent manner. High-resolution TEM showed that nfGNPs can directly interact with HPV16 PsVs. The nfGNP–PsV complex prevented the characteristic red to blue color shift in aggregation assays and, in the presence of ethanol, revealed that the interaction is essentially hydrophobic. The PsVs’ aggregate size in solution decreased rapidly in the presence of nfGNPs, as previously determined with VLPs. The nfGNPs were capable of inhibiting virus entry in a pseudovirus model with no toxic effects. This is not unique to nanometric gold, as non-functionalized silver nanoparticles (nfSNPs) can also inhibit the viral cell entry process. We compared the

inhibition effect of non-functionalized metallic nanoparticles (nfMNPs) with heparin, the canonical inhibitor of HPV, and showed that nfGNPs can inhibit the infection process more efficiently than heparin.

Non-functionalized metallic nanoparticles (nfMNPs) can be useful to efficiently inhibit the HPV16 infection process and have the potential to be incorporated in prophylactic formulations as a functional component.

2. Results

2.1. Non-Functionalized Gold Nanoparticle (nfGNP) Characterization

HPV-16 L1/L2 pseudoviruses (PsVs) (a functional model for HPV infection) were incubated with nfGNPs in HPV pseudo-infection assays. The nfGNPs were synthesized by a modified citrate reduction method and characterized by high-angle annular dark-field scanning transmission electron microscopy (HAADF-STEM) as spheroidal shaped particles of about 10–20 nm in diameter (Figure 1A). Dynamic light scattering (DLS) analysis showed a narrow nfGNP size distribution of 18 nm with a standard deviation of 8.164, a polydispersity index of 0.245 and a zeta potential of -22.8 mV with a standard deviation of 6.63, in the synthesis reaction final conditions at pH 5.5 (Figure 1B). These results indicate that the synthesis produced a uniform nfGNP population. For functional characterization, nfGNP response to Na^{++} counterions was tested by incubating 100 μL of nfGNPs (2 nM) with increasing NaCl concentrations (20–100 mM) and measuring the red–blue color shift by absorbance at a 650/520 nm wavelength ratio. Color change was apparent from a 20-mM NaCl increase in the 650/520 ratio, showing that the produced nfGNPs were competent for further experimentation (Figure 1C).

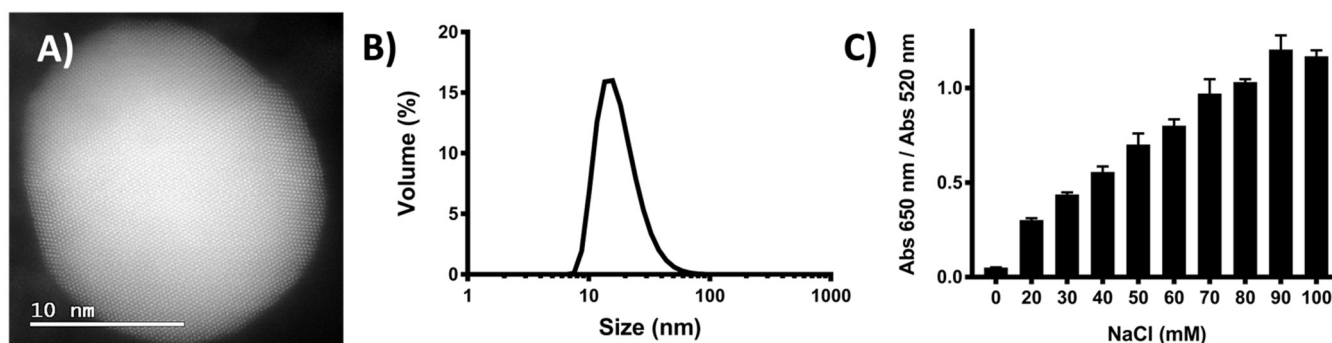


Figure 1. Characterization of non-functionalized gold nanoparticles (nfGNPs). (A) Quasispherical nfGNPs were directly visualized by HAADF-STEM (scale bar = 10 nm). (B) Hydrodynamic diameter of nfGNPs as determined by DLS. (C) Salt-induced aggregation of nfGNPs. Increasing NaCl concentrations were used to determine the minimum concentration required to trigger nfGNP aggregation (color shift from 650 to 520 nm). Bars represent the mean and standard deviation of three independent experiments.

2.2. Characterization of PsVs

HPV16 PsVs expressing the yellow fluorescent protein (YFP) reporter gene were produced in 293TT cells and purified through ultracentrifugation, as previously described [7]. The PsVs were immunoreactive to HPV16 L1 and L2 antibodies in immunoblot assays (Figure 2A). Transmission electron microscopy (TEM) analysis showed homogeneous 55 nm icosahedral capsids (Figure 2B).

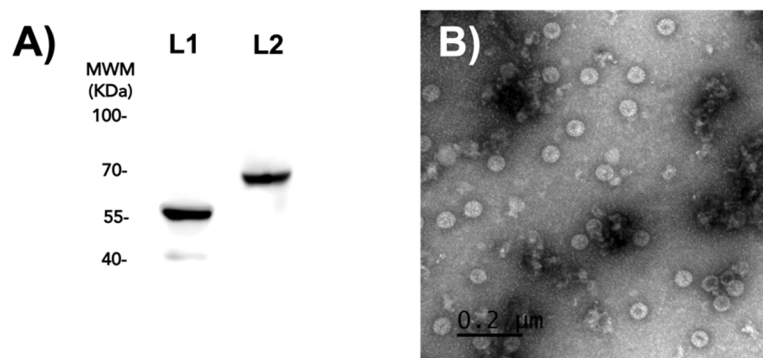


Figure 2. Characterization of PsVs. (A) HPV16 PsV immunoblotting. Purified PsVs were electrophoresed by SDS-PAGE and immunoblotted against HPV16 L1 and L2 protein monoclonal antibodies. Prominent 55 and 70 kDa bands corresponding to the L1 and L2 monomer confirmed the purity of PsVs. MWM, molecular weight marker. (B) Negative-stain TEM microphotography of PsVs (scale bar = 200 nm).

2.3. *nfGNPs Interact with PsVs*

As an initial approach to determining the effect of *nfGNPs* on HPV16 infection, the reported inhibitory effect of HPV16 L1 VLPs on the aggregation of *nfGNPs* was further tested with HPV16 L1/L2 VLPs and PsVs, which closely resemble the natural virion. Challenging *nfGNPs* (100 μL) with L1/L2 VLPs or PsVs (200–500 ng) in aggregation assays showed that the inhibition of *nfGNP* aggregation is not exclusive for L1 VLPs [6] but was also extensive to L1/L2 VLPs (Figure 3A). This was expected because the L1 protein that comprises most of the HPV capsid and L2 is minimally exposed on the virion surface [8]. Moreover, PsVs blocked salt-induced aggregation of *nfGNPs*, establishing that *nfGNP*–PsV and *nfGNP*–VLP interactions are very similar or identical. TEM and HAADF-STEM microphotography showed a direct interaction of *nfGNPs* with the PsV surface (Figure 3B,C), suggesting that an *nfGNP*–PsV interaction may have biological relevance to blocking the infection process [9].

As with VLPs, the PsVs tend to form clusters in suspension because of the relative high abundance of hydrophobic contacts on the virion surface [10]. Such contacts are likely destabilized by the hydrophobic interactions occurring with the *nfGNPs* [6]. The effect of *nfGNP* concentration on PsV clustering (size about 200 nm) was analyzed using purified HPV16 PsVs incubated with increasing amounts of *nfGNPs* (50–300 pM) and immediately analyzed by DLS. The *nfGNP* treatment resulted in the disaggregation of the PsV clusters into particles around 50 nm (Figure 3D), consistent with the previously reported *nfGNP*-induced disaggregation of HPV16 L1 VLP clusters [6].

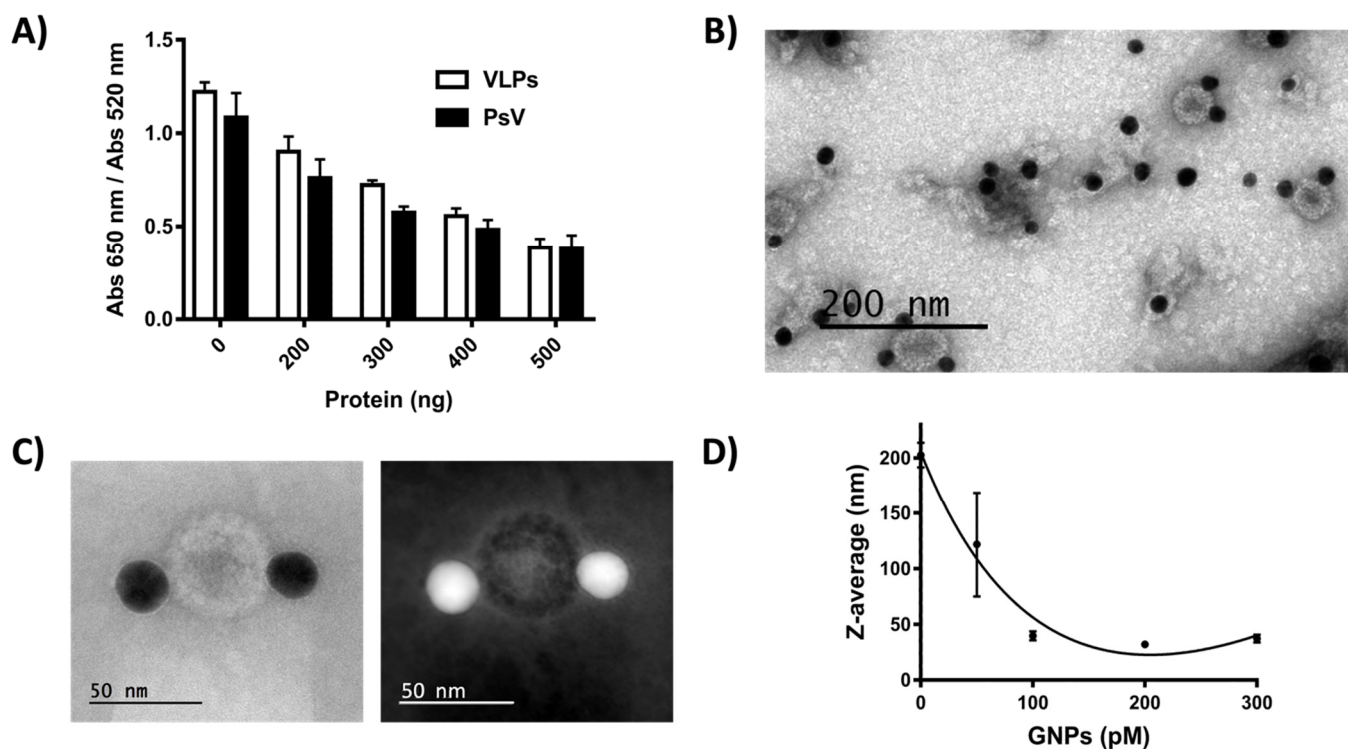


Figure 3. nfGNPs interact with PsV. (A) PsV inhibits aggregation of nfGNPs. nfGNPs (200 pM) were incubated with increasing amounts of L1/L2 VLPs (HPV16) and PsV (HPV16) (200, 300, 400 and 500 ng) in the presence of 70 mM NaCl. The graph represents the mean and standard deviation of three independent experiments. (B) Negative-stain TEM microphotography of PsV and nfGNPs (scale bar = 200 nm). nfGNPs decorate the surface of PsV. (C) Negative-stain HAADF-STEM of PsV and nfGNPs. (D) nfGNPs disaggregate PsV clusters. Purified PsV (400 ng) was incubated with increasing concentrations of nfGNPs (50, 100, 200 and 300 pM), and particle size was measure by DLS. The plot represents the average size of five measurements from the same sample.

2.4. nfGNP-PsV Interaction Is Mediated by Hydrophobic Interactions

Toward further insight into the nature of nfGNP–PsV interaction, aggregation assays were performed with rising EtOH concentrations to increase solubility as previously reported for HPV VLPs [6] (Figure 4). The observed recovery of aggregation suggests that, as with VLPs, the nfGNP–PsV interaction is mediated through the participation of hydrophobic interactions.

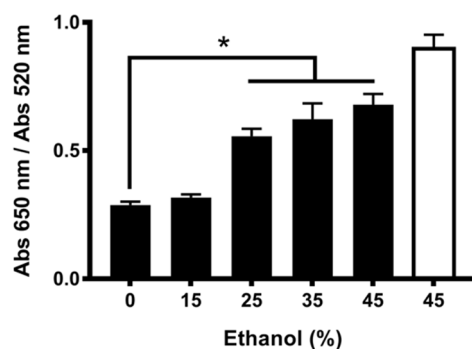


Figure 4. EtOH treatment recovers nfGNP aggregation in the presence of PsV. nfGNPs with increasing concentrations of ethanol were incubated with PsV (500 ng) in 70 mM NaCl. White bar, without PsV; black bars, with PsV. The plot represents the mean and standard deviation of three independent experiments. The asterisk indicates the statistical significance ($p = 0.0001$).

2.5. nfGNPs Inhibit HPV16 PsV Pseudo-Infection

Infection of 293TT cells with HPV16 PsV is the most widely used model for HPV infection. To evaluate the effect of nfGNPs on the HPV16 infection process, HPV16 PsV was treated with increasing amounts of nfGNPs before addition to monolayer 293TT cultures. A qualitative evaluation by fluorescence microscopy of the infected cells showed lower fluorescence levels relative to higher nfGNP concentrations (Figure 5A). Flow cytometry quantification of the pseudo-infected cultures showed that the nfGNP treatment decreased PsV-mediated fluorescence by up to 80–90% relative to the non-treated PsV control. Cell viability assays showed no harmful effects of the nfGNPs on 293TT cells (Figure 5B).

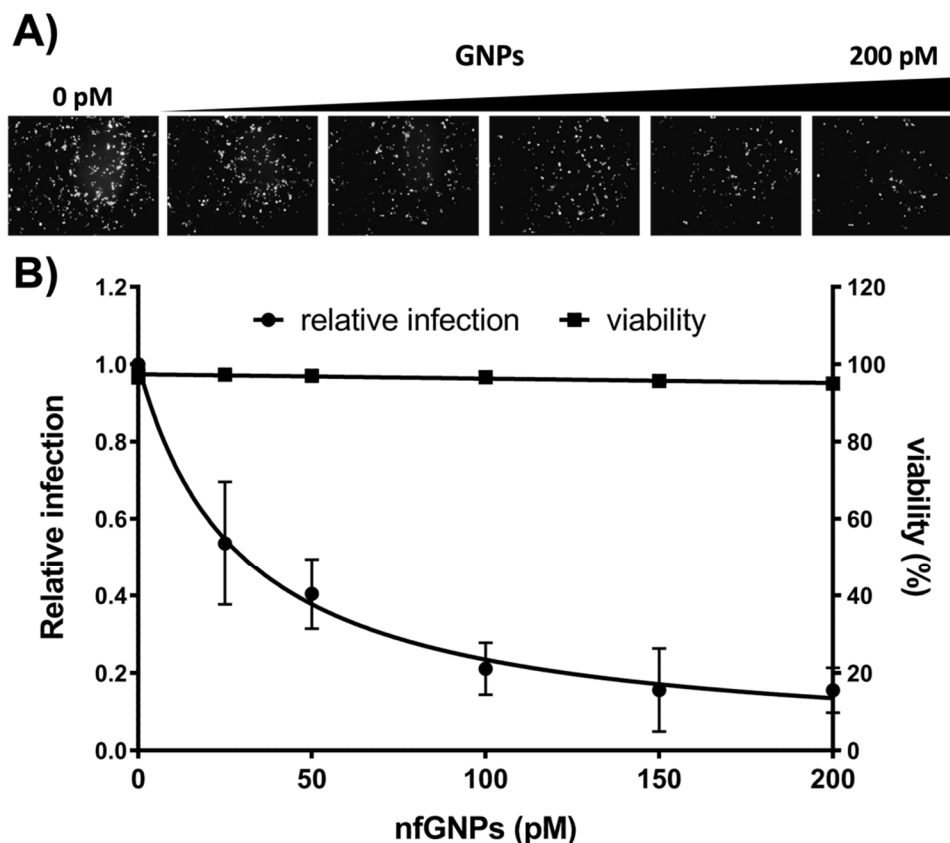


Figure 5. nfGNPs inhibit HPV16 PsV pseudo-infection. (A) Fluorescence microscopy of 293TT cells infected with PsV treated with nfGNPs. HPV16 PsV was incubated with increased concentrations of nfGNPs before 293TT cell infection. (B) Inhibition of PsV pseudo-infection by nfGNPs. Pseudo-infected 293TT cell fluorescence was quantified by flow cytometry and plotted relative to the non-treated PsV control. The graphs represent the mean and standard deviation of three independent experiments.

2.6. nfGNPs Efficiently Inhibit Pseudo-Infection at Ineffective Concentrations of Heparin

To evaluate whether the inhibition property of nfGNPs on HPV16 infection was restricted to nanometric gold, non-functionalized silver nanoparticles were tested. First, the nfSNP–PsV complex formation was confirmed by microscopy. TEM negative stain showed that nfSNPs interact with PsVs the way as nfGNPs; the nfSNP–PsV complex formation did not disturb the PsV three-dimensional structure visually (data not shown). Second, relative infection was determined to nfSNPs. Flow cytometry quantification of the pseudo-infected cultures showed 80% infection inhibition with nfSNPs in a dose-dependent manner (Figure 6), as previously shown with nfGNPs.

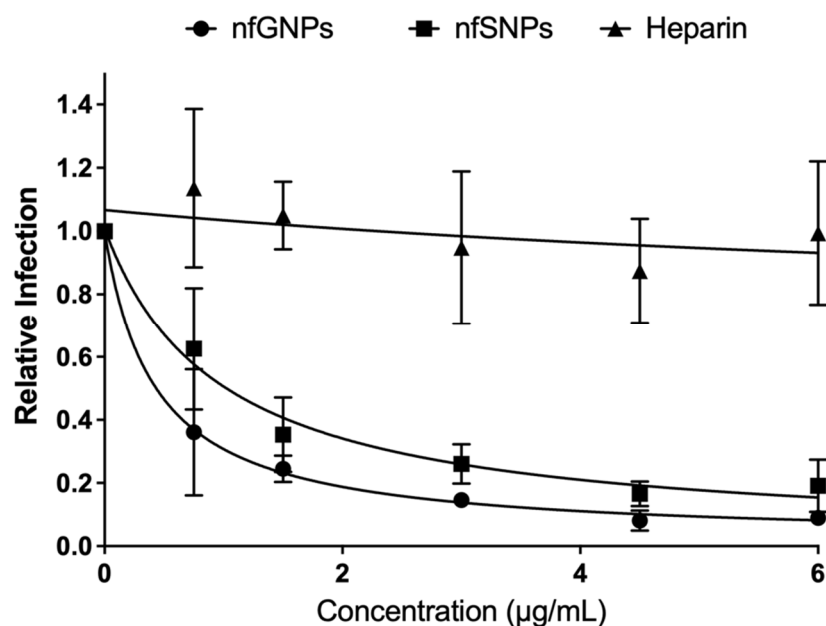


Figure 6. nfGNPs inhibit HPV16 PsV pseudo-infection better than heparin. Inhibition of PsV pseudo-infection by nfGNPs, nfSNPs and heparin. Pseudo-infected 293TT cell fluorescence was quantified by flow cytometry and plotted relative to the non-treated PsV control. The graphs represent the mean and standard deviation of three independent experiments.

Heparin is a potent HPV16 pseudo-infection inhibitor, as previously reported [7]. To compare with the HPV16 pseudo-infection inhibition potential of nfGNPs, HPV16 PsV was treated with increasing heparin concentrations before addition to monolayer 293TT cultures. Heparin did not show the HPV16 pseudo-infection inhibition effect for the tested concentrations (Figure 6), as previously reported [11].

3. Discussion

Pseudo-infection inhibition by nfGNPs was better than by heparin, a molecule structurally related to HS and widely accepted as an efficient inhibitor of the HPV infection [3]. However, the antiviral application of heparin is contraindicated due to its anticoagulant activity and inherent toxicity. On the other hand, nfGNPs have high specificity, even in a complex mixture of proteins, and have a hydrophobic surface that mediates nfGNP–PsV interaction, as recently reported for an influenza virus-sensing platform [11]. Metal nanoparticles (MNPs) have been widely used to inhibit viral infection, and this has been extensively reviewed by Kaminee Maduray and Raveen Parboosing [12]. Functionalized gold nanoparticles with polyethylene glycol (GNP-PEG) of 10 nm in size have been used to inhibit the HIV cell fusion process, supporting the idea of inhibiting the HIV infection process by gp120-CD4 recognition by raising 60% of inhibition at 0.8 mg/mL [13]. Poly-sulfated gold nanoparticles (GNP-SO₄Na) from 110 nm were used to efficiently inhibit the binding of vesicular stomatitis virus (VSV) by a three-dimensional network formation that prevents VSV from cell binding; conversely, 19 nm GNP-SO₄Na only decorate the virion at the concentration tested, probably inhibiting virus-cell binding by a complete steric shielding [14]. nfGNPs from 9.5 nm in size (initially 24 h after infection and every 24 h thereafter, for a total of three times at concentrations of 5 mg/kg and 20 mg/kg) were applied intranasally in 8–10-week-old female BALB/c mice against H2N2 influenza virus, obtaining 100% survival at eight days compared with zero survival for the control [15].

In perspective, nfGNPs could be a component of a novel topical application product as suggested for carrageenan (a polysaccharide such as heparin and a potent inhibitor of HPV infection) and the positively charged polymer AGMA1 [11]. Thus, incorporating nfGNPs into a mixture with carrageenan and AGM1 in a single treatment could completely

inhibit HPV entry in different ways, resulting in an effective prophylactic tool. The major concern with nanoparticle application in vivo is its potential toxicity; this concern has been widely reviewed by Sani et al. [16]. nfGNPs have a great potential to be incorporated as a functional component in a lubricant, where the nanoparticles would be in contact with the mucus-coated vaginal tissue—a non-keratinized stratified squamous epithelia. Vaginal epithelium is structured by basal membrane, stratum granulosum, stratum spinosum, intermediate cells, superficial squamous flat cells and stratum corneum cells. Stratum corneum cells, where nfGNP toxicity could occur, slough off by a natural process [17]. Ensign et al. exposed the difficulty of going through the mucous layer coating the vagina epithelium. Mucus traps particles efficiently by adhesive and steric interactions, preventing cell penetration. Particles and pathogens trapped in the upper mucus layer would be expected to rapidly clear [18].

This is the first report of nfGNPs blocking HPV infection. Although a full understanding of the molecular mechanisms governing the nfGNP–HPV interaction remains to be fully understood, the strong inhibitory effect of the nfGNPs on the PsV pseudo-infection process could provide a novel and affordable prophylactic method against HPV infection, thus preventing cervical cancer.

4. Materials and Methods

4.1. Synthesis of Non-Functionalized GNPs (nfGNPs)

Non-functionalized GNPs (nfGNPs) were prepared by a modified Turkevich method, as described [19,20]. Briefly, 45 mL of deionized water was added to a reaction flask and refluxed. A mixture of 5 mL of 0.1% tetrachloroauric acid, 2 mL of 1% trisodium citrate and 42.5 μ L of 0.1% silver nitrate was added dropwise. Synthesis reactions were carried out for 60 min and allowed to cool to room temperature. Colloidal nfGNPs were stored at 4 °C until used. The nfGNP characterization was made in the synthesis final reaction conditions (pH 5.5), nfGNP shape was determined by HAADF-STEM in a JEM-ARM200F transmission electron microscope (JEOL Ltd., Tokyo, Japan). nfGNP size was determined using dynamic light scattering (DLS) in a Zetasizer Nano-ZS90 (Malvern Panalytical Ltd., Cambridge, UK) with detection at 173°, and nfGNP concentration was determined by UV-visible spectra, using the equation $c = A_{450}/\epsilon_{450}$, where c is the concentration in mol per liter, A_{450} is the absorbance at 450 nm and ϵ_{450} is the molar extinction coefficient for GNPs of 18 nm ($3.87 \times 10^8 \text{ M}^{-1} \text{ cm}^{-1}$) [21]. The nfGNP suspension pH was changed to pH 7.2–7.7 through 1:100 dilution in DPBS buffer before incubation with the PsVs.

4.2. Production of HPV16 L1 Virus-Like Particles (VLPs)

HPV16 L1 virus-like particles (VLPs) were produced as we previously reported [1,22]. Briefly, *Spodoptera frugiperda* Sf21 cells (Life Technologies Corporation, Carlsbad, CA, USA) in Sf900TMII medium (Life Technologies) were infected with L1-producing recombinant baculovirus for 72 h at 26 °C. Infected cells were pelleted by centrifugation and resuspended in 1X Dulbecco's phosphate-buffered saline (D-PBS) (2.67 mM KCl, 1.47 mM KH_2PO_4 , 137.93 mM NaCl and 8.06 mM $\text{Na}_2\text{HPO}_4 \cdot 7\text{H}_2\text{O}$ pH 7.2–7.7) complemented with cComplete™ protease inhibitor cocktail (Sigma-Aldrich, St. Louis, MI, USA) in siliconized microtubes and lysed by sonication in a GEX 130 PB ultrasonic processor (Cole-Parmer Instrument Co., Vernon Hills, IL, USA) at 60% cycle duty 3 times (5 s each). Total lysates were incubated overnight at 37 °C for VLP maturation; digested at 37 °C for 1 h with *Serratia marcescens* nuclease (Sigma-Aldrich) at 0.1% final concentration; and immediately chilled on ice, mixed with a 0.17 volumes of 5 M NaCl and clarified by centrifugation at $2000 \times g$ for 15 min. The resulting supernatant was purified through CsCl isopycnic centrifugation and extensively dialyzed against 1X D-PBS at 4 °C. VLP production was verified by negative stain in TEM and immunoblotting, and VLP stock was stored in 1X D-PBS at 4 °C until use.

4.3. GNP Aggregation Assays

Non-functionalized GNP aggregation was carried out in 96-well microplates by adding nfGNPs (100 μ L), VLPs or PsV and NaCl for a 250 μ L final volume. Absorbance at 520 and 650 nm was measured immediately using an Epoch™ microplate spectrophotometer (Biotek Instruments, Winooski, VT, USA). The mean and standard deviation of the color-shift 650/520 ratio from each sample were plotted by triplicate.

4.4. Dynamic Light Scattering (DLS)

Sample measurements were performed at 25 °C using a Zetasizer Nano-ZS90 (Malvern Instruments, Malvern, UK) with detection at 90°. The hydrodynamic size of the VLPs was recorded as Z-average hydrodynamic diameter (Dh). The plotted data represent the average size of five measurements from the same sample.

4.5. Cell Culture

The human embryonic kidney 293TT (ATCC CRL-3467) cells were cultured in Gibco® Dulbecco's Modified Eagle's Medium (DMEM) (Thermo Fisher Scientific Inc., Waltham, MA, USA) supplemented with 5% Gibco® fetal bovine serum (FBS) (Thermo Fisher Scientific), 100 IU/mL penicillin, 100 μ g/mL streptomycin (PAA Laboratories Inc., Pasching, Austria) and 200 μ g/mL Gibco® hygromycin (Thermo Fisher Scientific) at 37 °C and 5% CO₂.

4.6. HPV16 Pseudovirus (PsVs) Production

HPV16 PsVs were produced as previously described [23]. Briefly, 293TT cells were co-transfected with the p16sheLL expression plasmid [11] and the reporter plasmid pSV-LYFP using the Lipofectin® transfection reagent (Thermo Fisher Scientific). Cells were harvested 72 h post-transfection, lysed in lysis buffer (DPBS-9.5 mM MgCl₂ and 0.25% Brij® 58) and incubated at 37 °C for 24 h for maturation. The mature mixture was digested with Benzonase® (Merck KGaA, Darmstadt, Germany) and clarified by centrifugation. Supernatant was placed on an OptiPrep™ gradient (Sigma-Aldrich) for ultracentrifugation at 170,000 \times g for 20 h. The fraction containing PsVs was recovered and filtered through a Sephadex® G25 column (Cytvia, Marlborough, MA, USA) in DPBS-0.5M NaCl. PsV production was verified by immunoblotting and transmission electron microscopy (TEM). Infectivity was a measure of the number of 293TT fluorescent cells generated by 1 μ L of viral stock after 72 h post infection. Each fluorescent cell was considered an infectious unit (InU). PsVs were stored at 4 °C until use.

4.7. Pseudovirus Infection Inhibition

293TT cells were seeded into 24-well plates (1×10^4 /well) and incubated overnight at 37 °C. Infection mixes were prepared with 5000 InU PsVs and increasing concentrations of nfGNPs (Thermo Fisher Scientific) until a final volume of 80 μ L of DPBS. Infection mixes were maintained on gentle agitation at room temperature for 20 min and then added to 293TT in 500 μ L of DMEM. PsV adsorption was allowed for 20 min before removal of the infection mix followed by addition of 1 mL of pre-warmed DMEM supplemented with 5% FBS. After 72 h, cells were harvested, washed with DPBS and resuspended in 0.5 mL of DPBS for analysis in a FACScalibur flow cytometer (BD Biosciences, San Jose, CA, USA) with a band-pass filter at 530/30 nm (FL1). Excitation was performed with a 488 nm argon laser (1×10^4 cells/read).

4.8. Cellular Viability Assay

293TT cells were treated as described in the Section 4.7. Seventy-two hours post treatment, the cells were harvested and an aliquot of the suspension cell was mixed with an equal volume of 0.4% blue trypan (Bio-Rad Laboratories, Hercules, CA, USA). The number of viable cells was evaluated in a TC10 automated cell counter (Bio-Rad Laboratories).

5. Conclusions

Nanomaterials used to integrate theranostic tools have become an essential part of health care research and development. In the present work, nfGNPs were tested as inhibitors for the infection of HPV16 (the main etiological agent of cervical cancer) in an in vitro PsV model that recapitulates the HPV16 L1 interaction with HS as an essential step for viral entry to the host cell. As with HPV16 VLPs, nfGNP NaCl-induced aggregation was inhibited by an interaction with HPV16 PsV, suggesting that nfGNPs can inhibit the viral entry process. Moreover, the nfGNPs stably interacted, disaggregating PsV–PsV complexes through direct hydrophobic contacts with the surface of the virions. Pseudo-infection experiments showed that the nfGNPs can significantly inhibit the HPV16 entry process in a dose-dependent manner without affecting cell viability and more efficiently than heparin, a classic inhibitor of HPV infection. A similar effect was observed with silver nanoparticles, suggesting a general mechanism for metallic nanoparticles.

Therefore, nfGNPs could be used as a part of topical formulations to prevent HPV infection on genital mucosa, thus providing a novel prophylactic alternative for the fight against cervical cancer.

Author Contributions: Conceptualization, G.P.-V., D.G.V.-R. and L.M.A.-S.; methodology, G.P.-V. and D.G.V.-R.; software, K.P.; validation, A.V., L.Q. and J.M.C.-B.; formal analysis, G.P.-V. and D.G.V.-R.; investigation, G.P.-V. and D.G.V.-R.; resources, L.M.A.-S.; data curation, D.B.; writing—original draft preparation, G.P.-V. and D.G.V.-R.; writing—review and editing, G.P.-V., D.G.V.-R. and L.M.A.-S.; visualization, A.V., L.Q. and J.M.C.-B.; supervision, L.M.A.-S.; project administration, L.M.A.-S.; funding acquisition, L.M.A.-S. All authors have read and agreed to the published version of the manuscript.

Funding: This research was funded by CONACyT grant numbers PEI222162 and A1-S-9160.

Institutional Review Board Statement: Not applicable.

Informed Consent Statement: Not applicable.

Data Availability Statement: Not applicable.

Acknowledgments: We thank the Faculty, the Medical and Dental Surgeon Educational Programs from the Facultad de Ciencias de la Salud, Valle de las Palmas and Campus Tijuana from The Autonomous University of Baja California for providing the lab facilities and academic support.

Conflicts of Interest: The authors declare no conflict of interest.

References

- Walboomers, J.; Jacobs, M.V.; Manos, M.M.; Bosch, F.X.; Kummer, J.A.; Shah, K.V.; Snijders, P.; Peto, J.; Meijer, C.; Munoz, N. Human Papillomavirus Is a Necessary Cause of Invasive Cervical Cancer Worldwide. *J. Pathol.* **1999**, *189*, 12–19. [CrossRef]
- Jit, M.; Prem, K.; Benard, E.; Brisson, M. From Cervical Cancer Elimination to Eradication of Vaccine-Type Human Papillomavirus: Feasibility, Public Health Strategies and Cost-Effectiveness. *Prev. Med.* **2021**, *144*, 106354. [CrossRef] [PubMed]
- Giroglou, T.; Florin, L.; Schafer, F.; Streeck, R.E.; Sapp, M. Human Papillomavirus Infection Requires Cell Surface Heparan Sulfate. *J. Virol.* **2001**, *75*, 1565–1570. [CrossRef] [PubMed]
- Grzelczak, M.; Vermant, J.; Furst, E.M.; Liz-Marzán, L.M. Directed Self-Assembly of Nanoparticles. *ACS Nano* **2010**, *4*, 3591–3605. [CrossRef]
- Ke, P.C.; Lin, S.; Parak, W.J.; Davis, T.P.; Caruso, F. A Decade of the Protein Corona. *ACS Nano* **2017**, *11*, 11773–11776. [CrossRef]
- Palomino-Vizcaino, G.; Valencia-Reséndiz, D.G.; Benítez-Hess, M.L.; Martínez-Acuña, N.; Tapia-Vieyra, J.V.; Bahena, D.; Díaz-Sánchez, M.; García-González, O.P.; Alvarez-Sandoval, B.A.; Alvarez-Salas, L.M. Effect of HPV16 L1 Virus-like Particles on the Aggregation of Non-Functionalized Gold Nanoparticles. *Biosens. Bioelectron.* **2018**, *100*, 176–183. [CrossRef]
- Valencia-Reséndiz, D.G.; Palomino-Vizcaino, G.; Tapia-Vieyra, J.V.; Benítez-Hess, M.L.; Leija-Montoya, A.G.; Alvarez-Salas, L.M. Inhibition of Human Papillomavirus Type 16 Infection Using an RNA Aptamer. *Nucleic Acid Ther.* **2018**, *28*, 97–105. [CrossRef]
- Buck, C.B.; Cheng, N.; Thompson, C.D.; Lowy, D.R.; Steven, A.C.; Schiller, J.T.; Trus, B.L. Arrangement of L2 within the Papillomavirus Capsid. *J. Virol.* **2008**, *82*, 5190–5197. [CrossRef]
- Buck, C.B.; Day, P.M.; Thompson, C.D.; Lubkowski, J.; Lu, W.; Lowy, D.R.; Schiller, J.T. Human Alpha-Defensins Block Papillomavirus Infection. *Proc. Natl. Acad. Sci. USA* **2006**, *103*, 1516–1521. [CrossRef]
- Shi, L.; Sanyal, G.; Ni, A.; Luo, Z.; Doshna, S.; Wang, B.; Graham, T.L.; Wang, N.; Volkin, D.B. Stabilization of Human Papillomavirus Virus-like Particles by Non-Ionic Surfactants. *J. Pharm. Sci.* **2005**, *94*, 1538–1551. [CrossRef]

11. Buck, C.B.; Thompson, C.D.; Roberts, J.N.; Müller, M.; Lowy, D.R.; Schiller, J.T. Carrageenan Is a Potent Inhibitor of Papillomavirus Infection. *PLoS Pathog.* **2006**, *2*, e69. [CrossRef] [PubMed]
12. Maduray, K.; Parboosing, R. Metal Nanoparticles: A Promising Treatment for Viral and Arboviral Infections. *Biol. Trace Elem. Res.* **2020**, *199*, 3159–3176. [CrossRef] [PubMed]
13. Vijayakumar, S.; Ganesan, S. Gold Nanoparticles as an HIV Entry Inhibitor. *Curr. HIV. Res.* **2012**, *10*, 643–646. [CrossRef] [PubMed]
14. Vonnemann, J.; Sieben, C.; Wolff, C.; Ludwig, K.; Böttcher, C.; Herrmann, A.; Haag, R. Virus Inhibition Induced by Polyvalent Nanoparticles of Different Sizes. *Nanoscale* **2014**, *6*, 2353–2358. [CrossRef]
15. Xiang, D.; Zheng, C.; Zheng, Y.; Li, X.; Yin, J.; Conner, M.O.; Marappan, M.; Miao, Y.; Xiang, B.; Duan, W.; et al. Inhibition of A/Human/Hubei/3/2005 (H3N2) Influenza Virus Infection by Silver Nanoparticles in Vitro and in Vivo. *Int. J. Nanomed.* **2013**, *8*, 4103–4112. [CrossRef]
16. Sani, A.; Cao, C.; Cui, D. Toxicity of Gold Nanoparticles (AuNPs): A Review. *Biochem. Biophys. Rep.* **2021**, *26*, 100991. [CrossRef]
17. Anderson, D.J.; Marathe, J.; Pudney, J. The Structure of the Human Vaginal Stratum Corneum and Its Role in Immune Defense. *Am. J. Reprod. Immunol.* **2014**, *71*, 618–623. [CrossRef]
18. Ensign, L.M.; Tang, B.C.; Wang, Y.-Y.; Tse, T.A.; Hoehn, T.; Cone, R.; Hanes, J. Mucus-Penetrating Nanoparticles for Vaginal Drug Delivery Protect Against Herpes Simplex Virus. *Sci. Transl. Med.* **2012**, *4*, 138ra79. [CrossRef]
19. Shwetha, N.; Selvakumar, L.S.; Thakur, M.S. Aptamer–Nanoparticle–Based Chemiluminescence for P53 Protein. *Anal. Biochem.* **2013**, *441*, 73–79. [CrossRef]
20. Turkevich, J.; Stevenson, P.C.; Hillier, J. A Study of the Nucleation and Growth Processes in the Synthesis of Colloidal Gold. *Discuss. Faraday Soc.* **1951**, *11*, 55. [CrossRef]
21. Haiss, W.; Thanh, N.T.K.; Aveyard, J.; Fernig, D.G. Determination of Size and Concentration of Gold Nanoparticles from UV–Vis Spectra. *Anal. Chem.* **2007**, *79*, 4215–4221. [CrossRef] [PubMed]
22. Baker, T.S.; Newcomb, W.W.; Olson, N.H.; Cowser, L.M.; Olson, C.; Brown, J.C. Structures of Bovine and Human Papillomaviruses. Analysis by Cryoelectron Microscopy and Three-Dimensional Image Reconstruction. *Biophys. J.* **1991**, *60*, 1445–1456. [CrossRef]
23. Buck, C.B.; Thompson, C.D. *Production of Papillomavirus-Based Gene Transfer Vectors*; John Wiley & Sons, Inc.: Hoboken, NJ, USA, 2001; Volume 78, ISBN 0471143030.



Article

Modulatory Effects of Biosynthesized Gold Nanoparticles Conjugated with Curcumin and Paclitaxel on Tumorigenesis and Metastatic Pathways—In Vitro and In Vivo Studies

Satish Kumar Vemuri ^{1,2,*}, Satyajit Halder ³, Rajkiran Reddy Banala ¹, Hari Krishnreddy Rachamalla ⁴, Vijaya Madhuri Devraj ¹ , Chandra Shekar Mallarpu ⁵, Uttam Kumar Neerudu ⁶, Ravikiran Bodlapati ⁷ , Sudip Mukherjee ⁸ , Subbaiah Goli Peda Venkata ¹, Gurava Reddy Annapareddy Venkata ¹, Malarvilli Thakkumalai ² and Kuladip Jana ^{3,*}



Citation: Vemuri, S.K.; Halder, S.; Banala, R.R.; Rachamalla, H.K.; Devraj, V.M.; Mallarpu, C.S.; Neerudu, U.K.; Bodlapati, R.; Mukherjee, S.; Venkata, S.G.P.; et al. Modulatory Effects of Biosynthesized Gold Nanoparticles Conjugated with Curcumin and Paclitaxel on Tumorigenesis and Metastatic Pathways—In Vitro and In Vivo Studies. *Int. J. Mol. Sci.* **2022**, *23*, 2150. <https://doi.org/10.3390/ijms23042150>

Academic Editors: Monica Terracciano, Ilaria Rea, Nicola Borbone and Chiara Tramontano

Received: 11 December 2021

Accepted: 7 February 2022

Published: 15 February 2022

Publisher's Note: MDPI stays neutral with regard to jurisdictional claims in published maps and institutional affiliations.



Copyright: © 2022 by the authors. Licensee MDPI, Basel, Switzerland. This article is an open access article distributed under the terms and conditions of the Creative Commons Attribution (CC BY) license (<https://creativecommons.org/licenses/by/4.0/>).

- ¹ Sunshine Medical Academy Research and Technology (SMART), Sunshine Hospitals, PG Road, Secunderabad 500003, Telangana, India; banala.neuroscience@gmail.com (R.R.B.); kbvijayamadhuri@gmail.com (V.M.D.); drgpvsubbaiahgoli@gmail.com (S.G.P.V.); guravareddy@gmail.com (G.R.A.V.)
- ² Department of Biochemistry, Bharathidasan University Constituent College for Women, Tiruchirappalli 620009, Tamil Nadu, India; malarsai96@gmail.com
- ³ Division of Molecular Medicine, Centenary Campus, Bose Institute, P-1/12 C.I.T. Scheme VII-M, Kolkata 700054, West Bengal, India; satyajithalder1.bira@gmail.com
- ⁴ Biomaterials Group, Indian Institute of Chemical Technology (IICT), Tarnaka, Hyderabad 500007, Telangana, India; rahakrireddy@gmail.com
- ⁵ Global Hospital, Lakdi-ka-Pool, Hyderabad 500004, Telangana, India; m.chandrashekar005@gmail.com
- ⁶ Department of Biochemistry, Osmania University, Hyderabad 500007, Telangana, India; jeevanuttam@gmail.com
- ⁷ TBRC, Business Research Private Limited, Hyderabad 500033, Telangana, India; ravikiran.b03@gmail.com
- ⁸ Department of Bioengineering, Rice University, Houston, TX 77030, USA; sudip.mukherjee1988@gmail.com
- * Correspondence: sathishk.vemuri@gmail.com (S.K.V.); kuladip.jana@gmail.com (K.J.); Tel.: +91-807-431-7348 (S.K.V.); +91-900-704-2850 (K.J.)

Abstract: Background: Breast cancer is the most common cancer in women globally, and diagnosing it early and finding potential drug candidates against multi-drug resistant metastatic breast cancers provide the possibilities of better treatment and extending life. Methods: The current study aimed to evaluate the synergistic anti-metastatic activity of Curcumin (Cur) and Paclitaxel (Pacli) individually, the combination of Curcumin–Paclitaxel (CP), and also in conjugation with gold nanoparticles (AuNP–Curcumin (Au–C), AuNP–Paclitaxel (Au–P), and AuNP–Curcumin–Paclitaxel (Au–CP)) in various in vitro and in vivo models. Results: The results from combination treatments of CP and Au–CP demonstrated excellent synergistic cytotoxic effects in triple-negative breast cancer cell lines (MDA MB 231 and 4T1) in in vitro and in vivo mouse models. Detailed mechanistic studies were performed that reveal that the anti-cancer effects were associated with the downregulation of the expression of VEGF, CYCLIN-D1, and STAT-3 genes and upregulation of the apoptotic Caspase-9 gene. The group of mice that received CP combination therapy (with and without gold nanoparticles) showed a significant reduction in the size of tumor when compared to the Pacli alone treatment and control groups. Conclusions: Together, the results suggest that the delivery of gold conjugated Au–CP formulations may help in modulating the outcomes of chemotherapy. The present study is well supported with observations from cell-based assays, molecular and histopathological analyses.

Keywords: Curcumin; Paclitaxel; gold nanoparticles; triple-negative breast cancer cell lines (4T1 and MDA MB 231); metastasis

1. Introduction

According to the published report by the International Agency for Research Cancer (IARC) on the global burden and the incidence of various cancer cases (36 types of cancers)

in the year 2020 using a statistical database (i.e., Globocan 2020), around 19.3 million active cases and 10 million cancer-related deaths were reported in over 185 countries. Among these 19.3 million cases, the incidence of breast cancer cases was higher in comparison to other cancer cases [1].

Triple-negative breast cancers (TNBC) are a type of breast cancer characterized by a lack of cell receptors such as ER (estrogen receptor), PR (progesterone receptor), and human epidermal growth factor receptor 2 (HER2). TNBC is considered a dreadful and highly malignant cancer, due to the high chances of re-emergence and frequency at which it metastasizes in comparison to the other breast cancers. Currently, there are no effective therapies available against TNBC due to the lack of molecular targets in cancer cells, which underscores the need for developing novel therapies for this subtype of breast cancer [2]. The literature suggests the role of a multitude of proteins in tumor growth, cell–cell interaction, and metastasis. E-cadherin (E-cad) is such a protein whose suppression is linked with increased invasiveness and metastasis of tumors. TNBC molecular phenotype presents a higher risk for the loss of E-cad expression in comparison to the tumors of non-TNBC molecular phenotypes [3]. Metastasis is an impenetrable event that involves multiple interrelated biochemical events that makes it less lucid. Metastasis is divided into four essential steps: invasion, adhesion, detachment, and migration of different signaling pathways, and extracellular matrix regulated in cancer metastasis. The metastatic genes are stress-related genes that contribute to wound healing, inflammation, and stress-induced angiogenesis [4]. Yang et al. (2019) [5] demonstrated the crucial role of a signaling molecule known as signal transducer and activator of transcription 3 (STAT3) in evading the immune system, proliferation, and metastasis of TNBC. TNBC continuously expresses the STAT gene for downregulating certain genes for gaining cellular responses by angiogenesis, anti-apoptosis, chemoresistance, immunosuppression, invasion, and migration. TNBC can be characterized by enhanced expression of vascular endothelial growth factor (VEGF) and vasculature [6]. Among the known chemotherapy drugs, Paclitaxel (Taxol) is the most extensively used chemotherapeutic drug for treating various cancers (i.e., breast, lung, ovarian cancer, and solid tumors). Paclitaxel exerts its anti-cancer effects by attaching itself to microtubules and inhibits cell division leading to induced apoptosis in cancer cells. However, the beneficial property of Paclitaxel as a chemotherapy drug has its limitations as it also causes adverse side effects including myelotoxicity and neurotoxicity [7] retinal vein occlusion, deep vein thrombosis, pulmonary embolism, stroke [8], and cataracts in cancer patients. Hence, the search for an alternate anti-cancer drug, which comes with the fewest side effects, is still on. Curcumin is a polyphenol known for its anti-inflammatory, anti-microbial, antioxidant, and anti-cancer properties [9,10]. Curcumin is known to act against many signaling molecules, including growth factors (VEGF-a/b/c/d), transcription factors, kinases, metalloproteases (MMP1/2) cytokines, and other receptors associated with angiogenesis and angiogenesis-dependent metastasis of tumor cells by downregulating respective genes [11]. Therefore, based on the extensive research findings regarding phytochemicals, and their derivatives, this can be a promising option for cancer treatment with lower toxicity and effectiveness [12,13]. After the selection of the phytochemicals, the focus shifts to the delivery systems that are inert and apt in delivering the drugs to the site of cancers. Scientists have researched varied delivery systems such as nanoparticles (silver and gold), liposomes, etc., both in vitro and in vivo for utilizing better therapeutic efficacies against different cancers, metastatic and drug-resistant tumors. Among the nanoparticles, gold nanoparticles (AuNPs) were extensively used as drug delivery systems (DDS) due to their easy synthesis, high surface volume, easy functionalization, and high biocompatibility. Nanoparticles exhibit better efficacy and a censorious role in drug delivery [3,14]. Our earlier publication on the evaluation of biosynthesized gold nanoparticles (i.e., Au-Cur, Au-Tur, Au-Qu, and Au-Pacli) alone and in combination in vitro has generated encouraging results giving us evidence on the synergistic effect of phytochemicals and Paclitaxel in employing significant anti-cancer properties with the regulation of gene expression playing a vital role in disease progression [15,16]. Based on the evidence from our earlier studies,

we developed an *in vivo* breast cancer model (i.e., Balb/c mice) by injecting the 4T1 cell line into the fourth inguinal (lower mammary fat pad) [17–20] of the mice for evaluating the anti-cancer properties of experimental drugs (Curcumin and Paclitaxel) and biosynthesized gold nanoparticles (Au-C, Au-P, and Au-CP) individually and in combination. The current study evaluates the anti-metastatic and synergistic effects of Curcumin and Au-CP in metastatic triple-negative breast cancer cell lines and mouse breast cancer models. Findings from the study exhibited anti-cancer and anti-metastatic properties of b-AuNPs (i.e., Curcumin alone and in combination with Paclitaxel) by controlling the expression of pro-oncogenes (MMPs, STAT, VEGF, Cyclin D) and enhancing the expression of the apoptotic gene (Caspase 9), anti-metastatic gene (E-cadherin), reduction in migration of cells *in vitro*, and reduction in the tumor size (*in vivo*). Based on the findings, it is evident and safe to promote to the phytochemical combinatorial chemotherapy approach in treating the triple-negative breast cancers as could be the future of nanomedicine in the field of cancer treatment.

2. Results

2.1. Characterization of Gold Nanoparticles (AuNPs) and Stability Study

After synthesis of drug conjugated gold nanoparticles, initially, we evaluated physicochemical parameters such as hydrodynamic diameter (HDD), zeta potentials, and polydispersity index (PDI) of Au-C, Au-P, and Au-CP by using dynamic light scattering spectroscopy (DLS) in various media (Mili-Q water and 10% serum containing media has a lot of BSA (bovine serum albumin) proteins, these proteins may bind to the surface of the gold nanoparticles and it may help to increase the surface diameter of the gold nanoparticles [21,22] (Table 1).

Table 1. Characterization of Au-C, Au-P, and Au-CP in water and cell culture media with serum.

Nanoparticles	In Water			In 10% Serum-Containing Medium		
	HDD (nm)	Zeta Potentials (mV)	PDI%	HDD (nm)	Zeta Potentials (mV)	PDI%
Au-C	101.5 ± 15	−0.2 ± 0.1	25.2 ± 2.5	152 ± 8	−6.9 ± 1.5	23.1 ± 1.5
Au-P	115 ± 9	−5.8 ± 2.1	23.9 ± 3.3	140 ± 15	−8.2 ± 2.3	20.2 ± 4.3
Au-CP	128 ± 10	−3.0 ± 1.1	25.5 ± 1.2	166 ± 6	−3.9 ± 1.12	22.41

We observed that these particles were in the nanometer range in water (101–128 nm) (Figure 1a, middle panel and Table 1) and serum-containing medium (Table 1) and negative zeta potentials in both the mediums (Figure 1a, lower panel and Table 1). Transmission electron microscopic images clearly showed that all three formulations were circular and uniformly distributed (Figure 1a, upper panel).

The stability of the particles was analyzed in water for up to 100 days. We observed that there was no significant change in the particle HDD (Figure 1b) indicating high stability of the nanoconjugates that are essential for any biomedical applications.

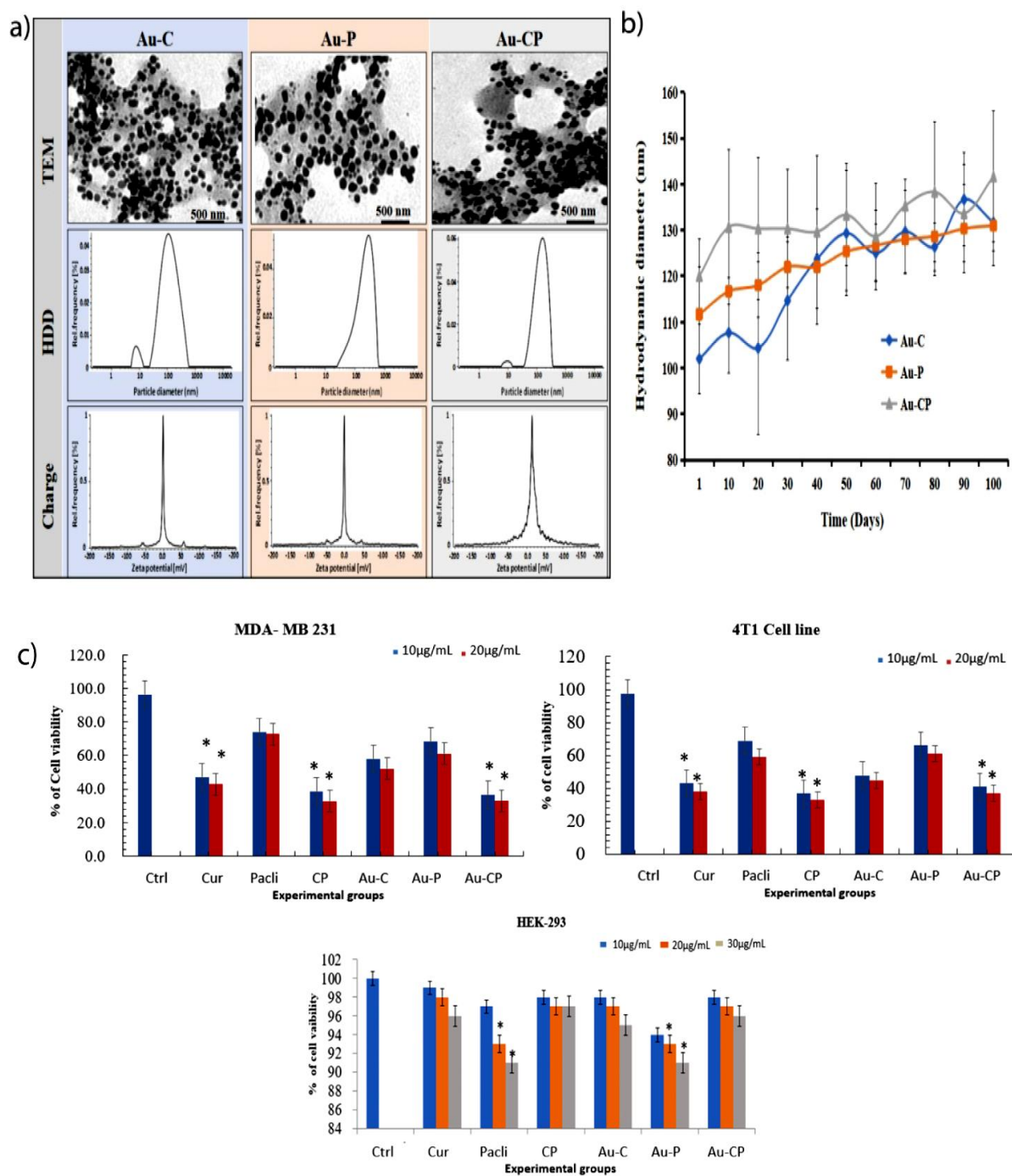


Figure 1. Cytotoxicity and cell viability assessment (MTT assay). (a) Characterization of gold nanoparticles conjugated with Cur, Pacli, and CP. Upper panel: Transmission electron microscopic (TEM) images of Au-C, Au-P, and Au-CP (scale bar 500 nm). Middle panel: Hydrodynamic diameter histograms of Au-C, Au-P, and Au-CP obtained by DLS in water. Lower panel: Zeta potential histograms of Au-C, Au-P, and Au-CP obtained by DLS in water. Each formulation was prepared and characterized thrice, and representative histograms are shown. (b) Stability analysis of Au-C (blue line), Au-P (orange line), and Au-CP (grey line) in deionized water at different time points at room temperature. (c) MTT assay (cytotoxicity and cell viability) was performed in cancer cell lines MDA-MB-231, 4T1 by treating with 10.0 and 20.0 µg/mL individually and in the combination of Au-CP at 5.0 and 10.0 µg/mL for 36 h. Similarly, HEK-293 cells were treated with three concentrations (10, 20, and 30 µg/mL). *p*-value < 0.05, * indicates significance.

2.2. Apoptotic Assay

The observations from the apoptotic assay highlight the treatments with Cur, Pacli, Au-C, Au-P, CP, and Au-CP, individual 10.0 µg/mL and in the combination of AuNPs-CP at 5.0 µg/mL for 36 h. The triple-negative metastatic cancer cell lines (4T1 and MDA MB 231 cell lines undergoing apoptosis) were quantified by the Annexin-V binding assay. The Annexin-V (apoptotic cells) phosphatidylserine (dead cells) showed 4T1 and MDA MB 231 cancer cells enhanced the apoptosis on treatment with the experimental drugs and the percentages of dead cells in the MDA MB 231 cell line are as follows: Cur (34.03% early apoptosis cell and 0.70% late apoptosis cell), Pacli (16.18% early apoptosis cell, 6.92% late apoptosis cell, and 4.96% necroptosis cell population), CP (52.40% early apoptosis cell and 12.67% late apoptosis cell), Au-C (32.57% early apoptosis cell, 18.22% late apoptosis cell, and 2.18% necroptosis cell population), Au-P (10.29% early apoptosis cell, 23.34% late apoptosis cell, and 5.74% necroptosis cell population), and Au-CP (38.36% early apoptosis cell, 35.20% late apoptosis cell, and 1.58 necroptosis cell population). The percentage of dead cells in the 4T1 cell line are as follows: Cur (26.39% early apoptosis cell, 4.67% late apoptosis cell, and 0.76% necroptosis), Pacli (17.87% early apoptosis cell, 6.54% late apoptosis cell, and 1.10% necroptosis cell population), CP (29.48% early apoptosis cell, 20.60% late apoptosis cell, and 6.32% necroptosis cell), Au-C (39.38% early apoptosis cell, 4.77% late apoptosis cell, and 0.58% necroptosis cell population), Au-P (32.36% early apoptosis cell, 2.20% late apoptosis cell, and 1.63% necroptosis cell population), and Au-CP (43.52% early apoptosis cell, 28.76% late apoptosis cell, and 0.09 necroptosis cell population). The results showed significant cytotoxicity in both 4T1 and MDA MB 231 cell lines on treatment with individual agents and also in combination, but the combination treatments demonstrated better apoptotic efficiencies in comparison to the individual treatments (Figure 2a,b) [23–27].

2.3. DCFDA Assay

To determine whether Cur, Pacli, Au-C, Au-P, CP, and Au-CP-mediated apoptotic cell death was due to intracellular reactive oxygen species (ROS) accumulation, we used an H2DCFDA fluorescence assay and ROS generation was measured using fluorescence microscopic analysis. Fluorescence microscopic images of treated MDA MB 231 and 4T1 cells showed enhancement in the level of green color fluorescent intensity (Cur (6.5 and 6.5), Au-C (10 and 10), Pacli (4.5 and 4.5), Au-P (8 and 7), CP (18 and 16), and Au-CP (22 and 18)) as compared to control untreated cells indicating intracellular ROS accumulation. The combination therapies demonstrated significant intracellular ROS accumulation in both 4T1 and MDA MB 231 cell lines in comparison to the individual treatments (Figure 2c,d) [28,29].

2.4. Retardation in MDA-MB 231 Cell Migration

To further investigate whether anti-proliferative changes in Cur, Pacli, Au-C, Au-P, CP, and Au-CP treated cells affected the migratory activity of MDA-MB 231 and 4T1 cells, a bidirectional scratch assay was performed. Decreased cellular migration in the wound areas which were treated with Cur, CP, Au-C, and Au-CP was observed, indicating that they could inhibit the mobility of breast cancer cells. The cells treated with Pacli and Au-P showed the least effect as a result of lesser inhibition of cellular migration in the wound area in comparison to control cells that gradually migrated and filled the wounded area after 24 h of treatment. To confirm our above-mentioned findings, the transwell migration assay was performed using Cur and Pacli (10.0 µg/mL) individually and in the combination of Au-CP at 5.0 µg/mL for 36 h. Consistent with our findings from the scratch assay, data from the transwell migration assay also showed in response to Cur, CP, Au-C, and Au-CP, lower numbers of cells migrating to the undersurface transwell insert in comparison to a significantly high number of migratory cells that migrated to the undersurface transwell insert in Pacli and Au-P-treated and control sets (number of cells migrated in different treatment groups, i.e., control (2500 and 1800), Cur (1250 and 1000), Au-C (600 and 600), Pacli (1600 and 1000), Au-P (800 and 700), CP (300 and 450), and Au-CP (200 and 300)).

Thus, these observations indicate that Curcumin in combination could be a very effective treatment regimen for controlling breast cancers (Figure 3a,b) [30].

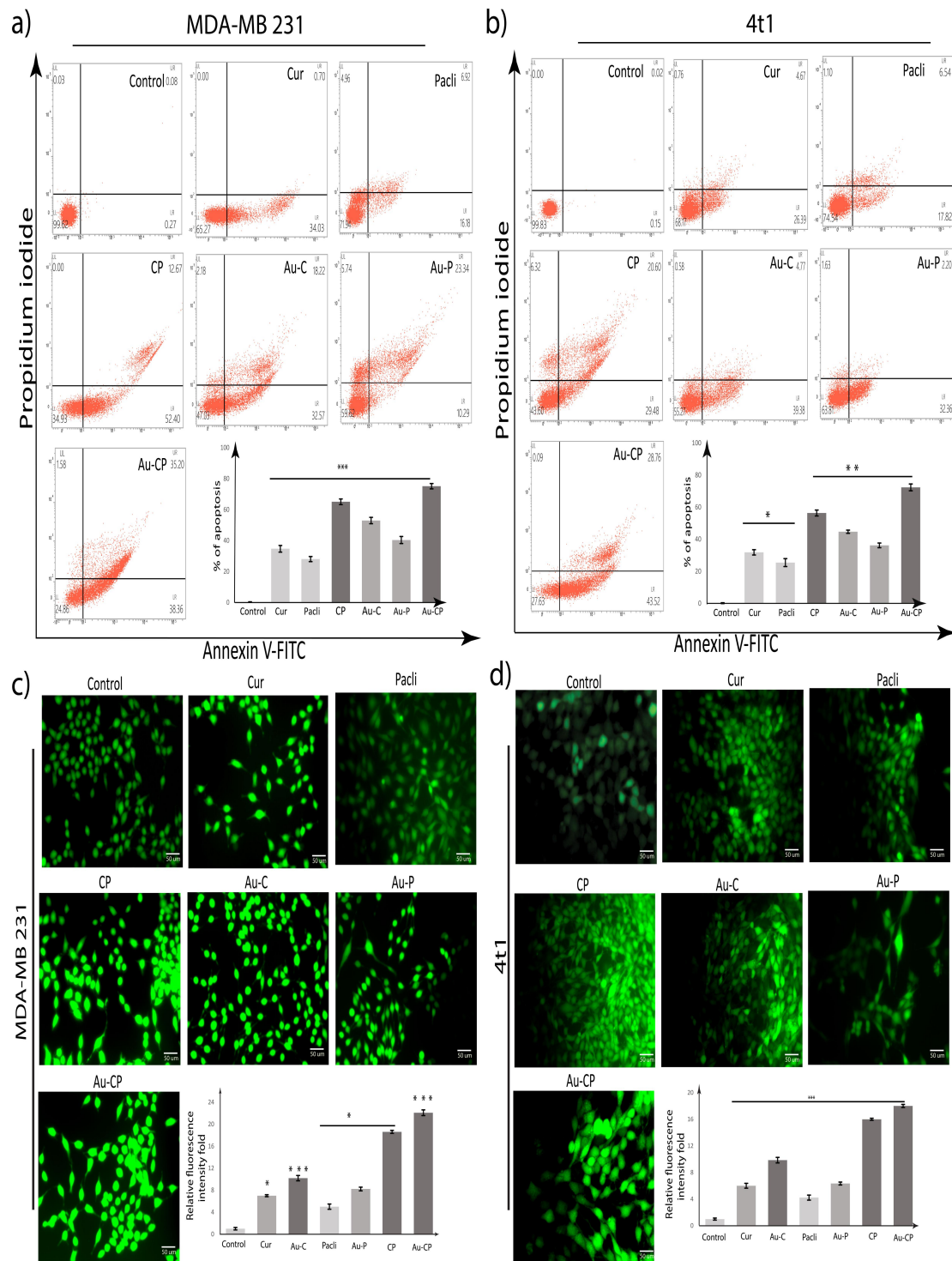


Figure 2. (a,b) Apoptotic assay—percentage of cells undergoing apoptosis in different breast cancer cell lines, (a) MDA MB 231 and (b) 4T1, after treatment with Cur, Pacli 10.0 µg/mL, and in the combination of Au-CP at 5.0 µg/mL for 36 h; Annexin V-PI assay. (c,d) DCFDA assay—fluorescence microscopic images of treated (c) MDA-MB 231 and (d) 4T1 cells showed enhancement in the level of green color fluorescent intensity as compared to control untreated cells indicating intracellular ROS accumulation. *p*-value: <0.05, 0.01, 0.001 indicates * significant, ** very significant, *** highly significant.

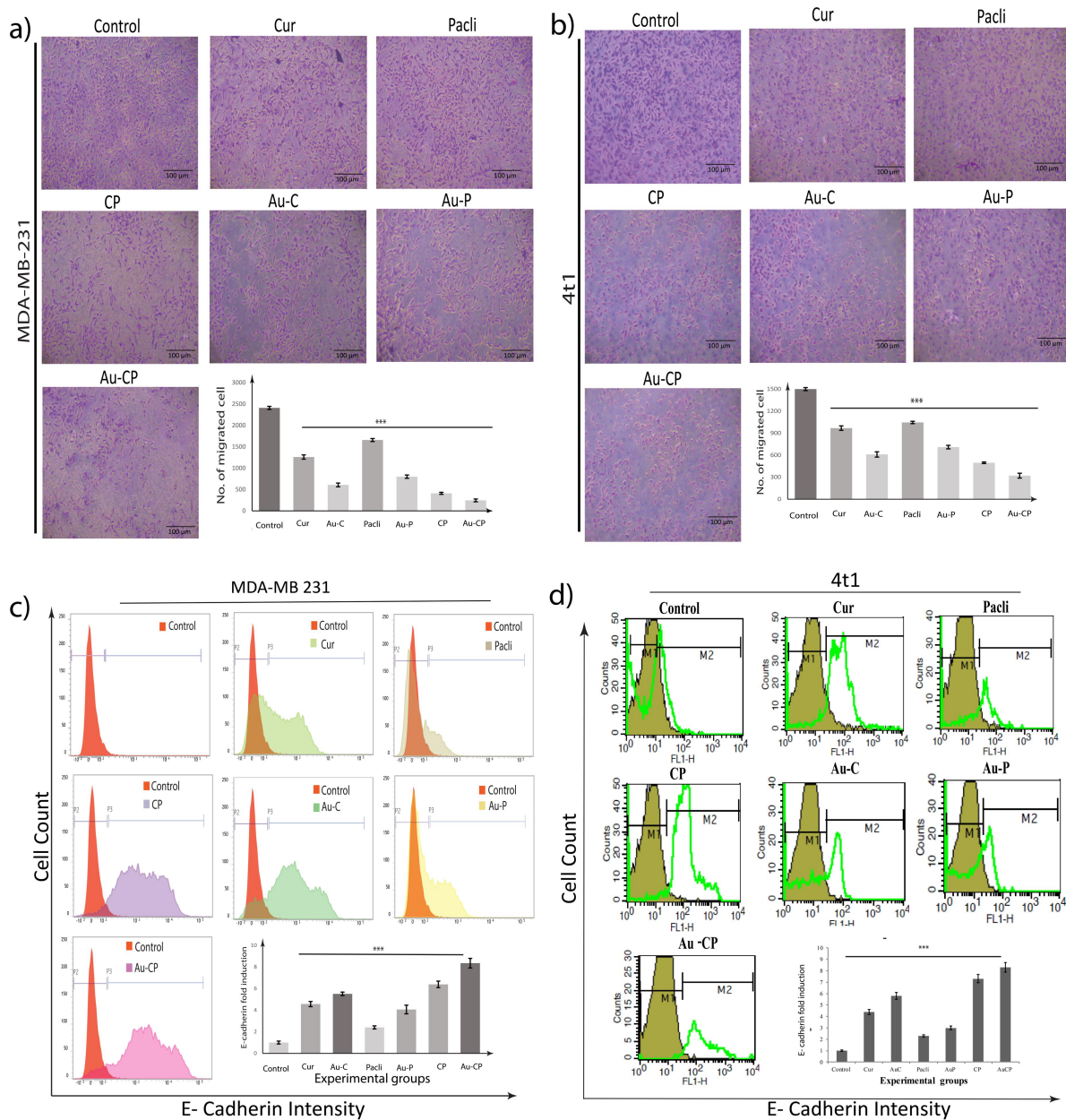


Figure 3. (a,b) Transwell migration assays of (a) MDA-MB 231 and (b) 4T1 were performed to assess the motility of metastatic cancer cells upon treatments with Cur and Pacli individually and both in combination CP in a transwell chamber with the non-coated membrane (24-well insert, pore size: 8 mm, Corning, Life Sciences). (c,d) Flow-cytometric analysis of E-cadherin in (c) MDA-MB 231 and (d) 4T1 metastatic breast cancer cell lines on treatment with Cur, Pacli at 10.0 µg/mL and the combination of AuNPs-CP at 5.0 µg/mL for 36 h. $p < 0.001$ *** signifies highly significant.

2.5. Flow Cytometer Analysis—E-Cadherin Expression in 4T1 and MDA-MB 231 Cell Lines

The below figure illustrates the efficacy of the anti-cancer treatments for controlling metastasis by enhancing the expression of E-cadherin in MDA-MB 231 and 4T1 cancer cells. E-cadherin expression signal was more evident in Cur, Pacli (10.0 µg/mL), and the combination of Au-CP at 5.0 µg/mL for 36 h treatments in comparison to the control group. The expression signals of E-cad in Pacli and Au-P treatment groups (MDA MB 231 and 4T1) were low in comparison to the other treatments groups (i.e., Cur, Au-C, CP, Au-CP) suggesting low efficacy against metastasis (Figure 3c,d) [31,32].

2.6. Scratch Assay

To determine the efficacy of different anti-cancer agents against cancer cell motility *in vitro*, the scratch assay was employed at different time points (0 and 24 h). The wound that was created was considered time zero. MDA-MB-231 cell migration was observed for 24 h and it was observed that the wound area increased in the cells, which were treated with Cur, CP, Au-C, and Au-CP, indicating that they could inhibit the motility of breast cancer cells. The cells treated with Pacli and Au-P showed the least effect as a result as the wound area appeared smaller which was similar to the control group [5,33]. Cur and Pacli at 10.0 µg/mL and the combination of Au-CP at 5.0 µg/mL for 36 h inhibited cell migration in MDA-MB-231 indicating that Curcumin in combination could be a very effective treatment regimen for controlling breast cancers (Figure 4a,b) [34].

2.7. Gene Marker Studies

MDA-MB 231 and 4T1 cell lines were treated with Cur, Pacli, CP, Au-C, Au-P, and Au-CP to assess their effect on the expression of Caspase 9, VEGF, STAT, and Cyclin D gene markers. The expression of different gene markers in the cells were treated individually and in combination with Cur, Pacli, CP. We observed that the combinational treatments significantly downregulated VEGF, CYCLIN D1, and STAT-3 genes and upregulated the Caspase-9 expression in comparison to the individual treatments in both 4T1 and MDAMB 231 cell lines. The individual and combinational treatments gave significant results in the case of the 4T1 cell line when compared to the MDA MB 231 cell line (Figure 4c,d) [30].

2.8. Tumor Induction and Treatment

A reduction in tumor size (primary xenografts) in BALB/c mice was observed. Curcumin decreased tumor size in primary breast cancer xenografts individually and in combination with Paclitaxel. BALB/c mice bearing 4T1 cells as xenografts were intraperitoneally treated with 50 mg/kg Curcumin and Paclitaxel daily for 3 weeks. Tumors in Cur, Pacli, and CP-treated mice were 50% of the size of control animals at the end of drug treatment. Xenografts were introduced into the breast fat pads of Balb/c mice and in a week the tumors were visible. The treatment with the Curcumin and Paclitaxel alone and in combination showed a reduction in tumor size. The mice that received Curcumin and CP combination showed a significant tumor reduction in comparison to the control and Pacli-treated mice. The use of AuNPs increased the therapeutic efficacy in all groups possibly due to the higher availability of drugs at disease sites using enhanced permeability and retention phenomena (Figure 5a) [35–37]. The size of tumors was measured externally in the experimental mice using a Vernier caliper at different time points (days 0, 10, and 21) and it was observed that the tumors regressed with the experimental treatments. The tumors significantly regressed in mice that received Cur, CP, Au-C, Au-CP, indicating the effectiveness of the treatments against breast cancers individually with Cur and Au-C and also in combination CP and Au-CP with the known anti-cancer drug Paclitaxel. The mice that received Paclitaxel showed minimal effects on tumors in comparison to other treatments, but the effect increased significantly when used as a combination with Curcumin, demonstrating the synergistic and beneficial effects in controlling tumor progression and disease (Figure 5b).

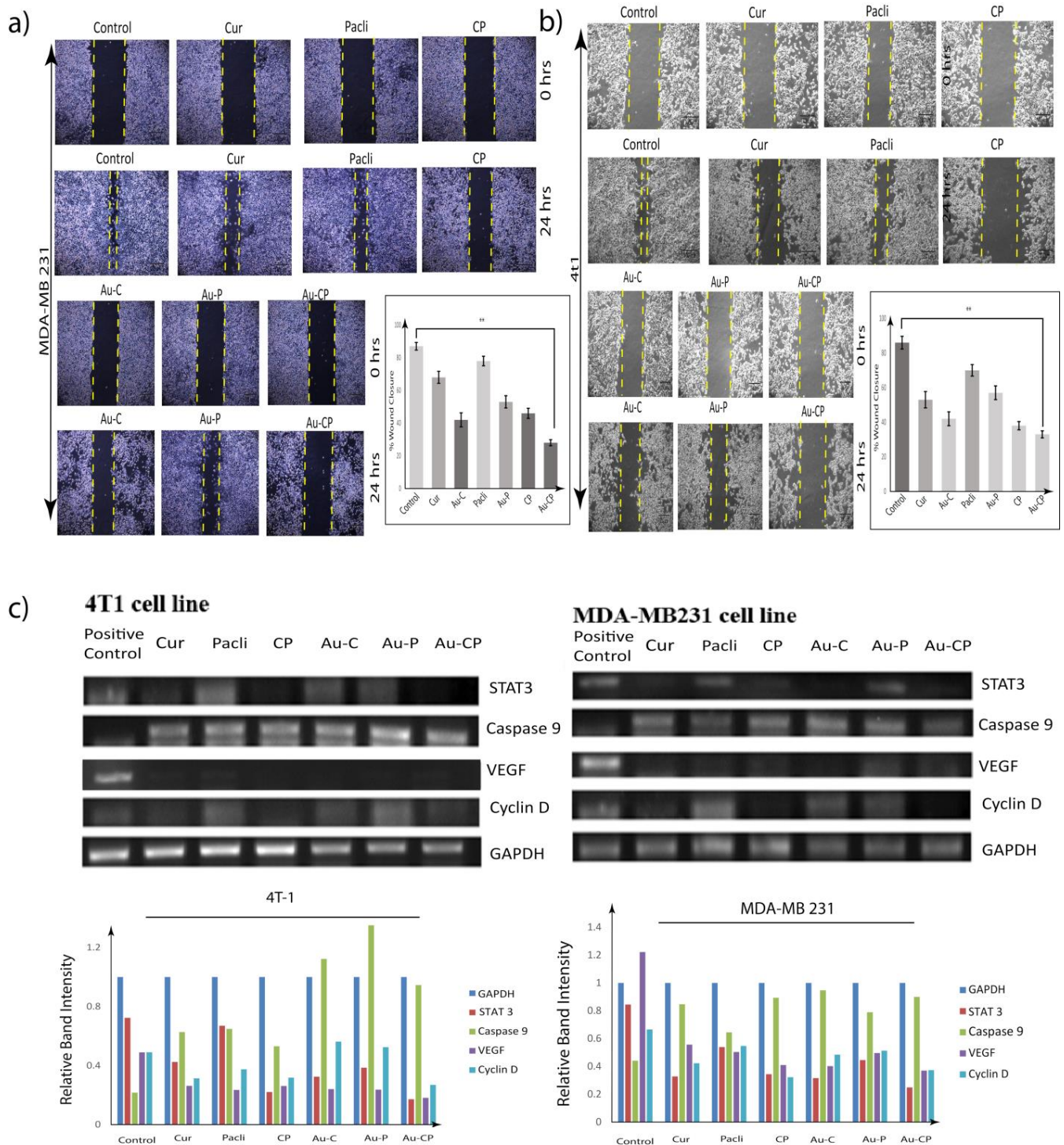


Figure 4. (a,b) Scratch assay—analysis of (a) MDA-MB 231 and (b) 4T1 cell migration by in vitro scratch assay upon treatment with sub-toxic concentrations of Cur and Pacli individually and both in combination CP, as indicated. Images were acquired under a phase-contrast microscope at 0 and 24 h. The dotted lines define the areas lacking cells. Cur, Au-C, CP, and Au-CP inhibited cell migration in MDA-MB-231 whereas Pacli and Au-P did not inhibit the cell migration. (c) The gene marker expression studies were undertaken in both in vitro 4T1 and MDA MB 231 cell lines. The in vitro expression of Caspase 9 was upregulated while STAT3, VEGF, Cyclin D were downregulated when compared with GAPDH in cell lines treated with Cur and Pacli 10.0 µg/mL and in the combination of Au-CP at 5.0 µg/mL for 36 h. *p*-value: < 0.01 ** signifies very significant.

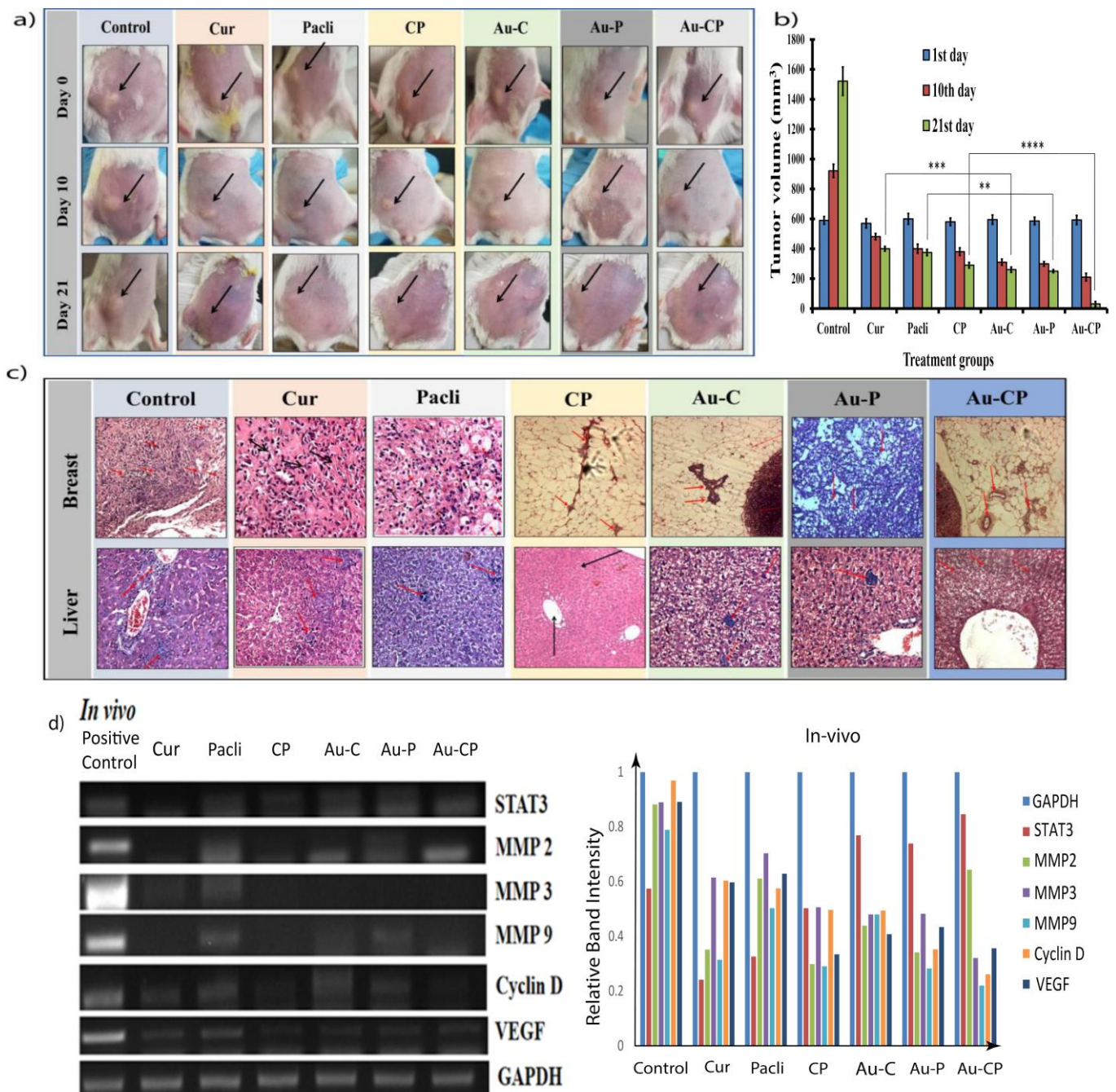


Figure 5. (a) Reduction in tumor size (primary xenografts) in BALB/c mice. BALB/c mice bearing 4T1 cells as xenografts were intraperitoneally treated with 50 mg/kg Cur and Pacli daily, individually and in combination with AuNP for 3 weeks. CP combination decreased tumor size more efficiently when conjugated with AuNP. (b) The size of tumors was measured externally in the experimental mice using a Vernier caliper at different time points (days 1, 10, and 21) and it was observed that the tumors regressed with the experimental treatments. (c) Histopathological evaluation of metastasis in breast fat pad and liver of the Balb/c mice that were treated with 50 mg/kg.bw Cur, Pacli, CP, Au-C, Au-P, and Au-CP. (d) The in vivo expression of STAT3, MMP2/3/9, Cyclin D, and VEGF was downregulated in rat tissues treated with 50 mg/kg Cur and Pacli individually and 25 mg/kg in combinations of CP with and without AuNPs groups [19]. **** *p*-value: <0.0001, *** *p*-value: <0.001, ** *p*-value: ≤0.01.

2.9. Histopathological Studies

Figure 5c demonstrates the histopathological evaluation of the breast and hepatic tissues of experimental mice for the status of metastasis and the potency of experimental drugs for controlling the progression of cancer and metastasis *in vivo*. Metastasis was prominently seen in the positive control, Pacli, and Au-P groups. Mild metastasis was observed in the groups that received Cur and Au-C, but the groups that received a combination of CP and Au-CP showed no signs of metastasis (i.e., neoplasticity in both mammary and hepatic tissues) indicating the effective therapeutic potential of CP and Au-CP [35].

3. Discussion

Over the years, focus has shifted towards phytochemical supplementation in cancer management that has become acceptable and cost-effective, but there is limited evidence that plant-derived constituents could decrease the risk or prognosis of cancer. In the last two decades, varied non-nutritive phytochemicals were isolated individually or as a mixture of agents, and their potency as chemo-preventive agents was evaluated. Despite scientific advancements in understanding of the incidence and progression of cancer, limitations in elucidating the chemo-preventive abilities of most phytochemicals are still encouraging researchers to conduct extensive research in this area of therapy. Anti-tumor activities of most phytoextracts are due to the combination of varied phytochemicals acting synergistically against carcinogenesis rather than an individual agent. It is hypothesized that an individual agent may not exert its anti-tumor properties similarly or may lose its bioactivity when isolated from the whole compound [36,37]. The challenge for researchers is the identification and characterization of compounds, molecular and cell signaling networks for better assessment of phytochemicals and the dosage to be administered to humans in a day.

The combination of Curcumin–Paclitaxel is potent for controlling the cancers by inhibiting the cell proliferation, metastasis, and enhancing the pro-apoptotic markers such as P53 and caspases 3, 7, 8, and 9 [38].

Gold nanoparticles are behaving as a delivery system as they can overcome the biological barriers, sustain the blood flow for a long duration, reach target specific cancer cells in distant areas, and accumulate densely in the tumor sites and release drugs [39].

The present study demonstrated the anti-cancer and anti-metastasis mechanisms of Curcumin, Paclitaxel, gold nanoparticle conjugated Curcumin, and Paclitaxel on metastatic cancers individually and in combination. Our earlier study reported the anti-metastatic properties of nanoparticle conjugated phytochemicals by targeting the STAT3, Cyclin D, and VEGF pathways *in vitro* [40,41]. STAT3 and MMPs hold a key role in proliferation and evasion of the apoptotic pathway in metastatic breast cancers. The authors of [42] reported on the tumor cells undergoing apoptosis, blebbing, necrosis, nuclear fragmentation, and formation of apoptotic bodies upon treatment with pectolinarigenin. Bcl-2 proteins are known as apoptosis regulators as they regulate the caspase-9 and caspase-3 genes in an apoptotic cascade and caspase-2/9 were mostly found in apoptotic pathways [43]. Observations in this study revealed that Cur, Pacli, CP, Au-C, Au-P, and Au-CP inhibited the metastasis of negative breast cancer cells by downregulating STAT3, MMP2/9, and cyclin D-1 and induced apoptosis in both *in vitro* and *in vivo* models and our findings co-relate with the literature [40–43].

TEM analysis was carried out to determine the size of monodispersed spherical nanoparticles of the Au-C and Au-P. The average size of Au-C and Au-P was found to be 5–40 nm (Figure 1a). DLS studies were carried out to calculate the hydrodynamic diameter and zeta potential. DLS results showed that the sizes of the nanoparticles for Au-C and Au-P were 101 and 128 nm; zeta potential was -0.2 ± 0.2 mV for Curcumin and 15.5 ± 0.9 mV for Paclitaxel (Figure 1b). It is important to mention that the size of the b-AuNPs obtained from DLS is greater than the size obtained from TEM [15].

The hydrodynamic diameter of AuNPs is shown to be higher in DLS in comparison to TEM analysis because DLS considers the water surrounding the nanoparticles and also

the coated phytochemicals, but TEM considers only the metallic part of the nanoparticles. We also measured the zeta potential of Au-C and Au-P, which provides the surface charge or surface potential of the nanoparticles. High positive or negative zeta potential data indicates the colloidal stability of nanoparticles. The result showed negative zeta potentials (Au-C: -0.2 ± 0.2 mV and Au-P: $-5.8 \text{ mV} \pm -6.7$ mV) for Au-C and Au-P that supports the colloidal stability of the nanoparticles (Table 1 and Figure 1b).

An MTT assay was performed to demonstrate the cytotoxic properties of Cur, Pacli, CP, Au-C, Au-P, and Au-CP in breast cancer cell lines (i.e., MDA MB 231, 4T1, and HEK 293). Cytotoxicity was successfully induced by phytochemical combination of anticancer drugs at 10–20 $\mu\text{g}/\text{mL}$ Cur, Pacli, and combinations of CP and Au-CP (5.0–10 $\mu\text{g}/\text{mL}$) concentrations in breast cancer cell lines. It was observed that combination treatments exerted better cytotoxicity in both MDA-MB 231 and 4T1 cell lines when a comparison was made between these individual and combination treatments in cell lines. Similarly, when these treatments were examined on the normal cell line (HEK-293) they did not exert any cytotoxic effects. Hence, we conclude that Cur, CP, Au-C, and Au-CP (10–30 $\mu\text{g}/\text{mL}$) selectively target the cancer cells. Our results are in agreement with earlier findings (Figure 1c).

Gene marker studies (qPCR) revealed the anti-metastatic and apoptotic properties Cur, Au-C, CP, Au-CP in both triple-negative cell lines (4T1 and MDA MB 231) by under-expressing the VEGF, Cyclin D, and STAT3 genes and enhancing caspase 9 gene expression. However, Pacli and Au-P treatments showed minimal effects on the expression profile of metastatic genes when compared to other treatment groups and their expression profile was similar to that of controls. Based on the results, it is convenient to say that Curcumin alone and in combination effectively controlled the metastatic process in comparison to the Paclitaxel treatment alone. Similar findings were observed in our *in vivo* studies (qPCR) which supported our *in vitro* findings. Based on the results, it is convenient to say that Curcumin alone and in combination effectively controlled the metastatic process in comparison to the Paclitaxel treatment alone. Our data is in agreement with existing literature [44].

Similar studies were reported, illustrating the role of nanoparticles in the treatment of various cancers by inducing increased apoptosis signals and activation of ER stress and Ca^{2+} signaling pathways. Varlamova et al. (2021) and Turovsky and Varlamova (2021) reported on cytotoxicity effects of Selenium nanoparticles (SeNPs) in cancer cells (A-172 and MCF-7) by activating the mitochondrial apoptosis pathway and by overexpression of pro-apoptotic gene markers such as BCL-2 and caspase 3 and by releasing cytochrome-C into the cytoplasm of cells by increasing the permeability of the mitochondrial membrane, when treated with 5 $\mu\text{g}/\text{mL}$ SeNP. As a consequence of SeNP treatment, higher expression of the caspase 4 gene in A-172 cells indicates modulation of the intrinsic ER-mediated pathway of apoptosis and Ca^{2+} signaling pathways [45,46].

Flow cytometric analysis of E-cadherin and apoptosis in MDA-MB-231 and 4T1 metastatic breast cancer cell line was undertaken after treatment with Cur, Pacli, CP, Au-C, Au-P, and Au-CP, and it was observed that combination treatments were exerting better cell apoptosis and inhibiting the metastatic E-cadherin pathway in both breast cancer cell lines in comparison with either substance alone in cancer cell lines. Therefore, breast cancer treatment may benefit from the use of a combination of drugs in chemotherapy (Figure 3c,d).

Observations from the *in vitro* study suggest the synergistic efficacy of Curcumin in combination with Paclitaxel for controlling the TNBC cells from metastasizing. Hence, the combination therapy could be a potential treatment regimen for controlling metastatic breast cancers (Figure 4c). Numerous *in vitro* and *in vivo* studies reported on the combination of Paclitaxel with phytochemicals and nanoparticles exhibiting synergistic anticancer effects in the treatment of breast cancer [47–49]. The physical and topical examination of induced tumor in the breast tissue revealed significant progression of disease and size of the tumor in the positive control, Pacli and Au-P groups, whereas reduced tumor size was observed

in groups that received individual treatments with Cur and Au-C, but the groups that received combinational treatments (CP, Au-CP) demonstrated the efficacy of combinational therapy against the induced tumor progression and metastasizing tumor cells (Figure 5a,b).

The status of metastasis in the breast and hepatic tissues of experimental mice was assessed. The neoplastic cells (Grade 3) with variation in size, shape, and multiple mitotic figures were also observed in the brain and liver of positive control and Paclitaxel-treated groups (Pacli and Au-P) indicated by arrows [50–58]. The mice that received Cur and Au-C showed the fewest neoplastic cells in mammary glands, whereas the observation in liver tissue revealed the presence of multiple nodular tumor mass with poorly differentiated neoplastic cells which were indicated by arrows. Whereas, the mice treated with CP and Au-CP showed normal cell morphology in the subcutaneous region in the mammary gland and normal portal triad with the portal vein and bile duct in the liver tissues (indicated by an arrow) (Figure 5c).

Our earlier studies demonstrated the apoptotic, anti-angiogenesis, anti-proliferative, anti-colony formation, and anti-spheroid formation properties of biosynthesized gold nanoparticles (i.e., Au-Cur, Au-Tur, Au-Qu, and Au-Pacli) when treated alone and in combination with Paclitaxel *in vitro* and provided evidence of the synergistic effects of phytochemicals and Paclitaxel in exerting significant anti-cancer effects by controlling the expression of various genes playing roles in disease progression [15]. The presence of Curcumin (non-conjugated and conjugated with gold nanoparticles) will enhance the anti-cancer properties of Paclitaxel even in the drug resistant and TNBC by activating different apoptotic pathways and reducing the expression of different metastatic genes. The biosynthesis of gold nanoparticles is an easy and economical process in reducing aurum chloride by using phytochemicals in the presence of heat. Developing an *in vivo* model for evaluating the potential therapeutic agents is very crucial for understanding the anti-metastatic mechanism in real-time. Therefore, it is speculated that the combination of Paclitaxel and Curcumin with gold nanoparticles may be an ideal strategy in clinical practice for cancer treatment. The advantages include lower cost, faster, and minimum ethical concerns.

4. Materials and Methods

4.1. Chemicals and Reagents

Chemicals and reagents were obtained from Merck (Mumbai, India), Himedia Mumbai, India), Invitrogen (Bengaluru, India), SRL (Hyderabad, India), DCFDA (#D6883) was purchased from Sigma-Aldrich (Bengaluru, India). Fetal bovine serum (#16000044) was obtained from Gibco, Cleveland, TN, USA, and MEM sodium pyruvate, MEM non-essential amino acids L-glutamine and Gentamicin, were procured from Hi-Media, India.

4.2. Preparation of Stock Solutions

A stock solution of 10^{-2} M was prepared by dissolving 1 gm of $\text{HAuCl}_{4.3}\text{H}_2\text{O}$ in 253.92 mL of autoclaved Milli-Q water (Millipore). We further prepared stocks of 10 mg/mL of Curcumin in 1 mL of DMSO. Moreover, we prepared a stock of Paclitaxel at a concentration of 10 mg/mL.

4.3. Synthesis of Gold Nanoparticles Using Phytochemicals (Curcumin and Paclitaxel)

HAuCl_4 (200 μL , 10^{-2} M) solution was added to a 4.8 mL water fraction of Curcumin and Paclitaxel (10 $\mu\text{g}/\text{mL}$). The total volume of the reaction mixture was adjusted to 5 mL in all experiments. The resulting Au-C and Au-P were purified by ultracentrifugation at 15,000 rpm ($25,000\times g$) for 40 min at 15 °C (Sorvall WX ultra-100, Thermo scientific, Bengaluru, India) [15,18].

Physicochemical Characterization of Curcumin and Paclitaxel Conjugated Gold Nanoparticles

Hydrodynamic diameter (HDD), zeta potentials, and poly-dispersity index (PDI) of Au-C, Au-P, and Au-CP were analyzed by photon correlation spectroscopy using a Lite Sizer TM 500 Particle Analyzer, manufactured by Anton Paar. The HDD, charges, and PDI of the particles were analyzed in deionized water and a 10% serum-containing medium. The stability of the particles was measured in deionized water up to 100 days DLS. The size and morphology of the particles were examined using transmission electron microscopy (TEM), Tecnai G2 F30 S-Twin Microscope, operated at 100 kV. Selected area electron diffraction patterns were also recorded using this instrument. Inductively, each experiment was carried out in triplicate in three different batches [15,18].

4.4. Cell Culture

The 4T1 cell line, mouse epithelial triple-negative breast metastatic cell line and MDA-MB 231 cell line, a human epithelial breast cancer cell line (4T1 cells and MDA-MB 231) were aseptically cultured in multi-well cell culture plates using Dulbecco's Modified Eagle's Medium, (DMEM High Glucose) supplemented with 10% fetal bovine serum, 50 units/mL penicillin, and 50 µg/mL streptomycin. Then, 24 h after seeding, these cell lines were treated with 10.0 µg/mL of Cur, Pacli, Au-C, and Au-P (optimized dose) when treated alone, and 5.0 µg/mL of CP and Au-CP as combination therapy. The 4T1 and MDA-MB 231 cell lines were processed for various tests at indicated post-treatment periods (36 h for cell apoptosis; 36 h for quantitative PCR) [15,19].

4.5. Cell Viability Assay/MTT Assay

4T1, MDA-MB 231, and HEK293 cell lines were plated in 96-well plates for cell viability assay. The cell lines were treated with vehicle control or different doses of Cur, Pacli, Au-C, and Au-P (10 and 20 µg/mL), and with combinations of CP and Au-CP (5 and 10 µg/mL) for 36 h. A dose of 5 µg/mL was selected for combination therapy which is precisely half of the dose of the pristine nanoconjugates. The reason behind this selection is to avoid unwanted cytotoxicity in normal cells as in the combination of b-AuNPs it is much more cytotoxic than its pristine form. After 36 h, cell viability was analyzed using the MTT assay using a published protocol and absorbance was recorded at 475 nm concerning 660 nm [20].

4.6. Annexin V-FITC/PI Staining for Apoptosis Assay

Induction of apoptosis was quantified via flow cytometric analysis of control and Cur, Pacli, CP, Au-C, Au-P, and Au-CP-treated cells that were stained with Annexin V-FITC/PI using the Annexin V-FITC apoptosis detection kit according to the manufacturer's protocol (BD Bioscience, San Jose, CA, USA). Briefly, 4T1 and MDA-MB-231 cells treated with compounds for 36 h were subjected to Annexin-V assay to quantify the number of apoptotic cells by flow cytometry. Cells were further trypsinized, washed once in PBS, and the pellets were collected after centrifugation and resuspended in binding buffer and to this 5 µL fluorescein isothiocyanate (FITC)-labeled Annexin-V and 10 µL propidium iodide (PI) were added. The resulting mixtures were incubated in the dark for 10 min at room temperature and the fluorescence of the cells was determined immediately using BD FACS Verse flow cytometer (BD Biosciences, San Jose, CA, USA). Annexin V/FITC positive cells were regarded as apoptotic cells analyzed using Cell Quest Software (BD Biosciences) [19].

4.7. Measurement of Cellular ROS Using DCFDA

To estimate the intracellular reactive oxygen species (ROS) production due to Cur, Pacli, CP, Au-C, Au-P, and Au-CP treatment, the DCFDA method was used (2, 7-Dichlorodihydrofluorescein diacetate). Briefly, MDA-MB 231 and 4T1 cells were seeded in a 6-well plate and treated with test compounds (10 mg/mL) for different periods. Post-treatment, the media was discarded and incubated with 10 µM H₂DCFDA for 30 min at 37 °C. For fluorescent imag-

ing, H2DCFDA incubated cells were washed, resuspended in 1x PBS, and directly imaged under a fluorescent microscope (Leica) [18,19].

4.8. Transwell Migration Assay

To assess cell migration and invasion capacities of Cur, Pacli, CP, Au-C, Au-P, and Au-CP-treated MDA-MB 231 and 4T1 cells, a transwell assay was undertaken using cell culture inserts with a pore size of 8 μm . Briefly, cell culture inserts were placed in 12-well companion plates containing 300 μL of serum-free DMEM media and MDA-MB 231 and 4T1 cells at a density of 2×10^5 cells were seeded in the upper half of the insert. Then, 700 μL DMEM media containing 10% FBS were then added into the lower chamber and treated with a respective concentration of compounds for 24 h. Post-treatment, the inserts were removed and the cells on the upper surface of the membrane were wiped off with cotton swabs. Then, the cells that had invaded into the micro-porous membrane were washed three times with 1X PBS, fixed with 3.7% formaldehyde, and were permeabilized using methanol. At last, cells were stained with Giemsa stain for 30 min, and the cells were observed with a microscope, and images were obtained. Cells present in the lower part of the inserts were counted in three microscopic fields per well, and the extent of migration was expressed as an average number of cells per microscopic field [19].

4.9. E-Cadherin Expression by Flow Cytometry

MDA-MB 231 and 4T1 cell lines were harvested after trypsinization then washed with 1X PBS and stained with primary antibody for E-cadherin, incubated for 30 min on ice at room temperature. After incubation, cells were then washed three times. E-cadherin and the control samples were then incubated with anti-rabbit-FITC IgG antibodies for 30 min under the same conditions. Cells were washed again, and flow cytometric analysis was performed [20].

4.10. Scratch Assay

A bidirectional scratch assay was used to determine the migration of breast cancer cells MDA-MB 231 and 4T1 under different conditions. Firstly, 4T1 and MDA-MB 231 cells were cultured in 6-well plates for 24 h to achieve 100% confluence followed by starvation in serum-free DMEM. After which, a scratch was done using a 200 μL sterile pipette tip to form a bidirectional wound. Cells were then treated with Cur, Pacli, CP, Au-C, Au-P, and Au-CP for different time periods (0 and 24 h). The migration width at each time point in each treatment group was measured at four different positions when microscopic images of the cells were captured and compared with the gap width at 0 h [19].

4.11. Quantitative RT-PCR

Total RNA was extracted with an RNASure mini-isolation kit Nucleo-pore, Genetix, and RNA (1 μg) was converted to cDNA using a Thermo fisher cDNA synthesis kit. The analysis of gene expression was performed using gene-specific primers (Table 1). The qRT-PCR steps were as follows: (1) denaturation at 95 $^{\circ}\text{C}$ for 3 min, (2) 30 cycles at 95 $^{\circ}\text{C}$ for 1 min, (3) 57 $^{\circ}\text{C}$ for 30 s (depending on primer sets), (4) 72 $^{\circ}\text{C}$ for 1 min, and (5) extension at 72 $^{\circ}\text{C}$ for 7 min. The melting curve examination verified a single product. Relative expression quantities were evaluated and normalized by comparing them to action [19,20].

4.12. Tumor Induction in Mice

Our study adopted the methodology and therapeutic strategies of [19] in developing the induced breast tumor model for safety and efficacy studies of our treatments. For the present study we used 8–10 weeks old female BALB/c mice, weighing about 25–32 g, for developing the tumor model. For developing the model, we sedated the mice by administering ketamine and xylazine (as per animal weight and accepted norms). Once the animals were completely in sedation, we identified the mammary gland (i.e., 3rd and 4th glands in abdomen area) and injected a low count of 4T1 breast cancer cells (1×10^4 cells)

into the BALB/c mouse mammary fat pad using a tuberculin syringe. Weekly assessments of weight and tumor size measurements, food and water intake were completed.

4.13. Statistical Analysis

The results were expressed as mean \pm SEM. One-way ANOVA was followed by Tukey's comparison test. The level of significance was set at **** (p -value: <0.0001) *** (p -value: <0.001); ** (p -value: ≤ 0.01); * (p -value: 0.05) in respect to the control. GraphPad Prim 5.0 software was used to statistically analyze the data.

5. Conclusions

The current study demonstrated the inhibitory role of various individual and combination treatments on different triple-negative metastatic breast cancers (in vitro and in vivo). The treatments controlled or reduced the progression, proliferation, and metastasis of cancer cell lines. Better efficacy was observed when drugs were delivered using gold nanoparticles that acted as a delivery vehicle and helped to provide targeted therapy. The present study was a comparative study between the individual and combination treatments to evaluate the synergistic activity of Curcumin and Paclitaxel for controlling the metastasis and disease progression. This study also provided rationale for considering the use of Curcumin, gold conjugated–Curcumin individually or in combination with Paclitaxel as an alternative therapeutic strategy to the existing chemotherapy regimens. The combination of Curcumin–Paclitaxel might help by ameliorating the side effects caused by Paclitaxel such as oxidative stress and induced cytotoxicity in cardiomyocytes. Further studies are still required before taking it into the clinics.

Author Contributions: Conceptualization, S.K.V. and R.R.B.; data curation, S.K.V., S.H., R.R.B., H.K.R., V.M.D., C.S.M. and U.K.N.; formal analysis, S.K.V., S.H. and K.J.; funding acquisition, S.M., S.G.P.V. and G.R.A.V.; investigation, S.K.V., R.R.B., S.M., M.T. and K.J.; methodology, S.K.V., S.H., R.R.B., H.K.R., V.M.D. and K.J.; project administration, S.K.V., R.R.B. and M.T.; resources, U.K.N., S.G.P.V., G.R.A.V. and K.J.; supervision, S.M., S.G.P.V., G.R.A.V., M.T. and K.J.; validation, S.K.V., S.M. and K.J.; visualization, S.K.V., S.H., R.R.B., H.K.R., V.M.D., C.S.M., U.K.N., R.B., S.M. and K.J.; writing—original draft, writing—review and editing, S.K.V., S.H., R.R.B., H.K.R., V.M.D., C.S.M., U.K.N., R.B. and K.J. All authors have read and agreed to the published version of the manuscript.

Funding: This research received no external funding.

Institutional Review Board Statement: The animal study was conducted according to the guidelines of the Declaration of Helsinki and approved by the Institutional Review Board (or Ethics Committee) of Institutional Animal Ethics committee (IAEC) at Sunshine Hospitals (Protocol No. CPCSEA/IAEC/JLS/011/11/19/002, 11 November 2019).

Informed Consent Statement: Not applicable.

Data Availability Statement: Data are contained within the article.

Acknowledgments: We sincerely thank Adarsh and Kushal Sunshine Hospitals for their timely help and support during the study.

Conflicts of Interest: The authors declare no conflict of interest. The funders had no role in the design of the study; in the collection, analyses, or interpretation of data; in the writing of the manuscript, or in the decision to publish the results.

References

1. CYTECARE. Statistics of Breast Cancer in India. Available online: <https://cytecare.com/blog/statistics-of-breast-cancer/> (accessed on 10 October 2020).
2. Nam, J.; Son, S.; Park, K.S.; Zou, W.; Shea, L.D.; Moon, J.J. Cancer nanomedicine for combination cancer immunotherapy. *Nat. Rev. Mater.* **2019**, *4*, 398–414. [CrossRef]
3. Tungsukruthai, S.; Petpiroon, N.; Chanvorachote, P. Molecular mechanisms of breast cancer metastasis and potential anti-metastatic compounds. *Anticancer Res.* **2018**, *38*, 2607–2618.

4. Wang, C.; Li, J.; Ye, S.; Zhang, Y.; Li, P.; Wang, L.; Wang, T.H. Oestrogen inhibits VEGF expression and angiogenesis in triple-negative breast cancer by activating GPER-1. *J. Cancer* **2018**, *9*, 3802–3811. [CrossRef]
5. Yang, L.; Lin, S.; Xu, L.; Lin, J.; Zhao, C.; Huang, X. Novel activators and small-molecule inhibitors of STAT3 in cancer. *Cytokine Growth Factor Rev.* **2019**, *49*, 10–22. [CrossRef]
6. Qin, J.J.; Yan, L.; Zhang, J.; Zhang, W.D. STAT3 as a potential therapeutic target in triple negative breast cancer: A systematic review. *J. Exp. Clin. Cancer Res.* **2019**, *38*, 195. [CrossRef]
7. Scripture, C.D.; Figg, W.D.; Sparreboom, A. Peripheral Neuropathy Induced by Paclitaxel: Recent Insights and Future Perspectives. *Curr. Neuropharmacol.* **2006**, *4*, 165–172. [CrossRef]
8. Athigakunagorn, K.S.; Nantavithya, C.; Shotelesak, K. A Case Report of Cerebral Venous Thrombosis after Taking Tamoxifen in Breast Cancer Patient Case Report. *J. Clin. Case Rep.* **2018**, *6*, 1–34. [CrossRef]
9. Avtanski, D.B.; Poretsky, L. Phyto-polyphenols as potential inhibitors of breast cancer metastasis. *Mol. Med.* **2018**, *24*, 24–29. [CrossRef]
10. Zhou, Q.; Wang, X.; Liu, X.; Zhang, H.; Lu, Y.; Su, S. Curcumin enhanced antiproliferative effect of mitomycin C in human breast cancer MCF-7 cells in vitro and in vivo. *Acta Pharmacol. Sin.* **2011**, *32*, 1402–1410. [CrossRef]
11. Landen, N.X.; Li, D.; Stahle, M. Transition from inflammation to proliferation: A critical step during wound healing. *Cell. Mol. Life Sci.* **2016**, *73*, 3861–3885. [CrossRef]
12. Kanai, M.; Otsuka, Y.; Otsuka, K.; Sato, M.; Nishimura, T.; Mori, Y.; Kawaguchi, M.; Hatano, E.; Kodama, Y.; Matsumoto, S.; et al. A phase I study investigating the safety and pharmacokinetics of highly bioavailable curcumin (Theracurmin) in cancer patients. *Cancer Chemother. Pharmacol.* **2013**, *71*, 1521–1530. [CrossRef]
13. Storka, A.; Vcelar, B.; Klikovic, U.; Gouya, G.; Weisshaar, S.; Aschauer, S.; Bolger, G.; Helson, L.; Wolzt, M. Safety, tolerability and pharmacokinetics of liposomal curcumin in healthy humans. *Int. J. Clin. Pharmacol. Ther.* **2015**, *53*, 54–65. [CrossRef] [PubMed]
14. Dykman, L.A.; Khlebtsov, N.G. Immunological properties of gold nanoparticles. *Chem. Sci.* **2017**, *8*, 1719. [CrossRef] [PubMed]
15. Vemuri, S.K.; Banala, R.R.; Sudip, M.; Uppula, P.; Subbaiah, G.P.V.; Reddy, A.V.G.; Mallarvili, T. Novel biosynthesized gold nanoparticles as anti-cancer agents against breast cancer: Synthesis, biological evaluation, molecular modelling studies. *Mater. Sci. Eng. C* **2019**, *99*, 417–429. [CrossRef] [PubMed]
16. Deng, Z.; Rong, Y.; Teng, Y.; Mu, J.; Zhuang, X.; Tseng, M.; Samykutty, A.; Zhang, L.; Yan, J.; Miller, D.; et al. Broccoli-Derived Nanoparticle Inhibits Mouse Colitis by Activating Dendritic Cell AMP-Activated Protein Kinase. *Mol. Ther.* **2017**, *25*, 1641–1654. [CrossRef]
17. Nigjeh, S.E.; Yeap, S.K.; Nordin, N.; Rahman, H.; Rosli, R. In Vivo Anti-Tumor Effects of Citral on 4T1 Breast Cancer Cells via Induction of Apoptosis and Downregulation of Aldehyde Dehydrogenase Activity. *Molecules* **2019**, *24*, 3241. [CrossRef]
18. Balakrishnan, S.; Mukherjee, S.; Das, S.; Bhat, F.; Rajasingh, A.P.; Patra, C.R. Gold nanoparticles–conjugated quercetin induces apoptosis via inhibition of EGFR/PI3K/Akt–mediated pathway in breast cancer cell lines (MCF-7 and MDA-MB 231). *Cell Biochem. Funct.* **2017**, *35*, 217–231. [CrossRef]
19. Laha, D.; Pal, K.C.; Pravat, K.P.; Sumanta, K.S.; Kuladip, J.; Parimal, K. Fabrication of curcumin loaded folic acid tagged metal organic framework for triple negative breast cancer therapy in in vitro and in vivo system. *New. J. Chem.* **2019**, *43*, 217–229. [CrossRef]
20. Vemuri, S.K.; Banala, R.R.; Subbaiah, G.P.V.; Srivastava, S.K.; Reddy, A.V.G.; Malarvili, T. The Anti-Cancer Activities of Natural Extract (NE) mix in Human Breast Cancer Cell Lines Are Mediated through Caspase-Dependent and p53-Independent Pathways. *Egypt. J. Basic Appl. Sci.* **2017**, *4*, 332–344. [CrossRef]
21. Marina, A.D.; Anil, K.P.; Jiwen, Z.; Jeffrey, D.C.; Nader, A.; Parag, A.; Barry, W.N.B.S.; McNeil, S.E. Interaction of colloidal gold nanoparticles with human blood: Effects on particle size and analysis of plasma protein binding profiles. *Nanomed. Nanotechnol. Biol. Med.* **2009**, *5*, 106–107.
22. Gunnarsson, S.B.; Bernfur, K.; Englund-Johansson, U.; Johansson, F.; Cedervall, T. Analysis of complexes formed by small gold nanoparticles in low concentration in cell culture media. *PLoS ONE* **2019**, *14*, e021821. [CrossRef] [PubMed]
23. Shakibaei, M.; Buhrmann, C.; Kraehe, P.; Shayan, P.; Lueders, C.; Goel, A. Curcumin chemosensitizes 5-fluorouracil resistant MMR-deficient human colon cancer cells in high density cultures. *PLoS ONE* **2014**, *9*, e85397. [CrossRef] [PubMed]
24. Banerjee, S.; Singh, S.K.; Chowdhury, I.; Lillard, J.W., Jr.; Singh, R. Combinatorial effect of curcumin with docetaxel modulates apoptotic and cell survival molecules in prostate cancer. *Front. Biosci.* **2017**, *9*, 235–245.
25. Lina, A.A.-A.; Farkaad, A.K.; Najihah, M.H.; Nurhidayatullaili, M.; Julkapli, A.S.; Jun, L.; Mohammed, A.A.; Wageeh, A.Y. The impact of curcumin-graphene based nanoformulation on cellular interaction and redox-activated apoptosis: An in vitro colon cancer study. *Heliyon* **2020**, *6*, e05360. [CrossRef]
26. Karimi, F.; Shaabani, E.; Martínez-Rovira, I.; Yousef, I.; Ghahremani, M.H.; Kharrazi, S. Infrared microspectroscopy studies on the protective effect of curcumin coated gold nanoparticles against H₂O₂-induced oxidative stress in human neuroblastoma SK-N-SH cells. *Analyst* **2021**, *146*, 6902–6916. [CrossRef]
27. Lee, W.H.; Loo, C.-Y.; Traini, D.; Young, P.M. Development and Evaluation of Paclitaxel and Curcumin Dry Powder for Inhalation Lung Cancer Treatment. *Pharmaceutics* **2021**, *13*, 9. [CrossRef] [PubMed]
28. Chang, P.; Peng, S.; Lee, C.; Lu, C.; Tsai, S.; Shieh, T.; Wu, T.; Tu, M.; Chen, M.Y.; Yang, J.S. Curcumin-loaded nanoparticles induce apoptotic cell death through regulation of the function of MDR1 and reactive oxygen species in cisplatin-resistant CAR human oral cancer cells. *Int. J. Oncol.* **2013**, *43*, 1141–1150. [CrossRef]

29. Chun, Y.S.; Bisht, S.; Chenna, V.; Pramanik, D.; Yoshida, T.; Hong, S.M.; de Wilde, R.F.; Zhang, Z.; Huso, D.L.; Zhao, M.; et al. Intraductal administration of a polymeric nanoparticle formulation of curcumin (NanoCurc) significantly attenuates incidence of mammary tumors in a rodent chemical carcinogenesis model: Implications for breast cancer chemoprevention in at-risk populations. *Carcinogenesis* **2012**, *33*, 2242–2249. [CrossRef]
30. Zhai, Z.; Qu, X.; Li, H.; Ouyang, Z.; Yan, W.; Liu, G.; Liu, X.; Fan, Q.; Tang, T.; Dai, K.; et al. Inhibition of MDA-MB-231 breast cancer cell migration and invasion activity by andrographolide via suppression of nuclear factor- κ B-dependent matrix metalloproteinase-9 expression. *Mol. Med. Rep.* **2015**, *11*, 1139–1145. [CrossRef]
31. Chen, D.; Dai, F.; Chen, Z.; Wang, S.; Cheng, X.; Sheng, Q.; Lin, J.; Chen, W. Dimethoxy curcumin induces apoptosis by suppressing survivin and inhibits invasion by enhancing E-cadherin in colon cancer cells. *Med. Sci. Monit.* **2016**, *22*, 3215–3222. [CrossRef]
32. Calaf, G.M.; Ponce-Cusi, R.; Carrión, F. Curcumin and paclitaxel induce cell death in breast cancer cell lines. *Oncol. Rep.* **2008**, *40*, 2381–2388. [CrossRef]
33. Liang, C.C.; Park, A.Y.; Guan, J.L. In vitro scratch assay: A convenient and inexpensive method for analysis of cell migration in vitro. *Nat. Protoc.* **2007**, *2*, 329–333. [CrossRef] [PubMed]
34. Kabala-Dzik, A.; Rzepecka-Stojko, A.; Robert, K.; Jastrzebska-Stojko, Z.; Rafał, S.; Robert, D.W.; Jerzy, S. Migration Rate Inhibition of Breast Cancer Cells Treated by Caffeic Acid and Caffeic Acid Phenethyl Ester: An In Vitro Comparison Study. *Nutrients* **2017**, *9*, 1144. [CrossRef] [PubMed]
35. Fu, Z.; Chen, X.; Guan, S.; Yan, Y.; Lin, H.; Hua, Z.C. Curcumin inhibits angiogenesis and improves defective hematopoiesis induced by tumor-derived VEGF in tumor model through modulating VEGF-VEGFR2 signaling pathway. *Oncotarget.* **2015**, *6*, 19469–19482. [CrossRef]
36. Li, Y.; Gan, C.; Zhang, Y.; Yu, Y.; Fan, C.; Deng, Y.; Zhang, Q.; Yu, X.; Zhang, Y.; Wang, L.; et al. Inhibition of Stat3 Signaling Pathway by Natural Product Pectolarigenin Attenuates Breast Cancer Metastasis. *Front. Pharmacol.* **2019**, *10*, 1195. [CrossRef] [PubMed]
37. Zhang, T.; Li, S.; Li, J.; Yin, F.; Hua, Y.; Wang, Z. Natural product pectolarigenin inhibits osteosarcoma growth and metastasis via SHP-1-mediated STAT3 signaling inhibition. *Cell Death Dis.* **2016**, *7*, 305. [CrossRef]
38. Quispe-Soto, E.T.; Calaf, G.M. Effect of curcumin and paclitaxel on breast carcinogenesis. *Int. J. Oncol.* **2016**, *49*, 2569–2577. [CrossRef] [PubMed]
39. Tang, X.; Loc, W.S.; Dong, C.; Matters, G.L.; Butler, P.J.; Kester, M.; Meyers, C.; Jiang, Y.; Adair, J.H. The use of nanoparticles to treat breast cancer. *Nanomedicine* **2017**, *12*, 2367–2388. [CrossRef]
40. Mahesh, P.M.; Sagar, R.P.; Gaurav, A.S.; Mahesh, N.S.; Prashant, K.D.; Jitendra, B.N.; Bhijeet, D.K. Recent advances in phytochemical-based Nano-formulation for drug-resistant Cancer. *Med. Drug Discov.* **2021**, *10*, 10008.
41. Balakrishnan, S.; Bhat, F.A.; Singh, P.R.; Mukherjee, S.; Elumalai, P.; Das, S.; Patra, C.R.; Arunakaran, J. Gold nanoparticle-conjugated quercetin inhibits epithelial-mesenchymal transition, angiogenesis and invasiveness via EGFR/VEGFR-2-mediated pathway in breast cancer. *Cell Prolif.* **2021**, *49*, 678–697. [CrossRef]
42. Mantle, D.; Lennard, T.W.; Pickering, A.T. Therapeutic applications of medicinal plants in the treatment of breast cancer: A review of their pharmacology, efficacy and tolerability. *Advers. Drug React. Toxicol. Rev.* **2000**, *19*, 223–240.
43. Kapinova, A.; Stefanicka, P.; Kubatka, P.; Zubor, P.; Uramova, S.; Kello, M. Are plant-based functional foods better choice against cancer than single phytochemicals? A critical review of current breast cancer research. *Biomed. Pharmacother.* **2017**, *96*, 1465–1477. [CrossRef] [PubMed]
44. Park, S.Y.; Chae, S.Y.; Park, J.O.; Lee, K.J.; Park, G. Gold-conjugated resveratrol nanoparticles attenuate the invasion and MMP-9 and COX-2 expression in breast cancer cells. *Oncol. Rep.* **2016**, *35*, 3248–3256. [CrossRef] [PubMed]
45. Varlamova, E.G.; Goltyaev, M.V.; Mal'tseva, V.N.; Turovsky, E.A.; Sarimov, R.M.; Simakin, A.V.; Gudkov, S.V. Mechanisms of the Cytotoxic Effect of Selenium Nanoparticles in Different Human Cancer Cell Lines. *Int. J. Mol. Sci.* **2021**, *22*, 7798. [CrossRef] [PubMed]
46. Turovsky, E.A.; Varlamova, E.G. Mechanism of Ca²⁺ Dependent Pro-Apoptotic Action of Selenium Nanoparticles, Mediated by Activation of Cx43 Hemichannels. *Biology* **2021**, *10*, 743. [CrossRef] [PubMed]
47. Lui, D.; Chen, Z.; Medarde, F.; Santos, E. The effect of curcumin on breast cancer cells. *J. Breast Cancer* **2013**, *16*, 133–137.
48. Liu, X.; Kim, C.N.; Yang, J.; Jemmerson, R.; Wang, X. Induction of apoptotic program in cell-free extracts: Requirement for dATP and cytochrome c. *Cell* **1996**, *86*, 147–157. [CrossRef]
49. Thakur, C.; Chen, B.; Li, L.; Zhang, Q.; Yang, Z.Q.; Chen, F. Loss of mdg expression enhances DNA and histone methylation and metastasis of aggressive breast cancer. *Signal Transduct. Target. Ther.* **2018**, *3*, 25. [CrossRef]
50. Flores, F.F.; Suarez, J.A.Q.; Pardi, P.C.; Maria, D.A. DM-1, sodium 4-(5-(4-hydroxy-3-methoxyphenyl)-3-oxo-penta-1,4-dienyl)-2-methoxy-phenolate: A curcumin analog with a synergic effect in combination with paclitaxel in breast cancer treatment. *Tumor Biol.* **2012**, *33*, 775–785. [CrossRef]
51. Banerjee, M.; Singh, P.; Panda, D. Curcumin suppresses the dynamic instability of microtubules, activates the mitotic checkpoint and induces apoptosis in MCF-7 cells. *FEBS J.* **2010**, *277*, 3437–3448. [CrossRef]
52. Zhang, J.; Haines, C.; Watson, A.J.M.; Hart, A.R.; Platt, M.J.; Pardoll, D.M.; Cosgrove, S.E.; Gebo, K.A.; Sears, C.L. Oral antibiotic use and risk of colorectal cancer in the United Kingdom, 1989–2012: A matched case-control study. *Gut* **2019**, *68*, 1971–1978. [CrossRef] [PubMed]

53. Karuppaiya, P.; Satheeshkumar, E.; Chao, W.T.; Kao, L.Y.; Chen, E.C.; Tsay, H.S. Anti-metastatic activity of biologically synthesized gold nanoparticles on human fibrosarcoma cell line HT-1080. *Colloids Surf. B. Biointerfaces* **2013**, *110*, 163–170. [CrossRef]
54. Zhan, Y.; Chen, Y.; Liu, R.; Zhang, H.; Zhang, Y. Potentiation of paclitaxel activity by curcumin in human breast cancer cell by modulating apoptosis and inhibiting EGFR signaling. *Arch. Pharm. Res.* **2014**, *37*, 1086–1095. [CrossRef]
55. Boztas, A.O.; Karakuzu, O.; Galante, G.; Ugur, Z.; Kocabas, F.; Altuntas, C.Z.; Yazaydin, A.O. Synergistic interaction of paclitaxel and curcumin with cyclodextrin polymer complexation in human cancer cells. *Mol. Pharm.* **2013**, *10*, 2676–2683. [CrossRef] [PubMed]
56. Bayet-Robert, M.; Kwiatkowski, F.; Leheurteur, M.; Gachon, F.; Planchat, E.; Abrial, C.; Mouret-Reynier, M.A.; Durando, X.; Bartheleuf, C.; Chollet, P. Phase I dose escalation trial of docetaxel plus curcumin in patients with advanced and metastatic breast cancer. *Cancer Biol. Ther.* **2010**, *9*, 8–14. [CrossRef] [PubMed]
57. Luo, C.Q.; Xing, L.; Cui, P.F.; Qiao, J.B.; He, Y.J.; Chen, B.A.; Jin, L.; Jiang, H.L. Curcumin-coordinated nanoparticles with improved stability for reactive oxygen species-responsive drug delivery in lung cancer therapy. *Int. J. Nanomed.* **2017**, *25*, 855–869. [CrossRef]
58. Epelbaum, R.; Schaffer, M.; Vigel, B.; Badmaev, V.; Bar-Sela, G. Curcumin and gemcitabine in patients with advanced pancreatic cancer. *Nutr. Cancer* **2010**, *62*, 1137–1141. [CrossRef]



Article

Modified Gold Nanoparticles for Efficient Delivery of Betulinic Acid to Cancer Cell Mitochondria

Olakunle Oladimeji, Jude Akinyelu, Aliscia Daniels and Moganavelli Singh *

Nano-Gene and Drug Delivery Group, Discipline of Biochemistry, University of KwaZulu-Natal, Private Bag X54001, Durban 4000, South Africa; kunle1433@gmail.com (O.O.); jude.akinyelu@fuoye.edu.ng (J.A.); DanielsA@ukzn.ac.za (A.D.)

* Correspondence: singhm1@ukzn.ac.za; Tel.: +27-3-1260-7170

Abstract: Advances in nanomedicine have seen the adaptation of nanoparticles (NPs) for subcellular delivery for enhanced therapeutic impact and reduced side effects. The pivotal role of the mitochondria in apoptosis and their potential as a target in cancers enables selective induction of cancer cell death. In this study, we examined the mitochondrial targeted delivery of betulinic acid (BA) by the mitochondriotropic TPP⁺-functionalized epigallocatechin gallate (EGCG)-capped gold NPs (AuNPs), comparing the impact of polyethylene glycol (PEG) and poly-L-lysine-graft-polyethylene glycol (PLL-g-PEG) copolymer on delivery efficacy. This included the assessment of their cellular uptake, mitochondrial localization and efficacy as therapeutic delivery platforms for BA in the human Caco-2, HeLa and MCF-7 cancer cell lines. These mitochondrial-targeted nanocomplexes demonstrated significant inhibition of cancer cell growth, with targeted nanocomplexes recording IC₅₀ values in the range of 3.12–13.2 μM compared to that of the free BA (9.74–36.31 μM) in vitro, demonstrating the merit of mitochondrial targeting. Their mechanisms of action implicated high amplitude mitochondrial depolarization, caspases 3/7 activation, with an associated arrest at the G₀/G₁ phase of the cell cycle. This nano-delivery system is a potentially viable platform for mitochondrial-targeted delivery of BA and highlights mitochondrial targeting as an option in cancer therapy.

Keywords: mitochondrial targeting; gold nanoparticles; cancer chemotherapy; drug delivery; betulinic acid; laminin receptor



Citation: Oladimeji, O.; Akinyelu, J.; Daniels, A.; Singh, M. Modified Gold Nanoparticles for Efficient Delivery of Betulinic Acid to Cancer Cell Mitochondria. *Int. J. Mol. Sci.* **2021**, *22*, 5072. <https://doi.org/10.3390/ijms22105072>

Academic Editors:
Monica Terracciano and
Chiara Tramontano

Received: 4 April 2021
Accepted: 28 April 2021
Published: 11 May 2021

Publisher's Note: MDPI stays neutral with regard to jurisdictional claims in published maps and institutional affiliations.



Copyright: © 2021 by the authors. Licensee MDPI, Basel, Switzerland. This article is an open access article distributed under the terms and conditions of the Creative Commons Attribution (CC BY) license (<https://creativecommons.org/licenses/by/4.0/>).

1. Introduction

The continuous rise in cancer-associated mortality against a backdrop of advances in drug discovery highlights the prevailing challenges of existing therapeutic interventions for cancer. Cancer remains the second leading cause of death worldwide, with approximately 9.6 million deaths recorded in 2018 and another 18 million new cases reported in the same year [1]. While traditional treatment approaches such as surgery and radiotherapy have their limitations, the major demerits of chemotherapy are poor bioavailability, a low therapeutic index, and a marked increase in normal cell cytotoxicity on any compensatory dose increase [2].

The idea of a “magic bullet” in the treatment of diseases proposed by Paul Ehrlich, suggesting the precise delivery of therapeutics to their active sites may have inspired the targeted delivery concept, which has gained traction in recent times [3]. In cancer therapy, the application of this concept has seen the development of nano-delivery systems engineered to target and accumulate in cancerous tissues. Their application significantly enhances drug pharmacokinetics, minimizes side effects, and improves the drug's therapeutic index [2,4]. Further advances in this research area have also led to the introduction of optimized systems suitable for efficient delivery of the cargo to molecular targets localized in intracellular organelles [5]. Recent reports revealed that nanoformulations targeted to organelles such as the mitochondria, endosome, lysosome, nucleus, ribosome and the Golgi apparatus, demonstrated efficacy in the delivery of genes, proteins and drugs, thus

highlighting their potential application in clinical scenarios [6,7]. It is anticipated that the preferential targeting of subcellular compartments with nanomedicines would significantly improve treatment selectivity and biocompatibility, with the potential of achieving higher therapeutic indices at lower doses. The central role of mitochondria in bioenergetics and apoptosis signaling has made them a focus of clinical research, and a therapeutic target for diseases in recent years. Although apoptosis is a well-regulated physiological process, certain extracellular agents have been shown to modulate mitochondria function and induce apoptosis, thus presenting an in-road to preferentially targeting the organelle in related disease conditions [8].

Betulinic acid (BA) is a pentacyclic triterpenoid, from a subclass of terpenes composed of isopentenyl pyrophosphate oligomers, that have been studied for their medicinal potential [9,10]. BA demonstrates potent activity against bacterial and viral infections, inflammation, malaria, and cancer [10,11]. Research has shown that the anticancer effect of BA is linked to its impact on the mitochondria. BA induces membrane permeability transition (MPT) in cancer mitochondria, consequently triggering the dissipation of mitochondrial membrane potential, cytochrome c release, caspase activation and finally, apoptosis [12–14]. A major drawback to BA's clinical potential is its poor solubility, which, coupled with other common limitations such as high blood clearance and low specificity, impacts its efficacy in vivo. To improve the therapeutic effectiveness of the drug on the cancer cell mitochondria, a nano-delivery system with the capacity to successfully navigate physiological and cellular barriers and ensure the delivery of the payload to the mitochondria for maximum impact is imperative [15].

Biocompatibility is a critical factor in the efficacy of nano-delivery platforms. The green or organic synthesis of inorganic nanoparticles (NPs) offers, among other things, the elimination of toxicities associated with chemical synthesis, as well as the transfer of bioactive properties from plant-based reductants. Green synthesis of inorganic NPs employs the reductive power of bio-extracts to affect the reduction of metallic salts from their initial oxidative state to zero [16]. Generally, green synthesized NPs adopt the unique features of bio-extracts employed in their synthesis. Organic synthesis with extracts from fungi, algae, plants, and bacteria have given rise to NPs with inherent antioxidant, antibacterial and self-targeting properties. EGCG has been reported to show an affinity for the 67 kD laminin receptor (67LR), that is overexpressed in most aggressive tumors [17–20]. The laminin receptor-dependent uptake of EGCG-reduced radioactive gold NPs (AuNPs) by cancer cells has been reported [21]. Considering the potential inherent in the preferential targeting of therapeutics to intracellular sites of action to bring about improved bioavailability and therapeutic efficacy at a lower dose with tolerable side effects, we have studied the capacity of EGCG-capped, laminin receptor-avid AuNPs for mitochondrial-targeted delivery of BA in selected cancer cells in vitro. The decoration of an inorganic NP surface with biodegradable polymers has been reported to improve NP biocompatibility, stability, and influence cargo release [22]. PLL, a biocompatible and biodegradable polymer of the amino acid L-lysine exerts these effects, and apart from the provision of functional amino groups for the easy conjugation of other components, its net electropositive charge promotes an electrostatic interaction with the electronegative cellular membrane, aiding NP uptake [23,24]. The pegylation of NPs, among other things, confers stealth properties and correlates with increased residence time in vivo [22,25]. Therefore, we assessed the impact of surface design on NP efficiency, comparing the activities of PEG-coated nanocomplexes to the PLL-g-PEG-coated variant. To the best of our knowledge, this study is the first attempt at preferentially targeting BA to the mitochondria.

2. Results

2.1. Synthesis and Functionalization of EGCG-Capped AuNPs

EGCG-capped AuNPs were synthesized by the reduction of gold (III) chloride with the green tea polyphenol, EGCG, as illustrated in Figure 1. Surface functionalization of EGCG-capped NPs involved coating with either PEG, or a graft polymer of PLL-PEG (PLL-

g-PEG) to produce two polymer-coated variants, the Au-PEG and the Au-[PLL-g-PEG] NPs, respectively. Further functionalization included the conjugation of the drug BA, and the lipophilic moiety, triphenylphosphine (TPP⁺) for enhanced mitochondria localization.

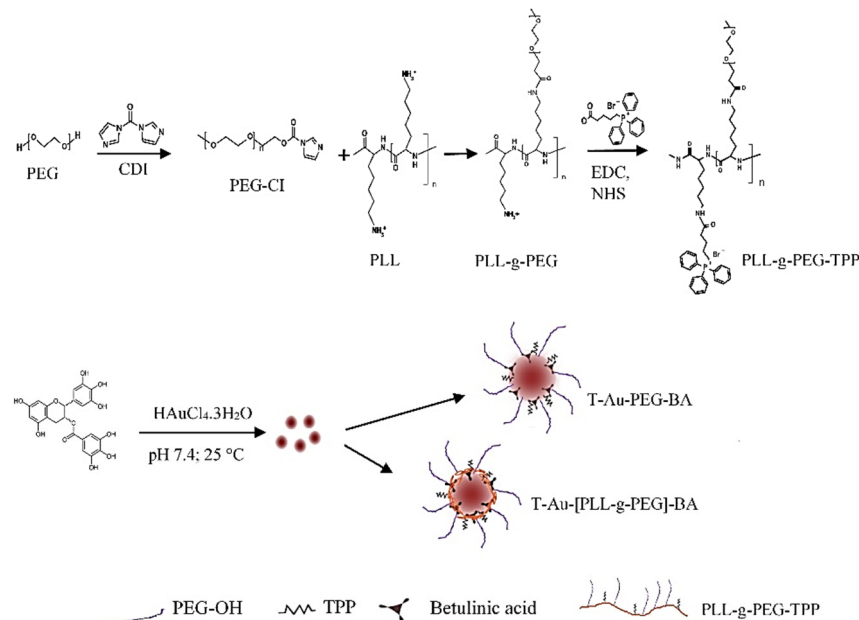


Figure 1. The synthesis of EGCG-capped NPs, and the engineering of the targeted T-Au-PEG-BA and T-Au-[PLL-g-PEG]-BA nanoparticles.

2.2. UV-Vis Spectroscopy

The synthesis and functionalization of EGCG-capped AuNPs were monitored by UV-vis spectroscopy. Inorganic NPs generally show distinct optical properties, which are representative of their physical features such as size and stability [26,27]. The successful functionalization of a NP results in changes in the oscillation state of its surface electrons, otherwise referred to as localized surface plasmon resonance (SPR), manifesting as change in optical properties. AuNPs generally show a strong absorbance peak between 500 and 600 nm, and in this study, EGCG capped AuNPs had a strong absorbance peak at 524 nm, comparable to citrate capped AuNPs (520 nm) [28,29]. Subsequent surface designs resulted in band shifts and reduction in peak intensities in Au-PEG (522 nm), T-Au-PEG and T-Au-PEG-BA (542 nm), with the blueshift on PEG conjugation indicating a reduction in size, the redshift to 542 nm on TPP⁺ and BA showing a slight reduction in NP stability compared to unfunctionalized AuNPs, with the widening of the peak indicating an increase in dispersity. Similarly, the coating with PLL-g-PEG resulted in a band shift to 534 nm, while the conjugation of TPP⁺ and BA resulted in a shift to 541 and 533 nm, respectively (Figure 2), indicating an increase in size or slight reduction in stability compared to the unfunctionalized AuNPs. Overall, the PLL-g-PEG coated NPs seemed to be the more stable of the two designs. The band shifts and reduction in peak intensity are suggestive of a successful binding of the polymer and drug.

2.3. Fourier-Transform Infrared Spectroscopy (FTIR)

The frequency of vibration of molecules upon absorption of electrochemical radiation is distinctive for individual molecules. These vibrations, represented as band shifts at characteristic wavelengths in the IR spectrum are applied in the analysis of organic compounds, especially in the identification of functional groups [30]. The synthesis and subsequent functionalization of NPs with polymers, drug, and the targeting moiety were monitored and confirmed by FTIR analysis. As represented in Figure 3, EGCG capped AuNPs showed stretching vibrations of O-H (3400 cm^{-1}) and C-H (3000 cm^{-1}) of the

aromatic rings characteristic of the polyphenol groups of EGCG. In addition, the aromatic skeletal vibrations at 1630 cm^{-1} also of the EGCG moiety further confirmed the successful capping of AuNPs by the polyphenol. The successful functionalization of AuNPs with PEG was evident from the stronger peak at 3000 and 1190 cm^{-1} due to the stretching vibrations of the C-H bonds and C-O bonds of the polymer, respectively.

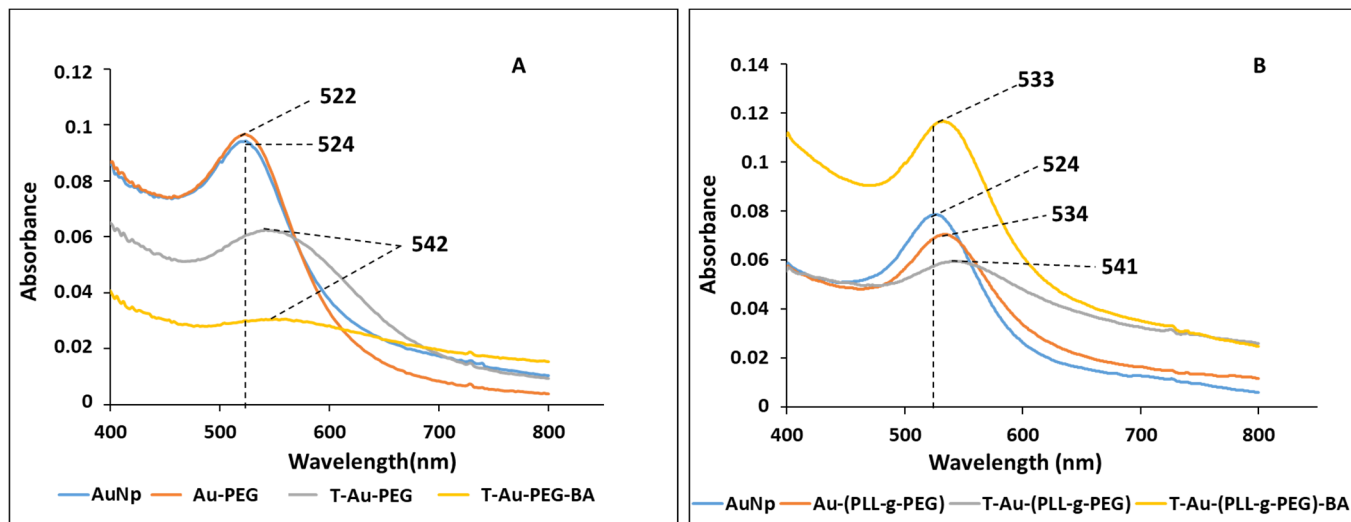


Figure 2. UV-vis of nanoparticles and drug nanocomplexes showing changes in surface plasmon resonance: (A) PEG functionalized AuNPs; (B) PLL-g-PEG coated AuNPs.

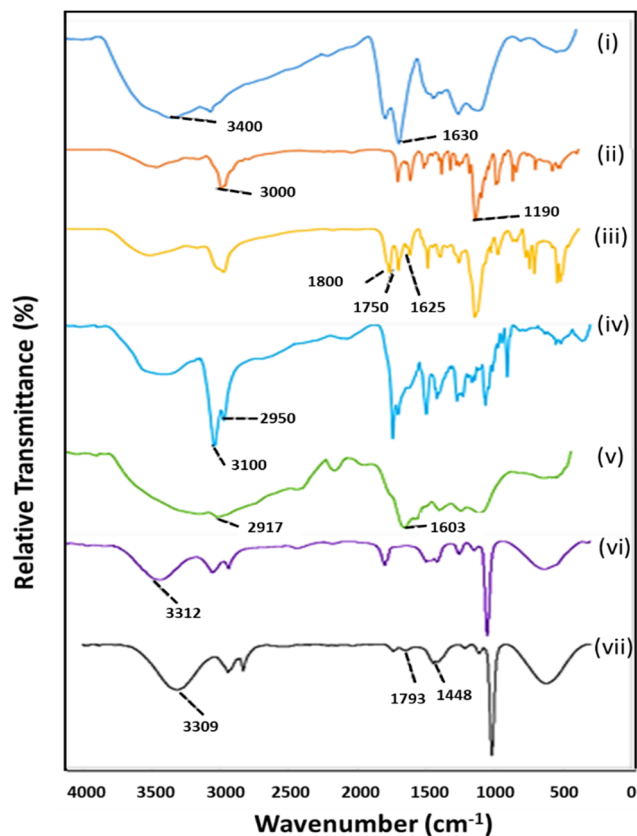


Figure 3. FTIR of nanoparticles showing changes in bond vibrations of respective functional groups. (i) AuNP, (ii) Au-PEG, (iii) T-Au-PEG, (iv) T-Au-PEG-BA, (v) Au-[PLL-g-PEG], (vi) T-Au-[PLL-g-PEG], (vii) T-Au-[PLL-g-PEG]-BA.

The lipophilic cation TPP⁺ moiety of the targeted NP (T-Au-PEG) coupled by Steglich esterification to the OH groups of Au-PEG, showed characteristic skeletal vibrations of its three aromatic rings at 1800, 1750 and 1625 cm⁻¹. Similarly, the very strong vibrations of the C=O group at 1681 cm⁻¹, and those of the CH₃, CH₂, and CH, at 2950 and 3000 cm⁻¹ in T-Au-PEG-BA, confirmed the loading of BA into the NPs [31]. The coating of NPs with PLL-g-PEG to yield the Au-PLL-g-PEG, showed the characteristic stretch vibration for the repeating CH₂ groups of PLL at 2917 cm⁻¹, and the secondary amine groups (NH) at 1603 cm⁻¹. The subsequent conjugation of TPP⁺ is evident from the stretching vibrations of the C-H bonds of the benzene rings at 3312 cm⁻¹, and the stretching vibration of CH₂ and CH₃ groups at 2945 and 2835 cm⁻¹, respectively. The loading of BA in T-Au-[PLL-g-PEG]-BA was confirmed by the amplification of IR peaks at 3309 cm⁻¹ for OH stretching vibration, and at 2943 cm⁻¹ for CH₃, CH₂ and CH groups. Furthermore, the bands at 1793 cm⁻¹ (shoulder) and 1648 cm⁻¹ are representative of the C=O group of BA, while the signal at 1448 cm⁻¹ is due to the bending vibrations of the CH₃ and CH₂ groups of the aliphatic ring of the drug [30].

2.4. Drug Loading, TEM and NTA

Au-PEG-BA and T-Au-PEG-BA had loading efficiencies of ~25.4%, while Au-PLL-g-PEG-BA and T-Au-PLL-g-PEG-BA had loading efficiencies of ~21% (Table 1). Table 1 also reflects the NTA hydrodynamic size, zeta potential and polydispersity indices of all NPs.

Table 1. Hydrodynamic size, zeta potential (ζ), polydispersity indices (PDI) and drug loading efficiencies of nanoparticles.

NPs	Hydrodynamic Size (nm)	PDI	ζ Potential (mV)	BA Loading Efficiency (%)
EGCG-AuNP	127.3 ± 3.1	0.10	-28.3 ± 1.6	-
Au-PEG-BA	110.1 ± 5.3	0.22	-25.0 ± 0.9	25.4 ± 0.04
T-Au-PEG-BA	97.1 ± 2.5	0.035	-23.1 ± 1.1	25.4 ± 0.12
Au-[PLL-g-PEG]-BA	147.2 ± 4.7	0.13	+11.8 ± 1.6	21.0 ± 1.2
T-Au-[PLL-g-PEG]-BA	119.2 ± 3.5	0.11	+23.4 ± 0.5	21.0 ± 0.7

TEM showed stable, spherical NPs (Figure 4) with an average size diameter of 15 nm. Analysis following surface design showed negligible change in particle size, and no agglomeration. The hydrodynamic diameter (NTA) for AuNPs was in the 127 nm range, while subsequent modification resulted in a reduction in the diameter to 110.1 and 97.1 nm for Au-PEG-BA and T-Au-PEG-BA, respectively. Upon coating with PLL-g-PEG and TPP⁺-PLL-g-PEG, an increase in NP diameter to 147.2 nm and a reduction to 119 nm were recorded, respectively (Table 1). The polydispersity index (PDI) provides information on the size distribution of NPs. Generally, NPs with low PDI values are monodispersed and uniform in size [32]. The PDI estimations for the nanocomplexes studied suggests moderate dispersity with values closer to 0.1, except for the Au-PEG-BA nano-construct with a PDI value of 0.22, suggesting some polydispersity.

The zeta potential measurement which informs on the surface charge of the NP with respect to that of the conducting fluid, in this case water (pH 7), is a marker for NP stability and biomolecular interactions. The PEG functionalization of the AuNPs only effected marginal changes, with the zeta potential remaining negative even upon further functionalization with TPP⁺. Conversely, coating with the cationic PLL-g-PEG and TPP⁺-PLL-g-PEG resulted in positive surface charge for the NPs, of 11.8 and 23.4 mV, respectively. Overall, the zeta potentials recorded indicated that the nanocomplexes were stable, however, the negative charge of T-Au-PEG-BA and Au-PEG-BA could have adversely influenced their interaction with the cell and mitochondria due to the negative potentials (Ψ) of both membranes.

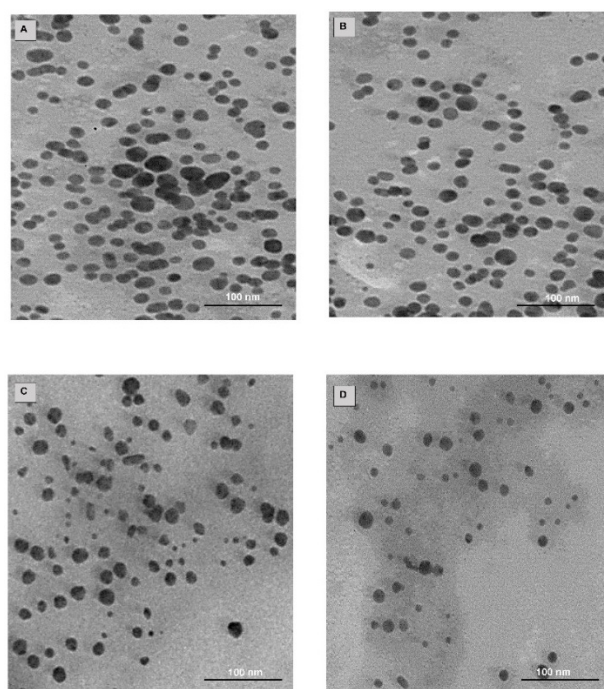


Figure 4. TEM images of nanoparticles: (A) AuNPs, (B) AuNP-BA, (C) T-Au-PEG-BA, (D) T-Au-[PLL-g-PEG]-BA.

2.5. Cellular Uptake and Mitochondrial Targeting

The ability of NPs to cross the cell membrane bilayer and translocate efficiently to subcellular targets is pivotal to their application in therapeutic delivery. Given earlier reports on the affinity of EGCG for the 67-kDa laminin receptor [21,33], the laminin receptor dependent uptake of T-Au-PEG and T-Au-PLL-g-PEG was studied in the HeLa cell line due to its high expression of the receptor [34]. Cellular uptake in cells preincubated with the laminin receptor antibody were generally lower compared to cells not treated with the antibody (Figure 5). For T-Au-PEG NPs, uptake was significantly lower in preincubated cells (T-Au-PEG: 51 980.98 particles/ μg protein; T-Au-PEG/+Ab: 12,059.37 particles/ μg protein), thus showing a strong dependence on laminin receptor mediated uptake. Although recording a lower level of uptake compared to T-Au-PEG, a statistically significant reduction in uptake upon receptor blocking was also recorded for the T-Au-[PLL-g-PEG] NPs with 30,451.87 particles/ μg protein, and T-Au-[PLL-g-PEG]/+Ab with 11,273.19 particles/ μg protein). The lower levels observed for T-Au-[PLL-g-PEG] NPs can be attributed to their larger size which may have an impact on the efficiency of NP uptake.

The distribution of NPs between the cytoplasm and mitochondria, in the Caco-2, MCF-7 and HeLa cell lines, was determined after a 12 h period by the differential centrifugation of the cell lysate to obtain the cytoplasmic and mitochondrial fractions, and thereafter analyzed by ICP-OES to obtain a quantitative estimate of the mitochondrial localization efficiency of these NPs. Significant mitochondrial localization was achieved by T-Au-PEG and T-Au-[PLL-g-PEG] NPs compared to their untargeted counterparts (Au-PEG and Au-[PLL-g-PEG]) (Figure 6).

Furthermore, in all three cell lines, mitochondrial localization was higher for T-Au-[PLL-g-PEG] NPs compared to T-Au-PEG NPs. Interestingly, mitochondrial localization for the two targeted NPs was highest in the MCF-7 and lowest in Caco-2 cells. While the presented data does not establish the rate of NP uptake in the different cell lines, it suggests that the intracellular trafficking of NPs may vary for the respective cell lines.

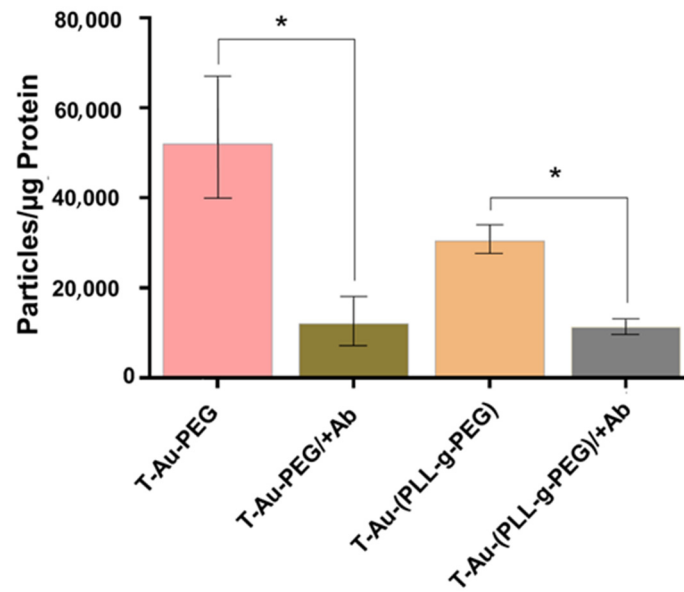


Figure 5. Graphical representation of the laminin dependent uptake of targeted nanoparticles in HeLa cells. Data is represented as mean \pm SD ($n = 3$). (* $p < 0.05$).

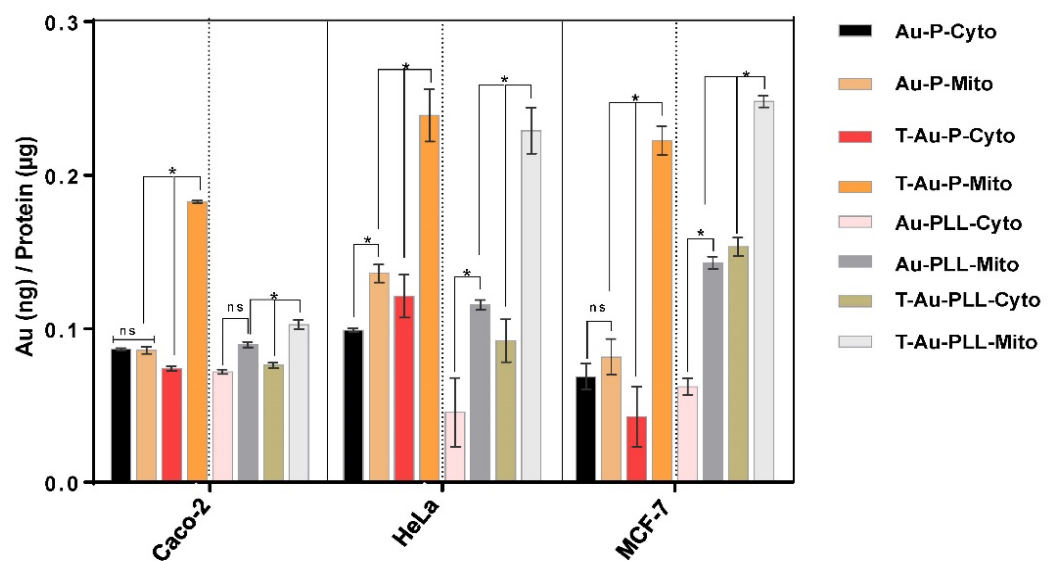


Figure 6. Cytosolic and mitochondrial distribution of mitochondrial targeted and nontargeted nanoparticles as determined by ICP-OES. Data is represented as mean \pm SD ($n = 3$); * $p < 0.05$; ns = no significant difference.

2.6. Cytotoxicity

The impact of targeted and untargeted nanocomplexes, and the free drug on cell proliferation was assessed in the HEK293, Caco-2, HeLa and MCF-7 cells, using the colorimetric MTT assay (Figure 7).

The drug-loaded nanocomplexes tested were reported in the concentrations of their respective BA content (μM) for easy comparison with free BA, while the corresponding volume of drug-loaded NPs used for each drug concentration was adopted for drug free nanocomplexes. Negligible cytotoxicity was recorded for all NPs in the HEK293 cells, suggesting that these normal cells showed good tolerance to these treatments. Similarly, drug loaded NPs showed low cytotoxicity, while free BA recorded marked cytotoxicity in normal HEK293 cells, recording an IC_{50} value of $32.4 \mu\text{M}$ compared to $>80 \mu\text{M}$ recorded for

T-Au-PEG-BA and T-Au[PLL-g-PEG]-BA. The efficacy of the NPs in mitochondrial accumulation, and subsequent delivery of their cargo is evident from the low IC₅₀ values recorded for targeted nanocomplexes compared to their nontargeted counterparts and the free drug. As presented in Table 2, the estimated IC₅₀ values for T-Au-PEG-BA in Caco-2, HeLa and MCF-7 cells are 3.13, 6.51 and 13.2 μM, respectively, which are markedly low compared to the 8.20, 25.37 and 53.74 μM recorded for Au-PEG-BA; and 9.74, 17.73 and 36.31 μM recorded for free drug. Similarly, T-Au[PLL-g-PEG]-BA inhibited proliferation at levels significantly higher compared to Au[PLL-g-PEG]-BA and BA, recording low IC₅₀ values in Caco-2, HeLa and MCF-7 cells (3.12, 3.26 and 13.13 μM, respectively), compared to the higher IC₅₀ values recorded by Au[PLL-g-PEG]-BA (5.72, 23.64 and 22.25 μM) and free BA (9.74, 17.73, 36.31 μM) in the same cells. In spite of the lower mitochondrial accumulation seen in T-Au-PEG-BA (Figure 6), its impact on cellular proliferation is not different from that of T-Au[PLL-g-PEG]-BA, which suggests the possibility of extra-mitochondrial targets for T-Au-PEG-BA.

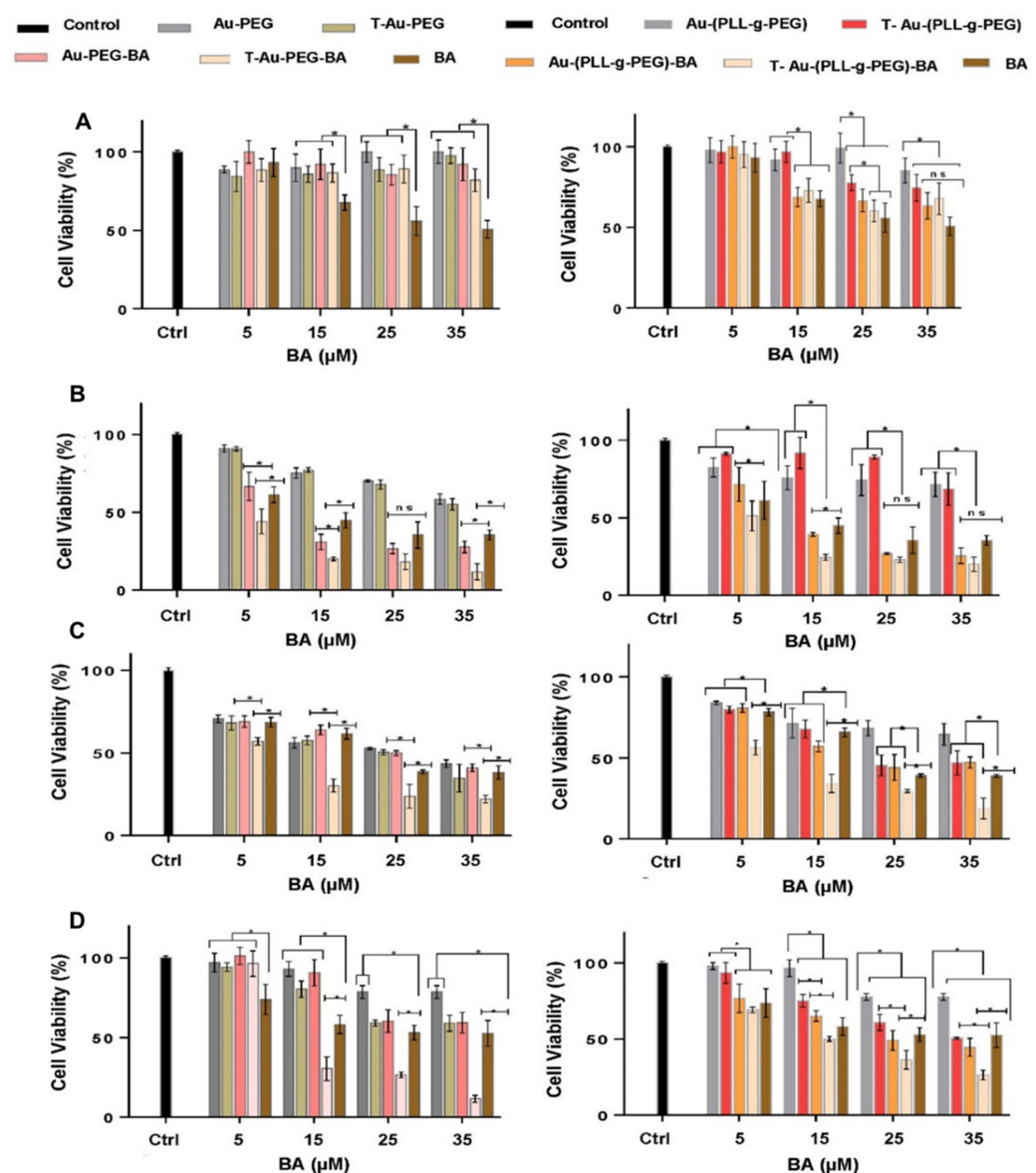


Figure 7. Effect of nanoparticles and drug nanocomplexes on cell viability in (A) HEK 293, (B) Caco-2, (C) HeLa and (D) MCF-7 cells. Au-PEG-BA; Au-[PLL-g-PEG]-BA = untargeted nanocomplexes, T-Au-PEG-BA; T-Au-[PLL-g-PEG]-BA = targeted nanocomplexes, and BA= free drug. Data is represented as mean \pm SD ($n = 3$); * $p < 0.05$); ns = no significant difference.

Table 2. Estimated IC₅₀ values of BA, targeted and untargeted nanocomplexes.

	Au-PEG-BA	T-Au-PEG-BA	Au-[PLL-g-PEG]-BA	T-Au-[PLL-g-PEG]-BA	BA
	Estimated IC ₅₀ Values (μM)				
Caco-2	8.20	3.13	5.72	3.12	9.74
HeLa	25.37	6.51	23.64	3.26	17.73
MCF-7	53.74	13.2	22.25	13.13	36.31

2.7. Effect on Mitochondrial Membrane Potential

To elucidate the impact of targeted nanocomplexes on the mitochondria and their underlying mechanism of action, the effects of all nanocomplexes and free drug on the mitochondria in the three cancer cell lines was investigated. Due to their efficient mitochondrial localization, the targeted nanocomplexes, T-Au-PEG-BA and T-Au-[PLL-g-PEG]-BA showed significant impact on mitochondrial membrane potential compared to the untargeted and free BA (Figures 8 and 9).

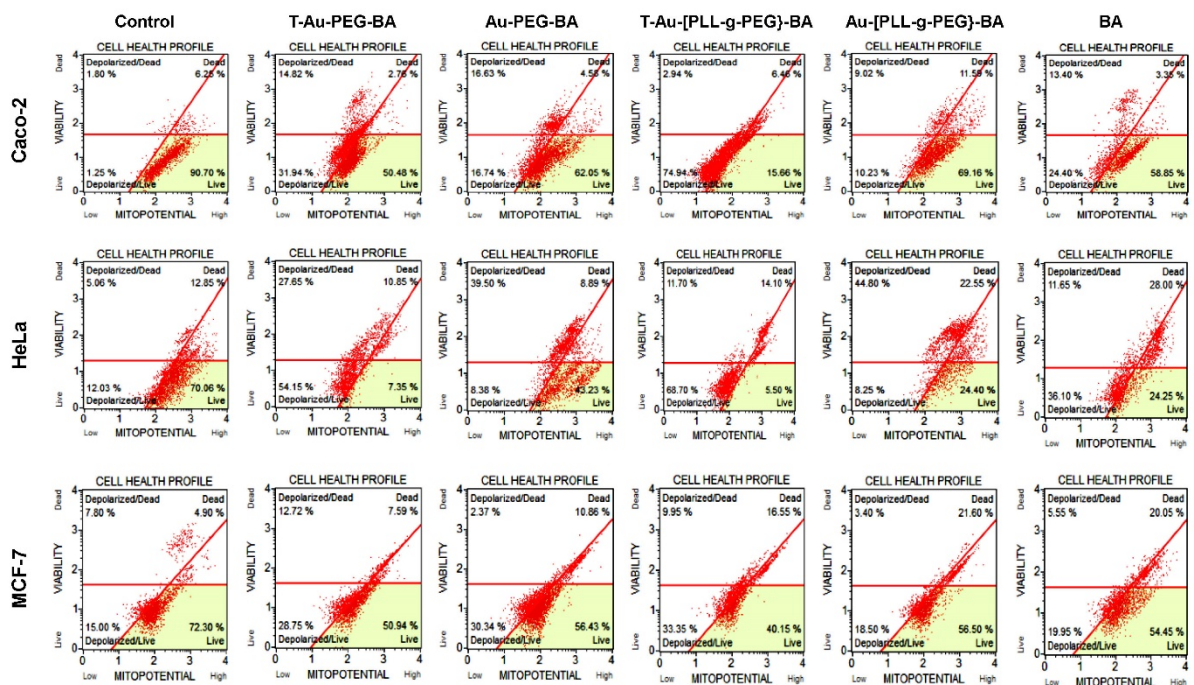


Figure 8. Cytographs of the effect of the targeted and untargeted nanocomplexes on the mitochondrial membrane potential in Caco-2, HeLa and MCF-7 cells. Au-PEG-BA; Au-[PLL-g-PEG]-BA = untargeted nanocomplexes, T-Au-PEG-BA; T-Au-[PLL-g-PEG]-BA = targeted nanocomplexes, and BA = free drug. Top left quadrat: cell death by mitochondrial depolarization; top right quadrat: non-mitochondria dependent cell death; lower left quadrat: mitochondrial depolarization in live cells; lower right quadrat: live cells.

Results suggest a significant impact by the cationic T-Au-[PLL-g-PEG]-BA recording 74.94%, 68.7% and 33.35% depolarization in the Caco-2, HeLa and MCF-7 cell lines, compared to the 31.94%, 54.15% and 28.75% observed for T-Au-PEG-BA. Furthermore, the activity of the nanocomplexes in the MCF-7 cells was generally lower in comparison with their activity in the other cells, highlighting the selective sensitivity of BA to certain cancers and confirming previous reports [10,35].

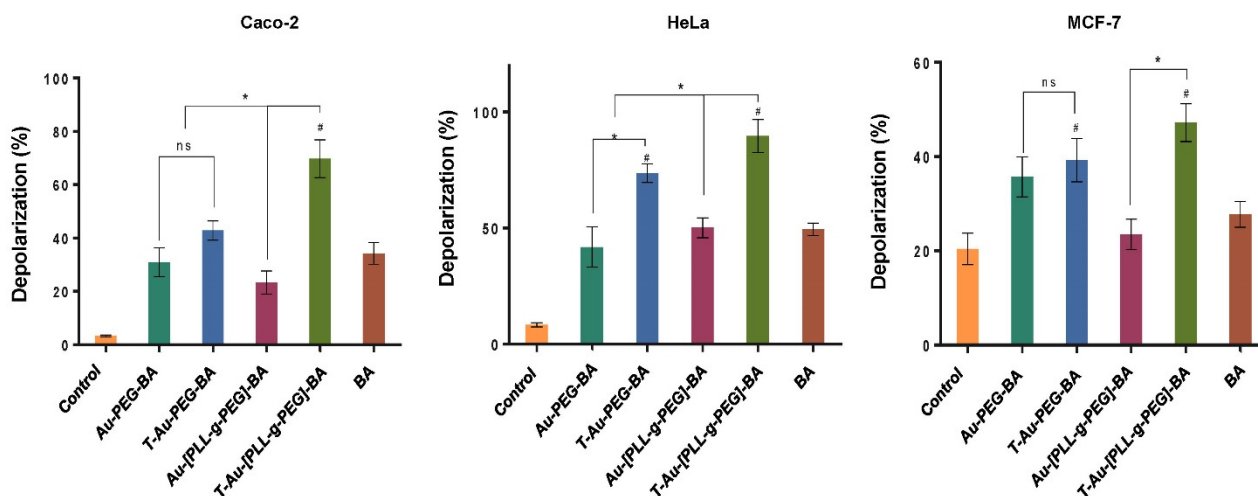


Figure 9. Graphical representation of the effect of targeted and untargeted nanocomplexes on the mitochondrial membrane potential in Caco-2, HeLa and MCF-7 cells. Data is represented as mean \pm SD ($n = 3$). * vs targeted or untargeted nanocomplex, # vs. free drug at $p < 0.05$. ns = no significant difference.

2.8. Impact on Caspases 3 and 7 Activity

The activity of caspases 3 and 7 (Figures 10 and 11) were assessed as markers of apoptosis initiation, using a fluorescent substrate—DEVD of the executioner proteases, and the cell death marker 7-AAD. From Figures 10 and 11 it can be observed that the highest levels of activation were recorded by T-Au-[PLL-g-PEG]-BA in all three cells, with a total of 52.81%, 67% and 32.84% apoptotic cell populations compared to the 35.71%, 49.95% and 24.25% for T-Au-PEG-BA, which is in tandem with results from the mitochondrial membrane potential dissipation. Apart from the demonstrated efficacy of the targeted nanocomplexes, they also demonstrated appreciable improvement over free BA in caspase induction.

2.9. The Effect of Targeted Nanocomplexes on Apoptosis Induction

Following incubation with the nanocomplexes and drug at predetermined concentrations, cells were stained with the AO/EB dual stain [28], to determine the extent of apoptosis in vitro. Fluorescent images showing cytomorphological changes indicative of apoptosis were noticed for treated cancer cell lines at varying degrees (Figure 12).

In comparison to the control cells (nontreated), morphological changes such as cell shrinkage and membrane blebbing indicative of apoptosis were observed in treated cells. These changes were moderate in BA treated cells, but generally severe in cells exposed to nanocomplexes. The dual staining technique is able to distinguish between early apoptotic cells, from cells at the final stage of apoptosis, with light yellow fluorescence indicating early apoptosis, and orange fluorescence suggesting cells are in the late stage of apoptosis. Overall, both targeted nanocomplexes showed significant improvement over free BA, demonstrating the importance of these NPs to enhance drug bioavailability and improve pharmacokinetics.

2.10. The Impact of Targeted Nanocomplexes on Cell Cycle Progression

The targeted nanocomplexes were then studied further to determine their impact on the cell cycle. Cells were incubated with an equimolar concentration of the drug and the nanocomplexes were assessed for distribution across the G0/G1, S and G2/M phases. There was appreciable cell distribution across the S and G2/M phases in the control group for the Caco-2, HeLa and MCF-7 cells, compared to the treated groups (Figure 13), which is indicative of the high rate of proliferation in this group of cells.

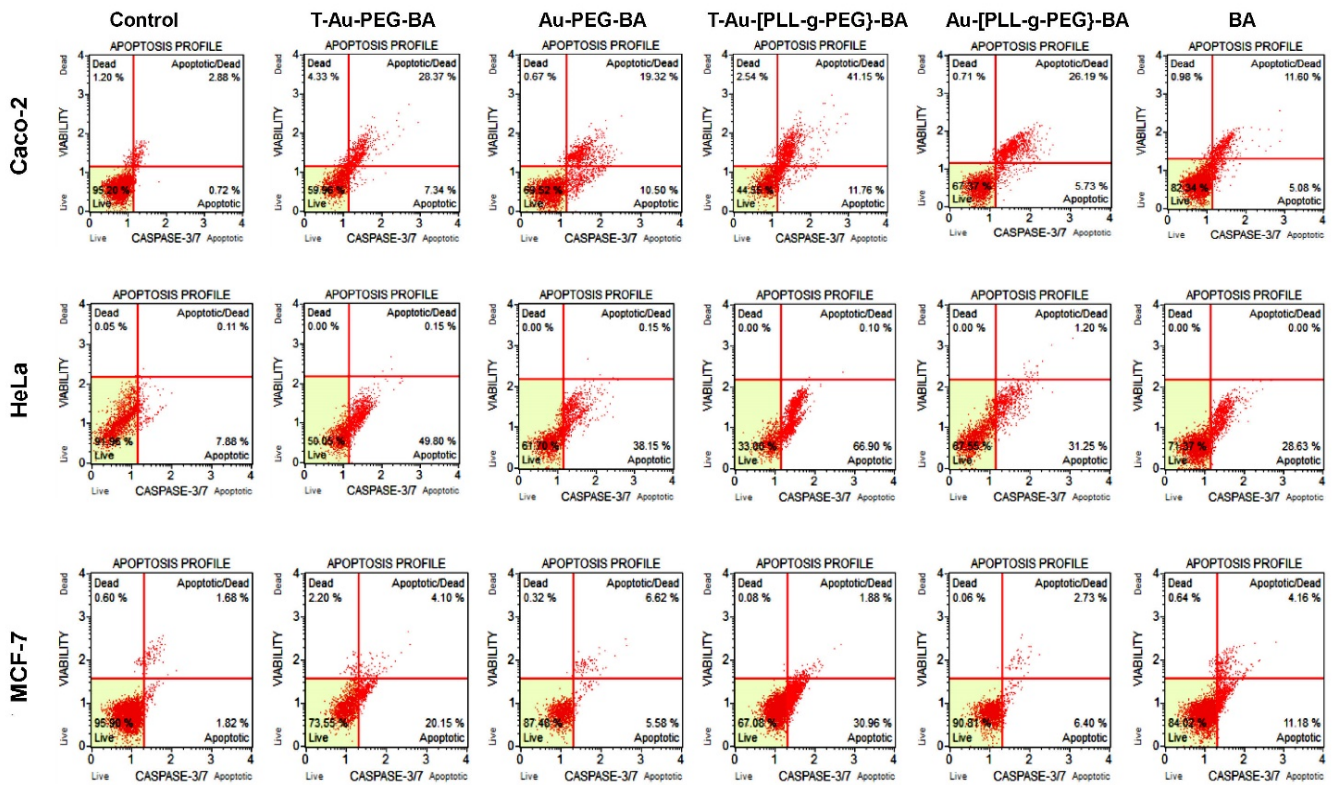


Figure 10. Cytographs showing the effect of targeted and untargeted nanocomplexes on caspases 3 and 7 in Caco-2, HeLa and MCF-7 cells. Au-PEG-BA; Au-[PLL-g-PEG]-BA = untargeted nanocomplexes, T-Au-PEG-BA; T-Au-[PLL-g-PEG]-BA = targeted nanocomplexes, and BA = free drug. Top left quadrat: cell death by non-apoptotic mechanisms; top right quadrat: cell death by caspase dependent apoptosis; lower left quadrat: Live cells; lower right quadrat: cells undergoing caspase dependent apoptosis.

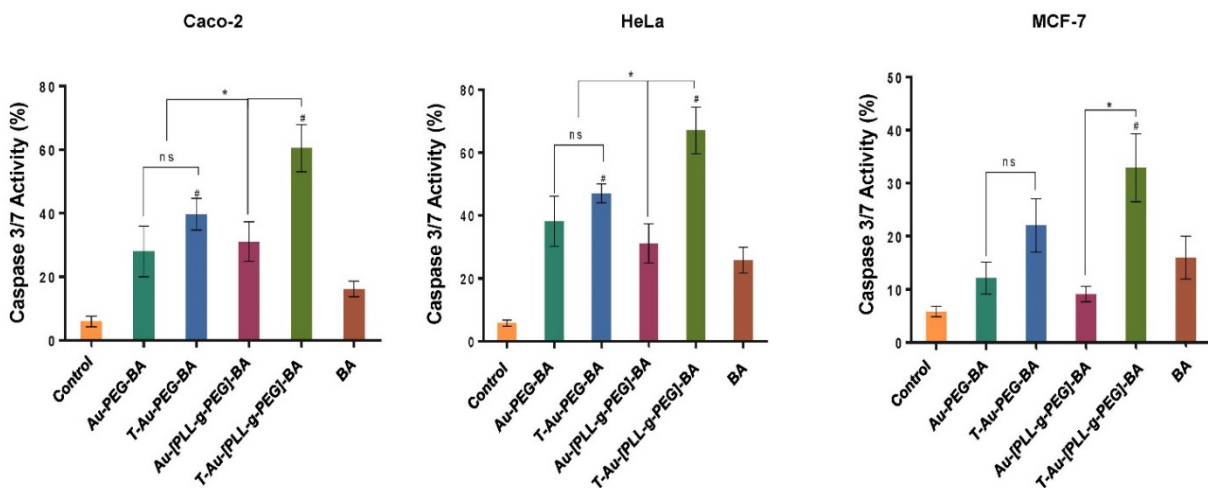


Figure 11. Graphical representation of the effect of targeted and untargeted nanocomplexes on caspases 3 and 7 in Caco-2, HeLa and MCF-7 cells. Data is represented as mean \pm SD ($n = 3$). * vs. targeted or untargeted nanocomplex, # vs. free drug at $p < 0.05$. ns = no significant difference.

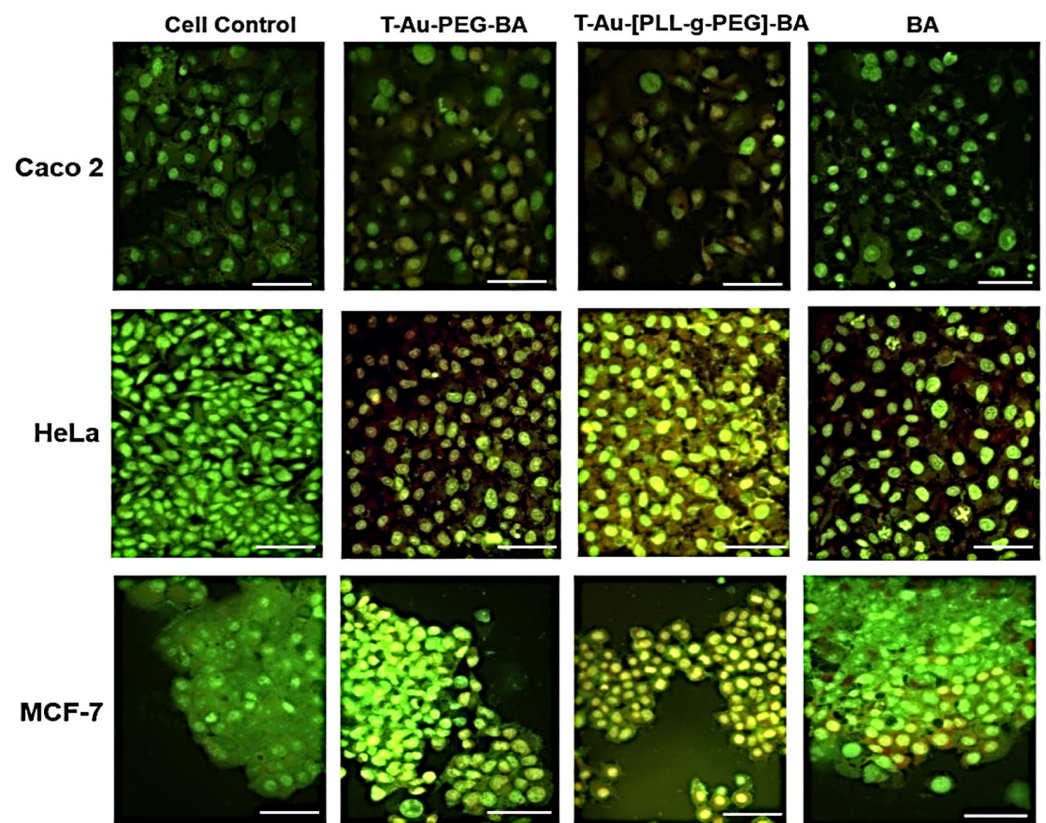


Figure 12. Sectional fluorescent images of acridine orange/ethidium bromide stained cells showing apoptosis induction by targeted nanocomplexes. T-Au-PEG-BA; T-Au-[PLL-g-PEG]-BA = targeted nanocomplexes, and BA = free drug. Untreated cells and BA served as controls. Scale bar = 100 μ m.

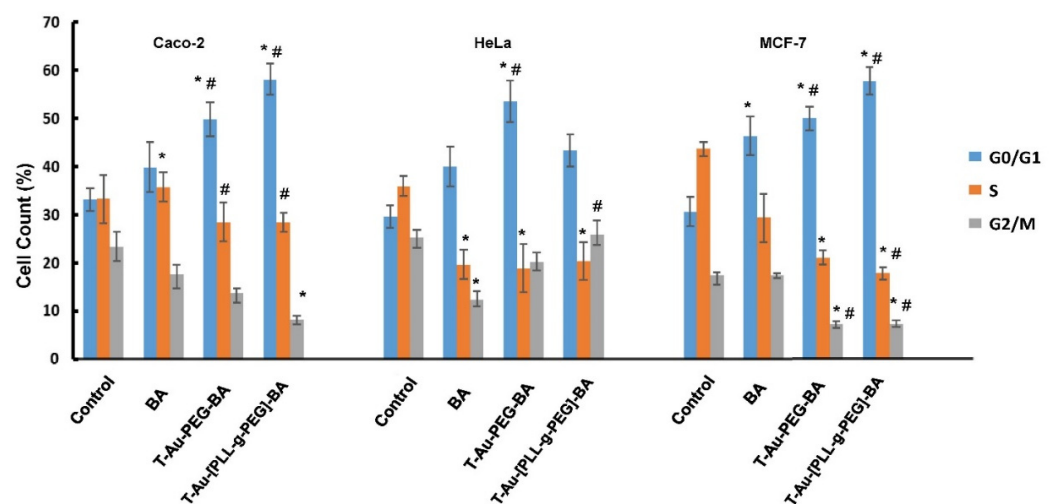


Figure 13. Graphical representation showing the effect of T-Au-PEG-BA, T-Au-[PLL-g-PEG]-BA and BA on cell cycle progression. T-Au-PEG-BA; T-Au-[PLL-g-PEG]-BA = targeted nanocomplexes, and BA= free drug. Data is represented as mean \pm SD ($n = 3$). * vs. control, # vs. free drug at $p < 0.05$.

Upon addition of the various treatments, a comparable decrease in cell population for the two phases was noticed, with a corresponding increase in cell number at the G0/G1 phase. In the Caco-2 cells, a significant increase in the number of cells arrested at the G0/G1 phase was observed for T-Au-[PLL-g-PEG], recording a 1.8-fold increase over the control. T-Au-PEG-BA and BA also recorded increases. In the MCF-7 cells, the trend was similar,

with the G₀/G₁ cell population increasing from 30% in the control to 46%, 57%, and 66% in BA, T-Au-PEG-BA, and T-Au-[PLL-g-PEG], respectively. However, in the HeLa cells, the highest G₀/G₁ arrest was observed for T-Au-PEG-BA, recording a 1.83-fold increase compared to that for T-Au-[PLL-g-PEG] (1.48-fold), further demonstrating the efficacy of the targeted nanocomplexes over the free drug.

Figure 14 provides an illustration depicting the cellular uptake, mitochondrial localization and mechanisms involved in cell death.

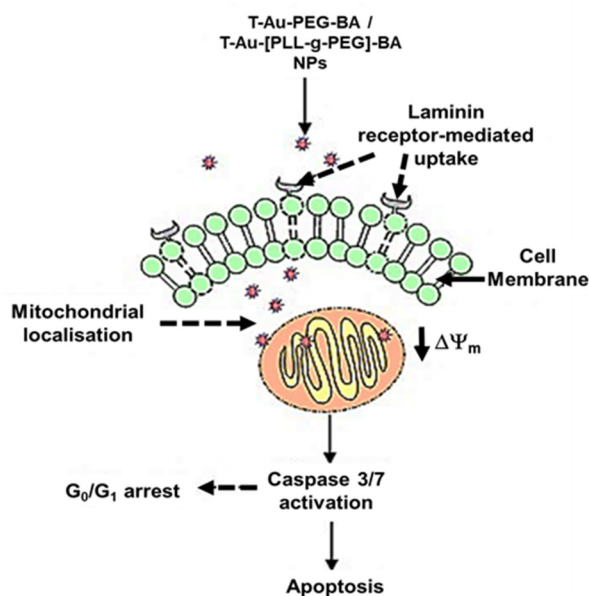


Figure 14. Illustration indicating possible mechanisms involved in cell death.

3. Discussion

The identification of the mitochondria as a therapeutic target for cancer chemotherapy initiated the search for therapeutics capable of impacting mitochondrial integrity and inducing apoptosis in cancer cells. Although studies have identified other cytoplasmic targets for BA, the merit for preferentially targeting the mitochondria lies in the high susceptibility of cancer mitochondria to mito-active agents owing to their dysfunctional status, thereby making the approach more specific as the impact on noncancer cells is generally negligible [36–38]. Therefore, for efficacy and specificity, the targeted delivery of mitochondrial-active principles has become an emerging area of research.

The organic synthesis of NPs which has seen increasing application in clinical research has shown significantly low environmental toxicity and ease of synthesis. AuNPs were successfully synthesized by exploiting the strong redox properties of the green tea polyphenol, EGCG to reduce the gold chloride. The EGCG-capped AuNPs were further functionalized with PLL and PEG to produce EGCG-capped laminin receptor-avid AuNPs for drug delivery to the mitochondria. The functionalization of NPs with polymers has been reported to improve NP stability, reduce agglomeration, allow for conjugation of bioactive moieties, and importantly, forestall NP immunogenicity while improving stealth properties in vivo [7,39,40]. The covalent attachment of PLL to AuNPs via its amide group has been reported to provide the gold-based nano-delivery system with favorable properties for gene delivery. The many active amino groups of PLL can accept protons at acidic pH and have been observed to significantly promote cell adhesion [41]. The amount of PEG in the formulation was sufficient to promote stabilization and produce NPs and nanocomplexes smaller than 150 nm. Higher densities of PEG may cause the PEG chains to extend further from the NP forming a brush border [42,43]. This may impact on the interaction between the NP and the cells.

The successful synthesis and functionalization of the NPs was confirmed by UV-vis spectroscopy, FTIR and ^1H NMR (Supplementary Materials Figures S1–S3), with NPs and nanocomplexes exhibiting varying color intensities. The magnitude of absorption and wavelength shifts observed from the UV spectra indicate changes in nanoparticle size and stability upon functionalization, due to its impact on the charge density and oscillation of electrons on NP surface. The presence of the AuNPs was confirmed by an excitation peak at 524 nm, while evidence for functionalization with PEG and PLL, and BA encapsulation were observed as red or blueshifts in the SPR, corresponding to a reduction or increase in NP size, respectively. It has been reported that modification of the surface of AuNPs is often denoted by a significant reduction in the absorption intensity in addition to marginal peak shifts [28], with the broadening of a peak suggesting NP aggregation due to low stability [44]. Upon PEG conjugation, a minimal blueshift in peak wavelength from 524 to 522 nm was observed, reflecting a change in the surface property of the NP, as reported previously [45]. TPP⁺ and BA conjugation resulted in a redshift to 542 nm, indicating a size increase, with the broadening of peaks and reduced intensity suggesting a tendency for agglomeration, especially for the T-Au-PEG-BA nanocomplexes. Although T-Au-PEG-BA had high a zeta potential (Table 2), indicating strong stabilizing repulsive forces between the colloidal particles, a mild to severe agglomeration has been associated with increasing ionic strength of NP suspensions in spite of high zeta potential values. It is suspected that an increase in ionic strength upon addition of TPP⁺ to Au-PEG may have impacted on the stability of T-Au-PEG-BA. In contrast, PLL-g-PEG coated NPs demonstrated significant stability, with the redshifts indicating changes in surface properties and size increase. This observed stability may be a combination of its high zeta potential (Table 1), the steric stabilization conferred by PEG, and the high density of positively charged amines on the NP surface which prevented aggregation. Furthermore, T-Au-[PLL-g-PEG]-BA (533 nm) produced a sharp peak and a blueshift compared to T-Au-[PLL-g-PEG] (541 nm) and Au-[PLL-g-PEG] (534 nm) indicating better stability.

For drug loading, BA was coupled to the NP's surface by Steglich esterification between the hydroxyl groups on the NP and the carboxylic groups of BA. Although, the functionalized NPs recorded low (<25%) loading efficiency which was lower than that for porous NPs with efficiencies >50%, the values recorded are higher than the 10% benchmark for ideal nanocarriers [46]. It has been suggested that significant therapeutic effects are achievable at lower drug concentrations for subcellular targets such as the mitochondria, with drug release proposed to involve the action of mitochondrial proteases [47]. NP size, surface charge and shape influence their delivery potential, distribution, clearance, accumulation at intended sites via enhanced permeability retention (EPR) and cellular and organellar interactions [48]. TEM revealed small spherical particles which were dark and dense due to the great light scattering properties of gold. As expected, the size of the NPs using TEM were in contrast with that of the hydrodynamic analysis (NTA) which determines the properties of NPs in an aqueous medium which could have resulted in some swelling of the NPs. NTA is a robust technique that provides the size, dispersity and colloidal stability of a NP in real time, by using laser light scattering to track individual particles based on their Brownian motion [2]. The hydrodynamic diameter, also referred to as the Stokes diameter, takes into consideration the presence of a hydration layer around the NP, and is also dependent on the diameter of the NP corona. The initial hydrodynamic diameter of the AuNPs resulted in size changes upon functionalization, which was not very clear from the TEM images. It has been reported that NPs of the sizes <200 nm have good interaction with the cellular membrane and are readily taken up via clathrin-mediated endocytosis [49,50]. All nanocomplexes in this study were favorably under 150 nm in size. Such small sizes are significant in drug delivery, since these drug nanocarriers can easily escape the leaky tumor vasculature to accumulate at the tumor site and induce their anticancer effects [2].

Zeta potential has become a powerful tool for examining the electrostatic forces within the bulk solution and on the surface of the NPs and nanocomplexes [51]. It is de-fined as

the magnitude of the electrostatic potential generated on the edge of the slipping plane between the particle and the dispersant medium. The NP interacts with the ions in the dispersant medium [52,53]. The zeta potential is a good measure of NP stability, with values of ± 20 mV irrespective of charge being regarded as highly stable. It can also inform on the net surface charge of a NP [54]. When zeta potentials are < -15 or $> +15$ mV, the attractive forces exceed the repulsive forces resulting in NP aggregation [2]. This was evident for Au-[PLL-g-PEG]-BA which had a low zeta potential (11.8 mV) in addition to being larger (147.4 nm) than the other nanocomplexes. Hence, these nanocomplexes had the tendency to aggregate which could account for the large size recorded. T-Au-PEG and T-Au-[PLL-g-PEG] recorded high zeta potential values of -23.1 and $+23.4$ mV, respectively, suggesting stability and low tendency for agglomeration. Since NPs with positive zeta potentials are assumed to interact favorably with anionic cell membranes, it is also possible for NPs with negative zeta potential to enter cells and induce their therapeutic activity [53]. The polydispersity index (PDI) provides us with an indication of the uniformity of a particle size in solution. The larger the PDI value, the larger the size distribution in the sample. The PDI value can also provide an insight into particle aggregation, consistency and the efficiency of the modifications on the NP. Generally, monodisperse samples have PDI values less than 0.1 [32], moderately dispersed samples have PDI values between 0.1 and 0.4, and PDI values > 0.4 have a broad size distribution [40]. Hence, the formulated NPs and nanocomplexes were close to homogeneity with only Au-PEG-BA being moderately dispersed. Importantly, the functionalization of the AuNPs did not greatly affect their dispersity in solution.

Charged NPs generally are capable of indiscriminate interaction with biomolecules, nevertheless, cationic NPs readily associate with the cellular membrane and enjoy significant cellular uptake by cells compared to anionic NPs. The uptake of NPs into cancer cells is mediated via three classical pathways, the clathrin mediated pathway, caveolae dependent endocytosis and macropinocytosis. However, the route of uptake is determined by the size, shape and surface charge of the NPs. Cellular targeting using receptor agonists as the homing moiety for NPs help improve uptake, allows for cell-specific delivery, and precludes toxicity to normal cells [55]. The avidity of the nanocomplexes to the laminin receptor in the presence of the laminin receptor-specific Laminin-R antibody (H-2), suggested that cellular uptake was largely receptor-dependent, with both targeted nanocomplexes recording a marked reduction in uptake in the presence of the antibody. Although cationic NPs are expected to easily cross the cell membrane due to the negative membrane potential across the bilayer, the lower count observed for the T-Au-[PLL-g-PEG] NPs in spite of its cationic nature may be due to its larger size (147 nm compared to the 98 nm of T-Au-PEG).

The high negative membrane potential (-180 mV) perpetuated by oxidative phosphorylation restricts the movement of negatively charged particles into the inner mitochondrial membrane. In its hyperpolarized state, as in cancers, mitochondrial membrane potential may increase to as high as -210 mV, encouraging a high amplitude translocation of cationic molecules across the inner membrane. This is one of the factors responsible for the higher susceptibility of cancer mitochondria to mitochondriotropic agents compared to those of noncancer cells. T-Au-[PLL-g-PEG] due to its highly cationic nature, showed the highest mitochondrial localization compared to Au-[PLL-g-PEG], T-Au-PEG and Au-PEG in all three cell lines. Although, T-Au-PEG also demonstrated appreciable mitochondrial localization, its lower mitochondrial accumulation compared to T-Au-[PLL-g-PEG] in spite of a high cellular uptake, may have been influenced by its negative surface charge hampering its interaction with the hyperpolarized mitochondrial membrane. Studies on the relationship between NP size and mitochondrial uptake reported optimum uptake at a particle size between 80 and 100 nm, with a gradual decline till about 210 nm, after which uptake is negligible [47].

The observed tolerance of NPs and drug loaded nanocomplexes in the noncancer HEK293 cells, compared to the toxicity of the free BA affirms their biocompatibility and potential to prevent cargo-associated toxicity in normal cells. Their negligible impact on

HEK293 cell viability may be associated with their high affinity for the laminin receptor, which is not overexpressed in these cells as in cancer cells, in addition to the normal functional state of the mitochondria in the HEK293 cells. In the cancer cells, drug-loaded nanocomplexes showed significant cytotoxicity compared to the free drug across all concentrations. T-Au-PEG-BA and T-Au[PLL-g-PEG]-BA displayed a concentration dependent inhibition of cell growth in all three cancer cell lines. Cancer cell mitochondria are dysfunctional and significantly hyperpolarized, enhancing the mitochondrial accumulation of cationic or mitochondrial targeted NPs and their cargo [47,56]. This explained their high susceptibility to T-Au-PEG-BA and T-Au[PLL-g-PEG]-BA treatments. Some studies have reported that negatively charged NPs do not readily translocate into the mitochondria due to their high negative membrane potential, while other studies have established the affinity of EGCG to the mitochondria [49,57]. A 90–95% accumulation of radioactive ^3Au -EGCG in the mitochondria of primary cultures of rat cerebellar granule neurons was reported [58]. Hence, T-Au-PEG-BA in spite of its negative surface charge may have been influenced by the EGCG component of the nanocomplex. Overall, the lower impact of free BA on the viability of the cancer cells compared to that of the targeted nanocomplexes emphasizes the challenge of poor pharmacokinetics in chemotherapy, while demonstrating the importance of specialized nanodelivery platforms such as T-Au-PEG and T-Au[PLL-g-PEG] in mitigating this challenge.

Tumors are reliant on anaerobic respiration for energy generation, and mitochondrial membrane hyperpolarization is a consequent anomaly arising from the accumulation of the proton motive force across the inner mitochondria membrane. The dissipation of this membrane potential compromises the mitochondrial membrane integrity, setting-off a cascade of events leading to cell death [59]. While its antiproliferative effect has been linked to a host of mechanisms, the impact of BA on the modulation of apoptotic signaling, the consequent opening of the mitochondria membrane permeability transition pore through ROS generation, and the release of cytochrome c has been established [13,60]. The assessment of the impact of free BA, and the nanocomplexes on mitochondrial membrane potential revealed highly significant membrane depolarizations by T-Au-PEG-BA and T-Au[PLL-g-PEG]-BA compared to the untargeted (Au-PEG-BA and Au-[PLL-g-PEG]-BA), and free BA, highlighting the efficacy of this targeted approach. Moreover, T-Au-[PLL-g-PEG]-BA showed higher depolarization of the cancer cells, compared to T-Au-PEG-BA. Considering the cytotoxicity initially recorded for T-Au-PEG-BA, and its low impact on the mitochondrial membrane potential, attests to the possibility of other cytoplasmic targets, and the induction of non-mitochondrial dependent auxiliary pathways of cell death, as reported by other investigators [60–63].

The cascade of events following the loss of mitochondrial membrane potential due to mitochondrial membrane disruption includes the release of cytochrome c from its intermembrane stores and the activation of initiator caspases, and the subsequent activation of executioner caspases such as caspases 3 and 7. A similar trend to that of the membrane potential analysis was noted, with targeted constructs eliciting the highest percentage of caspase 3/7-mediated cell death compared to both the untargeted and free BA treatments. Overall, T-Au-[PLL-g-PEG]-BA demonstrated a higher efficacy compared to T-Au-PEG-BA, corroborating earlier inference that the comparable cytotoxic effect of T-Au-PEG-BA is likely connected to its impact on other cytoplasmic targets as influenced by its higher cellular uptake and lower mitochondrial localization. Hence, the apparent effectiveness of T-Au-[PLL-g-PEG]-BA may be linked to its superior mitochondria targeting potential as demonstrated in the localization study. These findings further emphasize the potential of efficient mitochondria targeting platforms, especially, T-Au-[PLL-g-PEG] to enhance drug pharmacokinetics. The significant apoptogenic potential of T-Au-[PLL-g-PEG]-BA was again confirmed by fluorescent apoptotic studies employing the AO/EB dual stain.

Studies have established a relationship between cell cycle arrest and caspase dependent apoptosis [64,65]. The upregulation of the p53 protein, its downstream effector, p21, and the downregulation of cyclins D and E, and an arrest at the G1 phase of the cell cycle

are some of the consequent highlights of apoptosis induction [66]. The effect of the targeted nanocomplexes on the cell cycle revealed arrests at the G0/G1 phase compared to the control in all the cells, with T-Au-[PLL-g-PEG]-BA having a significant impact in the Caco-2 and MCF-7 cells, compared to the control, free BA and T-Au-PEG-BA. These findings are in consonance with earlier reports on the effect of BA-rich *Dillenia suffruticosa* root extracts in MCF-7 cells and as well as free BA in oral squamous cell cancer [67,68].

4. Materials and Methods

4.1. Materials

Tetrachloroaurate (III) trihydrate ($\text{HAuCl}_4 \cdot 3\text{H}_2\text{O}$), poly-L-lysine hydrobromide (PLL, Mw 1000–4000), (–)-epigallocatechin gallate (EGCG), N-hydroxysuccinimide (NHS), betulinic acid, N-(3-dimethyl aminopropyl)-N'-ethyl carbodiimide hydrochloride (EDC), 4-(dimethylamino)pyridine (DMAP), (4-Carboxybutyl)triphenyl-phosphonium bromide, dialysis tubing (MWCO 2000) and the bicinchoninic acid (BCA) assay kit were obtained from Sigma-Aldrich, St. Louis, MO, USA. Polyethyleneglycol 2000 (Mw 1800), acridine orange, ethidium bromide, and 3-(4-,5-dimethylthiazol-2-yl)-2,5-diphenyltetrazolium bromide (MTT) were supplied by Merck, Darmstadt, Germany, while cell lysis buffer (5x) was purchased from Promega Corporation, Madison, USA. The Muse[®] cell cycle, caspase and mitopotential kits were sourced from Luminex Corporation, Austin, TX, USA. All other reagents were locally purchased and of analytical grade. The human embryonic kidney (HEK293), colorectal adenocarcinoma (Caco-2), breast adenocarcinoma (MCF-7), and cervical adenocarcinoma (HeLa) cell lines were initially procured from the American Type Culture Collection (ATCC), Manassas, VA, USA. Minimum essential medium (EMEM), trypsin-versene and penicillin/streptomycin (10,000 U/mL penicillin, 10,000 U/mL streptomycin) were obtained from Lonza Bio Whittaker, Verviers, Belgium. Fetal bovine serum (FBS) was supplied by Hyclone, GE Healthcare, Utah, USA. All sterile tissue culture grade plasticware were obtained from Corning Inc. (New York, NY, USA). Cell culture medium was supplemented with 10% FBS and 1% penicillin/streptomycin amphotericin B mixture, and incubated at 37 °C in 5% CO₂.

4.2. Synthesis of EGCG Capped AuNPs

We synthesized EGCG-capped AuNPs by the reduction of hydrogen tetrachloroaurate (III) trihydrate ($\text{HAuCl}_4 \cdot 3\text{H}_2\text{O}$) with EGCG as previously described [21,40]. Briefly, 100 µL of 0.3 mM $\text{HAuCl}_4 \cdot 3\text{H}_2\text{O}$ was added to a 10 mL stirring 0.11 mM solution of EGCG in water. The mixture was stirred for an additional 10 min to allow for complete AuNP formation. Thereafter, the suspension was purified by dialysis (MWCO 2000 Da) against ultrapure water over 12 h. The formation of EGCG capped AuNPs was confirmed by UV spectroscopy.

4.3. Synthesis of AuNP-BA

BA was loaded into the EGCG capped AuNPs by Steglich esterification involving the carboxylic group of BA and the hydroxyl groups of EGCG [69]. BA (0.5 mM) and 4-dimethylaminopyridine (0.4 mM) were dissolved in 2 mL deionized water and stirred for 1 h. The mixture was then added with stirring to the AuNP suspension in a 1:5 final ratio (v/v). Thereafter, EDC (0.134 g, 0.7 mM in 2 mL deionized water) was added dropwise to the mixture, which was stirred overnight at room temperature for the reaction to proceed. The AuNP-BAs were purified by dialysis as in Section 4.2.

4.4. Synthesis of Poly-L-Lysine-Graft-(g)-Polyethylene Glycol Copolymer (PLL-g-PEG)

PEG-imidazole (PEG-CI) was first synthesized. Approximately, 0.2 g of 1, 1'-carbonyl diimidazole (CDI) was dissolved in 10 mL dioxane and added to a 0.1 g dry PEG solution in 25 mL of toluene. The mixture was stirred overnight at 50 °C and concentrated by rotary evaporation. The resultant yellow liquid was diluted with 50 mL dichloromethane and transferred to an ice bath where 20 mL of 1 M NaCl was added while stirring until

effervescence ceased. The organic layer was then separated from the cloudy aqueous layer, washed twice with water and dried for 12 h with anhydrous Na_2SO_4 . The Na_2SO_4 was then filtered and the filtrate concentrated and lyophilized. ^1H NMR (600 MHz, CDCl_3) δ 8.88, 8.11, 7.49, 7.30, 7.29, 3.75, 3.74, 3.74, 3.68, 3.68, 3.67, 3.66, 3.66, 3.63, 3.63, 2.97 (Supplementary Materials Figure S1).

Poly-L-lysine (PLL, 5 mg) was dissolved in freshly prepared sodium borate buffer (pH 9), followed by the addition of 20 mg of PEG-CI (based on the 82% yield) and stirred overnight. The solution was then dialyzed as in Section 4.2, concentrated and lyophilized. ^1H NMR (400 MHz, D_2O) δ 4.70, 4.23, 4.14, 3.62, 3.01, 2.86, 1.81, 1.58, 1.29 (Supplementary Materials Figure S2).

4.5. Synthesis of Triphenylphosphine-PLL-g-PEG (T-PLL-g-PEG)

The synthesis of T-PLL-g-PEG was accomplished by amide coupling between the free carboxylic end of (4-carboxybutyl) triphenyl-phosphonium bromide ($\text{TPP}-(\text{CH}_2)_4-\text{COOH}$) and the free amino groups of PLL. $\text{TPP}-(\text{CH}_2)_4-\text{COOH}$ (0.1 g, 0.226 mM), NHS (0.04 g, 0.339 mM) and EDC (0.0433 g, 0.226 mM) were dissolved in 5 mL of water and stirred for 1 h. To this was added PLL-g-PEG-OH (10 mg/mL) with stirring overnight at room temperature. The product was purified by dialysis as in Section 4.2 for 6 h and then concentrated and lyophilized. ^1H NMR (400 MHz, DMSO) δ 7.90, 7.81, 7.76, 6.07, 6.00, 3.51, 2.99, 2.89, 2.59, 2.46, 2.39, 1.71, 1.61, 0.99 (Supplementary Materials Figure S3).

4.6. Synthesis of T-Au-[PLL-g-PEG]-BA, Au-PLL-g-PEG-BA, and T-Au-PEG-BA

Lyophilized T-(PLL-g-PEG) was resuspended in ultrapure water (2 mg/mL) and added dropwise to a stirring AuNP-BA suspension in a 1:10 (*v/v*) final ratio. The mixture was stirred for 6 h, and thereafter dialyzed overnight against water to remove any unreacted T-(PLL-g-PEG). This procedure was repeated for formation of untargeted constructs using PLL-g-PEG. T-Au-PEG-BA NPs were synthesized by a sequential conjugation of PEG-CI and $\text{TPP}-(\text{CH}_2)_4-\text{COOH}$ to the OH groups on AuNP-BA. A PEG-CI solution (10 mg/mL) was added dropwise to a stirring AuNP-BA suspension (pH 9). The reaction was allowed to proceed overnight, and thereafter dialyzed, as previously for 8 h to remove unreacted PEG-CI. Thereafter, $\text{TPP}-(\text{CH}_2)_4-\text{COOH}$ (0.29 mM) and 4-dimethylaminopyridine (0.29 mM) were dissolved in 2 mL deionized water and stirred for 1 h. The mixture was then added to the AuNP-PEG-BA suspension in a 1:10 final ratio (*v/v*) with stirring. Thereafter, EDC (0.29 mM in 1 mL deionized water) was added dropwise to the stirring mixture. The reaction was allowed to proceed overnight at room temperature and thereafter, the product was purified by dialysis as in Section 4.2.

4.7. Drug Loading Efficiency

A 2 mL aliquot of the NP–drug complex (nanocomplex) was degraded by using 1.0 mM potassium iodide, and then centrifuged at $12,000\times g$ for 10 min to obtain a clear supernatant. The supernatant was subjected to UV-vis spectroscopy at 210 nm, while the corresponding BA concentration was deduced from a standard curve. The procedure was repeated 5 times, and loading efficiency determined from the average by the Equation below:

$$\text{Loading efficiency (\%)} = (\text{Encapsulated drug}) / (\text{Total drug added}) \times 100 \quad (1)$$

4.8. Nanoparticle Characterization

Changes in optical property and stability of the AuNPs upon synthesis and functionalization were monitored via UV-vis spectroscopy (Jasco V-730 Bio Spectrophotometer, JASCO Corporation, Hachioji City, Japan) over a wavelength range of 400–800 nm. Bond formation and functionalization of the AuNPs were determined by changes in absorption bands as evidenced by Fourier Transform Infra-red (FTIR) spectrometry (ATR-FTIR spectroscopy PerkinElmer, Inc. USA). NP shape, size and dispersity were determined from images generated by transmission electron microscopy (TEM) (JEM 1010, JEOL, Tokyo,

Japan). Hydrodynamic diameters, zeta-potential and stability were measured by nanoparticle tracking analysis (NTA) (Nanosight NS500, Malvern, Worcestershire, UK), at 25 °C, and analyzed using the NTA version 3.2 software.

4.9. Cell Culture

All cell culture protocols were conducted under sterile conditions in an Airvolution Class II biosafety laminar flow hood (United Scientific, South Africa). Human colorectal adenocarcinoma (Caco-2), cervical carcinoma (HeLa), breast adenocarcinoma (MCF-7) and embryonic kidney (HEK293) cells were grown as adherent cultures at 37 °C under 5% CO₂ (Steri-Cult CO₂ incubator with class 100 HEPA filtration, Thermo Electron Corporation), in 25 cm² culture flasks containing 5 mL of complete medium (EMEM supplemented with FBS 10% (*v/v*) and antibiotic (100 U/mL penicillin, 100 µg/mL streptomycin, 0.25 µg/mL amphotericin B)). Medium was routinely renewed until cells reached confluency. Confluent cells were trypsinized and cryopreserved, or propagated to increase cells numbers, or seeded into multiwell plates for cell-based experiments. All cell-based experiments were conducted in triplicate.

4.10. Cellular Uptake Studies

Cellular uptake was undertaken in HeLa cells that were seeded in 48-well plates (2.0 × 10³ cells/well) and incubated for 12 h. Cells in selected wells were incubated with the Laminin R antibody (H-2) (5 µg/mL) for 1 h prior to medium replacement. Targeted NPs (T-Au-[PLL-g-PEG] and T-Au-PEG) were then added at 80 µg/mL and cells incubated for 6 h. Thereafter, cells were washed with cold PBS to remove residual medium and NPs. Cells were then trypsinized, lysed and centrifuged at 3000 × *g* for 5 min to remove all cell debris. The resulting supernatant was then filtered through a 30-kDa MWCO Amicon[®] filter (Millipore) to remove other cellular contaminants. The filtrate was analyzed by NTA to determine the constituent nanoparticle concentration. Untreated cells were subjected to the same procedure and served as the control.

4.11. Quantitative Determination of Nanoparticle Distribution by ICP-OES Analysis

Caco-2, HeLa and MCF-7 cells (2.0 × 10⁵/mL) were seeded into 75 cm² flasks, containing 25 mL EMEM and incubated overnight at 37 °C in 5% CO₂. Following medium replacement, 1.58 mg/mL of targeted and untargeted NPs were added, and cells incubated for 12 h at 37 °C in 5% CO₂. The medium was then discarded, and the cells washed 3 times with cold PBS (pH 7.4.) Cells were harvested by trypsinization and subsequent centrifugation at 300 × *g* for 5 min at 4 °C. The cell pellet was resuspended in 50 µL of 10% cell lysis buffer (1×) and placed on ice for 5 min, with vortexing at 1 min intervals. Thereafter, 450 µL of a 0.25 M sucrose buffer (pH 7.4) was added and the cell suspension centrifuged twice at 700 × *g* at 4 °C to remove cellular debris. The supernatant was further centrifuged at 12,000 × *g* for 10 min at 4 °C, to obtain the mitochondrial fraction (pellet), and cytoplasmic fraction (supernatant). The mitochondrial fraction was washed once in sucrose buffer at 10,000 × *g* for 10 min at 4 °C. Both samples were digested in aqua regia (2 h at 90 °C) and subjected to inductively coupled plasma–optical emission spectrometry (ICP-OES) analysis for the determination of elemental gold concentration. ICP-OES was conducted on a Perkin Elmer Optima 5300 DV Optical Emission Spectrometer, and calibrated using 0, 50, 100, 200, 300, 400 and 500 parts per billion (ppb) of Au standard stock solution. Results were expressed in ng/µg protein. The analysis was conducted in triplicate.

4.12. MTT Assay

The MTT cytotoxicity assay determines the percentage viability of a cell population as a function of the ability of live cells to reduce the MTT ((3-(4,5-dimethylthiazol-2-yl)-2,5-diphenyltetrazolium bromide) to formazan by the NAD(P)H dependent oxido-reductase enzyme system [70]. Confluent HEK293, Caco-2, HeLa, and MCF-7 cells were seeded (2.0 × 10³ cells/well) into 96-well plates and incubated overnight at 37 °C in 5% CO₂. The

medium was then replaced, and NPs at varying concentrations were added, followed by incubation at 37 °C in 5% CO₂ for 48 h. At the end of the incubation period, the spent medium was replaced with fresh medium (100 µL) containing 10 µL (5 mg/mL in PBS) MTT reagent, and cells incubated as above for 4 h. Control wells containing untreated cells were treated similarly. Thereafter, the MTT/medium was removed and 100 µL DMSO was added to solubilize the formazan product. Absorbance was read against a DMSO blank at 540 nm using a Mindray MR-96A microplate reader (Vacutec, Hamburg, Germany). Cell viability was determined using the Equation below:

$$\text{Cell Viability (\%)} = (\text{OD}_{\text{treated cells}} / \text{OD}_{\text{control cells}}) \times 100 \quad (2)$$

4.13. Cell Cycle Analysis

Caco-2, HeLa, and MCF-7 cells were seeded (4.0×10^3 cells/well) into 48-well plates and incubated for 12 h (37 °C and 5% CO₂). After medium replacement, cells were treated with both targeted and untargeted nanocomplexes, and free BA at the equimolar BA concentration of 25 µM, and incubated for 48 h. The cells were then rinsed twice with cold PBS (pH 7.4), trypsinized and centrifuged at $300 \times g$ for 5 min. Cells were then washed once with PBS, suspended in 70% cold ethanol, and then incubated for 3 h at −20 °C. Ethanol was removed by centrifugation ($300 \times g$ for 5 min) and cells washed once with PBS. Thereafter, 200 µL of the Muse[®] cell cycle reagent (containing premixed propidium iodide and RNase A), was added to each tube, and incubated for 30 min in the dark, at room temperature. Thereafter, cells were assessed using the Muse[™] cell analyzer (Luminex Corporation, Austin, TX, USA).

4.14. Mitopotential Assay

Cells were seeded and treated as in Section 4.12. After a 48 h incubation, cells were trypsinized, centrifuged at $300 \times g$ for 5 min, washed once with PBS and resuspended in 100 µL PBS. Approximately, 95 µL Muse[®] mitopotential working solution was added to each tube, and cells incubated at 37 °C for 20 min. Thereafter, 5 µL of 7-aminoactinomycin D (7-AAD) was added, followed by incubation at room temperature for 5 min. Mitochondrial membrane potential was assessed using the Muse[™] cell analyzer.

4.15. Caspase 3/7 Analysis

Cells were seeded and treated as in Section 4.12. After incubation, cells were trypsinized, centrifuged and suspended in PBS. To a 50 µL cell suspension, 5 µL caspase-3/7 working reagent was added, and cells incubated at 37 °C for 30 min. Thereafter, 150 µL 7-AAD working solution was added to each tube, thoroughly mixed, and analyzed using the Muse[™] cell analyzer.

4.16. Apoptosis Assay

A qualitative assessment of apoptosis induction in the selected normal and cancer cells was conducted by the acridine orange/ethidium bromide (AO/EB) dual staining method [28]. Cells were seeded as in Section 4.12 and incubated for 24 h at 37 °C in 5% CO₂. Subsequently, the spent medium was replaced, and cells incubated for a further 48 h in the presence of the nanocomplexes and the free drug at their pre-determined IC₅₀ concentrations. Untreated cells were used as controls. After the incubation the cells were washed twice with cold PBS, 15 µL of the AO/EB dye mixture (0.1 mg/mL:0.1 mg/mL) was added, and cells incubated for 5 min at ambient temperature. The cells were then washed with PBS to remove any unabsorbed dye and viewed under an Olympus fluorescence microscope (Wirsam Scientific and Precision Eq. LTD., Johannesburg, South Africa). Images were captured using a CC12 fluorescence camera and Analysis Five Software (Olympus Soft Imaging Solutions, Olympus, Japan) at $200 \times$ magnification.

4.17. Statistical Analysis

Data are presented as mean \pm standard deviation (SD; $n = 3$). Data were analyzed using GraphPad Prism Version 7.3 (GraphPad Software Inc., San Diego, CA, USA). A two-way ANOVA with a post-hoc Tukey test was used to identify significant differences among the groups, while differences between two values were performed using an unpaired Student's *t* test. Differences were considered statistically significant at * $p < 0.05$. All experiments were conducted in triplicate.

5. Conclusions

This study highlights the merit of NP application in drug delivery as a tool for improving drug bioavailability and pharmacokinetics. Furthermore, it provides a proof of concept for the subcellular delivery of therapeutics as an alternative approach to improving selectivity. As demonstrated in this study, the targeted T-Au-[PLL-g-PEG]-BA and T-Au-PEG-BA showed measurable impact at lower doses with negligible side effects in normal cells. They effected significant cytotoxicity in the Caco-2, HeLa and MCF-7 cell lines, compared to the free drug. The underlying mechanism involved the mitochondrial dependent pathway of apoptosis, with T-Au-[PLL-g-PEG]-BA being the most efficient of the nanocomplexes. This study also confirmed the laminin receptor-dependent uptake of EGCG-capped NPs and demonstrated their potential suitability as a platform for mitochondrial targeted delivery of therapeutics, following functionalization. Importantly, we established the proficiency of the T-Au-[PLL-g-PEG] nano-construct as a favorable platform for mitochondrial delivery of BA, with attention to its enabling physicochemical properties. Further research is however required, especially in vivo studies, to assess its potential for clinical applications.

Supplementary Materials: The following are available online at <https://www.mdpi.com/article/10.3390/ijms22105072/s1>, Figure S1: ^1H NMR of PEG-CI in CDCl_3 ; Figure S2: ^1H NMR PLL-g-PEG in D_2O ; Figure S3: ^1H NMR PLL-g-PEG-TPP+ in DMSO.

Author Contributions: Conceptualization, O.O., J.A. and M.S.; methodology, O.O., J.A. and A.D., software, O.O., J.A. and A.D.; validation, M.S. and A.D.; data curation, O.O., J.A. and A.D.; resources, M.S.; writing—original draft preparation, O.O. and J.A.; writing—review and editing, M.S. and A.D.; supervision, M.S.; project administration, M.S.; funding acquisition, M.S. All authors have read and agreed to the published version of the manuscript.

Funding: This research was funded by the National Research Foundation of South Africa, grant numbers 120455 and 129263.

Institutional Review Board Statement: Not applicable.

Informed Consent Statement: Not applicable.

Data Availability Statement: The data and contributions presented in the study are included in the article and Supplementary Materials. Further inquiries can be directed to the corresponding author.

Acknowledgments: The authors acknowledge members of the Nano-Gene and Drug Delivery group for advice and technical support.

Conflicts of Interest: The authors declare no conflict of interest.

References

1. Bray, F.; Ferlay, J.; Soerjomataram, I.; Siegel, R.L.; Torre, L.A.; Jemal, A. Global cancer statistics 2018: GLOBOCAN estimates of incidence and mortality worldwide for 36 cancers in 185 countries. *CA Cancer J. Clin.* **2018**, *68*, 394–424. [[CrossRef](#)]
2. Rais, L.; Masood, A. Sulfur and Nitrogen Co-ordinately Improve Photosynthetic Efficiency, Growth and Proline Accumulation in Two Cultivars of Mustard Under Salt Stress. *J. Plant Biochem. Physiol.* **2013**, *1*. [[CrossRef](#)]
3. Maney, V.; Singh, M. The Synergism of Platinum-Gold Bimetallic Nanoconjugates Enhances 5-Fluorouracil Delivery In Vitro. *Pharmaceutics* **2019**, *11*, 439. [[CrossRef](#)]
4. Wang, W.; Ning, J.-Y.; Liu, J.-T.; Miao, J.-Y.; Zhao, B.-X. A mitochondria-targeted ratiometric fluorescence sensor for the detection of hypochlorite in living cells. *Dye. Pigment.* **2019**, *171*, 107708. [[CrossRef](#)]
5. Tran, S.; DeGiovanni, P.; Piel, B.; Rai, P. Cancer nanomedicine: A review of recent success in drug delivery. *Clin. Transl. Med.* **2017**, *6*, 44. [[CrossRef](#)] [[PubMed](#)]

6. Liu, C.-G.; Han, Y.-H.; Kankala, R.K.; Wang, S.-B.; Chen, A.-Z. Subcellular Performance of Nanoparticles in Cancer Therapy. *Int. J. Nanomed.* **2020**, *15*, 675–704. [[CrossRef](#)] [[PubMed](#)]
7. Akinyelu, J.; Singh, M. Nanomedicines for Subcellular Targeting: The Mitochondrial Perspective. *Curr. Med. Chem.* **2020**, *27*, 5480–5509. [[CrossRef](#)]
8. Neuzil, J.; Dong, L.-F.; Rohlena, J.; Truksa, J.; Ralph, S.J. Classification of mitocans, anti-cancer drugs acting on mitochondria. *Mitochondrion* **2013**, *13*, 199–208. [[CrossRef](#)]
9. Lee, K.L.; Shukla, S.; Wu, M.; Ayat, N.R.; El Sanadi, C.E.; Wen, A.M.; Edelbrock, J.F.; Pokorski, J.K.; Commandeur, U.; Dubyak, G.R.; et al. Stealth filaments: Polymer chain length and conformation affect the in vivo fate of PEGylated potato virus X. *Acta Biomater.* **2015**, *19*, 166–179. [[CrossRef](#)]
10. Hordyjewska, A.; Ostapiuk, A.; Horecka, A.; Kurzepa, J. Betulin and betulinic acid: Triterpenoids derivatives with a powerful biological potential. *Phytochem. Rev.* **2019**, *18*, 929–951. [[CrossRef](#)]
11. Alakurtti, S.; Mäkelä, T.; Koskimies, S.; Yli-Kauhaluoma, J. Pharmacological properties of the ubiquitous natural product betulin. *Eur. J. Pharm. Sci.* **2006**, *29*, 1–13. [[CrossRef](#)] [[PubMed](#)]
12. Fulda, S. Betulinic Acid for Cancer Treatment and Prevention. *Int. J. Mol. Sci.* **2008**, *9*, 1096–1107. [[CrossRef](#)]
13. Chintharlapalli, S.; Papineni, S.; Lei, P.; Pathi, S.; Safe, S. Betulinic acid inhibits colon cancer cell and tumor growth and induces proteasome-dependent and -independent downregulation of specificity proteins (Sp) transcription factors. *BMC Cancer* **2011**, *11*, 371. [[CrossRef](#)] [[PubMed](#)]
14. Ali-Seyed, M.; Jantan, I.; Vijayaraghavan, K.; Bukhari, S.N.A. Betulinic Acid: Recent Advances in Chemical Modifications, Effective Delivery, and Molecular Mechanisms of a Promising Anticancer Therapy. *Chem. Biol. Drug Des.* **2016**, *87*, 517–536. [[CrossRef](#)] [[PubMed](#)]
15. Kovarova, J.; Bajzikova, M.; Vondrusová, M.; Stursa, J.; Goodwin, J.; Nguyen, M.; Zobalova, R.; Pesdar, E.A.; Truksa, J.; Tomasetti, M.; et al. Mitochondrial targeting of α -tocopheryl succinate enhances its anti-mesothelioma efficacy. *Redox Rep.* **2014**, *19*, 16–25. [[CrossRef](#)] [[PubMed](#)]
16. Dahoumane, S.A.; Jeffryes, C.; Mechouet, M.; Agathos, S.N. Biosynthesis of Inorganic Nanoparticles: A Fresh Look at the Control of Shape, Size and Composition. *Bioengineers* **2017**, *4*, 14. [[CrossRef](#)]
17. Castronovo, V.; Campo, E.; Brùle, F.A.V.D.; Claysmith, A.P.; Cioce, V.; Liu, F.-T.; Fernandez, P.L.; Sobel, M.E. Inverse Modulation of Steady-State Messenger RNA Levels of Two Non-Integrin Laminin-Binding Proteins in Human Colon Carcinoma. *J. Natl. Cancer Inst.* **1992**, *84*, 1161–1169. [[CrossRef](#)] [[PubMed](#)]
18. Basolo, F.; Pollina, L.; Pacini, F.; Fontanini, G.; Ménard, S.; Castronovo, V.; Bevilacqua, G. Expression of the Mr 67,000 laminin receptor is an adverse prognostic indicator in human thyroid cancer: An immunohistochemical study. *Clin. Cancer Res.* **1996**, *2*, 1777–1780. [[PubMed](#)]
19. Satoh, K.; Narumi, K.; Abe, T.; Sakai, T.; Kikuchi, T.; Tanaka, M.; Shimo-Oka, T.; Uchida, M.; Tezuka, F.; Isemura, M.; et al. Diminution of 37-kDa laminin binding protein expression reduces tumour formation of murine lung cancer cells. *Br. J. Cancer* **1999**, *80*, 1115–1122. [[CrossRef](#)]
20. Tachibana, H.; Koga, K.; Fujimura, Y.; Yamada, K. A receptor for green tea polyphenol EGCG. *Nat. Struct. Mol. Biol.* **2004**, *11*, 380–381. [[CrossRef](#)]
21. Shukla, R.; Chanda, N.; Zambre, A.; Upendran, A.; Katti, K.V.; Kulkarni, R.R.; Nune, S.K.; Casteel, S.W.; Smith, C.J.; Vimal, J.; et al. Laminin receptor specific therapeutic gold nanoparticles (198AuNP-EGCG) show efficacy in treating prostate cancer. *Proc. Natl. Acad. Sci. USA* **2012**, *109*, 12426–12431. [[CrossRef](#)] [[PubMed](#)]
22. Amgoth, C.; Phan, C.; Banavoth, M.; Rompivalasa, S.; Tang, G. Polymer Properties: Functionalization and Surface Modified Nanoparticles. In *Role of Novel Drug Delivery Vehicles in Nanobiomedicine*; IntechOpen: London, UK, 2020; p. 446.
23. Yang, D.H.; Kim, H.J.; Park, K.; Kim, J.K.; Chun, H.J. Preparation of poly-L-lysine-based nanoparticles with pH-sensitive release of curcumin for targeted imaging and therapy of liver cancer in vitro and in vivo. *Drug Deliv.* **2018**, *25*, 950–960. [[CrossRef](#)] [[PubMed](#)]
24. Zheng, M.; Pan, M.; Zhang, W.; Lin, H.; Wu, S.; Lu, C.; Tang, S.; Liu, D.; Cai, J. Poly(α -L-lysine)-based nanomaterials for versatile biomedical applications: Current advances and perspectives. *Bioact. Mater.* **2021**, *6*, 1878–1909. [[CrossRef](#)] [[PubMed](#)]
25. Peltonen, L.; Singhal, M.; Hirvonen, J. Principles of nanosized drug delivery systems. In *Nanoengineered Biomaterials for Advanced Drug Delivery*; Elsevier BV: Amsterdam, The Netherlands, 2020; pp. 3–25.
26. Desai, R.; Mankad, V.; Gupta, S.; Jha, P. Size Distribution of Silver Nanoparticles: UV-Visible Spectroscopic Assessment. *Nanosci. Nanotechnol. Lett.* **2012**, *4*, 30–34. [[CrossRef](#)]
27. Mourdikoudis, S.; Pallares, R.M.; Thanh, N.T.K. Characterization techniques for nanoparticles: Comparison and complementarity upon studying nanoparticle properties. *Nanoscale* **2018**, *10*, 12871–12934. [[CrossRef](#)]
28. Akinyelu, J.; Singh, M. Folate-tagged chitosan-functionalized gold nanoparticles for enhanced delivery of 5-fluorouracil to cancer cells. *Appl. Nanosci.* **2018**, *9*, 7–17. [[CrossRef](#)]
29. Akinyelu, J.; Oladimeji, O.; Singh, M. Lactobionic acid-chitosan functionalised gold-coated poly(lactide-co-glycolide) nanoparticles for hepatocyte targeted gene delivery. *Adv. Nat. Sci. Nanosci. Nanotechnol.* **2020**, *11*, 045017. [[CrossRef](#)]
30. Coates, J. Interpretation of Infrared Spectra, A Practical Approach. In *Encyclopedia of Analytical Chemistry: Applications, Theory and Instrumentation*; John Wiley & Sons Ltd.: Chichester, UK, 2000; pp. 10815–10837.

31. Cinta-Pinzaru, S.; Dehelean, C.A.; Soica, C.; Culea, M.; Borcan, F. Evaluation and differentiation of the Betulaceae birch bark species and their bioactive triterpene content using analytical FT-vibrational spectroscopy and GC-MS. *Chem. Central J.* **2012**, *6*, 67. [[CrossRef](#)]
32. Clayton, K.N.; Salameh, J.W.; Wereley, S.T.; Kinzer-Ursem, T.L. Physical characterization of nanoparticle size and surface modification using particle scattering diffusometry. *Biomicrofluidics* **2016**, *10*, 054107. [[CrossRef](#)]
33. Fujimura, Y.; Sumida, M.; Sugihara, K.; Tsukamoto, S.; Yamada, K.; Tachibana, H. Green Tea Polyphenol EGCG Sensing Motif on the 67-kDa Laminin Receptor. *PLoS ONE* **2012**, *7*, e37942. [[CrossRef](#)] [[PubMed](#)]
34. Moodley, K.; Weiss, S.F.T. Downregulation of the Non-Integrin Laminin Receptor Reduces Cellular Viability by Inducing Apoptosis in Lung and Cervical Cancer Cells. *PLoS ONE* **2013**, *8*, e57409. [[CrossRef](#)]
35. Rzeski, W.; Stepulak, A.; Szymański, M.; Juszczak, M.; Grabarska, A.; Sifringer, M.; Kaczor, J.; Kandefor-Szerszeń, M. Betulin Elicits Anti-Cancer Effects in Tumour Primary Cultures and Cell Lines In Vitro. *Basic Clin. Pharmacol. Toxicol.* **2009**, *105*, 425–432. [[CrossRef](#)] [[PubMed](#)]
36. Liu, X.; Jutooru, I.; Lei, P.; Kim, K.; Lee, S.-O.; Brents, L.K.; Prather, P.L.; Safe, S. Betulinic Acid Targets YY1 and ErbB2 through Cannabinoid Receptor-Dependent Disruption of MicroRNA-27a:ZBTB10 in Breast Cancer. *Mol. Cancer Ther.* **2012**, *11*, 1421–1431. [[CrossRef](#)] [[PubMed](#)]
37. Boukalova, S.; Rohlenova, K.; Rohlena, J.; Neuzil, J. Mitocans: Mitochondrially Targeted Anti-cancer Drugs. In *Mitochondrial Biology and Experimental Therapeutics*; Springer: Cham, Switzerland, 2018; pp. 613–635.
38. Cai, Y.; Zheng, Y.; Gu, J.; Wang, S.; Wang, N.; Yang, B.; Zhang, F.; Wang, D.; Fu, W.; Wang, Z. Betulinic acid chemosensitizes breast cancer by triggering ER stress-mediated apoptosis by directly targeting GRP78. *Cell Death Dis.* **2018**, *9*, 636. [[CrossRef](#)] [[PubMed](#)]
39. Amoozgar, Z.; Yeo, Y. Recent advances in stealth coating of nanoparticle drug delivery systems. *Wiley Interdiscip. Rev. Nanomed. Nanobiotechnol.* **2012**, *4*, 219–233. [[CrossRef](#)]
40. Oladimeji, O.; Akinyelu, J.; Singh, M. Co-Polymer Functionalised Gold Nanoparticles Show Efficient Mitochondrial Targeted Drug Delivery in Cervical Carcinoma Cells. *J. Biomed. Nanotechnol.* **2020**, *16*, 853–866. [[CrossRef](#)] [[PubMed](#)]
41. Lazarus, G.G.; Singh, M. Cationic modified gold nanoparticles show enhanced gene delivery in vitro. *Nanotechnol. Rev.* **2016**, *5*, 425–434. [[CrossRef](#)]
42. Barenholz, Y. Liposome application: Problems and prospects. *Curr. Opin. Colloid Interface Sci.* **2001**, *6*, 66–77. [[CrossRef](#)]
43. Narainpersad, N.; Singh, M.; Ariatti, M. Novel Neo Glycolipid: Formulation into Pegylated Cationic Liposomes and Targeting of DNA Lipoplexes to the Hepatocyte-Derived Cell Line HepG₂. *Nucleosides Nucleotides Nucleic Acids* **2012**, *31*, 206–223. [[CrossRef](#)] [[PubMed](#)]
44. Huang, X.; El-Sayed, M.A. Gold nanoparticles: Optical properties and implementations in cancer diagnosis and photothermal therapy. *J. Adv. Res.* **2010**, *1*, 13–28. [[CrossRef](#)]
45. Kudgus, R.A.; Walden, C.A.; McGovern, R.M.; Reid, J.M.; Robertson, J.D.; Mukherjee, P. Tuning Pharmacokinetics and Biodistribution of a Targeted Drug Delivery System Through Incorporation of a Passive Targeting Component. *Sci. Rep.* **2014**, *4*, 5669. [[CrossRef](#)] [[PubMed](#)]
46. Shen, S.; Wu, Y.; Liu, Y.; Wu, D. High drug-loading nanomedicines: Progress, current status, and prospects. *Int. J. Nanomed.* **2017**, *12*, 4085–4109. [[CrossRef](#)] [[PubMed](#)]
47. Marrache, S.; Dhar, S. The energy blocker inside the power house: Mitochondria targeted delivery of 3-bromopyruvate. *Chem. Sci.* **2014**, *6*, 1832–1845. [[CrossRef](#)] [[PubMed](#)]
48. Greish, K.; Mathur, A.; Bakhiet, M.; Taurin, S. Nanomedicine: Is it lost in translation? *Ther. Deliv.* **2018**, *9*, 269–285. [[CrossRef](#)] [[PubMed](#)]
49. Marrache, S.; Dhar, S. Engineering of blended nanoparticle platform for delivery of mitochondria-acting therapeutics. *Proc. Natl. Acad. Sci. USA* **2012**, *109*, 16288–16293. [[CrossRef](#)] [[PubMed](#)]
50. Shang, L.; Nienhaus, K.; Nienhaus, G.U. Engineered nanoparticles interacting with cells: Size matters. *J. Nanobiotechnol.* **2014**, *12*, 5. [[CrossRef](#)] [[PubMed](#)]
51. Rodríguez-Pulido, A.; Martín-Molina, A.; Rodríguez-Beas, C.; Llorca, O.; Aicart, E.; Junquera, E.; Sospedra, E.A. A Theoretical and Experimental Approach to the Compaction Process of DNA by Dioctadecyldimethylammonium Bromide/Zwitterionic Mixed Liposomes. *J. Phys. Chem. B* **2009**, *113*, 15648–15661. [[CrossRef](#)] [[PubMed](#)]
52. Maney, V.; Singh, M. An in vitro assessment of novel chitosan/bimetallic PtAu nanocomposites as delivery vehicles for doxorubicin. *Nanomedicine* **2017**, *12*, 2625–2640. [[CrossRef](#)] [[PubMed](#)]
53. Habib, S.; Daniels, A.; Ariatti, M.; Singh, M. Anti-c-myc cholesterol based lipoplexes as onco-nanotherapeutic agents in vitro. *F1000Research* **2020**, *9*, 770. [[CrossRef](#)]
54. Samimi, S.; Maghsoudnia, N.; Eftekhari, R.B.; Dorkoosh, F. *Lipid-Based Nanoparticles for Drug Delivery Systems*; Elsevier BV: Amsterdam, The Netherlands, 2019; pp. 47–76.
55. Foroozandeh, P.; Aziz, A.A. Insight into Cellular Uptake and Intracellular Trafficking of Nanoparticles. *Nanoscale Res. Lett.* **2018**, *13*, 1–12. [[CrossRef](#)]
56. Boukalova, S.; Stursa, J.; Werner, L.; Ezrova, Z.; Cerny, J.; Bezawork-Geleta, A.; Pecinova, A.; Dong, L.; Drahota, Z.; Neuzil, J. Mitochondrial Targeting of Metformin Enhances Its Activity against Pancreatic Cancer. *Mol. Cancer Ther.* **2016**, *15*, 2875–2886. [[CrossRef](#)] [[PubMed](#)]

57. Piyaviriyakul, S.; Shimizu, K.; Asakawa, T.; Kan, T.; Siripong, P.; Oku, N. Anti-angiogenic Activity and Intracellular Distribution of Epigallocatechin-3-gallate Analogs. *Biol. Pharm. Bull.* **2011**, *34*, 396–400. [[CrossRef](#)] [[PubMed](#)]
58. Schroeder, E.K.; Kelsey, N.A.; Doyle, J.; Breed, E.; Bouchard, R.J.; Loucks, F.A.; Harbison, R.A.; Linseman, D.A. Green Tea Epigallocatechin 3-Gallate Accumulates in Mitochondria and Displays a Selective Antiapoptotic Effect Against Inducers of Mitochondrial Oxidative Stress in Neurons. *Antioxid. Redox Signal.* **2009**, *11*, 469–480. [[CrossRef](#)] [[PubMed](#)]
59. Dong, L.; Neuzil, J. Targeting mitochondria as an anticancer strategy. *Cancer Commun.* **2019**, *39*, 63–73. [[CrossRef](#)] [[PubMed](#)]
60. Saeed, M.E.M.; Mahmoud, N.; Sugimoto, Y.; Efferth, T.; Abdel-Aziz, H. Betulinic Acid Exerts Cytotoxic Activity Against Multidrug-Resistant Tumor Cells via Targeting Autocrine Motility Factor Receptor (AMFR). *Front. Pharmacol.* **2018**, *9*, 481. [[CrossRef](#)] [[PubMed](#)]
61. Rieber, M.; Rieber, M.S. Induction of p53 Without Increase in p21WAF1 in Betulinic Acid-Mediated Cell Death Is Preferential for Human Metastatic Melanoma. *DNA Cell Biol.* **1998**, *17*, 399–406. [[CrossRef](#)] [[PubMed](#)]
62. Chowdhury, A.R.; Mandal, S.; Mitra, B.; Sharma, S.; Mukhopadhyay, S.; Majumder, H.K. Betulinic acid, a potent inhibitor of eukaryotic topoisomerase I: Identification of the inhibitory step, the major functional group responsible and development of more potent derivatives. *Med. Sci. Monit.* **2002**, *8*, 254–265.
63. Kessler, J.H.; Mullauer, F.B.; De Roo, G.M.; Medema, J.P. Broad in vitro efficacy of plant-derived betulinic acid against cell lines derived from the most prevalent human cancer types. *Cancer Lett.* **2007**, *251*, 132–145. [[CrossRef](#)] [[PubMed](#)]
64. Pucci, B.; Kasten, M.; Giordano, A. Cell Cycle and Apoptosis. *Neoplasia* **2000**, *2*, 291–299. [[CrossRef](#)] [[PubMed](#)]
65. Alabsi, A.M.; Lim, K.L.; Paterson, I.C.; Ali-Saeed, R.; Muharram, B.A. Cell Cycle Arrest and Apoptosis Induction via Modulation of Mitochondrial Integrity by Bcl-2 Family Members and Caspase Dependence in *Dracaena cinnabari*-Treated H400 Human Oral Squamous Cell Carcinoma. *BioMed Res. Int.* **2016**, *2016*, 1–13. [[CrossRef](#)] [[PubMed](#)]
66. Li, J.; Li, T.-X.; Ma, Y.; Zhang, Y.; Li, D.-Y.; Xu, H.-R. Bursopentin (BP5) induces G1 phase cell cycle arrest and endoplasmic reticulum stress/mitochondria-mediated caspase-dependent apoptosis in human colon cancer HCT116 cells. *Cancer Cell Int.* **2019**, *19*, 130. [[CrossRef](#)] [[PubMed](#)]
67. Foo, J.B.; Yazan, L.S.; Tor, Y.S.; Wibowo, A.; Ismail, N.; How, C.W.; Armania, N.; Loh, S.P.; Ismail, I.S.; Cheah, Y.K.; et al. Induction of cell cycle arrest and apoptosis by betulinic acid-rich fraction from *Dillenia suffruticosa* root in MCF-7 cells involved p53/p21 and mitochondrial signalling pathway. *J. Ethnopharmacol.* **2015**, *166*, 270–278. [[CrossRef](#)] [[PubMed](#)]
68. Shen, H.; Liu, L.; Yang, Y.; Xun, W.; Wei, K.; Zeng, G. Betulinic Acid Inhibits Cell Proliferation in Human Oral Squamous Cell Carcinoma via Modulating ROS-Regulated p53 Signaling. *Oncol. Res. Featur. Preclin. Clin. Cancer Ther.* **2017**, *25*, 1141–1152. [[CrossRef](#)] [[PubMed](#)]
69. Neises, B.; Steglich, W. Simple Method for the Esterification of Carboxylic Acids. *Angew. Chem. Int. Ed.* **1978**, *17*, 522–524. [[CrossRef](#)]
70. Mosmann, T. Rapid colorimetric assay for cellular growth and survival: Application to proliferation and cytotoxicity assays. *J. Immunol. Methods* **1983**, *65*, 55–63. [[CrossRef](#)]



Article

Topical Capsaicin in Poly(lactic-co-glycolic)acid (PLGA) Nanoparticles Decreases Acute Itch and Heat Pain

Nathalie M. Malewicz^{1,2,*}, Zahra Rattray³, Sebastian Oeck^{4,5}, Sebastian Jung^{1,6},
Vicente Escamilla-Rivera^{1,7}, Zeming Chen⁸, Xiangjun Tang⁸, Jiangbing Zhou⁸ and Robert H. LaMotte^{1,*}

- ¹ Department of Anesthesiology, Yale University School of Medicine, 330 Cedar St, New Haven, CT 06510, USA; sebastian.jung@rub.de (S.J.); vicentee@arizona.edu (V.E.-R.)
 - ² Clinics for Anesthesiology, Intensive Care and Pain Medicine, Medical Faculty of Ruhr-University Bochum, BG University Hospital Bergmannsheil, 44789 Bochum, Germany
 - ³ Strathclyde Institute of Pharmacy and Biomedical Sciences, University of Strathclyde, Glasgow G4 0RE, UK; zahra.rattray@strath.ac.uk
 - ⁴ Department of Therapeutic Radiology, Yale University School of Medicine, New Haven, CT 06510, USA; sebastian.oeck@uk-essen.de
 - ⁵ Department of Medical Oncology, West German Cancer Center, University Hospital Essen, 45147 Essen, Germany
 - ⁶ ZEMOS Center for Solvation Science, Ruhr University Bochum, 44801 Bochum, Germany
 - ⁷ Department of Otolaryngology—Head and Neck Surgery, College of Medicine, The University of Arizona, Tucson, AZ 85724, USA
 - ⁸ Department of Neurosurgery, Yale University School of Medicine, New Haven, CT 06510, USA; czeming@hotmail.com (Z.C.); xiangjun.tang@yale.edu (X.T.); jiangbing.zhou@yale.edu (J.Z.)
- * Correspondence: nathalie.malewicz@rub.de (N.M.M.); robert.lamotte@yale.edu (R.H.L.)



Citation: Malewicz, N.M.; Rattray, Z.; Oeck, S.; Jung, S.; Escamilla-Rivera, V.; Chen, Z.; Tang, X.; Zhou, J.; LaMotte, R.H. Topical Capsaicin in Poly(lactic-co-glycolic)acid (PLGA) Nanoparticles Decreases Acute Itch and Heat Pain. *Int. J. Mol. Sci.* **2022**, *23*, 5275. <https://doi.org/10.3390/ijms23095275>

Academic Editor: Daniel Arcos

Received: 4 April 2022

Accepted: 6 May 2022

Published: 9 May 2022

Publisher's Note: MDPI stays neutral with regard to jurisdictional claims in published maps and institutional affiliations.



Copyright: © 2022 by the authors. Licensee MDPI, Basel, Switzerland. This article is an open access article distributed under the terms and conditions of the Creative Commons Attribution (CC BY) license (<https://creativecommons.org/licenses/by/4.0/>).

Abstract: Background: Capsaicin, the hot pepper agent, produces burning followed by desensitization. To treat localized itch or pain with minimal burning, low capsaicin concentrations can be repeatedly applied. We hypothesized that alternatively controlled release of capsaicin from poly(lactic-co-glycolic acid) (PLGA) nanoparticles desensitizes superficially terminating nociceptors, reducing burning. Methods: Capsaicin-loaded PLGA nanoparticles were prepared (single-emulsion solvent evaporation) and characterized (size, morphology, capsaicin loading, encapsulation efficiency, in vitro release profile). Capsaicin-PLGA nanoparticles were applied to murine skin and evaluated in healthy human participants (n = 21) for 4 days under blinded conditions, and itch and nociceptive sensations evoked by mechanical, heat stimuli and pruritogens cowhage, β -alanine, BAM8-22 and histamine were evaluated. Results: Nanoparticles (loading: 58 μ g capsaicin/mg) released in vitro 23% capsaicin within the first hour and had complete release at 72 h. In mice, 24 h post-application Capsaicin-PLGA nanoparticles penetrated the dermis and led to decreased nociceptive behavioral responses to heat and mechanical stimulation (desensitization). Application in humans produced a weak to moderate burning, dissipating after 3 h. A loss of heat pain up to 2 weeks was observed. After capsaicin nanoparticles, itch and nociceptive sensations were reduced in response to pruritogens cowhage, β -alanine or BAM8-22, but were normal to histamine. Conclusions: Capsaicin nanoparticles could be useful in reducing pain and itch associated with pruritic diseases that are histamine-independent.

Keywords: capsaicin; nanoparticles; human; pruritogens; desensitization; itch

1. Introduction

A persistent itch that accompanies neurological, dermatological and systemic diseases can cause suffering and a loss in the quality of life [1]. While receptors for pruritogens are expressed in cutaneous nociceptors, there are few treatments that block the pathological transmission of pruritic information in these neurons in disorders causing acute or chronic itch. There are two types of pruriceptive nociceptors that transduce and transmit

pruritic information from the skin [2–4]. One type responds to noxious mechanical and heat stimuli and to pruritogens that elicit a histamine independent itch [5]. These pruritogens include cysteine proteases, such as mucunain in the trichomes of cowhage, β -alanine, and bovine adrenal medulla 8-22 (BAM8-22) [5–10]. The other type of pruriceptive nociceptor is mechanically insensitive and responds to histamine [11–13]. In humans, monkeys and mice, pruriceptive nociceptors responsive to histamine or histamine-independent pruritogens typically express TRPV1, a non-selective cation channel responsive to capsaicin and noxious heat [14–16]. Thus, one treatment for itch that has shown some effectiveness is the topical application of capsaicin, which activates these nociceptors, leading to a longer lasting desensitization [17]. Commercially available topical preparations of capsaicin containing different concentrations have been used in the management of cutaneous neuropathic sensations including post-herpetic pain [18–20], brachioradial pruritus, and atopic dermatitis [21,22]. In an experimental study, daily topical application of capsaicin in humans elicited a persistent burning pain. After four days, there was a loss of transient heat pain and itch in response to cowhage spicules [23]. The itch to intradermal injection of histamine was unaffected by capsaicin. However, responses to β -alanine and BAM8-22 were not tested. In other studies, the transdermal delivery of higher concentrations of capsaicin, (e.g., 8% capsaicin in the Qutenza patch over 24 h) reduced or eliminated both histamine-dependent and histamine-independent itch and heat pain [24,25]. However, a major adverse event of capsaicin application experienced by patients is the painful burning sensation associated with the application of capsaicin. To treat localized itch or pain in humans through desensitization with low burning, very low concentrations of capsaicin are applied several times daily over a prolonged period of time. Strategies including the encapsulation of capsaicin in controlled release systems, such as poly(lactic-co-glycolic acid) nanoparticles (PLGA NPs) could reduce these adverse effects associated with capsaicin application. The slow-release effect of PLGA NPs as a carrier for bupivacaine or opioids to reduce nociceptive behavior in mice has been studied previously [26–28].

In the present study, we test the hypothesis that at single application of controlled release capsaicin-loaded PLGA NPs, over a period of hours to days, can achieve desensitization to histamine-independent pruritogens and to transient noxious heat, while eliciting a minimal ongoing burning pain sensation.

2. Results

2.1. Physicochemical Attributes of NPs

SEM analysis showed that both blank and capsaicin PLGA NPs are spherical in morphology and uniform in size (Figure 1A,B). All NPs were spherical in morphology, with a corresponding diameter of 108.11 ± 17.36 and 110.45 ± 18.33 nm as determined by analysis of SEM micrographs. No statistically significant difference in size was noted between blank and capsaicin NPs (Figure 1E). Data obtained from the dynamic light scattering analysis of capsaicin NP intensity-based particle size distribution showed a unimodal size distribution (Figure 1C), with a corresponding peak occurring at approximately 250 nm and a polydispersity index of 0.157. The zeta potential for capsaicin PLGA NPs was determined as -17.53 ± 0.13 mV.

Capsaicin drug loading and encapsulation efficiencies were determined using a capsaicin ELISA kit. Capsaicin loading was determined to be 58.01 ± 5.87 μ g per 1 mg for capsaicin-loaded PLGA NPs, and 0 μ g per 1 mg of blank PLGA NPs. Therefore, capsaicin loading was measured as 5.8% by weight, and the corresponding encapsulation efficiency was determined to be 16.57%.

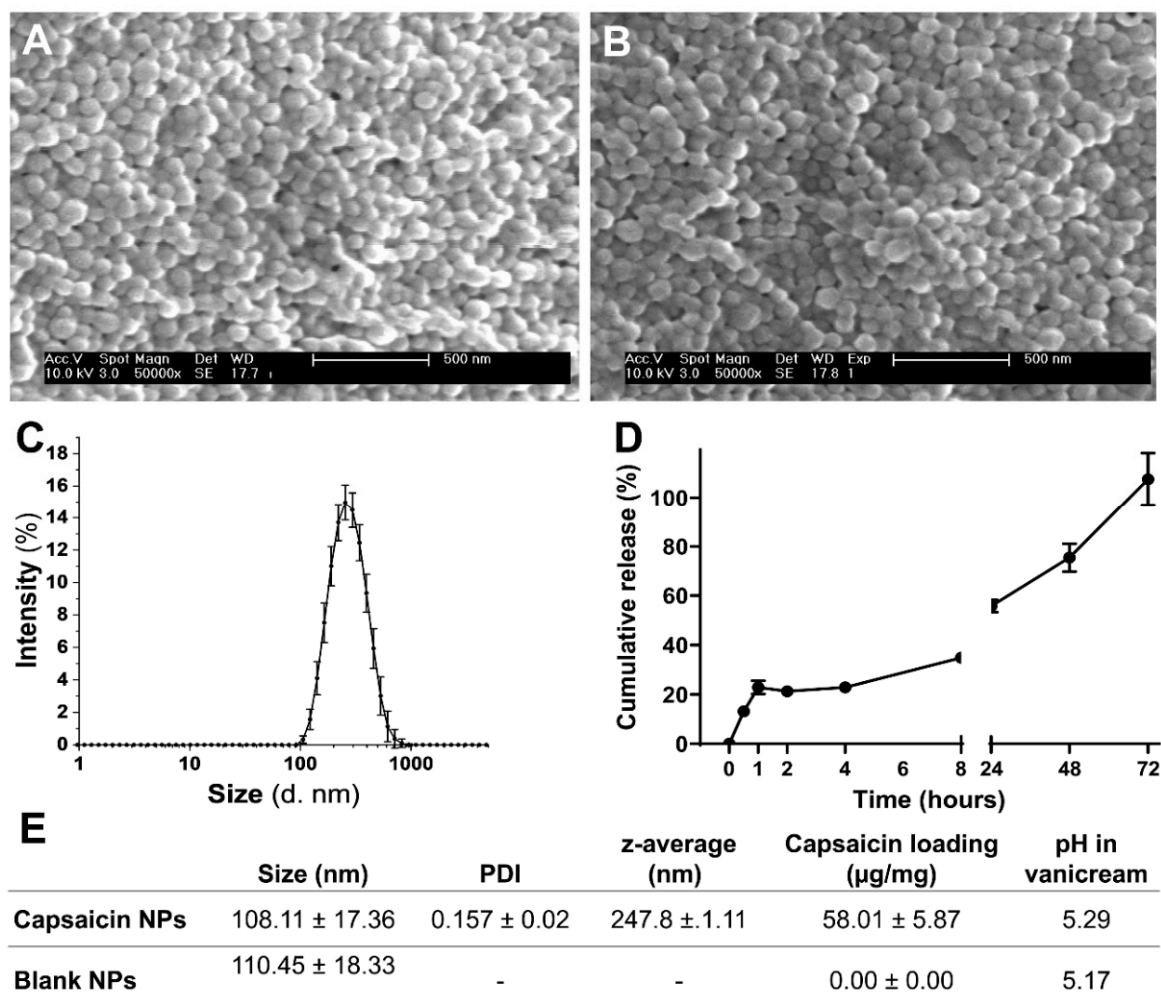


Figure 1. Characterization of the physicochemical attributes of NPs. (A) SEM of capsaicin NPs. (B) SEM of blank NPs. Scale bar is 500 nm. (C) Intensity-based particle size distribution as measured by dynamic light scattering. (D) Cumulative in vitro release of capsaicin from NPs over time under agitation. (E) Measurements of size, capsaicin loading, encapsulation efficiency and pH (in Vanicream) for capsaicin-loaded and blank NPs. Mean ± SEM.

In vitro capsaicin release from PLGA NPs under agitation showed an initial capsaicin release of approximately 22.9% from the NPs within the first hour (Figure 1B). This initial burst, leading to a release of 34% of the payload at 8 h, of capsaicin release from PLGA NPs continually increased until reaching a peak at about 72 h (Figure 1D).

The pH of Vanicream (5.28) was not changed by the addition of capsaicin-loaded (5.29) and blank PLGA NPs (5.17) (Figure 1E). The resultant pH was appropriate as to minimize pH-related irritation following topical application.

2.2. In Vivo Quantification of Capsaicin

The amount of capsaicin in murine cheek skin after 24 h of treatment with capsaicin NPs was measured as 0.16 µg/mL in 6 µg/µL total protein. In comparison, skin in which 30 µg of capsaicin was intradermally injected before harvesting exhibited a slightly higher amount of 0.25 µg/mL. In contrast, the amount of capsaicin in the skin treated with blank NPs was 0 µg/mL.

The in vivo skin penetration ability of capsaicin NPs containing red dye into the skin of the cheek was also assessed. The red colored areas were measured relative to the unstained skin. Untreated control tissue had only small amounts of red stain detected in 1 of 18 samples in the dermis and 3 of 18 in the epidermis, most likely due to autofluorescence

of high-density areas of the tissue (Figure 2A). Blank NPs and capsaicin NPs (Figure 2B,C) showed insignificantly higher amounts of red stain in the dermis and epidermis possibly due to agglomerated NPs. The amount of red stain after DiL NPs was detectable in all samples in the epidermis and in 17 of 18 samples in the dermis, mainly located in more superficial regions (Figure 2D). The amount of staining for the DiL NPs was significantly higher than in control tissue or tissue exposed to blank or capsaicin NPs (Figure 2E). This finding is consistent with a good penetration with NPs.

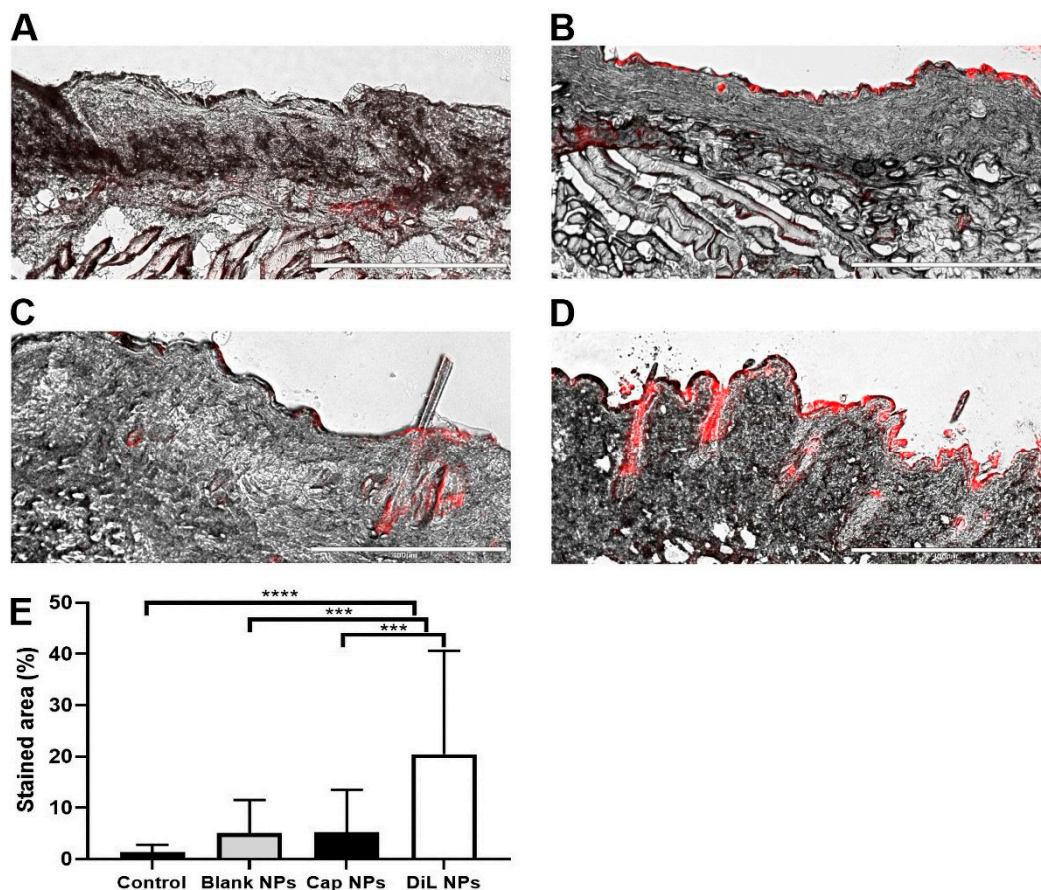


Figure 2. Intracutaneous penetration of NPs topically applied to the skin in the mouse. Exemplary microscope images (Scale bar is 400 μm) of (A) a potential autofluorescence (red area) of untreated skin from mouse cheek, (B) after treatment with blank NPs, (C) after treatment with capsaicin NPs, (D) treated with red dye (red area) containing DiL NPs. (E) Mean values of red color measured in cheek tissue from 18 samples per group. *** $p < 0.001$, **** $p < 0.0001$, mean \pm SD, one-way ANOVA with Bonferroni correction.

2.3. Behavioral Responses of Mice to Mechanical and Heat Stimuli

Mice were scored for aversive behavioral responses to punctate mechanical indentation and heat stimulation of the cheek prior to and 24 h after application of a Finn chamber containing either blank NPs or capsaicin-loaded NPs. In comparison with scores obtained before NP application, mice receiving capsaicin NPs exhibited significantly lower discomfort scores to filament indentations of 2, 20 and 20 mN and to the heat stimulus of 52 $^{\circ}\text{C}$ (Figure 3A,B). Responses to the lowest filament force of 0.23 mN and to the heat stimulus of 38 $^{\circ}\text{C}$ remained unchanged. In contrast, discomfort scores remained the same in response to each force of indentation and stimulus temperature before vs. after the application of blank NPs.

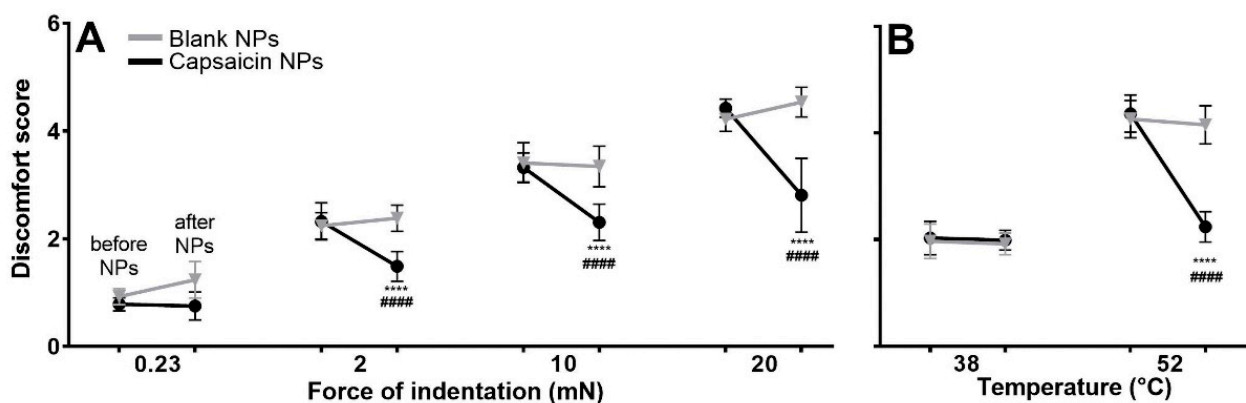


Figure 3. Discomfort scores to mechanical and heat stimuli applied to the cheek. The mechanical stimuli were produced by application of von-Frey type filaments with indentation forces (and tip diameters) of 0.23 mN (67 μ m) and 2, 10 and 20 mN (100 μ m). Heat stimuli were applied by a thermode preheated to the indicated temperature. Each stimulus was applied prior to and 24 h following removal of NPs. (**** $p < 0.0001$) for significance before and after treatment, ##### indicating significant differences between the blank vs. capsaicin NPs groups $p < 0.0001$, error bars: SD $n = 10$ male mice per group. RMANOVA—2 within timepoints (before, after treatment) \times treatments (capsaicin vs. blank NPs) \times forces (0.23, 2, 10, 20 mN) for (A) and temperatures for (B) (38, 52 $^{\circ}$ C) with Bonferroni correction.

For human subjects, the highest indentation force and the heat stimulus of 50 $^{\circ}$ C, but not the two lowest forces or 39 $^{\circ}$ C stimulus, readily elicited pain when applied to the volar forearm. Thus, capsaicin NPs decreased the aversive behavior of mice to stimuli that are nociceptive for humans (Figure 3B).

2.4. Evaluation of the Sensations Evoked by Treatment with Capsaicin PLGA NPs in Humans

Subjects used the generalized labeled magnitude scale [10,29,30] to rate the average perceived intensity of any burning, pricking/stinging and pain sensation originating from beneath each Finn chamber following application of NPs. Subjects made ratings every hour for 6 h followed by every 12 h from 12 to 84 and a final rating at 90 h. Between 1 and 3 h after application of the chambers, subjects reported significantly higher rating scores from capsaicin NPs, in comparison to placebo (blank) NPs for burning, described as moderate, and pain rated as barely detectable to weak on the scale (Figure 4). These sensations subsided after 3 h and mirrored the in vitro measurements reflecting the initial burst of capsaicin release from NPs. After 3 h there were no significant differences in ratings of any sensory quality or in pain for the two sites of NP application. Although there were more frequent reports of pricking/stinging sensation but not itch in response to capsaicin during the first 12 h (Fishers Exact Test, $p = 0.01$), these sensory qualities did not yield significant differences in magnitude for the two treatments.

2.5. Effects of Capsaicin NPs on Thresholds and Magnitude Estimates of Mechanical and Heat Stimuli

After removal of NP Finn chambers, mechanical pain thresholds for nociceptive sensations evoked by von Frey filaments were significantly higher for capsaicin in comparison to blank NP sites, but only on day 1 (Figure 5A).

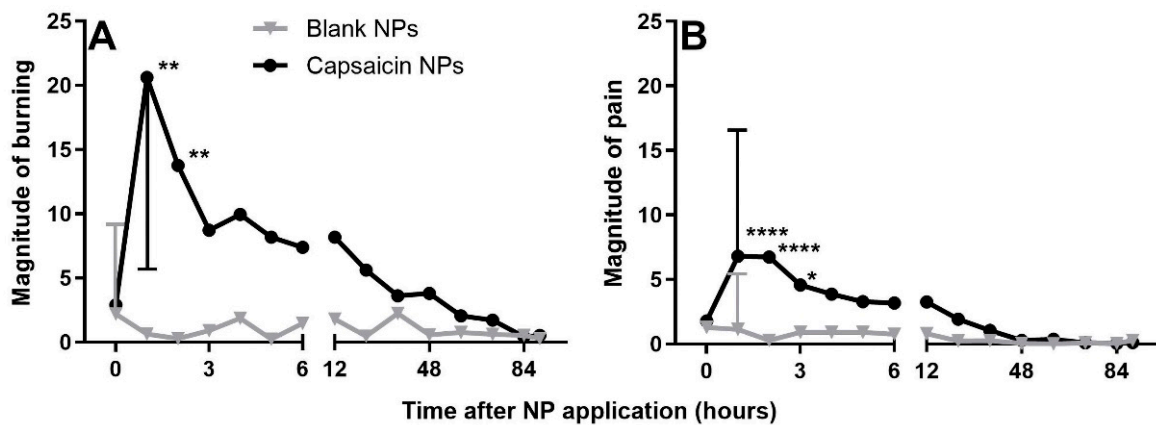


Figure 4. Magnitude ratings of spontaneous (background) sensations of burning and pain referred to the sites of application of blank and capsaicin filled NPs. (A) Magnitude of burning, (B) magnitude of pain. Mean \pm SD, $n = 21$, mixed effect model 2 within subject treatments (capsaicin vs. placebo treatment) \times 14 repeated timepoints (0–90 h) with Bonferroni correction. * $p < 0.05$, ** $p < 0.01$, **** $p < 0.0001$ for blank vs. NP comparison.

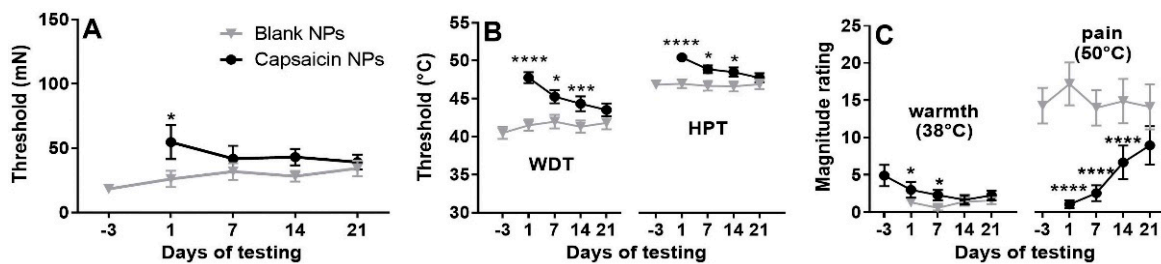


Figure 5. Mechanical pain thresholds, and thresholds and magnitude ratings of warmth and heat pain. (A) Thresholds for mechanically evoked pain (MPT) obtained at sites of blank and capsaicin NPs obtained 4 days before and on each designated day after removal of the NPs. (B) Detection thresholds for warmth (WDT) and heat pain (HPT, same format as in A). (C) Magnitude ratings of warmth and heat pain produced by 38 and 50 °C, respectively. $n = 21$, mixed effect model 2 within subject treatments (capsaicin vs. placebo treatment) \times 4 repeated timepoints (0, 7, 14, 21 days) with Bonferroni correction. Means with SEMs for capsaicin and blank NPs are black and gray, respectively. * $p < 0.05$, *** $p < 0.001$ and **** $p < 0.0001$ for blank vs. NP comparison.

The dominant sensory quality evoked by 50 °C was burning. The thresholds for detecting warmth (WDT) and painful heat (HPT) at the site of blank NPs administration were stable over the duration of the experiment. WDT and HPT increased on day 1 (after removal of Finn chambers with NP) in relation to prior tests after application of capsaicin NPs (Figure 5B). At this time, all subjects had a higher WDT and HPT on day 1 after capsaicin NP application in comparison with pre-treatment values at that site. A 2 treatment \times 4 days mixed effect model followed by Bonferroni correction revealed a significant interaction between treatment and days (WDT: $F(2.423, 48.46) = 6.976, p = 0.0012$; HPT: $F(2.651, 53.02) = 5.932, p = 0.0022$). Both WDTs and HPTs were significantly higher at the capsaicin than blank NP site on days 1, 7 and 14. Recovery of WDT and HPT was observed on day 21.

There were also decreased magnitude estimates of the intensity of suprathreshold warming and noxious heat. Magnitude ratings of the warmth evoked by sustained warming at 38 °C on the capsaicin vs. blank sites occurred on days 1 through 14 ($F = 9.657, p = 0.0055$). Pain in response to 50 °C heat for 7 s as suprathreshold stimulation was reduced in all subjects and abolished in 16 of 21. The mean magnitude estimate of pain elicited by

application of 50 °C heat was significantly lower on the capsaicin-treated side on days 1 through 14 (all $p < 0.0001$) but partially recovered on day 21 ($p = 0.087$); partial recovery was obtained ($F = 23.70$, $p < 0.0001$).

Noxious heat stimulation resulted in a local redness of the skin in 12 of 21 subjects before treatment and on the control site but in only one subject on the capsaicin-treated area. Another one of the capsaicin-treated subjects exhibited a white or vasoconstricted reaction. These findings suggest that capsaicin decreased heat-induced vascular dilation.

In contrast to the effects of capsaicin in decreasing the perceived intensity of warmth and heat pain, a RMANOVA revealed no significant differences between NPs and blank NPs sites in subjective magnitude estimates of mechanically evoked pain for any force on any day of testing (Supplementary Figure S1).

2.6. Effects of Capsaicin NPs on Itch, Nociceptive Sensations and Dysesthesias Evoked by Pruritogens

In response to cowhage application on the day of NP removal, there was a significant decrease in the peak magnitude, AUC, and duration of itch and each type of nociceptive sensation on the capsaicin vs. the blank NP site (Figure 6A–F). Eight subjects reported a complete abolition of itch as well as heat pain. In accordance with a decrease in sensations, capsaicin NPs also significantly decreased the areas of allodynia, hyperalgesia and hyperknesis induced by cowhage (Figure 6G).

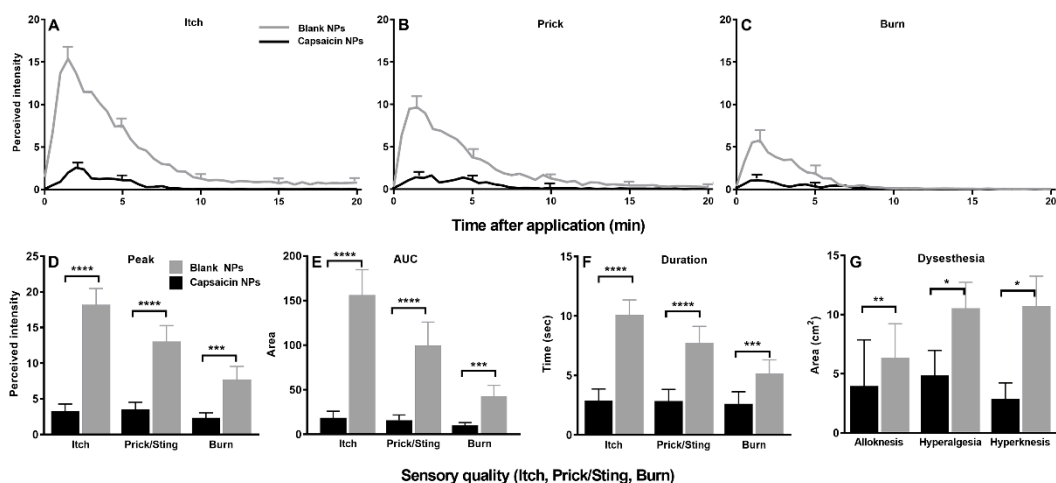


Figure 6. Effects of capsaicin NPs pretreatment on cowhage evoked sensations and dysesthesias applied by spicules. (A–C) Time course of perceived intensities of itch, pricking/stinging, and burning. Data are means with SEMs. For clarity, the SEMs are presented at the peak and every 5 min thereafter. (D) Peak magnitude (Peak) of each sensory quality. (E) Area under the rating curve (AUC). (F) Duration of response. (G) Area of each type of dysesthesia: allodynia, hyperalgesia and hyperknesis. $n = 21$, (A–C) repeated measures two-way ANOVA; two repeated treatment groups (capsaicin vs. placebo treatment) \times 40 repeated timepoints (0–20 min) with Bonferroni correction, (D–G) Wilcoxon test. * $p < 0.05$, ** $p < 0.01$, *** $p < 0.001$ and **** $p < 0.0001$.

In response to injections of β -alanine, the perceived intensities of itch and each nociceptive sensation were reduced early after injection, starting at 1 min after injection and lasting 2.5 min for itch and 3.5 min for the nociceptive sensations (Figure 7A–C). In relation to placebo (blank) NPs, capsaicin NPs resulted in significantly lower peak magnitude ratings and AUCs for both itch and pricking/stinging sensations but not for burning (Figure 6D,E). In contrast, there were no significant differences in the duration of each quality of sensation (Figure 7F). There was a significant decrease in the area of hyperalgesia (Figure 7G), and no significant differences in areas of allodynia or hyperknesis between the capsaicin and blank NP sites were reported.

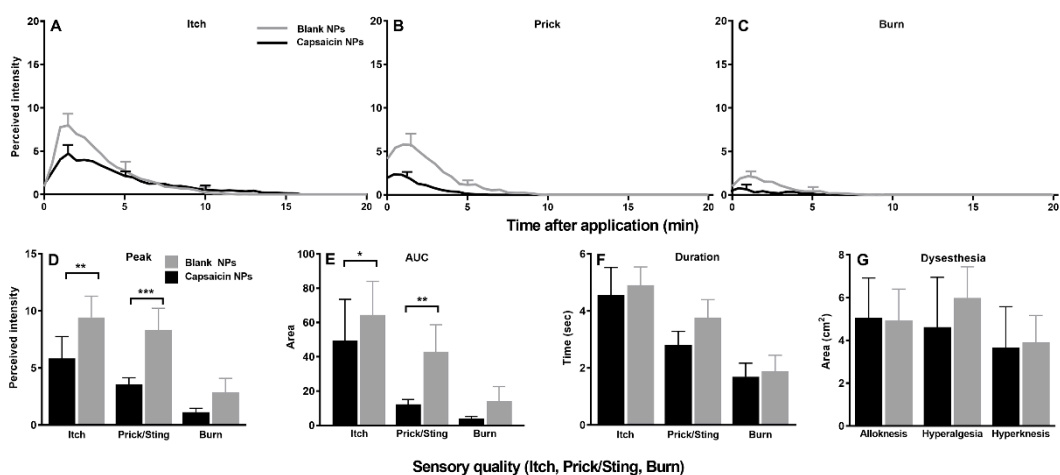


Figure 7. Effects of capsaicin NP pretreatment on sensations and dysesthesias evoked by injection of beta alanine. (A–C) Time course of perceived intensities of itch, pricking/stinging and burning. Same format as Figure 7. (D) Peak magnitude (Peak) of each sensory quality. (E) Area under the rating curve (AUC). (F) Duration of response. (G) Area of each type of dysesthesia: alloknesis, hyperalgesia and hyperknesis. $n = 21$, (A–C) repeated measures two-way ANOVA; two repeated treatment groups (capsaicin vs. placebo treatment) \times 40 repeated timepoints (0–20 min) with Bonferroni correction, (D–G) Wilcoxon test. Data are means with SEMs. * $p < 0.05$ and ** $p < 0.01$ and *** $p < 0.001$.

In response to injections of BAM8-22, the perceived intensities of itch and each nociceptive sensation were significantly lower for capsaicin in comparison with blank NP application (Figure 8A–C). The reduced ratings at the capsaicin application site were apparent within the first minutes after injection. Sensation at the capsaicin application site was reduced in comparison to blank for up to 3 min after injection for itch, up to 7 min for pricking/stinging and 5 min for burning. Similar to the effects of β -alanine, the peak ratings were significantly lower at the capsaicin site for each sensory quality (Figure 8D).

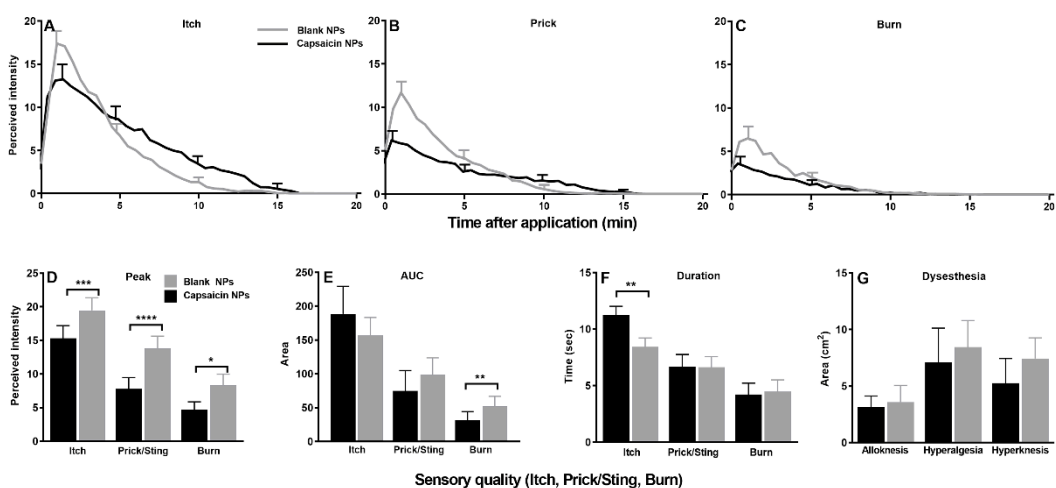


Figure 8. Effects of capsaicin NP pretreatment on sensations and dysesthesias evoked by injection of BAM8-22. (A–C) Time course of perceived intensities of itch, pricking/stinging, and burning. Same format as Figure 7. (D) Peak magnitude (Peak) of each sensory quality. (E) Area under the rating curve (AUC). (F) Duration of response. (G) Area of each type of dysesthesia: alloknesis, hyperalgesia and hyperknesis. $n = 21$, (A–C) repeated measures two-way ANOVA; two repeated treatment groups (capsaicin vs. placebo treatment) \times 40 repeated timepoints (0–20 min) with Bonferroni correction, (D–G) Wilcoxon test. Data are means with SEMs. * $p < 0.05$, ** $p < 0.01$, *** $p < 0.001$ and **** $p < 0.0001$.

In contrast to β -alanine, for injection of BAM8-22 the AUC was lower only for pricking/stinging and the duration of itch was significantly longer for the capsaicin site (Figure 8E,F). Differences in the areas of dysesthesia did not reach significance (Figure 8G). The only skin reaction to be affected was the area of local redness which was smaller on the capsaicin than the blank NP site (1.2 ± 2.2 vs. 5.4 ± 7.5 cm², $p = 0.0005$).

The effects of capsaicin on responses to spicules containing BAM8-22 were similar to those of cowhage, resulting in significantly lower peak ratings, AUCs and shorter durations of itch and pricking/stinging in comparison with the effects of blank NPs (Figure 9A–F). However, unlike cowhage there were no differences in the peak magnitude, rating, or duration for burning. Treatment with capsaicin NPs provoked a reduction in allodynia induced by BAM8-22 spicules (Figure 9G). There was also a decrease in the area of local redness at the application site within the capsaicin-treated area (0.8 ± 2.9 vs. 0.1 ± 0.1 cm², $p = 0.044$).

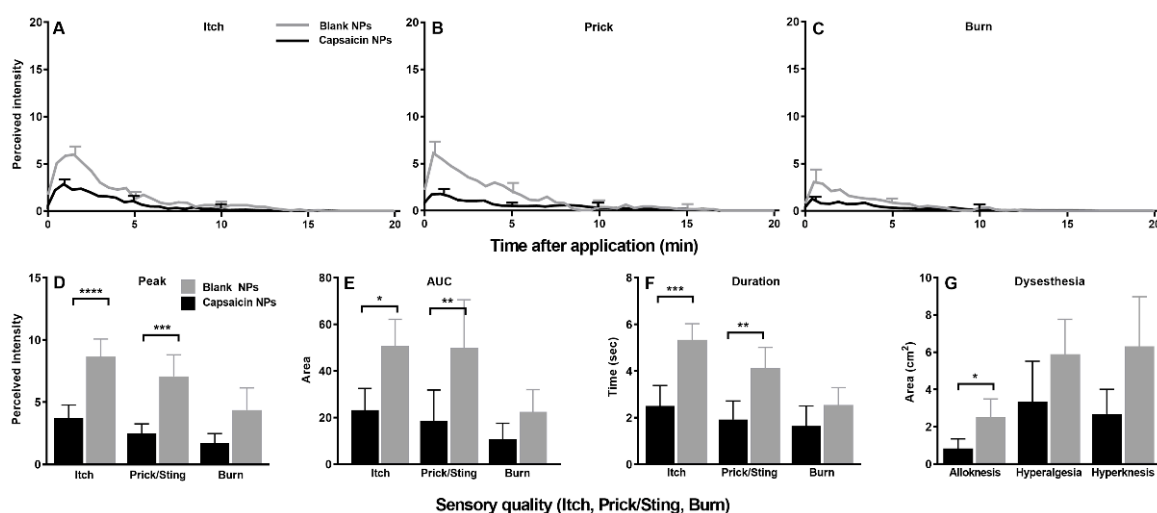


Figure 9. Effects of capsaicin NP pretreatment on sensations and dysesthesias evoked by BAM8-22 spicules. (A–C) Time course of perceived intensities of itch, pricking/stinging, and burning. Same format as Figure 7. (D) Peak magnitude (Peak) of each sensory quality. (E) Area under the rating curve (AUC). (F) Duration of response. (G) Area of each type of dysesthesia: allodynia, hyperalgesia and hyperknesis. $n = 21$, (A–C) repeated measures two-way ANOVA; two repeated treatment groups (capsaicin vs. placebo treatment) \times 40 repeated timepoints (0–20 min) with Bonferroni correction, (D–G) Wilcoxon test. Data are means with SEMs. * $p < 0.05$, ** $p < 0.01$, *** $p < 0.001$ and **** $p < 0.0001$.

Capsaicin NPs did not affect the maximum perceived intensity or duration of the histamine injection-evoked itch or pricking/stinging compared to the blank NPs (Supplementary Figure S2). Interestingly, 17 of 21 subjects exhibited a blanching of the skin, resembling a vasoconstriction around the histamine injection site. This effect was only observed on capsaicin-treated sites. In addition, treatment of capsaicin NP reduced the area of the local redness (27.2 ± 15.7 vs. 20.7 ± 19.0 cm², $p = 0.0239$). No significant differences were observed in areas of histamine-induced allodynia, hyperalgesia and hyperknesis.

Following the application of histamine spicules, the duration of each sensory quality was slightly but significantly decreased at the capsaicin vs. blank site without any change in peak magnitude (Supplementary Figure S3). The areas of hyperalgesia and hyperknesis were significantly smaller at the capsaicin vs. blank site (7.657 ± 13.09 vs. 4.769 ± 9.13 cm², $p = 0.0408$) and (4.982 ± 7.367 vs. 1.435 ± 2.792 cm², $p = 0.0136$), respectively. The area of local redness was also significantly decreased on the capsaicin site (7.0 ± 5.6 vs. 1.5 ± 2.9 cm², $p = 0.0003$) and the appearance of white areas around the capsaicin application area was observed in 10 out of 21 subjects.

Capsaicin had the major effect of reducing and in some instances eliminating the itch and nociceptive sensations evoked by the histamine-independent pruritogens cowhage, β -alanine and BAM8-22 but had little or no significant effect on the sensations evoked by histamine.

3. Discussion

In this study, capsaicin-loaded PLGA NPs were developed for topical application in humans and their *in vitro* physicochemical attributes were characterized. An initial *in vitro* release of 22.9% capsaicin within the first hour was observed (burst), followed by a lower continuous release until 72 h, where complete capsaicin release was observed. In a murine model, capsaicin NPs applied to the skin for 24 h penetrated the dermis and led to a behavioral desensitization to heat and mechanical stimuli. Application in humans caused weak to moderate burning sensation lasting approximately 2 h followed by a short-lasting elevation of mechanical pain threshold and a lasting desensitization to warm and noxious heat. During this period of heat desensitization there was also a significant decrease in the magnitude ratings of itch and nociceptive sensations evoked by cowhage, β -alanine, and BAM8-22 but little or no significant effect on sensations elicited by histamine.

PLGA NPs to alter pain or itch in humans have not yet been applied in practice [28]. Capsaicin-loaded PLGA NPs have been investigated for the treatment of chronic pain in animal models, due to their controllable prolonged release and biocompatibility and acceptable safety [26,31,32]. Our prototype PLGA NPs showed an initial low burst effect and a continuous release profile designed to desensitize while diminishing an unpleasant burning sensation. Using other PLGA compositions or biocompatible polymers to encapsulate capsaicin could alter the release profile [33].

Capsaicin has been applied in previous studies to desensitize the skin to noxious and pruritic stimuli experimentally applied to the skin in human volunteers. For example, three days of repeated topical applications of 0.1% capsaicin abolished transient heat pain and itch to cowhage but not itch to histamine [23]. A higher dose of 8% topically applied capsaicin was subsequently found to reduce both histaminergic and non-histaminergic cowhage itch [25].

A limitation of other topical applications of capsaicin is the associated prolonged burning pain sensation. Conversely, the slow release of the capsaicin from NPs in the present study leads to low pain and burning sensation. A positive control with active capsaicin was not applied in this study. However, lower burning pain was observed in comparison, for example to previously described for a 1 or 24 h application of 8% capsaicin in other studies [24,25] or capsaicin injection [34]. Therefore, capsaicin NP formulations could be a valuable treatment application for pain- and itch-associated diseases. The missing desensitization to histamine in our study could be due to the late testing after desensitization, when some functions had almost recovered. Other reasons could be the small area of desensitization which, after injection, was smaller than the wheal, indicating that the histamine diffused beyond the capsaicin-treated area into surrounding untreated skin. This was less likely to happen with the histamine spicules, whose effects were confined within the treated area. An effect of capsaicin after histamine injection was especially seen in a localized vasoconstriction or white area in the capsaicin application area surrounded by a local redness [24,35,36]. Other possibilities would be the amount of capsaicin being too low or the penetration depth not deep enough to reach the terminal endings of histamine-responsive mechanically insensitive nociceptors.

Capsaicin application decreased sensory responses to β -alanine and BAM8-22 spicules thought to activate mechanosensitive polymodal nociceptors mediating histamine-independent reactions [7,8,14,37,38]. Consequently, capsaicin could be effective in treating chronic pruritic disorders that elicit histamine-independent itch. Additionally, the capsaicin NP formulation is a feasible approach which should be investigated in further studies for its efficacy and safety to treat chronic pain and itch.

Experimental outcomes from the present work are clinically relevant and demonstrate the novel concept of controlled NP delivery of capsaicin for the future treatment of chronic, localized itch or pain that typically accompanies eczema or post-herpetic neuralgia. PLGA is readily hydrolyzed to its monomer components (lactic acid and glycolic acid), which are metabolized to non-toxic byproducts, with a demonstrated safety profile. Numerous FDA-approved PLGA formulations are routinely used in the clinical setting [39]. We anticipate that a single topical application of capsaicin-loaded NPs would minimize sensory discomfort and the need for multiple clinic visits for re-application. The minimization of discomfort would increase compliance of patients using the preparation. Thus, the present findings could motivate the use of capsaicin NPs for the clinical treatment of certain types of chronic inflammatory or neuropathic itch.

4. Materials and Methods

4.1. Nanoparticle Preparation

Capsaicin-loaded PLGA nanoparticles (NPs) were prepared under clean conditions using a single-emulsion, solvent evaporation approach previously described by Zhou et al. [26,32]. The PLGA (50:50 Poly(DL-lactide-co-glycolide)) and capsaicin (Sigma Aldrich, St. Louis, MO, USA) were mixed and dissolved in ethyl acetate (60 mg of capsaicin per 100 mg PLGA). The resultant solution was added dropwise to 5% polyvinyl alcohol (PVA). Following sonication, the resultant mixture was slowly added to a 0.3% *v/v* PVA solution while stirring. Over 5 to 6 h, the ethyl acetate was allowed to evaporate under a fume hood. Capsaicin-loaded PLGA NPs were collected through centrifugation ($18,000\times g$ for 20 min) and washed twice in sterile de-ionized water to remove unencapsulated capsaicin. Following the final wash step, the NPs were collected and resuspended in 5 mL sterile de-ionized water. Trehalose was added as a cryoprotectant to the NP suspension at a mass ratio of 0.1:1 (trehalose:NP). After flash freezing with liquid nitrogen, the NPs were lyophilized for 2 days using a freeze dryer (Labconco, Kansas City, MO, USA). The dry NP powder was stored at $-20\text{ }^{\circ}\text{C}$ until further use. Blank NPs (placebo control) were prepared under identical conditions in the absence of capsaicin.

4.2. Analysis of NP Physicochemical Attributes

Scanning Electron Microscopy (SEM): The morphology and size of NPs were characterized by SEM. NPs were mounted on a carbon tape and sputter-coated with gold in an argon atmosphere using a sputter current of 40 mA (Dynavac Mini Coater; Dynavac, Hingham, MA, USA). SEM analysis was carried out with a Philips XL30 SEM using a LaB electron gun with an accelerating voltage of 3 kV. NP size was determined from SEM micrographs using ImageJ software (version 1.5, National Institutes of Health (NIH), Bethesda, MD, USA).

Dynamic Light Scattering: Corresponding particle size distribution (hydrodynamic diameter) and polydispersity index were measured using a Zetasizer nano (Malvern, UK). The zeta potential of manufactured capsaicin NPs was measured using the electrophoretic light scattering function of the Zetasizer. All measurements were performed in triplicate.

4.3. Quantification of Drug Loading and Encapsulation Efficiency

A total of 1 mg of PLGA NPs was dissolved in 100 μL DMSO and made to a volume of 1 mL by adding PBS. An Enzyme-linked Immunosorbent Assay (ELISA) Capsaicin High Sensitivity Plate Kit (Beacon Analytical Cat.# 20-0027, Saco, ME, USA) was used for the quantification of capsaicin content as per manufacturer instructions. In brief, a serial dilution of PLGA NPs and a capsaicin standard for a calibration curve was made. Aliquots of 100 μL volume were pipetted in triplicates into the wells of antibody-coated stripes, mixed with 100 μL of enzyme conjugate and incubated for 30 min under agitation. Subsequently, the wells were washed five times with water, incubated with 100 μL reaction substrate for 10 min, and the reaction was stopped by adding 100 μL stop solution to each well. The resultant absorbance (450 nm–650 nm) was measured by a plate reader. The amount of capsaicin in the resultant solution was determined from the calibration

curve, and the corresponding NPs loading (Equation (1)) and encapsulation efficiency (Equation (2)) were determined from the following equations.

$$\text{NP capsaicin loading} = \frac{\text{Released Capsaicin (mg)}}{\text{NP weight (mg)}} \times 100 \quad (1)$$

$$\text{Encapsulation Efficiency} = \frac{\text{Measured capsaicin content (mg)}}{\text{Added capsaicin weight (mg)}} \times 100 \quad (2)$$

4.4. *In Vitro Release of Capsaicin from PLGA Nanoparticles*

The *in vitro* release of capsaicin from NPs was evaluated at various time points in phosphate buffer (pH 6.5) at 35 °C in an agitated system (150 rpm). Aliquots were removed at pre-determined time points and replaced with the same volume of fresh pre-warmed phosphate buffer. Sample aliquots removed were centrifuged at 18,000 rpm for 10 min and the resultant supernatant was removed for the quantification of released capsaicin using the aforementioned ELISA capsaicin quantification kit. Cumulative *in vitro* release of capsaicin from PLGA NPs was determined for each timepoint.

4.5. *Quantification of pH*

The pH of the combination of cream and NPs for topical application was determined in triplicate, on the same formulation composition used for the topical application. Briefly, a 1 mg aliquot of capsaicin-loaded PLGA NPs was dissolved in 20 µL of sterile water, vortexed for 1 min and sonicated for 5 min. The resultant NP suspension and pure sterile water were added to 80 mg of Vanicream dissolved in 50 µL DMSO and mixed in 15 mL of water. The resultant pH was quantified after 1 hr using a pH meter. The same procedure was carried out for the placebo (blank) NPs.

4.6. *Preparation of the NP Cream for Topical Application*

A 1 mg aliquot of NPs was suspended in 20 µL of sterile water by vortexing for 1 min, and then placed in an ultrasonic bath for 5 min. The resultant NP suspension was stirred into 80 mg of Vanicream. Then resultant preparation was filled into a 12 mm Finn chamber for human subjects. An equivalent dose corresponding to 1/8 of the human total dose was filled into an 8-mm Finn-type chamber for mice. Placebo controls included Vanicream and blank PLGA NP mixtures.

4.7. *In Vivo Application of Capsaicin NPs in a Murine Model*

4.7.1. *Animals*

C57BL/6 male mice (Charles River Laboratories), each weighing 20–25 g and aged 6–8 weeks old, were used for behavioral experiments, ultrasound, skin thickness measurements and histological evaluation. All experimental procedures were approved by the Institutional Animal Care and Use Committee of Yale University School of Medicine and were in accordance with guidelines provided by the National Institute of Health and the International Association for the Study of Pain. Mice were housed under a 12 h light/dark cycle with free access to standard laboratory food and water.

4.7.2. *In Vivo Application of Capsaicin NPs*

The Finn-like chambers for mice were constructed in the Yale Medical School Machine Shop from polyether ether ketone (PEEK) (Trident Plastics, Ivyland, PA, USA). The chamber had an outside diameter of 8 mm and a well that was 5 mm wide and 0.2–0.3 mm deep. PEEK is a medically compatible plastic and used for orthopedic surgery, bone replacement, dental implants, and other biomedical applications [40]. The chamber accommodated up to 10 mg of Vanicream filled with NPs in the same concentration as used for humans. This amount contained a maximal amount of 44 µg of capsaicin. The dermal LD50 for capsaicin was determined to be > 512 mg/kg in mice [41].

Under brief anesthesia (2% isoflurane in 300 mL/min oxygen), the PEEK chamber was applied on the shaved cheek of the mouse with a thin coat of cyanoacrylate glue on the rim. An Elizabethan collar prevented the animal from removing the cup for 24 h. After this time, the chamber was removed with a small amount of acetone and water under brief anesthesia. Then, the cheek was carefully wiped with ethanol, to eliminate remnants of glue, cream, superficial NPs and capsaicin.

4.7.3. In Vivo Quantification of Capsaicin from PLGA Nanoparticles in Mouse Skin

Skin from mice treated 24 h with NPs was harvested 1 hr after taking off the chamber filled with capsaicin or blank NPs. As a positive control, mice were injected with 30 µg/10 µL of capsaicin in 8% Tween 20 in normal saline (0.9 *w/v*) and the cheek skin was harvested 1 hr later. After euthanasia, the treated cheek skin (approximately 1 × 1 cm) was removed and directly frozen in a −80 °C freezer. For analysis, the tissue was cut into small pieces, mixed with 50 µL tissue extraction buffer (20 mM HEPES, pH 7, 420 mM NaCl, 0.2 mM EDTA, 1.5 mM MgCl₂, 1% NP40, 1 mM PMSF, 25% Glycerol, 0.4% PIC) and homogenized using a Biomasher II[®] Closed System Disposable Micro Tissue Homogenizer. Samples were centrifuged at 4 °C, 13,000 rpm for 20 min and the supernatant was isolated for further analysis. A Standard Bradford assay was used to measure the total protein concentration of samples. The samples were diluted to an equal total protein concentration of 6 µg/µL for the aforementioned ELISA capsaicin quantification kit in tissue. Three samples per group of mice were analyzed using the ELISA assay.

4.7.4. Analysis of Capsaicin Penetration Depth In Vivo

For the analysis of skin penetration of the NPs, either capsaicin, blank or capsaicin NPs each encapsulated with a dye (DiL) were applied to the cheek of mice for 24 h as described. One hour after cup removal, the cheek was carefully cleaned with 70% ethanol solution. Mice were euthanized under anesthesia and a section of the skin from the cheek was harvested (approximately 1 × 1 cm²). The skin was fixated with 4% *w/v* PFA/10% formalin for 24 h at −20 °C. Excess PFA was removed by rinsing with PBS and the samples were soaked in 40% *w/v* sucrose in PBS for 2 days. For cryoembedding, the tissue was equilibrated at room temperature in OCT-compound for 10 min, transferred and orientated in fresh cooled OCT in a cryomold surrounded by dry ice and isopentane. Samples were stored at −20 °C and cut with a cryostat on the next day into sections of 7 µm thickness. Sample sections were photographed using an EVOS FL Cell Imaging System with a EVOS Light Cube RFP (ThermoFisher, Waltham, MA, USA). For statistical comparisons, three images of random sections for six mice per condition were acquired to obtain a mean value. ImageJ software with a color deconvolution plugin [42,43] was used for detecting the percentage of area stained red or red autofluorescence signal compared to the whole tissue sample in the image [44]. Only the epidermis and dermis were included in the analysis and the rest were manually excluded. Colored tissue in each sample was automatically detected using an adaptation to an ImageJ macro, which was designed to count cells in a designated area of the tissue sample [44]. The color deconvoluting macro was used to separate the staining colors in each image. The Focinator tool was used to threshold and binarize the color-separated images, segmenting the stained and unstained regions and differential quantification of intensity for stained areas from each micrograph. The macro automatically detected regions of interest using a thresholded mask of the image and measuring the different areas across multiple regions of interest per image. Additionally, each image was surveyed for fluorescence in the dermis and epidermis by an operator who was blinded to the treatment conditions.

4.7.5. Testing Mice for Behavioral Responses to Mechanical and Heat Stimulation

Prior to collecting data, each mouse was placed daily for 5 days in a meshed test chamber for 30 min. After 15 min, mechanical and heat stimuli were periodically applied to the cheek as described for testing but with only 5 presentations of each stimulus, always ending

with the lowest intensity [45]. The mechanical stimuli consisted of nylon filaments with tip diameter (and delivering different bending forces) of 67 μm (0.23 mN) and 100 μm (2, 10 and 20 mN). A contact thermode with a chip resistor (2×3 mm) and a thermocouple were used for electronically servocontrolling temperature at the skin-probe interface, delivering stimulus temperatures of either 38 or 52 $^{\circ}\text{C}$.

After the 5 days of habituation to the testing chamber and stimuli, daily testing began 24 h after removal of the Finn chamber. The mechanical stimuli were presented first. Each stimulus force was presented five times and delivered in order of ascending force and again in descending order of applied force. Then five warm, 38 $^{\circ}\text{C}$ stimuli were delivered followed by five presentations of noxious 52 $^{\circ}\text{C}$ stimuli. Lastly, the same heat stimuli were presented again this time with stimuli of 52 $^{\circ}\text{C}$ delivered first. Each mechanical or heat stimulus was applied for a maximal contact time of one second or less if withdrawal occurred and with interstimulus intervals of at least 60 s.

During testing, mice were video recorded from the side, with a mirror positioned on one side to allow for a two-sided view. After each stimulation, the behavioral responses to each stimulus were documented and later confirmed or corrected in the videorecording. The operator performing the experiments was blinded to the placebo and treatment groups. Each behavioral reaction to a stimulus was assigned according to the following categories; a discomfort score (DS) according to whether “no reaction” (DS = 0), “looking” or turning the head or body towards the stimulating object (DS = 1), “withdrawal” from the stimulus by turning the head or body away or pulling backward after stimulation (DS = 2), rapid “flinching” (DS = 3), “biting”, consisting of a fast turning of the head toward the object and trying to bite it (DS = 4), “shaking”, a short, quick vibratory movement of the body (DS = 5), “jumping aside” from the stimulus (DS = 6), “jumping in the air” (DS = 7), or audible squeaking (DS = 8). In the case of observing a series of two immediate behaviors, only the behavior with the highest score was used. Each wipe directed towards the stimulated cheek was counted and added to the DS. The mean score from ten presentations of the same stimulus was calculated.

4.8. Testing Human Subjects for Responses to Heat, Mechanical Stimuli and to Pruritogens

Twenty-one healthy human subjects (10 females and 11 males, age: 28.9 ± 8.3) were included in this study. Subjects reporting a history of dermatological, neurological, immunological or cardiac disorders were excluded. In addition, subjects were required to refrain from taking antihistamines or analgesics at least 24 h prior to the first experiment and during the whole testing period. All protocols were approved by the Yale University Human Investigative Committee. Before the experiments, participants were trained to use the generalized Labeled Magnitude Scale (gLMS) to rate the perceived intensity of itch and pain-like (nociceptive) sensations of pricking/stinging and burning evoked by a given stimulus [29]. Itch was defined as a sensation that evokes a desire to scratch. Pricking/stinging was defined as a sensation that was sharp and well localized, either intermittent like a needle prick or continuous like an insect sting. Burning was defined as a sensation most often associated with sunburns or thermal burns, but also with skin abrasions, strong cold, or chemical irritants. Participants were instructed that the nociceptive sensations may or may not be painful (“hurt”).

Beginning with the application of a pruritogen and every 30 s thereafter, subjects were instructed to use a computer mouse to make three successive ratings using the gLMS presented on a video-screen using DAPSYS 8 software (<http://www.dapsys.net/> accessed on 3 April 2022, Brian Turnquist, Bethel University, St. Paul, MN, USA). The scale consisted of a vertical line with labels, positioned in a quasi-logarithmic manner, of “no sensation”, “barely detectable”, “weak”, “moderate”, “strong”, “very strong”, and “strongest imaginable sensation”. The subject was instructed to judge the maximal magnitude of each of the three qualities of sensation that occurred during the previous interval of 30 s, first “itch”, then “pricking/stinging” and lastly “burning” [46]. Ratings

were recorded every 30 s until either there occurred no sensation of any kind for three successive 30 sec periods or after a 20 min period had elapsed.

The subject's ratings were saved from the position of the cursor on the scale and converted to a numerical value between 0 and 100. The numbers were not visible to the subject. The positions of the labels were 0 for "no sensation", 1 for "barely detectable", 6 for "weak", 17 for "moderate", 35 for "strong", 53 for "very strong", and 100 for the "strongest imaginable sensation of any kind".

Once ratings of a pruritogen were completed, subjects were tested for the presence of any mechanically evoked hypersensitivity (dysesthesia) surrounding the application site. These were defined as (a) alloknesis, itch evoked by stroking the skin with a cotton swab attached to a coping-saw blade that exerted approximately 100 mN of compressional force; or, alternatively, allodynia, if stroking evoked tenderness, (b) hyperalgesia, characterized by a sensation of enhanced pricking pain to a one-second application of a von Frey filament with a tip diameter of 200 μm and exerting a bending force of 80 mN; (c) hyperknesis, defined as enhanced itch to pricking the skin with a von Frey filament having a tip diameter of 50 μm and exerting a bending force of 20 mN. Subjects were instructed to judge only the intensity of the sensation and not the perceived geometric features of the stimulus itself such as how small or "sharp" it was. Additionally, the borders of any skin reactions such as wheal, erythema, or changes in skin appearance such as lighter areas (blanching, white-reaction or vasoconstriction), were marked on the skin following each experiment.

4.9. Application of NPs

Following gentle cleaning of the arms with ethanol wipes and taking a picture of the skin, filled Finn chambers with an inner diameter of 12 mm were randomly placed on the volar forearm and held in place with Tegaderm film and additionally covered with white tape. The opposite forearm received the same treatment with Finn chambers filled with blank NPs. The chamber was left in place for four days. Subjects and investigators were blinded to the type of application. The locations of the Finn chambers on the arms were documented and photographed to be able to find the correct areas for further testing. The subjects were asked to refrain from sunbathing, bathing and strenuous physical activity to prevent alterations in the pharmacokinetics of the applied PLGA NPs, and received a cover for showering to ensure the integrity of the Tegaderm. The subjects were provided with four paper copies of the labeled magnitude rating scale to rate the mean and maximal perceived intensity of itch, pricking/stinging, burning, and pain and describe other experienced effects separately for left and right arm. Ratings were performed every hour for the first 8 h. The subjects were asked to continue the ratings in the morning and once in the evening every day for three days. On the day 4, the subjects returned to the laboratory, where the Finn chambers were removed, and the skin was cleaned with alcohol wipes and gently washed with soap and water.

4.10. Ratings of the Perceived Intensity of Pain Evoked by Punctate Mechanical Stimuli of Differing Indentation Force

Von-Frey type filaments having a tip diameter of 200 μm and delivering bending forces of 2, 8, 16, 32, 64, 128, 256 and 512 mN were initially each applied once to the treated area of skin in ascending order of force. The duration of indentation was 1 s and the interstimulus interval 30 s. In response to each stimulus the subject assigned a number of his/her own choosing for a rating in proportion to the perceived intensity of any "pain" sensation (here defined as any painful or pain-like quality such as pricking/stinging) according to the method of magnitude estimation [47]. If there occurred a sensation of touch-pressure with no pain or pain-like quality, the subject assigned the number zero. The stimuli were applied to the treated area of the arm prior to, and again 1, 7, 14 and 21 days after removal of the NPs. The ratings were normalized with respect to each subject's particular internal modulus as follows [47]. For each subject, the mean of the ratings for every stimulus was obtained and an overall grand mean of these means was calculated across all subjects. By

dividing each subject's mean into the grand mean, a normalizing factor was obtained which, when multiplied by the subject's mean, equaled the grand mean. This factor, varying for each subject, was multiplied by each of the subject's ratings to obtain a new set of now normalized data which were then averaged for the subjects for each stimulus applied on each day of testing.

4.11. Pain Threshold for Nociceptive Punctate Mechanical Stimuli of Differing Indentation Force

The "mechanical pain threshold" (MPT) was obtained on each day of testing in response to the same von-Frey filaments with the use of a Quantitative Sensory Testing (QST) protocol [48]. Each filament was applied first in order of ascending force, starting with the lowest value until the sensation of touch-pressure was accompanied by or changed to pain-like pricking or stinging sensation. This force was used as the first suprathreshold value. Then, the whole process was repeated first with the ascending and then descending series of forces until five supra- and five subthreshold values were obtained. The MPT was defined as the geometric mean of these values.

4.12. Thresholds for Warmth and Heat-Pain

The warmth detection threshold (WDT) and heat pain threshold (HPT) were determined in response to heat stimuli delivered with a Peltier contact thermode having a 1 cm² contact area and stimulus temperature electronically controlled within to 0.1 °C of the desired value via feedback from a thermocouple located at the skin-thermode interface [36]. The procedure of testing followed the QST protocol and instructions. The thermode was centered on the locus of prior NP application. An increasing ramp of temperature was delivered at 1 °C/s from a base temperature of 32 °C until reaching 50 °C. The thermode was programmed and the subject's reaction registered with DAPSYS 8 software. Warmth and heat sensations were registered by the subject using a button connected to the computer. Subjects were asked to press the button when a warming sensation was felt (for WDT) and again when the sensation of warmth changed to an additional, pain-like sensation of pricking/stinging or burning (for HPT). The WDT and HPT were calculated as the average threshold temperature of 3 measurements. Next, the subjects were presented with a warm stimulus of 38 °C for 40 s and a following suprathreshold stimulus 50 °C for 6 s. These suprathreshold stimuli were each an incremental heat stimulus with a trapezoidal temperature waveform. After these stimuli, the subjects were asked to rate the perceived magnitude of warmth, burning, pricking/stinging, and pain on the gLMS scale.

4.13. Ratings of Perceived Intensity of Itch and Nociceptive Sensations in Response to Pruritogens

Following removal of the Finn chambers, MPT, WDT and HPT were determined as on day 3, except that both arms were tested. After a 30 min break, subjects were asked to rate, the itch, pricking/stinging, and burning every 30 s after the application of a pruritogen to each test site. A different pruritogen was applied on each day of testing (Figure 10): day 1, cowhage spicules (trichomes from the plant, *Mucuna pruriens*) [10]; day 2, injection of either 90 mg β-alanine or 1 mg/mL BAM8-22 in 10 μL of normal saline (selected in randomized order and double-blinded); day 3, injection of the other pruritogen (β-alanine or BAM8-22); day 4, injection of 10 μg of histamine in 10 μL of normal saline; day 5, heat-inactivated spicules previously soaked in 3 mg/mL of BAM8-22; day 6, heat-inactivated spicules previously soaked in 10 mg/mL of histamine [10]. After all the sensations evoked by a particular pruritogen disappeared, or 20 min had elapsed, the borders of regions exhibiting any of the dysesthesias to the three mechanical stimuli were mapped on the skin. The mapped arms were photographed along with a scale bar; areas of dysesthesias were analyzed using ImageJ. Ratings of subjects were assessed using DAPSYS 6.

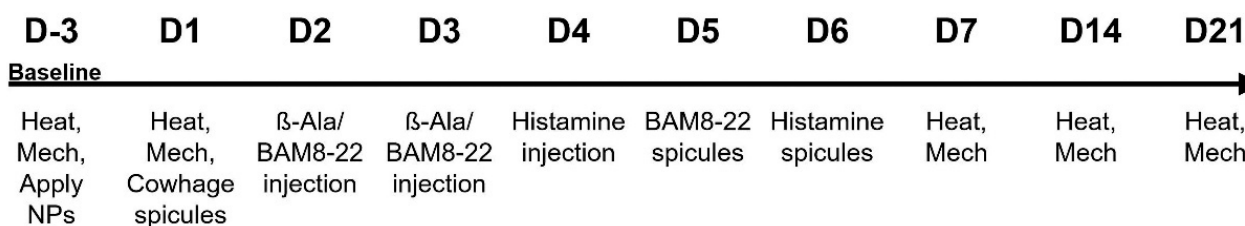


Figure 10. Timeline for human testing. Thresholds for warmth, painful heat and to mechanical stimuli (Mech) were obtained at the test site on each arm prior to application of blank and capsaicin NPs on Day 3 and again after NP removal four days later (D1) and again on D7, 14 and 21. Sensory ratings to cowhage spicules on D1, and to injection of β -alanine (β -Ala), BAM8-22 and histamine as indicated and subsequently to application in heat-inactivated spicules containing BAM8-22 and to histamine.

4.14. Statistical Analyses

Data evaluation and all analyses were performed by blinded investigators. For each pruritogen applied to the forearm and for each sensory quality (itch, pricking/stinging and burning) a comparison of differences in ratings of a pruritogen over time between blank- and capsaicin-treated areas were analyzed using a within subject repeated measures mixed effect model with Bonferroni post hoc correction.

For each pruritogen and each sensory quality, the means for peak magnitude, AUC and duration were analyzed for differences between the two NP treatments (placebo and capsaicin PLGA NPs) using a Wilcoxon signed-rank test.

Differences between groups in the proportions of subjects reporting a sensation were analyzed with the Fisher's exact test. Differences between areas of dysesthesias and skin reactions were analyzed with a Wilcoxon matched pairs signed-rank test. Behavioral responses to mechanical and heat stimuli in mice were assessed with a repeated measures two-way ANOVA. For statistical analysis, GraphPad Prism 8 (GraphPad Software, Inc., La Jolla, CA, USA) was applied.

Supplementary Materials: The following supporting information can be downloaded at: <https://www.mdpi.com/article/10.3390/ijms23095275/s1>.

Author Contributions: Conceptualization: R.H.L., J.Z. and N.M.M.; methodology: R.H.L., N.M.M., Z.C., S.O., Z.R., S.J.; investigation: N.M.M., Z.C., S.O., Z.R., S.J., X.T.; analysis: N.M.M., Z.R., S.O., V.E.-R.; writing original draft: N.M.M., Z.R., S.O.; writing review and editing: R.H.L., N.M.M.; visualization: S.O., N.M.M.; funding acquisition: R.H.L. All authors have read and agreed to the published version of the manuscript.

Funding: This work was supported by National Institute of Arthritis and Musculoskeletal and Skin Diseases (USA): Matthias Ringkamp, Robert H. LaMotte, R01 AR070875, National Institute of Neurological Disorders and Stroke (USA), NS014624, Robert H. LaMotte, Deutsche Forschungsgemeinschaft (DFG) Fellowship Grant, 326726541, Nathalie M. Malewicz, Fellowship grant and Engineering and Physical Sciences Research Council, EPSRC (EP/V028960/1), Zahra Rattray. For the purpose of open access, the authors have applied for a CC BY copyright license to any Author Accepted Manuscript version arising from this submission.

Institutional Review Board Statement: The study was conducted in accordance with the Declaration of Helsinki, and approved by the Institutional Review Board of Yale University School of Medicine (protocol #12780 approved 18 May 2016). The animal study protocol was approved by the Institutional Review Board of Yale University School of Medicine (protocol #07880, approved 31 March 2016).

Informed Consent Statement: Informed consent was obtained from all subjects involved in the study.

Data Availability Statement: The datasets used and/or analyzed are available from the corresponding author upon reasonable request.

Acknowledgments: We thank Steven G. Shimada for his contribution in the initiation of the study and his advice and support during the project. We thank Beacon for providing antibodies.

Conflicts of Interest: The authors declare no conflict of interest.

References

1. Mattered, U.; Apfelbacher, C.J.; Vogelgsang, L.; Loerbroks, A.; Weisshaar, E. Incidence and determinants of chronic pruritus: A population-based cohort study. *Acta Derm.-Venereol.* **2013**, *93*, 532–537. [CrossRef] [PubMed]
2. Johaneck, L.M.; Meyer, R.A.; Friedman, R.M.; Greenquist, K.W.; Shim, B.; Borzan, J.; Hartke, T.; LaMotte, R.H.; Ringkamp, M. A role for polymodal C-fiber afferents in nonhistaminergic itch. *J. Neurosci.* **2008**, *28*, 7659–7669. [CrossRef] [PubMed]
3. Ringkamp, M.; Schepers, R.J.; Shimada, S.G.; Johaneck, L.M.; Hartke, T.V.; Borzan, J.; Shim, B.; LaMotte, R.H.; Meyer, R.A. A role for nociceptive, myelinated nerve fibers in itch sensation. *J. Neurosci.* **2011**, *31*, 14841–14849. [CrossRef] [PubMed]
4. Ma, C.; Nie, H.; Gu, Q.; Sikand, P.; Lamotte, R.H. In vivo responses of cutaneous C-mechanosensitive neurons in mouse to punctate chemical stimuli that elicit itch and nociceptive sensations in humans. *J. Neurophysiol.* **2012**, *107*, 357–363. [CrossRef]
5. Han, L.; Ma, C.; Liu, Q.; Weng, H.J.; Cui, Y.; Tang, Z.; Kim, Y.; Nie, H.; Qu, L.; Patel, K.N.; et al. A subpopulation of nociceptors specifically linked to itch. *Nat. Neurosci.* **2013**, *16*, 174–182. [CrossRef]
6. Liu, Q.; Tang, Z.; Surdenikova, L.; Kim, S.; Patel, K.N.; Kim, A.; Ru, F.; Guan, Y.; Weng, H.J.; Geng, Y.; et al. Sensory neuron-specific GPCR Mrgprs are itch receptors mediating chloroquine-induced pruritus. *Cell* **2009**, *139*, 1353–1365. [CrossRef]
7. Sikand, P.; Dong, X.; LaMotte, R.H. BAM8-22 peptide produces itch and nociceptive sensations in humans independent of histamine release. *J. Neurosci.* **2011**, *31*, 7563–7567. [CrossRef]
8. Liu, Q.; Sikand, P.; Ma, C.; Tang, Z.; Han, L.; Li, Z.; Sun, S.; LaMotte, R.H.; Dong, X. Mechanisms of itch evoked by β -alanine. *J. Neurosci.* **2012**, *32*, 14532–14537. [CrossRef]
9. Dong, X.; Han, S.; Zylka, M.J.; Simon, M.I.; Anderson, D.J. A diverse family of GPCRs expressed in specific subsets of nociceptive sensory neurons. *Cell* **2001**, *106*, 619–632. [CrossRef]
10. LaMotte, R.H.; Shimada, S.G.; Green, B.G.; Zelterman, D. Pruritic and nociceptive sensations and dysesthesias from a spicule of cowhage. *J. Neurophysiol.* **2009**, *101*, 1430–1443. [CrossRef]
11. Wooten, M.; Weng, H.J.; Hartke, T.V.; Borzan, J.; Klein, A.H.; Turnquist, B.; Dong, X.; Meyer, R.A.; Ringkamp, M. Three functionally distinct classes of C-fibre nociceptors in primates. *Nat. Commun.* **2014**, *5*, 4122. [CrossRef] [PubMed]
12. Schmelz, M.; Schmidt, R.; Bickel, A.; Handwerker, H.O.; Torebjork, H.E. Specific C-receptors for itch in human skin. *J. Neurosci.* **1997**, *17*, 8003–8008. [CrossRef] [PubMed]
13. Namer, B.; Carr, R.; Johaneck, L.M.; Schmelz, M.; Handwerker, H.O.; Ringkamp, M. Separate peripheral pathways for pruritus in man. *J. Neurophysiol.* **2008**, *100*, 2062–2069. [CrossRef] [PubMed]
14. Klein, A.; Solinski, H.J.; Malewicz, N.M.; Jeong, H.F.; Sypek, E.I.; Shimada, S.G.; Hartke, T.V.; Wooten, M.; Wu, G.; Dong, X.; et al. Pruriception and neuronal coding in nociceptor subtypes in human and nonhuman primates. *Elife* **2021**, *10*, e64506. [CrossRef] [PubMed]
15. Imachi, N.; Park, G.H.; Lee, H.; Anderson, D.J.; Simon, M.I.; Basbaum, A.I.; Han, S.K. TRPV1-expressing primary afferents generate behavioral responses to pruritogens via multiple mechanisms. *Proc. Natl. Acad. Sci. USA* **2009**, *106*, 11330–11335. [CrossRef] [PubMed]
16. Shim, W.S.; Tak, M.H.; Lee, M.H.; Kim, M.; Kim, M.; Koo, J.Y.; Lee, C.H.; Kim, M.; Oh, U. TRPV1 mediates histamine-induced itching via the activation of phospholipase A2 and 12-lipoxygenase. *J. Neurosci.* **2007**, *27*, 2331–2337. [CrossRef] [PubMed]
17. Szolcsányi, J.; Pintér, E. Transient receptor potential vanilloid 1 as a therapeutic target in analgesia. *Expert Opin. Ther. Targets* **2013**, *17*, 641–657. [CrossRef]
18. Mason, L.; Moore, R.A.; Derry, S.; Edwards, J.E.; McQuay, H.J. Systematic review of topical capsaicin for the treatment of chronic pain. *BMJ* **2004**, *328*, 991. [CrossRef]
19. Mou, J.; Paillard, F.; Turnbull, B.; Trudeau, J.; Stoker, M.; Katz, N.P. Qutenza (capsaicin) 8% patch onset and duration of response and effects of multiple treatments in neuropathic pain patients. *Clin. J. Pain* **2014**, *30*, 286–294. [CrossRef]
20. Mainka, T.; Malewicz, N.M.; Baron, R.; Enax-Krumova, E.K.; Treede, R.D.; Maier, C. Presence of hyperalgesia predicts analgesic efficacy of topically applied capsaicin 8% in patients with peripheral neuropathic pain. *Eur. J. Pain* **2016**, *20*, 116–129. [CrossRef]
21. Zeidler, C.; Stander, S. Secondary generalized brachioradial pruritus. An uncommon but easy-to-use differential diagnostic approach to generalized pruritus. *Hautarzt* **2014**, *65*, 56–58. [CrossRef] [PubMed]
22. Andersen, H.H.; Elberling, J.; Solvsten, H.; Yosipovitch, G.; Arendt-Nielsen, L. Nonhistaminergic and mechanical itch sensitization in atopic dermatitis. *Pain* **2017**, *158*, 1780–1791. [CrossRef] [PubMed]
23. Johaneck, L.M.; Meyer, R.A.; Hartke, T.; Hobelmann, J.G.; Maine, D.N.; LaMotte, R.H.; Ringkamp, M. Psychophysical and Physiological Evidence for Parallel Afferent Pathways Mediating the Sensation of Itch. *J. Neurosci.* **2007**, *27*, 7490. [CrossRef] [PubMed]
24. Lo Vecchio, S.; Andersen, H.H.; Arendt-Nielsen, L. The time course of brief and prolonged topical 8% capsaicin-induced desensitization in healthy volunteers evaluated by quantitative sensory testing and vasomotor imaging. *Exp. Brain Res.* **2018**, *236*, 2231–2244. [CrossRef]

25. Andersen, H.H.; Marker, J.B.; Hoeck, E.A.; Elberling, J.; Arendt-Nielsen, L. Antipruritic effect of pretreatment with topical capsaicin 8% on histamine- and cowhage-evoked itch in healthy volunteers: A randomized, vehicle-controlled, proof-of-concept trial. *Br. J. Dermatol.* **2017**, *177*, 107–116. [CrossRef]
26. Wang, T.; Hurwitz, O.; Shimada, S.G.; Tian, D.; Dai, F.; Zhou, J.; Ma, C.; LaMotte, R.H. Anti-nociceptive effects of bupivacaine-encapsulated PLGA nanoparticles applied to the compressed dorsal root ganglion in mice. *Neurosci. Lett.* **2018**, *668*, 154–158. [CrossRef]
27. Lax, N.C.; Chen, R.; Leep, S.R.; Uhrich, K.; Yu, L.; Kolber, B. PolyMorphine provides extended analgesic-like effects in mice with spared nerve injury. *Mol. Pain* **2017**, *13*, 1744806917743479. [CrossRef]
28. Phạm, T.L.; Kim, D.W. Poly(lactic-co-glycolic acid) nanomaterial-based treatment options for pain management: A review. *Nanomedicine* **2020**, *15*, 1897–1913. [CrossRef]
29. Bartoshuk, L.M.; Duffy, V.B.; Green, B.G.; Hoffman, H.J.; Ko, C.W.; Lucchina, L.A.; Marks, L.E.; Snyder, D.J.; Weiffenbach, J.M. Valid across-group comparisons with labeled scales: The gLMS versus magnitude matching. *Physiol. Behav.* **2004**, *82*, 109–114. [CrossRef]
30. Green, B.G.; Dalton, P.; Cowart, B.; Shaffer, G.; Rankin, K.; Higgins, J. Evaluating the ‘Labeled Magnitude Scale’ for measuring sensations of taste and smell. *Chem. Senses* **1996**, *21*, 323–334. [CrossRef]
31. Raza, K.; Shareef, M.A.; Singal, P.; Sharma, G.; Negi, P.; Katare, O.P. Lipid-based capsaicin-loaded nano-colloidal biocompatible topical carriers with enhanced analgesic potential and decreased dermal irritation. *J. Liposome Res.* **2014**, *24*, 290–296. [CrossRef] [PubMed]
32. Zhou, J.; Patel, T.R.; Sirianni, R.W.; Strohbahn, G.; Zheng, M.Q.; Duong, N.; Schafbauer, T.; Huttner, A.J.; Huang, Y.; Carson, R.E.; et al. Highly penetrative, drug-loaded nanocarriers improve treatment of glioblastoma. *Proc. Natl. Acad. Sci. USA* **2013**, *110*, 11751–11756. [CrossRef] [PubMed]
33. Kim, S.; Kim, J.C.; Sul, D.; Hwang, S.W.; Lee, S.H.; Kim, Y.H.; Tae, G. Nanoparticle formulation for controlled release of capsaicin. *J. Nanosci. Nanotechnol.* **2011**, *11*, 4586–4591. [CrossRef] [PubMed]
34. Simone, D.A.; Baumann, T.K.; LaMotte, R.H. Dose-dependent pain and mechanical hyperalgesia in humans after intradermal injection of capsaicin. *Pain* **1989**, *38*, 99–107. [CrossRef]
35. Forstenpointner, J.; Naleschinski, D.; Wasner, G.; Hüllemann, P.; Binder, A.; Baron, R. Sensitized vasoactive C-nociceptors: Key fibers in peripheral neuropathic pain. *Pain Rep.* **2019**, *4*, e709. [CrossRef]
36. LaMotte, R.H.; Shain, C.N.; Simone, D.A.; Tsai, E.F. Neurogenic hyperalgesia: Psychophysical studies of underlying mechanisms. *J. Neurophysiol.* **1991**, *66*, 190–211. [CrossRef]
37. Wilson, S.R.; Gerhold, K.A.; Bifolck-Fisher, A.; Liu, Q.; Patel, K.N.; Dong, X.; Bautista, D.M. TRPA1 is required for histamine-independent, Mas-related G protein-coupled receptor-mediated itch. *Nat. Neurosci.* **2011**, *14*, 595–602. [CrossRef]
38. Zhang, Z.; Pan, J.; Zhu, T.; Malewicz, N.; Ye, K.; Rong, J.; Luo, Y.; Situ, Y.; Verkhatsky, A.; Wang, Y.; et al. Oxymatrine screened from *Sophora flavescens* by cell membrane immobilized chromatography relieves histamine-independent itch. *J. Pharm. Pharmacol.* **2021**, *73*, 1617–1629. [CrossRef]
39. Lu, J.M.; Wang, X.; Marin-Muller, C.; Wang, H.; Lin, P.H.; Yao, Q.; Chen, C. Current advances in research and clinical applications of PLGA-based nanotechnology. *Expert Rev. Mol. Diagn.* **2009**, *9*, 325–341. [CrossRef]
40. Panayotov, I.V.; Orti, V.; Cuisinier, F.; Yachouh, J. Polyetheretherketone (PEEK) for medical applications. *J. Mater. Sci. Mater. Med.* **2016**, *27*, 118. [CrossRef]
41. Glinsukon, T.; Stitmunnaithum, V.; Toskulkao, C.; Buranawuti, T.; Tangkrisanavinont, V. Acute toxicity of capsaicin in several animal species. *Toxicol. Off. J. Int. Soc. Toxicology* **1980**, *18*, 215–220. [CrossRef]
42. Ruifrok, A.C.; Johnston, D.A. Quantification of histochemical staining by color deconvolution. *Anal. Quant. Cytol. Histol.* **2001**, *23*, 291–299. [PubMed]
43. Schneider, C.A.; Rasband, W.S.; Eliceiri, K.W. NIH Image to ImageJ: 25 years of image analysis. *Nat. Methods* **2012**, *9*, 671–675. [CrossRef] [PubMed]
44. Oeck, S.; Malewicz, N.M.; Hurst, S.; Rudner, J.; Jendrossek, V. The Focinator—A new open-source tool for high-throughput foci evaluation of DNA damage. *Radiat. Oncol.* **2015**, *10*, 163. [CrossRef]
45. Zhang, Z.; Malewicz, N.M.; Xu, X.; Pan, J.; Kumowski, N.; Zhu, T.; Shimada, S.G.; Nie, H.; LaMotte, R.H. Differences in itch and pain behaviors accompanying the irritant and allergic contact dermatitis produced by a contact allergen in mice. *Pain Rep.* **2019**, *4*, e781. [CrossRef]
46. Sikand, P.; Shimada, S.G.; Green, B.G.; LaMotte, R.H. Similar itch and nociceptive sensations evoked by punctate cutaneous application of capsaicin, histamine and cowhage. *Pain* **2009**, *144*, 66–75. [CrossRef]
47. Stevens, S.S. *Psychophysics Introduction to Its Perceptual Neural and Social Prospects*; New York John Wiley-Scientific Research Publishing: New York, NY, USA, 1975.
48. Rolke, R.; Magerl, W.; Campbell, K.A.; Schalber, C.; Caspari, S.; Birklein, F.; Treede, R.D. Quantitative sensory testing: A comprehensive protocol for clinical trials. *Eur. J. Pain* **2006**, *10*, 77–88. [CrossRef]



Review

Recent Developments in Nanomaterials-Based Drug Delivery and Upgrading Treatment of Cardiovascular Diseases

Nura A. Mohamed^{1,*}, Isra Marei^{2,3}, Sergio Crovella¹ and Haissam Abou-Saleh^{1,4,*}

¹ Biological Science Program, Department of Biological and Environmental Sciences, College of Arts and Sciences, Qatar University, Doha P.O. Box 2713, Qatar; sgrovella@qu.edu.qa

² Department of Cardiothoracic Pharmacology, National Heart and Lung Institute, Imperial College, London SW7 2AZ, UK; iym2001@qatar-med.cornell.edu

³ Department of Pharmacology, Weill Cornell Medicine in Qatar, Doha P.O. Box 24144, Qatar

⁴ Biomedical Research Center (BRC), Qatar University, Doha P.O. Box 2713, Qatar

* Correspondence: nura.abdi11@imperial.ac.uk (N.A.M.); hasaleh@qu.edu.qa (H.A.-S.)

Abstract: Cardiovascular diseases (CVDs) are the leading causes of morbidity and mortality worldwide. However, despite the recent developments in the management of CVDs, the early and long outcomes vary considerably in patients, especially with the current challenges facing the detection and treatment of CVDs. This disparity is due to a lack of advanced diagnostic tools and targeted therapies, requiring innovative and alternative methods. Nanotechnology offers the opportunity to use nanomaterials in improving health and controlling diseases. Notably, nanotechnologies have recognized potential applicability in managing chronic diseases in the past few years, especially cancer and CVDs. Of particular interest is the use of nanoparticles as drug carriers to increase the pharmaco-efficacy and safety of conventional therapies. Different strategies have been proposed to use nanoparticles as drug carriers in CVDs; however, controversies regarding the selection of nanomaterials and nanoformulation are slowing their clinical translation. Therefore, this review focuses on nanotechnology for drug delivery and the application of nanomedicine in CVDs.

Keywords: nanotechnology; nanomedicine; nanoparticles; metal-organic framework; cardiovascular diseases



Citation: Mohamed, N.A.; Marei, I.; Crovella, S.; Abou-Saleh, H. Recent Developments in Nanomaterials-Based Drug Delivery and Upgrading Treatment of Cardiovascular Diseases. *Int. J. Mol. Sci.* **2022**, *23*, 1404. <https://doi.org/10.3390/ijms23031404>

Academic Editor: Christian Celia

Received: 14 November 2021

Accepted: 21 January 2022

Published: 26 January 2022

Publisher's Note: MDPI stays neutral with regard to jurisdictional claims in published maps and institutional affiliations.



Copyright: © 2022 by the authors. Licensee MDPI, Basel, Switzerland. This article is an open access article distributed under the terms and conditions of the Creative Commons Attribution (CC BY) license (<https://creativecommons.org/licenses/by/4.0/>).

1. Introduction

The concept of nanotechnology was first introduced to the public in December 1959 when Richard P. Feynman proclaimed, “There is Plenty of Room at the Bottom” [1] at an annual meeting of the American Physical Society. This new concept of nanotechnology gained more attention in 1986 when K. Eric Drexler published his book, *Engines of creation: the coming era of nanotechnology* [2]. This book further discussed how nanotechnology could be applied in the medical field to be used for drug delivery, diagnostic imaging of diseases, tissue engineering, and gene delivery systems [2]. Nonetheless, the term “nanomedicine” was first disclosed by K. Eric Drexler, Chris Peterson, and Gayle Pergamit in their book, *Unbounding the Future: The Nanotechnology Revolution*, published in 1991 [3]. The term became popular following the book, *Nanomedicine*, by Robert A. Freitas in 1999 [4]. Since then, nanomedicine has been investigated to revolutionize the therapeutic strategies to impacted different healthcare fields [1].

Nanomedicine is defined as “the use of materials, of which at least one of their dimensions that affects their function is in the scale range 1–100 nm, for a specific diagnostic or therapeutic purpose” [5]. This field expands to integrate biology, chemistry, pharmacology, and material sciences. Despite being described in the early 1990s, nanomedicine is still considered a new and rapidly evolving field that has drawn the attention of medical researchers, the biotech industry, engineers, legislatures, and public consideration. By 2009, 200,000 research articles [6] were published on the use of nanomaterials in medicine and

their potential to improve drug administration, implants, surgical devices (e.g., nanoneedles, nanoblades), nanorobotics, and nanosystems that combine therapeutics and real-time disease monitoring [6,7]. One of the emerging interests in nanomedicine is their application as drug carriers to improve the pharmacoefficacy and safety of conventional therapies [8]. In addition, nanotechnology for drug delivery holds the promise to improve the diagnosis and treatment of several diseases such as cardiovascular diseases (CVDs) [9], neurodegenerative diseases, inflammation, diabetes, orthopedic disorders, and cancer [1]. This review focuses on the use of nanotechnology for drug delivery and its application in CVDs.

2. Nanoparticles as Drug Carriers

The use of nanoparticles (NPs) as carriers for drugs can offer many advantages over conventional therapies due to their tunable physicochemical and structural properties [10,11]. Loading conventional therapeutics into NPs, combined with the precise design and accurate tuning, can improve pharmacokinetic/pharmacodynamic properties, efficacy, and solubility by changing the properties of the loaded drug in a way that sides with the therapeutic purposes [10]. Such nanoformulations may also increase the drug's safety and tolerability by reducing organ toxicity and non-selective drug delivery to undesirable sites. They could also be tuned to prevent the pre-activation and consequent early clearance of the drug by the immune system, thus enhancing drug stability. Furthermore, these formulations may promote a selective, guided, and sustained drug release to the affected tissues when labeled with a specific antibody, maintaining a specific and homogenous drug absorption and distribution [12,13].

Developing NPs from biocompatible and biodegradable materials has unceasingly been a major concern to improve drug delivery and bring considerable advances to other biomedical domains such as tissue engineering and biomaterial sciences [12]. Such development imperatively requires interdisciplinary networking involving biologists, chemists, engineers, and clinicians [12]. The careful and precise design of NPs, the choice of their material structure, and the methodology used to load the drugs into these NPs are all crucial aspects that affect the carried drug's stability, solubility, pharmacokinetics, and tissue distribution [8]. Thus, the following section provides an overview of the currently used material substrates for NPs, the parameters that influence drug delivery, the available methods to load drugs into NPs, their pharmacokinetics, and their interaction with the immune system. Moreover, the optimized protocols employed to achieve targeted drug delivery will be discussed.

2.1. Material Substrate

Different materials from organic or inorganic sources are being used to synthesize NPs, resulting in variable biological, toxicological, and chemical properties. Examples include proteins, micelles, liposomes, dendrimers, polymers, lipids, carbohydrates, nanocrystals, nanotubes, metals, and metal oxides, in addition to other inorganic materials. The efficacy of these NPs as drug delivery systems is affected by the properties of these materials and the NPs structures. NPs are composed of a surface layer, a shell, a core and may exhibit different sizes, shapes, and core/shell thicknesses [14]. The size, shape, polarity, and surface topography of NPs can significantly affect the drug's biodistribution, tissue absorption, cellular uptake, and accumulation. These properties can be tuned in a manner that facilitates the drug to cross biological barriers, increase its bioavailability, and provide a controlled clearance mechanism [15]. These same features can be used to customize treatments to be disease specific.

2.2. Size and Shape

Size is an important factor that ensures the safe travel of the nanoparticles in the bloodstream and determines their accumulation sites. Small nanoparticles are more likely to accumulate in leaky and deformed vessels in cancer and many cardiovascular diseases (due to angiogenesis), and they can also extravasate into normal tissues. In contrast, large

nanoparticles cannot easily accumulate in leaky vessels or extravasate into the surrounding normal tissues [16]. Once NPs are used up in the body, different body organs clear them out depending on their size. Small NPs with size <10 nm are removed by the kidney, while NPs > 10 nm are removed by the mononuclear-phagocyte system (MPS) [16]. This indicates that, by tuning and controlling NPs size, we can positively act on their uptake, tissue retention, distribution, and clearance from the body. In addition, NP shape influences their interaction *in vivo* and their body's retention due to its impact on fluid dynamics [16]. The shape has also been shown to impact cellular uptake and internalization, as well as cytotoxicity [17].

Nanoparticle functionalities can be tailored by altering the size, shape and/or surface chemistry of the nanoparticles. The purpose of functionalizing the nanoparticles is to help them reach the targeted tissue/organ, it also helps in enhancing the cellular uptake of the nanoparticles and their permeability. Choosing the nanoparticles optimal size depends on the specific type and the location of the targeted tissue/organ; this requires additional studies to understand the interactions between the nanoparticle and cells component of that tissue. Analytical models are also used to guide in designing and functionalization nanoparticles; these methods can help choose the NP shape. For instance, a comparison between spherical, cubic, and rod-like gold nanoparticles showed that spherical particles have the highest uptake in terms of weight; however, rod-like nanoparticles were higher in terms of quantity.

Furthermore, the size of the nanoparticle impacts cellular uptake, as it affects the adhesion strength between the nanoparticles and cellular receptors. Through the manipulation of that interaction, we can use the same nanoparticle (with different sizes) in many types of immune regulations. Small nanoparticles were shown to be great conjugates to vaccine antigens, with high cellular uptake rates compared to microsized particles. In addition, sizes between 25 and 40 nm showed high tissue penetration rates, which aid in activating the adaptive immune responses [18].

Variation in nanoparticles sizes can be accompanied with aggregation problems, where small nanoparticles are shown to aggregate into clusters up to several microns in size. Therefore, studying nanoparticles aggregation is crucial in determining the toxicity and nanoparticle risk in biological systems. Moreover, when small nanoparticles accumulate in organs and tissues with altered pH, it was shown that the more acidic the environment is, the greater the nanoparticles' aggregation tendency. In addition, nanoparticle aggregation can affect the size distribution, which in turn influences the toxicity and fate of the nanoparticles, altering the exposure location pathways [19].

Nanoparticle aggregation was also shown to affect the mode of cellular uptake in turn modifying the subsequent biological responses. Some nanoparticles use the aggregation on the cell membrane as a way to interact with the membrane proteins and to use it as a way to enter the desired cells. This is often seen with small-sized nanoparticles, when these nanoparticles fail to be wrapped by the cell membrane through receptor-mediated endocytosis, in which they often tend to aggregate, forming clusters of larger sizes to help in the internalization process. The rate of aggregation on the cell surface is regulated by the nanoparticles' size/shape/surface chemistry and by membrane tension. Therefore, nanoparticle aggregation is sometime beneficial, and understanding nanoparticle interactions with the cell membrane is important in the application of drug delivery systems [20,21].

2.3. Surface Chemistry

Similar to what is described for size/shape, nanoparticle surface chemistry properties impact their distribution in tissues/organs. Biocompatible nanoparticles often do not generate an immune response; therefore, biocompatibility of the nanoparticles should be first fully assessed, and the interactions between the nanoparticles and the serum proteins should be investigated. The surface chemistry of the nanoparticle not only affects its function, but it also determines its fate and clearance mood [21].

Nanoparticle surface charge, surface chemistry, and surface functional groups are important in determining the interaction between the nanoparticle and the cellular components of a particular tissue or organ. To do so, nanoparticles often come into contact with extracellular fluids (ECFs) (e.g., blood, lymph and interstitial fluid); this interaction forms a layer or shell that surrounds the nanoparticle, called the corona. This layer often contains the following ECFs components, proteins, ions, sugars, and lipids. The function of the corona is to mitigate nanoparticle cytotoxicity and to facilitate its clearance by the immune system. However, recent studies have shown the possibility of tailoring the nanoparticles' surface chemistry in order to recruit certain components of the ECFs to prolong its half-life, increase its permeability, tailor the immune response to the nanoparticles, and facilitate its cellular uptake [22].

The clearance of NPs from the bloodstream is primarily influenced by their hydrophobic/hydrophilic properties. For instance, hydrophobic nanoparticles are easily recognized by the reticuloendothelial system (RES), tagged with opsonin proteins [18] to be eliminated by the monocytes and macrophages and cleared from the body before reaching the affected tissue. Thus, coating them with a hydrophilic layer (e.g., polyethylene glycol (PGE) can mask their hydrophobicity. PEG can be used to coat hydrophobic drugs to improve their solubility, stability, and bioavailability and to enhance their retention by leaky vasculature [23,24]. However, materials used in the synthesis and the surface modification of nanoparticles should be carefully validated for their safety. Despite having Food and Drug Association (FDA) approved PGE nanoformulations, it still has some drawbacks, such as unfavorable physicochemical characteristics due to particle aggregation, post in vivo administration complications such as hypersensitivity reactions, and developing immune tolerance that limits their pharmacological effect [25].

2.4. NPs and the Immune System

Since the introduction of NPs as drug carriers and detection agents, concerns about their effect on the immune system have been raised. Historically, concerns were mainly centered on the immunostimulatory effect of the NPs; however, NPs unintended immunosuppressive and anti-inflammatory effects are currently drawing more attention [26]. For that particular purpose, monitoring immunosuppression, immunostimulation, anti-inflammatory effect of nanomaterials, and whether that effect is to the benefit of the studied disease is crucial to assure the nanomaterials safety [26]. Some of the currently existing nanoformulations possess anti-inflammatory effects on their own, as they reduce inflammatory, immune responses, and oxidative stress in diseased tissues [16]. Metals such as iron, gold, silver, copper, zinc oxide, zinc peroxide, magnesium oxide, nickel, selenium, cerium oxide, and titanium dioxide have been endowed to have anti-inflammatory as well as anti-proliferative effects [27]. Of these NPs, iron oxide NPs have drawn attention due to the many therapeutic properties they possess. Iron oxide NPs have been implicated in the treatment of many inflammatory disorders. For example, a study conducted by Saeidienik et al. showed that iron oxide NPs have neuroprotective and anti-inflammatory effects [28]. In this study, treatment of depressed mice with different doses of iron oxide NPs resulted in the attenuation of the depression symptoms through the modulation of neurotransmitters and the anti-inflammatory effects of these NPs [28]. Other NPs can be designed and engineered to specifically target the immune system causing an intended stimulatory or suppressive effect [29,30]. For example, several studies have shown that iron-oxide-containing NPs possess unintended immunosuppressive effects [29,30], which could be used in the field of organ and tissue transplantation to track the distribution of the administered stem cells and to study the viability of implanted cells within scaffolds intern monitoring the transplanted grafts; in addition, if loaded with other immunosuppressive drugs, they can be used to evaluate drug release and distribution in the tissues/scaffolds [31]. Therefore, NPs modulation of the immune responses led to the development of the nano-immunotherapy field [32,33]. This strategy is essentially used in cancer therapy to stimulate or boost the natural defenses of the immune system to recognize and kill cancer cells. Thus, nano-immunotherapy may

increase the ability of the body to recognize and destroy abnormal cells (e.g., cancer cells) while protecting the body from the side effects of chemotherapy [32,33].

2.5. Drug Loading and Release Pharmacokinetics

Drugs can be loaded into NPs by encapsulation, conjugation, linking, or other techniques [8]. In addition, they can be loaded with more than one drug to enable combined drug therapy. Examples of combined nanotherapies are the micellar nanoparticles loaded with both bortezomib and doxorubicin, which exhibited a synergistic antitumor effect on ovarian cancer [34]. Another example is the use of PLGA-NPs to carry multiple siRNAs either alone or in combination with drugs showed an increase in the tumor's sensitivity to the treatment [35,36]. The technicality by which drugs are loaded into NPs affects the carried drug's stability and solubility, as well as its pharmacokinetics and body distribution [8]. The mechanisms controlling the pharmacokinetics of drug-loaded NPs vary from those controlling conventional drugs and biologics. Therefore, understanding these processes is crucial to improving NPs efficacy and in vivo performance [37]. Glassman and Muzykantov have provided a comprehensive review of the differences between the pharmacokinetics of small drug molecules and drug-loaded NPs. In this review, we only highlight some of the key elements involved in NP pharmacokinetics [37].

One key element that affects drug pharmacokinetics is the duration by which the NPs can stay in the body, which varies according to the class of the NPs. Nanomedicine research reveals the involvement of a protein layer, called corona in defining the NPs half-life [24]. Protein corona is responsible for the NPs clearance from the body as it adheres and accumulates on the surface of the NPs. This accumulation acts as a signal and activates immune cells (e.g., macrophages) to clear the NPs [24]. This unwanted mechanism can be prevented by the surface functionalization and coating of the NPs with organic material such as PEG, which can inhibit the NPs early recognition by the immune system.

2.6. Surface Modifications for Targeted NPs Delivery

Some NPs have chemical properties that can help to achieve targeted delivery. Targeted delivery depends on the used nanoformulation and comprises either passive and/or active targeting. Passive targeting occurs due to the non-specific accumulations of NPs in the diseased tissues, a phenomenon seen in remodeled and impaired vessels [23]. These nanoparticles have high enhanced permeability and retention (EPR) properties, which help them to accumulate in the diseased tissues passively. This occurs in the damaged areas of the blood vessels, where the microvascular endothelial cell space is thin and damaged, making it easy for the drug-loaded nanoparticles to pass through the vascular wall [38]. Many CVDs such as acute ischemic stroke, myocardial infarction, atherosclerosis, abdominal aortic aneurysm, varicose veins, and hypertension have elevated vascular permeability [39,40]. Impaired or damaged vasculature is characterized by deformed and remodeled blood vessels with poor structural integrity and accumulation of inflammatory and progenitor cells. This results in having increased levels of the inflammatory cytokines such as TNF- α , TGF- β , IL-12, IL-6, IL-1 β , IFN- β , and cell adhesion molecules such as VCAM, ICAM-1, E selectin, and P-selectin [39–41]. Unfortunately, passive targeting cannot eliminate the accumulation of the nanocarriers in tissues that generally have fenestrated blood vessels, such as the liver or the spleen [42]. Conversely, active targeting occurs when NPs are tagged to selectively transport therapies to the desired sites. Tagging NPs surface with an endogenous guiding ligand (micro and/or macromolecule such as proteins antibodies, peptides) that are designed to single out diseased cells, tissues, and organs has the potential to increase the drug's intracellular and tissue accumulation [16,42].

3. Nanoimaging

Nanoimaging refers to the use of nanoformulation as detection agents. Some NPs on their own can offer both pharmacological and imaging properties [15]. In nanoimaging, NPs are used for disease detection and monitoring during follow-up. Similar to their effect with

drugs, NPs can improve the pharmacokinetics, efficacy, and safety of the loaded detecting agent and, in some cases, add some targeting benefits. In addition, they can provide better contrast compared to the conventional imaging techniques, thus promoting earlier and rapid disease detection [15]. This feature is a turning point in the prognosis of rapidly progressing diseases, such as cancer, making nanoimaging a valuable diagnostic tool [15]. Finding the proper nanoimaging tool is a herculean task that requires full knowledge of the targeted cell type, suitable photosensitive organic dye or radiolabeling the nanomaterial, and detection wavelength. The ability of the NP to accurately select the desired tissue is critical in nanoimaging to avoid non-specific cell binding and, therefore, to avoid false-positive results [10,43]. Examples of nanoimaging tools are the nanoscale crystals, quantum dots that can be attached to proteins to increase their cellular permeability, and they are often used in cancer detection [44].

Another example is the use of polymers to deliver detection agents such as the poly lactic-co-glycolic acid (PLGA), which is favored because of its biocompatibility and biodegradability. In one study, PLGA was used to encapsulate the highly toxic benzophenothiazinium dye EtNBS used in photodynamic therapy. The encapsulation reduced the amount of free EtNBS, which significantly reduced its toxicity [44]. Using nanoimaging-mediated cardiovascular theranosis is one of the recent areas in the CVD detection area. An example of this is the use of a nano-based theranostic approach in reducing the plaque volume. In that context, it was shown that rTPA tagged iron oxide nanoparticles were more efficient in dissolving clots. Once dissolved, it is important to monitor the migration and fate of any clot remains, which is performed using fluorophores coated nanoparticles.

Another example is the use of nanoparticles in the detection and inhibition of angiogenesis, which is an important step in the atherosclerotic plaque formation. To determine the presence of neovascularization ultra-small super paramagnetic iron oxide nanoparticle that can target integrin $\alpha_v\beta_3$ receptor have been developed, once iron nanoparticles target the integrin $\alpha_v\beta_3$, angiogenesis is determined and quantified using MR. Furthermore, supermagnetic iron nanoparticles tagged with fluorophores were shown to be effective in the detection and destruction of the inflammatory macrophages in atherosclerotic plaques.

Additionally, nanoimaging can also be used in labeling and tracking down the transplanted Stem cells. A study showed that transplanting mesenchymal stem cells can improve the cardiac activity in myocardial infarction (MI) patients. However, once transplanted, it is hard to know the % of the cells that reached the infarcted area. To overcome this problem, supermagnetic iron oxide nanoparticles (SPOIN) showed to be effective in marking the transplanted cells, tracking them down which aids in determining how many of these cells will reach the infarcted area as well as knowing the location of the others. Moreover, when patients undergo transplant (e.g., heart transplant), often the only way to determine the presence of organ rejection is through repeated biopsies. Recent studies have shown the possibility of using fluorophore-tagged iron-oxide nanoparticles, which were shown to be highly taken up by macrophages, which are found in abundance during organ rejection [45].

3.1. Smart NPs (Dynabeads)

The use of NPs in medicine is limited to nanopharmaceuticals and nanoimaging and blood disorders [46]. Smart nanomaterials (or Dynabeads) are used to magnetically activate and sort cells to purify the blood from harmful compounds such as pathogens and toxins, as well as proteins. This procedure is used to replace the ordinary dialysis methods and employs iron oxide or carbon-coated metal NPs. The iron atoms provide the ferromagnetic or super magnetic properties and can be linked to different antibodies, proteins, antibiotics, or other molecules. Once mixed with blood during dialysis, each linked molecule binds to the relevant target (i.e., cell, protein, other blood components). Then, the fluid is subjected to an external magnetic field whereby blood components attached to the Dynabeads will aggregate around the magnetic pole, whereas all the undesired components will pass by [46,47]. Although in the early stages, this technique can decidedly be used for other

blood disorders. Other uses of nanomaterials in medicine include nano-nephrology and nanorobots [46,47].

3.2. Multifunctional NPs

Multifunctional nanoparticles are defined as “nanoparticles that are capable of accomplishing multiple objectives such as imaging and therapy or performing a single advanced function through the incorporation of multiple functional units” [48]. These NPs are attractive due to their small size, which allows dosage reduction and improves their toxicity profile. These NPs have a large surface-area-to-volume ratio, which increases their solubility and improves their intracellular uptake. They can encapsulate drugs, thus protecting them from external agents. Most importantly, their size can be adjusted such that they readily diffuse through cell membranes and, in some cases, cross the BBB through different uptake mechanisms [49].

Furthermore, these NPs act as therapeutic cargo that allows controlled and sustained release of the therapeutic agent. Different parameters can be activated to ensure the controlled release of a drug, such as temperature, pH level, enzyme activity, magnetic field, etc. One of the most recent trends in NP formulation is the use of DNA as drug delivery systems, where researchers have focused their attention on DNA nanostructures due to their high biocompatibility and the fact that they are less prone to degradation when compared to synthetic NPs [50]. Similar to cancer, CVDs involve vasculature remodeling and lesion development with affected areas of high porosity. Porous vasculature can utilize the enhanced permeability retention (EPR) effect, allowing the nanoformulation to transport drugs to the affected cells. In ischemic tissue injury, the expression of vascular endothelial growth factor (VEGF) induces the breakdown of the endothelial lining by uncoupling endothelial cell-cell junctions, resulting in leaky vasculature. This results in the accumulation of excessive fluid in the affected area as well as the surrounding tissues. Therefore, tagging the nanoformulation with an anti-VEGF antibody might offer actively targeted drug delivery [51,52].

3.3. Nanomedicine and the COVID-19 Pandemic

The nanomedicine field has proven its effectiveness and uniqueness during the COVID-19 pandemic. A year after the COVID-19 pandemic, two nanomedicine-based mRNA vaccines have been developed, tested, validated, and authorized to be used in facing the still ongoing pandemic. The nanotechnology part of the COVID-19 vaccine which consists of the lipid, enabled the formulations of the first two COVID-19 vaccines in a way that advanced the clinical translation of the nanomedicine drug delivery systems from bench to bed use. The quick translation has distinguished the lipid based nanoparticles from the other forms as it showed its readiness to face the clinical challenge of the rapid development of mRNA vaccine [53]. The development of these two vaccines drew the world’s attention to the transformative potential of the RNA-based nanotherapeutics. Especially with recent findings suggesting the ability of RNA-based therapeutics in targeting previously “undruggable” pathways that are involved in the development of many diseases such as CVDs [54].

Thus far, there are three mRNA-nanotherapeutics approved clinically with many more in different clinical phases. Therefore, the further investigation of this field could have significant implications in the future of nanotechnology-based drug and gene delivery. Now more than ever, the successful delivery of advances such as vaccines, mRNA, and nucleic acid material depends on nanomedicine. Furthermore, the lessons learned from the translation of these lipid-based nanoparticles to the clinical phase can be used in forming the foundation for the safety COVID-19 pandemic tremendous scientific achievements caused by the COVID-19 helped in better shaping the translational of nanomedicines applications.

4. Approved and Clinically Tested Nanoformulations: State of the Art

Despite the numerous scientific articles published on nanomedicine every year, the number of nanomedicine formulations currently approved for clinical use is approximately one-tenth of what is reported in the scientific literature [49]. Experimental and regulatory barriers contribute to the low number of nanomedical formulations currently approved for clinical use. The main experimental obstacle is the full characterization scheme and extended toxicity profile of the tested NPs. In contrast, the main regulatory barrier is the lack of specified international regulatory guidelines and the need to illustrate the cost-benefit considerations for using nanomedicine formulations. Therefore, our expectations from the nanomedicine field should remain realistic until we fully understand the nanoformulations and their interactions with the human body [15].

Nevertheless, we still need to develop a more “precise” understanding of this field. This involves accurate characterization measures for the existing nanomedicines to understand their intrinsic properties and biological effects fully. This will enable the design of smart novel nanomedicines that are limited to precisely addressing diseases and personalizing nanotherapies.

As of November 2021, 91 clinical trials, including the term “nano,” were listed as “recruiting” or “active”, and 164 trials were under the term completed on ClinicalTrials.gov [55]. A quick screening through the progress in the nanoformulation clinical trials since 2000’ shows a steady increase starting from 2007, with the years 2013–2015 having the highest number of nanoformulation entering clinical trials [15,42]. In addition, a PubMed search of the word nanomedicine returns 37,170 results. Thus far, there are 52 nanomedicine formulations approved by the FDA [6,56,57], and 34 are approved by EMA (with one nanoformulation only approved in the Netherlands) [6,10,57] (see Supplementary Tables S1–S6 and Figure 1) [58–62]. Of these, three have been discontinued, which indicates the high success rate of the approved nanoformulations [6,10,56,57].

Nanomedicine is one of the hottest topics in cancer therapy, with more than 10,296 hits for “oncology” and “nanomedicine”, and 14,896 hits for “nanomedicine” and “cancer” on PubMed, making it the medical field that benefits the most from nanomedicine [9]. Other fields in medicine are picking up with infectious diseases and nanomedicine having 808 hits in PubMed and 84 hits in LitCOVID for COVID19 issues.

Despite having few clinically approved nanoformulations thus far, there is an abundance of available data, experimental research, and clinical trials reflecting the prevalence of this field [58]. Other medical fields should benefit from the knowledge gained from nanomedicine applications in cancer.

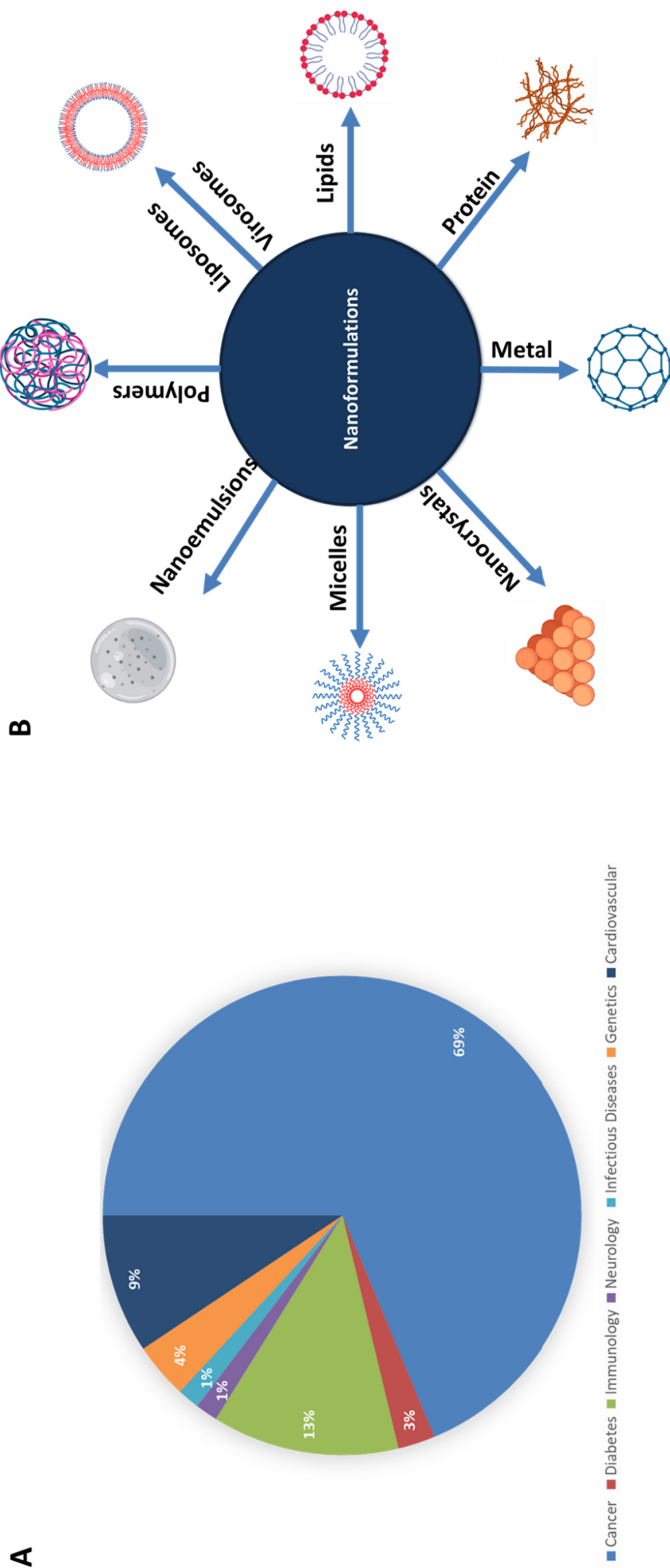


Figure 1. (A) Percentage of nanoformulations application in each medical field, and (B) different nanoformulations currently in use in the medical field.

5. Nanoformulations in Cardiovascular Diseases (CVDs)

CVDs are considered the major cause of disability and the number one cause of death worldwide [58], with 17.7 million deaths recorded in 2015, a figure that is expected to reach 23.6 million in 2030 (WHO 2017) [63]. In Europe, 45% of all deaths are due to CVDs, accounting for 3.9 million deaths/year [9]. In the United Kingdom, CVDs represent the second cause of death in the country, with 2 million people suffering from CVDs [63,64]. CVDs occurrence is either primary due to a defect in the heart, such as congenital heart disease [65], or secondary to other diseases such as diabetes [66] and hypertension [67]. Despite the advances in the treatment and control of CVDs, some diseases are still poorly managed and could benefit from nanomedicine such as hypertension [68], atherosclerosis [69], thrombosis [70], cardiovascular inflammatory disorders such as myocardium and endocarditis [71,72], stroke [68], myocardial infarction (MI) [73], and pulmonary arterial hypertension (PAH) [74,75]. There are many challenges that face CVDs such as: (i) failure in identifying the gaps in areas between CVDs prevention and treatment; (ii) failure to mark the risk factors and to learn how to modify them; (iii) failure in identifying and meeting individual needs; (iv) failure in diagnosing CVDs; (v) failure in accessing first line treatments; (vi) failure in identifying and using advanced CVDs treatments; and finally, (vii) failure in providing patients with supportive care [76]. Overcoming these challenges will lead to the development of new technologies, the development of new diagnostic approaches and the use of modern technologies that will help improve CVDs diagnosis and treatment [77]. In terms of the drug delivery systems, there are several grand challenges and hurdles that need to be addressed and overcome to improve the outcomes of patients with CVD. The first challenge is innovation, where scientists need to understand the basic molecular mechanisms that underlie the development of the CVD. By understanding these mechanisms relevant drug's delivery options can be selected. Second, different patients might require different delivery mechanisms, which has initiated the personalized therapeutic option. It is now clear more than ever that each patient comes with their individual: (i) risk factors, (ii) genetic background, (iii) lifestyle environment, and (iv) disease burden. Therefore, it is necessary to employ extensive diagnostics such as imaging, DNA sequencing, and proteomics to improve the clinical decision-making process [78].

Third, available CVD pharmacologic therapies are still combined with considerable drawbacks, these are the drug's low efficacy, side effects, and drug tolerability doses. A possible way to overcome CVDs challenges are the use of the advances made in the nanotechnology field in medicine and implement it in the CVD area. The use of nanoparticles as drug carriers can overcome these challenges, as there are nanoparticles that naturally interact with different biological pathways; others can be modified in terms of their charges, sizes, solubility to accumulate in the desired tissues. They can also be tagged with agents or ligands to make sure that they accumulate in the desired site. Upon accumulation, these nanoparticles will be stimulated by the intrinsic changes that occur at the disease site (e.g., PH) to release their payload a term called Smart Nanoparticles. Other extrinsic stimuli could be applied in other cases such as using ultrasound, light, magnetic or electrical fields directed at a specific region of the body [78]. This has highlighted the need for exploring new therapeutic strategies to overcome the limitations of current CVD conventional therapeutics. Thus, it has become crucial to apply the advances made in nanomedicine to improve CVDs diagnosis (e.g., Ferumoxytol) and treatment. Of relevance to CVDs is that many nanoformulations, such as polymeric NPs and metallic NPs (metal oxides), enable surface modification, allowing the NPs to code with ligands such as antibodies. This modulation improves their biodistribution and provides greater permeability into inflamed tissues [58].

Despite the late start of cardiovascular nanomedicine (CVN), this field is rushing with many promising lab-scale results. There are 1850 hits for "cardiovascular" and "nanomedicine" on PubMed, with studies working to establish innovative solutions for the current CVDs challenges. Many CVN trials remain focused on detecting, monitoring, and treating atherosclerosis; examples are BLAST, NANOM, and Nano-Athero [9]. The use of

stimuli-responsive NPs has also been reported [9]. These NPs are tailored to respond to internal vascular changes such as shear stress, with others responding to external stimuli such as magnetic and temperature-sensitive NPs [9].

5.1. Atherosclerosis

Atherosclerosis is a chronic inflammatory disease of the blood vessel walls resulting from the interaction between modified lipoproteins, circulating blood cells, and the endothelium. The etiology of atherosclerosis includes the slow and progressive build-up of vulnerable fatty plaques under the lining of the arterial wall, which gradually narrows the lumen of the artery and restricts blood flow to the heart, impelling myocardial ischemia. Acute myocardial infarction (AMI) is the major complication of atherosclerosis and is defined as a sudden, unpredictable plaque disruption (rupture or erosion) with superimposed thrombus formation. Atherosclerosis is a condition that can primarily benefit from nanomedicine due to the cellular and molecular mechanisms underlying the pathophysiology of the disease [79,80]. Atherosclerosis involves the formation of vascular lesions and the accumulation of inflammatory cells such as macrophages that express and upregulate cell surface receptors (e.g., vascular cell adhesion molecule-1, VCAM-1) that could be used as disease markers [79,80]. Several studies have been published investigating the use of nanoformulations that can target lesions sites and can be taken up by vascular cells through the surface modifying the NPs with either radiolabeled antibodies or fluorescent agents specific for the highly expressed receptors at the lesion site using protease-activatable nanosensors [81]. An example is the use of the surface modified copper sulfide (CuS) NPs to target the Transient Receptor Potential Vanilloid-1 (TRPV1) and reduce vascular lipid accumulation [82]. Elevated levels of blood lipids or hyperlipidemia are well-documented risk factors for atherosclerosis. The incorporation of the chemotherapeutic drug "Paclitaxel" into a cholesterol-rich nanoemulsion (LDE) was found to promote atherosclerosis regression and, when tested in vivo, showed a 65% reduction in the size of the atherosclerotic lesion with low toxicity [83].

5.2. Thrombosis

Thrombosis is defined as the formation of a malignant blood clot, and it is considered one of the leading causes of death. Despite knowing that in the process of the thrombus formation, platelets, and coagulation factors play a crucial role, the diagnosis of this disease is often limited to late stages, with treatment options being limited and unable to provide reasonable and effective results. Thus, identifying innovative diagnostic and treatment options are highly recommended in thrombosis [84]. Thrombosis underlines many CVDs, such as pulmonary embolism and myocardial infarction [70,85].

The clinical diagnostic of thrombosis relies on CT imaging, Doppler ultrasound, x-ray, and MRI. These techniques are routinely used in localizing the thrombi. Unfortunately, they fail in providing information about the composition and the age of the clots [86]. This kind of information can be obtained using nanomedicine techniques such as NPs radiolabeled with fibrin ligands and other coagulation factors and components involved in thrombus formation [87,88]. Another example of the use of nanomedicine in thrombosis is the development of the perfluorocarbon-core nanoparticle, which was functionalized by covalent binding to the Phe(D)-Pro-Arg-Chloromethylketone (PPACK) drug. PPACK is a synthetic peptide that can selectively and irreversibly inhibit thrombin activation. However, this drug has a short half-life in the body, and linking it to the perfluorocarbon-core nanoparticle prolonged its presence in circulation and, when tested in vivo, showed significant improvements in antithrombotic activity [89]. Another example is the use of iron oxide nanoworms (NWs) as carriers for a ligand-labeled peptide containing the Thrombin-activatable peptide (TAP); this nanoconjugate was shown to have high selectivity to thrombin [84].

5.3. Stroke

Stroke is a cerebrovascular disease that occurs when there is an abnormal cerebral blood flow (CBF), the disturbance then leads to either transient or permanent deficits in the function of one or more parts of the brain. Due to the metabolic and cellular changes caused by the disturbance, cellular death and disruption of the nervous system occurs, and if not intervened in time, the deficit can lead to disability, which is seen in high prevalence in developed countries. Therapeutic options available for stroke include recanalization and then using neuroprotective drugs. Despite the improvement in recovery strategies, there are still some major limitations that dramatically affect patients' lives in stroke. Some of the main limitations are the narrow therapeutic window, the limited ability to target the brain, and the side effects associated with the used drugs. For these reasons, nanomedicine seems perfect to be used in this area to overcome these limitations and to improve the treatments efficacy. In this area, nanoparticles could be used either as contrast agents or drug carriers [90].

An example of nanomedicine used in treating stroke is the liposome cytidine 5'-diphosphate conjugate tested to treat ischemic stroke. Liposomes and other NPs can be synthesized in a small size that can cross the blood-brain barrier (BBB) without compromising its integrity [91]. In addition, the use of liposome cytidine 5'-diphosphate conjugate can offer neuroprotective capacity in ischemia-reperfusion, which is an effective way of rescuing neural cells and avoiding the brain dead [91]. Another example is the emergence of a new micro-sized particle of the iron oxide (MPIOs) family that contains MRI contrast agents. Using MPIOs conjugated with monoclonal antibodies that targets vascular cell adhesion molecule-1 (VCAM-1) were shown to be effective in defining the "inflammatory penumbra" in ischemic stroke [90].

5.4. Myocardial Infarction (MI)

Adult cardiac tissues have limited regenerative capacity that is not enough in repairing the massive loss of heart tissue, which occurs following serious myocardial injuries (ischemia). Delivery of essential therapeutics agents (e.g., growth factors, cells, . . . etc.) is essential in facilitating the regeneration process. This is where using nanomedicine becomes essential due to the urgent need for the controlled release characteristics nanoparticles have. Applying the advances made in the nanomedicine field to enhance the drug's cardioprotective potential will revolutionize this area [92]. MI is associated with an inflammatory response, in which neutrophils and macrophages are recruited to the damaged area of the ischemic myocardium. These cells secrete different pro-inflammatory cytokines, chemokines, and proteolytic enzymes such as matrix metalloproteinases and cathepsin B [93]. This has enabled researchers to design probes that can carefully monitor and assess the pro-inflammatory secretome in subjects followed-up, especially for those with high-risk factors. Once fully established, this will help in the early detection of MI [94]. Conversely, iron oxide superparamagnetic nanoparticles possess remarkable magnetic properties that make them promising contrast agents. Furthermore, these NPs are biocompatible, and therefore, they have been used to monitor the homing of stem cells to ischemic myocardium. In addition, they can be used to sort and label stem cells [95]. Another example is the use of VEGF, stromal cell-derived factor-1 (SDF-1), FGF1 and/or Ang-1 loaded in nanoparticles to the ischemic myocardial tissue to stimulate angiogenesis. Recently, nanoparticle delivery through intravenous injection with targeting peptides has merged as a promising strategy. Another study reported an early targeting therapy property when anti-miR-1 antisense oligonucleotide (AMO-1) loaded and myocardium-targeting dendrimer: PEGylated dendrigraft poly-L-lysine with angiotensin II type 1 receptor (AT1-PEG-DGL AMO-1) were used with decreased cell death [92].

5.5. Hypertension and Pulmonary Arterial Hypertension (PAH)

Nanomedicine has been applied to improve hypertension treatment. Examples are gold and silica nanoparticles that were developed to enhance the bioavailability of the

nitric oxide (NO) supply to diseased vasculature [96]. Another example is cerium dioxide nanoparticles (CeO₂ NP) that have antioxidant potential, and when tested *in vivo*, they showed a significant decrease in both the levels of the antioxidants and the microvascular dysfunction [97]. PAH is a devastating, incurable disease with a poor prognosis and a low survival rate of 2–5 years [98]. Available treatments rely on restoring the normal pulmonary artery pressure by blocking the proliferative/vasoconstriction pathways and enhancing anti-proliferative/vasodilatory pathways [99–102]. When first introduced, PAH clinical treatment strategies were hampered by the short half-life of the drugs, implying the need for multiple doses or 24/7 infusion. Fortunately, these strategies have been improved to prolong the drug's half-life in circulation [103–107]. The utmost crucial limitation still facing scientists is the systemic side effects of the current drugs [108,109].

PAH drugs work better in preclinical animal models where PAH is prevented or reversed [110–112]. A possible explanation could be that these drugs are given to the tested animals at the early stages of PAH induction; thus, they work in a “prevention” setting, obviously, without predictors. In humans, this type of “pre-treatment” is often not applicable, as it is hard to identify an asymptomatic patient with PAH. Therefore, targeted delivery is of utmost importance to overcome current limitations and improve PAH detection/therapy by taking lessons from the advances made in other CVDs and cancer.

Despite the lack of clinically approved nanoformulations for PAH, preclinical studies are ongoing to investigate their use for this disease. An example is the NF-kappa B polymeric nanoformulation. Studies have shown that in the presence of the PAH lesions, there is an increase in the concentration of the transcription factor NF-kappa B. Blocking the NF-kappa B receptors with the polymeric nanoparticle-NF-kappa B antagonist conjugate can not only prevent PAH development, but can also improve PAH patient survival rate [113]. Most CVDs involve an inflammatory component in their pathogenesis; therefore, using nanoimmunotherapies could improve treatment strategies. A drug class called statins, composed of 3-hydroxy-3-methylglutaryl coenzyme A reductase inhibitor, is commonly used to lower lipid levels, and they have some vasculoprotective effects such as reducing antioxidant properties, inhibiting inflammation, and improving endothelial dysfunction. Statins can prevent inflammation and, therefore, can be utilized in the prevention and in slowing down the development of several CVDs, including PAH. In addition, statin has been incorporated in a polymeric NP to maximize its anti-inflammatory property [69]. Thus far, this application has been tested in various animal models, and its clinical applications are in progress [69]. It is well known that inflammation is involved in the development of PAH [114]. Patients with PAH have high levels of pro-inflammatory cytokines [115] and interferon (IFN) in their plasma [116]. Inflammation also causes the recruitment of immune cells such as macrophages and neutrophils as well as circulating progenitor cells [117]. Accumulated cells will then release an increased amount of cytokines and inflammatory mediators such as IFNs. This accumulation eventually leads to vascular remodeling that affects small pulmonary arteries (~500 μm) [118–120] and causes lesions in some cases (the so-called plexiform lesions) [121]. Targeting NPs to lesions and inflammation sites can improve the detection and targeted therapy of PAH and allow studying and characterizing the constituents of the plexiform lesions. Additionally, some NPs can be engineered to have a higher affinity to accumulate at the sites of inflammation and remodeled vessels, a phenomenon well studied in cancer [122,123].

Thus far, there is no drug available to explicitly stop the progressive cellular (inflammatory and progenitor cells) accumulation into the pulmonary artery vessel wall. This pulmonary vascular remodeling is a key pathological feature in PAH, contributing to the progressive narrowing of the lumen responsible for the functional decline and the right ventricle hypertrophy and dysfunction. In PAH, other cells are involved in vascular remodeling, such as the pericytes, which develop into pulmonary artery-like smooth muscle cells suggesting that these cells contribute to the excessive accumulation of pulmonary artery smooth muscle cells and fibroblasts within the pulmonary vascular wall of PAH patients [124]. Pericytes are central regulators of endothelial and smooth muscle cells pro-

liferation, vascular tone, and autoimmunity. Pericytes are responsible for regulating vessel maturation and for stabilization it. Furthermore, an accumulating body of evidence showed that in response to various pro-inflammatory stimuli they can participate in the onset of the innate immune responses. As a response, they then secrete a variety of chemokines and express different adhesion molecules including ICAM-1 and VCAM-1 which then causes the trafficking of the immune cells on the walls of the defected vessel [125,126]. Although pericytes appear to be an attractive therapeutic target in PAH, little is known about the intrinsic characteristics of lung pericytes and their role in the pathogenesis and particularly in the obstructive remodeling in PAH. Therefore, additional studies are needed. Although the contribution of altered immune responses in PAH pathogenesis is consensual, the exact role of inflammation in pulmonary vascular remodeling is still unclear. Whether immune dysregulation represents a cause, or an effect of PAH onset is still unknown [124]. Further studies are needed to assess the inadequate crosstalk between immune mediators and the components of the pulmonary vascular wall to identify novel therapeutical targets [124]. Another NP property that could be used is the affinity of iron nanoparticles to the lung [29], with studies showing the accumulation of the iron nanoparticle MIL-89 in the lung when tested *in vivo* [29].

Besides benefiting from the passive drug delivery offered by the NPs and the structural changes caused by the PAH prognosis, active targeting can also be achieved by coating the NPs with antibodies against antigens highly expressed in PAH endothelial cells. Examples of these antigens are: Nestin [127], BMPR2; EIF2AK4; TBX4; ATP13A3; GDF2; SOX17; AQP1; ACVRL1; SMAD9; ENG; KCNK3 and CAV1 [128]. A study conducted by Long et al. [129] reported the beneficial effects of BMP9 administration in heterozygous BMPR2 knockout mice, suggesting that compensating for BMPR2 haploinsufficiency by increasing dose of the ligand might constitute a targeted therapy for human PAH [129].

Designing an effective treatment strategy for PAH requires a complete understanding of the cellular mechanisms and the molecular pathways involved in the pathogenesis of the disease. This could explain why combined therapy for PAH has proven to be more effective than single therapy, with the European Society of Cardiology (ESC) and European Resuscitation Council (ERC) guidelines 2015, recommending the use of dual therapy in PAH by using a combination of the Phosphodiesterase type 5 inhibitor (PDE5) and Endothelin-1 (ET-1) drugs as the first-line therapy [130]. Therefore, encapsulating dual or triple PAH drugs might provide a “super” combination of PAH drugs to achieve a higher efficacy. In addition, this encapsulation may also protect the drugs from early immune clearance overcoming the drug tolerance issue seen with PAH drugs. In addition, we can take advantage of the fact that in PAH, endothelial cells are dysfunctional and express specific surface receptors. These receptors could be used as markers in synthesizing NP-coupled antibodies directed against dysfunctional endothelial cells to improve PAH treatment and detection.

The current clinical diagnostic detection for PAH relies on utilizing the suitable heart catheter, an invasive and inconvenient procedure [131]. Furthermore, some NPs, such as Fe-NPs, have shown a specific affinity to the lung, which could be used to direct drugs/agents to the lung for detection and treatment [29]. The ultimate treatment option in PAH is a lung transplant, which is subjected to organ failure [132]. NPs could also be used as a strategy for monitoring lung rejection [29] by detecting the presence of macrophage infiltration and measuring protease activity [75]. Thus, organ rejection could be predicted at the early stages to provide alternative options to save patients’ lives. Despite their promise, all these PAH drugs incorporating NPs have not yet been transitioned to clinical trials [75].

6. CVN: Bench to Bed Translation Challenges

Despite having many CVN formulations that are either being used in medicine (Supplementary Tables S1–S7) or being tested *in vitro* and *in vivo*, the effective translation of these nanoformulations is still in process, with most of these formulations struggling to beat the challenges of the preclinical stage as they are hampered by challenges that

significantly slows down this process. These challenges include: (i) nanoparticles development and manufacturing, (ii) validating the safety/tolerability of the NPs when intact and when metabolized by the body, (iii) NPs stability in bench and biological environments, (iv) NPs biocompatibility, (v) drug loading and release efficacy and pharmacokinetics, (vi) regulating their pathway requirements and finishing the clinical trials within reasonable time, and finally, (vii) the feasibility of scaling up the produced nanopharmaceuticals [9,78]. However, these challenges are also faced by other cardiovascular drugs that do not have advanced delivery system. Furthermore, these challenges should be met while adhering to the Good Manufacturing Practice, as compliant production is essential [133]. Achieving this will require multi-disciplinary collaborations between research experts, both basic and clinical, academia, and industry to successfully translate NPs with high potential from bench-studied materials to viable clinical products. During the last two years of the still ongoing pandemic, we have seen that a nano-based vaccine rose to the occasion and is now saving the lives of millions of people. This achievement will certainly reshape the way we view, study and implement nanomedicine in many fields, including in the CVDs area [78].

7. Conclusions

Nanoformulations represent an emerging tool in biology and medicine. They possess several physicochemical and biological properties attributed to their size, shape, and surface, making them a promising platform for launching alternative non-conventional therapies. We need to use all the advances made in the nanomedicine research field to develop a more “precise” understanding of this field to translate the findings to a clinical scenario. This involves gathering accurate information about the existing nanotherapeutics and thoroughly estimating their intrinsic properties and biological effects. This will enable the design of smart nanoformulations that are created to precisely address diseases and to personalize nanotherapies.

Furthermore, several aspects must be addressed for a nanoformulation to be translated from the laboratory to the drug market. These involve a comprehensive assessment of nanoformulation chemical and biological proprieties, identifying the required ethics and other regulatory guidelines, identifying the market size, costs, and commercial development. A strong network with pharmaceutical companies will allow the researchers to better and rapidly translate the considerable number of preclinical findings into novel drugs for precision medicine. An example of this network has been established during the current pandemic, which has allowed for the fast development of a lipid-based nano-vaccines that have saved the lives of millions. A lesson could be taken from this success to be applied in another field, such as in CVDs.

Supplementary Materials: The following supporting information can be downloaded at: <https://www.mdpi.com/article/10.3390/ijms23031404/s1>.

Author Contributions: Conceptualization, N.A.M., I.M., S.C. and H.A.-S.; Writing—original draft preparation, N.A.M. and I.M.; Writing—review and editing, N.A.M., S.C. and H.A.-S.; Visualization, N.A.M., I.M., S.C. and H.A.-S.; Supervision, S.C. and H.A.-S.; Funding acquisition: H.A.-S. The contents herein are solely the responsibility of the author. All authors have read and agreed to the published version of the manuscript.

Funding: N.A.M. and I.M. are recipient of the post-doctoral research award (PDRA3-0324-17001 and PDRA4-0129-18003 from the Qatar National Research Fund (a member of The Qatar Foundation). In addition, N.A.M. is a recipient of the Pickford Award from the British Pharmacological Society. This was supported by Qatar University Student Grant [QUST-1-CAS-2022-293]. The findings achieved herein are solely the responsibility of the authors.

Conflicts of Interest: The authors of this article declare no conflict of interest.

References

- Prasad, M.; Lambe, U.P.; Brar, B.; Shah, I.; Manimegalai, J.; Ranjan, K.; Rao, R.; Kumar, S.; Mahant, S.; Khurana, S.K.; et al. Nanotherapeutics: An insight into healthcare and multi-dimensional applications in medical sector of the modern world. *Biomed. Pharmacother.* **2018**, *97*, 1521–1537. [CrossRef] [PubMed]
- Farjadian, F.; Ghasemi, A.; Gohari, O.; Roointan, A.; Karimi, M.; Hamblin, M.R. Nanopharmaceuticals and nanomedicines currently on the market: Challenges and opportunities. *Nanomedicine* **2019**, *14*, 93–126. [CrossRef] [PubMed]
- Drexler, K.E.; Peterson, G.; Pergamit, G.; Brand, S. *Unbounding the Future: The Nanotechnology Revolution*; William Morrow: New York, NY, USA, 1991.
- Freitas, R.A. *Nanomedicine: Basic Capabilities*; Landes Bioscience: Georgetown, TX, USA, 1999; Volume 1, pp. 210–219.
- Kostarelos, K. The emergence of nanomedicine: A field in the making. *Nanomedicine* **2006**, *1*, 1–3. [CrossRef]
- Jones, A.D., 3rd; Mi, G.; Webster, T.J. A Status Report on FDA Approval of Medical Devices Containing Nanostructured Materials. *Trends Biotechnol.* **2019**, *37*, 117–120. [CrossRef] [PubMed]
- Mali, S. Nanotechnology for Surgeons. *Indian J. Surg.* **2013**, *75*, 485–492. [CrossRef] [PubMed]
- Jing Wang, Y.L.; Guangjun, N.; Yuliang, Z. Precise design of nanomedicines: Perspectives for cancer treatment. *Natl. Sci. Rev.* **2019**, *6*, 1107–1110. [CrossRef]
- Iafisco, M.; Alogna, A.; Miragoli, M.; Catalucci, D. Cardiovascular nanomedicine: The route ahead. *Nanomedicine* **2019**, *14*, 2391–2394. [CrossRef]
- Choi, Y.H.; Han, H.K. Nanomedicines: Current status and future perspectives in aspect of drug delivery and pharmacokinetics. *J. Pharm. Investig.* **2018**, *48*, 43–60. [CrossRef]
- Rosler, A.; Vandermeulen, G.W.; Klok, H.A. Advanced drug delivery devices via self-assembly of amphiphilic block copolymers. *Adv. Drug Deliv. Rev.* **2001**, *53*, 95–108. [CrossRef]
- Davoodi, P.; Lee, L.Y.; Xu, Q.; Sunil, V.; Sun, Y.; Soh, S.; Wang, C.-H. Drug delivery systems for programmed and on-demand release. *Adv. Drug Deliv. Rev.* **2018**, *132*, 104–138. [CrossRef]
- Anselmo, A.C.; Mitragotri, S. An overview of clinical and commercial impact of drug delivery systems. *J. Control. Release* **2014**, *190*, 15–28. [CrossRef] [PubMed]
- Ibrahim, K.; Saeed, K.; Idrees, K. Nanoparticles: Properties, applications and toxicities. *Arab. J. Chem.* **2019**, *12*, 908–931.
- Ventola, C.L. Progress in nanomedicine: Approved and investigational nanodrugs. *Pharm. Ther. Peer-Rev. J. Manag. Care Hosp. Formul. Manag.* **2017**, *42*, 742–755.
- Tran, S.; DeGiovanni, P.-J.; Piel, B.; Rai, P. Cancer nanomedicine: A review of recent success in drug delivery. *Clin. Transl. Med.* **2017**, *6*, 44. [CrossRef] [PubMed]
- Jindal, A.B. The effect of particle shape on cellular interaction and drug delivery applications of micro- and nanoparticles. *Int. J. Pharm.* **2017**, *1*, 450–465. [CrossRef]
- Hoshyar, N.; Gray, S.; Han, H.; Bao, G. The effect of nanoparticle size on in vivo pharmacokinetics and cellular interaction. *Nanomedicine* **2016**, *11*, 673–692. [CrossRef]
- Hotze, E.M.; Phenrat, T.; Lowry, G.V. Nanoparticle aggregation: Challenges to understanding transport and reactivity in the environment. *J. Environ. Qual.* **2016**, *39*, 1909–1924. [CrossRef]
- Tang, H.; Ye, H.; Zhang, H.; Zheng, Y. Aggregation of nanoparticles regulated by mechanical properties of nanoparticle-membrane system. *Nanotechnology* **2018**, *29*, 405102. [CrossRef]
- Soares, S.; Sousa, J.; Pais, A.; Vitorino, C. Nanomedicine: Principles, Properties, and Regulatory Issues. *Front. Chem.* **2018**, *6*, 360. [CrossRef]
- Stater, E.P.; Sonay, A.Y.; Hart, C.; Grimm, J. The ancillary effects of nanoparticles and their implications for nanomedicine. *Nat. Nanotechnol.* **2021**, *11*, 1180–1194. [CrossRef]
- Suk, J.S.; Xu, Q.; Kim, N.; Hanes, J.; Ensign, L.M. PEGylation as a strategy for improving nanoparticle-based drug and gene delivery. *Adv. Drug Deliv. Rev.* **2016**, *99*, 28–51. [CrossRef]
- Ahsan, S.M.; Rao, C.M.; Ahmad, M.F. Nanoparticle-Protein Interaction: The Significance and Role of Protein Corona. *Adv. Exp. Med. Biol.* **2018**, *1048*, 175–198. [PubMed]
- Sebak, A.A. Limitations of pegylated nanocarriers: Unfavourable physicochemical properties, biodistribution patterns and cellular and subcellular fates. *Int. J. Appl. Pharm. Impact Factor* **2018**, *10*, 6–12. [CrossRef]
- Ilinskaya, A.N.; Dobrovolskaia, M.A. Immunosuppressive and anti-inflammatory properties of engineered nanomaterials. *Br. J. Pharmacol.* **2014**, *171*, 3988–4000. [CrossRef] [PubMed]
- Agarwal, H.; Nakara, A.; Shanmugam, V.K. Anti-inflammatory mechanism of various metal and metal oxide nanoparticles synthesized using plant extracts: A review. *Biomed. Pharmacother.* **2019**, *109*, 2561–2572. [CrossRef] [PubMed]
- Saeidienik, F.; Shahraki, M.R.; Fanaei, H.; Badini, F. The Effects of Iron Oxide Nanoparticles Administration on Depression Symptoms Induced by LPS in Male Wistar Rats. *Basic Clin. Neurosci. J.* **2018**, *9*, 209–216. [CrossRef]
- Mohamed, N.A.; Davies, R.P.; Lickiss, P.D.; Ahmetaj-Shala, B.; Reed, D.M.; Gashaw, H.H.; Saleem, H.; Freeman, G.R.; George, P.M.; Wort, S.J.; et al. Chemical and biological assessment of metal organic frameworks (MOFs) in pulmonary cells and in an acute in vivo model: Relevance to pulmonary arterial hypertension therapy. *Pulm. Circ.* **2017**, *7*, 643–653. [CrossRef]
- Tsai, S.; Shameli, A.; Yamanouchi, J.; Clemente-Casares, X.; Wang, J.; Serra, P.; Yang, Y.; Medarova, Z.; Moore, A.; Santamaria, P. Reversal of Autoimmunity by Boosting Memory-like Autoregulatory T Cells. *Immunity* **2010**, *32*, 568–580. [CrossRef]

31. Hwang, J.; Lee, E.; Kim, J.; Seo, Y.; Lee, K.H.; Hong, J.W.; Gilad, A.A.; Park, H.; Choi, J. Effective delivery of immunosuppressive drug molecules by silica coated iron oxide nanoparticles. *Colloids Surf. B Biointerfaces* **2016**, *1*, 290–296. [CrossRef]
32. Kuai, R.; Yuan, W.; Son, S.; Nam, J.; Xu, Y.; Fan, Y.; Schwendeman, A.; Moon, J.J. Elimination of established tumors with nanodisc-based combination chemoimmunotherapy. *Sci. Adv.* **2018**, *4*, eaao1736. [CrossRef]
33. Nam, J.; Son, S.; Soo Park, K.; Zou, W.; Shea, L.D.; Moon, J.J. Cancer nanomedicine for combination cancer immunotherapy. *Nat. Rev. Mater.* **2019**, *4*, 398–414. [CrossRef]
34. Wang, L.; Shi, C.; Wright, F.A.; Guo, D.; Wang, X.; Wang, D.; Wojcikiewicz, R.J.; Luo, J. Multifunctional Telodendrimer Nanocarriers Restore Synergy of Bortezomib and Doxorubicin in Ovarian Cancer Treatment. *Cancer Res.* **2017**, *77*, 3293–3305. [CrossRef]
35. Ananta, J.S.; Paulmurugan, R.; Massoud, T.F. Tailored Nanoparticle Codelivery of anti-miR-21 and anti-miR-10b Augments Glioblastoma Cell Kill by Temozolomide: Toward a “Personalized” Anti-microRNA Therapy. *Mol. Pharm.* **2016**, *13*, 3164–3175. [CrossRef]
36. Meng, H.; Mai, W.X.; Zhang, H.; Xue, M.; Xia, T.; Lin, S.; Wang, X.; Zhao, Y.; Ji, Z.; Zink, J.I.; et al. Codelivery of an Optimal Drug/siRNA Combination Using Mesoporous Silica Nanoparticles To Overcome Drug Resistance in Breast Cancer in Vitro and in Vivo. *ACS Nano* **2013**, *7*, 994–1005. [CrossRef]
37. Glassman, P.M.; Muzykantov, V.R. Pharmacokinetic and Pharmacodynamic Properties of Drug Delivery Systems. *J. Pharmacol. Exp. Ther.* **2019**, *3*, 570–580. [CrossRef]
38. Deng, Y.; Zhang, X.; Shen, H.; He, Q.; Wu, Z.; Liao, W.; Yuan, M. Application of the Nano-Drug Delivery System in Treatment of Cardiovascular Diseases. *Front. Bioeng. Biotechnol.* **2020**, *7*, 489. [CrossRef]
39. Claesson-Welsh, L. Vascular permeability—The essentials. *Upsala J. Med. Sci.* **2015**, *120*, 135–143. [CrossRef]
40. Sprague, A.H.; Khalil, R.A. Inflammatory cytokines in vascular dysfunction and vascular disease. *Biochem. Pharmacol.* **2009**, *15*, 539–552. [CrossRef]
41. Brenner, J.S.; Greineder, C.; Shuvaev, V.; Muzykantov, V. Endothelial nanomedicine for the treatment of pulmonary disease. *Expert Opin. Drug Deliv.* **2015**, *12*, 239–261. [CrossRef]
42. Hua, S.; De Matos, M.B.C.; Metselaar, J.M.; Storm, G. Current Trends and Challenges in the Clinical Translation of Nanoparticulate Nanomedicines: Pathways for Translational Development and Commercialization. *Front. Pharmacol.* **2018**, *9*, 790. [CrossRef]
43. Liong, M.; Lu, J.; Kovichich, M.; Xia, T.; Ruehm, S.G.; Nel, A.E.; Tamanoi, F.; Zink, J.I. Multifunctional Inorganic Nanoparticles for Imaging, Targeting, and Drug Delivery. *ACS Nano* **2008**, *2*, 889–896. [CrossRef]
44. Hung, H.I.; Klein, O.J.; Peterson, S.W.; Rokosh, S.R.; Osseiran, S.; Nowell, N.H.; Evans, L. PLGA nanoparticle encapsulation reduces toxicity while retaining the therapeutic efficacy of EtNBS-PDT in vitro. *Sci. Rep.* **2016**, *6*, 33234. [CrossRef]
45. Deb, S.; Ghosh, K.; Shetty, S.D. Nanoimaging in cardiovascular diseases: Current state of the art. *Indian J. Med. Res.* **2015**, *141*, 285–298. [CrossRef]
46. Peng, H.; Brimijoin, S.; Hrabovska, A.; Targosova, K.; Krejci, E.; Blake, T.A.; Johnson, R.C.; Masson, P.; Lockridge, O. Comparison of 5 monoclonal antibodies for immunopurification of human butyrylcholinesterase on Dynabeads: KD values, binding pairs, and amino acid sequences. *Chem. Biol. Interact.* **2015**, *240*, 336–345. [CrossRef]
47. Wang, T.; Zhou, Y.; Lei, C.; Lei, J.; Yang, Z. Development of an ingenious method for determination of Dynabeads protein A based on a giant magnetoimpedance sensor. *Sens. Actuators B Chem.* **2013**, *186*, 727–733. [CrossRef]
48. Bao, G.; Mitragotri, S.; Tong, S. Multifunctional nanoparticles for drug delivery and molecular imaging. *Annu. Rev. Biomed. Eng.* **2013**, *15*, 253–282. [CrossRef]
49. Kleinstreuer, C.; Chari, S.V.; Vachhani, S. Potential Use of Multifunctional Nanoparticles for the Treatment of Cardiovascular Diseases. *Cardiol. Cardiovasc. Sci.* **2018**, *2*, 30–36. [CrossRef]
50. de Vries, J.W.; Schnichels, S.; Hurst, J.; Strudel, L.; Gruszka, A.; Kwak, M.; Bartz-Schmidt, K.-U.; Spitzer, M.S.; Herrmann, A. DNA nanoparticles for ophthalmic drug delivery. *Biomaterials* **2018**, *157*, 98–106. [CrossRef]
51. Weis, S.M. Vascular permeability in cardiovascular disease and cancer. *Curr. Opin. Hematol.* **2008**, *15*, 243–249. [CrossRef]
52. Ho, Y.T.; Poinard, B.; Kah, J.C. Nanoparticle drug delivery systems and their use in cardiac tissue therapy. *Nanomedicine* **2016**, *11*, 693–714. [CrossRef]
53. Milane, L.; Amiji, M. Clinical approval of nanotechnology-based SARS-CoV-2 mRNA vaccines: Impact on translational nanomedicine. *Drug Deliv. Transl. Res.* **2021**, *11*, 1309–1315. [CrossRef]
54. Boada, C.; Roman, S.; Pettigrew, R.; Cooke, J.P. RNA therapeutics for cardiovascular disease. *Curr. Opin. Cardiol.* **2021**, *36*, 256–263. [CrossRef]
55. U.S. National Library of Medicine. ClinicalTrials.gov. Available online: <https://clinicaltrials.gov/ct2/home2019> (accessed on 1 November 2021).
56. Patra, J.K.; Das, G.; Fraceto, L.F.; Campos, E.V.R.; del Pilar Rodriguez-Torres, M.; Acosta-Torres, L.S.; Diaz-Torres, L.A.; Grillo, R.; Swamy, M.K.; Sharma, S.; et al. Nano based drug delivery systems: Recent developments and future prospects. *J. Nanobiotechnol.* **2018**, *16*, 71. [CrossRef]
57. Anselmo, A.C.; Mitragotri, S. Nanoparticles in the clinic: An update. *Bioeng. Transl. Med.* **2019**, *4*, e10143. [CrossRef]
58. McCarthy, J.R. Nanomedicine and Cardiovascular Disease. *Curr. Cardiovasc. Imaging Rep.* **2010**, *3*, 42–49. [CrossRef]
59. Administration USAFaD. 2019. Available online: <https://www.fda.gov> (accessed on 15 January 2022).
60. Drugs, Know More, Be Sure. Available online: <https://www.drugs.com> (accessed on 15 January 2022).

61. Siyoung, A.; Lim, A.C.; Tung, M.; Chung, E.J. Clinical progress of nanomedicine-based RNA therapies. *Bioact. Mater.* **2021**, *12*, 203–213.
62. European Medicines Agency. Available online: <https://www.ema.europa.eu/en> (accessed on 15 January 2022).
63. Chandarana, M.; Hoskins, A.C.C. The use of nanotechnology in cardiovascular disease. *Appl. Nanosci.* **2018**, *8*, 1607–1619. [CrossRef]
64. Bhatnagar, P.; Wickramasinghe, K.; Wilkins, E.; Townsend, N. Trends in the epidemiology of cardiovascular disease in the UK. *Heart* **2016**, *102*, 1945–1952. [CrossRef]
65. Watkins, D.A.; Hasan, B.; Mayosi, B.; Bukhman, G.; Marin-Neto, A.; Rassi, A.J.; Rassi, A.; Kumar, K. Structural Heart Diseases. In *Diseases Control Priorities*; World Bank Publications: Washington, DC, USA, 2017; Volume 5.
66. Kovacic, J.C.; Castellano, J.M.; Farkouh, M.E.; Fuster, V. The relationships between cardiovascular disease and diabetes: Focus on pathogenesis. *Endocrinol. Metab. Clin. N. Am.* **2014**, *43*, 41–57. [CrossRef]
67. Kjeldsen, S.E. Hypertension and cardiovascular risk: General aspects. *Pharmacol. Res.* **2018**, *129*, 95–99. [CrossRef]
68. Martin Gimenez, V.M.; Kassuha, D.E.; Manucha, W. Nanomedicine applied to cardiovascular diseases: Latest developments. *Ther. Adv. Cardiovasc. Dis.* **2017**, *11*, 133–142. [CrossRef] [PubMed]
69. Katsuki, S.; Matoba, T.; Koga, J.I.; Nakano, K.; Egashira, K. Anti-inflammatory Nanomedicine for Cardiovascular Disease. *Front. Cardiovasc. Med.* **2017**, *4*, 87. [CrossRef] [PubMed]
70. Karagkiozaki, V.; Pappa, F.; Arvaniti, D.; Moumkas, A.; Konstantinou, D.; Logothetidis, S. The melding of nanomedicine in thrombosis imaging and treatment: A review. *Future Sci. OA* **2016**, *2*, 113. [CrossRef] [PubMed]
71. Molinaro, R.; Boada, C.; Del Rosal, G.M.; Hartman, K.A.; Corbo, C.; Andrews, E.D.; Toledano-Furman, N.E.; Cooke, J.P.; Tasciotti, E. Vascular Inflammation: A Novel Access Route for Nanomedicine. *Methodist Debaquey Cardiovasc. J.* **2016**, *12*, 169–174. [CrossRef]
72. Khaja, F.A.; Koo, O.M.; Onyuksel, H. Nanomedicines for inflammatory diseases. *Methods Enzymol.* **2012**, *508*, 355–375.
73. Ferreira, M.P.; Balasubramanian, V.; Hirvonen, J.; Ruskoaho, H.; Santos, H.A. Advanced Nanomedicines for the Treatment and Diagnosis of Myocardial Infarction and Heart Failure. *Curr. Drug Targets* **2015**, *16*, 1682–1697. [CrossRef]
74. Segura-Ibarra, V.; Wu, S.; Hassan, N.; Moran-Guerrero, J.A.; Ferrari, M.; Guha, A.; Karmouty-Quintana, H.; Blanco, E. Nanotherapeutics for Treatment of Pulmonary Arterial Hypertension. *Front. Physiol.* **2018**, *9*, 890. [CrossRef]
75. Nakamura, K.; Matsubara, H.; Akagi, S.; Sarashina, T.; Ejiri, K.; Kawakita, N.; Yoshida, M.; Miyoshi, T.; Watanabe, A.; Nishii, N.; et al. Nanoparticle-Mediated Drug Delivery System for Pulmonary Arterial Hypertension. *J. Clin. Med.* **2017**, *6*, 48. [CrossRef]
76. McClellan, M.; Brown, N.; Califf, R.M.; Warner, J.J. Call to Action: Urgent Challenges in Cardiovascular Disease: A Presidential Advisory From the American Heart Association. *Circulation* **2019**, *139*, e44–e54. [CrossRef]
77. Thompson, S.C.; Nedkoff, L.; Katzenellenbogen, J.; Hussain, M.A.; Sanfilippo, F. Challenges in Managing Acute Cardiovascular Diseases and Follow Up Care in Rural Areas: A Narrative Review. *Int. J. Environ. Res. Public Health* **2019**, *16*, 5126. [CrossRef]
78. Iwona, C. The Grand Challenges in Cardiovascular Drug Delivery. *Front. Drug Deliv.* **2021**, *1*, 2.
79. Jaffer, F.A.; Libby, P.; Weissleder, R. Optical and multimodality molecular imaging: Insights into atherosclerosis. *Arterioscler. Thromb. Vasc. Biol.* **2009**, *29*, 1017–1024. [CrossRef] [PubMed]
80. Nahrendorf, M.; Sosnovik, D.E.; French, B.A.; Swirski, F.K.; Bengel, F.; Sadeghi, M.M.; Lindner, J.R.; Wu, C.; Kraitchman, D.L.; Fayad, Z.A.; et al. Multimodality cardiovascular molecular imaging, Part II. *Circ. Cardiovasc. Imaging* **2009**, *2*, 56–70. [CrossRef] [PubMed]
81. Nahrendorf, M.; Waterman, P.; Thurber, G.; Groves, K.; Rajopadhye, M.; Panizzi, P.; Marinelli, B.; Aikawa, E.; Pittet, M.J.; Swirski, F.K.; et al. Hybrid in vivo FMT-CT imaging of protease activity in atherosclerosis with customized nanosensors. *Arterioscler. Thromb. Vasc. Biol.* **2009**, *29*, 1444–1451. [CrossRef] [PubMed]
82. Gao, W.; Sun, Y.; Cai, M.; Zhao, Y.; Cao, W.; Liu, Z.; Cui, G.; Tang, B. Copper sulfide nanoparticles as a photothermal switch for TRPV1 signaling to attenuate atherosclerosis. *Nat. Commun.* **2018**, *9*, 231. [CrossRef]
83. Deshpande, D.; Kethireddy, S.; Janero, D.R.; Amiji, M.M. Therapeutic Efficacy of an omega-3-Fatty Acid-Containing 17-beta Estradiol Nano-Delivery System against Experimental Atherosclerosis. *PLoS ONE* **2016**, *11*, e0147337. [CrossRef]
84. Su, M.; Dai, Q.; Chen, C.; Zeng, Y.; Chu, C.; Liu, G. Nano-Medicine for Thrombosis: A Precise Diagnosis and Treatment Strategy. *Nano-Micro Lett.* **2020**, *12*, 96. [CrossRef]
85. Balasubramanian, V.; Grabowski, E.; Bini, A.; Nemerson, Y. Platelets, circulating tissue factor, and fibrin colocalize in ex vivo thrombi: Real-time fluorescence images of thrombus formation and propagation under defined flow conditions. *Blood* **2002**, *100*, 2787–2792. [CrossRef]
86. Falati, S.; Gross, P.; Merrill-Skoloff, G.; Furie, B.C.; Furie, B. Real-time in vivo imaging of platelets, tissue factor and fibrin during arterial thrombus formation in the mouse. *Nat. Med.* **2002**, *8*, 1175–1181. [CrossRef]
87. Tung, C.-H.; Ho, N.-H.; Zeng, Q.; Tang, Y.; Jaffer, F.A.; Reed, G.L.; Weissleder, R. Novel factor XIII probes for blood coagulation imaging. *ChemBiochem* **2003**, *4*, 897–899. [CrossRef]
88. Bonnard, T.; Jayapadman, A.; Putri, J.A.; Cui, J.; Jum, Y.; Carmichael, C.; Angelovich, T.; Cody, S.H.; French, S.; Pascaud, K.; et al. Low-Fouling and Biodegradable Protein-Based Particles for Thrombus Imaging. *ACS Nano* **2018**, *12*, 6988–6996. [CrossRef] [PubMed]
89. Cicha, I. Thrombosis: Novel nanomedical concepts of diagnosis and treatment. *World J. Cardiol.* **2015**, *7*, 434–741. [CrossRef]

90. Correa-Paz, C.; da Silva-Candal, A.; Polo, E.; Parcq, J.; Vivien, D.; Maysinger, D.; Pelaz, B.; Campos, F. New Approaches in Nanomedicine for Ischemic Stroke. *Pharmaceutics* **2021**, *13*, 757. [CrossRef]
91. Panagiotou, S.; Saha, S. Therapeutic benefits of nanoparticles in stroke. *Front. Neurosci.* **2015**, *9*, 182. [CrossRef] [PubMed]
92. Fan, C.; Joshi, J.; Li, F.; Xu, B.; Khan, M.; Yang, J.; Zhu, W. Nanoparticle-Mediated Drug Delivery for Treatment of Ischemic Heart Disease. *Front. Bioeng. Biotechnol.* **2020**, *8*, 687. [CrossRef] [PubMed]
93. Sosnovik, D.E.; Nahrendorf, M.; Deliolani, N.; Novikov, M.; Aikawa, E.; Josephson, L.; Rosenzweig, A.; Weissleder, R.; Ntziachristos, V. Fluorescence tomography and magnetic resonance imaging of myocardial macrophage infiltration in infarcted myocardium in vivo. *Circulation* **2007**, *115*, 1384–1391. [CrossRef]
94. Nahrendorf, M.; Sosnovik, D.E.; Waterman, P.; Swirski, F.; Pande, A.N.; Aikawa, E.; Figueiredo, J.-L.; Pittet, M.J.; Weissleder, R. Dual channel optical tomographic imaging of leukocyte recruitment and protease activity in the healing myocardial infarct. *Circ. Res.* **2007**, *100*, 1218–1225. [CrossRef]
95. Santoso, M.R.; Yang, P.C. Magnetic Nanoparticles for Targeting and Imaging of Stem Cells in Myocardial Infarction. *Stem Cells Int.* **2016**, *2016*, 4198790. [CrossRef]
96. Das, A.; Mukherjee, P.; Singla, S.K.; Guturu, P.; Frost, M.; Mukhopadhyay, D.; Shah, V.H.; Patra, C.R. Fabrication and characterization of an inorganic gold and silica nanoparticle mediated drug delivery system for nitric oxide. *Nanotechnology* **2010**, *21*, 305102. [CrossRef]
97. Minarchick, V.C.; Stapleton, P.A.; Sabolsky, E.M.; Nurkiewicz, T.R. Cerium Dioxide Nanoparticle Exposure Improves Microvascular Dysfunction and Reduces Oxidative Stress in Spontaneously Hypertensive Rats. *Front. Physiol.* **2015**, *6*, 339. [CrossRef]
98. Benza, R.L.; Miller, D.P.; Barst, R.J.; Badesch, D.B.; Frost, A.E.; McGoon, M.D. An evaluation of long-term survival from time of diagnosis in pulmonary arterial hypertension from the REVEAL Registry. *Chest* **2012**, *142*, 448–456. [CrossRef] [PubMed]
99. Hampl, V.; Herget, J. Role of nitric oxide in the pathogenesis of chronic pulmonary hypertension. *Physiol. Rev.* **2000**, *80*, 1337–1372. [CrossRef] [PubMed]
100. Galie, N.; Manes, A.; Branzi, A. Medical therapy of pulmonary hypertension. The prostacyclins. *Clin. Chest Med.* **2001**, *22*, 529–537. [CrossRef]
101. Mitchell, J.A.; Ali, F.; Bailey, L.; Moreno, L.; Harrington, L.S. Role of nitric oxide and prostacyclin as vasoactive hormones = endothelium. *Exp. Physiol.* **2008**, *93*, 141–147. [CrossRef]
102. Rickert, V.; Haefeli, W.E.; Weiss, J. Pharmacokinetic interaction profile of riociguat, a new soluble guanylate cyclase stimulator, in vitro. *Pulm. Pharmacol. Ther.* **2014**, *28*, 130–137. [CrossRef]
103. McLaughlin, V.V.; Shillington, A.; Rich, S. Survival in primary pulmonary hypertension: The impact of epoprostenol therapy. *Circulation* **2002**, *106*, 1477–1482. [CrossRef]
104. Gombert-Maitland, M.; Olschewski, H. Prostacyclin therapies for the treatment of pulmonary arterial hypertension. *Eur. Respir. J.* **2008**, *31*, 891–901. [CrossRef]
105. Simonneau, G.; Barst, R.J.; Galie, N.; Naeije, R.; Rich, S.; Bourge, R.C.; Keogh, A.; Oudiz, R.; Frost, A.; Blackburn, S.D.; et al. Continuous subcutaneous infusion of treprostinil, a prostacyclin analogue, in patients with pulmonary arterial hypertension: A double-blind, randomized, placebo-controlled trial. *Am. J. Respir. Crit. Care Med.* **2002**, *165*, 800–804. [CrossRef]
106. Olschewski, H.; Simonneau, G.; Galiè, N.; Higenbottam, T.; Naeije, R.; Rubin, L.J.; Nikkho, S.; Speich, R.; Hoeper, M.M.; Behr, J.; et al. Inhaled iloprost for severe pulmonary hypertension. *N. Engl. J. Med.* **2002**, *347*, 322–329. [CrossRef]
107. Shibuya, M.; Hirai, S.; Seto, M.; Satoh, S.; Ohtomo, E. Effects of fasudil in acute ischemic stroke: Results of a prospective placebo-controlled double-blind trial. *J. Neurol. Sci.* **2005**, *238*, 31–39. [CrossRef]
108. Liu, Q.Q.; Jing, Z.C. The limits of oral therapy in pulmonary arterial hypertension management. *Ther. Clin. Risk Manag.* **2015**, *11*, 1731–1741. [PubMed]
109. Gupta, V.; Ahsan, F. Inhalational therapy for pulmonary arterial hypertension: Current status and future prospects. *Crit. Rev. Ther. Drug Carr. Syst.* **2010**, *27*, 313–370. [CrossRef] [PubMed]
110. Shinohara, T.; Sawada, H.; Otsuki, S.; Yodoya, N.; Kato, T.; Ohashi, H.; Zhang, E.; Saitoh, S.; Shimpo, H.; Maruyama, K.; et al. Macitentan reverses early obstructive pulmonary vasculopathy in rats: Early intervention in overcoming the survivin-mediated resistance to apoptosis. *Am. J. Physiol. Lung Cell Mol. Physiol.* **2015**, *308*, L523–L528. [CrossRef] [PubMed]
111. Schermuly, R.T.; Dony, E.; Ghofrani, H.A.; Pullamsetti, S.; Savai, R.; Roth, M.; Sydykov, A.; Lai, Y.J.; Weissmann, N.; Seeger, W.; et al. Reversal of experimental pulmonary hypertension by PDGF inhibition. *J. Clin. Investig.* **2005**, *115*, 2811–2821. [CrossRef]
112. Dony, E.; Lai, Y.J.; Dumitrescu, R.; Pullamsetti, S.S.; Savai, R.; Ghofrani, H.A.; Weissmann, N.; Schudt, C.; Flocknerzi, D.; Seeger, W.; et al. Partial reversal of experimental pulmonary hypertension by phosphodiesterase-3/4 inhibition. *Eur. Respir. J.* **2008**, *31*, 599–610. [CrossRef]
113. Kimura, S.; Egashira, K.; Chen, L.; Nakano, K.; Iwata, E.; Miyagawa, M.; Tsujimoto, H.; Hara, K.; Morishita, R.; Sueishi, K.; et al. Nanoparticle-mediated delivery of nuclear factor kappaB decoy into lungs ameliorates monocrotaline-induced pulmonary arterial hypertension. *Hypertension* **2009**, *53*, 877–883. [CrossRef]
114. Pugliese, S.C.; Poth, J.M.; Fini, M.A.; Olschewski, A.; El Kasbi, K.C.; Stenmark, K.R. The role of inflammation in hypoxic pulmonary hypertension: From cellular mechanisms to clinical phenotypes. *Am. J. Physiol. Lung Cell Mol. Physiol.* **2015**, *308*, L229–L252. [CrossRef]

115. Soon, E.; Holmes, A.M.; Treacy, C.M.; Doughty, N.J.; Southgate, L.; Machado, R.D.; Trembath, R.C.; Jennings, S.; Barker, L.; Nicklin, P.; et al. Elevated levels of inflammatory cytokines predict survival in idiopathic and familial pulmonary arterial hypertension. *Circulation* **2010**, *122*, 920–927. [CrossRef]
116. George, P.M.; Oliver, E.; Dorfmueller, P.; Dubois, O.D.; Reed, D.M.; Kirkby, N.S.; Mohamed, N.A.; Perros, F.; Antigny, F.; Fadel, E.; et al. Evidence for the Involvement of Type I Interferon in Pulmonary Arterial Hypertension. *Circ. Res.* **2013**, *114*, 677–688. [CrossRef]
117. Rabinovitch, M.; Guignabert, C.; Humbert, M.; Nicolls, M.R. Inflammation and immunity in the pathogenesis of pulmonary arterial hypertension. *Circ. Res.* **2014**, *115*, 165–175. [CrossRef]
118. Guignabert, C.; Dorfmueller, P. Pathology and pathobiology of pulmonary hypertension. *Semin. Respir. Crit. Care Med.* **2013**, *34*, 551–559. [CrossRef] [PubMed]
119. Voelkel, N.F.; Gomez-Arroyo, J.; Abbate, A.; Bogaard, H.J.; Nicolls, M.R. Pathobiology of pulmonary arterial hypertension and right ventricular failure. *Eur. Respir. J.* **2012**, *40*, 1555–1565. [CrossRef] [PubMed]
120. Rabinovitch, M. Molecular pathogenesis of pulmonary arterial hypertension. *J. Clin. Investig.* **2012**, *122*, 4306–4313. [CrossRef] [PubMed]
121. Tuder, R.M.; Groves, B.; Badesch, D.B.; Voelkel, N.F. Exuberant endothelial cell growth and elements of inflammation are present in plexiform lesions of pulmonary hypertension. *Am. J. Pathol.* **1994**, *144*, 275–285.
122. Sakao, S.; Tatsumi, K. Vascular remodeling in pulmonary arterial hypertension: Multiple cancer-like pathways and possible treatment modalities. *Int. J. Cardiol.* **2011**, *147*, 4–12. [CrossRef]
123. Lee, S.D.; Shroyer, K.R.; Markham, N.E.; Cool, C.D.; Voelkel, N.F.; Tuder, R.M. Monoclonal endothelial cell proliferation is present in primary but not secondary pulmonary hypertension. *J. Clin. Investig.* **1998**, *101*, 927–934. [CrossRef]
124. Tu, L.; De Man, F.S.; Girerd, B.; Huertas, A.; Chaumais, M.-C.; Lecerf, F.; Francois, C.; Perros, F.; Dorfmueller, P.; Fadel, E.; et al. A critical role for p130Cas in the progression of pulmonary hypertension in humans and rodents. *Am. J. Respir. Crit. Care Med.* **2012**, *186*, 666–676. [CrossRef]
125. Ross, C.L.; Ang, D.; Almeida-Porada, G. Targeting Mesenchymal Stromal Cells/Pericytes (MSCs) With Pulsed Electromagnetic Field (PEMF) Has the Potential to Treat Rheumatoid Arthritis. *Front. Immunol.* **2019**, *10*, 266. [CrossRef]
126. Navarro, R.; Compte, M.; Álvarez-Vallina, L.; Sanz, L. Immune Regulation by Pericytes: Modulating Innate and Adaptive Immunity. *Front. Immunol.* **2016**, *7*, 480. [CrossRef]
127. Bhagwani, A.R.; Hultman, S.; Farkas, D.; Moncayo, R.; Dandamudi, K.; Zadu, A.K.; Cool, C.D.; Farkas, L. Endothelial cells are a source of Nestin expression in Pulmonary Arterial Hypertension. *PLoS ONE* **2019**, *14*, e0213890.
128. Morrell, N.W.; Aldred, M.A.; Chung, W.K.; Elliot, C.G.; Nichols, W.C.; Soubrier, F.; Trembath, R.C.; Loyd, J.E. Genetics and genomics of pulmonary arterial hypertension. *Eur. Respir. J.* **2019**, *53*, 1801899. [CrossRef] [PubMed]
129. Long, L.; Ormiston, M.; Yang, X.; Southwood, M.; Graf, S.; Machado, R.D.; Mueller, M.; Kinzel, B.; Yung, L.M.; Wilkinson, J.; et al. Selective enhancement of endothelial BMPR-II with BMP9 reverses pulmonary arterial hypertension. *Nat. Med.* **2015**, *21*, 777–785. [CrossRef] [PubMed]
130. Badlam, J.B.; Bull, T.M. Steps forward in the treatment of pulmonary arterial hypertension: Latest developments and clinical opportunities. *Ther. Adv. Chronic Dis.* **2017**, *8*, 47–64. [CrossRef] [PubMed]
131. Rosenkranz, S.; Preston, I.R. Right heart catheterisation: Best practice and pitfalls in pulmonary hypertension. *Eur. Respir. Rev.* **2015**, *24*, 642–652. [CrossRef] [PubMed]
132. George, M.P.; Champion, C.H.; Pilewski, J.M. Lung transplantation for pulmonary hypertension. *Pulm. Circ.* **2011**, *1*, 182–191. [CrossRef]
133. Cicha, I.; Chauvierre, C.; Texier, I.; Cabella, C.; Metselaar, J.M.; Szebeni, J.; Dézsi, L.; Alexiou, C.; Rouzet, F.; Storm, G.; et al. From design to the clinic: Practical guidelines for translating cardiovascular nanomedicine. *Cardiovasc. Res.* **2018**, *1*, 1714–1727. [CrossRef]



Article

Pro-Apoptotic and Immunotherapeutic Effects of Carbon Nanotubes Functionalized with Recombinant Human Surfactant Protein D on Leukemic Cells

Haseeb A. Khan ^{1,*} , Uday Kishore ² , Hamed M. Alsulami ¹ and Salman H. Alrokayan ¹

¹ Department of Biochemistry, College of Science, King Saud University, Riyadh 11451, Saudi Arabia; halsulami@gmail.com (H.M.A.); salrokayan@ksu.edu.sa (S.H.A.)

² Biosciences, College of Health, Medicine and Life Sciences, Brunel University London, Uxbridge UB8 3PH, UK; ukishore@hotmail.com

* Correspondence: haseeb@ksu.edu.sa; Tel.: +966-11-4675859

Abstract: Nanoparticles are efficient drug delivery vehicles for targeting specific organs as well as systemic therapy for a range of diseases, including cancer. However, their interaction with the immune system offers an intriguing challenge. Due to the unique physico-chemical properties, carbon nanotubes (CNTs) are considered as nanocarriers of considerable interest in cancer diagnosis and therapy. CNTs, as a promising nanomaterial, are capable of both detecting as well as delivering drugs or small therapeutic molecules to tumour cells. In this study, we coupled a recombinant fragment of human surfactant protein D (rfhSP-D) with carboxymethyl-cellulose (CMC) CNTs (CMC-CNT, 10–20 nm diameter) for augmenting their apoptotic and immunotherapeutic properties using two leukemic cell lines. The cell viability of AML14.3D10 or K562 cancer cell lines was reduced when cultured with CMC-mwCNT-coupled-rfhSP-D (CNT + rfhSP-D) at 24 h. Increased levels of caspase 3, 7 and cleaved caspase 9 in CNT + rfhSP-D treated AML14.3D10 and K562 cells suggested an involvement of an intrinsic pathway of apoptosis. CNT + rfhSP-D treated leukemic cells also showed higher mRNA expression of p53 and cell cycle inhibitors (p21 and p27). This suggested a likely reduction in cdc2-cyclin B1, causing G2/M cell cycle arrest and p53-dependent apoptosis in AML14.3D10 cells, while p53-independent mechanisms appeared to be in operation in K562 cells. We suggest that CNT + rfhSP-D has therapeutic potential in targeting leukemic cells, irrespective of their p53 status, and thus, it is worth setting up pre-clinical trials in animal models.

Keywords: carbon nanotubes; human SP-D; cancer cells; apoptosis; immunotherapy



Citation: Khan, H.A.; Kishore, U.; Alsulami, H.M.; Alrokayan, S.H. Pro-Apoptotic and Immunotherapeutic Effects of Carbon Nanotubes Functionalized with Recombinant Human Surfactant Protein D on Leukemic Cells. *Int. J. Mol. Sci.* **2021**, *22*, 10445. <https://doi.org/10.3390/ijms221910445>

Academic Editors:
Monica Terracciano, Ilaria Rea,
Nicola Borbone
and Chiara Tramontano

Received: 31 July 2021

Accepted: 21 September 2021

Published: 28 September 2021

Publisher's Note: MDPI stays neutral with regard to jurisdictional claims in published maps and institutional affiliations.



Copyright: © 2021 by the authors. Licensee MDPI, Basel, Switzerland. This article is an open access article distributed under the terms and conditions of the Creative Commons Attribution (CC BY) license (<https://creativecommons.org/licenses/by/4.0/>).

1. Introduction

The innate immune system plays a key role in the clearance of pathogens and synthetic compounds including nanoparticles [1,2]. Nanoparticles have numerous biomedical applications [3–6], which can serve as drug delivery carriers or vaccine adjuvants [7]. Among nanoparticles, carbon nanotubes (CNTs) have unique physico-chemical properties, and hence, they are amenable as therapeutic nanocarriers [8–10]. CNTs can be single-walled (SWCNTs) and multiple-walled (MWCNTs), depending on length, diameter, and structure, and the layers of single CNT the wall is composed of [11].

Human surfactant protein D (SP-D) is a humoral, pathogen pattern recognition molecule, which is found to be associated with pulmonary surfactant, as well as mucosal surfaces outside the lungs [12,13]. SP-D belongs to the collectin family, a collagen containing C-type (calcium-dependent) lectin [14]. The primary structure of SP-D comprises a cross-linking amino-terminal region, a triple-helical collagen region, a coiled-coil neck region, and a C-type lectin domain or carbohydrate recognition domain (CRD) as a trimeric unit [15,16]. SP-D can bind to various carbohydrate and/or charge patterns on the surface of pathogens and become involved in clearing them by recruiting phagocytic

cells such as neutrophils and macrophages [15,16]. SP-D can also interact with a range of cancer cell lines (leukemic, lung, pancreatic, prostate, ovarian and breast). For example, a truncated form of recombinant human SP-D (rfhSP-D), composed of trimeric neck and C-type lectin domain, has been shown to interfere with tumour progression via apoptosis induction, invasion, and epithelial-to-mesenchymal transition [17–22]. These studies have thus suggested that SP-D has an immune surveillance role against tumors.

SP-D can associate with nanoparticles and modulate their uptake by macrophages [23,24]. SP-D can bind efficiently with oxidized (Ox) DWCNTs via their C-type lectin domain [2,25]. SP-D mediated enhancement of nanoparticle uptake by alveolar macrophages and dendritic cells in mice has been examined using polystyrene, carbon black and silica nanocarriers [23].

CNTs, when opsonized with rfhSP-D, can provoke a differential pro-inflammatory immune response [26]. Surface modifications of hydrophobic CNTs are used for their good dispersion via covalent or non-covalent surface coatings [27]. For instance, the dispersion of MWNTs via oxidation (Ox-CNT), or with carboxymethyl-cellulose (CMC-CNT), has been reported [27]. Soluble complement components, such as factor H and C1q, opsonize functionalized CNTs, suggesting that key innate immune molecules can bind CNTs and alter inflammatory response [27].

This study was aimed at examining the ability of CNT + rfhSP-D to induce apoptosis using an eosinophilic cell line, AML14.3D10 [28], and a chronic myelogenous leukemia cell line, K562, to assess if CNT + rfhSP-D nanomaterials are worth testing in animal models.

2. Results

2.1. CNT + rfhSP-D Treatment Reduces Cell Viability of AML14.3D10 and K562 Leukemic Cell Lines

First, we analysed and confirmed the stable binding of purified rfhSP-D with CMC-MWCNTs, as evident from the SDS-PAGE (Figure 1). Supernatant after centrifugation was also loaded, which did not show presence of rfhSP-D. rfhSP-D (10 µg/mL), without the addition of CNT, was used as a positive control. The quantitative analysis of viability in treated (cells + CNT + rfhSP-D; 5, 10, and 20 µg/mL in serum-free RPMI medium; cells + CNT as control) leukemic cells was carried out using trypan blue (Figure 2) and MTT (Figure 3) assays at 24 h time point. Trypan blue exclusion assay revealed a significant reduction in the cell viability in CNT + rfhSP-D treated cell lines (AML14.3D10: ~48%; K562: ~56%) at 24 h in a dose-dependent manner (Figure 2). This was confirmed by the MTT assay: AML14.3D10 (~37%) and K562 (~55%) (Figure 3). As evident by the MTT assay, rfhSP-D (20 µg/mL) alone was also able to reduce cell viability in both AML14.3D10 (~51%) and K562 (~69%) cell lines.

2.2. Proliferation of AML14.3D10 and K562 Cell Lines Is Reduced following CNT + rfhSP-D Treatment

Experiments were carried out to determine whether CNT + rfhSP-D (20 µg/mL) affected AML14.3D10 and K562 cell proliferation (Figure 4). Mouse anti-Ki-67 antibody staining was used to measure the percentage proliferation. CNT + rfhSP-D treated AML14.3D10 cells showed ~29% cell proliferation compared to rfhSP-D alone (20 µg/mL) (~57%) (Figure 4). However, a higher percentage of cell proliferation was noted in CNT-treated AML14.3D10 cells (~88%). In the case of K562 cell line (Figure 4B), approximately ~34% cell proliferation was noticed following CNT + rfhSP-D treatment (compared to CNT alone; ~107% proliferative cells stained with Ki-67 antibody), suggesting that cells treated only with CNT continued to proliferate and grow unhindered. rfhSP-D alone (20 µg/mL) treatment was also capable of reducing proliferation of AML14.3D10 (~57%) and K562 (~63%) cells when compared to CNT alone. These data suggested that CNT + rfhSP-D was more effective in reducing cell proliferation of both AML14.3D10 and K562 cell lines, indicating its therapeutic potential against acute and chronic leukemic cell lines.

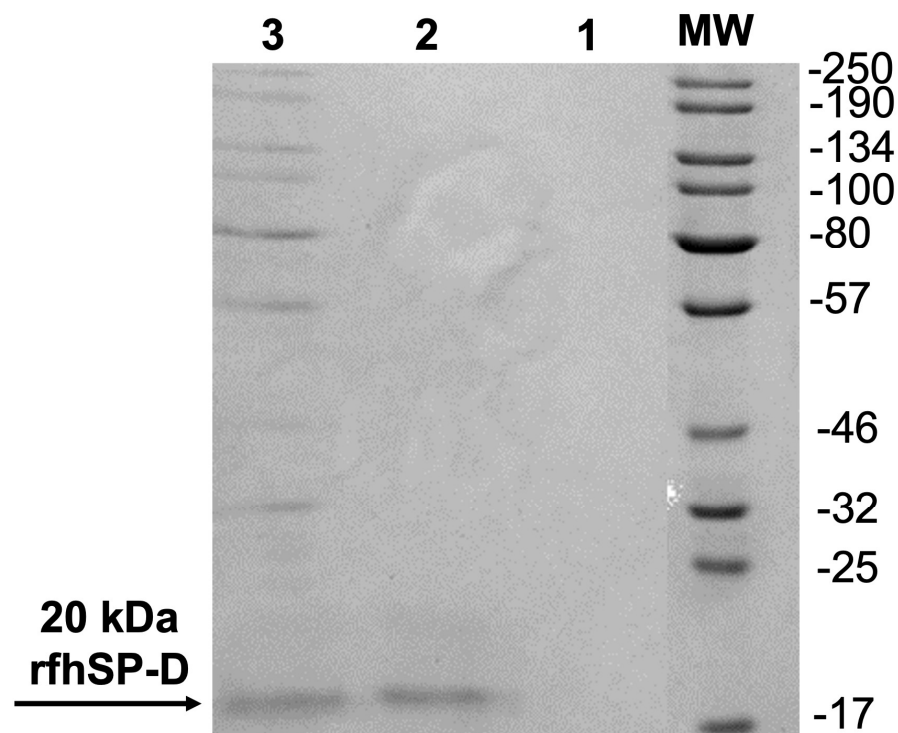


Figure 1. Purified rfhSP-D (10 $\mu\text{g}/\text{mL}$) or carboxymethyl cellulose-coated carbon nanotubes (rfhSP-D-CNTs) coupled-rfhSP-D (10 $\mu\text{g}/\text{mL}$) samples were subjected to an SDS-PAGE (15% *v/v*). Lane 1: Supernatant (10 $\mu\text{L}/\text{well}$) taken after centrifugation of rfhSP-D-CNT. Lane 2: purified rfhSP-D. Lane 3: rfhSP-D-CNT. The original image is available as a Supplementary Materials.

2.3. Apoptosis Induction by CNT + rfhSP-D in AML14.3D10 and K562 Cell Lines

The quantitative analysis of apoptosis induction by CNT + rfhSP-D was performed using flow cytometry. A significant proportion of AML14.3D10 or K562 (Figure 5) cells treated with CNT + rfhSP-D (20 $\mu\text{g}/\text{mL}$), or rfhSP-D (20 $\mu\text{g}/\text{mL}$) alone, resulted in increased apoptosis induction at 24 h, compared to CNT alone (untreated control). CNT + rfhSP-D was effective in inducing the maximum apoptosis at 24 h; AML14.3D10 (~71%) and K562 (~66%), when compared to CNT alone [AML14.3D10 (~12%) and K562 (~7%)]. rfhSP-D (20 $\mu\text{g}/\text{mL}$) alone was also able to reduce cell viability in both AML14.3D10 (~43%) (Figure 5) and K562 (~37%) cell lines (Figure 5; Supplementary Materials). This assay is based on the ability of annexin V/FITC to bind to phosphatidylserine (PS) on apoptosing cells. A higher percentage of PI positive AML14.3D10 compared to K562 cells appeared to suggest that these cells were late apoptotic/necrotic. Staurosporine (1 $\mu\text{M}/\text{mL}$), used as a positive control for triggering apoptosis, brought about ~72% apoptosis at 24 h.

2.4. Up-Regulation of Cell-Cycle Inhibitors by CNT + rfhSP-D Treatment

To further understand the mechanism of apoptosis induced by CNT + rfhSP-D in AML14.3D10 or K562 cells, we analysed the expression of cell cycle inhibitors by qRT-PCR. p21 was upregulated in CNT + rfhSP-D treated AML14.3D10 (\log_{10} 5.7-fold) and K562 (\log_{10} 2.7-fold) (Figure 6) [compared to CNT alone: AML14.3D10 (\log_{10} 1.2-fold) and K562 (\log_{10} 1-fold)]. p27 transcripts were also upregulated in CNT + rfhSP-D challenged AML14.3D10 (\log_{10} 2.5-fold) and K562 (\log_{10} 2-fold) cells. The level of upregulation was considerably higher compared to CNT or rfhSP-D alone that were negative and positive controls, respectively, suggesting that coating rfhSP-D on CNTs enhanced rfhSP-D potency for targeting tumors.

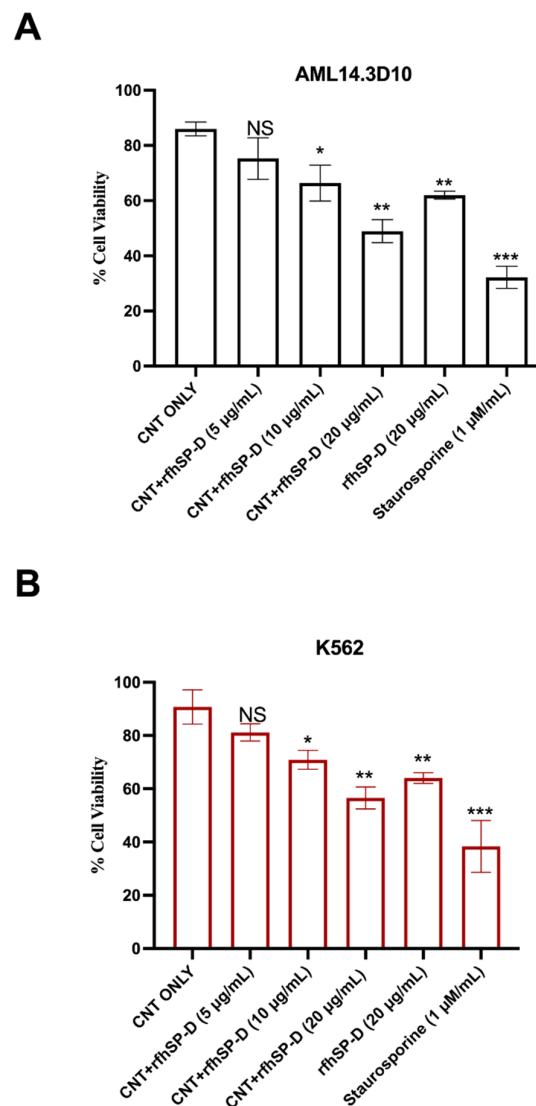


Figure 2. Cell viability following treatment with CNT + rfhSP-D-CNT in AML14.3D10 (A) and K562 (B) cell lines via trypan-blue-dye exclusion assay. Cells (0.1×10^5) were treated with CNT + rfhSP-D (5, 10, 20 $\mu\text{g}/\text{mL}$), rfhSP-D (20 $\mu\text{g}/\text{mL}$) or CNT alone (20 $\mu\text{g}/\text{mL}$) for 24 h at 37 °C. The data has been normalized with cells only as 100% of the cell viability. * $p < 0.05$, ** $p < 0.01$ and *** $p < 0.001$ compared to CNT only group.

2.5. rfhSP-D Upregulates p53 Expression in AML14.3D10 Cell Line

p53, a transcription factor, regulates oncogenic responses including DNA damage, cell cycle arrest, and apoptosis. CNT + rfhSP-D or rfhSP-D alone treated AML14.3D10 cells showed increased transcript levels of p53 when compared to untreated cells. CNT + rfhSP-D treated cells showed \log_{10} 8.2-fold increased mRNA levels, compared to rfhSP-D treated cells (approximately \log_{10} 5.2-fold) (Figure 7). p53 transcripts were not measured in K562 cells as these cells do not express wild type p53. These data suggest that CNT + rfhSP-D treatment can induce apoptosis in these cell lines regardless of their p53 status.

2.6. Apoptosis Induction in AML14.3D10 and K562 Cells by rfhSP-D-CNT via Intrinsic Pathway

Since apoptosis can be initiated via intrinsic or extrinsic pathways, expression of caspases was examined in AML14.3D10 or K562 cell lines treated with CNT + rfhSP-D (20 $\mu\text{g}/\text{mL}$) or rfhSP-D alone (20 $\mu\text{g}/\text{mL}$), using a fluorogenic substrate to detect the activation of caspase 3 and 7 (Figure 8). Higher levels of caspase 3 and 7 were observed

in CNT + rfhSP-D treated AML14.3D10 (Figure 8A) and K562 (Figure 8B) cells, when compared to rfhSP-D or CNT alone-treated cells. There was a time-dependent increase in caspase 3 and 7 activation, which peaked at 24 h. Cleaved caspase 9 level was observed in CNT + rfhSP-D (or rfhSP-D-treated) AML14.3D10 or K562 cells at 12h, reflecting an intrinsic pathway (Figure 9).

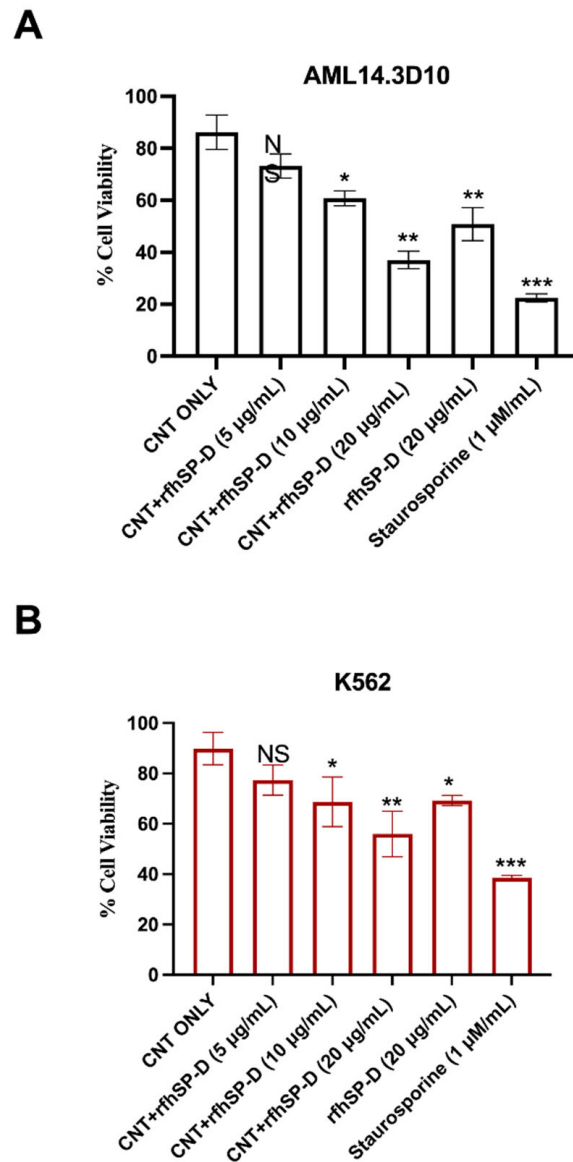


Figure 3. CNT + rfhSP-D treatment reduced viability of AML14.3D10 (A) and K562 (B) cells, as measured by MTT assay. The data have been normalized with cells only as 100% of the cell viability. Values are means \pm SEM ($n = 3$) * $p < 0.05$, ** $p < 0.01$ and *** $p < 0.001$ compared to CNT only group.

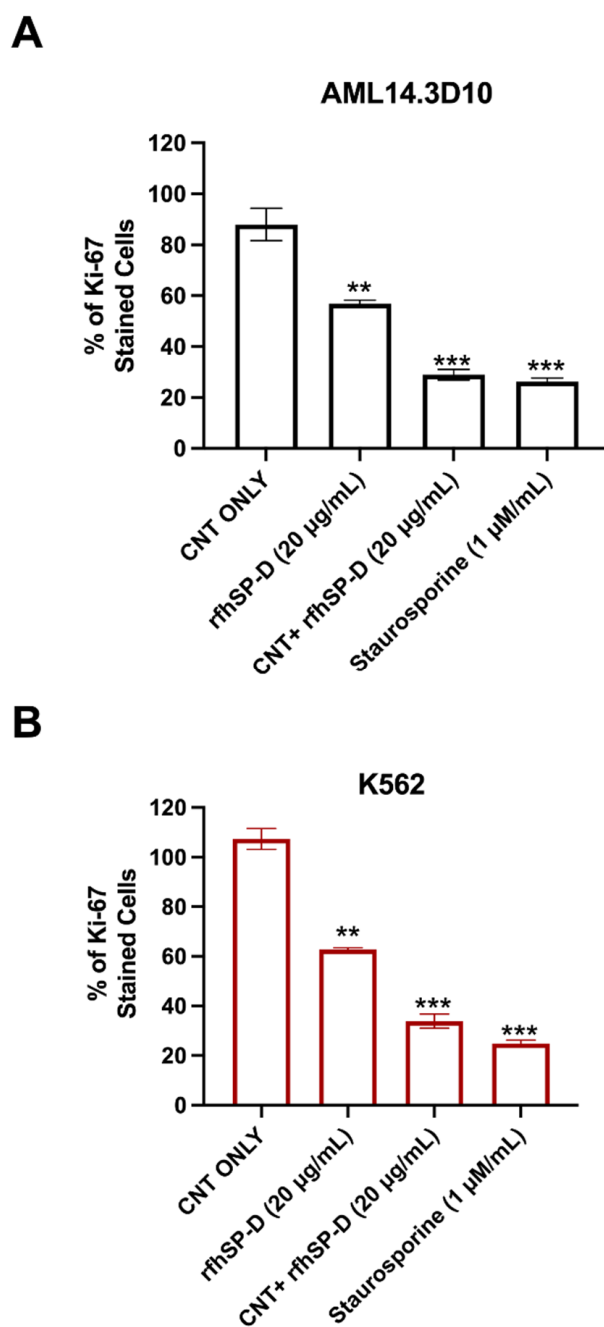


Figure 4. Anti-proliferative effects of CNT + rfhSP-D on AML14.3D10 (A) and K562 (B) cell lines. Values are means \pm SD. ** $p < 0.01$, and *** $p < 0.001$ compared to CNT group only. The raw data are available as Supplementary Materials.

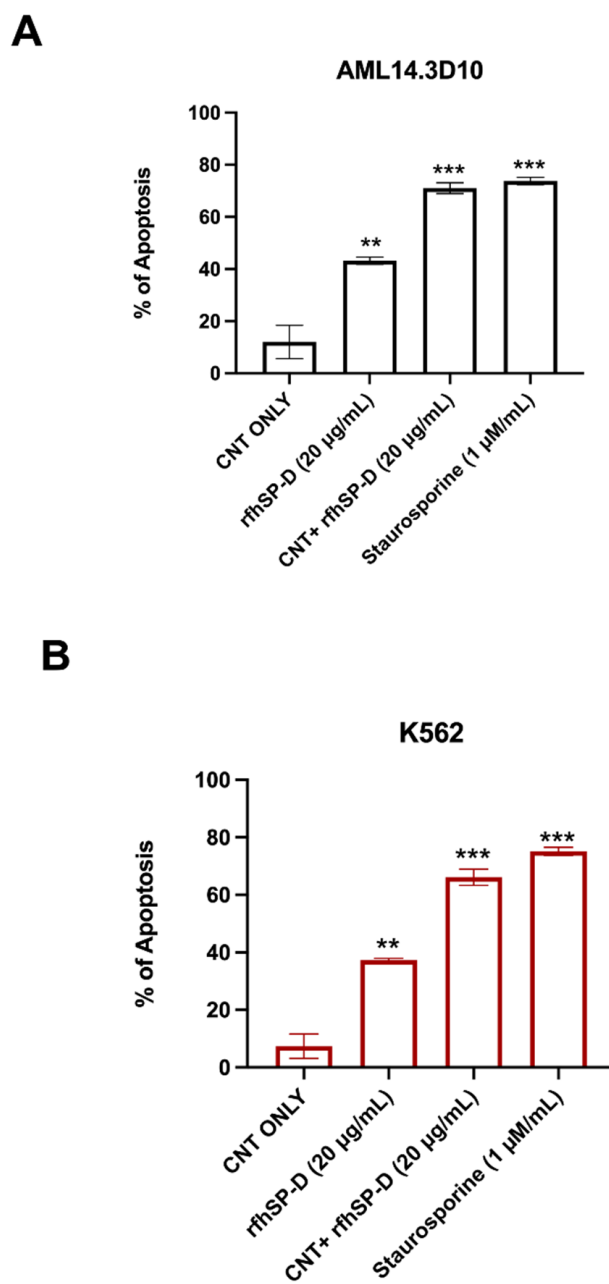


Figure 5. Flow cytometry analysis of apoptosis induction in AML14.3D10 (A) or K562 (B) cell lines treated with CNT + rfhSP-D. For Annexin V/FITC and DNA/PI staining, 12,000 cells were acquired and plotted. Values are means \pm SEM ($n = 3$). ** $p < 0.01$ and *** $p < 0.001$ compared to CNT only group. The raw data are available in the Supplementary Materials.

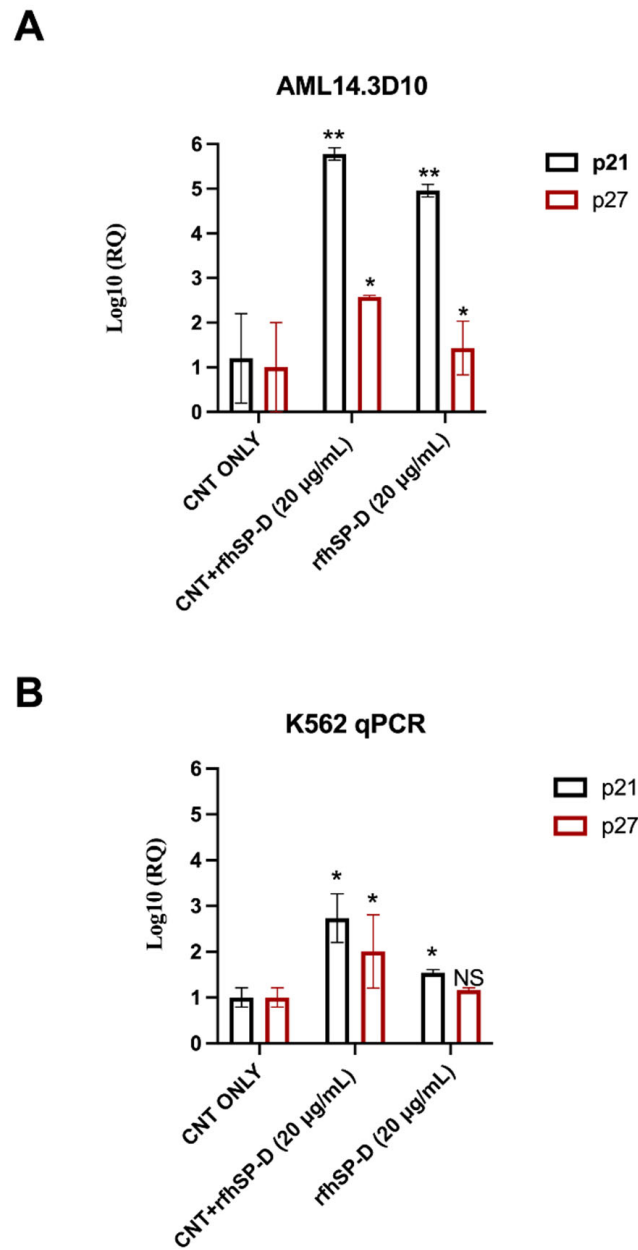


Figure 6. CNT + rfhSP-D treatment causes the upregulation of p21 and p27 cell cycle inhibitors in AML14.3D10 (A) and K562 (B) cell lines. AML14.3D10 or K562 (0.4×10^6) cells, treated with CNT + rfhSP-D (20 µg/mL) or rfhSP-D (20 µg/mL), plus untreated control (cells+ CNT) (20 µg/mL), were used for RNA extraction, cDNA synthesis and RT-qPCR, using 18S as an endogenous control. The RQ value was calculated using the formula: $RQ = 2^{-\Delta\Delta Ct}$. Values represent means \pm SEM ($n = 3$). * $p < 0.05$ and ** $p < 0.01$ compared to CNT only group.

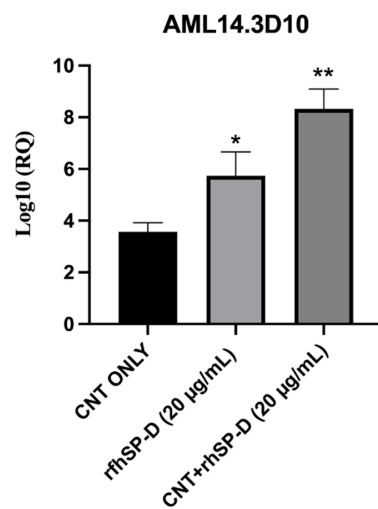
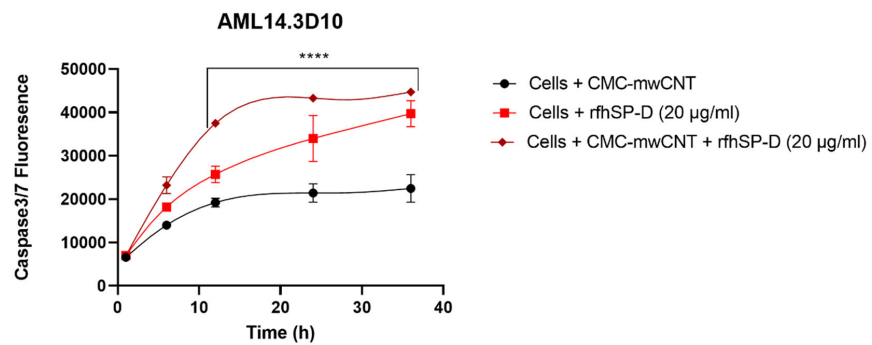


Figure 7. CNT + rfhSP-D treated AML14.3D10 cells show upregulation of the mRNA transcript levels of p53. AML14.3D10 (0.4×10^6) cells were treated with CNT + rfhSP-D or rfhSP-D alone, along with an untreated control (cells + CNT) (20 µg/mL each). The RQ value was calculated using the formula: $RQ = 2^{-\Delta\Delta Ct}$. * $p < 0.05$ and ** $p < 0.01$ compared to CNT only group.

A



B

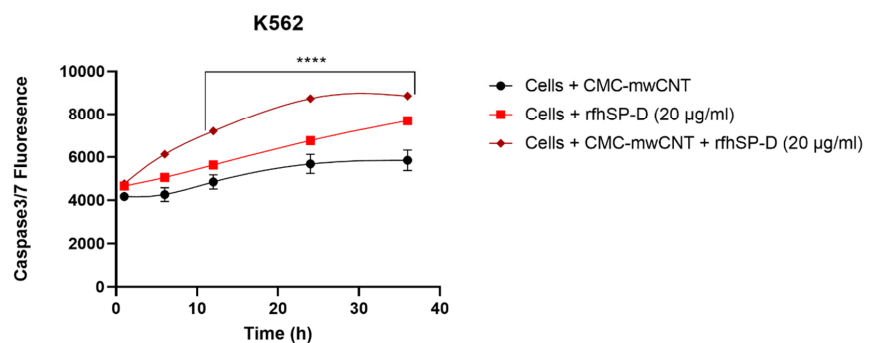


Figure 8. Activation of caspase 3/7 in AML14.3D10 (A) or K562 (B) cell lines following CNT + rfhSP-D treatment. AML14.3D10 or K562 cells (0.1×10^5) were seeded and challenged with CNT + rfhSP-D (20 µg/mL) or rfhSP-D (20 µg/mL) Cells + CNT was used as an untreated control. **** $p < 0.0001$ versus control group ($n = 3$).

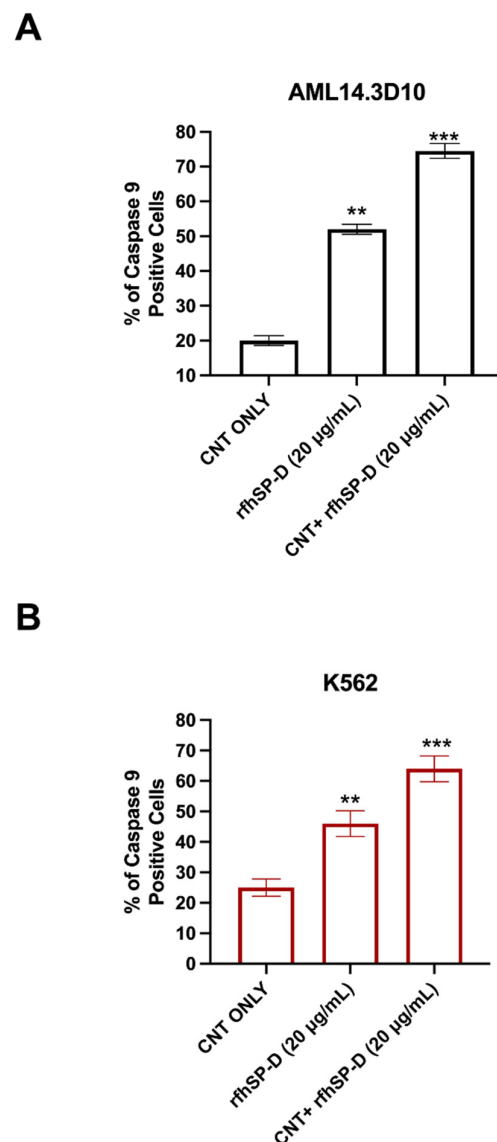


Figure 9. CNT + rfhSP-D treatment upregulates the levels of cleaved caspase 9 on AML14.3D10 (A) or K562 (B) cell lines at 24 h. AML14.3D10 or K562 cells (0.4×10^6) were treated with rfhSP-CNT or rfhSP-D, along with an untreated control (cells + CNT). Values are expressed as mean \pm SD ($n = 3$). ** $p < 0.01$, and *** $p < 0.001$ versus control group.

3. Discussion

The involvement of innate immune mechanisms in cancer progression and resistance has opened up opportunities for using innate immune molecules as a part of anti-tumour therapeutic strategies. Immune system, innate as well as adaptive, is a double-edged sword that can either foster tumour progression via immunosuppression, angiogenesis, and metastasis, or resist oncogenesis [29,30]. SP-D, especially the trimeric CRDs in its recombinant form (rfhSP-D), has recently been shown to be protective against a range of cancer, based on in vitro studies. Coupling rfhSP-D with nanoparticles triggers a differential immune response [26]. rfhSP-D-bound CNTs upregulate the pro-inflammatory response (IL-1 β , TNF- α , IL-6 and IL-12) in U937 and THP-1 cells [26]. Here, we examined the ability of CNT + rfhSP-D to act as a potent inducer of apoptosis in leukemic AML14.3D10 or K562 cell lines. CNT + rfhSP-D treatment reduced the cell viability of AML14.3D10 and K562 cells and induced apoptosis at 24 h in a dose- and time-dependent manner, peaking at 24 h and 20 μ g/mL. A significant reduction in viability was observed in

CNT + rfhSP-D treated AML14.3D10 (~37%) and K562 (~55%) cells compared to untreated control (cells + CNT), based on trypan blue and MTT assays.

FACS analysis revealed a significant increase in the percentage of Annexin V-/PI-positive leukemic cells following CNT + rfhSP-D treatment, characterized by the disruption of the asymmetric arrangement of the membrane, and appearance of PS on the outer side of the cell membrane in the cells undergoing apoptosis [31]. Annexin V, a 36 kDa protein, can bind PS, and also enter the entire plasma membrane in necrotic cells. CNT + rfhSP-D triggered the maximum apoptosis at 24 h [AML14.3D10 (~71%) and K562 (~66%)], when compared to CNT alone [AML14.3D10 (~12%) and K562 (~7%)]. However, no significant difference in terms of cell viability reduction/apoptosis induction was noticed following rfhSP-D treatment at 48 h in AML14.3D10 and K562 cells, suggesting recovery of the cells after 24 h. Apoptosis induction in AML14.3D10 and K562 cell lines by CNT + rfhSP-D may occur through the intrinsic pathway, supported by increased levels of caspase 3, 7 and cleaved caspase 9. This validates earlier studies on AML14.3D10, prostate and breast cancer cells [20,21,32], and the involvement of a mitochondrial pathway [20,21,32].

We also tried to understand the underlying mechanism of apoptosis induction by CNT + rfhSP-D and the associated signaling pathways. CNT + rfhSP-D caused increased transcript level of p53 in AML14.3D10 cell line, probably due to oxidative stress [17,33]. The upregulation of p53 in CNT + rfhSP-D treated AML14.3D10 cells may downregulate pAkt pathway, increasing Bad and Bax, which in turn, causes the release of the cytochrome c, and caspase 9 cleavage. In addition, the increased expression of p53 and cell cycle inhibitors (p21/p27) can cause inactivation of the cyclin B-cdc2 complex, crucial for G2/M cell cycle transition [17]. The existence of a lack of p53 wild type gene in K562 cell line, and its increased susceptibility to CNT + rfhSP-D, the protective effects of rfhSP-D bound to CNTs seem p53 independent. An involvement of cellular receptors expressed by these cancer cell lines is of paramount importance. SP-D interaction with HMGA1, CD14, CD91-calreticulin complex, SIRP α , EGFR, and GRP78 has been reported [20–22,33,34]. The presence of rfhSP-D on CNT as an array of therapeutic molecule is likely to have a clustering effect on these putative receptors, enhancing the potency of rfhSP-D.

In conclusion, CNT + rfhSP-D nanomaterial seems to be an attractive and novel therapeutic approach for targeting intracellular signaling cascades. There is a clear therapeutic potential of rfhSP-D against tumour cells. The advantage here is that the enhanced glycosylation of oncogenic targets can evade natural or therapeutic antibodies. Having established the specific nature of interactions between CNT + rfhSP-D and receptors found on leukemic cancer cells, we can hope to investigate host response in the murine models of cancer using wild type and SP-D knock-out mice.

4. Materials and Methods

4.1. Cell Culture

AML14.3D10 and K562 cells (ATCC) were cultured in RPMI media containing 10% *v/v* fetal calf serum (FCS), 2 mM L-glutamine, and penicillin (100 U/mL)/streptomycin (100 μ g/mL) (ThermoFisher Scientific, Oxford, UK). Cells were grown at 37 °C under 5% *v/v* CO₂ until 80–90% confluency was reached.

4.2. Dispersion and Functionalization of CNTs

The CNTs used in this study were characterized and functionalized as previously described [26,27]. Briefly, CNTs (diameters 10–20 nm, length 5–20 μ m; Aray Nano) were dispersed using CNT sulfuric acid/nitric acid (3:1 ratio) via sonication and functionalized using CMC (Sigma-Aldrich/Merck, Dorset, UK) in a 1:2 mass ratio [26,27].

4.3. Expression and Purification of rfhSP-D

A recombinant fragment of human SP-D (rfhSP-D) was expressed and purified as described previously [17,32]. Affinity purified rfhSP-D was then subjected to endotoxin

level measurement using QCL-1000 Limulus amoebocyte lysate system (Lonza, Slough, UK); the endotoxin levels were found to be ~5 pg/ μ g of rfhSP-D.

4.4. Sodium Dodecyl Sulfate Polyacrylamide Gel Electrophoresis (SDS-PAGE)

The binding of rfhSP-D to CMC-CNTs was assessed via SDS-PAGE (12% *v/v*). CNT + rfhSP-D samples were boiled in a treatment buffer containing SDS and β -mercaptoethanol at 95 °C for 10 min before loading on to the gel. The SDS-PAGE gel was stained for 2 h using brilliant blue stain containing methanol (50% *v/v*) and acetic acid (10% *v/v*). This followed submersion of the stained gel with gentle shaking with de-staining solution (staining solution without brilliant blue).

4.5. Trypan-Blue-Dye Exclusion Assay

AML14.3D10 or K562 cells (0.1×10^6) were seeded in a 12-well plate in complete RPMI complete medium overnight under 5% CO₂ at 37 °C. Next, the cells were washed with PBS and treated with CNT + rfhSP-D (5, 10 or 20 μ g/mL), or rfhSP-D alone (20 μ g/mL), in serum-free RPMI for 24 h. Cells + CNT and Staurosporine (1 μ M/mL) were used as an untreated/negative and positive control, respectively. Cells were then washed, detached using 5 mM EDTA, and centrifuged ($1200 \times g$). The cell pellet, re-suspended in RPMI, was treated with Trypan blue (10 μ L) (60%), and viable cells were counted using hemocytometer in 5 different optical fields with a threshold value of 200 cells per field.

4.6. MTT Assay

MTT [3-(4,5-dimethylthiazol-2-yl)-2,5-diphenyltetrazolium bromide] (Sigma-Aldrich, Dorset, UK) assay was performed to assess the cell metabolic activity (cells + CNT + rfhSP-D; cells + CNT). AML14.3D10 or K562 cells (0.1×10^5) were seeded in 96-well plates in RPMI complete medium until 85% confluency, and treated with CNT + rfhSP-D (5, 10 or 20 μ g/mL), or rfhSP-D (20 μ g/mL), in serum free RPMI medium for 24 h. MTT (50 μ g/ μ L) per well was added for 4 h at 37 °C. 25 μ L medium per well was then mixed with 50 μ L DMSO (10', 37 °C), and the absorbance was read at 570 nm using an ELISA plate reader.

4.7. Flow Cytometry

For apoptosis assays, AML14.3D10 or K562 cells (0.4×10^6) were seeded in culture petri dishes (Nunc) in complete RPMI medium for 24 h and treated with CNT + rfhSP-D (20 μ g/mL), or rfhSP-D (20 μ g/mL), in serum-free RPMI medium for 24 h. Other controls were used as described above. Detached, centrifuged and PBS washed cells were incubated with Alexa Fluor 488 (1:200) (Sigma-Aldrich/Merck, Dorset, UK) (15°, RT) in dark, and the extent of apoptosis was measured using Novocyte Flow Cytometer. Compensation parameters were acquired using unstained, untreated FITC stained, and untreated PI-stained samples for all the cell lines.

For proliferative studies, AML14.3D10 or K562 cells (0.4×10^6) were washed with PBS, probed with anti-mouse Ki-67 (BioLegend, San Diego, CA, USA) diluted in permeabilization reagent of the FIX&PERM kit (Fisher Scientific), and incubated for 30 min at room temperature (RT). Goat anti-mouse-FITC conjugate (1:200) (Fisher Scientific) was used as a probe at RT in the dark for 30 min. Cells (12,000) were acquired for each experiment and compensated before plotting the acquired data.

For caspase 9 and 8 studies, AML14.3D10 or K562 cells (0.4×10^6) were treated with CNT + rfhSP-D or rfhSP-D (cells + CNT as a control) for 24 h at 37 °C, and probed with rabbit anti-human cleaved caspase 9 or 8 (Cell Signaling Technology, Danvers, MA, USA) (1:200) for 1 h at RT. Cells were washed in PBS, incubated with Alexa Fluor 488 (1:200) (Sigma-Aldrich) at RT in dark for 30 min, acquired and compensated (12,000) prior to plotting the data.

4.8. Caspase-3/7 Analysis

AML14.3D10 or K562 cells (0.1×10^5) were seeded in 96 well plates in RPMI complete medium until 80% confluency. The cells were then treated with CNTs, as described above, in serum-free RPMI medium containing CellEvent™ Caspase-3/7 Green Detection Reagent (5 μ M; Thermo-Fisher) (0, 10, 20, 30 or 40 h). Cells + CNT was used as an untreated/negative control. CellEvent™ Caspase-3/7 Green Detection Reagent is a fluorogenic substrate for activated caspases 3 and 7 in cells undergoing apoptosis. The plates with treated and untreated samples were incubated at 37 °C with 5% CO₂ to detect the levels of Caspase 3/7 using a Clariostar plus microplate reader (BMG Labtech, Cary, NC, USA).

4.9. Quantitative RT-PCR

AML14.3D10 or K562 cells (0.5×10^6) were incubated with CNT + rfhSP-D (20 μ g/mL) or rfhSP-D (20 μ g/m in serum-free RPMI medium for 18 h and RNA was isolated using GenElute Mammalian Total RNA Purification Kit (Sigma-Aldrich) and treated with DNase I. 2 μ g of total RNA was used for cDNA synthesis using High Capacity kit (Applied Biosystems/ThermoFisher, Abingdon, UK). Primer sequences were designed using Primer-BLAST software (Table 1). Each PCR reaction, carried out in triplicates, contained SYBR Green (5 μ L) MasterMix (Applied Biosystems), primers (75 nM), and cDNA (500 ng) (7900HT; Applied Biosystems). The cycle involved 2'/50 °C and 10'/95 °C, and 40 cycles (15 s/95 °C; 1'/60 °C). Human 18S rRNA was used as a housekeeping gene control. Relative quantification (RQ) value and formula: $RQ = 2^{-\Delta\Delta Ct}$ were used to calculate the relative expression of each target. Cells + CNT was used as an untreated/negative control.

Table 1. Target genes and terminal primers used in the RT-qPCR analysis.

Target Gene	Forward Primer	Reverse Primer
18S	5'-ATGGCCGTTCTTAGTTGGTG-3'	5'-CGCTGAGCCAGTCAGTGTAG-3'
P53	5'-AGCACTGTCCAACAACACCA-3'	5'-CTTCAGGTGGCTGGAGTGAG-3'
p21	5'-TGGAGACTCTCAGGGTCGAAA-3'	5'-CGGCGTTTGGAGTGGTAGAA-3'
p27	5'-CCGGTGGACCACGAAGAGT-3'	5'-GCTCGCCTCTTCCATGTCTC-3'

4.10. Statistical Analysis

The graphs were generated using the GraphPad Prism 6.0 software. A one-way ANOVA test was carried out for statistical significance analysis. values less than 0.05 were considered as statistically significant.

Supplementary Materials: The following are available online at <https://www.mdpi.com/article/10.3390/ijms221910445/s1>.

Author Contributions: Conceptualization, H.A.K., U.K.; Data curation, U.K. and H.M.A.; Formal analysis, U.K. and S.H.A.; Funding acquisition, H.A.K.; Investigation, H.A.K., U.K. and S.H.A.; Methodology, U.K., H.M.A. and S.H.A.; Project administration, H.A.K.; Resources, H.A.K., U.K.; Software, U.K., H.M.A.; Writing—review & editing, H.A.K. and U.K. All authors have read and agreed to the published version of the manuscript.

Funding: This project was funded by the National Plan for Science, Technology and Innovation (MAARIFAH), King Abdulaziz City for Science and Technology, Kingdom of Saudi Arabia, Award Number (15-NAN-3664-02).

Institutional Review Board Statement: Not applicable.

Informed Consent Statement: Not applicable.

Data Availability Statement: Not applicable.

Acknowledgments: Technical assistance of Valarmathy Murugaiah, Khalid Ibrahim, Ashraf Hatamilah, and Adnan Khan is gratefully acknowledged.

Conflicts of Interest: The authors declare no conflict of interest.

References

- Boraschi, D.; Castellano, L.R.C.; Italiani, P. Interaction of Nanomaterials with the Immune System: Role in Nanosafety and Nanomedicine. *Front. Immunol.* **2017**, *8*, 1688. [[CrossRef](#)] [[PubMed](#)]
- Salvador-Morales, C.; Flahaut, E.; Sim, E.; Sloan, J.; Green, M.L.; Sim, R.B. Complement activation and protein adsorption by carbon nanotubes. *Mol. Immunol.* **2006**, *43*, 193–201. [[CrossRef](#)] [[PubMed](#)]
- Kang, S.H.; Nafiujjaman, M.; Nurunnabi, M.; Li, L.; Khan, H.A.; Cho, K.J.; Huh, K.M.; Lee, Y. Hybrid photoactive nanomaterial composed of gold nanoparticles, pheophorbide-A and hyaluronic acid as a targeted bimodal phototherapy. *Macromol. Res.* **2015**, *23*, 474–484. [[CrossRef](#)]
- Ibrahim, K.E.; Bakhiet, A.O.; Khan, A.; Khan, H.A. Recent trends in biomedical applications of nanomaterials. *Biosci. Biotechnol. Res. Asia* **2018**, *15*, 235–243. [[CrossRef](#)]
- Nafiujjaman, M.; Khan, H.A.; Lee, Y.K. Peptide-influenced graphene quantum dots on iron oxide nanoparticles for dual imaging of lung cancer cells. *J. Nanosci. Nanotechnol.* **2017**, *17*, 1704–1711. [[CrossRef](#)]
- Khan, H.A.; Sakharkar, M.; Nayak, A.; Kishore, U.; Khan, A. Nanoparticles for biomedical applications. In *Nanobiomaterials: Nanostructured Materials for Biomedical Applications*; Elsevier: New York, NY, USA, 2018; pp. 357–384.
- Du, J.; Zhang, Y.S.; Hobson, D.; Hydring, P. Nanoparticles for immune system targeting. *Drug Discov. Today* **2017**, *22*, 1295–1301. [[CrossRef](#)]
- Mishra, V.; Kesharwani, P.; Jain, N.K. Biomedical Applications and Toxicological Aspects of Functionalized Carbon Nanotubes. *Crit. Rev. Ther. Drug Carr. Syst.* **2018**, *35*, 293–330. [[CrossRef](#)] [[PubMed](#)]
- Vardharajula, S.; Ali, S.Z.; Tiwari, P.M.; Eroglu, E.; Vig, K.; Dennis, V.A.; Singh, S.R. Functionalized carbon nanotubes: Biomedical applications. *Int. J. Nanomed.* **2012**, *7*, 5361–5374.
- Liu, Z.; Tabakman, S.; Welsher, K.; Dai, H. Carbon Nanotubes in Biology and Medicine: In vitro and in vivo Detection, Imaging and Drug Delivery. *Nano Res.* **2009**, *2*, 85–120. [[CrossRef](#)]
- Li, W.; Tierce, N.T.; Bekyarova, E.; Bardeen, C.J. Protection of Molecular Microcrystals by Encapsulation under Single-Layer Graphene. *ACS Omega* **2018**, *3*, 8129–8134. [[CrossRef](#)]
- Crouch, E.; Wright, J.R. Surfactant proteins A and D and pulmonary host defense. *Annu. Rev. Physiol.* **2001**, *63*, 521–554. [[CrossRef](#)]
- Crouch, E.C. Surfactant protein-D and pulmonary host defense. *Respir. Res.* **2000**, *1*, 1–16. [[CrossRef](#)]
- Pastva, A.M.; Wright, J.R.; Williams, K.L. Immunomodulatory roles of surfactant proteins A and D: Implications in lung disease. *Proc. Am. Thorac. Soc.* **2007**, *4*, 252–257. [[CrossRef](#)] [[PubMed](#)]
- Nayak, A.; Dodagatta-Marri, E.; Tsolaki, A.G.; Kishore, U. An insight into the diverse roles of surfactant proteins, SP-A and SP-D in innate and adaptive immunity. *Front. Immunol.* **2012**, *3*, 131. [[CrossRef](#)] [[PubMed](#)]
- Murugaiah, V.; Tsolaki, A.G.; Kishore, U. Collectins: Innate Immune Pattern Recognition Molecules. *Lectin Host Def. Microb. Infect.* **2020**, *1204*, 75–127.
- Kaur, A.; Riaz, M.S.; Murugaiah, V.; Varghese, P.M.; Singh, S.K.; Kishore, U. A recombinant fragment of human surfactant protein D induces apoptosis in pancreatic cancer cell lines via fas-mediated pathway. *Front. Immunol.* **2018**, *9*, 1126. [[CrossRef](#)]
- Kaur, A.; Riaz, M.S.; Singh, S.K.; Kishore, U. Human surfactant protein D suppresses epithelial-to-mesenchymal transition in pancreatic cancer cells by downregulating TGF- β . *Front. Immunol.* **2018**, *9*, 1844. [[CrossRef](#)] [[PubMed](#)]
- Kumar, J.; Murugaiah, V.; Sotiriadis, G.; Kaur, A.; Jeyaneethi, J.; Sturniolo, I.; Alhamlan, F.; Chatterjee, J.; Hall, M.; Kishore, U. Surfactant protein D as a potential biomarker and therapeutic target in ovarian cancer. *Front. Oncol.* **2019**, *9*, 542. [[CrossRef](#)]
- Thakur, G.; Prakash, G.; Murthy, V.; Sable, N.; Menon, S.; Alrokayan, S.; Khan, H.A.; Murugaiah, V.; Bakshi, G.; Kishore, U. Human SP-D acts as an innate immune surveillance molecule against androgen-responsive and androgen-resistant prostate cancer cells. *Front. Oncol.* **2019**, *9*, 565. [[CrossRef](#)]
- Mahajan, L.; Pandit, H.; Madan, T.; Gautam, P.; Yadav, A.K.; Warke, H.; Sundaram, C.S.; Sirdeshmukh, R.; Sarma, P.U.; Kishore, U.; et al. Human surfactant protein D alters oxidative stress and HMGA1 expression to induce p53 apoptotic pathway in eosinophil leukemic cell line. *PLoS ONE* **2013**, *8*, e85046. [[CrossRef](#)]
- Hasegawa, Y.; Takahashi, M.; Ariki, S.; Asakawa, D.; Tajiri, M.; Wada, Y.; Yamaguchi, Y.; Nishitani, C.; Takamiya, R.; Saito, A. Surfactant protein D suppresses lung cancer progression by downregulation of epidermal growth factor signaling. *Oncogene* **2015**, *34*, 838–845. [[CrossRef](#)] [[PubMed](#)]
- Kendall, M.; Ding, P.; Mackay, R.M.; Deb, R.; McKenzie, Z.; Kendall, K.; Madsen, J.; Clark, H. Surfactant protein D (SP-D) alters cellular uptake of particles and nanoparticles. *Nanotoxicology* **2013**, *7*, 963–973. [[CrossRef](#)] [[PubMed](#)]
- Ruge, C.A.; Schaefer, U.F.; Herrmann, J.; Kirch, J.; Canadas, O.; Echaide, M.; Perez-Gil, J.; Casals, C.; Muller, R.; Lehr, C.M. The interplay of lung surfactant proteins and lipids assimilates the macrophage clearance of nanoparticles. *PLoS ONE* **2012**, *7*, e40775. [[CrossRef](#)]

25. Cirillo, G.; Hampel, S.; Klingeler, R.; Puoci, F.; Iemma, F.; Curcio, M.; Parisi, O.I.; Spizzirri, U.G.; Picci, N.; Leonhardt, A.; et al. Antioxidant multi-walled carbon nanotubes by free radical grafting of gallic acid: New materials for biomedical applications. *J. Pharm. Pharmacol.* **2011**, *63*, 179–188. [[CrossRef](#)] [[PubMed](#)]
26. Pondman, K.M.; Paudyal, B.; Sim, R.B.; Kaur, A.; Kouser, L.; Tsolaki, A.G.; Jones, L.A.; Salvador-Morales, C.; Khan, H.A.; Ten Haken, B.; et al. Pulmonary surfactant protein SP-D opsonises carbon nanotubes and augments their phagocytosis and subsequent pro-inflammatory immune response. *Nanoscale* **2017**, *9*, 1097–1109. [[CrossRef](#)] [[PubMed](#)]
27. Pondman, K.M.; Tsolaki, A.G.; Paudyal, B.; Shamji, M.H.; Switzer, A.; Pathan, A.A.; Abozaid, S.M.; Ten Haken, B.; Stenbeck, G.; Sim, R.B.; et al. Complement Deposition on Nanoparticles Can Modulate Immune Responses by Macrophage, B and T Cells. *J. Biomed. Nanotechnol.* **2016**, *12*, 197–216. [[CrossRef](#)]
28. Baumann, M.A.; Paul, C.C. The AML14 and AML14.3D10 cell lines: A long-overdue model for the study of eosinophils and more. *Stem Cells* **1998**, *16*, 16–24. [[CrossRef](#)]
29. Palucka, A.K.; Coussens, L.M. The Basis of Oncoimmunology. *Cell* **2016**, *164*, 1233–1247. [[CrossRef](#)]
30. Vesely, M.D.; Kershaw, M.H.; Schreiber, R.D.; Smyth, M.J. Natural innate and adaptive immunity to cancer. *Annu. Rev. Immunol.* **2011**, *29*, 235–271. [[CrossRef](#)]
31. Porter, A.G.; Janicke, R.U. Emerging roles of caspase-3 in apoptosis. *Cell Death Differ.* **1999**, *6*, 99–104. [[CrossRef](#)]
32. Murugaiah, V.; Agostinis, C.; Varghese, P.M.; Belmonte, B.; Vieni, S.; Alaql, F.A.; Alrokayan, S.H.; Khan, H.A.; Kaur, A.; Roberts, T.; et al. Hyaluronic Acid Present in the Tumor Microenvironment Can Negate the Pro-apoptotic Effect of a Recombinant Fragment of Human Surfactant Protein D on Breast Cancer Cells. *Front. Immunol.* **2020**, *11*, 1171. [[CrossRef](#)] [[PubMed](#)]
33. Janssen, W.J.; McPhillips, K.A.; Dickinson, M.G.; Linderman, D.J.; Morimoto, K.; Xiao, Y.Q.; Oldham, K.M.; Vandivier, R.W.; Henson, P.M.; Gardai, S.J. Surfactant proteins A and D suppress alveolar macrophage phagocytosis via interaction with SIRP alpha. *Am. J. Respir. Crit. Care Med.* **2008**, *178*, 158–167. [[CrossRef](#)] [[PubMed](#)]
34. Thakur, G.; Sathe, G.; Kundu, I.; Biswas, B.; Gautam, P.; Alkahtani, S.; Idicula-Thomas, S.; Sirdeshmukh, R.; Kishore, U.; Madan, T. Membrane Interactome of a Recombinant Fragment of Human Surfactant Protein D Reveals GRP78 as a Novel Binding Partner in PC3, a Metastatic Prostate Cancer Cell Line. *Front. Immunol.* **2021**, *11*, 3704. [[CrossRef](#)]



Article

Influence of Ce³⁺ Substitution on Antimicrobial and Antibiofilm Properties of ZnCe_xFe_{2-x}O₄ Nanoparticles (X = 0.0, 0.02, 0.04, 0.06, and 0.08) Conjugated with Ebselen and Its Role Subsidised with γ -Radiation in Mitigating Human TNBC and Colorectal Adenocarcinoma Proliferation In Vitro

Mohamed K. Abdel-Rafei ¹, Noura M. Thabet ^{1,*}, M. I. A. Abdel Maksoud ², M. Abd Elkodous ³, Go Kawamura ³, Atsunori Matsuda ^{3,*}, A. H. Ashour ², Ahmed I. El-Batal ⁴ and Gharieb S. El-Sayyad ⁴

- ¹ Radiation Biology Department, National Center for Radiation Research and Technology (NCRRT), Egyptian Atomic Energy Authority (EAEA), Cairo 11787, Egypt; mohamed.marawan2011@yahoo.com
 - ² Materials Science Lab., Radiation Physics Department, National Center for Radiation Research and Technology (NCRRT), Egyptian Atomic Energy Authority (EAEA), Cairo 11787, Egypt; muhamadmqsod@gmail.com (M.I.A.A.M.); ashourvip3@hotmail.com (A.H.A.)
 - ³ Department of Electrical and Electronic Information Engineering, Toyohashi University of Technology, 1-1 Hibarigaoka, Tempaku-cho, Toyohashi 441-8580, Aichi, Japan; mohamed.hamada.abdlekodous.xi@tut.jp (M.A.E.); kawamura.go.km@tut.jp (G.K.)
 - ⁴ Drug Microbiology Lab., Drug Radiation Research Department, National Center for Radiation Research and Technology (NCRRT), Egyptian Atomic Energy Authority (EAEA), Cairo 11787, Egypt; aelbatal2020@gmail.com (A.I.E.-B.); Gharieb.S.Elsayyad@eaea.org.eg (G.S.E.-S.)
- * Correspondence: noura_magdy@hotmail.com (N.M.T.); matsuda@ee.tut.ac.jp (A.M.)

Abstract: Cancers are a major challenge to health worldwide. Spinel ferrites have attracted attention due to their broad theranostic applications. This study aimed at investigating the antimicrobial, antibiofilm, and anticancer activities of ebselen (Eb) and cerium-nanoparticles (Ce-NPs) in the form of ZnCe_xFe_{2-x}O₄ on human breast and colon cancer cell lines. Bioassays of the cytotoxic concentrations of Eb and ZnCe_xFe_{2-x}O₄, oxidative stress and inflammatory milieu, autophagy, apoptosis, related signalling effectors, the distribution of cells through the cell-cycle phases, and the percentage of cells with apoptosis were evaluated in cancer cell lines. Additionally, the antimicrobial and antibiofilm potential have been investigated against different pathogenic microbes. The ZOI, and MIC results indicated that ZnCe_xFe_{2-x}O₄; X = 0.06 specimen reduced the activity of a wide range of bacteria and unicellular fungi at low concentration including *P. aeruginosa* (9.5 mm; 6.250 μ g/mL), *S. aureus* (13.2 mm; 0.390 μ g/mL), and *Candida albicans* (13.5 mm; 0.195 μ g/mL). Reaction mechanism determination indicated that after ZnCe_xFe_{2-x}O₄; X = 0.06 treatment, morphological differences in *S. aureus* were apparent with complete lysis of bacterial cells, a concomitant decrease in the viable number, and the growth of biofilm was inhibited. The combination of Eb with ZFO or ZnCe_xFe_{2-x}O₄ with γ -radiation exposure showed marked anti-proliferative efficacy in both cell lines, through modulating the oxidant/antioxidant machinery imbalance, restoring the fine-tuning of redox status, and promoting an anti-inflammatory milieu to prevent cancer progression, which may be a valuable therapeutic approach to cancer therapy and as a promising antimicrobial agent to reduce the pathogenic potential of the invading microbes.

Keywords: MDA-MB-231; HT-29; ebselen; cerium; ERK1/2; STAT-6; IL-4; STAT-1; antimicrobial activity



Citation: Abdel-Rafei, M.K.; Thabet, N.M.; Abdel Maksoud, M.I.A.; Abd Elkodous, M.; Kawamura, G.; Matsuda, A.; Ashour, A.H.; El-Batal, A.I.; El-Sayyad, G.S. Influence of Ce³⁺ Substitution on Antimicrobial and Antibiofilm Properties of ZnCe_xFe_{2-x}O₄ Nanoparticles (X = 0.0, 0.02, 0.04, 0.06, and 0.08) Conjugated with Ebselen and Its Role Subsidised with γ -Radiation in Mitigating Human TNBC and Colorectal Adenocarcinoma Proliferation In Vitro. *Int. J. Mol. Sci.* **2021**, *22*, 10171. <https://doi.org/10.3390/ijms221810171>

Academic Editors:

Monica Terracciano, Ilaria Rea,
Nicola Borbone and
Chiara Tramontano

Received: 9 September 2021

Accepted: 16 September 2021

Published: 21 September 2021

1. Introduction

Spinel ferrite is a class of magnetic materials that derives its name from its similarity to the naturally occurring mineral. Spinel ferrites have possible application in areas such as water treatment, data storage, the segregation of biomolecules, colour imaging, therapeutic diagnosis, antimicrobial activities, cores of transformers, bubble devices, electronic communication devices, sensors, and drug delivery [1–4]. Structure studies of spinels showed

Publisher's Note: MDPI stays neutral with regard to jurisdictional claims in published maps and institutional affiliations.



Copyright: © 2021 by the authors. Licensee MDPI, Basel, Switzerland. This article is an open access article distributed under the terms and conditions of the Creative Commons Attribution (CC BY) license (<https://creativecommons.org/licenses/by/4.0/>).

that the size of the cations in a sample plays a vital role in determining their site occupancy preferences. The presence of larger ions shifts the oxygen ions diagonally and expands the lattice parameter. The distribution of cations over the sub-lattices has a significant effect on both the chemical and physical properties of the spinel structure and subsequently affects their applications and performance [5,6]. Manipulation of the physical properties of Co-Zn spinel ferrite nanoparticles (NPs) by the incorporation of larger ions into their structure has attracted the attention of researchers. For example, Pawar et al. [7] have addressed the changes induced in the optical properties of cobalt–zinc ferrite $\text{Co}_{0.7}\text{Zn}_{0.3}\text{Ho}_x\text{Fe}_{2-x}\text{O}_4$ ($0 \leq x \leq 0.1$) due to the insertion of (Ho^{3+}), using a facile sol–gel method. These researchers found that the energy bandgap rose from 1.72 to 1.84 eV when the x increased from 0.0 to 0.1. Panda et al. [8] have described the consequences of the incorporation of chromium (Cr^{3+}) ions into the system $\text{CoFe}_{2-x}\text{Cr}_x\text{O}_4$ ($X = 0, 0.15, 0.3$). They found that the coercivity was lowered upon the insertion of Cr^{3+} due to the magnetic coupling with a weaker magnetic moment of Cr^{3+} ($3\mu_B$). Farid et al. [9] substituted praseodymium (Pr^{3+}) instead of Fe^{3+} into the system $\text{Co}_{0.6}\text{Zn}_{0.4}\text{Pr}_x\text{Fe}_{2-x}\text{O}_4$ ($X = 0.0, 0.025, 0.05, 0.075, 0.10$). They found that the insertion of Pr^{3+} increased the lattice constant due to the large difference between the ionic radii of Pr^{3+} and Fe^{3+} . The resistivity and activation energy also increased with the Pr^{3+} substitution. In our previous work, we synthesised Co-Zn spinel ferrites (ZCFO) NPs via a sol–gel method. The ZCFO sample showed a low crystallite size (11.7872 nm) and high surface area ($106.63 \text{ m}^2/\text{g}$), which made it suitable for environmental applications. ZCFO NPs have been used as antimicrobial agents [10], biosensors [11], and as a promising catalyst [12].

Colon cancer is the third most common cancer globally and is the second most common cause of cancer mortality after lung cancer. Approximately 5% of colon cancer patients have an additional primary cancer. In comparison, breast cancer is the single most common cancer of women worldwide, is responsible for 30% of all cancer diagnoses in women, and has a mortality rate of approximately 14% in women. About 3% of breast cancer patients have an additional primary cancer. Breast cancer susceptibility genes have been found to increase the susceptibility to colon cancer of patients with breast cancer [13].

The tumour microenvironment (TME) is a complex network composed of multipotent cells such as stromal cells, mesenchymal stem cells, fibroblasts, blood vessels, endothelial cell precursors and immune cells, and secreted mediators such as cytokines, growth factors, and reactive oxygen species (ROS), which are related to the initiation and maintenance of tumorigenesis. Oncogenic pathways can be associated with major changes in the TME to induce proliferation and inhibit apoptosis and promote angiogenesis and avoid hypoxia as well as inhibit the immune detection and activate immune cells to support invasion and metastasis [14]. Hence, cancer manipulation targeting the components of the TME including metabolites, ROS, hypoxia, and cytokine-mediated inflammation could be a valuable approach to cancer therapy. In radio-therapeutic oncology, radiation directly and indirectly, via radiolysis, induces damage to the structure of DNA, proteins, and lipids, leading to injury of the organelles and cell membranes of cancer cells. Irradiation also disrupts the immunogenicity and microenvironment of cancer cells. These factors have a vital role in regulating cancer cell mitosis, apoptosis, necrosis, proliferation, and other biological functions [15]. Radiotherapy is considered to be an effective treatment option after surgery. However, colorectal cancer exhibits resistance to ionising radiation (IR) as used in radiation oncology treatment. The high doses of radiation required to be delivered to a tumour also result in damage to adjacent normal tissues or organs [16]. Triple-negative breast cancer (TNBC) is the most aggressive breast cancer subtype and has a poor prognosis. Radiotherapy plays an important role in treating TNBC [17]. Hence, there is an urgent need for the development of drugs that serve as radiosensitisers to overcome the radioresistance exhibited by various cancers, including colorectal and TNBC [16,18].

In the current study, we supplemented radiotherapy with theranostic nanoparticles constructed using several approaches such as by conjugating therapeutic agents to imaging nanoparticles, then imaging agents to therapeutic nanoparticles, and hence engineering

unique nanoparticles possessing both therapeutic and diagnostic abilities [19]. Ebselen (Eb) (*N*-phenyl-1,2-benziselenazol-3(2H)-one) is one of the organo-selenium compounds that mimics glutathione peroxidase and exhibits a wide range of biological activities including antibacterial, cyto-protective, anti-inflammatory, antioxidant, and anticancer activities [20]. In biomedical applications, nanoparticles have attracted attention due to their physicochemical properties such as appropriate size, large surface-to-mass ratios, high reactivity, and the ability to modify the biological influence of diffusivity and immunogenicity [21]. The rare earth element cerium (Ce), which has the electronic configuration [Xe] 4f⁶s², has valuable properties due to its possession of shielded 4f electrons. Ce can exist in two common oxidation states, Ce³⁺ and Ce⁴⁺ [22]. In biology, cerium oxide nanoparticles (Ce-NPs) have attracted particular interest because of their regenerative and multi-enzymatic scavenging of ROS. The unique antioxidant/catalytic properties of Ce-NPs stem from their reversible switching between the oxidation states of Ce³⁺ and Ce⁴⁺ and their low reduction potential of around 1.52 V [23]. The bulk of crystals of cerium dioxide consists of Ce⁴⁺, but the nano-dimensions reduce the size to Ce³⁺, resulting in a higher activity of biological antioxidant processes [19,22]. We synthesised the ZnFeO₄ (ZFO) system using the sol-gel method. Ce³⁺ ions were then inserted into the pristine sample using Fe³⁺ ions with different concentrations: ZnCe_xFe_{2-x}O₄; X = 0.0–0.8; step = 0.02). We then investigated the antimicrobial and antibiofilm activities against some pathogenic microbes with the possible reaction mechanism determination (SEM imaging, and protein leakage assay) as well as anticancer effects of Eb and ZnCe_xFe_{2-x}O₄ nanoparticles (X = 0.0, 0.02, 0.04, 0.06, and 0.08) conjugated with Eb on human breast and colorectal cancer cell lines, evaluating their levels of ROS, inflammatory milieu, and related signalling effectors as well as investigating their effects on autophagy, cell cycle, and apoptosis.

2. Results and Discussion

2.1. Structural Studies

The X-ray diffraction (XRD) patterns of ZnCe_xFe_{2-x}O₄ (X = 0.0, 0.02, 0.04, 0.06, 0.08) NPs are presented in Figure 1. The diffraction peaks correspond to those of spinel ferrites, belonging to the Fd3m space group (JCPDS card nos. 88-1935, and 74-2082) [23,24]. The crystallite size (D) ranged between 7.75 and 11.63 nm, and the lattice constant, a_{exp} , was in the range 8.34–8.44 nm, as obtained in our previous work [25]. The change in a_{exp} and D is attributed to the replacement of the smaller ionic crystal radius of Fe³⁺ (0.064 nm) by the larger Ce³⁺ (0.103 nm) ions [26–29].

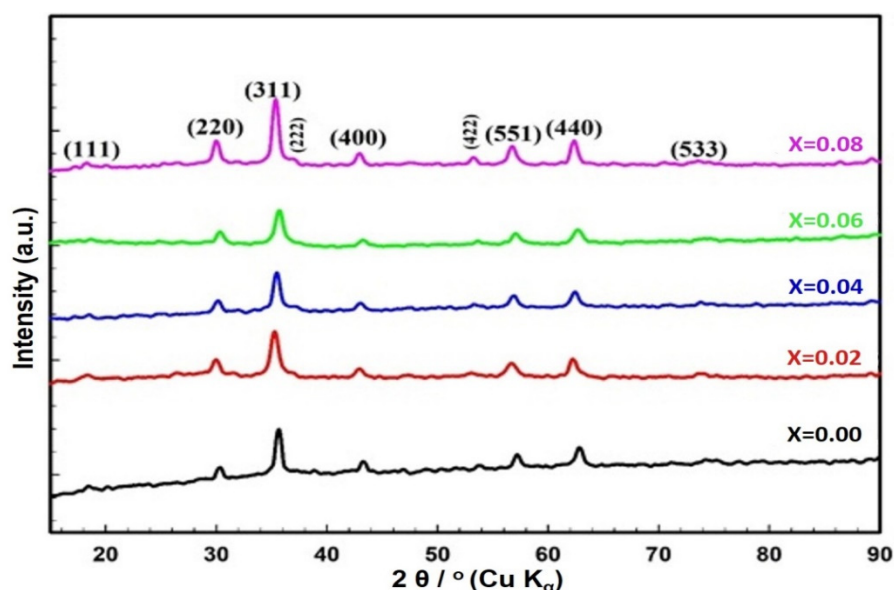


Figure 1. XRD patterns of ZnCe_xFe_{2-x}O₄ (X = 0.0, 0.02, 0.04, 0.06, 0.08) NPs.

Figure 2 shows the Fourier transform infrared (FTIR) spectra of $\text{ZnCe}_x\text{Fe}_{2-x}\text{O}_4$ ($X = 0.0, 0.02, 0.04, 0.06, 0.08$) samples. For the ZFO spinel ferrite sample used in this work, there were two peaks, $\nu_1 = 551.06 \text{ cm}^{-1}$ and $\nu_2 = 433.67 \text{ cm}^{-1}$. These peaks are fundamental and confirm the successful formation of the cubic spinel phase in the ZFO sample [30–32]. The positions of the vibrational bands are listed in Table 1. In general, spinel ferrites show two essential vibrational bands, ν_1 and ν_2 , which correspond to the stretching vibration of tetrahedral groups (A-site) and the stretching vibration of octahedral groups (B-site) [25]. From Figure 2, it is clear that the insertion of Ce^{3+} ions into the structure of $\text{ZnCe}_x\text{Fe}_{2-x}\text{O}_4$ shifted the bands of the tetrahedral and octahedral sites toward the lower-frequency side. The substitution of Ce^{3+} ions into the B-site resulted in the migration of an equal number of Fe^{3+} and Zn ions from A sites to B sites to ease the strain [26]. The ionic radii of the B sites increased due to the settlement of the Ce^{3+} ions. This augmentation in the ionic radii of the A and B sites reduced the fundamental frequency [26,33]. The peaks with a wave number of 2354 cm^{-1} were attributed to the presence of carbonyl groups, while the peak at around 2926 cm^{-1} was ascribed to O-H stretching [10–12,25,34,35].

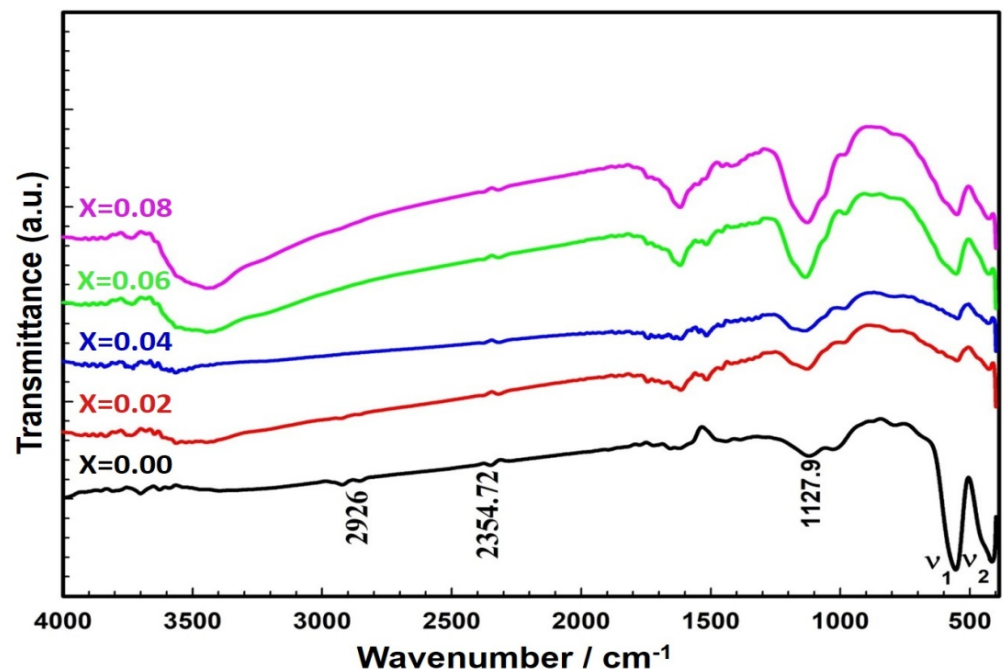


Figure 2. FTIR spectra of $\text{ZnCe}_x\text{Fe}_{2-x}\text{O}_4$ ($X = 0.0, 0.02, 0.04, 0.06, 0.08$) samples.

Table 1. Absorption bands at the tetrahedral and octahedral sites of $\text{ZnCe}_x\text{Fe}_{2-x}\text{O}_4$ ($X = 0.00, 0.02, 0.04, 0.06, \text{ and } 0.08$).

Doped Ferrites		ν_1	ν_2
	x	cm^{-1}	cm^{-1}
$\text{ZnCe}_x\text{Fe}_{2-x}\text{O}_4$	0.00	594.75	404.81
	0.02	549.12	429.17
	0.04	547.97	427.66
	0.06	553.24	426.81
	0.08	549.99	400.32

The scanning electron microscopy (SEM) images of $\text{ZnCe}_x\text{Fe}_{2-x}\text{O}_4$ ($X = 0.0, 0.02, 0.04, 0.06, 0.08$) NPs are shown in Figure 3a–e. The surface behaviour reveals an inhomogeneous grain appearance, in which the smooth agglomerates can be observed due to the occupation of a large quantity of Ce^{3+} ions at the grain boundary that could control the grain

growth [36]. The surface was markedly porous and presented a coalescing form of the agglomerated particles connected with the interfacial surface tension phenomena [25]. The composition of the $\text{ZnCe}_{0.8}\text{Fe}_{1.92}\text{O}_4$ sample was analysed using energy-dispersive X-ray spectra (EDX) (Figure 3f), and the presence of Ce, Zn, O, C, and Fe was confirmed [11,12].

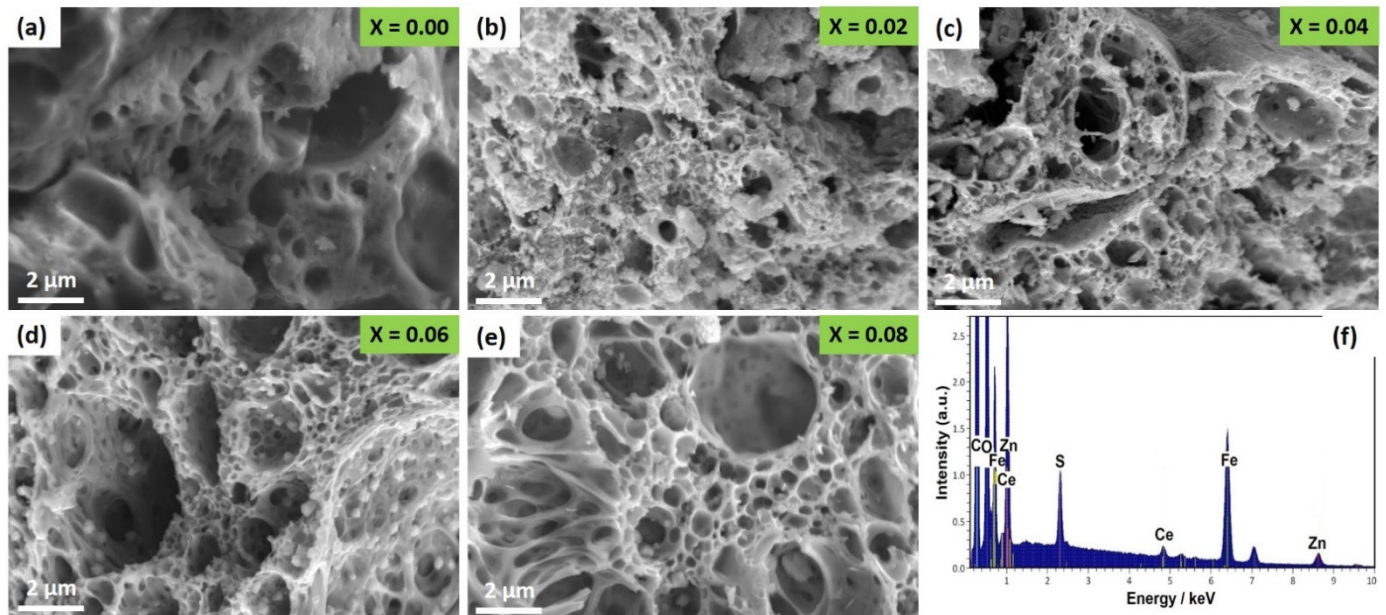


Figure 3. Surface morphology and elemental analysis where (a) SEM images of $\text{ZnCe}_x\text{Fe}_{2-x}\text{O}_4$ NPs; X = 0.0, (b) X = 0.02, (c) X = 0.04, (d) X = 0.06, (e) X = 0.08, and (f) EDX analysis of $\text{ZnCe}_x\text{Fe}_{2-x}\text{O}_4$ NPs.

To further illustrate the structural features of the samples, mapping of elements to the $\text{ZnCe}_{0.8}\text{Fe}_{1.92}\text{O}_4$ sample was carried out (Figure 4). It is evident from these images that the elements Zn, Fe, Ce, C, S, and O exist, an observation that agreed with the preceding EDX results. These elements were homogeneously distributed.

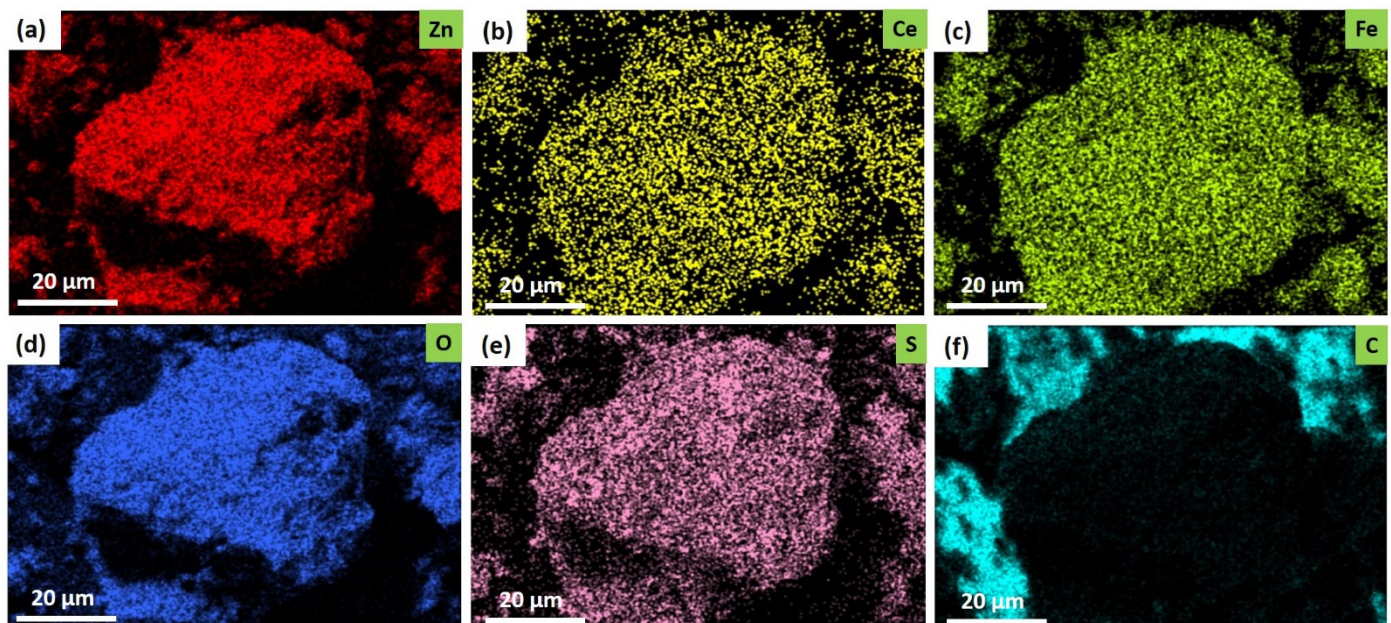


Figure 4. Elemental mapping images of $\text{ZnCe}_x\text{Fe}_{2-x}\text{O}_4$ (X = 0.08) NPs, where (a) for Zn atom, (b) for Ce atom, (c) for Fe atom, (d) for O atom, (e) for S atom, and (f) for C atom.

The Zeta potential of the synthesised $\text{ZnCe}_x\text{Fe}_{2-x}\text{O}_4$ ($X = 0.0, 0.02, 0.04, 0.06, 0.08$) NPs was examined at the culture media as used in the treatments to determine the surface charge of the synthesised samples, which in turn determine the stability, as observed in Figure 5. From the present results, it is notable that the Zeta potential of the $\text{ZnCe}_x\text{Fe}_{2-x}\text{O}_4$ ($X = 0.0, 0.02, 0.04, 0.06, 0.08$) NPs surface maintains a negative statement at pH 7 (cultural media pH). The initial Zeta potential of ZnFe_2O_4 NPs was -38.2 mV (Figure 5a), which completely agrees with the previous results obtained [37,38]. After the substitution of Ce^{3+} on ZnFe_2O_4 NPs (at different concentrations), the potential of substituent samples was slightly changed to be -37.7 , -36.5 , -30.5 , and -30.2 mV when $X = 0.02, 0.04, 0.06$, and 0.08 , respectively, due to the positive charge of Ce^{3+} and the net charge still negative at neutral medium (pH 7), as shown in Figure 5b,c,d,e, respectively. The magnitude of the zeta potential is predictive of the colloidal stability [39]. Nanoparticles with Zeta potential values from ± 30 to ± 40 have moderate stability [40], as shown in our synthesised samples. Dispersions with a low zeta potential value will eventually aggregate due to the Van Der Waal inter-particle attractions [41].

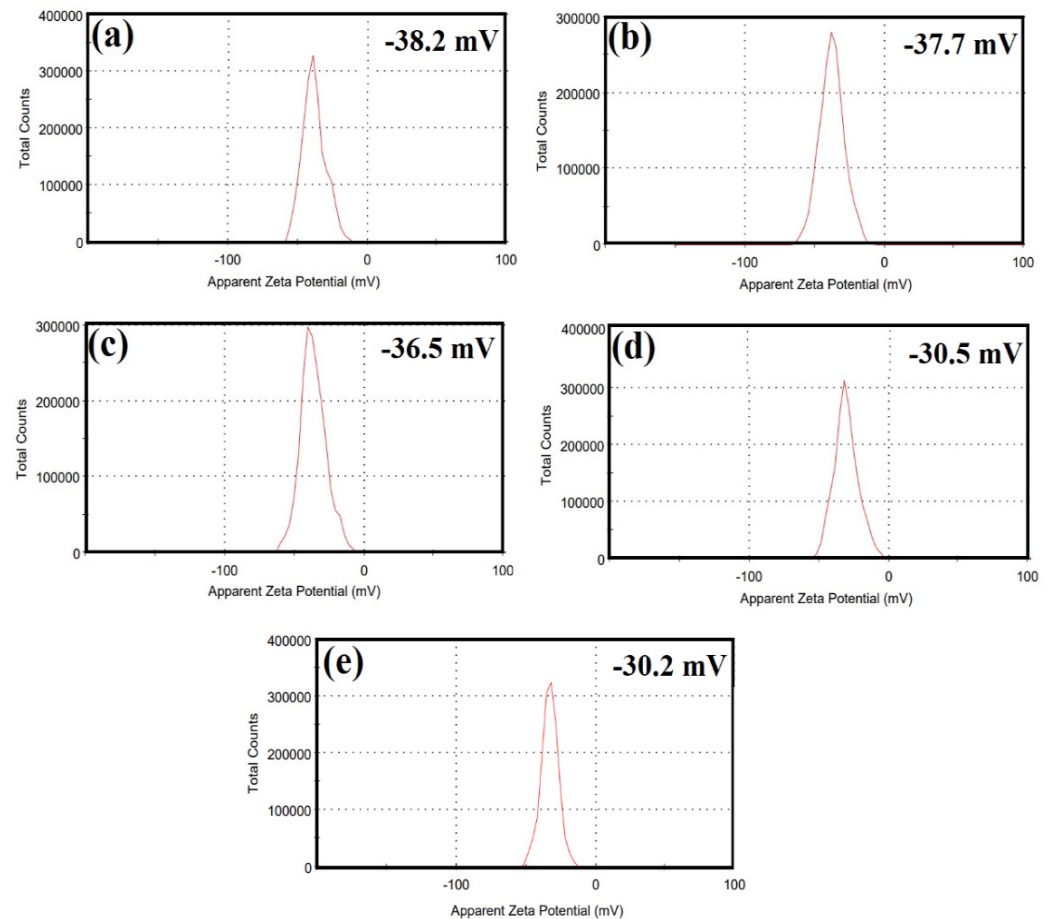


Figure 5. Surface charge determination of $\text{ZnCe}_x\text{Fe}_{2-x}\text{O}_4$ by Zeta potential when (a) $X = 0$, (b) $X = 0.02$, (c) $X = 0.04$, (d), $X = 0.06$, and (e) $X = 0.08$ at pH 7 (cultural media pH).

Dynamic light scattering (DLS) analysis was performed to evaluate particle size distribution and to calculate the average particle size of the synthesised $\text{ZnCe}_x\text{Fe}_{2-x}\text{O}_4$ ($X = 0.0, 0.02, 0.04, 0.06, 0.08$) NPs that was found as 36.71 nm when $X = 0$. Additionally, the particle size was found to be $43.20, 45.91, 49.27$, and 54.87 nm when $X = 0.02, 0.04, 0.06$, and 0.08 , respectively, in the synthesised $\text{ZnCe}_x\text{Fe}_{2-x}\text{O}_4$ NPs, as shown in Figure 6.

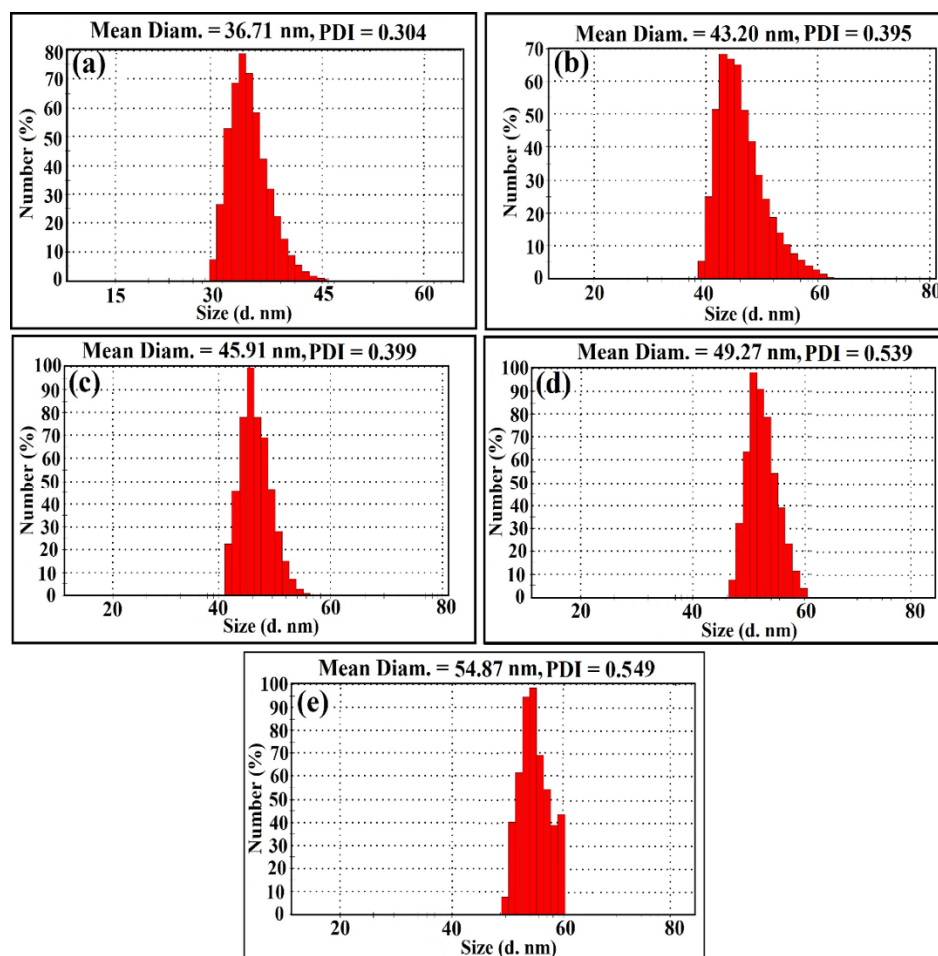


Figure 6. Particle size distribution and PDI determination of $\text{ZnCe}_x\text{Fe}_{2-x}\text{O}_4$ by DLS when (a) $X = 0$, (b) $X = 0.02$, (c) $X = 0.04$, (d) $X = 0.06$, and (e) $X = 0.08$ at pH 7 (cultural media pH).

It is important to state that the grown moderate mono-size distributed $\text{ZnCe}_x\text{Fe}_{2-x}\text{O}_4$ ($X = 0.0, 0.02, 0.04, 0.06, 0.08$) NPs were attributed to the synthesis method, and the particle size distribution was sharply increased as Ce^{3+} ions content increased in the prepared sample. It is common that DLS size measurements become higher than the crystallite size (D) measurements (Figure 1), as DLS analysis is estimating the hydrodynamic radius of $\text{ZnCe}_x\text{Fe}_{2-x}\text{O}_4$ ($X = 0.0, 0.02, 0.04, 0.06, 0.08$) NPs bounded by water molecules, resulting in larger particle sizes of the capped NPs, while XRD analysis is calculating the crystallite size of the powder material without water layer [42].

The polydispersity index (PDI) can be obtained from instruments that use DLS or are determined from electron micrographs. International standards organisations (ISOs) have established that PDI values < 0.05 are more common to monodisperse samples, while values > 0.7 are common to a broad size (e.g., polydisperse) distribution of particles [43]. Herein, for the obtained PDI values (Figure 6), we found that the PDI value increases as Ce^{3+} ions content increases in the prepared sample and was found to be 0.304, 0.395, 0.399, and 0.539 in $\text{ZnCe}_x\text{Fe}_{2-x}\text{O}_4$ NPs when $X = 0.0, 0.02, 0.04, 0.06, 0.08$, respectively. The present values indicate that the synthesised samples were moderate mono-size distributed.

2.2. Antimicrobial Potential

Antimicrobial agents have been used to treat and control the microbial infection [44]. The use of novel nanomaterial-based agents for the limitation of pathogenic microbes has received attention from several researchers [10]. In our study, the as-synthesised ferrite samples were checked for their antimicrobial activity using the agar-disc diffusion technique. The results indicated that the ferrite specimens reduced the activity of a wide range of bacteria

including *P. aeruginosa*, *P. mirabilis*, and *S. aureus*. $\text{ZnCe}_x\text{Fe}_{2-x}\text{O}_4$; $X = 0.06$ had the most powerful antimicrobial effects against all the microbes examined. The power of $\text{ZnCe}_x\text{Fe}_{2-x}\text{O}_4$; $X = 0.06$ as antimicrobial agent declines in the following order: *C. albicans* (13.5 ± 0.5000 mm), $>S. aureus$ (13.2 ± 0.2335 mm), $>P. aeruginosa$ (9.5 ± 0.5000 mm), $>P. mirabilis$ (9.5 ± 1.0000 mm), $>P. vulgaris$ (9.0 ± 0.2335 mm), $>S. typhi$ (9.0 ± 0.6545 mm), $>C. tropicalis$ (8.9 ± 0.6545 mm), $>E. coli$ (8.5 ± 0.6545 mm), and $>K. pneumoniae$ (8.0 ± 0.5755 mm) (Table 2).

Table 2. Antibacterial and antifungal activities of $\text{ZnCe}_x\text{Fe}_{2-x}\text{O}_4$ against some multi-drug resistant bacteria and pathogenic *Candida* species according to ZOI (mm) and MIC ($\mu\text{g}/\text{mL}$).

Pathogenic Microbes	ZOI (mm), $\text{ZnCe}_x\text{Fe}_{2-x}\text{O}_4$ (10 $\mu\text{g}/\text{mL}$)					$\text{ZnCe}_x\text{Fe}_{2-x}\text{O}_4$; $X = 0.06$ (Starting with 50 $\mu\text{g}/\text{mL}$ Concentration)	AX & NS
	$X = 0$	$X = 0.02$	$X = 0.04$	$X = 0.06$	$X = 0.08$		
<i>Staphylococcus aureus</i>	Nil	Nil	$9.0^c \pm 0.6545$	$13.2^d \pm 0.2335$	$10.1^c \pm 0.2335$	0.390	Nil
<i>Pseudomonas aeruginosa</i>	Nil	$7.0^a \pm 0.5000$	$9.0^c \pm 0.5000$	$9.5^{bc} \pm 0.5000$	$9.5^{bc} \pm 0.555$	6.250	Nil
<i>Escherichia coli</i>	$7.0^a \pm 0.5755$	Nil	$7.0^a \pm 1.0000$	$8.5^a \pm 0.6545$	$8.0^a \pm 0.6545$	12.50	Nil
<i>Klebsiella pneumoniae</i>	Nil	Nil	Nil	$8.0^a \pm 0.5755$	$\text{Nil} \pm 0.6387$	6.250	Nil
<i>Proteus vulgaris</i>	Nil	Nil	$8.0^b \pm 0.5755$	$9.0^b \pm 0.2335$	$8.5^{ab} \pm 0.2335$	12.50	Nil
<i>Salmonella typhi</i>	Nil	Nil	Nil	$9.0^b \pm 0.6545$	Nil	12.50	Nil
<i>Proteus mirabilis</i>	Nil	Nil	Nil	$9.5^c \pm 1.0000$	$8.5^b \pm 0.2335$	6.250	Nil
<i>Candida albicans</i>	Nil	Nil	$9.5^d \pm 0.6387$	$13.5^d \pm 0.5000$	$10.9^c \pm 0.2335$	0.195	Nil
<i>Candida tropicalis</i>	Nil	Nil	Nil	$8.9^{ab} \pm 0.6545$	$8.0^a \pm 0.6387$	12.50	Nil
LSD	—	—	0.33330	1.00500	0.12552	—	—

Values are means \pm SD ($n = 3$). Data within the groups were analysed using one-way ANOVA followed by ^{a,b,c,d} Duncan's multiple range test (DMRT) and LSD = least significant differences. Nil means that no ZOI had been measured and therefore no activity of the tested samples. AX = Amoxicillin (antibacterial standard). NS = Nystatin (antifungal standard).

The antimicrobial activity of the synthesised $\text{ZnCe}_x\text{Fe}_{2-x}\text{O}_4$ increased as the X value increased (Figure 7a). The highest zone of inhibition (ZOI) of *S. aureus* was observed when $X = 0.06$ in $\text{ZnCe}_x\text{Fe}_{2-x}\text{O}_4$ and slightly decreased when $X = 0.08$. In the case of *C. albicans*, the active sample was $\text{ZnCe}_x\text{Fe}_{2-x}\text{O}_4$ with $X = 0.06$ (Figure 7b).

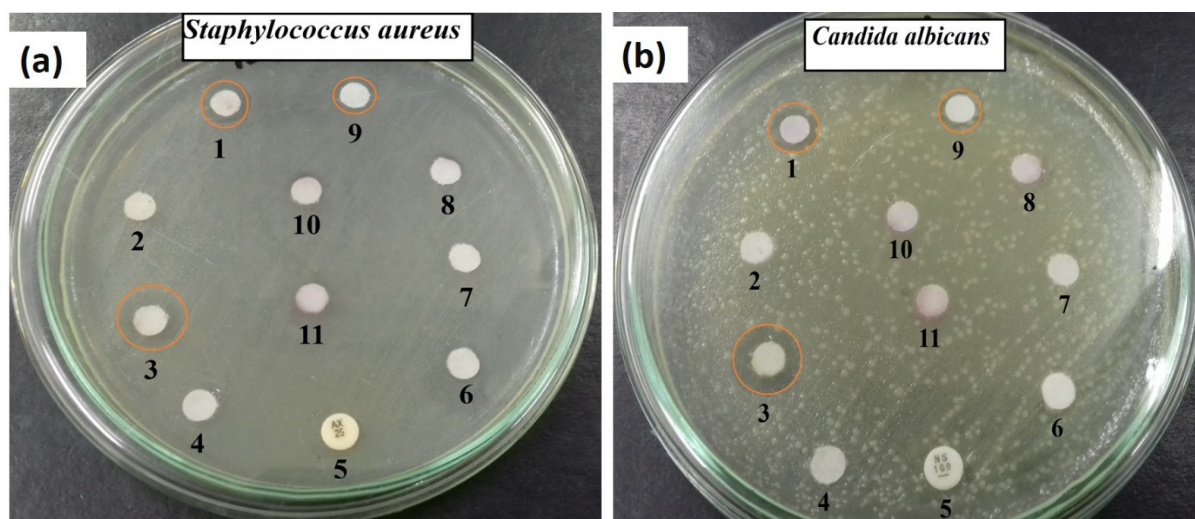


Figure 7. Antimicrobial activities and ZOI (mm) of tested ferrites ($\text{ZnCe}_x\text{Fe}_{2-x}\text{O}_4$) against the pathogenic microbes *Staphylococcus aureus* (a) and *Candida albicans* (b), where (1) $X = 0.08$, (2) $X = 0.02$, (3) $X = 0.06$, (4) $X = 0.00$, (5) standard positive control as amoxicillin (AX), and nystatin (NS), (6) DMSO (negative control), (7) $\text{Fe}(\text{NO}_2)_3 \cdot 9\text{H}_2\text{O}$, (8) $\text{ZnSO}_4 \cdot 7\text{H}_2\text{O}$, (9) $X = 0.04$, (10) $\text{Ce}(\text{NO}_3)_3 \cdot 6\text{H}_2\text{O}$, and (11) Eb; circle indicating the presence of ZOI.

The antimicrobial abilities of the as-synthesised samples were compared with the standard antibacterial amoxicillin (AX; $25.0 \mu\text{g}/\text{mL}$) and the antifungal agent nystatin (NS; $25.0 \mu\text{g}/\text{mL}$) as a positive control. Our samples were more active than the standard antibiotics, and the

microbes tested were resistant to the standard antibiotics. The synthesised ferrites samples (5.0 μL ; 1.0 $\mu\text{g}/\text{mL}$) were placed over 6.0 mm applied disks.

Next, nanoparticles were compared with the precursors used in the synthetic process, Eb alone and the dimethylsulfoxide (DMSO) organic solvent (as a negative control), and not all were active against the microbes tested (Figure 7a,b).

The synthesised $\text{ZnCe}_x\text{Fe}_{2-x}\text{O}_4$; $X = 0.06$ was more active against Gram-positive bacteria than against Gram-negative bacteria because the cell wall of Gram-negative bacteria contains a thick layer of lipopolysaccharides in addition to a small layer of peptidoglycans, whereas Gram-positive bacteria have a thicker layer of peptidoglycans [45]. In general, inorganic NPs have high surface-to-volume ratios and nanoscale sizes. Consequently, they can combine and interact with some pathogenic microbes such as yeasts, bacteria, and fungi [46]. The unique properties of the inorganic NPs make them potentially valuable in a wide range of biomedical applications. With the decreases in the effectiveness of traditional antibiotics due to the increases in drug resistance in some bacteria, NPs may be valuable as medications [47].

The results of the minimum inhibitory concentrations (MIC) tests (ranged from 0.195 to 12.50 $\mu\text{g}/\text{mL}$) of the samples against all microbes were tested. The MIC of $\text{ZnCe}_x\text{Fe}_{2-x}\text{O}_4$; $X = 0.06$ was 0.390 $\mu\text{g}/\text{mL}$ against *S. aureus*. The synthesised $\text{ZnCe}_x\text{Fe}_{2-x}\text{O}_4$; $X = 0.06$ had an MIC of 0.195 $\mu\text{g}/\text{mL}$ against *C. albicans*, suggesting that it could be used as an antifungal agent at low concentration, which means that the minimum concentration of our synthesised sample gave antimicrobial activity that was less than 0.5 part per million (ppm), which is a good and promising result, especially as they will not have any toxicity when applied in the in vivo studies.

The properties of the synthesised ferrites play a vital role in their antimicrobial characteristics: their elemental structure, purity, and size of the synthesised ferrites must be analysed to explain their antimicrobial activity [48]. The composition of the ferrites, their particle size, and the doping with Ce played an important part in improving the antimicrobial efficacy of the $\text{ZnCe}_x\text{Fe}_{2-x}\text{O}_4$ at very low concentrations (10.0 $\mu\text{g}/\text{mL}$) against all tested bacteria and yeasts. They possess encouraging physical and chemical behaviour, more than those of the usual organic and synthetic antimicrobial agents, such as a unique link to pathogens, leading to more interaction with pathogenic bacteria and yeasts and therefore increasing their antimicrobial potential [49]. The mechanisms of action were enhanced by the ability of the NPs to modify the distribution of ROS such as the superoxide anion O_2^- [50], the infiltration of $\text{ZnCe}_x\text{Fe}_{2-x}\text{O}_4$ within the pathogenic microbes, and an alkaline tendency [51]. $\text{ZnCe}_x\text{Fe}_{2-x}\text{O}_4$ might be able to alter the microbial morphology and the composition of the biofilms, change the microbial membrane permeability, and induce expression of the oxidative stress genes [52].

2.3. Antibiofilm Activity of $\text{ZnCe}_x\text{Fe}_{2-x}\text{O}_4$; $X = 0.06$

The production of biofilms by pathogenic microbes is characterised by the secretion of exo-polysaccharides [53]. The test tube method was applied to determine the antibiofilm potential of the synthesised ferrites against some familiar pathogenic microbes.

Figure 8 shows the antibiofilm action of the as-synthesised $\text{ZnCe}_x\text{Fe}_{2-x}\text{O}_4$; $X = 0.06$ against *S. aureus* and *C. albicans*. The complete steps were (I): normal microbial growth and production of a distinct ring in the absence of the synthesised $\text{ZnCe}_x\text{Fe}_{2-x}\text{O}_4$; $X = 0.06$ and interference with microbial growth in the vicinity of $\text{ZnCe}_x\text{Fe}_{2-x}\text{O}_4$; $X = 0.06$, (II): staining of the biofilm with crystal violet (CV), which produced qualitative results, and (III): elimination and separation of the adhered microbial cells after the addition of ethanol for the semi-quantitative measurement of the extent of biofilm hindrance (Table 3).

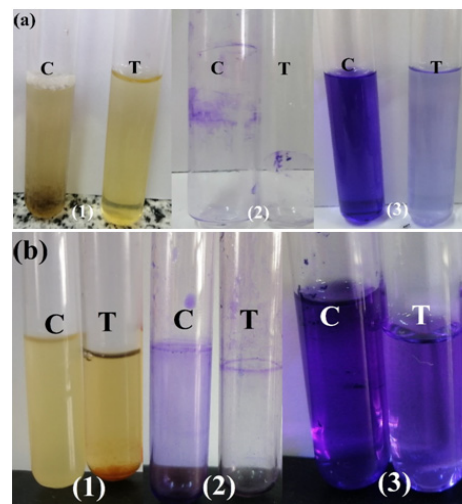


Figure 8. Antibiofilm potential of the synthesised $\text{ZnCe}_x\text{Fe}_{2-x}\text{O}_4$; $X = 0.06$ using the tube method against *Staphylococcus aureus* (a) and *Candida albicans* (b); where the steps are reported as follows: (1) growth of the bacterial and yeast cells and biofilm formation (rings) without the treatment with the synthesised $\text{ZnCe}_x\text{Fe}_{2-x}\text{O}_4$; $X = 0.06$ and inhibition of the bacterial and yeast growth after treatment with $\text{ZnCe}_x\text{Fe}_{2-x}\text{O}_4$; $X = 0.06$; (2) staining of the adherent bacterial and yeast cells with crystal violet, and (3) removal and dissolution of the adherent bacterial and yeast cells by ethanol for semi-quantitative biofilm inhibition determination.

Table 3. Semi-quantitative inhibition of biofilm formation for bacterial and yeast pathogens non-treated and treated with $\text{ZnCe}_x\text{Fe}_{2-x}\text{O}_4$; $X = 0.06$.

Bacterial and Yeast Strains	O.D. of Crystal Violet Stain at 570.0 nm		Inhibition %
	Control	$\text{ZnCe}_x\text{Fe}_{2-x}\text{O}_4$; $X = 0.06$ (10.0 $\mu\text{g}/\text{mL}$)	
<i>Staphylococcus aureus</i>	1.058 ^e \pm 0.0080	0.020 ^a \pm 0.0021	92.73%
<i>Pseudomonas aeruginosa</i>	0.945 ^d \pm 0.0062	0.241 ^c \pm 0.0047	78.83%
<i>Escherichia coli</i>	0.877 ^b \pm 0.0070	0.298 ^c \pm 0.0053	75.27%
<i>Klebsiella pneumoniae</i>	0.998 ^d \pm 0.0025	0.388 ^d \pm 0.0062	61.24%
<i>Proteus vulgaris</i>	0.899 ^c \pm 0.0046	0.444 ^e \pm 0.0036	56.29%
<i>Salmonella typhi</i>	1.222 ^f \pm 0.0070	0.831 ^a \pm 0.0053	26.18%
<i>Proteus mirabilis</i>	0.989 ^d \pm 0.0062	0.211 ^c \pm 0.0047	79.54%
<i>Candida albicans</i>	0.999 ^d \pm 0.0080	0.099 ^b \pm 0.0021	90.18%
<i>Candida tropicalis</i>	0.557 ^a \pm 0.0080	0.451 ^e \pm 0.0021	34.16%
LSD	0.01767	0.01267	—

Values are means \pm SD (n = 3). Data within the groups were analysed using one-way analysis of variance (ANOVA) followed by ^{a,b,c,d,e,f} Duncan's multiple range test (DMRT) and LSD = least significant difference.

Figure 8a displays the start of the tube design for the determination of the antibiofilm potential of $\text{ZnCe}_x\text{Fe}_{2-x}\text{O}_4$; $X = 0.06$ against *S. aureus*. This bacterium produced a thick whitish-yellow layer at the air-liquid interface in the $\text{ZnCe}_x\text{Fe}_{2-x}\text{O}_4$; $X = 0.06$ control. The matte layers produced were fully adhered across the walls of the tubes and developed a blue colour following staining with CV. A dark blue colour was created in the solution subsequent to dissolving CV with absolute ethanol (Figure 8a).

The managed tubes that included *S. aureus* cells and 10.0 $\mu\text{g}/\text{mL}$ $\text{ZnCe}_x\text{Fe}_{2-x}\text{O}_4$; $X = 0.06$ showed a marked negative effect on biofilm and ring formation. The colour of the adherent cells was muted, and the blue colour was faint after the addition of ethanol (Figure 8a). Similar results were observed for the repression of biofilms of the yeast *C. albicans* (Figure 8b).

The semi-quantitative determination of the inhibition percentage was performed using a UV-Vis spectrophotometer at 570.0 nm. The optical density (O.D) was estimated following the elimination of CV-stained biofilms.

Table 3 discerns the percentage of inhibition. The highest percentage was observed for *S. aureus* (92.73%), *P. mirabilis* (79.54%), and *C. albicans* (90.18%) following the addition of 10.0 µg/mL $\text{ZnCe}_x\text{Fe}_{2-x}\text{O}_4$; $X = 0.06$.

$\text{ZnCe}_x\text{Fe}_{2-x}\text{O}_4$; $X = 0.06$ controlled the growth of biofilm at a constant degree of adhesion, the first step in the antimicrobial behaviour [54]. The difference in the inhibitory percentage may be produced by many factors, such as the potential of the antimicrobial agents, the attraction on the surface because of the large surface area of the $\text{ZnCe}_x\text{Fe}_{2-x}\text{O}_4$; $X = 0.06$, physical features such as $\text{ZnCe}_x\text{Fe}_{2-x}\text{O}_4$ particle sizes, invasion skills, and different chemical characteristics influencing the relationship and communication of $\text{ZnCe}_x\text{Fe}_{2-x}\text{O}_4$ with biofilm-producing microbes. $\text{ZnCe}_x\text{Fe}_{2-x}\text{O}_4$; $X = 0.06$ repressed the growth of *S. aureus* by more than 98% at 0.390 µg/mL, as mentioned in the MIC results. By arresting exopolysaccharide synthesis, which is a precursor to biofilm formation, the creation of *S. aureus* biofilm was then prevented [53].

2.4. Reaction Mechanism Determination Using SEM Analysis

To explain the antimicrobial behaviour of the synthesised $\text{ZnCe}_x\text{Fe}_{2-x}\text{O}_4$; $X = 0.06$, we tried to define the mechanism of action toward *S. aureus* after the SEM analysis. The SEM analysis showed the appearance of the bacterial cells (*S. aureus*) following $\text{ZnCe}_x\text{Fe}_{2-x}\text{O}_4$; $X = 0.06$ treatment of the control sample. In the control sample, bacterial groups were constantly developed and displayed typical cellular forms, including the normal bacterial surface and semi-formed biofilm (Figure 9a).

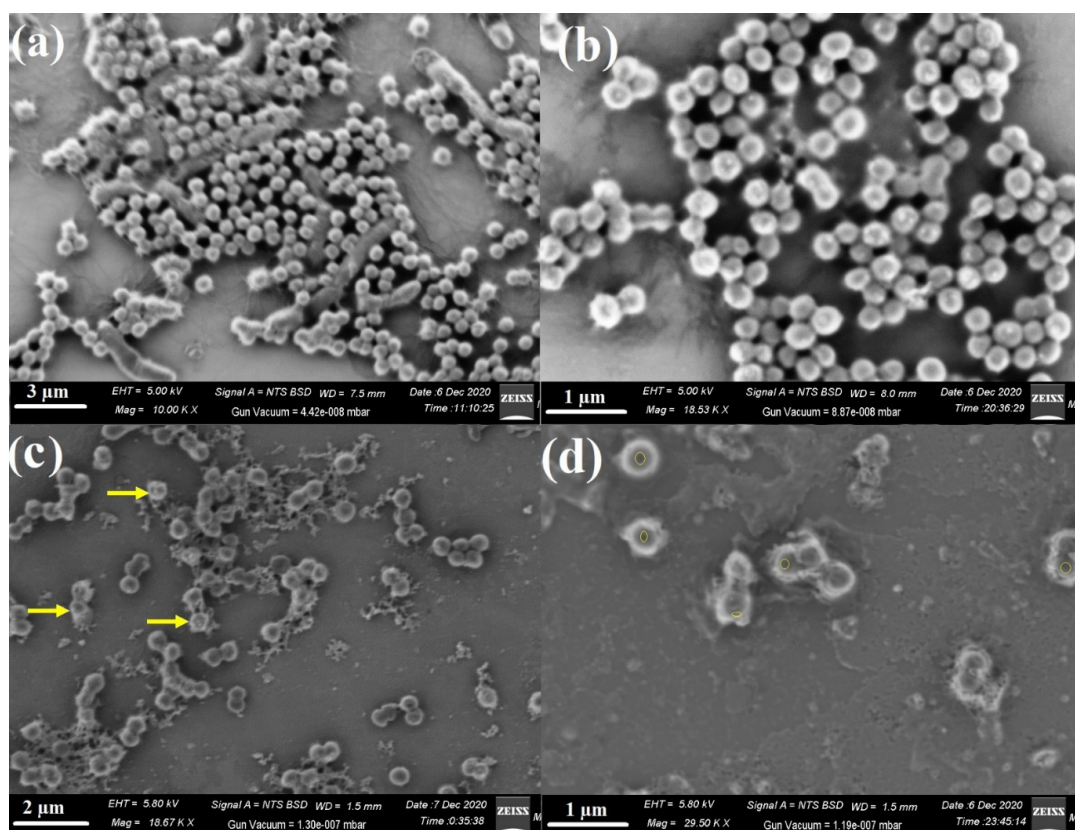


Figure 9. SEM images of *S. Aureus*; (a) regular bacterial cells (*S. aureus*) without $\text{ZnCe}_x\text{Fe}_{2-x}\text{O}_4$; $X = 0.06$ treatment, (b) other magnified area regarding control *S. aureus*, (c) malformed and an irregular bacterial cells after $\text{ZnCe}_x\text{Fe}_{2-x}\text{O}_4$; $X = 0.06$ treatment showing full lysis (yellow arrows), and (d) other magnified area regarding treated *S. aureus* showing the formation of pits on the bacterial surface (yellow circles).

After treatment with $\text{ZnCe}_x\text{Fe}_{2-x}\text{O}_4$; $X = 0.06$, morphological differences in *S. aureus* were apparent (Figure 9b). We also observed the complete lysis of bacterial cells with a concomitant decrease in the viable number, and ultimately the growth of biofilm was inhibited (Figure 9b). These results reflected the antimicrobial activity of Ce addition in the synthesised $\text{ZnCe}_x\text{Fe}_{2-x}\text{O}_4$; $X = 0.06$ and confirmed the ZOI results (Table 2).

2.5. Determination of Protein Leakage from Bacterial Cell Membranes

The quantities of protein discharged in the suspension of the treated *S. aureus* cells were determined applying the Bradford method [55]. As shown in Figure 10, it is obvious that the quantity of cellular protein discharged from *S. aureus* is directly proportional to the concentration of $\text{ZnCe}_x\text{Fe}_{2-x}\text{O}_4$; $X = 0.06$ nanocomposite and was found to be $79.05 \mu\text{g}/\text{mL}$ after the treatment with $1.0 \text{ mg}/\text{mL}$ of the tested $\text{ZnCe}_x\text{Fe}_{2-x}\text{O}_4$; $X = 0.06$ nanocomposite, which proves the antibacterial characteristics of the synthesised nanocomposites and explains the creation of holes and destruction in the cell membrane of *S. aureus*, causing the oozing out of the proteins from the *S. aureus* cytoplasm. On the other hand, the synthesised $\text{ZnCe}_x\text{Fe}_{2-x}\text{O}_4$; $X = 0$ nanocomposite exhibited reduced activity in membrane leakage after measured cellular protein release from *S. aureus* and was found to be $18.95 \mu\text{g}/\text{mL}$.

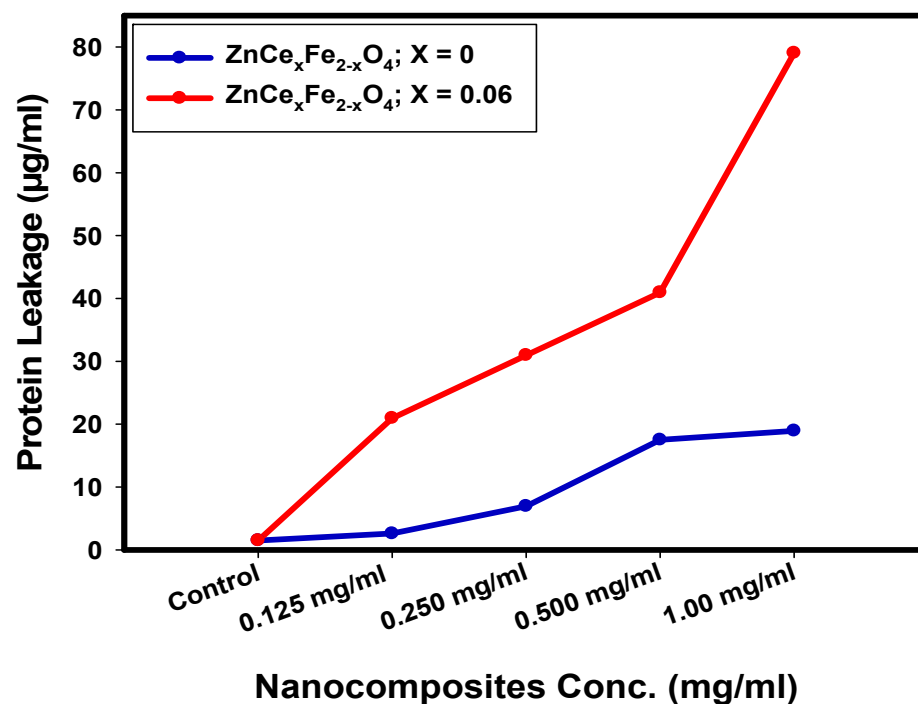


Figure 10. The effect of $\text{ZnCe}_x\text{Fe}_{2-x}\text{O}_4$; $X = 0$ and 0.06 on the protein leakage from *S. aureus* cell membranes.

These results revealed that $\text{ZnCe}_x\text{Fe}_{2-x}\text{O}_4$ nanocomposite; where $X = 0.06$ showed an improvement in the permeability of *S. aureus* cell membranes more than $\text{ZnCe}_x\text{Fe}_{2-x}\text{O}_4$; where $X = 0$ nanocomposite. Therefore, it could be assumed that confusion of membranous permeability would be a vital portion of the repression of bacterial mass. Related studies [56] and [57] described comparable outcomes when ferrites were incorporated, which revealed concentration-dependent destabilisation in the cell membrane of bacterial cells and pointed to leakage of their intracellular substance into the extracellular form (bacterial cell suspension).

Paul et al. [58] proved that the difference in bacterial cell membrane permeability was shown in percentage difference in corresponding electric conductivity. It was reported that the percentage of relative electric conductivities of all tested samples improves with the rise in the concentration of the treated nanocomposites. The integrity of the bacterial

cell membrane is defined by analysing the discharge of bacterial cell components such as proteins; the leakage developed with time, as there was constant cell membrane injury that pointed to the leakage of cell components deriving from the cell destruction, which confirms the results obtained in SEM analysis (Figure 9).

El-Batal et al. [59] have shown that there are four mechanisms that produce the effects of metal NPs on microbial cells. After comparison with our study, we recognise that $ZnCe_xFe_{2-x}O_4$; $X = 0.06$ start their activity by adhesion at the outer surface of the microbial cell, allowing membrane damage, formation of pits (as mentioned in membrane leakage assay), and switching off of the ions' transport activity (Figure 11).

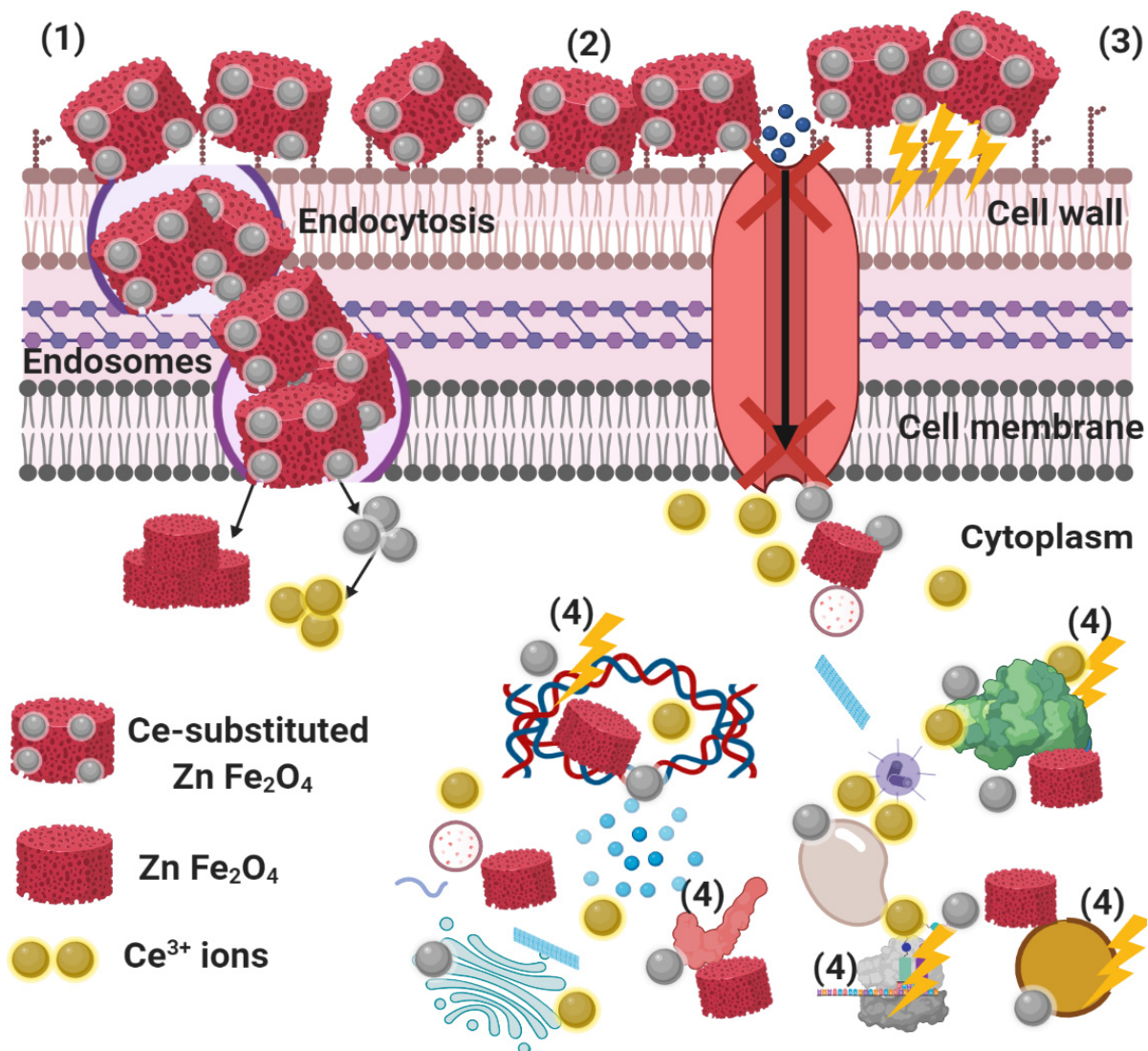


Figure 11. Proposed schematic representation illustrating the four prominent methods of antimicrobial activity of $ZnCe_xFe_{2-x}O_4$; $X = 0.06$, where (1) $ZnCe_xFe_{2-x}O_4$; $X = 0.06$ adheres to the bacterial cell surface and results in membrane damage and altered transport activity; (2) $ZnCe_xFe_{2-x}O_4$; $X = 0.06$ creates and increases ROS, leading to cell damage; (3) $ZnCe_xFe_{2-x}O_4$; $X = 0.06$ blocks the transport of ions to and from the bacterial cell; and (4) $ZnCe_xFe_{2-x}O_4$; $X = 0.06$ penetrates the bacterial cells and interacts with cellular organelles and biomolecules, affecting the cellular machinery, modulating the cellular signal system, and causing cell death. $ZnCe_xFe_{2-x}O_4$; $X = 0.06$ may serve as a vehicle to effectively deliver Ce^{3+} ions to the bacterial cytoplasm and membrane, where a proton motive force would decrease the pH to less than 3.0 and therefore improve the release of Ce^{3+} .

The nano-metals then modify the ionic structure (Ce^{3+}) inside the bacterial cell at pH 3 and interfere with the intracellular structures such as plasmids, DNA, and other vital

organelles. Cellular toxicity occurs due to the oxidative stress generated by the production of ROS (Figure 11). ZnFe_2O_4 NPs could withstand the acidic conditions inside the bacterial cells, and the conversion described above did not occur [60], but the antibacterial effect was caused by the presence of nano-structures inside the bacterial cells, which, in turn, affected signal transduction pathways. There were significant reaction mechanisms such as reactive oxygen species (ROS) division (superoxide anion; O_2^-) [59], and it is suggested that $\text{ZnCe}_x\text{Fe}_{2-x}\text{O}_4$; $X = 0.06$, could alter the microbial morphology, diminish the microbial membrane permeability, and induce the abundance of oxidative stress genes as a compensatory response due to the H_2O_2 production [49,59].

2.6. Antitumour Activity of Eb-ZFO and Eb- $\text{ZnCe}_x\text{Fe}_{2-x}\text{O}_4$; $X = 0.06$ Nanocomposites with or without γ -Radiation

2.6.1. Screening of the Cytotoxic Profile of Different Concentrations of Eb and $\text{ZnCe}_x\text{Fe}_{2-x}\text{O}_4$ Nanocomposites on Human Breast Cancer (MDA-MB-231; Triple-Negative Basal B Subtype) and Colon Cancer (HT-29; Colorectal Adenocarcinoma)

The cytotoxicity screening found the half-maximal inhibitory concentration (IC_{50}) of Eb to be 57.28 $\mu\text{g}/\text{mL}$ on MDA-MB-231 cells (Figure 12I(a)) and 60 $\mu\text{g}/\text{mL}$ on HT-29 cells (Figure 12II(a)). The optimal cytotoxic concentration of $\text{ZnCe}_x\text{Fe}_{2-x}\text{O}_4$ nanoparticles at different concentrations of (X) on MDA-MB-231 and HT-29 cell lines were 100 $\mu\text{M}/\text{L}$ for ZnFe_2O_4 (Figure 12I(b)) and 100 $\mu\text{M}/\text{L}$ for $\text{ZnCe}_{0.06}\text{Fe}_{1.94}\text{O}_4$ (Figure 12II(b)), respectively. Magnetic nanoparticles have valuable properties as theranostics, including hyperthermia and magnetic resonance imaging (MRI), and can be used in biosensors and drug delivery platforms [61,62]. Saquib et al. [63] reported that ZnFe_2O_4 NPs possess antitumour potential via the induction of apoptosis and necrosis in human amnion epithelial (WISH) cells, through the mitochondria-dependent intrinsic apoptotic pathway. It has also been found that ZnFe_2O_4 NPs cause genomic instability in the meristematic root cells of sunflowers, through induced chromosomal aberrations [64], supporting the contention that ZnFe_2O_4 NPs are cytotoxic. Several studies have found Ce oxide to have a unique electronic configuration, providing anti-inflammatory, non-invasive, and oxidative stress features. These characteristics result in the production of ROS at the microvascular stage level, owing to their natural reduction and oxidation reactions in the cells [65,66]. ROS generation relies on the production of defects caused by oxygen vacancies in the crystal structure of the nanoparticles, which could be boosted by selective metal ion doping of the lattice structure [67]. Apart from the stabilised dissolution of Zn from the ZnFe_2O_4 lattice owing to Fe doping, which contributes to the tumour cell growth inhibition, CeO_2 doping with metals resulted in an increased photocatalytic activity, due to a better separation of h^+/e^- pairs [68] owing to the electron accepting capability and/or hole donors, and facilitates charge carrier localisation [69]. In turn, these migrated holes contribute to the production of $\cdot\text{OH}$ radicals when reacted with chemisorbed H_2O molecules and form the free radicals $\cdot\text{OH}$ and $\text{O}_2\cdot$, which are the primary cause of cell death and the oxidation of organic matter such as bacterial cell walls and membranes [70]. This phenomenon might explain the potentiated cytotoxic activity of ZnFe_2O_4 lattice after CeO_2 doping observed in the current data. Furthermore, the antitumour efficacy of Eb, an organo-selenium compound, is attributed to its ability to induce apoptosis, inhibit angiogenesis, upregulate caspases and DNA fragmentation, cause cell-cycle arrest, and reduce oxidative stress in many cancers [71,72]. The IC_{50} of Eb was taken into account when determining the optimal concentration of ZnFe_2O_4 nanocarrier, which was then incorporated into the optimal concentration of ZnFe_2O_4 , afterwards applied to MDA-MB-231 cells, and the IC_{50} was found to be 25.7 $\mu\text{g}/\text{mL}$ (Figure 12I(c)). In HT-29 cells, the previously determined IC_{50} of Eb was incorporated into the optimal cytotoxic concentration in the $\text{ZnCe}_{0.06}\text{Fe}_{1.94}\text{O}_4$ nanocarrier, and the IC_{50} was found to be 15.29 $\mu\text{g}/\text{mL}$ (Figure 12II(c)). The incorporation of Eb to $\text{ZnCe}_x\text{Fe}_{2-x}\text{O}_4$ nanocomposite enhanced the cytotoxic effect against cancers cell lines, as shown in our study. However, incubation of normal Vero renal epithelial cells with Eb- ZnFe_2O_4 and Eb- $\text{ZnCe}_{0.06}\text{Fe}_{1.94}\text{O}_4$ at concentrations ranging from 1–100 μM over 24 h showed no cytotoxicity or morphological changes (Figure 12III) versus MDA-MB-

231 and HT-29 cells, which revealed a notable greater susceptibility against both NPs at corresponding concentrations. The morphological alterations represented reduced cell viability and population, detachment, rounding, and shrinkage, suggesting the incidence of apoptosis (as shown in Figure S1-I, II, and III). Accordingly, these data suggest the selective toxicity against MDA-MB-231 and HT-29 cells.

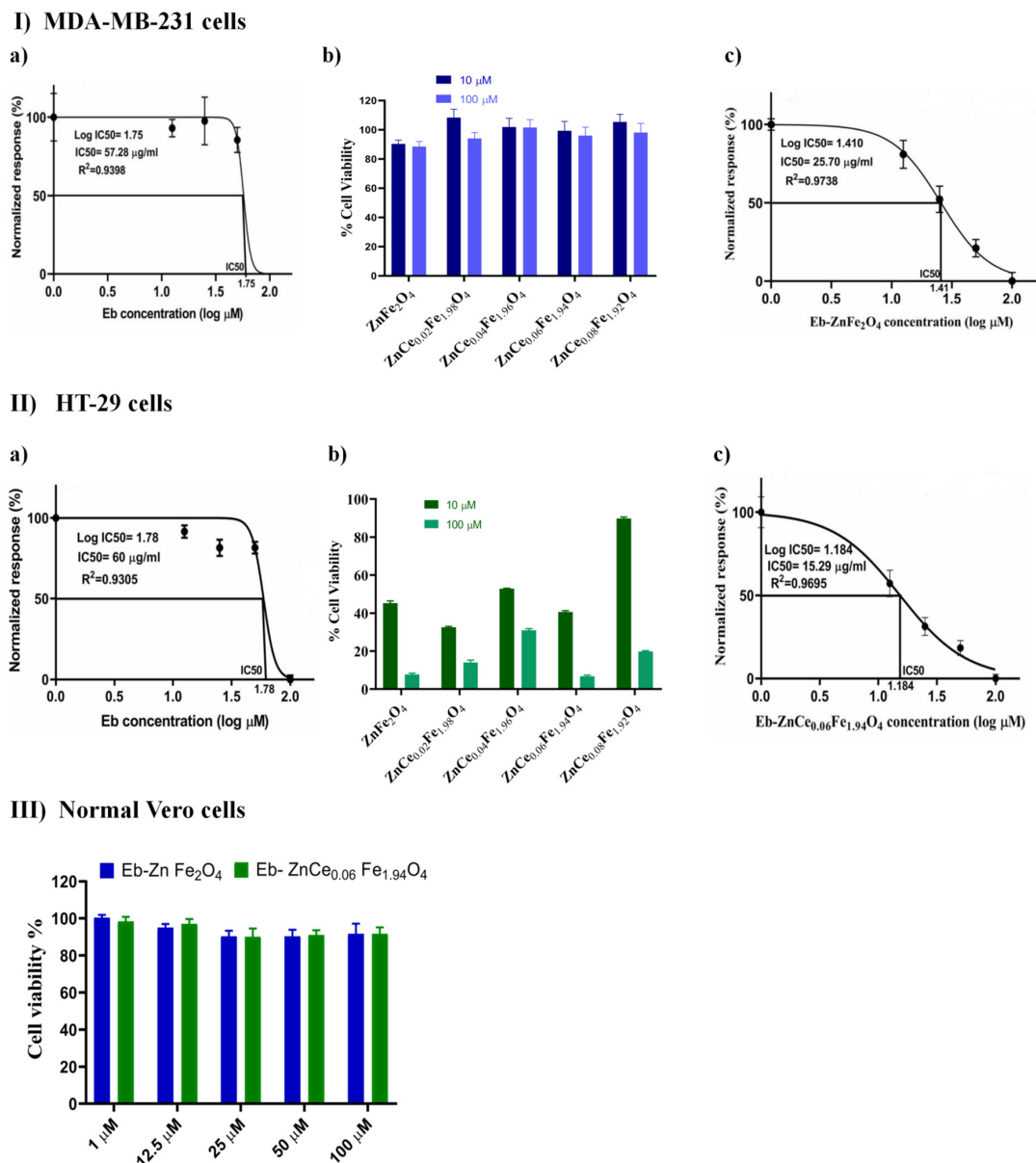


Figure 12. Cytotoxicity screening of various concentrations of Ebselen (Eb) and/or ZnCe_xFe₂-XO₄ nanoparticles. (I) MDA-MB-231 cells treated as follows: (a) Eb, (b) ZnCe_xFe₂-XO₄, and (c) Eb-ZnFe₂O₄. (II) HT-29 cells treated as follows: (a) Eb, (b) ZnCe_xFe₂-XO₄, and (c) Eb-ZnCe_{0.06}Fe_{1.94}O₄. (III) Normal Vero cells treated by Eb-ZnFe₂O₄ and Eb-ZnCe_{0.06}Fe_{1.94}O₄ at a concentration of 100 μM. The percent survival was calculated based on untreated cells of both cell lines and was set at 100% (n = 3). Inverted light microscopy images of all the above tests are represented as shown in Figure S1 (I, II and III).

2.6.2. ROS Status and Signaling Molecules ERK1/2, JNK and NRF-2 in MDA-MB-231 and HT-29 Cells

MDA-MB-231 Cell Line

The effect of Eb-ZFO on ROS status including hypoxia-inducible factor-1 alpha (HIF-1α), intracellular hydrogen peroxide (H₂O₂), malondialdehyde (MDA), and glutathione(GSH) levels

as well as superoxide dismutase (SOD), catalase (CAT), and glutathione peroxidase (GPX) activities, and the associated signalling molecules extracellular signal-regulated kinases 1 and 2 (ERK1/2), Jun N-terminal Kinase (JNK), and nuclear factor erythroid 2-related factor 2 (NRF-2) in MDA-MB-231 cells are shown in Figure 13. The data for the MDA + Eb-ZFO group showed a significant reduction ($p < 0.05$) in the levels of HIF-1 α (47.41%), intracellular H₂O₂ (50.52%), MDA (40.81%), the protein expression of p-ERK1/2 (46.03%), and p-JNK (58.82%) associated with a significant elevation in antioxidant system NRF-2 (2.96-fold) and GSH levels (1.47-fold) as well as SOD (2.17-fold), CAT (1.89-fold), and GPX (2.04-fold) activities when compared to the MDA group (MDA-MB-231 untreated cancer cells).

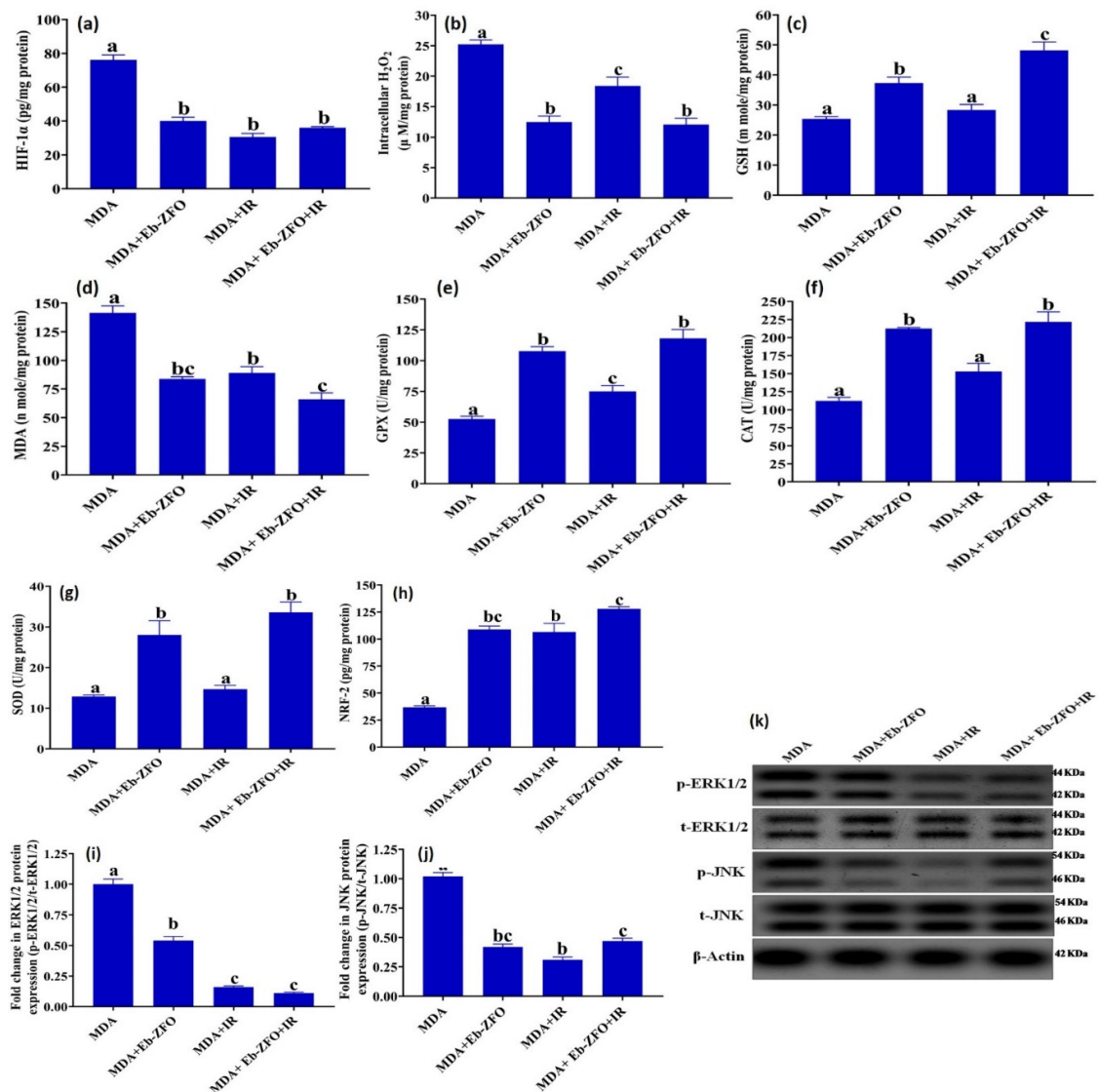


Figure 13. ROS status and associated signalling molecules ERK1/2, JNK, and NRF-2 in the MDA-MB-231 cell line. ROS status indicators were the levels of (a) HIF-1 α , (b) intracellular H₂O₂, (c) GSH, and (d) MDA; activities of (e) GPX, (f) CAT, and (g) SOD. ROS-sensing signalling molecules were (h) NRF-2 level; fold change in protein expression of (i) ERK1/2, (j) JNK, and (k) representative western blot analysis, SDS-PAGE of ERK1/2, JNK, and β -actin. Results are expressed as the mean and standard error of the mean (SEM) (n = 3). Columns with dissimilar letters (a, b, c . . .) overhead within the same histogram are significantly different, and columns that have the same letters are not significantly different at $p < 0.05$. MDA group: untreated MDA-MB-231 cells served as control, MDA + Eb-ZFO group: MDA-MB-231 cells treated with Ebselen (Eb) and ZnFe₂O₄ nanoparticles (ZFO), MDA + IR group: MDA-MB-231 cells exposed to γ -radiation; and MDA + Eb-ZFO + IR group: MDA-MB-231 cells treated with Eb-ZFO and exposed to IR.

The exposure of MDA-MB-231 cells to γ -radiation (IR) produced insignificant changes in SOD and CAT activities. GSH levels showed a significant decrease ($p < 0.05$), as did the levels of HIF-1 α (59.84%), intracellular H₂O₂ (26.98%), MDA (37.03%), the protein expression of p-ERK1/2 (83.99%), and p-JNK (69.54%), paralleled by a significant increase in NRF-2 level (1.89-fold) and GPX (0.43-fold) activity when compared to the MDA group (Figure 13).

The data from the MDA + Eb-ZFO + IR group revealed a significant decline ($p < 0.05$) in the levels of HIF-1 α (52.69%), intracellular H₂O₂ (52.10%), MDA (53.31%), and the protein expression of p-ERK1/2 (87%) and p-JNK (65%) associated with a significant upregulation in antioxidant system in terms of NRF-2 (3.48-fold) and GSH levels (1.89-fold) along with SOD (2.60-fold), CAT (1.97-fold), and GPX (2.24-fold) activities when compared to the MDA group. The combination of Eb-ZFO with IR induced a significant modulation ($p < 0.05$) in ROS/antioxidant machinery imbalance, and the fine-tuning of redox status, compared to either each one alone and the MDA group (Figure 13).

HT-29 Cell Line

As shown in Figure 14, the effect of Eb-ZCFO on ROS status and the levels of the signalling molecules ERK1/2, JNK, and NRF-2 in the HT-29 cell line showed a significant reduction ($p < 0.05$) in the levels of HIF-1 α (19.39%), intracellular H₂O₂ (55.95%), and MDA (66.24%), as well as p-ERK1/2 (45.39%) and p-JNK (47.00%) protein expression associated with a significant elevation in the antioxidant system (NRF-2 1.64-fold, SOD 1.84-fold, and GSH 1.40-fold) along with a non-significant change in CAT and GPX activities as compared to the HT-29 group. The exposure of HT-29 cells to IR caused insignificant changes in SOD and CAT activities, though a significant decrease ($p < 0.05$) in the levels of HIF-1 α (30.77%), intracellular H₂O₂ (60.75%), MDA (35.56%), GSH (35.76%), and GPX activity (28.64%) as well as the protein expression of p-ERK1/2 (75.00%) and p-JNK (51.02%) coupled with a marked elevation ($p < 0.05$) in NRF-2 level (1.89-fold) was observed as compared to the HT-29 group (Figure 14). Combining Eb-ZCFO with IR induced a significant reduction ($p < 0.05$) in HIF-1 α (61.30%), intracellular H₂O₂ (62.88%), MDA (64.54%), p-ERK1/2 (80.54%), and p-JNK (58.07%) and a significant increase ($p < 0.05$) in SOD activity (1.39-fold) and NRF-2 level (2.02-fold) compared with the HT-29 group (Figure 14). A delicate balance of the intracellular ROS levels is essential for cancer cells. High levels of ROS encourage tumour development and progression. Thus, the fine-tuning of intracellular ROS signalling is a challenge for novel therapeutic strategies. This, achieved through depriving cells of ROS-sensing signalling pathways, induces tumour progression, versus tipping the balance to ROS-induced apoptotic signalling [73]. In many types of cancers, ROS-sensitive signalling pathways such as mitogen-activated protein kinase/ERK cascade, signal transducer and activator of transcription (STAT), and nuclear factor κ -B (NF- κ B)-activating pathways are elevated and participate in cell proliferation, regulate protein synthesis and activity, induce inflammation, and promote cell survival [73,74]. In response to inflammatory signals, interferon gamma (IFN- γ) and lipopolysaccharide (LPS) sensitised macrophages polarise into the classical or "M1" state, which is characterised by the secretion of pro-inflammatory signals, such as tumour necrosis factor-alpha (TNF- α), interleukin 6 (IL-6), and IL-12. In contrast, alternatively activated macrophages, known as M2 macrophages, are polarised by anti-inflammatory signals such as IL-4, IL-10, and IL-13 [75]. Ohmori and Hamilton [76] and Hobson-Gutierrez and Carmona-Fontaine [75] demonstrated that the JAK-STAT pathway is an essential part of the pro-inflammatory (via STAT-1, which is activated by IFN- γ) and anti-inflammatory (via STAT-6, which is activated by IL-4) responses that generate "M1" and "M2" macrophages, respectively. The health of tissues and the quality of the cellular compartments are actively maintained by a range of cell-cell interactions, in a process known as cell competition. Through cell competition, cells sense fitness level heterogeneities across cell populations, resulting in the elimination of the less-fit cells (or losers) when they are in the presence of fitter cells (or winners), in a process akin to natural selection. It could be postulated that cell competition for healthy life is present

between normal (winners) and cancers (losers) in the TME. The stress response pathways, including the Jun N-terminal kinase (JNK), STAT, and the transcription factor NRF-2 that targets many genes involved in the oxidative stress response pathways, play vital roles in cellular competition and induce the three main aspects of the competition process: slow proliferation of losers, over-proliferation of winners, and loser cell elimination [77]. Owing to the complexity of ROS interconnections with stress-sensing signalling pathways, tight regulation and fine-tuning of intracellular ROS and scavengers is a recent approach in cancer therapy [78]. Cancer-associated fibroblasts (CAFs), which are highly represented in the TME, actively contribute to the regulation of tumour homeostasis, the promotion of tumour progression, and the invasion of cancer cells [79]. ROS and CAFs participate in two-way crosstalk: on the one hand, fibroblasts are targeted by ROS, particularly H_2O_2 , which is able to transform them into active CAFs via the upregulation of HIF1 α . On the other hand, CAFs are critical for the increase in ROS levels observed in cancer [80]. ROS largely impacts the redox-sensitive kinases ERK1/2 and JNK and induces proto-oncogenes [81,82]. Upon phosphorylation of the target proteins, these kinases can induce cell proliferation and survival [81]. Tumour cells have more abundant ROS levels than their normal counterparts, which are responsible for the maintenance of the malignant phenotype. Tenacious ROS stress enables cancer cells to adapt and survive [83]. Therefore, utilising drugs that decrease ROS and enhance the antioxidant machinery in tumour cells overwhelms the stress-sensing signalling pathways and renders them more vulnerable to external stimuli, especially when combined with therapies that elevate ROS, such as γ -radiation, as seen in our data. The antitumour efficiency of the ZFO and ZCFO nano-platform could be attributed to Eb, which blocked ADAM-9, a disintegrin and metalloprotease-9, by inhibiting ROS production, and reduced the progression of human prostate cancer cells [84]. Gao et al. [85] and Kang et al. (2019) [86] found that the expression of apoptosis-related proteins and antioxidant enzymes was increased through the upregulation of NRF-2 in cancer cells. Kucinski et al. [77] found that NRF-2 overexpression abolishes JNK expression, indicating that NRF-2 is not upstream of constitutive JNK activation, and therefore JNK activation is not necessary for cells to acquire loser status. As well as Eb, zinc oxide nanoparticles (ZnO-NPs) are known for toxicity and the ability to form nanoparticle–cell contacts [87].

Walkey et al. [88] showed that nanoceria selectively protect normal cells, but not cancer cells, from damage; in cancer cells, nanoceria are pro-apoptotic. This selective toxicity of nanoceria against cancer cells is due to the inhibition of nanoceria catalase-like activity occurring in acidic (pH 4.3) environments, and this is based on the assumption that the pH of cancer microenvironment is low due to the Warburg effect. Das et al. [89] reported that Ce-NPs in the A2780 ovarian cancer cell line had decreased ROS generation compared with control. These researchers explored the pro-oxidant effect of Ce-NPs as radiation sensitisers for pancreatic cancer radiotherapy. Pešić et al. [90] suggested the potential of using Ce-NP as a treatment for colorectal carcinoma, as it would selectively eliminate cancer cells and leave healthy cells intact. Ce-NPs serve as an enduring redox metabolism regulator rather than as simple scavengers, efficiently eliminating ROS when needed and thus maintaining basal cellular activities. They could therefore be used as a bio-compatible antioxidant system [91]. Their ROS-scavenging properties make Ce-NPs an attractive countermeasure against the detrimental effects of IR on normal cells [92]. Owing to their unique ROS-scavenging properties, Ce-NPs offer a valuable tool to aid in achieving ROS fine-tuning within the TME and prevent IR-associated NRF-2 over activation. Rice et al. [93] reported that a diminished level of phosphorylated ERK-1/2-MAPK protein was detected after CeO₂ instillation into rat lung. McDonald et al. [94] demonstrated that the MCF-7 cell line displayed a dose-dependent cytostatic, rather than cytotoxic, response to radiation, instead of rapid inter-phase death within hours by apoptosis like most cell lineages that exhibit mitotic cell death, autophagy, or senescence, and respond only over a period of many days, through the activation of NRF-2.

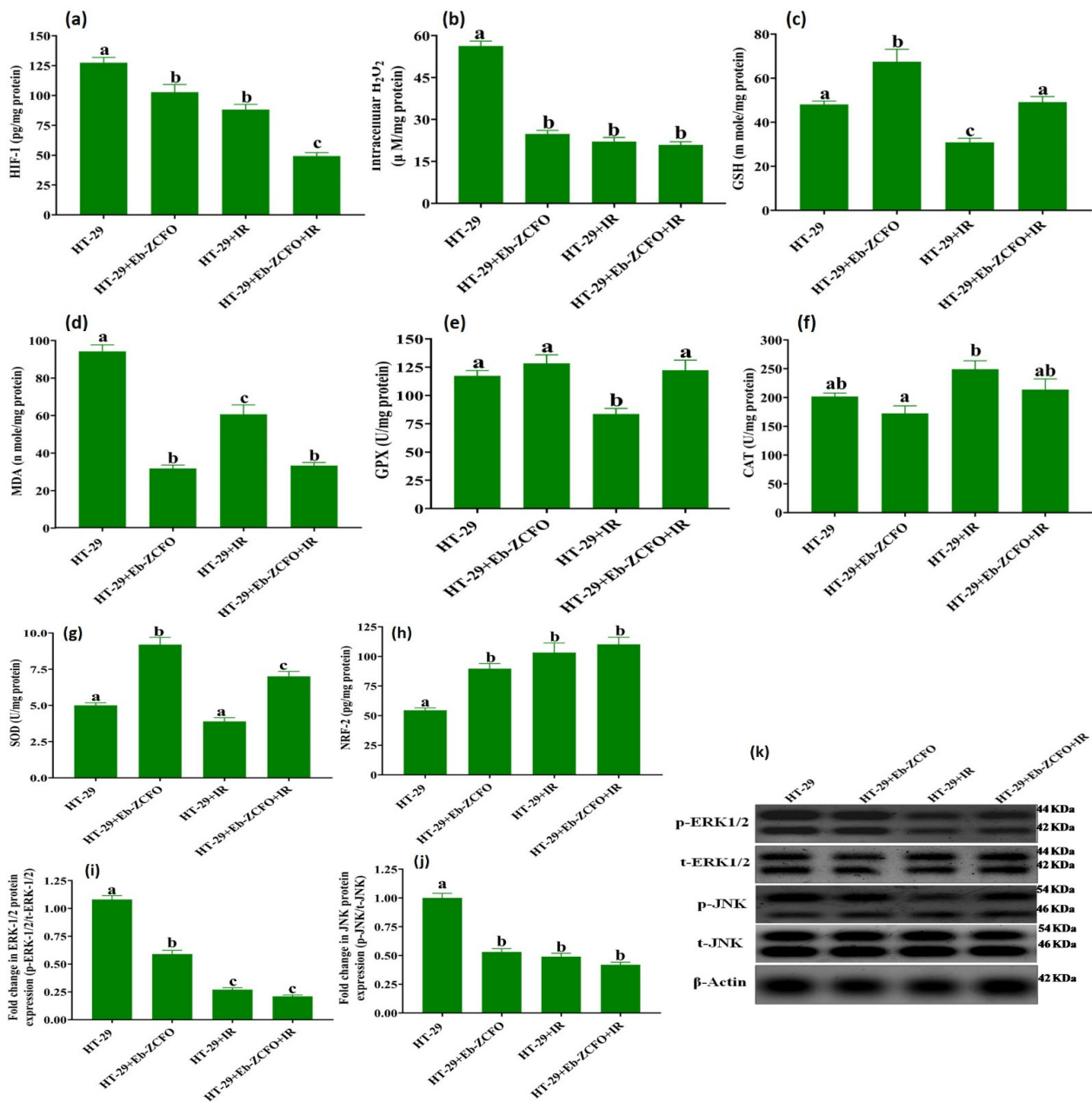


Figure 14. ROS status and associated signalling molecules ERK1/2, JNK, and NRF-2 in HT-29 cells lines. ROS status measured as follows: the levels of (a) HIF-1 α , (b) intracellular H₂O₂, (c) GSH, and (d) MDA; activities of (e) GPX, (f) CAT, and (g) SOD. ROS-sensing signalling molecules as follows: (h) NRF-2 level; fold change in protein expression of (i) ERK1/2, (j) JNK, and (k) representative western blot analysis, SDS-PAGE of ERK1/2, JNK, and β -actin. Results are expressed as the mean and standard error of the mean (SEM) (n = 3). Columns with dissimilar letters (a, b, c . . .) overhead within the same histogram are significantly different, and columns with the same letters are not significantly different at $p < 0.05$. HT-29 group: untreated HT-29 cells served as control, HT-29 + Eb-ZCFO group: HT-29 cells treated with Ebselen (Eb) and ZnCe_{0.06}Fe_{1.94}O₄ nanoparticles (ZCFO), HT-29 + IR group: HT-29 cells exposed to γ -radiation, and HT-29 + Eb-ZCFO + IR group: HT-29 cells treated with Eb-ZCFO and exposed to IR.

2.6.3. Inflammatory Status and Crosstalk of Signalling Pathways TNF- α /NF- κ B, INF- γ /STAT-1, and IL-4/STAT-6 in MDA-MB-231 and HT-29 Cell MDA-MB-231 Cell Line

The application of Eb-ZFO, IR, and Eb-ZFO + IR to MDA-MB-231 cells induced a significant decline ($p < 0.05$) in the inflammatory mediators NF- κ B by 59.33%, 60.52%, and

68.28%; IL-4 by 25.41%, 62.71%, and 66.09%; INF- γ by 62.33%, 65.71%, and 63.07%; and TNF- α by 64.44%, 63.98%, and 67.63%, respectively. The protein expression of p-STAT-1 signalling effector declined by 69.80%, 46.54%, and 67.55%, respectively, linked with a significant increase ($p < 0.05$) in IL-10 level by 2.25-fold, 1.51-fold, and 2.29-fold, respectively, and p-STAT-6 protein expression by 3.697-fold, 3.799-fold, and 5.199-fold, respectively, as compared to the MDA group (Figure 15).

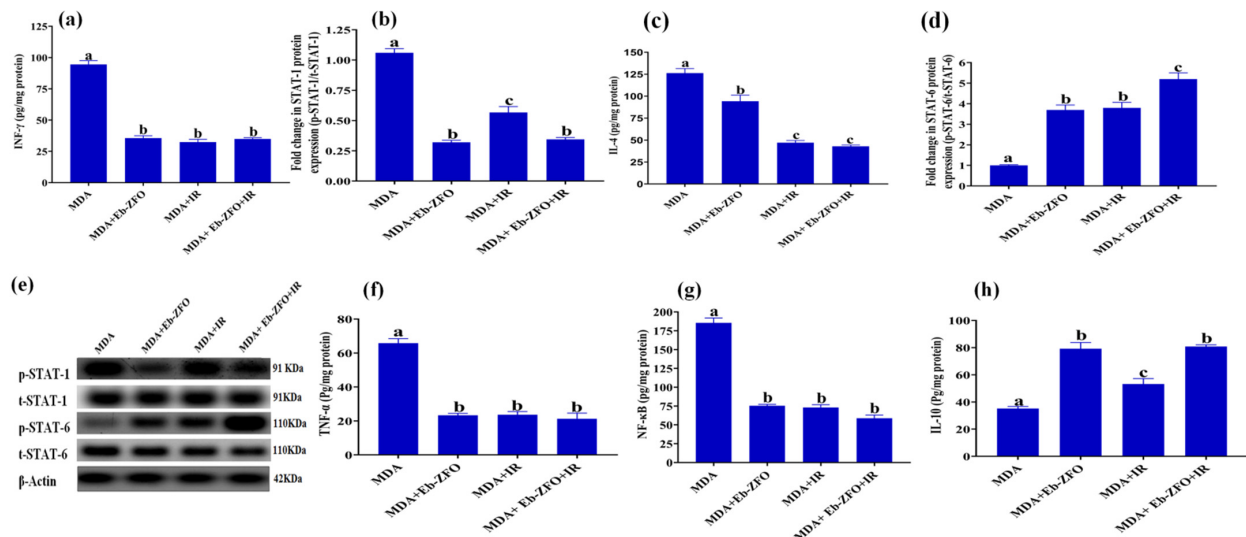


Figure 15. Inflammatory status and crosstalk of the signalling pathways TNF- α /NF- κ B, INF- γ /STAT-1, and IL-4/STAT-6 in MDA-MB-231 cells. Represented as follows; levels of (a) INF- γ , (b) protein expression of STAT-1, (c) IL-4, (d) protein expression of STAT-6, (e) representative western blot analysis, SDS-PAGE of STAT-1, STAT-6, and β -actin, (f) TNF- α , (g) NF- κ B and (h) IL-10. Results are expressed as the mean and standard error of the mean (SEM) ($n = 3$). Columns with dissimilar letters (a, b, c . . .) overhead within the same histogram are significantly different, and columns with the same letters are not significantly different at $p < 0.05$. MDA group: untreated MDA-MB-231 cells served as control, MDA + Eb-ZCFO group: MDA-MB-231 cells line treated with Ebselen (Eb) and ZnFe₂O₄ nanoparticles (ZFO), MDA + IR group: MDA-MB-231 cells exposed to γ -radiation, and MDA + Eb-ZFO + IR group: MDA-MB-231 cells treated with Eb-ZFO and exposed to IR.

HT-29 Cell Line

Treatment of HT-29 cells with either Eb-ZCFO or IR exposure or both Eb-ZCFO + IR showed a significant decrease ($p < 0.05$) in the inflammatory mediators NF- κ B 40.71%, 64.10%, and 69.49%; IL-4 30.90%, 21.31%, and 38.37%; INF- γ 58.29%, 43.82%, and 64.38%; and TNF- α 50.56%, 41.14%, and 73.43%, and the protein expression of STAT-1 by 78.41%, 40.18%, and 71.55%; signalling effector showed a significant rise ($p < 0.05$) in IL-10 level of 1.73-fold, 1.92-fold, and 2.42-fold; and its signalling effector STAT-6 protein expression by 4.03-fold, 4.09-fold, and 4.1-fold, respectively, as compared to the HT-29 group (Figure 16). The link between chronic inflammation and tumour development is well-established, and it has become evident that an inflammatory microenvironment is a prerequisite for all tumours, including those that emerge in the absence of overt inflammation [95]. Chronic inflammation affects the TME and impacts cell plasticity through the epithelial–mesenchymal transition, dedifferentiation, the polarisation of immune cells, production of ROS and cytokines, epigenetic mechanisms, miRNAs, and complex regulatory cascades in tumour and stromal cells [96]. The current data showed a considerable reduction in pro-inflammatory TME through the activation of STAT-6 expression. Consistently with our data, a study by Ohmori and Hamilton [76] found that STAT-6 mediates the suppression of INF- γ /STAT-1 and TNF- α /NF- κ B-dependent transcription by distinct mechanisms. Park et al. (2019) [97] found that the restoration of STAT-6 levels in glioblastoma (GBM) suppresses HIF-1 α protein synthesis and induces STAT-6-regulated immune responses and apoptosis, thereby leading to the suppression of GBM proliferation. Tissue hypoxia in cancer induces cell growth, neovascularisation, invasion, resistance to chemo

and radiotherapy, and ultimately recurrence after treatment [97]. IL-10 is a potentially valuable target of immunomodulatory therapy, as observed by Brunn et al. [98], who postulated a dual role for macrophages during initiation and recovery from experimental autoimmune neuritis (EAN), especially in the imbalance between autoimmune pro-inflammatory milieu and the net effect of various immunoregulatory mediators, such as IL-10, IL-4, and STAT-6. It was found that the absence of a single anti-inflammatory Th2-derived cytokine, such as IL-10 or IL-4, and even the absence of a single downstream signalling molecule of the IL-4 pathway, STAT6, markedly interferes with recovery from EAN. Tewari et al. [99] found that Eb not only down-regulated the enhanced ROS production of TNF- α treated glioma cells but also overcame TNF- α -induced pro-inflammatory mediators to prevent the build-up of a deleterious pro-inflammatory TME. Based on the current data, Eb appears to efficiently modulate the pro-inflammatory TME via augmentation of STAT-6 expression and its antioxidant and immunoregulatory activity. Irradiation was found to promote M2 phenotype macrophages in hypoxic TME, thereby directing the pro-inflammatory milieu within tumours toward an alternative anti-inflammatory TME [100]. Thabet and Moustafa [101] found that Eb and γ -radiation at 1, 3, and 6 Gy induced apoptosis and anti-angiogenic and antiproliferative effects by reducing NF- κ B signalling and increasing IL-10 in MCF-7 cells. One of the factors contributing to the anti-inflammatory effect of IR in the current study is NRF-2 upregulation in response to irradiation. Considering the biphasic role of NRF-2 in cancer therapy [102], constitutive activation of NRF-2 is associated with the promotion of development of several cancers, poor diagnosis in clinical settings, and resistance to therapies [103]. NRF-2 hyperactivity in cancer cells confers chemo- and radioresistant characteristics [102]. However, activation of the Nrf2/ARE signalling pathway plays a critical role in the alleviation of chronic inflammation, which is associated with cancers, since Nrf2 positively regulates a large number of cytoprotective proteins. Elimination of ROS has been widely accepted as the molecular basis of Nrf2-mediated anti-inflammation [104,105]. Hence, the boost in NRF-2 and STAT-6 expression elicited by Eb-ZCFO or IR exposure, or their combination, produces an anti-inflammatory response within the TME that might hinder tumour progression, as revealed in the present study.

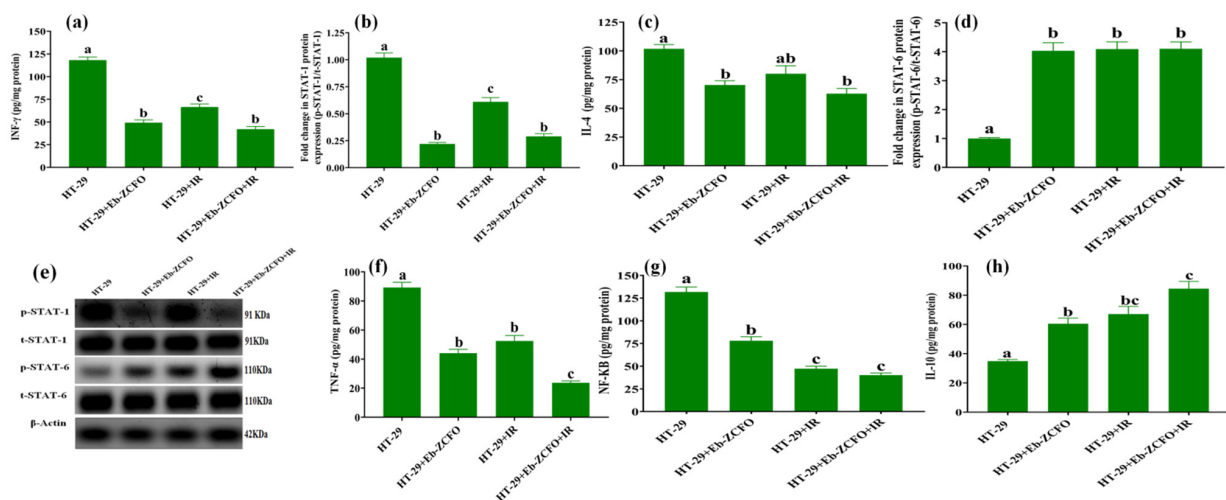


Figure 16. Inflammatory status and crosstalk of the signalling pathways TNF- α /NF- κ B, INF- γ /STAT-1, and IL-4/STAT-6 in HT-29 cells. Represented as follows: levels of (a) INF- γ , (b) protein expression of STAT-1, (c) IL-4, (d) protein expression of STAT-6, (e) representative western blot analysis, SDS-PAGE of STAT-1, STAT-6, and β -actin, (f) TNF- α , (g) NF- κ B, and (h) IL-10. Results are expressed as the mean and standard error of the mean (SEM) (n = 3). Columns with dissimilar letters (a, b, c . . .) overhead within the same histogram are significantly different, and columns with the same letters are not significantly different at $p < 0.05$. HT-29 group: untreated HT-29 cells line served as control, HT-29 + Eb-ZCFO group: HT-29 cells line treated with Ebselen (Eb) and ZnCe_{0.06}Fe_{1.94}O₄ nanoparticles (ZCFO), HT-29 + IR group: HT-29 cells exposed to γ -radiation, and HT-29 + Eb-ZCFO + IR group: HT-29 cells treated with Eb-ZCFO and exposed to IR.

2.6.4. Assessment of Autophagy and Apoptosis-Related Proteins in MDA-MB-231 and HT-29 Cells

MDA-MB-231 Cell Line

The data shown in Figure 17 show a significant increase ($p < 0.05$) in autophagy markers (Beclin-1 3.92-fold, 4.21-fold, and 5.09-fold and LC3B-II/I 3.8-fold, 3.9-fold, and 5.3-fold) and apoptosis-related protein cleaved caspase-3 (3.85-fold, 5.23-fold, and 6.14-fold) associated with a significant diminishment ($p < 0.05$) in p62 (49.52%, 72.27%, and 55.46%), caspase-dependent cleaved poly (ADP-ribose) polymerase (PARP), an apoptosis marker and enzyme responsible for DNA repair (61.39%, 74.26%, and 68.35%) and anti-apoptotic B-cell lymphoma 2 (BCL-2) (45.87%, 49.66%, and 73.64%) in MDA-MB-231 cells treated with Eb-ZFO, IR, and Eb-ZFO + IR, respectively, when compared to the MDA group (Figure 17).

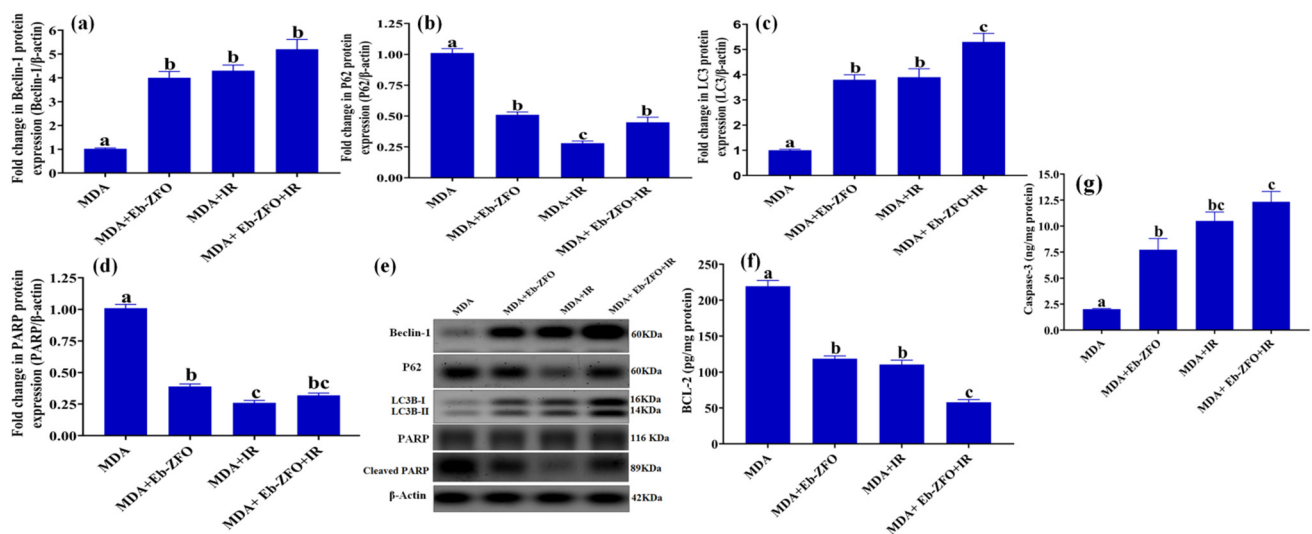


Figure 17. Autophagy and apoptosis in MDA-MB-231 cells. Represented as follows: fold change in protein expression of (a) beclin-1, (b) P62, (c) LC3B-II, (d) cleaved PARP-1, (e) representative western blot analysis, SDS-PAGE of beclin-1, P62, LC3B-II/LC3B-I, cleaved PARP-1 and β -actin, (f) BCL-2, and (g) cleaved caspase-3 protein levels. Results are expressed as the mean and standard error of the mean (SEM) ($n = 3$). Columns with dissimilar letters (a, b, c . . .) overhead within the same histogram are significantly different, and columns with the same letters are not significantly different at $p < 0.05$. MDA group: untreated MDA-MB-231 cells served as control; MDA + Eb-ZFO group: MDA-MB-231 cells treated with Ebselen (Eb) and $ZnFe_2O_4$ nanoparticles (ZFO); MDA + IR group: MDA-MB-231 cells exposed to γ -radiation; and MDA + Eb-ZFO + IR group: MDA-MB-231 cells treated with Eb-ZFO and exposed to IR.

HT-29 Cell Line

A significant increase ($p < 0.05$) was observed in the expression of autophagy proteins (Beclin-1 4.62-fold, 4.04-fold, and 5.78-fold and LC3B-II/I 2.67-fold, 2.98-fold, and 3.86-fold) and apoptosis-related protein; cleaved caspase-3 (3.27-fold, 4.83-fold, and 5.61-fold) was observed in HT-29 cells treated with Eb-ZCFO or exposed to IR or both (Figure 18). Eb-ZCFO + IR groups associated with a significant reduction ($p < 0.05$) in p62 (52.93%, 69.00%, and 57.00%) and cleaved PARP protein expression (52.46%, 81.18%, and 60.39%) as well as the anti-apoptosis protein; BCL-2 level (26.61%, 34.39%, and 62.39%), respectively, as compared to the HT-29 group (Figure 18). Autophagy is a recently recognised response of tumour cells to various anticancer therapies, including radiotherapy and chemotherapy [106]. It is a highly conserved cellular catabolic process that degrades and recycles cellular components through lysosomes [107]. During starvation, cells can supply self-nutrition via lysosomal enzyme-induced degradation of macromolecules and damaged proteins [108]. Autophagy, however, can serve as a double-edged sword and activate cellular apoptosis through type II programmed cell death. Through the interaction between the C-terminal cleavage of light chain 3 (LC3)-associated microtubule protein (LC3B peptide) and autophagy-related

gene 4, which is a type of cysteine protease, autophagy is induced. It produces LC3BI, which conjugates with phosphatidylethanolamine (PE) to yield LC3BII [109], which can integrate with autophagy-related proteins 5, 7, and 12 to create autophagosomes, along with phospholipid bilayers. In contrast, LC3 interacts with p62/sequestome-1 (SQSTM1), which functions as a ubiquitin-binding protein to break down damaged organelles and macromolecules [110]. Therefore, the levels of proteins LC3 and p62 are broadly recognised as prominent markers of autophagy [111,112]. As shown in our data, an increase in the autophagic flux was detected in MDA-MB-231 and HT-29 cells, as indicated by enhanced beclin-1 and LC3BII protein expression, paralleled by boosted cleaved caspase-3 along with reduced BCL-2 and p62 protein levels, suggesting a switch from cytoprotective to cytotoxic autophagy, which resulted in apoptotic death induced by Eb-ZCFO or IR, or their combination. Ample evidence has shown an association between the induction of autophagy and radioresistance in a wide range of tumours, including pancreatic cancer, breast carcinoma, and glioma [113–115].

The antitumour effect of Beclin-1 has been confirmed in many types of tumours such as breast [116], colon [117], cervical [118], ovarian [119], and glioblastoma [120]. Huang et al. (2014) [121] found that the autophagy gene Beclin-1 promotes apoptosis and reduces cell proliferation by increasing the expression of LC3 and caspase-3, associated with a decreased expression of p62 and Bcl-2. Thus, Beclin-1 plays an important role in the fine-tuning of autophagy and apoptosis. Song et al. [122] found that AKT inactivation-induced elevation of Beclin-1 cleavage resulted in disruption of the R-BiP/Beclin-1/p62 complex, which led to switching from autophagy to the synergistic induction of apoptosis. Baek et al. [123] found that Eb decreased the phosphorylation of I κ B, PI3K, and AKT in lipopolysaccharide-induced inflammatory bone destruction models. A study by Kaczor-Keller et al. [20] demonstrated that Eb efficiently inhibits cancer cell proliferation, induces G2/M cell-cycle arrest, and promotes cell death in prostate cancer by switching from apoptotic cell death to necrosis via a significant decrease in the level of cleaved PARP after 24 h exposure to Eb. Although necrosis as an uncontrolled modality of cell death is generally associated with damage to peripheral tissues and increased systemic inflammation, recent observations highlight a positive role for necrosis induction during cancer therapy [20]. PARP-1 plays an important role in the response to IR-induced DNA damage and may confer radioresistance [124]. Hampering PARP-1 activity may therefore be a successful approach to the sensitisation of TNBC and colorectal adenocarcinoma to radiotherapy, a process that was achieved by Eb-ZFO and Eb-ZnCe_{0.06}Fe_{1.94}O₄ nanocomposites in our study.

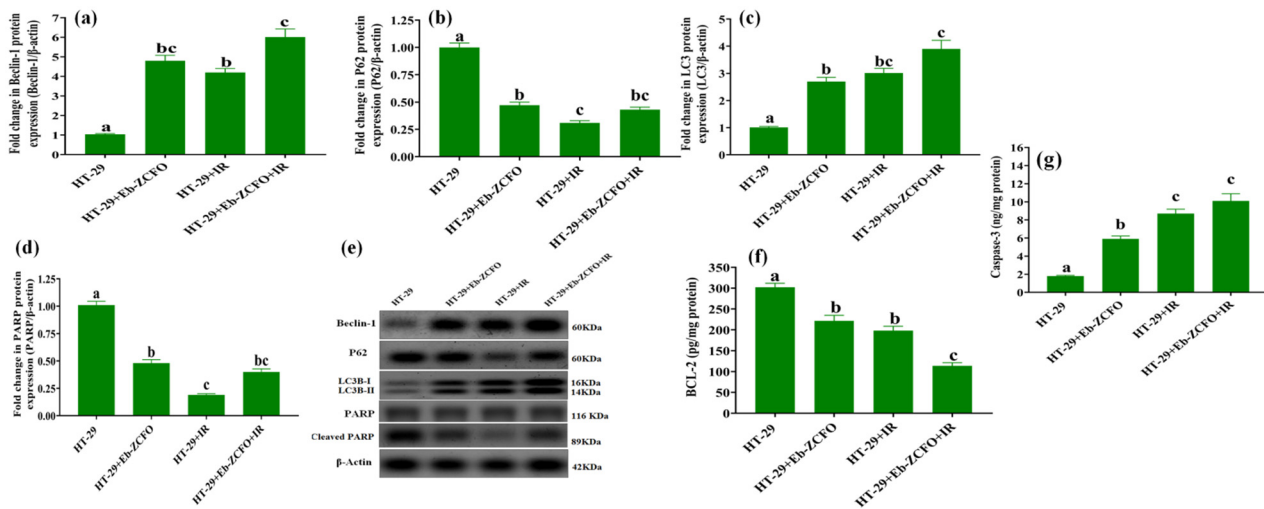


Figure 18. Autophagy and apoptosis in HT-29 cells. Represented as follows: fold change in protein expression of (a) Beclin-1; (b) P62; (c) LC3B-II; (d) cleaved PARP-1; (e) representative western blot analysis, SDS-PAGE of Beclin-1, P62, LC3B-II/LC3B-I, cleaved PARP-1, and β -actin; (f) BCL-2; and (g) cleavedcaspase-3 protein levels. Results are expressed as the mean and standard error of the mean (SEM) ($n = 3$). Columns with dissimilar letters (a, b, c . . .) overhead within the same histogram are significantly different, and columns with the same letters are not significantly different at $p < 0.05$. HT-29 group: untreated HT-29 cells served as control. HT-29 + Eb-ZCFO group: HT-29 cells treated with Ebselen (Eb) and $\text{ZnCe}_{0.06}\text{Fe}_{1.94}\text{O}_4$ nanoparticles (ZCFO). HT-29 + IR group: HT-29 cells exposed to γ -radiation. HT-29 + Eb-ZCFO + IR group: HT-29 cells treated with Eb-ZCFO and exposed to IR.

2.6.5. Flow Cytometric Analysis of Cell Cycle inMDA-MB-231 and HT-29 Cells

The flow cytometric analysis of the cell-cycle distribution was used to study the anti-cancer effects of Eb + ZnFe_2O_4 (Eb-ZFO) on MDA-MB-231 cells and Eb + $\text{ZnCe}_{0.06}\text{Fe}_{1.94}\text{O}_4$ (Eb-ZCFO) on HT-29 cells alone and in combination with γ -radiation (IR; 4 Gy) for 24 h.

MDA-MB-231 Cell Line

The data from the MDA + Eb-ZFO group showed a significant decrease ($p < 0.05$) in the percentage of cells in the G0/G1and S phases, associated with a noticeable accumulation of cells in the G2/M and pre-G1 phases. This distribution caused cell-cycle arrest at the G2/M phase as compared to the MDA group (Figure 19a). After exposure to γ -radiation, the MDA + Eb-ZFO + IR group showed a significant decrease ($p < 0.05$) in the percentage of cells in G0/G1 phase, associated with an accumulation of cells in the G2/M and pre-G1 phases, causing cell-cycle arrest at the pre-G1phase as compared to the MDA group (Figure 19a).

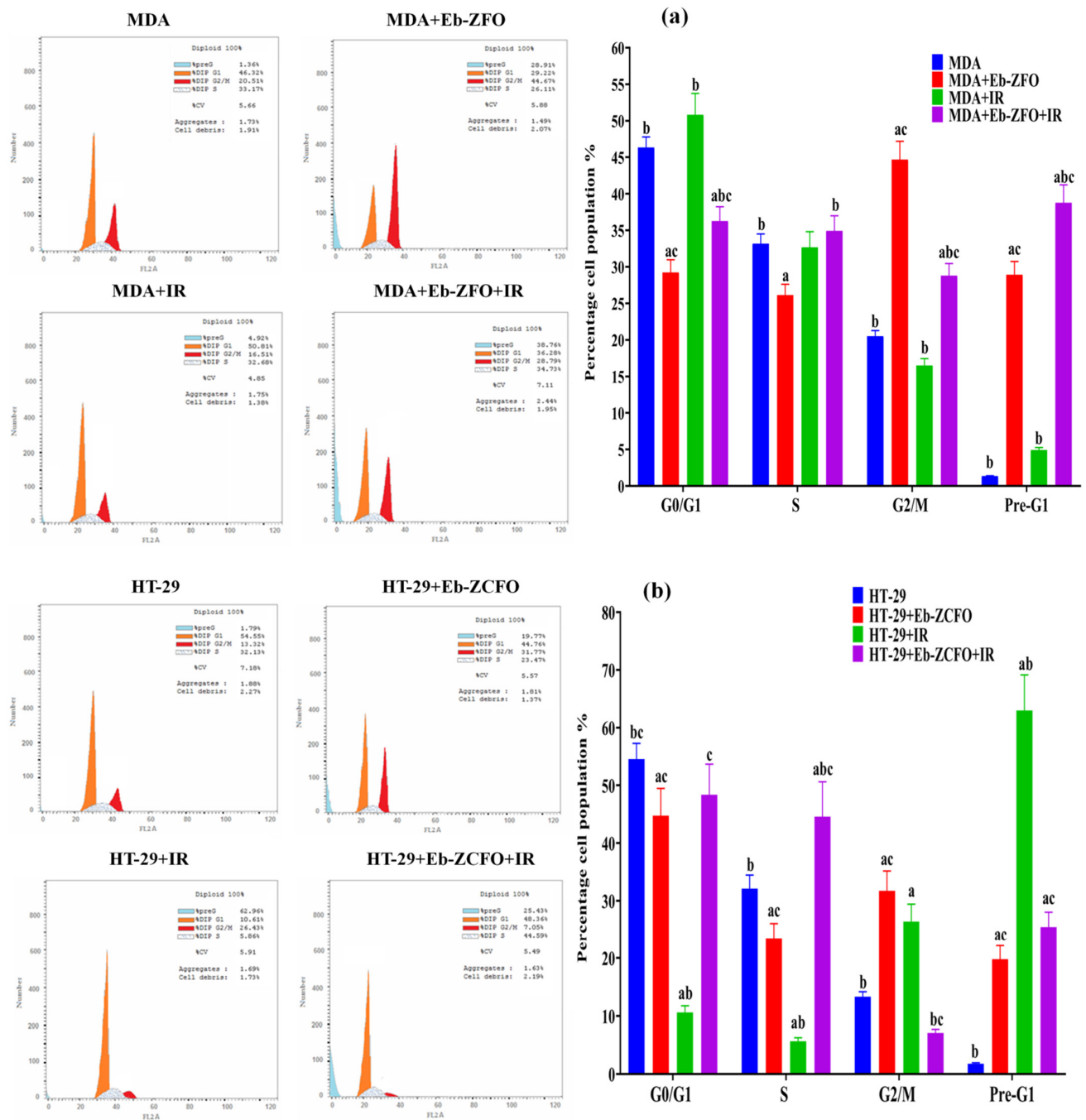


Figure 19. Cell-cycle analysis via flow cytometry. (a) Distribution of MDA-MB-231 cells through the cell-cycle phases after treatment with Eb-ZFO alone or in combination with 4 Gy γ -radiation for 24 h. MDA group: untreated MDA-MB-231 cells served as control. MDA + Eb-ZFO group: MDA-MB-231 cells treated with Ebselen (Eb) doped into ZnFe₂O₄ nanoparticles (ZFO). MDA + IR group: MDA-MB-231 cells exposed to γ -radiation. MDA + Eb-ZCFO + IR group: MDA-MB-231 cells treated with Eb-ZFO and exposed to IR. (b) Distribution of HT-29 cells through the cell-cycle phases after treatment with Eb-ZCFO alone or in combination with 4 Gy γ -radiation for 24 h. HT-29 group: untreated HT-29 cells served as control. HT-29 + Eb-ZCFO group: HT-29 cells treated with Ebselen (Eb) and ZnCe_{0.06}Fe_{1.94}O₄ nanoparticles (ZCFO). HT-29 + IR group: HT-29 cells exposed to γ -radiation. HT-29 + Eb-ZCFO + IR group: HT-29 cells treated with Eb-ZCFO and exposed to IR. Results are expressed as the mean and standard error of the mean (SEM) (n = 3). Columns with a, b, and c letters overhead within the same phase are significantly different from the control, treated group, or IR group of each cell line, respectively, at *p* < 0.05.

HT-29 Cell Lines

The data from the HT-29 + Eb-ZCFO group showed a significant decrease ($p < 0.05$) in the percentage of cells in the G0/G1 and S phases associated with an accumulation of cells in the G2/M- and pre-G1 phases, causing cell-cycle arrest at the G2/M phase as compared to the HT-29 group (Figure 19b). After exposure to γ -radiation, the results from the HT-29 + Eb-ZCFO + IR group displayed a significant increase in S- and pre-G1 phases and caused cell-cycle arrest at the S-phase, compared with the HT-29 group (Figure 19b). The cell cycle includes a number of checkpoints that allow the cell to repair its damaged DNA. Checkpoints at the G1/S and G2/M transitions are essential regulatory gates during cell-cycle progression, whereas loss of cell-cycle checkpoints ahead of completing DNA repair can activate the apoptotic cascade and result in cell death [125]. Our data indicated that Eb-ZFO and Eb-ZCFO induced cell-cycle arrest at the G2/M phase in both MDA-MB-231 and HT-29 cells, suggesting that cells undergo apoptosis or mitotic catastrophe, but when exposed to IR, as observed in the MDA + Eb-ZFO + IR and HT-29 + Eb-ZCFO + IR groups, caused cell-cycle arrest at the sub-G1 (total apoptosis) and S-phases, respectively, suggesting the fragmentation of DNA and impairment of DNA synthesis and replication. Most antitumour agents interrupt the cell-cycle checkpoints at the G0/G1, S, and G2/M phases and then trigger apoptosis [126]. The G2 checkpoint prevent cells from entering mitosis when the DNA is damaged, providing an opportunity for repair and prevention of the proliferation of damaged cells [127]. Cytotoxic drugs that cause S-phase arrest prevent accurate DNA synthesis and replication [128].

2.6.6. Detection of Apoptosis in MDA-MB-231 and HT-29 Cells Lines by Flow Cytometry

Apoptosis and necrotic cell death were assessed using flow cytometric analysis with Annexin-V-FITC and PI dual-staining to evaluate the pro-apoptotic effects of Eb + ZnFe₂O₄ (Eb-ZFO) on MDA-MB-231 cells and Eb + ZnCe_{0.06}Fe_{1.94}O₄ (Eb-ZCFO) on HT-29 cells, alone and in combination with γ -radiation (IR; 4 Gy) for 24 h.

MDA-MB-231 Cell Lines

The proportion of apoptotic and necrotic cells in a population of MDA-MB-231 cells treated with IC₅₀ is shown in Figure 20a. In Figure 20a, the data from the MDA + Eb-ZFO and MDA + Eb-ZFO + IR groups show a significant increase ($p < 0.05$) in the total apoptotic cells (early and late) compared to the MDA group. The MDA + Eb-ZFO + IR group showed a significant increase ($p < 0.05$) in necrotic cells compared to the MDA, MDA + Eb-ZFO, and MDA + IR groups. Based on these observations, it could be concluded that γ -radiation (IR) elevates both apoptotic and necrotic death in TNBC cells when coupled with Eb-ZFO nanocomposite (Figure 20a).

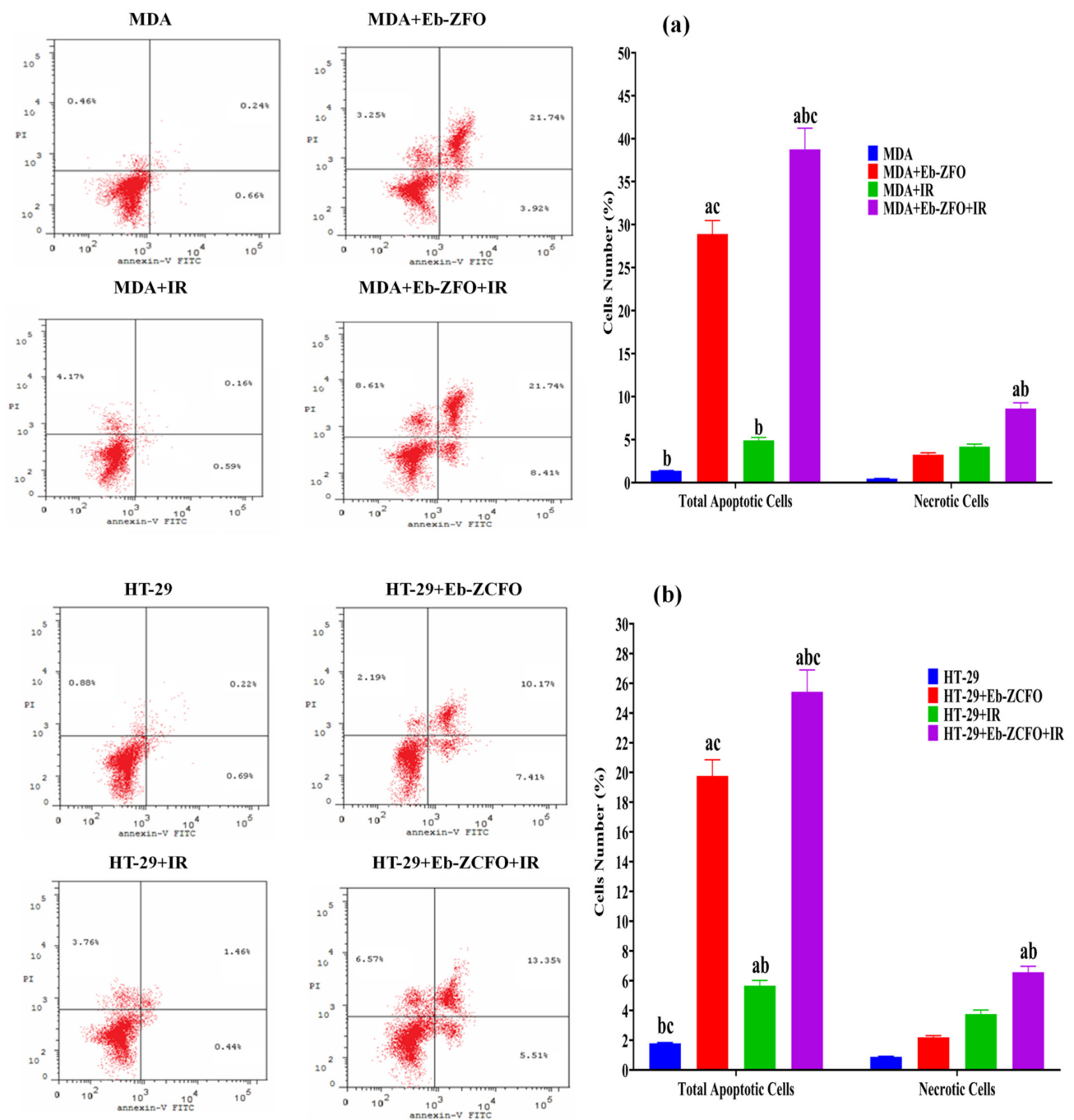


Figure 20. Detection of apoptosis via flow cytometry. (a) Eb-ZFO and IR induced apoptosis and necrosis in MDA-MB-231 cells after 24 h. The upper-left panel shows representative images of cell apoptosis. The percentage of apoptotic and necrotic cells was determined and is represented in the upper-right panel. MDA group: untreated MDA-MB-231 cells line served as control. MDA + Eb-ZFO group: MDA-MB-231 cells treated with Ebselen (Eb) and ZnFe₂O₄ nanoparticles (ZFO). MDA + IR group: MDA-MB-231 cells exposed to γ -radiation. MDA + Eb-ZFO + IR group: MDA-MB-231 cells treated with Eb-ZFO and exposed to IR. (b) Eb-ZCFO and IR induced apoptosis and necrosis in HT-29 cells after 24 h. HT-29 group: untreated HT-29 cells served as control. HT-29 + Eb-ZCFO group: HT-29 cells treated with Ebselen (Eb) and ZnCe_{0.06}Fe_{1.94}O₄ nanoparticles (ZCFO). HT-29 + IR group: HT-29 cells exposed to γ -radiation. HT-29 + Eb-ZCFO + IR group: HT-29 cells treated with Eb-ZCFO and exposed to IR. The lower-left panel shows representative images of cell apoptosis. The percentage of apoptotic and necrotic cells was determined and is shown in the lower-right panel. The results are expressed as the mean and standard error of the mean (SEM) (n = 3). Columns with a, b, and c letters overhead within the same phase are significantly different from control, treated group, or IR group of each cell line at $p < 0.05$.

HT-29 Cell Lines

Figure 20b shows data from the HT-29 + Eb-ZCFO, HT-29 + IR, and HT-29 + Eb-ZCFO + IR groups, revealing a significant increase ($p < 0.05$) in the total apoptotic cells (early and late) compared to the MDA group. The HT-29 + Eb-ZCFO + IR group showed a significant elevation ($p < 0.05$) in necrotic cells compared to the HT-29 and HT-29 + Eb-ZCFO groups. Accordingly, it could be concluded that γ -radiation (IR) promotes apoptotic and necrotic death in colorectal adenocarcinoma cells when combined with Eb-ZCFO nanocomposites (Figure 20b). A complex relationship is evident between autophagy and apoptosis. Autophagy frequently occurs with or before apoptosis. In the latter case, a surge in autophagic flux regulates tumour cell growth by facilitating the induction of apoptosis or necrosis [129,130]. As a crucial cellular process, apoptosis is modulated by multiple regulatory molecules and different pathways [131]. These modulators are essential for regulating the growth of various cancers. Both the blockage of pro-apoptotic Bcl-2 family molecules and the enhancement of anti-apoptotic family signals are required for the modulation of apoptotic dysregulation in tumours [132]. Caspases, a family of cysteine acid proteases, are key regulators of cell survival and apoptosis [133]. Our findings indicated that Eb-ZFO or Eb-ZCFO alone or in combination with IR could reduce the level of BCL-2 protein, which is known to be an essential anti-apoptotic signal in MDA-MB-231 and HT-29 cells, accompanied by an increase in cleaved caspase-3 protein, coupled with a marked curtailment of PARP-1 cleavage. In a mouse proximal tubular cell ATP depletion model, Lieberthal et al. [134] found that mild ATP depletion led to apoptosis, whereas severe ATP depletion led to necrosis. ATP is required for apoptosis, such that severe ATP depletion inhibits the apoptotic pathway in a number of cell types [135,136]. This phenomenon might explain the dual induction of apoptotic and necrotic cells in Eb-ZFO and Eb-ZCFO nanocomposites alone or when combined with IR, suggesting the radiosensitisation of MDA-MB-231 and HT-29 cells. A marked increase in the population of necrotic cells in the MDA-Eb-ZFO + IR and HT-29 + Eb-ZCFO + IR groups suggests the strong inhibition of ATP with the activation of ATP-independent necrosis.

Overall, as shown in Figure 21, the mechanism of Eb-ZFO in the MDA-MB-231 cell line depends primarily on the Eb antioxidant/anti-inflammatory capability and the cytotoxicity profile of the ZnO-NPs. However, the exhibited antitumour activity of Eb-ZCFO in HT-29 cell line depends on Ce nanoparticles as ROS scavenger and Eb as immunomodulatory of TME. The findings of the current study agree with those obtained by Barrera et al. [137] and Liu et al. [138].

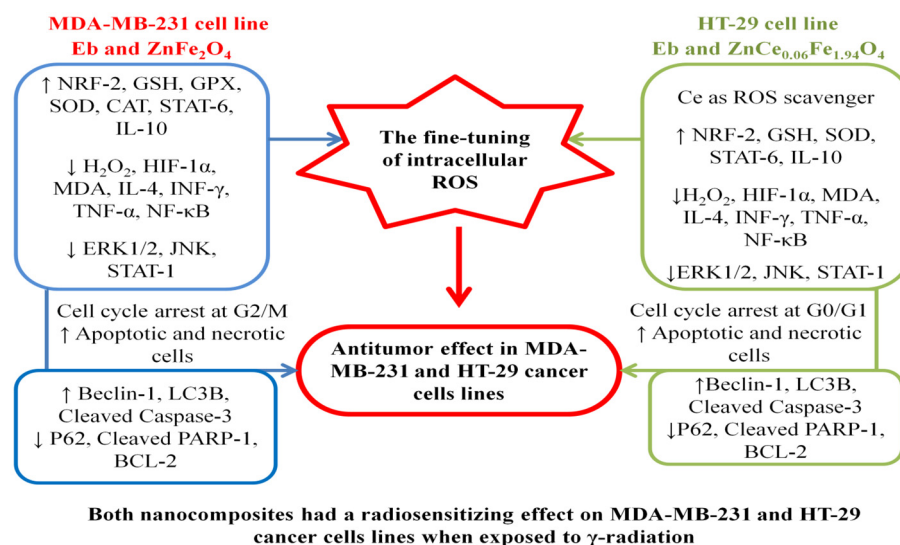


Figure 21. Signalling pathways involved in the antitumour activity of Eb + ZnFe₂O₄ and ZnCe_xFe_{2-x}O₄; X = 0.06 nanocomposites, where the effect is mediated through the antioxidant,

anti-inflammatory, and immunomodulatory effects of Eb, plus the cytotoxicity of ZnO-NPs in MDA-MB-231 cells, whereas the cytotoxic effect of $\text{ZnCe}_{0.06}\text{Fe}_{1.94}\text{O}_4$ relies mainly on Ce^{3+} as a ROS scavenger and the immunomodulatory capability of Eb in HT-29 cells, leading to an overwhelming response in the tumour antioxidant machinery, coupled with reversion of the pro-inflammatory TME to an anti-inflammatory milieu. This reversion, in turn, resulted in an alteration in the tumour proliferation pathways, accompanied by a switch from cytoprotective to cytotoxic autophagy, and eventually a marked rise in pro-apoptotic and decrease in anti-apoptotic proteins. Treatment of both cells with Eb-ZFO or Eb-ZCFO alone or in combination with IR provoked cell-cycle arrest at the major checkpoints, with elevated levels of apoptotic and necrotic cells, suggesting an excellent antitumour effect and radiosensitisation of TNBC and colorectal adenocarcinoma cells.

3. Materials and Methods

3.1. Synthesis of $\text{ZnCe}_x\text{Fe}_{2-x}\text{O}_4$ Nanoferrites

The $(\text{Ce}(\text{NO}_3)_3 \cdot 6\text{H}_2\text{O}, 99.99\%)$, $(\text{Fe}(\text{NO}_3)_3 \cdot 9\text{H}_2\text{O}, 98.0\%)$, $(\text{ZnSO}_4 \cdot 7\text{H}_2\text{O}, 98\%)$, $(\text{C}_6\text{H}_8\text{O}_7, 99.57\%)$, and $(\text{C}_2\text{H}_6\text{O}_2, 99.8\%)$ were purchased from Sigma-Aldrich, Germany and used as received without further purification. The synthesis of $\text{ZnCe}_x\text{Fe}_{2-x}\text{O}_4$ ($X = 0.0, 0.02, 0.04, 0.06, 0.08$) powders was carried out using a facile sol-gel method as described in detail in our previous work [10–12,25,34,35].

3.2. Characterisation of the Nanoferrites

The stoichiometry of the $\text{ZnCe}_x\text{Fe}_{2-x}\text{O}_4$ ($X = 0.0, 0.02, 0.04, 0.06, 0.08$) samples was examined using energy dispersive X-ray spectra (EDX) (JEOL JSM-5600 LV, Japan). In order to confirm the formation of the spinel ferrite phase, Fourier transform infrared (FTIR) spectroscopy using a NICOLET iS10 model instrument was conducted over a range from 350 to 3000 cm^{-1} . The crystal structure of the samples was investigated using X-ray diffraction (XRD) (Shimadzu XRD-6000, Japan). XRD patterns were obtained in a range of 2θ from 17° to 90° at room temperature. $\text{Cu K}\alpha$ was used as the radiation source of wavelength $\lambda = 0.15408$ nm, with a scan rate of $0.8^\circ/\text{min}$, an operating voltage of 50 kV, and a current of 40 mA [139,140]. Information about the shape and grain size of the sample particles was obtained using high resolution scanning electron microscopy (SEM) (JEOL JSM-5600 LV, Japan). Finally, the particle size distribution, the hydrodynamic radius, and the polydispersity index (PDI) of the synthesised $\text{ZnCe}_x\text{Fe}_{2-x}\text{O}_4$ ($X = 0.0, 0.02, 0.04, 0.06, 0.08$) samples were determined by dynamic light scattering (DLS; Malvern devise, UK) and the indirect measurement of the surface charges of $\text{ZnCe}_x\text{Fe}_{2-x}\text{O}_4$ ($X = 0.0, 0.02, 0.04, 0.06, 0.08$) samples was estimated by the zeta potential analyser (Malvern devise, UK) at the culture media as used in the treatments.

3.3. Antimicrobial Activities of $\text{ZnCe}_x\text{Fe}_{2-x}\text{O}_4$ Nanoparticles and Ebselen

The antimicrobial potential of the as-synthesised Zn ferrites and ferrites substituted with Ce and Ebselen against different pathogenic microbes, both yeast and bacteria, were examined using the agar-disc diffusion method [141].

The as-synthesised $\text{ZnCe}_x\text{Fe}_{2-x}\text{O}_4$ nanoparticles ($X = 0.0, 0.02, 0.04, 0.06, \text{ and } 0.08$) and Ebselen were dissolved in DMSO at a concentration of 0.01 mg/mL, equivalent to 10 ppm.

The synthesised nanocomposite powder must be dispersed into solvent (DMSO) and applied as solution to be diffused on the surface of the agar plate, so they have single nanoparticles rather than agglomerated nanoparticles. The activity of the as-synthesised compounds were examined against Gram-positive bacteria (*Staphylococcus aureus* ATCC 25923, *Proteus vulgaris* ATCC 26325, and *Proteus mirabilis* ATCC 26659) and Gram-negative bacteria (*Pseudomonas aeruginosa* ATCC 27853, *Escherichia coli* ATCC 25922, *Klebsiella pneumoniae* ATCC 28896, and *Salmonella typhi* ATCC 26510). All of the above bacteria were established and fixed from 2 to 5×10^8 CFU/mL (0.5 McFarland; at 600 nm). The inhibition of bacterial growth was defined by the zone of inhibition (ZOI) after 24 h of incubation.

The antifungal potential of the as-synthesised $\text{ZnCe}_x\text{Fe}_{2-x}\text{O}_4$ nanoparticles ($X = 0.0, 0.02, 0.04, 0.06, \text{ and } 0.08$) and Ebselen against the pathogenic unicellular fungi *Candida albicans* ATCC 90028, and *Candida tropicalis* ATCC 90159 was also examined. The inoculums of the yeast cells were set from $1 \text{ to } 4 \times 10^7$ CFU/mL. Nystatin (NS) and amoxicillin (AX) were used as standard antibiotics. AX is similar to penicillin in its bactericidal action against susceptible bacteria during the stage of active multiplication. It acts through the inhibition of cell wall biosynthesis that leads to the death of the bacteria [142]. NS is an antifungal that is both fungistatic and fungicidal in vitro against a wide-variety of yeasts and yeast-like fungi. It exerts its antifungal effects via disruption of the fungal cell membrane [143].

The investigation of minimum inhibitory concentrations (MIC) was performed using a serially diluted Luria–Bertani (LB) broth of the synthesised NPs. A positive control consisting of the microorganism and the nutrient, a negative control consisting of the nutrient alone, and the $\text{ZnCe}_x\text{Fe}_{2-x}\text{O}_4$ nanoparticles ($X = 0.0, 0.02, 0.04, 0.06, \text{ and } 0.08$) and Ebselen (beginning with 0.1 mg/mL concentration; 100 ppm) were used. The MIC was defined following 24 h of incubation at 37°C . The inocula of the bacteria were $3\text{--}5 \times 10^8$ CFU/mL and $2\text{--}3 \times 10^7$ CFU/mL for *Candida* species. The MICs were defined using enzyme-linked immunosorbent assays (ELISA) plates at 600 nm .

3.4. Antibiofilm Activities of $\text{ZnCe}_x\text{Fe}_{2-x}\text{O}_4$ Nanoparticles ($X = 0.0 \text{ and } 0.06$)

Qualitative measurement of biofilm inhibition was carried out as described by Christensen et al. [144]. The extent of the biofilm that formed at the tube wall in the absence and presence of the synthesised $\text{ZnCe}_x\text{Fe}_{2-x}\text{O}_4$ nanoparticles was measured. The antibiofilm activity of the as-synthesised $\text{ZnCe}_x\text{Fe}_{2-x}\text{O}_4$ nanoparticles at $10.0 \mu\text{g/mL}$ was measured in the selected bacteria and *Candida* spp. and compared with the non-treated control.

Five millilitres of the nutrient broth medium was added to each tube, and the bacteria and yeast were inoculated after adjusting 0.5 McFarland to $1\text{--}2.5 \times 10^8$ CFU/mL. The tubes were incubated at $37.0 \pm 0.5^\circ\text{C}$ for 24 h. The contents of the control and treated tubes were removed, mixed with phosphate buffered saline (PBS; pH 7.0), and desiccated. The bacterial and yeast cells that adhered to the tube walls were fixed with 5 mL sodium acetate (3.0%) for about 15 min and then rinsed with de-ionised water.

The biofilms that developed inside the tubes were stained with 15 mL of 0.1% crystal violet (CV) and washed with de-ionised water to remove the rest of the CV. For the semi-quantitative estimation of the antibiofilm activity, 5 mL of absolute ethanol was added to dissolve the stained bacterial and yeast biofilms. The optical density (O.D.) of the stained bacterial and yeast biofilms with CV was examined using a UV-Vis spectrophotometer at 570.0 nm . The percentage of inhibition bacterial and yeast biofilms was estimated using Equation (1):

$$\text{Biofilm inhibition \%} = (\text{O.D.}_{\text{Control sample}} - \text{O.D.}_{\text{treated sample}}) / \text{O.D.}_{\text{Control sample}} \times 100 \quad (1)$$

3.5. Reaction Mechanism Using SEM Analysis

The bacterial cells that were determined by the antibiofilm tests to be sensitive were cleaned with PBS three times and fixed using 3.5% glutaraldehyde solution. The microbial cells were repeatedly rinsed with PBS and dried using different concentrations of ethyl alcohol: 30%, 50%, 70%, 90%, and 100% for 15 min at $27 \pm 2^\circ\text{C}$. The prepared samples were then fixed on an aluminium substrate for SEM/EDX analysis. The morphological features of the control and the $\text{ZnCe}_x\text{Fe}_{2-x}\text{O}_4$ nanoparticles ($X = 0.06$)-treated bacteria were examined using SEM.

3.6. Effect of the Synthesised Nanocomposites on Protein Leakage from Bacterial Cell Membranes

To confirm the SEM reaction mechanism of the synthesised nanocomposites against the microbial cell, the protein leakage assay has been conducted [145]. Pure 18 hr bacterial culture was set at 0.5 McFarland ($1\text{--}3 \times 10^8$ CFU/mL), and $100 \mu\text{L}$ was injected into 10 mL of the nutrient broth, including well-sonicated and dispersed $\text{ZnCe}_x\text{Fe}_{2-x}\text{O}_4$ nanoparticles

($X = 0$, and 0.06) at various concentrations (0.125, 0.25, 0.5, and 1.0 mg/mL). Nanocomposites-free broth injected with culture has been used as the control. All the treated samples were incubated at 37 °C for 5 h and then centrifuged at 15 min at 5500 rpm [146]. For the different samples, 100 μ L supernatant was combined with 1 mL of Bradford reagent. Optical density was measured at 595 nm for 10 min of dark incubation [146].

3.7. Cell Lines, Treatment, and Reagents

Human breast cancer (MDA-MB-231; triple negative basal B subtype), colon cancer (HT-29; colorectal adenocarcinoma), and Vero kidney epithelial (normal epithelial cells derived from the African green monkey) cell lines provided via the American Type Culture Collection (Rockville, MD, USA) were bought from the Tissue Culture Unit in the Holding Company for Biological Products and Vaccines (VACSERA-Giza, Egypt). Ebselen (Eb) was purchased from Sigma-Aldrich (St. Louis, MO, USA). For western blot analysis, antibodies against Beclin-1 (CAT# ab137161), LC3B (CAT#192890), and P62 (CAT# ab91526) were obtained from Abcam. t-STAT-1 (rabbit polyclonal antibody, PA1-41383), p-STAT-1^(Tyr701) (rabbit polyclonal antibody, CAT# 44-376G), t-STAT-6 (mouse monoclonal antibody, CAT#MA5-15659), p-STAT-6^(Tyr641) (mouse monoclonal antibody, CAT#700247), t-ERK1/2 (mouse monoclonal antibody, CAT# 14-9108-82), p-ERK1/2^(Thr202,Tyr204) (mouse monoclonal antibody, CAT# 14-9109-82), t-JNK (rabbit polyclonal antibody, CAT#51151-1-AP), p-JNK^(Thr183,Tyr185) (mouse monoclonal antibody, CAT#MA5-15228), and PARP-1 (mouse monoclonal antibody, CAT#436400) were obtained from ThermoFisher Scientific. ELISA kits for the determination of INF- γ (CAT# MBS824507), TNF- α (CAT# MBS175820), IL-4 (CAT# MBS268288), MDA (CAT# MBS728071), GSH (CAT# MBS042904), GPX (CAT# MBS284182), SOD (CAT# MBS005068), and CAT (CAT#MBS165657) were purchased from MyBioSource (San Diego, CA, USA). ELISA kits for assaying IL-10 (CAT# ab100549), human active caspase-3 (Ser29) (CAT# ab181418), BCL-2 (CAT# ab119506), HIF-1 α (CAT# ab82832), and NRF-2 (CAT# ab207223) were obtained from Abcam, and NF- κ B (CAT# 85-86081-11) was provided by ThermoFisher Scientific. The other chemicals and reagents used in this study were purchased from Sigma-Aldrich (St Louis, MO, USA).

3.8. Culture Media

The cell lines MDA-MB-231, HT-29, and Vero were maintained in DMEM media supplemented with streptomycin (100 mg/mL), penicillin (100 units/mL), and heat-inactivated fetal bovine serum (10%) in a humidity of CO₂ (5% *v/v*) and a temperature of 37 °C.

3.9. Subculture of Cell Lines

The cultures were viewed under an inverted microscope (CKX41; Olympus, Japan), to estimate the degree of confluence and to verify the lack of bacterial and fungal contaminants. Cells of MDA-MB-231, HT-29, and Vero were washed with PBS free of Ca²⁺/Mg²⁺, with a volume equivalent to half of the volume of the culture medium. Trypsin/EDTA was then added at 1 mL/25 cm² of surface area, and the flask rotated to merge the trypsin/EDTA with the monolayer. The flasks were incubated for 10 min. Finally, an inverted microscope was used to confirm that the cells had detached.

3.10. Sulforhodamine B (SRB) Assay

The cytotoxicity screening of Eb at various concentrations ranging from 0–100 μ M and Ce nanoparticles at 10 and 100 μ M Ce³⁺ ranging from 0–0.08 in ZnCe_xFe_{2-x}O₄ nanoparticles individually on the MDA-MB-231 and HT-29 cell lines was assessed using SRB assays as described by Vichai and Kirtikara [147]. In a 96-well plate, aliquots of 100 μ L of cell suspension (5×10^3 cells) were incubated in complete media for 24 h. Then, the cells were treated with another aliquot of 100 μ L of medium containing the Eb and Ce nanoparticles at different concentrations. After 72 h of exposure, cells were fixed by replacing the media with 150 μ L of 10% TCA and incubating them at 4 °C for 1 h. The TCA solution was removed, and the cells were washed five times with distilled water. Aliquots of 70 μ L

SRB solution (0.4% *w/v*) were added, and the cells were incubated in the dark at room temperature for 10 min. Plates were washed three times with 1% acetic acid and allowed to air-dry overnight. Then, 150 μ L of TRIS (10 mM) was added to dissolve the protein-bound SRB stain. The absorbance was measured at 540 nm using a BMG LABTECH®-FLUOstar Omega microplate reader. The half-maximal inhibitory concentration (IC_{50}) of Eb or Ce in $ZnCe_xFe_{2-x}O_4$ nanoparticles was investigated individually in the MDA-MB-231 and HT-29 cell lines. Then, the Eb and Ce in $ZnCe_xFe_{2-x}O_4$ nanoparticles were used in conjunction to examine their cytotoxicity profiles on the MDA-MB-231 and HT-29 cell lines (based on the IC_{50} identified for each one individually previously) to obtain the final IC_{50} of each nanocomposite on the MDA-MB-231 and HT-29 cell lines. Afterwards, these two final IC_{50} were examined for their cytotoxicity profiles on Vero cells.

3.11. Irradiation

The cultured MDA-MB-231 and HT-29 cells were irradiated with a Canadian gamma cell-40 exactor, (^{137}Cs) (Best Theratronics Gamma cell 40 Exactor, Ottawa, ON, Canada) at the NCRRT (Cairo, Egypt) at a dose of 4 Gy, with a dose rate of 0.427 Gy/min.

3.12. Culture Models and Experimental Protocol

In the current study, the cultures of MDA-MB-231 and HT-29 cells were divided into two sets, as follows:

1. The MDA-MB-231 cell line was divided into four groups. The MDA group: untreated MDA-MB-231 cells line served as control; the MDA + Eb-ZFO group: MDA-MB-231 cells treated with Ebselen (Eb) and $ZnFe_2O_4$ nanoparticles (ZFO); the MDA + IR group: MDA-MB-231 cells exposed to ionising radiation; and the MDA + Eb-ZFO + IR group: MDA-MB-231 cells treated with Eb-ZFO and exposed to IR.
2. The HT-29 cell line was divided into four groups. The HT-29 group: untreated HT-29 cells served as a control; the HT-29 + Eb-ZCFO group: HT-29 cells treated with Eb and $ZnCe_{0.06}Fe_{1.94}O_4$ nanoparticles (ZCFO); the HT-29 + IR group: HT-29 cells exposed to ionising radiation; and the HT-29 + Eb-ZCFO + IR group: HT-29 cells treated with Eb-ZCFO and exposed to IR.

3.13. Cell-Cycle Analysis and Apoptosis Detection Using Flow Cytometry

MDA-MB-231 and HT-29 cells were stained with propidium iodide (PI) (Sigma-Aldrich) for cell-cycle analysis, or with PI and annexin V-FITC (BD Biosciences) for the detection of apoptosis. The distribution of cells in the different phases of the cell cycle, based on the differences in DNA content, and the apoptosis positive cells were determined using flow cytometry with a FACS Calibur flow cytometer (BD Biosciences). MDA-MB-231 and HT-29 cells were seeded at a density of 5×10^5 /mL in six-well tissue culture plates. After the cells adhered, the MDA-MB-231 cells were treated with Eb- $ZnFe_2O_4$, and the HT-29 cells were treated with $ZnCe_{0.06}Fe_{1.94}O_4$ at the concentrations determined from the IC_{50} obtained from the cytotoxicity screening. Cells were exposed to 4Gy irradiation (either with or without pre-treatment) and cultured for 24 h. The cells were harvested by trypsinisation, washed with PBS, and fixed with pre-chilled 70% ethyl alcohol at 4 °C overnight. The cells were then again washed with PBS and incubated with RNase A for 30 min, followed by staining with 400 μ L PI (50 μ g/mL PI, 0.1% Triton X-100, and 0.1% sodium citrate in PBS) for 30 min at room temperature in the dark. The percentage of cells in each phase of the cell cycle was calculated using an Accuri C6Flow Cytometer (BD Biosciences, Mountain View, CA, USA). For the detection of apoptosis and necrosis, the cells were harvested using trypsinisation, washed with PBS, and resuspended in 0.5 mL of binding buffer containing 0.5 μ g/mL Annexin-V-FITC and 5 μ g/mL PI for 30 min in the dark, according to the protocol supplied with the FITC Annexin V apoptosis detection kit (CAT# ab139418, Abcam) and the percent of apoptotic and necrotic cells was assessed using a BD Flow Cytometer (BD Biosciences, USA).

3.14. Determination of Intracellular Hydrogen Peroxide (H_2O_2)

The concentration of intracellular H_2O_2 was measured using colorimetric assay kits (ICT Technologies, CAT#9132).

3.15. Quantification of Pro- and Anti-Inflammatory Cytokines, Pro- and Anti-Apoptotic, and Oxidative Stress Markers by ELISA

Levels of INF- γ , TNF- α , IL-4, IL-10, HIF-1, Caspase-3, BCL-2, NF- κ B NRF-2, MDA, GSH, GPX, SOD, and CAT were determined according to the protocols accompanying the ELISA kits.

3.16. Western Blot Analysis

In a cold homogeniser tube, MDA-MB-231 and HT-29 cells lines were homogenised using a homogenisation lysis buffer (Sigma–Aldrich, St. Louis, MD, USA) according to the method published by [148]. The lysate was centrifuged at $8678 \times g$ for 20 min at $-4\text{ }^\circ\text{C}$, and the protein concentration was measured using BCA protein kits (Thermo Fisher Scientific). Protein aliquots of $7.5\text{ }\mu\text{g}$ from each sample were denatured and loaded onto 8% sodium dodecyl sulphate-polyacrylamide gel electrophoresis, (SDS-PAGE) and transferred to a nitrocellulose membrane (Amersham Bioscience, Piscataway, NJ, USA) using a semidry transfer apparatus (Bio-Rad, Hercules, CA, USA). The membranes were then incubated at $4\text{ }^\circ\text{C}$ with 5% non-fat milk blocking buffer, which consisted of Tris–HCl (10 mmol/L^{-1} —pH 7.4), Tris-buffered saline with Tween-20 (TBST) (0.05%), and NaCl (150 mmol/L^{-1}). The membranes were then washed with TBST and incubated overnight with a 1:1000 dilution of Beclin-1, LC3B II, P62, total and phosphorylated STAT-1 and STAT-6, ERK1/2, JNK, and PARP on a roller shaker at $4\text{ }^\circ\text{C}$. Immunoblotting was performed using the indicated primary antibody and the appropriate horseradish peroxidase (HRP), which was conjugated with goat immunoglobulin (Amersham Biosciences, Piscataway, NJ, USA). Using Amersham[®] detection kits, chemiluminescence detection was performed according to the manufacturer’s protocols and exposed to X-ray film. The protein levels obtained were estimated using β -actin as a housekeeping arbitrary unit [149].

3.17. Statistics

In the analysis of antimicrobial and antibiofilm data, the results were analysed using the least significant difference (LSD) and one-way analysis of variance (ANOVA) followed by Duncan’s multiple range using SPSS version 15. In the analysis of anticancer data, the data were analysed using ANOVA followed by Tukey multiple comparison. Kolmogorov–Smirnov and Bartlett’s tests were used to evaluate the normality of the distribution and the homology of the variance, respectively. Statistical analyses were performed using GraphPad Prism, Version 6 (GraphPad Software, San Diego, CA, USA, www.graphpad.com). All tests were two-tailed, and p -values < 0.05 were considered to be statistically significant.

4. Conclusions

A cost-effective sol–gel method was used to prepare ZFO or ZCFO ferrites, which were later conjugated with Eb. The antimicrobial and antibiofilm were proved against a wide array of pathogens. Moreover, the antiproliferative, antioxidant, and anti-inflammatory abilities of the prepared systems against human breast cancer (MDA-MB-231) and colon cancer (HT-29) cell lines were studied in detail. XRD analysis confirmed the chemical structure and crystallinity of the prepared samples, which possessed Fd3 m space groups. The chemical composition and purity of the materials were confirmed by EDX and FTIR analyses. Finally, the external morphology and the porous nature of the prepared samples were investigated using SEM analysis. The antimicrobial activity of the synthesised $ZnCe_xFe_{2-x}O_4$ increased as the x value increased. The highest ZOI of *S. aureus* was observed when $X = 0.06$ in $ZnCe_xFe_{2-x}O_4$ and slightly decreased when $X = 0.08$. In the case of *C. albicans*, the active sample was $ZnCe_xFe_{2-x}O_4$ with $X = 0.06$. The semi-quantitative determination of the inhibition percentage was estimated following the elimination of

CV-stained biofilms, and the results showed the percentage of inhibition for *S. aureus* (92.73%), *P. mirabilis* (79.54%), and *C. albicans* (90.18%) following the addition of 10.0 µg/mL $ZnCe_xFe_{2-x}O_4$; $X = 0.06$. After treatment with $ZnCe_xFe_{2-x}O_4$; $X = 0.06$, morphological differences in *S. aureus* were apparent, and a complete lysis of bacterial cells, with a concomitant decrease in the viable number, and ultimately the growth of biofilm was inhibited. These results reflected the antimicrobial activity of Ce addition in the synthesised $ZnCe_xFe_{2-x}O_4$; $X = 0.06$. Overall, we conclude that Eb-ZFO or Eb-ZCFO with or without IR affected the fine-tuning of intracellular ROS signalling in MDA-MB-231 and HT-29 cells by reducing ROS production through altering the antioxidant defence machinery associated with the deactivation of the ERK1/2, JNK, NRF-2, TNF- α /NF- κ B, INF- γ /STAT-1, and IL-4/STAT-6 signalling pathways. The mechanism of Eb-ZFO in the MDA-MB-231 cell line depends primarily on the Eb antioxidant/anti-inflammatory capability and the cytotoxicity profile of the ZnO-NPs. However, the antitumour activity of Eb-ZCFO in the HT-29 cell line depends on Ce nanoparticles as ROS scavengers and Eb as an immune modulator of the TME.

Supplementary Materials: Supplementary Materials are available online at <https://www.mdpi.com/article/10.3390/ijms221810171/s1>.

Author Contributions: M.K.A.-R.: experiments design, data acquisition, analysis, manuscript writing, and manuscript revision and editing. N.M.T.: experiments design, data acquisition, analysis, manuscript writing, and manuscript revision and editing. M.I.A.A.M.: synthetic experiments design, characterization methods, data acquisition, analysis, manuscript writing, and manuscript revision and editing. M.A.E.: characterization methods, data analysis, manuscript writing, and editing. G.K.: manuscript revision and editing. A.M.: manuscript revision and editing. A.H.A.: manuscript revision and editing. A.I.E.-B.: manuscript revision and editing. G.S.E.-S.: microbiology experiments design, characterization methods, data acquisition, analysis, manuscript writing, and manuscript revision and editing. All authors have read and agreed to the published version of the manuscript.

Funding: This study was partly funded by Japan Society for Promotion of Science (JSPS) KAKENHI Grant No. 18H03841 and No. 21K18823.

Institutional Review Board Statement: Not applicable.

Informed Consent Statement: Not applicable.

Data Availability Statement: Not applicable.

Acknowledgments: We acknowledge BioRender for posting the tools free of charge to allow the creation of professional science figures in minutes that we have used to create Figure 8.

Conflicts of Interest: The authors declare no competing interests as defined by Nature Research or other interests that might be perceived to influence the results and/or discussion reported in this paper.

References

- Supriya, S.; Kumar, S.; Kar, M. Electrical Properties and Dipole Relaxation Behavior of Zinc-Substituted Cobalt Ferrite. *J. Electron. Mater.* **2017**, *46*, 6884–6894. [\[CrossRef\]](#)
- Rani, R.; Kumar, G.; Batoor, K.M.; Singh, M. Influence of temperature on the electric, dielectric and AC conductivity properties of nano-crystalline zinc substituted cobalt ferrite synthesized by solution combustion technique. *Appl. Phys. A* **2014**, *115*, 1401–1407. [\[CrossRef\]](#)
- Sinfrônio, F.; Santana, P.; Coelho, S.; Silva, F.; de Menezes, A.; Sharma, S. Magnetic and structural properties of cobalt-and zinc-substituted nickel ferrite synthesized by microwave-assisted hydrothermal method. *J. Electron. Mater.* **2017**, *46*, 1145–1154. [\[CrossRef\]](#)
- Rani, B.J.; Mageswari, R.; Ravi, G.; Ganesh, V.; Yuvakkumar, R. Physico-chemical properties of pure and zinc incorporated cobalt nickel mixed ferrite ($Zn_xCo_{0.005-x}Ni_{0.005}Fe_2O_4$, where $x = 0, 0.002, 0.004$ M) nanoparticles. *J. Mater. Sci. Mater. Electron.* **2017**, *28*, 16450–16458. [\[CrossRef\]](#)
- Sodaee, T.; Ghasemi, A.; Razavi, R.S. Cation distribution and microwave absorptive behavior of gadolinium substituted cobalt ferrite ceramics. *J. Alloy. Compd.* **2017**, *706*, 133–146. [\[CrossRef\]](#)
- Vaithyanathan, V.; Ugendar, K.; Arout Chelvane, J.; Kamala Bharathi, K.; Inbanathan, S.S.R. Structural and magnetic properties of Sn and Ti doped Co ferrite. *J. Magn. Magn. Mater.* **2015**, *382*, 88–92. [\[CrossRef\]](#)

7. Pawar, R.A.; Patange, S.M.; Tamboli, Q.Y.; Ramanathan, V.; Shirsath, S.E. Spectroscopic, elastic and dielectric properties of Ho³⁺ substituted Co-Zn ferrites synthesized by sol-gel method. *Ceram. Int.* **2016**, *42*, 16096–16102. [[CrossRef](#)]
8. Panda, R.; Muduli, R.; Jayarao, G.; Sanyal, D.; Behera, D. Effect of Cr³⁺ substitution on electric and magnetic properties of cobalt ferrite nanoparticles. *J. Alloy. Compd.* **2016**, *669*, 19–28. [[CrossRef](#)]
9. Farid, H.M.T.; Ahmad, I.; Bhatti, K.; Ali, I.; Ramay, S.M.; Mahmood, A. The effect of praseodymium on Cobalt-Zinc spinel ferrites. *Ceram. Int.* **2017**, *43*, 7253–7260. [[CrossRef](#)]
10. Ashour, A.H.; El-Batal, A.I.; Maksoud, M.I.A.A.; El-Sayyad, G.S.; Labib, S.; Abdeltwab, E.; El-Okr, M.M. Antimicrobial activity of metal-substituted cobalt ferrite nanoparticles synthesized by sol-gel technique. *Particuology* **2018**, *40*, 141–151. [[CrossRef](#)]
11. Abdel Maksoud, M.I.A.A.; El-Sayyad, G.S.; Ashour, A.H.; El-Batal, A.I.; Abd-Elmonem, M.S.; Hendawy, H.A.M.; Abdel-Khalek, E.K.; Labib, S.; Abdeltwab, E.; El-Okr, M.M. Synthesis and characterization of metals-substituted cobalt ferrite [M_xCo_(1-x)Fe₂O₄; (M = Zn, Cu and Mn; x = 0 and 0.5)] nanoparticles as antimicrobial agents and sensors for Anagrelide determination in biological samples. *Mater. Sci. Eng. C* **2018**, *92*, 644–656. [[CrossRef](#)] [[PubMed](#)]
12. Maksoud, M.I.A.A.; El-Sayyad, G.S.; Ashour, A.H.; El-Batal, A.I.; Elsayed, M.A.; Gobara, M.; El-Khawaga, A.M.; Abdel-Khalek, E.K.; El-Okr, M.M. Antibacterial, antibiofilm, and photocatalytic activities of metals-substituted spinel cobalt ferrite nanoparticles. *Microb. Pathog.* **2019**, *127*, 144–158. [[CrossRef](#)] [[PubMed](#)]
13. Weissman, S.; S. Brow, J.; Gonzalez, H.H.; Weingarten, M.J.; Rosenblatt, S.; Mehta, T.I.; Thaker, R.; Krzyzak, M.; Saleem, S. Diagnosis of Primary Colorectal Carcinoma with Primary Breast Cancer: Associations or Connections? *Cureus* **2019**, *11*, e4287. [[CrossRef](#)] [[PubMed](#)]
14. Casey, S.C.; Amedei, A.; Aquilano, K.; Azmi, A.S.; Benencia, F.; Bhakta, D.; Bilsland, A.E.; Boosani, C.S.; Chen, S.; Ciriolo, M.R. Cancer prevention and therapy through the modulation of the tumor microenvironment. In *Seminars in Cancer Biology*; Elsevier: Amsterdam, The Netherlands, 2015; pp. S199–S223.
15. Wang, J.-S.; Wang, H.-J.; Qian, H.-L. Biological effects of radiation on cancer cells. *Mil. Med. Res.* **2018**, *5*, 1–10. [[CrossRef](#)]
16. Lee, S.H.; Jun, B.-H. Silver nanoparticles: Synthesis and application for nanomedicine. *Int. J. Mol. Sci.* **2019**, *20*, 865. [[CrossRef](#)]
17. Johnson, J.; Chow, Z.; Napier, D.; Lee, E.; Weiss, H.L.; Evers, B.M.; Rychahou, P. Targeting PI3K and AMPK α Signaling Alone or in Combination to Enhance Radiosensitivity of Triple Negative Breast Cancer. *Cells* **2020**, *9*, 1253. [[CrossRef](#)]
18. Speers, C.W.; Chandler, B.; Zhao, S.; Liu, M.; Wilder-Romans, K.; Olsen, E.; Nyati, S.; Rae, J.M.; Hayes, D.F.; Spratt, D.E. Radiosensitization of androgen receptor (AR)-positive triple-negative breast cancer (TNBC) cells using seviteronel (SEVI). In *A Selective CYP17 Lyase and AR Inhibitor*; American Society of Clinical Oncology: Alexandria, VA, USA, 2017.
19. Eriksson, P.; Tal, A.A.; Skallberg, A.; Brommesson, C.; Hu, Z.; Boyd, R.D.; Olovsson, W.; Fairley, N.; Abrikosov, I.A.; Zhang, X. Cerium oxide nanoparticles with antioxidant capabilities and gadolinium integration for MRI contrast enhancement. *Sci. Rep.* **2018**, *8*, 1–12.
20. Kaczor-Keller, K.B.; Pawlik, A.; Scianowski, J.; Pacuła, A.; Obieziurska, M.; Marcheggiani, F.; Cirilli, I.; Tiano, L.; Antosiewicz, J. In vitro anti-prostate cancer activity of two ebselen analogues. *Pharmaceuticals* **2020**, *13*, 47. [[CrossRef](#)]
21. Zhang, L.; Gu, F.; Chan, J.; Wang, A.; Langer, R.; Farokhzad, O. Clinical Pharmacol. *Therapeutics* **2008**, *83*, 761.
22. Dhall, A.; Self, W. Cerium oxide nanoparticles: A brief review of their synthesis methods and biomedical applications. *Antioxidants* **2018**, *7*, 97. [[CrossRef](#)]
23. Reyes-Rodríguez, P.Y.; Cortés-Hernández, D.A.; Escobedo-Bocardo, J.C.; Almanza-Robles, J.M.; Sánchez-Fuentes, H.J.; Jasso-Terán, A.; De León-Prado, L.E.; Méndez-Nonell, J.; Hurtado-López, G.F. Structural and magnetic properties of Mg-Zn ferrites (Mg_{1-x}Zn_xFe₂O₄) prepared by sol-gel method. *J. Magn. Magn. Mater.* **2017**, *427*, 268–271. [[CrossRef](#)]
24. Ghodake, U.; Kambale, R.C.; Suryavanshi, S. Effect of Mn²⁺ substitution on structural, electrical transport and dielectric properties of Mg-Zn ferrites. *Ceram. Int.* **2017**, *43*, 1129–1134. [[CrossRef](#)]
25. Alshahrani, B.; ElSaeedy, H.I.; Fares, S.; Korna, A.H.; Yakout, H.A.; Maksoud, M.I.A.A.; Fahim, R.A.; Gobara, M.; Ashour, A.H. The effect of Ce³⁺ doping on structural, optical, ferromagnetic resonance, and magnetic properties of ZnFe₂O₄ nanoparticles. *J. Mater. Sci. Mater. Electron.* **2020**. [[CrossRef](#)]
26. Murugesan, C.; Chandrasekaran, G. Impact of Gd³⁺ substitution on the structural, magnetic and electrical properties of cobalt ferrite nanoparticles. *RSC Adv.* **2015**, *5*, 73714–73725. [[CrossRef](#)]
27. Yadav, R.S.; Havlica, J.; Masilko, J.; Kalina, L.; Wasserbauer, J.; Hajdúchová, M.; Enev, V.; Kuřitka, I.; Kožáková, Z. Impact of Nd³⁺ in CoFe₂O₄ spinel ferrite nanoparticles on cation distribution, structural and magnetic properties. *J. Magn. Magn. Mater.* **2016**, *399*, 109–117. [[CrossRef](#)]
28. Abbas, M.K.; Khan, M.A.; Mushtaq, F.; Warsi, M.F.; Sher, M.; Shakir, I.; Aboud, M.F.A. Impact of Dy on structural, dielectric and magnetic properties of Li-Tb-nanoferrites synthesized by micro-emulsion method. *Ceram. Int.* **2017**, *43*, 5524–5533. [[CrossRef](#)]
29. Bahhar, S.; Lemziouka, H.; Boutahar, A.; Bioud, H.; Lassri, H.; Hlil, E. Influence of La³⁺ site substitution on the structural, magnetic and magnetocaloric properties of ZnFe_{2-x}LaxO₄ (x = 0.00, 0.001, 0.005 and 0.01) spinel zinc ferrites. *Chem. Phys. Lett.* **2019**, *716*, 186–191. [[CrossRef](#)]
30. Amer, M.; Matsuda, A.; Kawamura, G.; El-Shater, R.; Meaz, T.; Fakhry, F. Characterization and structural and magnetic studies of as-synthesized Fe²⁺Cr_xFe_(2-x)O₄ nanoparticles. *J. Magn. Magn. Mater.* **2017**, *439*, 373–383. [[CrossRef](#)]
31. Amer, M.; Meaz, T.; Mostafa, A.; El-Ghazally, H. Structural and physical properties of the nano-crystalline Al-substituted Cr-Cu ferrite. *J. Magn. Magn. Mater.* **2013**, *343*, 286–292. [[CrossRef](#)]

32. Kadam, R.H.; Alone, S.T.; Mane, M.L.; Biradar, A.R.; Shirsath, S.E. Phase evaluation of Li⁺ substituted CoFe₂O₄ nanoparticles, their characterizations and magnetic properties. *J. Magn. Magn. Mater.* **2014**, *355*, 70–75. [[CrossRef](#)]
33. Kounsalye, J.S.; Humbe, A.V.; Chavan, A.R.; Jadhav, K. Rietveld, cation distribution and elastic investigations of nanocrystalline Li_{0.5+0.5x}ZrxFe_{2.5-1.5x}O₄ synthesized via sol-gel route. *Phys. B Condens. Matter* **2018**, *547*, 64–71. [[CrossRef](#)]
34. Maksoud, M.I.A.A.; El-ghandour, A.; El-Sayyad, G.S.; Awed, A.S.; Fahim, R.A.; Atta, M.M.; Ashour, A.H.; El-Batal, A.I.; Gobara, M.; Abdel-Khalek, E.K.; et al. Tunable structures of copper substituted cobalt nanoferrites with prospective electrical and magnetic applications. *J. Mater. Sci. Mater. Electron.* **2019**, *30*, 4908–4919. [[CrossRef](#)]
35. Abdel Maksoud, M.I.A.; El-ghandour, A.; El-Sayyad, G.S.; Awed, A.S.; Ashour, A.H.; El-Batal, A.I.; Gobara, M.; Abdel-Khalek, E.K.; El-Okr, M.M. Incorporation of Mn²⁺ into cobalt ferrite via sol-gel method: Insights on induced changes in the structural, thermal, dielectric, and magnetic properties. *J. Sol.-Gel. Sci. Technol.* **2019**, *90*, 631–642. [[CrossRef](#)]
36. Zipare, K.; Bandgar, S.; Shahane, G. Effect of Dy-substitution on structural and magnetic properties of MnZn ferrite nanoparticles. *J. Rare Earths* **2018**, *36*, 86–94. [[CrossRef](#)]
37. Hafezi, M.; Rostami, M.; Hosseini, A.; Rahimi-Nasrabadi, M.; Fasihi-Ramandi, M.; Badiiei, A.; Ahmadi, F. Cur-loaded ZnFe₂O₄@mZnO@N-GQDs biocompatible nano-carriers for smart and controlled targeted drug delivery with pH-triggered and ultrasound irradiation. *J. Mol. Liq.* **2021**, *322*, 114875. [[CrossRef](#)]
38. Borthakur, S.; Saikia, L. ZnFe₂O₄@g-C₃N₄ nanocomposites: An efficient catalyst for Fenton-like photodegradation of environmentally pollutant Rhodamine B. *J. Environ. Chem. Eng.* **2019**, *7*, 103035. [[CrossRef](#)]
39. Xu, R.; Wu, C.; Xu, H. Particle size and zeta potential of carbon black in liquid media. *Carbon* **2007**, *45*, 2806–2809. [[CrossRef](#)]
40. Soema, P.C.; Willems, G.-J.; Jiskoot, W.; Amorij, J.-P.; Kersten, G.F. Predicting the influence of liposomal lipid composition on liposome size, zeta potential and liposome-induced dendritic cell maturation using a design of experiments approach. *Eur. J. Pharm. Biopharm.* **2015**, *94*, 427–435. [[CrossRef](#)]
41. Ravindran, S.; Williams, M.; Ward, R.; Gillies, G. Understanding how the properties of whey protein stabilized emulsions depend on pH, ionic strength and calcium concentration, by mapping environmental conditions to zeta potential. *Food Hydrocoll.* **2018**, *79*, 572–578. [[CrossRef](#)]
42. Abdel Maksoud, M.I.A.; El-Sayyad, G.S.; El-Khawaga, A.M.; Abd Elkodous, M.; Abokhadra, A.; Elsayed, M.A.; Gobara, M.; Soliman, L.I.; El-Bahnasawy, H.H.; Ashour, A.H. Nanostructured Mg substituted Mn-Zn ferrites: A magnetic recyclable catalyst for outstanding photocatalytic and antimicrobial potentials. *J. Hazard. Mater.* **2020**, *399*, 123000. [[CrossRef](#)] [[PubMed](#)]
43. Franks, K.; Kestens, V.; Braun, A.; Roebben, G.; Linsinger, T.P. Non-equivalence of different evaluation algorithms to derive mean particle size from dynamic light scattering data. *J. Nanoparticle Res.* **2019**, *21*, 1–10. [[CrossRef](#)]
44. El-Sayyad, G.S.; El-Bastawisy, H.S.; Gobara, M.; El-Batal, A.I. Gentamicin-Assisted Mycogenic Selenium Nanoparticles Synthesized Under Gamma Irradiation for Robust Reluctance of Resistant Urinary Tract Infection-Causing Pathogens. *Biol. Trace Elem. Res.* **2020**, *195*, 323–342. [[CrossRef](#)] [[PubMed](#)]
45. Wong, C.W.; Chan, Y.S.; Jeevanandam, J.; Pal, K.; Bechelany, M.; Abd Elkodous, M.; El-Sayyad, G.S. Response Surface Methodology Optimization of Mono-dispersed MgO Nanoparticles Fabricated by Ultrasonic-Assisted Sol-Gel Method for Outstanding Antimicrobial and Antibiofilm Activities. *J. Clust. Sci.* **2020**, *31*, 367–389. [[CrossRef](#)]
46. El-Batal, A.I.; El-Sayyad, G.S.; Al-Hazmi, N.E.; Gobara, M. Antibiofilm and Antimicrobial Activities of Silver Boron Nanoparticles Synthesized by PVP Polymer and Gamma Rays Against Urinary Tract Pathogens. *J. Clust. Sci.* **2019**, *30*, 947–964. [[CrossRef](#)]
47. Awed, A.S.; El-Sayyad, G.S.; El-ghandour, A.; Hameed, M.F.O.; Abdel Maksoud, M.I.A.; El-Batal, A.I.; Obayya, S.S.A. Unveiling Antimicrobial Activity of Metal Iodide (CuI, AgI, and PbI₂) Nanoparticles: Towards Biomedical Surfaces Applications. *J. Clust. Sci.* **2021**, *32*, 1–16. [[CrossRef](#)]
48. Abd Elkodous, M.; El-Sayyad, G.S.; Youssry, S.M.; Nada, H.G.; Gobara, M.; Elsayed, M.A.; El-Khawaga, A.M.; Kawamura, G.; Tan, W.K.; El-Batal, A.I. Carbon-dot-loaded CoxNi_{1-x}Fe₂O₄; x = 0.9/SiO₂/TiO₂ nanocomposite with enhanced photocatalytic and antimicrobial potential: An engineered nanocomposite for wastewater treatment. *Sci. Rep.* **2020**, *10*, 1–22.
49. Abd Elkodous, M.; El-Sayyad, G.S.; Abdelrahman, I.Y.; El-Bastawisy, H.S.; Mosallam, F.M.; Nasser, H.A.; Gobara, M.; Baraka, A.; Elsayed, M.A.; El-Batal, A.I. Therapeutic and diagnostic potential of nanomaterials for enhanced biomedical applications. *Colloids Surf. B Biointerfaces* **2019**, *180*, 411–428. [[CrossRef](#)]
50. El-Batal, A.I.; Nada, H.G.; El-Behery, R.R.; Gobara, M.; El-Sayyad, G.S. Nystatin-mediated bismuth oxide nano-drug synthesis using gamma rays for increasing the antimicrobial and antibiofilm activities against some pathogenic bacteria and Candida species. *RSC Adv.* **2020**, *10*, 9274–9289. [[CrossRef](#)]
51. Pal, K.; Si, A.; El-Sayyad, G.S.; Elkodous, M.A.; Kumar, R.; El-Batal, A.I.; Kralj, S.; Thomas, S. Cutting edge development on graphene derivatives modified by liquid crystal and CdS/TiO₂ hybrid matrix: Optoelectronics and biotechnological aspects. *Crit. Rev. Solid State Mater. Sci.* **2020**, 1–65. [[CrossRef](#)]
52. Karthik, K.; Dhanuskodi, S.; Gobinath, C.; Prabukumar, S.; Sivaramkrishnan, S. Fabrication of MgO nanostructures and its efficient photocatalytic, antibacterial and anticancer performance. *J. Photochem. Photobiol. B Biol.* **2019**, *190*, 8–20. [[CrossRef](#)]
53. Ansari, M.A.; Khan, H.M.; Khan, A.A.; Cameotra, S.S.; Pal, R. Antibiofilm efficacy of silver nanoparticles against biofilm of extended spectrum β-lactamase isolates of Escherichia coli and Klebsiella pneumoniae. *Appl. Nanosci.* **2014**, *4*, 859–868. [[CrossRef](#)]
54. Ashajyothi, C.; Harish, K.H.; Dubey, N.; Chandrakanth, R.K. Antibiofilm activity of biogenic copper and zinc oxide nanoparticles-antimicrobials collegiate against multiple drug resistant bacteria: A nanoscale approach. *J. Nanostructure Chem.* **2016**, *6*, 329–341. [[CrossRef](#)]

55. Bradford, N. A rapid and sensitive method for the quantitation microgram quantities of a protein isolated from red cell membranes. *Anal. Biochem.* **1976**, *72*, e254. [[CrossRef](#)]
56. Rajesh, S.; Dharanishanthi, V.; Kanna, A.V. Antibacterial mechanism of biogenic silver nanoparticles of *Lactobacillus acidophilus*. *J. Exp. Nanosci.* **2015**, *10*, 1143–1152. [[CrossRef](#)]
57. Azam, Z.; Ayaz, A.; Younas, M.; Qureshi, Z.; Arshad, B.; Zaman, W.; Ullah, F.; Nasar, M.Q.; Bahadur, S.; Irfan, M.M. Microbial synthesized cadmium oxide nanoparticles induce oxidative stress and protein leakage in bacterial cells. *Microb. Pathog.* **2020**, *144*, 104188. [[CrossRef](#)] [[PubMed](#)]
58. Paul, D.; Maiti, S.; Sethi, D.P.; Neogi, S. Bi-functional NiO-ZnO nanocomposite: Synthesis, characterization, antibacterial and photo assisted degradation study. *Adv. Powder Technol.* **2021**, *32*, 131–143. [[CrossRef](#)]
59. El-Batal, A.I.; Mosallam, F.M.; El-Sayyad, G.S. Synthesis of Metallic Silver Nanoparticles by Fluconazole Drug and Gamma Rays to Inhibit the Growth of Multidrug-Resistant Microbes. *J. Clust. Sci.* **2018**, *29*, 1003–1015. [[CrossRef](#)]
60. Liu, W.; Sun, W.; Borthwick, A.G.; Ni, J. Comparison on aggregation and sedimentation of titanium dioxide, titanate nanotubes and titanate nanotubes-TiO₂: Influence of pH, ionic strength and natural organic matter. *Colloids Surf. A Physicochem. Eng. Asp.* **2013**, *434*, 319–328. [[CrossRef](#)]
61. Taylor, E.N.; Webster, T.J. The use of superparamagnetic nanoparticles for prosthetic biofilm prevention. *Int. J. Nanomed.* **2009**, *4*, 145.
62. Klostergaard, J.; Seeney, C.E. Magnetic nanovectors for drug delivery. *Nanomed. Nanotechnol. Biol. Med.* **2012**, *8*, S37–S50. [[CrossRef](#)]
63. Saquib, Q.; Al-Khedhairi, A.A.; Ahmad, J.; Siddiqui, M.A.; Dwivedi, S.; Khan, S.T.; Musarrat, J. Zinc ferrite nanoparticles activate IL-1b, NFKB1, CCL21 and NOS2 signaling to induce mitochondrial dependent intrinsic apoptotic pathway in WISH cells. *Toxicol. Appl. Pharmacol.* **2013**, *273*, 289–297. [[CrossRef](#)] [[PubMed](#)]
64. Vochita, G.; Creanga, D.; Focanici-Ciurlica, E.-L. Magnetic nanoparticle genetic impact on root tip cells of sunflower seedlings. *Water Air Soil Pollut.* **2012**, *223*, 2541–2549. [[CrossRef](#)]
65. Gliga, A.R.; Edoff, K.; Caputo, F.; Källman, T.; Blom, H.; Karlsson, H.L.; Ghibelli, L.; Traversa, E.; Ceccatelli, S.; Fadeel, B. Cerium oxide nanoparticles inhibit differentiation of neural stem cells. *Sci. Rep.* **2017**, *7*, 1–20.
66. Atif, M.; Iqbal, S.; Ismail, M.; Mansoor, Q.; Mughal, L.; Aziz, M.H.; Hanif, A.; Farooq, W. Manganese-doped cerium oxide nanocomposite induced photodynamic therapy in MCF-7 cancer cells and antibacterial activity. *BioMed Res. Int.* **2019**, *2019*. [[CrossRef](#)] [[PubMed](#)]
67. Abbas, F.; Jan, T.; Iqbal, J.; Naqvi, M.S.H.; Ahmad, I. Inhibition of Neuroblastoma cancer cells viability by ferromagnetic Mn doped CeO₂ monodisperse nanoparticles mediated through reactive oxygen species. *Mater. Chem. Phys.* **2016**, *173*, 146–151. [[CrossRef](#)]
68. Mittal, M.; Gupta, A.; Pandey, O. Role of oxygen vacancies in Ag/Au doped CeO₂ nanoparticles for fast photocatalysis. *Sol. Energy* **2018**, *165*, 206–216. [[CrossRef](#)]
69. Kusmirek, E. A CeO₂ Semiconductor as a Photocatalytic and Photoelectrocatalytic Material for the Remediation of Pollutants in Industrial Wastewater: A Review. *Catalysts* **2020**, *10*, 1435. [[CrossRef](#)]
70. Maqbool, Q.; Nazar, M.; Naz, S.; Hussain, T.; Jabeen, N.; Kausar, R.; Anwaar, S.; Abbas, F.; Jan, T. Antimicrobial potential of green synthesized CeO₂ nanoparticles from *Olea europaea* leaf extract. *Int. J. Nanomed.* **2016**, *11*, 5015. [[CrossRef](#)] [[PubMed](#)]
71. Sundaram, N.; Pahwa, A.K.; Ard, M.D.; Lin, N.; Perkins, E.; Bowles, A.P. Selenium causes growth inhibition and apoptosis in human brain tumor cell lines. *J. Neuro-Oncol.* **2000**, *46*, 125–133. [[CrossRef](#)] [[PubMed](#)]
72. Venkateswaran, V.; Klotz, L.H.; Fleshner, N.E. Selenium modulation of cell proliferation and cell cycle biomarkers in human prostate carcinoma cell lines. *Cancer Res.* **2002**, *62*, 2540–2545.
73. Storz, P. Reactive oxygen species in tumor progression. *Front. Biosci.* **2005**, *10*, 1881–1896. [[CrossRef](#)] [[PubMed](#)]
74. Wang, Y.; Yu, X.; Song, H.; Feng, D.; Jiang, Y.; Wu, S.; Geng, J. The STAT-ROS cycle extends IFN-induced cancer cell apoptosis. *Int. J. Oncol.* **2018**, *52*, 305–313. [[CrossRef](#)]
75. Hobson-Gutierrez, S.A.; Carmona-Fontaine, C. The metabolic axis of macrophage and immune cell polarization. *Dis. Models Mech.* **2018**, *11*, dmm034462. [[CrossRef](#)]
76. Ohmori, Y.; Hamilton, T.A. Interleukin-4/STAT6 represses STAT1 and NF-κB-dependent transcription through distinct mechanisms. *J. Biol. Chem.* **2000**, *275*, 38095–38103. [[CrossRef](#)] [[PubMed](#)]
77. Kucinski, I.; Dinan, M.; Kolahgar, G.; Piddini, E. Chronic activation of JNK/JAK/STAT and oxidative stress signalling causes the loser cell status. *Nat. Commun.* **2017**, *8*, 1–13. [[CrossRef](#)]
78. Perillo, B.; Di Donato, M.; Pezone, A.; Di Zazzo, E.; Giovannelli, P.; Galasso, G.; Castoria, G.; Migliaccio, A. ROS in cancer therapy: The bright side of the moon. *Exp. Mol. Med.* **2020**, *52*, 192–203. [[CrossRef](#)] [[PubMed](#)]
79. Chan, J.S.K.; Tan, M.J.; Sng, M.K.; Teo, Z.; Phua, T.; Choo, C.C.; Liang, L.; Zhu, P.; Tan, N.S. Cancer-associated fibroblasts enact field cancerization by promoting extratumoral oxidative stress. *Cell Death Dis.* **2018**, *8*, e2562. [[CrossRef](#)]
80. Toullec, A.; Gerald, D.; Despouy, G.; Bourachot, B.; Cardon, M.; Lefort, S.; Richardson, M.; Rigault, G.; Parrini, M.C.; Lucchesi, C. Oxidative stress promotes myofibroblast differentiation and tumour spreading. *EMBO Mol. Med.* **2010**, *2*, 211–230. [[CrossRef](#)] [[PubMed](#)]
81. Son, Y.; Cheong, Y.-K.; Kim, N.-H.; Chung, H.-T.; Kang, D.G.; Pae, H.-O. Mitogen-activated protein kinases and reactive oxygen species: How can ROS activate MAPK pathways? *J. Signal Transduct.* **2011**, *2011*. [[CrossRef](#)]

82. Shi, Y.; Nikulenkov, F.; Zawacka-Pankau, J.; Li, H.; Gabdoulline, R.; Xu, J.; Eriksson, S.; Hedström, E.; Issaeva, N.; Kel, A. ROS-dependent activation of JNK converts p53 into an efficient inhibitor of oncogenes leading to robust apoptosis. *Cell Death Differ.* **2014**, *21*, 612–623. [[CrossRef](#)]
83. Gibellini, L.; Pinti, M.; Nasi, M.; De Biasi, S.; Roat, E.; Bertocelli, L.; Cossarizza, A. Interfering with ROS metabolism in cancer cells: The potential role of quercetin. *Cancers* **2010**, *2*, 1288–1311. [[CrossRef](#)] [[PubMed](#)]
84. Sung, S.-Y.; Kubo, H.; Shigemura, K.; Arnold, R.S.; Logani, S.; Wang, R.; Konaka, H.; Nakagawa, M.; Mousses, S.; Amin, M. Oxidative stress induces ADAM9 protein expression in human prostate cancer cells. *Cancer Res.* **2006**, *66*, 9519–9526. [[CrossRef](#)]
85. Gao, Y.; Ma, H.; Qu, G.; Su, L.; Ye, Q.; Jiang, F.; Zhao, B.; Miao, J. A hydrogen sulfide probe activates Nrf2, inhibits cancer cell growth and induces cell apoptosis. *RSC Adv.* **2017**, *7*, 42416–42421. [[CrossRef](#)]
86. Kang, K.A.; Piao, M.J.; Hyun, Y.J.; Zhen, A.X.; Cho, S.J.; Ahn, M.J.; Yi, J.M.; Hyun, J.W. Luteolin promotes apoptotic cell death via upregulation of Nrf2 expression by DNA demethylase and the interaction of Nrf2 with p53 in human colon cancer cells. *Exp. Mol. Med.* **2019**, *51*, 1–14. [[CrossRef](#)] [[PubMed](#)]
87. Moos, P.J.; Chung, K.; Woessner, D.; Honegger, M.; Cutler, N.S.; Veranth, J.M. ZnO particulate matter requires cell contact for toxicity in human colon cancer cells. *Chem. Res. Toxicol.* **2010**, *23*, 733–739. [[CrossRef](#)] [[PubMed](#)]
88. Walkey, C.; Das, S.; Seal, S.; Erlichman, J.; Heckman, K.; Ghibelli, L.; Traversa, E.; McGinnis, J.F.; Self, W.T. Catalytic properties and biomedical applications of cerium oxide nanoparticles. *Environ. Sci. Nano* **2015**, *2*, 33–53. [[CrossRef](#)]
89. Das, S.; Dowding, J.M.; Klump, K.E.; McGinnis, J.F.; Self, W.; Seal, S. Cerium oxide nanoparticles: Applications and prospects in nanomedicine. *Nanomedicine* **2013**, *8*, 1483–1508. [[CrossRef](#)]
90. Pešić, M.; Podolski-Renić, A.; Stojković, S.; Matović, B.; Zmejkoski, D.; Kojić, V.; Bogdanović, G.; Pavićević, A.; Mojović, M.; Savić, A. Anti-cancer effects of cerium oxide nanoparticles and its intracellular redox activity. *Chem. Biol. Interact.* **2015**, *232*, 85–93. [[CrossRef](#)]
91. Brenneisen, P.; Reichert, A.S. Nanotherapy and reactive oxygen species (ROS) in cancer: A novel perspective. *Antioxidants* **2018**, *7*, 31. [[CrossRef](#)]
92. Colon, J.; Hsieh, N.; Ferguson, A.; Kupelian, P.; Seal, S.; Jenkins, D.W.; Baker, C.H. Cerium oxide nanoparticles protect gastrointestinal epithelium from radiation-induced damage by reduction of reactive oxygen species and upregulation of superoxide dismutase 2. *Nanomed. Nanotechnol. Biol. Med.* **2010**, *6*, 698–705. [[CrossRef](#)]
93. Rice, K.M.; Nalabotu, S.K.; Manne, N.D.; Kolli, M.B.; Nandyala, G.; Arvapalli, R.; Ma, J.Y.; Blough, E.R. Exposure to cerium oxide Nanoparticles is associated with activation of Mitogen-activated protein Kinases signaling and apoptosis in rat lungs. *J. Prev. Med. Public Health* **2015**, *48*, 132. [[CrossRef](#)]
94. McDonald, J.T.; Kim, K.; Norris, A.J.; Vlashi, E.; Phillips, T.M.; Lagadec, C.; Della Donna, L.; Ratikan, J.; Szelag, H.; Hlatky, L. Ionizing radiation activates the Nrf2 antioxidant response. *Cancer Res.* **2010**, *70*, 8886–8895. [[CrossRef](#)]
95. Ritter, B.; Greten, F.R. Modulating inflammation for cancer therapy. *J. Exp. Med.* **2019**, *216*, 1234–1243. [[CrossRef](#)]
96. Varga, J.; Greten, F.R. Cell plasticity in epithelial homeostasis and tumorigenesis. *Nat. Cell Biol.* **2017**, *19*, 1133–1141. [[CrossRef](#)]
97. Park, S.J.; Kim, H.; Kim, S.H.; Joe, E.-H.; Jou, I. Epigenetic downregulation of STAT6 increases HIF-1 α expression via mTOR/S6K/S6, leading to enhanced hypoxic viability of glioma cells. *Acta Neuropathol. Commun.* **2019**, *7*, 1–19. [[CrossRef](#)]
98. Brunn, A.; Mihelcic, M.; Carstov, M.; Hummel, L.; Geier, F.; Schmidt, A.; Saupe, L.; Utermöhlen, O.; Deckert, M. IL-10, IL-4, and STAT6 Promote an M2 Milieu Required for Termination of P0106-125-Induced Murine Experimental Autoimmune Neuritis. *Am. J. Pathol.* **2014**, *184*, 2627–2640. [[CrossRef](#)] [[PubMed](#)]
99. Tewari, R.; Sharma, V.; Koul, N.; Ghosh, A.; Joseph, C.; Sk, U.H.; Sen, E. Ebselen abrogates TNF α induced pro-inflammatory response in glioblastoma. *Mol. Oncol.* **2009**, *3*, 77–83. [[CrossRef](#)] [[PubMed](#)]
100. Chiang, C.-S.; Fu, S.-Y.; Wang, S.-C.; Yu, C.-F.; Chen, F.-H.; Lin, C.-M.; Hong, J.-H. Irradiation promotes an m2 macrophage phenotype in tumor hypoxia. *Front. Oncol.* **2012**, *2*, 89. [[CrossRef](#)]
101. Thabet, N.M.; Moustafa, E.M. Synergistic effect of Ebselen and gamma radiation on breast cancer cells. *Int. J. Radiat. Biol.* **2017**, *93*, 784–792. [[CrossRef](#)]
102. Wu, S.; Lu, H.; Bai, Y. Nrf2 in cancers: A double-edged sword. *Cancer Med.* **2019**, *8*, 2252–2267. [[CrossRef](#)] [[PubMed](#)]
103. Solis, L.M.; Behrens, C.; Dong, W.; Suraokar, M.; Ozburn, N.C.; Moran, C.A.; Corvalan, A.H.; Biswal, S.; Swisher, S.G.; Bekele, B.N. Nrf2 and Keap1 abnormalities in non-small cell lung carcinoma and association with clinicopathologic features. *Clin. Cancer Res.* **2010**, *16*, 3743–3753. [[CrossRef](#)] [[PubMed](#)]
104. Iizuka, T.; Ishii, Y.; Itoh, K.; Kiwamoto, T.; Kimura, T.; Matsuno, Y.; Morishima, Y.; Hegab, A.E.; Homma, S.; Nomura, A. Nrf2-deficient mice are highly susceptible to cigarette smoke-induced emphysema. *Genes Cells* **2005**, *10*, 1113–1125. [[CrossRef](#)]
105. Thimmulappa, R.K.; Lee, H.; Rangasamy, T.; Reddy, S.P.; Yamamoto, M.; Kensler, T.W.; Biswal, S. Nrf2 is a critical regulator of the innate immune response and survival during experimental sepsis. *J. Clin. Investig.* **2016**, *116*, 984–995. [[CrossRef](#)] [[PubMed](#)]
106. Kondo, Y.; Kanzawa, T.; Sawaya, R.; Kondo, S. The role of autophagy in cancer development and response to therapy. *Nat. Rev. Cancer* **2005**, *5*, 726–734. [[CrossRef](#)] [[PubMed](#)]
107. Glick, D.; Barth, S.; Macleod, K.F. Autophagy: Cellular and molecular mechanisms. *J. Pathol.* **2010**, *221*, 3–12. [[CrossRef](#)] [[PubMed](#)]
108. Martinet, W.; De Meyer, G.R. Autophagy in atherosclerosis: A cell survival and death phenomenon with therapeutic potential. *Circ. Res.* **2009**, *104*, 304–317. [[CrossRef](#)]

109. Banduseela, V.C.; Chen, Y.-W.; Kultima, H.G.; Norman, H.S.; Aare, S.; Radell, P.; Eriksson, L.I.; Hoffman, E.P.; Larsson, L. Impaired autophagy, chaperone expression, and protein synthesis in response to critical illness interventions in porcine skeletal muscle. *Physiol. Genom.* **2013**, *45*, 477–486. [[CrossRef](#)] [[PubMed](#)]
110. Katsuragi, Y.; Ichimura, Y.; Komatsu, M. p62/SQSTM 1 functions as a signaling hub and an autophagy adaptor. *FEBS J.* **2015**, *282*, 4672–4678. [[CrossRef](#)]
111. Makowska, A.; Eble, M.; Prescher, K.; Hoß, M.; Kontny, U. Chloroquine sensitizes nasopharyngeal carcinoma cells but not nasoeptelial cells to irradiation by blocking autophagy. *PLoS ONE* **2016**, *11*, e0166766.
112. Wang, F.; Tang, J.; Li, P.; Si, S.; Yu, H.; Yang, X.; Tao, J.; Lv, Q.; Gu, M.; Yang, H. Chloroquine enhances the radiosensitivity of bladder cancer cells by inhibiting autophagy and activating apoptosis. *Cell. Physiol. Biochem.* **2018**, *45*, 54–66. [[CrossRef](#)]
113. Chaachouay, H.; Ohneseit, P.; Toulany, M.; Kehlbach, R.; Multhoff, G.; Rodemann, H.P. Autophagy contributes to resistance of tumor cells to ionizing radiation. *Radiother. Oncol.* **2011**, *99*, 287–292. [[CrossRef](#)] [[PubMed](#)]
114. Wang, P.; Zhang, J.; Zhang, L.; Zhu, Z.; Fan, J.; Chen, L.; Zhuang, L.; Luo, J.; Chen, H.; Liu, L. MicroRNA 23b regulates autophagy associated with radioresistance of pancreatic cancer cells. *Gastroenterology* **2013**, *145*, 1133–1143.e12. [[CrossRef](#)] [[PubMed](#)]
115. Koukourakis, M.I.; Mitrakas, A.G.; Giatromanolaki, A. Therapeutic interactions of autophagy with radiation and temozolomide in glioblastoma: Evidence and issues to resolve. *Br. J. Cancer* **2016**, *114*, 485–496. [[CrossRef](#)]
116. Jung, Y.Y.; Lee, Y.K.; Koo, J.S. The potential of Beclin 1 as a therapeutic target for the treatment of breast cancer. *Expert Opin. Ther. Targets* **2016**, *20*, 167–178. [[CrossRef](#)]
117. Wu, S.; Sun, C.; Tian, D.; Li, Y.; Gao, X.; He, S.; Li, T. Expression and clinical significances of Beclin1, LC3 and mTOR in colorectal cancer. *Int. J. Clin. Exp. Pathol.* **2015**, *8*, 3882.
118. Chen, Z.; Wang, B.; Yu, F.; Chen, Q.; Tian, Y.; Ma, S.; Liu, X. The roles of mitochondria in radiation-induced autophagic cell death in cervical cancer cells. *Tumor Biol.* **2016**, *37*, 4083–4091. [[CrossRef](#)] [[PubMed](#)]
119. Ju, L.; Zhao, C.; Ye, K.; Yang, H.; Zhang, J. Expression and clinical implication of Beclin1, HMGB1, p62, survivin, BRCA1 and ERCC1 in epithelial ovarian tumor tissues. *Eur. Rev. Med. Pharmacol. Sci* **2016**, *20*, 1993–2003. [[PubMed](#)]
120. Xue, S.; Xiao-Hong, S.; Lin, S.; Jie, B.; Li-Li, W.; Jia-Yao, G.; Shun, S.; Pei-Nan, L.; Mo-Li, W.; Qian, W. Lumbar puncture-administered resveratrol inhibits STAT3 activation, enhancing autophagy and apoptosis in orthotopic rat glioblastomas. *Oncotarget* **2016**, *7*, 75790. [[CrossRef](#)] [[PubMed](#)]
121. Huang, X.; Qi, Q.; Hua, X.; Li, X.; Zhang, W.; Sun, H.; Li, S.; Wang, X.; Li, B. Beclin 1, an autophagy-related gene, augments apoptosis in U87 glioblastoma cells. *Oncol. Rep.* **2014**, *31*, 1761–1767. [[CrossRef](#)]
122. Song, X.; Lee, D.-H.; Dilly, A.-K.; Lee, Y.-S.; Choudry, H.A.; Kwon, Y.T.; Bartlett, D.L.; Lee, Y.J. Crosstalk between apoptosis and autophagy is regulated by the arginylated BiP/Beclin-1/p62 complex. *Mol. Cancer Res.* **2018**, *16*, 1077–1091. [[CrossRef](#)]
123. Baek, J.M.; Kim, J.-Y.; Yoon, K.-H.; Oh, J.; Lee, M.S. Ebselen is a potential anti-osteoporosis agent by suppressing receptor activator of nuclear factor kappa-B ligand-induced osteoclast differentiation in vitro and lipopolysaccharide-induced inflammatory bone destruction in vivo. *Int. J. Biol. Sci.* **2016**, *12*, 478. [[CrossRef](#)] [[PubMed](#)]
124. Vormoor, B.; Schlosser, Y.T.; Blair, H.; Sharma, A.; Wilkinson, S.; Newell, D.R.; Curtin, N. Sensitizing Ewing sarcoma to chemo-and radiotherapy by inhibition of the DNA-repair enzymes DNA protein kinase (DNA-PK) and poly-ADP-ribose polymerase (PARP) 1/2. *Oncotarget* **2017**, *8*, 113418. [[CrossRef](#)] [[PubMed](#)]
125. Kastan, M.B.; Bartek, J. Cell-cycle checkpoints and cancer. *Nature* **2004**, *432*, 316–323. [[CrossRef](#)] [[PubMed](#)]
126. Murray, A.W. Recycling the cell cycle: Cyclins revisited. *Cell* **2004**, *116*, 221–234. [[CrossRef](#)]
127. Stark, G.R.; Taylor, W.R. Analyzing the G2/M checkpoint. *Checkp. Control. Cancer* **2004**, *280*, 51–82.
128. Li, Y.; Yu, H.; Han, F.; Wang, M.; Luo, Y.; Guo, X. Biochanin A induces S phase arrest and apoptosis in lung cancer cells. *BioMed Res. Int.* **2018**, *2018*, 3545376. [[CrossRef](#)] [[PubMed](#)]
129. Mariño, G.; Niso-Santano, M.; Baehrecke, E.H.; Kroemer, G. Self-consumption: The interplay of autophagy and apoptosis. *Nat. Rev. Mol. Cell Biol.* **2014**, *15*, 81–94. [[CrossRef](#)]
130. Singh, S.S.; Vats, S.; Chia, A.Y.-Q.; Tan, T.Z.; Deng, S.; Ong, M.S.; Arfuso, F.; Yap, C.T.; Goh, B.C.; Sethi, G. Dual role of autophagy in hallmarks of cancer. *Oncogene* **2018**, *37*, 1142–1158. [[CrossRef](#)]
131. Aubrey, B.J.; Kelly, G.L.; Janic, A.; Herold, M.J.; Strasser, A. How does p53 induce apoptosis and how does this relate to p53-mediated tumour suppression? *Cell Death Differ.* **2018**, *25*, 104–113. [[CrossRef](#)]
132. Adams, J.M.; Cory, S. The BCL-2 arbiters of apoptosis and their growing role as cancer targets. *Cell Death Differ.* **2018**, *25*, 27–36. [[CrossRef](#)] [[PubMed](#)]
133. Olsson, M.; Zhivotovsky, B. Caspases and cancer. *Cell Death Differ.* **2011**, *18*, 1441–1449. [[CrossRef](#)]
134. Lieberthal, W.; Menza, S.A.; Levine, J.S. Graded ATP depletion can cause necrosis or apoptosis of cultured mouse proximal tubular cells. *Am. J. Physiol.-Ren. Physiol.* **1998**, *274*, F315–F327. [[CrossRef](#)] [[PubMed](#)]
135. Chou, C.C.; Lam, C.Y.; Yung, B.Y.M. Intracellular ATP is required for actinomycin D-induced apoptotic cell death in HeLa cells. *Cancer Lett.* **1995**, *96*, 181–187. [[CrossRef](#)]
136. Stefanelli, C.; Bonavita, F.; Stanic, I.; Farruggia, G.; Falcieri, E.; Robuffo, I.; Pignatti, C.; Muscari, C.; Rossoni, C.; Guarnieri, C. ATP depletion inhibits glucocorticoid-induced thymocyte apoptosis. *Biochem. J.* **1997**, *322*, 909–917. [[CrossRef](#)] [[PubMed](#)]
137. Barrera, G.; Gentile, F.; Pizzimenti, S.; Canuto, R.A.; Daga, M.; Arcaro, A.; Cetrangolo, G.P.; Lepore, A.; Ferretti, C.; Dianzani, C. Mitochondrial dysfunction in cancer and neurodegenerative diseases: Spotlight on fatty acid oxidation and lipoperoxidation products. *Antioxidants* **2016**, *5*, 7. [[CrossRef](#)]

138. Liu, D.; Angelova, A.; Liu, J.; Garamus, V.M.; Angelov, B.; Zhang, X.; Li, Y.; Feger, G.; Li, N.; Zou, A. Self-assembly of mitochondria-specific peptide amphiphiles amplifying lung cancer cell death through targeting the VDAC1–hexokinase-II complex. *J. Mater. Chem. B* **2019**, *7*, 4706–4716. [[CrossRef](#)] [[PubMed](#)]
139. Reheem, A.A.; Atta, A.; Maksoud, M.A. Low energy ion beam induced changes in structural and thermal properties of polycarbonate. *Radiat. Phys. Chem.* **2016**, *127*, 269–275. [[CrossRef](#)]
140. Belavi, P.; Chavan, G.; Naik, L.; Somashekar, R.; Kotnala, R. Structural, electrical and magnetic properties of cadmium substituted nickel–copper ferrites. *Mater. Chem. Phys.* **2012**, *132*, 138–144. [[CrossRef](#)]
141. El-Shazly, A.N.; El-Sayyad, G.S.; Hegazy, A.H.; Hamza, M.A.; Fathy, R.M.; El Shenawy, E.; Allam, N.K. Superior visible light antimicrobial performance of facet engineered cobalt doped TiO₂ mesocrystals in pathogenic bacterium and fungi. *Sci. Rep.* **2021**, *11*, 1–14.
142. Hu, Y.; Liu, A.; Vaudrey, J.; Vaiciunaite, B.; Moigboi, C.; McTavish, S.M.; Kearns, A.; Coates, A. Combinations of β -lactam or aminoglycoside antibiotics with plectasin are synergistic against methicillin-sensitive and methicillin-resistant *Staphylococcus aureus*. *PLoS ONE* **2015**, *10*, e0117664.
143. Chandrika, K.M.; Sharma, S. Promising antifungal agents: A minireview. *Bioorganic Med. Chem.* **2020**, *28*, 115398. [[CrossRef](#)] [[PubMed](#)]
144. Christensen, G.D.; Simpson, W.A.; Bisno, A.L.; Beachey, E.H. Adherence of slime-producing strains of *Staphylococcus epidermidis* to smooth surfaces. *Infect. Immun.* **1982**, *37*, 318–326. [[CrossRef](#)] [[PubMed](#)]
145. Maksoud, M.A.; El-Sayyad, G.S.; El-Bastawisy, H.S.; Fathy, R.M. Antibacterial and antibiofilm activities of silver-decorated zinc ferrite nanoparticles synthesized by a gamma irradiation-coupled sol–gel method against some pathogenic bacteria from medical operating room surfaces. *RSC Adv.* **2021**, *11*, 28361–28374. [[CrossRef](#)]
146. Agarwal, H.; Nakara, A.; Menon, S.; Shanmugam, V. Eco-friendly synthesis of zinc oxide nanoparticles using *Cinnamomum Tamala* leaf extract and its promising effect towards the antibacterial activity. *J. Drug Deliv. Sci. Technol.* **2019**, *53*, 101212. [[CrossRef](#)]
147. Vichai, V.; Kirtikara, K. Sulforhodamine B colorimetric assay for cytotoxicity screening. *Nat. Protoc.* **2006**, *1*, 1112. [[CrossRef](#)] [[PubMed](#)]
148. Omar, H.A.; Sargeant, A.M.; Weng, J.-R.; Wang, D.; Kulp, S.K.; Patel, T.; Chen, C.-S. Targeting of the Akt-nuclear factor- κ B signaling network by [1-(4-chloro-3-nitrobenzenesulfonyl)-1H-indol-3-yl]-methanol (OSU-A9), a novel indole-3-carbinol derivative, in a mouse model of hepatocellular carcinoma. *Mol. Pharmacol.* **2009**, *76*, 957–968. [[CrossRef](#)] [[PubMed](#)]
149. Mingone, C.J.; Gupte, S.A.; Quan, S.; Abraham, N.G.; Wolin, M.S. Influence of heme and heme oxygenase-1 transfection of pulmonary microvascular endothelium on oxidant generation and cGMP. *Exp. Biol. Med.* **2003**, *228*, 535–539. [[CrossRef](#)]



Article

Structural Alterations of Antigens at the Material Interface: An Early Decision Toolbox Facilitating Safe-by-Design Nanovaccine Development

Litty Johnson , Lorenz Aglas, Wai Tuck Soh , Mark Geppert, Sabine Hofer , Norbert Hofstätter , Peter Briza , Fatima Ferreira , Richard Weiss, Hans Brandstetter , Albert Duschl and Martin Himly *

Department of Biosciences, University of Salzburg, 5020 Salzburg, Austria; litty.johnson@sbg.ac.at (L.J.); lorenz.aglas@sbg.ac.at (L.A.); waituck.soh@sbg.ac.at (W.T.S.); mark.geppert@sbg.ac.at (M.G.); sabine.hofer@sbg.ac.at (S.H.); norbert.hofstaetter@sbg.ac.at (N.H.); Peter.Briza@sbg.ac.at (P.B.); fatima.ferreira@sbg.ac.at (F.F.); richard.weiss@sbg.ac.at (R.W.); hans.brandstetter@sbg.ac.at (H.B.); albert.duschl@sbg.ac.at (A.D.)

* Correspondence: martin.himly@sbg.ac.at



Citation: Johnson, L.; Aglas, L.; Soh, W.T.; Geppert, M.; Hofer, S.; Hofstätter, N.; Briza, P.; Ferreira, F.; Weiss, R.; Brandstetter, H.; et al. Structural Alterations of Antigens at the Material Interface: An Early Decision Toolbox Facilitating Safe-by-Design Nanovaccine Development. *Int. J. Mol. Sci.* **2021**, *22*, 10895. <https://doi.org/10.3390/ijms221910895>

Academic Editors:
Monica Terracciano, Ilaria Rea,
Nicola Borbone and
Chiara Tramontano

Received: 24 August 2021

Accepted: 4 October 2021

Published: 8 October 2021

Publisher's Note: MDPI stays neutral with regard to jurisdictional claims in published maps and institutional affiliations.



Copyright: © 2021 by the authors. Licensee MDPI, Basel, Switzerland. This article is an open access article distributed under the terms and conditions of the Creative Commons Attribution (CC BY) license (<https://creativecommons.org/licenses/by/4.0/>).

Abstract: Nanomaterials have found extensive interest in the development of novel vaccines, as adjuvants and/or carriers in vaccination platforms. Conjugation of protein antigens at the particle surface by non-covalent adsorption is the most widely used approach in licensed particulate vaccines. Hence, it is essential to understand proteins' structural integrity at the material interface in order to develop safe-by-design nanovaccines. In this study, we utilized two model proteins, the wild-type allergen Bet v 1 and its hypoallergenic fold variant (BM4), to compare SiO₂ nanoparticles with Alhydrogel[®] as particulate systems. A set of biophysical and functional assays including circular dichroism spectroscopy and proteolytic degradation was used to examine the antigens' structural integrity at the material interface. Conjugation of both biomolecules to the particulate systems decreased their proteolytic stability. However, we observed qualitative and quantitative differences in antigen processing concomitant with differences in their fold stability. These changes further led to an alteration in IgE epitope recognition. Here, we propose a toolbox of biophysical and functional in vitro assays for the suitability assessment of nanomaterials in the early stages of vaccine development. These tools will aid in safe-by-design innovations and allow fine-tuning the properties of nanoparticle candidates to shape a specific immune response.

Keywords: Alhydrogel[®]; silica nanoparticles; Bet v 1; BM4; SiO₂; allergen; structural integrity; alum

1. Introduction

Engineered nanomaterials have gained significant research interest as novel vaccination platforms. They have been utilized to enhance vaccine efficacy by modulating the quality, specificity and durability of immune responses towards a specific antigen [1]. Adjuvants and/or carriers are important in vaccine formulations as they are essential for the efficient activation of the immune system. In this regard, nanomaterials are attractive platforms as they can transport protein antigens effectively close to or even into antigen-presenting cells, leading to decreased systemic or local side effects concomitant with a reduction in the antigen dose [2], in addition to their intrinsic immunomodulatory properties [3,4]. Moreover, the huge diversity in the physicochemical properties of engineered nanomaterials along with their ability to be tailored can be harnessed for directing a specific immune response [5]. Together, these novel opportunities have contributed to an explosion in the exploration of nanoparticles (NPs) in novel vaccine technologies, especially in the field of infectious disease, allergy and cancer [6–8].

However, despite their promising potential, only a limited number of nanovaccines have been approved for clinical use thus far. This may be due to challenges in the clinical

translation and commercialization of nanomaterials, which include restrictions in large-scale manufacturing, establishment of biopharmaceutical correlations between the properties of the nanomaterial and their *in vivo* performance and the lack of clear regulatory and safety guidelines [9]. The structural and physicochemical diversity of nanomaterials complicates large-scale manufacturing and can pose difficulties for quality assessment [10]. Compared to other biopharmaceutical products (e.g., highly purified monoclonal antibody preparations), vaccines are, in general, more complex due to the often heterogeneous nature of the active components (live-attenuated or inactivated/chemically modified whole microbes, crude allergen extracts, etc.) and their interaction with adjuvants or other excipients [11]. This contributes to increased concerns regarding the safety and efficacy of vaccines and results in the scrutiny of novel vaccine technologies. To a great extent, vaccines still rely on *in vivo* testing; nevertheless, a strong demand for novel *in vitro* testing methods ensuring consistency of vaccine formulations has been articulated [12]. The establishment of *in vitro* testing methods which are applicable early in the development pipeline and have a satisfying predictive power is in high demand. These methods in combination with functional assays can be used to determine the safety, efficacy and consistency of nanovaccines.

One critical step in the development of nanovaccines includes the rational selection of a nanoparticulate adjuvant for a specific antigen aiming at eliciting a desired immune response. To attain a potent antitumor response, a nanoparticulate system that can enhance the host immunity is favored, whereas in the case of hypersensitivity or autoimmune disorders, materials suppressing a harmful immune response are beneficial [13]. Thus, tailoring the physical and biochemical properties of NPs is crucial in evoking a specific immune response, thereby improving the efficacy of vaccines with an optimum safety profile. Tailoring novel vaccine strategies is of particular interest for the elderly and immunocompromised population, who are more prone to diseases and less responsive to vaccines [14]. In the case of the SARS-CoV-2 pandemic, we can see a direct impact of age on the increased vulnerability to severe infection [15]. The increased susceptibility to infection and diminished responsiveness to vaccines can be explained by the reduced number of naïve T cells, reduced T cell receptor diversity and other defects in the innate immune cells usually associated with aging [16]. Hence, to increase the efficacy of vaccines in the immunocompromised or elderly population, NPs that can induce inflammatory responses in a well-controlled fashion may be favorable as they are reported to enhance T cell function [17]. Furthermore, the tunable properties of NPs can be used to manipulate and optimize the quantity and proteolytic accessibility of antigens [18]. The differences in an antigen's stability, spacing and orientation when linked to NPs can affect the immune response. For example, a desired antibody response with negligible adverse effects can be accomplished by intentionally masking the undesirable epitopes of the antigen and exposing the desired epitopes. Once the structural integrity of an antigen associated with a specific NP is established, it may be tuned in such a way that a desired outcome can be achieved. By understanding its structural integrity, we can predict the behavior of an antigen upon conjugation to NPs. The resulting insights in antigens' immunogenicity will ultimately facilitate a "safe-by-design" nanovaccine development strategy [19].

In this study, we established an *in vitro* test strategy to study the interaction of nanoparticulate adjuvants with antigens, investigating the structural integrity of antigens at the nanoparticulate surface by using biophysical methods and a set of functional assays. We aimed to evaluate the early events in immune modulation to fine-tune nanoparticulate adjuvants. The goal was to test for desired immunological outcomes of novel nanovaccines displaying an optimal safety and efficacy profile. SiO₂ NPs were used as a model nanoparticulate platform and were compared with Alhydrogel[®], the most-applied particulate adjuvant in vaccines. Alhydrogel[®] or alum is still considered as the gold standard among the clinically available adjuvants despite its recognized drawbacks [20,21]. SiO₂ NPs, on the other hand, are promising candidate adjuvants and/or vaccine carriers and are widely studied due to their biodegradability, biocompatibility, ease of surface mod-

ification, low production costs and low toxicity [22]. The model proteins used for this study included Bet v 1, the major birch pollen allergen, and BM4, a molten globule-like hypoallergenic variant of Bet v 1 [23]. Both proteins display almost identical amino acid sequences (with a deviation in five amino acids only) but differ in their conformational stability [24]. We deliberately opted for model allergens with different conformations to determine if the conformational stability of the antigens has an influence on the interaction of the proteins and the particulate systems. The model proteins were conjugated to both selected particulate systems by non-covalent surface adsorption. This is the best established approach in developing licensed particulate vaccines due to its simplicity and increased effectiveness [25].

2. Results and Discussion

2.1. Characterization of the Synthesized SiO₂ NPs and Alhydrogel[®]

As the initial step, we characterized the two particulate systems to determine differences in their physicochemical properties. We adopted the microemulsion method for the synthesis of SiO₂ NPs as this method has been reported to produce highly monodisperse NPs [26]. Characterization of the synthesized NPs by dynamic light scattering (DLS) indicated a highly monodisperse suspension of SiO₂ NPs with an average hydrodynamic diameter of 100.3 ± 3.4 nm and a zeta potential of -38.9 ± 2.8 mV. Consistently, monodispersity and a hydrodynamic diameter of 102.4 ± 39.3 nm were confirmed by nanoparticle tracking analysis (NTA) (Table 1). Furthermore, from the transmission electron microscopy (TEM) images, the primary particle size of the synthesized NPs along with the uniform spherical shape was further established. The average diameter of the NPs was calculated from the TEM images and was found to be 96.3 ± 4.9 nm (Figure 1A). On the contrary, Alhydrogel[®] was found to be highly polydisperse, with an average size of 585.9 ± 174.2 nm, and exhibited a surface zeta potential of $+18.0 \pm 1.5$ mV (Table 1). Alhydrogel[®] consisted of large clusters of nanofibers, which heavily agglomerated to form microstructures, as evident from the TEM images (Figure 1B and Figure S1A). The scanning electron microscopy (SEM) images further confirmed these heterogeneous microstructures (Figure S1B). The presence of these larger agglomerates impaired their characterization by NTA. The characterization data for Alhydrogel[®] concur with previously published reports [27,28]. From these characterization data, the morphological distinction of both particulate systems was evident.

Table 1. Physicochemical characterization of the synthesized SiO₂ NPs and Alhydrogel[®] by measurement of hydrodynamic size, polydispersity index and zeta potential by DLS (NP concentration of 0.1 mg/mL) and NTA (NP concentration of 0.02 mg/mL).

Sample	Technique	Number Mean Diameter (nm)	PDI	Size (Z Average) (nm)	Zeta Potential (mV)
SiO ₂ NPs	DLS	100.3 ± 3.4	0.025	120.2 ± 1.2	-38.9 ± 2.8
SiO ₂ NPs	NTA	102.4 ± 39.3	-	-	-
Alhydrogel [®]	DLS	585.9 ± 174.2	0.345	1082.0 ± 63.4	$+18.0 \pm 1.5$

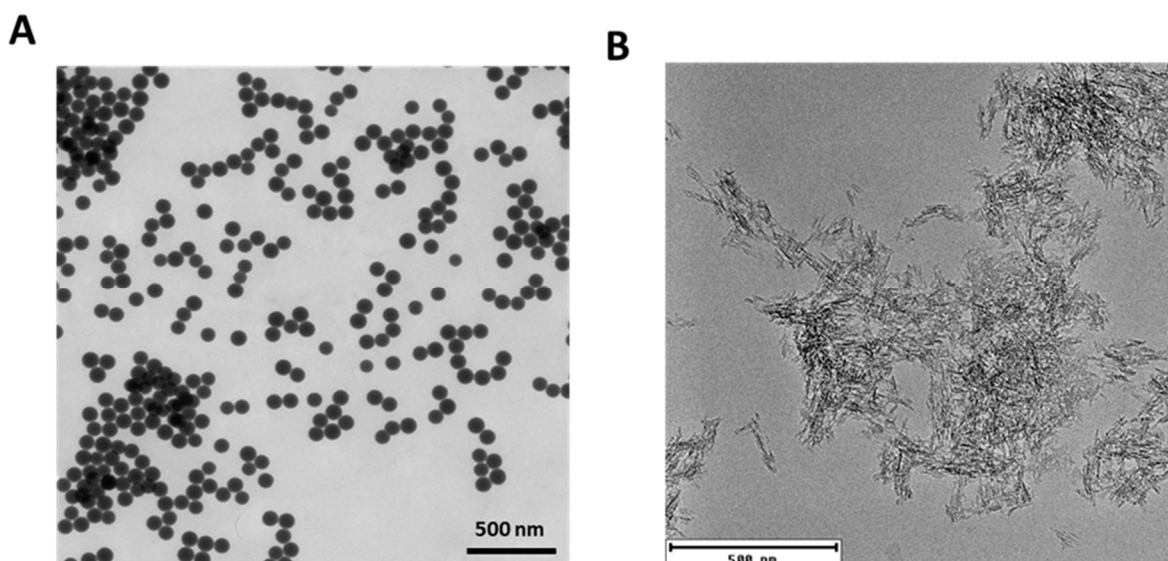


Figure 1. Characterization of the particulate systems by determining the morphology and primary size of particles. Transmission electron microscopy (TEM) image of synthesized SiO₂ NPs (A) and Alhydrogel[®] (B).

2.2. Efficient Conjugation of Allergens with SiO₂ NPs and Alhydrogel[®]

Following the characterization of particles, we examined their conjugation efficiency with the model allergens. The allergens were incubated with the particles, and the conjugated allergens were quantitatively and qualitatively analyzed. From the analysis of the centrifuged pellets by sodium dodecyl sulphate-polyacrylamide gel electrophoresis (SDS-PAGE), a conjugation efficiency of $14.5 \pm 3.5\%$ for Bet v 1 and $58.7 \pm 5.8\%$ for BM4 was obtained with SiO₂ NPs (Figure 2). To further confirm our observation, the supernatant, which contained the non-conjugated allergen, was quantified using standard protein assays such as Bradford and bicinchoninic acid (BCA) assays. The amounts of protein bound were back-calculated from the concentrations obtained from these assays. From the Bradford assay, the percentage of conjugation efficiency was found to be $16.8 \pm 6.2\%$ for Bet v 1 and $64.3 \pm 1.5\%$ for BM4. This was similar in the BCA assay, where $28.1 \pm 11.8\%$ of Bet v 1 and $63.7 \pm 4.8\%$ of BM4 were conjugated to SiO₂ NPs (Figure 2). These results are consistent with the SDS-PAGE analysis. Thus, we observed significant differences in conjugation efficiency with both allergens when bound to SiO₂ NPs. This discrepancy can be attributed to the conformational differences in both allergens [24]. We used only BCA and Bradford assays for the quantification with Alhydrogel[®] as we obtained comparable results from all three methods using SiO₂ NPs, and a lack of complete dissociation of allergens from Alhydrogel[®] leads to technical difficulties in their analysis by SDS-PAGE. Alhydrogel[®] exhibited a conjugation efficiency of $103.7 \pm 0.4\%$ for Bet v 1 and $97.0 \pm 0.3\%$ for BM4 from the Bradford assay. Similarly, we attained 99% efficiency with both allergens from the BCA assay (Figure 2). Furthermore, the conjugation efficiency of both candidate allergens and the particles was confirmed qualitatively by the changes in the zeta potential. Upon conjugation of the allergens to SiO₂ NPs or Alhydrogel[®], we observed a more positive zeta potential compared to the pristine NPs (Table 2). This further confirms the effective conjugation of the allergens. From all these data, it can be concluded that the conjugation efficiency of allergens with both candidate NPs is quite different. From previous reports, Alhydrogel[®] adsorbs proteins dominantly through ligand exchange and by electrostatic interactions [29], whereas SiO₂ NPs adsorb proteins mainly by hydrophobic and electrostatic forces [30,31]. As both model allergens have a pI of around 5 (Bet v 1, 5.4; BM4, 5.6), they exhibit a negative net charge at pH 7.4 [32]. Alhydrogel[®] displays a strongly positive zeta potential, which further indicates the possible role of strong electrostatic interactions leading to the increased conjugation efficiency in Alhydrogel[®]. Furthermore, the network of nanofibrillary structures of Alhydrogel[®] can create more binding sites for

the protein compared to the highly monodisperse spherical SiO₂ NPs used as model NPs here (Figure 1). SiO₂ NPs exhibit a negative zeta potential at neutral pH. Thus, theoretically the role of electrostatic interactions should be negligible or repulsive in SiO₂ NPs. However, there are reports indicating the adsorption of proteins to equally charged surfaces [33]. Even though a protein exhibits an overall negative charge, it can have local positively charged surface patches [34]. These areas in the allergen can attract the negatively charged SiO₂ NPs, leading to weak attractive electrostatic interactions resulting in effective protein conjugate formation.

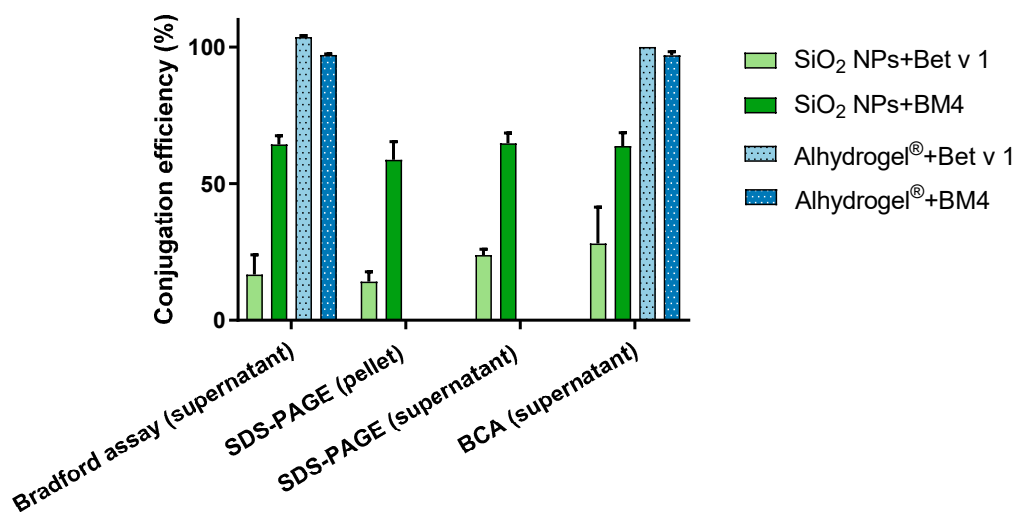


Figure 2. Conjugation efficiency of particulate systems. The quantitative analysis of percentage of allergen bound to SiO₂ NPs and Alhydrogel[®] was performed by SDS-PAGE, Bradford assay and BCA assay. A 100% conjugation efficiency here represents a conjugation of the total amount of allergen taken for the experiment (160 µg/mL).

Table 2. Zeta potential of the particles and particle–allergen conjugates determined by DLS.

Sample	Zeta Potential (mV)
SiO ₂ NPs	−38.9 ± 2.8
SiO ₂ NPs + Bet v 1	−25.7 ± 5.8
SiO ₂ NPs + BM4	−19.2 ± 5.5
Alhydrogel [®]	+18.0 ± 1.5
Alhydrogel [®] + Bet v 1	+31.2 ± 1.2
Alhydrogel [®] + BM4	+32.3 ± 1.4

2.3. Conjugation of Allergens Decreases Their Proteolytic Stability

The structural stability of proteins can affect the major molecular events leading to an immune response, from uptake to antigen presentation, thereby exerting a significant impact on the immunogenicity of the administered vaccine [35,36]. As an initial method to understand the structural integrity of the conjugated protein, we determined the proteolytic stability of the allergens conjugated to SiO₂ NPs and Alhydrogel[®] by comparing the degradation kinetics, using microsomal extracts of an immortalized murine dendritic cell line (JAWS II). The microsomal extracts are composed of several exo- and endoproteases which include cathepsin S, D, K and L and legumain, amongst others [37]. These proteases proteolytically process the protein antigens to smaller peptides for their presentation by MHC molecules. Initially, we confirmed that the conjugation of SiO₂ NPs and Alhydrogel[®] did not inhibit the activity of proteolytic enzymes by an enzymatic assay (Figure S2). Furthermore, the stability of allergen–NP conjugates in the microsomal degradation assay was verified (Figure S3). We observed that conjugation of allergens to both candidates increased the proteolytic susceptibility of the allergen. Bet v 1 bound to SiO₂ NPs and Alhydrogel[®]

was proteolytically cleaved much faster than the unconjugated allergen (Figure 3A,B). With BM4, we observed a similarly increased degradation upon conjugation (Figure 3A,B). This observation was further confirmed by simulating in vitro endolysosomal processing using recombinant human cathepsin S, a prominent endolysosomal cysteine protease (Figure S3). In accordance with the former results, a similar trend in the kinetics of degradation was evident. Subsequent analysis of the peptides derived from the endolysosomal degradation using liquid chromatography-mass spectrometry (LC-MS) resulted in qualitatively identical degradation patterns (Figure 4). However, we could observe a large diversity in the peptides generated for the conjugated samples. Interestingly, alterations in the kinetics of proteolytic processing also prompted the generation of more peptides in the immunodominant T cell epitope region [38] (Figure 4, highlighted in gray). For the quantitative analysis of the peptides, we grouped the generated peptides into eight main clusters based on the qualitative data and calculated the percentage of relative abundances for each peptide cluster (Figure 5). The conjugation of allergens to both particle systems clearly affected the rate of peptide production in different ways. Conjugation of both allergens to SiO₂ NPs significantly increased the relative abundance of peptides in clusters 1 and 8 compared to the unconjugated allergen. However, in Alhydrogel[®], we observed this shift towards peptide clusters 2 and 3 (Figure 5). The increased rate of core peptide production in cluster 8, thus, resulted in a more efficient generation of the immunodominant T cell epitope in the case of SiO₂-conjugated allergens. However, the increased or decreased peptide abundance in other clusters was, immunologically, not as significant as cluster 8. Even though both particles showed identical processing patterns, there is a deviation in their relative abundance of peptides. The fold or conformational stability of allergens has previously been shown to have a huge impact on the processing and immunogenicity of allergens [39]. Thus, the increased proteolytic processing of allergens upon conjugation to particles may be due to a change in the conformational stability of the allergens, and the deviation in the relative abundance of peptide clusters may indicate alterations in the interaction of allergens with the two different particulate systems, leading to differences in preferential exposure to the proteolytic enzymes.

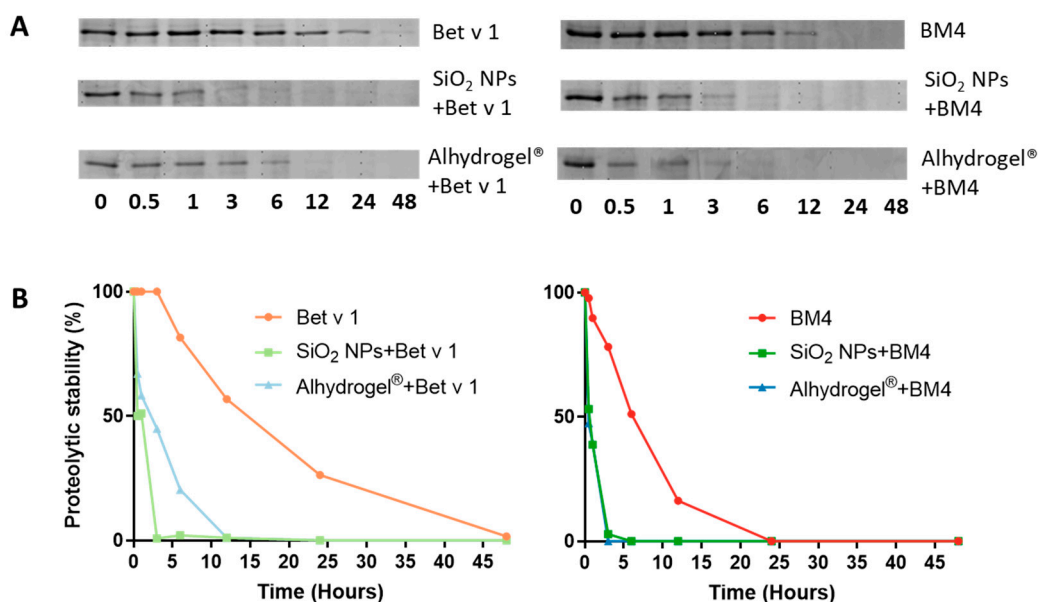


Figure 3. Impact of allergen conjugation to particles on the kinetics of allergen processing. (A) Comparison of the processing behavior of allergens conjugated to the particulate systems and the unconjugated allergens by assessing their proteolytic degradation at 37 °C for different time points (0, 0.5, 1, 3, 6, 12, 24 and 48 h) using the microsomal extracts from JAWS II determined by 15% SDS-PAGE and Coomassie staining (left panel denotes samples with Bet v 1 and right panel those with BM4), and (B) densitometric analysis of their proteolytic stability with Image lab 4.01 software (left panel denotes samples with Bet v 1 and right panel those with BM4).

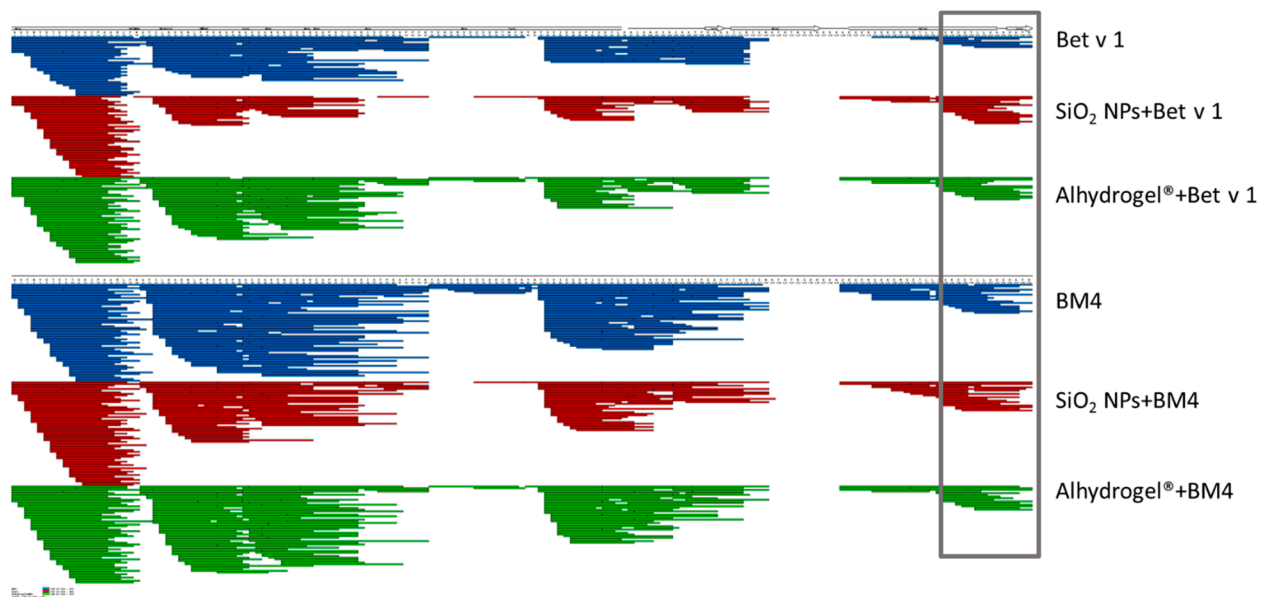


Figure 4. Impact of allergen conjugation to particles on the outcome of allergen processing determined qualitatively. The peptides obtained after 1 h of proteolytic degradation at 37 °C by LC-MS using the microsomal extract from JAWS II cells are displayed. The immunodominant T cell epitope region is highlighted in gray.

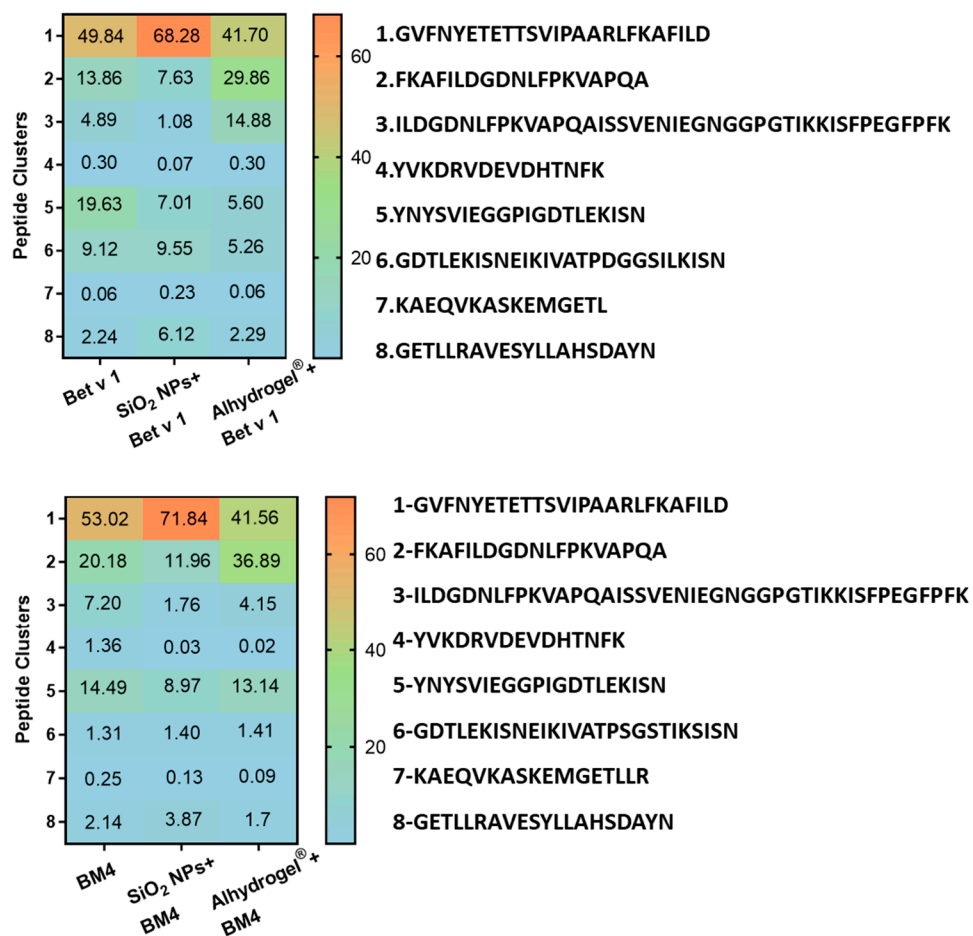


Figure 5. Impact of allergen conjugation to particles on the outcome of allergen processing determined quantitatively. Relative abundances of peptides obtained after 1 h of proteolytic degradation using the microsomal extract from JAWS II cells are shown (upper panel indicates samples with Bet v 1 and lower panel those with BM4). The peptides obtained by LC-MS analysis were grouped into eight clusters based on the qualitative data.

2.4. Changes in the 3D Fold of the Allergen upon (Nano)Particle Conjugation

The proteolytic resistance of allergens depends on their structural integrity; thus, a partial or complete unfolding of the allergen can make it more susceptible to proteolytic enzymes. The proteolytic cleavage sites for Bet v 1 are mostly located within its secondary structures, thus making Bet v 1 relatively proteolytically resistant [40,41]. Therefore, we investigated if the conjugation of the allergens to SiO₂ NPs or Alhydrogel[®] changed the conformational stability of both model allergens. From the circular dichroism (CD) spectroscopy data, it was evident that conjugation to SiO₂ NPs induced conformational changes in the allergens (Figure S5). The deconvoluted CD spectra indicated that upon conjugation to SiO₂ NPs, the allergen significantly lost its alpha-helical structures, as seen in the case of Bet v 1, whereas in the case of BM4 (partially unfolded allergen), it induced a partial stabilizing effect in the alpha-helical content (Figure 6A). This may be due to the interaction of the positively charged amino acid residues in both the allergens with the negatively charged surface of SiO₂ NPs. In the case of Alhydrogel[®], we observed that the alpha-helical structures were relatively stable, whereas there was notable depletion in the beta structures in both model allergens. However, in the case of BM4, an apparent re-folding effect was observed, as indicated by an increase in the alpha-helical content (Figure 6A). Thus, we hypothesize that in a well-folded allergen (Bet v 1), the interaction disrupts the fold stability, while in a molten globule-like allergen (BM4), the interaction with particles partially induces fold stabilization, as indicated by the increase in beta structures in BM4 conjugated to SiO₂ NPs and alpha structures in Alhydrogel[®]. The distinct stabilizing effects on BM4 by the two types of particles are intriguing and may occur due to the differently charged surfaces of SiO₂ NPs and Alhydrogel[®]. The observed beta-stabilizing effect in BM4 by SiO₂ NPs may result from their high curvature and their potential for electrostatic interactions, whereas in Alhydrogel[®], the interaction stabilizes the alpha-helical content of BM4 with a concomitant decrease in the beta structure content. We observed that the negatively charged SiO₂ NPs induced a relative destabilization of the alpha-helical structures in both Bet v 1 and BM4, suggesting that the interaction tends to distort the alpha helices in the protein. Conversely, the positively charged Alhydrogel[®] repels the alpha helices and attracts the beta structures, thereby destabilizing the beta structures and stabilizing the alpha helices. To further confirm this observation, we carried out infrared spectroscopy, which, in general, is more sensitive to the beta structures of proteins. The results additionally verify that the conjugation of allergens to SiO₂ NPs did not alter the beta structures (Figure 6B). However, in the case of allergens conjugated to Alhydrogel[®], interpretation of the data was not possible as Alhydrogel[®] interfered with the results by exhibiting a strong peak similar to the allergen in the amide I region (Figure S6). The anilino-naphthalene sulfonic acid (ANS) fluorescence spectroscopy data reveal that conjugation to SiO₂ NPs decreased the fluorescence intensity at least two-fold, which is an indication that the interaction of the allergens with the SiO₂ NPs further prevents the accessibility of hydrophobic regions of Bet v 1. Bet v 1 in its native state exhibits a solvent-exposed hydrophobic cavity favoring the binding of ANS [42]. In the case of the molten globule-like allergen (BM4), conjugation to SiO₂ NPs led to a slight decrease in the fluorescence intensity, whereas in Alhydrogel[®], the fluorescence intensity increased to a level seen in native Bet v 1, which suggests that conjugation induces a stabilization of the correctly folded allergen (Figure 6C). This may be an indication that SiO₂ NPs interact with positive charges in the C-terminal alpha helix of Bet v 1 in close proximity to the solvent-accessible hydrophobic cavity.

The conjugation of the well-folded allergen Bet v 1 to SiO₂ NPs or Alhydrogel[®] resulted in fold destabilization (at pH 7.4). During the process of allergen processing, these candidates are subjected to further chemical or physical stress. This includes a change in pH (acidic environment in the endolysosomes). It is obvious that the change to a more acidic environment can further pose chemical stress to the allergens and thereby induce further destabilization or unfolding of the allergen, making it more accessible for proteases [43].

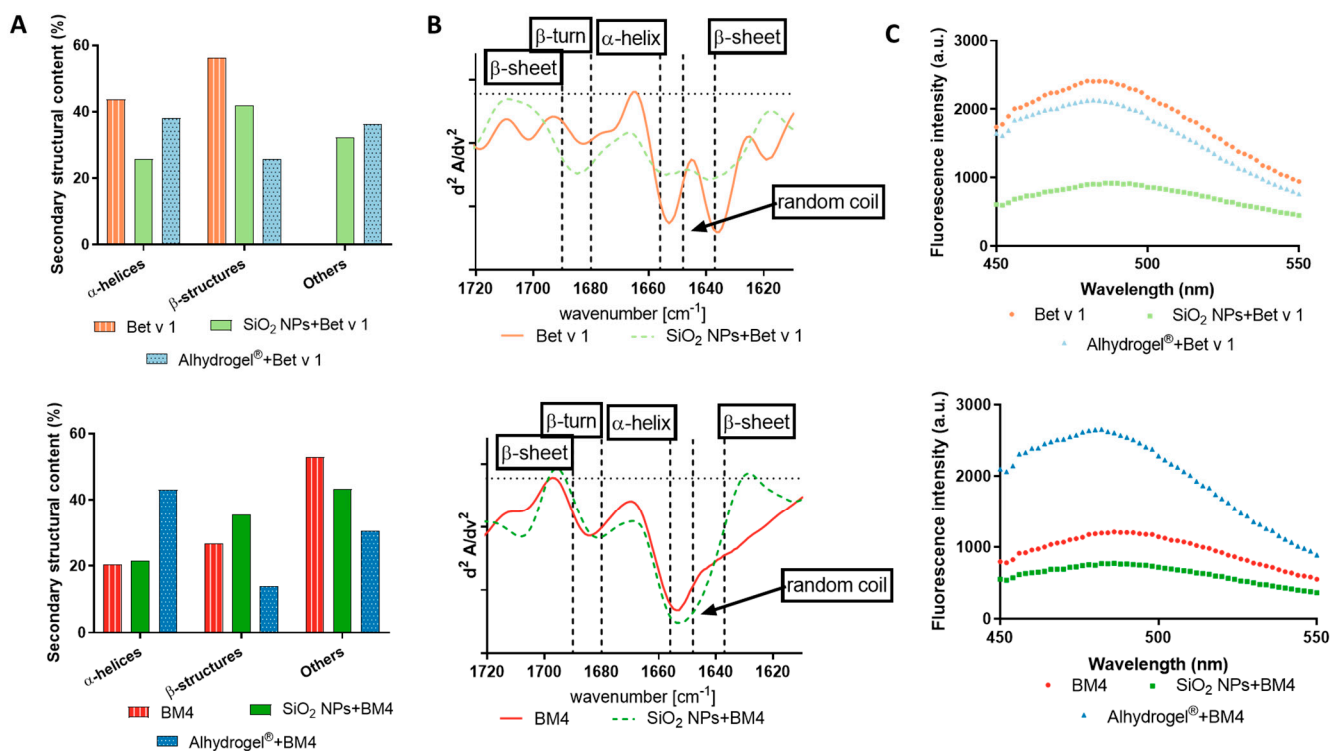


Figure 6. Determination of the fold stability of allergens conjugated to SiO₂ NPs and Alhydrogel[®]. (A) Comparison of the secondary structural contents of the allergens conjugated to particulate systems and unconjugated allergens by CD spectroscopy and (B) 2nd derivatives of amide I by Bio-ATR-FTIR spectroscopy, and (C) determination of the accessibility of the hydrophobic cavity by ANS spectroscopy. The upper panel indicates samples with Bet v 1 and the lower panel those with BM4.

2.5. Structural Integrity of T Cell and IgE Epitopes

The conformational stability of allergens has been reported to alter their allergenicity and immunogenicity [35]. We, therefore, sought to investigate if the changes in the fold stability of the allergens upon conjugation resulted in any differences in the immunological properties of the allergens. We determined T cell activation using a dominant T cell epitope recognizing T cell hybridoma by measuring the concentration of secreted interleukin (IL)-2, a cytokine indicative of T cell proliferation, but we could not detect any significant differences between the conjugated and the unconjugated allergens. However, we observed a tendency for an increase in the IL-2 concentration when conjugated to SiO₂ NPs. This increase most likely resulted from the activation of T cells by SiO₂ NPs alone (Figure S7). This observation also corresponds to the appearance of more peptides in the immunodominant T cell epitope cluster (Figures 4 and 5). Even though the conjugation affected the 3D fold of the allergens, it did not drastically affect the integrity of T cell epitopes. This confirms the functional integrity of T cell epitopes in both conjugated forms (Figure 7A). Decreased fold stability of an allergen can also lead to the loss of conformational epitopes. This property has been applied for hypoallergenic variants, where the T cell epitope is still intact and functional, whereas conformational B cell epitopes recognized by IgE are reduced [44,45]. We investigated the integrity of IgE epitopes by a mediator release assay using a humanized rat basophil leukemia cell line assay. As shown in Figure 7B, conjugation of both allergens to SiO₂ NPs did not change their capacity to crosslink cell-bound IgE. However, allergens conjugated to Alhydrogel[®] significantly reduced their IgE crosslinking capacity compared to the unconjugated allergens. Thus, we could confirm that the surface structure of the SiO₂ NP-conjugated allergens resembled the native Bet v 1, whereas in Alhydrogel[®], it was significantly altered or blocked by Alhydrogel[®] binding. The IgE epitope binding in Bet v 1 has been established to be strongly conformation-dependent [46]. There are also reports

on amino acids that may be involved in the recognition of IgE antibodies. This includes amino acids E42, N43, I44, E45, G46, N47, G48, G49, P50, G51 and T52, and R70, D72, H76, I86 and K97 [47,48]. These amino acids are predominantly located in the beta structures of Bet v 1. In the case of SiO₂ NPs, the beta structures are stabilized, whereas in Alhydrogel[®], they are distorted and electrostatically attracted, i.e., blocked. It is likely that this distortion, and potential blockage, of beta structures is the reason for the decreased IgE crosslinking.

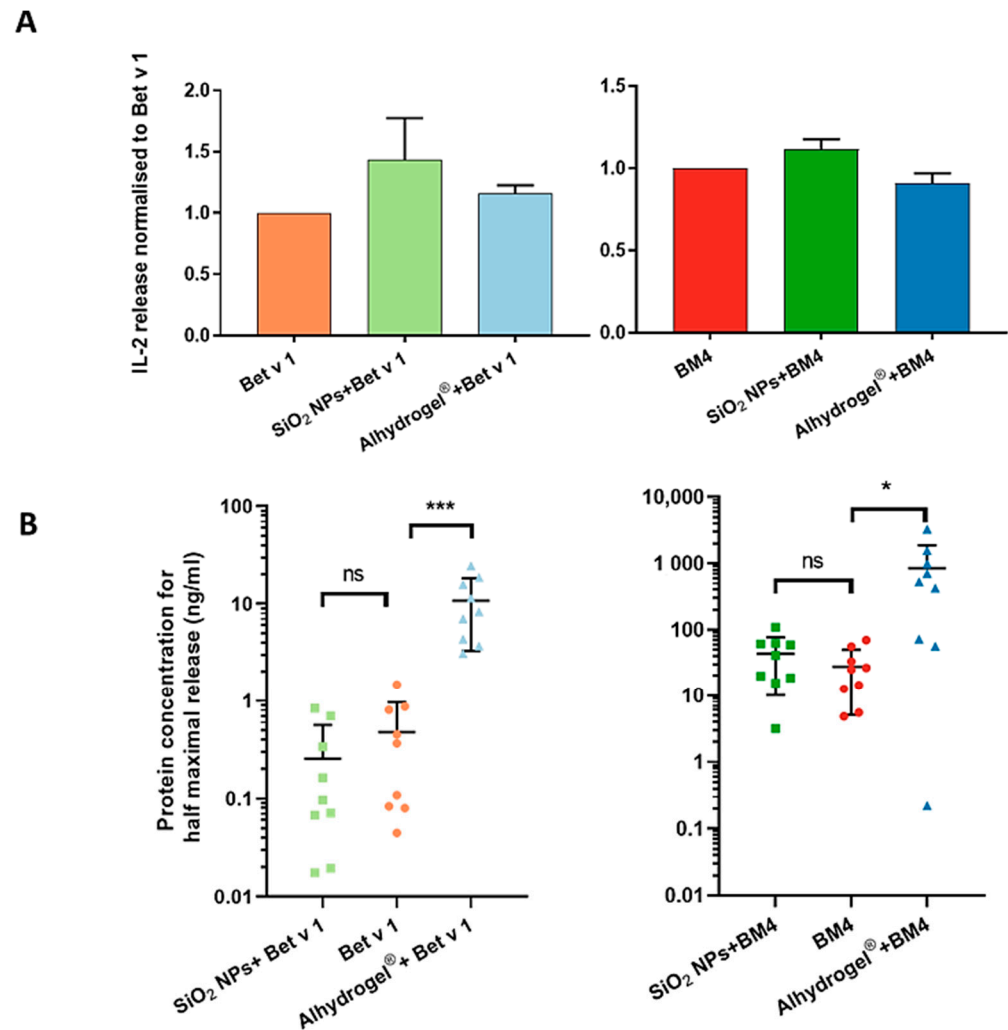


Figure 7. Immunologic properties of conjugated allergens. (A) The integrity of the dominant T cell epitope was determined as the concentration of IL-2 (indicator of T cell activation) released from T cell epitope-recognizing T cell hybridoma (panel on the left shows particulate systems with Bet v 1 and that on the right those with BM4). (B) The integrity of IgE epitopes was determined by mediator release assay using a humanized rat basophil leukemia cell line (panel on the left shows particulate systems with Bet v 1 and that on right those with BM4). Values are expressed as the protein concentration required to attain half-maximal release compared to the maximum release attained with 10% Triton X-100. Stars indicate the significance of difference in the protein concentration for half-maximal release: *** $p < 0.0001$, * $p < 0.01$.

3. Materials and Methods

3.1. Patients and Sera

Sera from birch pollen-allergic patients were collected for the mediator release assay and were selected ($n = 10$) based on their allergen-specific IgE reactivity. The procedure was approved by the local ethics committees of the Medical University and General Hospital of Vienna (No. EK1263/2014) and Salzburg (No. 415-E/1398/4-2011).

3.2. Synthesis and Physicochemical Characterization of SiO₂ NPs

SiO₂ NPs were synthesized by the microemulsion method using tetraethylorthosilicate (TEOS) (Sigma, Darmstadt, Germany) as the precursor, as previously described [49]. A detailed description of the synthesis can be found in the Supplementary Materials File. Alhydrogel[®] was purchased from Brenntag, Germany. The size distribution, polydispersity index and zeta potential of particulate systems were determined using dynamic light scattering (Malvern Zetasizer Nano ZS, Malvern instruments Ltd., Malvern, UK) and nanoparticle tracking analysis (NanoSight LM10, Malvern instruments Ltd., Malvern, UK). The morphology of the particulate systems was observed by a transmission electron microscope (EM 910, Zeiss, Oberkochen, Germany; JEM F-200, JEOL, Freising, Germany). The average primary particle size of the SiO₂ NPs was calculated from the TEM images by utilizing 30 particles.

3.3. Determination of the Efficiency of Conjugation

Two recombinant pollen allergens, Bet v 1.0101 and BM4 (hypoallergenic variant of Bet v 1), were chosen as the model allergens for this study. Both allergens were produced and characterized in our laboratory according to previously published protocols [24,50]. NPs and Alhydrogel[®] (2 mg/mL) were incubated with 160 µg/mL of allergens in an isotonic environment by maintaining a pH of 7.4 and a temperature of 4 °C for 17 h on a rotator. After incubation, the samples were centrifuged at 18,000 × *g* for 1 h at 4 °C, and the supernatant and pellet were separated. The obtained pellet was then washed with endotoxin-free water to remove the unbound proteins. The protein content of the pellet was determined by SDS-PAGE by successfully separating the allergen bound to the NPs using a reducing buffer, whereas the supernatant was analyzed by colorimetric protein assays, which included Bradford and BCA assays (Sigma-Aldrich, St. Louis, MI, USA). The supernatant was also quantified using SDS-PAGE, and the amount of adsorbed allergen was back-calculated from the value obtained. The identity of the allergens was confirmed using standard molecular weight markers, while the quantity of adsorbed allergens was determined by comparing the intensity of the bands of the samples with the standard allergen concentration after Coomassie brilliant blue R250 staining (Bio-Rad, Irvine, CA, USA). The absolute quantity of adsorbed allergens was calculated using the quantity tool function of Image lab 6.01 software. The efficiency of conjugation was calculated by determining the percentage of allergen bound to the NPs. Furthermore, allergen corona formation was qualitatively confirmed by DLS.

3.4. Simulation of In Vitro Endolysosomal Degradation Using Microsomes

The endolysosomal degradation assay was performed with SiO₂ NPs and Alhydrogel[®] conjugated to both model allergens and compared to unconjugated allergens, as previously described [37,51]. The samples containing 5 µg equivalent allergen were incubated with 7.5 µg of microsomal extract of JAWS II (American Type Culture Collection, Manassas, VA, USA) in 0.1 M citrate buffer pH 4.8 and 2 mM Dithiothreitol (DTT) for 0, 0.5, 1, 3, 6, 12, 24 and 48 h at 37 °C. At the end of incubation, the digestion was halted by incubation of samples at 95 °C for 5 min. The intact protein after different time points was analyzed by SDS-PAGE and quantitatively determined using Image lab 6.01 software. The proteolytic stability of conjugated allergens was compared with the unconjugated allergens. The quantitative amount of allergen at the zero time point was considered as 100%. The abundance of generated peptides obtained after 1 h of digestion was further analyzed by mass spectrometry (MS) using a Q-Exactive Orbitrap Mass Spectrometer (Thermo Fisher Scientific, Waltham, MA, USA), nanoelectrospray ionization and nano-HPLC (Dionex Ultimate 3000, Thermo Fisher Scientific) [35]. The MS data were qualitatively analyzed using MS Tools software [52]. Furthermore, the generated MS data were quantitatively analyzed by calculating the relative abundance of the generated peptides at 1 h of degradation. This was achieved by clustering the obtained peptide sequences into 8 groups according to their amino acid sequence. For Bet v 1, the clusters

are cluster 1: GVFNYETETTSVIPAARLFKAFILD, cluster 2: FKAFILDGDNLFKVPQA2, cluster 3: ILDGDNLFPKVPQAISVENIEGNGGPGTIKKISFPEGFPFK, cluster 4: YVKDRVDEVDHTNFK, cluster 5: YNYSVIEGGPIGDTLEKISN, cluster 6: GDTLEKISNEIKIVATPDGGSILKISN, cluster 7: KAEQVKASKEMGETL and cluster 8: GETLLRAVESYLLAHS-DAYN. Similarly, for BM4, the clusters include cluster 1: GVFNYETETTSVIPAARLFKAFILD, cluster 2: FKAFILDGDNLFKVPQA2, cluster 3: ILDGDNLFPKVPQAISVENIEGNGGPGTIKKISFPEGFPFK, cluster 4: YVKDRVDEVDHTNFK, cluster 5: YNYSVIEGGPIGDTLEKISN, cluster 6: GDTLEKISNEIKIVATPSGSTIKSISN, cluster 7: KAEQVKASKEMGETL and cluster 8: GETLLRAVESYLLAHS-DAYN. The peak areas of each cluster were calculated by summing up the sequences appearing under each cluster, and this was expressed in percentage by counting the total sum of the peptide sequences.

3.5. Evaluation of the Changes in the Protein Structure

The changes in the conformation of the proteins with allergen–(nano)particle conjugation were determined by techniques such as ANS spectroscopy, circular dichroism spectroscopy and Fourier transform infrared spectroscopy (FTIR). The changes in the accessibility of hydrophobic regions of allergens when bound to particles were monitored by using the fluorescent probe ANS. The samples (SiO₂ NPs and Alhydrogel[®] conjugated with both model allergens) and controls (unconjugated allergens) at a concentration of 19 µM (90 µL) were incubated with 1 mM of ANS (10 µL). The fluorescence intensity was measured after 30 min using an Infinite M200 Pro plate reader (Tecan, Grödig, Austria). The excitation wavelength was set at 370 nm, and an emission scan was performed from 450 to 550 nm. For CD spectroscopy, samples (Alhydrogel[®] and SiO₂ NPs with BM4 and Bet v 1 and unconjugated allergens) were diluted to a concentration of 0.12 mg/mL using 10 mM sodium phosphate buffer, pH 7.4, and the ellipticity was measured with a JASCO J-815 spectropolarimeter fitted with a PTC-423S Peltier-type single position cell holder (Jasco, Tokyo, Japan) over the wavelength range of 190 to 260 nm. The CD spectra obtained were deconvoluted using Bestsel software [53]. The changes in protein structure were confirmed using FTIR where the spectra in the range of the amide I and amide II peaks (1500–1700 cm⁻¹) were recorded at a constant temperature (25 °C) using a Bio-ATR II transmission cell adapted to a Tensor II FTIR system (Bruker Optics, Bremen, Germany). Protein concentrations of 1.0 mg/mL were used for the measurement. The analysis of the software was accomplished by using OPUS spectroscopy software 6.0 (Bruker Optics). The second derivative of the amide I vibration was calculated after vector normalization (25 smoothing points) using the Savitzky–Golay algorithm [46].

3.6. Determination of the Structural and Functional Integrity of T Cell Epitope by T Cell Activation Assay

To determine the structural and functional integrity of the T cell epitopes of the conjugated allergens to SiO₂ NPs or Alhydrogel[®], a T cell activation assay was performed. SiO₂ NPs and Alhydrogel[®] bound to both model allergens along with unconjugated allergens, as controls, were incubated with murine bone marrow-derived dendritic cells (BMDCs) from BALB/c mice at a concentration of 10 µg/mL or 5 µg/mL for a defined period of 16 h. After incubation, BMDCs were washed and cocultured with CD4+ T cell hybridoma cells specific for the immunodominant epitope of both proteins (amino acids 142–153) in a ratio of 1:10 for 16 h. The supernatants were harvested, and the concentration of IL-2 release was measured by ELISA (ELISA MAX[™] standard set mouse IL-2, Biolegend, CA, San Diego, USA). To avoid the variability within repeated experiments, the concentration of IL-2 release was normalized to unconjugated Bet v 1 and BM4.

3.7. Determination of the Structural and Functional Integrity of IgE Epitopes by Mediator Release Assay

To determine the structural and functional integrity of the IgE epitopes of the allergens when conjugated to SiO₂ NPs or Alhydrogel[®], a mediator release assay was performed [54]. Human high-affinity IgE receptor (FcεRI)-transfected rat basophilic leukemia cells (RBL-

2H3) were sensitized with the sera (containing allergen-specific IgE antibodies) of birch pollen-allergic patients overnight at 37 °C, 5% CO₂. Sera from birch pollen-allergic patients were selected ($n = 10$) based on their allergen-specific IgE reactivity. All of the patients' sera were preincubated with AG-8 cells (ATCC, Germany) in order to deactivate the complement system. After incubation, cells were washed with Tyrode's buffer (9.5 g/L Tyrode's salts (Sigma), 1 g/L sodium bicarbonate and 0.1% (*w/v*) BSA) and incubated with either SiO₂ NP- or Alhydrogel[®]-bound model allergens as well as the unconjugated allergen controls for 1 h at 37 °C, 5% CO₂. The concentrations of allergens used for the assay ranged from 10,000 to 0.0001 ng/mL (8 serial dilutions). After the incubation time, the supernatants were collected, and the fluorogenic substrate 4-methyl umbelliferyl-N-acetyl- β -glucosaminide (Sigma-Aldrich, St. Louis, MO, USA) was added. The release of β -hexosaminidase into the supernatant cleaves the fluorogenic substrate, leading to fluorescence. The reaction was stopped after 1 h using 0.2 M glycine buffer pH 10.7. The fluorescence intensity was measured at an excitation wavelength of 360 nm and emission at 440 nm, and the percentage of release was calculated by comparing it with the maximum release attained with 10% Triton X 100 (Sigma-Aldrich). The viability of the cells was confirmed with an MTT assay. The results were statistically evaluated by ANOVA followed by a Bonferroni post hoc test. A *p* value greater than 0.05 was considered as not statistically significant.

4. Conclusions

In this study, we utilized an *in vitro* test strategy that is suitable to analyze antigens at the material interface during the early stage of product development. The strategy comprises biophysical methods and functional assays to understand the structural integrity of proteins, using allergens as models here, at the particle surface. Our findings indicate the dominant role of electrostatic interactions in modulating protein–particle interaction, and we were able to prove that both particulate systems induced structural alterations in the model allergens. These changes significantly altered the immunological response, as confirmed by the biophysical and functional assays. This is a strong indication that the structural stability of antigens should be thoroughly investigated in the initial stages of nanovaccine development. In our study, when we compared the safety of the two particulate systems, the results revealed Alhydrogel[®] was still a better candidate for allergen-specific immunotherapy, as it exhibited a decreased IgE crosslinking potential, which is an indication of lower adverse effects. Furthermore, it showed better conjugation efficiency putatively due to its nanofibrillar, highly agglomerated and polydisperse state. For SiO₂ NPs, IgE crosslinking was similar to the unconjugated allergen, thereby indicating a risk of adverse effects during allergen-specific immunotherapy. However, fine-tuning of these NPs through surface functionalization could potentially attenuate this fold destabilization effect, thereby maintaining structural integrity. This could be a desirable property for other types of nanovaccine development. Thus, our early decision toolbox can readily be employed to compare an array of different NP and/or antigen candidates.

In summary, we herein described an early-stage *in vitro* test strategy applied for nanomaterial candidates for use as adjuvants and/or carriers of allergens, but which can also be applied for other diverse antigens in nanovaccine development, allowing fine-tuning of the nanovaccine properties in order to achieve a desired immune response. This approach, integrated early into the development process, can contribute to the establishment of safe and efficacious nanovaccines in a cost-effective and time-efficient manner and, thus, aid safe-by-design approaches in nanovaccine innovation.

Supplementary Materials: The following are available online at <https://www.mdpi.com/article/10.3390/ijms221910895/s1>.

Author Contributions: Conceptualization: L.J., L.A., H.B., A.D. and M.H.; Investigation: L.J., M.G., S.H. and N.H.; Methodology: W.T.S., L.A., R.W. and P.B.; Formal analysis: M.G., W.T.S., R.W. and H.B.; Visualization: L.J., S.H. and N.H.; Funding acquisition and supervision: F.F., A.D. and M.H.; Writing-original draft preparation: L.J.; Writing-review and editing: L.J., L.A., W.T.S., M.G., S.H.,

N.H., F.F., R.W., H.B., A.D. and M.H. All authors have read and agreed to the published version of the manuscript.

Funding: This work was funded by the international PhD program “Immunity in Cancer and Allergy—ICA” of the Austrian Science Fund (FWF, grant no. W01213), by the Austrian Science Funds Project P32189 and by the Allergy Cancer BioNano Research Centre of the Paris Lodron University of Salzburg (PLUS). Open Access Funding by the Austrian Science Fund (FWF).

Institutional Review Board Statement: Sera from birch pollen-allergic patients were collected for the mediator release assay. The procedure was approved by the local ethics committees of the Medical University and General Hospital of Vienna (No. EK1263/2014) and Salzburg (No. 415-E/1398/4-2011). The animal study was reviewed and approved by the Austrian Ministry of Education, Science and Research (permit No. BMWF-66.012/0013-WF/V/3b/2017).

Informed Consent Statement: Not applicable.

Data Availability Statement: All data generated or analyzed during this study are included in this manuscript and its supplementary information files.

Acknowledgments: The authors thank Stephan Drothler, BSc, for helping with the isolation of BMDCs, Athanasios Bethanis, BSc, scientific project staff, Robert Mills-Goodlet, MSc, for their scientific inputs, and Wright Jacob, Faculty of Medical Science, UCL, UK, for the scientific inputs and proofreading the manuscript.

Conflicts of Interest: The authors declare no conflict of interest.

References

1. Yun, C.-H.; Cho, C.-S. Nanoparticles to improve the efficacy of vaccines. *Pharmaceutics* **2020**, *12*, 418. [[CrossRef](#)]
2. Ilyinskii, P.O.; Roy, C.J.; O’Neil, C.P.; Browning, E.A.; Pittet, L.A.; Altreuter, D.H.; Alexis, F.; Tonti, E.; Shi, J.; Basto, P.A. Adjuvant-carrying synthetic vaccine particles augment the immune response to encapsulated antigen and exhibit strong local immune activation without inducing systemic cytokine release. *Vaccine* **2014**, *32*, 2882–2895. [[CrossRef](#)]
3. Getts, D.R.; Shea, L.D.; Miller, S.D.; King, N.J. Harnessing nanoparticles for immune modulation. *Trends Immunol.* **2015**, *36*, 419–427. [[CrossRef](#)]
4. Thakur, N.; Thakur, S.; Chatterjee, S.; Das, J.; Sil, P.C. Nanoparticles as smart carriers for enhanced cancer immunotherapy. *Front. Chem.* **2020**, *8*, 1217. [[CrossRef](#)]
5. Perciani, C.T.; Liu, L.Y.; Wood, L.; MacParland, S.A. Enhancing immunity with nanomedicine: Employing nanoparticles to harness the immune system. *ACS Nano* **2020**, *15*, 7–20. [[CrossRef](#)] [[PubMed](#)]
6. Johnson, L.; Duschl, A.; Himly, M. Nanotechnology-based vaccines for allergen-specific immunotherapy: Potentials and challenges of conventional and novel adjuvants under research. *Vaccines* **2020**, *8*, 237. [[CrossRef](#)] [[PubMed](#)]
7. Bhardwaj, P.; Bhatia, E.; Sharma, S.; Ahamad, N.; Banerjee, R. Advancements in prophylactic and therapeutic nanovaccines. *Acta Biomater.* **2020**, *108*, 1–21. [[CrossRef](#)] [[PubMed](#)]
8. Zhu, G.; Zhang, F.; Ni, Q.; Niu, G.; Chen, X. Efficient nanovaccine delivery in cancer immunotherapy. *ACS Nano* **2017**, *11*, 2387–2392. [[CrossRef](#)] [[PubMed](#)]
9. Hua, S.; De Matos, M.B.; Metselaar, J.M.; Storm, G. Current trends and challenges in the clinical translation of nanoparticulate nanomedicines: Pathways for translational development and commercialization. *Front. Pharmacol.* **2018**, *9*, 790. [[CrossRef](#)]
10. Tinkle, S.; McNeil, S.E.; Mühlebach, S.; Bawa, R.; Borchard, G.; Barenholz, Y.; Tamarkin, L.; Desai, N. Nanomedicines: Addressing the scientific and regulatory gap. *Ann. N. Y. Acad. Sci.* **2014**, *1313*, 35–56. [[CrossRef](#)] [[PubMed](#)]
11. De Mattia, F.; Chapsal, J.-M.; Descamps, J.; Halder, M.; Jarrett, N.; Kross, I.; Mortiaux, F.; Ponsar, C.; Redhead, K.; McKelvie, J. The consistency approach for quality control of vaccines—A strategy to improve quality control and implement 3rs. *Biologicals* **2011**, *39*, 59–65. [[CrossRef](#)] [[PubMed](#)]
12. Akkermans, A.; Chapsal, J.-M.; Coccia, E.M.; Depraetere, H.; Dierick, J.-F.; Duangkhae, P.; Goel, S.; Halder, M.; Hendriksen, C.; Levis, R. Animal testing for vaccines. Implementing replacement, reduction and refinement: Challenges and priorities. *Biologicals* **2020**, *68*, 92–107. [[CrossRef](#)]
13. Liu, Y.; Hardie, J.; Zhang, X.; Rotello, V.M. *Effects of Engineered Nanoparticles on the Innate Immune System*; Seminars in Immunology; Elsevier: Amsterdam, The Netherlands, 2017; pp. 25–32.
14. Ciabattini, A.; Nardini, C.; Santoro, F.; Garagnani, P.; Franceschi, C.; Medaglini, D. *Vaccination in the Elderly: The Challenge of Immune Changes with Aging*; Seminars in Immunology; Elsevier: Amsterdam, The Netherlands, 2018; pp. 83–94.
15. Kang, S.-J.; Jung, S.I. Age-related morbidity and mortality among patients with covid-19. *Infect. Chemother.* **2020**, *52*, 154. [[CrossRef](#)] [[PubMed](#)]
16. Nikolich-Zugich, J. The twilight of immunity: Emerging concepts in aging of the immune system. *Nat. Immunol.* **2018**, *19*, 10–19. [[CrossRef](#)] [[PubMed](#)]

17. Haynes, L.; Eaton, S.M.; Burns, E.M.; Rincon, M.; Swain, S.L. Inflammatory cytokines overcome age-related defects in cd4 t cell responses in vivo. *J. Immunol.* **2004**, *172*, 5194–5199. [[CrossRef](#)]
18. Hamad-Schifferli, K. Exploiting the novel properties of protein coronas: Emerging applications in nanomedicine. *Nanomedicine* **2015**, *10*, 1663–1674. [[CrossRef](#)]
19. Schmutz, M.; Borges, O.; Jesus, S.; Borchard, G.; Perale, G.; Zinn, M.; Sips, Ä.A.; Soeteman-Hernandez, L.G.; Wick, P.; Som, C. A methodological safe-by-design approach for the development of nanomedicines. *Front. Bioeng. Biotechnol.* **2020**, *8*, 258. [[CrossRef](#)]
20. HogenEsch, H.; O'Hagan, D.T.; Fox, C.B. Optimizing the utilization of aluminum adjuvants in vaccines: You might just get what you want. *NPJ Vaccines* **2018**, *3*, 1–11. [[CrossRef](#)] [[PubMed](#)]
21. Willhite, C.C.; Karyakina, N.A.; Yokel, R.A.; Yenugadhati, N.; Wisniewski, T.M.; Arnold, I.M.; Momoli, F.; Krewski, D. Systematic review of potential health risks posed by pharmaceutical, occupational and consumer exposures to metallic and nanoscale aluminum, aluminum oxides, aluminum hydroxide and its soluble salts. *Crit. Rev. Toxicol.* **2014**, *44*, 1–80. [[CrossRef](#)] [[PubMed](#)]
22. Navarro-Tovar, G.; Palestino, G.; Rosales-Mendoza, S. An overview on the role of silica-based materials in vaccine development. *Expert Rev. Vaccines* **2016**, *15*, 1449–1462. [[CrossRef](#)]
23. Kitzmüller, C.; Wallner, M.; Deifl, S.; Mutschlechner, S.; Walterskirchen, C.; Zlabinger, G.; Ferreira, F.; Bohle, B. A hypoallergenic variant of the major birch pollen allergen shows distinct characteristics in antigen processing and t-cell activation. *Allergy* **2012**, *67*, 1375–1382. [[CrossRef](#)] [[PubMed](#)]
24. Wallner, M.; Himly, M.; Neubauer, A.; Erler, A.; Hauser, M.; Asam, C.; Mutschlechner, S.; Ebner, C.; Briza, P.; Ferreira, F. The influence of recombinant production on the immunologic behavior of birch pollen isoallergens. *PLoS ONE* **2009**, *4*, e8457. [[CrossRef](#)] [[PubMed](#)]
25. Oyewumi, M.O.; Kumar, A.; Cui, Z. Nano-microparticles as immune adjuvants: Correlating particle sizes and the resultant immune responses. *Expert Rev. Vaccines* **2010**, *9*, 1095–1107. [[CrossRef](#)] [[PubMed](#)]
26. Finnie, K.S.; Bartlett, J.R.; Barbé, C.J.; Kong, L. Formation of silica nanoparticles in microemulsions. *Langmuir* **2007**, *23*, 3017–3024. [[CrossRef](#)]
27. Harris, J.R.; Soliakov, A.; Lewis, R.J.; Depoix, F.; Watkinson, A.; Lakey, J.H. Alhydrogel@adjuvant, ultrasonic dispersion and protein binding: A tem and analytical study. *Micron* **2012**, *43*, 192–200. [[CrossRef](#)]
28. Shardlow, E.; Mold, M.; Exley, C. From stock bottle to vaccine: Elucidating the particle size distributions of aluminum adjuvants using dynamic light scattering. *Front. Chem.* **2017**, *4*, 48. [[CrossRef](#)]
29. Huang, M.; Wang, W. Factors affecting alum–protein interactions. *Int. J. Pharm.* **2014**, *466*, 139–146. [[CrossRef](#)]
30. Lee, J.G.; Lannigan, K.; Shelton, W.A.; Meissner, J.; Bharti, B. Adsorption of myoglobin and corona formation on silica nanoparticles. *Langmuir* **2020**, *36*, 14157–14165. [[CrossRef](#)]
31. Kubiak-Ossowska, K.; Tokarczyk, K.; Jachimska, B.; Mulheran, P.A. Bovine serum albumin adsorption at a silica surface explored by simulation and experiment. *J. Phys. Chem. B* **2017**, *121*, 3975–3986. [[CrossRef](#)] [[PubMed](#)]
32. Himly, M.; Nony, E.; Chabre, H.; Van Overtvelt, L.; Neubauer, A.; Van Ree, R.; Buchheit, K.H.; Vieths, S.; Moingeon, P.; Ferreira, F. Standardization of allergen products: 1. Detailed characterization of gmp-produced recombinant bet v 1.0101 as biological reference preparation. *Allergy* **2009**, *64*, 1038–1045. [[CrossRef](#)]
33. Kubiak-Ossowska, K.; Jachimska, B.; Mulheran, P.A. How negatively charged proteins adsorb to negatively charged surfaces: A molecular dynamics study of bsa adsorption on silica. *J. Phys. Chem. B* **2016**, *120*, 10463–10468. [[CrossRef](#)] [[PubMed](#)]
34. Henzler, K.; Haupt, B.R.; Lauterbach, K.; Wittemann, A.; Borisov, O.; Ballauff, M. Adsorption of β -lactoglobulin on spherical polyelectrolyte brushes: Direct proof of counterion release by isothermal titration calorimetry. *J. Am. Chem. Soc.* **2010**, *132*, 3159–3163. [[CrossRef](#)] [[PubMed](#)]
35. Machado, Y.; Freier, R.; Scheiblhofer, S.; Thalhamer, T.; Mayr, M.; Briza, P.; Grutsch, S.; Ahammer, L.; Fuchs, J.E.; Wallnoefer, H.G. Fold stability during endolysosomal acidification is a key factor for allergenicity and immunogenicity of the major birch pollen allergen. *J. Allergy Clin. Immunol.* **2016**, *137*, 1525–1534. [[CrossRef](#)] [[PubMed](#)]
36. Scheiblhofer, S.; Laimer, J.; Machado, Y.; Weiss, R.; Thalhamer, J. Influence of protein fold stability on immunogenicity and its implications for vaccine design. *Expert Rev. Vaccines* **2017**, *16*, 479–489. [[CrossRef](#)] [[PubMed](#)]
37. Egger, M.; Jürets, A.; Wallner, M.; Briza, P.; Ruzek, S.; Hainzl, S.; Pichler, U.; Kitzmüller, C.; Bohle, B.; Huber, C.G. Assessing protein immunogenicity with a dendritic cell line-derived endolysosomal degradome. *PLoS ONE* **2011**, *6*, e17278. [[CrossRef](#)]
38. Jahn-Schmid, B.; Radakovics, A.; Lüttkopf, D.; Scheurer, S.; Vieths, S.; Ebner, C.; Bohle, B. Bet v 1142-156 is the dominant t-cell epitope of the major birch pollen allergen and important for cross-reactivity with bet v 1-related food allergens. *J. Allergy Clin. Immunol.* **2005**, *116*, 213–219. [[CrossRef](#)]
39. Winter, P.; Stubenvoll, S.; Scheiblhofer, S.; Joubert, I.A.; Strasser, L.; Briganser, C.; Soh, W.T.; Hofer, F.; Kamenik, A.S.; Dietrich, V. In silico design of phl p 6 variants with altered folding stability significantly impacts antigen processing, immunogenicity and immune polarization. *bioRxiv* **2020**, *11*, 1824.
40. Kamenik, A.S.; Hofer, F.; Handle, P.H.; Liedl, K.R. Dynamics rationalize proteolytic susceptibility of the major birch pollen allergen bet v 1. *Front. Mol. Biosci.* **2020**, *7*, 18. [[CrossRef](#)]
41. Freier, R.; Dall, E.; Brandstetter, H. Protease recognition sites in bet v 1a are cryptic, explaining its slow processing relevant to its allergenicity. *Sci. Rep.* **2015**, *5*, 1–9. [[CrossRef](#)]
42. Kofler, S.; Asam, C.; Eckhard, U.; Wallner, M.; Ferreira, F.; Brandstetter, H. Crystallographically mapped ligand binding differs in high and low ige binding isoforms of birch pollen allergen bet v 1. *J. Mol. Biol.* **2012**, *422*, 109–123. [[CrossRef](#)]

43. Kishore, D.; Kundu, S.; Kayastha, A.M. Thermal, chemical and pH induced denaturation of a multimeric β -galactosidase reveals multiple unfolding pathways. *PLoS ONE* **2012**, *7*, e50380. [[CrossRef](#)] [[PubMed](#)]
44. Thalhamer, T.; Dobias, H.; Stepanoska, T.; Pröll, M.; Stutz, H.; Dissertori, O.; Lackner, P.; Ferreira, F.; Wallner, M.; Thalhamer, J. Designing hypoallergenic derivatives for allergy treatment by means of in silico mutation and screening. *J. Allergy Clin. Immunol.* **2010**, *125*, 926–934.e910. [[CrossRef](#)] [[PubMed](#)]
45. Ferreira, F.; Ebner, C.; Kramer, B.; Casari, G.; Briza, P.; Kungl, A.J.; Grimm, R.; Jahn-schmid, B.; Breiteneder, H.; Kraft, D. Modulation of ige reactivity of allergens by site-directed mutagenesis: Potential use of hypoallergenic variants for immunotherapy. *FASEB J.* **1998**, *12*, 231–242. [[CrossRef](#)] [[PubMed](#)]
46. Aglas, L.; Bethanis, A.; Chrusciel, P.; Stolz, F.; Gruen, M.; Jaakkola, U.-M.; Jongejan, L.; Yarkin, E.; Van Ree, R. In vivo induction of functional inhibitory ige antibodies by a hypoallergenic bet v 1 variant. *Front. Immunol.* **2020**, *11*, 2118. [[CrossRef](#)] [[PubMed](#)]
47. Spangfort, M.D.; Mirza, O.; Ipsen, H.; Van Neerven, R.J.; Gajhede, M.; Larsen, J.N. Dominating ige-binding epitope of bet v 1, the major allergen of birch pollen, characterized by x-ray crystallography and site-directed mutagenesis. *J. Immunol.* **2003**, *171*, 3084–3090. [[CrossRef](#)] [[PubMed](#)]
48. Mirza, O.; Henriksen, A.; Ipsen, H.; Larsen, J.N.; Wissenbach, M.; Spangfort, M.D.; Gajhede, M. Dominant epitopes and allergic cross-reactivity: Complex formation between a fab fragment of a monoclonal murine ige antibody and the major allergen from birch pollen bet v 1. *J. Immunol.* **2000**, *165*, 331–338. [[CrossRef](#)]
49. Malik, M.A.; Wani, M.Y.; Hashim, M.A. Microemulsion method: A novel route to synthesize organic and inorganic nanomaterials: 1st nano update. *Arab. J. Chem.* **2012**, *5*, 397–417. [[CrossRef](#)]
50. Wallner, M.; Hauser, M.; Himly, M.; Zaborsky, N.; Mutschlechner, S.; Harrer, A.; Asam, C.; Pichler, U.; van Ree, R.; Briza, P. Reshaping the bet v 1 fold modulates th polarization. *J. Allergy Clin. Immunol.* **2011**, *127*, 1571–1578.e1579. [[CrossRef](#)]
51. Soh, W.T.; Aglas, L.; Mueller, G.A.; Gilles, S.; Weiss, R.; Scheiblhofer, S.; Huber, S.; Scheidt, T.; Thompson, P.M.; Briza, P. Multiple roles of bet v 1 ligands in allergen stabilization and modulation of endosomal protease activity. *Allergy* **2019**, *74*, 2382–2393. [[CrossRef](#)]
52. Kavan, D.; Man, P. Mstools—Web based application for visualization and presentation of hxms data. *Int. J. Mass Spectrom.* **2011**, *302*, 53–58. [[CrossRef](#)]
53. Micsonai, A.; Wien, F.; Bulyáki, É.; Kun, J.; Moussong, É.; Lee, Y.-H.; Goto, Y.; Réfrégiers, M.; Kardos, J. Bestsel: A web server for accurate protein secondary structure prediction and fold recognition from the circular dichroism spectra. *Nucleic Acids Res.* **2018**, *46*, W315–W322. [[CrossRef](#)] [[PubMed](#)]
54. Vogel, L.; Lüttkopf, D.; Hatahet, L.; Hausteiner, D.; Vieths, S. Development of a functional in vitro assay as a novel tool for the standardization of allergen extracts in the human system. *Allergy* **2005**, *60*, 1021–1028. [[CrossRef](#)] [[PubMed](#)]



Review

Protein-Based Nanoparticle Vaccines for SARS-CoV-2

Hyo-Dong Sung [†], Nayeon Kim [†], Yeram Lee and Eun Jung Lee ^{*†}

Department of Chemical Engineering, School of Applied Chemical Engineering, Kyungpook National University, Daegu 41566, Korea; gyehtd0314@knu.ac.kr (H.-D.S.); nykim0310@knu.ac.kr (N.K.); yeram0301@knu.ac.kr (Y.L.)

* Correspondence: eunjunglee@knu.ac.kr; Tel.: +82-53-950-7557

[†] These authors contributed equally to this work.

Abstract: The pandemic caused by the severe acute respiratory syndrome coronavirus-2 (SARS-CoV-2) has upended healthcare systems and economies around the world. Rapid understanding of the structural biology and pathogenesis of SARS-CoV-2 has allowed the development of emergency use or FDA-approved vaccines and various candidate vaccines. Among the recently developed SARS-CoV-2 candidate vaccines, natural protein-based nanoparticles well suited for multivalent antigen presentation and enhanced immune stimulation to elicit potent humoral and cellular immune responses are currently being investigated. This mini-review presents recent innovations in protein-based nanoparticle vaccines against SARS-CoV-2. The design and strategy of displaying antigenic domains, including spike protein, receptor-binding domain (RBD), and other domains on the surface of various protein-based nanoparticles and the performance of the developed nanoparticle-based vaccines are highlighted. In the final part of this review, we summarize and discuss recent advances in clinical trials and provide an outlook on protein-based nanoparticle vaccines.

Keywords: SARS-CoV-2; protein nanoparticles; vaccines; nanovaccine; nanomedicine; protein-based nanotechnology



Citation: Sung, H.-D.; Kim, N.; Lee, Y.; Lee, E.J. Protein-Based Nanoparticle Vaccines for SARS-CoV-2. *Int. J. Mol. Sci.* **2021**, *22*, 13445. <https://doi.org/10.3390/ijms222413445>

Academic Editor: Monica Terracciano

Received: 30 October 2021

Accepted: 10 December 2021

Published: 14 December 2021

Publisher's Note: MDPI stays neutral with regard to jurisdictional claims in published maps and institutional affiliations.



Copyright: © 2021 by the authors. Licensee MDPI, Basel, Switzerland. This article is an open access article distributed under the terms and conditions of the Creative Commons Attribution (CC BY) license (<https://creativecommons.org/licenses/by/4.0/>).

1. Introduction

Coronavirus disease 2019 (COVID-19) is an infectious disease caused by severe acute respiratory syndrome coronavirus-2 (SARS-CoV-2), which first appeared in Wuhan, People's Republic of China, in late 2019 and has since spread around the world, resulting in a pandemic [1,2]. The SARS-CoV-2 pandemic has disrupted global public health and economies in 216 countries, with over 49 million deaths since 29 December, 2019 [3].

Among the recently developed vaccine candidates for SARS-CoV-2, natural protein-based nanoparticles that can confer stronger and broader protective immunity have been shown to be effective [4–14]. A recent phase 3 clinical trial has demonstrated the Novavax vaccine, a recombinant nanoparticle vaccine made of a stabilized form of the coronavirus spike (S) protein, to be safe with an efficacy of 89.7% [15,16]. Additionally, ferritin-based protein nanoparticles presenting the SARS-CoV-2 S protein are entering phase 1 clinical trials (NCT04784767). These nanoparticle-based vaccine technologies can enhance the immunogenicity and stability of soluble antigens by multivalent antigen display on their surface [17–23]. They can facilitate numerous immunological processes, including the efficient delivery of antigens to lymph nodes, retention of follicular dendritic and helper T cells, and generation, activation, and expansion of B cells, including memory B cells and long-lived plasma cells [18,24–34]. In particular, protein-based nanoparticles have no special biosafety environmental issues in their manufacturing procedures and potentially greater accessibility to the public with reduced production costs [12,35–39]. Thus, protein-based nanoparticles have been widely used as a delivery platform for various vaccines and drugs. A more detailed description of the biological function, structure, and geometry of various protein nanoparticles and their application in nanomedicine, including the development of other vaccines, are described in excellent recent reviews [40–46].

This review mainly focuses on recent innovations in protein-based nanoparticle vaccines for protection against SARS-CoV-2 (Figure 1). First, the design and strategy of displaying antigenic domains, including S protein, receptor-binding domain (RBD), and other domains, into various protein nanoparticles are discussed. The performance of these engineered protein nanoparticle vaccines for protection against SARS-CoV-2 in mice, human angiotensin-converting enzyme 2 (ACE2) transgenic mice, rabbits, hamsters, ferrets, and macaques, and their ability to protect against other viruses in the Coronaviridae family is highlighted. Finally, we present a summary and perspective of recent advances in protein nanoparticle vaccines involving clinical trials.

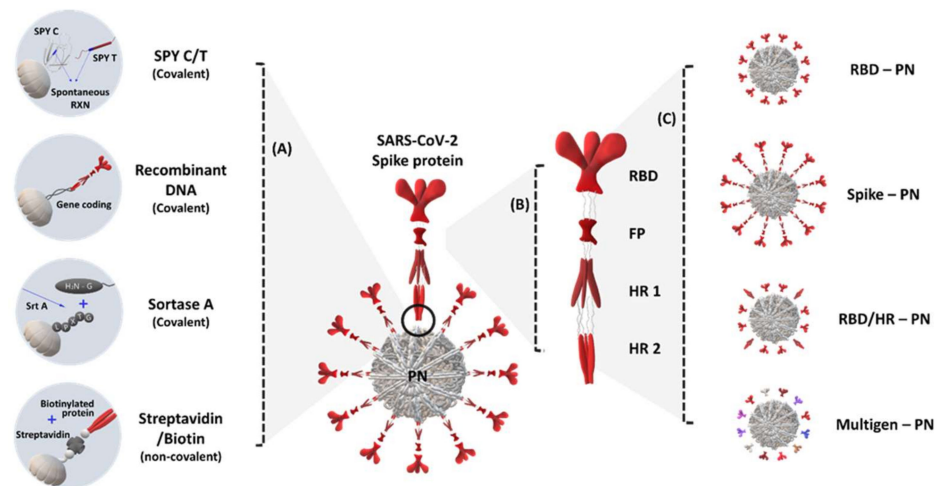


Figure 1. Application of protein nanoparticles (PN) that elicit severe acute respiratory syndrome coronavirus-2 (SARS-CoV-2)- and SARS variant-specific immune response: (A) methods for ligating PN components, nanoparticles, and immunogens based on covalent (SpyCatcher/SpyTag, recombinant DNA, and sortase-mediated bonding) and non-covalent (streptavidin/biotin) interactions; (B) schematic structure of the SARS-CoV-2 spike (S) protein; (C) type of immunogen applications for displaying PNs from the partial epitope region of SARS-CoV-2 to other types of receptor-binding domains (RBDs) and S proteins; SPY C/T, SpyCatcher/SpyTag; HR, heptad repeat.

2. S Protein Domain-Conjugated (Presenting) Protein Nanoparticles

SARS-CoV-2 is a positive-strand genomic RNA virus, and its RNA encodes non-structural proteins such as proteases and RNA polymerase and major structural proteins, including nucleocapsid, membrane, envelope, and S protein [47]. SARS-CoV-2 has a similar cell entry mechanism to other coronaviruses. The S protein protruding from the viral surface mediates host cell receptor recognition, viral attachment, and entry into the host cell via the formation of a trimeric hairpin structure [7]. The S protein mainly consists of S1 and S2 domains. First, the S1 domain binds to the ACE2 receptor on human cell surfaces through its RBD. Then, the S1 domain is cleaved by the host cellular protease furin, followed by the mediation of fusion of the viral envelope and host cell membrane by the S2 domain through its heptad repeat 1 (HR1), heptad repeat 2 (HR2), and fusion peptide domain. Therefore, the S protein is an ideal target for vaccine development due to its biological functions, and most of the currently developed vaccines against SARS-CoV-2 mainly target the S protein as an immunogen.

Powell et al. first reported S protein-conjugated protein nanoparticles based on *Helicobacter pylori* ferritin (Table 1) [48]. *H. pylori* ferritin self-assembles into 24 multimeric spherical nanoparticles approximately 12 nm in size [49]. Primarily, three-fold symmetric axes of the ferritin N-terminus have been used to display trimeric complexes, including surface glycoprotein antigens such as human immunodeficiency virus-1 (HIV-1) and the Epstein-Barr virus [12,36]. Using a similar approach, the full-length S protein or a C-terminal 70 amino acid-deleted S protein was genetically fused to the N-terminus of *H. pylori*

ferritin and successfully produced in human Expi293 cells. Cryogenic electron microscopy (cryo-EM) images showed S protein-displaying nanoparticles, and two-dimensional class averages and single-particle analysis confirmed that the octahedral nanoparticles had eight trimeric S antigens on their surfaces. The S protein-displaying nanoparticles with Quil-A/monophosphoryl lipid A successfully elicited a more consistent neutralizing antibody response compared with that with a trimeric form of S protein using the trimeric coiled-coil protein GCN4 and higher S-pseudotyped viral neutralizing titers than those in convalescent COVID-19 patient plasma, even in a single dose.

Table 1. Summary of advances in protein nanoparticle vaccines for severe acute respiratory syndrome coronavirus-2 (SARS-CoV-2).

Nanoparticle	Immunogen	In Vivo Model	Adjuvant	Route	Dose (μ g)	Infection	Ref.
Ferritin (Bullfrog and <i>Helicobacter pylori</i>)	S protein RBD protein RBD protein and N-terminal domain	BALB/c mouse C57BL/6 mouse K18-hACE2 mouse	ALFQ or Alhydrogel	Intramuscular	0.08–10	Intranasal (1.25×10^4 PFU)	[13]
	S protein	C57BL/6 mouse	ALFQ or Alhydrogel	Intramuscular	10	N/A	[50]
	S protein	Rhesus macaque	ALFQ	Intramuscular	5–50	Intranasal and Intratracheal (1.00×10^6 TCID50)	[51]
	RBD protein	Ferret	AddaVax	Intramuscular Intramuscular and Intranasal	15	Intranasal (1.00×10^5 – 1.00×10^6 TCID50)	[7]
Ferritin (<i>Helicobacter pylori</i>)	RBD protein	Cynomol gusmacaque Rhesus macaque	3M-052 and Alhydrogel	Intramuscular	100	Intranasal and Intratracheal (1.00×10^5 PFU)	[52]
	RBD protein and HR domain	BALB/c mouse C57BL/6 mouse(hACE2 transgenic)	Sigma Adjuvant System	Subcutaneous	10	Intranasal (4.00×10^4 FFU)	[35]
	S protein	Rhesus macaque C57BL/6 mouse Syrian golden hamster	Sigma Adjuvant System	Intramuscular Subcutaneous	50 20	N/A	[53]
	S protein	BALB/c mouse	Quil-A and MPLA	Intramuscular	100	Intranasal (1.99×10^4 TCID50)	[48]
Ferritin (<i>Pyrococcus furiosus</i>)	RBD protein	BALB/c mouse	CpG 1826	Subcutaneous	12.3–30.7	N/A	[54]
I53-50 (Artificial)	S protein	BALB/c mouse	Poly(I:C) Squalene emulsion	Subcutaneous	13	N/A	[55]
		New Zealand white rabbit		Intramuscular	39		
	RBD protein	Cynomolgus macaque	MPLA liposome	Intramuscular	50	Intranasal and Intratracheal (1.00×10^6 PFU)	[56]
	BALB/c mouse	AddaVax	Intramuscular	0.9–5	Intranasal (1.00×10^5 PFU)		
		Kymab Darwin mouse				N/A	
Mi3 (Artificial)	RBD protein (4a, 4b, or 8)	BALB/c mouse	AddaVax	Intraperitoneal	5	N/A	[57]
MS2 (<i>Emesvirus zinderi</i>)	S protein	Syrian golden hamster	Alhydrogel	Subcutaneous	60	Intranasal (1.00×10^3 PFU)	[58]
Dps (<i>Sulfolobus islandicus</i>)	RBD protein	C57BL/6J mouse	CpG 1668	Subcutaneous	25–50	N/A	[59]
		K18 mouse			25	Intranasal (1.00×10^4 PFU)	
	(hACE2 transgenic) C57BL/6J mouse	25–50			N/A		
	S protein Nucleocapsid protein	C57BL/6J mouse			25–50	N/A	
I3-01v9 (Artificial) E2p (<i>Geobacillus sterothermophilus</i>) Ferritin (<i>Helicobacter pylori</i>)	S protein	BALB/c mouse	AddaVax or Adju-Phos	Intraperitoneal	50	N/A	[60]
	S protein						
	S protein RBD protein						

Table 1. Cont.

Nanoparticle	Immunogen	In Vivo Model	Adjuvant	Route	Dose (μ g)	Infection	Ref.
Bann (Tomato bushy stunt virus)	RBD protein	BALB/c mouse	N/A	Intramuscular, Intranasal, or Sublingual	20 (Plasmid)	Intranasal (70 μ L of VSV-S pseudovirus)	[61]
Foldon (T4 bacteriophage fibrin)			AddaVax	Intramuscular	100 (protein)		
Ferritin (Bullfrog and <i>Helicobacter pylori</i>)			N/A	Intramuscular	20 (Plasmid)		
AaLS (<i>Aquifex aeolicus</i>)			N/A	Intramuscular	20 (Plasmid)		
I53-50 (Artificial) Mi3 (Artificial) Ferritin (<i>Helicobacter pylori</i>)	RBD protein	BALB/c mouse	AddaVax or Sigma Adjuvant System	Subcutaneous	11.91 9.51 9.34	N/A	[20]

Abbreviations: ALFQ, army liposome formulation containing QS-21; COVID-19, coronavirus disease 2019; PFU, plaque-forming units; RBD, receptor-binding domain; Th1, T helper 1 cells; APC, antigen-presenting cells; TCID50, tissue culture infectious dose 50; HR, heptad repeat; hACE2, human angiotensin-converting enzyme 2; MPLA, monophosphoryl lipid A; sgRNA, subgenomic RNA; 4a, (SARS-CoV-2, SHC014, RaTG13, Rs4081); 4b, (pang17, RmYN02, Rf1, WIV1); 8, (4a and 4b).

Icosahedral protein nanoparticles with 120 subunits have been computationally designed and developed as vaccines against HIV-1, the respiratory syncytial virus, and influenza via two-component self-assembly, such as I53-50 and dn5 [10,62,63]. Brouwer et al. developed a SARS-CoV-2 vaccine based on I53-50 nanoparticles composed of 20 trimeric (I53.50A.1NT1) and 12 pentameric (I53.50B.4PT1) subunits [55]. I53.50A.1NT1 was genetically conjugated with the S protein, and the recombinant fusion protein was purified as a trimeric complex using size exclusion chromatography. Then, the trimeric SARS-CoV-2 S-I53.50A.1NT1 was incubated with pentameric I53.50B.4PT1, resulting in S protein-displaying nanoparticles with a diameter of ~30 nm. The multivalent display of the S protein of I53-50 nanoparticles enhances cognate B cell activation in vitro compared with a trimeric form of the S protein (SARS-CoV-2 S-I53.50A.1NT1). The S protein-displaying I53-50 nanoparticles successfully induced neutralizing antibody responses in mice and rabbit models and S protein-specific B and T cell responses in cynomolgus macaques. Furthermore, these nanoparticles showed potent protective efficacy against 10- to 100-fold higher doses of SARS-CoV-2 challenge compared with other studies with reduced viral subgenomic RNA replication in tracheal and nasopharyngeal swabs.

As SARS-CoV-2 vaccine candidates, other types of protein nanoparticles such as the coat protein of the RNA bacteriophage MS2, dihydrolipoyl acetyltransferase (E2p) from *Bacillus stearothermophilus*, and computationally designed I3-01v9 have been utilized to display the S protein [45,47]. MS2 consists of 90 homodimers, resulting in 180-subunit icosahedral nanoparticles with a diameter of ~30 nm. Biotin-fused S protein was added to the surface of streptavidin-MS2 nanoparticles using streptavidin and biotin-specific binding systems [58]. Specifically, in addition to a prefusion-stabilized S protein (S2Pro), which contains two proline substitutions and is mostly used in other studies, Hexapro (S6Pro), a variant of S2Pro that contains six proline substitutions and higher stability and expression yield than that of S2Pro, was used in this study. A single immunization of S2Pro or S6Pro-displaying MS2 with Alhydrogel (AH) effectively protected Syrian hamsters from SARS-CoV-2 infection with rapid elimination of the virus in the nasal turbinates and viral titers more than 150- (S2Pro-MS2) and 700-fold (S6Pro-MS2) lower than those in controls.

Zhu et al. developed various SARS-CoV-2 nanoparticle vaccines using 24-mer ferritin, 60-mer E2p, and 60-mer I3-01v9 [60]. They designed a stable S protein (S2G Δ HR2) with a deleted HR-2 stalk and two substituted glycine residues, and genetically conjugated S2G Δ HR2 with ferritin, E2p, and I3-01v9. Additionally, S2G Δ HR2-E2p and -I3-01v9 had genetically fused locking domains and PADRE, a 13-amino acid pan-DR epitope that activated CD4⁺ T cells, in their inner cavity. These nanoparticles produced higher neutralizing antibody responses in mouse models than did soluble full-length SP2 and

S2GΔHR2, with their average EC50 titers corresponding to their size (ferritin < E2p < I3-01v9).

A recently developed nanoparticle vaccine called S protein ferritin nanoparticle (SpFN) developed by the Walter Reed Army Institute of Research of the US Army Medical Research and Development Command (USAMRDC) is being actively investigated in phase 1 trials [13,50,51]. SpFN was developed by the genetic fusion of prefusion-stabilized S protein and *H. pylori* ferritin. First, the efficacy of SpFN was evaluated in a mouse model with two different adjuvants, AH and army liposome formulation containing QS-21 (ALFQ) [50]. SpFN with ALFQ showed significantly higher recruitment and activation of classical and non-classical antigen-presenting cells and a T helper 1 cell (Th1)-based cellular response than SpFN with AH. Moreover, this combination induced a SARS-CoV2 spike epitope (VNFNFNGL; aa 539–546)-specific polyfunctional CD8+ T cell response and killed the peptide-pulsed target cells. This epitope is also present in SARS-CoV1, possibly suggesting the generation of cross-reactive T cells. The vaccination efficacy of SpFN with ALFQ was further evaluated for potent neutralizing antibody responses and neutralizing activity against live virus, pseudovirus, and SARS-CoV-2 protection in rhesus macaques [51]. In this study, SpFN with ALFQ showed a strong cellular immune response, including a Th1-based S protein-specific CD4+ T cell response and reduced viral titer upon high-dose SARS-CoV-2 infection in the lung parenchyma and the upper and lower airways. Neutralizing activity against authentic and pseudo-SARS-CoV-2 variants of concern (VOC) and SARS-CoV-1 was induced by vaccination with SpFN. Therefore, the generation of cross-reactive T cells by SpFN with ALFQ may provide protection against other coronavirus strains and SARS-CoV-2 VOCs.

3. RBD and Other Domain-Conjugated (Presenting) Protein Nanoparticles

A high-resolution cryo-EM study of the SARS-CoV-2 structure and interface mutation scanning revealed that the RBD in the S protein of SARS-CoV-2, the key binding interface, recognizes the ACE2 receptor in host cells [64,65]. Therefore, the RBD domain is being studied as a promising target for designing candidate SARS-CoV-2 vaccines.

Walls et al. first reported a SARS-CoV-2 nanoparticle vaccine using the RBD domain [56]. I53-50, a two-component icosahedral protein nanoparticle, was used to display the RBD domain. Trimeric I53-50A was genetically fused to the RBD domain with 8, 12, or 16 glycine and serine flexible linkers to present the native trimeric form of RBD and mixed with pentameric I53-50B, resulting in a SARS-CoV-2 nanoparticle vaccine displaying 60 copies of RBD on its surface. This nanoparticle vaccine showed an enhanced binding profile against human ACE2 (hACE2) and physical and antigenic stability compared with the monomeric form of RBD and the trimeric form of S2Pro. In BALB/c mice and mice with human immune repertoire (Kymab Darwin mice), strong neutralizing antibody responses can be induced by I53-50-based nanoparticle vaccines. These nanoparticle vaccines present potent neutralizing activity against pseudo and live SARS-CoV-2, whereas the monomeric form of RBD and S2Pro showed little to no neutralizing effect. In particular, although linker length and antigenic valency do not substantially affect the overall immunogenicity, RBD I53-50 nanoparticles with 12 and 16 glycine and serine linkers induced 10-fold higher neutralizing antibody titers and neutralizing activity compared with S2Pro. Furthermore, RBD-specific germinal center B cells, which are essential for forming a durable B cell memory, were significantly increased with RBD I53-50 nanoparticle treatment compared with those with treatment with the monomeric forms of RBD and S2Pro.

Various types of protein nanoparticles of different sizes and antigen valencies are being compared as potential SARS-CoV-2 vaccine platforms [20,60,61]. Zeng et al. utilized 24-subunit *H. pylori* ferritin, computationally designed and optimized 60-subunit mi3 and 120-subunit I53-50, and developed three different RBD-displaying nanoparticle vaccines using a spy catcher (SpyCatcher) and tag (SpyTag) system [20]. The bacteria-derived SpyCatcher and SpyTag pair efficiently formed covalent bonds by simple mixing. Therefore, the ligation strategy based on SpyCatcher-SpyTag has been utilized to display HIV, hepatitis

B virus, and SARS-CoV-2 antigens on the nanoparticle scaffold [30,66]. The produced RBD-SpyTag in HEK293F cells was incubated with the produced SpyCatcher nanoparticles in *Escherichia coli*, resulting in RBD-displaying nanoparticles. The three RBD-displaying nanoparticles (RBD-ferritin, RBD-mi3, and RBD-I53-50) showed high thermal stability, which may benefit commercial production and supply. Additionally, they presented significantly higher binding ability against hACE2 and RBD-specific neutralizing antibody (CB6) and neutralizing antibody titers in mouse models than monomeric RBD. In particular, RBD-mi3 and RBD-I53-50 elicited a higher neutralization effect than RBD-ferritin, indicating that nanoparticle vaccines with higher antigen valency could produce more effective immune responses.

Other nano-scaffolds, including bann (β -annulus-scaffold peptide from the tomato bushy stunt virus), bullfrog-*H. pylori* hybrid ferritin, AaLS (lumazine synthase from *Aquifex aeolicus*), and foldon from T4 bacteriophage fibritin have been investigated and compared as potential RBD-nano-scaffold plasmid DNA vaccines [61]. As a result, these nano-scaffold vaccines showed potent neutralizing antibody responses compared with RBD alone. However, in this study, given that foldon with six copies of RBD elicits stronger neutralization effects than AaLS with 60 copies of RBD, nano-scaffold sizes and antigen valency on the surface are not the only main factors contributing to vaccine efficacy. Therefore, bann, a small scaffolding domain with many antigen valencies, might be an ideal vaccine platform because of its strongly augmented immune response against the antigen and minimal antibody response against the nano-scaffold itself compared with those with large scaffold domains.

Currently, owing to the risk of emerging variants of SARS-CoV-2 and other zoonotic viruses, research into vaccine development and cross-reaction efficacy analysis against other viruses is being expedited [35,52,57,67]. Haynes et al. developed RBD-displaying ferritin using the sortase A reaction [52]. RBD with a sortase A donor sequence was conjugated to *H. pylori* ferritin with a sortase A acceptor sequence, resulting in 24 RBD-displaying ferritin nanoparticle vaccines. The nanoparticle vaccine successfully induced neutralizing SARS-CoV-2 RBD-specific antibody responses and protection against SARS-CoV-2 in a macaque model. In particular, cross-neutralizing antibody responses against SARS-CoV-2 variants B.1.1.7, P.1, and B.1.351., bat CoV, and SARS-CoV-1 were elicited in macaques with RBD-ferritin immunization. Similarly, Halfmann et al. designed RBD-conjugated mi3 nanoparticles using SpyCatcher-SpyTag systems and tested their efficacy against various viruses [67]. The nanovaccine induced potent cross-reactive antibodies against SARS-CoV-2, SARS-CoV-1, and SARS-CoV-2 variants B.1.1.7, P.1, and B.1.351. Moreover, neutralizing antibody responses against the above five viruses and important VOC Delta variants (B.1.617.2) were demonstrated.

In another report, given that 97.9% of patients who recovered from SARS-CoV-2 showed a high IgG-specific antibody titer against the HR domain, ferritin nanoparticle vaccines have been developed with additional HR-labeled surfaces along with RBD [35]. Based on sequence homology analyses, HR1 and HR2 are more highly conserved than RBD against three SARS-CoV-2 strains (Wuhan-HU-1, SYSU-IHV, and USA-IA-6399) and six human pathogenic coronaviruses (SARS-CoV Tor2, Middle East respiratory syndrome-related coronavirus [MERS-CoV] EMC, human coronavirus [hCoV]-HKU1, hCoV-OC43, hCoV-NL63, and hCoV-229E), five bat coronaviruses, and two pangolin coronaviruses. Both RBD- and HR-displaying nanoparticle vaccines elicited cross-reactive neutralizing antibody responses against SARS-CoV, MERS-CoV, HCoV-229E, HCoVOC43, and RATG13.

Cohen et al. designed heterotypic mosaic nanoparticle vaccines by co-displaying SARS-CoV-2 RBD with RBDs from other animal coronaviruses to evaluate whether the heterotypic nanoparticles can elicit cross-reactive antibody responses. They displayed four or eight of the 12 RBDs on the surface of mosaic nanoparticles using SpyCatcher-SpyTag ligation. Heterotypic nanoparticle vaccines successfully induced broader anti-coronavirus responses than homotypic nanoparticle vaccines displaying SARS-CoV-2 RBD

alone, suggesting that the co-display strategy is advantageous for inducing cross-immunity against zoonotic sarbecoviruses.

4. Conclusions and Perspectives

Viral vector vaccines from Astra Zeneca and Johnson & Johnson, mRNA-based vaccines from Pfizer and Moderna, and inactivated vaccines from Sinovac Biotech have been distributed worldwide, and hundreds of SARS-CoV-2 vaccine candidates are currently being evaluated in clinical trials. Among them, recombinant protein subunit vaccines using S protein or RBD are an attractive alternative to inactivated, viral vector, and mRNA-based vaccines owing to their track records of safety. However, despite extensive efforts to develop and apply the S protein or RBD-based subunit as vaccine candidates, their low immunogenicity remains a hindrance.

Compared with the monomeric form of recombinant S protein subunit vaccines, nanoparticle-based vaccines provide multivalent S protein or RBD display. This repetitive array promotes various immunological events, including robust B cell activation, memory B cell expansion, and retention of follicular dendritic cells. Therefore, protein nanoparticle-based vaccines have proven to have enhanced efficacy, neutralizing antibody responses, and specific humoral and cellular immune responses at lower doses than the S protein subunit vaccine. Additionally, inherent stability, the lack of a strict cold-chain supply, and no special biosafety environment concern in manufacturing procedures with reduced production costs are major advantages of protein nanoparticle-based SARS-CoV-2 vaccines [38]. Therefore, nanoparticle vaccines against SARS-CoV-2 (IVX-411) and other viruses (malaria (NCT04296279), Epstein–Barr virus (NCT04645147), and influenza (NCT03186781; NCT03814720; NCT04579250)) are currently being investigated in clinical trials.

On the other hand, the protein nanoparticle-based vaccine platform generates strong cross-reactive immunity against emerging SARS-CoV-2 VOCs and other zoonotic coronaviruses such as SARS-CoV and MERS-CoV. Despite mRNA-based vaccines from Pfizer and Moderna and viral vector vaccines from Astra Zeneca and Johnson & Johnson showing strong protective efficacy against the original Wuhan-Hu-1 strain (wild-type) and slowing the infection rate, the recent emergence of rapidly evolving SARS-CoV-2 VOCs, including Delta and Mu coronavirus variants, presents new challenges. Additionally, two other zoonotic betacoronaviruses, SARS-CoV and MERS-CoV, have appeared in human populations over the past 20 years, and the possibility of future potential zoonotic coronavirus emergence exists, making the next pandemic imminent. From this point of view, protein nanoparticle-based vaccines allow the development of a next-generation vaccine platform for protecting against SARS-CoV-2 VOCs and other zoonotic coronaviruses. They could provide strong protection against the destructive effects of pandemics on the public health system and economy.

Author Contributions: Conceptualization, E.J.L., H.-D.S. and N.K.; writing—original draft preparation, E.J.L., H.-D.S. and N.K.; writing—review and editing, E.J.L., H.-D.S., N.K. and Y.L.; supervision, E.J.L.; funding acquisition, E.J.L. All authors have read and agreed to the published version of the manuscript.

Funding: This work was supported by a grant from the National Research Foundation (NRF) of Korea funded by the Korean government (NRF-2021R1C1C1008217).

Conflicts of Interest: The authors declare no conflict of interest.

References

1. WHO Director-General's Opening Remarks at the Media Briefing on COVID-19—7 September 2020. Available online: <https://www.who.int/director-general/speeches/detail/who-director-general-s-opening-remarks-at-the-media-briefing-on-covid-19---7-september-2020> (accessed on 30 September 2021).
2. Coronavirus Resource Center. COVID-19 Dashboard by the Center for Systems Science and Engineering (CSSE) at Johns Hopkins University (JHU). Available online: <https://coronavirus.jhu.edu/map.html> (accessed on 30 September 2021).

3. WHO Coronavirus (COVID-19) Dashboard. Available online: <https://covid19.who.int/> (accessed on 30 September 2021).
4. Wrapp, D.; Wang, N.; Corbett Kizzmekia, S.; Goldsmith Jory, A.; Hsieh, C.-L.; Abiona, O.; Graham Barney, S.; McLellan Jason, S. Cryo-EM structure of the 2019-nCoV spike in the prefusion conformation. *Science* **2020**, *367*, 1260–1263. [[CrossRef](#)]
5. Shang, J.; Ye, G.; Shi, K.; Wan, Y.; Luo, C.; Aihara, H.; Geng, Q.; Auerbach, A.; Li, F. Structural basis of receptor recognition by SARS-CoV-2. *Nature* **2020**, *581*, 221–224. [[CrossRef](#)] [[PubMed](#)]
6. Wang, Q.; Zhang, Y.; Wu, L.; Niu, S.; Song, C.; Zhang, Z.; Lu, G.; Qiao, C.; Hu, Y.; Yuen, K.-Y.; et al. Structural and Functional Basis of SARS-CoV-2 Entry by Using Human ACE2. *Cell* **2020**, *181*, 894–904.e9. [[CrossRef](#)] [[PubMed](#)]
7. Kim, Y.-I.; Kim, D.; Yu, K.-M.; Seo, H.D.; Lee, S.-A.; Casel, M.A.B.; Jang, S.-G.; Kim, S.; Jung, W.; Lai, C.-J.; et al. Development of Spike Receptor-Binding Domain Nanoparticles as a Vaccine Candidate against SARS-CoV-2 Infection in Ferrets. *mBio* **2021**, *12*, e00230-21. [[CrossRef](#)]
8. Ingale, J.; Stano, A.; Guenaga, J.; Sharma, S.K.; Nemazee, D.; Zwick, M.B.; Wyatt, R.T. High-Density Array of Well-Ordered HIV-1 Spikes on Synthetic Liposomal Nanoparticles Efficiently Activate B Cells. *Cell Rep.* **2016**, *15*, 1986–1999. [[CrossRef](#)]
9. Thompson, E.A.; Ols, S.; Miura, K.; Rausch, K.; Narum, D.L.; Spångberg, M.; Juraska, M.; Wille-Reece, U.; Weiner, A.; Howard, R.F.; et al. TLR-adjuvanted nanoparticle vaccines differentially influence the quality and longevity of responses to malaria antigen Pfs25. *JCI Insight* **2018**, *3*, e120692. [[CrossRef](#)] [[PubMed](#)]
10. Marcandalli, J.; Fiala, B.; Ols, S.; Perotti, M.; de van der Schueren, W.; Snijder, J.; Hodge, E.; Benhaim, M.; Ravichandran, R.; Carter, L.; et al. Induction of Potent Neutralizing Antibody Responses by a Designed Protein Nanoparticle Vaccine for Respiratory Syncytial Virus. *Cell* **2019**, *176*, 1420–1431.e17. [[CrossRef](#)]
11. Yu, F.; Wang, J.; Dou, J.; Yang, H.; He, X.; Xu, W.; Zhang, Y.; Hu, K.; Gu, N. Nanoparticle-based adjuvant for enhanced protective efficacy of DNA vaccine Ag85A-ESAT-6-IL-21 against Mycobacterium tuberculosis infection. *Nanomedicine* **2012**, *8*, 1337–1344. [[CrossRef](#)] [[PubMed](#)]
12. Kanekiyo, M.; Wei, C.-J.; Yassine, H.M.; McTamney, P.M.; Boyington, J.C.; Whittle, J.R.R.; Rao, S.S.; Kong, W.-P.; Wang, L.; Nabel, G.J. Self-assembling influenza nanoparticle vaccines elicit broadly neutralizing H1N1 antibodies. *Nature* **2013**, *499*, 102–106. [[CrossRef](#)]
13. Joyce, M.G.; Chen, W.-H.; Sankhala, R.S.; Hajduczek, A.; Thomas, P.V.; Choe, M.; Chang, W.; Peterson, C.E.; Martinez, E.; Morrison, E.B.; et al. SARS-CoV-2 ferritin nanoparticle vaccines elicit broad SARS coronavirus immunogenicity. *bioRxiv* **2021**. [[CrossRef](#)]
14. Pati, R.; Shevtsov, M.; Sonawane, A. Nanoparticle Vaccines Against Infectious Diseases. *Front. Immunol.* **2018**, *9*, 2224. [[CrossRef](#)]
15. Bangaru, S.; Ozorowski, G.; Turner, H.L.; Antanasijevic, A.; Huang, D.; Wang, X.; Torres, J.L.; Diedrich, J.K.; Tian, J.H.; Portnoff, A.D.; et al. Structural analysis of full-length SARS-CoV-2 spike protein from an advanced vaccine candidate. *Science* **2020**, *370*, 1089–1094. [[CrossRef](#)] [[PubMed](#)]
16. Heath, P.T.; Galiza, E.P.; Baxter, D.N.; Boffito, M.; Browne, D.; Burns, F.; Chadwick, D.R.; Clark, R.; Cosgrove, C.; Galloway, J.; et al. Safety and Efficacy of NVX-CoV2373 Covid-19 Vaccine. *N. Engl. J. Med.* **2021**, *385*, 1172–1183. [[CrossRef](#)] [[PubMed](#)]
17. Gause, K.T.; Wheatley, A.K.; Cui, J.; Yan, Y.; Kent, S.J.; Caruso, F. Immunological Principles Guiding the Rational Design of Particles for Vaccine Delivery. *ACS Nano* **2017**, *11*, 54–68. [[CrossRef](#)]
18. Link, A.; Zabel, F.; Schnetzler, Y.; Titz, A.; Brombacher, F.; Bachmann, M.F. Innate immunity mediates follicular transport of particulate but not soluble protein antigen. *J. Immunol.* **2012**, *188*, 3724–3733. [[CrossRef](#)]
19. Wang, N.; Shang, J.; Jiang, S.; Du, L. Subunit Vaccines against Emerging Pathogenic Human Coronaviruses. *Front. Microbio.* **2020**, *11*, 298. [[CrossRef](#)]
20. Kang, Y.-F.; Sun, C.; Zhuang, Z.; Yuan, R.-Y.; Zheng, Q.; Li, J.-P.; Zhou, P.-P.; Chen, X.-C.; Liu, Z.; Zhang, X.; et al. Rapid Development of SARS-CoV-2 Spike Protein Receptor-Binding Domain Self-Assembled Nanoparticle Vaccine Candidates. *ACS Nano* **2021**, *15*, 2738–2752. [[CrossRef](#)]
21. Kih, M.; Lee, E.J.; Lee, N.K.; Kim, Y.K.; Lee, K.E.; Jeong, C.; Yang, Y.; Kim, D.-H.; Kim, I.-S. Designed trimer-mimetic TNF superfamily ligands on self-assembling nanocages. *Biomaterials* **2018**, *180*, 67–77. [[CrossRef](#)] [[PubMed](#)]
22. Je, H.; Nam, G.-H.; Kim, G.B.; Kim, W.; Kim, S.R.; Kim, I.-S.; Lee, E.J. Overcoming therapeutic efficiency limitations against TRAIL-resistant tumors using re-sensitizing agent-loaded trimeric TRAIL-presenting nanocages. *J. Control. Release* **2021**, *331*, 7–18. [[CrossRef](#)]
23. Choi, Y.; Nam, G.-H.; Kim, G.B.; Kim, S.; Kim, Y.K.; Kim, S.A.; Kim, H.-J.; Lee, E.J.; Kim, I.-S. Nanocages displaying SIRP gamma clusters combined with phagocytic stimulus of phagocytes potentiate anti-tumor immunity. *Cancer Gene Ther.* **2021**, *28*, 960–970. [[CrossRef](#)] [[PubMed](#)]
24. Hu, X.; Deng, Y.; Chen, X.; Zhou, Y.; Zhang, H.; Wu, H.; Yang, S.; Chen, F.; Zhou, Z.; Wang, M.; et al. Immune Response of A Novel ATR-AP205-001 Conjugate Anti-hypertensive Vaccine. *Sci. Rep.* **2017**, *7*, 12580. [[CrossRef](#)]
25. Pardi, N.; Hogan, M.J.; Naradikian, M.S.; Parkhouse, K.; Cain, D.W.; Jones, L.; Moody, M.A.; Verkerke, H.P.; Myles, A.; Willis, E.; et al. Nucleoside-modified mRNA vaccines induce potent T follicular helper and germinal center B cell responses. *J. Exp. Med.* **2018**, *215*, 1571–1588. [[CrossRef](#)] [[PubMed](#)]
26. López-Sagaseta, J.; Malito, E.; Rappuoli, R.; Bottomley, M.J. Self-assembling protein nanoparticles in the design of vaccines. *Comput. Struct. Biotechnol. J.* **2016**, *14*, 58–68. [[CrossRef](#)]
27. Slifka, M.K.; Amanna, I.J. Role of Multivalency and Antigenic Threshold in Generating Protective Antibody Responses. *Front. Immunol.* **2019**, *10*, 956. [[CrossRef](#)] [[PubMed](#)]

28. Kelly, H.G.; Kent, S.J.; Wheatley, A.K. Immunological basis for enhanced immunity of nanoparticle vaccines. *Expert Rev. Vaccines* **2019**, *18*, 269–280. [[CrossRef](#)] [[PubMed](#)]
29. Tokatlian, T.; Read, B.J.; Jones, C.A.; Kulp, D.W.; Menis, S.; Chang, J.Y.H.; Steichen, J.M.; Kumari, S.; Allen, J.D.; Dane, E.L.; et al. Innate immune recognition of glycans targets HIV nanoparticle immunogens to germinal centers. *Science* **2019**, *363*, 649–654. [[CrossRef](#)] [[PubMed](#)]
30. Wang, W.; Zhou, X.; Bian, Y.; Wang, S.; Chai, Q.; Guo, Z.; Wang, Z.; Zhu, P.; Peng, H.; Yan, X.; et al. Dual-targeting nanoparticle vaccine elicits a therapeutic antibody response against chronic hepatitis B. *Nat. Nanotechnol.* **2020**, *15*, 406–416. [[CrossRef](#)]
31. Kato, Y.; Abbott, R.K.; Freeman, B.L.; Haupt, S.; Groschel, B.; Silva, M.; Menis, S.; Irvine, D.J.; Schief, W.R.; Crotty, S. Multifaceted Effects of Antigen Valency on B Cell Response Composition and Differentiation In Vivo. *Immunity* **2020**, *53*, 548–563.e8. [[CrossRef](#)]
32. Zhang, Y.-N.; Lazarovits, J.; Poon, W.; Ouyang, B.; Nguyen, L.N.M.; Kingston, B.R.; Chan, W.C.W. Nanoparticle Size Influences Antigen Retention and Presentation in Lymph Node Follicles for Humoral Immunity. *Nano Lett.* **2019**, *19*, 7226–7235. [[CrossRef](#)]
33. Kim, G.B.; Sung, H.-D.; Nam, G.-H.; Kim, W.; Kim, S.; Kang, D.; Lee, E.J.; Kim, I.-S. Design of PD-1-decorated nanocages targeting tumor-draining lymph node for promoting T cell activation. *J. Control. Release* **2021**, *333*, 328–338. [[CrossRef](#)] [[PubMed](#)]
34. Lee, E.J.; Nam, G.H.; Lee, N.K.; Kih, M.; Koh, E.; Kim, Y.K.; Hong, Y.; Kim, S.; Park, S.Y.; Jeong, C.; et al. Nanocage-Therapeutics Prevailing Phagocytosis and Immunogenic Cell Death Awakens Immunity against Cancer. *Adv. Mater.* **2018**, *30*. [[CrossRef](#)]
35. Ma, X.; Zou, F.; Yu, F.; Li, R.; Yuan, Y.; Zhang, Y.; Zhang, X.; Deng, J.; Chen, T.; Song, Z.; et al. Nanoparticle Vaccines Based on the Receptor Binding Domain (RBD) and Heptad Repeat (HR) of SARS-CoV-2 Elicit Robust Protective Immune Responses. *Immunity* **2020**, *53*, 1315–1330.e9. [[CrossRef](#)] [[PubMed](#)]
36. Kanekiyo, M.; Bu, W.; Joyce, M.G.; Meng, G.; Whittle, J.R.; Baxa, U.; Yamamoto, T.; Narpala, S.; Todd, J.P.; Rao, S.S.; et al. Rational Design of an Epstein-Barr Virus Vaccine Targeting the Receptor-Binding Site. *Cell* **2015**, *162*, 1090–1100. [[CrossRef](#)] [[PubMed](#)]
37. Kelly, H.G.; Tan, H.-X.; Juno, J.A.; Esterbauer, R.; Ju, Y.; Jiang, W.; Wimmer, V.C.; Duckworth, B.C.; Groom, J.R.; Caruso, F.; et al. Self-assembling influenza nanoparticle vaccines drive extended germinal center activity and memory B cell maturation. *JCI Insight* **2020**, *5*, e136653. [[CrossRef](#)] [[PubMed](#)]
38. He, D.; Marles-Wright, J. Ferritin family proteins and their use in bionanotechnology. *New Biotechnol.* **2015**, *32*, 651–657. [[CrossRef](#)] [[PubMed](#)]
39. Lee, N.K.; Lee, E.J.; Kim, S.; Nam, G.H.; Kih, M.; Hong, Y.; Jeong, C.; Yang, Y.; Byun, Y.; Kim, I.S. Ferritin nanocage with intrinsically disordered proteins and affibody: A platform for tumor targeting with extended pharmacokinetics. *J. Control. Release* **2017**, *267*, 172–180. [[CrossRef](#)]
40. Lv, C.; Zhang, X.; Liu, Y.; Zhang, T.; Chen, H.; Zang, J.; Zheng, B.; Zhao, G. Redesign of protein nanocages: The way from 0D, 1D, 2D to 3D assembly. *Chem. Soc. Rev.* **2021**, *50*, 3957–3989. [[CrossRef](#)]
41. Ren, H.; Zhu, S.; Zheng, G. Nanoreactor Design Based on Self-Assembling Protein Nanocages. *Int. J. Mol. Sci.* **2019**, *20*, 592. [[CrossRef](#)]
42. Diaz, D.; Care, A.; Sunna, A. Bioengineering Strategies for Protein-Based Nanoparticles. *Genes* **2018**, *9*, 370. [[CrossRef](#)]
43. Bhaskar, S.; Lim, S. Engineering protein nanocages as carriers for biomedical applications. *NPG Asia Mater.* **2017**, *9*, e371. [[CrossRef](#)]
44. Lee, E.J.; Lee, N.K.; Kim, I.-S. Bioengineered protein-based nanocage for drug delivery. *Adv. Drug Del. Rev.* **2016**, *106*, 157–171. [[CrossRef](#)]
45. Demchuk, A.M.; Patel, T.R. The biomedical and bioengineering potential of protein nanocompartments. *Biotechnol. Adv.* **2020**, *41*, 107547. [[CrossRef](#)]
46. Nguyen, B.; Tolia, N.H. Protein-based antigen presentation platforms for nanoparticle vaccines. *NPJ Vaccines* **2021**, *6*, 70. [[CrossRef](#)]
47. Huang, Y.; Yang, C.; Xu, X.-F.; Xu, W.; Liu, S.-W. Structural and functional properties of SARS-CoV-2 spike protein: Potential antiviral drug development for COVID-19. *Acta Pharmacolol. Sin.* **2020**, *41*, 1141–1149. [[CrossRef](#)]
48. Powell, A.E.; Zhang, K.; Sanyal, M.; Tang, S.; Weidenbacher, P.A.; Li, S.; Pham, T.D.; Pak, J.E.; Chiu, W.; Kim, P.S. A Single Immunization with Spike-Functionalized Ferritin Vaccines Elicits Neutralizing Antibody Responses against SARS-CoV-2 in Mice. *ACS Cent. Sci.* **2021**, *7*, 183–199. [[CrossRef](#)] [[PubMed](#)]
49. Cho, K.J.; Shin, H.J.; Lee, J.-H.; Kim, K.-J.; Park, S.S.; Lee, Y.; Lee, C.; Park, S.S.; Kim, K.H. The Crystal Structure of Ferritin from *Helicobacter pylori* Reveals Unusual Conformational Changes for Iron Uptake. *J. Mol. Biol.* **2009**, *390*, 83–98. [[CrossRef](#)]
50. Carmen, J.M.; Shrivastava, S.; Lu, Z.; Anderson, A.; Morrison, E.B.; Sankhala, R.S.; Chen, W.-H.; Chang, W.C.; Bolton, J.S.; Matyas, G.R.; et al. A spike-ferritin nanoparticle vaccine induces robust innate immune activity and drives polyfunctional SARS-CoV-2-specific T cells. *bioRxiv* **2021**. [[CrossRef](#)]
51. Joyce, M.G.; King, H.A.D.; Naouar, I.E.; Ahmed, A.; Peachman, K.K.; Cincotta, C.M.; Subra, C.; Chen, R.E.; Thomas, P.V.; Chen, W.-H.; et al. Efficacy of a Broadly Neutralizing SARS-CoV-2 Ferritin Nanoparticle Vaccine in Nonhuman Primates. *bioRxiv* **2021**. [[CrossRef](#)]
52. Saunders, K.O.; Lee, E.; Parks, R.; Martinez, D.R.; Li, D.; Chen, H.; Edwards, R.J.; Gobeil, S.; Barr, M.; Mansouri, K.; et al. Neutralizing antibody vaccine for pandemic and pre-emergent coronaviruses. *Nature* **2021**, *594*, 553–559. [[CrossRef](#)] [[PubMed](#)]
53. Gu, M.; Torres, J.L.; Greenhouse, J.; Wallace, S.; Chiang, C.-I.; Jackson, A.M.; Porto, M.; Kar, S.; Li, Y.; Ward, A.B.; et al. One dose of COVID-19 nanoparticle vaccine REVC-128 protects against SARS-CoV-2 challenge at two weeks post-immunization. *Emerg Microbes Infect.* **2021**, *10*, 2016–2029. [[CrossRef](#)] [[PubMed](#)]

54. Wang, W.; Huang, B.; Zhu, Y.; Tan, W.; Zhu, M. Ferritin nanoparticle-based SARS-CoV-2 RBD vaccine induces a persistent antibody response and long-term memory in mice. *Cell. Mol. Immunol.* **2021**, *18*, 749–751. [[CrossRef](#)]
55. Brouwer, P.J.M.; Brinkkemper, M.; Maisonnasse, P.; Dereuddre-Bosquet, N.; Grobben, M.; Claireaux, M.; de Gast, M.; Marlin, R.; Chesnais, V.; Diry, S.; et al. Two-component spike nanoparticle vaccine protects macaques from SARS-CoV-2 infection. *Cell* **2021**, *184*, 1188–1200.e19. [[CrossRef](#)]
56. Walls, A.C.; Fiala, B.; Schäfer, A.; Wrenn, S.; Pham, M.N.; Murphy, M.; Tse, L.V.; Shehata, L.; O'Connor, M.A.; Chen, C.; et al. Elicitation of Potent Neutralizing Antibody Responses by Designed Protein Nanoparticle Vaccines for SARS-CoV-2. *Cell* **2020**, *183*, 1367–1382.e17. [[CrossRef](#)] [[PubMed](#)]
57. Cohen, A.A.; Gnanapragasam, P.N.P.; Lee, Y.E.; Hoffman, P.R.; Ou, S.; Kakutani, L.M.; Keeffe, J.R.; Wu, H.-J.; Howarth, M.; West, A.P.; et al. Mosaic nanoparticles elicit cross-reactive immune responses to zoonotic coronaviruses in mice. *Science* **2021**, *371*, 735. [[CrossRef](#)]
58. Chiba, S.; Frey, S.J.; Halfmann, P.J.; Kuroda, M.; Maemura, T.; Yang, J.E.; Wright, E.R.; Kawaoka, Y.; Kane, R.S. Multivalent nanoparticle-based vaccines protect hamsters against SARS-CoV-2 after a single immunization. *Commun. Bio.* **2021**, *4*, 597. [[CrossRef](#)] [[PubMed](#)]
59. Salzer, R.; Clark, J.J.; Vaysburd, M.; Chang, V.T.; Albecka-Moreau, A.; Kiss, L.; Sharma, P.; Llamazares, A.G.; Kipar, A.; Hiscox, J.A.; et al. Single-dose immunisation with a multimerised SARS-CoV-2 receptor binding domain (RBD) induces an enhanced and protective response in mice. *FEBS Lett.* **2021**, *595*, 2323–2340. [[CrossRef](#)] [[PubMed](#)]
60. He, L.; Lin, X.; Wang, Y.; Abraham, C.; Sou, C.; Ngo, T.; Zhang, Y.; Wilson, I.A.; Zhu, J. Single-component, self-assembling, protein nanoparticles presenting the receptor binding domain and stabilized spike as SARS-CoV-2 vaccine candidates. *Sci. Adv.* **2021**, *7*, eabf1591. [[CrossRef](#)] [[PubMed](#)]
61. Lainšček, D.; Fink, T.; Forstnerič, V.; Hafner-Bratkovič, I.; Orehek, S.; Strmšek, Ž.; Manček-Keber, M.; Pečan, P.; Esih, H.; Malenšek, Š.; et al. A Nanoscaffolded Spike-RBD Vaccine Provides Protection against SARS-CoV-2 with Minimal Anti-Scaffold Response. *Vaccines* **2021**, *9*, 431. [[CrossRef](#)]
62. Boyoglu-Barnum, S.; Ellis, D.; Gillespie, R.A.; Hutchinson, G.B.; Park, Y.-J.; Moin, S.M.; Acton, O.; Ravichandran, R.; Murphy, M.; Pettie, D.; et al. Elicitation of broadly protective immunity to influenza by multivalent hemagglutinin nanoparticle vaccines. *bioRxiv* **2020**. [[CrossRef](#)]
63. Brouwer, P.J.M.; Antanasijevic, A.; Berndsen, Z.; Yasmeen, A.; Fiala, B.; Bijl, T.P.L.; Bontjer, I.; Bale, J.B.; Sheffler, W.; Allen, J.D.; et al. Enhancing and shaping the immunogenicity of native-like HIV-1 envelope trimers with a two-component protein nanoparticle. *Nat. Commun.* **2019**, *10*, 4272. [[CrossRef](#)]
64. Li, F.; Li, W.; Farzan, M.; Harrison, S.C. Structure of SARS coronavirus spike receptor-binding domain complexed with receptor. *Science* **2005**, *309*, 1864–1868. [[CrossRef](#)] [[PubMed](#)]
65. Lan, J.; Ge, J.; Yu, J.; Shan, S.; Zhou, H.; Fan, S.; Zhang, Q.; Shi, X.; Wang, Q.; Zhang, L.; et al. Structure of the SARS-CoV-2 spike receptor-binding domain bound to the ACE2 receptor. *Nature* **2020**, *581*, 215–220. [[CrossRef](#)]
66. Escolano, A.; Gristick, H.B.; Abernathy, M.E.; Merckenschlager, J.; Gautam, R.; Oliveira, T.Y.; Pai, J.; West, A.P.; Barnes, C.O.; Cohen, A.A.; et al. Immunization expands B cells specific to HIV-1 V3 glycan in mice and macaques. *Nature* **2019**, *570*, 468–473. [[CrossRef](#)] [[PubMed](#)]
67. Halfmann, P.J.; Castro, A.; Loeffler, K.; Frey, S.J.; Chiba, S.; Kawaoka, Y.; Kane, R.S. Potent neutralization of SARS-CoV-2 including variants of concern by vaccines presenting the receptor-binding domain multivalently from nanoscaffolds. *Bioeng. Transl. Med.* **2021**, *6*, e10253. [[CrossRef](#)] [[PubMed](#)]



Communication

Cationic Surfactants as Disinfectants against SARS-CoV-2

Eduard V. Karamov ^{1,2} , Viktor F. Larichev ¹, Galina V. Kornilaeva ¹, Irina T. Fedyakina ¹, Ali S. Turgiev ^{1,2}, Andrey V. Shibaev ³ , Vyacheslav S. Molchanov ³ , Olga E. Philippova ^{3,*} and Alexei R. Khokhlov ³

¹ Gamaleya National Research Center for Epidemiology and Microbiology of the Russian Ministry of Health, 123098 Moscow, Russia; karamov2004@yandex.ru (E.V.K.); vlaritchev@mail.ru (V.F.L.); kornilaeva@yandex.ru (G.V.K.); irfed2@mail.ru (I.T.F.); turgiev@ld.ru (A.S.T.)

² National Medical Research Center of Phthisiopulmonology and Infectious Diseases of the Russian Ministry of Health, 127473 Moscow, Russia

³ Physics Department, Moscow State University, 119991 Moscow, Russia; shibaev@polly.phys.msu.ru (A.V.S.); molchan@polly.phys.msu.ru (V.S.M.); khokhlov@polly.phys.msu.ru (A.R.K.)

* Correspondence: phil@polly.phys.msu.ru

Abstract: The virucidal activity of a series of cationic surfactants differing in the length and number of hydrophobic tails (at the same hydrophilic head) and the structure of the hydrophilic head (at the same length of the hydrophobic n-alkyl tail) was compared. It was shown that an increase in the length and number of hydrophobic tails, as well as the presence of a benzene ring in the surfactant molecule, enhance the virucidal activity of the surfactant against SARS-CoV-2. This may be due to the more pronounced ability of such surfactants to penetrate and destroy the phospholipid membrane of the virus. Among the cationic surfactants studied, didodecyldimethylammonium bromide was shown to be the most efficient as a disinfectant, its 50% effective concentration (EC50) being equal to 0.016 mM. Two surfactants (didodecyldimethylammonium bromide and benzalkonium chloride) can deactivate SARS-CoV-2 in as little as 5 s.

Keywords: SARS-CoV-2; COVID-19; cationic surfactants; virucidal activity; quaternary ammonium compounds; disinfectants



Citation: Karamov, E.V.; Larichev, V.F.; Kornilaeva, G.V.; Fedyakina, I.T.; Turgiev, A.S.; Shibaev, A.V.;

Molchanov, V.S.; Philippova, O.E.; Khokhlov, A.R. Cationic Surfactants as Disinfectants against SARS-CoV-2.

Int. J. Mol. Sci. **2022**, *23*, 6645.

<https://doi.org/10.3390/ijms23126645>

ijms23126645

Academic Editors:

Monica Terracciano, Ilaria Rea,
Nicola Borbone and
Chiara Tramontano

Received: 2 June 2022

Accepted: 12 June 2022

Published: 14 June 2022

Publisher's Note: MDPI stays neutral with regard to jurisdictional claims in published maps and institutional affiliations.



Copyright: © 2022 by the authors. Licensee MDPI, Basel, Switzerland. This article is an open access article distributed under the terms and conditions of the Creative Commons Attribution (CC BY) license (<https://creativecommons.org/licenses/by/4.0/>).

1. Introduction

The ongoing coronavirus disease (COVID-19) pandemic caused by severe acute respiratory syndrome coronavirus 2 (SARS-CoV-2) is the most dramatic public health crisis in the last 100 years. By 30 May 2022, there were over 531 million infected people and 6.3 million deaths worldwide [1]. Therefore, it is extremely important to use multiple means of controlling the disease. Although airborne, and droplet transmission are the most common ways of SARS-CoV-2 spreading, contact transmission (through contaminated hands and surfaces touched by infected persons) also takes place. It was demonstrated that at room temperature SARS-CoV-2 survives for up to 3–4 days on plastic [2–4] and stainless-steel surfaces [2,3] and for up to 2 days on glass and banknotes [3]. To avoid contact transmission, it is necessary to use hand sanitizers and efficiently disinfect surfaces, especially in public places like hospitals, transport, stores, malls, etc. At present, most of the hand sanitizers used for SARS-CoV-2 control are represented by alcohol-based solutions [5]. Some of them (containing alcohol at high concentrations) are flammable; also, they evaporate rapidly thereby shortening the exposure time; among other disadvantages is their ability to cause skin drying/cracking [6] and induce contact and atopic dermatitis [7]. As an alternative, one can consider another commonly used wide class of disinfectants—quaternary ammonium compounds (quats) [8,9] often called the “workhorses” of modern disinfection [10]. They are non-flammable and some of them (for example, benzalkonium chloride (BAC)) are less irritating to the skin [5]. Quaternary ammonium compounds exert antiviral effects by disrupting the lipid bilayer of viral envelopes [5,11] (all coronaviruses, including SARS-CoV-2, belong to enveloped viruses) [12]. The spike (S) of SARS-CoV-2, responsible for its entry, is an integral glycoprotein of the lipid membrane of the virions. After binding to its cellular receptor, S-protein

undergoes conformational changes resulting in the fusion of the cellular and viral membranes. Virions with damaged lipid membranes cannot enter the cells and initiate the infection. Therefore, disruption of the virion membrane contributes to SARS-CoV-2 inactivation. Another mechanism of the antiviral activity of quaternary ammonium compounds consists in their lysosome tropism and accumulation in lysosomes or endosomes, ultimately blocking viral entry [11].

The most common quaternary ammonium disinfectants are probably BAC, cetylpyridinium chloride (C16Py), and didodecyltrimethylammonium chloride/bromide [8]. BAC is utilized in hand sanitizers, soaps, cleaning wipes, hospital sanitation kits, surface disinfectants [5,10,11], etc. C16Py is widely used in mouthwash, toothpaste, cough lozenges, and so on [13,14]. The newer fourth-generation quaternary ammonium compounds, referred to as twin-chain or dialkyl quaternaries (e.g., didodecyltrimethylammonium bromide (C12-C12DMA)), are used for the stabilization of emulsions [15]. They have some advantages since they remain active in hard water and are tolerant to anionic residues [16].

Even now, little is known about the resistance of SARS-CoV-2 to cationic surfactant-based common disinfectants. In particular, it was shown that a 0.2 wt% aqueous BAC solution reduces the infectious titer of SARS-CoV-2 by 3 orders of magnitude in 1 min [5,17]; in another paper [3], it was claimed that SARS-CoV-2 becomes undetectable after 5 min treatment with a less concentrated (0.1 wt%) BAC. As for the twin-chain cationic surfactant di-N-decyltrimethylammonium chloride (C10-C10DMA), it was shown to reduce SARS-CoV-2 by almost 5 orders of magnitude at concentrations exceeding 283 mg/L (0.028 wt%) [18]. Moreover, virucidal activity against SARS-CoV-2 was found for the cationic surfactant C16Py [11,13] *in vitro* and for a mouthwash with 0.075 wt% C16Py (Colgate Plax) *in vivo* [14]. However, none of those studies compared the virucidal activities of the different cationic disinfectants against SARS-CoV-2.

Therefore, the aim of the present work is to assess the virucidal efficacy against SARS-CoV-2 for diverse cationic surfactant-based disinfectants and to reveal the role of their structure (length and number of their hydrophobic tails and type of head) on the activity. For these studies, we selected the three most common disinfectants based on cationic surfactants (BAC, C16Py, and C12-C12DMA) as well as their analogs differing in the length and number of surfactant tails and the structure of hydrophilic head (as depicted in Figure 1). We believe that the results obtained will help prepare cationic disinfectants of optimum composition, e.g., for surfaces and hands contaminated with SARS-CoV-2.

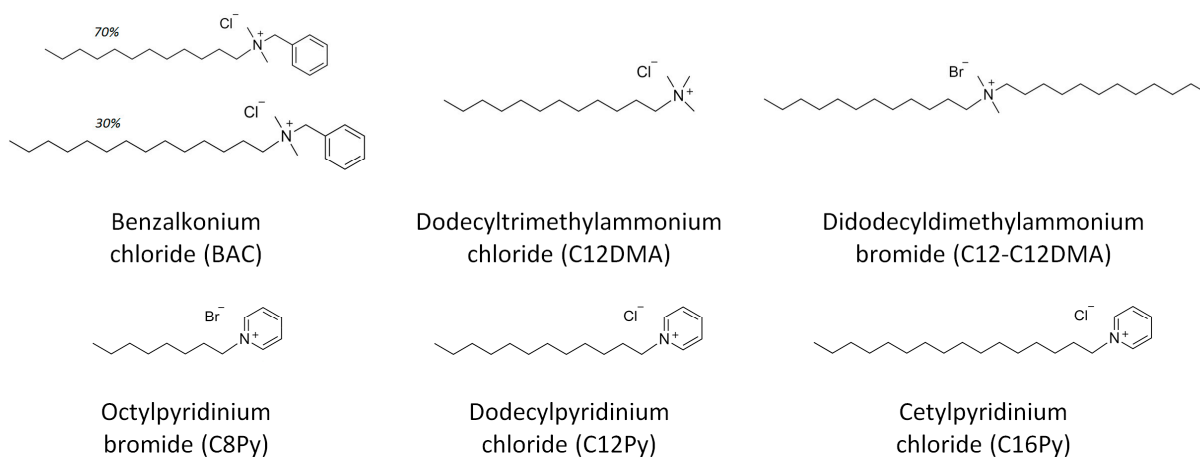


Figure 1. Molecular structure of cationic surfactants under study.

2. Results and Discussion

2.1. Effect of the Surfactant Structure on the Virucidal Efficacy

Comparative studies of the virucidal activity were carried out at fixed surfactant concentration (0.28 mM) and contact time (1 h). For most of the surfactants (except C12-C12DMA) the concentration used was below the critical micelle concentration (cmc). The

results are summarized in Table 1. They demonstrate that, under those conditions, four surfactants (C12BAC, BAC, C12-C12DMA, and C16Py) ensure complete inhibition of the infection (inhibition coefficient IC = 100%) and reduce SARS-CoV-2 titer by 7 orders of magnitude.

Table 1. SARS-CoV-2 inactivation by 0.28 mM solutions of different cationic surfactants (contact time 1 h).

Surfactant	Abbreviation	Hydrophobic Tail	Critical Micelle Concentration (cmc), mM	Hydrophile-Lipophile Balance (HLB)	Virus Titer			Inhibition Coefficient IC, %
					Control A _c	Experiment A _e	Log ₁₀ Reduction A	
Benzyltrimethylammonium chloride	C12BAC	C12	1.2 *	14.2 **	7.00	0.00	7.00	100
Benzalkonium chloride	BAC	C12 (70%), C14 (30%)	0.37 *, 0.43 [19]	13.9 **	7.00	0.00	7.00	100
Didodecyltrimethylammonium bromide	C12-C12DMA	C12-C12	0.08 [20], 0.15 [21]	10 [22]	7.00	0.00	7.00	100
Dodecyltrimethylammonium chloride	C12DMA	C12	21.3 [23]	15 [22], 17.1 [24], 18.5 [25]	7.00	5.75	1.25	18
Cetylpyridinium chloride	C16Py	C16	0.9 [26–28]	14.5 **	7.00	0.00	7.00	100
Dodecylpyridinium chloride	C12Py	C12	15 [29]	16.4 [30]	7.00	4.75	2.25	32
Octylpyridinium bromide	C8Py	C8	190 [29]	18.3 **	6.50	6.25	0.25	3.8

* in 0.9 wt% NaCl. ** calculated by group contribution method according to Refs. [30,31].

Structural determinants of the virucidal activity of the surfactants were studied. We first assessed the effect of the length of hydrophobic tails. For that, we compared activities of a series of N-alkylpyridinium surfactants (C16Py, C12Py, and C8Py), which have the same hydrophilic pyridinium head and hydrophobic n-alkyl tails of different lengths (Figure 1). As shown in Table 1 and Figure 2, increasing the length of the hydrophobic tail of a surfactant enhances its activity against SARS-CoV-2. Previously, C16Py was shown to destabilize the SARS-CoV-2 membrane through electrostatic interactions of the cationic head groups of the surfactant with the negatively charged viral membrane, as was detected by the shift in zeta potential [13]. Simultaneously, the hydrophobic groups of the surfactant penetrate the hydrophobic interior of the phospholipid bilayer of the viral membrane, thereby destroying it [32]. Higher surfactant hydrophobicity favors this process.

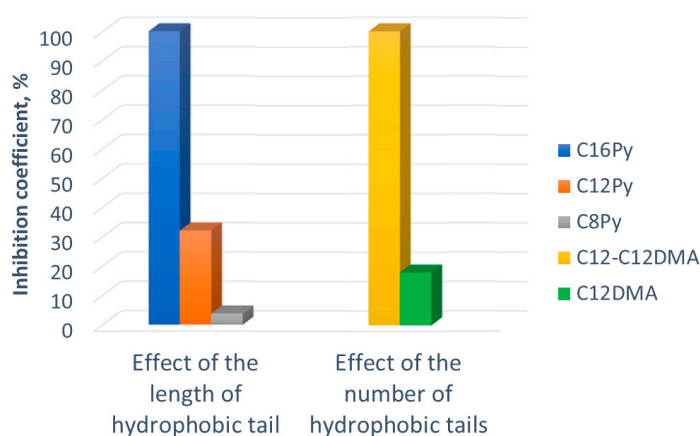


Figure 2. Effects of hydrophobicity on the virucidal activity of cationic surfactants against SARS-CoV-2: (left) effect of the length of the hydrophobic tail (for C8Py, C12Py, and C16Py surfactants having the same hydrophilic pyridinium head group) and (right) effect of the number of hydrophobic tails (for C12DMA and C12-C12DMA surfactants) on the values of the inhibition coefficient, observed at 0.28 mM concentration of each surfactant.

A comparison of the data obtained for alkylammonium surfactants C12-C12DMA (with two C12 tails) and dodecyltrimethylammonium chloride C12DMA (with one C12 tail), having similar ammonium head group (Figure 1), shows that the two-tailed surfactant is 5.5-fold more active against the virus (as judged by IC values; Table 1 and Figure 2). This finding lends support to the idea that surfactant hydrophobicity is a key factor in

virucidal activity. Note that the change of the type of counterion from chloride to bromide does not affect the virucidal activity against SARS-CoV-2 as was clearly demonstrated for di-N-decyldimethylammonium chloride and bromide recently [18].

One can also compare the virucidal activity of C12BAC and C12DMA, which have the same hydrophobic tail (C12), but differ in the presence of an additional substituent (benzene ring) at the surfactant head (Figure 1). It follows from Table 1 that the introduction of this substituent causes a 5.5-fold increase in IC. This also appears to be underlain by enhanced hydrophobicity of the surfactant molecule.

The contribution of surfactant head type to the antiviral effects was further studied using two surfactants with the same hydrophobic tail (C12) and different heads, i.e., pyridinium chloride C12Py and trimethylammonium chloride C12DMA (Figure 1). The data in Table 1 demonstrate that C12Py exhibits a more pronounced virucidal activity. This effect can also be related to the higher hydrophobicity of the pyridinium chloride head, which contains more nonpolar groups as compared to the trimethylammonium head [30].

Now let us consider the correlations between the virucidal activity and such characteristics of surfactants as cmc and hydrophile-lipophile balance (HLB) values. The cmc value (i.e., the concentration at which surfactant molecules start to aggregate into micelles) is an important characteristic related to the free energy of micelle formation, ΔG_{mic} , as [33,34]:

$$RT \ln cmc = \Delta G_{mic}. \quad (1)$$

One can see from Figure 3a that the virucidal activity increases with decreasing cmc. Therefore, the surfactants more prone to aggregation possess better virucidal properties against SARS-CoV-2. This may be related to the fact that such surfactants are easily incorporated into the virion's phospholipid bilayer.

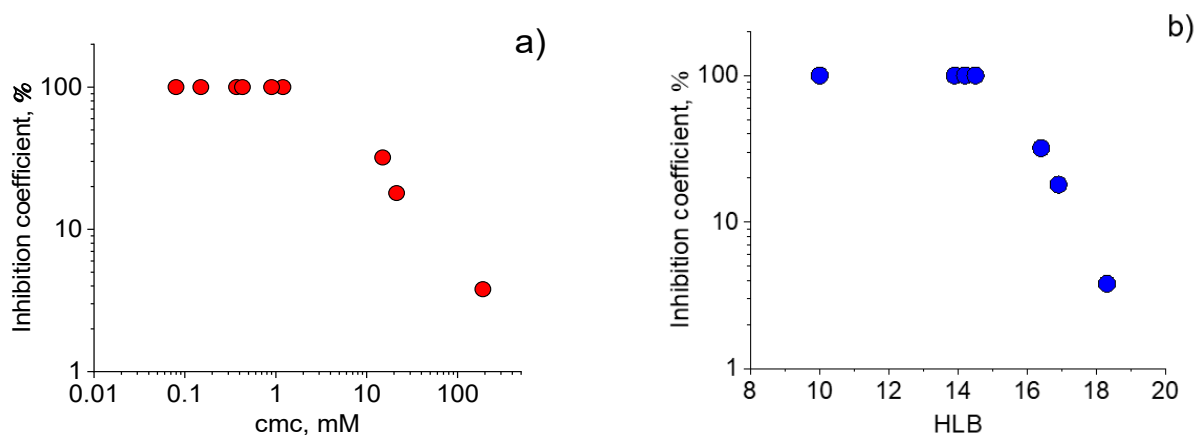


Figure 3. Inhibition coefficient as a function of: (a) critical micelle concentration cmc and (b) hydrophile-lipophile balance HLB of different cationic surfactants for SARS-CoV-2 inactivation by 0.28 mM surfactant solutions (contact time 1 h).

Another important characteristic of surfactants is the HLB value - the number related to the hydrophilic to lipophilic moieties ratio. This value, connected to the work of surfactant transfer from water to oil phase [35], serves as an empirical measure of the relative hydrophobicity [36,37]: the lower the HLB, the stronger the hydrophobicity. Figure 3b shows that HLB values correlate with virucidal activity demonstrating that the activity increases with surfactant hydrophobicity. Note that Figure 3b presents the HLB values for C12DMA surfactant averaged over three values obtained in different papers (Table 1).

Thus, our study of the effect of the structure of cationic surfactants on the virucidal activity against SARS-CoV-2 showed that the introduction of additional hydrophobic groups into surfactants augments their activity. This may be due to the more pronounced capacity of such surfactants for penetrating and destroying the phospholipid membrane of SARS-CoV-2.

2.2. Concentration Dependence of Virucidal Activity of the Most Efficient Surfactants

Table 2 shows the effect of the concentration of cationic surfactants on SARS-CoV-2 inactivation at constant contact time (1 h). For those studies, the four most efficient surfactants (C12BAC, BAC, C12-C12DMA, and C16Py) were used. From Table 2 it is clear that the virucidal activity increases with increasing surfactant concentration. It appears that the density of surfactant ions acting on the lipid membrane is an important factor. At 0.0048 mM, even prolonged incubation (1 h) favoring a gradual influx of surfactant ions does not result in pronounced SARS-CoV-2 inactivation. Complete inactivation occurs at surfactant concentrations exceeding 0.112 mM.

Table 2. SARS-CoV-2 inactivation by cationic surfactants of different concentrations (contact time 1 h).

Surfactant	Concentration		Virus Titer			Inhibition Coefficient IC, %
	mM	wt%	Control A _c	Experiment A _e	Log10 Reduction A	
Benzyltrimethylammonium chloride (C12BAC)	0.0224	0.0008	6.5	5.5	1.0	15
	0.112	0.0038	6.5	2.0	4.5	69
	0.56	0.0190	6.5	0	6.5	100
	2.8	0.0950	6.5	0	6.5	100
	50% effective concentration (EC50) 0.081 mM					
Benzalkonium chloride (BAC)	0.0048	0.0002	6.5	6.0	0.5	7.7
	0.0224	0.0008	6.5	5.5	1.0	15
	0.112	0.0039	6.5	0	6.5	100
	0.56	0.0195	6.5	0	6.5	100
	2.8	0.0970	6.5	0	6.5	100
50% effective concentration (EC50) 0.072 mM						
Didodecyltrimethylammonium bromide (C12-C12DMA)	0.0048	0.0002	6.75	6.5	0.25	3.7
	0.0224	0.0010	6.75	2.0	4.75	70
	0.112	0.0052	6.75	0	6.75	100
	0.56	0.0259	6.75	0	6.75	100
	2.8	0.1295	6.75	0	6.75	100
50% effective concentration (EC50) 0.016 mM						
Cetylpyridinium chloride (C16Py)	0.0048	0.0002	6.75	6.5	0.25	3.7
	0.0224	0.0008	6.75	6.0	0.75	11
	0.112	0.0038	6.75	0	6.75	100
	0.56	0.0190	6.75	0	6.75	100
	2.8	0.0950	6.75	0	6.75	100
50% effective concentration (EC50) 0.101 mM						

The 50% effective concentrations (EC50) were derived from concentration dependences of virucidal activity (expressed as IC values). The double-chain surfactant C12-C12MA exhibits the lowest EC50 (0.016 mM; Table 2) and, therefore, maximum efficiency in inactivating SARS-CoV-2. This may be due to its highest hydrophobicity among the surfactants under study. In addition, the presence of two chains may facilitate the penetration of the viral membrane, thereby accounting for the stronger antiviral activity of double-chain surfactants. Indeed, the second hydrophobic group (lying some distance off the first one) likely augments the membrane-perturbing effect.

The values of EC50 for BAC and C12BAC are equal to 0.072 and 0.081 mM, respectively (Table 2). Those surfactants possess the same hydrophilic head but differ in the length of hydrophobic groups (C12BAC contains only C12 tails, whereas BAC has 70% of C12 tails and 30% of C14 tails). Thus, the lower EC50 for BAC correlates well with its higher hydrophobicity.

As regards C16Py, its EC50 value (0.101 mM; Table 2) exceeds those of other surfactants under study. Note that C16Py and C12BAC have the same number of carbon atoms contributing to hydrophobicity (21 carbon atoms), the same empirical formula (C₂₁H₃₈CIN), and close HLB values. Moreover, each of the two surfactants has hydrophobic fragments (a long n-alkyl chain and an aromatic ring) on either side of its cationic group (Figure 1). Nevertheless, C12BAC exhibits a higher activity against SARS-CoV-2. It is conceivable that the difference in the activity may be due to the presence in C12BAC of a CH₂-group separating the aromatic ring from the cationic group. This additional group likens C12BAC to two-chain surfactants capable of perturbing the membrane more efficiently.

For all substances under study, their EC50s are 5–10-fold lower than their respective cmc values (Tables 1 and 2), suggesting that the virucidal effects are produced by the nonaggregated surfactants. This implies that surfactant monomers (rather than aggregates) are interacting with the lipid structures, which is consistent with the results obtained for solubilization of phosphatidylcholine bilayers of liposomes by cationic alkyl pyridinium

surfactants [38]. Figure 4 shows that the EC₅₀ values decrease with decreasing cmc. Note that the three first points of the dependence of EC₅₀ on the logarithm of cmc lie on the same line (Figure 4) suggesting that, in this range of cmc values, EC₅₀ is directly proportional to the free energy of micelle formation, ΔG_{mic} , since $\ln cmc \sim \Delta G_{mic}$ (Equation (1)).

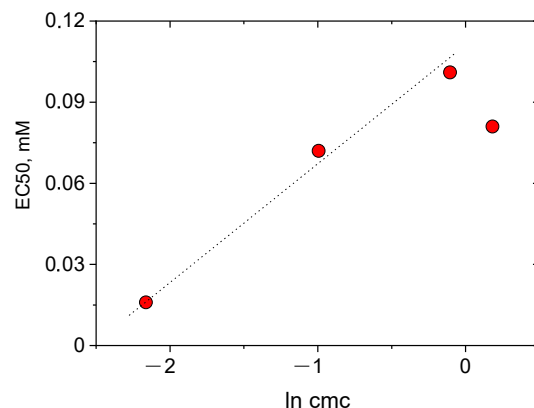


Figure 4. 50% effective concentrations EC₅₀ for SARS-CoV-2 inactivation as a function of critical micelle concentration cmc of different cationic surfactants in semi-logarithmic representation.

From Tables 1 and 2 it is evident that for all surfactants the EC₅₀ values decrease with HLB, that is with increasing hydrophobicity. This is related to the enhanced ability of the surfactants to interact with lipophilic lipid bilayers of the virus.

Thus, among the studied surfactants, C12-C12DMA has the lowest EC₅₀ value (0.016 mM). It may be accounted for by its double-chain structure in addition to the overall greater hydrophobicity.

2.3. Time Dependence of Virucidal Activity of the Most Efficient Surfactants

Figure 5 demonstrates time dependence of SARS-CoV-2 inactivation by 0.14 mM (0.005 wt%) BAC. It is evident that BAC starts to inactivate the virus after a 5-min contact and completes the inactivation in 15 min. It can be assumed that, for faster inactivation, higher surfactant concentrations are needed.

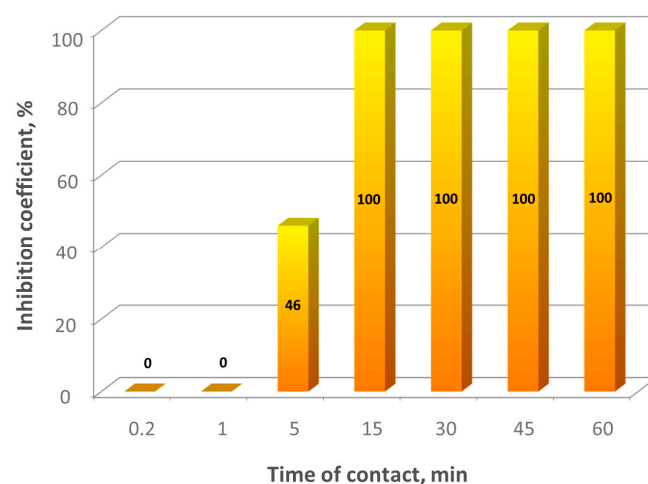


Figure 5. Kinetics of SARS-CoV-2 inactivation by 0.14 mM benzalkonium chloride at different virus-disinfectant contact times.

Therefore, subsequent experiments were performed at 20-fold higher surfactant concentrations, 2.8 mM. For those studies, we used three cationic surfactants, BAC, C16Py, and C12-C12DMA. The results are summarized in Table 3. It is seen that two surfactants (BAC and C12-C12DMA) completely inactivate SARS-CoV-2 at contact times as short as 5 s. The

efficiency of BAC against SARS-CoV-2 was reported previously in several papers [3,5,17]. For instance, a 0.1 wt% aqueous solution of BAC was shown to inactivate the virus after 5 min of treatment [3]. In the present study, we demonstrate that a 5-s incubation with 0.1 wt% solution of this surfactant is sufficient to ensure complete SARS-CoV-2 inactivation (Table 3). These results also indicate that BAC efficiency is much higher than found in another report [17], where SARS-CoV-2 treatment with 0.2 wt% BAC for 5 s led to as little as 1.83 log reduction of the virus titer. As regards C12-C12DMA, the data obtained are consistent with those reported for another two-chain cationic surfactant, di-N-decyldimethylammonium chloride [18]; in the present study, however, a much shorter contact time was sufficient (5 s instead of 30 s).

Table 3. SARS-CoV-2 inactivation by 2.8 mM cationic surfactants at different virus-disinfectant contact times.

Surfactant	Contact Time	Virus Titer			Inhibition Coefficient IC, %
		Control A _c	Experiment A _e	Log10 Reduction A	
Benzalkonium chloride (BAC)	5 s	7.50	0.00	7.50	100
	15 s	7.50	0.00	7.50	100
	30 s	7.50	0.00	7.50	100
	5 min	7.50	0.00	7.50	100
Didodecyldimethylammonium bromide (C12-C12DMA)	5 s	8.00	0.00	8.00	100
	15 s	8.00	0.00	8.00	100
	30 s	8.00	0.00	8.00	100
	5 min	8.00	0.00	8.00	100
Cetylpyridinium chloride (C16Py)	5 s	7.75	6.00	1.75	23
	15 s	7.75	4.50	3.25	42
	30 s	7.75	3.25	4.25	55
	5 min	7.75	0.00	7.75	100

In addition, Table 3 shows that 2.8 mM C16Py inactivates SARS-CoV-2 completely after no less than 5 min of contact. This is consistent with the weaker antiviral activity of this surfactant, evidenced by its higher EC₅₀ value (as compared to those of the other two surfactants; Table 2).

Thus, BAC and C12-C12DMA, which ensure SARS-CoV-2 inactivation in as little as 5 s of contact, are the most promising disinfectants among the surfactants under study.

3. Materials and Methods

3.1. Surfactants

Benzyltrimethylammonium chloride C12BAC (>99%) from Sigma Aldrich (Saint Louis, MO, USA, product number 13380), benzalkonium chloride BAC (>95%) containing 70% C12BAC and 30% benzyltrimethyltetradecylammonium chloride from Sigma Aldrich (product number 12060), didodecyldimethylammonium bromide C12-C12DMA (>98%) from ABCR (Karlsruhe, Germany), cetylpyridinium chloride C16Py (>98%) from Sigma Aldrich, dodecylpyridinium chloride C12Py (>99%) from ABCR, octylpyridinium bromide C8Py (>99%) from Chemos GmbH (Altdorf, Germany), dodecyltrimethylammonium chloride C12DMA (>97%) from ABCR, pyrene for fluorescence (>99%) from Sigma Aldrich were used as received. All solutions were prepared by weighing with dissolving the surfactant in physiological solution (0.9 wt% NaCl) as a solvent. Distilled deionized water for the preparation of the solutions was obtained using an ultrapure water purification system Milli Q (Millipore, Burlington, MA, USA).

3.2. Cells

Vero E6 cells (ATCC, Manassas, VA, USA; catalog number CRL-1586), a continuous line isolated from African green monkey (*Chlorocebus* sp.) kidney epithelium, were cultured in high glucose Dulbecco's modified Eagle's medium (DMEM; Sigma-Aldrich, St. Louis, MO, USA) supplemented with 5% fetal calf serum (FCS), 2 mM L-glutamine, 150 u/mL penicillin, and 150 u/mL streptomycin (all from Thermo Fisher Scientific, Waltham, MA,

USA) (growth medium) at 37 °C in 5% CO₂. This lineage is widely documented to be sensible and permissive to SARS-CoV-2 infection, leading to high titer replication [39].

3.3. Virus and Virus Titration

SARS-CoV-2 used in this work was a clinical isolate (hCoV-19/Russia/Moscow-PMVL-12/2020; GISAID reference EPI_ISL_572398) belonging to B.1.1.4 lineage [40]. The viral stock was propagated in confluent Vero E6 monolayers, harvested on day 5, concentrated by centrifugation at 140,000× *g* and 4 °C for 1 h (Optima XPN 100, Beckman Coulter, Brea, CA, USA) to achieve 1 × 10⁸ median tissue culture infectious doses (TCID₅₀) per 1 mL, and stored at −80 °C.

TCID₅₀ is the measure of infectious virus titer; this endpoint dilution assay quantifies the amount of virus required to produce cytopathic effects (CPE; structural changes in host cells, caused by the viral invasion and leading to cell death) in 50% of inoculated tissue cultures. Determination of TCID₅₀ is one of the established methods of SARS-CoV-2 quantification [41]; 10 TCID₅₀ were shown to be equivalent to 2–4 infectious virions [42,43], which is somewhat less than the theoretical value (equal to 7 [44]).

In brief, a suspension of Vero E6 cells in a growth medium (1.2 × 10⁶ cells/mL) was introduced in 96-well flat-bottomed Costar tissue culture plates (Corning, Corning, NY, USA) at 100 µL/well and cultured at 37 °C in 5% CO₂ for 24 h (until the formation of confluent monolayers). Thereafter, the monolayers were washed with FCS-free DMEM (2 × 5 min) and inoculated with serial 10-fold dilutions of the virus (10¹–10⁸ TCID₅₀/mL) in a support medium (DMEM, 1% FCS) at 100 µL/well. Each dilution was tested in eight replicates; in every plate, eight wells were used as no-virus control. Following a 2-h incubation (at 37 °C in 5% CO₂) for virus adsorption, the inoculum was removed, and the plates were washed twice with FCS-free DMEM, filled with (DMEM, 2% FCS), and further incubated (at 37 °C in 5% CO₂) for 96 h. The plates were observed daily to monitor the development of virus-induced CPE, which was completed in 72–96 h (Figure 6).

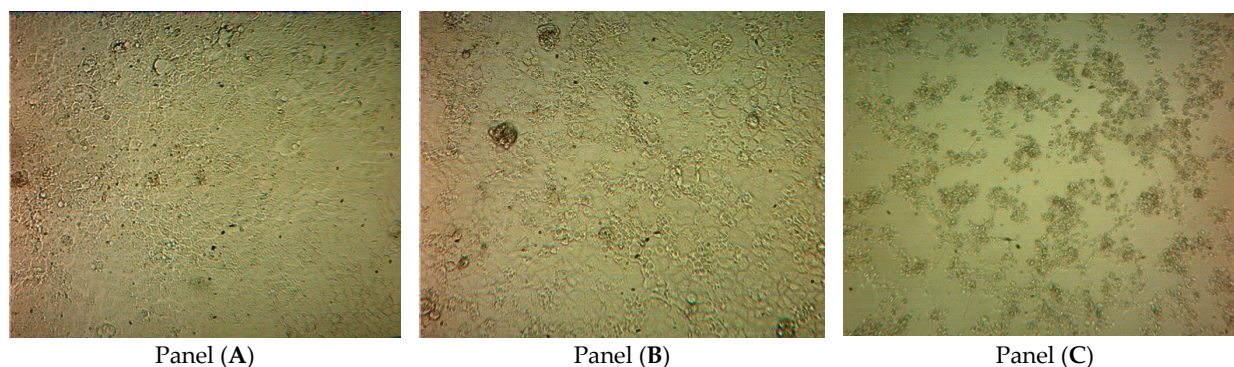


Figure 6. Micrographs displaying the time course of the development of SARS-CoV-2-induced cytopathic effects CPE in the Vero E6 cell monolayer. The CPE were visually scored for each well in a blinded fashion by two independent observers. Wells with 0, 25, 50, 75, and 100% cells exhibiting CPE or viability loss were scored, respectively, CPE−, CPE+, CPE++, CPE+++, and CPE++++. The photo in Panel (A) shows non-infected cells (no-virus control) after 72 h of incubation (no CPE or dead cells). Panels (B) and (C) show, respectively, cells inoculated with 10³ TCID₅₀/mL 36 and 72 h post-infection. About 50% of cells in Panel B exhibit CPE or loss of viability (score: CPE++). In Panel (C), all cells are dead (score: CPE++++). The photos were taken using an inverted microscope (×200 magnification; Leitz Diavert, Wetzlar, Germany).

To confirm the results of visual observation, cell viability was further assessed by the MTS test (CellTiter 96[®] AQueous One Solution Cell Proliferation Assay; Promega, Madison, MI, USA; catalog number G3582) based on the ability of live cells to convert 3-(4,5-dimethylthiazol-2-yl)-5-(3-carboxymethoxyphenyl)-2-(4-sulfophenyl)-2H-tetrazolium, inner salt (MTS) into a colored formazan product that is soluble in tissue culture medium (this

conversion, presumably accomplished by NADPH or NADH produced by dehydrogenase enzymes in metabolically active cells [45,46], is to a certain extent directly proportional to the concentration of viable cells). When the incubation was completed, the culture medium was removed from the wells, and 100 μL of support medium (DMEM, 2% FCS) and 20 μL MTS reagent were added to each well, and the plate was incubated at 37 $^{\circ}\text{C}$ for additional 3 h. Absorbance was measured at 490 nm on an iMark plate reader (Bio-Rad Laboratories, Hercules, CA, USA) using 630 nm as a reference wavelength. No discrepancies between the two methods of CPE assessment have been observed. The percentages of cultures with virus-induced CPE or viability loss were recorded for each virus dilution; the titer was calculated using the Spearman–Kärber method and presented as $\text{TCID}_{50}/0.1 \text{ mL}$ or $\lg \text{TCID}_{50}/0.1 \text{ mL}$ [47,48].

3.4. Fluorescence Spectroscopy

Fluorescence spectroscopy measurements with pyrene as a probe were performed with the Perkin Elmer LS-55 spectrofluorimeter. The excitation wavelength was 338 nm, and 7 and 3 nm spectral slits were used for excitation and emission, respectively. Samples for measurements were prepared by first pipetting 0.01 mL of pyrene stock solution (10^{-4} M in ethanol) into a flask, and evaporating ethanol at ambient conditions. Then, 1 mL of a surfactant solution of a given concentration was added to the flask and stirred for 1 day before the measurements. The ratio of the first (371 nm) to the third (383 nm) vibronic peaks in fluorescence spectra of pyrene I_1/I_3 is known to be sensitive to the polarity of its microenvironment [49,50]. The formation of micelles and the penetration of hydrophobic pyrene molecules in their cores leads to the drop in the polarity parameter I_1/I_3 (Figure 7). The cmc was determined as an inflection point of the dependence of I_1/I_3 on surfactant concentration. The cmc of the surfactants are displayed in Table 1.

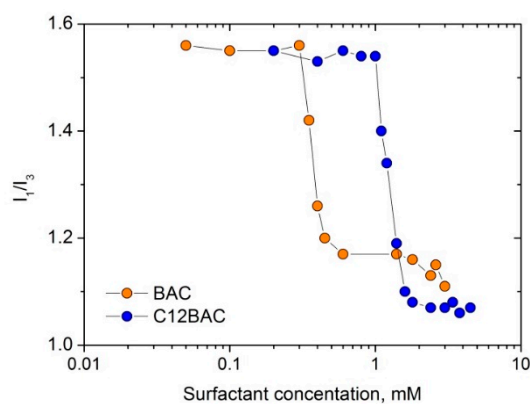


Figure 7. Polarity parameter of pyrene I_1/I_3 as a function of the concentration of cationic surfactants: benzalkonium chloride BAC and benzyldimethyldodecylammonium chloride C12BAC.

3.5. Evaluation of Virucidal Activity

Virucidal activity is defined as the ability to kill viruses [51], i.e., to cause them to lose “viability”. In its turn, the “viability” of a virus is equivalent to its capacity for replication [52,53]; if the replication competence of a virus is irreversibly disrupted, the virus is no longer “alive”. To assess the virucidal activity of surfactants under study, we compared the replicability of surfactant- and mock-treated SARS-CoV-2 virions in permissive cells.

Surfactant solutions of a given concentration (0.0096 mM, 0.0448 mM, 0.224 mM, 0.56 mM, 1.12 mM, or 5.6 mM; in a volume of 1 mL) were incubated with an equal volume of the virus stock ($10^8 \text{ TCID}_{50}/\text{mL}$) at room temperature for a certain period (contact time: 5 s, 10 s, 15 s, 30 s, 1 min, 5 min, 15 min, 30 min, 45 min, 60 min). To avoid the presence of surfactant during infection and its toxic effects on the cells, the samples (surfactant + virus) were centrifuged at $140,000 \times g$ (Optima XPN 100, Beckman Coulter, Brea, CA, USA) for 1 h.

A positive control (the virus stock without surfactants) was used in every run. Viral pellets were resuspended in 300 μ L of support medium (DMEM, 1% FCS), and, for each pellet, 10-fold dilutions in support medium were prepared. The titer of infectious SARS-CoV-2 was determined as described in Section 3.3 above. This endpoint dilution assay measures the amount of replication-competent SARS-CoV-2 particles directly: by the extent, to which the infection they induce is pronounced.

The virucidal efficacy of surfactants was assessed by the difference in the virus titers (A) between control (A_c) and experimental (A_e) samples:

$$A = A_c - A_e$$

The protection index, or inhibition coefficient IC, was calculated for all concentrations and contact times using the formula:

$$IC = [(A_c - A_e)/A_c] \times 100\%$$

The values of the 50% effective concentrations EC50 were derived from IC dependences on surfactant concentrations, using non-linear regression analysis (Prism 6; GraphPad Software, San Diego, CA, USA).

4. Conclusions

In the present paper, we report on establishing a relationship between the molecular structure of the “workhorses” of modern disinfection [10], cationic surfactants, and their virucidal efficacy against SARS-CoV-2. It was shown that increasing the overall hydrophobicity and/or the number of hydrophobic fragments attached to the cationic head group of a surfactant enhances its virucidal activity. Those structural features presumably facilitate the incorporation of the surfactant into the lipid membrane of the virus and its subsequent disintegration.

Among the cationic surfactants studied, didodecyldimethylammonium bromide was the most effective. It has the lowest 50% effective concentration (EC50) – 0.016 mM (7.4×10^{-4} wt%). Didodecyldimethylammonium bromide, as well as benzalkonium chloride, were demonstrated to ensure fast (in 5 s) inactivation of SARS-CoV-2 at a surfactant concentration of 2.8 mM. Those surfactants may serve as a base of highly efficient disinfectants for hands and surfaces, which will limit the spread of COVID-19.

Author Contributions: Conceptualization, E.V.K. and O.E.P.; methodology, V.F.L., I.T.F., G.V.K. and A.S.T.; formal analysis, E.V.K. and O.E.P.; investigation, V.F.L., I.T.F., A.V.S. and V.S.M.; resources, A.R.K.; writing-original draft preparation, O.E.P.; writing-review and editing, A.V.S., V.S.M., G.V.K., A.S.T. and O.E.P.; supervision, E.V.K. and O.E.P.; funding acquisition, A.R.K. All authors have read and agreed to the published version of the manuscript.

Funding: This research was funded by Russian Foundation for Basic Research, project number 20-04-60302.

Institutional Review Board Statement: Not applicable.

Informed Consent Statement: Not applicable.

Data Availability Statement: Not applicable.

Acknowledgments: This financial support provided by Russian Foundation for Basic Research (project number 20-04-60302) is gratefully acknowledged.

Conflicts of Interest: The authors declare no conflict of interest.

References

1. Worldometer. Coronavirus. Available online: <https://www.worldometers.info/coronavirus/#countries> (accessed on 30 May 2022).





2. Aboubakr, H.A.; Sharafeldin, T.A.; Goyal, S.M. Stability of SARS-CoV-2 and other coronaviruses in the environment and on common touch surfaces and the influence of climatic conditions: A review. *Transbound. Emerg. Dis.* **2021**, *68*, 296–312. [CrossRef] [PubMed]
3. Chin, A.W.H.; Chu, J.T.S.; Perera, M.R.A.; Hui, K.P.Y.; Yen, H.-L.; Chan, M.C.W.; Peiris, M.; Poon, L.L.M. Stability of SARS-CoV-2 in different environmental conditions. *Lancet Microbe* **2020**, *1*, E10. [CrossRef]
4. Van Doremalen, N.; Bushmaker, T.; Morris, D.H.; Holbrook, M.G.; Gamble, A.; Williamson, B.N.; Tamin, A.; Harcourt, J.L.; Thornburg, N.J.; Gerber, S.I.; et al. Aerosol and Surface Stability of SARS-CoV-2 as Compared with SARS-CoV-1. *N. Engl. J. Med.* **2020**, *382*, 1564–1567. [CrossRef]
5. Ogilvie, B.H.; Solis-Leal, A.; Lopez, J.B.; Poole, B.D.; Robinson, R.A.; Berges, B.K. Alcohol-free hand sanitizer and other quaternary ammonium disinfectants quickly and effectively inactivate SARS-CoV-2. *J. Hosp. Infect.* **2021**, *108*, 142–145. [CrossRef] [PubMed]
6. Gold, N.A.; Mirza, T.M.; Avva, U. *Alcohol Sanitizer*; StatPearls Publishing: Treasure Island, FL, USA, 2022; PMID: 30020626.
7. Basak, D.; Deb, S. Sensitivity of SARS-CoV-2 towards alcohols: Potential for alcohol related toxicity in humans. *Life* **2021**, *11*, 1334. [CrossRef] [PubMed]
8. Vereshchagin, A.N.; Frolov, N.A.; Egorova, K.S.; Seitkalieva, M.M.; Ananikov, V.P. Quaternary ammonium compounds (QACs) and ionic liquids (ILs) as biocides: From simple antiseptics to tunable antimicrobials. *Int. J. Mol. Sci.* **2021**, *22*, 6793. [CrossRef]
9. Druvari, D.; Antonopoulou, A.; Lainioti, G.C.; Vlamis-Gardikas, A.; Bokias, G.; Kallitsis, J.K. Preparation of antimicrobial coatings from cross-linked copolymers containing quaternary dodecyl-ammonium compounds. *Int. J. Mol. Sci.* **2021**, *22*, 13236. [CrossRef]
10. Schrank, C.L.; Minbiole, K.P.C.; Wuest, W.M. Are Quaternary Ammonium Compounds, the Workhorse Disinfectants, Effective against Severe Acute Respiratory Syndrome-Coronavirus-2? *ACS Infect. Dis.* **2020**, *6*, 1553–1557. [CrossRef]
11. Baker, N.; Williams, A.J.; Tropsha, A.; Ekins, S. Repurposing quaternary ammonium compounds as potential treatments for COVID-19. *Pharm. Res.* **2020**, *37*, 104. [CrossRef]
12. Gorbalenya, A.E.; Baker, S.C.; Baric, R.S.; de Groot, R.J.; Drosten, C.; Gulyaeva, A.A.; Haagmans, B.L.; Lauber, C.; Leontovich, A.M.; Neuman, B.W.; et al. The species Severe acute respiratory syndrome-related coronavirus: Classifying 2019-nCoV and naming it SARS-CoV-2. *Nat. Microbiol.* **2020**, *5*, 536–544. [CrossRef]
13. Munos-Basagoiti, J.; Perez-Zsolt, D.; Leon, R.; Blanc, V.; Raich-Regué, D.; Cano-Sarabia, M.; Trinité, B.; Pradenas, E.; Blanco, J.; Gispert, J.; et al. Mouthwashes with CPC reduce the infectivity of SARS-CoV-2 variants in vitro. *J. Dent. Res.* **2021**, *100*, 1265–1272. [CrossRef] [PubMed]
14. Seneviratne, C.J.; Balan, P.; Ko, K.K.K.; Udawatte, N.S.; Lai, D.; Ng, D.H.L.; Venkatachalam, I.; Lim, K.S.; Ling, M.L.; Oon, L.; et al. Efficacy of commercial mouth-rinses on SARS-CoV-2 viral load in saliva: Randomized control trial in Singapore. *Infection* **2021**, *49*, 305–311. [CrossRef] [PubMed]
15. Eastoe, J.; Hetherington, K.J.; Dalton, J.S.; Sharpe, D.; Lu, J.R.; Heenan, R.K. Microemulsions with didodecyldimethylammonium bromide studied by neutron contrast variation. *J. Colloid Interface Sci.* **1997**, *190*, 449–455. [CrossRef]
16. McKeen, L. Introduction to food irradiation and medical sterilization. In *The Effect of Sterilization on Plastics and Elastomers*, 3rd ed.; McKeen, L., Ed.; William Andrew Publishing: Amsterdam, The Netherlands, 2012; pp. 1–40. [CrossRef]
17. Hirose, R.; Bandou, R.; Ikegaya, H.; Watanabe, N.; Yoshida, T.; Daidoji, T.; Naito, Y.; Itoh, Y.; Nakaya, T. Disinfectant effectiveness against SARS-CoV-2 and influenza viruses present on human skin: Model-based evaluation. *Clin. Microbiol. Infect.* **2021**, *27*, 1042-e1. [CrossRef] [PubMed]
18. Guo, X.; Chen, Y.; Wang, L.; Wu, X.; Fan, J.; Li, F.; Zeng, X.; Ge, Y.; Chi, Y.; Zhang, L.; et al. In vitro inactivation of SARS-CoV-2 by commonly used disinfection products and methods. *Sci. Rep.* **2021**, *11*, 2418. [CrossRef]
19. Nandni, D.; Mahajan, R.K. Micellar and interfacial behavior of cationic benzalkonium chloride and nonionic polyoxyethylene alkyl ether based mixed surfactant systems. *J. Surfact. Deterg.* **2013**, *16*, 587–599. [CrossRef]
20. Griffin, L.R.; Browning, K.L.; Truscott, C.L.; Clifton, L.A.; Webster, J.; Clarke, S.M. A comparison of didodecyldimethylammonium bromide adsorbed at mica/water and silica/water interfaces using neutron reflection. *J. Colloid Interface Sci.* **2016**, *478*, 365–373. [CrossRef]
21. Manne, S.; Gaub, H.E. Molecular organization of surfactants at solid-liquid interfaces. *Science* **1995**, *270*, 1480–1482. [CrossRef]
22. Godfrey, K.M. Cationic emulsifiers in cosmetics. *J. Soc. Cosmet. Chem.* **1966**, *17*, 17–27.
23. Mehta, S.K.; Bhasin, K.K.; Chauhan, R.; Dham, S. Effect of temperature on critical micelle concentration and thermodynamic behavior of dodecyldimethylethylammonium bromide and dodecyltrimethylammonium chloride in aqueous media. *Colloids Surf. A Physicochem. Eng. Asp.* **2005**, *255*, 153–157. [CrossRef]
24. ChemBK. Online Chemical Database for PC. Available online: <https://www.chembk.com/en/chem/DTAC> (accessed on 23 May 2022).
25. Geyer, U.; Schönherr, J. In vitro test for effects of surfactants and formulations on permeability of plant cuticles. In *Pesticide Formulations Innovations and Developments*; ACS Symposium Series; Cross, B., Scher, H.B., Eds.; American Chemical Society: Washington, DC, USA, 1988; Volume 371, pp. 22–33. [CrossRef]
26. Philippova, O.E.; Hourdet, D.; Audebert, R.; Khokhlov, A.R. Interaction of hydrophobically modified poly(acrylic acid) hydrogels with ionic surfactants. *Macromolecules* **1996**, *29*, 2822–2830. [CrossRef]
27. Philippova, O.E.; Chitchevlova, L.A.; Karybians, N.S.; Khokhlov, A.R. Two mechanisms of gel/surfactant binding. *Polym. Gels Netw.* **1998**, *6*, 409–421. [CrossRef]

28. Mukhim, T.; Dey, J.; Das, S.; Ismail, K. Aggregation and adsorption behavior of cetylpyridinium chloride in aqueous sodium salicylate and sodium benzoate solutions. *J. Colloid Interface Sci.* **2010**, *350*, 511–515. [CrossRef] [PubMed]
29. Fisicaro, E.; Pelizzetti, E.; Barbieri, M.; Savarino, P.; Viscardi, G. Aqueous micellar solutions of some N-alkylpicotinic acid and N-alkylpyridinium halide surfactants: Apparent and partial molar enthalpies. *Thermochim. Acta* **1990**, *168*, 143–159. [CrossRef]
30. Proverbio, Z.E.; Bardavid, S.M.; Arancibia, E.L.; Schulz, P.C. Hydrophile-lipophile balance and solubility parameter of cationic surfactants. *Colloids Surf. A Physicochem. Eng. Asp.* **2003**, *214*, 167–171. [CrossRef]
31. Sowada, R.; McGowan, J.C. Calculation of HLB values. *Tenside Surf. Deterg.* **1992**, *29*, 109–113. [CrossRef]
32. Al-Sayah, M.H. Chemical disinfectants of COVID-19: An overview. *J. Water Health* **2020**, *18*, 843–848. [CrossRef]
33. Nagarajan, R.; Ruckenstein, E. Theory of surfactant self-assembly: A predictive molecular thermodynamic approach. *Langmuir* **1991**, *7*, 2934–2969. [CrossRef]
34. Mosquera, V.; Garcia, M.; Varela, L.M. Association colloids: Cmc a property to calculate. In *Handbook of Surfaces and Interfaces of Materials*; Halva, H.S., Ed.; Academic Press: Cambridge, MA, USA, 2001; pp. 405–426. [CrossRef]
35. Kruglyakov, P.M. *Hydrophile-Lipophile Balance of Surfactants and Solid Particles. Physicochemical Aspects and Applications*; Elsevier: Amsterdam, The Netherlands, 2000; pp. 216–222.
36. Storm, D.R.; Field, S.O.; Ryan, J. The HLB dependency for detergent solubilization of hormonally sensitive adenylate cyclase. *J. Supramol. Struct.* **1976**, *4*, 221–231. [CrossRef]
37. Ho, O.B. Electrokinetic studies on emulsions stabilized by ionic surfactants: The electroacoustophoretic behavior and estimation of Davies' HLB increments. *J. Colloid Interface Sci.* **1998**, *198*, 249–260. [CrossRef]
38. De la Maza, A.; Parra, J.L. Solubilizing effects caused by alkyl pyridinium surfactants in phosphatidylcholine liposomes. *Chem. Phys. Lipids* **1995**, *77*, 79–87. [CrossRef]
39. Brandolini, M.; Taddei, F.; Marino, M.M.; Grumiro, L.; Scalcione, A.; Turba, M.E.; Gentilini, F.; Fantini, M.; Zannoli, S.; Dirani, G.; et al. Correlating qRT-PCR, dPCR and viral titration for the identification and quantification of SARS-CoV-2: A new approach for infection management. *Viruses* **2021**, *13*, 1022. [CrossRef] [PubMed]
40. Gorchakov, A.A.; Kulemzin, S.V.; Guselnikov, S.V.; Baranov, K.O.; Belovezhets, T.N.; Mechetina, L.V.; Volkova, O.Y.; Najakshin, A.M.; Chikaev, N.A.; Chikaev, A.N.; et al. Isolation of a panel of ultra-potent human antibodies neutralizing SARS-CoV-2 and viral variants of concern. *Cell Discov.* **2021**, *7*, 96. [CrossRef] [PubMed]
41. Bullen, C.K.; Davis, S.L.; Looney, M.M. Quantification of infectious SARS-CoV-2 by the 50% tissue culture infectious dose endpoint dilution assay. *Methods Mol. Biol.* **2022**, *2452*, 131–146. [CrossRef] [PubMed]
42. Sun, Z.; Cai, X.; Gu, C.; Zhang, R.; Han, W.; Qian, Y.; Wang, Y.; Xu, W.; Wu, Y.; Cheng, X.; et al. Survival of SARS-COV-2 under liquid medium, dry filter paper and acidic conditions. *Cell Discov.* **2020**, *6*, 57. [CrossRef]
43. Shrivastava, S.; Patil, H.P.; Mhaske, S.T.; Palkar, S.; Lalwani, S.; Mishra, A.C.; Arankalle, V.A. Isolation and genetic characterization of SARS-CoV-2 from Indian patients in a single family without H/O travel abroad. *Virus Genes* **2021**, *57*, 245–249. [CrossRef]
44. Carter, J.; Saunders, V. *Virology: Principles and Applications*; John Wiley & Sons: Hoboken, NJ, USA, 2007; p. 23.
45. Barltrop, J.A.; Owen, T.C.; Cory, A.H.; Cory, J.G. 5-(3-carboxymethoxyphenyl)-2-(4,5-dimethylthiazolyl)-3-(4-sulfophenyl)tetrazolium, inner salt (MTS) and related analogs of 3-(4,5-dimethylthiazolyl)-2,5-diphenyltetrazolium bromide (MTT) reducing to purple water-soluble formazans as cell-viability indicators. *Bioorg. Med. Chem. Lett.* **1991**, *1*, 611–614. [CrossRef]
46. Berridge, M.V.; Tan, A.S. Characterization of the cellular reduction of 3-(4,5-dimethylthiazol-2-yl)-2,5-diphenyltetrazolium bromide (MTT): Subcellular localization, substrate dependence, and involvement of mitochondrial electron transport in MTT reduction. *Arch. Biochem. Biophys.* **1993**, *303*, 474–482. [CrossRef]
47. Flint, S.J.; Racaniello, V.R.; Rall, G.F.; Skalka, A.M.; Enquist, L.W. The infectious cycle. In *Principles of Virology*, 4th ed.; ASM Press: Washington, DC, USA, 2015; Volume 1, pp. 24–52.
48. Kärber, G. Beitrag zur kollektiven Behandlung pharmakologischer Reihenversuche. *Naunyn-Schmiedeberg's Arch. Für Exp. Pathol. Und Pharmakol.* **1931**, *162*, 480–483. [CrossRef]
49. Kalyanasundaram, K.; Thomas, J.K. Environmental effects on vibronic band intensities in pyrene monomer fluorescence and their application in studies of micellar systems. *J. Am. Chem. Soc.* **1977**, *99*, 2039–2044. [CrossRef]
50. Blagodatskikh, I.V.; Sutkevich, M.V.; Sitnikova, N.L.; Churochkina, N.A.; Pryakhina, T.A.; Philippova, O.E.; Khokhlov, A.R. Molecular mass characterization of polymers with strongly interacting groups using gel permeation chromatography–light scattering detection. *J. Chrom. A* **2002**, *976*, 155–164. [CrossRef]
51. Regulatory Framework | Disinfection & Sterilization Guidelines | Guidelines Library | Infection Control | CDC. Available online: <https://www.cdc.gov/infectioncontrol/guidelines/disinfection/glossary.html#V> (accessed on 1 June 2022).
52. Forterre, P. Defining life: The virus viewpoint. *Orig. Life Evol. Biosph.* **2010**, *40*, 151–160. [CrossRef] [PubMed]
53. Koonin, E.V.; Starokadomskyy, P. Are viruses alive? The replicator paradigm sheds decisive light on an old but misguided question. *Stud. Hist. Philos. Biol. Biomed. Sci.* **2016**, *59*, 125–134. [CrossRef] [PubMed]



Review

Antimicrobial Resistance and Inorganic Nanoparticles

Andrea-Sarahí Balderrama-González ¹, Hilda-Amelia Piñón-Castillo ^{2,*} ,
Claudia-Adriana Ramírez-Valdespino ¹ , Linda-Lucila Landeros-Martínez ² , Erasmo Orrantia-Borunda ¹
and Hilda-Esperanza Esparza-Ponce ^{1,*} 

¹ Centro de Investigación en Materiales Avanzados, S. C. Miguel de Cervantes 120, Complejo Industrial Chihuahua, Chihuahua 31136, Mexico; andrea.balderrama@cimav.edu.mx (A.-S.B.-G.); claudia.ramirez@cimav.edu.mx (C.-A.R.-V.); erasmo.orrantia@cimav.edu.mx (E.O.-B.)

² Facultad de Ciencias Químicas, Universidad Autónoma de Chihuahua, Chihuahua 31125, Mexico; lilanderos@uach.mx

* Correspondence: hpinon@uach.mx (H.-A.P.-C.); hilda.esparza@cimav.edu.mx (H.-E.E.-P.)

Abstract: Antibiotics are being less effective, which leads to high mortality in patients with infections and a high cost for the recovery of health, and the projections that are had for the future are not very encouraging which has led to consider antimicrobial resistance as a global health problem and to be the object of study by researchers. Although resistance to antibiotics occurs naturally, its appearance and spread have been increasing rapidly due to the inappropriate use of antibiotics in recent decades. A bacterium becomes resistant due to the transfer of genes encoding antibiotic resistance. Bacteria constantly mutate; therefore, their defense mechanisms mutate, as well. Nanotechnology plays a key role in antimicrobial resistance due to materials modified at the nanometer scale, allowing large numbers of molecules to assemble to have a dynamic interface. These nanomaterials act as carriers, and their design is mainly focused on introducing the temporal and spatial release of the payload of antibiotics. In addition, they generate new antimicrobial modalities for the bacteria, which are not capable of protecting themselves. So, nanoparticles are an adjunct mechanism to improve drug potency by reducing overall antibiotic exposure. These nanostructures can overcome cell barriers and deliver antibiotics to the cytoplasm to inhibit bacteria. This work aims to give a general vision between the antibiotics, the nanoparticles used as carriers, bacteria resistance, and the possible mechanisms that occur between them.

Keywords: nanoparticles; antimicrobial resistance; bacteria; resistance mechanism



Citation:

Balderrama-González, A.-S.; Piñón-Castillo, H.-A.; Ramírez-Valdespino, C.-A.; Landeros-Martínez, L.-L.; Orrantia-Borunda, E.; Esparza-Ponce, H.-E. Antimicrobial Resistance and Inorganic Nanoparticles. *Int. J. Mol. Sci.* **2021**, *22*, 12890. <https://doi.org/10.3390/ijms222312890>

Academic Editors: Monica Terracciano, Ilaria Rea, Nicola Borbone and Chiara Tramontano

Received: 29 October 2021

Accepted: 17 November 2021

Published: 29 November 2021

Publisher's Note: MDPI stays neutral with regard to jurisdictional claims in published maps and institutional affiliations.



Copyright: © 2021 by the authors. Licensee MDPI, Basel, Switzerland. This article is an open access article distributed under the terms and conditions of the Creative Commons Attribution (CC BY) license (<https://creativecommons.org/licenses/by/4.0/>).

1. Introduction

The application of scientific knowledge to manipulate and control matter predominantly in the nanoscale to make use of size and structure dependent properties, and phenomena distinct from those associated with individual atoms or molecules, or extrapolation from larger sizes of the same material [1], which consist of the ability to synthesize, manipulate, and modify materials below 100 nanometers [2–5], has postulated as nanotechnology a fundamental discipline in scientific and technological advances in different areas, such as medicine and the pharmaceutical industry, to provide solutions for various existing problems in these areas.

It is considered that a nanostructured material must have dimensions within 1 to 100 nm [5,6]. However, in medicine, these values can range up to 200 nm in diameter [7]. Among these materials, the use of nanoparticles (NPs) stands out metallic, bimetallic, metal oxide, and magnetic [8–10].

The use of metallic and metal oxide NPs has been increasing due to the chemical and physical intrinsic properties acquired by NPs synthesized [11]. Depending on their application, the optical, catalytic, and electrical behavior, mechanical and chemical stability [12,13], as well as morphology and particle size, can be controlled [14], which makes them suitable for the pharmaceutical industry.

Metallic NPs allow the possibility of interacting at biomolecular levels [15]. This improves detection, treatment, and monitoring of pathologies, through the specific targeting of cells and tissues. In addition, it helps with the administration of drugs, evaluation of diseases, and treatment of degenerative conditions [16], which makes them promising materials for directing chemotherapeutic drugs.

The pharmaceutical and medical industry was presented with one of the biggest problems worldwide since 2015, when the World Health Organization (WHO) declared the increase of antimicrobial resistance by pathogenic bacteria as a priority to study. The WHO published in 2017 a list of pathogens with the highest risk worldwide (Table 1) [17]. These bacteria are resistant to antibiotics and have been classified based on various criteria, such as mortality and resistance prevalence, among others, classifying them as critical, high, and medium priority [18].

Table 1. The official list of pathogen bacteria with declared priority by the WHO. Adapted with permission from WHO (permission 387722) [17].

Priority	Pathogenic Bacteria	Antibiotics for Which There is Resistance
Critical	<i>Acinetobacter baumannii</i>	Carbapenem
	<i>Pseudomonas aeruginosa</i>	
	Enterobacteriaceae	Carbapenem and 3rd generation cephalosporins
	Mycobacteria	
	<i>Mycobacterium tuberculosis</i>	
High	<i>Enterococcus faecium</i>	3rd generation cephalosporins
	<i>Staphylococcus aureus</i>	Vancomycin and methicillin
	<i>Helicobacter pylori</i>	Vancomycin
	<i>Campylobacter</i>	Clarithromycin
	<i>Salmonella</i> spp.	Fluoroquinolones
	<i>Neisseria gonorrhoeae</i>	3rd generation fluoroquinolone
Medium	<i>Streptococcus pneumoniae</i>	Non-sensible to penicillin Ampicillin and fluoroquinolones
	<i>Haemophilus influenza</i> <i>Shigella</i> spp.	

Antimicrobials are organic small molecules (they vary in size at angstrom level) that prevent the development of pathogenic microorganisms, which are generally used in bacteria. Antimicrobial agents can be divided into three groups according to their characteristics: disinfectants, antiseptics, and those for clinical-therapeutic use [19]; the latter are known as antibiotics capable of reducing and controlling the presence of bacteria that have invaded the patient's body.

Before the use of antibiotics, the mortality rate caused by pathogenic bacteria was high [18]. However, at the end of the 19th century and the beginning of the 20th century, antibiotics began to be studied. This led to the discovery of penicillin, using it clinically in 1930, together with sulfamide. These antibiotics were effective against Gram-positive and Gram-negative bacteria [20]. Unfortunately, the capacity of these antibiotics to treat infectious diseases caused by bacteria has not been enough, and this represents a danger for the population [21].

Excessive and uncontrolled use of antibiotics have generated resistance to antimicrobials by bacteria, as well as the spread of resistant bacteria in hospitals, and have become some of the most important problems in recent years [22].

In the United States alone, according to the Centers for Disease Control and Prevention (CDC), the first report on threats by antimicrobial resistance was published in 2013. This report mentions that, in the U.S., at least 2 million people contract an infection by bacteria resistant to antibiotics, and at least 23,000 people died because of this [23]. However, in 2019, an increase to 2.8 million infected patients by resistant bacteria was reported, of which more than 35,000 people died every year. Thus, producing an economic impact of more than 4.6 billion dollars annually in the United States alone [24].

On the other hand, in the publication of projections made by the Organization for Economic Co-operation and Development (OECD), it is predicted that, by 2030, the increase

in deaths caused by resistant bacteria will increase up to 60% in less developed countries, while the increase is approximately 5 to 20% in more developed countries [25].

In this work, we discuss some articles on metal and metal oxide nanoparticles having been used as a means of transportation of antibiotics to reduce antimicrobial resistance and also to analyze the various inhibition mechanisms. In summary, the NP size, morphology, and surface functionalization of the antibiotic, type of resistance mechanism, and nanoparticle toxicity are analyzed.

2. Methodology

This review was done to answer the following questions: what are synthetic antibiotics, and what is their classification? What is antimicrobial resistance, and why does it develop? What are the mechanisms of resistance of bacteria to antibiotics? What are the mechanisms of action of inorganic nanoparticles against antimicrobial resistance? What are the mechanisms of action of inorganic nanoparticles against antimicrobial resistance? In addition, how has the use of inorganic nanoparticles against antimicrobial resistance influenced the development of antimicrobial resistance? Which nanoparticles are being used to combat antimicrobial resistance? What are the mechanisms of action of inorganic nanoparticles against resistance? How has the use of inorganic nanoparticles functionalized with antibiotics influenced resistance?

We started to study articles from different official databases, such as Elsevier, ScienceDirect, PubMed, Google Scholar, Scopus, and SciFinder, to identify relevant papers according to the topic.

To describe the current situation and discuss research on inorganic nanoparticles functionalized with synthetic antibiotics, we chose to search for articles between the years 2015–2021. While, for basic information articles, such as what are antimicrobials and the types of resistance presented by bacteria, information was obtained from research, books, and review articles from 2005–2021.

The keywords used throughout the literature search were: nanoparticles, gold nanoparticles, silver nanoparticles, copper oxide nanoparticles, titanium oxide nanoparticles, zinc oxide nanoparticles, antimicrobial mechanism nanoparticles, ROS generation, antimicrobial resistance, bacteria, antibiotics, chromosomal mutation, biochemical mechanisms, pathogens, antibiotic mechanisms of action, World Health Organization, biofilm generation, and bacterial cell membrane inhibition.

A total of 300 to 400 articles were read, of which only 246 are cited because they were those that provided relevant, basic information or contributed something of importance to the review.

3. Antibiotics

Antibiotics are antimicrobial drugs capable of reducing and controlling the presence of bacteria that have invaded the tissues of a subject. Antibiotics are grouped into classes according to their chemical structure, effect, spectrum, and action mechanism [26–29].

3.1. By Chemical Structure

According to their chemical structure, the antibiotics can be grouped as β -lactam antibiotics, macrolides, aminoglycosides, and tetracycline antibiotics [30].

3.2. By Effect

This group corresponds to those that caused the death of the most sensitive microorganism, in the bacteria growth phase (bactericidal) or those that inhibit bacterial growth (bacteriostatic) [31].

3.3. By Spectrum

This classification is divided into three branches: the broad spectrum, the limited spectrum, and the narrow spectrum. When talking about broad spectrum antibiotics, it

emphasizes that the drug acts on a wide range of bacteria which can be Gram-positive and Gram-negative. Limited spectrum antibiotics are those acting only against Gram-positive or Gram-negative cocci, as well as Gram-positive bacilli and spirochetes, as is the case with penicillin. Lastly, narrow spectrum antibiotics, which attack only a very small sector of bacteria [32].

3.4. By the Mechanism of Action

The classification of antibiotics according to their mechanism is divided into four main ones which consist of inhibiting cell wall synthesis, protein synthesis, nucleic acid synthesis, and antimetabolites.

According to Murray et al. [32], in Medical Microbiology, antibiotics for inhibiting cell wall synthesis are the penicillins, cephalosporins, carbapenems, and cephamycins, since they bind to penicillin-binding proteins (PBP) and enzymes responsible for peptidoglycan synthesis. On the other hand, vancomycin, such as the other antibiotics, usually damages the cell wall; however, the mechanism of vancomycin is to inhibit the cross-linking of the peptidoglycan layers, such as cycloserine, thus causing cell death. Bacitracin is responsible for inhibiting the cytoplasmic membrane of the bacterium, as well as the movement of peptidoglycan precursors. Antibiotics of the polymyxin family often damage the bacterial membrane [27].

In the case of inhibiting protein synthesis, in Murray et al. [32], drugs, such as aminoglycosides, are used because they are responsible for the premature release of peptide chains from the 30S ribosome. Likewise, tetracyclines damage proteins by preventing polypeptide elongation in the 30S ribosome. Antibiotics of the macrolide, ketolide, clindamycin, oxazolidinone, and streptogramins groups are responsible for preventing protein synthesis and polypeptide elongation on the 50S ribosome.

The groups of quinoline, rifampicin, rifabutin, and metronidazole are antibiotics that usually impair nucleic acid synthesis, i.e., their mechanism of action is given by binding the DNA gyrase subunit, preventing transcription by binding DNA dependent RNA polymerase [32].

Finally, according to Murray et al. [32], antibiotics of the sulfonamide, dapsone, and trimethoprim families are responsible for damaging the metabolic pathways of bacteria, as they tend to inhibit dihydropteroate synthase and dihydrofolate reductase, which triggers the folic acid synthesis disruptions.

4. Antimicrobial Resistance

Antimicrobial resistance (AMR) is a natural phenomenon of bacteria [33] that develops thanks to its intrinsic evolutionary nature, as well as its easy and rapid adaptability to various environments [34]. However, the abuse and excessive use of antibiotics has given bacteria the ability to create greater resistance to antimicrobials [35–42], which translates into the lack of ability of antibiotics to inhibit the growth of pathogens [43]. This has alerted public health organizations worldwide and has led to major regulated and controlled antibiotic administration measures, to improve treatments in patients [44,45].

Resistance levels can vary greatly according to the groups of bacteria. Susceptibility and resistance are generally measured as a function of the minimum inhibitory concentration (MIC), which is the minimum concentration of the drug that will inhibit bacteria growth [46]. Susceptibility is a range of the average MICs for any given drug in the same bacterial species. If the average MIC for a species is in the resistant part of the range, such species are considered to have intrinsic resistance to that drug. Bacteria can also acquire resistance genes from other related organisms, and the level of resistance will vary according to the species and the genes acquired [47,48].

When referring to intrinsic resistance, it means that bacteria can be naturally resistant to some antibiotics [49], and this is due to the particular characteristics of each bacterium, which depend on its structure and function [50]. That is when the composition and chemical structure of the antibiotic is unable to penetrate or react with the structure of

the bacterial membrane. An example of this type of resistance is *Pseudomonas aeruginosa* because it has a membrane with low permeability, and this makes it naturally resistant to most antimicrobials [51–54].

On the other hand, bacteria can also acquire various AMR mechanisms either by gene transfer mechanisms or by biochemical mechanisms [55]. Among the genetic mechanisms are the chromosomal and extra chromosomal mutation [56], which is called acquired resistance [57]. This type of AMR is due to the evolutionary pressure that bacteria develop against the attack of antibiotics, changing their genome through genomic mutation or by cellular selection. This exchange of genes is carried out through transformation, transduction, or conjugation [32].

Mutations develop after excessive exposure to antibiotics, which provides pathogens with strong resistance mechanisms and, therefore, greater virulence, which complicates drug treatment against bacterial infections and can result in a greater complication [48].

The biochemical mechanisms of AMR can occur due to the modification of the antibiotic bacterial target, but the enzymes that modify antibiotics are only capable of affecting certain antimicrobials [55,58]. The enzymatic inactivation of antimicrobial drugs is when there are mutations in genes that can encode porin proteins around the bacterial membrane to slow down the action of antibiotics. Another biochemical mechanism is the flow pump system that can expel antimicrobial drugs without being damaged and the reduction of intracellular concentrations because of the decrease in permeability and flow [59,60].

AMR can be caused not only by chromosomal or extrachromosomal mutations but also by cross-transfer. This means that a bacterium resistant to one antibiotic or a family of antibiotics, in particular, when encountering another antibiotic or another group of antibiotics with a similar chemical structure, will likely recognize such structure and create this immunity to this new family of antimicrobials [61–63].

4.1. Mechanisms of AMR Gene Transfer

Two types of AMR gene transfer exist: chromosome mutation and extra chromosomal mutation.

4.1.1. Chromosome Mutation

This type of resistance occurs when changes are produced in the genomic sequence of bacteria, specifically in the main chromosome, and it is presented by vertical transmission, i.e., they are transmitted through offspring [62]. This type of mutation appears spontaneously and is irreversible, resulting in changes in the bacterial chromosome due to various factors that can be chemical and physical or both, which leads to changes in the bacterial cell [53] that modifies the permeability and drug target to prevent the effect of antibiotics on bacteria.

The chromosomal mutation depends on whether there are changes in the suitability or virulence of the pathogen and whether these genetically modified microorganisms prevail or arise more frequently; consequently, they would begin to replicate and would continue to cause pathologies [60].

4.1.2. Extra Chromosomal Mutation

Extra chromosomal resistance is when transmission of genetic material occurs through plasmids, transposons, and integrons [64], which are extra chromosomal material. This type of resistance is also known as horizontal genetic transmission mutation [58,65–68].

According to the National Human Genome Research Institute (NHGRI), plasmids are small circular DNA biomolecules that contain small groups of genes, which are generally associated with genes resistant to antibiotics [69]. These molecules can be separated from the chromosome and can be replicated independently of the chromosome; likewise, plasmids can be transferred between different bacterial cells [70–72]. Plasmids are generally responsible for developing enzymes that inactivate antibiotics [62,73,74].

On the other hand, transposons are sequences present in the genome that show a high recombination and mobility capacity, which means that they can be easily integrated into

the bacterial genome [75]. These can be transferred from one plasmid to another, or from a plasmid to a chromosome, and vice versa [76]. However, unlike plasmids, transposons are not capable of self-replicate [47]. The transposition process is catalyzed by an enzyme called transposase which is encoded by the genetic element itself; for example, in Gram-negative bacteria, various transposable elements will play a crucial role in the dispersal of resistance, and some will also contribute to the mobilization of integrons [61].

Through these transposons, the AMR genes may be transferred from one bacterium to another. An important characteristic of these is that they present extra genes that encode at least one function that changes the phenotype of the recipient cell in a predictable way, such as AMRs [77].

In the case of integrons able to encode cassettes of AMR genes specialized in capturing and expressing genes that encode the integrase enzyme [78], such integrons are responsible for recognizing the exogenous gene and integrating it at points of the integron [79]. These integrons also present sites specific for recombination where they can integrate genes and the promoter to express the integrated sequences [52,80–83].

What these genomic mutation methods have in common are the mechanisms of AMR gene transfer which are presented as transformation, conjugation, and transduction (Figure 1).

Transformation.

The transformation occurs when the bacterium can capture the exogenous from the DNA and manages to incorporate it into its genome through recombination. This process takes place in some bacteria that are from the same species; therefore, the DNA has a certain resemblance and homology [84].

Conjugation.

The mechanism of genetic transfer between two bacteria employing pili is known as conjugation; generally, by this mechanism, resistant plasmids are transferred [85].

Transduction.

Transduction occurs when a virus is capable of infecting bacteria, where said virus can transfer genetic material. The best-known strains to which this type of mechanism is attributed are *Staphylococcus* spp. [86].

4.2. Biochemical Mechanisms of AMR

The bacteria have four AMR biochemical mechanisms which are focused on inactivating the antibiotic and protecting its structure.

4.2.1. Inactivation of the Antibiotic

This mechanism can use enzymatic inactivation, which is responsible for modifying existing cellular enzymes that react with the antibiotic [87], thus avoiding cell damage [88]. An example is β -lactamase enzymes, which can hydrolyze the most common antibiotics, such as penicillins and cephalosporins. Likewise, bacteria can inactivate antibiotics through the transfer of acetyl, phosphoryl, and adenyl chemical groups into the antimicrobial drug, with acetylation being one of the mechanisms best known for the inactivation of aminoglycosides and chloramphenicol, among other groups of antibiotics [89].

4.2.2. Antibiotic Excretion

Another way to avoid cellular damage caused by antibiotics is the excretion of antimicrobial drugs through the activation of outlet pumps [90], which are proteins that can eliminate or get rid of a wide variety of antibiotics and compounds from the periplasm to the outside of the cell [91]. They are outlet pumps responsible for eliminating all toxic substances for bacteria, preventing their death. Five main families of pumps have been observed, which are classified according to their structure and the available energy source (Figure 2) [62,92].

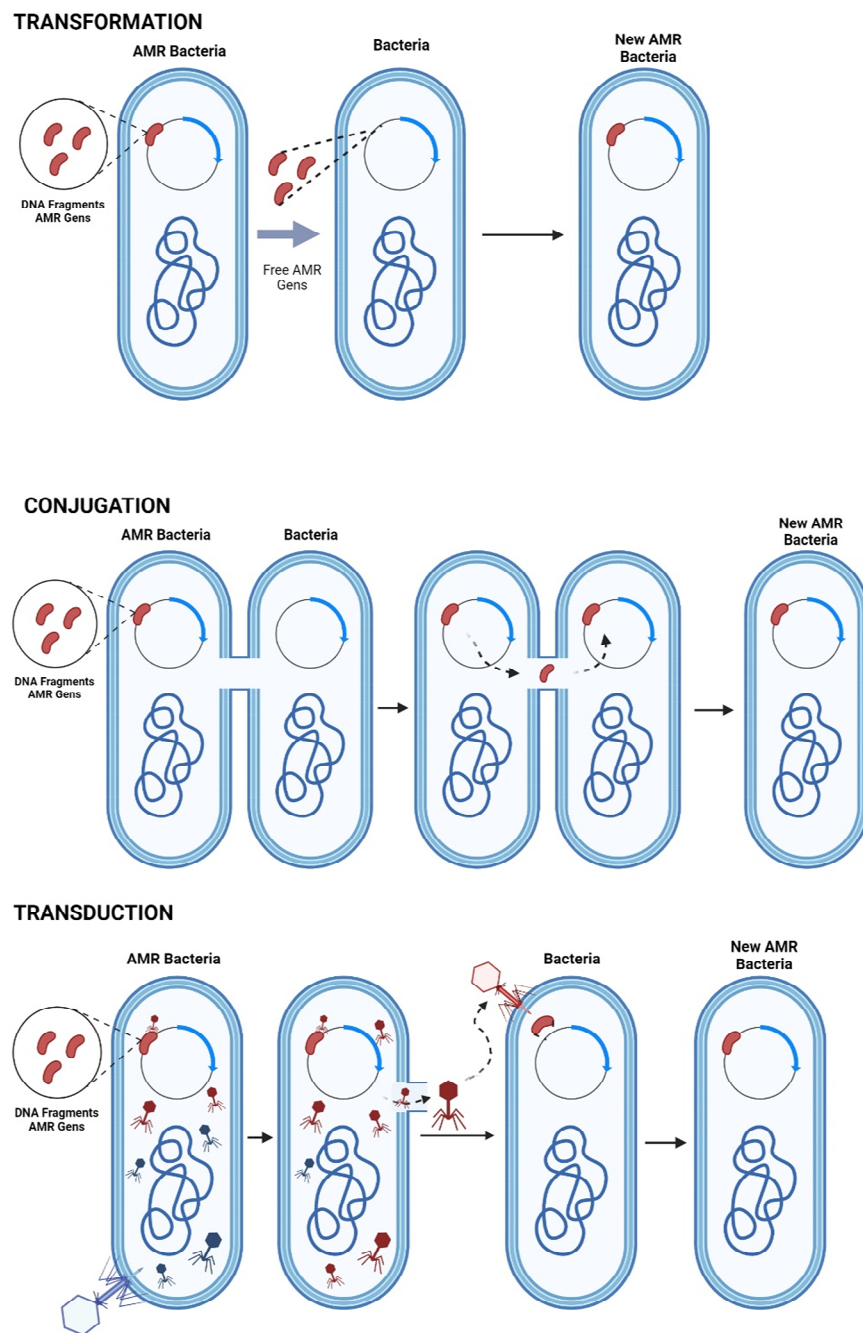


Figure 1. Extra chromosomal mutation: transformation, conjugation, and transduction. Created with BioRender.com (accessed on 17 November 2021).

The ABC Family handles ATP-binding cassettes, through the transport of amino acids, drugs, ions, polysaccharides, proteins, and glucose [93–95].

The MATE Family or of extrusion of toxic compounds through Na^+ used as an energy source. This type of pump can eliminate efflux cationic dyes, fluoroquinolone antibiotics, and some aminoglycosides [96–98].

The SMR Family is a group of small resistance to multiple antibiotics, which uses the energy of the H^+ protons, and, because these have hydrophobic nature, these can expel lipophilic cations [99,100].

The MFS Family are facilitator superfamily pumps that can dispose of antibiotics through the transport of anions, metabolites, and glucose [101–103].

The RND Family is given by resistance nodulation cell division, as these can catalyze the flow of substrates through the substrate/H⁺ anti-transport mechanism. This type of pump can not only get rid of antibiotics but other antimicrobials, such as detergents, heavy metals, solvents, etc., that compromise the life of the bacteria [104,105].

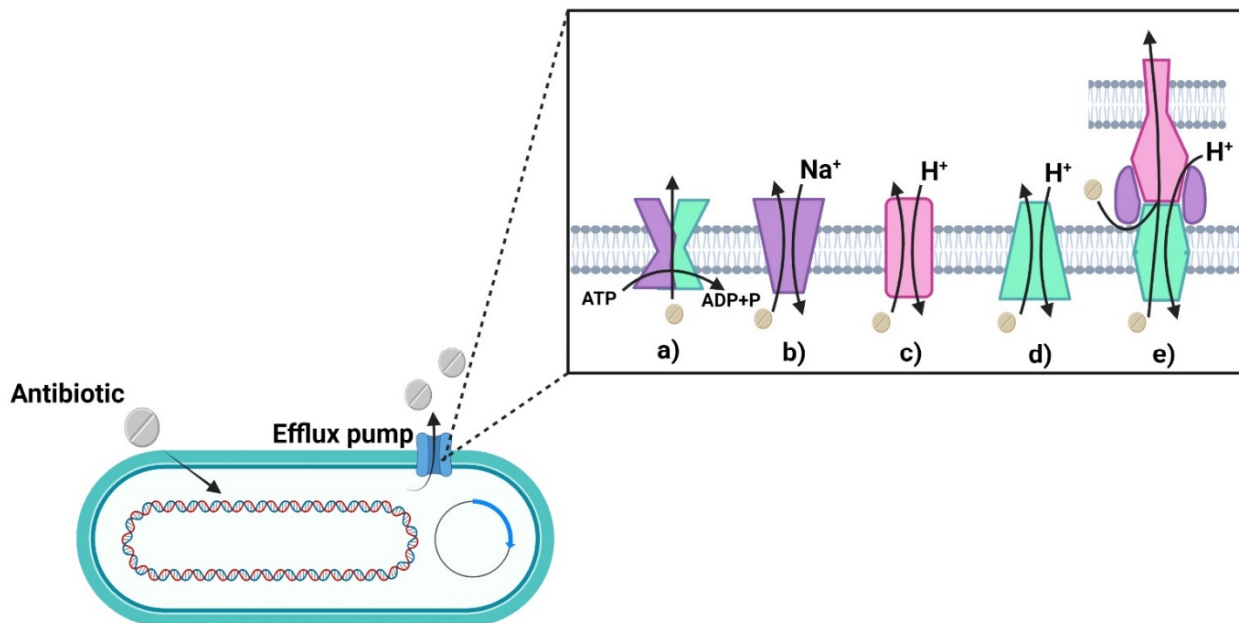


Figure 2. Efflux pump families: (a) ABC, (b) MATE, (c) SMR, (d) MFS, (e) RND. Created with BioRender.com (accessed on 17 November 2021).

4.2.3. Permeability of the Outer Membrane

This mechanism is given by generating changes in the lipid bilayer regardless of whether the permeability of the membrane is altered by changes in the porins, i.e., nothing can be absorbed, resulting in the entry of small molecules, such as antibiotics, to be limited. Likewise, some bacteria have managed to generate biofilms that enter into this resistance mechanism [106], where they manage to create through the same colony a kind of shell that protects them through different biomolecules to prevent the antibiotic from penetrating the membrane [18,107,108]. These biofilms are made up of lipids, polysaccharides, proteins, and extracellular DNA, which are responsible for interacting with antimicrobial agents, whether antibiotics or nanoparticles, modifying surface charge, size, concentration, and particle shape in the case of NPs, while, in the case of antibiotics, these are capable of modifying the chemical structure [109–111].

4.2.4. Target Modification

This type of mechanism is characterized by modifying or generating changes in the structures of antibiotics in specific places or in the target, which causes the inactivation of the drug. This mechanism takes place when the bacteria can alter the site where the antibiotic binds with it to deactivate the main function of the antimicrobial [112].

5. Nanotechnology Applied to Antimicrobial Resistance

Nanotechnology currently plays a key role in scientific and technological advances in medicine and the pharmaceutical industry, this concerns the use of materials controlling their size and shape [2]. In these senses, the nanoparticles (NPs) are particulate materials on a nanometric scale that allow modifying both the physical and chemical properties of materials, as well as their morphology and size, which ranges from 1 to 100 nm [113–115]. The smaller and more spherical the NPs are, the greater the surface-volume ratio is achieved, which helps to enhance the chemical and biological activities of the NPs [116,117].

The NPs which have been used for different applications [118,119], such as drug administration, photo ablation therapy, biological imaging, applications in biosensors, and even as an alternative to reduce antimicrobial resistance, have stood out with great relevance [120–122].

These applications include the use of NPs as antimicrobial components on advanced materials for medical devices as catheters walls, valves, stents, and a surface that could be found inside or outside the body or could be designed for in vivo therapies. The development of advanced materials includes the use of Fe_3O_4 functionalized with chitosan and lysozyme to produce a coating for producing biofilm-resistance surfaces [123]. The NPs designed for in vitro applications include their use as a drug administration; in these applications, the NPs can load with different molecules as an essential oil, such as the ZnONPs have been loaded with *Citronella* essential oil [124] or Oxide-Silica Core-Shell with essential oil [125], both with antimicrobial activity. In addition, Fe_2O_3 NPs have been used as carrier paclitaxel and β -cyclodextrin [126] or PdNPs capping with polyvinylpyrrolidone load with quercetin [114], and Silica Core-Shell Au [127] for Cancer Therapy.

NPs can be classified as metallic, metal oxide, bimetallic, and magnetic [8,128,129]. It has been demonstrated that this type of particle can obtain antimicrobial properties so that, when increasing the surface area of the particles, a greater contact area with microorganisms is generated [15,130–132], thus enhancing its antimicrobial activity.

As well as acting as antibacterial agents that can cause alterations in the bacterial membrane, metallic, bimetallic, and metal oxide NPs usually produce reactive oxygen species (ROS) by releasing metallic ions that alter the cellular components of bacteria [133,134], and the smaller nanoparticles are the damage created by them will be greater because they tend to be better absorbed on the bacterial surface. This is because, in some cases, the NPs have a positive surface charge that facilitates the union with the negative charge on the surface of bacteria [129,135,136]. Likewise, the photodynamic and photothermic effects of NPs generate a greater impact as antimicrobial agents (Figure 3), which is directly related to the release of metallic ions and ROS [6].

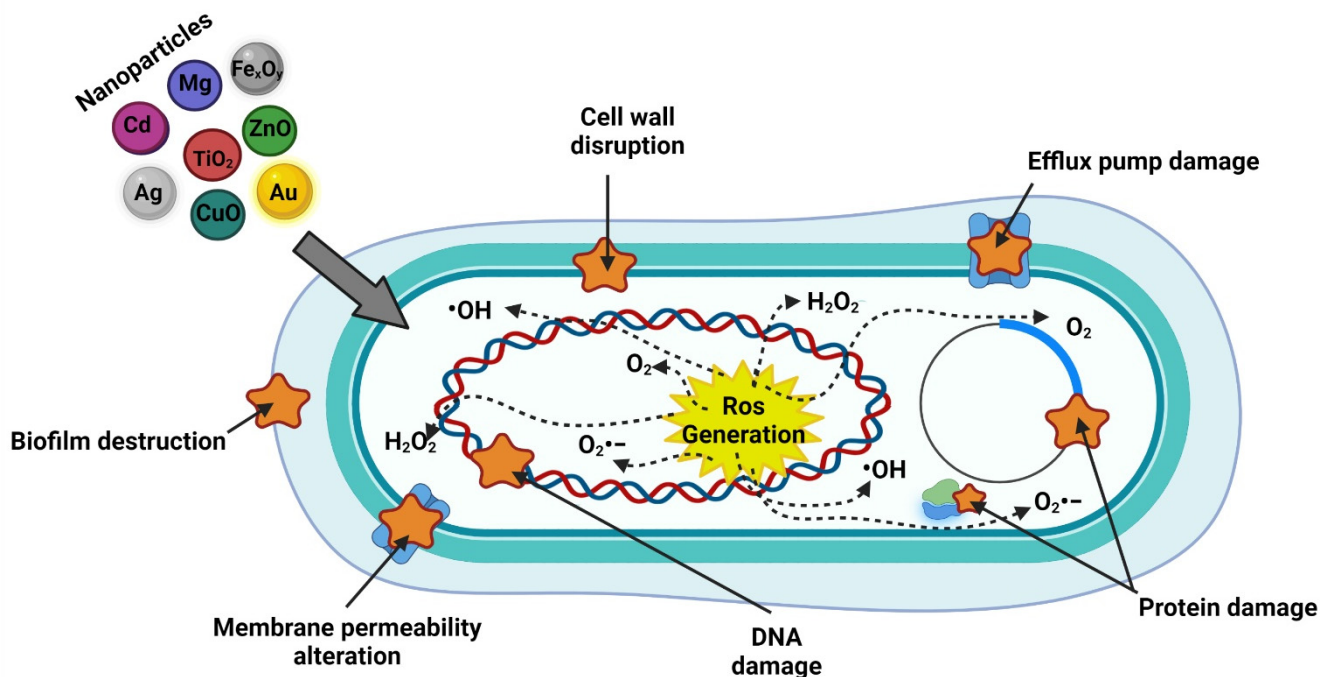


Figure 3. Action mechanism of inorganic nanoparticles. Created with BioRender.com (accessed on 17 November 2021).

NPs sizes are largest than antibiotics which allow the use of these as carriers of antibiotics or other small molecules as antibodies or chemotherapeutic agents [126].

5.1. Nanoparticles Antimicrobial Effects

There are six main antimicrobial effects of nanoparticles: (1) Interaction with cell wall and membrane, (2) Generation of ROS, (3) Penetration of the cell membrane, (4) Inhibition of protein synthesis and DNA damage, (5) Damage to metabolic pathways, and (6) Biofilm inhibition (Figure 3) [137–140].

5.1.1. Interaction with the Cell Wall and Membrane

Cell membrane and cell wall are one of the main resistance barriers that bacteria have, which are constituted by several molecules that help the adsorption of nanoparticles.

In the case of Gram-positive bacteria, the main component is teichoic acid, which causes the NPs to be distributed along the phosphate molecule chain, thus preventing their aggregation [141]. However, the fact that Gram-positive bacteria have a thick peptidoglycan wall and pores allows the penetration of smaller molecules that can cause damage to the cell wall, as well as the death of the bacteria [142].

On the other hand, in Gram-negative bacteria, this is the opposite, since having a higher concentration of lipopolysaccharides, lipoproteins, and phospholipids allows the bacteria to have a negatively charged cell wall and, thus, be able to attract NPs with greater intensity. However, these bacteria are the most prone to generate a barrier that prevents the penetration of small molecules [143,144].

5.1.2. Generation of ROS

The main mechanism by which nanoparticles can damage bacteria is through oxidative stress caused by ROS because, under normal conditions, bacteria can maintain a balance in the generation of ROS. However, when in contact with some NP, this balance is affected. This causes an excess of ROS that will inevitably in an alteration of the oxide-reduction state of molecules that will favor cellular oxidation.

Main Types of ROS:

There are four main types of ROS: radical hydroxyl ($\cdot\text{OH}$), singlet oxygen (O_2), superoxide radical ($\text{O}_2\cdot^-$), and hydrogen peroxide (H_2O_2) [145,146]. For both H_2O_2 and $\text{O}_2\cdot^-$, there have been reports that these come from the stress of short-term reactions and are reduced by antioxidants, such as catalases. Therefore, when it comes to physiological damage, it can be attributed largely to oxidative stress caused by O_2 [147].

5.1.3. Penetration of the Cell Membrane

Once the nanoparticles manage to penetrate the cell wall, they tend to release ions and generate ROS by diffusion. In the case of the release of metal ions, one of the main mechanisms that have been observed is the affinity of the ions to bind to the negatively charged functional groups of the cell membrane, such as phosphate and carboxyl groups. This phenomenon is known as adsorption [141,148–150].

5.1.4. Inhibition of Protein Synthesis and DNA Damage

Another of the most reported mechanisms attributed to metal nanoparticles is DNA damage and inhibition of protein synthesis. These usually cause a breakdown in the ribosomal subunit proteins, enzymes, and other proteins synthesized in the membranes of the bacterial cell. Likewise, a degradation, compression, and fragmentation of bacterial DNA have been observed, resulting in a reduction of the physiological activity of genes [151,152].

This was demonstrated in a study by Su et al. [153] using ZnONPs against *E. coli* DNA. They found that concentrations and the greatest damage caused by the NPs were found in 10 areas of the bacterial genome, as well as gene expression, ribosome composition, molecular structure-activity, and RNA modification, were altered in the presence of the NPs.

Similarly, Nagy et al. [154] used silver NPs to cause DNA damage by positively regulating various antioxidant genes, metal depletion, ATPase pumps, and genes encoding metal transport in *S. aureus* and *E. coli*. In this study, they concluded that silver nanoparti-

cles have an antibacterial mechanism that causes a depletion of the antioxidant capacity of bacteria.

5.1.5. Damage to Metabolic Pathways

Metabolic pathways of bacteria are not isolated and are integrated in a complex way in the activity of the cells since their main role is to maintain the growth and reproduction of bacteria. However, it has been observed that, when nanostructures enter the bacterial cell, alterations in metabolism occur, causing damage to the cell membrane, inducing oxidative stress and, finally, the death of the bacteria [155,156]. It has also been proposed that NPs can regulate and damage the metabolic processes directly of the target proteins of the bacteria, which is why they can affect the adhesion of bacteria and the formation of biofilms [155].

5.1.6. Biofilm Inhibition

One of the main mechanisms that nanoparticles present when interacting with biofilms generated by bacteria is the interaction with EPS, which will allow the access of any chemical molecule agentive to the bacteria and, thus, cause damage to the cell [157,158]. It has also been reported that NPs in contact with bacteria can affect the bacterial adhesion rate causing damage to biofilms, which is attributed to metabolic inhibition processes by releasing metal ions; however, the specific mechanisms cannot yet be fully explained.

5.2. Interaction between Antibiotics, Nanoparticles and Bacteria

The inorganic nanoparticles most used to inhibit the growth of bacteria due to their antimicrobial properties are those made of gold (Au), silver (Ag), silicon (Si), iron (Fe), silver oxide (Ag₂O), copper oxide (CuO), titanium oxide (TiO₂), zinc oxide (ZnO), and magnesium oxide (MgO) [2,8,119]. However, not all of the NPs are usually used for medical applications because they could have toxicity [138,139,159]. In addition, they can be accumulated on different organisms [160,161] and tissues [162]. Such is the case of apatite NPs in lipids that surround the site where the NPs was collocated. As well, the NPs were preferentially taken up by macrophages [163]. The mice exposition to AuNPs showed an increase in the Au accumulation after 6 h and liver and spleen accumulation of it [164].

The use of NPs together with antibiotics have been proved to act in a synergic way [124,165], reduce the dose used of antibiotic and NPs, achieve a high local concentration [166] or inclusive reverse the antibiotic resistance [165,167].

As with antibiotics, NPs also have various mechanisms of action against bacteria because they can alter the metabolic activity of pathogens. It has been observed that NPs act when they are in contact with the bacterial cell walls, and, because of this, the following interactions have been proposed to explain how the contact between the NP and the bacteria is: electrostatic attraction, by ligand-receptor interactions, hydrophobic reactions, and Vander Waals forces [168–171].

Likewise, there are metallic ions that are released through the metal oxides that are to be absorbed in the membranes of the bacteria, allowing them to interact with the functional groups of biomolecules, such as proteins and nucleic acids. This will trigger direct changes in the structures of bacteria, as well as the overproduction of enzymes, which will generate physiological disturbances [172–174].

It has been observed that bacteria produce an extracellular matrix that is responsible for nanoparticles agglomeration. This generates bacterial resistance to nanoparticles with a size larger than 10 nm [175,176]. Regarding nanoparticles smaller than 10 nm, bacteria have been mutating their genes, achieving to make changes in the regulation of reduction of porins, which prevents NPs from entering the cells.

Such was the case of *P. putida* which was able to change the composition of unsaturated fatty acids found in the membrane, generating a less permeable membrane [177].

The same happens when bacteria are attacked through the surface charge of both the nanostructure and the bacterial membrane because bacteria are capable of regulating and modifying the electrical charge of their surface, which will cause the nanoparticles

to be repelled [178,179]. According to Niño-Martínez et al. [157], this phenomenon is supported by the envelope stress response (ESR) mechanism present in Gram-positive and Gram-negative bacteria. This one is responsible for monitoring biogenesis, as well as protecting the integrity of the bacterial envelope.

Unlike antibiotics, NPs have dimensions smaller than 100 nm, resulting in novel physicochemical properties which can have greater interaction with cells due to a higher volume-to-surface ratio, making them versatile for strategic adjuvants. The mechanisms of action of antibiotics are usually relatively basic and simple, resulting in genomic mutation of bacteria to resist their mechanisms. However, NPs alone often have complex mechanisms that act simultaneously to prevent the generating genomic mutations of bacteria and inhibit their growth.

NPs used as transport media, loaded or functionalized with antibiotics, can enhance the mechanisms of action of the drug. This is because the particle size >100 nm is so small that the bacterial phagocytes can easily phagocytose them, in addition to the fact that the morphology of the particle itself allows greater flexibility to penetrate the cell and cause endocytosis, allowing the drug to be released intracellularly [180].

Another advantage of NPs as an antibiotic adjuvant is that they function as protectors, which means that the NPs can increase the serum levels of the drugs and, in this way, can protect from the enzymatic action of the target [181].

Likewise, by having an NP functionalized with an antibiotic, a more controlled and potent administration of the drug can be obtained, activating the effect of the NP through controlled stimuli of light, pH, photothermal, and magnetic, among others, which, unlike the antibiotic, would only need to be exceeded in doses and repeatedly to achieve the same effect [182,183].

The efficiency of antibiotics gets lower as time passes, and additionally, the human body can only absorb 50% of the antibiotic, while the other 50% is excreted in the urine [184], which further lowers its efficiency. It has been reported in the literature how complicated it is to stimulate the absorption of antibiotics in high doses due to the toxicity that the drug can present in the organism, as well as the development of side effects in the patient [185].

Such was the case of the research proposed by Qi et al. [185], where they explain that vancomycin has a strong mechanism of action against Gram-positive bacteria; however, the level of toxicity it has in the organism is high, causing side effects in kidneys and ears. Therefore, they proposed the synthesis of mesoporous silica nanoparticles functionalized with vancomycin with which they were able to inhibit the cell growth of Gram-positive pathogens selectively in macrophage-like cells.

For this reason, the targeting of antibiotic-functionalized nanoparticles employing an active targeting, which can be magnetic or by temperature, has been used. Table 2 shows some studies reported by different researchers, in which a greater inhibition of multi-resistant bacteria is reported when using metal nanoparticles functionalized with antibiotics.

In the next sections, a compilation of works with different compositions of NPs for inhibition of bacteria are analyzed.

5.2.1. Silver Nanoparticles

Silver nanoparticles (AgNPs) have become one of the most studied protagonists for the inhibition of bacteria due to their high antibacterial properties in concentrations that are not cytotoxic for humans, and they have become strong candidates to replace antibiotics for clinical use against bacterial resistance.

The mechanisms of action of AgNPs as antimicrobial agents depend on physicochemical properties [186], that is, on their morphology, size, whether they are linked or functionalized with any biomolecule or metal [177,187]. However, it has been reported that one of the main mechanisms of AgNPs is their binding to the cell wall and membrane, damaging biomolecules and structures found within the cell, as well as oxidative stress causing the release of silver ions [188–191].

The use of silver as an antimicrobial agent dates back to 1852 when it was used by Dr. J. Marion Sims for the treatment of vesicovaginal fistulas. In 2007, Pal et al. [192] studied the antimicrobial effects of silver by varying particle size, obtaining results that show that, by decreasing the particle size, it was possible to increase the surface area, which would result in a greater affinity when interacting with the biomolecules in bacterial cells. They observed that the morphology of the particle had a great influence to enhance the antimicrobial activity, thus concluding that the triangle-shaped nanoparticles generated a greater cell death compared to the ones with a spherical shape or nano-rods.

This was also confirmed by Nanda et al. [193] as they conducted a study about the biosynthesis of AgNPs with *Staphylococcus aureus* and its antimicrobial activity against Methicillin-Resistant *S. aureus* (MRSA) and Methicillin-Resistant *Staphylococcus epidermis* (MRSE), including Methicillin-Resistant *Streptococcus pyogenes*, *Salmonella typhi*, and *Klebsiella pneumoniae*. They reported AgNPs of approximately 160 to 180 nm and of irregular shape, which was characterized by the AFM technique. In the toxicity trials, for the inhibition of the bacteria they used a concentration of 20 μ L (0.002 mg) of AgNPs, bacteria Gram-positive was the affected bacteria. Was observed a diameter reduction of the bacterial cultures to 18 mm for MRSE, 17.5 mm for MRSA, and 16 mm for *S. pyogenes*. They concluded that the susceptibility for Gram-positive bacteria, and especially for MRSA bacteria, is because of the inhibition of the synthesis of the bacterial cell wall.

In 2010, Lara et al. [194] conducted a very similar study in which they sought to inhibit the growth of the pathogens *S. pyogenes* resistant to erythromycin, *E. coli* 0157:H7 resistant to ampicillin, and *P. aeruginosa* resistant to multiple antibiotics, using a concentration of 6.25, 12.5, 25, and 50 mM of AgNPs of 100 nm. They reported the inhibition of 99.7% of *S. pyogenes*, 95.7% for *E. coli*, and *P. aeruginosa* 92.8%, concluding that the higher the concentration, the greater the death of bacteria, and also confirming that time is not an important factor for AgNPs to cause bacterial inhibition. However, they decided to carry out studies to see if bacteria could become resistant to the AgNPs functionalized with antibiotics, leaving the bacteria exposed to the AgNPs for 3 weeks. They reported that MRSA could grow at a concentration of nanoparticles of 100 mM, *S. aureus* at 200 mM, and, finally, for *P. aeruginosa* and *E. coli*, they achieved to generate resistance at the concentration of 75 mM. These results show that lipopolysaccharides could trap and block positive charges of silver nanoparticles and make Gram-negative bacteria less vulnerable to nanoparticles. However, it has also been proposed that AgNPs adhere to the surface of the cell membrane, thus altering their function, penetrating the cells, and releasing silver ions that cause oxidative stress through ROS. On the other hand, resistance to AgNPs implies changes in the inhibited cell target, so, if there is a change in proteins or in how antibiotics are directed, the bacterial sensitivity to the antibiotic used can be modified.

In 2018, Panáček et al. [179] demonstrated the resistance of the Gram-negative strains *E. coli* and *P. aeruginosa* to AgNPs after repeated exposures. They determined the minimum inhibitory concentrations (MIC) of AgNPs at 432 mg/L. Their results focus on bacteria repeatedly exposed to sub-inhibitory concentrations of AgNPs, where pathogens were able to rapidly develop AMR. They state that said resistance is due to the production of flagellin, which is an adhesive protein of the bacterial flagellum that causes the aggregation of AgNPs, eliminating its antimicrobial effect against Gram-negative bacteria.

Ashraf et al. [195], in their study of bacterial extracellular proteins interacting with silver ions for the production of AgNPs encapsulated in proteins, found the potential that the *E. cloacae* protein has within the synthesis of AgNPs. It assists in the elimination of the risk of toxic agents, and this could have a great impact on medical applications, since it generates greater biocompatibility. In this study, they carried out various nanoparticle's synthesis by chemical and biological methods, where they obtained nanoparticles with a size approximate of 58 nm, to which they exposed various Gram-positive and Gram-negative strains, proposing the mechanism of interaction between the extracellular protein and the silver ions that are released to cause cell death. However, they emphasize the need for more research to confirm their hypothesis.

The discovery of antibacterial and catalytic activities of AgNPs that are biosynthesized with *Convolvulus fruticosus* (CF-AgNPs) to inhibit the growth of pathogens resistant to multiple drugs was studied by Shirzadi-Ahodashi et al. [196]. They obtained nanoparticles of 45 nm with spherical morphology. AgNPs have been exposed to the strains *S. aureus*, *E. faecalis*, *A. baumannii*, *E. coli*, *P. mirabilis*, *K. pneumoniae*, and *P. aeruginosa*, using a MIC of 0.1 µg/mL for *S. aureus*, *A. baumannii*, and *E. faecalis*, which had a greater inhibitory response compared to the exposure of the reference antibiotic ciprofloxacin, while *E. coli* showed the same inhibitory activity for both the antibiotic and AgNPs. Finally, *K. pneumoniae* and *P. mirabilis* showed a lower sensitivity to CF-AgNPs with MIC. The authors report various mechanisms of action of nanoparticles, such as the release of lipopolysaccharides, electrostatic interactions, and alterations in the permeability of the cell membrane. However, they specifically describe that a binding and penetration of CF-AgNPs into the bacterial membrane was observed through the destruction of the cell wall; likewise, some reactions occurred with the thiol groups (-SH) of proteins, and, finally, DNA replication was prevented, causing bacterial death.

5.2.2. Zinc Oxide Nanoparticles

Zinc oxide nanoparticles (ZnONPs) have been of interest to researchers because they are inorganic semiconductors, which can be easily absorbed by organisms in regulated concentrations [197]. It has caused the fact that the research of ZnONPs focuses on environmental, biological, cosmetic [198], and renewable energy applications [199], such as catalysts [200], biosensors, and even microbial enzyme inhibition, among many other applications. Its application in the medicine and pharmaceutical industry is not behind because, recently, its use as anti-inflammatories, for drug administration, cancer therapy, and as antimicrobial agents [201] on their own or as a potentiator for antibiotics [202] has been studied.

As in other metal or metal oxide nanoparticles, ZnONPs have mechanisms of action against bacteria. However, their exact mechanism remains difficult to confirm. For this reason, various authors have supported the interactions caused by ROS, since inducing oxidative stress in cells interrupts the synthesis of biomolecules, such as lipids, proteins, and even DNA, resulting in bacterial death [173,203]. In addition, it has been proposed that particle size, as well as the morphology they present, can cause less or more damage, depending on what is intended, since these can enter the cells and damage the integrity of bacteria by attacking the membrane [202,204]. Finally, there is a discussion about the possibility that Zn⁺² ions can delay the growth of bacteria by binding with the receptors located in the membranes [205–207].

In 2010, Banoee et al. [208] conducted a study of ZnONPs where they improved the antibacterial activity of the antibiotic ciprofloxacin in *S. aureus* and *E. coli* bacteria. The authors report nanoparticles of 10 and 45 nm in diameter with a concentration of 500 µg and obtained an increase in the zone of inhibition by 27% for *S. aureus* and by 22% for *E. coli*. They concluded that ZnONPs are powerful adjuvants for antimicrobial inhibition when working together with antibiotics because the mechanism of action of antimicrobials is potentiated.

Patra et al. [209] carried out the study of ZnONPs with a size of 18 to 20 nm and with a semispherical morphology, which was functionalized with the antibiotics ciprofloxacin (CIP), whose ligands were verified by the FTIR spectroscopic technique. Inhibition of *S. aureus*, *Klebsiella* sp., and *E. coli* was given with a MIC of 10 µg/mL of ZnONPs-CIP, obtaining favorable results for bacterial death compared to the trial carried out of the pathogens with the antibiotic. The authors reported that the combination between the nanoparticle improve the antibiotic activity, causing damage to the bacterium cell membrane, which allowed ciprofloxacin to enter into the cell, causing ROS and, thus, interrupting cell division.

The biocompatibility of ZnONPs has been demonstrated, Zhong et al. [210] incorporated ZnONPs into carboxy methyl chitosan (CMCS) by spray drying. They demonstrated

that both ZnONPs and CMCS-ZnO microspheres of sizes from 1 to 6 μm in diameter had the same antimicrobial activity, which was dose dependent. The activity against *E. coli* showed that the ZnONPs alone have better activity with the smallest NPs (10 nm). These NPs exhibit an 87% of inhibition with 125 $\mu\text{g}/\text{mL}$ while the ZnONPs with a size of 30 nm, while ZnONPs with a size of 10 nm showed a 97% of inhibition with 62.5 $\mu\text{g}/\text{mL}$. The use of CMCS-ZnO microsphere showed an increase of concentration for the *E. coli* inhibition until 2 $\mu\text{g}/\text{mL}$. The explanation for this is that the CMCS-covered ZnONPs turned out to have a better interaction when binding to the cell membrane through the $-\text{NH}_2$ group of the CS group, thus, improving the permeability of the membrane and making the cytoplasm capable of filtering the nanostructure causing cell death.

The ZnONPs antimicrobial mechanism is based on their ability to damage the integrity of the cell membrane, slow down the replication of AMR genes in bacteria, prevent the formation of biofilms, and decrease the hydrophobicity of the cell surface. Likewise, the antibacterial action of these nanoparticles depends significantly on their size, since it is a crucial factor due to the ease of entry of small particles through the pores on the surface of the bacterial cell. These pores on the surface of the bacterial cell are in the nano-size range. Furthermore, the ZnONPs exhibited anticancer activity compared to normal cells. Two mechanisms based on ROS production, ZnONPs toxicity and induction of apoptosis, were predicted [211–214].

5.2.3. Gold Nanoparticles

AuNPs arrived at the pharmaceutical and medical industry due to their intrinsic properties because they can be synthesized in different sizes and morphologies. In addition, the reduction from Au^{+3} to Au^0 facilitates their functionalization with ligands, such as aptamers, polymers, drugs, and genetic material, among others [215–217]. In addition, the chemical inertness of gold allows good in vitro and in vivo biocompatibility [218], so there has been a proposal to functionalize AuNPs surfaces with antibiotics to increase antibacterial efficacy against resistant pathogens [219].

In 2016, a new approach was reported using gold nanoparticles functionalized with chitosan streptomycin (CANP). These ligands were characterized by various techniques, such as UV-Vis, SEM, TEM, and DLS. The 35 nm size spherical nanoparticles were studied to avoid the formation of biofilms in microorganisms, such as *Listeria monocytogenes*, *S. aureus*, *E. coli*, *P. aeruginosa*, and *Salmonella typhimurium*, obtaining favorable results for research, by inhibiting the survival of bacteria up to 95%, whose mechanism of action by the nanostructure was focused on cell wall damage [220].

Kalita et al. [167] demonstrated the increase in the bactericidal activity of the beta-lactam broad spectrum drug against Methicillin-Resistant *Staphylococcus aureus* (MRSA). In this research, they functionalized gold nanoparticles with amoxicillin (Amox) through the electrostatic interaction of the attraction forces regulated by the protonated amino and the thioether group. The AuNPs-Amox complexes were tested in in vitro and in vivo trials, where they revealed a potent anti-MRSA activity, improving the survival rate of clinical patients. They reported that the use of the nanostructure could assist the antibiotic in penetrating inside the cell. In addition, it inhibits the cell wall synthesis.

Hu et al. [221], proposed biofilms based on gold nanoparticles for photothermal ablation treatment to fight the resistance of Methicillin-Resistant *Staphylococcus aureus*. The AuNPs were 14 nm in diameter with a mixed charge of hybrid ions, which adapt to the surface of any biomolecule, and were functionalized with 10-mercaptodecyl and electrolytic 11-mercaptopundecanoic acid. The obtained favorable in vivo results, in which healthy tissues did not show damage by AuNPs due to NIR light irradiation, showing damage and inhibition of the spread of bacteria.

Due to generalized multidrug resistance caused by antibiotic abuse, Xie et al. [222] proposed the use of 2 nm diameter gold nanoparticle (AuNP) to fight multi-resistant bacteria (MDR), coating AuNP with quaternary ammonium (QA) as a solution to MDR Gram-positive bacteria, including Methicillin-Resistant *Staphylococcus aureus* (MRSA) and

Vancomycin-Resistant *Enterococci* (VRE) in vivo assays. They present results where QA-AuNP kills bacteria through combined physicochemical mechanisms without causing damage to surrounding tissues in the living organism.

In 2019, a study in which there was an evaluation of the antibacterial activity of gold nanoparticles of 10 nm in diameter, functionalized with gentamicin and amikacin in *Acinetobacter baumannii* strains from patients with severe burn infections, was reported. They obtained results of 94.5% in the bacterial inhibition of AuNP with amikacin, while AuNPs functionalized with gentamicin had an antimicrobial effect 50% superior to the use of gentamicin alone. They concluded that the combination of amikacin and gentamicin with AuNPs has a very significant antibacterial efficacy against *A. baumannii* [223].

Khan et al. [224] used gold nanoparticles bound to chitosan oligosaccharide (COS-AuNPs) to inhibit the formation of *Pseudomonas aeruginosa* biofilms, where they obtained favorable results for the eradication of biofilms and were able to reduce bacterial hemolysis and different virulence factors produced by *P. aeruginosa*. They concluded that the hybrid COS-AuNPs nanoformulation could act as a potential agent to exhibit inhibitory properties against pathogenesis derived from biofilm formation as a result of a resistance mechanism of *P. aeruginosa*.

In more recent studies, Riaz et al. [225] reported the effects of gold nanoparticles coated with flavonoids (FauNP) with spherical shape and 23 nm in diameter in mice, against the resistance of *Enterococcus faecalis*, which mainly colonize tissues in the liver and the kidneys. They obtained significant results in the reduction in bacterial counts in vivo and in vitro in organs compared to free flavonoids.

Chavan et al. [166] synthesized 25 nm AuNPs coated with ampicillin (AuNPs-Amp) and evaluated their interaction with *Escherichia coli* bacterial cells. The results showed a successful accumulation of AuNPs-Amp on the surface of the bacterial cell, forming pores in the bacterial membrane. They evaluated membrane damage by atomic force and fluorescent microscopy, and functionalized particles showed promising antimicrobial activity against resistance to ampicillin in *E. coli* bacteria resistant to ampicillin with an increase of 95%.

5.2.4. TiO₂ Nanoparticles

Another clear example of materials that have been of interest to researchers is titanium oxide nanoparticles (TiO₂NPs), due to their chemical and physical stability, as well as their strong corrosion resistance. These nanoparticles have low toxicity at low concentrations without altering their antimicrobial activity, which makes them even more interesting. In general, TiO₂NPs are reported in conjunction with other types of antimicrobial nanoparticles. Such is the case in the study carried out by Stoyanova et al. [226], where they prepared TiO₂-ZnO nanocompounds to study their bactericidal properties in *E. coli* strains. Another similar case was that of Menazea et al. [227], where they studied a ZnO compound spiked with TiO₂ to evaluate its antimicrobial effect against resistant strains *E. coli*, *P. aeruginosa*, *S. aureus*, and *B. subtilis*, obtaining results of an increase in inhibition when ZnO NPs were spiked with TiO₂ compared to when they were each separately.

Sunscreen with TiO₂/Zn₂ and TiO₂/Ag has been developed to inhibition of UV radiation and bacteria protection. Nanocomposite showed a correlation between concentration and inhibition efficiency. The most effective concentration to inhibit in 60–70% of *E. coli* and *S. aureus* bacteria was 100 mg/mL [228].

It has been proven that the interaction between the phospholipid presented in the bacteria membrane and TiO₂ nanoparticles. This interaction has a direct relationship with the superficial charge and the pH. With acid pH, the nanoparticles have a positive charge that allowed the interaction with the membrane cell. In addition, UV irradiation has a greater effect on membrane stabilization, triggering oxidative stress [229].

TiO₂ photoactivity has been increased with sodium nitrite, increasing nanoparticle ability to inhibit MRSA *Staphylococcus aureus* and kill *E. coli*. The reported mechanisms

to inhibit these bacteria were the production of nitrogen reactive species as peroxyxynitrite, tyrosine nitration [230].

5.2.5. Other Nanoparticles

The antimicrobial activity presented by magnetic iron, manganese, and magnesium nanoparticles has aroused the interest of researchers in recent years due to the damaging effect they have on bacteria by interfering with their respiratory and metabolic processes [40,211,231,232]. Likewise, Davarpanah et al. [233] mention in their study that the release of metal ions, the destruction of the cell membrane and wall, and the generation of ROS, as well as the internalization of nanoparticles in bacteria, are the mechanisms most representative of inhibiting the growth of pathogens.

In 2019, Madubuonu et al. [234] used magnetic nanoparticles to inhibit the growth of Gram-positive bacteria mainly, they said nanostructures were synthesized by the sol-gel method with sizes of approximately 71–90 nm. In this investigation they tested the cytotoxicity of the nanoparticles with a concentration of 256 to 2040 µg/mL approximately in *E. coli*, *Shigella*, *P. aeruginosa*, *S. aureus*, and *Salmonella typhi*, obtaining favorable inhibition results with Gram-positive bacteria, while, in Gram-negative bacteria, they failed to inhibit the growth, attributing it to the natural resistance of the bacteria by having a double lipid membrane.

On the other hand, cobalt oxide nanoparticles have been studied in the last three years after discovering their antibacterial properties [211,235]. In 2019, Dogra et al. [236] evaluated cobalt hydroxide and oxide nanostructures synthesized by the microemulsion method, obtaining favorable results for the antimicrobial property against the multi-resistant bacterium *S. aureus*, reporting that said bacterium presented a cellular contraction, rupture of the cell wall, and membrane, as well as a change in the morphology of the microorganism.

Table 2. Recent studies on metallic nanoparticles against pathogenic bacteria resistance.

Elemental Composition	Size and Morpho	Concentration (µg/mL)	Bacteria	Antibiotic	Inhibit	Mechanims	Author
AgNPs	10 nm	2.5	<i>P. aeruginosa</i>	N/A	~90%	AgNPs can enter cells and inhibits enzymatic systems in the respiratory chain, thereby altering their DNA synthesis	Salomoni et al. (2017) [4]
AgNPs	35 ± 15 nm Spheroides	0.35 0.5 0.05 8 0.05 0.1 16 0.12	<i>E. coli</i> <i>S. typhimurium</i> <i>S. aureus</i> <i>B. subtilis</i>	Chloramphenicol Kanamycin	50% 95%	The combination of the AgNPs + antibiotic produced membrane damage	Vazquez-Muñoz et al. (2019) [237]

Table 2. Cont.

Elemental Composition	Size and Morpho	Concentration (µg/mL)	Bacteria	Antibiotic	Inhibit	Mechanims	Author
AgNPs	~26 nm Spheras	1 + 5 E 1 + 10 AMP 1 + 30 C 1 + 30 KF 1 + 2 DA 1 + 30 TE 1 + 10 GEN 1 + 30 AMC 1 + 10 CFP 1 + 30 CXM	<i>S. aureus</i> MRSA <i>E. coli</i> <i>P. aeruginosa</i> <i>A. actinomycetemcomitans</i>	Erythromycin (E) Ampicillin (AMP) Chloramphenicol (C) Cephalothin (KF) Clindamycin (DA) Tetracycline (TE) Gentamycin (GEN) Amoxycillin (AMC) Cefpodoxime (CFP) Cefuroxime (CXM)	~80%	ROS generation and mechanism of action of antibiotic	Ipe et al. (2020) [238]
AgNPs	8–21 nm Spherical	15.62 15.62 7.8 31.25	<i>S. epidermis</i> <i>S. haemolyticus</i>	Ciprofloxacin Methicillin Gentamycin Rifampicin	0.25 mm 0.06 mm 0.12 mm 1 mm	ROS generation and enhancement	Thomas et al. (2020) [239]
Mesoporous silica	50–100 nm Spherical	426 170	<i>A. baumannii</i>	Cefepime Meropenem	11 mm 11 mm	Antibiotic mechanims The combination of antibiotic and NPs increase the concentration of antibiotic at the site of bacterium-antibiotic interaction; in addition the multivalent presentation of amoxicillin blockade of the bacterial efflux pump	Najafi et al. (2021) [240]
AuNPs	33 ± 14 nm	2/4 1/2 1/2	<i>E. coli</i> <i>S. aureus</i> <i>S. epidermis</i>	Amoxicillin	31 mm 30 mm 19 mm	The NPs improve the mechanism of action of antibiotic	Kalita et al. (2016) [167]
AuNPs	35 nm 200 nm	0.72 0.73	<i>Klebsiella pneumoniae</i> <i>A. baumannii</i>	Impinem Meropenem	72 mm I/35 & 48 mm I/200 73 mm M/35 & 46 mm M/200	The NPs improve the mechanism of action of antibiotic	Shaker et al. (2017) [241]
AuNPs	8 ± 2 nm	0.15 1.5	<i>S aureus</i> MRSA	Amoxicillin	85%	ROS generation by the antibiotic effect	Silvero et al. (2018) [242]
AuNPs	30 ± 20 nm Irregular	1.5	<i>P aeruginosa</i>	Amoxicillin	60–70%	Biofilm damage	Rocca et al. (2020) [243]
AuNPs	5 nm	1.18 0.23	<i>E. coli</i>	Colistin	- 6.8% fold	N/A	Fuller et al. (2020) [244]

Table 2. Cont.

Elemental Composition	Size and Morpho	Concentration (µg/mL)	Bacteria	Antibiotic	Inhibit	Mechanims	Author
AuNPs	25 nm	62.5	<i>P. aeruginosa</i> <i>S. aureus</i>	N/A	19 mm 15.8 mm	AuNPs have a significant inhibitory effect on bacteria, to their ability to associate with the bacteria cell wall and rupture it, as well as disrupting bacterial metabolism by interfering with bacterial DNA The antibiotic in combination with the nanostructure increases the synergistic effect of an antibiotic as can inhibit the cell	Abdulazeem et al. (2021) [245]
TiO ₂ NPs	64 ± 0.14 nm Irregular spheres	8–64	<i>P. aeruginosa</i>	Ceftriaxone Amikacin Ciprofloxacin Cefepime	96% 88% 80% 100%		Youssef et al. (2020) [246]

6. Conclusions

The inorganic nanoparticles composed of metals, including silver, magnetic metals, such as iron and magnesium, cobalt, zinc oxide, titanium dioxide, and gold, have been shown to possess high antibacterial activity. However, limited information is available on the in vivo antibacterial efficacy of nanostructures, their ability to inhibit pathogenic strains, and mechanisms of action. In general, metal nanoparticles have some advantages, such as a large surface area and multimodal applications. However, there are obstacles of toxicity, instability, and storage which prevent its replication and the limitation of information.

It has been proposed that, once NPs accumulate in the metabolic pathway and cross the bacterial membrane, they can interact with lysosomes, DNA, enzymes, and ribosomes, which triggers oxidative stress, changes in membrane permeability, cell electrolyte imbalances, heterologous alterations, protein inactivation, inhibition of resistant enzymes, and decoding of genomic expression.

The NPs' toxicity depends on both the NPs and bacterial characteristics. Differences between experimental conditions make it difficult to compare results. However, NPs can interrupt the AMR and make the cells more sensitive to the antibiotic, generating a new use of the ancient antibiotic with improved characteristics.

Finally, nanoparticles not only improve the therapeutic activity of antimicrobials but also restrict the stimulation of resistance generated by bacteria. Thus, there is a need for developing simultaneous strategies to deactivate beta-lactamase, deactivating enzymes, efflux pumps, as well as generate damage to cell wall, and membrane, protein and DNA damage, change in cell permeability, and generation of ROS.

Author Contributions: A.-S.B.-G. was responsible of conceptualization, original draft preparation, writing review and editing, while H.-A.P.-C. and H.-E.E.-P. of conceptualization, original draft preparation, writing review, editing and supervision, C.-A.R.-V., L.-L.L.-M. and E.O.-B. review and editing. All authors have read and agreed to the published version of the manuscript.

Funding: This research received no external funding.

Acknowledgments: A.S. Balderrama González acknowledge CONACYT for her scholarship.

Conflicts of Interest: The authors declare no conflict of interest.

References

- Econom, D.E. *NORMA MEXICANA NMX-R-80004-1-SCFI-2013 Nanotecnologías—Vocabulario—Parte 1: Conceptos Básicos Nanotechnologies—Vocabulary—Part 1: Core Terms, Dirección General de Normas (DGN); Dirección General de Normas (DGN): Cuauhtémoc, México, 2013.*
- Bayda, S.; Adeel, M.; Tuccinardi, T.; Cordani, M.; Rizzolio, F.; Baeza, A. The History of Nanoscience and Nanotechnology: From Chemical-Physical Applications to Nanomedicine. *Molecules* **2020**, *25*, 112. [[CrossRef](#)] [[PubMed](#)]
- Kandi, V.; Kandi, S. Antimicrobial properties of nanomolecules: Potential candidates as antibiotics in the era of multi-drug resistance. *Epidemiol. Health* **2015**, *37*, e2015020. [[CrossRef](#)] [[PubMed](#)]
- Salomoni, R.; Léo, P.; Montemor, A.; Rinaldi, B.; Rodrigues, M. Antibacterial effect of silver nanoparticles in *Pseudomonas aeruginosa*. *Nanotechnol. Sci. Appl.* **2017**, *10*, 115–121. [[CrossRef](#)]
- NNI. Nanotechnology. Available online: www.nano.gov (accessed on 15 March 2021).
- Yougbare, S.; Chang, T.-K.; Tan, S.-H.; Kuo, J.-C.; Hsu, P.-H.; Su, C.-Y.; Kuo, T.-R. Antimicrobial Gold Nanoclusters: Recent Developments and Future Perspectives. *Int. J. Mol. Sci.* **2019**, *20*, 2924. [[CrossRef](#)]
- Contera, S.; Bernardino de la Serna, J.; Tetley, T.D. Biotechnology, nanotechnology and medicine. *Emerg. Top. Life Sci.* **2020**, *4*, 551–554. [[CrossRef](#)]
- Allahverdiyev, A.M.; Kon, K.V.; Abamor, E.S.; Bagirova, M.; Rafailovich, M. Coping with antibiotic resistance: Combining nanoparticles with antibiotics and other antimicrobial agents. *Expert Rev. Anti. Infect. Ther.* **2011**, *9*, 1035–1052. [[CrossRef](#)] [[PubMed](#)]
- Roy, J.; Chandra, S.; Maitra, S. Nanotechnology in castable refractory. *Ceram. Int.* **2019**, *45*, 19–29. [[CrossRef](#)]
- Peigneux, A.; Oltolina, F.; Colangelo, D.; Iglesias, G.R.; Delgado, A.V.; Prat, M.; Jimenez-Lopez, C. Functionalized Biomimetic Magnetic Nanoparticles as Effective Nanocarriers for Targeted Chemotherapy. *Part. Part. Syst. Charact.* **2019**, *36*, 1900057. [[CrossRef](#)]
- Kuo, Y.-L.; Wang, S.-G.; Wu, C.-Y.; Lee, K.-C.; Jao, C.-J.; Chou, S.-H.; Chen, Y.-C. Functional gold nanoparticle-based antibacterial agents for nosocomial and antibiotic-resistant bacteria. *Nanomedicine* **2016**, *11*, 2497–2510. [[CrossRef](#)] [[PubMed](#)]
- Kumari, A.; Singla, R.; Guliani, A.; Yadav, S.K. Nanoencapsulation for drug delivery. *EXCLI J.* **2014**, *13*, 265–286.
- Menon, S.; Rajeshkumar, S.; Kumar, V. A review on biogenic synthesis of gold nanoparticles, characterization, and its applications. *Resour. Technol.* **2017**, *3*, 516–527. [[CrossRef](#)]
- Kim, B.Y.S.; Rutka, J.T.; Chan, W.C.W. Nanomedicine. *N. Engl. J. Med.* **2010**, *363*, 2434–2443. [[CrossRef](#)] [[PubMed](#)]
- Blecher, K.; Nasir, A.; Friedman, A. The growing role of nanotechnology in combating infectious disease. *Virulence* **2011**, *2*, 395–401. [[CrossRef](#)] [[PubMed](#)]
- Ratner, B.D. Biomaterials: Been There, Done That, and Evolving into the Future. *Annu. Rev. Biomed. Eng.* **2019**, *21*, 171–191. [[CrossRef](#)] [[PubMed](#)]
- OMS. Global Priority List of Antibiotic-Resistant Bacteria to Guide Research, Discovery, and Development of New Antibiotics. Available online: https://www.who.int/medicines/publications/WHO-PPL-Short_Summary_25Feb-ET_NM_WHO.pdf?ua=1 (accessed on 25 February 2020).
- Li, B.; Webster, T.J. Bacteria antibiotic resistance: New challenges and opportunities for implant-associated orthopedic infections. *J. Orthop. Res.* **2017**, *36*, 22–32. [[CrossRef](#)]
- Kumar, L.; Verma, S.; Vaidya, B.; Mehra, N.K. *Nanocarrier-Assisted Antimicrobial Therapy against Intracellular Pathogens*; Chapter 13; Elsevier: Amsterdam, The Netherlands, 2017; pp. 293–324. ISBN 9780323461528. [[CrossRef](#)]
- Hutchings, M.I.; Truman, A.W.; Wilkinson, B. Antibiotics: Past, present and future. *Curr. Opin. Microbiol.* **2019**, *51*, 72–80. [[CrossRef](#)] [[PubMed](#)]
- Laxminarayan, R.; Duse, A.; Wattal, C.; Zaidi, A.K.M.; Wertheim, H.F.L.; Sumpradit, N.; Vlieghe, E.; Hara, G.L.; Gould, I.M.; Goossens, H.; et al. Antibiotic resistance—the need for global solutions. *Lancet Infect. Dis.* **2013**, *13*, 1057–1098. [[CrossRef](#)]
- Feng, Q.; Huang, Y.; Chen, M.; Li, G.; Chen, Y. Functional synergy of α -helical antimicrobial peptides and traditional antibiotics against Gram-negative and Gram-positive bacteria in vitro and in vivo. *Eur. J. Clin. Microbiol. Infect. Dis.* **2015**, *34*, 197–204. [[CrossRef](#)]
- CDC. Antimicrobial Resistance. Available online: https://www.cdc.gov/drugresistance/biggest-threats.html?CDC_AA_refVal=https%3A%2F%2Fwww.cdc.gov%2Fdrugresistance%2Fbiggest_threats.html (accessed on 15 March 2021).
- CDC. *Antibiotic Resistance Threats in the United States*; U.S. Centers for Disease Control and Prevention: Atlanta, GA, USA, 2019.
- OCDE. *Stemming the Superbug Tide*; OECD Health Policy Studies; OECD: Paris, France, 2018; ISBN 9789264307582.
- Eyler, R.F.; Shvets, K. Clinical Pharmacology of Antibiotics. *Clin. J. Am. Soc. Nephrol.* **2019**, *14*, 1080–1090. [[CrossRef](#)]
- Brunton, L.; Hilal-Dandan, R.; Knollmann BCMacDougall, C. Penicillins, cephalosporins and other β -lactam antibiotics. In *Goodman & Gilman's: The Pharmacological Basis of Therapeutics*; Brunton, L., Hilal-Dandan, R., BC, K., Eds.; McGraw-Hill Education: New York, NY, USA, 2017; pp. 1023–1038.
- Lodise, T.P.; Lomaestro, B.; Drusano, G.L. Piperacillin-Tazobactam for *Pseudomonas aeruginosa* Infection: Clinical Implications of an Extended-Infusion Dosing Strategy. *Clin. Infect. Dis.* **2007**, *44*, 357–363. [[CrossRef](#)]

29. Koomanachai, P.; Bulik, C.C.; Kuti, J.L.; Nicolau, D.P. Pharmacodynamic modeling of intravenous antibiotics against gram-negative bacteria collected in the United States. *Clin. Ther.* **2010**, *32*, 766–779. [[CrossRef](#)]
30. Lingzhi, L.; Haojie, G.; Dan, G.; Hongmei, M.; Yang, L.; Mengdie, J.; Chengkun, Z.; Xiaohui, Z. The role of two-component regulatory system in β -lactam antibiotics resistance. *Microbiol. Res.* **2018**, *215*, 126–129. [[CrossRef](#)] [[PubMed](#)]
31. Werth, B.J. Overview of Antibiotics. Available online: <https://www.msdmanuals.com/home/infections/antibiotics/overview-of-antibiotics> (accessed on 3 March 2020).
32. Murray, P.R.; Rosenthal, K.S.; Pfaller, M.A. Bacteriology. In *Medical Microbiology*; Saunders, E., Ed.; Elsevier: Amsterdam, The Netherlands, 2020; p. 872. ISBN 9780323673228.
33. Brown, E.D.; Wright, G.D. Antibacterial drug discovery in the resistance era. *Nature* **2016**, *529*, 336–343. [[CrossRef](#)] [[PubMed](#)]
34. D’Costa, V.M.; King, C.E.; Kalan, L.; Morar, M.; Sung, W.W.L.; Schwarz, C.; Froese, D.; Zazula, G.; Calmels, F.; Debruyne, R.; et al. Antibiotic resistance is ancient. *Nature* **2011**, *477*, 457–461. [[CrossRef](#)] [[PubMed](#)]
35. Banin, E.; Hughes, D.; Kuipers, O.P. Editorial: Bacterial pathogens, antibiotics and antibiotic resistance. *FEMS Microbiol. Rev.* **2017**, *41*, 450–452. [[CrossRef](#)]
36. Luepke, K.H.; Suda, K.J.; Boucher, H.; Russo, R.L.; Bonney, M.W.; Hunt, T.D.; Mohr, J.F. Past, Present, and Future of Antibacterial Economics: Increasing Bacterial Resistance, Limited Antibiotic Pipeline, and Societal Implications. *Pharmacother. J. Hum. Pharmacol. Drug Ther.* **2017**, *37*, 71–84. [[CrossRef](#)] [[PubMed](#)]
37. Chung, P.Y.; Khanum, R. Antimicrobial peptides as potential anti-biofilm agents against multidrug-resistant bacteria. *J. Microbiol. Immunol. Infect.* **2017**, *50*, 405–410. [[CrossRef](#)]
38. Cárdenas, L.L.; Merchán, M.A.; López, D.P. New antibiotics against bacterial resistance. *Infectio* **2019**, *23*, 382. [[CrossRef](#)]
39. MacFadden, D.R.; McGough, S.F.; Fisman, D.; Santillana, M.; Brownstein, J.S. Antibiotic resistance increases with local temperature. *Nat. Clim. Chang.* **2018**, *8*, 510–514. [[CrossRef](#)]
40. Imran, M.; Das, K.R.; Naik, M.M. Co-selection of multi-antibiotic resistance in bacterial pathogens in metal and microplastic contaminated environments: An emerging health threat. *Chemosphere* **2019**, *215*, 846–857. [[CrossRef](#)]
41. Aslam, B.; Wang, W.; Arshad, M.I.; Khurshid, M.; Muzammil, S.; Rasool, M.H.; Nisar, M.A.; Alvi, R.F.; Aslam, M.A.; Qamar, M.U.; et al. Antibiotic resistance: A rundown of a global crisis. *Infect. Drug Resist.* **2018**, *11*, 1645–1658. [[CrossRef](#)]
42. Frieri, M.; Kumar, K.; Boutin, A. Antibiotic resistance. *J. Infect. Public Health* **2017**, *10*, 369–378. [[CrossRef](#)] [[PubMed](#)]
43. Troncoso, C.; Pavez, M.; Santos, A.; Salazar, R.; Barrientos, L. Implicancias Estructurales y Fisiológicas de la Célula Bacteriana en los Mecanismos de Resistencia Antibiótica. *Int. J. Morphol.* **2017**, *35*, 1214–1223. [[CrossRef](#)]
44. Bullington, W.; Hempstead, S.; Smyth, A.R.; Drevinek, P.; Saiman, L.; Waters, V.J.; Bell, S.C.; VanDevanter, D.R.; Flume, P.A.; Elborn, S.; et al. Antimicrobial resistance: Concerns of healthcare providers and people with CF. *J. Cyst. Fibros.* **2020**, *20*, 407–412. [[CrossRef](#)]
45. Płusa, T.; Konieczny, R.; Baranowska, A.; Szymczak, Z. The growing resistance of bacterial strains to antibiotics. *Pol. Merkur. Lek.* **2019**, *47*, 106–110.
46. Mobarki, N.; Almerabi, B.; Hattan, A. Antibiotic Resistance Crisis. *Int. J. Med. Dev. Ctries* **2019**, 561–564. [[CrossRef](#)]
47. Reygaert, W.C. An overview of the antimicrobial resistance mechanisms of bacteria. *AIMS Microbiol.* **2018**, *4*, 482–501. [[CrossRef](#)] [[PubMed](#)]
48. Mandsberg, L.F.; Ciofu, O.; Kirkby, N.; Christiansen, L.E.; Poulsen, H.E.; Høiby, N. Antibiotic Resistance in *Pseudomonas aeruginosa* Strains with Increased Mutation Frequency Due to Inactivation of the DNA Oxidative Repair System. *Antimicrob. Agents Chemother.* **2009**, *53*, 2483–2491. [[CrossRef](#)] [[PubMed](#)]
49. Kapoor, G.; Saigal, S.; Elongavan, A. Action and resistance mechanisms of antibiotics: A guide for clinicians. *J. Anaesthesiol. Clin. Pharmacol.* **2017**, *33*, 300. [[CrossRef](#)]
50. Ruddaraju, L.K.; Pammi, S.V.N.; Guntuku, G.S.; Padavala, V.S.; Kolapalli, V.R.M. A review on anti-bacterials to combat resistance: From ancient era of plants and metals to present and future perspectives of green nano technological combinations. *Asian J. Pharm. Sci.* **2020**, *15*, 42–59. [[CrossRef](#)]
51. Nas, F. Mechanisms of Bacterial Antibiotics Resistance: A Review. *J. Adv. Microbiol.* **2017**, *7*, 1–6. [[CrossRef](#)]
52. Partridge, S.R.; Kwong, S.M.; Firth, N.; Jensen, S.O. Mobile Genetic Elements Associated with Antimicrobial Resistance. *Clin. Microbiol. Rev.* **2018**, *31*, e00088-17. [[CrossRef](#)]
53. Majeed, H.T.; Aljanaby, A.A.J. Antibiotic Susceptibility Patterns and Prevalence of Some Extended Spectrum Beta-Lactamases Genes in Gram-Negative Bacteria Isolated from Patients Infected with Urinary Tract Infections in Al-Najaf City, Iraq. *Avicenna J. Med. Biotechnol.* **2019**, *11*, 192–201.
54. Bassetti, M.; Vena, A.; Croxatto, A.; Righi, E.; Guery, B. How to manage *Pseudomonas aeruginosa* infections. *Drugs Context* **2018**, *7*, 1–18. [[CrossRef](#)]
55. Henrichfreise, B.; Wiegand, I.; Pfister, W.; Wiedemann, B. Resistance Mechanisms of Multiresistant *Pseudomonas aeruginosa* Strains from Germany and Correlation with Hypermutation. *Antimicrob. Agents Chemother.* **2007**, *51*, 4062–4070. [[CrossRef](#)]
56. Blair, J.M.A.; Webber, M.A.; Baylay, A.J.; Ogbolu, D.O.; Piddock, L.J.V. Molecular mechanisms of antibiotic resistance. *Nat. Rev. Microbiol.* **2015**, *13*, 42–51. [[CrossRef](#)] [[PubMed](#)]
57. Arzanlou, M.; Chai, W.C.; Venter, H. Intrinsic, adaptive and acquired antimicrobial resistance in Gram-negative bacteria. *Essays Biochem.* **2017**, *61*, 49–59. [[CrossRef](#)] [[PubMed](#)]

58. Yang, Y.; Mathieu, J.M.; Chattopadhyay, S.; Miller, J.T.; Wu, T.; Shibata, T.; Guo, W.; Alvarez, P.J.J. Defense Mechanisms of *Pseudomonas aeruginosa* PAO1 against Quantum Dots and Their Released Heavy Metals. *ACS Nano* **2012**, *6*, 6091–6098. [CrossRef]
59. Hancock, R.E.W.; Brinkman, F.S.L. Function of *Pseudomonas* Porins in Uptake and Efflux. *Annu. Rev. Microbiol.* **2002**, *56*, 17–38. [CrossRef]
60. Bradford, P.A. Epidemiology of Bacterial Resistance. In *Antimicrobial Resistance in the 21st Century*; Springer International Publishing: Cham, Switzerland, 2018; pp. 299–339. ISBN 978-3-319-78538-7.
61. Bockstael, K.; Aerscot, A. Antimicrobial resistance in bacteria. *Open Med.* **2009**, *4*, 141–155. [CrossRef]
62. Hasan Abusaiba, T.; AL-Harmoosh, R. Mechanisms of Antibiotics Resistance in Bacteria. *Syst. Rev. Pharm.* **2020**, *11*, 817–823. [CrossRef]
63. Begum, S.; Begum, T.; Rahman, N.; Khan, R.A. A review on antibiotic resistance and way of combating antimicrobial resistance. *GSC Biol. Pharm. Sci.* **2021**, *14*, 087–097. [CrossRef]
64. Orellana, J.; Contreras, R. Bacterial Resistance Algorithm. An Application to CVRP. In *International Work-Conference on the Interplay between Natural and Artificial Computation*; Springer: Cham, Switzerland, 2019; Volume 11487, pp. 204–211. [CrossRef]
65. Stevenson, C.; Hall, J.P.; Harrison, E.; Wood, A.; Brockhurst, M.A. Gene mobility promotes the spread of resistance in bacterial populations. *ISME J.* **2017**, *11*, 1930–1932. [CrossRef] [PubMed]
66. Gyles, C.; Boerlin, P. Horizontally Transferred Genetic Elements and Their Role in Pathogenesis of Bacterial Disease. *Vet. Pathol.* **2014**, *51*, 328–340. [CrossRef]
67. Wang, X.; Yang, F.; Zhao, J.; Xu, Y.; Mao, D.; Zhu, X.; Luo, Y.; Alvarez, P.J.J. Bacterial exposure to ZnO nanoparticles facilitates horizontal transfer of antibiotic resistance genes. *NanoImpact* **2018**, *10*, 61–67. [CrossRef]
68. Dodd, M.C. Potential impacts of disinfection processes on elimination and deactivation of antibiotic resistance genes during water and wastewater treatment. *J. Environ. Monit.* **2012**, *14*, 1754. [CrossRef]
69. NHGRI. Available online: <https://www.genome.gov/genetics-glossary/Plasmid> (accessed on 10 April 2021).
70. Julin, D. Plasmid Cloning Vectors. In *Molecular Life Sciences*; Springer: New York, NY, USA, 2014; pp. 1–12.
71. Santos López, A. Importancia de los Plásmidos ColE1 en la Resistencia a Antibióticos. Ph.D. Thesis, Universidad Complutense de Madrid, Madrid, Spain, 2017.
72. Thomas, C.M.; Frost, L.S. Plasmid Genomes, Introduction to. In *Molecular Life Sciences*; Springer: New York, NY, USA, 2014; pp. 1–20.
73. Redondo-Salvo, S.; Fernández-López, R.; Ruiz, R.; Vielva, L.; de Toro, M.; Rocha, E.P.C.; Garcillán-Barcia, M.P.; de la Cruz, F. Pathways for horizontal gene transfer in bacteria revealed by a global map of their plasmids. *Nat. Commun.* **2020**, *11*, 3602. [CrossRef]
74. Bennett, P.M. Plasmid encoded antibiotic resistance: Acquisition and transfer of antibiotic resistance genes in bacteria. *Br. J. Pharmacol.* **2008**, *153*, S347–S357. [CrossRef]
75. Cain, A.K.; Barquist, L.; Goodman, A.L.; Paulsen, I.T.; Parkhill, J.; van Opijnen, T. A decade of advances in transposon-insertion sequencing. *Nat. Rev. Genet.* **2020**, *21*, 526–540. [CrossRef] [PubMed]
76. Asif, M.; Alvi, I.A.; Rehman, S.U. Insight into *Acinetobacter baumannii*: Pathogenesis, global resistance, mechanisms of resistance, treatment options, and alternative modalities. *Infect. Drug Resist.* **2018**, *11*, 1249–1260. [CrossRef]
77. Fan, C.; Wu, Y.-H.; Decker, C.M.; Rohani, R.; Gesell Salazar, M.; Ye, H.; Cui, Z.; Schmidt, F.; Huang, W.E. Defensive Function of Transposable Elements in Bacteria. *ACS Synth. Biol.* **2019**, *8*, 2141–2151. [CrossRef]
78. Pournajaf, A.; Razavi, S.; Irajian, G.; Ardebili, A.; Erfani, Y.; Solgi, S.; Yaghoubi, S.; Raseaiean, A.; Yahyapour, Y.; Kafshgari, R.; et al. Integron types, antimicrobial resistance genes, virulence gene profile, alginate production and biofilm formation in Iranian cystic fibrosis *Pseudomonas aeruginosa* isolates. *Infez. Med.* **2018**, *26*, 226–236. [PubMed]
79. Barlow, R.S.; Gobijs, K.S. Diverse class 2 integrons in bacteria from beef cattle sources. *J. Antimicrob. Chemother.* **2006**, *58*, 1133–1138. [CrossRef] [PubMed]
80. Huang, J.; Lan, F.; Lu, Y.; Li, B. Characterization of Integrons and Antimicrobial Resistance in *Escherichia coli* Sequence Type 131 Isolates. *Can. J. Infect. Dis. Med. Microbiol.* **2020**, *2020*, 3826186. [CrossRef] [PubMed]
81. Kaushik, M.; Kumar, S.; Kapoor, R.K.; Virdi, J.S.; Gulati, P. Integrons in Enterobacteriaceae: Diversity, distribution and epidemiology. *Int. J. Antimicrob. Agents* **2018**, *51*, 167–176. [CrossRef]
82. Khosravi, A.D.; Motahar, M.; Abbasi Montazeri, E. The frequency of class 1 and 2 integrons in *Pseudomonas aeruginosa* strains isolated from burn patients in a burn center of Ahvaz, Iran. *PLoS ONE* **2017**, *12*, e0183061. [CrossRef]
83. Zhao, X.; Hu, M.; Zhang, Q.; Zhao, C.; Zhang, Y.; Li, L.; Qi, J.; Luo, Y.; Zhou, D.; Liu, Y. Characterization of integrons and antimicrobial resistance in *Salmonella* from broilers in Shandong, China. *Poult. Sci.* **2020**, *99*, 7046–7054. [CrossRef]
84. Bello-López, J.M.; Cabrero-Martínez, O.A.; Ibáñez-Cervantes, G.; Hernández-Cortez, C.; Pelcastre-Rodríguez, L.I.; Gonzalez-Avila, L.U.; Castro-Escarpulli, G. Horizontal Gene Transfer and Its Association with Antibiotic Resistance in the Genus *Aeromonas* spp. *Microorganisms* **2019**, *7*, 363. [CrossRef]
85. Lermينياux, N.A.; Cameron, A.D.S. Horizontal transfer of antibiotic resistance genes in clinical environments. *Can. J. Microbiol.* **2019**, *65*, 34–44. [CrossRef]
86. Schneider, C.L. Bacteriophage-Mediated Horizontal Gene Transfer: Transduction. In *Bacteriophages*; Springer International Publishing: Cham, Switzerland, 2021; pp. 151–192.

87. Melander, R.J.; Melander, C. The Challenge of Overcoming Antibiotic Resistance: An Adjuvant Approach? *ACS Infect. Dis.* **2017**, *3*, 559–563. [[CrossRef](#)]
88. Baker, S.; Thomson, N.; Weill, F.-X.; Holt, K.E. Genomic insights into the emergence and spread of antimicrobial-resistant bacterial pathogens. *Science* **2018**, *360*, 733–738. [[CrossRef](#)]
89. Holmes, A.H.; Moore, L.S.P.; Sundsfjord, A.; Steinbakk, M.; Regmi, S.; Karkey, A.; Guerin, P.J.; Piddock, L.J. V Understanding the mechanisms and drivers of antimicrobial resistance. *Lancet* **2016**, *387*, 176–187. [[CrossRef](#)]
90. Blair, J.M.; Richmond, G.E.; Piddock, L.J. Multidrug efflux pumps in Gram-negative bacteria and their role in antibiotic resistance. *Future Microbiol.* **2014**, *9*, 1165–1177. [[CrossRef](#)] [[PubMed](#)]
91. Zgurskaya, H.I.; Rybenkov, V.V. Permeability barriers of Gram-negative pathogens. *Ann. N. Y. Acad. Sci.* **2020**, *1459*, 5–18. [[CrossRef](#)]
92. Hernando-Amado, S.; Blanco, P.; Alcalde-Rico, M.; Corona, F.; Reales-Calderón, J.A.; Sánchez, M.B.; Martínez, J.L. Multidrug efflux pumps as main players in intrinsic and acquired resistance to antimicrobials. *Drug Resist. Updat.* **2016**, *28*, 13–27. [[CrossRef](#)] [[PubMed](#)]
93. Li, N.; Wu, J.-X.; Ding, D.; Cheng, J.; Gao, N.; Chen, L. Structure of a Pancreatic ATP-Sensitive Potassium Channel. *Cell* **2017**, *168*, 101–110.e10. [[CrossRef](#)]
94. Johnson, Z.L.; Chen, J. Structural Basis of Substrate Recognition by the Multidrug Resistance Protein MRP1. *Cell* **2017**, *168*, 1075–1085.e9. [[CrossRef](#)]
95. Verhalen, B.; Dastvan, R.; Thangapandian, S.; Peskova, Y.; Koteiche, H.A.; Nakamoto, R.K.; Tajkhorshid, E.; Mchaourab, H.S. Energy transduction and alternating access of the mammalian ABC transporter P-glycoprotein. *Nature* **2017**, *543*, 738–741. [[CrossRef](#)]
96. Mousa, J.J.; Yang, Y.; Tomkovich, S.; Shima, A.; Newsome, R.C.; Tripathi, P.; Oswald, E.; Bruner, S.D.; Jobin, C. MATE transport of the *E. coli*-derived genotoxin colibactin. *Nat. Microbiol.* **2016**, *1*, 15009. [[CrossRef](#)] [[PubMed](#)]
97. Radchenko, M.; Symersky, J.; Nie, R.; Lu, M. Structural basis for the blockade of MATE multidrug efflux pumps. *Nat. Commun.* **2015**, *6*, 7995. [[CrossRef](#)]
98. Radchenko, M.; Nie, R.; Lu, M. Disulfide Cross-linking of a Multidrug and Toxic Compound Extrusion Transporter Impacts Multidrug Efflux. *J. Biol. Chem.* **2016**, *291*, 9818–9826. [[CrossRef](#)]
99. Zwama, M.; Yamasaki, S.; Nakashima, R.; Sakurai, K.; Nishino, K.; Yamaguchi, A. Multiple entry pathways within the efflux transporter AcrB contribute to multidrug recognition. *Nat. Commun.* **2018**, *9*, 124. [[CrossRef](#)]
100. Sun, J.; Deng, Z.; Yan, A. Bacterial multidrug efflux pumps: Mechanisms, physiology and pharmacological exploitations. *Biochem. Biophys. Res. Commun.* **2014**, *453*, 254–267. [[CrossRef](#)]
101. Radestock, S.; Forrest, L.R. The Alternating-Access Mechanism of MFS Transporters Arises from Inverted-Topology Repeats. *J. Mol. Biol.* **2011**, *407*, 698–715. [[CrossRef](#)] [[PubMed](#)]
102. Kaback, H.R. A chemiosmotic mechanism of symport. *Proc. Natl. Acad. Sci. USA* **2015**, *112*, 1259–1264. [[CrossRef](#)]
103. Heng, J.; Zhao, Y.; Liu, M.; Liu, Y.; Fan, J.; Wang, X.; Zhao, Y.; Zhang, X.C. Substrate-bound structure of the *E. coli* multidrug resistance transporter MdfA. *Cell Res.* **2015**, *25*, 1060–1073. [[CrossRef](#)]
104. Su, C.-C.; Yin, L.; Kumar, N.; Dai, L.; Radhakrishnan, A.; Bolla, J.R.; Lei, H.-T.; Chou, T.-H.; Delmar, J.A.; Rajashankar, K.R.; et al. Structures and transport dynamics of a *Campylobacter jejuni* multidrug efflux pump. *Nat. Commun.* **2017**, *8*, 171. [[CrossRef](#)]
105. Poonsuk, K.; Tribuddharat, C.; Chuanchuen, R. Simultaneous overexpression of multidrug efflux pumps in *Pseudomonas aeruginosa* non-cystic fibrosis clinical isolates. *Can. J. Microbiol.* **2014**, *60*, 437–443. [[CrossRef](#)] [[PubMed](#)]
106. Saxena, P.; Joshi, Y.; Rawat, K.; Bisht, R. Biofilms: Architecture, Resistance, Quorum Sensing and Control Mechanisms. *Indian J. Microbiol.* **2019**, *59*, 3–12. [[CrossRef](#)]
107. Felden, B.; Cattoir, V. Bacterial Adaptation to Antibiotics through Regulatory RNAs. *Antimicrob. Agents Chemother.* **2018**, *62*, e02503-17. [[CrossRef](#)] [[PubMed](#)]
108. Hall, C.W.; Mah, T.-F. Molecular mechanisms of biofilm-based antibiotic resistance and tolerance in pathogenic bacteria. *FEMS Microbiol. Rev.* **2017**, *41*, 276–301. [[CrossRef](#)]
109. Gou, N.; Onnis-Hayden, A.; Gu, A.Z. Mechanistic Toxicity Assessment of Nanomaterials by Whole-Cell-Array Stress Genes Expression Analysis. *Environ. Sci. Technol.* **2010**, *44*, 5964–5970. [[CrossRef](#)]
110. Nevius, B.A.; Chen, Y.P.; Ferry, J.L.; Decho, A.W. Surface-functionalization effects on uptake of fluorescent polystyrene nanoparticles by model biofilms. *Ecotoxicology* **2012**, *21*, 2205–2213. [[CrossRef](#)]
111. Tkachenko, A.G. Stress Responses of Bacterial Cells as Mechanism of Development of Antibiotic Tolerance (Review). *Appl. Biochem. Microbiol.* **2018**, *54*, 108–127. [[CrossRef](#)]
112. Santajit, S.; Indrawattana, N. Mechanisms of Antimicrobial Resistance in ESKAPE Pathogens. *Biomed. Res. Int.* **2016**, *2016*, 2475067. [[CrossRef](#)]
113. Miller, K.P.; Wang, L.; Benicewicz, B.C.; Decho, A.W. Inorganic nanoparticles engineered to attack bacteria. *Chem. Soc. Rev.* **2015**, *44*, 7787–7807. [[CrossRef](#)] [[PubMed](#)]
114. Piñón-Castillo, H.A.; Martínez-Chamarro, R.; Reyes-Martínez, R.; Salinas-Vera, Y.M.; Manjarrez-Nevárez, L.A.; Muñoz-Castellanos, L.N.; López-Camarillo, C.; Orrantia-Borunda, E. Palladium Nanoparticles Functionalized with PVP-Quercetin Inhibits Cell Proliferation and Activates Apoptosis in Colorectal Cancer Cells. *Appl. Sci.* **2021**, *11*, 1988. [[CrossRef](#)]

115. Shrestha, A.; Kishen, A. Antibacterial Nanoparticles in Endodontics: A Review. *J. Endod.* **2016**, *42*, 1417–1426. [[CrossRef](#)] [[PubMed](#)]
116. Bi, J.; Li, T.; Ren, H.; Ling, R.; Wu, Z.; Qin, W. Capillary electrophoretic determination of heavy-metal ions using 11-mercaptopundecanoic acid and 6-mercapto-1-hexanol co-functionalized gold nanoparticle as colorimetric probe. *J. Chromatogr. A* **2019**, *1594*, 208–215. [[CrossRef](#)]
117. Thakkar, K.N.; Mhatre, S.S.; Parikh, R.Y. Biological synthesis of metallic nanoparticles. *Nanomed. Nanotechnol. Biol. Med.* **2010**, *6*, 257–262. [[CrossRef](#)]
118. Brewer, M.; Zhang, T.; Dong, W.; Rutherford, M.; Tian, Z.R. Future Approaches of Nanomedicine in Clinical Science. *Med. Clin. N. Am.* **2007**, *91*, 963–1016. [[CrossRef](#)]
119. McNamara, K.; Tofail, S.A.M. Nanosystems: The use of nanoalloys, metallic, bimetallic, and magnetic nanoparticles in biomedical applications. *Phys. Chem. Chem. Phys.* **2015**, *17*, 27981–27995. [[CrossRef](#)]
120. Kaweeterawat, C.; Na Ubol, P.; Sangmuang, S.; Aueviriyavit, S.; Maniratanachote, R. Mechanisms of antibiotic resistance in bacteria mediated by silver nanoparticles. *J. Toxicol. Environ. Health Part. A* **2017**, *80*, 1276–1289. [[CrossRef](#)] [[PubMed](#)]
121. Li, X.; Xu, H.; Chen, Z.-S.; Chen, G. Biosynthesis of Nanoparticles by Microorganisms and Their Applications. *J. Nanomater.* **2011**, *2011*, 270974. [[CrossRef](#)]
122. Liu, J.; Qiao, S.Z.; Hu, Q.H.; Max Lu, G.Q. Magnetic Nanocomposites with Mesoporous Structures: Synthesis and Applications. *Small* **2011**, *7*, 425–443. [[CrossRef](#)]
123. Spirescu, V.A.; Niculescu, A.-G.; Slave, S.; Bircă, A.C.; Dorcioman, G.; Grumezescu, V.; Holban, A.M.; Oprea, O.-C.; Vasile, B.S.; Grumezescu, A.M.; et al. Anti-Biofilm Coatings Based on Chitosan and Lysozyme Functionalized Magnetite Nanoparticles. *Antibiotics* **2021**, *10*, 1269. [[CrossRef](#)]
124. Motelica, L.; Fikai, D.; Oprea, O.; Fikai, A.; Trusca, R.D.; Andronescu, E.; Holban, A.M. Biodegradable alginate films with ZnO nanoparticles and citronella essential oil—a novel antimicrobial structure. *Pharmaceutics* **2021**, *13*, 1020. [[CrossRef](#)] [[PubMed](#)]
125. Vasile, B.S.; Chircov, C.; Matei, M.; Neacs, I.A. Iron Oxide—Silica Core—Shell Nanoparticles Functionalized with Essential Oils for Antimicrobial Therapies. *Antibiotics* **2021**, *10*, 1138.
126. Puiu, R.A.; Balaure, P.C.; Constantinescu, E.; Grumezescu, A.M.; Andronescu, E.; Oprea, O.C.; Vasile, B.S.; Grumezescu, V.; Negut, I.; Nica, I.C.; et al. Anti-cancer nanopowders and maple-fabricated thin coatings based on spions surface modified with paclitaxel loaded β -cyclodextrin. *Pharmaceutics* **2021**, *13*, 1356. [[CrossRef](#)]
127. Isela Ruvalcaba Ontiveros, R.; Alberto Duarte Moller, J.; Rocío Carrasco Hernandez, A.; Esperanza Esparza-Ponce, H.; Orrantia Borunda, E.; Deisy Gómez Esparza, C.; Manuel Olivares Ramírez, J. A Simple Way to Produce Gold Nanoshells for Cancer Therapy. In *Current Topics in Biochemical Engineering*; IntechOpen: London, UK, 2019. [[CrossRef](#)]
128. Khameneh, B.; Diab, R.; Ghazvini, K.; Fazly Bazzaz, B.S. Breakthroughs in bacterial resistance mechanisms and the potential ways to combat them. *Microb. Pathog.* **2016**, *95*, 32–42. [[CrossRef](#)]
129. Slavin, Y.N.; Asnis, J.; Häfeli, U.O.; Bach, H. Metal nanoparticles: Understanding the mechanisms behind antibacterial activity. *J. Nanobiotechnol.* **2017**, *15*, 65. [[CrossRef](#)]
130. AlMatar, M.; Makky, E.A.; Var, I.; Koksai, F. The Role of Nanoparticles in the Inhibition of Multidrug-Resistant Bacteria and Biofilms. *Curr. Drug Deliv.* **2018**, *15*, 470–484. [[CrossRef](#)]
131. Franci, G.; Falanga, A.; Galdiero, S.; Palomba, L.; Rai, M.; Morelli, G.; Galdiero, M. Silver Nanoparticles as Potential Antibacterial Agents. *Molecules* **2015**, *20*, 8856–8874. [[CrossRef](#)]
132. Nisar, P.; Ali, N.; Rahman, L.; Ali, M.; Shinwari, Z.K. Antimicrobial activities of biologically synthesized metal nanoparticles: An insight into the mechanism of action. *JBIC J. Biol. Inorg. Chem.* **2019**, *24*, 929–941. [[CrossRef](#)]
133. Abdal Dayem, A.; Hossain, M.; Lee, S.; Kim, K.; Saha, S.; Yang, G.-M.; Choi, H.; Cho, S.-G. The Role of Reactive Oxygen Species (ROS) in the Biological Activities of Metallic Nanoparticles. *Int. J. Mol. Sci.* **2017**, *18*, 120. [[CrossRef](#)]
134. Snezhkina, A.V.; Kudryavtseva, A.V.; Kardymon, O.L.; Savvateeva, M.V.; Melnikova, N.V.; Krasnov, G.S.; Dmitriev, A.A. ROS Generation and Antioxidant Defense Systems in Normal and Malignant Cells. *Oxid. Med. Cell. Longev.* **2019**, *2019*, 6175804. [[CrossRef](#)] [[PubMed](#)]
135. Gupta, A.; Mumtaz, S.; Li, C.-H.; Hussain, I.; Rotello, V.M. Combatting antibiotic-resistant bacteria using nanomaterials. *Chem. Soc. Rev.* **2019**, *48*, 415–427. [[CrossRef](#)] [[PubMed](#)]
136. Ulloa-Ogaz, A.L.; Piñón-Castillo, H.A.; Muñoz-Castellanos, L.N.; Athie-García, M.S.; Ballinas-Casarrubias, M.D.L.; Murillo-Ramirez, J.G.; Flores-Ongay, L.Á.; Duran, R.; Orrantia-Borunda, E. Oxidative damage to *Pseudomonas aeruginosa* ATCC 27833 and *Staphylococcus aureus* ATCC 24213 induced by CuO-NPs. *Environ. Sci. Pollut. Res.* **2017**, *24*, 22048–22060. [[CrossRef](#)] [[PubMed](#)]
137. Amini, S.M. Preparation of antimicrobial metallic nanoparticles with bioactive compounds. *Mater. Sci. Eng. C* **2019**, *103*, 109809. [[CrossRef](#)]
138. Buzea, C.; Pacheco, I.I.; Robbie, K. Nanomaterials and nanoparticles: Sources and toxicity. *Biointerphases* **2007**, *2*, MR17–MR71. [[CrossRef](#)]
139. El-Ansary, A.; Al-Daihan, S. On the Toxicity of Therapeutically Used Nanoparticles: An Overview. *J. Toxicol.* **2009**, *2009*, 754810. [[CrossRef](#)]

140. Pérez-Díaz, M.A.; Boegli, L.; James, G.; Velasquillo, C.; Sánchez-Sánchez, R.; Martínez-Martínez, R.-E.; Martínez-Castañón, G.A.; Martínez-Gutiérrez, F. Silver nanoparticles with antimicrobial activities against *Streptococcus mutans* and their cytotoxic effect. *Mater. Sci. Eng. C* **2015**, *55*, 360–366. [[CrossRef](#)] [[PubMed](#)]
141. Padmavathy, N.; Vijayaraghavan, R. Interaction of ZnO Nanoparticles with Microbes—A Physio and Biochemical Assay. *J. Biomed. Nanotechnol.* **2011**, *7*, 813–822. [[CrossRef](#)]
142. Yu, J.; Zhang, W.; Li, Y.; Wang, G.; Yang, L.; Jin, J.; Chen, Q.; Huang, M. Synthesis, characterization, antimicrobial activity and mechanism of a novel hydroxyapatite whisker/nano zinc oxide biomaterial. *Biomed. Mater.* **2014**, *10*, 015001. [[CrossRef](#)]
143. Lesniak, A.; Salvati, A.; Santos-Martinez, M.J.; Radomski, M.W.; Dawson, K.A.; Åberg, C. Nanoparticle Adhesion to the Cell Membrane and Its Effect on Nanoparticle Uptake Efficiency. *J. Am. Chem. Soc.* **2013**, *135*, 1438–1444. [[CrossRef](#)] [[PubMed](#)]
144. Sarwar, A.; Katas, H.; Samsudin, S.N.; Zin, N.M. Regioselective Sequential Modification of Chitosan via Azide-Alkyne Click Reaction: Synthesis, Characterization, and Antimicrobial Activity of Chitosan Derivatives and Nanoparticles. *PLoS ONE* **2015**, *10*, e0123084. [[CrossRef](#)]
145. Ahmed, B.; Hashmi, A.; Khan, M.S.; Musarrat, J. ROS mediated destruction of cell membrane, growth and biofilms of human bacterial pathogens by stable metallic AgNPs functionalized from bell pepper extract and quercetin. *Adv. Powder Technol.* **2018**, *29*, 1601–1616. [[CrossRef](#)]
146. Yang, B.; Chen, Y.; Shi, J. Reactive Oxygen Species (ROS)-Based Nanomedicine. *Chem. Rev.* **2019**, *119*, 4881–4985. [[CrossRef](#)] [[PubMed](#)]
147. Shaikh, S.; Nazam, N.; Rizvi, S.M.D.; Ahmad, K.; Baig, M.H.; Lee, E.J.; Choi, I. Mechanistic Insights into the Antimicrobial Actions of Metallic Nanoparticles and Their Implications for Multidrug Resistance. *Int. J. Mol. Sci.* **2019**, *20*, 2468. [[CrossRef](#)]
148. Pan, W.-Y.; Huang, C.-C.; Lin, T.-T.; Hu, H.-Y.; Lin, W.-C.; Li, M.-J.; Sung, H.-W. Synergistic antibacterial effects of localized heat and oxidative stress caused by hydroxyl radicals mediated by graphene/iron oxide-based nanocomposites. *Nanomed. Nanotechnol. Biol. Med.* **2016**, *12*, 431–438. [[CrossRef](#)]
149. Zhang, W.; Li, Y.; Niu, J.; Chen, Y. Photogeneration of Reactive Oxygen Species on Uncoated Silver, Gold, Nickel, and Silicon Nanoparticles and Their Antibacterial Effects. *Langmuir* **2013**, *29*, 4647–4651. [[CrossRef](#)] [[PubMed](#)]
150. Lin, J.; Zhang, H.; Chen, Z.; Zheng, Y. Penetration of Lipid Membranes by Gold Nanoparticles: Insights into Cellular Uptake, Cytotoxicity, and Their Relationship. *ACS Nano* **2010**, *4*, 5421–5429. [[CrossRef](#)] [[PubMed](#)]
151. Yamanaka, M.; Hara, K.; Kudo, J. Bactericidal Actions of a Silver Ion Solution on *Escherichia coli*, Studied by Energy-Filtering Transmission Electron Microscopy and Proteomic Analysis. *Appl. Environ. Microbiol.* **2005**, *71*, 7589–7593. [[CrossRef](#)]
152. Cui, Y.; Zhao, Y.; Tian, Y.; Zhang, W.; Lü, X.; Jiang, X. The molecular mechanism of action of bactericidal gold nanoparticles on *Escherichia coli*. *Biomaterials* **2012**, *33*, 2327–2333. [[CrossRef](#)] [[PubMed](#)]
153. Su, G.; Zhang, X.; Giesy, J.P.; Musarrat, J.; Saquib, Q.; Alkhedairy, A.A.; Yu, H. Comparison on the molecular response profiles between nano zinc oxide (ZnO) particles and free zinc ion using a genome-wide toxicogenomics approach. *Environ. Sci. Pollut. Res.* **2015**, *22*, 17434–17442. [[CrossRef](#)]
154. Nagy, A.; Harrison, A.; Sabbani, S.; Munson, R.S., Jr.; Dutta, P.K.; Waldman, W.J. Silver nanoparticles embedded in zeolite membranes: Release of silver ions and mechanism of antibacterial action. *Int. J. Nanomed.* **2011**, *6*, 1833. [[CrossRef](#)]
155. Qiu, W.; Zheng, X.; Wei, Y.; Zhou, X.; Zhang, K.; Wang, S.; Cheng, L.; Li, Y.; Ren, B.; Xu, X.; et al. D-Alanine metabolism is essential for growth and biofilm formation of *Streptococcus mutans*. *Mol. Oral Microbiol.* **2016**, *31*, 435–444. [[CrossRef](#)] [[PubMed](#)]
156. Su, H.-L.; Chou, C.-C.; Hung, D.-J.; Lin, S.-H.; Pao, I.-C.; Lin, J.-H.; Huang, F.-L.; Dong, R.-X.; Lin, J.-J. The disruption of bacterial membrane integrity through ROS generation induced by nanohybrids of silver and clay. *Biomaterials* **2009**, *30*, 5979–5987. [[CrossRef](#)] [[PubMed](#)]
157. Niño-Martínez, N.; Salas Orozco, M.F.; Martínez-Castañón, G.-A.; Torres Méndez, F.; Ruiz, F. Molecular Mechanisms of Bacterial Resistance to Metal and Metal Oxide Nanoparticles. *Int. J. Mol. Sci.* **2019**, *20*, 2808. [[CrossRef](#)] [[PubMed](#)]
158. Salas-Orozco, M.; Niño-Martínez, N.; Martínez-Castañón, G.-A.; Méndez, F.T.; Jasso, M.E.C.; Ruiz, F. Mechanisms of Resistance to Silver Nanoparticles in Endodontic Bacteria: A Literature Review. *J. Nanomater.* **2019**, *2019*, 7630316. [[CrossRef](#)]
159. Webster, T.J.; Seil, I. Antimicrobial applications of nanotechnology: Methods and literature. *Int. J. Nanomed.* **2012**, *7*, 2767. [[CrossRef](#)]
160. Poyedinok, N.; Mykhaylova, O.; Sergiichuk, N.; Tugay, T.; Tugay, A.; Lopatko, S.; Matvieieva, N. Effect of Colloidal Metal Nanoparticles on Biomass, Polysaccharides, Flavonoids, and Melanin Accumulation in Medicinal Mushroom *Inonotus obliquus* (Ach.:Pers.) Pilát. *Appl. Biochem. Biotechnol.* **2020**, *191*, 1315–1325. [[CrossRef](#)] [[PubMed](#)]
161. Courtois, P.; Rorat, A.; Lemiere, S.; Levard, C.; Pradas, A.; Lors, C.; Vandenbulcke, F. Accumulation and Localization of Silver Nanoparticles in *Eisenia Fetida* Earthworms. *Environ. Sci. Pollut. Res.* **2021**, *28*, 3756–3765. [[CrossRef](#)] [[PubMed](#)]
162. Yarjanli, Z.; Ghaedi, K.; Esmaili, A.; Rahgozar, S.; Zarrabi, A. Iron oxide nanoparticles may damage to the neural tissue through iron accumulation, oxidative stress, and protein aggregation. *BMC Neurosci.* **2017**, *18*, 1–12. [[CrossRef](#)] [[PubMed](#)]
163. Matter, M.T.; Li, J.H.; Lese, I.; Schreiner, C.; Bernard, L.; Scholder, O.; Hubeli, J.; Keevend, K.; Tsolaki, E.; Bertero, E.; et al. Multiscale Analysis of Metal Oxide Nanoparticles in Tissue: Insights into Biodistribution and Biotransformation. *Adv. Sci.* **2020**, *7*, 1–11. [[CrossRef](#)] [[PubMed](#)]
164. Morales-Dalmau, J.; Vilches, C.; Sanz, V.; De Miguel, I.; Rodríguez-Fajardo, V.; Berto, P.; Martínez-Lozano, M.; Casanovas, O.; Durduran, T.; Quidant, R. Quantification of gold nanoparticle accumulation in tissue by two-photon luminescence microscopy. *Nanoscale* **2019**, *11*, 11331–11339. [[CrossRef](#)] [[PubMed](#)]

165. Arya, S.S.; Sharma, M.M.; Das, R.K.; Rookes, J.; Cahill, D.; Lenka, S.K. Heliyon Vanillin mediated green synthesis and application of gold nanoparticles for reversal of antimicrobial resistance in *Pseudomonas aeruginosa* clinical isolates. *Heliyon* **2019**, *5*, e02021. [CrossRef]
166. Chavan, C.; Kamble, S.; Murthy, A.V.R.; Kale, S.N. Ampicillin-mediated functionalized gold nanoparticles against ampicillin-resistant bacteria: Strategy, preparation and interaction studies. *Nanotechnology* **2020**, *31*, 215604. [CrossRef]
167. Kalita, S.; Kandimalla, R.; Sharma, K.K.; Kataki, A.C.; Deka, M.; Kotoky, J. Amoxicillin functionalized gold nanoparticles reverts MRSA resistance. *Mater. Sci. Eng. C* **2016**, *61*, 720–727. [CrossRef]
168. Armentano, I.; Arciola, C.R.; Fortunati, E.; Ferrari, D.; Mattioli, S.; Amoroso, C.F.; Rizzo, J.; Kenny, J.M.; Imbriani, M.; Visai, L. The Interaction of Bacteria with Engineered Nanostructured Polymeric Materials: A Review. *Sci. World J.* **2014**, *2014*, 410423. [CrossRef]
169. Gao, W.; Thamphiwatana, S.; Angsantikul, P.; Zhang, L. Nanoparticle approaches against bacterial infections. *Wiley Interdiscip. Rev. Nanomed. Nanobiotechnol.* **2014**, *6*, 532–547. [CrossRef]
170. Li, H.; Chen, Q.; Zhao, J.; Urmila, K. Enhancing the antimicrobial activity of natural extraction using the synthetic ultrasmall metal nanoparticles. *Sci. Rep.* **2015**, *5*, 11033. [CrossRef] [PubMed]
171. Luan, B.; Huynh, T.; Zhou, R. Complete wetting of graphene by biological lipids. *Nanoscale* **2016**, *8*, 5750–5754. [CrossRef]
172. McBee, M.E.; Chionh, Y.H.; Sharaf, M.L.; Ho, P.; Cai, M.W.L.; Dedon, P.C. Production of Superoxide in Bacteria Is Stress- and Cell State-Dependent: A Gating-Optimized Flow Cytometry Method that Minimizes ROS Measurement Artifacts with Fluorescent Dyes. *Front. Microbiol.* **2017**, *8*, 459. [CrossRef]
173. Ye, Q.; Chen, W.; Huang, H.; Tang, Y.; Wang, W.; Meng, F.; Wang, H.; Zheng, Y. Iron and zinc ions, potent weapons against multidrug-resistant bacteria. *Appl. Microbiol. Biotechnol.* **2020**, *104*, 5213–5227. [CrossRef] [PubMed]
174. Zou, L.; Wang, J.; Gao, Y.; Ren, X.; Rottenberg, M.E.; Lu, J.; Holmgren, A. Synergistic antibacterial activity of silver with antibiotics correlating with the upregulation of the ROS production. *Sci. Rep.* **2018**, *8*, 11131. [CrossRef]
175. Xu, R.; Wang, D.; Zhang, J.; Li, Y. Shape-Dependent Catalytic Activity of Silver Nanoparticles for the Oxidation of Styrene. *Chem.-Asian J.* **2006**, *1*, 888–893. [CrossRef]
176. Agnihotri, S.; Mukherji, S.; Mukherji, S. Size-controlled silver nanoparticles synthesized over the range 5–100 nm using the same protocol and their antibacterial efficacy. *RSC Adv.* **2014**, *4*, 3974–3983. [CrossRef]
177. Hachicho, N.; Hoffmann, P.; Ahlert, K.; Heipieper, H.J. Effect of silver nanoparticles and silver ions on growth and adaptive response mechanisms of *Pseudomonas putida* mt-2. *FEMS Microbiol. Lett.* **2014**, *355*, 71–77. [CrossRef]
178. Graves, J.L.; Tajkarimi, M.; Cunningham, Q.; Campbell, A.; Nonga, H.; Harrison, S.H.; Barrick, J.E. Rapid evolution of silver nanoparticle resistance in *Escherichia coli*. *Front. Genet.* **2015**, *6*, 42. [CrossRef]
179. Panáček, A.; Kvítek, L.; Smékalová, M.; Večeřová, R.; Kolář, M.; Röderová, M.; Dyčka, F.; Šebela, M.; Pucek, R.; Tomanec, O.; et al. Bacterial resistance to silver nanoparticles and how to overcome it. *Nat. Nanotechnol.* **2018**, *13*, 65–71. [CrossRef]
180. Lellouche, J.; Friedman, A.; Lahmi, R.; Gedanken, A.; Banin, E. Antibiofilm surface functionalization of catheters by magnesium fluoride nanoparticles. *Int. J. Nanomed.* **2012**, *7*, 1175. [CrossRef]
181. Yun, S.; Huang, J.J. Routes for Drug Delivery: Sustained-Release Devices. *Retinal Pharmacotherapeut.* **2016**, *55*, 84–92.
182. Peng, Z.; Ni, J.; Zheng, K.; Shen, Y.; Wang, X.; He, G.; Jin, S.; Tang, T. Dual effects and mechanism of TiO₂ nanotube arrays in reducing bacterial colonization and enhancing C3H10T1/2 cell adhesion. *Int. J. Nanomed.* **2013**, *8*, 3093. [CrossRef]
183. Wunderink, R.G.; Giamarellos-Bourboulis, E.J.; Rahav, G.; Mathers, A.J.; Bassetti, M.; Vazquez, J.; Cornely, O.A.; Solomkin, J.; Bhowmick, T.; Bishara, J.; et al. Effect and Safety of Meropenem–Vaborbactam versus Best-Available Therapy in Patients with Carbapenem-Resistant Enterobacteriaceae Infections: The TANGO II Randomized Clinical Trial. *Infect. Dis. Ther.* **2018**, *7*, 439–455. [CrossRef]
184. Jijie, R.; Barras, A.; Teodorescu, F.; Boukherroub, R.; Szunerits, S. Advancements on the molecular design of nanoantibiotics: Current level of development and future challenges. *Mol. Syst. Des. Eng.* **2017**, *2*, 349–369. [CrossRef]
185. Qi, G.; Li, L.; Yu, F.; Wang, H. Vancomycin-Modified Mesoporous Silica Nanoparticles for Selective Recognition and Killing of Pathogenic Gram-Positive Bacteria Over Macrophage-Like Cells. *ACS Appl. Mater. Interfaces* **2013**, *5*, 10874–10881. [CrossRef]
186. Tang, S.; Zheng, J. Antibacterial Activity of Silver Nanoparticles: Structural Effects. *Adv. Healthc. Mater.* **2018**, *7*, 1701503. [CrossRef]
187. Cheon, J.Y.; Kim, S.J.; Rhee, Y.H.; Kwon, O.H.; Park, W.H. Shape-dependent antimicrobial activities of silver nanoparticles. *Int. J. Nanomed.* **2019**, *14*, 2773–2780. [CrossRef] [PubMed]
188. Burdușel, A.-C.; Gherasim, O.; Grumezescu, A.M.; Mogoantă, L.; Ficai, A.; Andronescu, E. Biomedical Applications of Silver Nanoparticles: An Up-to-Date Overview. *Nanomaterials* **2018**, *8*, 681. [CrossRef]
189. Lee, S.; Jun, B.-H. Silver Nanoparticles: Synthesis and Application for Nanomedicine. *Int. J. Mol. Sci.* **2019**, *20*, 865. [CrossRef] [PubMed]
190. Helmlinger, J.; Sengstock, C.; Groß-Heitfeld, C.; Mayer, C.; Schildhauer, T.A.; Köller, M.; Epple, M. Silver nanoparticles with different size and shape: Equal cytotoxicity, but different antibacterial effects. *RSC Adv.* **2016**, *6*, 18490–18501. [CrossRef]
191. Raza, M.; Kanwal, Z.; Rauf, A.; Sabri, A.; Riaz, S.; Naseem, S. Size- and Shape-Dependent Antibacterial Studies of Silver Nanoparticles Synthesized by Wet Chemical Routes. *Nanomaterials* **2016**, *6*, 74. [CrossRef]
192. Pal, S.; Tak, Y.K.; Song, J.M. Does the Antibacterial Activity of Silver Nanoparticles Depend on the Shape of the Nanoparticle? A Study of the Gram-Negative Bacterium *Escherichia coli*. *Appl. Environ. Microbiol.* **2007**, *73*, 1712–1720. [CrossRef]

193. Nanda, A.; Saravanan, M. Biosynthesis of silver nanoparticles from *Staphylococcus aureus* and its antimicrobial activity against MRSA and MRSE. *Nanomed. Nanotechnol. Biol. Med.* **2009**, *5*, 452–456. [[CrossRef](#)]
194. Lara, H.H.; Ayala-Núñez, N.V.; del Carmen Ixtepan Turrent, L.; Rodríguez Padilla, C. Bactericidal effect of silver nanoparticles against multidrug-resistant bacteria. *World J. Microbiol. Biotechnol.* **2010**, *26*, 615–621. [[CrossRef](#)]
195. Ashraf, N.; Ahmad, F.; Lu, Y.; Yin, D.-C. Bacterial extracellular protein interacts with silver ions to produce protein-encapsulated bactericidal AgNPs. *Process. Biochem.* **2021**, *106*, 120–129. [[CrossRef](#)]
196. Shirzadi-Ahodashi, M.; Mizwari, Z.M.; Hashemi, Z.; Rajabalipour, S.; Ghoreishi, S.M.; Mortazavi-Derazkola, S.; Ebrahimzadeh, M.A. Discovery of high antibacterial and catalytic activities of biosynthesized silver nanoparticles using *C. fruticosus* (CF-AgNPs) against multi-drug resistant clinical strains and hazardous pollutants. *Environ. Technol. Innov.* **2021**, *23*, 101607. [[CrossRef](#)]
197. Gudkov, S.V.; Burmistrov, D.E.; Serov, D.A.; Rebezov, M.B.; Semenova, A.A.; Lisitsyn, A.B. A Mini Review of Antibacterial Properties of ZnO Nanoparticles. *Front. Phys.* **2021**, *9*, 641481. [[CrossRef](#)]
198. Rabani, I.; Lee, S.; Kim, H.; Yoo, J.; Hussain, S.; Maqbool, T.; Seo, Y. Journal of Environmental Chemical Engineering Engineering-safer-by design ZnO nanoparticles incorporated cellulose nanofiber hybrid for high UV protection and low photocatalytic activity with mechanism. *J. Environ. Chem. Eng.* **2021**, *9*, 105845. [[CrossRef](#)]
199. Sevcik, J.; Urbanek, P.; Skoda, D.; Jamatia, T.; Nadazdy, V.; Urbanek, M.; Antos, J.; Munster, L.; Kuritka, I. Materials & Design Energy resolved-electrochemical impedance spectroscopy investigation of the role of Al-doped ZnO nanoparticles in electronic structure modification of polymer nanocomposite LEDs. *Mater. Des.* **2021**, *205*, 109738. [[CrossRef](#)]
200. Bankar, D.B.; Hawaldar, R.R.; Arbuj, S.S.; Shinde, S.T.; Gadde, J.R.; Rakshe, D.S.; Amalnerkar, D.P.; Kanade, K.G. Palladium loaded on ZnO nanoparticles: Synthesis, characterization and application as heterogeneous catalyst for Suzuki–Miyaura cross-coupling reactions under ambient and ligand-free conditions. *Mater. Chem. Phys.* **2019**, *243*, 122561. [[CrossRef](#)]
201. Sathish, P.; Dineshbabu, N.; Ravichandran, K.; Arun, T.; Karuppasamy, P. Combustion synthesis, characterization and antibacterial properties of pristine ZnO and Ga doped ZnO nanoparticles. *Ceram. Int.* **2021**, *47*, 27934–27941. [[CrossRef](#)]
202. Anwar, M.A.; Aqib, A.I.; Ashfaq, K.; Deeba, F.; Khan, M.K.; Khan, S.R.; Muzammil, I.; Shoaib, M.; Naseer, M.A.; Riaz, T.; et al. Antimicrobial resistance modulation of MDR *E. coli* by antibiotic coated ZnO nanoparticles. *Microb. Pathog.* **2020**, *148*, 104450. [[CrossRef](#)] [[PubMed](#)]
203. Prasad, A.R.; Williams, L.; Garvasis, J.; Shamsheera, K.O.; Basheer, S.M.; Kuruvilla, M.; Joseph, A. Applications of phytogetic ZnO nanoparticles: A review on recent advancements. *J. Mol. Liq.* **2021**, *331*, 115805. [[CrossRef](#)]
204. Benitez-salazar, M.I.; Ni, V.E.; Rodríguez-p, J.E.; Caldas-arias, L.; Fern, I. Chemical synthesis versus green synthesis to obtain ZnO powders: Evaluation of the antibacterial capacity of the nanoparticles obtained by the chemical method. *J. Environ. Chem. Eng.* **2021**, *9*, 106544. [[CrossRef](#)]
205. Gold, K.; Slay, B.; Knackstedt, M.; Gaharwar, A.K. Antimicrobial Activity of Metal and Metal-Oxide Based Nanoparticles. *Adv. Ther.* **2018**, *1*, 1700033. [[CrossRef](#)]
206. Saha, R.K.; Debanath, M.K.; Paul, B.; Medhi, S.; Saikia, E. Antibacterial and nonlinear dynamical analysis of flower and hexagon-shaped ZnO microstructures. *Sci. Rep.* **2020**, *10*, 2598. [[CrossRef](#)]
207. Turner, R.J. Metal-based antimicrobial strategies. *Microb. Biotechnol.* **2017**, *10*, 1062–1065. [[CrossRef](#)]
208. Banoee, M.; Seif, S.; Nazari, Z.E.; Jafari-Fesharaki, P.; Shahverdi, H.R.; Moballegheh, A.; Moghaddam, K.M.; Shahverdi, A.R. ZnO nanoparticles enhanced antibacterial activity of ciprofloxacin against *Staphylococcus aureus* and *Escherichia coli*. *J. Biomed. Mater. Res. Part B Appl. Biomater.* **2010**, *93B*, 557–561. [[CrossRef](#)]
209. Patra, P.; Mitra, S.; Debnath, N.; Pramanik, P.; Arunava, G. Ciprofloxacin conjugated zinc oxide nanoparticle: A camouflage towards multidrug resistant bacteria. *Bull. Mater. Sci.* **2014**, *3*, 199–206. [[CrossRef](#)]
210. Zhong, Q.; Tian, J.; Liu, T.; Guo, Z.; Ding, S.; Li, H. Preparation and antibacterial properties of carboxymethyl chitosan/ZnO nanocomposite microspheres with enhanced biocompatibility. *Mater. Lett.* **2018**, *212*, 58–61. [[CrossRef](#)]
211. Eleraky, N.E.; Allam, A.; Hassan, S.B.; Omar, M.M. Nanomedicine Fight against Antibacterial Resistance: An Overview of the Recent Pharmaceutical Innovations. *Pharmaceutics* **2020**, *12*, 142. [[CrossRef](#)]
212. Petros, R.A.; DeSimone, J.M. Strategies in the design of nanoparticles for therapeutic applications. *Nat. Rev. Drug Discov.* **2010**, *9*, 615–627. [[CrossRef](#)] [[PubMed](#)]
213. Pati, R.; Mehta, R.K.; Mohanty, S.; Padhi, A.; Sengupta, M.; Vaseeharan, B.; Goswami, C.; Sonawane, A. Topical application of zinc oxide nanoparticles reduces bacterial skin infection in mice and exhibits antibacterial activity by inducing oxidative stress response and cell membrane disintegration in macrophages. *Nanomed. Nanotechnol. Biol. Med.* **2014**, *10*, 1195–1208. [[CrossRef](#)] [[PubMed](#)]
214. Premanathan, M.; Karthikeyan, K.; Jeyasubramanian, K.; Manivannan, G. Selective toxicity of ZnO nanoparticles toward Gram-positive bacteria and cancer cells by apoptosis through lipid peroxidation. *Nanomed. Nanotechnol. Biol. Med.* **2011**, *7*, 184–192. [[CrossRef](#)]
215. Alex, S.; Tiwari, A. Functionalized gold nanoparticles: Synthesis, properties and applications-A review. *J. Nanosci. Nanotechnol.* **2015**, *15*, 1869–1894. [[CrossRef](#)]
216. Xu, G.; Hou, J.; Zhao, Y.; Bao, J.; Yang, M.; Fa, H.; Yang, Y.; Li, L.; Huo, D.; Hou, C. Dual-signal aptamer sensor based on polydopamine-gold nanoparticles and exonuclease I for ultrasensitive malathion detection. *Sens. Actuators B Chem.* **2019**, 428–436. [[CrossRef](#)]

217. Yang, H.; Xu, W.; Zhou, Y. Signal amplification in immunoassays by using noble metal nanoparticles: A review. *Microchim. Acta* **2019**, *186*, 859. [[CrossRef](#)] [[PubMed](#)]
218. Elbially, N.S.; Fathy, M.M.; Khalil, W.M. Doxorubicin loaded magnetic gold nanoparticles for in vivo targeted drug delivery. *Int. J. Pharm.* **2015**, *490*, 190–199. [[CrossRef](#)]
219. Khandelwal, P.; Singh, D.K.; Poddar, P. Advances in the Experimental and Theoretical Understandings of Antibiotic Conjugated Gold Nanoparticles for Antibacterial Applications. *ChemistrySelect* **2019**, *4*, 6719–6738. [[CrossRef](#)]
220. Mu, H.; Liu, Q.; Niu, H.; Sun, Y.; Duan, J. Gold nanoparticles make chitosan–streptomycin conjugates effective towards Gram-negative bacterial biofilm. *RSC Adv.* **2016**, *6*, 8714–8721. [[CrossRef](#)]
221. Hu, D.; Li, H.; Wang, B.; Ye, Z.; Lei, W.; Jia, F.; Jin, Q.; Ren, K.-F.; Ji, J. Surface-Adaptive Gold Nanoparticles with Effective Adherence and Enhanced Photothermal Ablation of Methicillin-Resistant Staphylococcus aureus Biofilm. *ACS Nano* **2017**, *11*, 9330–9339. [[CrossRef](#)] [[PubMed](#)]
222. Xie, Y.; Liu, Y.; Yang, J.; Liu, Y.; Hu, F.; Zhu, K.; Jiang, X. Gold Nanoclusters for Targeting Methicillin-Resistant Staphylococcus aureus In Vivo. *Angew. Chem. Int. Ed.* **2018**, *57*, 3958–3962. [[CrossRef](#)]
223. Rad, M.R.; Kazemian, H.; Yazdani, F.; Monfared, M.R.Z.; Rahdar, H.; Javadi, A.; Kodori, M. Antibacterial Activity of Gold Nanoparticles Conjugated by Aminoglycosides against *A. baumannii* Isolates from Burn Patients. *Recent Pat. Antiinfect. Drug Discov.* **2019**, *13*, 256–264. [[CrossRef](#)]
224. Khan, F.; Lee, J.-W.; Manivasagan, P.; Pham, D.T.N.; Oh, J.; Kim, Y.-M. Synthesis and characterization of chitosan oligosaccharide-capped gold nanoparticles as an effective antibiofilm drug against the Pseudomonas aeruginosa PAO1. *Microb. Pathog.* **2019**, *135*, 103623. [[CrossRef](#)] [[PubMed](#)]
225. Riaz, S.; Fatima Rana, N.; Hussain, I.; Tanweer, T.; Nawaz, A.; Mena, F.; Janjua, H.A.; Alam, T.; Batool, A.; Naeem, A.; et al. Effect of Flavonoid-Coated Gold Nanoparticles on Bacterial Colonization in Mice Organs. *Nanomaterials* **2020**, *10*, 1769. [[CrossRef](#)] [[PubMed](#)]
226. Stoyanova, A.; Hitkova, H.; Bachvarova-Nedelcheva, A.; Iordanova, R.; Ivanova, N.; Sredkova, M. Synthesis and antibacterial activity of TiO₂/ZnO nanocomposites prepared via nonhydrolytic route. *J. Chem. Technol. Metall.* **2013**, *48*, 154–161.
227. Menazea, A.A.; Awwad, N.S. Antibacterial activity of TiO₂ doped ZnO composite synthesized via laser ablation route for antimicrobial application. *J. Mater. Res. Technol.* **2020**, *9*, 9434–9441. [[CrossRef](#)]
228. Torbat, T.V.; Javanbakht, V. *Fabrication of TiO₂/Zn₂TiO₄/Ag Nanocomposite for Synergic Effects of UV Radiation Protection and Antibacterial Activity in Sunscreen*; Elsevier: Amsterdam, The Netherlands, 2019; ISBN 8415683111.
229. Häffner, S.M.; Parra-ortiz, E.; Skoda, M.W.A.; Saerbeck, T.; Browning, K.L.; Malmsten, M. Composition effects on photooxidative membrane destabilization by TiO₂ nanoparticles. *J. Colloid Interface Sci.* **2021**, *584*, 19–33. [[CrossRef](#)]
230. Huang, Y.-Y.; Rajda, P.J.; Szewczyk, G.; Bhayana, B.; Chiang, L.Y.; Sarna, T.; Hamblin, M.R. Sodium nitrite potentiates antimicrobial photodynamic inactivation: Possible involvement of peroxyxynitrate. *Photochem. Photobiol. Sci.* **2019**, *18*, 505–515. [[CrossRef](#)] [[PubMed](#)]
231. Mohammed, L.; Gomaa, H.G.; Ragab, D.; Zhu, J. Magnetic nanoparticles for environmental and biomedical applications: A review. *Particuology* **2017**, *30*, 1–14. [[CrossRef](#)]
232. Flores-González, M.; Talavera-Rojas, M.; Soriano-Vargas, E.; Rodríguez-González, V. Practical mediated-assembly synthesis of silver nanowires using commercial Camellia sinensis extracts and their antibacterial properties. *New J. Chem.* **2018**, *42*, 2133–2139. [[CrossRef](#)]
233. Davarpanah, A.M.; Rahdar, A.; Dastnae, M.A.; Zeybek, O.; Beyzaei, H. (1-x)BaFe₁₂O₁₉/xCoFe₂O₄ hard/soft magnetic nanocomposites: Synthesis, physical characterization, and antibacterial activities study. *J. Mol. Struct.* **2019**, *1175*, 445–449. [[CrossRef](#)]
234. Madubuonu, N.; Aisida, S.O.; Ali, A.; Ahmad, I.; Zhao, T.; Botha, S.; Maaza, M.; Ezema, F.I. Biosynthesis of iron oxide nanoparticles via a composite of Psidium guajava-Moringa oleifera and their antibacterial and photocatalytic study. *J. Photochem. Photobiol. B Biol.* **2019**, *199*, 111601. [[CrossRef](#)]
235. Khalil, A.T.; Ovais, M.; Ullah, I.; Ali, M.; Shinwari, Z.K.; Maaza, M. Physical properties, biological applications and biocompatibility studies on biosynthesized single phase cobalt oxide (Co₃O₄) nanoparticles via *Sageretia thea* (Osbeck.). *Arab. J. Chem.* **2020**, *13*, 606–619. [[CrossRef](#)]
236. Dogra, V.; Kaur, G.; Jindal, S.; Kumar, R.; Kumar, S.; Singhal, N.K. Bactericidal effects of metallosurfactants based cobalt oxide/hydroxide nanoparticles against Staphylococcus aureus. *Sci. Total Environ.* **2019**, *681*, 350–364. [[CrossRef](#)]
237. Vazquez-Muñoz, R.; Meza-Villezcás, A.; Fournier, P.G.J.; Soria-Castro, E.; Juárez-Moreno, K.; Gallego-Hernández, A.L.; Bogdanchikova, N.; Vazquez-Duhalt, R.; Huerta-Saquero, A. Enhancement of antibiotics antimicrobial activity due to the silver nanoparticles impact on the cell membrane. *PLoS ONE* **2019**, *14*, e0224904. [[CrossRef](#)] [[PubMed](#)]
238. Ipe, D.S.; Kumar, P.T.S.; Love, R.M.; Hamlet, S.M. Silver Nanoparticles at Biocompatible Dosage Synergistically Increases Bacterial Susceptibility to Antibiotics. *Front. Microbiol.* **2020**, *11*, 1074. [[CrossRef](#)] [[PubMed](#)]
239. Thomas, R.; Jishma, P.; Snigdha, S.; Soumya, K.R.; Mathew, J.; Radhakrishnan, E.K. Enhanced antimicrobial efficacy of biosynthesized silver nanoparticle based antibiotic conjugates. *Inorg. Chem. Commun.* **2020**, *117*, 107978. [[CrossRef](#)]
240. Najafi, A.; Khosravian, P.; Validi, M.; Porgham Daryasari, M.; Drees, F.; Gholipour, A. Antimicrobial action of mesoporous silica nanoparticles loaded with cefepime and meropenem separately against multidrug-resistant (MDR) Acinetobacter baumannii. *J. Drug Deliv. Sci. Technol.* **2021**, *65*, 102757. [[CrossRef](#)]

241. Shaker, M.A.; Shaaban, M.I. Formulation of carbapenems loaded gold nanoparticles to combat multi-antibiotic bacterial resistance: In vitro antibacterial study. *Int. J. Pharm.* **2017**, *525*, 71–84. [[CrossRef](#)]
242. Silvero C, M.J.; Rocca, D.M.; de la Villarmois, E.A.; Fournier, K.; Lanterna, A.E.; Perez, M.F.; Becerra, M.C.; Scaiano, J.C. Selective Photoinduced Antibacterial Activity of Amoxicillin-Coated Gold Nanoparticles: From One-Step Synthesis to in Vivo Cytocompatibility. *ACS Omega* **2018**, *3*, 1220–1230. [[CrossRef](#)] [[PubMed](#)]
243. Rocca, D.M.; Silvero, C.M.J.; Aiassa, V.; Cecilia Becerra, M. Rapid and effective photodynamic treatment of biofilm infections using low doses of amoxicillin-coated gold nanoparticles. *Photodiagnosis Photodyn. Ther.* **2020**, *31*, 101811. [[CrossRef](#)] [[PubMed](#)]
244. Fuller, M.; Whiley, H.; Köper, I. Antibiotic delivery using gold nanoparticles. *SN Appl. Sci.* **2020**, *2*, 1022. [[CrossRef](#)]
245. Abdulazeem, L.; Abdalkareem Jasim, S.; Rajab, W.J. Anti-bacterial activity of gold nanoparticles against two type of antibiotic resistance pathogenic bacteria in Al-Hilla city. *Mater. Today Proc.* **2021**, in press. [[CrossRef](#)]
246. Youssef, F.; Farghaly, U.; Abd El-Baky, R.M.; Waly, N. Comparative Study of Antibacterial Effects of Titanium Dioxide Nanoparticles Alone and in Combination with Antibiotics on MDR *Pseudomonas aeruginosa* Strains. *Int. J. Nanomed.* **2020**, *15*, 3393–3404. [[CrossRef](#)]



Article

Hyaluronic Acid Derivative Molecular Weight-Dependent Synthesis and Antimicrobial Effect of Hybrid Silver Nanoparticles

Guillem Ferreres, Sílvia Pérez-Rafael, Juan Torrent-Burgués and Tzanko Tzanov *

Grup de Biotecnologia Molecular i Industrial, Department of Chemical Engineering, Universitat Politècnica de Catalunya, Rambla Sant Nebridi 22, 08222 Terrassa, Spain; guillem.ferreres@upc.edu (G.F.); silvia.perez.rafael@upc.edu (S.P.-R.); juan.torrent@upc.edu (J.T.-B.)

* Correspondence: tzanko.tzanov@upc.edu

Abstract: Silver nanoparticles (Ag NPs) appeared as promising antimicrobial candidates to face the development of antibiotic resistance. Although reported as toxic towards mammalian cells, their combination with biomolecules have shown reduced toxicity, while maintaining the antimicrobial function. Herein, hyaluronic acid (HA) with low (40 kDa), medium (200 and 600 kDa) and high (2 MDa) molecular weight (Mw) was modified with adipic acid dihydrazide (ADH) and used as reducing and capping agents to synthesise antimicrobial hybrid Ag NPs. The Mw of the polymer played a crucial role in the morphology, size and antibacterial activity of the Ag NPs. The 600 and 200 kDa HA-ADH-Ag NPs were able to reduce the *Escherichia coli* and *Staphylococcus aureus* concentration by more than 3 logs, while the 40 kDa NPs reached ~2 logs reduction. The 2 MDa HA-ADH failed to form homogenous NPs with strong bactericidal activity. A mechanistic study of the interaction with a model bacterial membrane using Langmuir isotherms confirmed the greater interaction between bacteria and higher Mw polymers and the effect of the NP's morphology. The nanocomposites low toxicity to human skin cells was demonstrated in vitro, showing more than 90% cell viability after incubation with the NPs.

Keywords: hyaluronic acid; adipic acid dihydrazide; silver nanoparticles; polymer molecular weight; antimicrobial



Citation: Ferreres, G.; Pérez-Rafael, S.; Torrent-Burgués, J.; Tzanov, T. Hyaluronic Acid Derivative Molecular Weight-Dependent Synthesis and Antimicrobial Effect of Hybrid Silver Nanoparticles. *Int. J. Mol. Sci.* **2021**, *22*, 13428. <https://doi.org/10.3390/ijms222413428>

Academic Editors: Monica Terracciano, Ilaria Rea, Nicola Borbone and Chiara Tramontano

Received: 23 November 2021
Accepted: 9 December 2021
Published: 14 December 2021

Publisher's Note: MDPI stays neutral with regard to jurisdictional claims in published maps and institutional affiliations.



Copyright: © 2021 by the authors. Licensee MDPI, Basel, Switzerland. This article is an open access article distributed under the terms and conditions of the Creative Commons Attribution (CC BY) license (<https://creativecommons.org/licenses/by/4.0/>).

1. Introduction

Inefficacy of antibiotics due to the advent of multidrug resistance of pathogens has become a global health emergency, causing complicated infections and even death. Conventional antibiotics have very specific mechanisms of action, which enable the development of resistance associated to single mutations sufficient to counteract the effect of the drug [1,2]. Conversely, metal (silver [3] and copper [4]) and metal oxide (zinc oxide [5]) nanoparticles (NPs), possess multiple antimicrobial mechanisms, comprising membrane disruption, ion release, ROS formation, inactivation of bacterial enzymes and metabolic pathways and damage of pathogen's DNA [6]. Simultaneous and unspecific mechanisms broaden the spectrum of antibacterial activity and hamper the resistance acquisition due to multiple mutations required to overcome the antimicrobial action. Compared to their bulk forms, NPs possess larger surface area to volume ratio allowing stronger interaction with bacterial cell structures, resulting in higher antimicrobial efficiency. Despite the potential of these materials as antimicrobial agents, they have been described as toxic towards mammalian cells [7]. To avoid their intrinsic toxicity these nano-antimicrobials can be combined with biomolecules, for both enhanced biocompatibility [8] and antimicrobial efficacy [9].

Silver is still by far the most extensively used antimicrobial metal for biomedical applications. Biopolymers, such as polysaccharides, have been increasingly employed as natural alternatives to traditional chemical reducing and capping agents for Ag NPs synthesis, providing multiple benefits as: (i) NPs' stabilisers prolonging their shell-life, (ii) protective agents that decrease the NP toxicity to human cells, (iii) enhancers of the antimicrobial

properties of Ag NP and (iv) providers of functional groups allowing immobilisation on solid substrates or further surface functionalisation. Positively charged biopolymers, such as chitosan and aminocellulose, are well-known antimicrobials agents, which interact with bacterial membranes, producing changes in their permeability, homeostasis failure and membrane hydrolysis, ultimately resulting in cell death [10]. Conversely, biopolymers without antimicrobial activity, e.g., hyaluronic acid, enhance the biocompatibility of toxic antimicrobial agents towards mammalian cells [11]. Moreover, their functional groups allow for further modifications to provide additional bioactivities. In the synthesis of metal NPs, these biomacromolecules may serve as reducing agents of the corresponding metal salt to generate stable NPs dispersion [12–14].

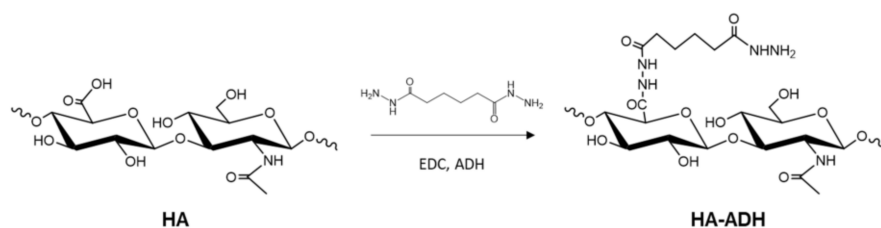
Herein, a hydrazide-modified hyaluronic acid (HA) was synthesised and used for production of antimicrobial silver-enabled nanocomposites. HA is a linear glycosaminoglycan formed by alternating units of β -1,4-linked D-glucuronic acid and β -1-3-linked N-acetyl-D-glucosamine. It is the main structural component of the extracellular matrix involved in signalling processes, inflammation, wound repair and morphogenesis, among others. Furthermore, the biological function of HA is determined by its molecular weight (Mw). For instance, low Mw stimulates inflammation, while higher chain length induce anti-inflammatory response [15]. On the other hand, adipic acid dihydrazide (ADH) is a low toxicity ligand that have been described to form complexes with metal ions such as Ag^+ or Cu^{2+} [16,17].

This study attempts to achieve green synthesis of stable and concentrated dispersions of antimicrobial HA-derivative capped Ag NPs using biopolymer-assisted Ag^+ reduction into Ag NPs. HA was modified with adipic acid dihydrazide (HA-ADH) in order to promote the interaction between silver ions and the biopolymer, and thus enhancing its potential as a reducing and capping agent in the synthesis of Ag NPs. Since little is known on how the polymer Mw influences the NPs synthesis, the size/distribution and antibacterial efficacy of HA-ADH-Ag NPs were studied using HA-derivatives with increasing molecular weight (40, 200, 600 kDa and 2 MDa).

2. Results and Discussion

2.1. Amination of HA

Biopolymers have been widely used to synthesise nanocomposite materials, yielding hybrid structures with a broad range of functionalities and superior performance compared to their individual constituents. In the synthesis of Ag NPs, the biopolymers are involved in both silver ion reduction and capping, thus overcoming the major drawbacks of traditional chemical synthetic methods, such as the use of chemical reducers or high temperature. However, pristine HA is not able to produce metal NPs without these conditions [18,19]. In the current work, the modification of HA with ADH moieties was expected to promote the metal coordination-driven interaction between the silver ions and HA, and enhance the hybrid HA-ADH-Ag NPs formation. The conjugation reaction was performed using 1-ethyl-3-(3-dimethylaminopropyl)carbodiimide (EDC), which activated the carboxylic groups in HA for reacting with the amino groups of ADH (Scheme 1) [20]. In the FTIR spectrum of HA-ADH, compared to unmodified HA, the presence of the signal at 1281 cm^{-1} corresponded to the stretching vibration of C-N bonds from the ADH functional groups. The new amide I (1650 cm^{-1}) and amide II (1535 cm^{-1}) peaks confirmed the presence of the amide groups of ADH [21]. The signal at 3000 cm^{-1} in the pristine HA samples split into two signals in the modified samples due to the stretching vibration of the C-H bonds of ADH. Finally, the subtle change in the shape of the signal at 3300 cm^{-1} could correlate with N-H vibration [16]. These changes were observed in the spectra of the four modified HA samples when compared to their unmodified counterparts, indicating that the ADH-grafting reaction was successful regardless the Mw of HA (Figure 1). The degree of HA amination ($\sim 60\%$), quantified by the trinitrobenzene sulfonic acid (TNBSA) assay, was similar for the low and medium Mw HA samples. On the other hand, the 2 MDa showed slightly lower modification ($\sim 45\%$) (Figure S1).



Scheme 1. Hyaluronic acid modification with adipic acid dihydrazide.

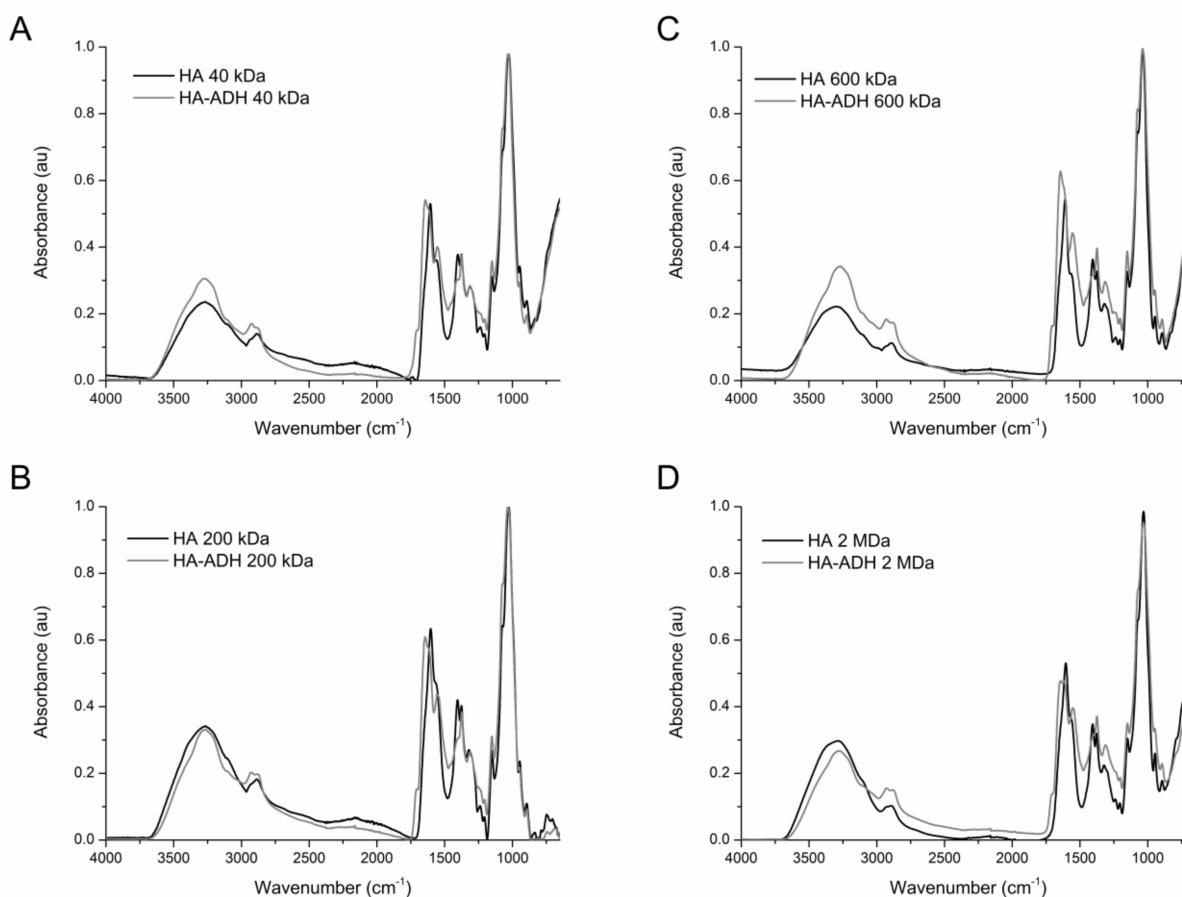


Figure 1. FTIR spectra of pristine and ADH-modified hyaluronic acid: (A) 40 kDa, (B) 200 kDa, (C) 600 kDa and (D) 2 MDa.

2.2. HA-ADH-Ag NPs Characterisation

The synthesis of stable and concentrated dispersion of HA-ADH-Ag NPs were achieved upon mechanical stirring of four different Mw HA-ADH (40, 200, 600 kDa and 2 MDa) solutions with silver nitrate at room temperature for 24 h. In this study, the different polymer molecular weights were used to investigate the effect of the chain length on the NPs size/distribution and their antimicrobial performance. After centrifugation and separation process to remove the unreacted precursors, the NPs dispersions presented turbidity and brownish colour [22]. The Ag NP formation was confirmed by UV-vis spectrophotometry. Unlike the unmodified HA (Figure S2), all the samples prepared with HA-ADH showed absorbance spectra with the characteristic peak of nano-silver at 420 nm (Figure 2) [23]. Besides this, the spectra corresponding to medium Mw polymer (200 and 600 kDa) showed narrower and more intense absorbance peak than the low and high molecular weight counterparts [24]. TEM analysis demonstrated that the Mw of the biopolymer determined the particle size and polydispersity. HA-ADH with 200 and 600 kDa produced uniform spherical HA-ADH-Ag NPs of approximately 18 nm, whereas

the Ag NPs prepared with low Mw (40 kDa) displayed irregular form and heterogeneous size distribution (Figure 3). The nanoparticulate conjugates obtained with 2 MDa HA-ADH were larger (around ~20–40 nm), with irregular forms (images showed spherical, amorphous, oval and triangular morphologies) and higher polydispersity (Figures 3D and S3). The size and polydispersity of hybrid NPs are typically controlled by varying the temperature, reaction time and ratio of the reagents used. Herein, the results indicated that the size and polydispersity of the NPs could be tuned simply by varying the biopolymer Mw. The presence of the hydrophilic biopolymer on the surface of the NPs provided a molecular barrier that acts as a stabiliser for the nanocomposites through steric repulsions, preventing them from agglomeration. As reported, such effect is enhanced by the length of the polymer chain [25–27]. Similarly, higher Mw polyvinyl alcohol and chitosan used as silver reducing agents yielded smaller and more stable Ag NPs than their lower Mw counterparts [28,29]. At the same mass concentration, the HA-ADH solution of low Mw contains more macromolecules than the corresponding solutions of higher Mw biopolymer. Higher HA-ADH molecular concentration might boost the HA-ADH/silver nanostructures aggregation, resulting in larger nanoparticles. It is reported that high Mw HA solutions present pseudo-gel-like behaviour due to polymer chain entanglement [30]. The viscosity of 2 MDa solutions drastically increased compared to the 40, 200 and 600 kDa samples, which may hinder the diffusion of the metal ions through the polymeric matrix, favouring the formation of bigger metal-polymer clusters with irregular shape.

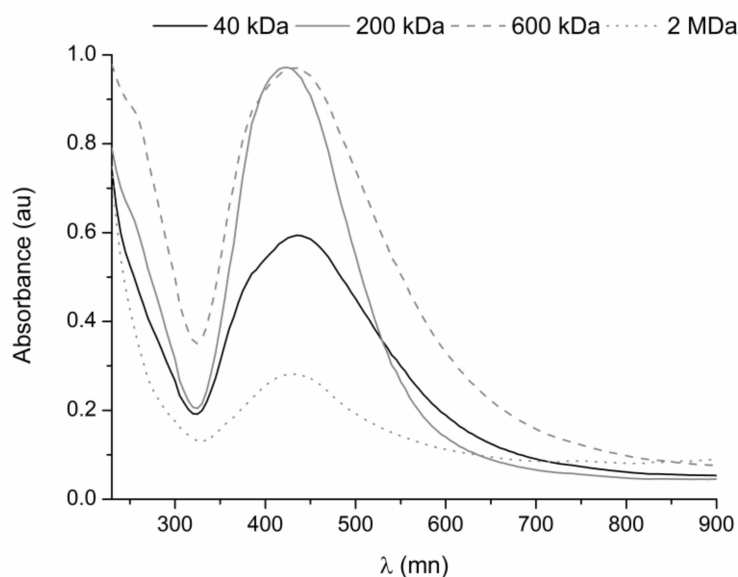


Figure 2. UV-vis spectra of HA-ADH-Ag NPs dispersions synthesised with different Mw HA-ADH derivatives.

2.3. Mechanism of HA-ADH-Ag NPs Formation

Metal ion-biopolymer interaction has been identified as a key factor in the hybrid metal-organic NPs synthesis. Although HA could interact with Ag^+ through glucosidic groups, the unmodified polymer failed to form NPs. Therefore, the capacity of hydrazides to form complexes with metal ions was explored to enhance the interaction of the polymer with Ag^+ during the NPs formation [31,32]. In order to assess the interaction between the silver ions and HA-ADH, the UV-vis spectra of HA-ADH/ Ag^+ mixtures were recorded. The addition of silver salt increased the signal at ~220 nm and shifted it towards longer wavelength, which correlate with a coordination reaction between HA-ADH and Ag^+ (Figures 4A and S4). This interaction makes available and exposes Ag^+ to reduction by the -OH groups in HA, yielding HA-ADH-Ag NPs. The FTIR analysis of the NPs revealed the increase of the following signals in HA-ADH spectrum: at 2859 and 1297 cm^{-1} corresponding to C-H stretching and bending vibration from aldehydes, at 1693 cm^{-1}

assigned to C=O stretching vibration, and at 1420 cm^{-1} corresponding to the increase of carboxylic groups. These changes were observed in the spectra of 200, 40 and 600 kDa (Figures 4B and S5). The same signals appear in HA-ADH treated with sodium periodate (Figure 4B) due to the formation of carbonyl groups by oxidation of C2 and C3 and opening of the glucuronic acid ring of HA [33]. Thus, we hypothesised that the oxidation of HA-ADH during the Ag NPs formation follows a similar pattern.

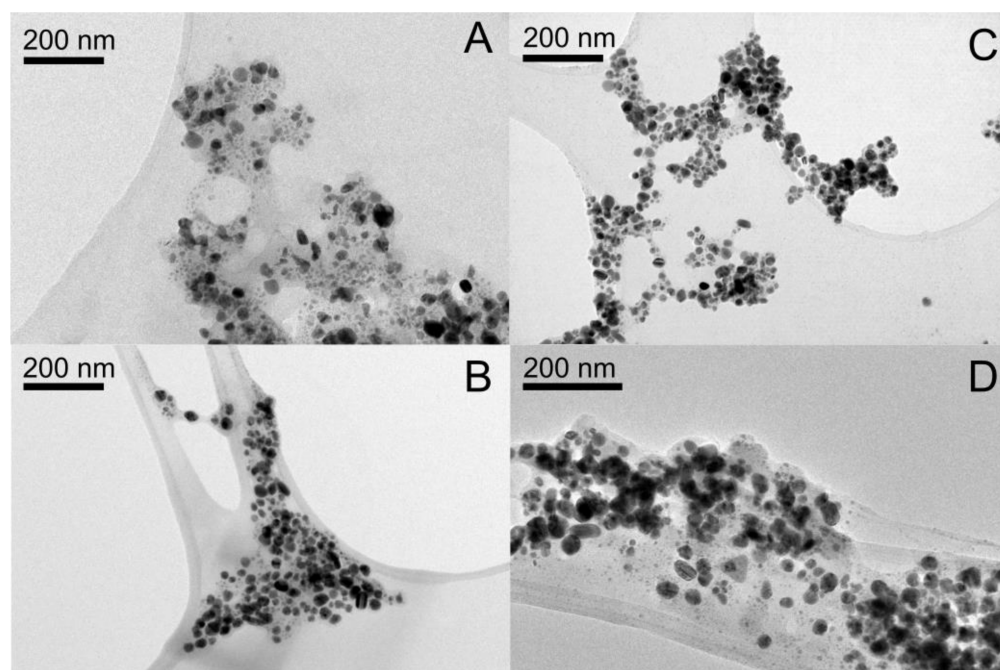


Figure 3. TEM images of HA-ADH-Ag NPs synthesised with (A) 40 kDa, (B) 200 kDa, (C) 600 kDa and (D) 2 MDa.

2.4. Antibacterial Activity of HA-ADH-Ag NPs

The antibacterial efficacy of HA-ADH-Ag NPs were assessed towards two medically relevant bacterial pathogens: the Gram-negative *E. coli* and the Gram-positive *S. aureus*. Biocidal activity of the nanocomposites was expected due to the generation of ROS and release of Ag^+ [34,35]. In order to compare the antibacterial activity of HA-ADH NPs obtained from HA-ADH of different Mw (40, 200, 600 kDa and 2 MDa), each NPs solution was prepared at the same silver concentration. Interestingly, significant differences in the antibacterial performance of the four sets of NPs were observed. At a total silver concentration of 12 ppm, both bacteria were completely eradicated by 40, 200 and 600 kDa HA-ADH-Ag NPs, however, the 2 MDa NPs were only able to reduce ~ 2.5 logs of the bacterial concentration. The NPs of 600 kDa HA-ADH, containing 6 ppm silver, efficiently eradicated both bacteria, while those prepared with 200 kDa HA-ADH at the same silver concentration caused full killing of *E. coli* and 3 logs reduction of *S. aureus* concentration. On the other hand, the HA-ADH-Ag NPs made of 40 kDa HA-ADH at 6 ppm of silver presented lower activity, reducing less than 3 logs the bacterial concentration. Finally, the ones prepared with 2 MDa HA-ADH did not show bactericidal activity at this concentration towards any of the tested bacterial species (Figure 5). Although HA-ADH in bulk form did not display antimicrobial activity, different Mw HA derivatives unexpectedly modulated the antimicrobial activity of the nanocomposite. The impact of the chain length on the antimicrobial activity has been previously described for other biomolecules, such as chitooligosaccharides [36]. On the other hand, the size and shape play a crucial role in the NPs activity. It has been reported that small changes in the size of the particles can affect their antimicrobial potential, generally improving with smaller particle sizes [37,38]. Accord-

ingly, the irregular morphology of the 40 kDa and 2 MDa NPs may reduce their interaction with the bacterial membranes, and therefore, their antimicrobial efficacies [39,40].

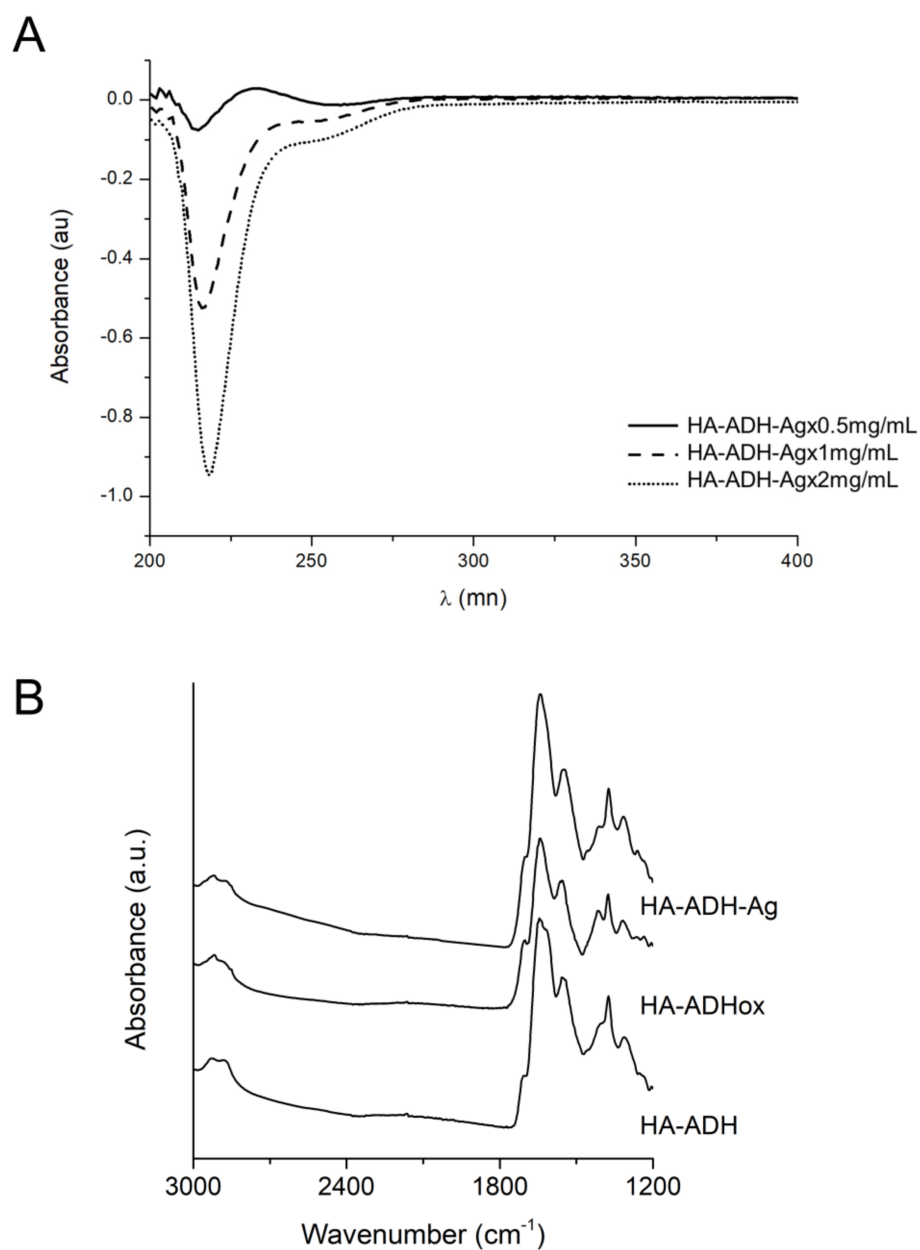


Figure 4. (A) UV-vis spectrum of the HA-ADH subtracted to the spectra of HA-ADH/Ag⁺ mixtures. (B) FTIR spectra of 200 kDa HA-ADH, HA-ADH-Ag NPs and HA-ADH oxidised with sodium periodate (HA-ADHox).

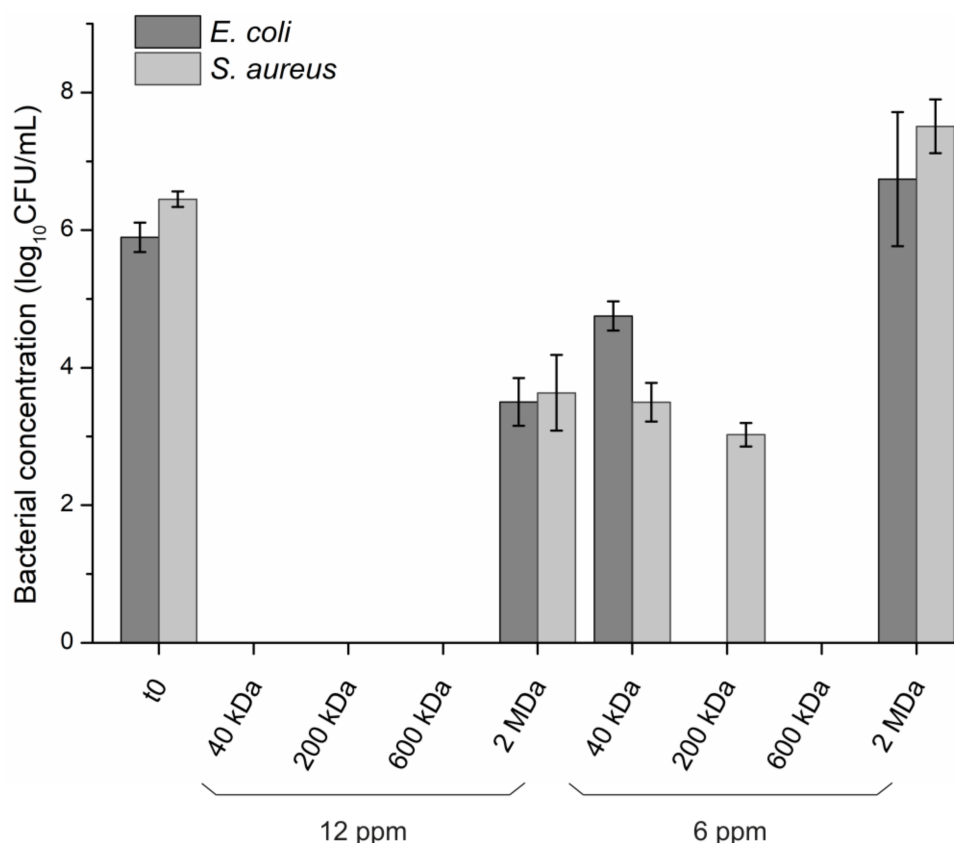


Figure 5. Antimicrobial activity of HA-ADH-Ag NPs synthesised using 40, 200, 600 kDa and 2 MDa HA-ADH towards *E. coli* and *S. aureus*. t₀ indicates the initial bacterial concentration of the test.

2.5. HA-ADH-Ag NPs Interaction with a Bacterial Model Membrane

In order to elucidate the effect of the Mw on the antimicrobial performance of the nanocomposites, the interactions between the HA derivatives and a mimetic Gram-negative bacterial membrane model were studied using Langmuir isotherms. The monolayer was formed using the two main phospholipids of the *E. coli* membrane-phosphatidylethanolamine (PE): phosphatidylglycerol (PG) [41]. Similar to previous studies, the PE:PG π -A isotherm presented a monotonic increase until the collapse pressure (CP) at $\pi \sim 48 \text{ mN}\cdot\text{m}^{-1}$ [42]. As expected, unmodified HA did not produce significant changes in the compression isotherm for *E. coli* model membrane (Figure S6). In contrast, at low lateral pressures ($\pi < 25 \text{ mN}\cdot\text{m}^{-1}$), the addition of HA-ADH and HA-ADH NPs shifted the control PE:PG isotherm (Figure 6A,B, black line) towards higher values of area per molecule. Analogous behaviour has been reported for membrane disturbing biopolymers such as chitosan [43]. The increase of the area observed may be due either to intercalation of the polymer/NPs between the phospholipids chains, or to electrostatic interactions [44]. At $\pi > 25 \text{ mN}\cdot\text{m}^{-1}$, the 40 kDa HA-ADH in bulk and nanoform behave similar to the PE:PG, but presented slightly lower CP. In the case of 200 and 600 kDa HA-ADH in both forms, the initial shift was maintained, increasing the area per molecule, however, the CP was the same as in the PE:PG isotherm. Finally, the highest Mw HA-ADH (2 MDa) promoted the interaction and shifted the position of the isotherm towards higher area per molecule values (Figure 6A). On the other hand, 2 MDa capped Ag NPs did not interact with a detectable affinity with *E. coli* model membrane (Figure 6B).

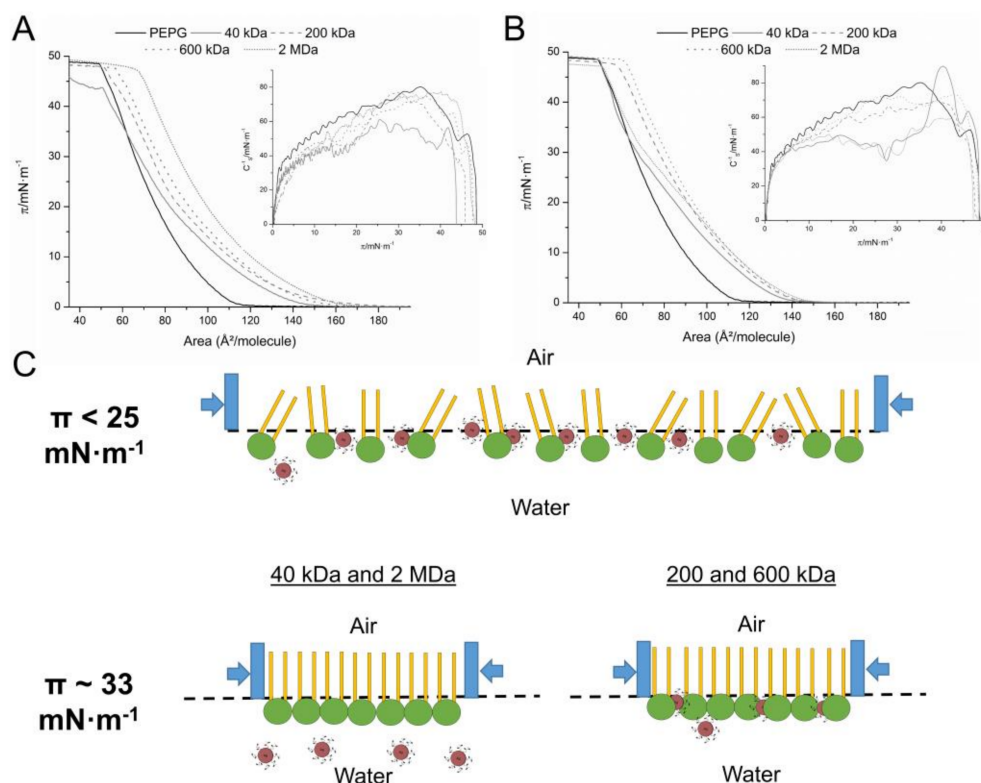


Figure 6. π -A isotherms of a PE:PG 8:2 mix monolayers in PBS subphase (solid black), or with HA-ADH in bulk form (A) or in nano-form (B) of 40 kDa (grey solid), 200 kDa (grey dash), 600 kDa (grey dot) and 2 MDa (grey short dot). Insets: the inverse of the compressibility modulus. (C) Cartoon illustrating the interactions of the HA-ADH-Ag NPs with the model membrane.

The effect of the NPs and biopolymers on the lipid monolayer was measured comparing the area of the isotherms at 33 mN·m⁻¹, corresponding to the physiological membrane pressure [45]. At this pressure, the PE:PG monolayers with PBS, 40 kDa HA-ADH and 40 kDa HA-ADH-Ag NPs presented an area of ~ 63 Å²/molecule, indicating that at this pressure, the 40 kDa samples were not interacting with the model membrane. On the other hand, the 200 kDa and the 600 kDa HA-ADH showed areas of 71 and 74 Å²/molecule in bulk form, and 73 and 78 Å²/molecule in nanoform, respectively. Finally, 2 MDA HA-ADH presented an area of 82.4 Å²/molecule and 65.3 Å²/molecule in NPs form. Despite not having antibacterial activity, the HA-ADH polymer displayed almost a linear area increment (from 63–82.4 Å²/molecule) with higher Mw, which may be correlated with stronger interactions with the bacterial membrane (Figure S7). From low to medium Mw polymer NPs, the interaction with the PE:PG monolayer is clearly enhanced by HA-ADH polymer chain length. In agreement with the antibacterial properties, polymer-capped Ag NPs with higher Mw (600 kDa) presented stronger activity than NPs with similar sizes and morphology (40 and 200 kDa). The drastic interaction loss of the 2 MDA NPs (65.3 Å²/molecule) may be due to the higher size, polydispersity and heterogeneous shape of the NPs. The Langmuir study results showed the contribution of both factors: (i) biopolymer Mw and (ii) NPs size, morphology and polydispersity, in the interaction of the nanocomposite with the bacterial surface.

In the case of the inverse of the compressibility module curves, although the PE:PG monolayer is maintained in a fluid or liquid state, the NPs induced a decrease in the C_s^{-1} values (Figure 6A,B), indicating an increase of the membrane fluidity [46]. As this effect could not be correlated with the antimicrobial-Mw tendency observed in the antimicrobial assay, we assumed that it may not have an important contribution in the antimicrobial mechanism of the NPs.

2.6. Biocompatibility of the HA-ADH-Ag NPs

The unspecific and multiple antimicrobial mechanism of Ag NPs has been reported to cause toxicity towards mammalian cells [47]. Although the HA used in this work has been modified, it did not show any toxicity against human skin cells at a concentration of 0.9% (*w/v*) (Figure S8) [48]. The NPs synthesised with different Mw HA-ADH were tested with fibroblasts (BJ5t α) and keratinocytes (HaCat) at antimicrobial concentration of 6 ppm silver for 24 h. After one day of direct incubation and a further recovery time of 24 h, none of the four HA-ADH-Ag NPs was toxic towards the skin cells, which showed viability higher than 90% (Figure 7A). The fluorescence microscopy images confirmed that the HA-ADH-Ag NPs did not affect the morphology of the human skin cells (Figure 7B).

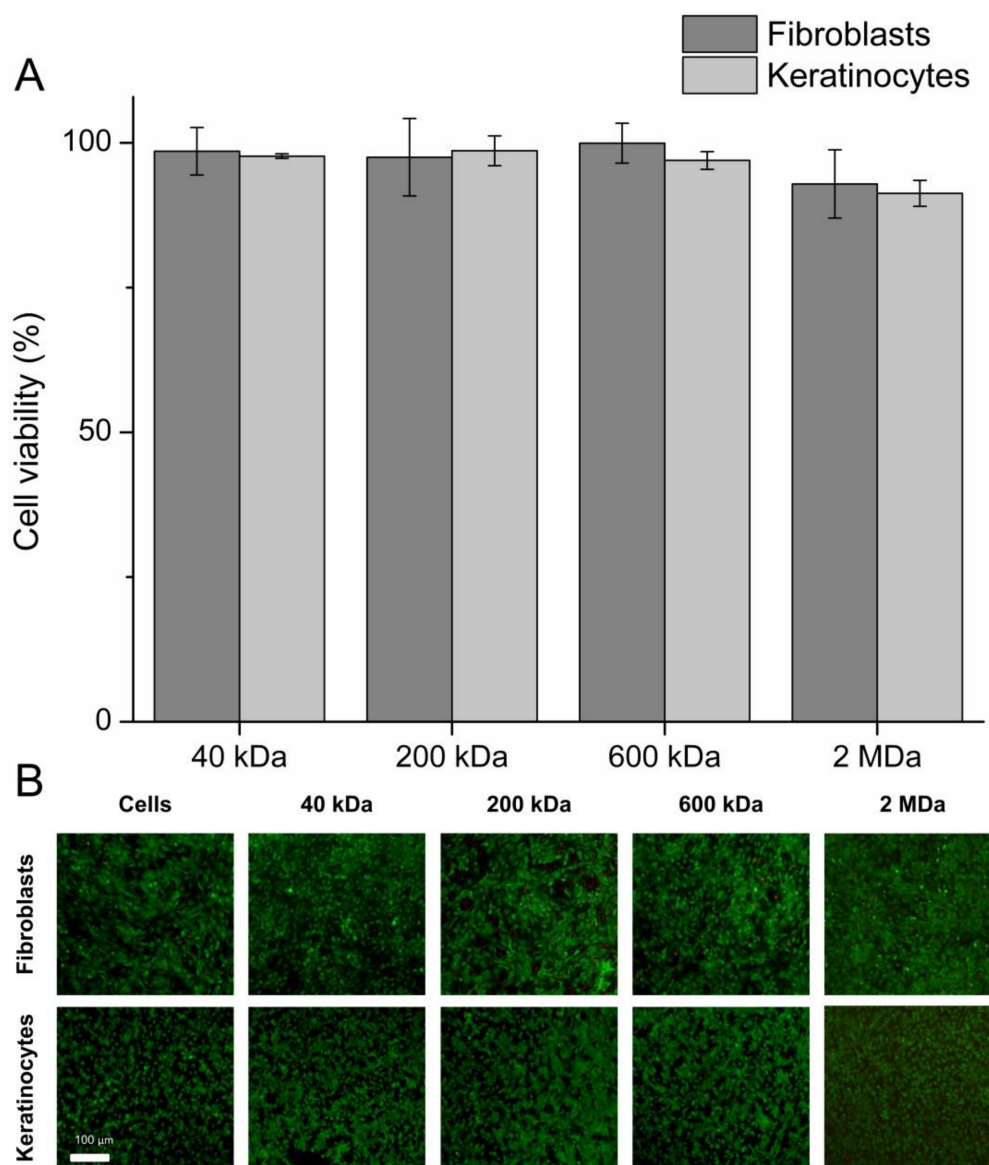


Figure 7. Cytotoxicity of HA-ADH-Ag NPs synthesised using 40, 200, 600 kDa and 2 MDa HA-ADH at 6 ppm of silver content. **(A)** AlamarBlue assay for assessment of the cellular metabolic activity of fibroblast (BJ5t α) and keratinocytes (HaCat) after 24 h incubation with HA-ADH-Ag NPs. **(B)** Fluorescence microscopy images of fibroblasts (BJ5t α) and keratinocytes (HaCat) after 24 h incubation with HA-ADH-Ag NPs. The green (live cells) and red (dead cells) fluorescence images are overlaid in one picture for better comparison.

3. Materials and Methods

3.1. Reagents and Enzymes

Pharmaceutical grade hyaluronic acid (HA) sodium salt from *Streptococcus Equi* (MW = 40, 200, 600 kDa and 2 MDa) was obtained from Lehvoss Iberia (Barcelona, Spain). Silver nitrate, Muller-Hinton Broth (MHB), Coliform ChromoSelect agar, Braid-Parker agar, Dulbecco's modified Eagle's medium—high glucose (DMEM) were supplied by Sigma-Aldrich (Madrid, Spain). Invitrogen Life Technologies Corporation (Sant Cugat del Vallès, Spain) provided the alamarBlue cell viability reagent. Adipic acid dihydrazide (ADH), hydrochloric acid, nitric acid, 1-ethyl-3-(3-dimethylaminopropyl)carbodiimide (EDC) and 2,4,6-trinitrobenzene sulfonic acid (TNBSA) were supplied by Thermo Fischer Scientific (Sant Cugat del Vallès, Spain). Sodium dodecyl sulfate was purchased from Fisher Bioreagent (Madrid, Spain). Bacterial strains *Staphylococcus aureus* (ATCC 25923) and *Escherichia coli* (ATCC 25922), and human fibroblast (ATCC-CRL-4001, BJ-5ta) and keratinocyte (HaCaT cell line) cells were obtained from the American Type Culture Collection (ATCC LGC Standards, Barcelona, Spain).

3.2. Hyaluronic Acid Modification

Four HA Mws (40, 200, 600 kDa and 2 MDa) were modified with adipic acid dihydrazide as previously described [49]. Briefly, each HA was dissolved in MilliQ water at a final concentration of 2.5 mg/mL. When the HA was completely dissolved, adipic acid dihydrazide (ADH) was added in 1:40 (HA:ADH) molar ratio. After 30 min of stirring at room temperature, the pH was adjusted to 4.8 with hydrochloric acid. Subsequently, EDC was added in a molar ratio of 1:4 (HA:EDC). The reaction was performed for 2 h, adjusting the pH every 10 min to 4.8. Then, the HA was dialysed four times with distilled water to remove the unreacted compounds, the first one in 20% (*v/v*) of ethanol, and subsequently freeze it overnight at $-80\text{ }^{\circ}\text{C}$. Thereafter, the HA was freeze-dried for 3 days. The HA modification was assessed through FTIR, performing 64 scans over $4000\text{--}650\text{ cm}^{-1}$ range with PerkinElmer Spectrum 100 (PerkinElmer, Boston, MA, USA). In order to assess the modification degree of the polymer, the TNBSA assay was performed. Briefly, 500 μL of sample and standard solutions were reacted with 250 μL TNBSA solution 0.01% (*w/v*) prepared in 0.1 M sodium bicarbonate buffer pH 8.5. After 2 h of incubation at $37\text{ }^{\circ}\text{C}$, 250 μL of 10% SDS and 125 μL of 1 M HCl were added to each sample to stop the reaction. Finally, 200 μL of all reaction were transferred to a 96-well plate and the absorbance of the solutions was measured at 335 nm.

3.3. Synthesis of NPs

Modified-HA of each Mw was resuspended in water to obtain 1.5% (*w/v*) solution. After complete dissolution, 2 mg/mL silver nitrate was added in a volume ratio of 1.5:1 (HA: silver nitrate) and stirred at 300 rpm for 24 h at room temperature. Since the 2 MDa polymer was not dissolved at a concentration of 1.5% (*w/v*), the HA-ADH solution was prepared at the final concentration of synthesis reaction 0.9% (*w/v*) and the silver salt was added in solid and subsequently the mix was strongly vortexed in order to dissolve the salt. After that, the particles were separated by centrifugation at $18,000\times g$ for 40 min. The particles were washed twice with miliQ water, and finally resuspended in miliQ water.

3.4. Characterisation of the NPs

The study of NPs size and morphology was performed using a JEOL JEM-2100 LaB6 transmission electron microscope (TEM) operating at an accelerating voltage of 200 kV with holey carbon grid.

The NPs were analysed spectrophotometrically over the 230–930 nm range, using a microplate reader Infinite M200 (Tecan, Grödig, Austria) to identify the characteristic absorption peak of nano-silver at 420 nm. The silver content of the HA-ADH-Ag NPs was assessed using ICP. The sample preparation consisted in dissolving the NPs with 20% (*v/v*) nitric acid at $100\text{ }^{\circ}\text{C}$ for 60 min. Thereafter, the volume was completed to 5 mL with

ultrapure water to reach a final concentration of 2% (*v/v*) nitric acid. Then the samples were filtered to remove any remaining solid and the measurement was performed using an ICP-MS 7800 (Agilent Technologies, Madrid, Spain) calibrated by internal standard with ^{45}Rh and a standard curve of ^{107}Ag .

3.5. Mechanism of NPs Formation

HA-ADH and ADH with 0.5, 1 and 2 mg/mL silver nitrate were analysed spectrophotometrically using a Varian Cary 100 Bio spectrophotometer (Varian, Belrose, Australia) over a wavelength range of 200 to 400 nm in 1 cm quartz cuvettes. The HA-ADH-Ag NPs were lyophilised and compared to the HA-ADH by FTIR, performing 64 scans over the 4000–650 cm^{-1} range with PerkinElmer Spectrum 100 (PerkinElmer, Boston, MA, USA).

3.6. Antibacterial Activity of HA-ADH-Ag NPs

The antibacterial activity of the HA-ADH-Ag NPs was assessed towards *Escherichia coli* and *Staphylococcus aureus*. The NPs solutions at different concentrations were mixed with 50 μL bacterial inoculum at optical density (OD) at $\lambda = 600 \text{ nm}$ $\text{OD}_{600} = 0.01$ ($\sim 10^5$ – 10^6 colony forming units (CFU) mL^{-1}) in a 96-well polystyrene plates. The samples were incubated for 24 h at 37 °C with shaking at 230 rpm. A microplate reader was used to assess the bacterial growth in presence of the NPs measuring at 600 nm (OD_{600}). Samples without turbidity ($\text{OD}_{600} \sim 0$) were considered antibacterial. Afterwards, the number of survived CFU was assessed by plating 10 μL of the suspensions onto coliform Agar for *E. coli* and Braid Parker Agar for *S. aureus*. The agar plates were incubated for 24 h at 37 °C and counted. All results are reported as mean value \pm standard deviation ($n = 3$).

3.7. Langmuir Experiments

The capacity of the modified HA and NPs to interact with a model Gram-negative membrane was studied under biomimetic conditions by means of the Langmuir technique. Monolayers of phosphatidylethanolamine (PE): phosphatidylglycerol (PG) in a ratio of 8:2, using subphases with PBS, PBS + HA-ADH and PBS + NPs, were formed in a Langmuir trough (KSV NIMA Langmuir–Blodgett Deposition Troughs, model KN2002, Finland) equipped with two mobile barriers mounted on an antivibration table, housed in an insulation box at 23 ± 1 °C. The surface pressure (π) was measured using a Wilhelmy plate connected to the trough. The system was cleaned twice with chloroform and several times with water until the pristine subphase confirmed the cleanliness of the system. The experiments were performed with a barrier closing rate of $15 \text{ cm}^2 \cdot \text{min}^{-1}$. The subphases were prepared using 100 mM PBS at pH 7.4 and 0.05% (*w/v*) of HA-ADH, and the NPs samples were normalised regarding the HA-ADH content determined by TNBSA. After the establishment of the subphases, 30 μL of the phospholipid mixture at a concentration of 0.5 mg/mL dissolved in chloroform was gently added on the surface of the subphase. The recording of the surface pressure-area per molecule (π -A) isotherm started after 10 min of lagging for complete chloroform evaporation. All the experiments were carried out at least three times. The physical states of the monolayers were estimated by the inverse of the compressibility modulus C_s^{-1} that is obtained from the π -A isotherms calculated according to the following equation, where A is the mean area per molecule ($\text{\AA}^2 \cdot \text{molecule}^{-1}$), π the surface pressure ($\text{mN} \cdot \text{m}^{-1}$) and T the absolute temperature (K):

$$C_s^{-1} = -A \left(\frac{d\pi}{dA} \right)_T$$

3.8. Biocompatibility of the HA-ADH-Ag NPs

Human fibroblast cell line BJ5t α and human keratinocytes cell line HaCaT were used to determine the toxicity of the hybrid NPs towards mammalian cells as previously described. NPs suspensions were put in contact with the previously cultured in a 96-well plate (6×10^4 cells per plate) cells, and after 24 h the particles were removed and the cells

were let for 24 h to recover. Thereafter, the number of viable cells was detected using alamarBlue assay kit. All results are reported as mean value \pm standard deviation ($n = 3$). In parallel, 20 μ L of a PBS solution containing 0.1% (v/v) of calcein AM and 0.1% (v/v) of ethidium homodimer-1 were added to each well and the cells were stained for 15 min in the dark. The stained cells were observed using a fluorescence microscope (Nikon/Eclipse Ti-S, Amstelveen, The Netherlands), the stained live cells are displayed in green and the dead cells in red.

4. Conclusions

Silver NPs have been postulated as a powerful tool against the rising drug-resistant bacteria. In this work, we developed a safe to human cells antimicrobial nanocomposite through reduction of silver nitrate with HA-ADH of increasing Mw. The adipic acid-modified polymer was not only used as a silver reducing agent to obtain Ag NPs, but also stabilised the NP dispersion, decreased the NPs toxicity to human cells and enhanced their antimicrobial efficacy. TEM analysis revealed that the Mw of the biopolymer determined the size, morphology and polydispersity of the NPs, being the ones produced with medium molecular weight polymer (600 and 200 kDa) smaller and less polydisperse than those produced with 40 kDa or 2 MDa HA-ADH. The hybrid HA-ADH-Ag NPs showed strong antimicrobial effect towards the planktonic form of Gram-negative *E. coli* and Gram-positive *S. aureus* without affecting the viability of fibroblast and keratinocytes cells. Mw-related antimicrobial activity of the HA derivatives and developed nanocomposites was studied through Langmuir isotherms. Interestingly, higher Mw of HA-ADH in bulk form, presented greater interaction with a model bacterial membrane. The Langmuir characterisation of NPs-*E. coli* model membrane interaction also showed correlation with their antimicrobial activity. At physiological membrane pressure, 200 and 600 kDa HA-ADH-Ag NPs displayed the strongest interaction, followed by 2 MDa and 40 kDa. From low to medium Mw HA-ADH-generated NPs, the antibacterial capacity is clearly influenced by higher polymer Mw. On the contrary, although strong effect of 2 MDa HA-ADH in bulk form was observed in the Langmuir isotherm, the low interaction of the corresponding NPs, being larger and irregular in shape, with the model membrane confirmed the role of the NP size/morphology in their antimicrobial activity. Thus, the polymer Mw not only determines the NPs synthesis outcomes in terms of size, stability and dispersity, but also endowed them with the ability to interact with the bacterial membrane conferring enhanced antibacterial activity.

Supplementary Materials: The following are available online at <https://www.mdpi.com/article/10.3390/ijms222413428/s1>.

Author Contributions: G.F.: NPs synthesis and characterization, Langmuir data acquisition and analysis, manuscript writing. S.P.-R.: experiments design, polymer modification and characterization, data acquisition, analysis, manuscript writing, figure design. J.T.-B.: Langmuir experiments design and analysis, manuscript writing. T.T.: experiments design, manuscript writing and revision, project administration, funding acquisition. All authors have read and agreed to the published version of the manuscript.

Funding: This research was funded by the European project PROTECT—Pre-commercial lines for production of surface nanostructured antimicrobial and anti-biofilm textiles, medical devices and water treatment membranes (H2020—720851). G.F. acknowledges Universitat Politècnica de Catalunya and Banco Santander for his PhD grant (113 FPI-UPC 2018).

Institutional Review Board Statement: Not applicable.

Informed Consent Statement: Not applicable.

Data Availability Statement: All data generated or analysed during this study are included in this manuscript and its supplementary information files.

Conflicts of Interest: The authors declare no conflict of interest.

References

- Woodford, N.; Ellington, M.J. The Emergence of Antibiotic Resistance by Mutation. *Clin. Microbiol. Infect.* **2007**, *13*, 5–18. [[CrossRef](#)] [[PubMed](#)]
- Albrich, W.C.; Monnet, D.L.; Harbarth, S. Antibiotic Selection Pressure and Resistance in Streptococcus Pneumoniae and Streptococcus Pyogenes. *Emerg. Infect. Dis.* **2004**, *10*, 514–517. [[CrossRef](#)]
- Raffi, M.; Akhter, J.I.; Hamed, A.; Hassan, M.U. Antibacterial Characterization of Silver Nanoparticles against E.Coli ATCC-15224. *J. Mater. Sci. Technol.* **2008**, *24*, 192–196.
- Raffi, M.; Mehrwan, S.; Bhatti, T.M.; Akhter, J.I.; Hameed, A.; Yawar, W.; Ul Hasan, M.M. Investigations into the Antibacterial Behavior of Copper Nanoparticles against *Escherichia coli*. *Ann. Microbiol.* **2010**, *60*, 75–80. [[CrossRef](#)]
- Xie, Y.; He, Y.; Irwin, P.L.; Jin, T.; Shi, X. Antibacterial Activity and Mechanism of Action of Zinc Oxide Nanoparticles against *Campylobacter Jejuni*. *Appl. Environ. Microbiol.* **2011**, *77*, 2325–2331. [[CrossRef](#)]
- Slavin, Y.N.; Asnis, J.; Häfeli, U.O.; Bach, H. Metal Nanoparticles: Understanding the Mechanisms behind Antibacterial Activity. *J. Nanobiotechnol.* **2017**, *15*, 1–20. [[CrossRef](#)] [[PubMed](#)]
- Karlsson, H.L.; Cronholm, P.; Gustafsson, J.; Möller, L. Copper Oxide Nanoparticles Are Highly Toxic: A Comparison between Metal Oxide Nanoparticles and Carbon Nanotubes. *Chem. Res. Toxicol.* **2008**, *21*, 1726–1732. [[CrossRef](#)]
- Cao, X.L.; Cheng, C.; Ma, Y.L.; Zhao, C.S. Preparation of Silver Nanoparticles with Antimicrobial Activities and the Researches of Their Biocompatibilities. *J. Mater. Sci. Mater. Med.* **2010**, *21*, 2861–2868. [[CrossRef](#)]
- Ferreres, G.; Bassegoda, A.; Hoyo, J.; Torrent-Burgués, J.; Tzanov, T. Metal-Enzyme Nanoaggregates Eradicate Both Gram-Positive and Gram-Negative Bacteria and Their Biofilms. *ACS Appl. Mater. Interfaces* **2018**, *10*, 40434–40442. [[CrossRef](#)]
- Shahidi, F.; Arachchi, J.K.V.; Jeon, Y.-J. Food Applications of Chitin and Chitosans. *Trend Food Sci. Technol.* **1999**, *10*, 37–51. [[CrossRef](#)]
- Karakocak, B.B.; Iang, J.; Biswas, P.; Ravi, N. Hyaluronate Coating Enhances the Delivery and Biocompatibility of Gold Nanoparticles. *Carbohydr. Polym.* **2019**, *186*, 243–251. [[CrossRef](#)]
- Rahme, K.; Chen, L.; Hobbs, R.G.; Morris, M.A.; O'Driscoll, C.; Holmes, J.D. PEGylated Gold Nanoparticles: Polymer Quantification as a Function of PEG Lengths and Nanoparticle Dimensions. *RSC Adv.* **2013**, *3*, 6085–6094. [[CrossRef](#)]
- Francesco, A.; Cano Fossas, M.; Petkova, P.; Fernandes, M.M.; Mendoza, E.; Tzanov, T. Sonochemical Synthesis and Stabilization of Concentrated Antimicrobial Silver-Chitosan Nanoparticle Dispersions. *J. Appl. Polym. Sci.* **2017**, *134*, 1–8. [[CrossRef](#)]
- Zain, N.M.; Stapley, A.G.F.; Shama, G. Green Synthesis of Silver and Copper Nanoparticles Using Ascorbic Acid and Chitosan for Antimicrobial Applications. *Carbohydr. Polym.* **2014**, *112*, 195–202. [[CrossRef](#)] [[PubMed](#)]
- Dovedytis, M.; Liu, Z.J.; Bartlett, S. Hyaluronic Acid and Its Biomedical Applications: A Review. *Eng. Regen.* **2020**, *1*, 102–113. [[CrossRef](#)]
- Zheng, E.; Dang, Q.; Liu, C.; Fan, B.; Yan, J.; Yu, Z.; Zhang, H. Preparation and Evaluation of Adipic Acid Dihydrazide Cross-Linked Carboxymethyl Chitosan Microspheres for Copper Ion Adsorption. *Colloids Surf. A Physicochem. Eng. Asp.* **2016**, *502*, 34–43. [[CrossRef](#)]
- Jeragh, B.; El-Asmy, A.A. Structure and Spectroscopic Studies of Homo-and Heterometallic Complexes of Adipic Acid Dihydrazide. *Spectrochim. Acta—Part A Mol. Biomol. Spectrosc.* **2014**, *125*, 25–35. [[CrossRef](#)] [[PubMed](#)]
- Zhang, X.; Yao, M.; Chen, M.; Li, L.; Dong, C.; Hou, Y.; Zhao, H.; Jia, B.; Wang, F. Hyaluronic Acid-Coated Silver Nanoparticles As a Nanoplatform for in Vivo Imaging Applications. *ACS Appl. Mater. Interfaces* **2016**, *8*, 25650–25653. [[CrossRef](#)]
- Lee, M.-Y.; Yang, J.-A.; Sang Jung, H.; Songeun, B.; Eun, C.J.; Wonhee, H.; Koo, H.; Kwangmeyung, K.; Kew, Y.S.; Hahn, S.K. Hyaluronic Acid-Gold Nanoparticle / Interferon α Complex for Targeted Treatment of Hepatitis C Virus. *ACS Nano* **2012**, *6*, 9522–9531. [[CrossRef](#)]
- Park, S.N.; Lee, H.J.; Lee, K.H.; Suh, H. Biological Characterization of EDC-Crosslinked Collagen-Hyaluronic Acid Matrix in Dermal Tissue Restoration. *Biomaterials* **2003**, *24*, 1631–1641. [[CrossRef](#)]
- Zhang, L.; Xiao, Y.; Jiang, B.; Fan, H.; Zhang, X. Effect of Adipic Dihydrazide Modification on the Performance of Collagen/Hyaluronic Acid Scaffold. *J. Biomed. Mater. Res.—Part B Appl. Biomater.* **2010**, *92*, 307–316. [[CrossRef](#)]
- Goia, D.V. Preparation and Formation Mechanisms of Uniform Metallic Particles in Homogeneous Solutions. *J. Mater. Chem.* **2004**, *14*, 451–458. [[CrossRef](#)]
- Smitha, S.L.; Nissamudeen, K.M.; Philip, D.; Gopchandran, K.G. Studies on Surface Plasmon Resonance and Photoluminescence of Silver Nanoparticles. *Spectrochim. Acta—Part A Mol. Biomol. Spectrosc.* **2008**, *71*, 186–190. [[CrossRef](#)]
- Schaadt, D.M.; Feng, B.; Yu, E.T. Enhanced Semiconductor Optical Absorption via Surface Plasmon Excitation in Metal Nanoparticles. *Appl. Phys. Lett.* **2008**, *86*, 063106. [[CrossRef](#)]
- Yin, B.; Ma, H.; Wang, S.; Chen, S. Electrochemical Synthesis of Silver Nanoparticles under Protection of Poly(N-Vinylpyrrolidone). *J. Phys. Chem. B* **2003**, *107*, 8898–8904. [[CrossRef](#)]
- Elbasuney, S. Sustainable Steric Stabilization of Colloidal Titania Nanoparticles. *Appl. Surf. Sci.* **2017**, *409*, 438–447. [[CrossRef](#)]
- Kvítek, L.; Panáček, A.; Soukupová, J.; Kolář, M.; Večeřová, R.; Prucek, R.; Holecová, M.; Zbořil, R. Effect of Surfactants and Polymers on Stability and Antibacterial Activity of Silver Nanoparticles (NPs). *J. Phys. Chem. C* **2008**, *112*, 5825–5834. [[CrossRef](#)]
- Van Phu, D.; Thi, V.; Lang, K.; Thi, N.; Lan, K.; Duy, N.N.; Chau, N.D.; Du, B.D.; Cam, B.D.; Hien, N.Q. Synthesis and Antimicrobial Effects of Colloidal Silver Nanoparticles in Chitosan by γ -Irradiation. *J. Exp. Nanosci.* **2010**, *5*, 169–179.

29. Temgire, M.K.; Joshi, S.S. Optical and Structural Studies of Silver Nanoparticles. *Radiat. Phys. Chem.* **2004**, *71*, 1039–1044. [[CrossRef](#)]
30. Snetkov, P.; Zakharova, K.; Morozkina, S.; Olekhovich, R. Hyaluronic Acid : The Influence of Molecular Weight and Degradable Properties of Biopolymer. *Polymers* **2020**, *12*, 1800. [[CrossRef](#)] [[PubMed](#)]
31. Vujčić, M.; Lazić, M.; Milenković, M.; Sladić, D.; Radulović, S.; Filipović, N.; Anđelković, K. A Comparative Study of DNA Binding and Cell Cycle Phase Perturbation by the Dinuclear Complex of Cd(II) with the Condensation Product of 2-Acetylpyridine and Malonic Acid Dihydrazide N',N' 2-Bis[(1E)-1-(2-Pyridyl)Ethylidene]Propanedihydrazide. *J. Biochem. Mol. Toxicol.* **2011**, *25*, 175–182. [[CrossRef](#)]
32. De Souza, G.D.; Rodrigues, M.A.; Fernandes, L.E.; Silva, P.P.; Ruggiero, R.; Pereira-Maia, E.C.; Guerra, W. Complexes of Platinum and Palladium with 4-Nitrobenzoic Hydrazide: Synthesis and Cytotoxic Activity. *Cent. Eur. J. Chem.* **2013**, *11*, 290–294. [[CrossRef](#)]
33. Su, W.Y.; Chen, Y.C.; Lin, F.H. Injectable Oxidized Hyaluronic Acid/Adipic Acid Dihydrazide Hydrogel for Nucleus Pulposus Regeneration. *Acta Biomater.* **2010**, *6*, 3044–3055. [[CrossRef](#)]
34. Rai, M.K.; Deshmukh, S.D.; Ingle, A.P.; Gade, A.K. Silver Nanoparticles: The Powerful Nanoweapon against Multidrug-Resistant Bacteria. *J. Appl. Microbiol.* **2012**, *112*, 841–852. [[CrossRef](#)] [[PubMed](#)]
35. Kandi, V.; Kandi, S. Antimicrobial Properties of Nanomolecules: Potential Candidates as Antibiotics in the Era of Multi-Drug Resistance. *Epidemiol. Health* **2015**, *37*, e2015020. [[CrossRef](#)] [[PubMed](#)]
36. Jeon, Y.J.; Park, P.J.; Kim, S.K. Antimicrobial Effect of Chitooligosaccharides Produced by Bioreactor. *Carbohydr. Polym.* **2001**, *44*, 71–76. [[CrossRef](#)]
37. Pal, S.; Tak, Y.K.; Song, J.M. Does the Antibacterial Activity of Silver Nanoparticles Depend on the Shape of the Nanoparticle? A Study of the Gram-Negative Bacterium Escherichia Coli. *Appl. Environ. Microbiol.* **2007**, *73*, 1712–1720. [[CrossRef](#)]
38. Adams, C.P.; Walker, K.A.; Obare, S.O.; Docherty, K.M. Size-Dependent Antimicrobial Effects of Novel Palladium Nanoparticles. *PLoS ONE* **2014**, *9*, e85981. [[CrossRef](#)]
39. Wani, I.A.; Ahmad, T. Size and Shape Dependant Antifungal Activity of Gold Nanoparticles: A Case Study of Candida. *Colloids Surf. B Biointerfaces* **2013**, *101*, 162–170. [[CrossRef](#)]
40. Linklater, D.P.; Baulin, V.A.; Le Guével, X.; Fleury, J.B.; Hanssen, E.; Nguyen, T.H.P.; Juodkazis, S.; Bryant, G.; Crawford, R.J.; Stoodley, P.; et al. Antibacterial Action of Nanoparticles by Lethal Stretching of Bacterial Cell Membranes. *Adv. Mater.* **2020**, *32*, 1–15. [[CrossRef](#)]
41. Morein, S.; Andersson, A.; Rilfors, L. Wild-Type Escherichia Coli Cells Regulate the Membrane Lipid Composition in a Window between Gel and Non-Lamellar Structures. *J. Biol. Chem.* **1996**, *271*, 6801–6809. [[CrossRef](#)] [[PubMed](#)]
42. Hoyo, J.; Torrent-burgués, J.; Tzanov, T. Physical States and Thermodynamic Properties of Model Gram-Negative Bacterial Inner Membranes. *Chem. Phys. Lipids* **2019**, *218*, 57–64. [[CrossRef](#)]
43. Fernandes, M.M.; Francesko, A.; Torrent-burgués, J.; Tzanov, T. Effect of Thiol-Functionalisation on Chitosan Antibacterial Activity : Interaction with a Bacterial Membrane Model. *React. Funct. Polym.* **2013**, *73*, 1384–1390. [[CrossRef](#)]
44. Ładniak, A.; Jurak, M.; Ewa, A. Langmuir Monolayer Study of Phospholipid DPPC on the Titanium Dioxide—Chitosan—Hyaluronic Acid Subphases. *Adsorption* **2019**, *25*, 469–476. [[CrossRef](#)]
45. Raju, R.; Torrent-burgués, J.; Bryant, G. Interactions of Cryoprotective Agents with Phospholipid Membranes—A Langmuir Monolayer Study. *Chem. Phys. Lipids* **2020**, *231*, 104949. [[CrossRef](#)]
46. Fernandes, M.M.; Francesko, A.; Torrent-burgués, J.; Carrio, F.J.; Heinze, T.; Tzanov, T. Sonochemically Processed Cationic Nanocapsules: Efficient Antimicrobials with Membrane Disturbing Capacity. *Biomacromolecules* **2014**, *15*, 1365–1374. [[CrossRef](#)] [[PubMed](#)]
47. Beer, C.; Foldbjerg, R.; Hayashi, Y.; Sutherland, D.S.; Autrup, H. Toxicity of Silver Nanoparticles—Nanoparticle or Silver Ion ? *Toxicol. Lett.* **2012**, *208*, 286–292. [[CrossRef](#)]
48. Rampersad, S.N. Multiple Applications of Alamar Blue as an Indicator of Metabolic Function and Cellular Health in Cell Viability Bioassays. *Sensors* **2012**, *12*, 12347–12360. [[CrossRef](#)] [[PubMed](#)]
49. Kwang, S.; Kyu, J.; Tomimatsu, T.; Shimoboji, T. Synthesis and Degradation Test of Hyaluronic Acid Hydrogels. *Int. J. Biol. Macromol.* **2007**, *40*, 374–380.



Article

Thymoquinone-Loaded Chitosan Nanoparticles as Natural Preservative Agent in Cosmetic Products

María Mondéjar-López ¹, Alberto José López-Jiménez ¹, Joaquín C. García Martínez ^{2,3} , Oussama Ahrazem ¹ , Lourdes Gómez-Gómez ¹ and Enrique Niza ^{1,*}

¹ Instituto Botánico, Departamento de Ciencia y Tecnología Agroforestal y Genética, Universidad de Castilla-La Mancha, Campus Universitario s/n, 02071 Albacete, Spain; maria.mondejar3@alu.uclm.es (M.M.-L.); alberto.jose.lopez@uclm.es (A.J.L.-J.); Oussama.ahrazem@uclm.es (O.A.); MariaLourdes.gomez@uclm.es (L.G.-G.)

² Departamento de Química Inorgánica, Orgánica y Bioquímica, Facultad de Farmacia, Universidad de Castilla-La Mancha, C/José María Sánchez Ibáñez s/n, 02008 Albacete, Spain; Joaquin.c.garcia@uclm.es

³ Regional Center for Biomedical Research (CRIB), Universidad de Castilla-La Mancha, C/Almansa 13, 02008 Albacete, Spain

* Correspondence: enrique.niza@uclm.es

Abstract: The current status of controversy regarding the use of certain preservatives in cosmetic products makes it necessary to seek new ecological alternatives that are free of adverse effects on users. In our study, the natural terpene thymoquinone was encapsulated in chitosan nanoparticles. The nanoparticles were characterized by DLS and TEM, showing a particle size of 20 nm. The chemical structure, thermal properties, and release profile of thymoquinone were evaluated and showed a successful stabilization and sustained release of terpenes. The antimicrobial properties of the nanoparticles were evaluated against typical microbial contaminants found in cosmetic products, showing high antimicrobial properties. Furthermore, natural moisturizing cream inoculated with the aforementioned microorganisms was formulated with thymoquinone-chitosan nanoparticles to evaluate the preservative efficiency, indicating its promising use as a preservative in cosmetics.

Keywords: nanotechnology; cosmetic; chitosan; essential oils; antimicrobial; preservative agents; nanoparticles



Citation: Mondéjar-López, M.; López-Jiménez, A.J.; Martínez, J.C.G.; Ahrazem, O.; Gómez-Gómez, L.; Niza, E. Thymoquinone-Loaded Chitosan Nanoparticles as Natural Preservative Agent in Cosmetic Products. *Int. J. Mol. Sci.* **2022**, *23*, 898. <https://doi.org/10.3390/ijms23020898>

Academic Editors: Monica Terracciano, Ilaria Rea, Nicola Borbone and Chiara Tramontano

Received: 23 December 2021

Accepted: 13 January 2022

Published: 14 January 2022

Publisher's Note: MDPI stays neutral with regard to jurisdictional claims in published maps and institutional affiliations.



Copyright: © 2022 by the authors. Licensee MDPI, Basel, Switzerland. This article is an open access article distributed under the terms and conditions of the Creative Commons Attribution (CC BY) license (<https://creativecommons.org/licenses/by/4.0/>).

1. Introduction

Microorganism contaminants are one of the most usual causes of alteration in cosmetic products (CPs) due to over-exposition to atmospheric oxygen [1]. When the CPs are opened for daily use, the microorganisms present in the atmosphere make contact with the cosmetic formulation, producing problems such as the appearance of mold, separation of phases of the emulsions, loss of viscosity, change in aroma, or rancidity of fats [2]. Moreover, the presence of pathogenic microorganisms in CPs has been associated with the development of some adverse effects, such as dermatitis, irritation, or peeling as well as conjunctivitis, asthma, urticaria, angioedema, or pneumonia [3].

The rising CP market, which is projected to reach \$429.8 billion by 2022, is linked to an increased consumption of long shelf-life products. The cosmetic industry uses several compounds to prolong the period of use in cosmetics. One of the most common approaches is the incorporation of preservative agents, i.e., substances that inhibit the growth of microorganisms and counteract the generation of reactive oxygen species and oxidation processes [4]. Some cosmetic preservatives such as parabens, triclosan, benzalkonium chloride, formaldehyde, phenoxyethanol, and chlorphenesin produce adverse effects in humans such as DNA damage, antiandrogenic activity, cytotoxicity and genotoxic effects on human lymphocytes, cytotoxicity in meibomian glands, risk of cancer, and allergic reactions and also produce environmental and animal toxicity [5,6]. Due to these results,

the traditional use of preservatives in cosmetics is leading us to search for new “eco-friendly” and efficient alternatives.

Essential oils (EO) are volatile compounds present in some aromatic plants and spices. Terpenes and isoprenoids are compounds derived from isoprenes and are the main component of several EOs that are widely used in medicine due to their varied biological and pharmacological activity, including high antimicrobial and antioxidant properties [7]. Thymoquinone (TQ) is the most abundant constituent of the volatile oil of *Nigella sativa* seeds, contributing to most of the properties of *N. sativa*. Different pharmacological properties of TQ have been previously described, e.g., immunomodulatory [8], anti-histaminic [9], anti-tumor [10], hepatoprotective [11], gastroprotective [12], nephroprotective [13], neuroprotective [14], antioxidant [15], and antimicrobial activity [16]. However, its high volatility and easy degradation can make its applications difficult.

The encapsulation of terpenes in different raw materials can improve the stability of compounds and increase their therapeutic efficacy. One of the most promising approaches is through the use of nanotechnology, with the encapsulation of terpenes in different formulations with a range of sizes between 1–1000 nm, thus improving their effect and stability [17].

Chitosan (CH), a linear polysaccharide consisting of 1, 4-linked glucosamine and *N*-acetylglucosamine, is a natural polymer derived through deacetylation of chitin in an alkaline media, with chitosan being the major component in shrimp and other crustaceans' cuticular exoskeletons [18]. CH is one of the most popular polysaccharides used as a raw material to encapsulate active compounds such as essential oils, terpenes, and several drugs due to its structure-forming, biocompatibility, and high stability [19,20]. Due to its versatile and easy manipulation, several formulations of chitosan have been formulated such as gel beads [21], polyelectrolyte complex-based hydrogels [22], microparticles [23], and nanoparticles, among others. The encapsulation of TQ into chitosan nanoparticles has been tested in different medical areas [14], where the TQ encapsulation is evaluated in radioiodinated folic acid-chitosan nanoparticles in order to target ovarian cancer, showing lower cytotoxicity in healthy cells [24]. Encapsulation of TQ in chitosan nanoparticles coated with polysorbate 80 showed an improvement in the antidepressant effect of terpene in Wistar rodents [25]. Moreover, in the cosmetic industry, CH is widely applied in CPs as an antioxidant, emulsifying agent, and skin protective agent in chitosan form or in different chitosan forms such as carboxymethyl chitosan [26].

Thus, the present study shows, for the first time, the assessment of TQ encapsulated in chitosan nanoparticles (NPCH-TQ) as a cosmetic preservative agent through the evaluation of antimicrobial activity in natural formulated moisturizing cream.

2. Results

2.1. Particle Size and Z Potential of NPCH and NPCH-TQ

Photon correlation spectroscopy or dynamic light scattering (DLS) is a technique based on the scattering of a laser beam of a given wavelength by particles or macromolecules in a liquid medium due to their Brownian motion, which is widely used to determine particle size and surface charge. The results presented in Table 1 show an average range of nanoparticle size from 48.6 to 65.0 nm, showing an increase in size from non-encapsulated nanoparticles due to the incorporation of terpenes into raw material. The results of the polydispersity index (PDI) show values below 0.5, achieving PDI values of 0.2 in the formulations of ratios 1:0.75 and 1:1. All nano-formulations present positive Z values from +23.9 up to +49.8 mV due to the use of chitosan as a raw material. The results presented in Table 1 show a decreasing trend in Z values related to the amount of TQ encapsulated in nanoparticles.

Table 1. DLS measures, encapsulation efficiency (EE%), and efficient loading (EL%) of nano-formulations.

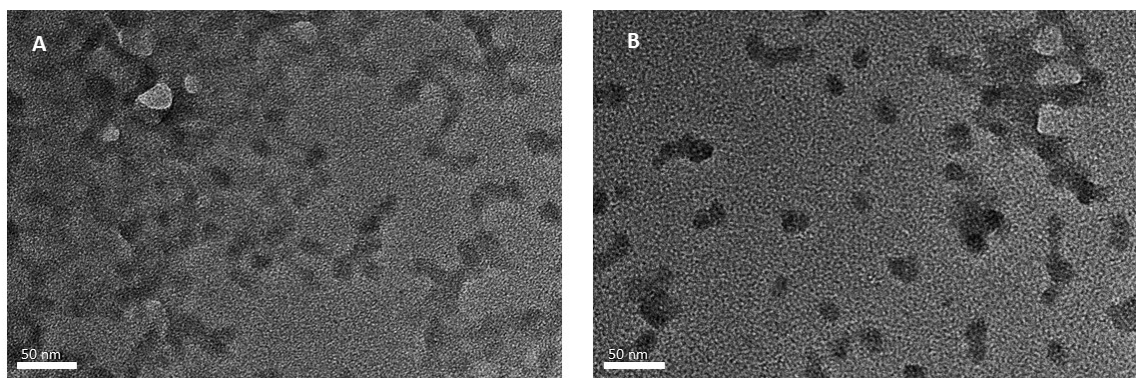
Formulation	Average Size (nm)	PDI	Z-Value (mV)	EE%	EL%
NPCH	48.6 ± 3.40	0.4 ± 0.02	+49.8 ± 0.75	-	-
NPCH-TQ 1:0.25	65.0 ± 1.40	0.4 ± 0.01	+35.8 ± 3.23	88.2 ± 6.39	44.8 ± 0.70
NPCH-TQ 1:0.5	57.5 ± 0.36	0.3 ± 0.01	+27.8 ± 1.13	93.2 ± 2.05	48.4 ± 1.14
NPCH-TQ 1:0.75	57.5 ± 0.33	0.2 ± 0.01	+25.3 ± 0.76	94.5 ± 1.94	48.8 ± 1.24
NPCH-TQ 1:1	63.4 ± 0.65	0.2 ± 0.01	+23.9 ± 0.58	90.6 ± 10.4	50.7 ± 8.70

2.2. Successful Encapsulation of Thymoquinone in Chitosan Nanoparticles

Encapsulation efficiency and efficient loading are parameters related to the capacity of encapsulation of drugs by different raw materials and the quality of formulation. These parameters mainly depend on the type of raw material, drug polarity, and approach used in nanoparticle preparation. The results presented in Table 1 show different EE% and EL% obtained by the different ratios used to obtain NPCH-TQ. The EE% values are between 88.2% and 94.5%, showing the maximum value in the 1:0.75 ratio. The maximum EL% value reached 50.7% in the 1:1 ratio corresponding to the formulation with the highest amount of initial thymoquinone used.

2.3. Morphology Characterization of Nanoparticles

Transmission Electron Microscope (TEM) is a common microscope technique to determine the surface properties and morphology characteristics of nanoparticles and nano-formulations [27]. Figure 1 shows two different micrographs which correspond to (A) NPCH and (B) NPCH-TQ 1:1. Both images show nanoparticles with non-defined surfaces, clearly trending toward forming aggregates or gel-like structures. All nanoparticles have a size smaller than 50 nm with approximately 20 nm with narrow size distribution.

**Figure 1.** TEM micrograph of (A) NPCH and (B) NPCH-TQ 1:1.

2.4. Chemical Structure of NPCH-TQ

The chemical composition of NPCH-TQ was determined by identification of the principal functional groups through the FTIR technique. The attenuated total reflectance (ATR) accessory allowed us to identify the main functional groups present directly from the nanoparticles or essential oils without the need to use matrices. FTIR is typically employed to investigate the interaction between functional groups. However, this technique allows us to verify the existence of functional groups whose vibrational modes are characteristic. FTIR spectra of TQ, NPCH, and NPCH-TQ are shown in Figure S1. In the TQ spectrum, the signals corresponding to the stretching vibrations of the most important functional groups are observed. The most intense signal in the spectrum is broadband at 1636 cm^{-1} , which corresponds to the overlap of two vibrations, the C=O double bond strain and the C=C double bond strain. The conjugate system between the C=O and C=C of the TQ makes these vibrations overlap in the spectrum. Moreover, intense bands corresponding to the sp^3 car-

bon C-H bonds (2969 cm^{-1}) and the C-O bond strain (1249 cm^{-1}) are observed. The NPCH and NPCH-TQ spectra are very similar since their content is mainly chitosan. A broadband between 3750 cm^{-1} and 2500 cm^{-1} , associated with the stretch of the O-H and N-H bonds, was clearly observed. As shown in the gravimetric analysis, chitosan nanoparticles were hygroscopic and had a great tendency to absorb water. This signal includes both chitosan O-H structure and water in its different strengths due to the hydrogen bonds formed. From the spectra, additional characteristic peaks of chitosan were observed at 2916 cm^{-1} and 2864 cm^{-1} due to C-H bond stretching of sp^3 carbon, 1634 cm^{-1} due to carbonyl stretching C=O of the amide, 1533 cm^{-1} due to N-H bending of the chitosan, and 1066 cm^{-1} due to the tension of the different C-O bonds. Because the most important TQ signals overlap with important bands in the NPCH, it is difficult to appreciate significant changes, although variations in signal intensities indicate the presence of TQ in the nanoparticles [28].

2.5. Thermal Properties of NPCH-TQ

Thermo Gravimetric Analysis/Differential Scanning Calorimetry (TGA/DSC) was used to evaluate the absorbed material, thermal stability, and decomposition temperatures of the TQ, NPCH, and NPCH-TQ. TQ is a volatile yellowish solid. Figure S1a shows the combination of TGA and DSC for TQ. In DSC, an endothermic peak is observed at $45\text{ }^\circ\text{C}$ (119 J/g) which correlates with the loss of virtually all mass in TGA. This indicates that the compound is volatile and sublimates at this temperature. Previously, we showed that chitosan nanoparticles have two degradation steps, the initial step starting from the very beginning of the experiment and ending at $100\text{ }^\circ\text{C}$, and the second one starting at $170\text{ }^\circ\text{C}$ up to $333\text{ }^\circ\text{C}$ (Figure S2). The first transition corresponds to a 3% mass drop and is attributed to the loss of adsorbed/bound water/moisture vaporization [28]. The degradation of the pure chitosan biopolymer resulted in a 60% weight loss in the second stage. This has been found previously for various chitosan polymers, where the amount of moisture and the range of breakdown temperatures are dependent on the chitosan polymer's molecular weight. A similar trend is observed in the NPCH-TQ thermogram (Figure S2b), coinciding in the temperature ranges. In the second transition, the mass loss was 58%, matching with the degree of NPCH decomposition [28]. In first transition, the mass loss is considerably higher, reaching 9.4% and, even though the water absorbed by both particles may differ, this may indicate that this 9.4% loss could correspond not only to water but also to TQ loss. These data were confirmed by comparing the endothermic peaks between $25\text{ }^\circ\text{C}$ and $100\text{ }^\circ\text{C}$. There is a considerable difference between the NPCH and NPCH-TQ evaporation enthalpies. For NPCH, an enthalpy of 145 J/g has been determined, while NPCH-TQ shows a higher value, reaching 274 J/g , which indicates that TQ-loaded nanoparticles need more energy to evaporate both water and TQ.

2.6. In Vitro Drug Release of NPCH-TQ

Drug release studies can offer information concerning nanoparticle behavior to release its encapsulated drugs. In this study, the pH of the buffer release medium was chosen according to the nanoparticle application. In this case, the pH of the CPs was close to 6. The results presented in Figure 2 show a triphasic release profile of TQ, achieving a maximum of 62% of TQ release at 28 days. Nanoparticles showed a slow initial release reaching 11% TQ in the first 24 h. Then, the release of TQ was governed by diffusion and degradation of the polymer matrix showing a slow-release profile due to the high hydrophobicity of TQ, resulting in the release mechanism being dependent on the nature of the raw material.

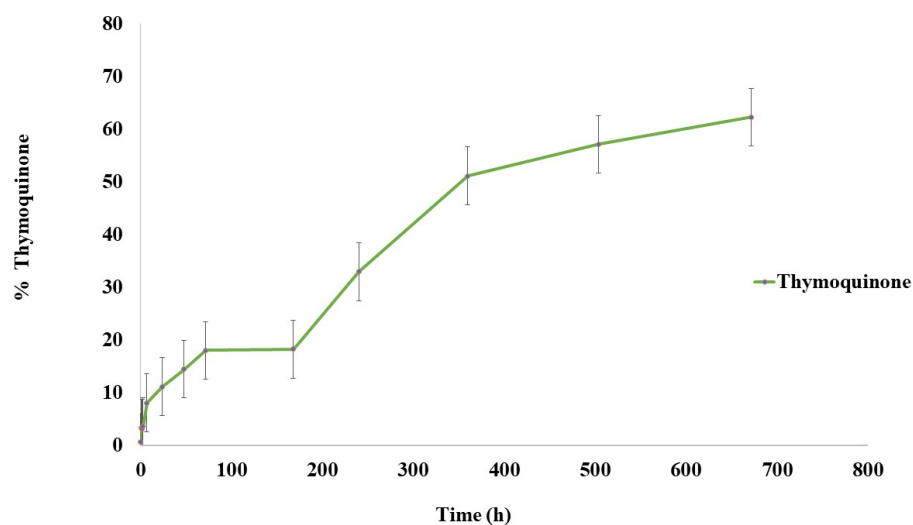


Figure 2. In vitro drug release of NPCH-TQ in PBS at pH 6.

2.7. DPPH Scavenging Activity of Free TQ and Nano-Formulations

To determine the antioxidant properties of nano-formulations, we used the DPPH scavenging method. DPPH was chosen for its simplicity since it is one of the few organic radicals with nitrogen atoms in its structure. This structure confers stability because of the delocalization of an unpaired electron on the molecule. This delocalization also causes an intensification in the purplish color characteristic of the radical, which in an ethanolic medium absorbs at 515 nm. This purplish coloration of the solution is attenuated in the presence of an antioxidant that can donate or transfer a hydrogen atom, giving a yellowish color due to the reduced form of DPPH-H [5]. Figure 3 presents the % of DPPH scavenging of free TQ, NPCH and NPCH-TQ on the range of concentrations between 0.125 and 1 of tested material. NPCH did not show antioxidant properties against DPPH in the concentration range tested. Free TQ shows a maximum of 83.6% of inhibition of DPPH at 1 mg/mL of TQ, higher than NPCH-TQ, which showed a maximum inhibition of 29.3% at 1 mg/mL of total material corresponding to 0.48 mg/mL of pure TQ.

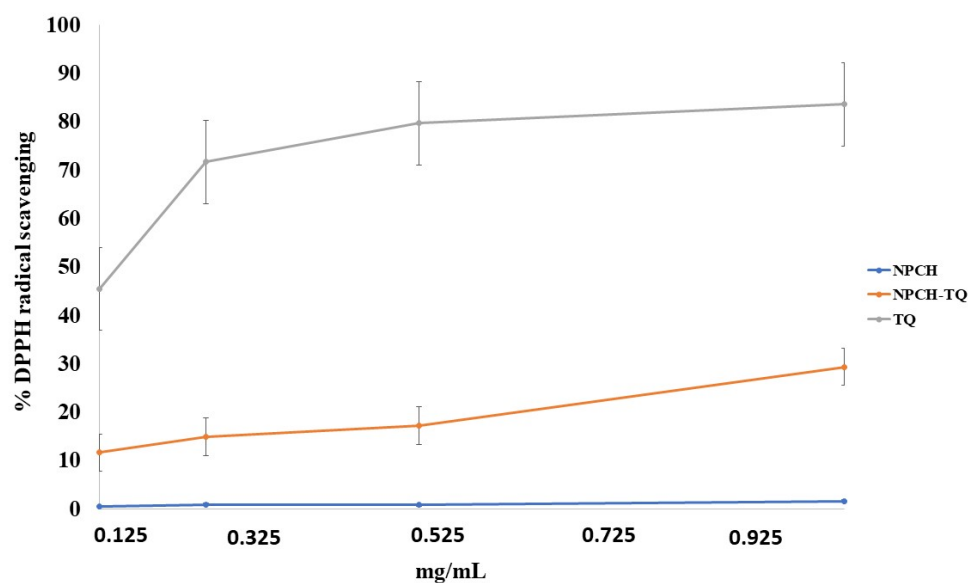


Figure 3. DPPH scavenging of free TQ, NPCH, and NPCH-TQ.

2.8. Antimicrobial Evaluation of Free Terpene and Its Nano-Formulation

The microorganisms used to check the activity in preservative agents in CPs are *P. aeruginosa*, *E. coli*, *S. aureus*, *A. brasiliensis*, and *C. albicans*. The broth microdilution method is a widely used technique to evaluate the antimicrobial properties of volatile compounds such as essential oil and terpenes [17,29]. The Minimum Inhibitory Concentrations (MICs) after 24 h of treatment for bacteria and 48 h for fungi are presented in Table 2. The minimum inhibitory concentrations ($\mu\text{g/mL}$) of different treatments are presented in Table 2. NPCH did not display an increase in the antimicrobial effect with respect to the control treatments against tested microorganisms, showing the same MICs in *E. coli* and *P. aeruginosa* (1000 $\mu\text{g/mL}$) and lower MICs against *S. aureus*, *C. albicans*, and *A. brasiliensis* (>1000 $\mu\text{g/mL}$). The encapsulation of TQ in chitosan nanoparticles resulted in improved antimicrobial activity reaching 292 $\mu\text{g/mL}$, 417 $\mu\text{g/mL}$, and 333 $\mu\text{g/mL}$ in *E. coli*, *P. aeruginosa*, and *S. aureus*, respectively. However, the NPCH-TQ showed lower MICs than free TQ against *C. albicans* and *A. brasiliensis*, obtaining 250 $\mu\text{g/mL}$ and 500 $\mu\text{g/mL}$, respectively.

Table 2. Minimum inhibitory concentrations ($\mu\text{g/mL}$) of control drugs (Gentamicin (*)) and Tebucanazole (**), TQ, NPCH, and NPCH-TQ.

Microorganism	Control MIC ($\mu\text{g/mL}$)	TQ ($\mu\text{g/mL}$)	NPCH ($\mu\text{g/mL}$)	NPCH-TQ ($\mu\text{g/mL}$)
<i>E. coli</i>	* 1000	1000	1000	292
<i>P. aeruginosa</i>	* 1000	>1000	1000	417
<i>S. aureus</i>	* 1000	>1000	>1000	333
<i>C. albicans</i>	** 250	333	>1000	250
<i>A. brasiliensis</i>	** 250	250	>1000	500

2.9. Evaluation of NPCH-TQ as a New Preservative Agent in Cosmetic Products

In order to evaluate the effect of NPCH-TQ as new preservative agent in cosmetic products, we formulated a natural moisturizing cream with the ingredients shown in Table 3. After formulation, control cream and NPCH-TQ cream were both inoculated with common contaminant microorganisms in CPs as recommended by UNI EN ISO 11930:2012, detailed in Section 4.8. At different intervals of days, 1 g of the creams was inoculated in different culture media, and the UFC/g was counted for each microorganism. The results of the antimicrobial activity of NPCH-TQ in the formulated cream are presented in Figure 4. The control cream did not display any preservative activity against all tested microorganisms, showing an increasing trend over the days in all bacteria and fungi reaching 10^8 UFC/gr for *P. aeruginosa* and *E. coli* and 10^7 for *S. aureus*. Preserved cream with NPCH-TQ displayed high antibacterial activity against *E. coli* and *S. aureus*, reducing the UFC/g to zero. Meanwhile, in *P. aeruginosa*, NPCH-TQ showed bacteriostatic properties during the time of the experiment, maintaining stable CFU/g. The antifungal effects of NPCH-TQ in formulated cream against *A. brasiliensis* and *C. albicans* are shown in Figure 4 revealed a total reduction in the number of UFC/g to zero.

Table 3. Cream composition. A (Aqueous phase), B (Oil phase), and C (thermolabile compounds).

Ingredient	Control Cream (%)	NPCH-TQ Cream (%)
Water (A)	47	46.5
Vegetable glycerin (A)	10	10
Urea (A)	3	3
Glyceryl monostearate (B)	8	8
Argania spinosa kernel oil (B)	28	28
Allantoin (C)	0.4	0.4
Avena sativa extract (C)	3	3
Vitamin E (C)	0.5	0.5
Parfum (C)	0.1	0.1
NPCH-TQ (C)	-	0.5

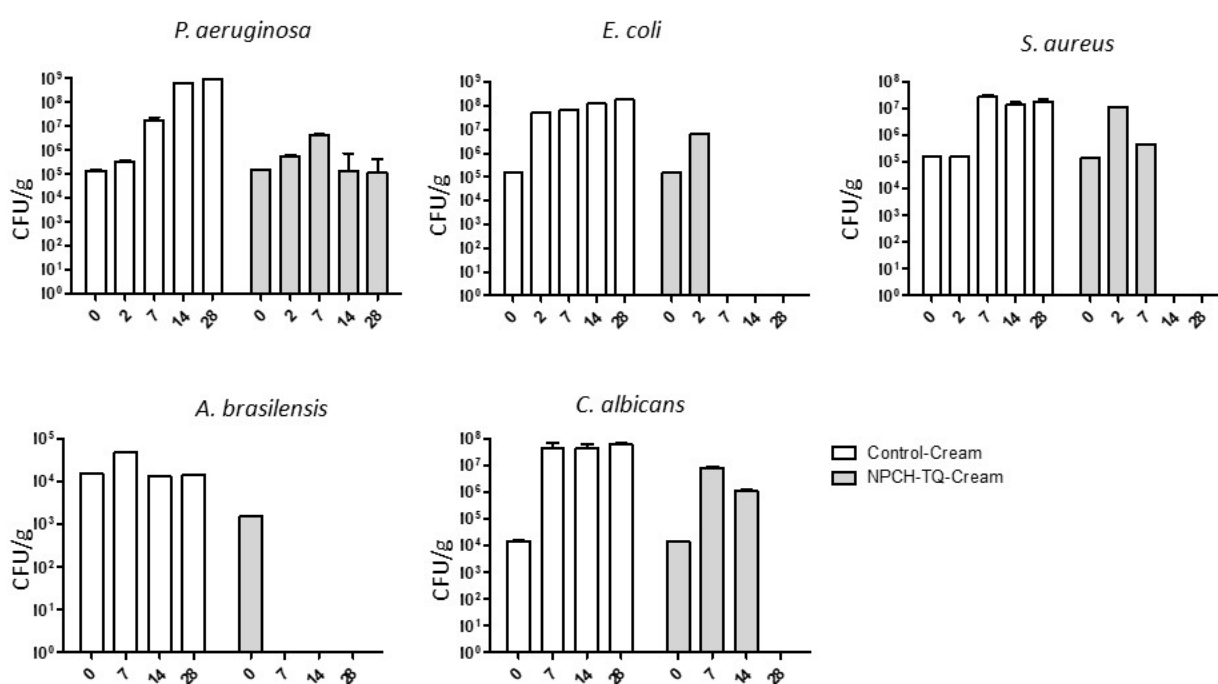


Figure 4. Preservative activity of control cream vs. NPCH-TQ.

3. Discussion

The main objective of this work is to develop a new alternative to conventional preservative agents based on green nanotechnology through the encapsulation of the natural terpene thymoquinone in chitosan nanoparticles. There is a lack of studies on TQ encapsulation in chitosan formulations; studies have focused mainly on the treatment of breast adenocarcinoma [30], ovarian cancer [24], nose-to-brain targeting [31], and depression treatments [25], among others.

In this study, we obtained four types of nano-formulations of NPCH-TQ through the utilization of different ratios of NPCH:TQ, where the particle size measured by the DLS technique did not show too many differences among obtained nano-formulations. The particle size ranged from 48.6 to 65.0 nm. However, the TEM micrograph presented in Figure 1 shows nanoparticles with a size close to 20 nm. Other works obtained the same trend with terpenes encapsulated in chitosan nanoparticles, obtaining different data regarding particle sizes in DLS and TEM. This was the case in the study performed by Woranuch et al., where chitosan-eugenol nanoparticles showed an average particle size of 683 nm by DLS and close to 100 nm by TEM due to the swelling and aggregation effect of chitosan in water solutions [32]. All NPCH-TQ revealed a positive surface charge with a decreasing trend related to the incorporation of TQ into the polymer matrix. The same

pattern is shown in the encapsulation of other volatile compounds such as garlic essential oil in chitosan nanoparticles with a Z potential range from +45.8 to +19.8 mV [28]. The positive surface charge of nanoparticles is associated with increased antimicrobial activity due to their ease of interaction with the wall of microorganisms [17]. Our nano-formulations showed a successful encapsulation of TQ in all tested ratios, with a maximum of 94.5% of EE% and 50.7% of EL for the ratio 1:1. Other works with chitosan-TQ nanoparticles coated with polysorbate 80 reported an EE% of 85.6% and 16.26% of EL% [25]. The encapsulation of TQ has also been explored in other polymeric raw materials such as PLGA, showing EE% values of 79.9% [33].

The release profile in long-term experiments gives us an idea of how the nanoparticles release the encapsulated compound with a suitable pH for CPs as well as the release profile during 28 days of storage. NPCH-TQ showed a triphasic release profile with a maximum release of 62% at 28 days. The insolubility of TQ in water results in a slow burst release and diffusion phase showing a slower release profile than other water-soluble drugs such as doxorubicin encapsulated in chitosan nanoparticles, which reached 100% of release at 170 h [34]. Another work in which TQ was encapsulated in pegylated poly-lactide co-glycolide nanoparticles (TF-PEG-PLGA-TQ NPs) for the treatment of non-small cell lung carcinoma achieved a maximum of 50% cumulative release of TQ in 24 h at pH 7.4, showing a faster release than NPCH-TQ due to the more hydrophilic nature of PEG-PLGA, facilitating the release of the hydrophobic compound from raw materials [35]. More hydrophilic terpenes, such as eugenol, showed a faster release than the TQ profile encapsulated in chitosan nanoparticles, with a maximum release of 73% at 36 h [36].

The study of antioxidant properties of NPCH-TQ is suitable to increase the usefulness of this nano-formulation in CPs. NPCH-TQ showed a maximum DPPH scavenging of 29.3% at 1 mg/mL of total material, lower than other essential oil encapsulated in chitosan nanoparticles such as clove essential oil, which showed a maximum value of 71% at the same concentration. However, this low value might be due to the fact that at DPPH scavenging measure time (30 min) and based on the release profile shown in Figure 2, the TQ released to the medium only reached 3.3% of total encapsulated TQ, and the antioxidant properties were due mainly to the presence of TQ and not to the chitosan as shown in Figure 3. Another nano-formulation with eugenol encapsulated in chitosan nanoparticles showed a maximum of 70% inhibition of DPPH at 4.0 mg/mL. Meanwhile, carvacrol encapsulated in the same nano-formulation achieved close to 40% of DPPH inhibition [37].

The encapsulation of TQ in chitosan nanoparticles resulted in an improvement of antibacterial activity in the bacteria tested. The antibacterial activity of NPCH-TQ was higher against *E. coli* than *S. aureus* and *P. aeruginosa* with 292 µg/mL, 333 µg/mL, and 417 µg/mL, respectively. NPCH-TQ displayed a higher antibacterial activity against *E. coli* and *S. aureus* than other nanoparticles made of carvacrol and eugenol-chitosan nanoparticles, which showed MICs values of 0.5–1 µg/mL for the same bacteria [37]. However, the encapsulation of TQ in chitosan nanoparticles was not associated with an increase in the antifungal activity of TQ. TQ nanoparticles obtained through the ball milling method obtained lower MICs with values of 160 µg/mL against *C. albicans* [38]. The same trend was observed in *A. brasiliensis* after NPCH-TQ with an MIC value of 500 µg/mL. Garlic essential oil encapsulated in chitosan-TPP nanoparticles via crosslinking showed different MIC values against two different *Aspergillus* species, *A. niger* and *A. versicolor*, with 0.37 µg/mL and 3.33 µg/mL, respectively [28].

To confirm the preservative effect of NPCH-TQ in naturally formulated cream, we evaluate the antimicrobial activity in contaminated cream with the microorganisms described above. After 28 days of storage, non-preserved cream (control cream) shows an increase in total UFC/gr in all tested microorganisms, reaching an increase of 3 logs in *E. coli*, *P. aeruginosa*, and *A. brasiliensis*. However, the synthesized NPCH-TQ displayed a total reduction in UFC/gr in *E. coli*, *S. aureus*, *C. albicans*, and *A. brasiliensis* and a maintenance of the total UFC/gr of *P. aeruginosa* related to the lower activity of NPCH-TQ against this microorganism. These results confirm the preservative activity of NPCH-TQ in formulated

creams. Other works with biogenic silver nanoparticles from *Iris tuberosa* aqueous extract confirm the role of nanotechnology to be used as a platform to obtain new preservative agents [5].

In conclusion, the results shown in this work present a new and effective preservative agent based on the encapsulation of a terpene in chitosan nanoparticles to satisfy the regulations and the growing demands of the consumers of natural, green, and sustainable products. This approach achieves a sustained and controlled release of TQ, allowing for a greater stabilization of the terpene and a higher antimicrobial activity over time and offering a long-lasting, effective, and preservative effect in natural cosmetics. However, additional experiments are necessary to support the use of our nanoparticles in humans before commercialization.

4. Materials and Methods

Low molecular weight chitosan (CH) (50–190 kDa) with a 75–85% degree of deacetylation, tripolyphosphate (TPP), 3-(4-dimethylthiazol-2-yl)-2,5-diphenyltetrazolium bromide (MTT), thymoquinone (TQ), and all the solvents were supplied by Sigma-Aldrich (Madrid, Spain). Microorganisms were purchased from the American Type Culture Collection (Manassas, VA, USA), namely *E. coli* (ATCC25922), *P. aureginosa* (ATCC27853), *S. aureus* (ATCC 6538), *C. albicans* (ATCC 10231), and *A. brasiliensis* (ATCC16404).

4.1. Preparation of Loaded and Unloaded Thymoquinone-Chitosan Nanoparticles (NPCH-TQ)

4.1.1. Formulation of NPCH

Chitosan nanoparticles (NPCH) were formulated through the ionic-gelation method described by [28]. Briefly, CH solution at 0.2% was prepared by dissolving CH flakes in acetic acid at 1% under continuous stirring overnight. Then, 50 mL of CH solution was mixed at 1000 RPM in a 1% Tween 80 solution and heated to 50 °C. Finally, TPP aqueous solution at 0.2% was added dropwise at 2 mL/min under continuous stirring to induce the ionic gelation to form the nanoparticles. Afterward, agitation was carried out at 700 RPM for 40 min. The nanoparticles were collected after centrifugation at 15,000 RPM for 20 min at 4 °C and subsequently washed several times with mQ water. The nanoparticle suspension was frozen at –80 °C and freeze-dried for 48 h at –50 °C (LyoQuest-85/208 V 60 Hz, Teslar).

4.1.2. Formulation of NPCH-TQ

Encapsulation of TQ into chitosan nanoparticles (NPCH-TQ) was formulated in a two-step process. Firstly, oil-in-water emulsification (o/w) was carried out, followed by the ionic gelation method as described above. Briefly, 50 mL of previously prepared CH solution was mixed at 1000 RPM in a 1% Tween 80 solution and heated at 50 °C. Subsequently, different amounts of terpene, previously preheated at 50 °C to form the liquid state to perform different ratios of CH:terpenes (1:0, 1:0.25, 1:0.5, 1:0.75, and 1:1 w/w), were added dropwise under continuous agitation and emulsified at 1500 RPM during 10 min at room temperature. Finally, TPP aqueous solution at 0.2% was added dropwise at 2 mL min^{–1} under continuous stirring to induce the ionic gelation. Afterward, agitation was carried out at 700 RPM for 40 min. The nanoparticles were collected after centrifugation at 15,000 RPM for 20 min at 4 °C and subsequently washed several times with mQ water to eliminate unencapsulated terpenes. The nanoparticle suspension was frozen at –80 °C and freeze-dried for 48 h at –50 °C (LyoQuest-85/208 V 60 Hz, Teslar).

4.2. Determination of Encapsulation Efficiency and Loading Efficiency of Thymoquinone-Chitosan Nanoparticles (NPCH-TQ)

Determination of Encapsulated TQ in Nanoparticles

To determine the total amount of TQ encapsulated into chitosan nanoparticles, 2 mL acetonitrile was added to 5 mg of TQ-NPCH, and suspension was sonicated for 1 h at room temperature and left overnight with the solvent. Then, the supernatant was filtered

through 0.45 μm Millipore filter to measure in HPLC. The mobile phase employed was acetonitrile:water 70:30 and the amount of TQ was measured at 254 nm [39].

Loading capacity (LC) and encapsulation efficiency (EE) of terpenes were calculated according to the following equations (Equation (1), Equation (2)):

$$\text{LC\%} = (\text{weight of encapsulated terpene (mg)}) \div (\text{weight of total (terpene encapsulated + scaffold weight) (mg)}) \times 100 \quad (1)$$

$$\text{EE\%} = (\text{weight of encapsulated terpene (mg)}) \div (\text{weight of terpene feeding (mg)}) \times 100 \quad (2)$$

4.3. Instrumental Characterization of Nanoparticles

4.3.1. Particle Size Analysis

Characterization of nano-formulations (size, zeta potential, and polydispersity index (PDI)) was determined by dynamic light scattering (DLS) using a Zetasizer (3000 HSM Malvern Ltd., Madrid, Spain) with the following specifications: chitosan refractive index (IR) of 1.700, absorption index 0.010, and water solvent RI: 1.33, with a viscosity of 0.8872 cP. Measurements were performed in triplicate.

4.3.2. Chemical Analysis of Nanoparticles

R spectra were recorded on an attenuated total reflectance-Fourier transform infrared (ATR-FTIR) spectrophotometer (VARIAN 640-IR with a Pike Diamond/KRS-5 HS Performance Crystal Plate), and the main peaks were given in cm^{-1} . ATR allows us to use the samples directly in a solid or liquid state without the need of KBr or Lugol's iodine matrix. Specifically, for NPCH and NPCH-TQ, 20 mg of nanoparticles was powdered in a mortar, and the thin solid was placed on the diamond plate and pressed until a homogeneous pellet was obtained. For TQ, being liquid, a drop of approximately 200 μL was placed on the plate, and the tip was placed in such a way that the surface tension of the drop covered the diamond plate homogeneously. 256 scans were acquired at an instrument resolution of 1 cm^{-1} over the spectral range between 650 and 4000 cm^{-1} owing to the frequency cutoff of the ATR-FTIR internal reflection element (IRE) used.

4.3.3. Thermal Properties of Nanoparticles

The thermal decomposition mechanisms were determined on a thermogravimetric analyzer (TGA Q20, TA Instruments) fitted with a standard platinum pan. The differential scanning calorimetry (DSC) experiments were carried out using a DSC Q50 system (TA Instruments) equipped with a standard aluminum pan with 10 $^{\circ}\text{C}/\text{min}$ increasing heat rate (30–320 $^{\circ}\text{C}$) to investigate the thermal stability of pure TQ, NPCH, and NPCH-TQ. A sample of indium was used as reference. In all cases, samples of about 3 mg were heated at a 10 $^{\circ}\text{C min}^{-1}$ rate under nitrogen atmosphere.

4.3.4. Morphology Studies of Nanoparticles

High-resolution electron microscope images of NPCH-TQ were obtained on a Jeol JEM 210 TEM microscope operating at 200 kV and equipped with an Oxford Link EDS detector. The resulting images were analyzed using Digital MicrographTM software from Gatan.

4.4. In Vitro Release Studies of NPCH-TQ

One milligram of lyophilized nanoparticles was sealed in a dialysis membrane (molecular weight cut off 3500 Da) and suspended in 10 mL of phosphate-buffered saline at optimum pH in CPs (pH 6) in continuous stirring at 200 rpm to ensure homogeneity. At certain intervals of incubation time at 37 $^{\circ}\text{C}$, 3 mL of release medium was removed to evaluate the amount of released terpene and replaced with 3 mL of fresh medium. The concentration of released TQ was determined with a spectrophotometer at wavelengths of 258 nm. Terpene release was performed in triplicate.

4.5. 2,2-Diphenyl-1-Picrylhydrazyl (DPPH) Radical Scavenging Activity

FRS, free radical scavenging activity, was determined as described previously [5]. Briefly, 0.5 mL for each concentration (1 mg/mL, 500 µg/mL, 250 µg/mL, and 125 µg/mL) of synthesized NPCH-CAR, NPCH-EUG, and free terpenes was mixed with 0.1 mM ethanolic DPPH radical solution (1.5 mL) and then mixed and kept in the dark at room temperature for 30 min. The absorbance of the solution was measured at 517 nm. The FRS was calculated by $\% = (A_0 - A_1/A_0) \times 100$, where A_0 is absorbance at Time = 0 and A_1 is the absorbance after 30 min.

4.6. Antimicrobial Assay

Different ratios of CH:TQ (1:0.25, 1:0.5, 1:0.75, and 1:1) were evaluated in order to perform the optimal formulation. For antimicrobial analysis, the NPCH:TQ ratio 1:1 was chosen to perform the assay because this ratio has better loading efficiency values than the other ratios (50.7%) plus similar sizes and PDIs.

The antimicrobial activity and minimum inhibitory concentration (MIC) of terpenes and nanoparticles were tested against the most common pathogenic microorganisms in cosmetics and those that the UNI EN ISO 11930:2012 recommend for preservative efficacy evaluation. Antimicrobial activity of nanoparticles against *P. aeruginosa*, *E. coli*, *S. aureus*, *A. brasiliensis*, and *C. albicans* was tested using the broth microdilution method [17,40]. Stock cultures were prepared from Culti-Loops™ (Sigma-Aldrich, Madrid, Spain) in Nutrient Broth (NB) and Potato Dextrose Broth (PDB) at 37 °C. Standardized inoculum was then created by dilution in Müller–Hinton medium to a final density of 0.5 McFarland units by densitometer McFarland type DEN-1B (Biosan, Riga, Latvia). TQ, NPCH-TQ, and NPCH were tested in concentrations of 1000 µg/mL to 15.6 µg/mL. Gentamicin (for bacteria) and Tebuconazole (for mold and yeast) were used as standards. After treatment, plates were incubated 24 h at 37 °C for bacteria and 48 h at 30 °C for yeast and fungi.

4.7. Moisturizing Cream Formulation

Two types of moisturizing creams were formulated: control cream without any preservative agent and NPCH-TQ with the addition of nanoparticles on formulated cream. The composition of both creams is shown in Table 3 Oil phase (B) and water phase (A) were preheated at 70 °C to achieve the fusion of oils and waxes present in this phase. Then, B was added slowly under agitation in a homogenizer at 3000 RPM to form an oil/water emulsion. Upon cooling, the thermolabile compounds (C) and preservatives (NPCH-TQ) at a dose of 500 µg/mL (maximum of MIC value) were added to the cooled cream under continuous agitation.

4.8. Preservative Activity of AgNPs in Formulated Cream

The preservative efficacy of NPCH-TQ in the moisturizing creams was carried out comparing the antimicrobial activity of NPCH-TQ cream against non-preserved cream. Briefly, twenty grams of each cream (Control and NPCH-TQ) was diluted with a sterile NaCl solution at 0.9%. Then, each cream was inoculated with 10^5 UFC/mL for bacteria, 10^4 CFU/mL for yeast, and 10^3 CFU/mL for mold. Contaminated creams were stored at room temperature for 30 days. After 2, 7, 14, and 28 days, one gram of each contaminated cream was diluted and spread in Petri dishes to count CFUs of bacteria. Yeast and mold contaminations were evaluated at 7, 14, and 28 days using the same methodology.

Supplementary Materials: The following supporting information can be downloaded at: <https://www.mdpi.com/article/10.3390/ijms23020898/s1>.

Author Contributions: Conceptualization, E.N. and O.A.; methodology, M.M.-L. and J.C.G.M.; software, A.J.L.-J.; validation, E.N., O.A., and L.G.-G.; formal analysis and investigation, E.N.; writing—original draft preparation, E.N.; writing—review and editing, O.A.; supervision, E.N., O.A., and L.G.-G.; project administration, O.A.; funding acquisition, L.G.-G. All authors have read and agreed to the published version of the manuscript.

Funding: This research was funded by the University of Castilla-La Mancha (UCLM, Spain), grant number 2020-GRIN-28857.

Institutional Review Board Statement: Not applicable.

Informed Consent Statement: Not applicable.

Data Availability Statement: Not applicable.

Acknowledgments: Our thanks to Javier Argandoña for his technical assistance and to K.A. Walsh for language revision.

Conflicts of Interest: The authors declare no conflict of interest.

Sample Availability: Samples of the compounds are not available from the authors.

References

1. Michalek, I.; John, S.; Dos Santos, F.C. Microbiological contamination of cosmetic products—Observations from Europe, 2005–2018. *J. Eur. Acad. Dermatol. Venerol.* **2019**, *33*, 2151–2157. [CrossRef]
2. Halla, N.; Fernandes, I.P.; Heleno, S.A.; Costa, P.; Boucherit-Otmani, Z.; Boucherit, K.; Rodrigues, A.E.; Ferreira, I.C.F.R.; Barreiro, M.F. Cosmetics Preservation: A Review on Present Strategies. *Molecules* **2018**, *23*, 1571. [CrossRef]
3. Palacios, S.; Shaman, F.; Garcá, J.A. Prevalence of cosmetic sensitivity among beauticians. *Allergol. Immunopathol.* **1995**, *23*, 148–152.
4. Nowak, K.; Jabłońska, E.; Ratajczak-Wrona, W. Controversy around parabens: Alternative strategies for preservative use in cosmetics and personal care products. *Environ. Res.* **2021**, *198*, 110488. [CrossRef] [PubMed]
5. Mondéjar-López, M.; López-Jiménez, A.; Abad-Jordá, M.; Rubio-Moraga, A.; Ahrazem, O.; Gómez-Gómez, L.; Niza, E. Biogenic Silver Nanoparticles from *Iris tuberosa* as Potential Preservative in Cosmetic Products. *Molecules* **2021**, *26*, 4696. [CrossRef] [PubMed]
6. Wang, J.; Liu, Y.; Kam, W.R.; Li, Y.; Sullivan, D.A. Toxicity of the cosmetic preservatives parabens, phenoxyethanol and chlorphenesin on human meibomian gland epithelial cells. *Exp. Eye Res.* **2020**, *196*, 108057. [CrossRef]
7. De Matos, S.P.; Teixeira, H.F.; De Lima, Á.A.; Veiga-Junior, V.F.; Koester, L.S. Essential Oils and Isolated Terpenes in Nanosystems Designed for Topical Administration: A Review. *Biomolecules* **2019**, *9*, 138. [CrossRef]
8. Aslam, H.; Shahzad, M.; Shabbir, A.; Irshad, S. Immunomodulatory effect of thymoquinone on atopic dermatitis. *Mol. Immunol.* **2018**, *101*, 276–283. [CrossRef]
9. Darakhshan, S.; Pour, A.B.; Colagar, A.H.; Sisakhtnezhad, S. Thymoquinone and its therapeutic potentials. *Pharmacol. Res.* **2015**, *95–96*, 138–158. [CrossRef]
10. Mahmoud, Y.K.; Abdelrazek, H.M. Cancer: Thymoquinone antioxidant/pro-oxidant effect as potential anticancer remedy. *Biomed. Pharmacother.* **2019**, *115*, 108783. [CrossRef]
11. Kalam, M.A.; Raish, M.; Ahmed, A.; Alkharfy, K.M.; Mohsin, K.; Alshamsan, A.; Al-Jenoobi, F.I.; Al-Mohizea, A.M.; Shakeel, F. Oral bioavailability enhancement and hepatoprotective effects of thymoquinone by self-nanoemulsifying drug delivery system. *Mater. Sci. Eng. C Mater. Biol. Appl.* **2017**, *76*, 319–329. [CrossRef] [PubMed]
12. Magdy, M.-A.; Hanan, E.-A.; Nabila, E.-M. Thymoquinone: Novel gastroprotective mechanisms. *Eur. J. Pharmacol.* **2012**, *697*, 126–131. [CrossRef] [PubMed]
13. Shaterzadeh-Yazdi, H.; Noorbakhsh, M.-F.; Samarghandian, S.; Farkhondeh, T. An Overview on Renoprotective Effects of Thymoquinone. *Kidney Dis.* **2018**, *4*, 74–82. [CrossRef]
14. Tabeshpour, J.; Mehri, S.; Abnous, K.; Hosseinzadeh, H. Neuroprotective Effects of Thymoquinone in Acrylamide-Induced Peripheral Nervous System Toxicity Through MAPKinase and Apoptosis Pathways in Rat. *Neurochem. Res.* **2019**, *44*, 1101–1112. [CrossRef]
15. Abdel-Daim, M.M.; El-Ela, F.I.A.; Alshahrani, F.K.; Bin-Jumah, M.; Al-Zharani, M.; Almutairi, B.; Alyousif, M.S.; Bungau, S.; Aleya, L.; Alkahtani, S. Protective effects of thymoquinone against acrylamide-induced liver, kidney and brain oxidative damage in rats. *Environ. Sci. Pollut. Res.* **2020**, *27*, 37709–37717. [CrossRef]
16. Fan, Q.; Yuan, Y.; Jia, H.; Zeng, X.; Wang, Z.; Hu, Z.; Gao, Z.; Yue, T. Antimicrobial and anti-biofilm activity of thymoquinone against *Shigella flexneri*. *Appl. Microbiol. Biotechnol.* **2021**, *105*, 4709–4718. [CrossRef]
17. Niza, E.; Božik, M.; Bravo, I.; Clemente-Casares, P.; Sánchez, A.L.; Juan, A.; Klouček, P.; Alonso-Moreno, C. PEI-coated PLA nanoparticles to enhance the antimicrobial activity of carvacrol. *Food Chem.* **2020**, *328*, 127131. [CrossRef]
18. Kamkar, A.; Molaee-Aghaee, E.; Khanjari, A.; Akhondzadeh-Basti, A.; Noudoost, B.; Shariatifar, N.; Sani, M.A.; Soleimani, M. Nanocomposite active packaging based on chitosan biopolymer loaded with nano-liposomal essential oil: Its characterizations and effects on microbial, and chemical properties of refrigerated chicken breast fillet. *Int. J. Food Microbiol.* **2021**, *342*, 109071. [CrossRef] [PubMed]
19. Sani, M.A.; Tavassoli, M.; Hamishehkar, H.; McClements, D.J. Carbohydrate-based films containing pH-sensitive red barberry anthocyanins: Application as biodegradable smart food packaging materials. *Carbohydr. Polym.* **2021**, *255*, 117488. [CrossRef]

20. Tavassoli, M.; Sani, M.A.; Khezerlou, A.; Ehsani, A.; McClements, D.J. Multifunctional nanocomposite active packaging materials: Immobilization of quercetin, lactoferrin, and chitosan nanofiber particles in gelatin films. *Food Hydrocoll.* **2021**, *118*, 106747. [CrossRef]
21. Lisuzzo, L.; Cavallaro, G.; Parisi, F.; Milioto, S.; Fakhruddin, R.; Lazzara, G. Core/Shell Gel Beads with Embedded Halloysite Nanotubes for Controlled Drug Release. *Coatings* **2019**, *9*, 70. [CrossRef]
22. Potaś, J.; Szymańska, E.; Basa, A.; Hafner, A.; Winnicka, K. Tragacanth Gum/Chitosan Polyelectrolyte Complexes-Based Hydrogels Enriched with Xanthan Gum as Promising Materials for Buccal Application. *Materials* **2020**, *14*, 86. [CrossRef] [PubMed]
23. Szymańska, E.; Woś-Latosi, K.; Jacyna, J.; Dąbrowska, M.; Potaś, J.; Markuszewski, M.J.; Winnicka, K. The Correlation between Physical Crosslinking and Water-Soluble Drug Release from Chitosan-Based Microparticles. *Pharmaceutics* **2020**, *12*, 455. [CrossRef] [PubMed]
24. Ince, I.; Yıldırım, Y.; Güler, G.; Medine, E.I.; Ballica, G.; Kusdemir, B.C.; Göker, E. Synthesis and characterization of folic acid-chitosan nanoparticles loaded with thymoquinone to target ovarian cancer cells. *J. Radioanal. Nucl. Chem.* **2020**, *324*, 71–85. [CrossRef]
25. Fahmy, H.M.; Khadrawy, Y.A.; Daim, T.M.A.-E.; Elfeky, A.S.; Rabo, A.A.A.; Mustafa, A.B.; Mostafa, I.T. Thymoquinone-encapsulated chitosan nanoparticles coated with polysorbate 80 as a novel treatment agent in a reserpine-induced depression animal model. *Physiol. Behav.* **2020**, *222*, 112934. [CrossRef]
26. Aranaz, I.; Acosta, N.; Civera, C.; Elorza, B.; Mingo, J.; Castro, C.; Gandía, M.D.L.L.; Caballero, A.H. Cosmetics and Cosmeceutical Applications of Chitin, Chitosan and Their Derivatives. *Polymers* **2018**, *10*, 213. [CrossRef]
27. Estupiñán, Ó.; Niza, E.; Bravo, I.; Rey, V.; Tornín, J.; Gallego, B.; Clemente-Casares, P.; Moris, F.; Ocaña, A.; Blanco-Lorenzo, V.; et al. Mithramycin delivery systems to develop effective therapies in sarcomas. *J. Nanobiotechnol.* **2021**, *19*, 267. [CrossRef]
28. Mondéjar-López, M.; Rubio-Moraga, A.; López-Jimenez, A.J.; Martínez, J.C.G.; Ahrazem, O.; Gómez-Gómez, L.; Niza, E. Chitosan nanoparticles loaded with garlic essential oil: A new alternative to tebuconazole as seed dressing agent. *Carbohydr. Polym.* **2021**, *277*, 118815. [CrossRef]
29. Tullio, V.; Nostro, A.; Mandras, N.; Dugo, P.; Banche, G.; Cannatelli, M.; Cuffini, A.M.; Alonzo, V.; Carlone, N. Antifungal activity of essential oils against filamentous fungi determined by broth microdilution and vapour contact methods. *J. Appl. Microbiol.* **2007**, *102*, 1544–1550. [CrossRef]
30. Dehghani, H.; Hashemi, M.; Entezari, M.; Mohsenifar, A. The Comparison of Anticancer Activity of Thymoquinone and Nanothymoquinone on Human Breast Adenocarcinoma. *Iran. J. Pharm. Res* **2015**, *14*, 539–546. [PubMed]
31. Alam, S.; Mustafa, G.; Khan, Z.I.; Islam, F.; Bhatnagar, A.; Ahmad, F.J.; Kumar, M. Development and evaluation of thymoquinone-encapsulated chitosan nanoparticles for nose-to-brain targeting: A pharmacoscintigraphic study. *Int. J. Nanomed.* **2012**, *7*, 5705–5718. [CrossRef] [PubMed]
32. Woranuch, S.; Yoksan, R. Eugenol-loaded chitosan nanoparticles: I. Thermal stability improvement of eugenol through encapsulation. *Carbohydr. Polym.* **2013**, *96*, 578–585. [CrossRef]
33. Ahmad, R.; Kaus, N.H.M.; Hamid, S. Synthesis and Characterization of PLGA-PEG Thymoquinone Nanoparticles and Its Cytotoxicity Effects in Tamoxifen-Resistant Breast Cancer Cells. In *Cancer Biology and Advances in Treatment. Advances in Experimental Medicine and Biology*; Pham, P.V., Ed.; Springer: Cham, Switzerland, 2018; Volume 1292.
34. Bhatta, A.; Krishnamoorthy, G.; Marimuthu, N.; Dihingia, A.; Manna, P.; Biswal, H.T.; Das, M.; Krishnamoorthy, G. Chlorin e6 decorated doxorubicin encapsulated chitosan nanoparticles for photo-controlled cancer drug delivery. *Int. J. Biol. Macromol.* **2019**, *136*, 951–961. [CrossRef] [PubMed]
35. Upadhyay, P.; Sarker, S.; Ghosh, A.; Gupta, P.; Das, S.; Ahir, M.; Bhattacharya, S.; Chattopadhyay, S.; Ghosh, S.; Adhikary, A. Transferrin-decorated thymoquinone-loaded PEG-PLGA nanoparticles exhibit anticarcinogenic effect in non-small cell lung carcinoma via the modulation of miR-34a and miR-16. *Biomater. Sci.* **2019**, *7*, 4325–4344. [CrossRef] [PubMed]
36. Anand, T.; Anbukkarasi, M.; Thomas, P.A.; Geraldine, P. A comparison between plain eugenol and eugenol-loaded chitosan nanoparticles for prevention of in vitro selenite-induced cataractogenesis. *J. Drug Deliv. Sci. Technol.* **2021**, *65*, 102696. [CrossRef]
37. Chen, F.; Shi, Z.; Neoh, K.; Kang, E. Antioxidant and antibacterial activities of eugenol and carvacrol-grafted chitosan nanoparticles. *Biotechnol. Bioeng.* **2009**, *104*, 30–39. [CrossRef]
38. Randhawa, M.A.; Gondal, M.A.; Al-Zahrani, A.-H.J.; Rashid, S.G.; Ali, A. Synthesis, morphology and antifungal activity of nanoparticulated amphotericin-B, ketoconazole and thymoquinone against *Candida albicans* yeasts and *Candida* biofilm. *J. Environ. Sci. Health Part A* **2015**, *50*, 119–124. [CrossRef]
39. Xiao, X.-Y.; Zhu, Y.-X.; Bu, J.-Y.; Li, G.-W.; Zhou, J.-H.; Zhou, S.-P. Evaluation of Neuroprotective Effect of Thymoquinone Nanof ormulation in the Rodent Cerebral Ischemia-Reperfusion Model. *BioMed Res. Int.* **2016**, *2016*, 2571060. [CrossRef]
40. Qidwai, A.; Kumar, R.; Dikshit, A. Green synthesis of silver nanoparticles by seed of *Phoenix sylvestris* L. and their role in the management of cosmetics embarrassment. *Green Chem. Lett. Rev.* **2018**, *11*, 176–188. [CrossRef]

MDPI
St. Alban-Anlage 66
4052 Basel
Switzerland
www.mdpi.com

International Journal of Molecular Sciences Editorial Office

E-mail: ijms@mdpi.com
www.mdpi.com/journal/ijms



Disclaimer/Publisher's Note: The statements, opinions and data contained in all publications are solely those of the individual author(s) and contributor(s) and not of MDPI and/or the editor(s). MDPI and/or the editor(s) disclaim responsibility for any injury to people or property resulting from any ideas, methods, instructions or products referred to in the content.



Academic Open
Access Publishing

mdpi.com

ISBN 978-3-0365-9102-5